

Weibo Cai *Editor*

Engineering in Translational Medicine

Volume 1

 Springer

Engineering in Translational Medicine

Weibo Cai
Editor

Engineering in Translational Medicine

 Springer

Editor
Weibo Cai
Department of Radiology, Medical Physics,
and Biomedical Engineering
University of Wisconsin
Madison
USA

ISBN 978-1-4471-4371-0 ISBN 978-1-4471-4372-7 (eBook)
DOI 10.1007/978-1-4471-4372-7
Springer London Heidelberg New York Dordrecht

Library of Congress Control Number: 2013955301

© Springer-Verlag London 2014

This work is subject to copyright. All rights are reserved by the Publisher, whether the whole or part of the material is concerned, specifically the rights of translation, reprinting, reuse of illustrations, recitation, broadcasting, reproduction on microfilms or in any other physical way, and transmission or information storage and retrieval, electronic adaptation, computer software, or by similar or dissimilar methodology now known or hereafter developed. Exempted from this legal reservation are brief excerpts in connection with reviews or scholarly analysis or material supplied specifically for the purpose of being entered and executed on a computer system, for exclusive use by the purchaser of the work. Duplication of this publication or parts thereof is permitted only under the provisions of the Copyright Law of the Publisher's location, in its current version, and permission for use must always be obtained from Springer. Permissions for use may be obtained through RightsLink at the Copyright Clearance Center. Violations are liable to prosecution under the respective Copyright Law. The use of general descriptive names, registered names, trademarks, service marks, etc. in this publication does not imply, even in the absence of a specific statement, that such names are exempt from the relevant protective laws and regulations and therefore free for general use.

While the advice and information in this book are believed to be true and accurate at the date of publication, neither the authors nor the editors nor the publisher can accept any legal responsibility for any errors or omissions that may be made. The publisher makes no warranty, express or implied, with respect to the material contained herein.

Printed on acid-free paper

Springer is part of Springer Science+Business Media (www.springer.com)

Preface

This book provides a detailed discussion of the synergy between biology and engineering and the promise this convergence holds for advancing our understanding and practice of medicine. It is this complementary relationship between new discoveries in biology and the precise, quantitative, and predictable nature of engineering that underlies the significant advances described in each of chapters. When I was a young researcher, this type of multidisciplinary research was unprecedented. During the past decade I have been gratified to see it emerge and be validated as a powerful approach for addressing challenges in translational medicine.

The goal of this book is to highlight how invaluable engineering has become by describing an extensive range of fields. This book is organized into five parts, covering engineering of biological systems in the first two sections, followed by nanotechnology approaches and advances in instrumentation and concluding with the emerging field of theranostics. Although not written in the form of a college textbook, this book is well-suited for graduate students and researchers alike as the chapters contain both didactic materials and research findings.

It is impossible to describe all the areas where engineering has had an impact on medicine. The biology of living systems is extremely complex involving interactions over many spatial and temporal scales. For example, assessment of the structural and mechanical relationship of dynamic cell–cell interactions has been informed by quantitative metrics and engineering principles. Such interactions are vital to cellular processes and underpin the mechanism of disease such as cancer as evidenced by cell proliferation, cell adhesion, and extravasation of tumor cells in metastasis. These and other biological processes are discussed in this book from the perspective of engineering and the synergic impact with biology toward advances in medicine. The aim of each chapter is not to provide a complete survey, but to provide a commentary on the advances currently being made, to give the reader a sense of the opportunities and challenges in each field while providing extensive references to permit the interested reader to learn more about a particular subject or advance.

There are common challenges running through the book related to sensitivity, specificity, and efficacy that underlie the need for systematic and quantitative solutions. There are also disease-specific challenges that are highlighted, involving diagnosis, monitoring, and treatment. The targeted delivery of therapy has

emerged as one crucial area for engineering to have an impact. This book devotes several chapters on the various delivery systems and includes discussions of the increasing adoption of targeted versus systemic approaches. Topics include delivery system designs, cell entry, drug clearance, biodistribution, cellular absorption, etc.

As well as treating disease, engineering also holds the promise of renewing function. Regenerative medicine and tissue engineering are discussed through the book, highlighting another broad area where engineering approaches are leading to significant advances. For example, stem cell therapies are discussed based on research with quantitative metrics of the stem cell niche, innovatively engineered scaffolds, and the biology of pluripotent cells. The convergence of these disciplines has resulted in advances in the regeneration of nerves, blood vessels, and tissue repair.

This book is the culmination of a community of dedicated scientists whose contributions to this book are invaluable. Weibo Cai has worked tirelessly over the past year to coordinate, edit, and provide a framework for each of the chapters. I am indebted to him for his efforts in promoting engineering as an indispensable component of translational medicine.

NIBIB, USA

Belinda Seto

Acknowledgments

I would like to thank Anthony Doyle from Springer for the kind invitation to edit this book, which has been the experience of a lifetime and I am extremely satisfied with how this book has turned out. I would also like to thank Christine Velarde for her tremendous effort in helping me assemble this book, who has thoroughly answered all my seemingly endless questions regarding minute details. I hope we get to work again in the future on other exciting journeys like this.

I truly appreciate the excellent contribution of the more than 80 scientists to this book, who have devoted enormous amount of time to writing the 35 chapters. I am truly touched by their professionalism and wholehearted support to this book, who are all international leading experts in the topic of each chapter. Special thanks are due to Belinda Seto, Deputy Director of the National Institute of Biomedical Imaging and Bioengineering (NIBIB) in the United States, who has kindly agreed to write both the Preface and [Chap. 18](#).

I am deeply grateful for the tremendous support from my wife, Yunlin Sun, and two beautiful daughters, Emily and Michelle. Organizing and editing this book was primarily done outside my normal business hours, which had an enormous impact on the family time and I hope I can make up for it in the future. This book is dedicated to them.

Weibo Cai

Contents

1	Engineering in Translational Medicine: An Introduction	1
	Weibo Cai	

Part I Cell and Tissue Engineering

2	Stem Cells: The Holy Grail of Regenerative Medicine	19
	Ram K. Singh, Snehal M. Gaikwad, Subhoshree Chatterjee and Pritha Ray	

3	Engineering T Cells to Target Tumor Cells	71
	Hiroki Torikai, Judy S. Moyes and Laurence J. N. Cooper	

4	Engineering Biomaterials for Anchorage-Dependent and Non-anchorage-Dependent Therapeutic Cell Delivery in Translational Medicine	103
	Wenyan Leong and Dong-An Wang	

5	Tissue Engineering Applications for Peripheral Nerve Repair . . .	133
	Hakan Orbay and Weibo Cai	

6	Structure, Function, and Development of Blood Vessels: Lessons for Tissue Engineering	155
	Hamisha Ardalani, Amir H. Assadi and William L. Murphy	

7	Engineering Gene-Activated Matrices for the Repair of Articular Cartilage Defect	183
	Junfeng Zhang and Zhen Huang	

Part II Genetic and Protein Engineering

8	Engineering Luciferases for Assays and Imaging	203
	Andreas M. Loening and Zachary F. Walls	

9	Engineered Split Reporter Systems for Molecular Imaging of Protein–Protein Interactions in Living Subjects	233
	Tarik F. Massoud and Ramasamy Paulmurugan	
10	Engineering Aspects of Bioluminescence Resonance Energy Transfer Systems	257
	Abhijit De, Rohit Arora and Akshi Jasani	
11	Antibody Engineering in Translational Medicine	301
	Eliane Fischer	
12	Engineered Affibodies in Translational Medicine	317
	Xiang Hu, Hongguang Liu and Zhen Cheng	
13	Alternative Protein Scaffolds for Molecular Imaging and Therapy	343
	Benjamin J. Hackel	
14	Engineering Multivalent and Multispecific Protein Therapeutics	365
	Cassie J. Liu and Jennifer R. Cochran	
15	Engineering Aptamers for Biomedical Applications: Part I	397
	Ya Cao and Genxi Li	
16	Engineering Aptamers for Biomedical Applications: Part II.	427
	Laura Cerchia, Luciano Cellai and Vittorio de Franciscis	
17	Engineering DNA Vaccines for Cancer Therapy	449
	Brian M. Olson and Douglas G. McNeel	
 Part III Nanoengineering		
18	Multifunctional Nanoscale Delivery Systems for Nucleic Acids	475
	Richard Conroy and Belinda Seto	
19	Engineering Nanomaterials for Biosensors and Therapeutics	513
	Tse-Ying Liu, Chun-Liang Lo, Chih-Chia Huang, Syue-Liang Lin and C. Allen Chang	
20	Engineering Fluorescent Nanoparticles for Biomedical Applications	535
	Oscar F. Silvestre and Xiaoyuan Chen	

21	Magnetic Nanoparticles for Biomedical Applications: From Diagnosis to Treatment to Regeneration.	567
	Yu Gao, Yi Liu and Chenjie Xu	
22	Engineering Upconversion Nanoparticles for Biomedical Imaging and Therapy	585
	Feng Chen, Wenbo Bu, Weibo Cai and Jianlin Shi	
23	Engineering of Mesoporous Silica Nanoparticles for In Vivo Cancer Imaging and Therapy	611
	Feng Chen, Weibo Cai and Hao Hong	
24	Engineering Carbon Nanomaterials for Stem Cell-Based Tissue Engineering	641
	Tapas R. Nayak and Weibo Cai	
25	Engineering Peptide-based Carriers for Drug and Gene Delivery	667
	Jo-Ann Chuah, David L. Kaplan and Keiji Numata	
26	Activation Approaches on Delivery of Imaging and Therapeutic Agents	691
	Mitul Kumar A. Patel and Benedict Law	
27	Opportunities for New Photodynamic Molecular Beacon Designs.	733
	Kun Lou and Jonathan F. Lovell	
Part IV Biomedical Instrumentation		
28	Engineering the Next-Generation PET Detectors	761
	Arne Vandenbroucke and Craig S. Levin	
29	Photoacoustic Imaging: Development of Imaging Systems and Molecular Agents.	799
	Adam de la Zerda	
30	Engineering Miniature Imaging Instruments	835
	Zhen Qiu and Thomas D. Wang	
31	Engineering Small Animal Conformal Radiotherapy Systems.	853
	Magdalena Bazalova and Edward E. Graves	

Part V Theranostics and Other Novel Approaches

- 32 Plasmonic Nanobubbles for Cancer Theranostics** 879
Ekaterina Y. Lukianova-Hleb and Dmitri O. Lapotko
- 33 Cell-based Microfluidic Assays in Translational Medicine** 927
Eric K. Sackmann, Benjamin P. Casavant,
S. Farshid Moussavi-Harami, David J. Beebe and Joshua M. Lang
- 34 Engineering of Photomanipulatable Hydrogels
for Translational Medicine** 957
Mingtao He and Yan Zhang
- 35 Engineering Apeptides for Translational Medicine** 983
Haifan Wu and Jianfeng Cai

Contributors

Hamisha Ardalani Department of Biomedical Engineering, University of Wisconsin, Madison, WI, USA, e-mail: hardalani@wisc.edu

Rohit Arora Molecular Functional Imaging Lab, ACTREC, Tata Memorial Centre, Sector 22, Kharghar, Navi Mumbai, Maharashtra 410210, India, e-mail: rohit0288@gmail.com

Amir H. Assadi Department of Mathematics, University of Wisconsin, Madison, WI, USA, e-mail: ahassadi@wisc.edu

Magdalena Bazalova Department of Radiation Oncology, Stanford University, 875 Blake Wilbur, Stanford, CA, USA, e-mail: bazalova@stanford.edu

David J. Beebe University of Wisconsin Carbone Cancer Center and Wisconsin Institutes for Medical Research, Room 6009, 1111 Highland Avenue, Madison, WI 53705, USA, e-mail: djbeebe@wisc.edu

Wenbo Bu State Key Laboratory of High Performance Ceramics and Superfine Microstructure, Shanghai Institute of Ceramics, Chinese Academy of Sciences, Shanghai 200050, People's Republic of China, e-mail: wbbu@mail.sic.ac.cn

Jianfeng Cai Department of Chemistry, University of South Florida, 4202 E. Fowler Ave, Tampa, FL 33620, USA, e-mail: jianfengcai@usf.edu

Weibo Cai Departments of Radiology and Medical Physics, University of Wisconsin Carbone Cancer Center, Room 7137, 1111 Highland Avenue, Madison, WI 53705-2275, USA, e-mail: wcai@uwhealth.org

Ya Cao Laboratory of Biosensing Technology, School of Life Science, Shanghai University, Shanghai 200444, China, e-mail: conezimint@shu.edu.cn

Benjamin P. Casavant University of Wisconsin Carbone Cancer Center and Wisconsin Institutes for Medical Research, Room 6028, 1111 Highland Avenue, Madison, WI 53705, USA, e-mail: bcasavant@wisc.edu

Luciano Cellai CNR-Istituto di Cristallografia, 00015 Monterotondo Stazione, Rome, Italy, e-mail: luciano.cellai@ic.cnr.it

Laura Cerchia Istituto per l'Endocrinologia e l'Oncologia Sperimentale del CNR "G. Salvatore", via Pansini 5, 80131 Naples, Italy, e-mail: cerchia@unina.it

C. Allen Chang Department of Biomedical Imaging and Radiological Sciences, National Yang Ming University, 7199, No. 155, Sec. 2, Li-Nong Street, Taipei 112, Taiwan, ROC, e-mail: cachang@ym.edu.tw

Subhoshree Chatterjee Advanced Centre for Treatment, Research and Education in Cancer, Tata Memorial Centre, Navi Mumbai, Maharashtra, India, e-mail: srchatterjee@actrec.gov.in

Feng Chen Department of Radiology, University of Wisconsin, Madison, WI 53705, USA, e-mail: FChen@uwhealth.org

Xiaoyuan Chen Laboratory of Molecular Imaging and Nanomedicine, National Institute of Biomedical Imaging and Bioengineering, National Institutes of Health, Bethesda, MD 20892, USA, e-mail: shawn.chen@nih.gov

Zhen Cheng Molecular Imaging Program at Stanford, Department of Radiology, Stanford University, 1201 Welch Road, Lucas Expansion, P095, Stanford, CA 94305, USA, e-mail: zcheng@stanford.edu

Jo-Ann Chuah Biomass Engineering Program, Enzyme Research Team, RIKEN, 2-1, Hirosawa, Wako-shi, Saitama 351-0198, Japan, e-mail: jo-ann.chuah@riken.jp

Jennifer R. Cochran Department of Bioengineering, Stanford University, Stanford, CA, USA, e-mail: jennifer.cochran@stanford.edu

Richard Conroy National Institute of Biomedical Imaging and Bioengineering, National Institutes of Health, 6707 Democracy Blvd, Suite 200, Bethesda MD, 20892, USA, e-mail: richard.conroy@nih.gov

Laurence J. N. Cooper Division of Pediatrics, The University of Texas M. D. Anderson Cancer Center, Unit 907, 1515 Holcombe Boulevard, Houston, TX 77030, USA, e-mail: ljncooper@mdanderson.org

Abhijit De Molecular Functional Imaging Lab, ACTREC, Tata Memorial Centre, Sector 22, Kharghar, Navi Mumbai, Maharashtra 410210, India, e-mail: ade@actrec.gov.in

Eliane Fischer Paul Scherrer Institute, 5232 Villigen, Switzerland, e-mail: eliane.fischer@psi.ch

Vittorio de Franciscis Istituto per l'Endocrinologia e l'Oncologia Sperimentale del CNR "G. Salvatore", via Pansini 5, 80131 Naples, Italy, e-mail: defranci@unina.it

Snehal M. Gaikwad Advanced Centre for Treatment, Research and Education in Cancer, Tata Memorial Centre, Navi Mumbai, Maharashtra, India, e-mail: smgaikwad@actrec.gov.in

Yu Gao Division of Bioengineering, School of Chemical and Biomedical Engineering, Nanyang Technological University, Building N1.3, Level B2, Room 06, 70 Nanyang Drive, Singapore 637457, Singapore, e-mail: gaoyu@ntu.edu.sg

Edward E. Graves Department of Radiation Oncology, Stanford University, 875 Blake Wilbur, Stanford, CA, USA, e-mail: egraves@stanford.edu

Benjamin J. Hackel Department of Chemical Engineering and Materials Science, University of Minnesota, 421 Washington Avenue SE, Minneapolis, MN 55455, USA, e-mail: hackel@umn.edu

Mingtao He State Key Laboratory of Analytical Chemistry for Life Science, School of Chemistry and Chemical Engineering, Nanjing University, Nanjing 210093, People's Republic of China, e-mail: he.mingtao@163.com

Hao Hong University of Wisconsin Carbone Cancer Center, Madison, WI, USA, e-mail: HHong@uwhealth.org

Xiang Hu Molecular Imaging Program at Stanford, Department of Radiology, Stanford University, 1201 Welch Road, Lucas Expansion, P095, Stanford, CA 94305, USA, e-mail: xianghu@stanford.edu

Chih-Chia Huang Institute of Biophotonics, National Yang Ming University, 7959, No. 155, Sec. 2, Li-Nong Street, Taipei 112, Taiwan, ROC, e-mail: huang.chihchia@gmail.com

Zhen Huang State Key Laboratory of Pharmaceutical Biotechnology, School of Life Sciences, Nanjing University, Nanjing 210093, China, e-mail: njuhenery@gmail.com

Akshi Jasani Molecular Functional Imaging Lab, ACTREC, Tata Memorial Centre, Sector 22, Kharghar, Navi Mumbai, Maharashtra 410210, India, e-mail: akshi.aj@gmail.com

David L. Kaplan Biomass Engineering Program, Enzyme Research Team, RIKEN, 2-1, Hirosawa, Wako-shi, Saitama 351-0198, Japan, e-mail: David.Kaplan@tufts.edu

Joshua M. Lang Department of Medicine, University of Wisconsin Carbone Cancer Center and Wisconsin Institutes for Medical Research, Room 7151, 1111 Highland Avenue, Madison, WI 53705, USA, e-mail: jmlang@medicine.wisc.edu

Dmitri O. Lapotko Department of Biochemistry and Cell Biology, Department of Physics and Astronomy, Rice University, 6100 Main Street, MS-140, Houston 77005, TX, USA, e-mail: dl5@rice.edu

Benedict Law Department of Pharmaceutical Sciences, Department 2665, College of Pharmacy, North Dakota State University, PO Box 6050, Fargo, ND 58108, USA, e-mail: Shek.law@ndsu.edu

Wenyan Leong Division of Bioengineering, School of Chemical and Biomedical Engineering, Nanyang Technological University, 70 Nanyang Drive, N1.3-B2-13, Singapore 637457, Singapore, e-mail: wleong1@e.ntu.edu.sg

Craig S. Levin Molecular Imaging Program at Stanford, Department of Radiology, Physics, Electrical Engineering and Bioengineering, Stanford University, Stanford, CA, USA, e-mail: cslevin@stanford.edu

Genxi Li Laboratory of Biosensing Technology, School of Life Science, Shanghai University, Shanghai 200444, China; National Key Laboratory of Pharmaceutical Biotechnology, Department of Biochemistry, Nanjing University, Nanjing 210093, China, e-mail: genxili@nju.edu.cn

Syue-Liang Lin Department of Biotechnology and Laboratory Science in Medicine, National Yang Ming University, 5540, No. 155, Sec. 2, Li-Nong Street, Taipei 112, Taiwan, ROC, e-mail: g39919041@ym.edu.tw

Cassie J. Liu Department of Bioengineering, Stanford University, Stanford, CA, USA, e-mail: casliu@stanford.edu

Hongguang Liu Molecular Imaging Program at Stanford, Department of Radiology, Stanford University, 1201 Welch Road, Lucas Expansion, P095, Stanford, CA 94305, USA, e-mail: hongguangliu@stanford.edu

Tse-Ying Liu Department of Biomedical Engineering, National Yang Ming University, 7923, No. 155, Sec. 2, Li-Nong Street, Taipei 112, Taiwan, ROC, e-mail: tyliu5@ym.edu.tw

Yi Liu Division of Bioengineering, School of Chemical and Biomedical Engineering, Nanyang Technological University, Building N1.3, Level B2, Room 06, 70 Nanyang Drive, Singapore 637457, Singapore, e-mail: liu.yi@ntu.edu.sg

Chun-Liang Lo Department of Biomedical Engineering, National Yang Ming University, 7914, No. 155, Sec. 2, Li-Nong Street, Taipei 112, Taiwan, ROC, e-mail: cllou@ym.edu.tw

Andreas M. Loening Department of Radiology, Stanford University School of Medicine, Stanford, CA, USA, e-mail: loening@stanford.edu

Kun Lou Departments of Chemical and Biological Engineering, State University of New York, Buffalo, NY 14260, USA, e-mail: jflovell@buffalo.edu

Jonathan F. Lovell Departments of Chemical and Biological Engineering, State University of New York, Buffalo, NY 14260, USA, e-mail: jflovell@buffalo.edu

Ekaterina Y. Lukianova-Hleb Department of Biochemistry and Cell Biology, Department of Physics and Astronomy, Rice University, 6100 Main Street, MS-140, Houston 77005, TX, USA, e-mail: kh11@rice.edu

Tarik F. Massoud Molecular Imaging Program at Stanford, Laboratory of Experimental and Molecular Neuroimaging, Department of Radiology, Section of

Neuroradiology, Stanford University School of Medicine and Medical Center, 300 Pasteur Drive, Grant S-047A, Stanford, CA 94305-5105, USA, e-mail: tmassoud@stanford.edu

Douglas G. McNeel Department of Medicine, Wisconsin Institutes for Medical Research, University of Wisconsin, Room 7007, 1111 Highland Avenue, Madison, WI 53705, USA, e-mail: dm3@medicine.wisc.edu

S. Farshid Moussavi-Harami University of Wisconsin Carbone Cancer Center and Wisconsin Institutes for Medical Research, Room 6028, 1111 Highland Avenue, Madison, WI 53705, USA, e-mail: moussavihara@wisc.edu

Judy S. Moyes Division of Pediatrics, The University of Texas M. D. Anderson Cancer Center, Unit 907, 1515 Holcombe Boulevard, Houston, TX 77030, USA, e-mail: jsmoyes@mdanderson.org

William L. Murphy Departments of Biomedical Engineering and Orthopedic and Rehabilitation, University of Wisconsin, Madison, WI, USA, e-mail: wlmurphy@wisc.edu

Tapas R. Nayak University of Wisconsin, 1111 Highland Avenue, Madison, WI 53705-2275, USA, e-mail: tnayak@uwhealth.org

Keiji Numata Biomass Engineering Program, Enzyme Research Team, RIKEN, 2-1, Hirosawa, Wako-shi, Saitama 351-0198, Japan, e-mail: keiji.numata@riken.jp

Brian M. Olson Department of Medicine, Wisconsin Institutes for Medical Research, University of Wisconsin, Room 7007, 1111 Highland Avenue, Madison, WI 53705, USA, e-mail: bmo@medicine.wisc.edu

Hakan Orbay University of Wisconsin, 1111 Highland Avenue, Madison, WI 53705-2275, USA, e-mail: Horbay@uwhealth.org

Mitulkumar A. Patel Department of Pharmaceutical Sciences, Department 2665, College of Pharmacy, North Dakota State University, PO Box 6050, Fargo, ND 58108, USA, e-mail: mitulkumar.patel@my.ndsu.edu

Ramasamy Paulmurugan Molecular Imaging Program at Stanford, Cellular Pathway Imaging Laboratory, Canary Center, Stanford University School of Medicine, 1501 S. California Avenue, Stanford, CA 94304, USA, e-mail: paulmur8@stanford.edu

Zhen Qiu Department of Biomedical Engineering, University of Michigan, 1728, 109 Zina Pitcher Place, Ann Arbor, MI 48109, USA, e-mail: zqiu@umich.edu

Pritha Ray Advanced Centre for Treatment, Research and Education in Cancer, Tata Memorial Centre, Navi Mumbai, Maharashtra, India, e-mail: pray@actrec.gov.in

Eric K. Sackmann 5860 Charter Oaks Drive, Castro Valley, CA 94552, USA, e-mail: eric.sackmann@me.com

Belinda Seto National Institute of Biomedical Imaging and Bioengineering, National Institutes of Health, 6707 Democracy Blvd, Suite 200, Bethesda MD, 20892, USA, e-mail: setob@mail.nih.gov

Jianlin Shi State Key Laboratory of High Performance Ceramics and Superfine Microstructure, Shanghai Institute of Ceramics, Chinese Academy of Sciences, Shanghai 200050, People's Republic of China, e-mail: jlshi@sunm.shcnc.ac.cn

Oscar F. Silvestre Laboratory of Molecular Imaging and Nanomedicine, National Institute of Biomedical Imaging and Bioengineering, National Institutes of Health, Bethesda, MD 20892, USA

Ram K. Singh Advanced Centre for Treatment, Research and Education in Cancer, Tata Memorial Centre, Navi Mumbai, Maharashtra, India, e-mail: rksingh@actrec.gov.in

Hiroki Torikai Division of Pediatrics, The University of Texas M. D. Anderson Cancer Center, Unit 907, 1515 Holcombe Boulevard, Houston, TX 77030, USA, e-mail: htorikai@mdanderson.org

Arne Vandenbroucke Molecular Imaging Program at Stanford, Department of Radiology, Stanford University, Stanford, CA, USA, e-mail: arnevdb@stanford.edu

Zachary F. Walls Department of Pharmaceutical Sciences, East Tennessee State University, Johnson City, TN, USA, e-mail: wallsz@etsu.edu

Dong-An Wang Division of Bioengineering, School of Chemical and Biomedical Engineering, Nanyang Technological University, 70 Nanyang Drive, N1.3-B2-13, Singapore 637457, Singapore, e-mail: DAWang@ntu.edu.sg

Thomas D. Wang Department of Medicine, Biomedical Engineering and Mechanical Engineering, University of Michigan, Ann Arbor, MI 48109, USA, e-mail: thomaswa@umich.edu

Haifan Wu Department of Chemistry, University of South Florida, 4202 E. Fowler Ave, Tampa, FL 33620, USA, e-mail: jianfengcai@usf.edu

Chenjie Xu Division of Bioengineering, School of Chemical and Biomedical Engineering, Nanyang Technological University, Building N1.3, Level B2, Room 06, 70 Nanyang Drive, Singapore 637457, Singapore, e-mail: cjxu@ntu.edu.sg

Adam de la Zerda Department of Structural Biology and Bio-X Program, School of Medicine, Stanford University, Fairchild Building, D141, 299, Campus Drive W, Stanford, CA 94305, USA, e-mail: adlz@stanford.edu

Junfeng Zhang State Key Laboratory of Pharmaceutical Biotechnology, School of Life Sciences, Nanjing University, Nanjing 210093, China, e-mail: jfzhang@nju.edu.cn

Yan Zhang State Key Laboratory of Analytical Chemistry for Life Science, School of Chemistry and Chemical Engineering, Nanjing University, Nanjing 210093, People's Republic of China, e-mail: njzy@nju.edu.cn

Chapter 1

Engineering in Translational Medicine: An Introduction

Weibo Cai

1.1 Man Text

Translational medicine has attracted tremendous attention over the last decade. Personalized medicine is the future for twenty-first century healthcare, where translational research is the indispensable bridge between basic science discoveries and clinical patient management. In the broadest sense, translational research is a continuum that spans the majority of preclinical and clinical research. In a more strict sense, translational research is referring to research that can be immediately translated into clinical investigation, as well as those that can be translated into the clinic within a decade. In many cases, the biggest hurdle for clinical translation is not the lack of adequate technology development for clinical applications; instead it is the regulatory requirement that causes a “valley of death” for translational research. Given the recent crisis in global economy and significant budget cut in virtually all agencies that fund research over the last decade, which may not change dramatically in the near future, translational research is facing unprecedented challenges since it is quite costly to translate new discoveries (e.g., agents and devices) into clinical investigation [1, 2].

Nonetheless, scientists and researchers remain highly enthusiastic and devoted to translational research. To provide a forum to disseminate research findings in cutting-edge translational research, many major publishers have launched peer-reviewed journals that are focused on translational research/medicine. The words “research” and “medicine” are often used interchangeably, and there is no clear-cut boundary regarding where “research” stops and “medicine” begins, although the latter is certainly more clinically oriented than the former. Some representative

W. Cai (✉)

Departments of Radiology and Medical Physics, University of Wisconsin,
Madison, WI, USA

University of Wisconsin Carbone Cancer Center, Madison, WI, USA
e-mail: wcai@uwhealth.org

journals that are focused on this topic include *Science Translational Medicine* (Science), *American Journal of Translational Research* (e-Century Publishing Corporation), *Translational Research* (Elsevier Science Inc.), and *Journal of Translational Medicine* (Biomed Central Ltd.).

The field of engineering has witnessed spectacular advancement over the last several decades, which has affected the everyday life of billions of people worldwide in all areas ranging from energy to medicine. However, currently, a comprehensive reference book that focuses on “Engineering” and “Translational Medicine” does not exist. To fill this gap and meet the urgent need, I have worked with an international ensemble of leading experts in the field to organize this book entitled “Engineering in Translational Medicine”, which covers most major topics of the field in the 34 subsequent chapters of this book. I am deeply grateful to the total of ~80 contributors of this book for their tremendous effort in writing these exceptional chapters on a diverse array of topics that are related to “Engineering in Translational Medicine”, which we all firmly believe will be an invaluable resource for scientists/students/clinicians both new to this topic and currently working in this area for many years to come.

Encompassing a broad spectrum of state-of-the-art engineering research in translational medicine, the book is categorized into 5 parts: “Cell and Tissue Engineering” which includes 6 chapters, “Genetic and Protein Engineering” which has 10 chapters, “Nanoengineering” which also contains 10 chapters, “Biomedical Instrumentation” which is composed of 4 chapters, and “Therapeutics and Other Novel Approaches” with 4 chapters (Fig. 1.1).

Part I of this book, which includes [Chaps. 2–7](#), is focused on cell and tissue engineering. Regenerative medicine holds tremendous potential in the treatment of a wide variety of human diseases; for many of those, it may be the only solution [3]. In [Chap. 2](#), Dr. Ray and co-workers discussed about these “therapeutic wonders” (i.e., stem cells) and reviewed the ongoing investigations on stem cell biology, as well as their clinical applicability which can bring revolutions to future clinical care. Engineering of stem cells, non-invasive imaging of stem cells, as well as clinical applications of stem cells in a number of human diseases were all covered in this chapter. In [Chap. 3](#), Dr. Cooper and co-workers focused on the treatment of cancer with engineered T cells. Since tumor microenvironment is often immune suppressive, which protects cancer cells from recognition and elimination by effector cells, engineered T cells can be used for effective cancer cell killing. This chapter provided a comprehensive summary of adoptive cell therapy with genetically modified T cells to redirect specificity to tumor cell antigens using a number of approaches, to improve T-cell effector function, as well as to control these T cells with suicide genes to ensure safety.

Much recent research effort has been devoted to the development of various scaffold systems that can carry cells, using a broad array of biomaterials. In [Chap. 4](#), Dr. Wang and his co-worker gave a thorough review on engineering biomaterials for the delivery of anchorage-dependent and non-anchorage-dependent therapeutic cells. Some cells (e.g., muscle cells and neurons) are dependent on anchorage to the extracellular matrix. Therefore, they require extensive cell adhesion to a substrate

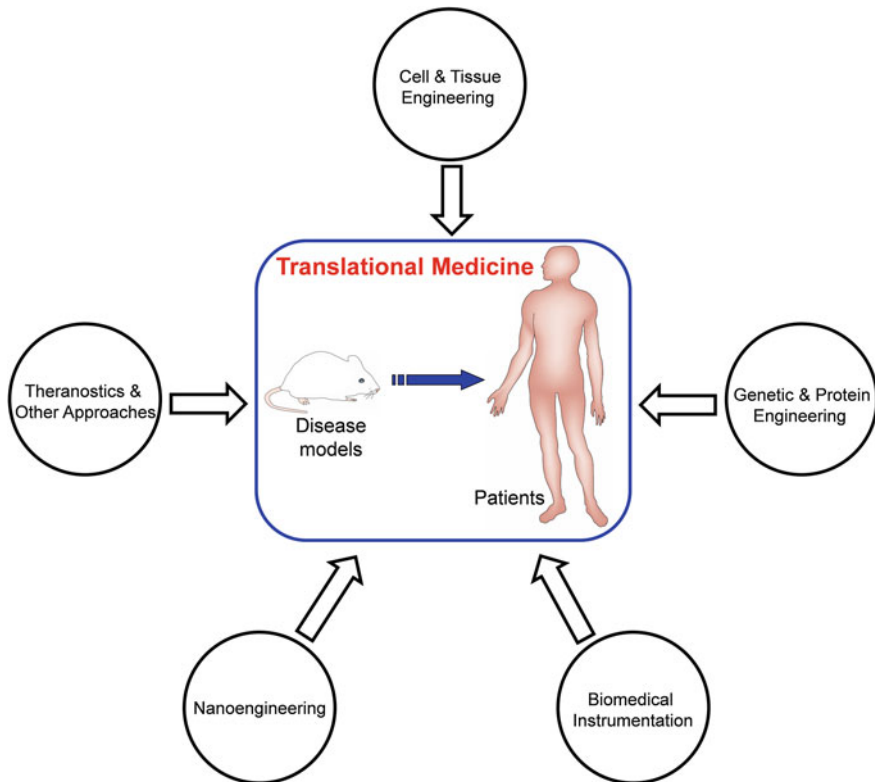


Fig. 1.1 An outline of this book, which is organized into 5 parts

to survive and elicit biological function upon transplantation. On the other hand, non-anchorage-dependent cells (e.g., chondrocytes and hepatocytes) do not have such requirement, which often exhibit a rounded morphology in their native environment. Clearly, different cell delivery structures are needed for these cells to achieve maximal therapeutic effect, which were illustrated in detail in this chapter.

The next three chapters in Part I of this book are focused on tissue repair. Peripheral nerve injuries can lead to variable levels of functional loss, depending on the extent of injury. In [Chap. 5](#), Dr. Orbay and I had a detailed survey into the components of tissue-engineered nerve grafts, as well as reviewed the relevant clinical studies. A tissue-engineered nerve is typically composed of a biodegradable scaffold, a neurogenic cell line, and growth factors. Therefore, how to improve the cell–scaffold and scaffold–tissue interactions is a key challenge for peripheral nerve repair. Perhaps even more important than nerve repair, the establishment of blood vessel networks is a matter of life and death for tissues and organisms. In [Chap. 6](#), Dr. Murphy and co-workers discussed about the structure of blood vessels and key signaling molecules, which play significant role in vasculogenesis, angiogenesis, and maturation of nascent blood vessels. A description of

promising approaches specific to tissue-engineered blood vessels, various tissue engineering approaches to identify the appropriate sources of endothelial cells, a brief introduction to some clinical results, as well as the regulatory challenges were all included in this chapter. Cartilage tissue is prone to significant dysfunction after damage, which also lacks the innate ability to effectively repair itself. [Chapter 7](#), written by Dr. Zhang and his co-worker, was focused on engineering gene-activated matrices for the repair of articular cartilage defect. Although growth factors were shown to promote cartilage repair, the structure of cartilage tissue can hinder direct addition of growth factors into the traditional system, due to the difficulty in controlling the amount of growth factors added and the short biological half-lives. Therefore, gene-activated matrix systems have been developed for the repair of articular cartilage damage, which can secrete large quantity of growth factors continuously and serve as a promising therapeutic approach for repairing cartilage damage.

The ten following chapters in Part II of this book cover a broad array of areas related to genetic and protein engineering. Many luciferases have been isolated and investigated for broad biomedical applications, ranging from cell-based studies to in vivo applications in small animal models [4, 5]. In [Chap. 8](#), Dr. Walls and Dr. Loening provided an excellent and comprehensive review of engineered luciferases. They discussed in detail about how protein engineering can be used to improve their stability, light output, emission wavelength, chemical sensitivity, and substrate specificity among others for better in vitro/in vivo performances and broader biomedical applications. After significant improvement and optimization of the naturally occurring luciferases (e.g., firefly luciferase and Renilla luciferase, as discussed in [Chap. 8](#)) and other enzymes (e.g., herpes simplex virus type-1 thymidine kinase), they can be employed for a wide variety of biomedical applications, two of which are detailed in the two following chapters.

In [Chap. 9](#), Dr. Massoud and Dr. Paulmurugan focused on the use of engineered split reporter systems for in vivo molecular imaging of protein–protein interactions, which can pave the way for functional proteomics in living animals and provide a tool for whole-body evaluation of new pharmaceuticals that can modulate protein–protein interactions. The main strategies currently available for imaging protein–protein interactions in living subjects using molecularly engineered and rationally designed split reporter gene, as well as the broad (potential) uses of these strategies, were illustrated in exquisite detail. A few of the major strategies adopted for split reporter gene-based imaging include intein-mediated reconstitution and protein fragment complementation (which can be achieved via a variety of different mechanisms), which can enable the interrogation of many protein–protein interactions through in vitro assays and/or non-invasive imaging. Besides split reporter gene techniques, bioluminescence resonance energy transfer (BRET)-based sensors are rapidly expanding, which can also be adopted for investigation of protein–protein interactions, protein dimerization, signal transduction, etc. [6, 7]. In [Chap. 10](#), Dr. De and co-workers presented an in-depth overview on the engineering requirements of BRET components such as donor, acceptor, substrate chemistry, and instrumentation. Both genetically engineered

and synthetic BRET systems were described, which have witnessed significant advancement over the last decade and can be used in a variety of systems including both *in vitro* assays and *in vivo* applications.

Besides luciferases and other enzymes, a variety of other engineered proteins can be used for biomedical applications, which are the topics of the subsequent 4 chapters. Antibodies are a major constituent of the human immune system and have become an indispensable class of therapeutics in cancer and many other diseases [8, 9]. In [Chap. 11](#), Dr. Fischer summarized the topic of antibody engineering in translational medicine, which offered an overview of current strategies to tailor antibodies for biomedical applications. After a brief introduction, this chapter covers many related topics which include approaches to reduce immunogenicity of therapeutic antibodies, optimize pharmacokinetics, and enhance therapeutic efficacy (e.g., with Fc engineering to improve effector function, generation of antibody–drug conjugates, and radioimmunoconjugates). In addition, engineered antibody fragments and bispecific antibodies were also discussed, which can be advantageous than intact antibodies for many applications due to the much shorter circulation half-life and other desirable properties (e.g., the capability to bind to two different antigens simultaneously). Together with the conventional antibodies, many of which have been approved for clinical use over the last two decades, these novel engineered antibody-based imaging agents and therapeutics will have a major impact on future diagnosis and treatment of many diseases, including but not limited to cancer.

Affibodies are an emerging class of small (7 kDa) protein scaffold-based affinity ligands, which have attracted much attention recently and are the focus of [Chap. 12](#), written by Dr. Cheng and co-workers. Because of the small size (58 amino acid residues), affibodies can be readily produced via both peptide synthesis and recombinant expression in *Escherichia coli*. General structures and engineering strategies used to optimize affibody molecules for imaging and therapy applications are described in this chapter. As evidenced by the constantly emerging literature reports on this class of exciting proteins, affibodies have been extensively investigated for imaging applications with different techniques (e.g., upon labeling with various radionuclides for positron emission tomography or single-photon emission computed tomography, fluorescent dyes or quantum dots for optical imaging, and magnetic nanoparticles for magnetic resonance imaging), and most of the current research effort is focused on cancer research. In addition, affibodies have been explored for therapeutic applications as well (e.g., upon labeling with ^{177}Lu or ^{90}Y , or used as targeting ligands to redirect cytotoxic T lymphocytes and natural killer cells). With recent clinical studies indicating safety and efficacy of affibody-based imaging agents, affibodies hold promising potential in future clinical patient management.

In [Chap. 13](#), Dr. Hackel provided a comprehensive summary of various protein scaffolds that can be used for molecular imaging and therapy applications. Since effective targeting of imaging/therapeutic agents requires specific binding with high-affinity, facile and robust conjugation of effectors (e.g., drugs, genes, radioisotopes, and therapeutic proteins) without compromising the binding/biological

activity, and efficient in vivo delivery, protein scaffolds can serve as promising platforms for these applications. Aside from affibodies that were covered in [Chap. 12](#), other validated scaffolds include the fibronectin domain, knottin, designed ankyrin repeat protein, anticalin, etc. With clinical trials in therapy or imaging already ongoing with many of these scaffolds, the future is bright for newly developed agents that are based on these protein scaffolds.

In [Chap. 14](#), Dr. Cochran and Miss Liu focused on the topic of engineering multivalent and multispecific protein therapeutics. Since many proteins utilize the principles of multivalency and multispecificity to ensure optimal biological function in nature [10], their mechanisms of action have inspired the development of next-generation protein therapeutics with improved efficacy and safety profiles. The main advantages conferred by multivalency and multispecificity include increased target-binding affinity through avidity effects and selectivity for a diseased versus normal state, which can lead to better therapeutic control over an intended biological response and in the meantime offer reduced side effects. Both the basic biophysical principles underlying multivalency/multispecificity and how they influence protein design parameters were illustrated in detail in this chapter, which also included several examples regarding how these principles can be utilized to develop next-generation protein therapeutics.

After seven chapters covering many aspects of protein engineering, as described above, the next three chapters focus on DNA/RNA. Aptamers are single-stranded DNA or RNA oligonucleotides that can be selected for specific binding to a wide range of targets, primarily through the systematic evolution of ligands by exponential enrichment (SELEX) technology [11]. [Chapter 15](#) is the first of two chapters focusing on engineering aptamers for biomedical applications, written by Dr. Li and Dr. Cao. Because of their many desirable properties such as small size, ease of synthesis, and versatile chemistry, aptamers have attracted considerable attention in many disciplines of biomedicine. After a brief introduction and description of the different strategies for selecting optimal aptamers for biomedical applications, this chapter provided a detailed overview of engineering aptamers for use in biosensors. A number of approaches were covered, which include engineering aptamers to improve the bioavailability, to generate detectable signals (e.g., through incorporation of functional nucleic acids or molecular reporters) and to achieve signal amplification for high-sensitivity/selectivity biosensing. In [Chap. 16](#), Dr. Cerchia and co-workers provided a comprehensive summary on the development of multifunctional aptamer-based bioconjugates for targeted delivery of therapeutics and imaging agents to diseased cells and tissues. Many approaches have been utilized to conjugate aptamers with a broad array of agents, which include siRNA/miRNA, drugs, synthetic polymers, nanoparticles (e.g., synthetic nanoparticles, liposomes, gold nanoparticles, quantum dots, magnetic nanoparticles, and silica-coated nanoparticles), and radioisotopes (e.g., ^{99m}Tc for single-photon emission computed tomography imaging). Lastly, various strategies used to enhance the resistance of aptamers to nuclease degradation were also described in this chapter.

One intriguing approach for the treatment of cancer is to use vaccines. Dozens of DNA vaccines have entered clinical trials for a variety of malignancies, with demonstrated efficacy in eliciting immune responses and potential clinical responses [12, 13]. Recently, a DNA vaccine was approved for the treatment of canine melanoma, which represents a landmark achievement in this area [14]. In Chap. 17, Dr. McNeel and Dr. Olson presented an excellent overview of engineering DNA vaccines for cancer therapy. Generally speaking, a DNA vaccine for cancer is a bacterial DNA plasmid that encodes the cDNA of a tumor antigen, which can elicit humoral and/or cellular immunity against tumor cells expressing the encoded antigen when injected into recipients. A distinct advantage of DNA vaccines over other methods of antigen delivery is that DNA vaccines can be easily constructed, purified, and delivered to recipients. In this chapter, the engineering efforts to enhance the immune and anti-cancer efficacy of DNA vaccines were illustrated in extensive detail, focusing on specific modifications that can be made to the DNA backbone to enhance the expression, processing, and presentation of the encoded antigen, in addition to improve the inherent immunogenicity of the vaccine itself.

The next ten chapters, part III of this book, are related to the exciting topic of nanoengineering. Nanotechnology, an interdisciplinary research field involving physics, chemistry, engineering, biology, and medicine among others, holds tremendous potential for early detection, accurate diagnosis, and personalized treatment of diseases [15–17]. With the sizes several orders of magnitude smaller than human cells, nanoscale agents/devices can offer unprecedented interactions with biomolecules both on the surface of and inside cells, which can revolutionize disease diagnosis and treatment. In light of this, there has been numerous nanotechnology centers established worldwide over the last two decades [18–20]. One major area of applications for nanotechnology is biomedicine, and it is expected that nanotechnology will mature into a clinically useful field in the near future, which has already made significant impact in many aspects to date.

In Chap. 18, Dr. Seto and Dr. Conroy gave an excellent overview of the multifunctional nanoscale delivery systems for nucleic acids. Although nanoscale systems are attractive platforms for *in vivo* delivery of nucleic acids, their potential for improving human health has yet to be fully realized in the clinic. Engineering efforts is critical for modifying and optimizing synthetic and viral delivery systems to include drugs, imaging agents, and targeting moieties, which can simultaneously minimize toxicity and increase delivery efficiency/specificity. This chapter focuses on the recent advances in RNA/DNA delivery with an emphasis on the progress toward human therapies, the challenges that have been encountered, and the engineering approaches that have been employed. The delivery systems used (e.g., viral, non-viral, and directed delivery) and the therapeutic components incorporated (e.g., DNA, RNA, and nucleic acid analogs) were all described in exquisite detail. Lastly, three major challenges were identified, namely the development of optimal systems for preclinical testing, integration of clinically useful imaging approaches, and rapid translation of directed delivery technologies, which should all be adequately addressed before broad future clinical applications.

In [Chap. 19](#), Dr. Chang and co-workers centered on engineering nanomaterials for biosensing and therapeutic applications, which provided a timely overview on the synthetic methodology, surface engineering, physiological itinerary, and theranostic applications for various inorganic and organic nanostructures. After an introduction and a brief review of the applications and preparative methods of inorganic nanomaterials, the effects of surface modification with polymers and morphology on the physiological itinerary and toxicity of these nanomaterials were discussed, which can offer critical insights for future design of targeted imaging/therapeutic agents. Subsequently, in this chapter, several examples of promising nanotechnologies and theranostic applications were given, such as biosensors, magnetic hyperthermia, and photodynamic therapy for diagnosis and treatment of cancer. To take full advantage of these innovative ideas and demonstrated proof of principles of nanomaterials for biomedical applications, it is crucial to emphasize and expand efforts on translational research and development in the near future.

The following five chapters in part III of this book are related to several classes of nanomaterials that have been extensively investigated over the last decade, all of which hold tremendous potential for clinical applications: fluorescent nanoparticles ([Chap. 20](#)), magnetic nanoparticles ([Chap. 21](#)), upconversion nanoparticles ([Chap. 22](#)), mesoporous silica nanoparticles ([Chap. 23](#)), and carbon nanomaterials ([Chap. 24](#)). Fluorescent nanoparticles have been extensively studied in preclinical research for cancer imaging and/or theranostic applications [[21](#), [22](#)]. In [Chap. 20](#), Dr. Chen and Dr. Silvestre offered in-depth discussions about the design of fluorescent nanoparticles, which has to take into consideration not only the parameters that are related to enhanced fluorescence (e.g., absorption coefficient, quantum yield, stability, and excitation/emission wavelengths), but also characteristics that can lead to optimal blood circulation half-life, tumor specificity, efficient delivery, biocompatibility, and low toxicity. Three major classes of fluorescent nanoparticles were discussed: quantum dots and fluorescent dye-loaded inorganic and organic nanoparticles (e.g., those that are based on calcium phosphate, silica, lipid, or polymer). The characteristics, advantages, limitations, and the engineering strategies employed to enhance their *in vivo* use were discussed for each class of nanoparticles with ample preclinical examples. Significant emphasis was also devoted to clinical translation, which has remained a major challenge for most nanoparticles, and a few examples as well as the hurdles that exist were illustrated and discussed.

Magnetic nanoparticles are also popular candidates for many biomedical applications because of their low toxicity, biocompatibility, and unique magnetic properties [[23](#)]. In [Chap. 21](#), Dr. Xu and co-workers gave a general overview of their applications in diverse areas such as separation of biological samples, *in vitro* diagnostics, *in vivo* imaging, drug/gene delivery, treatment of iron deficiency, cancer therapy with hyperthermia, anti-bacterial agents, tissue engineering, and regenerative medicine. Although magnetic nanoparticles hold great promise for numerous biomedical applications, as listed above, many challenges still exist and should be addressed before newly developed magnetic nanoparticle-based agents can be translated into clinical investigation.

Upconversion nanoparticles are a relatively new class of materials with intriguing properties for biomedical applications, such as sharp emission lines, long signal lifetime, large anti-Stokes shift, superb photostability, and no blinking/bleaching [24]. In addition, doping of these intriguing nanoparticles with rationally selected ions (e.g., Gd^{3+} , $\text{Er}^{3+}/\text{Yb}^{3+}$, $\text{Tm}^{3+}/\text{Yb}^{3+}$, or combination of these ions) can lead to many exciting new features. In Chap. 22, Dr. Shi and co-workers summarized the recent advances in engineering upconversion nanoparticles for biological imaging and therapy, focusing on size/morphology, optimization of properties for in vivo multimodality imaging (e.g., to achieve near-infrared emission or confer sensitivity for magnetic resonance imaging), as well as the integration of therapeutic entities for cancer therapy.

Another class of promising nanoparticles is mesoporous silica nanoparticles, which possess many attractive properties such as excellent biocompatibility, large surface area, high pore volume, and uniform/tunable pore size [25, 26]. In Chap. 23, Dr. Chen, Dr. Hong, and I reviewed the progress to date and potential future directions of engineering these nanoparticles for biological imaging and/or therapy in vivo. After a brief introduction, efforts in engineering the morphology and surface of these nanoparticles were summarized, followed by a systematic review of in vivo imaging with functionalized mesoporous silica nanoparticles, which include the use of optical techniques, positron emission tomography, magnetic resonance imaging, as well as various combinations of multiple techniques. Subsequently, the use of (hollow) mesoporous silica nanoparticles for cancer therapy was discussed, which include loading of these nanoparticles with chemotherapeutic drugs, genes, or photodynamic therapy agents. Furthermore, mesoporous silica nanoparticles have also been investigated for image-guided ultrasound therapy and combination therapy applications, which were also covered in this chapter.

The 2010 Nobel Prize in Physics was awarded to Andre Geim and Konstantin Novoselov “for groundbreaking experiments regarding the two-dimensional material graphene,” which is a class of carbon nanomaterials that have attracted tremendous attention over the last decade [27–29]. In Chap. 24, Dr. Nayak and I focused on the recent studies pertaining to engineering and development of carbon nanomaterials and their composite for applications as synthetic scaffolds in tissue engineering and regenerative medicine. Because of the unique intrinsic physical and chemical properties, carbon nanotubes and graphene have been engineered via different methods to develop suitable two-dimensional and three-dimensional scaffolds, which were reported to sustain growth, proliferation, and adhesion of many types of stem cells [29]. Whereas some of these scaffolds were found to accelerate the osteogenic, neurogenic, and adipogenic differentiation of certain stem cells in the presence of specific medium, many other reports supported spontaneous differentiation of stem cells into specific adult tissues even in normal medium. Several underlying mechanisms such as nanopopography, preconcentration of growth factors, and electrostatic/chemical interactions have been proposed for such behavior of stem cells growing on different carbon nanomaterial-based scaffolds. Since most of the literature reports to date are based on in vitro studies,

more *in vivo* studies with relevant toxicity and biocompatibility data need to be in place for their future applications as implantable biomaterials for tissue engineering and regenerative medicine.

Some of the major goals of optimizing drug/gene delivery systems include increasing cell specificity, incorporating organelle targeting, and improving overall delivery efficiency [30]. Peptides/proteins can potentially meet the requirement for reaching these goals because of several desirable properties, such as the ability to condense DNA into compact particles for transport, to disrupt endosomal membrane, to escape proteasomal degradation, to traffic various therapeutic molecules to targeted intracellular compartments, and to minimize cytotoxicity/immunogenicity. In [Chap. 25](#), Dr. Numata and co-workers gave a comprehensive overview of engineering peptide-based carriers for drug and gene delivery. Since silk is well known for its biodegradability and biocompatibility, silk proteins derived from spiders and insects can be utilized for various biomedical applications such as drug/gene delivery, which is the focus of this chapter. The ability of silk to self-assemble, in combination with many other inherent features, makes it a unique and versatile delivery platform for small molecules, large proteins, as well as DNA/RNA. Not limited to drug/gene delivery, it may also be useful for tissue engineering, imaging, and regenerative medicine applications.

To achieve effective therapy and minimize toxic effects to the normal tissue, the drug/gene delivery systems need to target the disease sites (e.g., tumor) effectively. An alternative approach to enhance the therapeutic efficacy while minimizing side effects is to use activatable agents, which can be designed to release biologically active agents (e.g., drugs and genes) in response to internal or external stimuli upon systemic administration. In [Chap. 26](#), Dr. Law and his co-worker presented a comprehensive summary of activatable agents and provided specific examples to illustrate their mechanisms and potential applications for imaging and therapy of various diseases (e.g., cancer, diabetes, and pulmonary embolism). Complementary to nanotechnology, such activatable agents with various built-in sophisticated mechanisms have been engineered, which can dramatically facilitate broad future use of nanotechnology for clinical applications. The activation approaches described in this chapter include pH (e.g., with the use of acid-sensitive linkers or microgels, disassembly of micelles under certain pH range, and decomposition/desorption of inorganic materials), enzyme (e.g., proteases, esterases, myeloperoxidase, and many other enzymes), heat, light, and magnetic field. Although most of these agents are still in the preclinical development stage, for many of which only *in vitro* data are available, continued research effort in this exciting area will ultimately lead to more sophisticated activatable systems that are biocompatible and possess favorable pharmacokinetic properties as prospective candidates for future clinical trials.

Molecular beacons are useful in a number of biomedical applications, since they can provide fluorescence readout upon biomolecular recognition [31, 32]. With the use of photosensitizers, photodynamic molecular beacons hold potential as new tools for not only disease diagnosis but also therapy. In [Chap. 27](#), Dr. Lovell and his co-worker discussed about the opportunities for new photodynamic molecular

beacon designs. After an introduction to the classic molecular beacons and photodynamic molecular beacons, they offered important insights into the design considerations for next-generation molecular beacons, including the optimization of fluorophores and quenchers, rational design of loops and stems, as well as several other aspects. Enormous opportunities lie ahead in converting some of the already existing molecular beacons into new photodynamic molecular beacons, where seamless conversion of an imaging probe to a therapeutic agent can be achieved by replacing the fluorophores with light-activatable photosensitizers.

The design/optimization of new agents should proceed in parallel with the development of new instrumentation that can offer sensitive detection of various imaging agents described above, as well as providing high-resolution real-time images in preclinical animal models and cancer patients. Part IV of this book, composed of the next four chapters, is focused on biomedical instrumentation which has witnessed tremendous recent advances in terms of engineering. Three of the chapters (Chaps. 28–30) are related to the development of new imaging systems for various contrast agents, whereas the last chapter (Chap. 31) is focused on preclinical radiotherapy systems.

With the use of contrast agents that contain positron emitters, positron emission tomography (PET) is widely used in the clinic for disease diagnosis and treatment monitoring, particularly in oncology [33, 34]. In Chap. 28, Dr. Levin and Dr. Vandembroucke provide the readers with an overview of novel techniques in the engineering of next-generation PET detectors. After a brief introduction to PET and current state-of-the-art commercially available clinical systems, the characteristics of current and novel scintillating materials used for detection were discussed in detail. Subsequently, improvements in spatial resolution through depth-of-interaction measurements and novel optical photon extraction methods were illustrated, followed by a discussion on various photodetectors which include photomultiplier tubes (widely used in current clinical PET scanners) and silicon-based solid-state photodetectors (e.g., avalanche photodiodes and silicon photomultipliers), as well as semiconductor detectors that do not require the use of photodetectors. Since accurate time-of-flight information can significantly improve image signal-to-noise ratio, how to improve time resolution and the consequences for time-of-flight imaging was also covered in this chapter. With the recent commercial availability of clinical PET/MR scanners, the compatibility of various detector materials with magnetic resonance imaging was also reviewed. Lastly, improvements in image reconstruction techniques were briefly discussed. The authors believe that many of these techniques currently being developed will make their way into the clinic, which will significantly improve patient management.

Photoacoustic imaging, which converts short light pulses into ultrasound waves for detection, can generate three-dimensional maps of tissues with high spatial resolution and good signal penetration depth [35]. As a relatively new technique, photoacoustic imaging can overcome many limitations of conventional optical imaging. In Chap. 29, Dr. de la Zerda gave a thorough review on the development of imaging systems and molecular contrast agents for photoacoustic imaging. After an introduction and brief review of the physical basis for photoacoustic imaging,

different photoacoustic scanner implementations were discussed (e.g., photoacoustic tomography and photoacoustic microscopy), along with their biomedical applications. Since the basic mechanism that gives rise to a photoacoustic signal is light absorption, many endogenous molecules can be used for photoacoustic imaging, such as hemoglobin and melanin. To fully realize the potential of photoacoustic imaging, exogenous contrast agents (both molecularly targeted and non-targeted) have also been developed, which were comprehensively covered in detail in this chapter.

Aside from scanners that can be used for non-invasive imaging in humans or preclinical animal models, miniature imaging instruments are also needed for endoscopy applications. Many such instruments have been developed, which exhibit millimeter dimensions for in vivo imaging with performance approaching that of conventional microscopy [36]. In [Chap. 30](#), Dr. Wang and Dr. Qiu presented representative miniature imaging technologies that are currently under active development, including scanning fiber endoscopy, optical coherence tomography endomicroscopy, photoacoustic endomicroscopy, confocal endomicroscopy, dual-axes confocal endomicroscopy, and multi-photon endomicroscopy. Significant advances have been made in endomicroscopy technology such as optical designs/fibers, light sources, and miniature scanners, which can allow for improved resolution, greater signal penetration in tissue, as well as multi-spectral imaging. With the significant reduction in size, these systems can enable minimally invasive visualization of pathology in hollow organs to guide biopsy, identify surgical margins, and localize diseases. Major engineering challenges in this field include the need for large displacements, high scan speed, linear motion, and mechanical stability in a miniature instrument. To ultimately achieve fast two- and three-dimensional beam scanning, novel methods for cross-sectional imaging with deep tissue penetration, wide-area surveillance, and high-resolution microscopy were also illustrated in this chapter.

[Chapter 31](#), written by Dr. Graves and Dr. Bazalova, was focused on engineering small animal conformal radiotherapy systems which are important tools for translational research in radiation oncology. Since it is critical that the effects of radiotherapy on preclinical animal models are studied under the same conditions as how clinical radiotherapy is delivered, the engineering aspects of small animal radiotherapy systems were thoroughly discussed in this chapter, which include the sources of radiation, beam collimation, and imaging techniques. Quality assurance (e.g., mechanics, dose output, beam targeting, and imaging) of small animal conformal radiotherapy systems was also illustrated, which is an extremely important aspect in radiotherapy. Many preclinical radiotherapy systems have been developed at various institutions, which were also reviewed and compared. Lastly, various applications of such small animal conformal radiotherapy systems were briefly described. The authors are convinced that the models derived from small animal studies will facilitate the development of future personalized medicine, which can help physicians to decide on the best treatment protocol for individual cancer patients.

Part V of this book, which includes the remaining four chapters, is related to theranostics and other novel approaches. The area of theranostics has been an extremely vibrant field over the last decade, which can integrate diagnosis and therapy [37, 38]. Since the field has evolved so rapidly, the journal *Theranostics* was launched in 2011, which has already gained widespread recognition with an impressive 2012 impact factor of 7.806. In Chap. 32, Dr. Lapotko and Dr. Lukianova-Hleb gave a comprehensive review regarding cancer theranostics with plasmonic nanobubbles. After an introduction and description of the limitations of various other approaches, the physical properties of plasmonic nanobubbles were described (e.g., generation, detection, tunability, and spectral properties). Next, generation and detection of plasmonic nanobubbles in cells and tissues were reviewed in exquisite detail. In addition, theranostic applications of plasmonic nanobubbles were also discussed with concrete and specific examples, both in vitro and in vivo. Lastly, the translational potential/challenges of these plasmonic nanobubbles were mentioned, which are mainly associated with the limited penetration of light and gold nanoparticles into heterogeneous tumors, as well as possible phototoxicity. As a new paradigm of nanomedicine, plasmonic nanobubble-based theranostics was expected to achieve cell-level efficacy and safety, as well as high speed through the novel intracellular diagnostic and therapeutic mechanisms for potential future clinical applications.

Microfluidics, the study and use of fluid flow at small volumes (e.g., microliter or less), has been an exciting area of research over the last decade [39, 40]. In Chap. 33, Dr. Lang and co-workers focused on cell-based microfluidic assays in translational medicine, which hold great potential in many engineering and medical arenas such as point-of-care diagnostic tests. Two major areas where microfluidic cell-based assays have been used for clinical applications are chemotaxis (i.e., gradient-dependent cell migration) and the isolation/analysis of rare cells (e.g., circulating tumor cells), which were both reviewed in this chapter.

Chapter 34 is focused on engineering of photo-manipulatable hydrogels for translational medicine, which was written by Dr. Zhang and her co-worker. Since spatial and temporal resolved control of their property and function can be realized through light irradiation, photo-manipulatable biomaterials are of high significance in translational medicine. Hydrogels, an important class of biomaterials that are based on natural or synthetic polymers [41, 42], have been engineered to have photo-reactive chemical moieties for post-gelation photo-manipulation. In this chapter, the chemistry involved in the engineering of photo-manipulatable hydrogels was summarized, followed by representative examples of photo-manipulatable hydrogels (e.g., those that are photo-polymerizable, photo-degradable, or photo-patternable, as well as smart supramolecular hydrogels with sensitive photo-response). In addition, the applications of these photo-manipulatable biomaterials in regenerative medicine and tissue engineering were illustrated using recent examples. With the continued discovery of new bio-orthogonal reactions, it is certainly possible to engineer photo-manipulatable and multi-functional biomaterials for translational medicine in the near future.

In the last chapter of this book, written by Dr. Cai and his co-worker, a new class of peptidomimetics termed “AApeptides” was comprehensively reviewed. Peptidomimetics, designed to mimic the structure and function of bioactive peptides, have found numerous applications in the biomedical arena, and novel classes of peptidomimetics have continued to emerge [43, 44]. Dr. Cai’s research group recently developed AApeptides, which have unnatural backbones and hence are much more resistant to protease degradation than the naturally occurring peptides. Furthermore, they have limitless potential for derivatization with straightforward synthesis. In this chapter, the chemical development of AApeptides was illustrated with ample examples of AApeptides as potential therapeutics such as anti-microbial agents and anti-cancer agents.

Together, there are about 80 contributors to this book. Since they are all international leaders in the topic of each chapter, I am convinced that this book will be a comprehensive and authoritative reference book in the area of engineering and/in translational medicine. Several more chapters on other important topics were planned in the initial book proposal. However, due to various unforeseen circumstances, many authors were not able to write the book chapters that they initially committed to contribute. Since such situations were only discovered with very short notices, there was not sufficient time to find other experts in the field to write on these topics. A list of topics that would have been covered in this book include the following: engineering induced pluripotent stem cells for biomedical applications, carbohydrate-engineered cells for regenerative medicine, engineering tissues with spatial and temporal control of microenvironmental cues, engineering HaloTag for biomedical applications, engineering FRET sensors for biomedical applications, engineering nanoneedle systems for transdermal vaccine delivery, engineering combinatorial drug delivery systems, engineering fluorescence optical devices for non-invasive and intraoperative molecular imaging in patients, engineering small animal optical imaging systems, engineering tumor ablation systems, and a few others. Given the extremely competitive funding situation across the globe with grant funding rate at all-time low, I completely understand their time constraint and priorities. If there will be a second edition of this book in the future, I hope I will be able to include these exciting topics and other newly emerged areas.

I am deeply indebted to the scientists who have contributed to this book and will be forever grateful for their enthusiasm, support, tremendous effort, and scientific insight. Thank you very much for reading this introductory book chapter, and now, I present you the rest of the book which I am sure you will be as intrigued by each chapter as I was during the editing process.

References

1. DiMasi JA, Hansen RW, Grabowski HG (2003) The price of innovation: new estimates of drug development costs. *J Health Econ* 22(2):151–185
2. Josephson L, Rudin M (2013) Barriers to clinical translation with diagnostic drugs. *J Nucl Med* 54(3):329–332. doi:[10.2967/jnumed.112.107615](https://doi.org/10.2967/jnumed.112.107615)
3. Passier R, van Laake LW, Mummery CL (2008) Stem-cell-based therapy and lessons from the heart. *Nature* 453(7193):322–329. doi:[10.1038/nature07040](https://doi.org/10.1038/nature07040)
4. Contag CH, Bachmann MH (2002) Advances in in vivo bioluminescence imaging of gene expression. *Annu Rev Biomed Eng* 4:235–260
5. Badr CE, Tannous BA (2011) Bioluminescence imaging: progress and applications. *Trends Biotechnol* 29(12):624–633. doi:[10.1016/j.tibtech.2011.06.010](https://doi.org/10.1016/j.tibtech.2011.06.010)
6. Bacart J, Corbel C, Jockers R, Bach S, Couturier C (2008) The BRET technology and its application to screening assays. *Biotechnol J* 3(3):311–324. doi:[10.1002/biot.200700222](https://doi.org/10.1002/biot.200700222)
7. Pfleger KD, Eidne KA (2006) Illuminating insights into protein–protein interactions using bioluminescence resonance energy transfer (BRET). *Nat Methods* 3(3):165–174. doi:[10.1038/nmeth841](https://doi.org/10.1038/nmeth841)
8. Elbakri A, Nelson PN, Abu Odeh RO (2010) The state of antibody therapy. *Hum Immunol* 71(12):1243–1250. doi:[10.1016/j.humimm.2010.09.007](https://doi.org/10.1016/j.humimm.2010.09.007)
9. Scott AM, Wolchok JD, Old LJ (2012) Antibody therapy of cancer. *Nat Rev Cancer* 12(4):278–287. doi:[10.1038/nrc3236](https://doi.org/10.1038/nrc3236)
10. Mammen M, Chio S, Whitesides GM (1998) Polyvalent interactions in biological systems: implications for design and use of multivalent ligands and inhibitors. *Angew Chem Int Ed Engl* 37(20):2755–2794
11. Keefe AD, Pai S, Ellington A (2010) Aptamers as therapeutics. *Nat Rev Drug Discov* 9(7):537–550. doi:[10.1038/nrd3141](https://doi.org/10.1038/nrd3141)
12. Rice J, Ottensmeier CH, Stevenson FK (2008) DNA vaccines: precision tools for activating effective immunity against cancer. *Nat Rev Cancer* 8(2):108–120. doi:[10.1038/nrc2326](https://doi.org/10.1038/nrc2326)
13. Stevenson FK, Rice J, Ottensmeier CH, Thirdborough SM, Zhu D (2004) DNA fusion gene vaccines against cancer: from the laboratory to the clinic. *Immunol Rev* 199:156–180. doi:[10.1111/j.0105-2896.2004.00145.x](https://doi.org/10.1111/j.0105-2896.2004.00145.x)
14. USDA licenses DNA vaccine for treatment of melanoma in dogs (2010). *J Am Vet Med Assoc* 236(5):495. doi:[10.2460/javma.236.5.488](https://doi.org/10.2460/javma.236.5.488)
15. Farrell D, Alper J, Ptak K, Panaro NJ, Grodzinski P, Barker AD (2010) Recent advances from the National Cancer Institute Alliance for Nanotechnology in Cancer. *ACS Nano* 4(2):589–594. doi:[10.1021/nn100073g](https://doi.org/10.1021/nn100073g)
16. Ferrari M (2005) Cancer nanotechnology: opportunities and challenges. *Nat Rev Cancer* 5(3):161–171
17. Service RF (2005) Materials and biology nanotechnology takes aim at cancer. *Science* 310(5751):1132–1134
18. Horton MA, Khan A (2006) Medical nanotechnology in the UK: a perspective from the London Centre for Nanotechnology. *Nanomedicine* 2(1):42–48
19. Ptak K, Farrell D, Panaro NJ, Grodzinski P, Barker AD (2010) The NCI Alliance for Nanotechnology in Cancer: achievement and path forward. *Wiley Interdiscip Rev Nanomed Nanobiotechnol* 2(5):450–460. doi:[10.1002/wnan.98](https://doi.org/10.1002/wnan.98)
20. Pero H, Faure JE (2007) European research infrastructures for the development of nanobiotechnologies. *Trends Biotechnol* 25(5):191–194. doi:[10.1016/j.tibtech.2007.03.001](https://doi.org/10.1016/j.tibtech.2007.03.001)
21. Michalet X, Pinaud FF, Bentolila LA, Tsay JM, Doose S, Li JJ, Sundaresan G, Wu AM, Gambhir SS, Weiss S (2005) Quantum dots for live cells, in vivo imaging, and diagnostics. *Science* 307(5709):538–544
22. Cai W, Hsu AR, Li ZB, Chen X (2007) Are quantum dots ready for in vivo imaging in human subjects? *Nanoscale Res Lett* 2:265–281

23. Shubayev VI, Pisanic TR II, Jin S (2009) Magnetic nanoparticles for theragnostics. *Adv Drug Deliv Rev* 61(6):467–477. doi:[10.1016/j.addr.2009.03.007](https://doi.org/10.1016/j.addr.2009.03.007)
24. Zhou J, Liu Z, Li F (2012) Upconversion nanophosphors for small-animal imaging. *Chem Soc Rev* 41(3):1323–1349. doi:[10.1039/c1cs15187h](https://doi.org/10.1039/c1cs15187h)
25. Li Z, Barnes JC, Bosoy A, Stoddart JF, Zink JI (2012) Mesoporous silica nanoparticles in biomedical applications. *Chem Soc Rev* 41(7):2590–2605. doi:[10.1039/c1cs15246g](https://doi.org/10.1039/c1cs15246g)
26. Tang F, Li L, Chen D (2012) Mesoporous silica nanoparticles: synthesis, biocompatibility and drug delivery. *Adv Mater* 24(12):1504–1534. doi:[10.1002/adma.201104763](https://doi.org/10.1002/adma.201104763)
27. Novoselov KS, Fal'ko VI, Colombo L, Gellert PR, Schwab MG, Kim K (2012) A roadmap for graphene. *Nature* 490(7419):192–200. doi:[10.1038/nature11458](https://doi.org/10.1038/nature11458)
28. Yang K, Feng L, Shi X, Liu Z (2012) Nano-graphene in biomedicine: theranostic applications. *Chem Soc Rev* 42(2):530–547. doi:[10.1039/c2cs35342c](https://doi.org/10.1039/c2cs35342c)
29. Zhang Y, Nayak TR, Hong H, Cai W (2012) Graphene: a versatile nanoplatform for biomedical applications. *Nanoscale* 4(13):3833–3842. doi:[10.1039/c2nr31040f](https://doi.org/10.1039/c2nr31040f)
30. Peer D, Karp JM, Hong S, Farokhzad OC, Margalit R, Langer R (2007) Nanocarriers as an emerging platform for cancer therapy. *Nat Nanotechnol* 2(12):751–760. doi:[10.1038/nnano.2007.387](https://doi.org/10.1038/nnano.2007.387)
31. Huang K, Marti AA (2012) Recent trends in molecular beacon design and applications. *Anal Bioanal Chem* 402(10):3091–3102. doi:[10.1007/s00216-011-5570-6](https://doi.org/10.1007/s00216-011-5570-6)
32. Tan W, Wang K, Drake TJ (2004) Molecular beacons. *Curr Opin Chem Biol* 8(5):547–553. doi:[10.1016/j.cbpa.2004.08.010](https://doi.org/10.1016/j.cbpa.2004.08.010)
33. Gambhir SS, Czernin J, Schwimmer J, Silverman DH, Coleman RE, Phelps ME (2001) A tabulated summary of the FDG PET literature. *J Nucl Med* 42(5):1S–93S
34. Alauddin MM (2012) Positron emission tomography (PET) imaging with ¹⁸F-based radiotracers. *Am J Nucl Med Mol Imaging* 2(1):55–76
35. Wang LV, Hu S (2012) Photoacoustic tomography: in vivo imaging from organelles to organs. *Science* 335(6075):1458–1462. doi:[10.1126/science.1216210](https://doi.org/10.1126/science.1216210)
36. Khondee S, Wang TD (2013) Progress in molecular imaging in endoscopy and endomicroscopy for cancer imaging. *J Healthc Eng* 4(1):1–22. doi:[10.1260/2040-2295.4.1.1](https://doi.org/10.1260/2040-2295.4.1.1)
37. Kelkar SS, Reineke TM (2011) Theranostics: combining imaging and therapy. *Bioconjug Chem* 22(10):1879–1903. doi:[10.1021/bc200151q](https://doi.org/10.1021/bc200151q)
38. Chen XS (2011) Introducing theranostics journal-from the editor-in-chief. *Theranostics* 1:1–2
39. Becker H, Gartner C (2012) Microfluidics and the life sciences. *Sci Prog* 95(2):175–198
40. Holmes D, Gawad S (2010) The application of microfluidics in biology. *Methods Mol Biol* 583:55–80. doi:[10.1007/978-1-60327-106-6_2](https://doi.org/10.1007/978-1-60327-106-6_2)
41. Cabral J, Moratti SC (2011) Hydrogels for biomedical applications. *Future Med Chem* 3(15):1877–1888. doi:[10.4155/fmc.11.134](https://doi.org/10.4155/fmc.11.134)
42. Vermonden T, Censi R, Hennink WE (2012) Hydrogels for protein delivery. *Chem Rev* 112(5):2853–2888. doi:[10.1021/cr200157d](https://doi.org/10.1021/cr200157d)
43. Goodman M, Zapf C, Rew Y (2001) New reagents, reactions, and peptidomimetics for drug design. *Biopolymers* 60(3):229–245. doi:[10.1002/1097-0282\(2001\)60:3<229:aid-bip10034>3.0.co;2-p](https://doi.org/10.1002/1097-0282(2001)60:3<229:aid-bip10034>3.0.co;2-p)
44. Vagner J, Qu H, Hruby VJ (2008) Peptidomimetics, a synthetic tool of drug discovery. *Curr Opin Chem Biol* 12(3):292–296. doi:[10.1016/j.cbpa.2008.03.009](https://doi.org/10.1016/j.cbpa.2008.03.009)

Part I
Cell and Tissue Engineering

Chapter 2

Stem Cells: The Holy Grail of Regenerative Medicine

Ram K. Singh, Snehal M. Gaikwad, Subhoshree Chatterjee and Pritha Ray

2.1 Introduction

Stem cells occupy a special position in cellular hierarchy during differentiation and development of any organism. These undifferentiated cells have the potential to form any other cell type with specialized function and are characterized by their ability to self-renew and to differentiate. Both these cellular properties are prime requisites for the success of current regenerative medicine.

Depending upon the potential to differentiate into a particular lineage, stem cells could be grouped into five types (Fig. 2.1).

1. **Totipotent:** A single cell capable of dividing and forming various differentiated cells including extraembryonic tissues is known as totipotent or omnipotent cell, e.g., a zygote.
2. **Pluripotent:** The pluripotent stem cells have the ability to differentiate into all cell types of the three germ layers, i.e., ectoderm, mesoderm, and endoderm. Inability to form extraembryonic tissues such as placenta is the only limitation that makes them inferior to totipotent stem cells, e.g., embryonic stem (ES) cells.
3. **Multipotent:** Stem cells that demonstrate a restricted pattern of differentiation toward few lineages are termed as multipotent cells such as hematopoietic stem cell (HSC), which can develop into various types of blood cells but not into brain or liver cells.

R. K. Singh · S. M. Gaikwad · S. Chatterjee · P. Ray (✉)
Advanced Centre for Treatment, Research and Education in Cancer (ACTREC),
Tata Memorial Centre, Navi Mumbai, Maharashtra, India
e-mail: pray@actrec.gov.in

R. K. Singh
e-mail: rksingh@actrec.gov.in

S. M. Gaikwad
e-mail: smgaikwad@actrec.gov.in

S. Chatterjee
e-mail: srchatterjee@actrec.gov.in

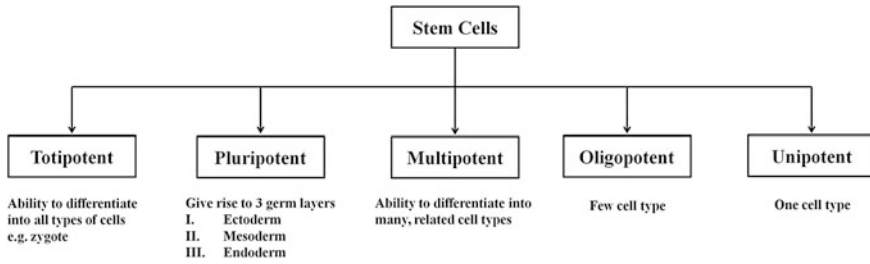


Fig. 2.1 Classification of stem cells: Depending upon the differentiation potential into different lineages, stem cells are categorized as totipotent, pluripotent, multipotent, oligopotent, and unipotent

4. **Oligopotent:** Oligopotent stem cells are able to differentiate into few cell types of specific lineages such as lymphoid stem cells that can be differentiated only into basophil, neutrophil, eosinophil, monocyte, and thrombocytes.
5. **Unipotent:** Unipotent stem cells can only differentiate into one particular cell type such as hepatoblasts forming hepatocytes.

Besides normal developmental functions in multicellular organisms, these mother cells are believed to be the holy grail of medical therapy with high promise for regenerative medicine.

2.2 Engineering of Stem Cells

Stem cells with their unique differentiation potential may act as therapeutic tool to cure diseases which are beyond treatment with routine drug therapy including genetic disorders. Since stem cells are able to generate functionally active healthy cells/tissues, ailments such as neurodegenerative diseases, cardiovascular diseases, liver failure, diabetes, and renal failure where unhealthy cells that are at fault may achieve significant alleviation by stem cell therapy (Fig. 2.2). Current medical practices have not adapted these new therapy regimes routinely as most of them are under clinical trials and not approved yet. The main challenges involve modulation of stem cells toward lineage-specific differentiation in vitro and in vivo, monitor the differentiation, and finally assess the success rate in clinic. Preliminary results appear to be quite promising, which are discussed in the following sections.

2.2.1 Human Embryonic Stem Cells

The unique potential of human ESCs (hESCs) to differentiate into three main germ layers and subsequent to any cell type of human body brought them into forefront of biomedical research with a caveat of forming teratoma in vivo during differentiation. However, recent progress in cell fate control, directed differentiation,

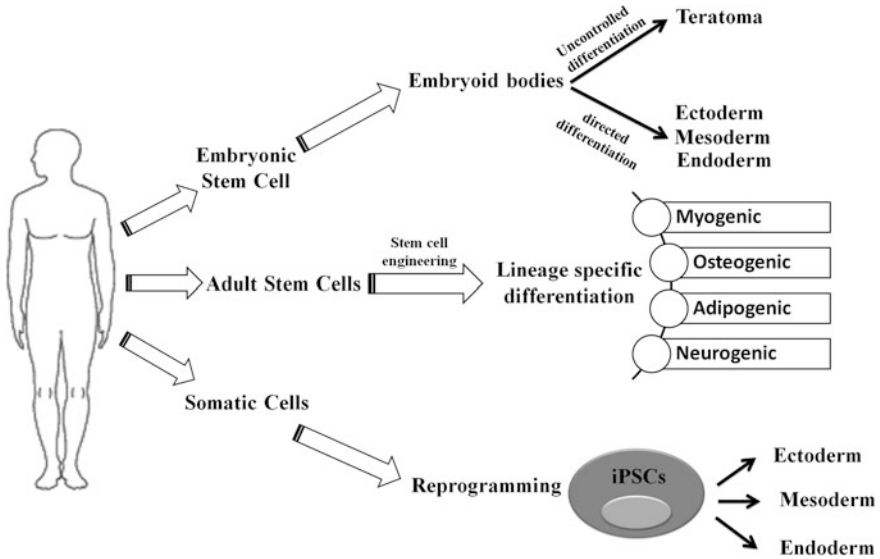


Fig. 2.2 Schematic representation of differentiation process of embryonic stem cell (ESC), adult stem cell (ASC), and induced pluripotent stem cells (iPSCs): While ESCs can generate three germ layers via directed differentiation, it may give rise to teratomas through uncontrolled differentiation in vivo. The ASCs have restricted potential to generate myogenic, osteogenic, adipogenic, and neurogenic lineages under specified conditions. In contrary to ESC and ASC that only differentiate toward specific lineage, iPSCs follow a dedifferentiation (from somatic cell) and then differentiation to germ-layer-specific cellular lineages

and tissue engineering crossed the boundaries of laboratory and extended to the arena of regenerative medicine. hESC lines are conventionally derived from the inner cell mass (ICM) of preimplantation-stage blastocysts, morula-stage embryos, or late-stage blastocysts and express pluripotency markers (transcription factors—Oct4, Sox2, Nanog; surface antigens—SSEA-4, SSEA-3; proteoglycans—TRA-1-60, TRA-1-81) [1]. To maintain the undifferentiated state, these cells are co-cultured with a support or feeder layer derived from mouse embryonic fibroblast (MEF) that provides all the essential growth factors [1]. The reported success rate for hESC derivation is highly variable, possibly due to variation in embryo quality and culture conditions. Major progress had happened in derivation, propagation, cryopreservation, and efficient passaging of hESCs. Since clinical application of hESCs critically depends on well-characterized growth and differentiation of stem cells, much effort was put in developing conditioned media that will enable feeder-free growth of ESC cells and eliminate animal products [2, 3]. The original culture system for the maintenance of hESC using MEF feeder cell layer support possesses risk of zoonosis transmitted by animal pathogens, potential activation of animal retroviruses, and possibility of immune rejection due to the presence of nonhuman sialic acid. Several approaches such as use of extracellular matrix (ECM) derived from MEF than living feeder cells, hESC-derived fibroblasts,

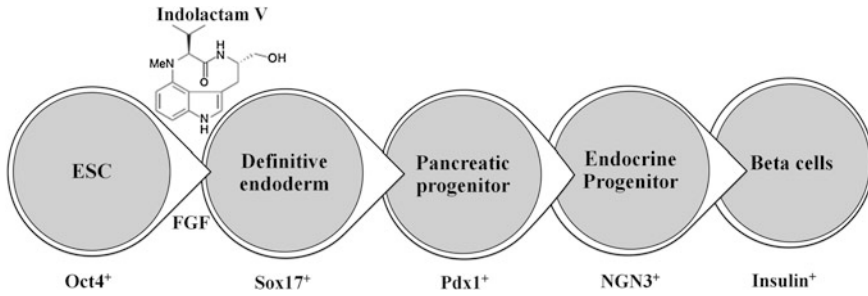


Fig. 2.3 In vitro differentiation of ESCs into insulin-producing beta-cells: Indolactam-V guides the differentiation of ESC into insulin-producing beta-cells via definitive endoderm, pancreatic progenitor, endocrine progenitor, and beta-cells

defined culture medium containing components solely derived from purified human material, MEF-conditioned Matrigel layer to establish and maintain clinical-grade hESCs cell lines are in progress [4]. However, these xeno-free and feeder-independent culture systems are costly and laborious and may lead to abnormal karyotype during long-term culture. Recently, Akopian et al. in conjunction with the Internal Stem Cell Initiative Consortium (ISCIC) compared several commercially available ESC culture media with Knockout Serum Replacer, FGF-2, and MEF cell layers for propagation of several hESC cell lines established in five different laboratories and showed that only mTeSR1 and STEMPRO were able to support most cell lines up to 10 passages [2].

The next major challenge for translational application of hESC is to direct their differentiation toward a specific cell lineage. The pioneer study by Itskovtz-eldor et al. [5] showed that hESC cells were capable of forming “embryoid bodies” (EB) comprised of three embryonic germ layers. In this study, hESCs were grown in suspension to induce their differentiation into EBs. Formation of in vitro EB required special cocktail of supplements and growth factors such as glutamine, beta-mercaptoethanol, nonessential amino acids, leukemia inhibitory factor (LIF), and basic fibroblast growth factor (bFGF). Under these conditions, majority of the cells remained in an undifferentiated state. For the formation of EBs, ES cells were transferred using either collagenase or trypsin/EDTA to plastic petri plates to allow aggregation and prevent adherence. About one million ES cells were plated in each of the 50-mm petri plates, and the hEBs were grown in the same culture medium without LIF and bFGF. The differentiation status of the human ES cells and EBs was determined by the expression pattern of several lineage-specific markers such as gamma-globin (hematopoietic cells), alpha-cardiac actin (myocardial cells), neurofilament (neuronal cells), and alpha-fetoprotein (endodermal cells).

Recently, Chen et al. performed a stepwise differentiation of ESCs to insulin-secreting functional beta-cells where ESCs first formed a definitive endoderm in the presence of indolactam-V and FGF, then Pdx1-expressing pancreatic progenitors, followed by the formation of endocrine progenitors and eventually insulin-producing beta-cells (Fig. 2.3) [6, 7].

Thus, strategic development of tissue-specific adult cells with fully functional potential from undifferentiated ES cells is possible and holds great promise for translational application.

Transplantation of hESC-derived cells into human patients:

The first clinical trial using hESC-derived retinal pigment epithelium (RPE) to establish the safety and tolerability in patients suffering from Stargardt's macular dystrophy and dry age-related macular degeneration was reported by Schwartz et al. [8]. They transplanted a low number of (5×10^4) RPE cells into subretinal space of patient's eye suffering from different forms of macular degeneration. Preoperative and postoperative ophthalmic examinations such as visual acuity, fluorescein angiography, optical coherence tomography, and visual field testing were performed for its validation (clinicaltrials.gov #NCT01345006 and #NCT01344993). This pilot study generated enthusiasm and hope for cell therapy trials in humans with ESCs, which was sidelined due to the adverse effect of generation of teratoma and ethical regulation. Since isolation of ESCs requires creation, treatment, and destruction of human embryos, hESC research always faces criticism and tight ethical regulation. The effort then moved toward using of adult stem cells, which in spite of limited differential potential has turned out to be a great source for cell therapy application.

2.2.2 Adult Stem Cells

Each adult organ in human body harbors a small population of stem cells that have the ability to maintain tissue homeostasis. These "adult stem cells" remain in quiescent or nondividing state until activated by any injury or disease, and they have limited ability to differentiate into organ/tissue-specific lineages. The common ones are HSCs, mesenchymal stem cells (MSCs), neuronal stem cells, umbilical stem cells, cardiac stem cells, retinal stem cells, and limbal stem cells that reside in their respective tissues. Unlike ES cells, adult stem cells do not require a feeder layer or supporting cells for their growth and thus easier to be engineered using different media, growth factors, and small molecules. They also do not pose a risk for developing teratoma and thus preferable in regenerative medicine and stem cell therapy. However, immune rejections of adult stem cells pose serious challenge in certain cases.

2.2.2.1 Hematopoietic Stem Cells

Pioneering studies in engineering of HSCs started in early 1990s at National Institute of Health for the treatment of patients suffering from adenosine deaminase (ADA) deficiency. These patients were treated with genetically modified CD34+ hematopoietic progenitors using retroviral vectors carrying different transgenes. Out of four successfully treated patients suffering from SCID, three

continued doing well up to 3.6 years after gene therapy, whereas one patient suffered serious adverse effect. During a routine checkup after 30 months of gene therapy, lymphocytosis consisting of a monoclonal population of $V_{\gamma}9/V_{\delta}1$, γ/δ T cells of mature phenotype was detected. One pro-viral integration site was found on chromosome 11 within the LMO-2 locus. This insertion leads to an aberrant expression of the LMO-2 transcript in the monoclonal T-cell population (characteristics of acute lymphoblastic leukemia) [9].

These adverse events have resulted in discontinuation of the use of such long terminal repeat (LTR)-driven gamma-retroviral vectors for the genetic manipulations of HSCs, but at the same time, it provided a major thrust for developing novel approaches. New and modified types of retroviral vector such as a “self-inactivating” (SIN) vector [10], lentiviral vectors [11], and lineage-restricted vectors [12] are now entering the clinic. These vectors might reduce the risk of reactivation of proto oncogenes after semi random integrations.

Thrombocytopenia, a deficiency in blood platelets, is a major consequence of several hematological malignancies and chemotherapy [13]. In vitro platelet production from hematopoietic stem and progenitor cells (HSPCs)-derived megakaryocytes (Mks) could augment the supply and elude problems associated with bacterial and viral contamination, as well as immune rejection. Panuganti et al. [14] using HSPCs developed a three-stage strategy for ex vivo expansion of high-ploidy megakaryocytic cells for large-scale platelet production (Fig. 2.4). The $CD34^+$ HSPCs culture was started in a cytokine cocktail at 5 % O_2 (pH 7.2). At day 5, cells were shifted to 20 % O_2 (pH 7.4) and maintained in 1 of the 17 cytokine cocktails (identified using a 2^4 factorial design of experiment method to evaluate the effects of interleukin (IL)-3, IL-6, IL-9, and high- or low-dose stem cell factor (SCF) in conjunction with thrombopoietin (Tpo) and IL-11) for expansion of mature Mks from progenitors. The combination of Tpo, high-dose SCF, IL-3, IL-9, and IL-11 produced maximum Mk expansion. These Mks when cultured in IMDM + 20 % BIT 9,500 gave rise to platelets with functional activity similar to that of fresh platelets from normal donors, as validated by basal tubulin distribution and the expression of surface markers.

Later Eric Lagasse showed in vivo differentiation of purified HSCs into hepatocytes in a mouse model of a lethal hereditary liver disease. As few as 50 adult HSCs injected intravenously had the capacity to reconstitute hematopoiesis and produce hepatocytes [15].

2.2.2.2 Mesenchymal Stem Cells

MSCs comprised of the major portion of adult stem cells were first identified by Friedenstein from adult bone marrow [16]. These MSCs were shown to differentiate into osteoblasts, chondrocytes, adipocytes, and hematopoietic supporting stroma when a single colony-forming unit-fibroblast (CFU-F) was transplanted in vivo [17].



Fig. 2.4 Production of platelet forming MK cells from HSCs: Schematic representation of step-by-step differentiation of HSCs into MK progenitor, mature MK, polyloid MK, and proplatelet forming MK under a series of cytokine cocktails with increasing pH and pO₂

MSCs can easily be cultured on petri dishes, and their lineages are determined by specific cell markers or enzyme assays. Researchers have shown that MSC can differentiate toward adipocytes or osteocytes *in vitro* when cultured in adipogenic or osteogenic induction media. During adipogenic induction, the differentiated adipocyte cells stain oil red O-positive indicating a lipid-laden adipocyte phenotype. Similarly, differentiated osteocytes show calcification when stained with alizarin red for calcium deposits [18]. However, determination of the lineage identity *in vivo* is quite challenging and active research is going on to identify lineage/differentiation-specific biomarkers. A tabulated form of lineage-specific differentiation of MSCs is shown in Fig. 2.5. MSCs can be isolated during routine surgical procedures such as tooth extraction, baby delivery (from placenta and cord blood), or through some special isolation techniques from adipose tissues or bone marrow. These cells can be directed toward lineage-specific differentiation even toward bone using synthetic or natural scaffolds to attain the proper three-dimensional structures. A wide variety of natural and synthetic materials are being tested as scaffolds for bone regeneration. Natural proteins such as collagen [19–21], fibrin [22], silk [23–25], and polysaccharides such as hyaluronic acid and chitosan [26–29] are optimal choices as bone scaffolds. These materials have the advantages of biocompatibility and biodegradability with limited toxicity and may be molded to maintain mechanical flexibility of human bones [22]. Recently, Hassani et al. showed the potential of human endometrial stem cells (EnSCs) to form urinary bladder epithelial cells (urothelium) on nanofibrous silk–collagen scaffolds for construction of the urinary bladder wall [30].

A major thrust area for stem cell therapy is acute myocardial infarction where disruptions of blood supply to the heart muscle cells lead to myocardial infarction or death of cardiomyocytes. Attempts to use stem cells to reduce infarct size and enhance cardiac function in animal models and patients have been exponentially increased in the last decade [31]. Bone marrow and fat tissues serve as the major source of MSCs for cardiovascular disease [32]. Differentiation of mouse BM-MSc into myogenic lineage *in vitro* has been reported using culture medium supplemented with 5-azacytidine at a concentration of 3 $\mu\text{mol/L}$ for 24 h [33]. The purified hMSCs from adult bone marrow engrafted in the myocardium appeared to differentiate into cardiomyocytes. The persistence of the engrafted hMSCs and their *in situ* differentiation in the small animal models paved the way to use these adult stem cells for human cellular cardiomyoplasty [34].

The enormous potential of various adult stem cells in curing diverse diseases encouraged researchers to explore their potential systematically either *in vitro* or

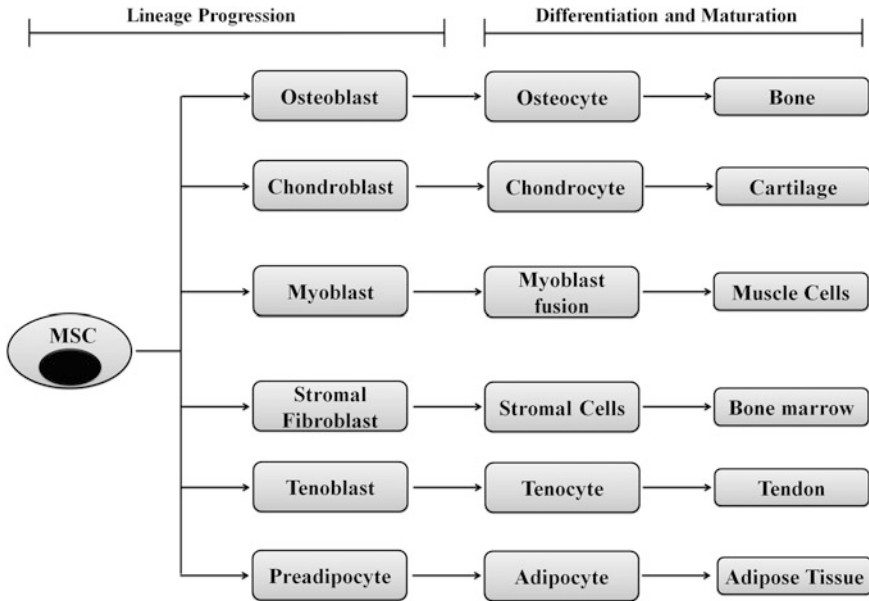


Fig. 2.5 Schematic representation showing differentiation of MSCs to various lineages: MSCs are like gold mines for the regenerative medicine since they could be directed toward any of the cell types through commitment, lineage progression, differentiation, and maturation. A single MSC can differentiate into bone, cartilage, muscle, bone marrow, tendon/ligament, adipose tissue, and connective tissue using appropriate developmental cues

in vivo condition. Some of these examples on MSC-based applications are mentioned in Table 2.1.

2.2.3 Induced Pluripotent Stem Cell

While stem cell therapy is emerging as a promising alternative for diseases and genetic disorders where drugs or gene therapy fail, it is limited by availability and stringent culture conditions. Exploiting epigenetic influence on phenotypic outcome, researchers have developed powerful genetic platforms for reversal of differentiated adult cells back to an embryonic state. Such reprogrammed cells are known as “induced pluripotent stem cells (iPSCs),” and the reprogramming strategies include “**therapeutic cloning**” and “**nuclear reprogramming.**” Both these strategies act through ectopic introduction of a small number of pluripotency-associated transcription factors into differentiated tissue-specific cells. iPSCs have the ability to differentiate into any of the three germ layers, ectoderm, mesoderm, and endoderm and the respective lineage-specific fully differentiated and functional cells/tissues.

Table 2.1 In vitro differentiation of adult stem cells to their respective lineages using small molecules, appropriate scaffold stiffness, cocktail of drugs and culture media

Cell type	Culture condition	Lineage	Reference
hESC	Ascorbic acid	Cardiac myocytes	[35]
BM-MSCs	Ascorbic acid, BMP2, dexamethasone, TGF-beta, and insulin	Osteogenic	[36]
	DMEM/10 % FBS + 0.5 μ M dexamethasone, 0.5 mM isobutyl-1-methylxanthine, and 10 μ g/ml insulin	Adipogenic	[37]
	DMEM/10 % FBS, 100 nM dexamethasone, 10 mM β -glycerophosphate, and 50 μ M ascorbic acid	Chondrogenic	[37]
	Laminin-1 without serum and differentiation growth factors, valproic acid, insulin, and butylated hydroxyanisole	Neurogenic	[36, 38]
Cardiac MSC	5 % FBS in 5 mM all-trans retinoic acid, 5 mM phenyl butyrate, and 200 mM diethylenetriamine/nitric oxide Transferrin, IL3, IL6, and VEGF	Myogenic	[36, 39]
MSC	1. Osteogenic differentiation on stiffness (45–49 kPa)	Osteogenic	[40]
	2. Myogenic differentiation (13–17 kPa)	Myogenic	
Limbal stem cell	Human amniotic membrane + human corneal epithelial cell medium + autologous serum	Limbal epithelium	[41]

The concept of iPSCs demonstrated long back by Sir John Gurdon when he successfully cloned a frog using intact nuclei from intestinal epithelium cells of [42]. Later, he showed that even nuclei from terminally differentiated adult cells (e.g., blood cells, skeletal muscle, and kidney cells) could generate *Xenopus* larvae with nuclear transfer [42]. Decades later, in 2006, Takahashi et al. demonstrated the ability of adult mouse fibroblasts to reprogram themselves into pluripotent stem cells by introduction of four key transcription factors (Oct3/4, Sox2, c-Myc, and Klf4) [43]. In November 2007, two independent studies were published simultaneously on successful transformation of differentiated human cells into pluripotent stem cells. While Takahashi et al. used retroviral delivery Oct3/4, Sox2, Klf4, and c-Myc combinations to induce pluripotency in human fibroblasts, Yu et al. delivered Oct4, Nanog, Sox2, and LIN28 by lentiviral transduction in hESC-derived mesenchymal cells to induce pluripotency [44, 45]. These groundbreaking experiments by Sir Gurdon and Yamanaka and his group were acknowledged by Nobel Prize award in 2010.

The most exciting and oversimplified part of iPSC generation is that a combination of only four transcription factors is able to reverse the differentiation process. To identify this main core of pluripotent factors, Yamanaka et al. (2006) evaluated twenty-four candidate genes and Thomson et al. (2007) screened sixteen transcription factors in an assay system in which the induction of the pluripotent state could be detected through the development of resistance to neomycin gene.

Both the groups identified Oct4, Sox2, and Nanog as the major pluripotency determinants. Though promising, the current iPSC reprogramming method experiences certain drawbacks such as

1. Requires host cell to be genetically engineered to express a drug resistance gene driven by a marker of pluripotency.
2. Requires viral-mediated integration of transgenes into the genome.
3. Reactivation of c-Myc in differentiated progeny of the induced ES-like cells is common and may result in tumor formation [46].

Thus, alternative approaches such as use of purified transcription factors, replacement of c-Myc, and strategy to avoid drug resistance selection method are being explored [47].

Their et al. [48] reported generation of TAT-modified cell permeate versions of recombinant Oct4 and Sox2 proteins (Oct4 TAT and Sox2 TAT), and later, Zhou et al. generated protein-piPSCs from murine embryonic fibroblasts. The deleterious effects of c-Myc could be circumvented by using *n-myc*, and host cell need not be drug resistant if using serum-free condition for iPSCs generation [49]. Recently, miRNA particularly the miR302/367 cluster was used to generate iPSCs from mouse and human somatic cells without adding the exogenous transcription factors. This miRNA-based reprogramming was found to be more efficient (twofold) than the standard Oct4/Sox2/Klf4/Myc-mediated reprogramming and ultimately overcome the deleterious effect of c-Myc reactivation [50].

Using the above-mentioned methods, one can now generate individual-specific iPSC cell lines to derive patient-specific progenitor cells and eliminate immune rejection crisis. Moreover, iPSC-based technology will facilitate the production of cell line panels that closely reflect the genetic diversity of a population enabling the discovery, development, and validation of therapies tailored for each individual. Till today, iPSCs has been generated from ten different species mouse, human, rhesus monkey, rat, dog, rabbit, horse, and bird [43, 44, 51–58] and into various lineages as listed in Table 2.2.

However, it still would be a long way for iPSCs to reach the clinic, which requires stringent and systematic validation of lineage-specific differentiation.

2.3 Monitoring of Stem Cells

Success of regenerative medicine and stem cell therapy depends on efficient *in vivo* differentiation of stem cells into specific lineages. Monitoring of engineered stem cells in cell cultures and *in vivo* before and after transplantation is a prerequisite for any stem cell application. It is also necessary to perform such studies directly in living subjects in a longitudinal, reliable, and accurate manner. Various microscopic techniques are extensively used for detail visualization of growth, differentiation, and functional validation of stem cells and iPSCs in cultures. Some of these techniques are also utilized for monitoring of the stem cells in

Table 2.2 In vitro differentiations of species-specific iPSCs toward various lineages in their respective culture condition

iPSCs	Culture condition	Lineage	Species	Reference
Murine	Valproic acid, zonisamide, and estradiol	Neural	Rat model of ALS	[59]
	ES medium without LIF for the first 4 days and day 5 onwards in differentiating medium supplemented with RPE-conditioned medium	RPE	Mouse	[60]
Human	Serum-free embryoid-body-like aggregates	Dopaminergic neurons	Mouse	[61]
	Keratinocyte growth factor and fibroblast growth factor	Hepatocyte-like cell	Human	[62, 63]
	Embryoid bodies EGF and bFGF	Erythropoietin Oligodendrocyte progenitors	Human Rat model	[64] [65]
Porcine	Activin A, bFGF, BMP-4, and oncostatin	Hepatic	Porcine	[66]

living subjects with high resolution. In parallel, macroscopic or noninvasive in vivo imaging modalities turn out to be indispensable for longitudinal monitoring of translational applications. Commonly used noninvasive imaging modalities for stem cell therapy are radioisotopic imaging (PET or positron emission tomography and SPECT or single-photon emission computed tomography), CT, ultrasound, magnetic resonance imaging (MRI), and optical imaging (bioluminescence and fluorescence). The next two sections will elaborate microscopic and macroscopic imaging of stem cells, an essential requirement for clinical application (Fig. 2.6).

2.3.1 Microscopic Techniques

For centuries, microscopy is an indispensable tool for visualizing dynamics of biomolecules in live cells. Optical microscopic techniques including conventional light (phase contrast) microscopy, fluorescence microscopy, confocal and multi-photon microscopy, intravital microscopy (IVM) have emerged as powerful tools for noninvasive monitoring and characterization of engineered stem cells and tissues [67].

2.3.1.1 Phase Contrast Microscopy

The age-old phase contrast microscopy is routinely required to monitor the culture conditions and kinetics of HSCs during their expansion for therapeutic use. Recently, these microscopes were improved with automated time-lapse system to

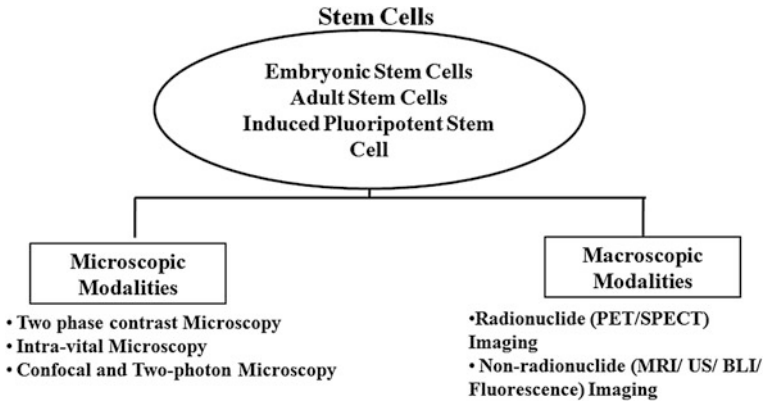


Fig. 2.6 Imaging modalities for in vitro and in vivo monitoring of stem cells: Naive or engineered stem cells in in vitro culture or transplanted in living subjects can be visualized noninvasively either by microscopic or by macroscopic imaging techniques. Microscopic modalities include phase contrast microscopy, intravital microscopy, confocal and two-photon microscopy, whereas macroscopic modalities include radionuclide-based (positron emission tomography or PET and single-photon emission computed tomography or SPECT) and nonradionuclide-based (MRI, ultrasonography imaging, bioluminescence, and fluorescence) imaging

capture the mitotic divisions of stem cells such as multipotent C3H10T1/2 mesenchymal and C2C12 myoblastic stem cells in real time [68, 69].

2.3.1.2 Fluorescence Microscopy

The complexity of the biological samples can be unraveled by labeling specimen with a fluorophore to achieve single-cell resolution when monitored with fluorescent microscopes. Stem cell labeling for fluorescence microscopy includes DNA binding dyes (such as Hoechst dye, BrdU, DAPI), nanoparticles and quantum dots, the later ones are also suitable for in vivo imaging. These labeling methods can only be used for short-term cell tracking due to loss of fluorophores through cell division. For long-term monitoring, tracking, engraftment and differentiation of stem cells, genetic manipulation with fluorescent proteins of different excitation and emission spectra (GFP and RFP and their mutants) is an ideal approach. These proteins can also be coupled to another protein to act as molecular reporters in living cells [70].

Tumbar et al. [71] developed a new strategy to identify multipotent epithelial stem cells (ESC) in their native environment by fluorescent labeling. These quiescent cells residing in the bulge of hair follicles can differentiate into various cell types upon stimulation. Transgenic mice expressing a H2B-GFP fusion protein under tetracycline-regulated keratinocyte-specific K5 promoter showed specific GFP expression only in rapidly dividing skin epithelium. Administration of doxycycline led to the loss of GFP expression in the keratinocytes but not in the

SCs due to their slow cycling and quiescent nature. The fluorescence microscopy of the sections from the keratinocytes clearly demonstrated the label-retaining capability of SC niche. This method was later used by many research groups to isolate and purify the label-retaining cells (LRCs) or SCs for further characterization [70, 71].

Fluorescent probes with emission wavelengths in the near-infrared (NIR) spectra ($\sim 700\text{--}800$ nm) enhance the feasibility of tracking cells in vitro and in small animal models due to high depth penetration and lower absorption and scattering [72]. Several dyes including NIR fluorochrome DiD, a lipophilic dye that binds to the cell membrane, have proven effective for both in vitro labeling of MSCs and in vivo cell tracking with optical imaging [73, 74].

As described in Sect. 2.2.3, direct reprogramming of somatic cells into iPSCs can be achieved by overexpression of four reprogramming factors (RFs). A dynamic fluorescence microscopy study of iPSCs expressing Nanog-GFP suggests that the number of cell divisions is a key parameter of driving epigenetic reprogramming to pluripotency [75]. Similarly, fluorescence microscopy combined with long-term time-lapse imaging and single-cell tracking revealed the “birth” of pluripotent cells and early iPSC clusters from murine embryonic fibroblasts transduced with multicistronic lentiviral vectors carrying RFs (Klf4, Sox2, Oct4, Myc) tagged with different fluorescence proteins (GFP, RFP, YFP) [76].

2.3.1.3 Confocal Microscopy and Multiphoton Microscopy

A major drawback of fluorescence microscopy is that irrespective of the vertical focusing of the specimen, illumination causes the entire specimen to fluoresce and is unable to produce tomographic images. Confocal microscopy, multiphoton microscopy, and intravital microscopy are competent of generating tomographic imaging essential for localizing fluorescent targets in three-dimensional space [77–79].

In a recent study, transgenic ES cells co-expressing myristoylated RFP (labels plasma membrane) and histone H2B-GFP (labels active chromatin) fusions were introduced into a nontransgenic embryo and then dissected out of the maternal uterus at mid-gestation period and cultured ex utero on the stage of a confocal microscope. These labeled ES cells produced information on dynamic changes in morphology and chromatin distribution that occurred during mitotic progression [80]. The powerful confocal/two-photon hybrid microscopy can also track the clonal history of HSPCs expressing various fluorescence proteins noninvasively in intact tissues, including bone marrow with long-term monitoring after transplantation [81].

2.3.1.4 Intravital Microscopy

Intravital microscope (IVM) can be referred as “microscope for living subjects,” which enables single-cell imaging in thin sections of live tissues [82]. In a remarkable study, Rompolas et al. [83] monitored the regeneration of hair follicles temporarily in a transgenic mouse expressing H2B-GFP driven by keratin 14 promoter. They demonstrated that stem cells are quiescent during initial stages of hair regeneration and their progeny is actively dividing within follicular organization [83].

In another elegant study, Takayama et al. [84, 85] imaged the functioning of human iPSC-derived platelets during thrombus formation by intravital microscopy in live mice. The study demonstrated that transient expression of c-Myc was critical for efficient platelet generation from human iPSCs, which were capable of mediating hemostasis and thrombosis in a laser-induced vessel wall injury.

2.3.2 Macroscopic Imaging Modalities

Though microscopic imaging techniques can generate critical information, they are restricted at cellular level and do not depict the kinetics, distribution, and location of in vivo differentiation of stem cells in a living subject. Even IVM requires an artificially created “window chamber” or “tissue flap” at the body surface and is not applicable for deep tissue imaging. Recent developments in macroscopic or in vivo imaging modalities enable the “visualization, characterization, and measurement of biological processes at the molecular and cellular levels in humans and other living systems.” Along with other applications, these modalities are now widely used for imaging stem cell delivery, migration and localization, cell viability, and therapeutic effects in various diseases [86–88].

The Six commonly used modalities for imaging stem cell therapy are ultrasound, CT, SPECT, PET, MRI, and optical. For many instances, multimodality approaches that can collectively assess different parameters specific for each modality are gaining popularity. For imaging the stem cells in vivo, it is required to label the cells with an appropriate probe. The two important methods for labeling cells are as follows:

- (a) Direct labeling such as with magnetic resonance contrast agents, radionuclides, fluorophores, and nanoparticles.
- (b) Indirect labeling with reporter genes.

Direct labeling of cells poses limitation to long-term monitoring since the signal gets diminished by dilution or loss of labeling agents via cell division or differentiation. This limitation can be overcome with “indirect-labeling strategy” where cells are exogenously labeled with reporter genes (bioluminescence, fluorescence, PET, SPECT, or MR reporters) and then implanted for imaging. Indirect labeling requires genetic manipulation of the cells that are often not possible to follow in

Table 2.3 Stem cell therapy studies using PET imaging approach in human

Stem cells	Radionuclides	Applications	Reference
HSCs	^{18}F -FDG	Homing and tissue distribution of intracoronary injected peripheral HSCs	[106]
MSCs	^{18}F -FDG	Functional efficacy of MSC therapy in patients with multiple system atrophy	[107]
Cord blood stem cells (CBSC)	^{18}F -FDG	CBSC transplant in patients for local engraftment and reconstitution of haematopoiesis	[108]
CD33 + bone marrow stem cells	^{13}N -ammonia and ^{18}F -FDG	Improvement in the myocardial perfusion in patients AMI	[109]
HSCs	^{18}F -FDG	HSC therapy for osteosarcoma	[110]

clinics [86–90]. However, both the strategies have own advantages and disadvantages and should be implemented by experimental need.

2.3.2.1 Radionuclide Imaging

Majority of the radionuclide imaging techniques follow direct-labeling strategies and are extensively used in human studies. Both radionuclide imaging techniques, i.e., PET and SPECT, have picomolar sensitivity and high tissue penetration with least attenuation and are tomographic in nature.

Positron Emission Tomography (PET)

In PET, two 180° apart high-energy (511 keV) gamma rays produced by the annihilation of a positron (from the radioactive atom) with a neighboring tissue electron are captured by detectors and produce a three-dimensional image of functional processes in living subjects. The commonly used positron-emitting isotopes are ^{11}C , ^{13}N , ^{15}O , ^{124}I , ^{64}Cu , and ^{18}F . The widely used PET tracers in clinic are 2-deoxy-2- ^{18}F fluoro-D-glucose (^{18}F -FDG, which images glucose metabolism) and 3-deoxy-3- ^{18}F fluorothymidine (^{18}F -FLT, which images cell proliferation). Several studies have elaborated the use of PET imaging approach for the stem cells therapy in various human disorders [91–100] (Table 2.3). Some studies have also used small animal models for studying the role of human stem cells in homing, engraftment, and survival through PET imaging [101–105].

Herpes simplex virus type 1 thymidine kinase (HSV-tk) is the most widely used reporter gene for PET imaging for preclinical as well as clinical studies [90]. ^{18}F Fluorine-labeled FIAU (2'-fluoro-2'-deoxy- β -D-arabinofuranosyl-5-iodouracil) and FHBG (9-(4-fluoro-3-hydroxy-methyl-butyl) guanine) are the two common reporter probes used for HSV1-tk. This reporter gene–reporter probe approach has been used to monitor viability of stem cells after transplantation in myocardium,

tracking, and survival of autologous MSCs in pig myocardium and tumor stroma [111, 112].

Recently, human sodium iodide symporter (hNIS) gene has emerged as an important PET reporter gene that could be used for SPECT imaging as well. Uptake of ^{124}I was seen in areas deficit of myocardial perfusion in rat myocardium injected with MSCs expressing hNIS gene by PET imaging [113]. NIS-mediated ^{124}I PET imaging was also used to monitor the delivery and survival of endothelial progenitor cells (EPCs) after transplantation into the rat heart [114]. Some other promising PET reporter genes for stem cell therapy are dopamine 2-like receptor (D2R), human somatostatin receptor subtype 2 (hSSTR2), human norepinephrine transporter (hNET), neurotensin receptors, and cytosine deaminase [115].

Stem cell therapy is often benefited from multimodality imaging approaches. In an elegant study, Cao et al. [116] monitored the survival, proliferation, and migration of ESCs expressing a triple fusion (TF) reporter comprised of a fluorescence (mrfp), a bioluminescence (fluc), and a PET reporter (ttk) gene after transplantation into rat myocardium for 40 days (Fig. 2.7). Some studies have used bifusion reporters such as tk-GFP to monitor neuronal stem cell, therapy in treatment of malignant glioma [117].

Single-Photon Emission Computed Tomography (SPECT)

In contrast to PET imaging, SPECT imaging is a log-order less sensitive technique due to the presence of collimators (to restrict detection of nonspecific random gamma rays) between the detectors. The widely used SPECT radionuclides are $^{99\text{m}}\text{Tc}$, ^{111}In , and ^{123}I . SPECT imaging probes are extensively applied to image in vivo trafficking and biodistribution of MSCs in myocardial injuries in large animal models [118–120]. Some human clinical studies have also used ^{111}In -oxine to track bone marrow stem cells or pro-angiogenic progenitor cells in acute and chronic myocardial injuries. Goussetis et al. [121] performed SPECT imaging with $^{99\text{m}}\text{Tc}$ hexamethylpropyleneamine-oxime-labeled autologous $\text{CD133}^-\text{CD34}^+$ bone marrow progenitor cells transplanted in patients with ischemic cardiomyopathy. Higher uptake of radioactivity was observed in the infarcted area of the heart, suggesting preferential migration and retention of stem cells in the chronic ischemic myocardium.

Both HSV1-tk and hNIS genes can serve as SPECT reporter genes in combination with probes labeled with SPECT isotopes ($^{123}\text{I}/^{125}\text{I}$ -labeled probes FIAU or $^{99\text{m}}\text{Tc}$) [113, 122]. Table 2.4 summarizes various studies involved in stem cell visualization by SPECT in human. Studies related to small animal models can be found in other articles [123–125].

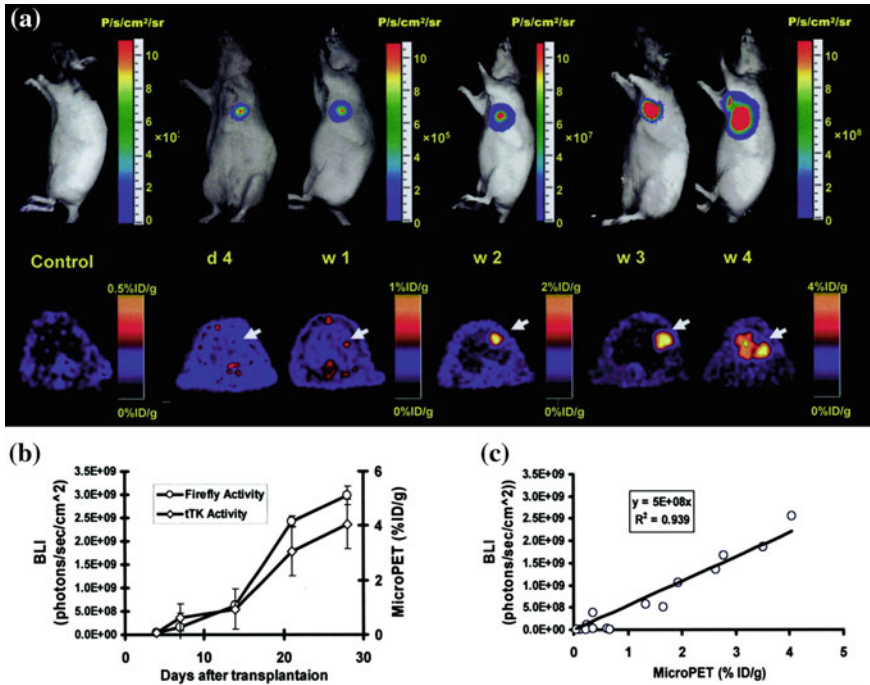


Fig. 2.7 Multimodality imaging for long-term monitoring of mouse embryonic stem cells expressing a triple fusion reporter (ES-TF): **a** Representative images of animal injected with ES-TF in infarcted rat heart showed significant increase in bioluminescence (top) and PET (bottom) signals from day 4, week 1, week 2, week 3, and week 4. **b** Quantification of imaging signals showed a drastic increase in luciferase and thymidine kinase activities from week 2 to week 4. **c** Quantification of cell signals showed a robust in vivo correlation between bioluminescence and PET imaging ($r^2 = 0.92$). (Reprinted from Cao et al. [116] with permission)

2.3.2.2 Optical Imaging

Optical imaging has emerged as an established tool to assess efficacy and treatment outcomes for cell-based therapeutics in preclinical models. Two optical imaging methods, bioluminescence, and fluorescence are extensively used in stem cell research.

Fluorescence Imaging (FLI)

Fluorescence imaging is the only modality that directly translates the finding/observation from live cell to live animals. However, due to inherent autofluorescence and signal attenuation issues, whole-body FLI has not been extensively used for stem cell therapy. Tzukerman et al. [133] applied fluorescence imaging to demonstrate the growth and invasiveness of cancer cells in the niche of teratomas

Table 2.4 Stem cell therapy studies using SPECT imaging approach in human

Stem cell types	Radionuclides	Applications	Reference
MSCs	¹¹¹ In-tropolone	Delivery, tracking, and differentiation of stem cells	[126]
BM-MSCs	¹¹¹ In-oxide	Monitoring blood flow and bone metabolism after cell transplantation	[127]
CD34 ⁺ stem cells	^{99m} Tc hexamethylpropyleneamine oxime	5-year follow-up of CD34 ⁺ stem cell in nonischemic cardiomyopathy patients	[128]
MSCs	^{99m} Tc-pertechnetate	Demonstrate the feasibility of MSCs as virus carriers to ovarian tumors in phase I clinical trails	[129]
BM-MSCs	^{99m} Tc-sestamibi	Improvement in cardiac function after BMMSCs transplantation in patients with acute myocardial infarction	[130]
Autologous CD34 ⁺ cells	^{99m} Tc-exametazime	Homing of transplanted cells to injured myocardium	[131]
BM-HSCs	^{99m} Tc	Repair efficacy for ischemic heart	[132]

derived from hESCs. Tao et al. [134] reported that e-GFP is a better probe than DS-Red protein for long-term monitoring of HSCs.

Other than reporter gene strategy, FLI can be performed with exogenous contrast agents such as quantum dots, nanoparticles, and fluorescent dyes that emit light in the visible, red, and near-infrared region. Inorganic fluorescent semiconductor nanocrystals (quantum dots, QDs) are rapidly replacing organic fluorophores like indocyanine green with NIR emission due to their ability for multiplex imaging [135]. Lin et al. [136] for the first time demonstrated the *in vivo* multiplex imaging of mouse ES cells labeled with six quantum dots (QDs). The six emission spectra from all the six QDs were recorded with a single excitation light source. These QDs are emerging as a promising tool for tracking stem cells within deep tissues noninvasively *in vivo*. Human ESC-derived cardiomyocytes (hESCs-CM) were also labeled with indocyanine green for noninvasive tracking by fluorescent imaging [137].

Bioluminescence Imaging (BLI)

Among all the functional imaging modalities, BLI acts only through reporter gene–reporter probe strategy and has been extensively used for monitoring stem cell therapy. Though restricted to small animals, bioluminescence imaging

generates essential clues on differentiation, behavior, and viability of stem cells after transplanted in small animals, assisting to predict the behavior of stem cell therapy in humans. A glimpse of the large number of BLI-based studies is summarized in Table 2.5, and a few important studies are discussed.

Tsuji et al. [138], using iPSC-derived neurospheres in a mouse model of spinal cord injury, demonstrated that iPSCs can “safely” promote locomotor function recovery in injured mouse models with BLI. They observed that these cells can even differentiate into trilineage neural cells in the injured spinal cord. In another study, Daadi et al. [139] investigated the efficacy of human neural stem cells (hNSCs) derived from human ES cells to repair brain injury. In this study, rats with neonatal HI (hypoxic-ischemic) brain injury were implanted with hNSCs expressing luciferase and their survival was monitored using BLI. The study suggests that hNSCs transplants are able to enhance brain injury repair in response to HI brain injury and that the location and survival can be monitored noninvasively. Further, the deleterious effect of ESC differentiation on teratomas was spatially and temporally monitored by Cao et al. [116] with high sensitivity, which was not possible with other imaging modalities (Fig. 2.7).

2.3.2.3 Magnetic Resonance Imaging

MRI is the sole imaging modality that generates both functional information and anatomical information. Among all the other noninvasive imaging techniques, MRI has the highest spatial resolution ($\sim 100 \mu\text{m}$) and thus is the most preferred strategy for stem cell imaging. Since endogenous molecules (such as H_2 atoms) do not generate enough contrast to achieve that high resolution, supra-paramagnetic iron oxide (SPIOs) and paramagnetic nanoparticles are often used to label the cells to enhance image contrast. However, SPIO-based MRI is not well suited for long-term monitoring since SPIOs get diluted with cell proliferation and are often engulfed by macrophages [86]. Chelated gadolinium (Gd^{3+}), manganese (Mn^{2+}), and iron (Fe^{3+}) could also act as contrast agents. Recently, certain metal-ion-based enzymes namely metalloproteinase, transferrin, ferritin, tyrosinase are being evaluated as reporter genes in MR imaging [87].

In contrast to optical imaging where smaller animals such as mouse and rat are preferred as model systems, MR-based stem cell imaging is tested both in smaller and larger animals and in humans. The first autologous transplantation of iron oxide-labeled iPSCs reprogrammed from canine adipose stromal cells and fibroblasts showed repair of infarcted myocardium and hindlimb ischemia by MR imaging in adult mongrel dogs [158]. Similarly, an enhanced effect of combining human cardiac stem cells and bone marrow MSCs to reduce infarct size and restore cardiac function after myocardial infarction was followed by MR imaging in a Yorkshire swine model [159].

To overcome the shortcoming of the contrast agents, reporter-gene-based strategies are also being employed in stem cell imaging by MR. Liu et al. [160] showed that engraftment of transgenic mouse ESCs expressing human ferritin

Table 2.5 Studies involving BLI approach for stem cell therapy

Stem cell types	Origin	Applications	Reference
HSCs	Human	Longitudinal monitoring of human HSC engraftment	[140]
Neural progenitor cells	Murine	Migratory capability of NPCs and their preferential accumulation in brain tumors on CNS	[141]
Embryonic rat H9C2 cardiomyoblast	Rat	Location, magnitude, and survival duration of embryonic cardiomyoblast	[142]
ESC-derived insulin-producing cells (IPCs)	Murine	Novel source of unlimited cells for transplantation to treat type 1	[143]
ESCs	Murine	Longitudinal monitoring and tumorigenic potential of ESCs	[144]
	Human	Longitudinal monitoring of differentiation in the tumors	[145]
	Human	Preferential differentiation of hESC-derived CD34 ⁺ cells into endothelial cells	[146]
	Mouse	Longitudinal monitoring of implanted ESCs in rat corpus cavernosum	[147]
	Human	Serial imaging of human embryonic stem cell engraftment and teratoma formation in murine model	[122]
Neural stem cells	Mouse	Improved engraftment of neural stem cells	[148]
MSCs	Mouse	Migration and engraftment of transplanted cell into primary breast tumor sites	[149]
		Monitoring survival of transplanted MSCs injected intramyocardially	[150]
		Homing to kidneys in mice with ischemia- and reperfusion-induced acute kidney injury (AKI)	[151]
MSCs expressing bone morphogenetic protein 2 (BMP2)	Human	Bone and cartilage repair in articular fractures	[152]
Umbilical cord blood HSCs	Human	Cell engraftment of HSCs after bone marrow transplantation in nonobese diabetic/SCID mice	[153]
BM-MSCs	Human	Monitoring inhibition and eradication of glioma with BM-MSCs labeled with Delta-24-RGD	[154]
MSCs	Murine	Localization, survival, proliferation, and differentiation of MSCs to osteoblasts and adipocytes	[155]
iPSCs	Human and Murine	Long-term tracking of iPSCs in the gastrocnemius muscle of recipient mice monitored	[156]
ESCs-derived cardiomyocytes (CM)	Murine	Tracking of immature (ESCs-CM) demonstrate longer survival than the mature CM	[157]

heavy chain (FTH) resulted in increased cellular iron uptake and MRI contrast and did not interfere with stem cell pluripotency, neural differentiation, and teratoma formation.

Stem cell therapy has immense potential to treat neurodegenerative diseases, traumatic injury, and stroke. However, risk is associated with intracranial surgery used to deliver the cells to the brain. In some studies, MRI was combined with ultrasound modality to obtain higher sensitivity and resolution. For targeted delivery of neural stem cells to brain, Burgess et al. [161] employed MRI-guided focused ultrasound (MRIgFUS) imaging to monitor noninvasive delivery of stem cells from the blood to the brain by opening the blood–brain barrier at specific regions (striatum and hippocampus) in rat brain. Entry of cells crossing the BBB to brain was verified by MRI. The study also demonstrated that these stem cells started expressing double cortin, a marker of immature neurons, indicating occurrence of *in vivo* differentiation. An excellent review by Qiu et al. [162] described many such MRI-based studies for stem cell therapy such as migration and homing of hematopoietic stem–progenitor cells to injured arteries and atherosclerosis, stem–progenitor-cell-mediated vascular gene therapy, and several novel techniques for magnetic labeling of stem or progenitor cells. Table 2.6 describes some of the MRI-based stem cell tracking studies in living subjects.

2.3.2.4 Ultrasound Imaging

Ultrasound imaging (US) utilizes the interaction of sound waves with living tissue to produce an anatomical image. Since US imaging is the only modality that generates real-time images during scanning, several investigators are using this technology for longitudinal monitoring of stem-cell-mediated tissue repair and vessel formation. One such application was shown by Watts et al. [173] where equine fetal-derived embryonic-like stem cells (fdESCs) expressing Oct 4, Nanog, SSEA-4, TRA-1-60, TRA-1-81 stem cell markers and telomerase were implanted in equine flexor tendonitis model through intralesional injection. Thoroughbred horses ($n = 8$) were induced with tendon injury in the mid-metacarpal region of the superficial digital flexor tendon and injected with fdESCs, and serial ultrasound examinations were performed. After 8 weeks, significant improvement in tissue architecture, tendon size, tendon lesion size, and tendon linear fiber pattern was found by US imaging, which was further corroborated by tissue histology.

To enhance the contrast of signal intensity of US imaging, microbubbles (MBs) tagged with nanoparticles, antibodies, or other signatures are being developed. Such an approach was demonstrated by Leng et al. [174] where biocompatible polymer MBs were internalized by human bone-marrow-derived MSCs (MB-MSCs) and used for US imaging. Nude mice injected with MSCs and MB-MSCs in the hindlimb region were temporally imaged by ultrasound, which showed that the MB-MSCs are acoustically active *in vivo* and can be imaged for at least 4 h from the time of injection [174].

Table 2.6 MRI-based stem cell tracking studies in living subjects

Stem cells	Contrast agents (CAs)/reporter genes	Applications	Reference
hESCs	SPIO	Comparison between two CAs to monitor stem cell therapy for failing heart	[163]
hESCs	MnCl ₂ SPIO	Long-term monitoring of transplanted cells in mouse myocardial infarction model	[164]
hESC-derived neural stem cells	SPIO	Long-term monitoring of differentiation in rat brain injury model	[165]
Rat MSCs	Gadolinium–diethylene triamine penta-acetic acid (Gd-DTPA)	Transplanted cells are used to track spinal cord injury	[166]
ESCs/MSCs	Iron oxide nanoparticles	Evaluation of migration and fate of transplanted cells in rat central nervous system (CNS)	[167]
Pig cardiospheres (Cs): clusters of cardiac stem cells	Ferritin	In vivo tracking of stem cells in rat model of myocardial infarction	[168]
BM-MSCs	Gd-DTPA	Improvement in cardiac function in swine myocardial infarction model	[169]
Canine adipose-derived MSCs	FeO	Engraftment and migration of MSCs	[170]
Canine-MSCs	SPIO	Tracking of MSCs delivered intraarterially	[171]
Swine BM-derived stem progenitor cells	0.032-inch MR imaging-guidewire (MRIG)	Monitoring cell-based arterial repair	[172]

2.3.2.5 Computed Tomography

X-ray CT is a purely anatomical imaging modality, which generates high-resolution three-dimensional anatomical images. CT imaging, however, can be applied to monitor degree of differentiation of embryonic or adult stem cells. Arpornmaeklong et al. [175] demonstrated that undifferentiated hESCs can be cultivated in osteogenic medium to increase the quantity of osteoblast-like cells (hESCs-OS). These hESCs-OS when transplanted in mice with calvarial defects showed limited mineralization of tissue in central region, margin of defect, and calvarial bone adjacent to the defect site by micro-CT imaging. Image analysis revealed that bone mineral density of the new bone in the cranial defect generated by the transplanted cells at passage 5 was significantly higher than that in the controls (without cell implantation). However, CT being purely anatomical imaging modality has limited use in measurement and monitoring of stem cell differentiation. Integrated PET-CT and SPECT-CT are better approaches for such evaluations.

2.4 Applications of Stem Cells

The previous two sections describe the advances in stem cell research and monitoring the outcome in live cells as well as in live animals. The most challenging phase is to get “biological solutions to biological diseases” with an aim to achieve success in curing patients. To estimate the extent of success, a large number of clinical trials are ongoing with stem cell transplantation in various pathological conditions.

In this section, we will provide an overview of these studies categorized by the disease types based on the information obtained from trials mostly initiated by the National Institute of Health (Figs. 2.8 and 2.9). Due to overwhelming number of animal studies, we have limited this section only to human trials. The animal studies can be found in other excellent reviews [176, 177].

2.4.1 Stem Cells and Neurodegenerative Diseases

Two percent of worldwide death is contributed by neurodegenerative diseases such as Alzheimer’s and Parkinson’s, and medical science is still unable to cure these diseases. Recent progress in stem cell science showed that functional neuronal replacement is possible, raising the hope for ultimate cure for these dreadful diseases. The idea of stem-cell-based therapy for neurodegenerative diseases is not new. The first neuronal transplantation was reported in 1890 by Thompson who made a very bold attempt to transplant cortical tissue from a cat into the brain of a dog [178]. This encouraged scientists to consider cell transplantation to treat deadly neurodegenerative diseases such as Parkinson’s and Alzheimer’s.

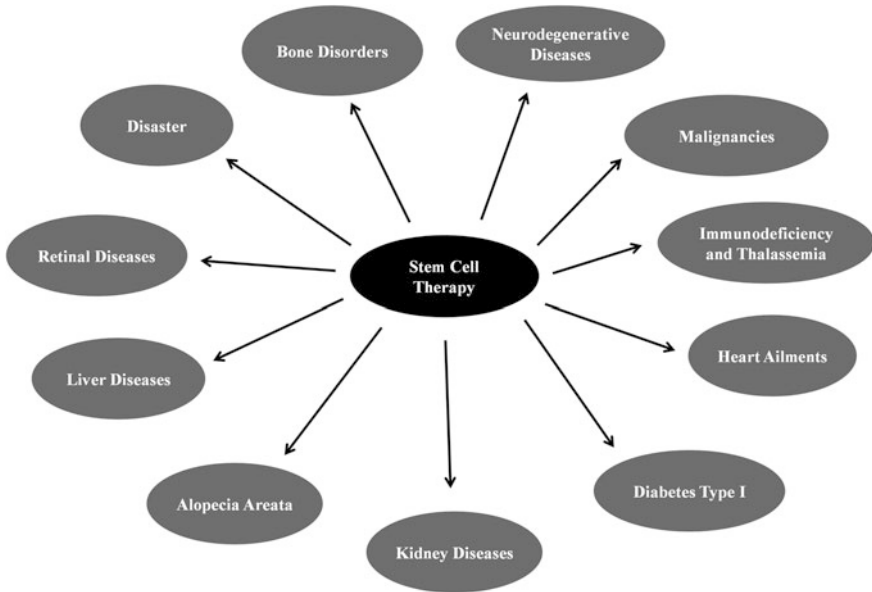


Fig. 2.8 Diseases treated with stem cells: Stem cells are emerging as an alternate or sole option for treating a wide spectrum of diseases such as neurodegenerative diseases, immune disorders, diabetes type 1, cardiac ailments, kidney disease, malignancies, liver disease, bone and retinal disorders. At certain times, health damages caused by disasters could also be managed with stem cell therapy

Earlier, the Parkinson's disease (PD) patients received a transplant of the adrenal medullary tissue, which did not result in significant improvement. Later, transplantation with fetal tissue and human embryonic neural tissue for cell-based therapy was also explored. However, serious ethical issues with these tissue replacements led to search for the alternate cell source. One such cell source was found to be the neural stem cells [179]. Clinical trials with transplantation of human fetal mesencephalic tissues rich in neuronal stem cells have produced satisfactory results. In a trial by Freed et al. [180], 40 patients between the age of 35–75 years were divided into transplantation group (mesencephalic tissue was implanted bilaterally into the putamen) and sham surgery group (tissue implanted by drilling a hole into the brain but not disturbing the dura mater) and received mesencephalic tissue transplantation. At the end of the surgery, younger patients in the transplantation group showed better signs of improvement as compared to the sham surgery, while significant improvement was seen in the group of the older patients. A small trial by Venketaramana et al. [181] generated a lot of hope for the PD patients. In this pilot study, seven advanced-stage PD patients between the age of 22 and 65 years were subjected to bone-marrow-derived MSC transplantation extracted from the iliac crest. Patients were reported to show improvement and a reduction in the levels of L-DOPA. Spinal muscular dystrophy is a dreadful

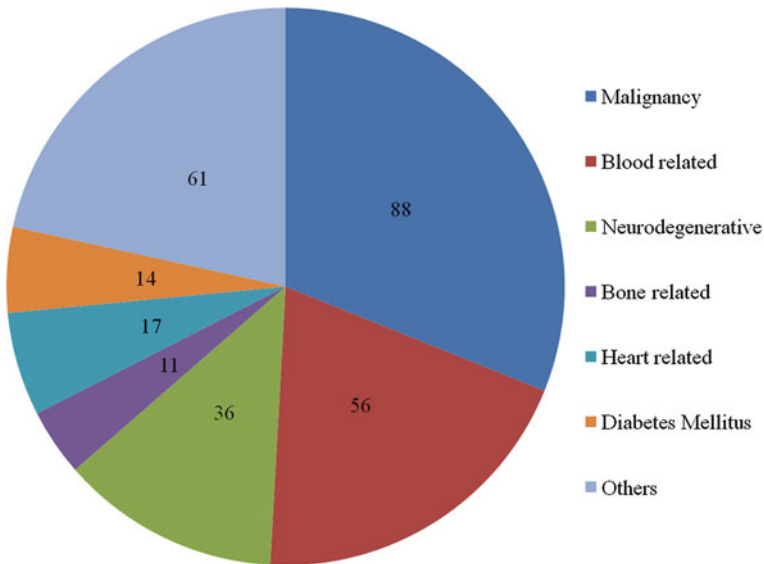


Fig. 2.9 Clinical trials with stem cells: A graphical representation of various disease-specific trials undertaken by US government around the world involving stem-cell-mediated therapy ($n = 283$). (Source Clinicaltrials.gov, accessed: 28/3/2013)

neurodegenerative disease characterized by the loss of motor neurons in the spinal cord leading to overall muscle weakness. Remarkable results were obtained with stem cells in animal models, but clinical trials are yet to be initiated [182].

Like PD, MSCs are also used as a powerful therapy regime against Huntington's disease as they can enhance tissue repair by secreting various neurotrophic factors leading to neural growth, inhibition of apoptosis, and regulation of inflammation. Bachoud-Lévi AC et al. (2006) have shown that 3 out of 5 patients showed some degree of improvement with fetal neural grafts, but the other two had no signs of benefit. This trial proved that such transplantations provide relief for a short period of time but offers no permanent cure [183]. Many of the clinical trials for Huntington's disease have shown mixed results. Gaura et al. [184] transplanted fetal striatal neuroblasts (progenitor cells derived from the neural stem cells) as allograft in five Huntington's disease patients. The patients were assessed based on the neural hypometabolism and glucose metabolism rate in the brain. While two patients showed drastic improvement, patient 3 actually showed a slight decline in condition. Patient 4 and patient 5 deteriorated during course of the experiment [184].

In amyotrophic lateral sclerosis (ALS), upper and lower motor neurons gradually degenerate and lead to muscular atrophy and severe weakness. In a clinical trial by Mazzini et al. [185, 186], autologous MSCs were transplanted into the spinal cord of seven ALS patients. In the follow-up of 2 years, no permanent clinical side effects or change in the spinal cord was reported as assessed by MRI.

A relatively slow linear decline of the forced vital capacity was seen in four out of seven patients, indicating that MSCs might have the ability to repair tissue damage and prolong the survival of the patients. A similar exercise was performed by Mazzini et al. [187] with 10 patients. The results obtained indicated that stem cell therapy could be extremely beneficial for ALS patients. Thus, stem cell therapy upon proper guidance and validation is finally bringing hope for patients with neurodegenerative diseases such as ALS, chronic spinal injuries, advanced PD [188].

2.4.2 Stem Cells and Kidney Diseases

Both human ES cells and allogenic/autologous HSC transplantations are used to correct kidney disorders in clinics. Trivedi et al. [189, 190] was the first group to report their clinical experience with 24 patients. In their experiment, they introduced unfractionated HSCs into the thymus and bone marrow before surgery and infused them peripherally after transplantation. The aim of the study was to design strategy to enhance tolerance to cadaver renal transplantation and thus prevent graft rejection. Patients were divided into two groups of which group-A received infusion of the concentrated marrow before and after surgery and group-B underwent direct transplantation. Since this procedure did not yield any graft rejection, the study continued, and by 2011, more than 1,000 transplantations were performed with further modifications.

2.4.3 Stem Cells in Immunodeficiency and Thalassemia

Life-threatening immunodeficiency can be induced either by drugs or by malfunction of immune system for which cell-based gene transfer is a good treatment option. Unfortunately, several such trials are reported with little benefit. Thrasher et al. [191, 192] reported a trial in which engineered CD34⁺ bone marrow cells failed to produce any effect in the subjects. Gaspar et al. [192] treated 10 patients with autologous CD34⁺HSPCs transduced with (gamma c) γc retroviral vectors. Follow-up of 80 months showed all patients to be alive with functional T cells, though mild pulmonary infections in most patients and development of acute T-cell lymphoblastic leukemia in one patient were seen. Another strikingly similar attempt was made by Hacein-Bey-Abina et al. [193] where CD34⁺ cells isolated from five X-SCID patients were transduced with a retroviral vector expressing gamma c(γc) transgene and then transplanted back in patients. The follow-up data for four out of five patients were quite promising. Their T cells and the natural killer cells carrying the transduced gene appeared normal in number, in phenotype, and in proliferative response for at least 2 years after therapy.

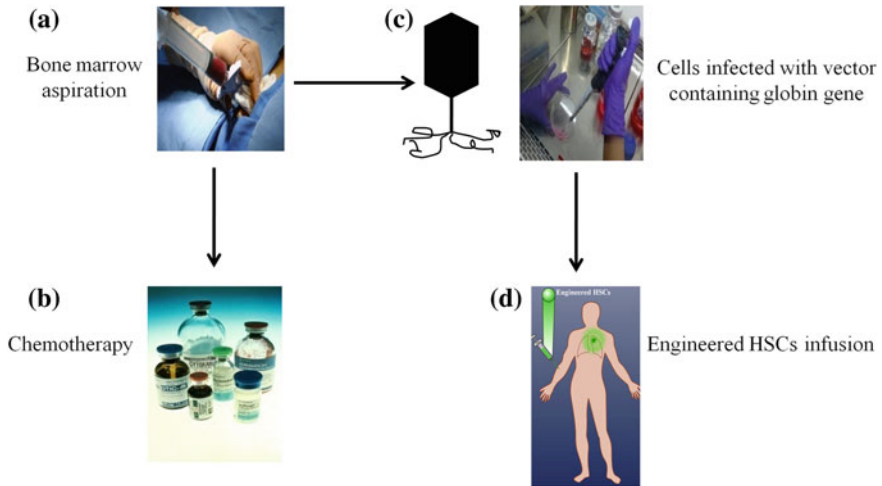


Fig. 2.10 Schematic representation of the trial conducted by Cavazzana-Calvo et al.: HSCs are isolated from patient by bone marrow aspiration (a) followed by patients treated with chemotherapy (b) cells mobilized in culture subjected to retroviral transduction with appropriate gene (c), and finally, these engineered $CD34^+$ HSC cells are infused into the body of the patient (d)

Stem-cell-mediated gene therapy was attempted to tackle thalassemia, a blood-related disorder that affects 7 % of population worldwide. The first trial involving transfer of β -globin gene into the $CD34^+$ bone marrow cells using lentiviral vectors was performed by Cavazzana-Calvo et al. Among three patients, the first one failed to engraft. Fortunately, the second patient accepted the graft and was continuously followed up for the next 5 years. The third patient was engrafted after a few months without complications. In a detailed report, Cavazzana-Calvo et al. [176, 194] have discussed the health of the second patient who had become transfusion independent for a period of 21 months after transplantation. The process of the trial is diagrammatically represented in Fig. 2.10.

In the last few years, a few trials were done on diseases such as ADA, gaucher, X-SCID using engineered HSCs with limited success [195].

2.4.4 Stem Cells and Type 1 Diabetes

Type 1 diabetes is an autoimmune disease associated with T-cell-mediated destruction of insulin-producing cells, which results in a lifelong dependence on insulin. Several attempts such as pancreas transplantation and islet transplantation have been attempted by scientists and clinicians to improve the quality of life of the patients [196].

Autologous and allogenic transplantations of hematopoietic cells were found to rescue patients from their diabetic symptoms. Recently, Gu et al. [197] published a clinical trial in which 28 patients who were having type 1 diabetes, antiglutamine decarboxylase antibody, and devoid of conditions such as cardiorespiratory insufficiency, renal or kidney failure or chronic and acute infection enrolled for autologous HSC transplantation between the years 2007 and 2010. After the administration of cyclophosphamide and rabbit antithymocyte globulin, autologous HSCs were infused. The daily requirement of insulin started decreasing in these patients within a month, and the decrease was found to be significant during the course of next 3 months and remained stable for the next 24 months. A similar observation was made in a group of patients with diabetes ketoacidosis (DKA) in which 20 out of 23 patients showed a remarkable insulin-free state. Twelve out of the twenty patients maintained the state of complete remission (CR) for 31 months, and the rest came back with the disease [197].

The umbilical cord blood rich in T regulatory cells and stem cells preserved at the time of birth also proves to be beneficial to combat such disease conditions. In a clinical study, Haller et al. [198] reported the results of infusion (about 100 ml cord blood/year) of own stored cord blood in 23 patients with diabetes type 1. No significant adverse effects were observed in 15 of these patients who were a part of the follow-up regime. In fact, the study illustrated the process of cord blood infusion in young to be feasible. However, the infusion failed to preserve the C-peptide levels in children.

Human placenta being a rich source of pluripotent and multipotent stem cells has become an attractive resource to the translational researchers. In one such trial performed, Hou et al. [199, 200] have shown that human amnion epithelial cells can be differentiated into insulin-producing cells of the pancreas and can reverse the state of hyperglycemia in C57 diabetic mouse. Unfortunately, no such trial has been initiated in patients.

2.4.5 Stem Cells and Malignancies

Stem cell transplantation has become a standard of care for the hematological cancers but yet to reach clinic for all types of solid tumors. HSC transplantation is a process in which HSCs are injected into the patients receiving bone-marrow-toxic drugs with or without whole-body radiation therapy. HSC transplantation could be of two types: allogenic transplantation when the stem cells come from another person with matched immune profile and autologous transplantation where the stem cells come from own body.

Allogenic transplantation is used to treat acute myelogenous leukemia (AML), chronic myelogenous leukemia (CML), chronic lymphocytic leukemia (CLL), and non-Hodgkin's lymphoma. CLL accounts for 25 % of all leukemia in which

allogenic stem cell transplantation is a good option of treatment. However, due to the lack of sufficient matching donors, this transplantation method is rarely followed. A trial by Michallet et al. (2011) enrolled 223 patients between the age of 31–65 years and in a stage of CR who were divided into two groups, 112 for transplantation arm or ACST arm and 111 for observation arm. Eighty of the 112 patients were subjected to transplantation of autologous stem cells, and the rest were spared due to collection failure, refusal, or secondary malignancies. According to the results published in 2011, no significant difference was found between ASCT and observation arm with respect to mortality without relapse even after 43.7 months of follow-up. However, a statistically significantly improved event-free survival was obtained in the ASCT arm. Only occurrence of myelodysplastic syndrome was reported. Thus, the transplantation study proved to be beneficial for CLL patients in CR. In contrary to the above-mentioned trial, a study by Sutton et al. [203] did not show beneficial effects of ASCT over combined chemotherapy of fludarabine and cyclophosphamide in patients aged between 18 and 65 years with Binet stage B or C CLL who were not treated before [201–203].

A few more randomized clinical trials were performed with allogenic HSC transplantation. The main focus of these trials was to overcome the chances of developing chronic graft versus host disease (GVHD), which is a very common complication encountered by clinicians after allogenic stem cell transplantation. Socie et al. [201, 204] performed a randomized trial that assessed prophylactic treatment regime with ATGs. Administration of corticosteroids or antithymocyte globulin along with drugs such as methotrexate and tacrolimus was shown to reduce the chances of GVHD.

Apart from trials on hematological malignancies, few very interesting clinical trials have been performed on solid tumors such as neuroblastoma, Wilms' tumor, retinoblastoma. In an attempt by George et al. 205, high-risk neuroblastoma patients enrolled between the years 1999 and 2002 were initially subjected to five cycles of standard chemotherapy and peripheral blood stem cell transplantation was performed after recovery from the second or the third cycle of chemotherapy. Out of the selected 97 patients, 51 died, and in the remaining 46, patient's progression-free survival was estimated to be around 47 and 45 % at the end of 5 and 7 years, respectively. The overall survival rate was found to be around 60 and 53 % at the end of 5 and 7 years, respectively. Thus, a combination of high-dose therapy with autologous stem cell rescue proved to be beneficial for high-risk neuroblastoma patients. An identical study was performed by Berthold et al. [206] with increased number of high-risk neuroblastoma patients. Patients subjected to high-dose chemotherapy with autologous stem cell transplantation were shown to have an extended 3-year event-free survival as compared to the batch of subjects given a maintenance therapy.

2.4.6 Stem Cells and Heart Ailments

Heart ailments such as myocardial infarction and ischemic heart failure lead to drastic loss of cardiomyocytes, interstitial cells, and vascular cells, which make recovery slow and difficult. A number of clinical trials are being conducted with mononuclear bone marrow cells rich in MSCs transplantation and are summarized in Table 2.7 [207].

In a recent report, Vrtovec and his colleagues (2013) discussed a clinical trial registered under NIH (NCT01350310) performed on 110 dilated cardiomyopathy patients. In phase I, the patients received doses of granulocyte-stimulating factor, and in phase II, 55 out of 110 patients were given an infusion of bone-marrow-derived autologous CD34⁺ cells. During the 5-year follow-up, patients were assessed by echocardiography and walking test. However, the most significant feature of the trial was the use of 99 m Tc hexamethylpropyleneamine oxime tracer accumulation method, which was used to determine the homing of the infused CD34⁺ cells. The stem cell transplantation was hence seen to be well associated with longtime survival of the patients [128].

2.4.7 Stem Cells and Retinal Diseases

Age-related macular degeneration (AMD), glaucoma, and diabetic retinopathy are the three most common causes of retinal degeneration, visual impairment, and complete blindness. In the recent years, a number of studies have been performed on animal models that have explored the potential of mouse or human adult bone-marrow-derived stem cells containing endothelial precursor to stabilize and rescue retinal blood vessels in experimental retinal dystrophies. Fewer numbers of clinical studies were done. Jonas et al. [177, 216, 217] produced case reports of trials performed in three patients with end-stage macular degeneration and glaucoma. Bone marrow was harvested, and mononuclear cells were separated by Ficoll density gradient sedimentation. The cells were then injected into the intraocular space. After the procedure was completed, a regular follow-up was done till 12 months. In spite of the trial being technically feasible, no significant improvement was obtained.

2.4.8 Stem Cells and Alopecia Areata

Alopecia areata is a common T-cell-mediated autoimmune disease leading to chronic and recurrent hair loss. The incidence of the disease is 0.1–0.2 % worldwide. Cell therapy is extremely limited and discouraging for alopecia areata. A clinical trial was initiated in August 2012 using the technique of “stem cell educator.” This technique is extremely useful in treating autoimmune diseases

Table 2.7 Trials on the various cardiac diseases

Disease	Trial	Patients	Cell type used	Result
Myocardial infraction	Boost Trial [207]	60	Nucleated BMC	Effect prominent in 6 months but diminished between 18 and 61 months
	Leuven AMI trial [208, 209]	67	Mononucleated BMC	Fast recovery
	Astami trial [210]	100	Mononucleated BMC	No significant effect observed after 6 and 12 months
	Fincell trial [211]	80	Thrombolytic therapy	Improvement seen before and after 6 months
	Regent trial [212]	200	Mononucleated BMC	Specific marker expressing cell population associated with the observed effects
Chronic myocardial ischemia	HEBE Trial [213]	20	Mononucleated BMC and standard therapy as control	Subjects showed either enhanced ventricular recovery or remodeling. Results need further validation
	[214]	24	CD34 ⁺ cells collected from peripheral blood	Satisfactory results

such as alopecia areata and type 1 diabetes. The principle of this technique is to change the behavior of the immune cells of the body so that they do not function against self-immune system. This phase I/II trial was performed with an objective to see how the stem cells modulate autoimmunity. The date of completion of the trial is expected to be in July 2013 [218].

2.4.9 Stem Cells and Disasters

Disasters are always unpredictable and could be either natural or man-made. At times, human errors can lead to accidents such as radiation exposure, road mishaps that may cause irreversible damages. Strategies such as isolating cells from an autologous healthy source and transplanting them into the damaged sites for generating functional cells with desired characteristics are adopted to cope up with such events. A case study was published by Lataillade et al. [219] in which a 27-year-old Chilean man overexposed to gammagraphy radioactive source was treated using dosimetry-guided lesion excision and mesenchymal stem cell therapy. Autologous total bone marrow cells were obtained from unexposed iliac crest by aspiration and were grown in culture using medium supplemented with 8 % platelet lysate. MSCs characterized by surface markers, clonogenic assays, and telomerase activity were infused into the patient body at day 90 and day 99. Within

five and a half months postirradiation, the patient showed signs of improvement with complete healing. After a series of successful animal experiments, a phase I/II clinical trial was initiated in the year 2011 (NCT01298830). The trial was designed based on the use of encapsulated and engineered human bone-marrow-derived MSCs to cure traumatic brain injury. In spite of obtaining some positive results from 11 patients, the trial was terminated in 2013 [220].

2.4.10 Stem Cells and Bone Disorders

Bone loss has always been a challenge for the clinicians. Marcacci et al. [221] published a trial report that they conducted on four subjects of whom two patients had an affected ulna and the other two had defective tibia and humerus. As mentioned in Sect. 2.2.3, a porous bioceramics was used as the scaffold in this study. Bone marrow stem cells isolated from the patients were cultured with minor modifications and seeded on the scaffold within 36 h from harvest. During the follow-up course, no complications in terms of pain, swelling, or infections were observed. Even after 6–7 years of postsurgery, a good integration of implants was observed in patients 1 and 3. Angiographic evaluation performed even after 6.5 years postsurgery indicated vascularization of the grafted zone. Pre/postoperative radiography and 2D and 3D CT scans were used to monitor bone development.

Apart from the above-mentioned bone disease, osteogenesis imperfecta is a very painful genetic disorder caused by a defect in the collagen type I encoding gene. The disease is characterized by bony deformities, fragility, fractures, and short stature. Two identical clinical trials were performed by Horwitz et al. (1999 and 2001). Analysis was conducted using techniques such as dual-energy X-ray absorptiometry and bone histologic examination from bone biopsy samples taken before and after transplantation using the technique of microscopy as explained previously. In the first trial, three patients were infused with unmanipulated bone marrow from HLA-matched identical siblings. In the second trial, a similar approach was adopted for the three patients, while the two patients in the control arm were not given any specific therapy. Improvement in bone histology and a significant increase in the number of osteoblasts were observed. Unlike the second trial, the first one also accounted for a significant increase in bone mineral content. However, complications such as sepsis, pulmonary insufficiency, and bifrontal hygroma were commonly seen in both trials. In spite of the aftereffects as mentioned above, these trials indeed generated a lot of hope in patients suffering from this tragic genetic defect [222, 223].

2.4.11 Stem Cells and Liver Diseases

Liver diseases such as liver cirrhosis and hepatitis B are considered to be extremely life threatening. No effective treatment regime has been designed for almost a decade now. Hence, intensive research is carried out using HSCs due to their promising results in other fatal diseases. A phase I trial was designed and published by Gordon et al. and Levicar et al. [224, 225] in which CD34⁺ HSCs in granulocyte-stimulating-factor-mobilized blood were infused into the portal vein of 5 patients with chronic liver diseases. Further, the data collected during the follow-up period of 12–18 months were discussed in the report published in 2008. During the follow-up period of 12–18 months, patients were assessed on the basis of CT and levels of bilirubin and alpha-fetoproteins in serum and they showed no side effects. The study implicated that the treatment with stem cells lasts for about 12 months. Terai et al. [226] in 2006 conducted autologous bone marrow transplantation in patients with liver cirrhosis. One of the successful trials reported by Gasbarrini et al. [227–229] showed a reversal of drug-induced liver failure by transplanting CD34⁺ BMSCs. Zang et al. [230] discussed a trial on infusion of umbilical cord MSCs in 30 patients with 15 controls (only saline). Reduction in the amount of ascites, improvement in liver function with increased serum albumin, and decrease in serum bilirubin levels were achieved. Another remarkable clinical trial on end-stage liver disease was reported by Kharaziha [231] in which autologous MSCs were used. The cells were isolated from the iliac crest and grown in vitro to get a count of 30 to 50 millions. Posttransplantation follow-ups were regularly done in the 1st, 2nd, 4th, 8th, and 24th weeks. The transplantation was well tolerated as seen in the improved liver function test results that were reflected in the levels of serum creatinine, serum albumin, and serum bilirubin.

2.4.12 Stem Cells and Pharmaceutical Companies

Cell therapy by using stem cells has been a subject of interest for clinicians and scientists for almost a decade. The recent years have seen many pharmaceutical companies participating in stem cell research, therefore making regenerative medicine a vibrant industry. The first FDA-approved trial for patients with spinal cord injury with ESC-derived oligodendrocyte progenitor cells (GRNOPC1) (#NCT01217008) was conducted by Geron, which is currently on hold. Recently, Genzyme reported a quality control program conducted on 303 patients subjected to autologous transplantation of cultured chondrocytes to repair knee damages. The follow-up of these patients produced positive results [232]. Many companies are also involved in iPSC research for future like Progenitor Labs involved in stem cell engineering [233, 234]. Some company-sponsored trials are listed in Table 2.8.

Table 2.8 Companies and their contribution in the stem-cell-therapy-based trials

Companies	Trials
TCA Cellular Therapy	NCT00518401; NCT00643981; NCT00721006; NCT00790764; NCT00548613
Shenzhen Beike Biotechnology Co. Ltd	NCT01360164; NCT01343511; NCT01610440; NCT01742533; NCT01443689
Manipal Acunova Ltd	NCT01501773
Banc de Sang i Teixits	NCT01227694
NCIC Clinical Trial Group	NCT00003032
TECAM Group	NCT00984178
Cellonis Biotechnology Co. Ltd	NCT01143168; NCT01142050
Osiris Therapeutics	NCT00482092; NCT01233960
International Stem Cell Service Ltd	NCT01152125

Table 2.9 describes ongoing and completed trials categorized on the basis of the different types of stem cells used for transplantation.

2.5 Conclusion and Future Prospect

Self-renewal and multilineage differentiation properties of stem cells are keys to the lifelong homeostatic maintenance of tissues and organs. These properties could also make the cells as potential therapeutic tool for many incurable diseases where traditional “chemical solution to biological diseases” fails to work. Last few decades of biomedical research have seen extensive experimentation on stem cell therapy for regenerative medicine. Most early work was carried out with pluripotent ES cells derived from the inner mass of blastocyst embryo that can differentiate into any type of cells belong to all the three germ layers. However, significant challenge was met in successfully culturing the hESCs on MEF cells and induction of directed differentiation toward a specific cell lineage. An ongoing effort is going to establish feeder-independent culture system under the supervision of International Stem Cell Initiative Consortium. Various combinations of growth factors, chemicals, cell densities, and matrices are being tested to achieve proper differentiation of hESCs. A remarkable success was reported by Chen et al. [6] who were able to differentiate hESCs to functionally active insulin-secreting beta-cells in a stepwise manner. However, application of hESCs in regenerative medicine is still limited due to the formation of teratoma in vivo and ethical issues. A potential future solution for overcoming teratoma formation would be implantation of hESC-derived progenitor cells with specific lineage memory instead of implantation of undifferentiated hESC.

The next and most widely accepted choice for cell therapy after hESC is the adult stem cells, which beat the major limitations of hESCs. Adult stem cells, majority of which are known as MSCs, reside in various organs and are potential

Table 2.9 Ongoing or completed clinical trials on various diseases using stem cells

Stem Cells	Disease	Trials completed/in progress
Autologous HSCs transplantation	Severe systemic lupus erythematosus	NCT00076752
	Retinoblastoma	NCT00554788
Peripheral blood stem cell transplantation	Type 1 diabetes	NCT01285934; NCT01341899
	Neuroblastoma	NCT00004188; NCT01526603
Allogenic HSCs transplantation	Ewing's tumor	NCT00003081
	Hematological malignancies	NCT00152139; NCT00176930
Autologous transplantation of CD34 ⁺ cells	Ewing's tumor	NCT00357396
	Coronary artery disease, angina, myocardial infarction, and chronic ischemia	NCT00081913; NCT00221182
Bone-marrow-derived mononuclear cell transplantation	Retinitis pigmentosa	NCT01068561
	Liver cirrhosis	NCT01120925; NCT01724697
	Wilms' tumor	NCT00025103
HLA-matched bone-marrow-derived stem cells	Alopecia areata	NCT01758510
Mesenchymal stem cell	Amyotrophic lateral sclerosis	NCT01609283
	Osteonecrosis of the femoral head	NCT01605383
Umbilical cord-derived MSCs	Liver cirrhosis and liver failure	NCT01573923; NCT01724398; NCT01728727
	Hereditary ataxia	NCT01360164
	Diabetes type 1	NCT01374854
Autologous bone marrow mononuclear cells and umbilical cord mesenchymal stem cell transplantation	Diabetes type 1	NCT01143168
Cord blood stem cells (educator therapy)	Diabetes type 1	NCT01350219
	Alopecia areata	NCT01673789
Autologous adipose-tissue-derived stem cells	Diabetes type 1	NCT00703599
Development of iPSCs from cell culture established from skin biopsies	Neurodegenerative diseases	NCT00874783
Combined stem cell therapy	Severe leg ischemia	NCT00721006

to form different types of cells through proper differentiation. An extensive overview of MSC and other adult stem cell (such as HSC)-based applications are discussed in the main sections. The wide application of MSCs in preclinical and clinical trials with many of them displaying effective prevention and control of a diversity of diseases brings them to forefront of stem cell therapy research. A number of clinical trials are currently going on with MSCs to treat

neurodegenerative diseases, thalassemia, diabetes, cardiovascular diseases, and malignancies and even in disaster-related injuries. However, success rate is still low and more number of trials would be required to assess the real potential of stem cell therapy.

The low abundance and need of large-scale culture of adult stem cells for clinical application can overcome by iPSCs, which shows great promise for regenerative medicine. However, application of iPSCs is still limited in preclinical stages and expected to reach clinic soon.

Finally, monitoring the efficacy of stem cell therapy is an extremely important component and a large number of microscopic and macroscopic techniques are being implemented to check for in vitro differentiation, in vivo differentiation, and functional output. Each of these cell based and preclinical imaging techniques has own merits and demerits and is often used in combination to achieve a multimodal approach. Since stem cell imaging requires high resolution, MRI despite having lower sensitivity is probably the most suitable technology. A large number of preclinical applications are using bioluminescence imaging as well. These imaging techniques are also important in understanding the interactions of local microenvironment with stem cells. Overall, the excitement and hope for effective treatment for many incurable diseases by stem cells are quite promising but require a thorough and long-term monitoring at preclinical level, followed by practical protocols. It is highly expected that detailed investigations of stem cell biology and clinical applicability will result in revolutions in medical technologies.

References

1. Thomson JA, Itskovitz-Eldor J, Shapiro SS, Waknitz MA, Swiergiel JJ, Marshall VS, Jones JM (1998) Embryonic stem cell lines derived from human blastocysts. *Science* 282(5391):1145–1147
2. Akopian V, Andrews PW, Beil S, Benvenisty N, Brehm J, Christie M, Ford A, Fox V, Gokhale PJ, Healy L, Holm F, Hovatta O, Knowles BB, Ludwig TE, McKay RD, Miyazaki T, Nakatsuji N, Oh SK, Pera MF, Rossant J, Stacey GN, Suemori H (2010) Comparison of defined culture systems for feeder cell free propagation of human embryonic stem cells. *Vitro Cell Dev Biol Anim* 46(3–4):247–258. doi:10.1007/s11626-010-9297-z
3. Xu C, Inokuma MS, Denham J, Golds K, Kundu P, Gold JD, Carpenter MK (2001) Feeder-free growth of undifferentiated human embryonic stem cells. *Nat Biotechnol* 19(10):971–974. doi:10.1038/nbt1001-971
4. Lei T, Jacob S, Ajil-Zaraa I, Dubuisson JB, Irion O, Jaconi M, Feki A (2007) Xeno-free derivation and culture of human embryonic stem cells: current status, problems and challenges. *Cell Res* 17(8):682–688. doi:10.1038/cr.2007.61
5. Itskovitz-Eldor J, Schuldiner M, Karsenti D, Eden A, Yanuka O, Amit M, Soreq H, Benvenisty N (2000) Differentiation of human embryonic stem cells into embryoid bodies comprising the three embryonic germ layers. *Mol Med* 6(2):88–95
6. Chen S, Borowiak M, Fox JL, Maehr R, Osafune K, Davidow L, Lam K, Peng LF, Schreiber SL, Rubin LL, Melton D (2009) A small molecule that directs differentiation of human ESCs into the pancreatic lineage. *Nat Chem Biol* 5(4):258–265. doi:10.1038/nchembio.154

7. Kroon E, Martinson LA, Kadoya K, Bang AG, Kelly OG, Eliazar S, Young H, Richardson M, Smart NG, Cunningham J, Agulnick AD, D'Amour KA, Carpenter MK, Baetge EE (2008) Pancreatic endoderm derived from human embryonic stem cells generates glucose-responsive insulin-secreting cells in vivo. *Nat Biotechnol* 26(4):443–452. doi:[10.1038/nbt1393](https://doi.org/10.1038/nbt1393)
8. Schwartz SD, Hubschman JP, Heilwell G, Franco-Cardenas V, Pan CK, Ostrick RM, Mickunas E, Gay R, Klimanskaya I, Lanza R (2012) Embryonic stem cell trials for macular degeneration: a preliminary report. *Lancet* 379(9817):713–720. doi:[10.1016/S0140-6736\(12\)60028-2](https://doi.org/10.1016/S0140-6736(12)60028-2)
9. Hacein-Bey-Abina S, von Kalle C, Schmidt M, Le Deist F, Wulffraat N, McIntyre E, Radford I, Villeval JL, Fraser CC, Cavazzana-Calvo M, Fischer A (2003) A serious adverse event after successful gene therapy for X-linked severe combined immunodeficiency. *N Engl J Med* 348(3):255–256. doi:[10.1056/NEJM200301163480314](https://doi.org/10.1056/NEJM200301163480314)
10. Yu SF, von Ruden T, Kantoff PW, Garber C, Seiberg M, Ruther U, Anderson WF, Wagner EF, Gilboa E (1986) Self-inactivating retroviral vectors designed for transfer of whole genes into mammalian cells. *Proc Natl Acad of Sci USA*. 83(10):3194–3198
11. Naldini L, Blomer U, Gally P, Ory D, Mulligan R, Gage FH, Verma IM, Trono D (1996) In vivo gene delivery and stable transduction of nondividing cells by a lentiviral vector. *Science* 272(5259):263–267
12. May C, Rivella S, Callegari J, Heller G, Gaensler KM, Luzzatto L, Sadelain M (2000) Therapeutic haemoglobin synthesis in beta-thalassaemic mice expressing lentivirus-encoded human beta-globin. *Nature* 406(6791):82–86. doi:[10.1038/35017565](https://doi.org/10.1038/35017565)
13. Vadhan-Raj S, Patel S, Bueso-Ramos C, Folloder J, Papadopolous N, Burgess A, Broemeling LD, Broxmeyer HE, Benjamin RS (2003) Importance of predosing of recombinant human thrombopoietin to reduce chemotherapy-induced early thrombocytopenia. *J Clin Oncol* 21(16):3158–3167. doi:[10.1200/JCO.2003.08.003](https://doi.org/10.1200/JCO.2003.08.003)
14. Panuganti S, Schlinker AC, Lindholm PF, Papoutsakis ET, Miller WM (2013) Three-stage ex vivo expansion of high-ploidy megakaryocytic cells: toward large-scale platelet production. *Tissue Eng Part A* 19(7–8):998–1014. doi:[10.1089/ten.TEA.2011.0111](https://doi.org/10.1089/ten.TEA.2011.0111)
15. Lagasse E, Connors H, Al-Dhalimy M, Reitsma M, Dohse M, Osborne L, Wang X, Finegold M, Weissman IL, Grompe M (2000) Purified hematopoietic stem cells can differentiate into hepatocytes in vivo. *Nat Med* 6(11):1229–1234. doi:[10.1038/81326](https://doi.org/10.1038/81326)
16. Friedenstein AJ, Deriglasova UF, Kulagina NN, Panasuk AF, Rudakowa SF, Luria EA, Ruadkow IA (1974) Precursors for fibroblasts in different populations of hematopoietic cells as detected by the in vitro colony assay method. *Exp Hematol* 2(2):83–92
17. Friedenstein AJ, Chailakhyan RK, Latsinik NV, Panasyuk AF, Keiliss-Borok IV (1974) Stromal cells responsible for transferring the microenvironment of the hemopoietic tissues. Cloning in vitro and retransplantation in vivo. *Transplantation* 17(4):331–340
18. Polisetty N, Fatima A, Madhira SL, Sangwan VS, Vemuganti GK (2008) Mesenchymal cells from limbal stroma of human eye. *Mol Vis* 14:431–442
19. Chan BP, Hui TY, Wong MY, Yip KH, Chan GC (2010) Mesenchymal stem cell-encapsulated collagen microspheres for bone tissue engineering. *Tissue Eng Part C Methods* 16(2):225–235. doi:[10.1089/ten.tec.2008.0709](https://doi.org/10.1089/ten.tec.2008.0709)
20. Sumanasinghe RD, Bernacki SH, Loba EG (2006) Osteogenic differentiation of human mesenchymal stem cells in collagen matrices: effect of uniaxial cyclic tensile strain on bone morphogenetic protein (BMP-2) mRNA expression. *Tissue Eng* 12(12):3459–3465. doi:[10.1089/ten.2006.12.3459](https://doi.org/10.1089/ten.2006.12.3459)
21. Sumanasinghe RD, Osborne JA, Loba EG (2009) Mesenchymal stem cell-seeded collagen matrices for bone repair: effects of cyclic tensile strain, cell density, and media conditions on matrix contraction in vitro. *J Biomed Mater Res A* 88(3):778–786. doi:[10.1002/jbm.a.31913](https://doi.org/10.1002/jbm.a.31913)
22. Ahmed TA, Dare EV, Hincke M (2008) Fibrin: a versatile scaffold for tissue engineering applications. *Tissue Eng Part B Rev* 14(2):199–215. doi:[10.1089/ten.teb2007.0435](https://doi.org/10.1089/ten.teb2007.0435)

23. Kim HJ, Kim UJ, Kim HS, Li C, Wada M, Leisk GG, Kaplan DL (2008) Bone tissue engineering with premineralized silk scaffolds. *Bone* 42(6):1226–1234. doi:[10.1016/j.bone.2008.02.007](https://doi.org/10.1016/j.bone.2008.02.007)
24. Li C, Vepari C, Jin HJ, Kim HJ, Kaplan DL (2006) Electrospun silk-BMP-2 scaffolds for bone tissue engineering. *Biomaterials* 27(16):3115–3124. doi:[10.1016/j.biomaterials.2006.01.022](https://doi.org/10.1016/j.biomaterials.2006.01.022)
25. Mieszawska AJ, Fourligas N, Georgakoudi I, Ouhib NM, Belton DJ, Perry CC, Kaplan DL (2010) Osteoinductive silk-silica composite biomaterials for bone regeneration. *Biomaterials* 31(34):8902–8910. doi:[10.1016/j.biomaterials.2010.07.109](https://doi.org/10.1016/j.biomaterials.2010.07.109)
26. Patterson J, Siew R, Herring SW, Lin AS, Guldberg R, Stayton PS (2010) Hyaluronic acid hydrogels with controlled degradation properties for oriented bone regeneration. *Biomaterials* 31(26):6772–6781. doi:[10.1016/j.biomaterials.2010.05.047](https://doi.org/10.1016/j.biomaterials.2010.05.047)
27. Kim J, Kim IS, Cho TH, Kim HC, Yoon SJ, Choi J, Park Y, Sun K, Hwang SJ (2010) In vivo evaluation of MMP sensitive high-molecular weight HA-based hydrogels for bone tissue engineering. *J Biomed Mater Res A* 95(3):673–681. doi:[10.1002/jbm.a.32884](https://doi.org/10.1002/jbm.a.32884)
28. Kim J, Kim IS, Cho TH, Lee KB, Hwang SJ, Tae G, Noh I, Lee SH, Park Y, Sun K (2007) Bone regeneration using hyaluronic acid-based hydrogel with bone morphogenic protein-2 and human mesenchymal stem cells. *Biomaterials* 28(10):1830–1837. doi:[10.1016/j.biomaterials.2006.11.050](https://doi.org/10.1016/j.biomaterials.2006.11.050)
29. Venkatesan J, Kim SK (2010) Chitosan composites for bone tissue engineering—an overview. *Mar Drugs* 8(8):2252–2266. doi:[10.3390/md8082252](https://doi.org/10.3390/md8082252)
30. Shoaie-Hassani A, Mortazavi-Tabatabaei SA, Sharif S, Seifalian AM, Azimi A, Samadikuchaksaraei A, Verdi J (2013) Differentiation of human endometrial stem cells into urothelial cells on a three-dimensional nanofibrous silk-collagen scaffold: an autologous cell resource for reconstruction of the urinary bladder wall. *J Tissue Eng Regen Med*. doi:[10.1002/term.1632](https://doi.org/10.1002/term.1632)
31. Mummery CL, Davis RP, Krieger JE (2010) Challenges in using stem cells for cardiac repair. *Sci Transl Med* 2(27):27ps17. doi:[10.1126/scitranslmed.3000558](https://doi.org/10.1126/scitranslmed.3000558)
32. Lee RH, Kim B, Choi I, Kim H, Choi HS, Suh K, Bae YC, Jung JS (2004) Characterization and expression analysis of mesenchymal stem cells from human bone marrow and adipose tissue. *Cell Physiol Biochem* 14(4–6):311–324. doi:[10.1159/000080341](https://doi.org/10.1159/000080341)
33. Makino S, Fukuda K, Miyoshi S, Konishi F, Kodama H, Pan J, Sano M, Takahashi T, Hori S, Abe H, Hata J, Umezawa A, Ogawa S (1999) Cardiomyocytes can be generated from marrow stromal cells in vitro. *J Clin Invest* 103(5):697–705. doi:[10.1172/JCI5298](https://doi.org/10.1172/JCI5298)
34. Toma C, Pittenger MF, Cahill KS, Byrne BJ, Kessler PD (2002) Human mesenchymal stem cells differentiate to a cardiomyocyte phenotype in the adult murine heart. *Circulation* 105(1):93–98
35. Takahashi T, Lord B, Schulze PC, Fryer RM, Sarang SS, Gullans SR, Lee RT (2003) Ascorbic acid enhances differentiation of embryonic stem cells into cardiac myocytes. *Circulation* 107(14):1912–1916. doi:[10.1161/01.CIR.0000064899.53876.A3](https://doi.org/10.1161/01.CIR.0000064899.53876.A3)
36. Dominici M, Le Blanc K, Mueller I, Slaper-Cortenbach I, Marini F, Krause D, Deans R, Keating A, Prockop D, Horwitz E (2006) Minimal criteria for defining multipotent mesenchymal stromal cells. The International Society for Cellular Therapy position statement. *Cytotherapy* 8(4):315–317. doi:[10.1080/14653240600855905](https://doi.org/10.1080/14653240600855905)
37. Pittenger MF, Mackay AM, Beck SC, Jaiswal RK, Douglas R, Mosca JD, Moorman MA, Simonetti DW, Craig S, Marshak DR (1999) Multilineage potential of adult human mesenchymal stem cells. *Science* 284(5411):143–147
38. Mruthyunjaya S, Manchanda R, Godbole R, Pujari R, Shiras A, Shastry P (2010) Laminin-1 induces neurite outgrowth in human mesenchymal stem cells in serum/differentiation factors-free conditions through activation of FAK-MEK/ERK signaling pathways. *Biochem Biophys Res Commun* 391(1):43–48. doi:[10.1016/j.bbrc.2009.10.158](https://doi.org/10.1016/j.bbrc.2009.10.158)
39. Vecellio M, Meraviglia V, Nanni S, Barbuti A, Scavone A, DiFrancesco D, Farsetti A, Pompilio G, Colombo GI, Capogrossi MC, Gaetano C, Rossini A (2012) In vitro epigenetic

- reprogramming of human cardiac mesenchymal stromal cells into functionally competent cardiovascular precursors. *PLoS ONE* 7(12):e51694. doi:[10.1371/journal.pone.0051694](https://doi.org/10.1371/journal.pone.0051694)
40. Zouani OF, Kalisky J, Ibarboure E, Durrieu MC (2013) Effect of BMP-2 from matrices of different stiffnesses for the modulation of stem cell fate. *Biomaterials* 34(9):2157–2166. doi:[10.1016/j.biomaterials.2012.12.007](https://doi.org/10.1016/j.biomaterials.2012.12.007)
 41. Fatima A, Sangwan VS, Iftekhar G, Reddy P, Matalia H, Balasubramanian D, Vemuganti GK (2006) Technique of cultivating limbal derived corneal epithelium on human amniotic membrane for clinical transplantation. *J Postgrad Med* 52(4):257–261
 42. Gurdon JB (1962) The developmental capacity of nuclei taken from intestinal epithelium cells of feeding tadpoles. *J Embryol Exp Morphol* 10:622–640
 43. Takahashi K, Yamanaka S (2006) Induction of pluripotent stem cells from mouse embryonic and adult fibroblast cultures by defined factors. *Cell* 126(4):663–676. doi:[10.1016/j.cell.2006.07.024](https://doi.org/10.1016/j.cell.2006.07.024)
 44. Takahashi K, Tanabe K, Ohnuki M, Narita M, Ichisaka T, Tomoda K, Yamanaka S (2007) Induction of pluripotent stem cells from adult human fibroblasts by defined factors. *Cell* 131(5):861–872. doi:[10.1016/j.cell.2007.11.019](https://doi.org/10.1016/j.cell.2007.11.019)
 45. Yu J, Vodyanik MA, Smuga-Otto K, Antosiewicz-Bourget J, Frane JL, Tian S, Nie J, Jonsdottir GA, Ruotti V, Stewart R, Slukvin II, Thomson JA (2007) Induced pluripotent stem cell lines derived from human somatic cells. *Science* 318(5858):1917–1920. doi:[10.1126/science.1151526](https://doi.org/10.1126/science.1151526)
 46. Okita K, Ichisaka T, Yamanaka S (2007) Generation of germline-competent induced pluripotent stem cells. *Nature* 448(7151):313–317. doi:[10.1038/nature05934](https://doi.org/10.1038/nature05934)
 47. Kawai H, Yamashita T, Ohta Y, Deguchi K, Nagotani S, Zhang X, Ikeda Y, Matsuura T, Abe K (2010) Tridermal tumorigenesis of induced pluripotent stem cells transplanted in ischemic brain. *J Cereb Blood Flow Metab* 30(8):1487–1493. doi:[10.1038/jcbfm.2010.32](https://doi.org/10.1038/jcbfm.2010.32)
 48. Zhou H, Wu S, Joo JY, Zhu S, Han DW, Lin T, Trauger S, Bien G, Yao S, Zhu Y, Siuzdak G, Scholer HR, Duan L, Ding S (2009) Generation of induced pluripotent stem cells using recombinant proteins. *Cell Stem Cell* 4(5):381–384. doi:[10.1016/j.stem.2009.04.005](https://doi.org/10.1016/j.stem.2009.04.005)
 49. Brelloch R, Veneri M, Yen J, Ramalho-Santos M (2007) Generation of induced pluripotent stem cells in the absence of drug selection. *Cell Stem Cell* 1(3):245–247. doi:[10.1016/j.stem.2007.08.008](https://doi.org/10.1016/j.stem.2007.08.008)
 50. Anokye-Danso F, Trivedi CM, Juhr D, Gupta M, Cui Z, Tian Y, Zhang Y, Yang W, Gruber PJ, Epstein JA, Morrissey EE (2011) Highly efficient miRNA-mediated reprogramming of mouse and human somatic cells to pluripotency. *Cell Stem Cell* 8(4):376–388. doi:[10.1016/j.stem.2011.03.001](https://doi.org/10.1016/j.stem.2011.03.001)
 51. Liu H, Zhu F, Yong J, Zhang P, Hou P, Li H, Jiang W, Cai J, Liu M, Cui K, Qu X, Xiang T, Lu D, Chi X, Gao G, Ji W, Ding M, Deng H (2008) Generation of induced pluripotent stem cells from adult rhesus monkey fibroblasts. *Cell Stem Cell* 3(6):587–590. doi:[10.1016/j.stem.2008.10.014](https://doi.org/10.1016/j.stem.2008.10.014)
 52. Liao J, Cui C, Chen S, Ren J, Chen J, Gao Y, Li H, Jia N, Cheng L, Xiao H, Xiao L (2009) Generation of induced pluripotent stem cell lines from adult rat cells. *Cell Stem Cell* 4(1):11–15. doi:[10.1016/j.stem.2008.11.013](https://doi.org/10.1016/j.stem.2008.11.013)
 53. Ezashi T, Telugu BP, Alexenko AP, Sachdev S, Sinha S, Roberts RM (2009) Derivation of induced pluripotent stem cells from pig somatic cells. *Proc Natl Acad of Sci USA* 106(27):10993–10998. doi:[10.1073/pnas.0905284106](https://doi.org/10.1073/pnas.0905284106)
 54. Shimada H, Nakada A, Hashimoto Y, Shigeno K, Shionoya Y, Nakamura T (2010) Generation of canine induced pluripotent stem cells by retroviral transduction and chemical inhibitors. *Mol Reprod Dev* 77(1):2. doi:[10.1002/mrd.21117](https://doi.org/10.1002/mrd.21117)
 55. Wu Y, Zhang Y, Mishra A, Tardif SD, Hornsby PJ (2010) Generation of induced pluripotent stem cells from newborn marmoset skin fibroblasts. *Stem Cell Res* 4(3):180–188. doi:[10.1016/j.scr.2010.02.003](https://doi.org/10.1016/j.scr.2010.02.003)
 56. Honda A, Hirose M, Hatori M, Matoba S, Miyoshi H, Inoue K, Ogura A (2010) Generation of induced pluripotent stem cells in rabbits: potential experimental models for human generative medicine. *J Biol Chem* 285(41):31362–31369. doi:[10.1074/jbc.M110.150540](https://doi.org/10.1074/jbc.M110.150540)

57. Nagy K, Sung HK, Zhang P, Laflamme S, Vincent P, Agha-Mohammadi S, Woltjen K, Monetti C, Michael IP, Smith LC, Nagy A (2011) Induced pluripotent stem cell lines derived from equine fibroblasts. *Stem Cell Rev* 7(3):693–702. doi:[10.1007/s12015-011-9239-5](https://doi.org/10.1007/s12015-011-9239-5)
58. Lu Y, West FD, Jordan BJ, Mumaw JL, Jordan ET, Gallegos-Cardenas A, Beckstead RB, Stice SL (2012) Avian-induced pluripotent stem cells derived using human reprogramming factors. *Stem Cells Dev* 21(3):394–403. doi:[10.1089/scd.2011.0499](https://doi.org/10.1089/scd.2011.0499)
59. Yoshikawa T, Samata B, Ogura A, Miyamoto S, Takahashi J (2013) Systemic administration of valproic acid and zonisamide promotes differentiation of induced pluripotent stem cell-derived dopaminergic neurons. *Front Cell Neurosci* 7:11. doi:[10.3389/fncel.2013.00011](https://doi.org/10.3389/fncel.2013.00011)
60. Mekala SR, Vauhini V, Nagarajan U, Maddileti S, Gaddipati S, Mariappan I (2013) Derivation, characterization and retinal differentiation of induced pluripotent stem cells. *J Biosci* 38(1):123–134
61. Nishimura K, Takahashi J (2013) Therapeutic application of stem cell technology toward the treatment of Parkinson's disease. *Biol Pharma Bull.* 36(2):171–175
62. Song Z, Cai J, Liu Y, Zhao D, Yong J, Duo S, Song X, Guo Y, Zhao Y, Qin H, Yin X, Wu C, Che J, Lu S, Ding M, Deng H (2009) Efficient generation of hepatocyte-like cells from human induced pluripotent stem cells. *Cell Res* 19(11):1233–1242. doi:[10.1038/cr.2009.107](https://doi.org/10.1038/cr.2009.107)
63. Sullivan GJ, Hay DC, Park IH, Fletcher J, Hannoun Z, Payne CM, Dalgetty D, Black JR, Ross JA, Samuel K, Wang G, Daley GQ, Lee JH, Church GM, Forbes SJ, Iredale JP, Wilmot I (2010) Generation of functional human hepatic endoderm from human induced pluripotent stem cells. *Hepatology* 51(1):329–335. doi:[10.1002/hep.23335](https://doi.org/10.1002/hep.23335)
64. Kobari L, Yates F, Oudrhiri N, Francina A, Kiger L, Mazurier C, Rouzbeh S, El-Nemer W, Hebert N, Giarratana MC, Francois S, Chapel A, Lapillonne H, Luton D, Bennaceur-Griscelli A, Douay L (2012) Human induced pluripotent stem cells can reach complete terminal maturation: in vivo and in vitro evidence in the erythropoietic differentiation model. *Haematologica* 97(12):1795–1803. doi:[10.3324/haematol.2011.055566](https://doi.org/10.3324/haematol.2011.055566)
65. Pouya A, Satarian L, Kiani S, Javan M, Baharvand H (2011) Human induced pluripotent stem cells differentiation into oligodendrocyte progenitors and transplantation in a rat model of optic chiasm demyelination. *PLoS ONE* 6(11):e27925. doi:[10.1371/journal.pone.0027925](https://doi.org/10.1371/journal.pone.0027925)
66. Aravalli RN, Cressman EN, Steer CJ (2012) Hepatic differentiation of porcine induced pluripotent stem cells in vitro. *Vet J* 194(3):369–374. doi:[10.1016/j.tvjl.2012.05.013](https://doi.org/10.1016/j.tvjl.2012.05.013)
67. Georgakoudi I, Rice WL, Hronik-Tupaj M, Kaplan DL (2008) Optical spectroscopy and imaging for the noninvasive evaluation of engineered tissues. *Tissue Eng Part B Rev* 14(4):321–340. doi:[10.1089/ten.teb.2008.0248](https://doi.org/10.1089/ten.teb.2008.0248)
68. Huh S, Ker DF, Bise R, Chen M, Kanade T (2011) Automated mitosis detection of stem cell populations in phase-contrast microscopy images. *IEEE Trans Med Imaging* 30(3):586–596. doi:[10.1109/TMI.2010.2089384](https://doi.org/10.1109/TMI.2010.2089384)
69. S-iH Sungeun Eom, Ker Dai Fei Elmer, Bise Ryoma, Kanade Takeo (2007) Tracking of hematopoietic stem cells in microscopy images for lineage determination. *J Latex Class Files* 6(01–09):9
70. Jang YY, Ye Z, Cheng L (2011) Molecular imaging and stem cell research. *Mol Imagings* 10(2):111–122
71. Tumber T, Guasch G, Greco V, Blanpain C, Lowry WE, Rendl M, Fuchs E (2004) Defining the epithelial stem cell niche in skin. *Science* 303(5656):359–363. doi:[10.1126/science.1092436](https://doi.org/10.1126/science.1092436)
72. Giepmans BN, Adams SR, Ellisman MH, Tsien RY (2006) The fluorescent toolbox for assessing protein location and function. *Science* 312(5771):217–224. doi:[10.1126/science.1126171](https://doi.org/10.1126/science.1126171)
73. Sutton EJ, Henning TD, Pichler BJ, Bremer C, Daldrup-Link HE (2008) Cell tracking with optical imaging. *Eur Radiol* 18(10):2021–2032. doi:[10.1007/s00330-008-0984-z](https://doi.org/10.1007/s00330-008-0984-z)

74. Sutton EJ, Boddington SE, Nedopil AJ, Henning TD, Demos SG, Baehner R, Sennino B, Lu Y, Daldrup-Link HE (2009) An optical imaging method to monitor stem cell migration in a model of immune-mediated arthritis. *Opt Express* 17(26):24403–24413. doi:[10.1364/OE.17.024403](https://doi.org/10.1364/OE.17.024403)
75. Hanna J, Saha K, Pando B, van Zon J, Lengner CJ, Creyghton MP, van Oudenaarden A, Jaenisch R (2009) Direct cell reprogramming is a stochastic process amenable to acceleration. *Nature* 462(7273):595–601. doi:[10.1038/nature08592](https://doi.org/10.1038/nature08592)
76. Warlich E, Kuehle J, Cantz T, Brugman MH, Maetzig T, Galla M, Filipczyk AA, Halle S, Klump H, Scholer HR, Baum C, Schroeder T, Schambach A (2011) Lentiviral vector design and imaging approaches to visualize the early stages of cellular reprogramming. *Mol Ther* 19(4):782–789. doi:[10.1038/mt.2010.314](https://doi.org/10.1038/mt.2010.314)
77. Conchello JA, Lichtman JW (2005) Optical sectioning microscopy. *Nat Methods* 2(12):920–931. doi:[10.1038/nmeth815](https://doi.org/10.1038/nmeth815)
78. Helmchen F, Denk W (2005) Deep tissue two-photon microscopy. *Nat Methods* 2(12):932–940. doi:[10.1038/nmeth818](https://doi.org/10.1038/nmeth818)
79. Rice WL, Kaplan DL, Georgakoudi I (2010) Two-photon microscopy for non-invasive, quantitative monitoring of stem cell differentiation. *PLoS ONE* 5(4):e10075. doi:[10.1371/journal.pone.0010075](https://doi.org/10.1371/journal.pone.0010075)
80. Jérôme Artus A-KH (2007) Live imaging genetically-encoded fluorescent proteins in embryonic stem cells using confocal microscopy. In: Méndez-Vilas A, Díaz J (eds) *Modern research and educational topics in microscopy*. Sloan-Kettering Institute, New York
81. Malide D, Metais JY, Dunbar CE (2012) Dynamic clonal analysis of murine hematopoietic stem and progenitor cells marked by 5 fluorescent proteins using confocal and multiphoton microscopy. *Blood* 120(26):e105–e116. doi:[10.1182/blood-2012-06-440636](https://doi.org/10.1182/blood-2012-06-440636)
82. Ntziachristos V (2010) Going deeper than microscopy: the optical imaging frontier in biology. *Nat Methods* 7(8):603–614. doi:[10.1038/nmeth.1483](https://doi.org/10.1038/nmeth.1483)
83. Rompolas P, Deschene ER, Zito G, Gonzalez DG, Saotome I, Haberman AM, Greco V (2012) Live imaging of stem cell and progeny behaviour in physiological hair-follicle regeneration. *Nature* 487(7408):496–499. doi:[10.1038/nature11218](https://doi.org/10.1038/nature11218)
84. Takayama N, Eto K (2012) Pluripotent stem cells reveal the developmental biology of human megakaryocytes and provide a source of platelets for clinical application. *Cell Mol Life Sci* 69(20):3419–3428. doi:[10.1007/s00018-012-0995-4](https://doi.org/10.1007/s00018-012-0995-4)
85. Takayama N, Nishimura S, Nakamura S, Shimizu T, Ohnishi R, Endo H, Yamaguchi T, Otsu M, Nishimura K, Nakanishi M, Sawaguchi A, Nagai R, Takahashi K, Yamanaka S, Nakauchi H, Eto K (2010) Transient activation of c-MYC expression is critical for efficient platelet generation from human induced pluripotent stem cells. *J Exp Med* 207(13):2817–2830. doi:[10.1084/jem.20100844](https://doi.org/10.1084/jem.20100844)
86. Rodriguez-Porcel M, Wu JC, Gambhir SS (2008) *Molecular imaging of stem cells*. Stem Book, Cambridge
87. Shah K, Jacobs A, Breakefield XO, Weissleder R (2004) Molecular imaging of gene therapy for cancer. *Gene Ther* 11(15):1175–1187. doi:[10.1038/sj.gt.3302278](https://doi.org/10.1038/sj.gt.3302278)
88. Nguyen PK, Lan F, Wang Y, Wu JC (2011) Imaging: guiding the clinical translation of cardiac stem cell therapy. *Circ Res* 109(8):962–979. doi:[10.1161/CIRCRESAHA.111.242909](https://doi.org/10.1161/CIRCRESAHA.111.242909)
89. Beeres SL, Bengel FM, Bartunek J, Atsma DE, Hill JM, Vanderheyden M, Penicka M, Schaliq MJ, Wijns W, Bax JJ (2007) Role of imaging in cardiac stem cell therapy. *J Am Col Cardiol* 49(11):1137–1148. doi:[10.1016/j.jacc.2006.10.072](https://doi.org/10.1016/j.jacc.2006.10.072)
90. Rodriguez-Porcel M (2010) In vivo imaging and monitoring of transplanted stem cells: clinical applications. *Curr Cardiol Rep* 12(1):51–58. doi:[10.1007/s11886-009-0073-1](https://doi.org/10.1007/s11886-009-0073-1)
91. Chan AT, Abraham MR (2012) SPECT and PET to optimize cardiac stem cell therapy. *J Nucl Cardiol* 19(1):118–125. doi:[10.1007/s12350-011-9485-6](https://doi.org/10.1007/s12350-011-9485-6)
92. Dimayuga VM, Rodriguez-Porcel M (2011) Molecular imaging of cell therapy for gastroenterologic applications. *Pancreatol* 11(4):414–427. doi:[10.1159/000327395](https://doi.org/10.1159/000327395)
93. Kircher MF, Gambhir SS, Grimm J (2011) Noninvasive cell-tracking methods. *Nat Rev Clin Oncol* 8(11):677–688. doi:[10.1038/nrclinonc.2011.141](https://doi.org/10.1038/nrclinonc.2011.141)

94. Manley NC, Steinberg GK (2012) Tracking stem cells for cellular therapy in stroke. *Curr Pharm Des* 18(25):3685–3693
95. Sandu N, Schaller B (2010) Stem cell transplantation in brain tumors: a new field for molecular imaging? *Mol Med* 16(9–10):433–437. doi:[10.2119/molmed.2010.00035](https://doi.org/10.2119/molmed.2010.00035)
96. Shah P, Choi BG, Mazhari R (2011) Positron emission tomography for the evaluation and treatment of cardiomyopathy. *Ann New York Acad Sci* 1228:137–149. doi:[10.1111/j.1749-6632.2011.06017.x](https://doi.org/10.1111/j.1749-6632.2011.06017.x)
97. Wang J, Tian M, Zhang H (2011) PET molecular imaging in stem cell therapy for neurological diseases. *Eur J Nucl Med Mol Imaging* 38(10):1926–1938. doi:[10.1007/s00259-011-1860-7](https://doi.org/10.1007/s00259-011-1860-7)
98. Wu C, Ma G, Li J, Zheng K, Dang Y, Shi X, Sun Y, Li F, Zhu Z (2013) In vivo cell tracking via (1)(8)F-fluorodeoxyglucose labeling: a review of the preclinical and clinical applications in cell-based diagnosis and therapy. *Clin Imaging* 37(1):28–36. doi:[10.1016/j.clinimag.2012.02.023](https://doi.org/10.1016/j.clinimag.2012.02.023)
99. Zhou R, Acton PD, Ferrari VA (2006) Imaging stem cells implanted in infarcted myocardium. *J Am Col Cardiol* 48(10):2094–2106. doi:[10.1016/j.jacc.2006.08.026](https://doi.org/10.1016/j.jacc.2006.08.026)
100. Bengel FM (2011) Noninvasive stem cell tracking. *J Nucl Cardiol* 18(5):966–973. doi:[10.1007/s12350-011-9436-2](https://doi.org/10.1007/s12350-011-9436-2)
101. Cao F, Li Z, Lee A, Liu Z, Chen K, Wang H, Cai W, Chen X, Wu JC (2009) Noninvasive de novo imaging of human embryonic stem cell-derived teratoma formation. *Cancer Res* 69(7):2709–2713. doi:[10.1158/0008-5472.CAN-08-4122](https://doi.org/10.1158/0008-5472.CAN-08-4122)
102. Martinez-Quintanilla J, Bhare D, Heidari P, He D, Mahmood U, Shah K (2013) In vivo Imaging of the therapeutic efficacy and fate of bimodal engineered stem cells in malignant brain tumors. *Stem Cells*. doi:[10.1002/stem.1355](https://doi.org/10.1002/stem.1355)
103. Rueger MA, Backes H, Walberer M, Neumaier B, Ullrich R, Simard ML, Emig B, Fink GR, Hoeft M, Graf R, Schroeter M (2010) Noninvasive imaging of endogenous neural stem cell mobilization in vivo using positron emission tomography. *J Neurosci* 18:6454–6460. doi:[10.1523/JNEUROSCI.6092-09.2010](https://doi.org/10.1523/JNEUROSCI.6092-09.2010)
104. Shields AF, Grierson JR, Dohmen BM, Machulla HJ, Stayanoff JC, Lawhorn-Crews JM, Obradovich JE, Muzik O, Mangner TJ (1998) Imaging proliferation in vivo with [¹⁸F]FLT and positron emission tomography. *Nat Med* 4(11):1334–1336. doi:[10.1038/3337](https://doi.org/10.1038/3337)
105. Tarantal AF, Lee CC, Batchelder CA, Christensen JE, Prater D, Cherry SR (2012) Radiolabeling and in vivo imaging of transplanted renal lineages differentiated from human embryonic stem cells in fetal rhesus monkeys. *Mol Imaging Biol* 14(2):197–204. doi:[10.1007/s11307-011-0487-1](https://doi.org/10.1007/s11307-011-0487-1)
106. Kang WJ, Kang HJ, Kim HS, Chung JK, Lee MC, Lee DS (2006) Tissue distribution of 18F-FDG-labeled peripheral hematopoietic stem cells after intracoronary administration in patients with myocardial infarction. *J Nucl Med* 47(8):1295–1301
107. Lee PH, Kim JW, Bang OY, Ahn YH, Joo IS, Huh K (2008) Autologous mesenchymal stem cell therapy delays the progression of neurological deficits in patients with multiple system atrophy. *Clin Pharmacol Ther* 83(5):723–730. doi:[10.1038/sj.clpt.6100386](https://doi.org/10.1038/sj.clpt.6100386)
108. Marini C, Podesta M, Massollo M, Capitanio S, Fiz F, Morbelli S, Brignone M, Bacigalupo A, Piana M, Frassoni F, Sambucetti G (2012) Intrabone transplant of cord blood stem cells establishes a local engraftment store: a functional PET/FDG study. *J Biomed Biotechnol* 2012:767369. doi:[10.1155/2012/767369](https://doi.org/10.1155/2012/767369)
109. Castellani M, Colombo A, Giordano R, Pusineri E, Canzi C, Longari V, Piccaluga E, Palatresi S, Dellavedova L, Soligo D, Rebulli P, Gerundini P (2010) The role of PET with 13 N-ammonia and 18F-FDG in the assessment of myocardial perfusion and metabolism in patients with recent AMI and intracoronary stem cell injection. *J Nucl Med* 51(12):1908–1916. doi:[10.2967/jnumed.110.078469](https://doi.org/10.2967/jnumed.110.078469)
110. Loebe DM, Hobbs RF, Okoli A, Chen AR, Cho S, Srinivasan S, Sgouros G, Shokek O, Wharam MD Jr, Scott T, Schwartz CL (2010) Tandem dosing of samarium-153 ethylenediamine tetramethylene phosphoric acid with stem cell support for patients with high-risk osteosarcoma. *Cancer* 116(23):5470–5478. doi:[10.1002/cncr.25518](https://doi.org/10.1002/cncr.25518)

111. Li Z, Wu JC, Sheikh AY, Kraft D, Cao F, Xie X, Patel M, Gambhir SS, Robbins RC, Cooke JP (2007) Differentiation, survival, and function of embryonic stem cell derived endothelial cells for ischemic heart disease. *Circulation* 116(11 Suppl):I46–I54. doi:[10.1161/CIRCULATIONAHA.106.680561](https://doi.org/10.1161/CIRCULATIONAHA.106.680561)
112. Hung SC, Deng WP, Yang WK, Liu RS, Lee CC, Su TC, Lin RJ, Yang DM, Chang CW, Chen WH, Wei HJ, Gelovani JG (2005) Mesenchymal stem cell targeting of microscopic tumors and tumor stroma development monitored by noninvasive in vivo positron emission tomography imaging. *Clin Cancer Res* 11(21):7749–7756. doi:[10.1158/1078-0432.CCR-05-0876](https://doi.org/10.1158/1078-0432.CCR-05-0876)
113. Terrovitis J, Kwok KF, Lautamaki R, Engles JM, Barth AS, Kizana E, Miake J, Leppo MK, Fox J, Seidel J, Pomper M, Wahl RL, Tsui B, Bengel F, Marban E, Abraham MR (2008) Ectopic expression of the sodium-iodide symporter enables imaging of transplanted cardiac stem cells in vivo by single-photon emission computed tomography or positron emission tomography. *J Am Col Cardiol*. 52(20):1652–1660. doi:[10.1016/j.jacc.2008.06.051](https://doi.org/10.1016/j.jacc.2008.06.051)
114. Higuchi T, Anton M, Saraste A, Dumler K, Pelisek J, Nekolla SG, Bengel FM, Schwaiger M (2009) Reporter gene PET for monitoring survival of transplanted endothelial progenitor cells in the rat heart after pretreatment with VEGF and atorvastatin. *J Nucl Med* 50(11):1881–1886. doi:[10.2967/jnumed.109.067801](https://doi.org/10.2967/jnumed.109.067801)
115. Yaghoubi SS, Campbell DO, Radu CG, Czernin J (2012) Positron emission tomography reporter genes and reporter probes: gene and cell therapy applications. *Theranostics* 2(4):374–391. doi:[10.7150/thno.3677](https://doi.org/10.7150/thno.3677)
116. Cao F, Lin S, Xie X, Ray P, Patel M, Zhang X, Drukker M, Dylla SJ, Connolly AJ, Chen X, Weissman IL, Gambhir SS, Wu JC (2006) In vivo visualization of embryonic stem cell survival, proliferation, and migration after cardiac delivery. *Circulation* 113(7):1005–1014. doi:[10.1161/CIRCULATIONAHA.105.588954](https://doi.org/10.1161/CIRCULATIONAHA.105.588954)
117. Rath P, Shi H, Maruniak JA, Litofsky NS, Maria BL, Kirk MD (2009) Stem cells as vectors to deliver HSV/tk gene therapy for malignant gliomas. *Curr Stem Cell Res Ther* 4(1):44–49
118. Kraitchman DL, Tatsumi M, Gilson WD, Ishimori T, Kedziorek D, Walczak P, Segars WP, Chen HH, Fritzges D, Izbudak I, Young RG, Marcelino M, Pittenger MF, Solaiyappan M, Boston RC, Tsui BM, Wahl RL, Bulte JW (2005) Dynamic imaging of allogeneic mesenchymal stem cells trafficking to myocardial infarction. *Circulation* 112(10):1451–1461. doi:[10.1161/CIRCULATIONAHA.105.537480](https://doi.org/10.1161/CIRCULATIONAHA.105.537480)
119. Blackwood KJ, Lewden B, Wells RG, Sykes J, Stodilka RZ, Wisenberg G, Prato FS (2009) In vivo SPECT quantification of transplanted cell survival after engraftment using (111)In-tropolone in infarcted canine myocardium. *J Nucl Med* 50(6):927–935. doi:[10.2967/jnumed.108.058966](https://doi.org/10.2967/jnumed.108.058966)
120. Gu E, Chen WY, Gu J, Burrige P, Wu JC (2012) Molecular imaging of stem cells: tracking survival, biodistribution, tumorigenicity, and immunogenicity. *Theranostics* 2(4):335–345. doi:[10.7150/thno.3666](https://doi.org/10.7150/thno.3666)
121. Goussetis E, Manginas A, Koutelou M, Peristeri I, Theodosaki M, Kollaros N, Leontiadis E, Theodorakos A, Paterakis G, Karatasakis G, Cokkinos DV, Graphakos S (2006) Intracoronary infusion of CD133+ and CD133-CD34+ selected autologous bone marrow progenitor cells in patients with chronic ischemic cardiomyopathy: cell isolation, adherence to the infarcted area, and body distribution. *Stem Cells* 24(10):2279–2283. doi:[10.1634/stemcells.2005-0589](https://doi.org/10.1634/stemcells.2005-0589)
122. Pomper MG, Hammond H, Yu X, Ye Z, Foss CA, Lin DD, Fox JJ, Cheng L (2009) Serial imaging of human embryonic stem-cell engraftment and teratoma formation in live mouse models. *Cell Res* 19(3):370–379. doi:[10.1038/cr.2008.329](https://doi.org/10.1038/cr.2008.329)
123. Zhou R, Thomas DH, Qiao H, Bal HS, Choi SR, Alavi A, Ferrari VA, Kung HF, Acton PD (2005) In vivo detection of stem cells grafted in infarcted rat myocardium. *J Nucl Med* 46(5):816–822
124. Zhou Y, Sun M, Li H, Yan M, He Z, Wang W, Lu S (2013) Recovery of behavioral symptoms in hemi-parkinsonian rhesus monkeys through combined gene and stem cell therapy. *Cytotherapy* 15(4):467–480. doi:[10.1016/j.jcyt.2013.01.007](https://doi.org/10.1016/j.jcyt.2013.01.007)

125. Mitkari B, Kerkela E, Nystedt J, Korhonen M, Mikkonen V, Huhtala T, Jolkkonen J (2013) Intra-arterial infusion of human bone marrow-derived mesenchymal stem cells results in transient localization in the brain after cerebral ischemia in rats. *Exp Neurol* 239:158–162. doi:[10.1016/j.expneurol.2012.09.018](https://doi.org/10.1016/j.expneurol.2012.09.018)
126. Bindslev L, Haack-Sorensen M, Bisgaard K, Kragh L, Mortensen S, Hesse B, Kjaer A, Kastrup J (2006) Labelling of human mesenchymal stem cells with indium-111 for SPECT imaging: effect on cell proliferation and differentiation. *Eur J Nucl Med Mol Imaging* 33(10):1171–1177. doi:[10.1007/s00259-006-0093-7](https://doi.org/10.1007/s00259-006-0093-7)
127. Phulpin B, Dolivet G, Marie PY, Poussier S, Huger S, Bravetti P, Graff P, Merlin JL, Tran N (2011) Feasibility of treating irradiated bone with intramedullary delivered autologous mesenchymal stem cells. *J Biomed Biotechnol* 2011:560257. doi:[10.1155/2011/560257](https://doi.org/10.1155/2011/560257)
128. Vrtovc B, Poglajen G, Lezaic L, Sever M, Domanovic D, Cernelc P, Socan A, Schrepfer S, Torre-Amione G, Haddad F, Wu JC (2013) Effects of intracoronary CD34 + stem cell transplantation in nonischemic dilated cardiomyopathy patients: 5-year follow-up. *Circ Res* 112(1):165–173. doi:[CIRCRESAHA.112.276519](https://doi.org/10.1161/CIRCRESAHA.112.276519)
129. Mader EK, Butler G, Dowdy SC, Mariani A, Knutson KL, Federspiel MJ, Russell SJ, Galanis E, Dietz AB, Peng KW (2013) Optimizing patient derived mesenchymal stem cells as virus carriers for a phase I clinical trial in ovarian cancer. *J Transl Med* 11:20. doi:[10.1186/1479-5876-11-20](https://doi.org/10.1186/1479-5876-11-20)
130. Chen SL, Fang WW, Qian J, Ye F, Liu YH, Shan SJ, Zhang JJ, Lin S, Liao LM, Zhao RC (2004) Improvement of cardiac function after transplantation of autologous bone marrow mesenchymal stem cells in patients with acute myocardial infarction. *Chin Med J (Engl)* 117(10):1443–1448
131. Musialek P, Tekieli L, Kostkiewicz M, Majka M, Szot W, Walter Z, Zebzda A, Pieniazek P, Kadzielski A, Banys RP, Olszowska M, Pasowicz M, Zmudka K, Tracz W (2011) Randomized transcoronary delivery of CD34(+) cells with perfusion versus stop-flow method in patients with recent myocardial infarction: Early cardiac retention of (9)(9)(m)Tc-labeled cells activity. *J Nucl Cardiol* 18(1):104–116. doi:[10.1007/s12350-010-9326-z](https://doi.org/10.1007/s12350-010-9326-z)
132. Perin EC, Silva GV, Zheng Y, Gahremanpour A, Canales J, Patel D, Fernandes MR, Keller LH, Quan X, Coulter SA, Moore WH, Herlihy JP, Willerson JT (2012) Randomized, double-blind pilot study of transendocardial injection of autologous aldehyde dehydrogenase-bright stem cells in patients with ischemic heart failure. *Am Heart J* 163(3):415–421, 421 e411. doi:[10.1016/j.ahj.2011.11.020](https://doi.org/10.1016/j.ahj.2011.11.020)
133. Tzukerman M, Rosenberg T, Ravel Y, Reiter I, Coleman R, Skorecki K (2003) An experimental platform for studying growth and invasiveness of tumor cells within teratomas derived from human embryonic stem cells. *Proc Natl Acad Sci USA* 100(23):13507–13512. doi:[10.1073/pnas.2235551100](https://doi.org/10.1073/pnas.2235551100)
134. Tao W, Evans BG, Yao J, Cooper S, Cornetta K, Ballas CB, Hangoc G, Broxmeyer HE (2007) Enhanced green fluorescent protein is a nearly ideal long-term expression tracer for hematopoietic stem cells, whereas DsRed-express fluorescent protein is not. *Stem Cells* 25(3):670–678. doi:[10.1634/stemcells.2006-0553](https://doi.org/10.1634/stemcells.2006-0553)
135. Frangioni JV (2003) In vivo near-infrared fluorescence imaging. *Curr Opin Chem Biol* 7(5):626–634
136. Lin S, Xie X, Patel MR, Yang YH, Li Z, Cao F, Gheysens O, Zhang Y, Gambhir SS, Rao JH, Wu JC (2007) Quantum dot imaging for embryonic stem cells. *BMC Biotechnol* 7:67. doi:[10.1186/1472-6750-7-67](https://doi.org/10.1186/1472-6750-7-67)
137. Boddington SE, Henning TD, Jha P, Schlieve CR, Mandrussow L, DeNardo D, Bernstein HS, Ritner C, Golovko D, Lu Y, Zhao S, Daldrup-Link HE (2010) Labeling human embryonic stem cell-derived cardiomyocytes with indocyanine green for noninvasive tracking with optical imaging: an FDA-compatible alternative to firefly luciferase. *Cell Transplant* 19(1):55–65. doi:[10.3727/096368909X478579](https://doi.org/10.3727/096368909X478579)
138. Tsuji O, Miura K, Okada Y, Fujiyoshi K, Mukaino M, Nagoshi N, Kitamura K, Kumagai G, Nishino M, Tomisato S, Higashi H, Nagai T, Katoh H, Kohda K, Matsuzaki Y, Yuzaki M, Ikeda E, Toyama Y, Nakamura M, Yamanaka S, Okano H (2010) Therapeutic potential of

- appropriately evaluated safe-induced pluripotent stem cells for spinal cord injury. *Proc Natl Acad Sci USA* 107(28):12704–12709. doi:[10.1073/pnas.0910106107](https://doi.org/10.1073/pnas.0910106107)
139. Daadi MM, Davis AS, Arac A, Li Z, Maag AL, Bhatnagar R, Jiang K, Sun G, Wu JC, Steinberg GK (2010) Human neural stem cell grafts modify microglial response and enhance axonal sprouting in neonatal hypoxic-ischemic brain injury. *Stroke* 41(3):516–523. doi:[10.1161/STROKEAHA.109.573691](https://doi.org/10.1161/STROKEAHA.109.573691)
 140. Wang X, Rosol M, Ge S, Peterson D, McNamara G, Pollack H, Kohn DB, Nelson MD, Crooks GM (2003) Dynamic tracking of human hematopoietic stem cell engraftment using in vivo bioluminescence imaging. *Blood* 102(10):3478–3482. doi:[10.1182/blood-2003-05-1432](https://doi.org/10.1182/blood-2003-05-1432)
 141. Tang Y, Shah K, Messerli SM, Snyder E, Breakefield X, Weissleder R (2003) In vivo tracking of neural progenitor cell migration to glioblastomas. *Hum Gene Ther* 14(13):1247–1254. doi:[10.1089/104303403767740786](https://doi.org/10.1089/104303403767740786)
 142. Wu JC, Chen IY, Sundaresan G, Min JJ, De A, Qiao JH, Fishbein MC, Gambhir SS (2003) Molecular imaging of cardiac cell transplantation in living animals using optical bioluminescence and positron emission tomography. *Circulation* 108(11):1302–1305. doi:[10.1161/01.CIR.0000091252.20010.6E](https://doi.org/10.1161/01.CIR.0000091252.20010.6E)
 143. Raikwar SP, Zavazava N (2012) PDX1-engineered embryonic stem cell-derived insulin producing cells regulate hyperglycemia in diabetic mice. *Transplant Res* 1(1):19. doi:[10.1186/2047-1440-1-19](https://doi.org/10.1186/2047-1440-1-19)
 144. Cao F, van der Bogt KE, Sadrzadeh A, Xie X, Sheikh AY, Wang H, Connolly AJ, Robbins RC, Wu JC (2007) Spatial and temporal kinetics of teratoma formation from murine embryonic stem cell transplantation. *Stem Cells Dev* 16(6):883–891. doi:[10.1089/scd.2007.0160](https://doi.org/10.1089/scd.2007.0160)
 145. Priddle H, Grabowska A, Morris T, Clarke PA, McKenzie AJ, Sottile V, Denning C, Young L, Watson S (2009) Bioluminescence imaging of human embryonic stem cells transplanted in vivo in murine and chick models. *Cloning Stem Cells* 11(2):259–267. doi:[10.1089/clo.2008.0056](https://doi.org/10.1089/clo.2008.0056)
 146. Tian X, Hexum MK, Penchev VR, Taylor RJ, Shultz LD, Kaufman DS (2009) Bioluminescent imaging demonstrates that transplanted human embryonic stem cell-derived CD34(+) cells preferentially develop into endothelial cells. *Stem Cells* 27(11):2675–2685. doi:[10.1002/stem.204](https://doi.org/10.1002/stem.204)
 147. Jung-Joon Min UCNL, Han Ho Jae, Lee Hyun-Suk, Moon Sung-Min, Heo Jung-Sun, Lee Yun Jung, Ahn Kyuyoun, Park Kwangsung (2008) Visualization of embryonic stem cell survival in vivo by adenoviral-driven bioluminescence reporter in rat corpus cavernosum. *Tissue Eng Regen Med* 5(4):743–749
 148. Sher F, van Dam G, Boddeke E, Copray S (2009) Bioluminescence imaging of Olig2-neural stem cells reveals improved engraftment in a demyelination mouse model. *Stem Cells* 27(7):1582–1591. doi:[10.1002/stem.76](https://doi.org/10.1002/stem.76)
 149. Ling X, Marini F, Konopleva M, Schober W, Shi Y, Burks J, Clise-Dwyer K, Wang RY, Zhang W, Yuan X, Lu H, Caldwell L, Andreeff M (2010) Mesenchymal stem cells overexpressing IFN-beta inhibit breast cancer growth and metastases through Stat3 signaling in a syngeneic tumor model. *Cancer Microenviron* 3(1):83–95. doi:[10.1007/s12307-010-0041-8](https://doi.org/10.1007/s12307-010-0041-8)
 150. Deuse T, Peter C, Fedak PW, Doyle T, Reichenspurner H, Zimmermann WH, Eschenhagen T, Stein W, Wu JC, Robbins RC, Schrepfer S (2009) Hepatocyte growth factor or vascular endothelial growth factor gene transfer maximizes mesenchymal stem cell-based myocardial salvage after acute myocardial infarction. *Circulation* 120(11 Suppl):S247–S254. doi:[10.1161/CIRCULATIONAHA.108.843680](https://doi.org/10.1161/CIRCULATIONAHA.108.843680)
 151. Togel F, Yang Y, Zhang P, Hu Z, Westenfelder C (2008) Bioluminescence imaging to monitor the in vivo distribution of administered mesenchymal stem cells in acute kidney injury. *Am J Physiol Renal Physiol* 295(1):F315–F321. doi:[10.1152/ajprenal.00098.2008](https://doi.org/10.1152/ajprenal.00098.2008)

152. Zachos T, Diggs A, Weisbrode S, Bartlett J, Bertone A (2007) Mesenchymal stem cell-mediated gene delivery of bone morphogenetic protein-2 in an articular fracture model. *Mol Ther* 15(8):1543–1550. doi:[10.1038/sj.mt.6300192](https://doi.org/10.1038/sj.mt.6300192)
153. Gao J, Li Y, Lu S, Wang M, Yang Z, Yan X, Zheng Y (2009) Enhanced in vivo motility of human umbilical cord blood hematopoietic stem/progenitor cells introduced via intra-bone marrow injection into xenotransplanted NOD/SCID mouse. *Exp Hematol* 37(8):990–997. doi:[10.1016/j.exphem.2009.05.006](https://doi.org/10.1016/j.exphem.2009.05.006)
154. Yong RL, Shinojima N, Fueyo J, Gumin J, Vecil GG, Marini FC, Bogler O, Andreeff M, Lang FF (2009) Human bone marrow-derived mesenchymal stem cells for intravascular delivery of oncolytic adenovirus Delta24-RGD to human gliomas. *Cancer Res* 69(23):8932–8940. doi:[10.1158/0008-5472.CAN-08-3873](https://doi.org/10.1158/0008-5472.CAN-08-3873)
155. Wang H, Cao F, De A, Cao Y, Contag C, Gambhir SS, Wu JC, Chen X (2009) Trafficking mesenchymal stem cell engraftment and differentiation in tumor-bearing mice by bioluminescence imaging. *Stem Cells* 27(7):1548–1558. doi:[10.1002/stem.81](https://doi.org/10.1002/stem.81)
156. Pearl JI, Lee AS, Leveson-Gower DB, Sun N, Ghosh Z, Lan F, Ransohoff J, Negrin RS, Davis MM, Wu JC (2011) Short-term immunosuppression promotes engraftment of embryonic and induced pluripotent stem cells. *Cell Stem Cell* 8(3):309–317. doi:[10.1016/j.stem.2011.01.012](https://doi.org/10.1016/j.stem.2011.01.012)
157. Boheler KR, Joodi RN, Qiao H, Juhasz O, Urick AL, Chuppa SL, Gundry RL, Wersto RP, Zhou R (2011) Embryonic stem cell-derived cardiomyocyte heterogeneity and the isolation of immature and committed cells for cardiac remodeling and regeneration. *Stem Cells Int* 2011:214203. doi:[10.4061/2011/214203](https://doi.org/10.4061/2011/214203)
158. Lee AS, Xu D, Plews JR, Nguyen PK, Nag D, Lyons JK, Han L, Hu S, Lan F, Liu J, Huang M, Narsinh KH, Long CT, de Almeida PE, Levi B, Kooreman N, Bangs C, Pacharinsak C, Ikeno F, Yeung AC, Gambhir SS, Robbins RC, Longaker MT, Wu JC (2011) Preclinical derivation and imaging of autologously transplanted canine induced pluripotent stem cells. *J Biol Chem* 286(37):32697–32704. doi:[10.1074/jbc.M111.235739](https://doi.org/10.1074/jbc.M111.235739)
159. Williams AR, Hatzistergos KE, Addicott B, McCall F, Carvalho D, Suncion V, Morales AR, Da Silva J, Sussman MA, Heldman AW, Hare JM (2013) Enhanced effect of combining human cardiac stem cells and bone marrow mesenchymal stem cells to reduce infarct size and to restore cardiac function after myocardial infarction. *Circulation* 127(2):213–223. doi:[10.1161/CIRCULATIONAHA.112.131110](https://doi.org/10.1161/CIRCULATIONAHA.112.131110)
160. Liu J, Cheng EC, Long RC, Yang SH, Wang L, Cheng PH, Yang J, Wu D, Mao H, Chan AW (2009) Noninvasive monitoring of embryonic stem cells in vivo with MRI transgene reporter. *Tissue Eng Part C Methods* 15(4):739–747. doi:[10.1089/ten.TEC2008.0678](https://doi.org/10.1089/ten.TEC2008.0678)
161. Burgess A, Ayala-Grosso CA, Ganguly M, Jordao JF, Aubert I, Hynynen K (2011) Targeted delivery of neural stem cells to the brain using MRI-guided focused ultrasound to disrupt the blood-brain barrier. *PLoS ONE* 6(11):e27877. doi:[10.1371/journal.pone.0027877](https://doi.org/10.1371/journal.pone.0027877)
162. Qiu B, Yang X (2008) Molecular MRI of hematopoietic stem-progenitor cells: in vivo monitoring of gene therapy and atherosclerosis. *Nat Clin Pract Cardiovas Med* 5(7):396–404. doi:[10.1038/npcardio1217](https://doi.org/10.1038/npcardio1217)
163. Chung J, Yamada M, Yang PC (2009) Magnetic resonance imaging of human embryonic stem cells. *Curr Protoc Stem Cell Biol*. Chapter 5 (Unit 5A):3. doi:[10.1002/9780470151808.sc05a03s10](https://doi.org/10.1002/9780470151808.sc05a03s10)
164. Himes N, Min JY, Lee R, Brown C, Shea J, Huang X, Xiao YF, Morgan JP, Burstein D, Oettgen P (2004) In vivo MRI of embryonic stem cells in a mouse model of myocardial infarction. *Magn Res Med* 52(5):1214–1219. doi:[10.1002/mrm.20220](https://doi.org/10.1002/mrm.20220)
165. Daadi MM, Li Z, Arac A, Grueter BA, Sofilos M, Malenka RC, Wu JC, Steinberg GK (2009) Molecular and magnetic resonance imaging of human embryonic stem cell-derived neural stem cell grafts in ischemic rat brain. *Mol Ther* 17(7):1282–1291. doi:[10.1038/mt.2009.104](https://doi.org/10.1038/mt.2009.104)
166. Shen J, Zhong XM, Duan XH, Cheng LN, Hong GB, Bi XB, Liu Y (2009) Magnetic resonance imaging of mesenchymal stem cells labeled with dual (MR and fluorescence)

- agents in rat spinal cord injury. *Acad Radiol* 16(9):1142–1154. doi:[10.1016/j.acra.2009.03.016](https://doi.org/10.1016/j.acra.2009.03.016)
167. Sykova E, Jendelova P (2006) Magnetic resonance tracking of transplanted stem cells in rat brain and spinal cord. *Neurodegener Dis* 3(1–2):62–67. doi:[10.1159/000092095](https://doi.org/10.1159/000092095)
168. Campan M, Lionetti V, Aquaro GD, Forini F, Matteucci M, Vannucci L, Chiuppesi F, Di Cristofano C, Faggioni M, Maioli M, Barile L, Messina E, Lombardi M, Pucci A, Pistello M, Recchia FA (2011) Ferritin as a reporter gene for in vivo tracking of stem cells by 1.5-T cardiac MRI in a rat model of myocardial infarction. *Am J Physiol Heart Circ Physiol* 300(6):H2238–H2250. doi:[10.1152/ajpheart.00935.2010](https://doi.org/10.1152/ajpheart.00935.2010)
169. Amado LC, Saliaris AP, Schuleri KH, St John M, Xie JS, Cattaneo S, Durand DJ, Fitton T, Kuang JQ, Stewart G, Lehrke S, Baumgartner WW, Martin BJ, Heldman AW, Hare JM (2005) Cardiac repair with intramyocardial injection of allogeneic mesenchymal stem cells after myocardial infarction. *Proc Natl Acad Sci USA* 102(32):11474–11479. doi:[10.1073/pnas.0504388102](https://doi.org/10.1073/pnas.0504388102)
170. Wood JA, Chung DJ, Park SA, Zwigenberger AL, Reilly CM, Ly I, Walker NJ, Vernau W, Hayashi K, Wisner ER, Cannon MS, Kass PH, Cherry SR, Borjesson DL, Russell P, Murphy CJ (2012) Periocular and intra-articular injection of canine adipose-derived mesenchymal stem cells: an in vivo imaging and migration study. *J Ocul Pharmacol Ther* 28(3):307–317. doi:[10.1089/jop.2011.0166](https://doi.org/10.1089/jop.2011.0166)
171. Lu SS, Liu S, Zu QQ, Xu XQ, Yu J, Wang JW, Zhang Y, Shi HB (2013) In vivo MR imaging of intraarterially delivered magnetically labeled mesenchymal stem cells in a canine stroke model. *PLoS ONE* 8(2):e54963. doi:[10.1371/journal.pone.0054963](https://doi.org/10.1371/journal.pone.0054963)
172. Meng Y, Zhang F, Blair T, Gu H, Feng H, Wang J, Yuan C, Zhang Z, Qiu B, Yang X (2012) MRI of auto-transplantation of bone marrow-derived stem-progenitor cells for potential repair of injured arteries. *PLoS ONE* 7(2):e31137. doi:[10.1371/journal.pone.0031137](https://doi.org/10.1371/journal.pone.0031137)
173. Watts AE, Yeager AE, Kopyov OV, Nixon AJ (2011) Fetal derived embryonic-like stem cells improve healing in a large animal flexor tendonitis model. *Stem Cell Res Ther* 2(1):4. doi:[10.1186/scrt45](https://doi.org/10.1186/scrt45)
174. Leng X, Wang J, Fu H, Fisher A, Chen X, Villanueva FS (2009) In-vivo stem cell tracking using ultrasound imaging. *Circulation* 120(Suppl 18):S326
175. Arpornmaeklong P, Wang Z, Pressler MJ, Brown SE, Krebsbach PH (2010) Expansion and characterization of human embryonic stem cell-derived osteoblast-like cells. *Cell Reprogram* 12(4):377–389. doi:[10.1089/cell.2009.0079](https://doi.org/10.1089/cell.2009.0079)
176. Nienhuis AW, Persons DA (2012) Development of gene therapy for thalassemia. *Cold Spring Harb Perspect Med* 2(11). doi:[2/11/a011833](https://doi.org/10.1101/a011833)
177. Siqueira RC (2011) Stem-cell therapy for retinal diseases In: Kallos PMS (ed) *Embryonic stem cells—differentiation and pluripotent alternatives*. InTech, p 506
178. Dunnett SB, Bjorklund A (1987) Mechanisms of function of neural grafts in the adult mammalian brain. *J Exp Biol* 132:265–289
179. Drucker-Colin R, Verdugo-Diaz L (2004) Cell transplantation for Parkinson's disease: present status. *Cell Mol Neurobiol* 24(3):301–316
180. Freed CR, Greene PE, Breeze RE, Tsai WY, DuMouchel W, Kao R, Dillon S, Winfield H, Culver S, Trojanowski JQ, Eidelberg D, Fahn S (2001) Transplantation of embryonic dopamine neurons for severe Parkinson's disease. *New Engl J Med* 344(10):710–719. doi:[10.1056/NEJM200103083441002](https://doi.org/10.1056/NEJM200103083441002)
181. Venkataramana NK, Kumar SK, Balaraju S, Radhakrishnan RC, Bansal A, Dixit A, Rao DK, Das M, Jan M, Gupta PK, Totey SM (2010) Open-labeled study of unilateral autologous bone-marrow-derived mesenchymal stem cell transplantation in Parkinson's disease. *Transl Res* 155(2):62–70. doi:[S1931-5244\(09\)00220-5](https://doi.org/10.1016/j.trsl.2010.09.002)
182. Davies T, Amy Greenwood P, Opitz S, Girard L (2008) Stem cell science: overviews of selected disease areas stem cells and neurodegenerative disease
183. Bachoud-Levi AC, Gaura V, Brugieres P, Lefaucheur JP, Boisse MF, Maison P, Baudic S, Ribeiro MJ, Bourdet C, Remy P, Cesaro P, Hantraye P, Peschanski M (2006) Effect of fetal neural transplants in patients with Huntington's disease 6 years after surgery: a long-term

- follow-up study. *Lancet Neurol.* 5 (4):303–309. doi:[S1474-4422\(06\)70381-7](https://doi.org/10.1016/S1474-4422(06)70381-7)[pii] 10.1016/S1474-4422(06)70381-7
184. Gaura V, Bachoud-Levi AC, Ribeiro MJ, Nguyen JP, Frouin V, Baudic S, Brugieres P, Mangin JF, Boisse MF, Palfi S, Cesaro P, Samson Y, Hantraye P, Peschanski M, Remy P (2004) Striatal neural grafting improves cortical metabolism in Huntington's disease patients. *Brain.* 127(Pt 1):65–72. doi:[10.1093/brain/awh003](https://doi.org/10.1093/brain/awh003)
 185. Mazzini L, Fagioli F, Boccaletti R (2004) Stem-cell therapy in amyotrophic lateral sclerosis. *Lancet* 364(9449):1936–1937. doi:[S0140673604174709](https://doi.org/10.1016/S0140673604174709)
 186. Mazzini L, Fagioli F, Boccaletti R, Mareschi K, Oliveri G, Olivieri C, Pastore I, Marasso R, Madon E (2003) Stem cell therapy in amyotrophic lateral sclerosis: a methodological approach in humans. *Amyotroph Lateral Scler Other Motor Neuron Disord* 4(3):158–161. doi:[WEYT8N4CMFY5MVM6](https://doi.org/10.1080/14737170310001638888)
 187. Mazzini L, Ferrero I, Luparello V, Rustichelli D, Gunetti M, Mareschi K, Testa L, Stecco A, Tarletti R, Miglioretti M, Fava E, Nasuelli N, Cisari C, Massara M, Vercelli R, Oggioni GD, Carriero A, Cantello R, Monaco F, Fagioli F (2010) Mesenchymal stem cell transplantation in amyotrophic lateral sclerosis: a phase I clinical trial. *Exp Neurol* 223(1):229–237. doi:[S0014-4886\(09\)00317-3](https://doi.org/10.1016/j.expneurol.2009.09.031)
 188. Trounson A, Thakar RG, Lomax G, Gibbons D (2011) Clinical trials for stem cell therapies. *BMC Med.* 9:52. doi:[1741-7015-9-52](https://doi.org/10.1186/1745-7189-9-52)
 189. Acharya VN (2012) Stem cell therapy for kidney disease—present and future. *J Assoc Physicians India* 60:32–33
 190. Trivedi HL, Vanikar AV, Vakil JM, Shah VR, Modi PR, Trivedi VB (2004) A strategy to achieve donor-specific hyporesponsiveness in cadaver renal allograft recipients by donor haematopoietic stem cell transplantation into the thymus and periphery. *Nephrol Dial Transplant* 19(9):2374–2377. doi:[10.1093/ndt/gfh27419/9/2374](https://doi.org/10.1093/ndt/gfh27419/9/2374)
 191. Thrasher AJ, Hacein-Bey-Abina S, Gaspar HB, Blanche S, Davies EG, Parsley K, Gilmour K, King D, Howe S, Sinclair J, Hue C, Carlier F, von Kalle C, de Saint Basile G, le Deist F, Fischer A, Cavazzana-Calvo M (2005) Failure of SCID-X1 gene therapy in older patients. *Blood* 105(11):4255–4257. doi:[2004-12-4837](https://doi.org/10.1182/blood-2004-12-4837)
 192. Gaspar HB, Cooray S, Gilmour KC, Parsley KL, Adams S, Howe SJ, Al Ghonaium A, Bayford J, Brown L, Davies EG, Kinnon C, Thrasher AJ (2011) Long-term persistence of a polyclonal T cell repertoire after gene therapy for X-linked severe combined immunodeficiency. *Sci Transl Med* 3(97):97ra79. doi:[3/97/97ra79](https://doi.org/10.1126/scitranslmed.3002799)
 193. Hacein-Bey-Abina S, Le Deist F, Carlier F, Bouneaud C, Hue C, De Villartay JP, Thrasher AJ, Wulffraat N, Sorensen R, Dupuis-Girod S, Fischer A, Davies EG, Kuis W, Leiva L, Cavazzana-Calvo M (2002) Sustained correction of X-linked severe combined immunodeficiency by ex vivo gene therapy. *New Engl J Med* 346(16):1185–1193. doi:[10.1056/NEJMoa012616346/16/1185](https://doi.org/10.1056/NEJMoa012616346/16/1185)
 194. Cavazzana-Calvo M, Payen E, Negre O, Wang G, Hehir K, Fusil F, Down J, Denaro M, Brady T, Westerman K, Cavallesco R, Gillet-Legrand B, Caccavelli L, Sgarra R, Maouche-Chretien L, Bernaudin F, Girot R, Dorazio R, Mulder GJ, Polack A, Bank A, Soulier J, Larghero J, Kabbara N, Dalle B, Gourmel B, Socie G, Chretien S, Cartier N, Aubourg P, Fischer A, Cornetta K, Galacteros F, Beuzard Y, Gluckman E, Bushman F, Hacein-Bey-Abina S, Leboulch P (2010) Transfusion independence and HMGA2 activation after gene therapy of human beta-thalassaemia. *Nature* 467(7313):318–322. doi:[nature09328](https://doi.org/10.1038/nature09328)
 195. Riviere I, Dunbar CE, Sadelain M (2012) Hematopoietic stem cell engineering at a crossroads. *Blood* 119(5):1107–1116. doi:[blood-2011-09-349993](https://doi.org/10.1182/blood-2011-09-349993)
 196. Lehmann R, Pavlicek V, Spinass GA, Weber M (2005) Islet transplantation in type I diabetes mellitus. *Ther Umsch* 62(7):481–486
 197. Gu W, Hu J, Wang W, Li L, Tang W, Sun S, Cui W, Ye L, Zhang Y, Hong J, Zhu D, Ning G (2012) Diabetic ketoacidosis at diagnosis influences complete remission after treatment with hematopoietic stem cell transplantation in adolescents with type 1 diabetes. *Diabetes Care* 35(7):1413–1419. doi:[dc11-2161](https://doi.org/10.2337/dc11-2161)

198. Haller MJ, Wasserfall CH, McGrail KM, Cintron M, Brusko TM, Wingard JR, Kelly SS, Shuster JJ, Atkinson MA, Schatz DA (2009) Autologous umbilical cord blood transfusion in very young children with type 1 diabetes. *Diabetes Care* 32(11):2041–2046. doi:[dc09-0967](#)
199. Miki T (2011) Amnion-derived stem cells: in quest of clinical applications. *Stem Cell Res Ther* 2(3):25. doi:[s crt66](#)
200. Hou Y, Huang Q, Liu T, Guo L (2008) Human amnion epithelial cells can be induced to differentiate into functional insulin-producing cells. *Acta Biochim Biophys Sin (Shanghai)* 40(9):830–839
201. Rancea M, Skoetz N, Monsef I, Hubel K, Engert A, Bauer K (2012) Fourteenth biannual report of the Cochrane haematological malignancies group—focus on autologous stem cell transplantation in hematological malignancies. *J Natl Cancer Inst* 104(14):NP. doi:[djs278](#)
202. Michallet M, Dreger P, Sutton L, Brand R, Richards S, van Os M, Sobh M, Choquet S, Corront B, Dearden C, Gratwohl A, Herr W, Catovsky D, Hallek M, de Witte T, Niederwieser D, Leporrier M, Milligan D (2011) Autologous hematopoietic stem cell transplantation in chronic lymphocytic leukemia: results of European intergroup randomized trial comparing autografting versus observation. *Blood* 117(5):1516–1521. doi:[blood-2010-09-308775](#)
203. Sutton L, Chevret S, Tourmilhac O, Divine M, Leblond V, Corront B, Lepretre S, Eghbali H, Van Den Neste E, Michallet M, Maloisel F, Bouabdallah K, Decaudin D, Berthou C, Brice P, Gonzalez H, Chapiro E, Radford-Weiss I, Leporrier N, Maloum K, Nguyen-Khac F, Davi F, Lejeune J, Merle-Beral H, Leporrier M (2011) Autologous stem cell transplantation as a first-line treatment strategy for chronic lymphocytic leukemia: a multicenter, randomized, controlled trial from the SFGM-TC and GFLLC. *Blood* 117(23):6109–6119. doi:[blood-2010-11-317073](#)
204. Socie G, Schmoor C, Bethge WA, Ottinger HD, Stelljes M, Zander AR, Volin L, Ruutu T, Heim DA, Schwerdtfeger R, Kolbe K, Mayer J, Maertens JA, Linkesch W, Holler E, Koza V, Bornhauser M, Einsele H, Kolb HJ, Bertz H, Egger M, Grishina O, Finke J (2011) Chronic graft-versus-host disease: long-term results from a randomized trial on graft-versus-host disease prophylaxis with or without anti-T-cell globulin ATG-Fresenius. *Blood* 117(23):6375–6382. doi:[blood-2011-01-329821](#)
205. George RE, Li S, Medeiros-Nancarrow C, Neuberger D, Marcus K, Shamberger RC, Pulsipher M, Grupp SA, Diller L (2006) High-risk neuroblastoma treated with tandem autologous peripheral-blood stem cell-supported transplantation: long-term survival update. *J Clin Oncol* 24(18):2891–2896. doi:[24/18/2891](#)
206. Berthold F, Boos J, Burdach S, Erttmann R, Henze G, Hermann J, Klingebiel T, Kremens B, Schilling FH, Schrappe M, Simon T, Hero B (2005) Myeloablative megatherapy with autologous stem-cell rescue versus oral maintenance chemotherapy as consolidation treatment in patients with high-risk neuroblastoma: a randomised controlled trial. *Lancet Oncol* 6(9):649–658. doi:[S1470-2045\(05\)70291-6](#)
207. Wollert KC, Drexler H (2010) Cell therapy for the treatment of coronary heart disease: a critical appraisal. *Nat Rev Cardiol*. 7(4):204–215. doi:[nrcardio.2010.1](#)
208. Wollert KC, Meyer GP, Lotz J, Ringes-Lichtenberg S, Lippolt P, Breidenbach C, Fichtner S, Korte T, Hornig B, Messinger D, Arseniev L, Hertenstein B, Ganser A, Drexler H (2004) Intracoronary autologous bone-marrow cell transfer after myocardial infarction: the BOOST randomised controlled clinical trial. *Lancet* 364(9429):141–148. doi:[10.1016/S0140-6736\(04\)16626-9S0140673604166269](#)
209. Janssens S, Dubois C, Bogaert J, Theunissen K, Deroose C, Desmet W, Kalantzi M, Herbots L, Sinnaeve P, Dens J, Maertens J, Rademakers F, Dymarkowski S, Gheysens O, Van Cleemput J, Bormans G, Nuyts J, Belmans A, Mortelmans L, Boogaerts M, Van de Werf F (2006) Autologous bone marrow-derived stem-cell transfer in patients with ST-segment elevation myocardial infarction: double-blind, randomised controlled trial. *Lancet* 367(9505):113–121. doi:[S0140-6736\(05\)67861-0](#)
210. Schachinger V, Erbs S, Elsasser A, Haberbosch W, Hambrecht R, Holschermann H, Yu J, Corti R, Mathey DG, Hamm CW, Suselbeck T, Assmus B, Tonn T, Dimmeler S, Zeiher AM

- (2006) Intracoronary bone marrow-derived progenitor cells in acute myocardial infarction. *New Engl J Med* 355(12):1210–1221. doi:[355/12/1210](https://doi.org/10.1056/NEJMoa052163)
211. Lunde K, Solheim S, Aakhus S, Arnesen H, Abdelnoor M, Egeland T, Endresen K, Ilebakk A, Mangschau A, Fjeld JG, Smith HJ, Taraldsrud E, Groggaard HK, Bjornerheim R, Brekke M, Muller C, Hopp E, Ragnarsson A, Brinchmann JE, Forfang K (2006) Intracoronary injection of mononuclear bone marrow cells in acute myocardial infarction. *New Engl J Med* 355(12):1199–1209. doi:[355/12/1199](https://doi.org/10.1056/NEJMoa052163)
 212. Huikuri HV, Kervinen K, Niemela M, Ylitalo K, Saily M, Koistinen P, Savolainen ER, Ukkonen H, Pietila M, Airaksinen JK, Knuuti J, Makikallio TH (2008) Effects of intracoronary injection of mononuclear bone marrow cells on left ventricular function, arrhythmia risk profile, and restenosis after thrombolytic therapy of acute myocardial infarction. *Eur Heart J* 29(22):2723–2732. doi:[ehn436](https://doi.org/10.1093/eurheartj/ehn436)
 213. Tendera M, Wojakowski W, Ruzyllo W, Chojnowska L, Kepka C, Tracz W, Musialek P, Piwowarska W, Nessler J, Buszman P, Grajek S, Breborowicz P, Majka M, Ratajczak MZ (2009) Intracoronary infusion of bone marrow-derived selected CD34+ CXCR4+ cells and non-selected mononuclear cells in patients with acute STEMI and reduced left ventricular ejection fraction: results of randomized, multicentre myocardial regeneration by intracoronary infusion of selected population of stem cells in acute myocardial infarction (REGENT) trial. *Eur Heart J* 30(11):1313–1321. doi:[ehp073](https://doi.org/10.1093/eurheartj/ehp073)
 214. van der Laan A, Hirsch A, Nijveldt R, van der Vleuten PA, van der Giessen WJ, Doevendans PA, Waltenberger J, Ten Berg JM, Aengevaeren WR, Zwaginga JJ, Biemond BJ, van Rossum AC, Tijssen JG, Zijlstra F, Piek JJ (2008) Bone marrow cell therapy after acute myocardial infarction: the HEBE trial in perspective, first results. *Neth Heart J* 16(12):436–439
 215. Losordo DW, Schatz RA, White CJ, Udelson JE, Veereshwarayya V, Durgin M, Poh KK, Weinstein R, Kearney M, Chaudhry M, Burg A, Eaton L, Heyd L, Thorne T, Shturman L, Hoffmeister P, Story K, Zak V, Dowling D, Traverse JH, Olson RE, Flanagan J, Sodano D, Murayama T, Kawamoto A, Kusano KF, Wollins J, Welt F, Shah P, Soukas P, Asahara T, Henry TD (2007) Intramyocardial transplantation of autologous CD34+ stem cells for intractable angina: a phase I/IIa double-blind, randomized controlled trial. *Circulation* 115(25):3165–3172. doi:[CIRCULATIONAHA.106.687376](https://doi.org/10.1161/CIRCULATIONAHA.106.687376)
 216. Jonas JB, Witzens-Harig M, Arseniev L, Ho AD (2010) Intravitreal autologous bone-marrow-derived mononuclear cell transplantation. *Acta Ophthalmol* 88(4):e131–e132. doi:[AOS1564](https://doi.org/10.1093/aos1564)
 217. Jonas JB, Witzens-Harig M, Arseniev L, Ho AD (2008) Intravitreal autologous bone marrow-derived mononuclear cell transplantation: a feasibility report. *Acta Ophthalmol* 86(2):225–226. doi:[AOS987](https://doi.org/10.1093/aos987)
 218. Yong Zhao M, PhD phase 1/phase 2 study of stem cell educator therapy in alopecia areata
 219. Lataillade JJ, Doucet C, Bey E, Carsin H, Huet C, Clairand I, Bottollier-Depois JF, Chapel A, Ernou I, Gourven M, Boutin L, Hayden A, Carcamo C, Buglova E, Joussemet M, de Revel T, Gourmelon P (2007) New approach to radiation burn treatment by dosimetry-guided surgery combined with autologous mesenchymal stem cell therapy. *Regen Med* 2(5):785–794. doi:[10.2217/17460751.2.5.785](https://doi.org/10.2217/17460751.2.5.785)
 220. Heile A, Brinker T (2011) Clinical translation of stem cell therapy in traumatic brain injury: the potential of encapsulated mesenchymal cell biodelivery of glucagon-like peptide-1. *Dialogues Clin Neurosci* 13(3):279–286
 221. Marcacci M, Kon E, Moukhachev V, Lavroukov A, Kutepov S, Quarto R, Mastrogiacomio M, Cancedda R (2007) Stem cells associated with macroporous bioceramics for long bone repair: 6- to 7-year outcome of a pilot clinical study. *Tissue Eng* 13(5):947–955. doi:[10.1089/ten.2006.0271](https://doi.org/10.1089/ten.2006.0271)
 222. Horwitz EM, Prockop DJ, Fitzpatrick LA, Koo WW, Gordon PL, Neel M, Sussman M, Orchard P, Marx JC, Pyeritz RE, Brenner MK (1999) Transplantability and therapeutic

- effects of bone marrow-derived mesenchymal cells in children with osteogenesis imperfecta. *Nat Med* 5(3):309–313. doi:[10.1038/6529](https://doi.org/10.1038/6529)
223. Horwitz EM, Prockop DJ, Gordon PL, Koo WW, Fitzpatrick LA, Neel MD, McCarville ME, Orchard PJ, Pyeritz RE, Brenner MK (2001) Clinical responses to bone marrow transplantation in children with severe osteogenesis imperfecta. *Blood* 97(5):1227–1231
224. Gordon MY, Levicar N, Pai M, Bachellier P, Dimarakis I, Al-Allaf F, M'Hamdi H, Thalji T, Welsh JP, Marley SB, Davies J, Dazzi F, Marelli-Berg F, Tait P, Playford R, Jiao L, Jensen S, Nicholls JP, Ayav A, Nohandani M, Farzaneh F, Gaken J, Dodge R, Alison M, Apperley JF, Lechler R, Habib NA (2006) Characterization and clinical application of human CD34+ stem/progenitor cell populations mobilized into the blood by granulocyte colony-stimulating factor. *Stem Cells* 24(7):1822–1830. doi:[2005-0629](https://doi.org/2005-0629)
225. Levicar N, Pai M, Habib NA, Tait P, Jiao LR, Marley SB, Davis J, Dazzi F, Smadja C, Jensen SL, Nicholls JP, Apperley JF, Gordon MY (2008) Long-term clinical results of autologous infusion of mobilized adult bone marrow derived CD34+ cells in patients with chronic liver disease. *Cell Prolif* 41(Suppl 1):115–125. doi:[CPR491](https://doi.org/CPR491)
226. Terai S, Ishikawa T, Omori K, Aoyama K, Marumoto Y, Urata Y, Yokoyama Y, Uchida K, Yamasaki T, Fujii Y, Okita K, Sakaida I (2006) Improved liver function in patients with liver cirrhosis after autologous bone marrow cell infusion therapy. *Stem Cells* 24(10):2292–2298. doi:[2005-0542](https://doi.org/2005-0542)
227. Lyra AC, Soares MB, da Silva LF, Fortes MF, Silva AG, Mota AC, Oliveira SA, Braga EL, de Carvalho WA, Genser B, dos Santos RR, Lyra LG (2007) Feasibility and safety of autologous bone marrow mononuclear cell transplantation in patients with advanced chronic liver disease. *World J Gastroenterol* 13(7):1067–1073
228. Gasbarrini A, Rapaccini GL, Rutella S, Zocco MA, Tittoto P, Leone G, Pola P, Gasbarrini G, Di Campli C (2007) Rescue therapy by portal infusion of autologous stem cells in a case of drug-induced hepatitis. *Dig Liver Dis* 39(9):878–882. doi:[S1590-8658\(06\)00312-4](https://doi.org/S1590-8658(06)00312-4)
229. Pai M, Spalding D, Xi F, Habib N (2012) Autologous bone marrow stem cells in the treatment of chronic liver disease. *Int J Hepatol* 2012:307165. doi:[10.1155/2012/307165](https://doi.org/10.1155/2012/307165)
230. Zhang Z, Lin H, Shi M, Xu R, Fu J, Lv J, Chen L, Lv S, Li Y, Yu S, Geng H, Jin L, Lau GK, Wang FS (2012) Human umbilical cord mesenchymal stem cells improve liver function and ascites in decompensated liver cirrhosis patients. *J Gastroenterol Hepatol* 27(Suppl 2):112–120. doi:[10.1111/j.1440-1746.2011.07024.x](https://doi.org/10.1111/j.1440-1746.2011.07024.x)
231. Kharaziha P, Hellstrom PM, Noorinayer B, Farzaneh F, Aghajani K, Jafari F, Telkabadi M, Atashi A, Honardoost M, Zali MR, Soleimani M (2009) Improvement of liver function in liver cirrhosis patients after autologous mesenchymal stem cell injection: a phase I-II clinical trial. *Eur J Gastroenterol Hepatol* 21(10):1199–1205. doi:[10.1097/MEG.0b013e32832a1f6c](https://doi.org/10.1097/MEG.0b013e32832a1f6c)
232. Persidis A (1999) Tissue engineering. *Nat Biotechnol* 17(5):508–510. doi:[10.1038/8700](https://doi.org/10.1038/8700)
233. McKernan R, McNeish J, Smith D (2010) Pharma's developing interest in stem cells. *Cell Stem Cell* 6(6):517–520. doi:[S1934-5909\(10\)00222-5](https://doi.org/S1934-5909(10)00222-5)
234. Kim HJ, Jin CY (2012) Stem cells in drug screening for neurodegenerative disease. *Korean J Physiol Pharmacol* 16(1):1–9. doi:[10.4196/kjpp.2012.16.1.1](https://doi.org/10.4196/kjpp.2012.16.1.1)

Chapter 3

Engineering T Cells to Target Tumor Cells

Hiroki Torikai, Judy S. Moyes and Laurence J. N. Cooper

3.1 Introduction

The observation that viral-associated tumor formation is increased in the immunocompromised host reveals a role of immune surveillance in tumor biology [1]. Recent analysis of cells at the tumor site shows that memory T cell infiltration is associated with a favorable outcome [2]. These observations support the view that immune effector cells such as T cells or NK cells play a role in eradication of tumor cells. However, immunocompetent cells do not always eliminate malignancy. Evidence suggests that tumor cells may also be protected by other classes of immune cells or by an immunosuppressive microenvironment [3]. Indeed, “tumor immunoediting” is recognized as one of the emerging hallmarks in cancer therapy [4]. Passive immunotherapy aimed at enhancing host T cell responses has not met with significant success in part due to the presence of an immunosuppressive microenvironment [5]. Adoptive immunotherapy infusing tumor antigen-specific T cells expanded in vitro is an attractive alternative way to enhance immune-mediated tumor destruction. Clinical trials administering T cells have shown improved results when compared to passive immunotherapy [6]. However, the burdens to manufacture such T cells for individual patients and the length of time it may take to generate T cells in sufficient numbers and quality remain obstacles to the widespread distribution of this therapy. To improve their therapeutic potential, T cells need to be able to be produced in a timely manner. The development and human application of genetic engineering technologies now

H. Torikai · J. S. Moyes · L. J. N. Cooper (✉)
Division of Pediatrics, The University of Texas MD Anderson Cancer Center, Unit 907,
1515 Holcombe Boulevard, Houston, TX 77030, USA
e-mail: ljncooper@mdanderson.org

H. Torikai
e-mail: htorikai@mdanderson.org

J. S. Moyes
e-mail: jsmoyes@mdanderson.org

enable T cells to be modified as desired and their efficacy (effector function, long-term survival, and migration) to be maximized for a tumor and its microenvironment. To enhance adoptive immunotherapy, T cells need to be equipped with (1) specificity to tumor cells, (2) cytotoxicity to destroy the tumor cell, (3) longevity to survive long-term in vivo, and (4) the ability to disrupt the immunosuppressive tumor microenvironment.

We will discuss the strategies to enhance T cell function and generate ideal tumor-specific T cells using genetic engineering.

3.2 Redirect T Cell Specificity

T cells can kill target cells using multiple mechanisms (e.g., granzymes, perforin, Fas, and TRAIL). T cells can also proliferate and survive in vivo if they receive appropriate signals in the context of receptors. Antigen-specific T cell lines or clones expressing T cell receptors (TCRs) with defined and desired specificities can be isolated from patients. However, this process is time consuming, and the resulting tumor-specific T cells often have an exhausted phenotype compromising long-term in vivo survival. To improve this process, T cell specificity can be redirected against the tumor-associated antigens (TAAs) by genetic engineering. Currently, two technologies exist to achieve this: TCR gene therapy and the stable and transient introduction of a chimeric antigen receptor (CAR).

3.2.1 TCR Gene Therapy

Each $\alpha\beta$ T cell expresses a unique TCR $\alpha\beta$, which recognizes a small peptide in the context of a human leukocyte antigen (HLA) molecule. These small peptides are derived from either intracellular or cell surface proteins. Since the pioneering identification of the melanoma-associated epitope derived from MAGE-A1 [7], numerous other TAAs have been identified [8]. However, the majority of TAAs identified so far are self-proteins except for peptides derived from tumor-specific chimeric proteins (e.g., bcr-abl in CML or ALL [9]) or mutations (e.g., NPM in AML [10]). This hampers attempts to induce a patient's own TAA-specific T cells in vitro and in vivo since T cells expressing high-affinity TCR $\alpha\beta$ against self-proteins are typically eliminated during their selection in the thymus. Gene therapy has thus been used to enforce expression of a TCR harvested from the T cells of an allogeneic donor [11]. The transduction of a high-affinity TCR α and β chain from a pre-characterized TAA-specific T cell clone can redirect T cell specificity to the same TAA recognized by the original T cell clone. For successful TCR $\alpha\beta$ gene therapy, the high-affinity TCR $\alpha\beta$ must be isolated, introduced into recipient T cells, and efficiently expressed.

3.2.1.1 Isolating High-Affinity TCR $\alpha\beta$

A prototypical TCR $\alpha\beta$ typically has low affinity for self-protein, and therefore, the initial challenge is to isolate and identify high-affinity TCR $\alpha\beta$ sequences. Several methods have been developed to achieve this. One is to create a complementarity determining region (CDR3) library using low-affinity TAA-specific TCR $\alpha\beta$ and screen their binding affinity to target using the phage display system. CDR3 is generated during V-J-(D) recombination of TCR α or β and known to bind peptide expressed on HLA. By randomly introducing a mutation within this region, the affinity of TCR $\alpha\beta$ can be manipulated, and TCR $\alpha\beta$ generated with 2–3 log higher affinity than that of original TCR $\alpha\beta$ [12].

A second approach to isolate high-affinity TCR $\alpha\beta$ is to use HLA transgenic mice. Immunizing these mice with candidate TAA-derived peptide(s) engenders immune response and enables the isolation of murine T cells that recognize desired TAAs. Using this system, murine TCR $\alpha\beta$ chains with high affinity to target TAA have been isolated [13]. Potentially, these TCR $\alpha\beta$ may be immunogenic when infused on human T cells, but so far no evidence has been obtained to support this.

Recently, several researchers have isolated high-affinity TCR $\alpha\beta$ from third-party donors that do not share restricted HLA [14–17]. This is based on the fact that the self-antigen expressed on nonself HLA is not displayed in these donors. Careful evaluation is needed of high-affinity TCR $\alpha\beta$ isolated from mismatched donors as they may exhibit promiscuity for off-target sequences [18].

Some antigen-specific TCR $\alpha\beta$ also respond to nonrestricted HLA molecules. This is evident as virus-specific cytotoxic T lymphocytes (CTL) respond to nonself HLAs [19]. No graft-versus-host-disease (GVHD) has been reported after infusing virus-specific CTL after HLA-mismatched allogeneic hematopoietic stem cell transplantation [20]. Potential off-target cytotoxicity may be avoided by predefining the cross-reactivity of TCR $\alpha\beta$ and careful patient selection.

3.2.1.2 Tools to Transduce TCR $\alpha\beta$ Gene into T Cells

An efficient way to introduce the TCR $\alpha\beta$ gene into T cells is the use of γ -retroviral vectors. Transduction results in multiple integrations of the transgene into the T cell genome, thereby enabling the rapid production of clinically significant numbers of TCR⁺ T cells. Retroviral vectors are being used in the majority of current clinical trials. However, a concern with using the γ -retroviral vector is the mutagenesis associated with the random integration of a strong promoter upstream of the oncogenes. This was made evident by the high incidence of T cell acute lymphocytic leukemia (T-ALL) in patients who received hematopoietic stem cell (HSC) genetically modified with a γ -retroviral vector. This was due to the transgene insertion in the promoter region of the oncogenes (such as in association with *LMO2* locus). However, this concern may be offset in T cells since such cells are more differentiated than HSC. This assumption is supported by the observation that genetically modified T cells may safely reside over the long term in patients [21].

Furthermore, mouse experiments demonstrate that enforced expression of oncogene related to T-ALL in HSCs generates leukemic T cells, but that is not the case when these oncogenes are expressed in T cells [22]. Another method to introduce a transgene into T cells is to use a self-inactivating lentivirus vector. Genotoxicity is expected to be less than with a γ -retrovirus vector because this vector lacks the promoter/enhancer element in the long terminal repeat region, which is a major determinant of genotoxicity [23]. An additional potential benefit is that unlike γ -retrovirus, the lentivirus vector has the ability to integrate into naïve T cells.

The manufacture and production of clinical-grade recombinant viral vectors require the use of a specific facility and extensive validation processing of the final products, both of which are expensive and labor intensive. Use of synthetic DNA plasmid is a less expensive approach to modifying T cells, and naked DNA transfection is currently being used in clinical trials. However, since the efficiency of stable integration of a transgene is much lower in a naked DNA plasmid when compared to that of virus vector, extensive culture and drug selection may be needed to obtain clinically useful numbers of genetically modified T cells [24].

Within the last decade, the integration efficiency of DNA plasmids has benefited from an understanding of transposition. A transposon is a mobile element that is able to integrate into the human genome with the help of a transposase. The *Sleeping Beauty* (SB) transposon/transposase system is based on a Tc1-like transposon from fish [25]. In this nonviral system, the gene of interest has to be flanked by approximately 230 bp of inverted repeats, which contain two nonidentical direct repeats (DR) in the transposon DNA. Upon co-transfection of this plasmid with SB11 hyperactive transposase (or SB100X), which is modified to enhance enzymatic activity, the gene of interest can be readily integrated into the human genome. This insertion occurs in two steps. First, SB11 binds the DR sequence at each end and generates a synaptic formation. When this complex docks with a TA dinucleotide sequence, the SB11 catalyzes the integration of the transposon (cargo load) into that site. The SB system has been used to introduce therapeutic genes into T cells [26–28]. It is also being used to stable express CARs into T cells. When combined with artificial antigen-presenting cells, which specifically activate CAR-expressing T cells, clinically significant numbers of CAR T cells can be prepared in a relatively short period of time [26]. The *piggyBac* system represents another class of a transposon/transposase system that has been used to introduce exogenous genes into human cells [29–31]. Here, the insertion of the transgene is preferentially at a TTAA sequence. Compared to viral vector or SB, the *piggyBac* transposon system can integrate a larger transgene product (over 10 kb) [32]. An advantage of the transposon/transposase system is that it is an inexpensive way to prepare genetically engineered T cells. Safety of these systems regarding their potential genotoxicity related to transgene insertion is being addressed by assessing the genome-wide integration profile of a transposon. The integration profile of the SB system appears to be safer than that of other transposon systems (*piggyBac* or *Tol2*). Although the *piggyBac* system theoretically randomly targets the TTAA site, the integration pattern tends to occur near the transcription start sites, CpG islands, or DNase I hypersensitive site. This is in contrast to SB which integrates transgenes into such

sites less often [33]. The apparent safer integration profile of the SB system has been commented upon [34–36]. Currently, the use of SB mediated genetically engineered CAR⁺ T cells is being investigated in a clinical setting at MD Anderson Cancer Center [37].

As an alternative to stably expressing a transgene from a viral vector or DNA plasmids, in vitro-transcribed mRNA can also be used to engineer T cells. Investigators have demonstrated that this technology can be applied to efficiently express exogenous genes into T cells [38, 39]. However, despite its efficiency, the mRNA cannot integrate into the host genome and is subject to degradation. The clinical application of this technology may therefore be limited and likely needs to be combined with an approach to infuse and reinfuse T cells to achieve a clinical benefit [40].

3.2.1.3 Improving TCR $\alpha\beta$ Gene Therapy

Most gene transfer of TCR $\alpha\beta$ sequences use murine leukemia virus derived γ -retrovirus vector in which the expression of the immunoreceptor is driven by the strong promoter in the LTR. The effect of promoter choice in self-inactivating lentivirus vector has been studied [41]. Based on a comparison of GFP expression in T cells transduced with lentivirus vectors employing a panel of promoters, it was observed that the murine stem cell virus (MSCV) U3 promoter showed higher transduction efficiency and GFP intensity in both CD4 and CD8 T cells. TCR $\alpha\beta$ transgene expression was also compared, and MSCV-driven bicistronic vector (2A) was identified as superior. Optimization of the TCR $\alpha\beta$ transgene cassette aims to enhance TCR $\alpha\beta$ expression and function. Many vendors provide inexpensive custom gene synthesis enabling codon optimization of TCR $\alpha\beta$ genes to enhance their expression. Introducing desired noncoding changes into cDNA increases the TCR $\alpha\beta$ expression compared to the wild-type sequences in many TCR $\alpha\beta$ constructs [42, 43]. The two TCR $\alpha\beta$ genes are usually transduced as a bicistronic construct since both genes (TCR α and TCR β) must be introduced to express a functional TCR $\alpha\beta$ heterodimer. A bicistronic construct including a 2A ribosomal skip peptide appears to be superior to the internal ribosome entry site (IRES) [44]. This 2A peptide can be optimized by adding a furin-cleavage domain and a small amino acid spacer [45]. Functional avidity of TCR $\alpha\beta$ can be increased by removing *N*-glycosylation sites in the constant region [46]. To efficiently introduce TCR $\alpha\beta$ gene into a subset of T cells, lentivirus has been recently developed that specifically targets CD8 T cells based on the expression of a single-chain antibody against CD8 on the packaged lentivirus particle (CD8-LV) [47]. CD8 T cells transduced with CD8-LV have increased cytotoxicity against cells expressing TCR $\alpha\beta$ target antigens than conventional vector.

A major concern for TCR $\alpha\beta$ gene therapy is the potential to form an inappropriate TCR $\alpha\beta$ heterodimer between the introduced and endogenous TCR $\alpha\beta$ chains leading to the creation of an immunoreceptor that has not undergone thymic selection and can cause unwanted autoreactivity (Fig. 3.1a). Although these miss-paired

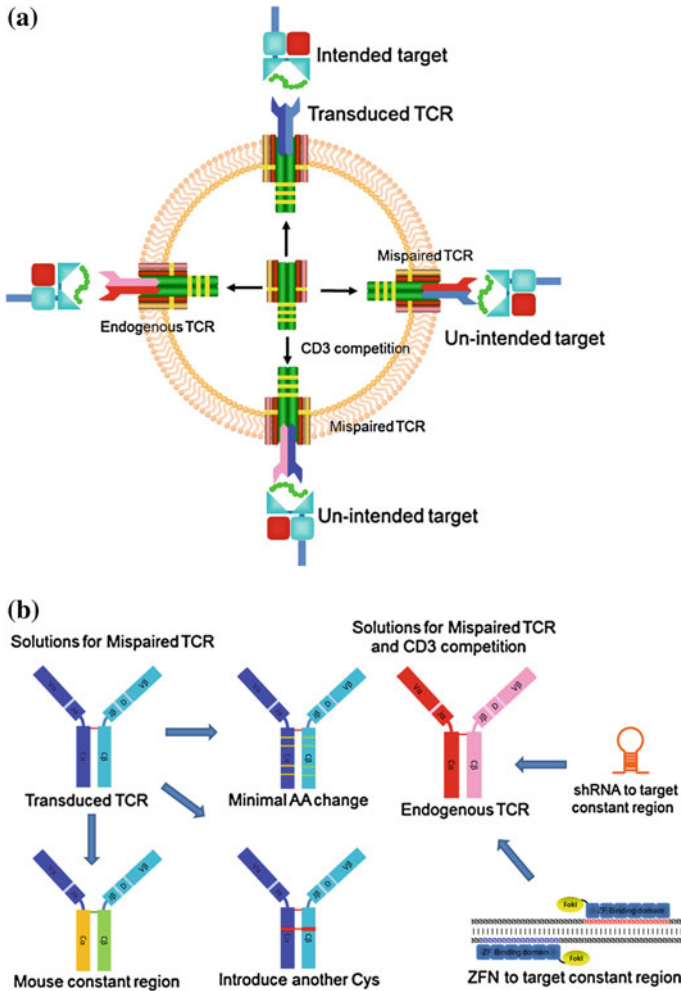


Fig. 3.1 Problems of TCR $\alpha\beta$ gene therapy and their solution. **a** Formation of mispaired TCR $\alpha\beta$. Mispairing between endogenous TCR $\alpha\beta$ and introduced TCR $\alpha\beta$ may generate specificity for un-intended targets. Shown are the possible combinations generating four different TCRs that may compete CD3 complex which is needed for TCR $\alpha\beta$ to be expressed on the T cell surface. **b** Reported solution for mispaired TCR $\alpha\beta$. Modifications to the constant region may improve desired heterodimer formation between introduced TCR chains. These include (1) use mouse constant region, (2) amino acid substitutions in constant region, and (3) insertion of another disulfide bond in constant region. Another solution uses shRNA or ZFN targeting constant region to down-regulate or prevent TCR $\alpha\beta$ expression

TCR $\alpha\beta$ have been shown to respond as allogeneic antigens in vitro or cause GVHD-like symptom in mice [48, 49], this has not occurred in clinical trials. Another concern for the expression of four different TCR $\alpha\beta$ heterodimers is the competition

for CD3 complex (CD3 ζ , ϵ , γ , and δ), which is needed to transduce activation signal in T cells. If CD3 is limiting, then the ability of introduced TCR to be expressed and to activate T cells may be compromised.

Several solutions for this issue have been developed (Fig. 3.1b). As an alternative to using $\alpha\beta$ T cell, Heemskerk et al. employ $\gamma\delta$ T cells as the recipient cell for gene transfer since introduced TCR $\alpha\beta$ chains cannot pair with endogenous TCR $\gamma\delta$ chains [50]. However, TCR $\alpha\beta$ -transduced TCR $\gamma\delta$ cells typically need CD8 transduction to induce robust antigen-specific activation which may not be available on $\gamma\delta$ T cells that fail to express (CD4 and) CD8. One strategy to prevent mismatched TCR $\alpha\beta$ formation is to facilitate heterodimer formation between the introduced TCR $\alpha\beta$ chains. This has been accomplished (1) using full or partial mouse TCR α and β sequences [51–53], (2) introducing another disulfide bond within the introduced TCR constant regions [54, 55], and (3) designing a knob-into-hole configuration [56]. These systems have been shown to successfully reduce mismatched TCR $\alpha\beta$ formation. However, introduced TCR $\alpha\beta$ cannot avoid competing for the CD3 complex with endogenous TCR $\alpha\beta$. As a result, the copy number of introduced TCR $\alpha\beta$ on the surface may be decreased leading to insufficient TCR $\alpha\beta$ -mediated effector functioning.

Recently, two groups showed that endogenous TCR $\alpha\beta$ expression can be disrupted by different molecular technologies. One team used short hairpin RNAs (shRNAs) against TCR $\alpha\beta$ constant regions to suppress endogenous TCR $\alpha\beta$ expression [57]. They designed a plasmid containing both shRNAs and introduced TCR $\alpha\beta$ genes in a single retrovirus vector and demonstrated both enhanced expression of introduced TCR $\alpha\beta$ and suppression of endogenous TCR $\alpha\beta$. This resulted in enhanced function of the introduced TCR $\alpha\beta$ compared with expressing transgenic TCR $\alpha\beta$ in T cells without shRNAs. The other team used zinc-finger nucleases (ZFNs) to completely disrupt endogenous TCR $\alpha\beta$ expression at the genomic level [58]. ZFN employs an engineered nuclease which consists of the zinc-finger-binding domain and the cleavage domain from type II endonuclease *FokI*. A pair of ZFNs can induce a DNA double-strand break (DSB) at an intended genomic target site. The nonhomologous end-joining DNA DSB repair mechanism creates an indel at ZFN target sites to disrupt target gene expression by frame shift mutation. The sequential introduction of ZFNs targeting TCR α chain and then β chain was used by the authors to demonstrate that endogenous TCR $\alpha\beta^{\text{null}}$ WT1-specific TCR $\alpha\beta^+$ T cells could be generated. This strategy enhances TCR $\alpha\beta^+$ T cell function and avoids mispaired TCR $\alpha\beta$ mediated xenogeneic GVHD in a mouse model.

3.2.1.4 TCR $\alpha\beta$ Specificity Recapitulated Through the Introduction of a Single Chain

An alternative strategy to define TCR $\alpha\beta$ specificity uses a single-chain TCR $\alpha\beta$ (scTCR). This is an artificial TCR $\alpha\beta$ chain is comprised of a variable domain, including the CDR3 region of TCR α and β chains, linked through a peptide and

fused in frame to the CD3 ζ signaling domain [59–61]. This technology avoids the potential for mispairing between the introduced immunoreceptor and the endogenous TCR $\alpha\beta$; however, the expression and affinity of scTCR $\alpha\beta$ may be less than that of the original TCR $\alpha\beta$ heterodimer [62]. Efforts to enhance the avidity of scTCR chain have been undertaken, and in some cases, the resultant scTCR has been shown to induce a comparable response to heterodimeric TCR $\alpha\beta$ [56, 60, 61]. Modification of the signaling domain and increasing the affinity of the scTCR domain will be needed to improve the therapeutic potential of this approach. Recently, several groups have isolated monoclonal antibodies (mAbs) having TCR $\alpha\beta$ -like specificity [63–69]. Although the cross-reactivity of these antibodies has not been extensively studied (such as to the superstructure of HLA molecules), these mAbs may be used to construct CARs to target a peptide/HLA complex, instead of using TCR $\alpha\beta$ gene transfer.

3.2.1.5 Clinical Trial in TCR $\alpha\beta$ Gene Therapy

As of February 2013, five reports have been published by the NCI group describing the translation of TCR gene therapy into the clinical setting. In the seminal paper in 2006 [70], 15 patients with metastatic melanoma were treated with MART1-specific TCR $\alpha\beta$ gene transduced autologous peripheral blood lymphocytes. These patients were treated with lymphocyte depleting chemotherapy before T cell infusions, followed by IL-2 administration and MART-1 peptide vaccination. Two of 15 patients exhibited a partial response to this therapy. A follow-up study employing the same TCR $\alpha\beta$ specificity reported a response rate (tumor regression) of 13 % (Four out of 31 patients). A follow-up study using a high-affinity murine TCR $\alpha\beta$ against MART-1 and gp100 resulted in a superior response (tumor regression was observed in 30 % of patients receiving MART1-specific TCR $\alpha\beta$ -modified T cells and 19 % of patients receiving gp100-specific TCR $\alpha\beta$ -modified T cells). However, on-target adverse events (e.g., skin rash related to destruction of melanocyte, uveitis, and vitiligo) were observed [71]. T cells genetically modified to target NY-ESO1 have also been tested in the clinic. Five of 11 patients with metastatic melanoma showed a clinical response, and two patients showed a complete response lasting more than 1 year. Furthermore, four of 6 patients with metastatic synovial sarcoma also showed a clinical response [72]. Mouse-derived TCR $\alpha\beta$ genes against CEA have also been tested in patients with metastatic colorectal cancer. Tumor regression occurred in one out of three treated patients, but severe colitis was the dose-limiting toxicity [73]. T cells expressing a MAGE-A3-specific mouse TCR $\alpha\beta$ have been administered, but a high incidence of neurological toxicity was observed due to unpredicted expression of MAGE-A family gene in human brain [74].

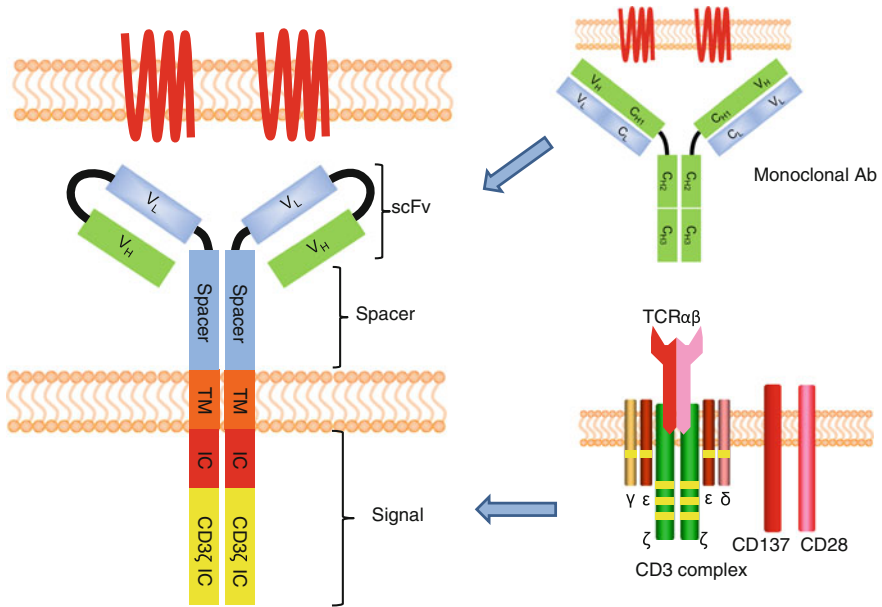


Fig. 3.2 Structure of chimeric antigen receptor. Variable regions from heavy and light chain (scFv) of mAb are linked with spacer domain and signaling domain from CD3 ζ and co-stimulatory molecules (e.g., CD28 and CD137)

3.2.2 CAR

One of the first CARs (“T-body”) was developed by Eshhar [75]. Upon expression, T cells can recognize cell surface TAAs independent of HLA. Thus, one CAR design has application for a tumor type common to multiple patients. Recent advances in CAR design, especially in the intracellular signaling domain, the affinity of the antigen recognition domain, and the extracellular scaffold make this a promising immunotherapy. Currently, multiple clinical trials are underway to evaluate this technology.

3.2.2.1 Structure of CAR

The structure of a prototypical CAR can be divided into three segments: (1) Single chain fragment of variable (scFv) which determines the specificity, (2) extracellular spacer, and (3) intracellular signaling domain(s) (Fig. 3.2). Other aspects of CAR design may impact the ability to recycle T cell effector functions in the tumor microenvironment such as the transmembrane domain [76], where the CAR binds the TAA [77], and the density of CAR on the T cell surface.

Table 3.1 Target molecules of chimeric antigen receptor for tumor therapy (as of March 2013)

Target	Target tumors	State of evaluation
<i>Hematological malignancies</i>		
CD19	B cell malignancies	Clinical
CD20	B cell malignancies	Clinical
CD22	B-ALL	Preclinical
CD23	B-CLL	Preclinical
CD30	Hodgkin's lymphoma	Clinical
CD38	B cell malignancies including multiple myeloma	Preclinical
CD70	Hematological malignancies and some solid tumor (e.g. renal cell carcinoma)	Preclinical
Igk	Mature B cell malignancies	Clinical
ROR1	B-CLL	Preclinical
BCMA	Multiple myeloma	Preclinical
CD33	Acute myelogenous leukemia	Preclinical
Lewis (Y)	Hematological malignancies	Clinical
CD123	Acute myelogenous leukemia	Preclinical
<i>Solid tumors</i>		
EphA2	Glioblastoma	Preclinical
GD2	Neuroblastoma, myeloma	Clinical
IL11R α	Osteosarcoma	Preclinical
IL13R α 2	Glioblastoma, medulloblastoma	Clinical
EGFRvIII	Glioblastoma	Clinical
Her2/ErbB2	Breast cancer, osteosarcoma (low), glioblastoma, pancreatic cancer, etc	Clinical
CAIX	Renal cell carcinoma	Clinical
MUC1	Hematological malignancies, many types of cancers	Preclinical
FAP	Malignant pleural mesothelioma	Clinical
PSMA	Prostate cancer	Clinical
PSCA	Prostate cancer	Preclinical
fAChR	Rhabdomyosarcoma	Preclinical
FR α	Ovarian cancer	Clinical
CD24	Pancreatic cancer	Preclinical
CEA	Colon cancer, pancreatic cancer	Clinical
Mesothelin	Breast cancer	Clinical
EpCAM	Many types of cancer	Preclinical
HMW-MAA	Melanoma	Preclinical
GUCY2C	Colon cancer	Preclinical
GD3	Melanoma	Preclinical
VEGFR2	Tumor vasculature	Clinical

scFv

The scFv consists of the variable regions of heavy and light chains from a mAb with desired specificity for TAA. Indeed, this determines the specificity of the CAR. Many cell surface TAAs expressed on a variety of tumor cells have been targeted by CARs using scFvs from specific mAb (Table 3.1). In addition to these

specific scFvs, a universal CAR has recently been described [78, 79]. Here, scFv from anti-FITC or avidin dimer was used to construct CARs. For example, after infusing T cells expressing a fluorescein-specific CAR, multiple cell surface molecules expressed on tumors can be targeted by infusion of FITC-labeled mAbs. This technology enables the target tumor antigens to be changed after infusing CAR-expressing T cells.

Spacer

The spacer domain is gaining importance in its ability to influence the ability of T cells to target tumor and protect the genetically modified T cells from activation-induced cell death [80]. A panel of spacers has been used including the CH₂–CH₃ Fc hinge domain from IgG1 or IgG4, CD8 α , as well as small hinges. The IgG1 CH₂–CH₃ Fc hinge domain is widely used spacers, but the potential to bind to the Fc γ receptor raises concerns for deleterious side effects. Modification of this construct may avoid this issue [81]. Information regarding the impact of spacer is beginning to be published. For example, CAR-mediated activation is less efficient in T cells expressing a CAR containing a spacer sequence (IgG1 Fc domain) compared to CAR containing no spacer sequence [82]. This report was restricted to the use of first-generation (described later) signaling domain. The role that spacer sequence plays in the function of a second- or third-generation CAR constructs is being evaluated.

Intracellular domain

CD3 ζ or Fc receptor γ has multiple ITAM motifs to transduce an activation signal in T cells and as such have been widely used as intracellular signaling domains. Construct containing just these ITAMs are referred to as a “first-generation” CARs. Although these signaling domains can induce an activation signal in T cells, they are usually suboptimal and curtail the therapeutic impact after adoptive transfer [83–87].

Co-stimulatory molecules that provide a “2nd signal” are required to trigger a fully competent T cell activation event. To improve CAR-mediated signaling, multiple co-stimulatory molecules have been combined with chimeric CD3 ζ . CD28 is one of the well-known co-stimulatory molecules which are important for T cell survival [88]. Enforced expression of CD28 in CD28^{neg} virus-specific CTL clones restores production of IL-2 and proliferation in these cells [89]. CD28 was first tested as a single intracellular domain instead of CD3 ζ [90, 91]. T cells transduced with this construct showed increased IL-2 production and proliferation. Following this observation, Maher et al. generated prostate-specific membrane antigen (PSMA) target CAR containing both CD28 and CD3 ζ signaling domain (“2nd generation”) [92]. T cells expressing this CAR construct produced increased amounts of IL-2, showed increased proliferation, and maintained specificity for target PSMA. The authors also showed that the functional activity was dependent on the order of CD28 and CD3 ζ within the CAR. Improved function was observed in the CAR having transmembrane and proximal intracellular domain of CD28 fused to CD3 ζ . The improved function afforded by the CAR design that employs CD28 and CD3 ζ CAR has been confirmed in vitro [83, 93] and in the clinical setting [94]. Co-stimulatory molecules belonging to the tumor necrosis factor

(TNF) ligand superfamily (e.g., 4-1BB (CD137), OX40 (CD134), and CD27) are also important for co-stimulation of T cells and promote long-term T cell survival [95, 96]. These molecules associate with TNF receptor-associated factor (TRAF) and link to many molecules which are important for cell survival (e.g., BCL2, BCL-X, phosphoinositide 3 kinase, AKT, and NF κ B pathway) [97]. As anticipated, CAR constructs containing chimeric CD134 [98, 99] or CD137 [100–102] have been shown to sustain *in vivo* persistence of CAR⁺ T cells. Combining signaling from multiple signaling molecules, such as CD3, CD28, and CD137 (or CD134) to form a third-generation CAR, has also been tested [103–105]. Several groups have reported that CAR containing three activation motifs have potent anti-tumor efficacy in models [106, 107]. A CAR signaling through chimeric CD27 has also been shown to result in improved function and *in vivo* survival, comparable to CAR containing CD137 [108]. In addition to anti-apoptotic molecules, CD27 has been reported to activate the Wnt pathway in chronic myeloid leukemia stem cells [109]. Since the Wnt pathway has recently been identified as the key signaling pathway of stem-cell-like memory T cells [110], it will be intriguing to see how the Wnt pathway is regulated in T cells expressing CAR that include the CD27 signaling domain. Although much progress has been made in the intracellular signaling domain of CARs, many of these constructs still need to be evaluated in clinical trials.

3.2.2.2 Improving the Human Application of T Cells Expressing CAR

Targeting one TAA that is exclusively expressed on tumor cells is difficult, especially given the heterogeneity of antigen expression on solid tumors. An approach to increase the specificity of genetically modified T cells is to synchronously target two cell surface TAAs expressed on tumors, thereby enabling CAR⁺ T cells to distinguish tumor cells from normal cells. This can apparently be achieved using two CAR designs which activate T cells via CD3 ζ on one CAR and a co-stimulatory molecule (CD28 or CD137) on the other CAR. Kloss et al. developed CARs targeting PSMA and prostate stem cell antigen (PSCA) as model antigens and showed that T cells expressing both anti-PSMA CAR (CD28 + CD137) and low-affinity anti-PSCA CAR (CD3 ζ) kill only those tumor cells that express both TAAs [111]. A probable limitation is that the affinity of scFv linked with CD3 ζ should be low as described by the authors. The antigen density and affinity of scFv vary with each CAR to tumor combination, and therefore, this needs to be taken into consideration when applying this strategy to the clinical setting.

Autologous T cells are infused in many current clinical trials, but T cells from heavily pre-treated patients may be damaged in quality and compromised in quantity, and (due to the time required for production and manufacture) they may not be available where and when the patient needs them. Any time delay before infusion allows disease progression to take place, and the possibility that treatment is therefore not possible for some patients. “Off-the-shelf” (OTS) therapy

administering T cells expressing a CAR would resolve these issues. Toward this end, CAR⁺ T cells have been pre-prepared from healthy donors, using either peripheral blood mononuclear cells (PBMC) or umbilical cord blood (UCB) derived mononuclear cells, for infusion when the patient needs them rather than when the T cells are available. A potential problem using OTS T cells is the development of an allogeneic immune reaction (either from donor to patient or from patient to donor). Zakezewski et al. generated precursor CAR⁺ T cells by *in vitro* differentiation of CAR-transduced HSCs activated and propagated on Notch-1 ligand expressing OP9 cell lines [112]. When precursor CAR⁺ T cells were infused into irradiated mice they became host MHC restricted and host tolerant. This technology may be used to generate “OTS” CAR⁺ T cell precursors.

We have shown that the endogenous TCR $\alpha\beta$ can be eliminated from CAR⁺ T cells by ZFNs targeting either TCR α constant region or TCR β constant region [113]. These TCR $\alpha\beta$ ^{neg} CAR⁺ T cells can then be enriched by clinically compatible paramagnetic bead-based sorting. TCR $\alpha\beta$ ^{neg} CAR⁺ T cells cannot proliferate by TCR $\alpha\beta$ stimulation while maintaining activity through CAR. We have also shown that HLA can be eliminated from CAR⁺ T cells, thus enabling these cells to evade attack from patient T cells recognizing allogeneic antigens. Although further evaluation is needed, CAR⁺ T cells may be used as an OTS “drug” in the growing field of immunotherapy.

3.2.2.3 Clinical Trials Infusing CARs

Multiple phase I clinical trials administering T cells expressing first-generation CARs have been reported [84–87, 114, 115]. Overall clinical responses in these studies are limited presumably due to incomplete T cell activation. To provide additional stimulation to these T cells, Pule et al. reported that half the patients treated with anti-GD2 CAR expressed in EBV-specific T cells showed clinical responses. These EBV-specific T cells presumably retained sufficient stimulation through the EBV-specific TCR $\alpha\beta$ to enable targeting of tumor via first-generation CAR. This observation reinforces that co-stimulation is important to improve anti-tumor function.

The results of early-phase clinical studies using second-generation CAR (including CD28 or CD137 intracellular domain) are promising [94, 116–121]. The improved anti-tumor responses appear to correlate with sustained *in vivo* persistence of CAR⁺ T cells. For example, Kalos et al. reported that all three patients with advanced chronic lymphocytic leukemia who received CD19-specific T cells expressing a CAR that signaled through chimeric CD137 showed marked clinical responses [117]. It was calculated that on average one CAR⁺ T cell can act as a serial killer and eradicate 1,000 tumor cells. Most adverse events related to CAR⁺ T cell infusion were tolerable with intensive clinical support. Expected on-target toxicity occurred as these CAR⁺ T cells do not distinguish between CD19 on malignant versus normal B cells. Thus, eradication of normal B lineage has served as a biomarker and has been observed. The loss of humoral immunity can lead to

complications as one patient has died from viral infection after receiving CD19-specific T cells [119]. However, unexpected on-target related severe adverse events have also reported. In a trial targeting carbonic anhydrase IX (CAIX) CAR T cells were attributed to causing hepatotoxicity due to the low level of CAIX expression on the liver [115]. One patient with metastatic colon cancer treated with ERBB2 target CAR therapy suffered from fatal respiratory distress due to the low level of expression of ERBB2 on lung epithelial cells [122]. Another unforeseen, an adverse event was also reported in a patient with CLL treated with CD19 target CAR. Although the precise cause of death was not reported, this patient showed elevated serum cytokine levels after infusion of CAR⁺ T cells [123].

3.3 Improving T Cell Function

One of the major challenges in adoptive transfer of genetically engineered T cells is improving T cell function and survival in vivo. One approach to achieving this is to include co-stimulatory signals with the CAR construct. In addition, cytokines known to enhance T cell survival and chemokines that guide T cells to the tumor site(s) have also been tested.

3.3.1 *Engineering T Cells to Improve Function and Survival*

In vivo survival of infused T cells is important to eradicate residual tumor cells and maintain immune surveillance. BCL2 and BCL-XL are anti-apoptotic molecules that contribute to T cell differentiation and survival [124]. Pro-survival function of cytokines, especially cytokines that signal through the common γ chain, relies on the induction of BCL2 or BCL-XL expression [125]. BCL-XL is also an anti-apoptotic molecule reported to be associated with T cell survival mediated through CD28 co-stimulation [88]. Enforced expression of BCL2 in TAA-specific T cells has been tested in vitro and in vivo [126, 127]. These T cells have augmented resistant to apoptosis, survive in the absence of cytokine support, and exhibit enhanced anti-tumor activity in a mouse model. Genetic modification with BCL-XL protects T cells from Fas-mediated death and enhances survival in vitro and in vivo [127, 128]. Fas-mediated T cell death can be also reduced by introduction of siRNA targeting Fas [129]. hTERT is the catalytic subunit of telomerase and overexpression of hTERT prevents the shortening of a chromosomal ends after multiple cell divisions. Because of this, transduction of hTERT is used for immortalization of cells. hTERT-transduced T cells have been evaluated and found to have enhanced survival [130]. The clinical translation of all these approaches to improve T cell survival needs to be balanced against the risk of infusing a product capable of autonomous proliferation. Thus, at a minimum, these T cells will need to be engineered for conditional ablation through the expression of a suicide gene.

3.3.2 Cytokines to Support T Cell Function and Survival

T cell survival is dependent on factors intrinsic to the T cells and extrinsic as exerted by microenvironment. Cytokines that signal through the common γ chain are indispensable for T cell expansion and survival [131]. These cytokines have been shown to enhance in vivo T cell survival animals and human trials [132–134]. However, the exogenous administration of supraphysiologic concentrations of recombinant human cytokines is expensive, requires repeated injection, and can cause toxicity. Genetic engineering of T cells with enforced expression of cytokines may be an alternative approach to enhancing T cell persistence. The enforced expression of IL-15 has been tested in CD19-specific CAR⁺ T cells. These T cells secreted IL-15 and proliferated upon encounter with TAA resulting in an improved anti-tumor effect in vivo [135]. However, prolonged expression of IL-15 may lead to genetic alteration and lead to malignant transformation [136]; thus, the co-expression of suicide genes is recommended. IL-7 is an important cytokine for homeostatic expansion of naïve and memory T cells, and IL-7R α is the important cellular marker that identifies long-lived T cells. However, many T cells lose IL-7R α after ex vivo culture. The transduction of IL-7R α into EBV-specific CTL restores responsiveness to IL-7 [137]. Although enforced expression of IL-21 in effector T cells has not been published, IL-21 transduction into T cells capable of antigen presentation (T-APC) has been evaluated. IL-21-secreting T-APCs enhance the generation and proliferation of MART-1-specific CTLs [138]. IL-12 is a heterodimer consisting of a light chain (*p35*) and a heavy chain (*p40*) [139]. IL-12 has an important role in T cell priming, effector function, and survival [140]. Several groups have transduced TAA-specific T cells to express IL-12. This resulted in the enhanced cytotoxic function of T cells, but IL-12 alone did not sustain the long-term survival of T cells [141]. Of note, IL-12 expressing CAR T cells acquired resistance to suppression mediated regulatory T cells [142], attracted activated macrophages in tumor site [143], and also reduced tumor infiltration by myeloid suppressor cells [144]. Thus, it appears that IL-12 from T cells has the potential to disrupt a suppressive tumor microenvironment as well as to enhance effector functioning.

3.3.3 Disruption of Inhibitory Molecules

The long-term efficacy of adoptive T cell therapy is subject to immune checkpoint regulation. Interaction of inhibitory molecules on activated T cells and their ligand on tumor cells compromises T cell function. These checkpoints include CTLA-4, PD-1, TIM-3, and LAG3. Such molecules can be targeted by therapeutic mAbs. Promising clinical results infusing mAbs that block the interaction of CTLA-4 with B7.1 (or B7.2) [145, 146] or the interaction between PD-1 and PD-L1 (or PD-L2) [147, 148] in patients with solid tumors have been reported. Combining these mAbs

with genetically engineered T cells may enhance their therapeutic efficacy. Alternatively, inhibitory molecules expressed on T cells may also be eliminated by post-transcriptional suppression with shRNA. This has been tested by suppressing PD-1 expression on T cells. Increased production of IFN γ and T cell degranulation was noted although PD-1 suppression was incomplete [149]. With the emergence of gene targeting technologies such as ZFN [150], TALEN [151], and CRISPR/Cas9 [152], these molecules may be targeted to completely disrupt their expression.

3.4 Expression of Chemokine/Chemokine Receptor to Guide T Cells to Desired Sites

In order to completely eradicate tumor cells, intravenously administered T cells need to home to tumor sites. In many types of cancer, the degree of infiltration of T cells at the tumor site, especially memory CD8 T cells, correlates positively with a favorable outcome [2]. Chemokines and their receptors affect the migration of immune cells. Chemokine expression in tumor cells likely guides immune cell infiltration and therefore may alter clinical outcomes [153]. CCL2 chemokine is known to be expressed on many types of cancer cells. Its receptor CCR2 is found on myeloid cells in greater amounts than on T cells. Tumors may defend themselves from T cell attack by producing nitrotyrosine which converts CCL2 on tumor cells to a nitrotyrosinated CCL2 [154]. Cells expressing high levels of CCR2 can migrate to tumor via the CCR2–CCL2 axis which is co-opted by tumor cells to load their tumor microenvironment with suppressor myeloid cells. The enforced expression of CCR2 on TAA-specific T cells has been tested to improve the trafficking [155, 156]. Such T cells infiltrate into the tumor site at increased efficiency resulting in augmented antitumor activity. Also, the enforced expression of CCR4 in CD30-specific CAR⁺ T cells enhances migration to sites of Hodgkin lymphoma [157]. The strategy to express chemokine or its receptor on T cells can be generalized by profiling chemokine expression on target tumor cells and enforced expression of corresponding ligand on TAA-specific T cells. Transient expression of chemokine may be sufficient to guide T cells to a tumor site, and therefore, the introduction of in vitro-transcribed mRNA coding for chemokine receptor may be desirable.

3.5 Control of Aberrant T Cell Activity

Suicide gene therapy was first adapted for clinical use in the treatment for cancer. Targeted transduction of a suicide gene into tumor cells was used to destroy tumor by subsequent administration of substrate. This technology was then adapted to enhance the safety of donor leukocyte infusion (DLI) after allogeneic HSCT.

Although DLI may induce remission in certain types of hematological malignancies, it can result in life-threatening GVHD. These transgenes capable of conditional ablation were introduced to eliminate genetically modified T cells severe GVHD occurred after DLI. This technology can also be applied to eliminate any type of cells or transformed cells which are potentially harmful to the patient.

3.5.1 Conditional T Cell Ablation Mediated by Kinases

Thymidine kinase is involved in the pyrimidine salvage pathway. Herpes simplex virus type 1 thymidine kinase (HSV-TK) is desirable for gene therapy because of its broad substrate specificity (e.g., pyrimidines, pyrimidine analogs, and purine analogs). Of these potential substrates, ganciclovir (GCV) is favored for TK-mediated suicide gene therapy because of the need for a low drug concentration and that it is clinically available. The administration of GCV leads to DNA chain termination and cell death in cells expressing HSV-TK. The first use for the HSV-TK gene in T cells was to control GVHD after DLI in allogeneic HSCT [158]. Since this first study, hundreds of patients have been treated using this technology in phases I–II studies. Control of GVHD was observed in all patients who developed GVHD [159]. The ability to control GVHD with HSV-TK has also been proved in the more challenging setting of HLA-haploidentical transplantation [160]. In addition to use as a suicide gene, HSV-TK can be used for noninvasive imaging. T cells expressing variants of HSV-TK can be tracked by injection of radiolabeled 2'-fluoro-2'-deoxy-1-beta-D-arabinofuranosyl-5-iodouracil (FIAU) as imaged by positron emission tomography [161]. This is achieved by the trapping of FIAU in the T cell cytoplasm after phosphorylation by HSV-TK [162]. A drawback to HSV-TK is its immunogenicity and the myelosuppression due to GCV infusion. Mutants of HSV-TK have been developed to overcome GCV mediated myelotoxicity. These need lower concentrations of GCV than wild-type HSV-TK gene, thus reducing the potential for myelosuppression [163, 164]. Immunogenicity of HSV-TK leads to the induction of HSV-TK-specific T cells in the host which compromises persistence of the infused genetically modified T cells [165]. A variant of the less immunogenic human-derived thymidine monophosphate kinase (TMPK) can also be used to conditionally ablate T cells upon addition of 3'-azido-3'-deoxythymidine (AZT) [166]. One concern is the amount of AZT that is needed to achieve ablation of T cells if used in humans.

3.5.2 Conditional T Cell Ablation Mediated by Dimerization

Another class of suicide genes is based on the use of a small molecule to dimerize recombinant Fas. This uses a variant of FK506-binding protein (FKBP) fused to Fas and AP1903 that is a chemical inducer of dimerization (CID). T cells

expressing this fusion can be conditionally eliminated by administration of CID as a result of cross-linked Fas initiating caspase-dependent apoptosis. This construct has been tested in human [136] and macaque T cells [137]. The extent of drug-mediated T cell death was comparable to that of HSV-TK-transduced T cells (up to 90 %), but the pace of inducing apoptosis in this system was improved. Moreover, because this system is derived from human proteins, this fusion transgene may avoid the immunogenicity of HSV-TK. Straathof et al. generated an alternative using caspase 9 instead of Fas intracellular domain [135]. Several constructs were evaluated, and the construct of one copy of FKBP fused to large and small subunits of caspase 9 (referred to as iCasp9) was preferred. A clinically appealing approach has been developed to generate T cells that all express the iCasp9 and thus are all susceptible to conditional ablation. This was based on co-expression of iCasp9 with recombinant CD19 and using paramagnetic beads to positively select successfully genetically modified T cells with mAb against CD19. The initial clinical reports infused haploidentical CD19⁺ (iCasp9⁺) T cells after HSCT [136]. Four out of 5 patients infused with transduced T cells developed GVHD. Their GVHD resolved after one infusion of CID due to the rapid elimination of the genetically modified transduced T cells. Although further clinical experience with this suicide gene therapy is necessary, iCasp9 may be the best alternative to HSV-TK.

3.5.3 Conditional T Cell Ablation Mediated by mAbs

Clinical-grade mAbs can be adapted to eliminate genetically modified T cells. For example, CD20-specific mAb (rituximab) is used for treatment of B cell lymphoma. Enforced expression of recombinant CD20 in T cells does not affect function, and rituximab can eliminate T cells expressing CD20 [167, 168]. Wang et al. developed truncated human EGFR (EGFRt) [169] as an antigen that can be targeted by infusion of EGFR-specific mAb (cetuximab). Furthermore, the aberrant expression of these molecules can serve as a marker for transduced T cells and used for tracking. A downside to the administration of these mAbs in vivo is any toxicity that might occur due to the toxicity of the mAb itself, for example, loss of normal B cells after anti-CD20 and skin toxicity after anti-EGFR.

3.6 Conclusion and Future Perspective

The development of technologies to insert therapeutic transgenes into the genome has enabled multiple investigators to genetically modify T cells for human application. This genetic engineering can equip T cells with desired specificities and functions. Genetic editing to prevent expression of unwanted genes can further enhance therapeutic potential. The pace of gene therapy is currently limited by

sites that can undertake manufacturing and release of clinical-grade T cell products and an ability to select and target TAAs that precludes unacceptable toxicity due to deleterious damage of normal cells. An ability to undertake in-depth correlative studies retrieving T cells from the patient after infusion will lead to the discovery of pathways and T cell subsets that have enhanced persistence and ability to home to tumor. These data will guide the selection of transgenes to express and endogenous genes to remove to genetically modify T cells for next generation clinical trials targeting tumor.

References

1. Grulich AE, van Leeuwen MT, Falster MO, Vajdic CM (2007) Incidence of cancers in people with HIV/AIDS compared with immunosuppressed transplant recipients: a meta-analysis. *Lancet* 370(9581):59–67. doi:[10.1016/s0140-6736\(07\)61050-2](https://doi.org/10.1016/s0140-6736(07)61050-2)
2. Fridman WH, Pages F, Sautes-Fridman C, Galon J (2012) The immune contexture in human tumours: impact on clinical outcome. *Nat Rev Cancer* 12(4):298–306. doi:[10.1038/nrc3245](https://doi.org/10.1038/nrc3245)
3. Lindau D, Gielen P, Kroesen M, Wesseling P, Adema GJ (2013) The immunosuppressive tumour network: myeloid-derived suppressor cells, regulatory T cells and natural killer T cells. *Immunology* 138(2):105–115. doi:[10.1111/imm.12036](https://doi.org/10.1111/imm.12036)
4. Hanahan D, Weinberg RA (2011) Hallmarks of cancer: the next generation. *Cell* 144(5):646–674. doi:[10.1016/j.cell.2011.02.013](https://doi.org/10.1016/j.cell.2011.02.013)
5. Rosenberg SA, Yang JC, Restifo NP (2004) Cancer immunotherapy: moving beyond current vaccines. *Nat Med* 10(9):909–915. doi:[10.1038/nm1100](https://doi.org/10.1038/nm1100)
6. Dudley ME, Rosenberg SA (2003) Adoptive-cell-transfer therapy for the treatment of patients with cancer. *Nat Rev Cancer* 3(9):666–675. doi:[10.1038/nrc1167](https://doi.org/10.1038/nrc1167)
7. van der Bruggen P, Traversari C, Chomez P, Lurquin C, De Plaen E, Van den Eynde B, Knuth A, Boon T (1991) A gene encoding an antigen recognized by cytolytic T lymphocytes on a human melanoma. *Science* 254(5038):1643–1647
8. Cheever MA, Allison JP, Ferris AS, Finn OJ, Hastings BM, Hecht TT, Mellman I, Prindiville SA, Viner JL, Weiner LM, Matrisian LM (2009) The prioritization of cancer antigens: a national cancer institute pilot project for the acceleration of translational research. *Clin Cancer Res* 15(17):5323–5337. doi:[10.1158/1078-0432.ccr-09-0737](https://doi.org/10.1158/1078-0432.ccr-09-0737)
9. Bocchia M, Korontsvit T, Xu Q, Mackinnon S, Yang SY, Sette A, Scheinberg DA (1996) Specific human cellular immunity to bcr-abl oncogene-derived peptides. *Blood* 87(9):3587–3592
10. Greiner J, Ono Y, Hofmann S, Schmitt A, Mehring E, Gotz M, Guillaume P, Dohner K, Mytilineos J, Dohner H, Schmitt M (2012) Mutated regions of nucleophosmin 1 elicit both CD4(+) and CD8(+) T-cell responses in patients with acute myeloid leukemia. *Blood* 120(6):1282–1289. doi:[10.1182/blood-2011-11-394395](https://doi.org/10.1182/blood-2011-11-394395)
11. Schumacher TN (2002) T-cell-receptor gene therapy. *Nat Rev Immunol* 2(7):512–519. doi:[10.1038/nri841](https://doi.org/10.1038/nri841)
12. Li Y, Moysey R, Molloy PE, Vuidepot AL, Mahon T, Baston E, Dunn S, Liddy N, Jacob J, Jakobsen BK, Boulter JM (2005) Directed evolution of human T-cell receptors with picomolar affinities by phage display. *Nat Biotechnol* 23(3):349–354. doi:[10.1038/nbt1070](https://doi.org/10.1038/nbt1070)
13. Yu Z, Liu X, McCarty TM, Diamond DJ, Ellenhorn JD (1997) The use of transgenic mice to generate high affinity p53 specific cytolytic T cells. *J Surg Res* 69(2):337–343. doi:[10.1006/jsre.1997.5058](https://doi.org/10.1006/jsre.1997.5058)
14. Wilde S, Sommermeyer D, Frankenberger B, Schiemann M, Milosevic S, Spranger S, Pohla H, Uckert W, Busch DH, Schendel DJ (2009) Dendritic cells pulsed with RNA encoding

- allogeneic MHC and antigen induce T cells with superior antitumor activity and higher TCR functional avidity. *Blood* 114(10):2131–2139. doi:[10.1182/blood-2009-03-209387](https://doi.org/10.1182/blood-2009-03-209387)
15. Amrolia PJ, Reid SD, Gao L, Schultheis B, Dotti G, Brenner MK, Melo JV, Goldman JM, Stauss HJ (2003) Allorestricted cytotoxic T cells specific for human CD45 show potent antileukemic activity. *Blood* 101(3):1007–1014. doi:[10.1182/blood-2002-02-0525](https://doi.org/10.1182/blood-2002-02-0525)
 16. Mutis T, Blokland E, Kester M, Schrama E, Goulmy E (2002) Generation of minor histocompatibility antigen HA-1-specific cytotoxic T cells restricted by nonself HLA molecules: a potential strategy to treat relapsed leukemia after HLA-mismatched stem cell transplantation. *Blood* 100(2):547–552. doi:[10.1182/blood-2002-01-0024](https://doi.org/10.1182/blood-2002-01-0024)
 17. Kronig H, Hofer K, Conrad H, Guillaume P, Muller J, Schiemann M, Lennerz V, Cosma A, Peschel C, Busch DH, Romero P, Bernhard H (2009) Allorestricted T lymphocytes with a high avidity T-cell receptor towards NY-ESO-1 have potent anti-tumor activity. *Int J Cancer* 125(3):649–655. doi:[10.1002/ijc.24414](https://doi.org/10.1002/ijc.24414)
 18. Falkenburg WJ, Melenhorst JJ, van de Meent M, Kester MG, Hombrink P, Heemskerk MH, Hagedoorn RS, Gostick E, Price DA, Falkenburg JH, Barrett AJ, Jedema I (2011) Allogenic HLA-A*02-restricted WT1-specific T cells from mismatched donors are highly reactive but show off-target promiscuity. *J Immunol* 187(5):2824–2833. doi:[10.4049/jimmunol.1100852](https://doi.org/10.4049/jimmunol.1100852)
 19. Amir AL, D’Orsogna LJ, Roelen DL, van Loenen MM, Hagedoorn RS, de Boer R, van der Hoorn MA, Kester MG, Doxiadis II, Falkenburg JH, Claas FH, Heemskerk MH (2010) Allo-HLA reactivity of virus-specific memory T cells is common. *Blood* 115(15):3146–3157. doi:[10.1182/blood-2009-07-234906](https://doi.org/10.1182/blood-2009-07-234906)
 20. Melenhorst JJ, Leen AM, Bollard CM, Quigley MF, Price DA, Rooney CM, Brenner MK, Barrett AJ, Heslop HE (2010) Allogenic virus-specific T cells with HLA alloreactivity do not produce GVHD in human subjects. *Blood* 116(22):4700–4702. doi:[10.1182/blood-2010-06-289991](https://doi.org/10.1182/blood-2010-06-289991)
 21. Scholler J, Brady TL, Binder-Scholl G, Hwang WT, Plesa G, Hege KM, Vogel AN, Kalos M, Riley JL, Deeks SG, Mitsuyasu RT, Bernstein WB, Aronson NE, Levine BL, Bushman FD, June CH (2012) Decade-long safety and function of retroviral-modified chimeric antigen receptor T cells. *Sci Transl Med* 4(132):132ra153. doi:[10.1126/scitranslmed.3003761](https://doi.org/10.1126/scitranslmed.3003761)
 22. Newrzela S, Cornils K, Li Z, Baum C, Brugman MH, Hartmann M, Meyer J, Hartmann S, Hansmann ML, Fehse B, von Laer D (2008) Resistance of mature T cells to oncogene transformation. *Blood* 112(6):2278–2286. doi:[10.1182/blood-2007-12-128751](https://doi.org/10.1182/blood-2007-12-128751)
 23. Montini E, Cesana D, Schmidt M, Sanvito F, Bartholomae CC, Ranzani M, Benedicenti F, Sergi LS, Ambrosi A, Ponzoni M, Doglioni C, Di Serio C, von Kalle C, Naldini L (2009) The genotoxic potential of retroviral vectors is strongly modulated by vector design and integration site selection in a mouse model of HSC gene therapy. *J Clin Invest* 119(4):964–975. doi:[10.1172/jci37630](https://doi.org/10.1172/jci37630)
 24. Jensen MC, Clarke P, Tan G, Wright C, Chung-Chang W, Clark TN, Zhang F, Slovak ML, Wu AM, Forman SJ, Raubitschek A (2000) Human T lymphocyte genetic modification with naked DNA. *Mol Ther* 1(1):49–55. doi:[10.1006/mthe.1999.0012](https://doi.org/10.1006/mthe.1999.0012)
 25. Ivics Z, Hackett PB, Plasterk RH, Izsvak Z (1997) Molecular reconstruction of Sleeping Beauty, a Tc1-like transposon from fish, and its transposition in human cells. *Cell* 91(4):501–510
 26. Singh H, Manuri PR, Olivares S, Dara N, Dawson MJ, Huls H, Hackett PB, Kohn DB, Shpall EJ, Champlin RE, Cooper LJ (2008) Redirecting specificity of T-cell populations for CD19 using the sleeping beauty system. *Cancer Res* 68(8):2961–2971. doi:[10.1158/0008-5472.can-07-5600](https://doi.org/10.1158/0008-5472.can-07-5600)
 27. Peng PD, Cohen CJ, Yang S, Hsu C, Jones S, Zhao Y, Zheng Z, Rosenberg SA, Morgan RA (2009) Efficient nonviral Sleeping Beauty transposon-based TCR gene transfer to peripheral blood lymphocytes confers antigen-specific antitumor reactivity. *Gene Ther* 16(8):1042–1049. doi:[10.1038/gt.2009.54](https://doi.org/10.1038/gt.2009.54)

28. Huang X, Wilber AC, Bao L, Tuong D, Tolar J, Orchard PJ, Levine BL, June CH, McIvor RS, Blazar BR, Zhou X (2006) Stable gene transfer and expression in human primary T cells by the sleeping beauty transposon system. *Blood* 107(2):483–491. doi:[10.1182/blood-2005-05-2133](https://doi.org/10.1182/blood-2005-05-2133)
29. Nakazawa Y, Huye LE, Dotti G, Foster AE, Vera JF, Manuri PR, June CH, Rooney CM, Wilson MH (2009) Optimization of the piggyBac transposon system for the sustained genetic modification of human T lymphocytes. *J Immunother* 32(8):826–836. doi:[10.1097/CJI.0b013e3181ad762b](https://doi.org/10.1097/CJI.0b013e3181ad762b)
30. Manuri PV, Wilson MH, Maiti SN, Mi T, Singh H, Olivares S, Dawson MJ, Huls H, Lee DA, Rao PH, Kaminski JM, Nakazawa Y, Gottschalk S, Kebriaei P, Shpall EJ, Champlin RE, Cooper LJ (2010) PiggyBac transposon/transposase system to generate CD19-specific T cells for the treatment of B-lineage malignancies. *Hum Gene Ther* 21(4):427–437. doi:[10.1089/hum.2009.114](https://doi.org/10.1089/hum.2009.114)
31. Nakazawa Y, Huye LE, Salsman VS, Leen AM, Ahmed N, Rollins L, Dotti G, Gottschalk SM, Wilson MH, Rooney CM (2011) PiggyBac-mediated cancer immunotherapy using EBV-specific cytotoxic T-cells expressing HER2-specific chimeric antigen receptor. *Mol Ther* 19(12):2133–2143. doi:[10.1038/mt.2011.131](https://doi.org/10.1038/mt.2011.131)
32. Di Matteo M, Belay E, Chuah MK, Vandendriessche T (2012) Recent developments in transposon-mediated gene therapy. *Expert Opin Biol Ther* 12(7):841–858. doi:[10.1517/14712598.2012.684875](https://doi.org/10.1517/14712598.2012.684875)
33. Huang X, Guo H, Tammana S, Jung YC, Mellgren E, Bassi P, Cao Q, Tu ZJ, Kim YC, Ekker SC, Wu X, Wang SM, Zhou X (2010) Gene transfer efficiency and genome-wide integration profiling of sleeping beauty, Tol2, and piggyBac transposons in human primary T cells. *Mol Ther* 18(10):1803–1813. doi:[10.1038/mt.2010.141](https://doi.org/10.1038/mt.2010.141)
34. Hackett CS, Geurts AM, Hackett PB (2007) Predicting preferential DNA vector insertion sites: implications for functional genomics and gene therapy. *Genome Biol* 8(Suppl 1):S12. doi:[10.1186/gb-2007-8-s1-s12](https://doi.org/10.1186/gb-2007-8-s1-s12)
35. Yant SR, Wu X, Huang Y, Garrison B, Burgess SM, Kay MA (2005) High-resolution genome-wide mapping of transposon integration in mammals. *Mol Cell Biol* 25(6):2085–2094. doi:[10.1128/mcb.25.6.2085-2094.2005](https://doi.org/10.1128/mcb.25.6.2085-2094.2005)
36. Berry C, Hannehalli S, Leipzig J, Bushman FD (2006) Selection of target sites for mobile DNA integration in the human genome. *PLoS Comput Biol* 2(11):e157. doi:[10.1371/journal.pcbi.0020157](https://doi.org/10.1371/journal.pcbi.0020157)
37. Kebriaei P, Huls H, Jena B, Munsell M, Jackson R, Lee DA, Hackett PB, Rondon G, Shpall E, Champlin RE, Cooper LJ (2012) Infusing CD19-directed T cells to augment disease control in patients undergoing autologous hematopoietic stem-cell transplantation for advanced B-lymphoid malignancies. *Hum Gene Ther* 23(5):444–450. doi:[10.1089/hum.2011.167](https://doi.org/10.1089/hum.2011.167)
38. Barrett DM, Zhao Y, Liu X, Jiang S, Carpenito C, Kalos M, Carroll RG, June CH, Grupp SA (2011) Treatment of advanced leukemia in mice with mRNA engineered T cells. *Hum Gene Ther* 22(12):1575–1586. doi:[10.1089/hum.2011.070](https://doi.org/10.1089/hum.2011.070)
39. Zhao Y, Zheng Z, Cohen CJ, Gattinoni L, Palmer DC, Restifo NP, Rosenberg SA, Morgan RA (2006) High-efficiency transfection of primary human and mouse T lymphocytes using RNA electroporation. *Mol Ther* 13(1):151–159. doi:[10.1016/j.ymthe.2005.07.688](https://doi.org/10.1016/j.ymthe.2005.07.688)
40. Zhao Y, Moon E, Carpenito C, Paulos CM, Liu X, Brennan AL, Chew A, Carroll RG, Scholler J, Levine BL, Albelda SM, June CH (2010) Multiple injections of electroporated autologous T cells expressing a chimeric antigen receptor mediate regression of human disseminated tumor. *Cancer Res* 70(22):9053–9061. doi:[10.1158/0008-5472.can-10-2880](https://doi.org/10.1158/0008-5472.can-10-2880)
41. Jones S, Peng PD, Yang S, Hsu C, Cohen CJ, Zhao Y, Abad J, Zheng Z, Rosenberg SA, Morgan RA (2009) Lentiviral vector design for optimal T cell receptor gene expression in the transduction of peripheral blood lymphocytes and tumor-infiltrating lymphocytes. *Hum Gene Ther* 20(6):630–640. doi:[10.1089/hum.2008.048](https://doi.org/10.1089/hum.2008.048)
42. Scholten KB, Kramer D, Kueter EW, Graf M, Schoedl T, Meijer CJ, Schreurs MW, Hooijberg E (2006) Codon modification of T cell receptors allows enhanced functional

- expression in transgenic human T cells. *Clin Immunol* 119(2):135–145. doi:[10.1016/j.clim.2005.12.009](https://doi.org/10.1016/j.clim.2005.12.009)
43. Jorritsma A, Gomez-Eerland R, Dokter M, van de Kastele W, Zoet YM, Doxiadis II, Rufer N, Romero P, Morgan RA, Schumacher TN, Haanen JB (2007) Selecting highly affine and well-expressed TCRs for gene therapy of melanoma. *Blood* 110(10):3564–3572. doi:[10.1182/blood-2007-02-075010](https://doi.org/10.1182/blood-2007-02-075010)
 44. Leisegang M, Engels B, Meyerhuber P, Kieback E, Sommermeyer D, Xue SA, Reuss S, Stauss H, Uckert W (2008) Enhanced functionality of T cell receptor-redirected T cells is defined by the transgene cassette. *J Mol Med* 86(5):573–583. doi:[10.1007/s00109-008-0317-3](https://doi.org/10.1007/s00109-008-0317-3)
 45. Yang S, Cohen CJ, Peng PD, Zhao Y, Cassard L, Yu Z, Zheng Z, Jones S, Restifo NP, Rosenberg SA, Morgan RA (2008) Development of optimal bicistronic lentiviral vectors facilitates high-level TCR gene expression and robust tumor cell recognition. *Gene Ther* 15(21):1411–1423. doi:[10.1038/gt.2008.90](https://doi.org/10.1038/gt.2008.90)
 46. Kuball J, Hauptrock B, Malina V, Antunes E, Voss RH, Wolff M, Strong R, Theobald M, Greenberg PD (2009) Increasing functional avidity of TCR-redirected T cells by removing defined *N*-glycosylation sites in the TCR constant domain. *J Exp Med* 206(2):463–475. doi:[10.1084/jem.20082487](https://doi.org/10.1084/jem.20082487)
 47. Zhou Q, Schneider IC, Edes I, Honegger A, Bach P, Schonfeld K, Schambach A, Wels WS, Kneissl S, Uckert W, Buchholz CJ (2012) T-cell receptor gene transfer exclusively to human CD8(+) cells enhances tumor cell killing. *Blood* 120(22):4334–4342. doi:[10.1182/blood-2012-02-412973](https://doi.org/10.1182/blood-2012-02-412973)
 48. Bendle GM, Linnemann C, Hooijkaas AI, Bies L, de Witte MA, Jorritsma A, Kaiser AD, Pouw N, Debets R, Kieback E, Uckert W, Song JY, Haanen JB, Schumacher TN (2010) Lethal graft-versus-host disease in mouse models of T cell receptor gene therapy. *Nat Med* 16(5):565–570, 561p following 570. doi:[10.1038/nm.2128](https://doi.org/10.1038/nm.2128)
 49. van Loenen MM, de Boer R, Amir AL, Hagedoorn RS, Volbeda GL, Willemze R, van Rood JJ, Falkenburg JH, Heemskerk MH (2010) Mixed T cell receptor dimers harbor potentially harmful reactivity. *Proc Natl Acad Sci USA* 107(24):10972–10977. doi:[10.1073/pnas.1005802107](https://doi.org/10.1073/pnas.1005802107)
 50. van der Veken LT, Hagedoorn RS, van Loenen MM, Willemze R, Falkenburg JH, Heemskerk MH (2006) Alphabeta T-cell receptor engineered gammadelta T cells mediate effective antileukemic reactivity. *Cancer Res* 66(6):3331–3337. doi:[10.1158/0008-5472.can-05-4190](https://doi.org/10.1158/0008-5472.can-05-4190)
 51. Cohen CJ, Zheng Z, Bray R, Zhao Y, Sherman LA, Rosenberg SA, Morgan RA (2005) Recognition of fresh human tumor by human peripheral blood lymphocytes transduced with a bicistronic retroviral vector encoding a murine anti-p53 TCR. *J Immunol* 175(9):5799–5808
 52. Sommermeyer D, Uckert W (2010) Minimal amino acid exchange in human TCR constant regions fosters improved function of TCR gene-modified T cells. *J Immunol* 184(11):6223–6231. doi:[10.4049/jimmunol.0902055](https://doi.org/10.4049/jimmunol.0902055)
 53. Cohen CJ, Zhao Y, Zheng Z, Rosenberg SA, Morgan RA (2006) Enhanced antitumor activity of murine-human hybrid T-cell receptor (TCR) in human lymphocytes is associated with improved pairing and TCR/CD3 stability. *Cancer Res* 66(17):8878–8886. doi:[10.1158/0008-5472.can-06-1450](https://doi.org/10.1158/0008-5472.can-06-1450)
 54. Kuball J, Dossett ML, Wolff M, Ho WY, Voss RH, Fowler C, Greenberg PD (2007) Facilitating matched pairing and expression of TCR chains introduced into human T cells. *Blood* 109(6):2331–2338. doi:[10.1182/blood-2006-05-023069](https://doi.org/10.1182/blood-2006-05-023069)
 55. Cohen CJ, Li YF, El-Gamil M, Robbins PF, Rosenberg SA, Morgan RA (2007) Enhanced antitumor activity of T cells engineered to express T-cell receptors with a second disulfide bond. *Cancer Res* 67(8):3898–3903. doi:[10.1158/0008-5472.can-06-3986](https://doi.org/10.1158/0008-5472.can-06-3986)
 56. Voss RH, Willemsen RA, Kuball J, Grabowski M, Engel R, Intan RS, Guillaume P, Romero P, Huber C, Theobald M (2008) Molecular design of the Calphabeta interface favors specific pairing of introduced TCRalphabeta in human T cells. *J Immunol* 180(1):391–401

57. Okamoto S, Mineno J, Ikeda H, Fujiwara H, Yasukawa M, Shiku H, Kato I (2009) Improved expression and reactivity of transduced tumor-specific TCRs in human lymphocytes by specific silencing of endogenous TCR. *Cancer Res* 69(23):9003–9011. doi:[10.1158/0008-5472.can-09-1450](https://doi.org/10.1158/0008-5472.can-09-1450)
58. Provasi E, Genovese P, Lombardo A, Magnani Z, Liu PQ, Reik A, Chu V, Paschon DE, Zhang L, Kuball J, Camisa B, Bondanza A, Casorati G, Ponzoni M, Ciceri F, Bordignon C, Greenberg PD, Holmes MC, Gregory PD, Naldini L, Bonini C (2012) Editing T cell specificity towards leukemia by zinc finger nucleases and lentiviral gene transfer. *Nat Med* 18(5):807–815. doi:[10.1038/nm.2700](https://doi.org/10.1038/nm.2700)
59. Schaft N, Lankiewicz B, Drexhage J, Berrevoets C, Moss DJ, Levitsky V, Bonneville M, Lee SP, McMichael AJ, Gratama JW, Bolhuis RL, Willemsen R, Debets R (2006) T cell re-targeting to EBV antigens following TCR gene transfer: CD28-containing receptors mediate enhanced antigen-specific IFN γ production. *Int Immunol* 18(4):591–601. doi:[10.1093/intimm/dxh401](https://doi.org/10.1093/intimm/dxh401)
60. Voss RH, Thomas S, Pfirschke C, Hauptrock B, Klobuch S, Kuball J, Grabowski M, Engel R, Guillaume P, Romero P, Huber C, Beckhove P, Theobald M (2010) Coexpression of the T-cell receptor constant alpha domain triggers tumor reactivity of single-chain TCR-transduced human T cells. *Blood* 115(25):5154–5163. doi:[10.1182/blood-2009-11-254078](https://doi.org/10.1182/blood-2009-11-254078)
61. Aggen DH, Chervin AS, Schmitt TM, Engels B, Stone JD, Richman SA, Piepenbrink KH, Baker BM, Greenberg PD, Schreiber H, Kranz DM (2012) Single-chain V α V β T-cell receptors function without mispairing with endogenous TCR chains. *Gene Ther* 19(4):365–374. doi:[10.1038/gt.2011.104](https://doi.org/10.1038/gt.2011.104)
62. Zhang T, He X, Tsang TC, Harris DT (2004) Transgenic TCR expression: comparison of single chain with full-length receptor constructs for T-cell function. *Cancer Gene Ther* 11(7):487–496. doi:[10.1038/sj.cgt.7700703](https://doi.org/10.1038/sj.cgt.7700703)
63. Verma B, Neethling FA, Caseltine S, Fabrizio G, Largo S, Duty JA, Tabaczewski P, Weidanz JA (2010) TCR mimic monoclonal antibody targets a specific peptide/HLA class I complex and significantly impedes tumor growth in vivo using breast cancer models. *J Immunol* 184(4):2156–2165. doi:[10.4049/jimmunol.0902414](https://doi.org/10.4049/jimmunol.0902414)
64. Bernardeau K, Gouard S, David G, Ruellan AL, Devys A, Barbet J, Bonneville M, Chelid M, Davodeau F (2005) Assessment of CD8 involvement in T cell clone avidity by direct measurement of HLA-A2/Mage3 complex density using a high-affinity TCR like monoclonal antibody. *Eur J Immunol* 35(10):2864–2875. doi:[10.1002/eji.200526307](https://doi.org/10.1002/eji.200526307)
65. Chames P, Hufton SE, Coulie PG, Uchanska-Ziegler B, Hoogenboom HR (2000) Direct selection of a human antibody fragment directed against the tumor T-cell epitope HLA-A1-MAGE-A1 from a nonimmunized phage-Fab library. *Proc Natl Acad Sci USA* 97(14):7969–7974
66. Epel M, Carmi I, Soueid-Baumgarten S, Oh SK, Bera T, Pastan I, Berzofsky J, Reiter Y (2008) Targeting TARP, a novel breast and prostate tumor-associated antigen, with T cell receptor-like human recombinant antibodies. *Eur J Immunol* 38(6):1706–1720. doi:[10.1002/eji.200737524](https://doi.org/10.1002/eji.200737524)
67. Andersen PS, Stryhn A, Hansen BE, Fugger L, Engberg J, Buus S (1996) A recombinant antibody with the antigen-specific, major histocompatibility complex-restricted specificity of T cells. *Proc Natl Acad Sci USA* 93(5):1820–1824
68. Sergeeva A, Alatrash G, He H, Ruisaard K, Lu S, Wygant J, McIntyre BW, Ma Q, Li D, St John L, Clise-Dwyer K, Mollidrem JJ (2011) An anti-PR1/HLA-A2 T-cell receptor-like antibody mediates complement-dependent cytotoxicity against acute myeloid leukemia progenitor cells. *Blood* 117(16):4262–4272. doi:[10.1182/blood-2010-07-299248](https://doi.org/10.1182/blood-2010-07-299248)
69. Held G, Matsuo M, Epel M, Gnjatich S, Ritter G, Lee SY, Tai TY, Cohen CJ, Old LJ, Pfreundschuh M, Reiter Y, Hoogenboom HR, Renner C (2004) Dissecting cytotoxic T cell responses towards the NY-ESO-1 protein by peptide/MHC-specific antibody fragments. *Eur J Immunol* 34(10):2919–2929. doi:[10.1002/eji.200425297](https://doi.org/10.1002/eji.200425297)
70. Morgan RA, Dudley ME, Wunderlich JR, Hughes MS, Yang JC, Sherry RM, Royal RE, Topalian SL, Kammula US, Restifo NP, Zheng Z, Nahvi A, de Vries CR, Rogers-Freezer

- LJ, Mavroukakis SA, Rosenberg SA (2006) Cancer regression in patients after transfer of genetically engineered lymphocytes. *Science* 314(5796):126–129. doi:[10.1126/science.1129003](https://doi.org/10.1126/science.1129003)
71. Johnson LA, Morgan RA, Dudley ME, Cassard L, Yang JC, Hughes MS, Kammula US, Royal RE, Sherry RM, Wunderlich JR, Lee CC, Restifo NP, Schwarz SL, Cogdill AP, Bishop RJ, Kim H, Brewer CC, Rudy SF, VanWaes C, Davis JL, Mathur A, Ripley RT, Nathan DA, Laurencot CM, Rosenberg SA (2009) Gene therapy with human and mouse T-cell receptors mediates cancer regression and targets normal tissues expressing cognate antigen. *Blood* 114(3):535–546. doi:[10.1182/blood-2009-03-211714](https://doi.org/10.1182/blood-2009-03-211714)
 72. Robbins PF, Morgan RA, Feldman SA, Yang JC, Sherry RM, Dudley ME, Wunderlich JR, Nahvi AV, Helman LJ, Mackall CL, Kammula US, Hughes MS, Restifo NP, Raffeld M, Lee CC, Levy CL, Li YF, El-Gamil M, Schwarz SL, Laurencot C, Rosenberg SA (2011) Tumor regression in patients with metastatic synovial cell sarcoma and melanoma using genetically engineered lymphocytes reactive with NY-ESO-1. *J Clin Oncol* 29(7):917–924. doi:[10.1200/jco.2010.32.2537](https://doi.org/10.1200/jco.2010.32.2537)
 73. Parkhurst MR, Yang JC, Langan RC, Dudley ME, Nathan DA, Feldman SA, Davis JL, Morgan RA, Merino MJ, Sherry RM, Hughes MS, Kammula US, Phan GQ, Lim RM, Wank SA, Restifo NP, Robbins PF, Laurencot CM, Rosenberg SA (2011) T cells targeting carcinoembryonic antigen can mediate regression of metastatic colorectal cancer but induce severe transient colitis. *Mol Ther* 19(3):620–626. doi:[10.1038/mt.2010.272](https://doi.org/10.1038/mt.2010.272)
 74. Morgan RA, Chinnsamy N, Abate-Daga D, Gros A, Robbins PF, Zheng Z, Dudley ME, Feldman SA, Yang JC, Sherry RM, Phan GQ, Hughes MS, Kammula US, Miller AD, Hessman CJ, Stewart AA, Restifo NP, Quezado MM, Alimchandani M, Rosenberg AZ, Nath A, Wang T, Bielekova B, Wuest SC, Akula N, McMahon FJ, Wilde S, Mosetter B, Schendel DJ, Laurencot CM, Rosenberg SA (2013) Cancer regression and neurological toxicity following Anti-MAGE-A3 TCR gene therapy. *J Immunother*. doi:[10.1097/CJI.0b013e3182829903](https://doi.org/10.1097/CJI.0b013e3182829903)
 75. Eshhar Z, Waks T, Gross G, Schindler DG (1993) Specific activation and targeting of cytotoxic lymphocytes through chimeric single chains consisting of antibody-binding domains and the gamma or zeta subunits of the immunoglobulin and T-cell receptors. *Proc Natl Acad Sci USA* 90(2):720–724
 76. Bridgeman JS, Hawkins RE, Bagley S, Blaylock M, Holland M, Gilham DE (2010) The optimal antigen response of chimeric antigen receptors harboring the CD3 zeta transmembrane domain is dependent upon incorporation of the receptor into the endogenous TCR/CD3 complex. *J Immunol (Baltimore, Md: 1950)* 184(12):6938–6949. doi:[10.4049/jimmunol.0901766](https://doi.org/10.4049/jimmunol.0901766)
 77. Haso W, Lee DW, Shah NN, Stetler-Stevenson M, Yuan CM, Pastan IH, Dimitrov DS, Morgan RA, Fitzgerald DJ, Barrett DM, Wayne AS, Mackall CL, Orentas RJ (2012) Anti-CD22-chimeric antigen receptors targeting B cell precursor acute lymphoblastic leukemia. *Blood*. doi:[10.1182/blood-2012-06-438002](https://doi.org/10.1182/blood-2012-06-438002)
 78. Tamada K, Geng D, Sakoda Y, Bansal N, Srivastava R, Li Z, Davila E (2012) Redirecting gene-modified T cells toward various cancer types using tagged antibodies. *Clin Cancer Res* 18(23):6436–6445. doi:[10.1158/1078-0432.ccr-12-1449](https://doi.org/10.1158/1078-0432.ccr-12-1449)
 79. Urbanska K, Lanitis E, Poussin M, Lynn RC, Gavin BP, Kelderman S, Yu J, Scholler N, Powell DJ Jr (2012) A universal strategy for adoptive immunotherapy of cancer through use of a novel T-cell antigen receptor. *Cancer Res* 72(7):1844–1852. doi:[10.1158/0008-5472.can-11-3890](https://doi.org/10.1158/0008-5472.can-11-3890)
 80. Hudecek M, Lupo Stanghellini MT, Kosasih PL, Sommermeyer D, Jensen M, Rader C, Riddell S (2013) Receptor affinity and extracellular domain modifications affect tumor recognition by ROR1-specific chimeric antigen receptor T-cells. *Clin Cancer Res*. doi:[10.1158/1078-0432.ccr-13-0330](https://doi.org/10.1158/1078-0432.ccr-13-0330)
 81. Hombach A, Hombach AA, Abken H (2010) Adoptive immunotherapy with genetically engineered T cells: modification of the IgG1 Fc ‘spacer’ domain in the extracellular moiety

- of chimeric antigen receptors avoids ‘off-target’ activation and unintended initiation of an innate immune response. *Gene Ther* 17(10):1206–1213. doi:[10.1038/gt.2010.91](https://doi.org/10.1038/gt.2010.91)
82. Hombach A, Heuser C, Gerken M, Fischer B, Lewalter K, Diehl V, Pohl C, Abken H (2000) T cell activation by recombinant FcepsilonRI gamma-chain immune receptors: an extracellular spacer domain impairs antigen-dependent T cell activation but not antigen recognition. *Gene Ther* 7(12):1067–1075. doi:[10.1038/sj.gt.3301195](https://doi.org/10.1038/sj.gt.3301195)
 83. Kowolik CM, Topp MS, Gonzalez S, Pfeiffer T, Olivares S, Gonzalez N, Smith DD, Forman SJ, Jensen MC, Cooper LJ (2006) CD28 costimulation provided through a CD19-specific chimeric antigen receptor enhances in vivo persistence and antitumor efficacy of adoptively transferred T cells. *Cancer Res* 66(22):10995–11004. doi:[10.1158/0008-5472.can-06-0160](https://doi.org/10.1158/0008-5472.can-06-0160)
 84. Jensen MC, Popplewell L, Cooper LJ, DiGiusto D, Kalos M, Ostberg JR, Forman SJ (2010) Antitransgene rejection responses contribute to attenuated persistence of adoptively transferred CD20/CD19-specific chimeric antigen receptor redirected T cells in humans. *Biol Blood Marrow Transplant* 16(9):1245–1256. doi:[10.1016/j.bbmt.2010.03.014](https://doi.org/10.1016/j.bbmt.2010.03.014)
 85. Till BG, Jensen MC, Wang J, Chen EY, Wood BL, Greisman HA, Qian X, James SE, Raubitschek A, Forman SJ, Gopal AK, Pagel JM, Lindgren CG, Greenberg PD, Riddell SR, Press OW (2008) Adoptive immunotherapy for indolent non-Hodgkin lymphoma and mantle cell lymphoma using genetically modified autologous CD20-specific T cells. *Blood* 112(6):2261–2271. doi:[10.1182/blood-2007-12-128843](https://doi.org/10.1182/blood-2007-12-128843)
 86. Pule MA, Savoldo B, Myers GD, Rossig C, Russell HV, Dotti G, Huls MH, Liu E, Gee AP, Mei Z, Yvon E, Weiss HL, Liu H, Rooney CM, Heslop HE, Brenner MK (2008) Virus-specific T cells engineered to coexpress tumor-specific receptors: persistence and antitumor activity in individuals with neuroblastoma. *Nat Med* 14(11):1264–1270. doi:[10.1038/nm.1882](https://doi.org/10.1038/nm.1882)
 87. Park JR, DiGiusto DL, Slovak M, Wright C, Naranjo A, Wagner J, Meechoovet HB, Bautista C, Chang WC, Ostberg JR, Jensen MC (2007) Adoptive transfer of chimeric antigen receptor re-directed cytolytic T lymphocyte clones in patients with neuroblastoma. *Mol Ther* 15(4):825–833. doi:[10.1038/sj.mt.6300104](https://doi.org/10.1038/sj.mt.6300104)
 88. Boise LH, Minn AJ, Noel PJ, June CH, Accavitti MA, Lindsten T, Thompson CB (1995) CD28 costimulation can promote T cell survival by enhancing the expression of Bcl-XL. *Immunity* 3(1):87–98
 89. Topp MS, Riddell SR, Akatsuka Y, Jensen MC, Blattman JN, Greenberg PD (2003) Restoration of CD28 expression in CD28- CD8+ memory effector T cells reconstitutes antigen-induced IL-2 production. *J Exp Med* 198(6):947–955. doi:[10.1084/jem.20021288](https://doi.org/10.1084/jem.20021288)
 90. Krause A, Guo HF, Latouche JB, Tan C, Cheung NK, Sadelain M (1998) Antigen-dependent CD28 signaling selectively enhances survival and proliferation in genetically modified activated human primary T lymphocytes. *J Exp Med* 188(4):619–626
 91. Alvarez-Vallina L, Hawkins RE (1996) Antigen-specific targeting of CD28-mediated T cell co-stimulation using chimeric single-chain antibody variable fragment-CD28 receptors. *Eur J Immuno* 26(10):2304–2309. doi:[10.1002/eji.1830261006](https://doi.org/10.1002/eji.1830261006)
 92. Maher J, Brentjens RJ, Gunset G, Riviere I, Sadelain M (2002) Human T-lymphocyte cytotoxicity and proliferation directed by a single chimeric TCRzeta/CD28 receptor. *Nat Biotechnol* 20(1):70–75. doi:[10.1038/nbt0102-70](https://doi.org/10.1038/nbt0102-70)
 93. Loskog A, Giandomenico V, Rossig C, Pule M, Dotti G, Brenner MK (2006) Addition of the CD28 signaling domain to chimeric T-cell receptors enhances chimeric T-cell resistance to T regulatory cells. *Leukemia* 20(10):1819–1828. doi:[10.1038/sj.leu.2404366](https://doi.org/10.1038/sj.leu.2404366)
 94. Savoldo B, Ramos CA, Liu E, Mims MP, Keating MJ, Carrum G, Kamble RT, Bollard CM, Gee AP, Mei Z, Liu H, Grilley B, Rooney CM, Heslop HE, Brenner MK, Dotti G (2011) CD28 costimulation improves expansion and persistence of chimeric antigen receptor-modified T cells in lymphoma patients. *J Clin Invest* 121(5):1822–1826. doi:[10.1172/jci46110](https://doi.org/10.1172/jci46110)
 95. Bertram EM, Lau P, Watts TH (2002) Temporal segregation of 4-1BB versus CD28-mediated costimulation: 4-1BB ligand influences T cell numbers late in the primary

- response and regulates the size of the T cell memory response following influenza infection. *J Immunol* 168(8):3777–3785
96. Takahashi C, Mittler RS, Vella AT (1999) Cutting edge: 4-1BB is a bona fide CD8 T cell survival signal. *J Immunol* (Baltimore, Md: 1950) 162(9):5037–5040
 97. Croft M (2009) The role of TNF superfamily members in T-cell function and diseases. *Nat Rev Immunol* 9(4):271–285. doi:[10.1038/nri2526](https://doi.org/10.1038/nri2526)
 98. Finney HM, Akbar AN, Lawson AD (2004) Activation of resting human primary T cells with chimeric receptors: costimulation from CD28, inducible costimulator, CD134, and CD137 in series with signals from the TCR zeta chain. *J Immunol* 172(1):104–113
 99. Pule MA, Straathof KC, Dotti G, Heslop HE, Rooney CM, Brenner MK (2005) A chimeric T cell antigen receptor that augments cytokine release and supports clonal expansion of primary human T cells. *Mol Ther* 12(5):933–941. doi:[10.1016/j.ymt.2005.04.016](https://doi.org/10.1016/j.ymt.2005.04.016)
 100. Carpenito C, Milone MC, Hassan R, Simonet JC, Lakhali M, Suhoski MM, Varela-Rohena A, Haines KM, Heitjan DF, Albelda SM, Carroll RG, Riley JL, Pastan I, June CH (2009) Control of large, established tumor xenografts with genetically retargeted human T cells containing CD28 and CD137 domains. *Proc Natl Acad Sci USA* 106(9):3360–3365. doi:[10.1073/pnas.0813101106](https://doi.org/10.1073/pnas.0813101106)
 101. Milone MC, Fish JD, Carpenito C, Carroll RG, Binder GK, Teachey D, Samanta M, Lakhali M, Gloss B, Danet-Desnoyers G, Campana D, Riley JL, Grupp SA, June CH (2009) Chimeric receptors containing CD137 signal transduction domains mediate enhanced survival of T cells and increased antileukemic efficacy in vivo. *Mol Ther* 17(8):1453–1464. doi:[10.1038/mt.2009.83](https://doi.org/10.1038/mt.2009.83)
 102. Song DG, Ye Q, Carpenito C, Poussin M, Wang LP, Ji C, Figini M, June CH, Coukos G, Powell DJ Jr (2011) In vivo persistence, tumor localization, and antitumor activity of CAR-engineered T cells is enhanced by costimulatory signaling through CD137 (4-1BB). *Cancer Res* 71(13):4617–4627. doi:[10.1158/0008-5472.can-11-0422](https://doi.org/10.1158/0008-5472.can-11-0422)
 103. Wilkie S, Picco G, Foster J, Davies DM, Julien S, Cooper L, Arif S, Mather SJ, Taylor-Papadimitriou J, Burchell JM, Maher J (2008) Retargeting of human T cells to tumor-associated MUC1: the evolution of a chimeric antigen receptor. *J Immunol* 180(7):4901–4909
 104. Yvon E, Del Vecchio M, Savoldo B, Hoyos V, Dutour A, Anichini A, Dotti G, Brenner MK (2009) Immunotherapy of metastatic melanoma using genetically engineered GD2-specific T cells. *Clin Cancer Res* 15(18):5852–5860. doi:[10.1158/1078-0432.ccr-08-3163](https://doi.org/10.1158/1078-0432.ccr-08-3163)
 105. Marin V, Pizzitola I, Agostoni V, Attianese GM, Finney H, Lawson A, Pule M, Rousseau R, Biondi A, Biagi E (2010) Cytokine-induced killer cells for cell therapy of acute myeloid leukemia: improvement of their immune activity by expression of CD33-specific chimeric receptors. *Haematologica* 95(12):2144–2152. doi:[10.3324/haematol.2010.026310](https://doi.org/10.3324/haematol.2010.026310)
 106. Tammana S, Huang X, Wong M, Milone MC, Ma L, Levine BL, June CH, Wagner JE, Blazar BR, Zhou X (2010) 4-1BB and CD28 signaling plays a synergistic role in redirecting umbilical cord blood T cells against B-cell malignancies. *Hum Gene Ther* 21(1):75–86. doi:[10.1089/hum.2009.122](https://doi.org/10.1089/hum.2009.122)
 107. Hombach AA, Heiders J, Foppe M, Chmielewski M, Abken H (2012) OX40 costimulation by a chimeric antigen receptor abrogates CD28 and IL-2 induced IL-10 secretion by redirected CD4(+) T cells. *Oncoimmunology* 1(4):458–466
 108. Song DG, Ye Q, Poussin M, Harms GM, Figini M, Powell DJ Jr (2012) CD27 costimulation augments the survival and antitumor activity of redirected human T cells in vivo. *Blood* 119(3):696–706. doi:[10.1182/blood-2011-03-344275](https://doi.org/10.1182/blood-2011-03-344275)
 109. Church C, Riether C, Matter MS, Tzankov A, Ochsenbein AF (2012) CD27 signaling on chronic myelogenous leukemia stem cells activates Wnt target genes and promotes disease progression. *J Clin Invest* 122(2):624–638. doi:[10.1172/jci45977](https://doi.org/10.1172/jci45977)
 110. Gattinoni L, Lugli E, Ji Y, Pos Z, Paulos CM, Quigley MF, Almeida JR, Gostick E, Yu Z, Carpenito C, Wang E, Douek DC, Price DA, June CH, Marincola FM, Roederer M, Restifo NP (2011) A human memory T cell subset with stem cell-like properties. *Nat Med* 17(10):1290–1297. doi:[10.1038/nm.2446](https://doi.org/10.1038/nm.2446)

111. Kloss CC, Condomines M, Cartellieri M, Bachmann M, Sadelain M (2012) Combinatorial antigen recognition with balanced signaling promotes selective tumor eradication by engineered T cells. *Nat Biotechnol* 31(1):71–75. doi:[10.1038/nbt.2459](https://doi.org/10.1038/nbt.2459)
112. Zakrzewski JL, Suh D, Markley JC, Smith OM, King C, Goldberg GL, Jenq R, Holland AM, Grubin J, Cabrera-Perez J, Brentjens RJ, Lu SX, Rizzuto G, Sant'Angelo DB, Riviere I, Sadelain M, Heller G, Zuniga-Pflucker JC, Lu C, van den Brink MR (2008) Tumor immunotherapy across MHC barriers using allogeneic T-cell precursors. *Nat Biotechnol* 26(4):453–461. doi:[10.1038/nbt1395](https://doi.org/10.1038/nbt1395)
113. Torikai H, Reik A, Liu PQ, Zhou Y, Zhang L, Maiti S, Huls H, Miller JC, Kebriaei P, Rabinovitch B, Lee DA, Champlin RE, Bonini C, Naldini L, Rebar EJ, Gregory PD, Holmes MC, Cooper LJ (2012) A foundation for universal T-cell based immunotherapy: T cells engineered to express a CD19-specific chimeric-antigen-receptor and eliminate expression of endogenous TCR. *Blood* 119(24):5697–5705. doi:[10.1182/blood-2012-01-405365](https://doi.org/10.1182/blood-2012-01-405365)
114. Kershaw MH, Westwood JA, Parker LL, Wang G, Eshhar Z, Mavroukakis SA, White DE, Wunderlich JR, Canevari S, Rogers-Freezer L, Chen CC, Yang JC, Rosenberg SA, Hwu P (2006) A phase I study on adoptive immunotherapy using gene-modified T cells for ovarian cancer. *Clin Cancer Res* 12(20 Pt 1):6106–6115. doi:[10.1158/1078-0432.ccr-06-1183](https://doi.org/10.1158/1078-0432.ccr-06-1183)
115. Lamers CH, Sleijfer S, Vulto AG, Kruit WH, Kliffen M, Debets R, Gratama JW, Stoter G, Oosterwijk E (2006) Treatment of metastatic renal cell carcinoma with autologous T-lymphocytes genetically retargeted against carbonic anhydrase IX: first clinical experience. *J Clin Oncol* 24(13):e20–e22. doi:[10.1200/jco.2006.05.9964](https://doi.org/10.1200/jco.2006.05.9964)
116. Till BG, Jensen MC, Wang J, Qian X, Gopal AK, Maloney DG, Lindgren CG, Lin Y, Pagel JM, Budde LE, Raubitschek A, Forman SJ, Greenberg PD, Riddell SR, Press OW (2012) CD20-specific adoptive immunotherapy for lymphoma using a chimeric antigen receptor with both CD28 and 4-1BB domains: pilot clinical trial results. *Blood* 119(17):3940–3950. doi:[10.1182/blood-2011-10-387969](https://doi.org/10.1182/blood-2011-10-387969)
117. Kalos M, Levine BL, Porter DL, Katz S, Grupp SA, Bagg A, June CH (2011) T cells with chimeric antigen receptors have potent antitumor effects and can establish memory in patients with advanced leukemia. *Sci Transl Med* 3(95):95ra73. doi:[10.1126/scitranslmed.3002842](https://doi.org/10.1126/scitranslmed.3002842)
118. Porter DL, Levine BL, Kalos M, Bagg A, June CH (2011) Chimeric antigen receptor-modified T cells in chronic lymphoid leukemia. *N Engl J Med* 365(8):725–733. doi:[10.1056/NEJMoa1103849](https://doi.org/10.1056/NEJMoa1103849)
119. Kochenderfer JN, Dudley ME, Feldman SA, Wilson WH, Spaner DE, Maric I, Stetler-Stevenson M, Phan GQ, Hughes MS, Sherry RM, Yang JC, Kammula US, Devillier L, Carpenter R, Nathan DA, Morgan RA, Laurencot C, Rosenberg SA (2012) B-cell depletion and remissions of malignancy along with cytokine-associated toxicity in a clinical trial of anti-CD19 chimeric-antigen-receptor-transduced T cells. *Blood* 119(12):2709–2720. doi:[10.1182/blood-2011-10-384388](https://doi.org/10.1182/blood-2011-10-384388)
120. Kochenderfer JN, Wilson WH, Janik JE, Dudley ME, Stetler-Stevenson M, Feldman SA, Maric I, Raffeld M, Nathan DA, Lanier BJ, Morgan RA, Rosenberg SA (2010) Eradication of B-lineage cells and regression of lymphoma in a patient treated with autologous T cells genetically engineered to recognize CD19. *Blood* 116(20):4099–4102. doi:[10.1182/blood-2010-04-281931](https://doi.org/10.1182/blood-2010-04-281931)
121. Brentjens RJ, Riviere I, Park JH, Davila ML, Wang X, Stefanski J, Taylor C, Yeh R, Bartido S, Borquez-Ojeda O, Olszewska M, Bernal Y, Pegram H, Przybylowski M, Hollyman D, Usachenko Y, Pirraglia D, Hoseney J, Santos E, Halton E, Maslak P, Scheinberg D, Jurcic J, Heaney M, Heller G, Frattini M, Sadelain M (2011) Safety and persistence of adoptively transferred autologous CD19-targeted T cells in patients with relapsed or chemotherapy refractory B-cell leukemias. *Blood* 118(18):4817–4828. doi:[10.1182/blood-2011-04-348540](https://doi.org/10.1182/blood-2011-04-348540)
122. Morgan RA, Yang JC, Kitano M, Dudley ME, Laurencot CM, Rosenberg SA (2010) Case report of a serious adverse event following the administration of T cells transduced with a chimeric antigen receptor recognizing ERBB2. *Mol Ther* 18(4):843–851. doi:[10.1038/mt.2010.24](https://doi.org/10.1038/mt.2010.24)

123. Brentjens R, Yeh R, Bernal Y, Riviere I, Sadelain M (2010) Treatment of chronic lymphocytic leukemia with genetically targeted autologous T cells: case report of an unforeseen adverse event in a phase I clinical trial. *Mol Ther* 18(4):666–668. doi:[10.1038/mt.2010.31](https://doi.org/10.1038/mt.2010.31)
124. Marsden VS, Strasser A (2003) Control of apoptosis in the immune system: Bcl-2, BH3-only proteins and more. *Annu Rev Immunol* 21:71–105. doi:[10.1146/annurev.immunol.21.120601.141029](https://doi.org/10.1146/annurev.immunol.21.120601.141029)
125. Li XC, Demirci G, Ferrari-Lacraz S, Groves C, Coyle A, Malek TR, Strom TB (2001) IL-15 and IL-2: a matter of life and death for T cells in vivo. *Nat Med* 7(1):114–118. doi:[10.1038/83253](https://doi.org/10.1038/83253)
126. Charo J, Finkelstein SE, Grewal N, Restifo NP, Robbins PF, Rosenberg SA (2005) Bcl-2 overexpression enhances tumor-specific T-cell survival. *Cancer Res* 65(5):2001–2008. doi:[10.1158/0008-5472.can-04-2006](https://doi.org/10.1158/0008-5472.can-04-2006)
127. Kalbasi A, Shrimali RK, Chinnasamy D, Rosenberg SA (2010) Prevention of interleukin-2 withdrawal-induced apoptosis in lymphocytes retrovirally cotransduced with genes encoding an antitumor T-cell receptor and an antiapoptotic protein. *J Immunother* 33(7):672–683. doi:[10.1097/CJI.0b013e3181e475cd](https://doi.org/10.1097/CJI.0b013e3181e475cd)
128. Eaton D, Gilham DE, O'Neill A, Hawkins RE (2002) Retroviral transduction of human peripheral blood lymphocytes with Bcl-X(L) promotes in vitro lymphocyte survival in pro-apoptotic conditions. *Gene Ther* 9(8):527–535. doi:[10.1038/sj.gt.3301685](https://doi.org/10.1038/sj.gt.3301685)
129. Dotti G, Savoldo B, Pule M, Straathof KC, Biagi E, Yvon E, Vigouroux S, Brenner MK, Rooney CM (2005) Human cytotoxic T lymphocytes with reduced sensitivity to Fas-induced apoptosis. *Blood* 105(12):4677–4684. doi:[10.1182/blood-2004-08-3337](https://doi.org/10.1182/blood-2004-08-3337)
130. Rufer N, Migliaccio M, Antonchuk J, Humphries RK, Roosnek E, Lansdorp PM (2001) Transfer of the human telomerase reverse transcriptase (TERT) gene into T lymphocytes results in extension of replicative potential. *Blood* 98(3):597–603
131. Rochman Y, Spolski R, Leonard WJ (2009) New insights into the regulation of T cells by gamma(c) family cytokines. *Nat Rev Immunol* 9(7):480–490. doi:[10.1038/nri2580](https://doi.org/10.1038/nri2580)
132. Yee C, Thompson JA, Byrd D, Riddell SR, Roche P, Celis E, Greenberg PD (2002) Adoptive T cell therapy using antigen-specific CD8+ T cell clones for the treatment of patients with metastatic melanoma: in vivo persistence, migration, and antitumor effect of transferred T cells. *Proc Natl Acad Sci USA* 99(25):16168–16173. doi:[10.1073/pnas.242600099](https://doi.org/10.1073/pnas.242600099)
133. Berger C, Berger M, Hackman RC, Gough M, Elliott C, Jensen MC, Riddell SR (2009) Safety and immunologic effects of IL-15 administration in nonhuman primates. *Blood* 114(12):2417–2426. doi:[10.1182/blood-2008-12-189266](https://doi.org/10.1182/blood-2008-12-189266)
134. Mackall CL, Fry TJ, Gress RE (2011) Harnessing the biology of IL-7 for therapeutic application. *Nat Rev Immunol* 11(5):330–342. doi:[10.1038/nri2970](https://doi.org/10.1038/nri2970)
135. Hoyos V, Savoldo B, Quintarelli C, Mahendravada A, Zhang M, Vera J, Heslop HE, Rooney CM, Brenner MK, Dotti G (2010) Engineering CD19-specific T lymphocytes with interleukin-15 and a suicide gene to enhance their anti-lymphoma/leukemia effects and safety. *Leukemia* 24(6):1160–1170. doi:[10.1038/leu.2010.75](https://doi.org/10.1038/leu.2010.75)
136. Mishra A, Liu S, Sams GH, Curphey DP, Santhanam R, Rush LJ, Schaefer D, Falkenberg LG, Sullivan L, Jaronczyk L, Yang X, Fisk H, Wu LC, Hickey C, Chandler JC, Wu YZ, Heerema NA, Chan KK, Perrotti D, Zhang J, Porcu P, Racke FK, Garzon R, Lee RJ, Marcucci G, Caligiuri MA (2012) Aberrant overexpression of IL-15 initiates large granular lymphocyte leukemia through chromosomal instability and DNA hypermethylation. *Cancer Cell* 22(5):645–655. doi:[10.1016/j.ccr.2012.09.009](https://doi.org/10.1016/j.ccr.2012.09.009)
137. Vera JF, Hoyos V, Savoldo B, Quintarelli C, Giordano Attianese GM, Leen AM, Liu H, Foster AE, Heslop HE, Rooney CM, Brenner MK, Dotti G (2009) Genetic manipulation of tumor-specific cytotoxic T lymphocytes to restore responsiveness to IL-7. *Mol Ther* 17(5):880–888. doi:[10.1038/mt.2009.34](https://doi.org/10.1038/mt.2009.34)
138. Kaka AS, Shaffer DR, Hartmaier R, Leen AM, Lu A, Bear A, Rooney CM, Foster AE (2009) Genetic modification of T cells with IL-21 enhances antigen presentation and generation of central memory tumor-specific cytotoxic T-lymphocytes. *J Immunother* (Hagerstown, Md: 1997) 32(7):726–736. doi:[10.1097/CJI.0b013e3181ad4071](https://doi.org/10.1097/CJI.0b013e3181ad4071)

139. Kobayashi M, Fitz L, Ryan M, Hewick RM, Clark SC, Chan S, Loudon R, Sherman F, Perussia B, Trinchieri G (1989) Identification and purification of natural killer cell stimulatory factor (NKSF), a cytokine with multiple biologic effects on human lymphocytes. *J Exp Med* 170(3):827–845
140. Del Vecchio M, Bajetta E, Canova S, Lotze MT, Wesa A, Parmiani G, Anichini A (2007) Interleukin-12: biological properties and clinical application. *Clin Cancer Res* 13(16):4677–4685. doi:[10.1158/1078-0432.ccr-07-0776](https://doi.org/10.1158/1078-0432.ccr-07-0776)
141. Kerkar SP, Muranski P, Kaiser A, Boni A, Sanchez-Perez L, Yu Z, Palmer DC, Reger RN, Borman ZA, Zhang L, Morgan RA, Gattinoni L, Rosenberg SA, Trinchieri G, Restifo NP (2010) Tumor-specific CD8+ T cells expressing interleukin-12 eradicate established cancers in lymphodepleted hosts. *Cancer Res* 70(17):6725–6734. doi:[10.1158/0008-5472.can-10-0735](https://doi.org/10.1158/0008-5472.can-10-0735)
142. Pegram HJ, Lee JC, Hayman EG, Imperato GH, Tedder TF, Sadelain M, Brentjens RJ (2012) Tumor-targeted T cells modified to secrete IL-12 eradicate systemic tumors without need for prior conditioning. *Blood* 119(18):4133–4141. doi:[10.1182/blood-2011-12-400044](https://doi.org/10.1182/blood-2011-12-400044)
143. Chmielewski M, Kopecky C, Hombach AA, Abken H (2011) IL-12 release by engineered T cells expressing chimeric antigen receptors can effectively muster an antigen-independent macrophage response on tumor cells that have shut down tumor antigen expression. *Cancer Res* 71(17):5697–5706. doi:[10.1158/0008-5472.can-11-0103](https://doi.org/10.1158/0008-5472.can-11-0103)
144. Chinnasamy D, Yu Z, Kerkar SP, Zhang L, Morgan RA, Restifo NP, Rosenberg SA (2012) Local delivery of interleukin-12 using T cells targeting VEGF receptor-2 eradicates multiple vascularized tumors in mice. *Clin Cancer Res* 18(6):1672–1683. doi:[10.1158/1078-0432.ccr-11-3050](https://doi.org/10.1158/1078-0432.ccr-11-3050)
145. Hodi FS, O’Day SJ, McDermott DF, Weber RW, Sosman JA, Haanen JB, Gonzalez R, Robert C, Schadendorf D, Hassel JC, Akerley W, van den Eertwegh AJ, Lutzky J, Lorigan P, Vaubel JM, Linette GP, Hogg D, Ottensmeier CH, Lebbe C, Peschel C, Quirt I, Clark JI, Wolchok JD, Weber JS, Tian J, Yellin MJ, Nichol GM, Hoos A, Urba WJ (2010) Improved survival with ipilimumab in patients with metastatic melanoma. *N Engl J Med* 363(8):711–723. doi:[10.1056/NEJMoa1003466](https://doi.org/10.1056/NEJMoa1003466)
146. Robert C, Thomas L, Bondarenko I, O’Day S, M DJ, Garbe C, Lebbe C, Baurain JF, Testori A, Grob JJ, Davidson N, Richards J, Maio M, Hauschild A, Miller WH, Jr., Gascon P, Lotem M, Harmankaya K, Ibrahim R, Francis S, Chen TT, Humphrey R, Hoos A, Wolchok JD (2011) Ipilimumab plus dacarbazine for previously untreated metastatic melanoma. *N Engl J Med* 364(26):2517–2526. doi:[10.1056/NEJMoa1104621](https://doi.org/10.1056/NEJMoa1104621)
147. Brahmer JR, Tykodi SS, Chow LQ, Hwu WJ, Topalian SL, Hwu P, Drake CG, Camacho LH, Kauh J, Odunsi K, Pitot HC, Hamid O, Bhatia S, Martins R, Eaton K, Chen S, Salay TM, Alaparthi S, Grosso JF, Korman AJ, Parker SM, Agrawal S, Goldberg SM, Pardoll DM, Gupta A, Wigginton JM (2012) Safety and activity of anti-PD-L1 antibody in patients with advanced cancer. *N Engl J Med* 366(26):2455–2465. doi:[10.1056/NEJMoa1200694](https://doi.org/10.1056/NEJMoa1200694)
148. Topalian SL, Hodi FS, Brahmer JR, Gettinger SN, Smith DC, McDermott DF, Powderly JD, Carvajal RD, Sosman JA, Atkins MB, Leming PD, Spigel DR, Antonia SJ, Horn L, Drake CG, Pardoll DM, Chen L, Sharfman WH, Anders RA, Taube JM, McMiller TL, Xu H, Korman AJ, Jure-Kunkel M, Agrawal S, McDonald D, Kollia GD, Gupta A, Wigginton JM, Sznol M (2012) Safety, activity, and immune correlates of anti-PD-1 antibody in cancer. *N Engl J Med* 366(26):2443–2454. doi:[10.1056/NEJMoa1200690](https://doi.org/10.1056/NEJMoa1200690)
149. Borkner L, Kaiser A, van de Kastele W, Andreesen R, Mackensen A, Haanen JB, Schumacher TN, Blank C (2010) RNA interference targeting programmed death receptor-1 improves immune functions of tumor-specific T cells. *Cancer Immunol Immunother* 59(8):1173–1183. doi:[10.1007/s00262-010-0842-0](https://doi.org/10.1007/s00262-010-0842-0)
150. Urnov FD, Rebar EJ, Holmes MC, Zhang HS, Gregory PD (2010) Genome editing with engineered zinc finger nucleases. *Nat Rev Genet* 11(9):636–646. doi:[10.1038/nrg2842](https://doi.org/10.1038/nrg2842)
151. Miller JC, Tan S, Qiao G, Barlow KA, Wang J, Xia DF, Meng X, Paschon DE, Leung E, Hinkley SJ, Dulay GP, Hua KL, Ankoudinova I, Cost GJ, Urnov FD, Zhang HS, Holmes MC, Zhang L, Gregory PD, Rebar EJ (2011) A TALE nuclease architecture for efficient genome editing. *Nat Biotechnol* 29(2):143–148. doi:[10.1038/nbt.1755](https://doi.org/10.1038/nbt.1755)

152. Mali P, Yang L, Esvelt KM, Aach J, Guell M, DiCarlo JE, Norville JE, Church GM (2013) RNA-guided human genome engineering via Cas9. *Science* 339(6121):823–826. doi:[10.1126/science.1232033](https://doi.org/10.1126/science.1232033)
153. Franciszkiwicz K, Boissonnas A, Boutet M, Combadiere C, Mami-Chouaib F (2012) Role of chemokines and chemokine receptors in shaping the effector phase of the antitumor immune response. *Cancer Res* 72(24):6325–6332. doi:[10.1158/0008-5472.can-12-2027](https://doi.org/10.1158/0008-5472.can-12-2027)
154. Molon B, Ugel S, Del Pozzo F, Soldani C, Zilio S, Avella D, De Palma A, Mauri P, Monegal A, Rescigno M, Savino B, Colombo P, Jonjic N, Pecanic S, Lazzarato L, Fruttero R, Gasco A, Bronte V, Viola A (2011) Chemokine nitration prevents intratumoral infiltration of antigen-specific T cells. *J Exp Med* 208(10):1949–1962. doi:[10.1084/jem.20101956](https://doi.org/10.1084/jem.20101956)
155. Moon EK, Carpenito C, Sun J, Wang LC, Kapoor V, Predina J, Powell DJ Jr, Riley JL, June CH, Albelda SM (2011) Expression of a functional CCR2 receptor enhances tumor localization and tumor eradication by retargeted human T cells expressing a mesothelin-specific chimeric antibody receptor. *Clin Cancer Res* 17(14):4719–4730. doi:[10.1158/1078-0432.ccr-11-0351](https://doi.org/10.1158/1078-0432.ccr-11-0351)
156. Craddock JA, Lu A, Bear A, Pule M, Brenner MK, Rooney CM, Foster AE (2010) Enhanced tumor trafficking of GD2 chimeric antigen receptor T cells by expression of the chemokine receptor CCR2b. *J Immunother* 33(8):780–788. doi:[10.1097/CJI.0b013e3181ee6675](https://doi.org/10.1097/CJI.0b013e3181ee6675)
157. Di Stasi A, De Angelis B, Rooney CM, Zhang L, Mahendravada A, Foster AE, Heslop HE, Brenner MK, Dotti G, Savoldo B (2009) T lymphocytes coexpressing CCR4 and a chimeric antigen receptor targeting CD30 have improved homing and antitumor activity in a Hodgkin tumor model. *Blood* 113(25):6392–6402. doi:[10.1182/blood-2009-03-209650](https://doi.org/10.1182/blood-2009-03-209650)
158. Bonini C, Ferrari G, Verzeletti S, Servida P, Zappone E, Ruggieri L, Ponzoni M, Rossini S, Mavilio F, Traversari C, Bordignon C (1997) HSV-TK gene transfer into donor lymphocytes for control of allogeneic graft-versus-leukemia. *Science* 276(5319):1719–1724
159. Bonini C, Bondanza A, Perna SK, Kaneko S, Traversari C, Ciceri F, Bordignon C (2007) The suicide gene therapy challenge: how to improve a successful gene therapy approach. *Mol Ther* 15(7):1248–1252. doi:[10.1038/sj.mt.6300190](https://doi.org/10.1038/sj.mt.6300190)
160. Ciceri F, Bonini C, Stanghellini MT, Bondanza A, Traversari C, Salomoni M, Turchetto L, Colombi S, Bernardi M, Peccatori J, Pescarollo A, Servida P, Magnani Z, Perna SK, Valtolina V, Crippa F, Callegaro L, Spoldi E, Crocchiolo R, Fleischhauer K, Ponzoni M, Vago L, Rossini S, Santoro A, Todisco E, Apperley J, Olavarria E, Slavin S, Weissinger EM, Ganser A, Stadler M, Yannaki E, Fassas A, Anagnostopoulos A, Bregni M, Stampino CG, Bruzzi P, Bordignon C (2009) Infusion of suicide-gene-engineered donor lymphocytes after family haploidentical haemopoietic stem-cell transplantation for leukaemia (the TK007 trial): a non-randomised phase I–II study. *Lancet Oncol* 10(5):489–500. doi:[10.1016/s1470-2045\(09\)70074-9](https://doi.org/10.1016/s1470-2045(09)70074-9)
161. Koehne G, Doubrovin M, Doubrovina E, Zanzonico P, Gallardo HF, Ivanova A, Balatoni J, Teruya-Feldstein J, Heller G, May C, Ponomarev V, Ruan S, Finn R, Blasberg RG, Bornmann W, Riviere I, Sadelain M, O'Reilly RJ, Larson SM, Tjuvajev JG (2003) Serial in vivo imaging of the targeted migration of human HSV-TK-transduced antigen-specific lymphocytes. *Nat Biotechnol* 21(4):405–413. doi:[10.1038/nbt805](https://doi.org/10.1038/nbt805)
162. Tjuvajev JG, Stockhammer G, Desai R, Uehara H, Watanabe K, Gansbacher B, Blasberg RG (1995) Imaging the expression of transfected genes in vivo. *Cancer Res* 55(24):6126–6132
163. Kokoris MS, Black ME (2002) Characterization of herpes simplex virus type 1 thymidine kinase mutants engineered for improved ganciclovir or acyclovir activity. *Protein Sci: Publ Protein Soc* 11(9):2267–2272. doi:[10.1110/ps.2460102](https://doi.org/10.1110/ps.2460102)
164. Qasim W, Thrasher AJ, Buddle J, Kinnon C, Black ME, Gaspar HB (2002) T cell transduction and suicide with an enhanced mutant thymidine kinase. *Gene Ther* 9(12):824–827. doi:[10.1038/sj.gt.3301690](https://doi.org/10.1038/sj.gt.3301690)
165. Berger C, Flowers ME, Warren EH, Riddell SR (2006) Analysis of transgene-specific immune responses that limit the in vivo persistence of adoptively transferred HSV-TK-modified donor T cells after allogeneic hematopoietic cell transplantation. *Blood* 107(6):2294–2302. doi:[10.1182/blood-2005-08-3503](https://doi.org/10.1182/blood-2005-08-3503)

166. Sato T, Neschadim A, Konrad M, Fowler DH, Lavie A, Medin JA (2007) Engineered human tmpk/AZT as a novel enzyme/prodrug axis for suicide gene therapy. *Mol Ther: J Am Soc Gene Ther* 15(5):962–970. doi:[10.1038/mt.sj.6300122](https://doi.org/10.1038/mt.sj.6300122)
167. Introna M, Barbui AM, Bambacioni F, Casati C, Gaipa G, Borleri G, Bernasconi S, Barbui T, Golay J, Biondi A, Rambaldi A (2000) Genetic modification of human T cells with CD20: a strategy to purify and lyse transduced cells with anti-CD20 antibodies. *Hum Gene Ther* 11(4):611–620. doi:[10.1089/10430340050015798](https://doi.org/10.1089/10430340050015798)
168. Griffioen M, van Egmond EH, Kester MG, Willemze R, Falkenburg JH, Heemskerk MH (2009) Retroviral transfer of human CD20 as a suicide gene for adoptive T-cell therapy. *Haematologica* 94(9):1316–1320. doi:[10.3324/haematol.2008.001677](https://doi.org/10.3324/haematol.2008.001677)
169. Wang X, Chang WC, Wong CW, Colcher D, Sherman M, Ostberg JR, Forman SJ, Riddell SR, Jensen MC (2011) A transgene-encoded cell surface polypeptide for selection, in vivo tracking, and ablation of engineered cells. *Blood* 118(5):1255–1263. doi:[10.1182/blood-2011-02-337360](https://doi.org/10.1182/blood-2011-02-337360)

Chapter 4

Engineering Biomaterials for Anchorage-Dependent and Non-anchorage-Dependent Therapeutic Cell Delivery in Translational Medicine

Wenyan Leong and Dong-An Wang

4.1 Introduction

Translational medicine is an interdisciplinary field utilizing basic sciences and research findings to develop solutions to medical problems. Cell-based therapy, or utilizing biological cells as a medical intervention to replace lost or abnormal cells, tissues, and organs, has the potential to become an important therapeutic technology. Much research effort has thus been focused on developing cell delivery methods that can deliver and localize viable functional cells or undifferentiated stem cells to the target site with high efficiencies and at low cost. A multitude of biomaterials have been developed to act as contained cell carriers—confining cells within a scaffold structure to facilitate easy handling as well as prevent leakage or migration of cells from target site after implantation. This not only delivers cells into the target site, but it also creates a distinct separation between the host tissue and delivered cells, hence protecting against immune responses [1–4]. As different cells have different cell–cell and cell–material interactions, it is critical that biomaterials and their scaffolding structure are designed to suit the therapeutic cell type.

Ideally, materials used for cell delivery should be easy to fabricate at a low cost, be biocompatible, and biodegradable with no undesirable degradation products and with degradation rates matching those of tissue regeneration. They should also have suitable mechanical integrity for ease of handling. Furthermore, suitable biochemical and physical moieties that mimic the microenvironment niche of the cells to be delivered should ideally be present. The choice of appropriate biomaterials and their structure is therefore crucial for successful cell delivery [5]. In light of the complexity of these criteria for materials to ensure proper and efficient delivery of therapeutic cells, this chapter shall focus on the advancement

W. Leong · D.-A. Wang (✉)

Division of BioEngineering, School of Chemical and Biomedical Engineering, Nanyang Technological University, 70 Nanyang Drive, N1.3-B2-13, Singapore 637457, Singapore
e-mail: DAWang@ntu.edu.sg

of biomaterial research for the delivery of different cell types: anchorage-dependent cells (ADCs) and non-anchorage-dependent cells (non-ADCs). Furthermore, several key improvisations that are envisaged to propel cell delivery as a viable medical solution are discussed.

4.1.1 Anchorage-Dependent Versus Non-anchorage-Dependent Cells

Therapeutic biological cells can be broadly categorized into two types: anchorage dependent or non-anchorage dependent. ADCs in their native environment require extensive adhesion to the extracellular matrix (ECM) and exhibit a stretched or spreading morphology. ADCs include osteoblasts, fibroblasts, neural, epithelial, endothelial, and smooth muscle cells [6, 7]. On the other hand, non-ADCs exhibit a rounded morphology in native environment and do not require extensive cell adhesion to the surrounding ECM. These cells include blood cells, chondrocytes, hepatocytes, embryonic stem cells (ESCs), and induced pluripotent stem cells (iPSCs).

ADCs' survival depends on a homeostatic mechanism whereby a specific apoptotic pathway is activated when the cell is unable to adhere to the surrounding ECM [6]. This apoptotic process, coined *anoikis* meaning "homelessness" in Greek, functions to prevent detached cells from being able to survive and proliferate dysplastically in non-native locations, which is especially important for preventing tumorigenesis [6]. This attachment-dependent survival has been widely documented in various cell types, including epithelial and endothelial cells.

In *anoikis*, cells that are not attached to their native ECM sense the loss of integrin (comprising α - and β -subunits) contact and translate these mechanical cues into intracellular signaling cascades, leading to apoptosis (Fig. 4.1) [8, 9]. There are namely two pathways—intrinsic and extrinsic—that both ultimately effect a caspase cascade, leading to endonuclease activation and DNA fragmentation [10]. When cells are properly attached to their appropriate ECM, anti-apoptotic signals Bcl-2 and Bcl-XL are expressed to maintain mitochondrial membrane's integrity by binding to pro-apoptotic Bad and Bax and sequestering pro-apoptotic Bim [11, 12]. In the intrinsic pathway, when cells fail to attach to the ECM, integrin disengagement increases the amount of Bim in the cytoplasm by allowing its release from cytoskeleton while preventing its degradation (inhibition of ERK and PI3K/Akt-mediated phosphorylation of Bim) [10]. Apoptosis activators Bim and Bid as well as apoptosis sensitizers Bad, Puma, Bik, Noxa, Hrk, and Bmf are activated [10, 13]. Apoptosis sensitizers on the cell membrane act as competitive inhibitors of apoptosis activators for Bcl-2 [14, 15]. Apoptosis activators, which are usually repressed by anti-apoptotic Bcl-2 and Bcl-XL, then assemble Bax and Bak into Bax-Bak oligomers in the outer mitochondrial membrane (OMM) [16]. The OMM is hence permeabilized, and cytochrome c is

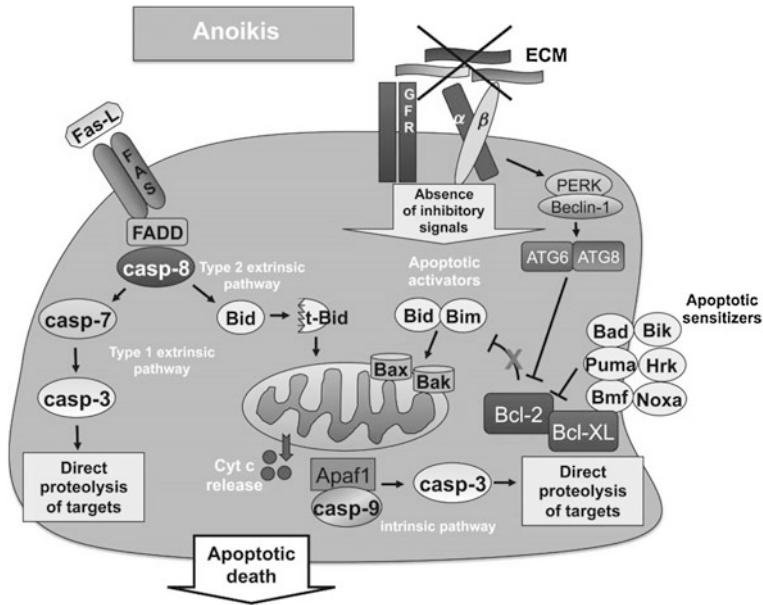


Fig. 4.1 *Anoikis* activation pathways. Lack of adhesion to the extracellular matrix via integrins (transmembrane proteins consisting of α - and β -subunits) reduces the anti-apoptotic signals Bcl-2 and Bcl-XL. The pro-apoptotic pathways involving increase in pro-apoptotic molecules Bid, Bim, Bad, Puma, and Noxa are therefore not inhibited, leading to an intracellular caspase cascade that causes cytochrome c (cyt-c) in mitochondria to be released and apoptosome assembly in the intrinsic pathway. The extrinsic pathways are activated by extracellular death ligands such as FasL binding to corresponding death receptors Fas. There are two branches of the extrinsic pathway: The first leads to a caspase cascade resulting in the direct proteolysis of target proteins, while the second results in a truncated Bid (t-Bid) that joins the intrinsic pathway to activate cytochrome release from mitochondria. [9] Recreated from Fig. 1 of Ref. [9] with kind permission from John Wiley and Sons (License Number 3125710475964)

released from the mitochondria into the cytoplasm [9]. Subsequently, cytochrome c binds with caspase-9 and apoptosis protease-activating factor (APAF) to form an apoptosome which activates caspase-3, resulting in a caspase signaling cascade concluding in apoptosis [17, 18].

There are two branches of the extrinsic pathway, both of which begin with the binding of extracellular death ligands Fas ligands (FasL) and tumor necrosis factor- α (TNF- α) to the cells' corresponding transmembrane receptors Fas and TNF- α receptor TNFR, which are upregulated upon disengagement from ECM [19, 20]. The morphological change into a rounded cell further causes the accumulation and activation of the mentioned receptors [21, 22]. FasL binds to its receptor present on the cellular membrane, causing death-inducing signaling complex (DISC) to be formed. Subsequently, DISC causes the activation of caspase-8 that activates a caspase cascade involving caspase-3 and caspase-7, causing the proteolysis and ultimately cell death (type I extrinsic apoptosis); caspase-8 also

can cleave pro-apoptotic Bid into a form (t-Bid) that encourages apoptosome assembly and cytochrome c release, facilitating cell death in the second type of apoptosis [9].

4.1.2 Biomaterials in Cell Delivery Vehicles

A wide variety of biomaterials, both naturally derived and synthetic, have been used in constructing three-dimensional (3D) cell delivery vehicles or cell-laden scaffolds. These scaffolding systems have to fulfill several basic criteria in order to successfully encapsulate cells *in vitro* and subsequently deliver the functional cells to the target site in the clinical setting. Most importantly, biomaterials used must be biocompatible, that is, they must possess the ability to perform *in vivo* without invoking any harmful effects such as immune response [23]. Secondly, they should provide a suitable microenvironment for cells to attach, reside, and proliferate within. Thirdly, biomaterials should be biodegradable with a controlled rate—degradation by-products should not be harmful to cells and the rate should match that of tissue growth. Lastly, as cell delivery vehicles, suitable mechanical integrity for ease of handling *ex vivo* and similar mechanical properties as surrounding tissues *in vivo* is critical. Simply put, the cell delivery vehicle should recapitulate both the micro- and macroenvironments of the target implantation site; therefore, the materials utilized in constructing the vehicle are of critical importance.

Biomaterials can either be naturally derived or be synthetically manufactured (Table 4.1), both of which possess respective pros and cons. Naturally derived biomaterials are popular because of their low toxicity, biodegradability, low cost of manufacture, and possession of cell-adhesive moieties. However, it is precisely this ability to interact with cells that also imparts the risk of immune response and disease transfer; strict screening and purification are required. Batch-to-batch variation and therefore uncontrollable mechanical properties and degradation rates are also cause for concern.

Synthetic biomaterials circumvent the need for purification and batch-to-batch variation. Synthetic polymers have predictable and controllable chemical and physical properties, but are more expensive and do not possess cell adhesion moieties. Furthermore, their degradation by-products may be toxic to cells. Therefore, synthetic materials require functionalization to be biocompatible. Popular synthetic biomaterials include poly(ethyl glycol) (PEG), polylactic acid (PLA), and poly(vinyl alcohol) (PVA). PEG is not naturally degradable and cell adhesive, requiring addition of cleavable segments such as polyester units and coatings with cell adhesion moieties.

Often, the best of both worlds—respective advantages of naturally derived and synthetic biomaterials—are combined by researchers in a bid to create an “ideal” biomaterial with the desired properties for the target delivery cell type and the target implantation site [24].

Table 4.1 List of popularly used naturally derived and synthetic biomaterials for cell delivery

Naturally derived	Synthetic
Alginate	Poly(acryl amide) (PAam)
Agarose	Poly(acrylic acid) (PAA)
Chitosan	Poly(ethyl glycol) (PEG)
Chondroitin sulfate	Poly(ethylene oxide) (PEO)
Collagen	Poly(lactic acid (PLA): poly-L-lactic acid (PLLA), poly-DL-lactic acid (PDLLA)
Elastin	Poly(lactide-co-glycolide) (PLGA)
Fibrin	
Gelatin	
Hydroxyapatite	Poly(vinyl alcohol) (PVA)
Hyaluronic acid	Poly(ϵ -caprolactone) (PCL)
Silk fibroin	

4.2 Engineering Basic Cell Delivery Structures

Cell delivery vehicles (or scaffolds) can be categorized into preformed or injectable systems. Preformed systems are fabricated *ex vivo*; cells are introduced either during or after the fabrication process of a macroscopic-sized scaffold. The cell-laden scaffolds are then cultured *in vitro* for a period of time prior to surgical implantation. On the other hand, injectable systems are either in cell-encapsulated microsized scaffold (microcarrier) form or in a cell suspension form, which can be easily injected into the target site, thereby providing a minimally invasive means of implantation. The latter refers to hydrogel solutions that can be gelled *in situ* under mild conditions, imparting the quality of filling up irregular defects.

In the subsections below, the different fundamental structures and their fabrication techniques, as well as the popular biomaterials used in cell delivery vehicles are discussed. Biomaterials are often engineered to achieve quick and simple polymerization as well as to suit the cell type and the target site; they can be conjugated with polymerizable segments, blended or copolymerized with other materials prior to fabricating the scaffold structures or fabricated with certain orientations. Table 4.2 summarizes and compares the four different basic structures.

4.2.1 Hydrogels

Hydrogels are a class of insoluble water-swollen polymeric networks formed from crosslinked water-soluble macromers. Usually, cells are mixed into the hydrogel precursor solution prior to gelation, hence achieving a homogeneous cell-laden hydrogel (Fig. 4.2a). Advantages of hydrogels are as follows: the highly hydrated environment and good diffusion of nutrients and waste as well as the mimicking of

Table 4.2 Features, fabrication techniques, and development of basic cell delivery structures

	Hydrogel	Fibrous mesh	Sponge	Decellularized scaffold
Features	<ul style="list-style-type: none"> ✓ Highly hydrated, mimicking biological tissue ✓ Good diffusion of nutrients and waste ✓ Mild conditions for polymerization (fabrication) ✓ Reversible gelation (responsive to external stimuli, e.g., change in temperature and ionic concentration) ✓ Typically degradable ✓ Fast and simple gelation ✓ Injectable – Weak mechanical properties, suitable for soft tissues only 	<ul style="list-style-type: none"> ✓ Fibers mimic ECM fiber architecture in structural tissues (collagen) ✓ Strong mechanical properties, suitable for structural tissues, e.g., bones ✓ Highly controllable physical and chemical parameters ✓ Controllable fiber diameters (nm to μm scale) – Time-consuming, labor intensive – Non-injectable – Require prefabrication before cell seeding 	<ul style="list-style-type: none"> ✓ Highly porous ✓ Strong mechanical properties, suitable for structural tissues – Small, thin templates for proper diffusion – Limited amount of pores for structural integrity, limited interconnectivity – Irregular pore size – Difficulty in ensuring well-distributed pores – Require removal of toxic components used in fabrication – Time-consuming, labor intensive post-fabrication washing – Require prefabrication before cell seeding 	<ul style="list-style-type: none"> ✓ Provides tissue-specific native ECM and growth factors (niche) by previous residing cells ✓ Able to retain complex structure and ECM architecture that cannot be easily mimicked (e.g., alveoli of lungs) ✓ Biocompatible ✓ Xenogenic and allogeneic sources used without eliciting immune response as ECM components are well conserved among species <ul style="list-style-type: none"> – Labor intensive, time-consuming as complete removal of cells and nuclear material required – Decellularization protocols may cause structural ECM changes • Physical (freeze–thaw, agitation, sonication) • Enzymatic (trypsin, endonucleases) • Chemical (SDS, Triton X-100)
Fabrication techniques	<ul style="list-style-type: none"> • Photoinitiated (conjugate with acrylate groups) • Enzymatic (conjugate with phenolic hydroxyl groups) • Temperature (e.g., agarose, gelatin) • pH (e.g., chitosan) • Ionic (e.g., alginate) • Self-assembly peptides/amphiphiles 	<ul style="list-style-type: none"> • Electrospinning • Extrusion • Phase separation 	<ul style="list-style-type: none"> • Gas foaming • Particulate leaching/solvent casting • Freeze-drying • Phase separation • Thermally induced phase separation (TIPS) 	

(continued)

Table 4.2 (continued)

	Hydrogel	Fibrous mesh	Sponge	Decellularized scaffold
Modification	<ul style="list-style-type: none"> • Interpenetrating network (IPN) of two hydrogels [27] • Saccharide-peptide hydrogels [43, 44] 	<ul style="list-style-type: none"> • Blending of materials [122, 123] • Coatings [56] • Aligned fibers [58] • Different shapes, e.g., tubes and mats • Zonal organization [55] 	<ul style="list-style-type: none"> • Blending of materials [62, 124] 	<ul style="list-style-type: none"> • Conversion into hydrogel [82] and sponge [79]

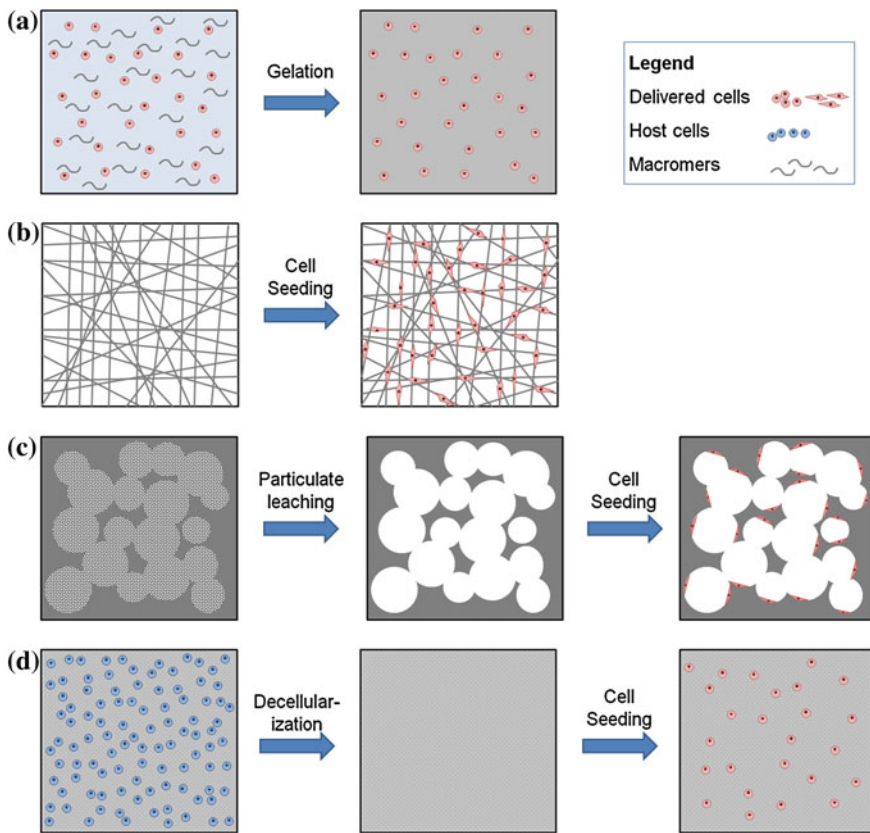


Fig. 4.2 Basic cell delivery structures. **(a)** Hydrogel formation from homogenous cell suspension in macromer solution; **(b)** fibrous mesh fabrication via electrospinning and subsequent cell seeding and attachment onto fibers; **(c)** sponge fabrication via particulate leaching by firstly forming a solid encapsulating particulates (porogens), leaching of particulates to leave behind pores, and finally seeding cells that attach to walls of pores; and **(d)** decellularized scaffolds fabrication by firstly isolating biological tissues and organs from allogeneic or xenogeneic sources, applying decellularization techniques to remove previous host cells without breaking down ECM structure and finally seeding therapeutic cells onto decellularized ECM scaffold

most tissues. Many hydrogels offer the advantage of being injectable: In other words, they can be quickly gelled in situ under mild physiological conditions, thereby allowing molding into irregularly sized defects via a minimally invasive means of implantation. These properties have thus made hydrogels popular for cell and drug delivery. Through altering the porosity and crosslinking density, mechanical properties of hydrogels can be adjusted to suit the targeted cell type and site of implantation. Mechanical strength, however, is usually low compared to the meshes and sponges, and hence, hydrogels are only suitable for soft tissues such as cartilage. Furthermore, as hydrogels are highly hydrophilic, cells typically

exhibit a rounded morphology when encapsulated within [25]. While this makes hydrogels suitable for the delivery of non-ADCs, successful delivery of ADCs using hydrogels would require modifications to include cell adhesion moieties within the hydrogels for ADCs to adhere onto.

Hydrogel formation (gelation) is attained via physical or chemical crosslinking mechanisms. Under suitable conditions, a solution consisting of macromers or unreacted monomers with crosslinking agents is converted into an insoluble 3D network upon gelation. Physically crosslinked gels are linked via ionic or hydrogen bonds or hydrophobic interactions, forming a gel upon a change in environmental conditions, e.g., temperature, pH, and ionic concentration. Temperature-responsive hydrogels such as agarose and gelatin have reversible properties. Alginate, derived from brown algae, is an ionic polysaccharide that is crosslinked upon presence of divalent cations such as calcium. These are usually reversible crosslinking reactions—upon reversal of conditions, the gel reverts to a solution form. Chemically crosslinked hydrogels are linked via covalent bonds—radical initiators activate crosslinking agents that link monomers to a certain critical density that converts the precursor solution form into a gel form. An example would be Photoinitiated polymerization using ultraviolet or visible light, which is a popular crosslinking technology because it offers injectability [26].

Photoinitiated crosslinking is a popular technique using ultraviolet (UV) radiation, whereby gelation is achieved at physiological temperature and pH under light exposure. Macromers such as PEG are firstly conjugated with acrylate groups and subsequently mixed with a small amount of photoinitiators and cells prior to exposure to light for gelling. Depending on the mechanical strength required which is dependent on crosslinking density, the density of conjugated acrylate groups or the duration of light exposure can be varied. Alginate was conjugated with methacrylate through an esterification reaction to become photoinitiated crosslinkable [27]. To provide the cell adhesion moieties, the alginate–methacrylate precursor was mixed with temperature-responsive collagen solution and gelled by firstly increasing the temperature to 37 °C for collagen gelling and then exposing to UV light for alginate crosslinking, thereby fabricating an interpenetrating network (IPN) of two different hydrogels. This IPN hydrogel was reported to have a denser network and hence had superior mechanical properties than photoinitiated crosslinked alginate gel (control). Furthermore, it was able to support murine preosteoblasts MC3T3-E1 (as an ADC type) for bone defect repair in terms of extensive cell spreading morphology, high proliferative rates, and maintenance of osteogenic gene expressions as compared to the control.

Enzymatically crosslinked gels have recently been gaining popularity due to its injectability and gelation under physiological conditions. A gel can be formed in situ by mixing the phenolic hydroxyl-conjugated macromer solution with hydrogen peroxide (H₂O₂) and horseradish peroxidase (HRP) enzyme in the target defect site. This peroxidase-catalyzed system has been applied in various polysaccharides including chitosan, hyaluronic acid, alginate, and dextran [28–32]. Notably, gelatin type A was modified to possess tyramine (phenolic hydroxyl

groups), which was subsequently used for the delivery of osteoblasts [33]. Murine preosteoblasts MC3T3 cells were mixed in the tyramine-conjugated gelatin solution and gelled upon the addition of HRP. The osteoblasts were observed to have a spreading morphology even though osteogenic gene and protein analyses were not significant. Inclusion of bioactive molecules that can promote the osteogenic phenotype, e.g., bone morphogenetic proteins (BMPs) and fibroblast growth factors (FGFs), may be beneficial [34, 35]. Recently, Mathieu et al. injected a suspension of mesenchymal stem cells (MSCs) and a pH-responsive hydrogel into infarcted myocardia of rats and observed an increased healing rate and functionality with little fibrosis [36]. The silane-grafted hydroxypropyl methylcellulose (Si-HPMC) gels upon a decrease in pH levels to the physiological pH 7–7.4, due to the condensation of silane groups.

Self-assembling peptides spontaneously assemble themselves into a stable macroscopic nanofibrous network via non-covalent interactions such as hydrogen bonding, hydrophobic and Van der Waals forces [37]. Being amphiphilic, i.e., containing both hydrophilic (polar) and hydrophobic (non-polar) amino acid residues, the peptides undergo self-assembly to undertake the most stable structure as a nanofiber in a polar environment (salt solution or cell culture media)—non-polar residues are orientated into the fiber center while exposing the polar residues to the environment. This phenomenon is ubiquitous in nature, e.g., phospholipids in forming micelles and plasma membranes. As the self-assembled scaffolds are simple and form under physiological conditions, have a fiber diameter of approximately 10 nm and pore diameter of 5–200 nm and mimic ECM structure, are highly hydrated, and can be functionalized with the addition of cell adhesion moieties, they have been extensively utilized as a tissue engineering scaffold [37, 38].

For example, to impart the cell adhesion capability to the self-assembled nanofibrous hydrogel, cell adhesion moieties such as arginine–glycine–aspartic acid (RGD) sequences can be conjugated to the peptides prior to assembly [39–41]. Zhou et al. [39] designed a self-assembled hydrogel based on two simple peptides, one of which possesses the RGD sequence. The sequence not only provides the hydrogel with cell-adhesive properties on the surface of the nanofibers, but it also influences the mechanical properties of the hydrogel. Human dermal fibroblasts encapsulated within the hydrogel were able to adhere through RGD-specific binding and exhibited a spreading morphology as ADCs do. Webber et al. [41] also demonstrated the potential of self-assembled hydrogels made up of RGD peptides in delivering bone marrow mononuclear cells (BMNCs) into mice. BMNCs were able to adhere and proliferate in the tested hydrogel *in vitro*, enhancing the cells' numbers by more than 5-folds in 5 days, whereas non-RGD-containing nanofibrous hydrogel control had no significant increase in cell number during the same time period. Furthermore, gene expression studies validated that BMNC phenotype was maintained *in vitro*; *in vivo* experiments also confirmed that BMNCs were successfully delivered subcutaneously with maintenance of high viability, albeit with a mild tissue reaction to the cell delivery material.

Gong et al. [42] made use of a naturally occurring phenomenon involving non-ADCs and the non-cell-adhesive property of hydrogel to develop a dense tissue construct for cartilage tissue engineering. A rapid and dense outgrowth of cells and ECM secretion at gel–medium boundaries, termed “edge flourish,” was exploited in a microcavitory gel (MCG)—chondrocytes and gelatin microspheres were co-encapsulated in temperature-responsive agarose hydrogel; upon raising the temperature to 37 °C, gelatin melts to leave behind microcavities within the hydrogel bulk. The strategy was named phase transfer cell culture (PTCC) to connote the dynamic culture of cells on the boundaries of two phases. Chondrocytes were then observed to infiltrate and fill up the cavities. By inducing cavities to increase the amount of gel–medium boundaries throughout the hydrogel bulk, not only was diffusion of nutrients and waste improved, a higher proliferation rate and hyaline cartilage-specific ECM secretion was observed [42]. In another study involving a temperature-responsive hybrid hydrogel of naturally derived heparin and synthetic PEG diacrylate (PEGDA) was shown to support primary hepatocyte spheroids more greatly than pure PEG-based hydrogels, as concluded from the high cell viability and albumin and urea secretion [24]. The heparin–PEG hydrogel gels at 37 °C within a short duration of 10 min under physiological conditions and was also able to retain hepatocyte growth factor (HGF) and maintain its bioactivity; this hydrogel is therefore envisaged to be a potential stem cell delivery vehicle with differentiation cues incorporated within.

A relatively new synthetic saccharide–peptide hydrogel has been designed and demonstrated to be highly supportive of non-ADC chondrocytes [43] and pancreatic islets [44]. Being composed of naturally derived monomers saccharides and peptides, the intrinsic advantages of biodegradability, non-toxicity, and low cost are combined with the controllable and predictable properties of synthetic biomaterials. The copolymer backbone is covalently crosslinked via Michael-type addition mechanism and subsequently functionalized with tyrosine amino acids which, in chondrocyte studies, supported extensive ECM secretion and higher mechanical strength [43]. In another study involving pancreatic islet delivery into rat models using the same gel, the diabetic condition was significantly reversed alongside the high insulin secretion by the functional islets and lack of detectable immune response, as compared to transplanted unencapsulated islets [44].

4.2.2 Fibrous Meshes

Fibrous meshes are a body of individual nanoscale fibers that have been spun into a 3D network. Its structural similarity to native ECM network, high surface area to volume ratio, porosity, tunable mechanical and degradation properties, and controllable fiber diameter [45] makes fibrous meshes as suitable cell delivery vehicle, especially for ADCs (Fig. 4.2b). Electrospinning is a common technique for fabricating fibrous meshes. The droplet of polymer solution forms a thin stream upon passing through an electric field and is collected as a mesh of fibers upon the

evaporation of solvent in the polymer. By modifying the collector and electric field, fiber orientation [46] as well as scaffold shape and size [47–49] can be varied. For example, tubular scaffolds were fabricated using a rotating rod collector [50]; tubular structures with longitudinally aligned nanofibers were fabricated using two extra parallel electrodes [47]. However, the difficulty in cell penetration into a dense scaffold is a shortfall [51]. Naturally derived materials including elastin [52], sulfated silk fibroin [53], collagen [54], and synthetic materials PCL [46, 55] and PLA [56] have been used in fabricating electrospun scaffolds.

While many previous studies utilized simple randomly aligned fibrous meshes, second-generation fibrous meshes with aligned fibers and multilayered structures have been engineered to better mimic the complex native ECM structure. Since fiber orientation can modulate cell phenotype and guide cell growth, many studies have deliberately aligned fibers for the culture of muscle cells and neurons. For example, smooth muscle cells (SMCs) cultured on longitudinal poly(L-lactide-co- ϵ -caprolactone) P(LLA-CL) 75:25 fibers had a contractile phenotype similar to those in physiological conditions [57]. Another research group demonstrated the effect of aligned PCL/collagen fibrous meshes on skeletal muscle cells [58]. The skeletal muscle cells were stretched along the fibers, exhibited high viability and functionality with formation of myotubes observed.

In a bid to restore the neural retina through cell-based therapy, biodegradable PLA was utilized in fabricating a scaffold of radially aligned nanofibers mimicking the ECM architecture in the retina, for the culture of retinal ganglion cells (neurons) [56]. The scaffold was then immersed in laminin to coat the fibers as neurons reside in a laminin-rich ECM [59]. Axons of the cells, as a type of ADCs, were observed to be of higher viability and were mostly aligned along the fibers, as opposed to control tissue culture plates and randomly aligned electrospun scaffolds. Cells cultured in the aligned scaffolds maintained electrophysiological functionality and exhibited similar radial patterns as axon bundles of the native retina. Furthermore, at higher densities, the cells were observed to form axon bundles *in vivo*. This cell delivery vehicle for the treatment of degenerated retina, e.g., due to glaucoma, is an important first step in delivering aligned functional nerve cells and can be developed further for delivering other nerve cells, especially for the repair of the central nervous system, since nerve cells have poor self-repair capability.

Homogeneous fibrous meshes have been widely used as ECM substitutes, but recently the paradigm shifted toward creating structures more similar to native tissue. For example, the zonal organization of articular cartilage was mimicked using PCL fibers of varying orientations to match the mechanical properties of each zone: The topmost superficial layer as a lubricating surface was made of aligned 1- μ m-thick fibers; the middle layer was composed of random 1- μ m fibers; and the deep layer was composed of random and thicker fibers of 5 μ m diameter, mimicking the architecture of collagen fibrils in native articular cartilage tissue [55]. Chondrocyte culture in the triple-layered electrospun scaffold was done *in vitro* for 5 weeks; analyses of mechanical properties and quality of engineered

cartilage revealed close similarity with native cartilage tissue. In another study, McClure et al. [60] designed a triple-layered electrospun scaffold with layer-specific compositions of PCL, elastin, and collagen fibers to mimic the structural architecture of arteries, namely the intima, media, and adventitia layers; the engineered construct was mechanically tested acellularly and demonstrated similar modulus and compliance values to those of native porcine femoral arteries. The potential of this artery-mimicking electrospun scaffold, however, would be better reflected with the culture of vascular cells—vascular endothelial cells and SMCs.

4.2.3 Sponges

Also known as porous scaffolds, sponges are made using gas foaming, particulate leaching, and freeze-drying techniques. The success of porous scaffolds as a cell delivery vehicle depends on its porosity, pore size, and pore interconnectivity—the pores provide surface area for cells to adhere on, while interconnectivity dictates the cell penetration as well as diffusion of nutrients and waste [25]. Pore size is critical: Small pores will impede cell penetration and proper diffusion, while larger pores may not be sensed by cells to be a 3D environment. Hence, engineering a cell delivery capable sponge requires consideration of pore design parameters.

Gas foaming involves the saturation of high-pressure gas (usually carbon dioxide) into the polymer particles; upon rapid decrease in pressure, gas bubbles nucleate and expand and the polymer fuses to form a continuous porous scaffold [61]. This method is quick and simple and allows the control of pore size by varying pressure without the use of high temperatures or harsh organic solvents to create the pores. Recently, PDLLA/PEG copolymer sponges were fabricated by gas foaming, achieving 84 % average porosity [62]. PDLLA possesses superior mechanical properties and biodegradability but is hydrophobic and therefore unsuitable for cell encapsulation. Hence, by copolymerizing with hydrophilic PEG, the advantageous properties of each material are combined. Although no cell-seeding studies were done on this sponge, this is a classic example of exploiting the advantages of two different materials by copolymerization, and with further optimization, the sponge is expected to work well as a cell delivery vehicle. Zhou et al. [63] combined foaming and blending of two immiscible polymers to create a more controllable, open, and porous scaffold with higher interconnectivity between pores. Firstly, two polymers PLA and polystyrene were blended in equal weight ratios together and molded by compression prior to carbon dioxide foaming, achieving a porous scaffold of PLA and polystyrene with tunable pore sizes. Then, polystyrene was removed via immersion of scaffold in cyclohexane, creating a PLA scaffold with much higher interconnectivity. After washing, osteoblasts were seeded onto the scaffold and compared against unfoamed control; although both scaffolds showed proper cell adhesion and spreading morphology of osteoblasts, the foamed sample had significantly higher number of cells, thereby reiterating the importance of porosity.

Particulate leaching using salt particles is an alternative method to create porous scaffolds (Fig. 4.2c) by mixing salt crystals (typically sodium chloride NaCl) into a polymer solution and then inducing the crosslinking to form a scaffold with salt particles entrapped within. Upon immersing in water, the salt dissolves and is removed from the scaffold, leaving behind empty spaces inside the scaffold. Sponges of silk fibroin/hyaluronic acid blends for cartilage tissue engineering were fabricated using this method [64]. Silk fibroin/PDLLA sponges were fabricated by NaCl particulate leaching; the silk fibroin was incorporated to increase the vascularization potential of the PDLLA sponge for bone tissue engineering, since silk fibroin is known to support the adhesion and growth of endothelial cells [65]. In this study, human umbilical vein endothelial cells (HUVECs) were shown to be properly adhered onto the silk fibroin/PDLLA sponges with high viability and proliferation while maintaining the cell phenotype *in vitro*; *in vivo* studies showed quicker vascularization and integration with the surrounding tissue.

PLA/PCL (70:30) sponges were also fabricated using NaCl particulate leaching and studied for the delivery of myoblasts for skeletal muscle repair [66]. Myoblasts were not only able to adhere and grow on the sponges, but they also differentiated and fused with each other into myotube structures with expression of skeletal muscle-specific genes and proteins, both *in vitro* and *in vivo*. Coupled with the biodegradability and biocompatibility of the materials, the PLA/PCL sponge exhibits great potential for skeletal muscle repair.

4.2.4 Decellularized Scaffolds

Biological tissues and organs comprised of ECM network and residing native cells can be extracted and then decellularized (removal of cells), leaving behind an intact ECM scaffold on which cells can be reseeded prior to implantation (Fig. 4.2d) [67]. Decellularized scaffolds provide a most suitable natural micro-environment as tissue- and organ-specific ECM cues produced and modeled by the previous residing cells can guide the newly seeded cells. Complete decellularization is important to remove the immunogenicity caused by previous cells' antigens, since the host tissue is of xenogeneic and allogeneic origin. This can be achieved by chemical (SDS, Triton X-100) [68], physical (freeze-thaw cycles), or enzymatic (trypsin, endonucleases) means [69]. Indeed, the excellent biocompatibility and lack of immunogenicity of decellularized scaffolds have been recognized and approved by FDA for bone [68], skin [70], and heart valve replacements [71] as acellular scaffolds, whereby host cells are allowed to penetrate and regrow tissue. Other decellularized scaffolds currently being studied and characterized include skin [72, 73], larynx [74], lung [75, 76], blood vessels [77, 78]. To accelerate the healing process, cells can be seeded within the decellularized scaffold and cultured *in vitro*, thereby generating a replacement tissue or organ ready for implantation [79, 80].

Wang et al. [80] characterized decellularized scaffolds from porcine musculo-fascial tissues and observed the presence of vascular endothelial growth factor (VEGF) in the decellularized ECM, which served to be pro-angiogenic and showed high healing capability when seeded with adipose stem cells (ASCs) into a rat muscle defect model. Lang et al. [81] optimized liver tissue decellularization and utilized decellularized liver tissue for studying the behavior of seeded human primary hepatocytes. The viability, phenotype, and functionality of the liver cells were highly conserved in a 3D environment for at least 21 days, which was significantly better than current collagen sandwich culture methods. In another study involving the complex lung tissue, Petersen et al. [76] decellularized rat lungs without disrupting the ECM architecture of airways, alveoli, and blood vessels, after which lung epithelial and endothelial cells were seeded onto the decellularized lung scaffold and subsequently tested both *in vitro* and *in vivo*. *In vitro* characterization showed maintenance of ECM components and lung structure, as well as seeded cells' phenotype. The engineered lungs were also able to function *in vivo*, as observed by the inflation of the organ, gas exchange, and hemoglobin saturation. Therefore, through the favorable results obtained in various studies, decellularized scaffolds of biological tissues and even whole organs were shown to be choice cell delivery methods in the form of whole-organ transplantation, if the abovementioned three engineered structures are unable to recreate complex architecture of tissues and organs.

However, decellularized tissues need not be used wholesale; instead, researchers have solubilized the ECM and converted them into porous scaffolds [79] and hydrogels [82–84]. In another study, Yu et al. [79] fabricated porous scaffolds from human decellularized adipose tissue: The decellularized tissue was solubilized by α -amylase, after which the solubilized proteins were made into porous scaffolds via freezing and lyophilization. The porous scaffolds were shown to support ASC adhesion and adipogenic differentiation. Wolf et al. [82] developed and characterized both *in vitro* and *in vivo* ECM-based hydrogels derived from decellularized dermal and urinary bladder tissues. The study validated that ECM and hence properties are tissue specific, therefore causing varied cell behaviors as well.

4.3 Improvising the Cell Delivery Systems

The basic cell delivery structures discussed above may still be inadequate on their own. As mentioned, research efforts based on combining different materials by copolymerization and blending to create a material with combined advantageous properties have been prevalent. Fabrication techniques are diverse and continuously improving to become milder, more elegant, and non-toxic. In this section, several key advancements that will potentially drive cell delivery toward the

clinical setting are noted. These include making the system injectable as an elegant and minimally invasive means of surgical implantation, functionalizing inert surfaces with bioactive ligands and molecules, controlling cell behavior using micro- and nanoscale topographical cues, as well as delivering intact masses of cells without delivering biomaterials. These promising developments not only make cell delivery vehicles simple systems, but they also can influence the delivered cells' behavior and phenotype.

4.3.1 Microcarriers for Injectability

Microcarriers are injectable cell or drug-eluting microscopic-sized vehicles that are downscaled versions of the abovementioned basic structures. Cell microcarriers can be further subcategorized into microsized scaffolds that ADCs can attach onto and microsized materials encapsulating cells within. The former are usually developed in two phases: The microcarriers are firstly fabricated, and the cells are subsequently seeded onto them. On the other hand, cell-encapsulating microcarriers are usually hydrogel based, using a one-step process of directly gelling microsized droplets of cell–material suspension. Several commercially available microcarriers such as Cultispher® (Sigma) have been used [85].

The emulsion technique, either a single or double emulsion, is a simple and therefore popular technique for microsphere fabrication. Huang et al. [86] fabricated gelatin type A porous microspheres using a single water-in-oil emulsion followed by freeze-drying; next, basic fibroblast growth factor (bFGF) was loaded into the rehydrated microspheres and finally fibroblasts were seeded. The typical spreading morphology of fibroblasts was exhibited on the microspheres, and implantation of the fibroblast/bFGF-loaded microspheres in critically sized dermal defects (which would require skin grafting) showed favorable healing—the epidermal layer was fully restored and was integrated with native tissue [86]. In another study, the same group utilized the same microsphere fabrication technique, but incorporated epidermal growth factor (EGF) instead of bFGF and mesenchymal stem cells (MSCs) instead of fibroblasts [87]. The MSC-laden microspheres were suspended in a type I collagen/Matrigel™ gel, which was subsequently studied for skin tissue regeneration. In vivo experiments showed quick and good healing with sweat gland-like structures restored.

Similarly, Leong et al. [88] also used gelatin type A to fabricate hydrogel microspheres using a water-in-oil emulsion; however, the focus was to directly encapsulate and deliver non-ADCs instead of ADCs. Using chondrocytes as the model non-ADC type, a chondrocyte–gelatin type A suspension was stirred in soya oil and cooled down in an iced water bath. Chondrocyte-encapsulated gelatin microspheres of mainly 75–100 μm diameters were retrieved after two washes in phosphate-buffered saline (PBS) and suspended in an alginate hydrogel. Upon incubation at 37 °C, these gelatin microspheres melted, suspending chondrocytes within the microcavities for growth; the microspheres were hence termed

temperature-cured dissolvable gelatin microsphere-based cell carrier (tDGMC) [88]. Dense islets of rounded and viable cells with little dead cells were observed by 21 days in culture, and merging of cell islets throughout was noticed by day 35. This technique can be used to culture other non-ADCs as well; the dense cell islets can be obtained by dissolving the alginate hydrogel to yield microsized injectable cell islets.

The double emulsion technique is more complicated as the innermost phase has to be thoroughly removed, but it allows the fabrication of hollow microspheres, which translates to less biomaterial, better diffusion, and more space for cell attachment and growth. Su et al. [89] proposed a novel microcarrier for ADCs that was derived from such a technique. Hollow gelatin spheres were firstly fabricated from the double oil-in-water-in-oil emulsion and then modified with a surface crosslinking process and removal of uncrosslinked material, resulting in a hollow open structure named “shell-structure cell microcarrier” (SSCM). Human fetal osteoblasts were used as the model ADC type—the cells were able to adhere onto and proliferate on both the external and internal walls of the microcarrier at a higher efficacy than control gelatin microspheres and express the osteogenic phenotype.

Another group aimed to develop neuronal cell-laden porous (sponge) microspheres for neural tissue engineering. Poly(3-hydroxybutyrate-co-3-hydroxyvalerate) (PHBV) microspheres were fabricated using double water-in-oil-in-water emulsion (W1/O/W2) and freeze-dried to remove the aqueous solvent [90]. Murine neuronal cell line PC12 cells, neural progenitor cells (NPCs), and primary cortical neurons were viable and supported on the microspheres, exhibiting extensive spreading morphology and neuronal proteins. NPC differentiation was promoted, while axon and dendrites of cortical neurons were observed to be discriminated as a sign of neuronal maturation and functionality. PHBV was proposed as a suitable biomaterial for neuronal cell-laden microspheres because of their biodegradability and slow degradation, which matches the relatively slow growth of neuronal cells. Poly(lactic-co-glycolic acid) (PLGA) porous microspheres were also fabricated using a similar emulsion method, except that the pores were created by gas foaming [91]. The W2 phase consisted of ammonium bicarbonate that formed ammonia and carbon dioxide gas bubbles upon evaporation, creating a highly porous structure in the microspheres.

To exploit the ECM-like architecture of fiber meshes, substantial progress on fibrous microcarriers has also been made. One of the most recent developments is the simple fabrication of hybrid nanofibrous network-containing hydrogel microparticles [92]. A nanofibrous PCL network is firstly fabricated by electrospinning and soaked in the photoinitiated crosslinkable PEGDA solution containing fibroblasts; subsequently, through photomasking for PEGDA polymerization and removal of excess solution as well as dissolution of non-encapsulated PCL nanofibers using chloroform, controllable shapes of polymerized PEGDA gels containing nanofibers and cells can be produced. The hybrid microcarrier was characterized for both protein and cell delivery, which were deemed favorable. Specifically, cell adhesion within the hydrogel was achieved without the need for chemical modification to include cell adhesion moieties on PEGDA

gels—fibroblasts exhibited a spreading and elongated morphology along the nanofibers of the hybrid microcarrier, whereas a rounded morphology was noted in the simple PEGDA gel.

4.3.2 *Post-fabrication Modification for Cell Adhesion*

For ADCs, proper cell adhesion is critical in determining the success of their delivery vehicles; otherwise, they may undergo *anoikis* and decrease the efficacy of cell delivery. Therefore, many studies have explored the post-fabrication incorporation of cell-adhesive moieties in cell delivery vehicles.

One of the major shortcomings of synthetic biomaterials is their biologically inertness, i.e., they do not support cell adhesion, which affects their survival and phenotype. They can be functionalized through coatings or grafting of ECM proteins and ligands known to promote cell adhesion, e.g., fibronectin and laminin [59]. One of the most popularly incorporated bioactive ligands is the RGD sequence derived from fibronectin. It is known that RGD is the minimal recognition and binding sequence of cells' integrins to fibronectin and can support adhesion and spreading of cells [93, 94]. Differentiated SMCs were demonstrated to express the contractile phenotype in PEGDA hydrogels coated with fibronectin or laminin, or functionalized with linear RGD sequences [95]. Cyclic RGD have been shown to have higher affinity and selectivity toward cell binding, as well as greater stability against enzymatic degradation [96]. Patel et al. [97] functionalized the synthetic polynorbornene hydrogel by grafting linear and cyclic RGD motifs and comparing between the two forms using HUVECs. The group found that cyclic RGD was significantly more efficient in promoting cell adhesion—not only was the minimal concentration of the cyclic form (0.05 %) required for cell adhesion 50 times lower than that required for linear RGD, the cyclic RGD-conjugated gel supported cell spreading within 15 min, while the other required at least 90 min to achieve a similar state.

Larger ECM molecules such as gelatin and elastin can also be coated onto the biomaterials following the formation of the vehicle structure. Human fibroblasts and osteoblasts (both of which are ADCs) were viable and functional throughout the culture period on novel gelatin-coated gellan gum microspheres [98]. A water-in-oil emulsion involving preheated FDA-approved gellan in peanut oil yielded microspheres upon cooling, onto which gelatin was then grafted. PCL sponges were permeated with elastin using carbon dioxide gas foaming and crosslinked with glutaraldehyde to create a mechanically suitable and cell-supportive scaffold for cartilage tissue engineering [99]. In vitro studies concluded that the integration of elastin not only increased the water content in the sponges, it was also able to support chondrocytes better than pure PCL sponges. As mentioned previously, laminin was coated onto electrospun fibers to present cell-adhesive moieties to implanted neural cells, mimicking the native laminin-rich environment [56]. The basic bioactive sequence isoleucine–lysine–valine–alanine–valine (IKVAV) that

interacts with neural cells and increases their adhesion and proliferation can also be isolated from laminin and conjugated onto biomaterials, such as self-assembled peptides [100, 101].

4.3.3 Controlling Cell Functionality Through Micropatterns

The materials' surface topography is able to directly interact with cells and influence cell adhesion and growth in a specific manner. As this is especially crucial for cells that require alignment to function, e.g., neurons, endothelial cells and SMCs, the effect of submicron levels of surface modification on cell behavior has gained attention and been incorporated in various biomaterials [102]. The patterns are popularly achieved through photomasking, casting, and lithography techniques, which allow the width and depth to be tuned to control cell behavior and growth.

Endothelial cells in the native vascular environment are stretched and aligned along the longitudinal axis of blood vessels, i.e., parallel to blood flow. When organized in this orientation on manufactured biomimetic scaffolds, endothelial cells were able to retain their morphology and cell-specific gene expressions and possess athero-resistant qualities with less adhesion of platelets and monocytes [103]. Nikkhah et al. [104] recently demonstrated the importance of topography in directing endothelial cell adhesion and attachment with the maintenance of its functionality in vascularization. Longitudinal tubes of photoinitiated crosslinkable gelatin methacrylate hydrogel were fabricated with micropatterns by exposing selective areas to light using a mask (photomasking) [104]. HUVECs were of an elongated and spreading morphology and reorganized themselves to align along the length of the tubes by day 5, forming a 3D stable cord-like structure in 15 days. On the other hand, HUVECs on the unpatterned gelatin methacrylate gel block were randomly aligned, therefore affirming the effect of topography on cell behavior and functionality. Another study by Liu et al. [105] micropatterned the collector via lithography, hence fabricating electrospun fibrous meshes with specific grooves and ridges. Fibroblasts seeded on the micropatterned fibrous meshes were observed in higher numbers in the ridges and secreted ECM with similar patterns. Uttayarat et al. [106] used spin casting to fabricate micro-sized grooves in the lumen of polyurethane (PU) fibrous tubes to guide endothelial cell orientation in a vascular tube. The cells were observed to reach a confluent monolayer with alignment along the micropatterned topography, while retaining cell phenotype.

To guide neuronal cell growth and their neurite outgrowth as neural replacements (for example, at the interface of neurons and prosthetic equipment for successful and conserved transmission of stimulus), micropatterning serves as a favorable and simple micro-sized guidance. As demonstrated by Tuft et al. [107], photomask-fabricated indents (slopes instead of defined edges of grooves) on a methacrylated substrate on which neurite and Schwann cells were subsequently seeded and shown to be aligned. Not only can surface topography guide cell

alignment, proteins (i.e., biochemical cues) can also be specifically patterned to influence cell adhesion and their orientation. For example, neuronal cells were strictly confined on 5–10- μm -thick lines of cell-adhesive collagen patterned through microcontact printing on tissue culture polystyrene (TCPS) surfaces, which were backfilled with cell-repelling poly-L-lysine-g-polyethylene glycol [108]. The cells and their nuclei were also aligned parallel to the lines. On 5- μm -thick collagen patterns, neurite extension was significantly enhanced compared to non-patterned surfaces; neurite outgrowth was further stimulated by adding soluble retinoic acid in the cell culture medium.

4.3.4 Biomaterial-Free Cell Delivery

Ultimately, biomaterials have to be removed prior to implantation in order to completely eliminate the possible risks of biomaterial-related problems—mismatch of degradation rate to that of tissue development, immune responses, and toxic degradation products. Yet, direct injection of therapeutic cells may not be an efficient and effective cell delivery method since cells are not retained within the target site (leakage) and survive poorly without proper homing [109, 110]. This can be achieved by transplanting biomaterial-free microtissues, which have been cultured *in vitro* using biomaterials as a temporary scaffolding system. In other words, cells can be firstly cultured on biomaterials in the laboratory for a predetermined duration until they form microsized pieces of tissue comprising cells held together by their secreted ECM; subsequently, they can be removed from the biomaterial-based scaffolding system for implantation in the target site.

A confluent monolayer of cells, known as cell sheets, can be easily engineered in tissue culture plates by making use of responsive biomaterial surfaces to force the detachment of cells from the biomaterial surface without disrupting the cell–cell interactions and ECM holding the cells together. This strategy was pioneered by Kushida et al. [111]: Temperature-responsive poly(N-isopropylacrylamide) (PIPAAm) was coated on TCPS surfaces, and cells were grown on this coating. At the physiological temperature of cell culture, i.e., 37 °C, the coating is mildly hydrophobic, which is suitable for cell adhesion and culture; upon lowering the temperature to below 32 °C (its lower critical solution temperature, LCST), the coating becomes hydrophilic and the cells are upheaved from the surface. This produces a biomaterial-free cell sheet held together by the cells' secreted ECM, which is removable from the attached surface without any enzymatic treatment that would have also broken down the ECM [112, 113]. The PIPAAm coating is currently commercially available as UpCell[®] and has been utilized in fabricating cell sheets of various cell types, including mesenchymal stem cells [114] and fibroblasts [115]. A monolayer of mesenchymal stem cells implanted into infarcted myocardia of rats was able to reverse the thinning of the scarred myocardial wall while promoting vascularization and differentiating into vascular cells, with the overall effect of improving function of the infarcted heart [114]. Other cell sheet

fabrication strategies include the use of magnetic force and polyelectrolytes [116]. Ito et al. [117] developed a magnetic nanoparticle—RGD-conjugated magnetite cationic liposomes (MCL)—that coated surfaces by applying magnetic force beneath the surface; fibroblasts as model cells were able to adhere to the RGD-conjugated surface coating, and upon removal of the magnetic force, the cell monolayer was detached. Kito et al. [118] successfully utilized a similar MCL strategy to retrieve an iPSC monolayer for implantation to induce angiogenesis in ischemic tissues, except that MCLs were labeled in the cells instead of on a surface coating. Likewise, cells can be detached from RGD-conjugated polyelectrolyte coatings via altering the polarization [119, 120].

The difficulty in handling an extremely fragile monolayer of cells is a severe limitation of cell sheets in the clinical setting. Furthermore, being monolayer, it is difficult to scale up to form and replace a 3D macrosized tissue defect since stacking multiple layers of monolayers is a laborious process. Biomaterial-free 3D systems are favorable for cell delivery as they can deliver a large amount of cells without unwanted leakage to non-target sites and circumventing any biomaterial-related problems. As an example, the engineered PTCC system for hyaline cartilage tissue engineering (mentioned in Sect. 4.2.1, Gong et al.) was further improvised by Su et al. [121] by replacing temperature-responsive agarose with ionic-responsive alginate as the gel bulk. Alginate, which crosslinks in the presence of calcium divalent ions, can be completely and quickly removed by immersing the scaffold in a sodium citrate-containing solution, whereby citrate ions act as calcium-chelating agents. After 35 days of culture, the extensive and dense ECM network secreted by chondrocytes was able to support the construct such that alginate was removed without a collapse in structure (compared to a conventional cell-laden hydrogel without microcavities), thereby leaving behind a hyaline cartilaginous construct free of biomaterials. Implantation into rabbit osteochondral defects in the knee joint showed good integration with host tissue and expression of hyaline cartilage phenotype with no visible fibrosis.

4.4 Conclusion

Cells interact with the surroundings; the biochemical and mechanical cues they receive from the surroundings are translated and lead to modification of cell behavior. Without proper cell adhesion in certain cells (ADCs), not only will the cell phenotype be affected, a specific apoptotic process named *anoikis* may also occur. Therefore, the importance of biomaterial properties and design cannot be further emphasized. In this chapter, the four basic cell delivery structures hydrogels, fibrous meshes, sponges, and decellularized ECM and their recent developments in cell delivery have been discussed. While hydrogels are more naturally suited for soft tissues and for delivery of non-ADCs, they have been modified to possess cell adhesion moieties that allow ADCs to be successfully delivered using hydrogels as well. Fibrous meshes, with their similarity to ECM architecture, have

been widely used for the delivery of many cell types. Developing aligned fibers for guiding cell growth and behavior has been the recent focus of electrospun meshes. Sponges are highly porous scaffolds in which ADCs adhere to walls of the pores; therefore, porosity and the interconnectivity of pores are important design factors. Finally, decellularized scaffolds, derived from biological tissues, offer site-specific ECM proteins to guide the newly seeded cells. They have been solubilized and converted into sponges and hydrogels of controllable shapes and sizes.

Cell delivery vehicles have been greatly improvised to better mimic the microenvironment of cells thus far. In order to create an ideal cell delivery vehicle, both biomaterials and structure have been researched on. Biomaterials are blended and copolymerized in order to offset the shortcomings and combine the advantages of the individual biomaterials. Also, modification of surfaces with cell adhesion moieties and ECM molecules and surface topography has become an established technique to maintain functionality of delivered cells. While some hydrogels are injectable, other structures (sponges and fibrous meshes) have also become injectable by downscaling them into microsized particles. Furthermore, biomaterials have been exploited as temporary scaffolding systems for *in vitro* culture to create micro- or macrosized biomaterial-free tissues for implantation, hence eliminating risks of biomaterial-related complications *in vivo*. This variety of improvisations to conventional cell delivery vehicles has brought us one step closer from the bench to the bedside.

Acknowledgments This work was made possible by financial support from AcRF Tier 1 Grant RG 36/12.

References

1. Bryers JD, Giachelli CM, Ratner BD (2012) Engineering biomaterials to integrate and heal: the biocompatibility paradigm shifts. *Biotechnol Bioeng* 109(8):1898–1911. doi:[10.1002/bit.24559](https://doi.org/10.1002/bit.24559)
2. Malda J, Frondoza CG (2006) Microcarriers in the engineering of cartilage and bone. *Trends Biotechnol* 24(7):299–304. doi:<http://dx.doi.org/10.1016/j.tibtech.2006.04.009>
3. Hernandez RM, Orive G, Murua A, Pedraz JL (2010) Microcapsules and microcarriers for *in situ* cell delivery. *Adv Drug Deliv Rev* 62(7–8):711–730
4. Nafea EH, Marson A, Poole-Warren LA, Martens PJ (2011) Immunoisolating semi-permeable membranes for cell encapsulation: focus on hydrogels. *J Control Release* 154(2):110–122
5. Shastri VP (2009) *In vivo* engineering of tissues: biological considerations, challenges, strategies, and future directions. *Adv Mater* 21(32–33):3246–3254. doi:[10.1002/adma.200900608](https://doi.org/10.1002/adma.200900608)
6. Frisch SM, Francis H (1994) Disruption of epithelial cell-matrix interactions induces apoptosis. *J Cell Biol* 124(4):619–626
7. Chen Z-L, Strickland S (1997) Neuronal death in the hippocampus is promoted by plasmin-catalyzed degradation of Laminin. *Cell* 91(7):917–925. doi:[http://dx.doi.org/10.1016/S0092-8674\(00\)80483-3](http://dx.doi.org/10.1016/S0092-8674(00)80483-3)

8. Damsky CH, Ilic D (2002) Integrin signaling: it's where the action is. *Curr Opin Cell Biol* 14(5):594–602. doi:[http://dx.doi.org/10.1016/S0955-0674\(02\)00368-X](http://dx.doi.org/10.1016/S0955-0674(02)00368-X)
9. Taddei ML, Giannoni E, Fiaschi T, Chiarugi P (2012) Anoikis: an emerging hallmark in health and diseases. *J Pathol* 226(2):380–393
10. Chiarugi P, Giannoni E (2008) Anoikis: a necessary death program for anchorage-dependent cells. *Biochem Pharmacol* 76(11):1352–1364
11. Vander Heiden MG, Chandel NS, Williamson EK, Schumacker PT, Thompson CB (1997) Bcl-xL regulates the membrane potential and volume homeostasis of mitochondria. *Cell* 91(5):627–637
12. Cheng EH, Wei MC, Weiler S, Flavell RA, Mak TW, Lindsten T, Korsmeyer SJ (2001) BCL-2, BCL-X(L) sequester BH3 domain-only molecules preventing BAX- and BAK-mediated mitochondrial apoptosis. *Mol Cell* 8(3):705–711
13. Taylor RC, Cullen SP, Martin SJ (2008) Apoptosis: controlled demolition at the cellular level. *Nat Rev Mol Cell Biol* 9(3):231–241
14. Kuwana T, Bouchier-Hayes L, Chipuk JE, Bonzon C, Sullivan BA, Green DR, Newmeyer DD (2005) BH3 domains of BH3-only proteins differentially regulate Bax-mediated mitochondrial membrane permeabilization both directly and indirectly. *Mol Cell* 17(4):525–535
15. Letai A, Bassik MC, Walensky LD, Sorcinelli MD, Weiler S, Korsmeyer SJ (2002) Distinct BH3 domains either sensitize or activate mitochondrial apoptosis, serving as prototype cancer therapeutics. *Cancer Cell* 2(3):183–192
16. Martinou JC, Green DR (2001) Breaking the mitochondrial barrier. *Nat Rev Mol Cell Biol* 2(1):63–67
17. Thornberry NA (1998) Caspases: key mediators of apoptosis. *Chem Biol* 5(5):R97–103
18. Zou H, Henzel WJ, Liu X, Lutschg A, Wang X (1997) Apaf-1, a human protein homologous to *C. elegans* CED-4, participates in cytochrome c-dependent activation of caspase-3. *Cell* 90(3):405–413
19. Wajant H (2002) The Fas signaling pathway: more than a paradigm. *Science* 296(5573):1635–1636. doi:[10.1126/science.1071553](http://dx.doi.org/10.1126/science.1071553)
20. Aoudjit F, Vuori K (2001) Matrix attachment regulates Fas-induced apoptosis in endothelial cells: a role for c-flip and implications for anoikis. *J Cell Biol* 152(3):633–643
21. Chen CS, Mrksich M, Huang S, Whitesides GM, Ingber DE (1997) Geometric control of cell life and death. *Science* 276(5317):1425–1428
22. Muzio M, Stockwell BR, Stennicke HR, Salvesen GS, Dixit VM (1998) An induced proximity model for caspase-8 activation. *J Biol Chem* 273(5):2926–2930
23. Williams DF (2008) On the mechanisms of biocompatibility. *Biomaterials* 29(20):2941–2953. doi:<http://dx.doi.org/10.1016/j.biomaterials.2008.04.023>
24. Kim M, Lee JY, Jones CN, Revzin A, Tae G (2010) Heparin-based hydrogel as a matrix for encapsulation and cultivation of primary hepatocytes. *Biomaterials* 31(13):3596–3603. doi:<http://dx.doi.org/10.1016/j.biomaterials.2010.01.068>
25. Chung C, Burdick JA (2008) Engineering cartilage tissue. *Adv Drug Deliv Rev* 60(2):243–262
26. Bryant SJ, Anseth KS (2001) The effects of scaffold thickness on tissue engineered cartilage in photocrosslinked poly(ethylene oxide) hydrogels. *Biomaterials* 22(6):619–626
27. Sun J, Xiao W, Tang Y, Li K, Fan H (2012) Biomimetic interpenetrating polymer network hydrogels based on methacrylated alginate and collagen for 3D pre-osteoblast spreading and osteogenic differentiation. *Soft Matter* 8(8):2398–2404
28. Sakai S, Yamada Y, Zenke T, Kawakami K (2009) Novel chitosan derivative soluble at neutral pH and in situ gellable via peroxidase-catalyzed enzymatic reaction. *J Mater Chem* 19(2):230–235
29. Kurisawa M, Chung JE, Yang YY, Gao SJ, Uyama H (2005) Injectable biodegradable hydrogels composed of hyaluronic acid-tyramine conjugates for drug delivery and tissue engineering. *Chem Commun* 14(34):4312–4314

30. Sakai S, Hashimoto I, Ogushi Y, Kawakami K (2007) Peroxidase-catalyzed cell encapsulation in subsieve-size capsules of alginate with phenol moieties in water-immiscible fluid dissolving H₂O₂. *Biomacromolecules* 8(8):2622–2626
31. Jin R, Hiemstra C, Zhong Z, Feijen J (2007) Enzyme-mediated fast in situ formation of hydrogels from dextran-tyramine conjugates. *Biomaterials* 28(18):2791–2800
32. Sakai S, Kawakami K (2007) Synthesis and characterization of both ionically and enzymatically cross-linkable alginate. *Acta Biomater* 3(4):495–501
33. Amini AA, Nair LS (2012) Enzymatically cross-linked injectable gelatin gel as osteoblast delivery vehicle. *J Bioact Compat Pol*. doi:[10.1177/0883911512444713](https://doi.org/10.1177/0883911512444713)
34. Chen D, Zhao M, Mundy GR (2004) Bone morphogenetic proteins. *Growth Factors* 22(4):233–241
35. Marie PJ, Miraoui H, Sévère N (2012) FGF/FGFR signaling in bone formation: progress and perspectives. *Growth Factors* 30(2):117–123. doi:[10.3109/08977194.2012.656761](https://doi.org/10.3109/08977194.2012.656761)
36. Mathieu E, Lamirault G, Toquet C, Lhommet P, Rederstorff E, Sourice S, Biteau K, Hulin P, Forest V, Weiss P, Guicheux J, Lemarchand P (2012) Intramyocardial delivery of mesenchymal stem cell-seeded hydrogel preserves cardiac function and attenuates ventricular remodeling after myocardial infarction. *PLoS ONE* 7(12):e51991. doi:[10.1371/journal.pone.0051991](https://doi.org/10.1371/journal.pone.0051991)
37. Zhang S (2003) Fabrication of novel biomaterials through molecular self-assembly. *Nat Biotechnol* 21(10):1171–1178
38. Hartgerink JD, Beniash E, Stupp SI (2001) Self-assembly and mineralization of peptide-amphiphile nanofibers. *Science* 294(5547):1684–1688. doi:[10.1126/science.1063187](https://doi.org/10.1126/science.1063187)
39. Zhou M, Smith AM, Das AK, Hodson NW, Collins RF, Ulijn RV, Gough JE (2009) Self-assembled peptide-based hydrogels as scaffolds for anchorage-dependent cells. *Biomaterials* 30(13):2523–2530. doi:[10.1016/j.biomaterials.2009.01.010](https://doi.org/10.1016/j.biomaterials.2009.01.010)
40. Zupancich JA, Bates FS, Hillmyer MA (2009) Synthesis and self-assembly of RGD-functionalized PEO-PB amphiphiles. *Biomacromolecules* 10(6):1554–1563. doi:[10.1021/bm900149b](https://doi.org/10.1021/bm900149b)
41. Webber MJ, Tongers J, Renault M-A, Roncalli JG, Losordo DW, Stupp SI (2010) Development of bioactive peptide amphiphiles for therapeutic cell delivery. *Acta Biomater* 6(1):3–11. doi:<http://dx.doi.org/10.1016/j.actbio.2009.07.031>
42. Gong Y, Su K, Lau TT, Zhou R, Wang DA (2010) Microcavitary hydrogel-mediating phase transfer cell culture for cartilage tissue engineering. *Tissue Eng Part A* 16(12):3611–3622
43. Chawla K, Yu T-b, Stutts L, Yen M, Guan Z (2012) Modulation of chondrocyte behavior through tailoring functional synthetic saccharide–peptide hydrogels. *Biomaterials* 33(26):6052–6060. doi:<http://dx.doi.org/10.1016/j.biomaterials.2012.04.058>
44. Liao SW, Rawson J, Omori K, Ishiyama K, Mozhdehi D, Oancea AR, Ito T, Guan Z, Mullen Y (2013) Maintaining functional islets through encapsulation in an injectable saccharide–peptide hydrogel. *Biomaterials* 34(16):3984–3991. doi:<http://dx.doi.org/10.1016/j.biomaterials.2013.02.007>
45. Kumbar SG, James R, Nukavarapu SP, Laurencin CT (2008) Electrospun nanofiber scaffolds: engineering soft tissues. *Biomed Mater* 3(3):034002. doi:[10.1088/1748-6041/3/3/034002](https://doi.org/10.1088/1748-6041/3/3/034002)
46. Choi JS, Lee SJ, Christ GJ, Atala A, Yoo JJ (2008) The influence of electrospun aligned poly(epsilon-caprolactone)/collagen nanofiber meshes on the formation of self-aligned skeletal muscle myotubes. *Biomaterials* 29(19):2899–2906. doi:[10.1016/j.biomaterials.2008.03.031](https://doi.org/10.1016/j.biomaterials.2008.03.031)
47. Yang L, Yuan W, Zhao J, Ai F, Chen X, Zhang Y (2011) A novel approach to prepare uniaxially aligned nanofibers and longitudinally aligned seamless tubes through electrospinning. *Macromol Mater Eng* 297(7):604–608. doi:[10.1002/mame.201100195](https://doi.org/10.1002/mame.201100195)
48. Teo WE, Kotaki M, Mo XM, Ramakrishna S (2005) Porous tubular structures with controlled fibre orientation using a modified electrospinning method. *Nanotechnology* 16(6):918–924. doi:[10.1088/0957-4484/16/6/049](https://doi.org/10.1088/0957-4484/16/6/049)

49. Fisher MB, Henning EA, Söegaard N, Esterhai JL, Mauck RL (2013) Organized nanofibrous scaffolds that mimic the macroscopic and microscopic architecture of the knee meniscus. *Acta Biomater* 9(1):4496–4504. doi:<http://dx.doi.org/10.1016/j.actbio.2012.10.018>
50. Browning MB, Dempsey D, Guiza V, Becerra S, Rivera J, Russell B, Höök M, Clubb F, Miller M, Fossum T, Dong JF, Bergeron AL, Hahn M, Cosgriff-Hernandez E (2012) Multilayer vascular grafts based on collagen-mimetic proteins. *Acta Biomater* 8(3):1010–1021. doi:[10.1016/j.actbio.2011.11.015](http://dx.doi.org/10.1016/j.actbio.2011.11.015)
51. Prestwich GD (2011) Hyaluronic acid-based clinical biomaterials derived for cell and molecule delivery in regenerative medicine. *J Control Release* 155(2):193–199. doi:<http://dx.doi.org/10.1016/j.jconrel.2011.04.007>
52. Nivison-Smith L, Weiss AS (2012) Alignment of human vascular smooth muscle cells on parallel electrospun synthetic elastin fibers. *J Biomed Mater Res A* 100(1):155–161. doi:[10.1002/jbm.a.33255](http://dx.doi.org/10.1002/jbm.a.33255)
53. Liu H, Li X, Zhou G, Fan H, Fan Y (2011) Electrospun sulfated silk fibroin nanofibrous scaffolds for vascular tissue engineering. *Biomaterials* 32(15):3784–3793. doi:[10.1016/j.biomaterials.2011.02.002](http://dx.doi.org/10.1016/j.biomaterials.2011.02.002)
54. Matthews JA, Wnek GE, Simpson DG, Bowlin GL (2002) Electrospinning of collagen nanofibers. *Biomacromolecules* 3(2):232–238
55. McCullen SD, Autebage H, Callanan A, Gentleman E, Stevens MM (2012) Anisotropic fibrous scaffolds for articular cartilage regeneration. *Tissue Eng Part A* 18(19–20):2073–2083
56. Kador KE, Montero RB, Venugopalan P, Hertz J, Zindell AN, Valenzuela DA, Uddin MS, Lavik EB, Muller KJ, Andreopoulos FM, Goldberg JL (2013) Tissue engineering the retinal ganglion cell nerve fiber layer. *Biomaterials* 34(17):4242–4250. doi:<http://dx.doi.org/10.1016/j.biomaterials.2013.02.027>
57. Xu CY, Inai R, Kotaki M, Ramakrishna S (2004) Aligned biodegradable nanofibrous structure: a potential scaffold for blood vessel engineering. *Biomaterials* 25(5):877–886. doi:[10.1016/s0142-9612\(03\)00593-3](http://dx.doi.org/10.1016/s0142-9612(03)00593-3)
58. Choi JS, Lee SJ, Christ GJ, Atala A, Yoo JJ (2008) The influence of electrospun aligned poly(ϵ -caprolactone)/collagen nanofiber meshes on the formation of self-aligned skeletal muscle myotubes. *Biomaterials* 29(19):2899–2906. doi:<http://dx.doi.org/10.1016/j.biomaterials.2008.03.031>
59. Anderson DG, Burdick JA, Langer R (2004) Smart biomaterials. *Science* 305(5692):1923–1924. doi:[10.1126/science.1099987](http://dx.doi.org/10.1126/science.1099987)
60. McClure MJ, Sell SA, Simpson DG, Walpoth BH, Bowlin GL (2010) A three-layered electrospun matrix to mimic native arterial architecture using polycaprolactone, elastin, and collagen: A preliminary study. *Acta Biomater* 6(7):2422–2433. doi:<http://dx.doi.org/10.1016/j.actbio.2009.12.029>
61. Harris LD, Kim B-S, Mooney DJ (1998) Open pore biodegradable matrices formed with gas foaming. *J Biomed Mater Res* 42(3):396–402. doi:[10.1002/\(sici\)1097-4636\(19981205\)42:3<396::aid-jbm7>3.0.co;2-e](http://dx.doi.org/10.1002/(sici)1097-4636(19981205)42:3<396::aid-jbm7>3.0.co;2-e)
62. Ji C, Annabi N, Hosseinkhani M, Sivaloganathan S, Dehghani F (2012) Fabrication of poly-DL-lactide/polyethylene glycol scaffolds using the gas foaming technique. *Acta Biomater* 8(2):570–578. doi:<http://dx.doi.org/10.1016/j.actbio.2011.09.028>
63. Changchun Z, Liang M, Wei L, Donggang Y (2011) Fabrication of tissue engineering scaffolds through solid-state foaming of immiscible polymer blends. *Biofabrication* 3(4):045003
64. Foss C, Merzari E, Migliaresi C, Motta A (2012) Silk Fibroin/Hyaluronic acid 3D matrices for cartilage tissue engineering. *Biomacromolecules* 14(1):38–47. doi:[10.1021/bm301174x](http://dx.doi.org/10.1021/bm301174x)
65. Stoppato M, Stevens HY, Carletti E, Migliaresi C, Motta A, Guldberg RE (2013) Effects of silk fibroin fiber incorporation on mechanical properties, endothelial cell colonization and vascularization of PDLA scaffolds. *Biomaterials* (2013). doi:<http://dx.doi.org/10.1016/j.biomaterials.2013.02.009>

66. Bandyopadhyay B, Shah V, Soram M, Viswanathan C, Ghosh D (2013) In vitro and in vivo evaluation of L-lactide/ ϵ -caprolactone copolymer scaffold to support myoblast growth and differentiation. *Biotechnol Progr* 29(1):197–205. doi:[10.1002/btpr.1665](https://doi.org/10.1002/btpr.1665)
67. Song JJ, Ott HC (2011) Organ engineering based on decellularized matrix scaffolds. *Trends Mol Med* 17(8):424–432. doi:<http://dx.doi.org/10.1016/j.molmed.2011.03.005>
68. Nakayama KH, Batchelder CA, Lee CI, Tarantal AF (2010) Decellularized rhesus monkey kidney as a three-dimensional scaffold for renal tissue engineering. *Tissue Eng Part A* 16(7):2207–2216
69. Gilbert TW, Sellaro TL, Badylak SF (2006) Decellularization of tissues and organs. *Biomaterials* 27(19):3675–3683. doi:<http://dx.doi.org/10.1016/j.biomaterials.2006.02.014>
70. Wainwright DJ (1995) Use of an acellular allograft dermal matrix (AlloDerm) in the management of full-thickness burns. *Burns* 21(4):243–248. doi:[http://dx.doi.org/10.1016/0305-4179\(95\)93866-1](http://dx.doi.org/10.1016/0305-4179(95)93866-1)
71. Brown JW, Elkins RC, Clarke DR, Tweddell JS, Huddleston CB, Doty JR, Fehrenbacher JW, Takkenberg JJM (2010) Performance of the CryoValve SG human decellularized pulmonary valve in 342 patients relative to the conventional CryoValve at a mean follow-up of four years. *J Thorac Cardiovasc Surg* 139(2):339–348. doi:<http://dx.doi.org/10.1016/j.jtcvs.2009.04.065>
72. Choi JS, Kim JD, Yoon HS, Cho YW (2013) Full-thickness skin wound healing using human placenta-derived extracellular matrix containing bioactive molecules. *Tissue Eng Part A* 19(3–4):329–339
73. Bannasch H, Stark GB, Knam F, Horch RE, Föhn M (2008) Decellularized dermis in combination with cultivated keratinocytes in a short- and long-term animal experimental investigation. *J Eur Acad Dermatol* 22(1):41–49. doi:[10.1111/j.1468-3083.2007.02326.x](https://doi.org/10.1111/j.1468-3083.2007.02326.x)
74. Ma R, Li M, Luo J, Yu H, Sun Y, Cheng S, Cui P (2013) Structural integrity, ECM components and immunogenicity of decellularized laryngeal scaffold with preserved cartilage. *Biomaterials* 34(7):1790–1798. doi:<http://dx.doi.org/10.1016/j.biomaterials.2012.11.026>
75. Ott HC, Clippinger B, Conrad C, Schuetz C, Pomerantseva I, Ikonomou L, Kotton D, Vacanti JP (2010) Regeneration and orthotopic transplantation of a bioartificial lung. *Nat Med* 16(8):927–933
76. Petersen TH, Calle EA, Zhao L, Lee EJ, Gui L, Raredon MB, Gavrilov K, Yi T, Zhuang ZW, Breuer C, Herzog E, Niklason LE (2010) Tissue-engineered lungs for in vivo implantation. *Science* 329(5991):538–541. doi:[10.1126/science.1189345](https://doi.org/10.1126/science.1189345)
77. Dahl SL, Koh J, Prabhakar V, Niklason LE (2003) Decellularized native and engineered arterial scaffolds for transplantation. *Cell Transplant* 12(6):659–666
78. Zhao Y, Zhang S, Zhou J, Wang J, Zhen M, Liu Y, Chen J, Qi Z (2010) The development of a tissue-engineered artery using decellularized scaffold and autologous ovine mesenchymal stem cells. *Biomaterials* 31(2):296–307. doi:<http://dx.doi.org/10.1016/j.biomaterials.2009.09.049>
79. Yu C, Bianco J, Brown C, Fuetterer L, Watkins JF, Samani A, Flynn LE (2013) Porous decellularized adipose tissue foams for soft tissue regeneration. *Biomaterials* 34(13):3290–3302. doi:<http://dx.doi.org/10.1016/j.biomaterials.2013.01.056>
80. Wang L, Johnson JA, Chang DW, Zhang Q (2013) Decellularized musculofascial extracellular matrix for tissue engineering. *Biomaterials* 34(11):2641–2654. doi:<http://dx.doi.org/10.1016/j.biomaterials.2012.12.048>
81. Lang R, Stern MM, Smith L, Liu Y, Bharadwaj S, Liu G, Baptista PM, Bergman CR, Soker S, Yoo JJ, Atala A, Zhang Y (2011) Three-dimensional culture of hepatocytes on porcine liver tissue-derived extracellular matrix. *Biomaterials* 32(29):7042–7052. doi:<http://dx.doi.org/10.1016/j.biomaterials.2011.06.005>
82. Wolf MT, Daly KA, Brennan-Pierce EP, Johnson SA, Carruthers CA, D'Amore A, Nagarkar SP, Velankar SS, Badylak SF (2012) A hydrogel derived from decellularized dermal extracellular matrix. *Biomaterials* 33(29):7028–7038. doi:<http://dx.doi.org/10.1016/j.biomaterials.2012.06.051>

83. Turner AEB, Yu C, Bianco J, Watkins JF, Flynn LE (2012) The performance of decellularized adipose tissue microcarriers as an inductive substrate for human adipose-derived stem cells. *Biomaterials* 33(18):4490–4499. doi:<http://dx.doi.org/10.1016/j.biomaterials.2012.03.026>
84. Duan Y, Liu Z, O'Neill J, Wan L, Freytes D, Vunjak-Novakovic G (2011) Hybrid gel composed of native heart matrix and collagen induces cardiac differentiation of human embryonic stem cells without supplemental growth factors. *J Cardiovasc Trans Res* 4(5):605–615. doi:[10.1007/s12265-011-9304-0](http://dx.doi.org/10.1007/s12265-011-9304-0)
85. Schrobback K, Klein TJ, Schuetz M, Upton Z, Leavesley DI, Malda J (2011) Adult human articular chondrocytes in a microcarrier-based culture system: expansion and redifferentiation. *J Orthop Res* 29(4):539–546. doi:[10.1002/jor.21264](http://dx.doi.org/10.1002/jor.21264)
86. Huang S, Deng T, Wang Y, Deng Z, He L, Liu S, Yang J, Jin Y (2008) Multifunctional implantable particles for skin tissue regeneration: Preparation, characterization, in vitro and in vivo studies. *Acta Biomater* 4(4):1057–1066. doi:<http://dx.doi.org/10.1016/j.actbio.2008.02.007>
87. Huang S, Lu G, Wu Y, Jirigala E, Xu Y, Ma K, Fu X (2012) Mesenchymal stem cells delivered in a microsphere-based engineered skin contribute to cutaneous wound healing and sweat gland repair. *J Dermatol Sci* 66(1):29–36. doi:[10.1016/j.jdermsci.2012.02.002](http://dx.doi.org/10.1016/j.jdermsci.2012.02.002)
88. Leong W, Lau TT, Wang D-A (2012) A temperature-cured dissolvable gelatin microsphere-based cell carrier for chondrocyte delivery in a hydrogel scaffolding system. *Acta Biomater* (2012). doi:<http://dx.doi.org/10.1016/j.actbio.2012.10.047>
89. Su K, Gong Y, Wang C, Wang D-A (2011) A novel shell-structure cell microcarrier (SSCM) for cell transplantation and bone regeneration medicine. *Pharm Res* 28(6):1431–1441. doi:[10.1007/s11095-010-0321-5](http://dx.doi.org/10.1007/s11095-010-0321-5)
90. Chen W, Tong YW (2012) PHBV microspheres as neural tissue engineering scaffold support neuronal cell growth and axon-dendrite polarization. *Acta Biomater* 8(2):540–548. doi:[10.1016/j.actbio.2011.09.026](http://dx.doi.org/10.1016/j.actbio.2011.09.026)
91. Kim TK, Yoon JJ, Lee DS, Park TG (2006) Gas foamed open porous biodegradable polymeric microspheres. *Biomaterials* 27(2):152–159. doi:<http://dx.doi.org/10.1016/j.biomaterials.2005.05.081>
92. Lee HJ, Park YH, Koh W-G (2013) Fabrication of nanofiber microarchitectures localized within hydrogel microparticles and their application to protein delivery and cell encapsulation. *Adv Funct Mater* 23(5):591–597. doi:[10.1002/adfm.201201501](http://dx.doi.org/10.1002/adfm.201201501)
93. Akiyama S, Olden K, Yamada K (1995) Fibronectin and integrins in invasion and metastasis. *Cancer Metast Rev* 14(3):173–189. doi:[10.1007/bf00690290](http://dx.doi.org/10.1007/bf00690290)
94. Pierschbacher MD, Ruoslahti E (1984) Cell attachment activity of fibronectin can be duplicated by small synthetic fragments of the molecule. *Nature* 309(5963):30–33
95. Beamish JA, Fu AY, Choi A-j, Haq NA, Kottke-Marchant K, Marchant RE (2009) The influence of RGD-bearing hydrogels on the re-expression of contractile vascular smooth muscle cell phenotype. *Biomaterials* 30(25):4127–4135. doi:<http://dx.doi.org/10.1016/j.biomaterials.2009.04.038>
96. Burkhart DJ, Kalet BT, Coleman MP, Post GC, Koch TH (2004) Doxorubicin-formaldehyde conjugates targeting alphavbeta3 integrin. *Mol Cancer Ther* 3(12):1593–1604
97. Patel PR, Kiser RC, Lu YY, Fong E, Ho WC, Tirrell DA, Grubbs RH (2012) Synthesis and cell adhesive properties of linear and cyclic RGD functionalized polynorbormene thin films. *Biomacromolecules* 13(8):2546–2553. doi:[10.1021/bm300795y](http://dx.doi.org/10.1021/bm300795y)
98. Wang C, Gong Y, Lin Y, Shen J, Wang DA (2008) A novel gellan gel-based microcarrier for anchorage-dependent cell delivery. *Acta Biomater* 4(5):1226–1234
99. Annabi N, Fathi A, Mithieux SM, Martens P, Weiss AS, Dehghani F (2011) The effect of elastin on chondrocyte adhesion and proliferation on poly (ϵ -caprolactone)/elastin composites. *Biomaterials* 32(6):1517–1525. doi:<http://dx.doi.org/10.1016/j.biomaterials.2010.10.024>

100. Song YL, Li YX, Zheng QX, Wu K, Guo XD, Wu YC, Yin M, Wu Q, Fu XL (2011) Neural progenitor cells survival and neuronal differentiation in peptide-based hydrogels. *J Biomat Sci-Polym E* 22(4–6):475–487. doi:[10.1163/092050610x487756](https://doi.org/10.1163/092050610x487756)
101. Silva GA, Czeisler C, Niece KL, Beniash E, Harrington DA, Kessler JA, Stupp SI (2004) Selective differentiation of neural progenitor cells by high-epitope density nanofibers. *Science* 303(5662):1352–1355. doi:[10.1126/science.1093783](https://doi.org/10.1126/science.1093783)
102. Gerberich BG, Bhatia SK (2013) Tissue scaffold surface patterning for clinical applications. *Biotechnol J* 8(1):73–84. doi:[10.1002/biot.201200131](https://doi.org/10.1002/biot.201200131)
103. Huang NF, Lai ES, Ribeiro AJS, Pan S, Pruitt BL, Fuller GG, Cooke JP (2013) Spatial patterning of endothelium modulates cell morphology, adhesiveness and transcriptional signature. *Biomaterials* 34(12):2928–2937. doi:<http://dx.doi.org/10.1016/j.biomaterials.2013.01.017>
104. Nikkhah M, Eshak N, Zorlutuna P, Annabi N, Castello M, Kim K, Dolatshahi-Pirouz A, Edalat F, Bae H, Yang Y, Khademhosseini A (2012) Directed endothelial cell morphogenesis in micropatterned gelatin methacrylate hydrogels. *Biomaterials* 33(35):9009–9018
105. Liu Y, Zhang L, Li H, Yan S, Yu J, Weng J, Li X (2012) Electrospun fibrous mats on lithographically micropatterned collectors to control cellular behaviors. *Langmuir* 28(49):17134–17142. doi:[10.1021/la303490x](https://doi.org/10.1021/la303490x)
106. Uttayarat P, Perets A, Li M, Pimton P, Stachelek SJ, Alferiev I, Composto RJ, Levy RJ, Lelkes PI (2010) Micropatterning of three-dimensional electrospun polyurethane vascular grafts. *Acta Biomater* 6(11):4229–4237. doi:<http://dx.doi.org/10.1016/j.actbio.2010.06.008>
107. Tuft BW, Li S, Xu L, Clarke JC, White SP, Guymon BA, Perez KX, Hansen MR, Guymon CA (2013) Photopolymerized microfeatures for directed spiral ganglion neurite and Schwann cell growth. *Biomaterials* 34(1):42–54. doi:<http://dx.doi.org/10.1016/j.biomaterials.2012.09.053>
108. Poudel I, Lee JS, Tan L, Lim JY (2013) Micropatterning–retinoic acid co-control of neuronal cell morphology and neurite outgrowth. *Acta Biomater* 9(1):4592–4598. doi:<http://dx.doi.org/10.1016/j.actbio.2012.08.039>
109. Zhang M, Method D, Poppa V, Fujio Y, Walsh K, Murry CE (2001) Cardiomyocyte grafting for cardiac repair: graft cell death and anti-death strategies. *J Mol Cell Cardiol* 33(5):907–921. doi:<http://dx.doi.org/10.1006/jmcc.2001.1367>
110. Pittenger MF, Martin BJ (2004) Mesenchymal stem cells and their potential as cardiac therapeutics. *Circ Res* 95(1):9–20. doi:[10.1161/01.RES.0000135902.99383.6f](https://doi.org/10.1161/01.RES.0000135902.99383.6f)
111. Kushida A, Yamato M, Konno C, Kikuchi A, Sakurai Y, Okano T (2000) Temperature-responsive culture dishes allow nonenzymatic harvest of differentiated Madin-Darby canine kidney (MDCK) cell sheets. *J Biomed Mater Res* 51(2):216–223. doi:[10.1002/\(sici\)1097-4636\(200008\)51:2<216::aid-jbm10>3.0.co;2-k](https://doi.org/10.1002/(sici)1097-4636(200008)51:2<216::aid-jbm10>3.0.co;2-k)
112. Kushida A, Yamato M, Isoi Y, Kikuchi A, Okano T (2005) A noninvasive transfer system for polarized renal tubule epithelial cell sheets using temperature-responsive culture dishes. *Eur Cell Mater* 10:23–30
113. Kushida A, Yamato M, Kikuchi A, Okano T (2001) Two-dimensional manipulation of differentiated Madin–Darby canine kidney (MDCK) cell sheets: The noninvasive harvest from temperature-responsive culture dishes and transfer to other surfaces. *J Biomed Mater Res* 54(1):37–46. doi:[10.1002/1097-4636\(200101\)54:1<37::aid-jbm5>3.0.co;2-7](https://doi.org/10.1002/1097-4636(200101)54:1<37::aid-jbm5>3.0.co;2-7)
114. Miyahara Y, Nagaya N, Kataoka M, Yanagawa B, Tanaka K, Hao H, Ishino K, Ishida H, Shimizu T, Kangawa K, Sano S, Okano T, Kitamura S, Mori H (2006) Monolayered mesenchymal stem cells repair scarred myocardium after myocardial infarction. *Nat Med* 12(4):459–465. doi:http://www.nature.com/nm/journal/v12/n4/supinfo/nm1391_S1.html
115. Arisaka Y, Kobayashi J, Yamato M, Akiyama Y, Okano T (2013) Switching of cell growth/detachment on heparin-functionalized thermoresponsive surface for rapid cell sheet fabrication and manipulation. *Biomaterials* 34(17):4214–4222. doi:<http://dx.doi.org/10.1016/j.biomaterials.2013.02.056>

116. Kelm JM, Fussenegger M (2010) Scaffold-free cell delivery for use in regenerative medicine. *Adv Drug Deliv Rev* 62(7–8):753–764. doi:<http://dx.doi.org/10.1016/j.addr.2010.02.003>
117. Ito A, Ino K, Kobayashi T, Honda H (2005) The effect of RGD peptide-conjugated magnetite cationic liposomes on cell growth and cell sheet harvesting. *Biomaterials* 26(31):6185–6193. doi:<http://dx.doi.org/10.1016/j.biomaterials.2005.03.039>
118. Kito T, Shibata R, Ishii M, Suzuki H, Himeno T, Kataoka Y, Yamamura Y, Yamamoto T, Nishio N, Ito S, Numaguchi Y, Tanigawa T, Yamashita JK, Ouchi N, Honda H, Isobe K, Murohara T (2013) iPS cell sheets created by a novel magnetite tissue engineering method for reparative angiogenesis. *Sci Rep* 3. doi:<http://www.nature.com/srep/2013/130311/srep01418/abs/srep01418.html#supplementary-information>
119. Zahn R, Thomasson E, Guillaume-Gentil O, Vörös J, Zambelli T (2012) Ion-induced cell sheet detachment from standard cell culture surfaces coated with polyelectrolytes. *Biomaterials* 33(12):3421–3427. doi: <http://dx.doi.org/10.1016/j.biomaterials.2012.01.019>
120. Guillaume-Gentil O, Akiyama Y, Schuler M, Tang C, Textor M, Yamato M, Okano T, Vörös J (2008) Polyelectrolyte coatings with a potential for electronic control and cell sheet engineering. *Adv Mater* 20(3):560–565. doi:[10.1002/adma.200700758](https://doi.org/10.1002/adma.200700758)
121. Su K, Lau TT, Leong W, Gong Y, Wang D-A (2012) Creating a living hyaline cartilage graft free from non-cartilaginous constituents: an intermediate role of a biomaterial scaffold. *Adv Funct Mater* 22(5):972–978. doi:[10.1002/adfm.201102884](https://doi.org/10.1002/adfm.201102884)
122. Gomes ME, Azevedo HS, Moreira AR, Ella V, Kellomaki M, Reis RL (2008) Starch-poly(epsilon-caprolactone) and starch-poly(lactic acid) fibre-mesh scaffolds for bone tissue engineering applications: structure, mechanical properties and degradation behaviour. *J Tissue Eng Regen M* 2(5):243–252. doi:[10.1002/term.89](https://doi.org/10.1002/term.89)
123. Chen ZG, Wang PW, Wei B, Mo XM, Cui FZ (2010) Electrospun collagen–chitosan nanofiber: a biomimetic extracellular matrix for endothelial cell and smooth muscle cell. *Acta Biomater* 6(2):372–382. doi:<http://dx.doi.org/10.1016/j.actbio.2009.07.024>
124. Rahman MM, Pervez S, Nesa B, Khan MA (2013) Preparation and characterization of porous scaffold composite films by blending chitosan and gelatin solutions for skin tissue engineering. *Polym Int* 62(1):79–86. doi:[10.1002/pi.4299](https://doi.org/10.1002/pi.4299)

Chapter 5

Tissue Engineering Applications for Peripheral Nerve Repair

Hakan Orbay and Weibo Cai

5.1 Introduction

Peripheral nerves are prone to physical injuries due to their relatively superficial location in most parts of the body. The physical trauma usually comes in the form of transportation and construction accidents, natural disaster and war damage, and other trauma, as well as iatrogenic side effects of surgery. Approximately, 2.8 % of trauma patients suffer from an accompanying peripheral nerve injury, and the number of patients with upper extremity paralysis reaches up to 360,000 per annum in the USA. Therefore, peripheral nerve repair and regeneration have always been a popular and challenging topic of clinical research [1].

The first attempts to repair peripheral nerves by Galen date back to second century [2]. Sporadic descriptions of nerve coaptation sutures were reported later by Paul von Aegina in the seventh century and Rahzes and Avicenna in the ninth century [3]. The treatment techniques have evolved to a great extent over the following centuries; however, even with the most advanced techniques, peripheral nerve injuries often result in residual sensory and functional losses [3–5].

5.2 Classification of Peripheral Nerve Injuries

Peripheral nerve injuries are classified according to the Sunderland's scale [6] which includes five degrees with an increasing severity of the injury: First-degree injury (also called neuropraxia) defines the injuries that cause a block in the action

H. Orbay (✉)

University of Wisconsin—Madison, 1111 Highland Avenue, Madison,
WI 53705-2275, USA
e-mail: Horbay@uwhealth.org

W. Cai

University of Wisconsin—Madison, Room 7137, 1111 Highland Avenue, Madison,
WI 53705-2275, USA
e-mail: Wcai@uwhealth.org

potential conduction, but axonal continuity is preserved. Complete healing is expected. Second-degree injury is associated with a loss in axonal continuity without damage to the surrounding glial and connective structures. Complete healing is expected since the regenerating axons can be properly oriented under the guidance of the original glial tubules in the distal nerve stump. Third-degree injuries include the endoneurial structures, and thus, although nerve continuity is maintained, the orientation of the regenerating axons to the proper target can be poorer than in second-degree lesions. Fourth-degree injuries refer to nerve injuries which cause the disruption of all nerve fibers and supporting structures except the epineurium. Regeneration can occur spontaneously; however, complete recovery is unlikely due to scar formation and improper orientation of regenerated axons. Finally, in fifth-degree injuries, complete nerve transection occurs. Healing is impossible unless nerve continuity is reconstructed surgically.

5.3 Conventional Treatment of Peripheral Nerve Injuries

Treatment for the simple cuts is direct coaptation, but severe injuries resulting in a wide gap require an autologous nerve graft or a nerve conduit to bridge the gap [7]. After the implantation of nerve graft, the axons within the graft are removed by phagocytes and Schwann cells with initial phagocytosis [4, 8]. In the next step, Schwann cells, which are responsible for the synthesis of the myelin sheath in the peripheral nerve tissue, proliferate and develop bands of Büngner. These are columns of cells lining the endoneurial tubes, eventually helping the regenerating axons to progress in the direction of denervated targets [5, 9].

Even though the autologous nerve grafting is currently the gold standard treatment for nerve defects, the drawbacks of the technique are as follows: limited donor tissue and donor site morbidity that may present as numbness and neuroma pain in the donor site [3, 4, 8]. Due to the limited regeneration capacity of human peripheral nerve tissue, the completion of the axonal regeneration is a time-consuming process even under ideal conditions, and a long period of rehabilitation is essential to obtain the maximum functional recovery [4, 5]. Functional recovery rates typically approach only 80 % for nerve injuries treated by autologous nerve grafts [1].

5.4 Tissue Engineering of Peripheral Nerves

Discovery of multipotent stem cells and the advancements in biomaterial engineering have enabled engineering of peripheral nerves in the laboratory medium. Tissue-engineered nerve grafts have attracted a large volume of interest as an alternative to autologous nerve grafting for the treatment for peripheral nerve defects considering the above-mentioned drawbacks of the latter technique.

Similarly, to the other fields of regenerative medicine, peripheral nerve tissue engineering has raised great expectations within the general public, as well as in the scientific community, regarding its potential clinical application in the treatment of damaged nerves. However, in spite of the significant scientific advancements, clinical application of tissue-engineered nerve grafts is still very limited. To optimize the engineering strategy and accelerate the process of clinical translation, we should bring together the main pillars of tissue engineering which are as follows: scaffolds; growth factors, genes, and drugs; and support cells [8].

5.4.1 Nerve Scaffolds

5.4.1.1 Structure of Nerve Scaffolds

As mentioned above, the axons in the autologous nerve grafts do not integrate into the structure of the regenerated nerves, but they are degraded in the early steps of nerve regeneration, subsequently leaving a hollow lumen through which the regenerating axons progress distally. Therefore, using hollow nerve scaffolds instead of nerve grafts for bridging wide nerve gaps may help to decrease the donor site morbidity related with autologous nerve grafting [4, 8]. Figure 5.1 gives a summary of the structure of nerve scaffolds and the way that they can be used for peripheral nerve tissue engineering.

Scaffolds should be non-cytotoxic, non-immunogenic, non-allergenic, and non-carcinogenic as well as being sufficiently porous to allow the diffusion of nutrients while inhibiting the invasion of scar tissue [5, 10]. The fabrication technique (cutting holes on the wall, rolling of meshes, fiber spinning, adding a pore-forming agent, or injection molding followed by solvent evaporation) affects the permeability by altering the porous structure of neural scaffolds [11, 12]. Permeability of neural scaffold is also affected by the hydrophilic property of the scaffold material [1]. For a routine clinical application, the neural scaffold has to be easily fabricated, sterilized, and moreover has to satisfy many biomechanical and biological requirements such as biocompatibility and biodegradability [1]. On biomechanical side, a neural scaffold must be flexible to allow bending without kinking; too stiff scaffolds are easily dislocated, while too flexible scaffolds fail to provide sufficient mechanical support for axonal regeneration [1]. On biocompatibility side, the surface properties (including pH and surface charge) are the determining factors in terms of interactions between the neural scaffolds and nerve cells and the ability of the scaffold to blend in the implantation site and promote cell–substrate interaction [1, 10]. For example, the longitudinally oriented surface texture of the neural scaffold has been shown to help directional outgrowth of axons and uniform alignment of Schwann cells *in vitro*, resulting in improved nerve regeneration [1]. Similarly, multichannel neural scaffolds have greater surface areas for cell attachment and local release of growth factors, thus theoretically can support the nerve regeneration across a larger nerve gap. The data published thus far support

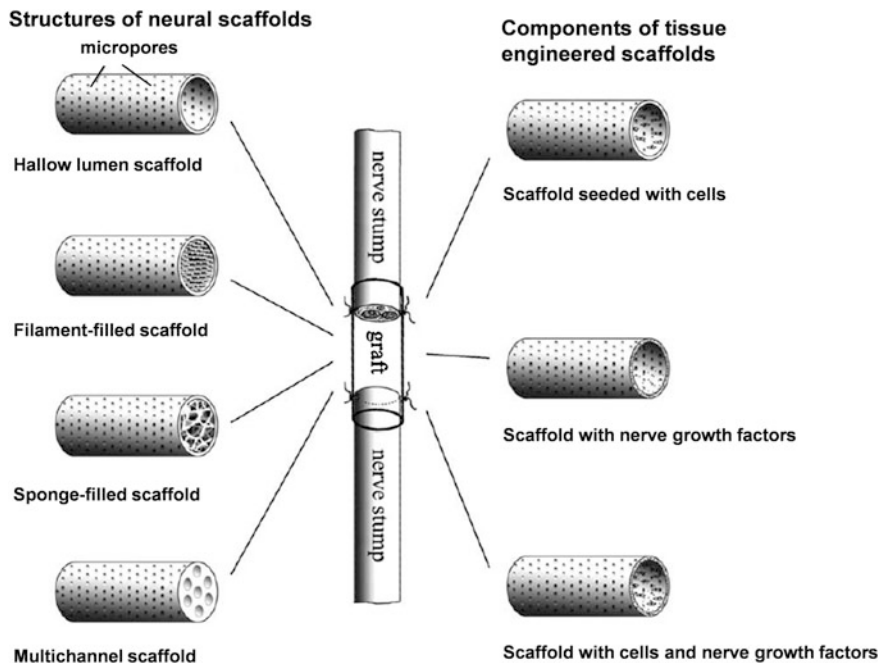


Fig. 5.1 The types of neural scaffolds are shown on the *left-hand side* of the diagram, and the components of tissue-engineered nerve grafts are shown on the *right-hand side*. Adapted with permission from [1]

the hypothesis that multichannel neural scaffolds reduce the dispersion of regenerating axons through the scaffold lumen; however, they displayed no significant benefit over single-lumen scaffolds [1, 13] probably because a complex multilayer internal structure may at the same time interfere with the permeability and flexibility of the neural scaffold [13].

5.4.1.2 Surface Properties of Nerve Scaffolds

In *in vivo*, the cells are located in three-dimensional microenvironments where they are surrounded by other cells and by the extracellular matrix, whose components, such as collagen, elastin, and laminin, are organized in nanostructures (i.e., fibers, triple helixes, etc.). This complex tissue network regulates the morphology, migration, and proliferation of Schwann cells, stimulates the release of nerve growth factors from Schwann cells, and also provides binding sites and directionality to the growing axons [14]. It is therefore essential to develop scaffolds that create synthetic microenvironments, providing 3D support, so as to control and direct the cellular behavior and to promote specific cell interactions [5].

Attempts to imitate the natural extracellular matrix by adding macromolecules (proteoglycans, collagen, elastin, laminin, fibronectin) to the internal environment of nerve scaffolds experienced a limited success [14–17]. However, nanomaterials provide a new dimension of interaction with biological systems that takes place on a subcellular level with a high degree of specificity [5, 18, 19]. For example, nanodiamond monolayers provide an excellent growth surface on various materials for functional neuronal networks and bypass the necessity of protein coating [20]. Furthermore, carbon nanotubes enhance nerve regeneration by rendering the scaffold more conductive [89].

The source of the scaffold is another aspect that effects the cell–scaffold and tissue–scaffold interactions. A scaffold may be derived from natural or synthetic materials [21].

5.4.1.3 Natural Nerve Scaffolds

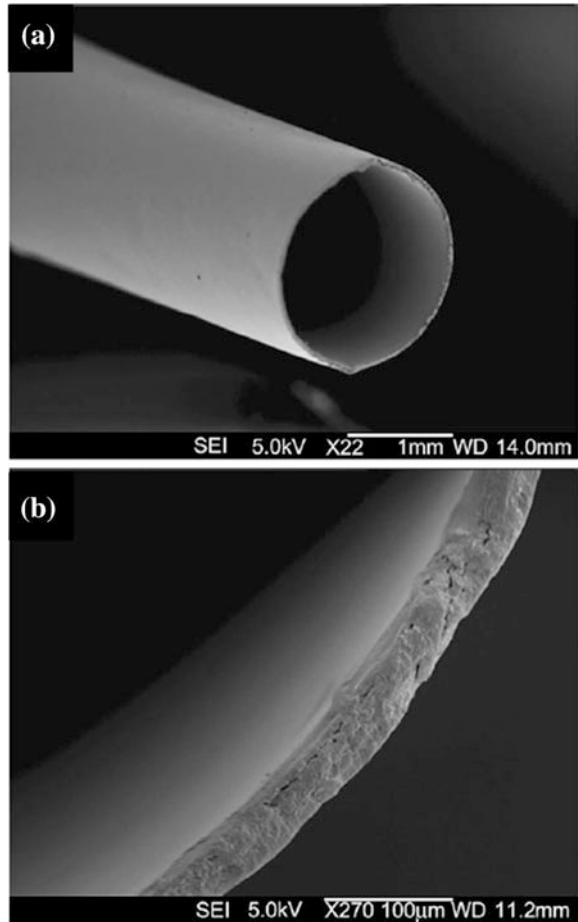
Natural scaffolds are made from tissues that already exist in human body or from materials that exist naturally outside human body [5]. Natural biomaterials are attractive sources for nerve tissue engineering since they constitute cell-friendly matrices that stimulate adhesion, migration, growth, and proliferation of neurogenic cells. These materials also exhibit similar properties to the soft tissues that they are replacing, and they do not elicit foreign body reaction upon implantation and therefore have an excellent biocompatibility [1, 22]. The concerns about natural materials are as follows: the necessity of a careful purification process and inconsistent homogeneity of products between the lots [22].

- *Acellular Allogeneic or Xenogeneic Tissues*

Acellular tissues from same or different species can be obtained by various physical, chemical, and enzymatic decellularization methods [23–25]. These methods aim to remove the immunogenic components and preserve the extracellular matrix components that are essential for the mechanical integrity of the tissue. Acellular tissues are especially useful in the repair of non-critical peripheral nerve gaps with a small length and diameter [1].

Acellular allogeneic and xenogeneic nerve tissues [25–32], tendon [33], and vein and muscle [34, 35] have been used by different groups in order to repair peripheral nerve defects. Avance1 (AxoGen Inc. Alachua, FL) is a commercially available acellular allogeneic nerve graft product which is fabricated from a donated cadaveric nerve through decellularization. Preliminary clinical applications of this product yielded favorable results [28]. However, the major concern about the use of acellular nerve scaffolds is the lack of axonal growth-stimulating bioactive components just like any other synthetic nerve scaffold. Recently, an increasing amount of effort has been directed toward incorporation of support cells or growth factors into the acellular allogeneic or xenogeneic-based neural scaffolds [30–32, 36]. The resultant tissue-engineered nerve grafts allow a better nerve regeneration than the acellular neural scaffolds alone.

Fig. 5.2 SEM views of a collagen nerve scaffold (Revolv[®] tube) with a smooth internal and external texture. Scale bars, 1 mm (a) and 100 μm (b). Adapted with permission from [37]



- *Extracellular Matrix Components*

Extracellular matrix is a network of proteins and fibers surrounding the cells that together form a complex 3-D structure crucial for proper biological functioning of the cells. Three main components of extracellular matrix, collagen, laminin, and fibronectin, have important roles in nerve regeneration.

Collagen has been extensively investigated as a potential scaffold for neural tissue engineering (Fig. 5.2) [37–41]. The properties of collagen scaffolds can be varied by using different concentrations of collagen or it can be denatured to gelatin that has also been used as a scaffold material [42]. The source of the collagen can be mammals such as rats, bovines, and humans; therefore, there is a risk of immune response if xenogeneic transplantation is used.

- *Chitin, Chitosan, and Other Natural Polysaccharides*

Chitin is a natural polysaccharide that is commonly found in the outer shells of crustaceans, insect exoskeletons, and fungal cell walls. It is extensively used in biomedical applications. Chitosan is closely related to chitin and can be obtained from chitin via deacetylation [22]. The molecular structure of chitosan has got a strong resemblance with the molecular structure of glycosaminoglycan; therefore, it can interact with the extracellular matrix molecules in a similar way. The favorable biological properties of chitin and chitosan made them useful materials for nerve tissue engineering [1, 43–46].

- *Silk Fibroin and Other Natural Molecules*

Silk fibroin, keratins, and other matrix proteins extracted from human hair, wool, nail, and feather have been used as natural materials for the production of nerve scaffolds [47–49].

5.4.1.4 Synthetic Nerve Scaffolds

Synthetic scaffolds can be made from non-degradable materials such as silicone [50, 51] and poly-2-hydroxyethyl methacrylate-co-methyl methacrylate (PHEMA-MMA) [52] or from biodegradable polymers such as poly-3-hydroxybutyrate [53, 54], polyglycolic acid (PGA) [55, 56], poly L-lactic acid (PLA) [57, 58], poly-lactide-co-glycolide (PLGA) (Fig. 5.3) [59–61], and poly-lactide-co-caprolactone (PLC) [62, 63].

The main advantage of synthetic nerve scaffolds is their tunable chemical and physical properties. However, their incompatibility with cell adhesion and tissue integration poses a challenge to nerve tissue engineering. Therefore, synthetic materials are often chemically modified to render them more biocompatible [1].

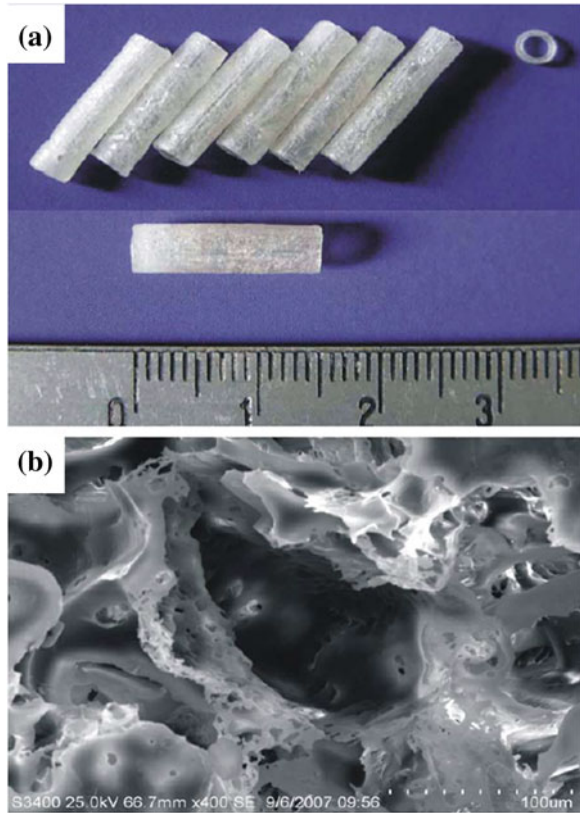
- *Non-degradable Synthetic Materials*

The early neural scaffolds were made of non-degradable synthetic materials such as silicone, rubber, acrylic polymer, polyethylene, elastomer, etc. Even though they achieved variable levels of success, their clinical use is currently limited because of the long-term complications such as chronic nerve compression, chronic foreign body reaction, and the necessity of a second surgical procedure to remove the scaffold [64, 65].

- *Biodegradable Synthetic Materials*

As the concerns rose over the use of non-degradable synthetic materials as nerve scaffolds, biodegradable synthetic scaffolds, which degrade within a reasonable time span after implantation, were developed. Ideally, the neural scaffolds should remain intact throughout the axon regeneration and then gradually degrade with minimal swelling and foreign body reaction [1]. In case of a 10-mm gap of

Fig. 5.3 PLGA conduits (a) and structure of the scaffold under scanning electron microscopy (SEM) (b). Scale bar, 100 μm . Adapted with permission from [61]



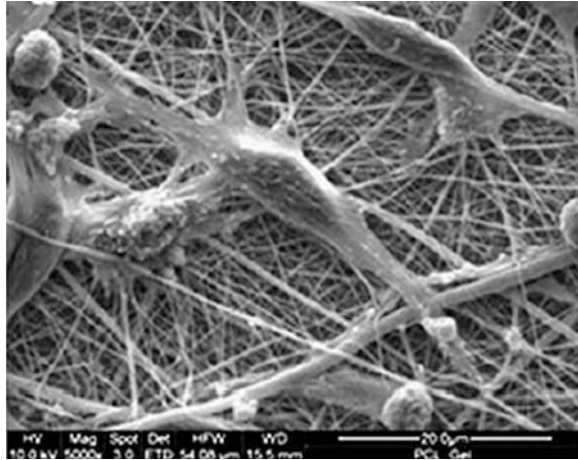
the rat sciatic nerve, the minimum time period that a biodegradable nerve scaffold must remain intact for sufficient nerve regeneration is 3 months [5]. Both the premature and delayed degradation of nerve scaffold might result in increased scar formation that further delays nerve regeneration [5, 66].

Further chemical modifications can be used to increase the biocompatibility of degradable scaffolds via adding sites for cell or extracellular matrix adhesion to allow cells to infiltrate into the scaffold lumen (Fig. 5.4) [19, 67, 68].

5.4.2 Growth Factors

Growth factors act in coordination with extracellular matrix to control the survival, proliferation, migration, and differentiation of various cell types involved in the nerve regeneration [69]. Incorporation of growth factors, such as nerve growth factor, glial cell line-derived neurotrophic factor, and brain-derived neurotrophic factor (BDNF), into the tissue-engineered nerve grafts has been actively attempted

Fig. 5.4 SEM image shows Schwann cells on PCL/gelatin nanofibrous scaffolds after 12 days of coculture. Nanofibers encourage the attachment of Schwann cells. Scale bar, 200 μm . Adapted with permission from [19]



in order to avoid the possible side effects and morbidity associated with cellular therapy [70–76]. However, growth factor therapy has fallen short of expectations because of the unpredictable side effects, unknown optimal dosage, and short half-life of the growth factors [5, 74, 75, 77].

5.4.3 Cell Sources for Peripheral Nerve Tissue Engineering

Due to the *in vivo* inefficiency of growth factors, some researchers implanted cells into the lumen of neural scaffolds in an attempt to provide a continuous supply of growth factors to the nerve defect area [35, 78–81]. Moreover, engineering a complete peripheral nerve is not possible without the *in vitro* culture and seeding of cells onto the nerve scaffolds. The major cell types used were as follows: Schwann cells, embryonic stem cells (ESCs), neural stem cells (NSCs), mesenchymal stem cells (MSCs), and induced pluripotent stem cells (iPSCs) (Table 5.1).

These cell lines could be implanted into the scaffolds via direct injection or coculturing methods before or after *in vitro* differentiation [33, 82]. The markers for successful neural differentiation are as follows: GFAP, p75NGFR, and S-100 for Schwann cells [83–86] and nestin and NeuN [84, 87] for neural progenitor cells.

- *Schwann Cells*

Schwann cells can be obtained from allogeneic, syngeneic, or autologous sources. Their function is to create a suitable environment for axonal growth by expressing cell adhesion molecules, secreting nerve growth factors, and forming an endoneurial myelin sheath that acts as a guide for the regenerating axons [3, 34]. This central role of Schwann cells in peripheral nerve regeneration made

Table 5.1 Cell lines used as support cells for nerve tissue engineering

Cell type	Advantages	Disadvantages
Schwann cells	Non-immunogenic; major role in myelination; secretes growth factors	Harvest and expansion are time consuming; harvest requires invasive procedures
Olfactory ensheathing cells	Secrete neurotropic factors; participate in myelination; non-immunogenic	Limited survival in cell cultures; limited donor site
Neural stem cells	Non-immunogenic; promote axonal regeneration	High risk of tumor formation in vivo
Bone-marrow-derived stem cells	Easy expansion, non-immunogenic	Harvest requires invasive procedures; low stem cell yield
Adipose-derived mesenchymal stem cells	Easy harvest and expansion; secrete growth factors	Action of mechanism needs to be clarified;
Skin-derived stem cells	Easy harvest and expansion; secrete growth factors; non-immunogenic	Donor site morbidity

them the most commonly used cell type for experimental nerve tissue engineering applications. Schwann cell-enriched nerve scaffolds improved both the quality and rate of axonal regeneration in rat sciatic nerve defect model [88, 89]. However, among the obstacles in front of their clinical use are; suboptimal attachment of Schwann cells to the nerve scaffolds and the difficulties in obtaining and in vitro expansion of autologous Schwann cells [1, 81].

- *ESCs*

As an alternative to Schwann cells, ESCs can easily be expanded and have a great potential to proliferate and differentiate into neurons under various protocols (Fig. 5.5) [87, 90]. However, the ethical concerns on the use of ESCs for clinical applications limit their use.

- *NSCs*

Neural stem cells, just like ESCs, are multipotent, highly mobile, and can easily be isolated and cultured in vitro. These properties make NSCs an attractive alternative source of support cells for nerve tissue engineering [91–93].

- *MSCs*

MSCs from various adult tissues (bone marrow, adipose tissue, etc.) became the subject of interest because of various advantages over the other cell lines. It is relatively easily to obtain *MSCs* through minimally invasive procedures such as the aspiration of the bone marrow or liposuction. *MSCs* can easily be expanded in a large scale by in vitro culture [94, 95].

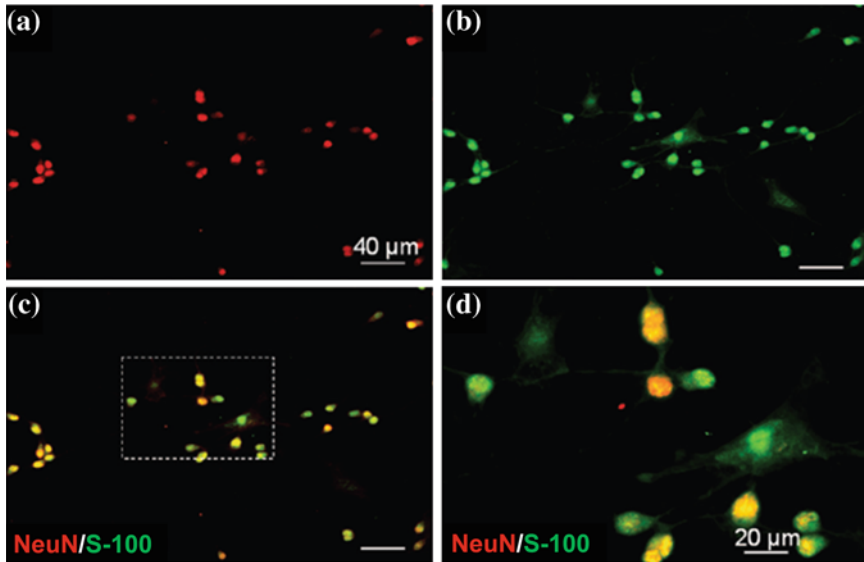


Fig. 5.5 Phenotype characterization of ESCs differentiated into neural progenitors. Confocal fluorescence microscopy imaging shows the cell phenotype 3 days after differentiation induction. Images demonstrate double staining of NeuN (*red*) (a) and S-100 (*green*) (b) in neural progenitor cells differentiated from ESCs. Merged image demonstrates the positivity of some of the cells for both NeuN and S-100, implying that these neural progenitors can further differentiate into either neuronal or glia/Schwann cells (c). A close-up view is seen in pane (d). *Scale bars*, 40 μm (a, b) and 20 μm (c, d). Adapted with permission from [87]

Even though they do not possess the wide range of differentiation of ESCs, adult MSCs are multipotent, secrete growth factors and other soluble mediators, and moreover can serve as a vehicle for drug delivery and gene therapy [96]. Several *in vitro* studies have shown that MSCs can be induced to differentiate into neural lineages including Schwann cell-like cells (Fig. 5.6) [85, 97–101]; however, MSCs promote nerve regeneration not only by direct differentiation but also via spontaneous fusion with host cells and possibly by secreting growth factors [102, 103].

- *iPSCs*

The latest and maybe the most significant advancement in stem cell field is the reprogramming of adult somatic cells (e.g., skin fibroblasts) into pluripotent stem cells by the introduction of genes Oct3/4, Sox2, c-Myc, and KLF4 [104]. These cells are named iPSCs, and since they are derived from somatic cells, they bypass the immune system of the host. Similar to ESCs, iPSCs possess an unlimited expansion potential, and they can be differentiated into almost every tissue in human body yet without any of the ethical concerns surrounding ESCs (Fig. 5.7). However, iPSCs require a significantly more genetic manipulation than any other stem cell type during the induction process that subsequently leads to some safety concerns in clinical application [105].

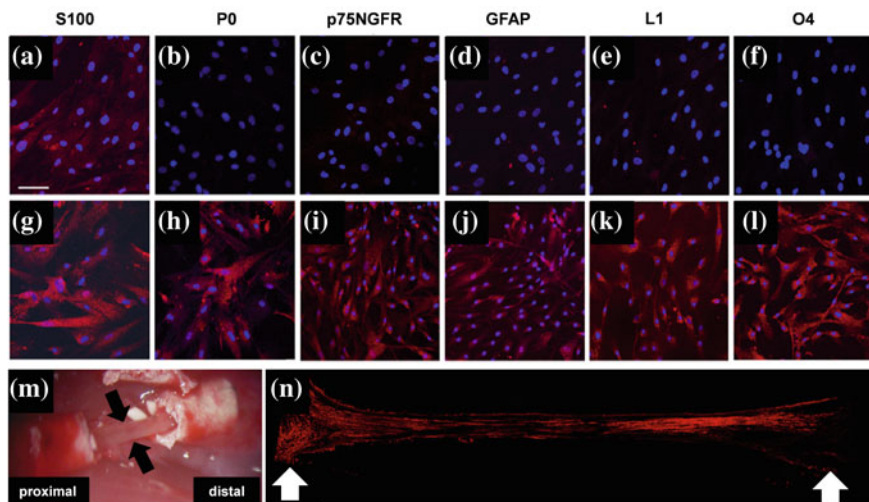


Fig. 5.6 Human MSCs can be differentiated into Schwann cell-like cells. This picture shows immunofluorescence staining for S100, P0, p75NGFR, GFAP, L1, O4 in human MSCs (a–f), and human MSC-derived Schwann cells (g–l). The untreated human MSCs slightly expressed S100 (a) but were negative for other Schwann cell markers before induction (b–f). However, after the induction, cells became positive for all the other Schwann cell markers and exhibited an increased immunoreactivity for S100 (g). Macroscopic view of the tissue within the nerve scaffold seeded with MSC-derived Schwann 3 weeks after transplantation of the scaffold into a rat sciatic nerve defect (*black arrows*) (m). Neurofilament-positive nerve fibers (*red*) observed in the newly formed tissue in the scaffold, *white arrows* mark the coaptation sites (n). Scale bar, 100 μ m. Adapted with permission from [101]

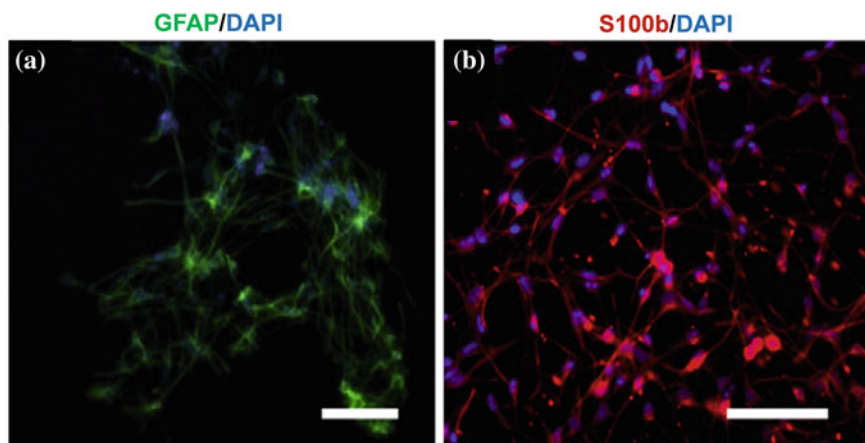


Fig. 5.7 In vitro differentiation of iPSC into Schwann cells. Differentiated cells are positive for GFAP (a) and S100b (b). Scale bar, 100 μ m. Adapted with permission from [105]

5.4.4 Toward Clinical Applications

The repair of critical-sized rat sciatic nerve defects by tissue-engineered nerve grafts has been the experiment model that supplied the major percentage of pre-clinical data on in vivo application of peripheral nerve tissue engineering. Studies with different cell lines and scaffolds yielded similar results [34, 36, 80, 81, 84, 86, 106, 107]. Even though it constitutes a strong background for clinical translation, the differences between the biology's of small animals and human beings should always be considered when interpreting the preclinical data.

Wakao et al. used a cynomolgus monkey peripheral nervous system injury model to examine the safety and efficacy of bone marrow MSCs differentiated into Schwann cells as a cell source for peripheral nerve tissue engineering [108]. Differentiated MSCs were seeded onto a collagen sponge at a concentration of 2×10^6 cells, and collagen sponge was placed into the lumen of a PLC scaffold to repair a 20-mm median nerve defect. For the evaluation, in addition to other techniques, they have performed ^{18}F -fluorodeoxyglucose positron emission tomography (^{18}F -FDG-PET) scanning for in vivo tracking of the injected cells. No abnormal accumulation of radioactivity except in regions with expected physiological accumulation was observed excluding a possible neoplastic transformation of the injected cells.

Hu et al. used rhesus monkey for two different experiments. In the first experiment, acellular allogeneic nerve segments were seeded either with autologous bone marrow MSCs or autologous Schwann cells to repair a 40 mm defect in the ulnar nerve of rhesus monkeys [30]. The concentration of the cells was 2×10^7 cells per graft, and the recovery with the MSC-seeded allografts was similar to that observed with Schwann cell-seeded allografts and autologous nerve grafts. This study demonstrated that MSCs could be a solid alternative to Schwann cells as a cell source for peripheral nerve tissue engineering given the difficulties in purifying sufficient quantities of Schwann cells for peripheral nerve regeneration. In the second study, they used chitosan/PLGA-based, autologous marrow MSC-containing tissue-engineered nerve grafts for bridging a 50 mm long median nerve defect in rhesus monkeys (Fig. 5.8) [30]. They injected 1×10^8 cells per ml of suspension. At 12 months after grafting, locomotive activity observation, electrophysiological assessments, and gold retrograde tracing tests were carried out, and the recovery of nerve function by tissue-engineered nerve was found to be more efficient than the one by scaffold alone. In addition, the authors performed a safety evaluation of MSC-based therapies. Blood test and histopathological examination demonstrated that tissue-engineered nerve graft could be safely used in the primate body. These two studies were milestone studies toward the clinical application, considering the striking similarity in the anatomy and function of forearm nerves between human and monkey hands.

Bone marrow MSCs seeded on a PLGA scaffold was used to repair a dog sciatic nerve defect in two different studies [107, 109]. Both of these studies demonstrated that repair of the peripheral nerve defects with tissue-engineered nerve grafts yielded similar results with autologous nerve graft repair.

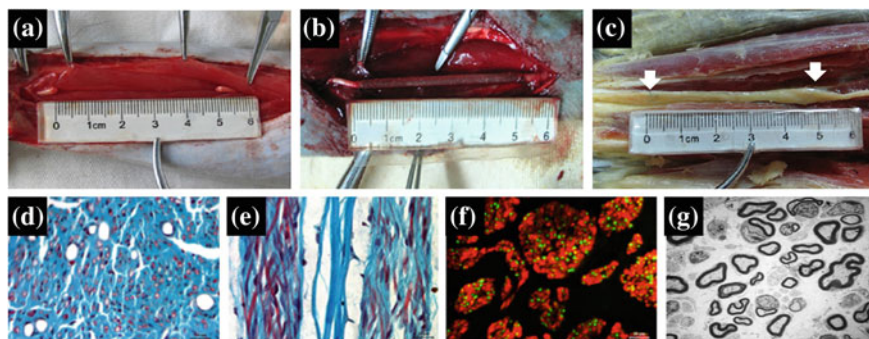


Fig. 5.8 Intra-operative views of the repair of a median nerve defect in a monkey forearm. A 5-cm median nerve segment was excised following the dissection of the nerve (a). The defect was bridged by a chitosan/PLGA scaffold injected with an autologous BMSC suspension (b). Macroscopic view of the regenerated nerve at 12 months after the operation. The *white arrows* mark the proximal and distal coaptation sites, respectively (c). Histological examination confirmed the nerve regeneration at 12 months: Meyer trichrome staining of transverse and longitudinal nerve sections depicts the myelinated axons within the regenerated nerve (myelin seen in *red*) (d, e); double immunostaining with anti-neurofilament 200 (*green color*) and anti-S100 (*red color*) of transverse nerve segments shows neurofilament-200-positive axons encircled by S-100-positive myelin (f). Scale bars, 20 μm . Transmission electron micrographs show myelin around the axons as dense *black circles* (g). Scale bar, 5 μm . Adapted with permission from [78]

The data obtained from the experiments using bigger animal models are more clinically relevant. The results of these experiments will definitely help to determine the guidelines of human applications of tissue-engineered nerve grafts. Nevertheless, more studies are warranted to find the appropriate cell type and number of cells for peripheral nerve tissue engineering and possible side effects of cellular treatment.

Among the preclinical studies, another one that deserves some emphasis is a recent study that reported *in vivo* transplantation of differentiated adipose-derived stem cells on a three-dimensional nerve scaffold composed of fibroblasts. This is an important study in terms of omitting the peripheral nerve tissue engineering problems related to scaffolds such as cell adhesion and biocompatibility [83].

5.4.5 Conclusion and Future Prospects

Unpredictable outcomes and morbidity associated with the traditional methods of treatment of nerve defects encouraged surgeons to consider alternative methods for peripheral nerve repair. Tissue engineering has recently emerged as a useful tool for the treatment for a variety of diseases that were previously known to be untreatable. The combination of bioengineered scaffolds and multipotent/pluripotent stem cells hold a great potential toward peripheral nerve tissue engineering.

However, the clinical translation of peripheral nerve tissue engineering is a delicate process that should proceed toward realistic expectations following a set of carefully determined guidelines. Further refinement of the available techniques is required for routine, safe, and efficient clinical application.

Even though the volume of the experimental data is encouraging, the clinical success of peripheral nerve tissue engineering depends on the controlled regulation of cell behavior and tissue progression in synthetic nerve scaffolds. To achieve this goal, 3D imitation of the extracellular matrix structure and a sophisticated cell–extracellular matrix interaction are crucial. In this regard, incorporation of nanofibers into the scaffold had greatly enhanced the biocompatibility of scaffolds. Altogether, addition of cells and growth factors into the lumens of scaffolds and surface modifications should help the scaffolds to mimic the natural conditions and improve the outcomes of surgical repair of peripheral nerve defects.

References

1. Gu X, Ding F, Yang Y, Liu J (2011) Construction of tissue engineered nerve grafts and their application in peripheral nerve regeneration. *Prog Neurobiol* 93(2):204–230. doi:[10.1016/j.pneurobio.2010.11.002](https://doi.org/10.1016/j.pneurobio.2010.11.002)
2. Terzis JK, Sun DD, Thanos PK (1997) Historical and basic science review: past, present, and future of nerve repair. *J Reconstr Microsurg* 13(3):215–225. doi:[10.1055/s-2007-1006407](https://doi.org/10.1055/s-2007-1006407)
3. Raimondo S, Fornaro M, Tos P, Battiston B, Giacobini-Robecchi MG, Geuna S (2011) Perspectives in regeneration and tissue engineering of peripheral nerves. *Ann Anat* 193(4):334–340. doi:[10.1016/j.aanat.2011.03.001](https://doi.org/10.1016/j.aanat.2011.03.001)
4. Sinis N, Kraus A, Drakotos D, Doser M, Schlosshauer B, Muller HW, Skouras E, Bruck JC, Werdin F (2011) Bioartificial reconstruction of peripheral nerves using the rat median nerve model. *Ann Anat* 193(4):341–346. doi:[10.1016/j.aanat.2011.02.018](https://doi.org/10.1016/j.aanat.2011.02.018)
5. Sedaghati T, Yang SY, Mosahebi A, Alavijeh MS, Seifalian AM (2011) Nerve regeneration with aid of nanotechnology and cellular engineering. *Biotechnol Appl Biochem* 58(5):288–300. doi:[10.1002/bab.51](https://doi.org/10.1002/bab.51)
6. Sunderland S (1951) A classification of peripheral nerve injuries producing loss of function. *Brain* 74(4):491–516
7. Millesi H, Meissl G, Berger A (1972) The interfascicular nerve-grafting of the median and ulnar nerves. *J Bone Joint Surg Am* 54(4):727–750
8. Battiston B, Raimondo S, Tos P, Gaidano V, Audisio C, Scevola A, Perroteau I, Geuna S (2009) Chapter 11: tissue engineering of peripheral nerves. *Int Rev Neurobiol* 87:227–249. doi:[10.1016/s0074-7742\(09\)87011-6](https://doi.org/10.1016/s0074-7742(09)87011-6)
9. Geuna S, Raimondo S, Ronchi G, Di Scipio F, Tos P, Czaja K, Fornaro M (2009) Chapter 3: histology of the peripheral nerve and changes occurring during nerve regeneration. *Int Rev Neurobiol* 87:27–46. doi:[10.1016/s0074-7742\(09\)87003-7](https://doi.org/10.1016/s0074-7742(09)87003-7)
10. Cunha C, Panseri S, Antonini S (2011) Emerging nanotechnology approaches in tissue engineering for peripheral nerve regeneration. *Nanomedicine* 7(1):50–59. doi:[10.1016/j.nano.2010.07.004](https://doi.org/10.1016/j.nano.2010.07.004)
11. Dellon AL, Mackinnon SE (1988) An alternative to the classical nerve graft for the management of the short nerve gap. *Plast Reconstr Surg* 82(5):849–856

12. Rodriguez FJ, Gomez N, Perego G, Navarro X (1999) Highly permeable polylactide-caprolactone nerve guides enhance peripheral nerve regeneration through long gaps. *Biomaterials* 20(16):1489–1500
13. de Ruiter GC, Spinner RJ, Malessy MJ, Moore MJ, Sorenson EJ, Currier BL, Yaszemski MJ, Windebank AJ (2008) Accuracy of motor axon regeneration across autograft, single-lumen, and multichannel poly (lactic-co-glycolic acid) nerve tubes. *Neurosurgery* 63(1):144–153. doi:[10.1227/01.NEU.0000335081.47352.78](https://doi.org/10.1227/01.NEU.0000335081.47352.78) (discussion 153–145)
14. Armstrong SJ, Wiberg M, Terenghi G, Kingham PJ (2007) ECM molecules mediate both Schwann cell proliferation and activation to enhance neurite outgrowth. *Tissue Eng* 13(12):2863–2870. doi:[10.1089/ten.2007.0055](https://doi.org/10.1089/ten.2007.0055)
15. Whitworth IH, Brown RA, Dore C, Green CJ, Terenghi G (1995) Orientated mats of fibronectin as a conduit material for use in peripheral nerve repair. *J Hand Surg Br* 20(4):429–436
16. Plow EF, Haas TA, Zhang L, Loftus J, Smith JW (2000) Ligand binding to integrins. *J Biol Chem* 275(29):21785–21788. doi:[10.1074/jbc.R000003200](https://doi.org/10.1074/jbc.R000003200)
17. Massia SP, Hubbell JA (1991) An RGD spacing of 440 nm is sufficient for integrin alpha V beta 3-mediated fibroblast spreading and 140 nm for focal contact and stress fiber formation. *J Cell Biol* 114(5):1089–1100
18. Behan BL, DeWitt DG, Bogdanowicz DR, Koppes AN, Bale SS, Thompson DM (2011) Single-walled carbon nanotubes alter Schwann cell behavior differentially within 2D and 3D environments. *J Biomed Mater Res A* 96(1):46–57. doi:[10.1002/jbm.a.32939](https://doi.org/10.1002/jbm.a.32939)
19. Gupta D, Venugopal J, Prabhakaran MP, Dev VR, Low S, Choon AT, Ramakrishna S (2009) Aligned and random nanofibrous substrate for the in vitro culture of Schwann cells for neural tissue engineering. *Acta Biomater* 5(7):2560–2569. doi:[10.1016/j.actbio.2009.01.039](https://doi.org/10.1016/j.actbio.2009.01.039)
20. Thalhammer A, Edgington RJ, Cingolani LA, Schoepfer R, Jackman RB (2010) The use of nanodiamond monolayer coatings to promote the formation of functional neuronal networks. *Biomaterials* 31(8):2097–2104. doi:[10.1016/j.biomaterials.2009.11.109](https://doi.org/10.1016/j.biomaterials.2009.11.109)
21. Siemionow M, Bozkurt M, Zor F (2010) Regeneration and repair of peripheral nerves with different biomaterials: review. *Microsurgery* 30(7):574–588. doi:[10.1002/micr.20799](https://doi.org/10.1002/micr.20799)
22. Willerth SM, Sakiyama-Elbert SE (2007) Approaches to neural tissue engineering using scaffolds for drug delivery. *Adv Drug Deliv Rev* 59(4–5):325–338. doi:[10.1016/j.addr.2007.03.014](https://doi.org/10.1016/j.addr.2007.03.014)
23. Gilbert TW, Sellaro TL, Badylak SF (2006) Decellularization of tissues and organs. *Biomaterials* 27(19):3675–3683. doi:[10.1016/j.biomaterials.2006.02.014](https://doi.org/10.1016/j.biomaterials.2006.02.014)
24. Hiles RW (1972) Freeze dried irradiated nerve homograft: a preliminary report. *Hand* 4(1):79–84
25. Sondell M, Lundborg G, Kanje M (1998) Regeneration of the rat sciatic nerve into allografts made acellular through chemical extraction. *Brain Res* 795(1–2):44–54
26. Yang LM, Liu XL, Zhu QT, Zhang Y, Xi TF, Hu J, He CF, Jiang L (2011) Human peripheral nerve-derived scaffold for tissue-engineered nerve grafts: histology and biocompatibility analysis. *J Biomed Mater Res B Appl Biomater* 96(1):25–33. doi:[10.1002/jbm.b.31719](https://doi.org/10.1002/jbm.b.31719)
27. Wang D, Liu XL, Zhu JK, Jiang L, Hu J, Zhang Y, Yang LM, Wang HG, Yi JH (2008) Bridging small-gap peripheral nerve defects using acellular nerve allograft implanted with autologous bone marrow stromal cells in primates. *Brain Res* 1188:44–53. doi:[10.1016/j.brainres.2007.09.098](https://doi.org/10.1016/j.brainres.2007.09.098)
28. Karabekmez FE, Duymaz A, Moran SL (2009) Early clinical outcomes with the use of decellularized nerve allograft for repair of sensory defects within the hand. *Hand (N Y)* 4(3):245–249. doi:[10.1007/s11552-009-9195-6](https://doi.org/10.1007/s11552-009-9195-6)
29. Jia H, Wang Y, Tong XJ, Liu GB, Li Q, Zhang LX, Sun XH (2012) Sciatic nerve repair by acellular nerve xenografts implanted with BMSCs in rats xenograft combined with BMSCs. *Synapse* 66(3):256–269. doi:[10.1002/syn.21508](https://doi.org/10.1002/syn.21508)

30. Hu J, Zhu QT, Liu XL, Xu YB, Zhu JK (2007) Repair of extended peripheral nerve lesions in rhesus monkeys using acellular nerve grafts implanted with autologous mesenchymal stem cells. *Exp Neurol* 204(2):658–666. doi:[10.1016/j.expneurol.2006.11.018](https://doi.org/10.1016/j.expneurol.2006.11.018)
31. Hess JR, Brenner MJ, Fox IK, Nichols CM, Myckatyn TM, Hunter DA, Rickman SR, Mackinnon SE (2007) Use of cold-preserved allografts seeded with autologous Schwann cells in the treatment of a long-gap peripheral nerve injury. *Plast Reconstr Surg* 119(1):246–259. doi:[10.1097/01.prs.0000245341.71666.97](https://doi.org/10.1097/01.prs.0000245341.71666.97)
32. Zhang Y, Luo H, Zhang Z, Lu Y, Huang X, Yang L, Xu J, Yang W, Fan X, Du B, Gao P, Hu G, Jin Y (2010) A nerve graft constructed with xenogeneic acellular nerve matrix and autologous adipose-derived mesenchymal stem cells. *Biomaterials* 31(20):5312–5324. doi:[10.1016/j.biomaterials.2010.03.029](https://doi.org/10.1016/j.biomaterials.2010.03.029)
33. Nishiura Y, Brandt J, Nilsson A, Kanje M, Dahlin LB (2004) Addition of cultured Schwann cells to tendon autografts and freeze-thawed muscle grafts improves peripheral nerve regeneration. *Tissue Eng* 10(1–2):157–164. doi:[10.1089/107632704322791808](https://doi.org/10.1089/107632704322791808)
34. Fansa H, Keilhoff G, Wolf G, Schneider W (2001) Tissue engineering of peripheral nerves: a comparison of venous and acellular muscle grafts with cultured Schwann cells. *Plast Reconstr Surg* 107(2):485–494 (discussion 495–486)
35. Hassan NH, Sulong AF, Ng MH, Htwe O, Idrus RB, Roohi S, Naicker AS, Abdullah S (2012) Neural-differentiated mesenchymal stem cells incorporated into muscle stuffed vein scaffold forms a stable living nerve conduit. *J Orthop Res* 30(10):1674–1681. doi:[10.1002/jor.22102](https://doi.org/10.1002/jor.22102)
36. Frerichs O, Fansa H, Schicht C, Wolf G, Schneider W, Keilhoff G (2002) Reconstruction of peripheral nerves using acellular nerve grafts with implanted cultured Schwann cells. *Microsurgery* 22(7):311–315. doi:[10.1002/micr.10056](https://doi.org/10.1002/micr.10056)
37. Alluin O, Wittmann C, Marqueste T, Chabas JF, Garcia S, Lavaut MN, Guinard D, Feron F, Decherchi P (2009) Functional recovery after peripheral nerve injury and implantation of a collagen guide. *Biomaterials* 30(3):363–373. doi:[10.1016/j.biomaterials.2008.09.043](https://doi.org/10.1016/j.biomaterials.2008.09.043)
38. Archibald SJ, Shefner J, Krarup C, Madison RD (1995) Monkey median nerve repaired by nerve graft or collagen nerve guide tube. *J Neurosci* 15(5 Pt 2):4109–4123
39. Farole A, Jamal BT (2008) A bioabsorbable collagen nerve cuff (NeuraGen) for repair of lingual and inferior alveolar nerve injuries: a case series. *J Oral Maxillofac Surg* 66(10):2058–2062. doi:[10.1016/j.joms.2008.06.017](https://doi.org/10.1016/j.joms.2008.06.017)
40. Goto E, Mukozawa M, Mori H, Hara M (2010) A rolled sheet of collagen gel with cultured Schwann cells: model of nerve conduit to enhance neurite growth. *J Biosci Bioeng* 109(5):512–518. doi:[10.1016/j.jbiosc.2009.11.002](https://doi.org/10.1016/j.jbiosc.2009.11.002)
41. Suri S, Schmidt CE (2010) Cell-laden hydrogel constructs of hyaluronic acid, collagen, and laminin for neural tissue engineering. *Tissue Eng Part A* 16(5):1703–1716. doi:[10.1089/ten.tea.2009.0381](https://doi.org/10.1089/ten.tea.2009.0381)
42. Gamez E, Goto Y, Nagata K, Iwaki T, Sasaki T, Matsuda T (2004) Photofabricated gelatin-based nerve conduits: nerve tissue regeneration potentials. *Cell Transplant* 13(5):549–564
43. Freier T, Montenegro R, Shan Koh H, Shoichet MS (2005) Chitin-based tubes for tissue engineering in the nervous system. *Biomaterials* 26(22):4624–4632. doi:[10.1016/j.biomaterials.2004.11.040](https://doi.org/10.1016/j.biomaterials.2004.11.040)
44. He Q, Zhang T, Yang Y, Ding F (2009) In vitro biocompatibility of chitosan-based materials to primary culture of hippocampal neurons. *J Mater Sci Mater Med* 20(7):1457–1466. doi:[10.1007/s10856-009-3702-8](https://doi.org/10.1007/s10856-009-3702-8)
45. Itoh S, Suzuki M, Yamaguchi I, Takakuda K, Kobayashi H, Shinomiya K, Tanaka J (2003) Development of a nerve scaffold using a tendon chitosan tube. *Artif Organs* 27(12):1079–1088
46. Kim IY, Seo SJ, Moon HS, Yoo MK, Park IY, Kim BC, Cho CS (2008) Chitosan and its derivatives for tissue engineering applications. *Biotechnol Adv* 26(1):1–21. doi:[10.1016/j.biotechadv.2007.07.009](https://doi.org/10.1016/j.biotechadv.2007.07.009)

47. Tang X, Ding F, Yang Y, Hu N, Wu H, Gu X (2009) Evaluation on in vitro biocompatibility of silk fibroin-based biomaterials with primarily cultured hippocampal neurons. *J Biomed Mater Res A* 91(1):166–174. doi:[10.1002/jbm.a.32212](https://doi.org/10.1002/jbm.a.32212)
48. Yang Y, Chen X, Ding F, Zhang P, Liu J, Gu X (2007) Biocompatibility evaluation of silk fibroin with peripheral nerve tissues and cells in vitro. *Biomaterials* 28(9):1643–1652. doi:[10.1016/j.biomaterials.2006.12.004](https://doi.org/10.1016/j.biomaterials.2006.12.004)
49. Apel PJ, Garrett JP, Sierpinski P, Ma J, Atala A, Smith TL, Koman LA, Van Dyke ME (2008) Peripheral nerve regeneration using a keratin-based scaffold: long-term functional and histological outcomes in a mouse model. *J Hand Surg Am* 33(9):1541–1547. doi:[10.1016/j.jhsa.2008.05.034](https://doi.org/10.1016/j.jhsa.2008.05.034)
50. Kim SM, Lee SK, Lee JH (2007) Peripheral nerve regeneration using a three dimensionally cultured schwann cell conduit. *J Craniofac Surg* 18(3):475–488. doi:[10.1097/01.scs.0000249362.41170.f3](https://doi.org/10.1097/01.scs.0000249362.41170.f3)
51. Lundborg G, Dahlin LB, Danielsen N (1991) Ulnar nerve repair by the silicone chamber technique. Case report. *Scand J Plast Reconstr Surg Hand Surg* 25(1):79–82
52. Belkas JS, Munro CA, Shoichet MS, Johnston M, Midha R (2005) Long-term in vivo biomechanical properties and biocompatibility of poly (2-hydroxyethyl methacrylate-co-methyl methacrylate) nerve conduits. *Biomaterials* 26(14):1741–1749. doi:[10.1016/j.biomaterials.2004.05.031](https://doi.org/10.1016/j.biomaterials.2004.05.031)
53. Kalbermatten DF, Pettersson J, Kingham PJ, Pierer G, Wiberg M, Terenghi G (2009) New fibrin conduit for peripheral nerve repair. *J Reconstr Microsurg* 25(1):27–33. doi:[10.1055/s-0028-1090619](https://doi.org/10.1055/s-0028-1090619)
54. Mosahebi A, Wiberg M, Terenghi G (2003) Addition of fibronectin to alginate matrix improves peripheral nerve regeneration in tissue-engineered conduits. *Tissue Eng* 9(2):209–218. doi:[10.1089/107632703764664684](https://doi.org/10.1089/107632703764664684)
55. Rosson GD, Williams EH, Dellon AL (2009) Motor nerve regeneration across a conduit. *Microsurgery* 29(2):107–114. doi:[10.1002/micr.20580](https://doi.org/10.1002/micr.20580)
56. Waitayawinyu T, Parisi DM, Miller B, Luria S, Morton HJ, Chin SH, Trumble TE (2007) A comparison of polyglycolic acid versus type I collagen bioabsorbable nerve conduits in a rat model: an alternative to autografting. *J Hand Surg Am* 32(10):1521–1529. doi:[10.1016/j.jhsa.2007.07.015](https://doi.org/10.1016/j.jhsa.2007.07.015)
57. Pierucci A, Duek EA, de Oliveira AL (2009) Expression of basal lamina components by Schwann cells cultured on poly (lactic acid) (PLLA) and poly (caprolactone) (PCL) membranes. *J Mater Sci Mater Med* 20(2):489–495. doi:[10.1007/s10856-008-3614-z](https://doi.org/10.1007/s10856-008-3614-z)
58. Wang HB, Mullins ME, Cregg JM, Hurtado A, Oudega M, Trombley MT, Gilbert RJ (2009) Creation of highly aligned electrospun poly-L-lactic acid fibers for nerve regeneration applications. *J Neural Eng* 6(1):016001. doi:[10.1088/1741-2560/6/1/016001](https://doi.org/10.1088/1741-2560/6/1/016001)
59. Bryan DJ, Tang JB, Holway AH, Rieger-Christ KM, Trantolo DJ, Wise DL, Summerhayes IC (2003) Enhanced peripheral nerve regeneration elicited by cell-mediated events delivered via a bioresorbable PLGA guide. *J Reconstr Microsurg* 19(2):125–134. doi:[10.1055/s-2003-37820](https://doi.org/10.1055/s-2003-37820)
60. Bini TB, Gao S, Xu X, Wang S, Ramakrishna S, Leong KW (2004) Peripheral nerve regeneration by microbraided poly (L-lactide-co-glycolide) biodegradable polymer fibers. *J Biomed Mater Res A* 68(2):286–295. doi:[10.1002/jbm.a.20050](https://doi.org/10.1002/jbm.a.20050)
61. Li BC, Jiao SS, Xu C, You H, Chen JM (2010) PLGA conduit seeded with olfactory ensheathing cells for bridging sciatic nerve defect of rats. *J Biomed Mater Res A* 94(3):769–780. doi:[10.1002/jbm.a.32727](https://doi.org/10.1002/jbm.a.32727)
62. Meek MF, Jansen K (2009) Two years after in vivo implantation of poly (DL-lactide-epsilon-caprolactone) nerve guides: has the material finally resorbed? *J Biomed Mater Res A* 89(3):734–738. doi:[10.1002/jbm.a.32024](https://doi.org/10.1002/jbm.a.32024)
63. Mligiliche NL, Tabata Y, Kitada M, Endoh K, Okamoto K, Fujimoto E, Ide C (2003) Poly lactic acid–caprolactone copolymer tube with a denatured skeletal muscle segment inside as a guide for peripheral nerve regeneration: a morphological and electrophysiological

- evaluation of the regenerated nerves. *Anat Sci Int* 78(3):156–161. doi:[10.1046/j.0022-7722.2003.00056.x](https://doi.org/10.1046/j.0022-7722.2003.00056.x)
64. Deng M, Chen G, Burkley D, Zhou J, Jamiolkowski D, Xu Y, Vetrecin R (2008) A study on in vitro degradation behavior of a poly (glycolide-co-L-lactide) monofilament. *Acta Biomater* 4(5):1382–1391. doi:[10.1016/j.actbio.2008.03.011](https://doi.org/10.1016/j.actbio.2008.03.011)
65. Braga-Silva J (1999) The use of silicone tubing in the late repair of the median and ulnar nerves in the forearm. *J Hand Surg Br* 24(6):703–706. doi:[10.1054/jhsb.1999.0276](https://doi.org/10.1054/jhsb.1999.0276)
66. den Dunnen WF, van der Lei B, Robinson PH, Holwerda A, Pennings AJ, Schakenraad JM (1995) Biological performance of a degradable poly (lactic acid-epsilon-caprolactone) nerve guide: influence of tube dimensions. *J Biomed Mater Res* 29(6):757–766. doi:[10.1002/jbm.820290612](https://doi.org/10.1002/jbm.820290612)
67. Elbert DL, Hubbell JA (2001) Conjugate addition reactions combined with free-radical cross-linking for the design of materials for tissue engineering. *Biomacromolecules* 2(2):430–441
68. Groll J, Fiedler J, Engelhard E, Ameringer T, Tugulu S, Klok HA, Brenner RE, Moeller M (2005) A novel star PEG-derived surface coating for specific cell adhesion. *J Biomed Mater Res A* 74(4):607–617. doi:[10.1002/jbm.a.30335](https://doi.org/10.1002/jbm.a.30335)
69. Terenghi G (1999) Peripheral nerve regeneration and neurotrophic factors. *J Anat* 194(Pt 1):1–14
70. Ho PR, Coan GM, Cheng ET, Niell C, Tarn DM, Zhou H, Sierra D, Terris DJ (1998) Repair with collagen tubules linked with brain-derived neurotrophic factor and ciliary neurotrophic factor in a rat sciatic nerve injury model. *Arch Otolaryngol Head Neck Surg* 124(7):761–766
71. Kokai LE, Bourbeau D, Weber D, McAtee J, Marra KG (2011) Sustained growth factor delivery promotes axonal regeneration in long gap peripheral nerve repair. *Tissue Eng Part A* 17(9–10):1263–1275. doi:[10.1089/ten.TEA.2010.0507](https://doi.org/10.1089/ten.TEA.2010.0507)
72. Sun H, Xu F, Guo D, Yu H (2012) Preparation and evaluation of NGF-microsphere conduits for regeneration of defective nerves. *Neurol Res* 34(5):491–497. doi:[10.1179/1743132812y.0000000037](https://doi.org/10.1179/1743132812y.0000000037)
73. Madduri S, di Summa P, Papaloizos M, Kalbermatten D, Gander B (2010) Effect of controlled co-delivery of synergistic neurotrophic factors on early nerve regeneration in rats. *Biomaterials* 31(32):8402–8409. doi:[10.1016/j.biomaterials.2010.07.052](https://doi.org/10.1016/j.biomaterials.2010.07.052)
74. Lee AC, Yu VM, Lowe JB 3rd, Brenner MJ, Hunter DA, Mackinnon SE, Sakiyama-Elbert SE (2003) Controlled release of nerve growth factor enhances sciatic nerve regeneration. *Exp Neurol* 184(1):295–303
75. Lin YC, Ramadan M, Hronik-Tupaj M, Kaplan DL, Philips BJ, Sivak W, Rubin JP, Marra KG (2011) Spatially controlled delivery of neurotrophic factors in silk fibroin-based nerve conduits for peripheral nerve repair. *Ann Plast Surg* 67(2):147–155. doi:[10.1097/SAP.0b013e3182240346](https://doi.org/10.1097/SAP.0b013e3182240346)
76. Fu KY, Dai LG, Chiu IM, Chen JR, Hsu SH (2011) Sciatic nerve regeneration by microporous nerve conduits seeded with glial cell line-derived neurotrophic factor or brain-derived neurotrophic factor gene transfected neural stem cells. *Artif Organs* 35(4):363–372. doi:[10.1111/j.1525-1594.2010.01105.x](https://doi.org/10.1111/j.1525-1594.2010.01105.x)
77. Madduri S, Gander B (2012) Growth factor delivery systems and repair strategies for damaged peripheral nerves. *J Control Release* 161(2):274–282. doi:[10.1016/j.jconrel.2011.11.036](https://doi.org/10.1016/j.jconrel.2011.11.036)
78. Hu N, Wu H, Xue C, Gong Y, Wu J, Xiao Z, Yang Y, Ding F, Gu X (2013) Long-term outcome of the repair of 50 mm long median nerve defects in rhesus monkeys with marrow mesenchymal stem cells-containing, chitosan-based tissue engineered nerve grafts. *Biomaterials* 34(1):100–111. doi:[10.1016/j.biomaterials.2012.09.020](https://doi.org/10.1016/j.biomaterials.2012.09.020)
79. Hou SY, Zhang HY, Quan DP, Liu XL, Zhu JK (2006) Tissue-engineered peripheral nerve grafting by differentiated bone marrow stromal cells. *Neuroscience* 140(1):101–110. doi:[10.1016/j.neuroscience.2006.01.066](https://doi.org/10.1016/j.neuroscience.2006.01.066)

80. Erba P, Mantovani C, Kalbermatten DF, Pierer G, Terenghi G, Kingham PJ (2010) Regeneration potential and survival of transplanted undifferentiated adipose tissue-derived stem cells in peripheral nerve conduits. *J Plast Reconstr Aesthet Surg* 63(12):e811–e817. doi:[10.1016/j.bjps.2010.08.013](https://doi.org/10.1016/j.bjps.2010.08.013)
81. Fansa H, Dodic T, Wolf G, Schneider W, Keilhoff G (2003) Tissue engineering of peripheral nerves: epineurial grafts with application of cultured Schwann cells. *Microsurgery* 23(1):72–77. doi:[10.1002/micr.10081](https://doi.org/10.1002/micr.10081)
82. Komiyama T, Nakao Y, Toyama Y, Vacanti CA, Vacanti MP, Ignatz RA (2004) Novel technique for peripheral nerve reconstruction in the absence of an artificial conduit. *J Neurosci Methods* 134(2):133–140. doi:[10.1016/j.jneumeth.2003.11.020](https://doi.org/10.1016/j.jneumeth.2003.11.020)
83. Adams AM, Arruda EM, Larkin LM (2012) Use of adipose-derived stem cells to fabricate scaffoldless tissue-engineered neural conduits in vitro. *Neuroscience* 201:349–356. doi:[10.1016/j.neuroscience.2011.11.004](https://doi.org/10.1016/j.neuroscience.2011.11.004)
84. Ao Q, Fung CK, Tsui AY, Cai S, Zuo HC, Chan YS, Shum DK (2011) The regeneration of transected sciatic nerves of adult rats using chitosan nerve conduits seeded with bone marrow stromal cell-derived Schwann cells. *Biomaterials* 32(3):787–796. doi:[10.1016/j.biomaterials.2010.09.046](https://doi.org/10.1016/j.biomaterials.2010.09.046)
85. Chen X, Wang XD, Chen G, Lin WW, Yao J, Gu XS (2006) Study of in vivo differentiation of rat bone marrow stromal cells into schwann cell-like cells. *Microsurgery* 26(2):111–115. doi:[10.1002/micr.20184](https://doi.org/10.1002/micr.20184)
86. Dezawa M, Takahashi I, Esaki M, Takano M, Sawada H (2001) Sciatic nerve regeneration in rats induced by transplantation of in vitro differentiated bone-marrow stromal cells. *Eur J Neurosci* 14(11):1771–1776
87. Cui L, Jiang J, Wei L, Zhou X, Fraser JL, Snider BJ, Yu SP (2008) Transplantation of embryonic stem cells improves nerve repair and functional recovery after severe sciatic nerve axotomy in rats. *Stem Cells* 26(5):1356–1365. doi:[10.1634/stemcells.2007-0333](https://doi.org/10.1634/stemcells.2007-0333)
88. Hadlock T, Sundback C, Hunter D, Cheney M, Vacanti JP (2000) A polymer foam conduit seeded with Schwann cells promotes guided peripheral nerve regeneration. *Tissue Eng* 6(2):119–127. doi:[10.1089/107632700320748](https://doi.org/10.1089/107632700320748)
89. Mosahebi A, Woodward B, Wiberg M, Martin R, Terenghi G (2001) Retroviral labeling of Schwann cells: in vitro characterization and in vivo transplantation to improve peripheral nerve regeneration. *Glia* 34(1):8–17
90. Craff MN, Zeballos JL, Johnson TS, Ranka MP, Howard R, Motarjem P, Randolph MA, Winograd JM (2007) Embryonic stem cell-derived motor neurons preserve muscle after peripheral nerve injury. *Plast Reconstr Surg* 119(1):235–245. doi:[10.1097/01.prs.0000244863.71080.f0](https://doi.org/10.1097/01.prs.0000244863.71080.f0)
91. Alessandri G, Emanuelli C, Madeddu P (2004) Genetically engineered stem cell therapy for tissue regeneration. *Ann N Y Acad Sci* 1015:271–284. doi:[10.1196/annals.1302.023](https://doi.org/10.1196/annals.1302.023)
92. Guo BF, Dong MM (2009) Application of neural stem cells in tissue-engineered artificial nerve. *Otolaryngol Head Neck Surg* 140(2):159–164. doi:[10.1016/j.otohns.2008.10.039](https://doi.org/10.1016/j.otohns.2008.10.039)
93. Hsu SH, Su CH, Chiu IM (2009) A novel approach to align adult neural stem cells on micropatterned conduits for peripheral nerve regeneration: a feasibility study. *Artif Organs* 33(1):26–35. doi:[10.1111/j.1525-1594.2008.00671.x](https://doi.org/10.1111/j.1525-1594.2008.00671.x)
94. Zuk PA, Zhu M, Ashjian P, De Ugarte DA, Huang JI, Mizuno H, Alfonso ZC, Fraser JK, Benhaim P, Hedrick MH (2002) Human adipose tissue is a source of multipotent stem cells. *Mol Biol Cell* 13(12):4279–4295. doi:[10.1091/mbc.E02-02-0105](https://doi.org/10.1091/mbc.E02-02-0105)
95. Mosna F, Sensebe L, Krampera M (2010) Human bone marrow and adipose tissue mesenchymal stem cells: a user's guide. *Stem Cells Dev* 19(10):1449–1470. doi:[10.1089/scd.2010.0140](https://doi.org/10.1089/scd.2010.0140)
96. Horwitz EM, Dominici M (2008) How do mesenchymal stromal cells exert their therapeutic benefit? *Cytherapy* 10(8):771–774. doi:[10.1080/14653240802618085](https://doi.org/10.1080/14653240802618085)
97. Lu J, Moochhala S, Moore XL, Ng KC, Tan MH, Lee LK, He B, Wong MC, Ling EA (2006) Adult bone marrow cells differentiate into neural phenotypes and improve functional

- recovery in rats following traumatic brain injury. *Neurosci Lett* 398(1–2):12–17. doi:[10.1016/j.neulet.2005.12.053](https://doi.org/10.1016/j.neulet.2005.12.053)
98. Munoz-Elias G, Woodbury D, Black IB (2003) Marrow stromal cells, mitosis, and neuronal differentiation: stem cell and precursor functions. *Stem Cells* 21(4):437–448. doi:[10.1634/stemcells.21-4-437](https://doi.org/10.1634/stemcells.21-4-437)
99. Suzuki H, Taguchi T, Tanaka H, Kataoka H, Li Z, Muramatsu K, Gondo T, Kawai S (2004) Neurospheres induced from bone marrow stromal cells are multipotent for differentiation into neuron, astrocyte, and oligodendrocyte phenotypes. *Biochem Biophys Res Commun* 322(3):918–922. doi:[10.1016/j.bbrc.2004.07.201](https://doi.org/10.1016/j.bbrc.2004.07.201)
100. Orbay H, Uysal AC, Hyakusoku H, Mizuno H (2012) Differentiated and undifferentiated adipose-derived stem cells improve function in rats with peripheral nerve gaps. *J Plast Reconstr Aesthet Surg* 65(5):657–664. doi:[10.1016/j.bjps.2011.11.035](https://doi.org/10.1016/j.bjps.2011.11.035)
101. Shimizu S, Kitada M, Ishikawa H, Itokazu Y, Wakao S, Dezawa M (2007) Peripheral nerve regeneration by the in vitro differentiated-human bone marrow stromal cells with Schwann cell property. *Biochem Biophys Res Commun* 359(4):915–920. doi:[10.1016/j.bbrc.2007.05.212](https://doi.org/10.1016/j.bbrc.2007.05.212)
102. Weimann JM, Charlton CA, Brazelton TR, Hackman RC, Blau HM (2003) Contribution of transplanted bone marrow cells to Purkinje neurons in human adult brains. *Proc Natl Acad Sci U S A* 100(4):2088–2093. doi:[10.1073/pnas.0337659100](https://doi.org/10.1073/pnas.0337659100)
103. Chen CJ, Ou YC, Liao SL, Chen WY, Chen SY, Wu CW, Wang CC, Wang WY, Huang YS, Hsu SH (2007) Transplantation of bone marrow stromal cells for peripheral nerve repair. *Exp Neurol* 204(1):443–453. doi:[10.1016/j.expneurol.2006.12.004](https://doi.org/10.1016/j.expneurol.2006.12.004)
104. Takahashi K, Tanabe K, Ohnuki M, Narita M, Ichisaka T, Tomoda K, Yamanaka S (2007) Induction of pluripotent stem cells from adult human fibroblasts by defined factors. *Cell* 131(5):861–872. doi:[10.1016/j.cell.2007.11.019](https://doi.org/10.1016/j.cell.2007.11.019)
105. Wang A, Tang Z, Park IH, Zhu Y, Patel S, Daley GQ, Li S (2011) Induced pluripotent stem cells for neural tissue engineering. *Biomaterials* 32(22):5023–5032. doi:[10.1016/j.biomaterials.2011.03.070](https://doi.org/10.1016/j.biomaterials.2011.03.070)
106. Blais M, Grenier M, Berthod F (2009) Improvement of nerve regeneration in tissue-engineered skin enriched with schwann cells. *J Invest Dermatol* 129(12):2895–2900. doi:[10.1038/jid.2009.159](https://doi.org/10.1038/jid.2009.159)
107. Ding F, Wu J, Yang Y, Hu W, Zhu Q, Tang X, Liu J, Gu X (2010) Use of tissue-engineered nerve grafts consisting of a chitosan/poly (lactic-co-glycolic acid)-based scaffold included with bone marrow mesenchymal cells for bridging 50-mm dog sciatic nerve gaps. *Tissue Eng Part A* 16(12):3779–3790. doi:[10.1089/ten.TEA.2010.0299](https://doi.org/10.1089/ten.TEA.2010.0299)
108. Wakao S, Hayashi T, Kitada M, Kohama M, Matsue D, Teramoto N, Ose T, Itokazu Y, Koshino K, Watabe H, Iida H, Takamoto T, Tabata Y, Dezawa M (2010) Long-term observation of auto-cell transplantation in non-human primate reveals safety and efficiency of bone marrow stromal cell-derived Schwann cells in peripheral nerve regeneration. *Exp Neurol* 223(2):537–547. doi:[10.1016/j.expneurol.2010.01.022](https://doi.org/10.1016/j.expneurol.2010.01.022)
109. Xue C, Hu N, Gu Y, Yang Y, Liu Y, Liu J, Ding F, Gu X (2012) Joint use of a chitosan/PLGA scaffold and MSCs to bridge an extra large gap in dog sciatic nerve. *Neurorehabil Neural Repair* 26(1):96–106. doi:[10.1177/1545968311420444](https://doi.org/10.1177/1545968311420444)

Chapter 6

Structure, Function, and Development of Blood Vessels: Lessons for Tissue Engineering

Hamisha Ardalani, Amir H. Assadi and William L. Murphy

The establishment of blood vessel networks is a matter of life and death for tissues and organisms. Failure to form a functional vascular network causes early death of embryos, and also dysfunction of ECs contributes to many diseases, including stroke, thrombosis, and atherosclerosis. Furthermore, there is a considerable clinical need for alternatives to the autologous vein and artery tissues used for vascular reconstructive surgeries such as lower limb bypass, arteriovenous shunts, and repairs of congenital defects to the pulmonary outflow tract. So far, synthetic materials, particularly in small-diameter applications, have not matched the efficacy of native tissues. Therefore, substantial resources are being directed toward research into the cellular, molecular, and physical factors that regulate the formation, stability, and functional responses of the vasculature. While academic research in the field of tissue engineering in general has been active, yet there has been no clear example of clinical and commercial success. The recent transition of cell-based therapies from experimental to clinical use, however, is a breakthrough in the field of cardiovascular tissue engineering.

Here, we discuss the structure of blood vessels and key signaling molecules, which play significant role in vasculogenesis, angiogenesis, and maturation of nascent blood vessels in [Sects. 6.1](#) and [6.2](#), respectively. The discussion is followed by a description of promising approaches specific to tissue-engineered blood vessels and a brief introduction to some clinical results in [Sect. 6.4](#). But before we explain about tissue engineering approaches, finding the appropriate

H. Ardalani

Department of Biomedical Engineering, University of Wisconsin, Madison, WI, USA
e-mail: hardalani@wisc.edu

A. H. Assadi

Department of Mathematics, University of Wisconsin, Madison, WI, USA
e-mail: ahasadi@wisc.edu

W. L. Murphy (✉)

Departments of Biomedical Engineering and Orthopedic and Rehabilitation,
University of Wisconsin, Madison, WI, USA
e-mail: wlmurphy@wisc.edu

sources of ECs is of utmost importance, which is discussed in [Sect. 6.3](#). The unique regulatory, reimbursement, and production challenges facing personalized medicine are also discussed in the last [Sect. 6.5](#).

6.1 Structure of Blood Vessels

Delivery of nutrients and other molecules as well as blood and immune cells to all tissues in our body is done by blood vessels. Nascent vessels consist of a tube of ECs that mature into three specialized structures: *capillaries*, *arteries*, and *veins*. ECs and mural cells that are surrounded by extracellular matrix (ECM) comprise the walls of vessels.

To form mature blood vessels, immature blood vessels formed by vasculogenesis and angiogenesis must mature at two levels: the *level of vessel wall* as well as *network level*. *Vessel wall* maturation is the result of mural cell recruitment, development of surrounding matrix and elastic laminae, and organ specific specialization of ECs, mural cells, and matrix. Optimal patterning of network by branching, expanding, and pruning to meet local demands leads to *network-level* maturation [1, 2].

6.1.1 Capillaries

The most abundant vessels in our body are capillaries. Capillaries consist of ECs covered with a sparse layer of pericytes that is surrounded by basement membrane (BM). Because of their wall structure and large surface-area-to-volume ratio, these vessels form the main site of exchange of nutrients between blood and tissue. Depending upon the organ or tissue, the capillary endothelial layer could be continuous (as in muscle), fenestrated (as in kidney or endocrine glands), or discontinuous (as in liver sinusoids). The endothelia of the blood–brain barrier or blood–retina barrier are further specialized to include tight junctions and are thus impermeable to various molecules [1].

6.1.2 Arterioles and Venules

Arterioles and venules are small-diameter blood vessels in the microcirculation that extend and branch out from an artery and vein, respectively, which lead to capillaries [1]. These vessels have an increased coverage of mural cells compared with capillaries. Pre-capillary arterioles are completely invested with vascular SMCs that form their own BM and are circumferentially arranged, closely packed and tightly associated with the endothelium. Extravasation of macromolecules and cells from the blood stream typically occurs from postcapillary venules [2, 3].

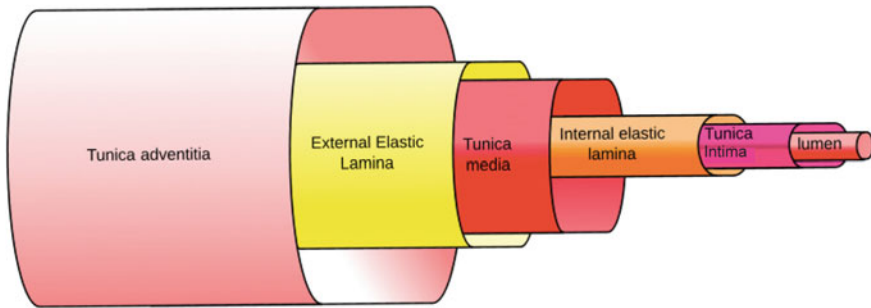


Fig. 6.1 Schematic representation of various layers in blood vessels

6.1.3 Arteries and Veins

Arteries are blood vessels that carry blood away from the heart. This blood is normally oxygenated, with the exception of the pulmonary and umbilical arteries. Veins are blood vessels that carry blood toward the heart. Most veins carry deoxygenated blood from the tissues back to the heart; exceptions are the pulmonary and umbilical veins, both of which carry oxygenated blood to the heart. Larger vessels, arteries and veins, consist of three specialized layers as shown in Fig. 6.1: tunica intima, the tunica media, and the tunica adventitia. The tunica intima is made of a monolayer of ECs with an underlying BM. The tunica media is generally composed of a dense population of concentrically organized SMCs and is separated from the tunica intima by an internal elastic lamina. The tunica adventitia forms the external layer and contains fibroblast cells, collagenous ECM, nerves, and vasa vasorum [4]. The vascular wall ECM composed of structural proteins like collagen and elastin and adhesion proteins like fibronectin and laminin, as well as glycosaminoglycans (GAGs), proteoglycans, growth factors, cytokines, and matrix-degrading enzymes and their inhibitors [5, 6].

6.2 Important Signaling Molecules in Vasculogenesis and Angiogenesis

Understanding important signaling molecules at each level of development of arteries, veins and capillaries and their maturation could help us to engineer blood vessels that are a more faithful mimic of the natural system. Here, we review briefly the important molecules and pathways in vasculogenesis, angiogenesis, and maturation. Tissue engineering strategies may benefit from generating materials that can guide these biological events in the formation of vascular networks. How scientists and researchers use this information to engineer the blood vessels is discussed in Sect. 6.4.

6.2.1 Formation of Immature Vasculature by Vasculogenesis and Angiogenesis

During embryonic development, angioblasts migrate to various regions of the developing embryo and differentiate into ECs in response to local cues such as growth factors and ECM components. The ECs then form a vascular plexus, which is a network built by connections (anastomoses) between blood vessels. This process is called vasculogenesis and it is not limited to the embryonic period, as a similar process can also occur in adults through the recruitment and participation of bone marrow-derived endothelial progenitor cells [3, 7, 8].

Angiogenesis is another mechanism of blood vessel formation that occurs through the sprouting of existing blood vessels. Angiogenesis is a sequential, multistep process that begins with activation of a quiescent endothelium by pro-angiogenic factors such as vascular endothelial growth factor (VEGF), fibroblast growth factor (FGF), and angiopoietin-2 (Ang2) that are often produced by hypoxic or tumorigenic tissues [3, 8]. Hypoxia up-regulates expression of a number of genes involved in vessel formation, patterning, and maturation, including nitric oxide synthase, VEGF, and Ang2. Nitric oxide, which is a product of nitric oxide synthase, dilates vessels and make them more responsive to VEGF because they becomes more leaky. Ang2 also facilitates sprout formation in the presence of VEGF. The sprouts anastomose to form vascular loops and networks [3].

Angiogenesis is also dependent on degradation of the BM, a thin layer of ECM between the epithelial cell layer and the endothelial cell lining of blood vessels. Degradation of BM is due to up-regulation of matrix metalloproteinases (MMPs) such as MMP2, MMP3, and MMP9, and suppression of protease inhibitors such as tissue inhibitor of metalloproteinase-2 (TIMP2). BM degradation is followed by migration of an endothelial tip cell from the leading edge of a vascular sprout; this leading edge defines the direction of the newly growing sprout [2, 6, 7].

6.2.2 Endothelial Cell Branching and Proliferation

High levels of proangiogenic factors (such as VEGFA and VEGFC) and of VEGF receptor 2 (VEGFR2) or VEGFR3 signaling select “tip cells” (TCs) for sprouting during angiogenesis. By contrast, Delta-like 4-notch signaling laterally inhibits TC fate in adjacent ECs. TC sprouting behavior is facilitated by the vascular endothelial cadherin-mediated loosening of EC–EC junctions, matrix metalloproteinase-mediated degradation of ECM and the detachment of pericytes. Guidance of TC sprouting is due to the gradients of proangiogenic growth factors and various environmental guidance cues, such as semaphorins and ephrins. During sprout elongation, TCs are trailed by endothelial “stalk cells” (SCs), which maintain connectivity with parental vessels and initiate partitioning-defective3 (PAR3)-mediated vascular lumen morphogenesis. Expression of VEGFR1 and activation of

notch, Roundabout homologue 4 and WNT signaling in SCs repress TC behavior to maintain the hierarchical organization of sprouting ECs. However, TCs and SCs may also shuffle and exchange positions during angiogenic sprouting. Upon contact with other vessels, TC behavior is repressed and vessels fuse by the process of anastomosis, which is assisted by associated myeloid cells. The ECs adjacent to the tip cells begin to proliferate and elongate to form capillary sprouts, which then assemble to form a vessel lumen. After the activation and proliferation stages, a nascent blood vessel must mature to become functional [6–11].

6.2.3 Stabilization of Immature Vasculature

After the activation and proliferation stages, a nascent blood vessel must mature to become functional. The nascent vessels are stabilized by recruiting mural cells and by deposition of an ECM, in a process known as arteriogenesis. There are at least four molecular pathways that regulate this process, including the following:

1. Platelet-derived growth factor PDGFB and PDGF receptor (PDGFR)- β .
2. Sphingosine-1-phosphate-1 (S1P)-endothelial differentiation sphingolipid G-protein-coupled receptor-1 (EDG1).
3. Ang1-Tie2.
4. Transforming growth factor TGF- β 1.

Recruitment of mural cells such as pericytes and smooth muscle cells (SMCs) to the developing immature vasculature by platelet-derived growth factor B (PDGFB) and transforming growth factor- β 1 (TGF- β 1) stabilize the vessel wall [2, 7, 12, 13]. The contact between ECs and mural cells is strengthened by bioactive lipid sphingosine 1 phosphate (S1P) through activating the guanine nucleotide-binding-coupled receptor, and S1P receptor 1 (S1PR1 or EDG1) signaling [7, 14]. Tie receptors (Tie1 and Tie2) and their ligands Ang1 and Ang2 are also critical for vessel formation and stabilization. Main sources of Ang1 and Ang2 are the mural cells and ECs, respectively. Ang1 stabilizes nascent vessels by facilitating communication between ECs and mural cells. Ang2 acts as an antagonist of Ang1 in the absence of VEGF and destabilizes vessels in the presence of VEGF [15].

TGF- β 1 is a multifunctional growth factor that promotes vessel maturation by stimulating ECM production and by inducing differentiation of mesenchymal cells to mural cells. It is expressed in a number of cell types, including ECs and mural cells, and depending on the context and concentration, could be pro- or anti-angiogenic. Recent in vitro studies indicate that the TGF- β 1–ALK1 pathway is a positive regulator of endothelial cell migration and proliferation by inducing ECs and fibroblasts to express Id1, a protein required for proliferation and migration. On the other hand, the TGF- β 1–ALK5 pathway is a positive regulator of vessel maturation by inducing the plasminogen activator inhibitor (PAI1) in ECs. PAI1

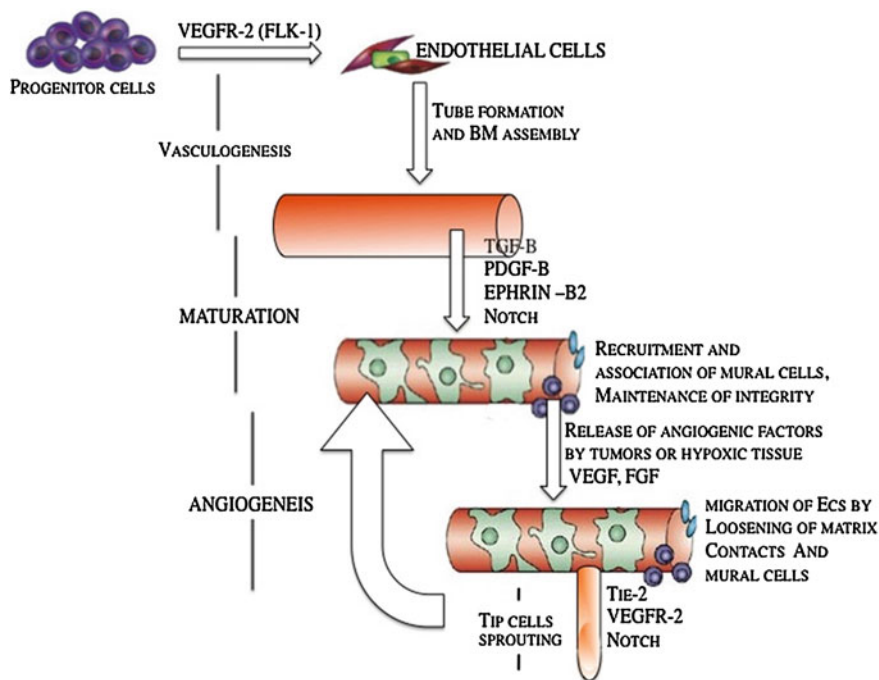


Fig. 6.2 Schematic of important signaling molecules that are involved in vasculogenesis, maturation of blood vessels, and angiogenesis, modified from Ref. [6]

promotes vessel maturation by preventing degradation of the provisional matrix around the nascent vessel. Thus, the degree to which TGF- β signals through ALK1 versus ALK5 can determine the pro- or anti-angiogenic effect of TGF- β [2, 10]. Figure 6.2 shows important signaling molecules that are involved in vasculogenesis, maturation of blood vessels and angiogenesis.

6.2.3.1 Role of Basement Membrane in Stabilization of Immature Blood Vessels

As mentioned earlier, BM degradation happens during the complicated multistep angiogenesis process. Direct contact between the BM and the EC layer provides important signals that control the stability of EC layer and facilitate EC tube stabilization. Vascular basement membrane matrices are largely composed of structural components, including laminin (particularly laminin IV), collagen IV, and fibronectin. Other proteins provide bridging functions such as nidogens 1 and 2, and the heparan sulfate proteoglycan perlecan, which facilitate the co-assembly of BM components [16–18]. It has long been known that ECs have the capacity to synthesize most if not all of these proteins, so it was generally assumed that BM

assembly occurred through ECs alone. However, in a variety of tissues, most notably the skin, it is clear that BM assembly requires more than keratinocytes and was strongly stimulated by the presence of fibroblasts in collagenous matrices underlying the keratinocyte layer. Thus, by analogy with these findings, it is likely that vascular basement membrane assembly may require heterotypic cell–cell contacts, which was originally suggested by Davis and Senger [19]. A recent study by Stratman et al. demonstrates that pericyte recruitment to EC-lined tubes *in vitro* and *in vivo* is necessary to stimulate vascular basement membrane matrix assembly, a key step in vascular maturation and stabilization [20].

Collectively, the matrix serves as a store for various growth factors and proenzymes involved in vessel development. The balance between proteases (such as MMP2, MMP3, MMP9, and urokinase plasminogen activator) and their inhibitors (such as tissue inhibitors of metalloproteinases and PAI1) controls BM and ECM degradation and could influence EC and mural cell migration [7, 20, 21]. These proteases also lead to the release of various proangiogenic growth factors, such as VEGF and basic fibroblast growth factor (bFGF), which are sequestered in the matrix. Protease activity can also generate anti-angiogenic molecules by cleaving plasma proteins (such as angiostatin from plasminogen), matrix molecules (such as tumstatin from collagen type IV), or the proteases themselves (such as PEX from MMP2). Thus, branching patterns of vessels are tightly regulated by spatial and temporal concentration profiles of growth factors and protein fragments that transport and bind to the matrix [2, 4].

6.3 Sources of Endothelial Cells and Their Progenitors

One potential source of ECs are embryonic stem cells, which are pluripotent and thus capable of differentiating into all cell types of the endoderm, ectoderm, and mesoderm. Although ESCs have the advantages of greater proliferative capacity and pluripotentiality when compared to other endothelial cell precursors, these properties also raise a concern. Specifically, the inadvertent administration of an undifferentiated (and thus pluripotent) ESC to a patient would risk teratoma formation. Accordingly, the clinical development of this cell therapy will require robust differentiation and purification protocols, supported by data showing the safety of these cells. The therapeutic use of these cells is further complicated because they are allogeneic and therapeutic engraftment may require immunosuppression, which carries additional risk. Finally, the clinical use of these cells may be influenced by the ethical debate surrounding the isolation of cells from human embryos. Accordingly, there is great interest in a new form of pluripotential cell that can obviate some of these concerns. Induced pluripotent stem cells (iPSCs) can be “reprogrammed” from adult somatic cells using a variety of methods, established primarily by Yamanaka and Thomson. iPSCs have the potential to generate patient-specific tissues for disease modeling and regenerative medicine applications. However, before iPSC technology can progress to the

translational phase, several obstacles must be overcome. These include uncertainty regarding the ideal somatic cell type for reprogramming, the low kinetics and efficiency of reprogramming, and karyotype discrepancies between iPSCs and their somatic precursors. In this section, we describe different sources of ECs and common endothelial cell markers that have been investigated so far by researchers, from embryonic and iPSCs to adult cells.

6.3.1 Embryonic Stem Cell-Derived Endothelial Cells

- *From Embryoid Bodies (EB)*

Mouse embryonic stem cells (mESCs) can differentiate into hemangioblasts after forming embryoid bodies (EBs). Hemangioblasts that form blood islands contain endothelial and haematopoietic progenitors [22]. Formation of a vessel-like network is the result of further differentiation of the EBs [23]. Moreover, it has been shown that endothelial cell markers differentiated from EBs are expressed in the same order that is expressed in endothelial differentiation during embryonic development [24].

During human EB differentiation, endothelial cell markers such as CD31, CD34, VE-cad, and GATA-2 show increasing trends in their expression [25, 26]. CD31, CD34, and VE-cad reach a maximum at days 13–15 and GATA-2 around day 18. Other endothelial markers such as VCAM1, FLT-1, FLT-2; vasculogenic growth factors such as VEGF, Ang1, Ang2, and PDGF; and transcription factors such as GATA1 and GATA3 are up-regulated as well [27]. Like mouse ESCs, human ESCs (hESCs) can spontaneously differentiate and organize within EBs into three-dimensional vessel-like structures, in a pattern that resembles embryonic vascularization. The capillary area in the human EBs increases during subsequent maturation steps, starting from cell clusters that later sprout into capillary-like structures and eventually organize in a network-like arrangement. These isolated CD31⁺ cells from human EBs (days 13–15), express endothelial markers and can form vascular tubes in vitro and in vivo [28].

- *On feeder layer and ECM*

Seeding ES cells on feeder cells or within an ECM can also induce differentiation into haematopoietic and endothelial lineages. For example, mouse endothelial progenitors (Flk-1⁺ cells) were isolated following the differentiation of ESCs on collagen. The isolated Flk-1⁺ cells in mouse systems are precursors for haematopoietic, endothelial, and SMCs and can also give rise to contracting cardiac cells, thus acting as cardiohemangioblasts [29, 30]. Culturing of human embryonic stem cells (hESC) on collagen IV resulted in two types of cell population that differ by size. The smaller cell population showed an upregulation of specific endothelial markers, such as CD31, CD34, Tei2, and GATA2. Cord-like organization of the cells (20 % ECs) was observed by re-plating the smaller population of cells on collagen IV with VEGF supplementation.

Moreover, addition of PDGFB induced differentiation into SMCs [31]. Seeding hESCs on stromal feeder cells (bone marrow and yolk sac) could lead to differentiation into CD34⁺ cells (1–2 %). Interestingly, about 50 % of the CD34⁺ cells also express CD31. The CD34⁺ cells were isolated and differentiated into haematopoietic cells [32].

6.3.2 Adult-Derived Endothelial Cells

Human umbilical vein endothelial cells (HUVECs) show relatively higher proliferative potential among the isolated CD31⁺ ECs that originate from veins and arteries of different tissues [28]. Isolation of CD34⁺ and Flk-1⁺ cells from peripheral blood using magnetic beads is another source of adult ECs [16]. These isolated progenitor cells could differentiate into ECs and incorporate into neo-vascularization sites in mouse and rabbit hindlimb ischemic models [34]. CD34⁺ cells, mobilized from the bone marrow following treatment with granulocyte macrophage colony stimulating factor, improved ventricular function and neoangiogenesis in ischemic nude rat myocardium [35]. CD133⁺ cells purified from bone marrow were also shown to enhance human myocardial perfusion and global function [36]. Another important source of adult ECs is the umbilical cord blood, which contains more CD133⁺ and CD34⁺ cells than adult peripheral blood and has higher proliferation capacity [37].

6.3.3 Induced Pluripotent Stem Cell-Derived Endothelial Cells

Yamanaka et al. have shown systematic differentiation of cardiovascular cells from mouse iPSCs. Induced pluripotent stem (iPS) cells were generated from mouse skin fibroblasts by introducing four transcription factors (Oct3/4, Sox2, Klf4, c-myc), and then, the same approach was applied on ES cells to induce cardiovascular differentiation. They showed that Flk1⁺ cells could differentiate into artery, vein, and mural cells [38]. Rufaihah et al. have differentiated human iPSCs (hiPSCs) into endothelial cells (hiPSC-ECs) to assess their ability to improve perfusion in a murine model of peripheral arterial disease [39, 40]. In brief, endothelial differentiation was initiated by culturing hiPSCs for 14 days in differentiation media supplemented with bone morphogenetic protein 4 and VEGF. They purified the heterogeneous mixture of cells by FACS using an antibody directed against CD31. The purified hiPSC-ECs generated capillary-like structures when grown in Matrigel and incorporated acetylated-LDL cholesterol. These cells expressed endothelial markers such as FLK-1 (KDR), CD31, CD144, and eNOS. When exposed to hypoxia, the hiPSC-ECs produced angiogenic cytokines and growth factors. Subsequently, they transduced the cells with a double-fusion

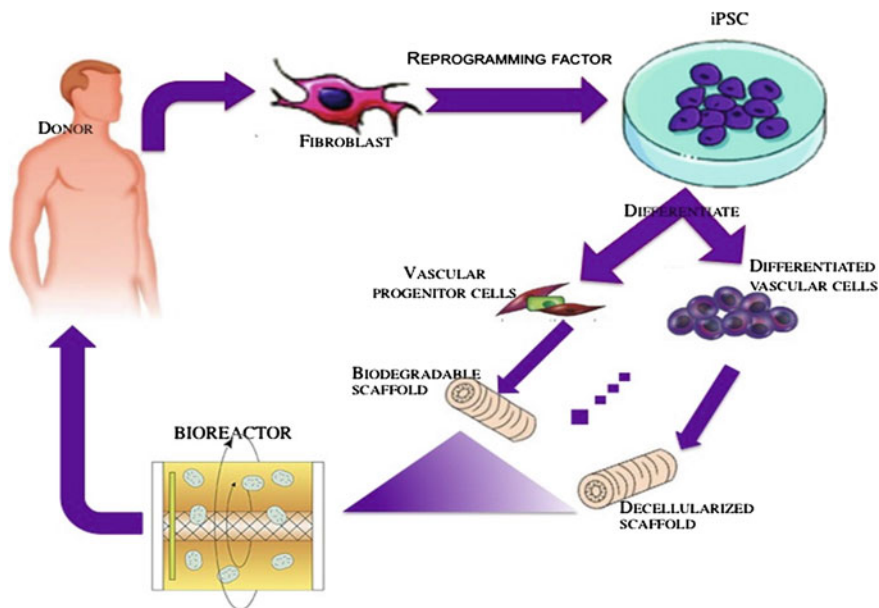


Fig. 6.3 Development of therapeutic cells from human-induced pluripotent cells

construct comprising firefly luciferase for BLI and green fluorescence protein for histochemistry. The hiPSC–ECs were administered on days 0 and 7 after femoral artery ligation into the ischemic hindlimb of immunodeficient mice. Over a two-week period, BLI revealed reduction of cells, but some hiPSC–ECs survived in the ischemic limb for at least 2 weeks. At that time, and for up to 4 weeks, perfusion was improved by over 30 % by comparison to the vehicle-treated group, as assessed by laser Doppler imaging. This effect was associated with a 60 % increase in the total number of capillaries in the ischemic limb of mice receiving hiPSC–EC injections by comparison to the vehicle-treated group. This preclinical work provided proof-of-concept for the use of hiPSC–EC in peripheral arterial disease [41].

Figure 6.3 shows development of therapeutic cells from human-induced pluripotent cells. Readily accessible somatic cells (e.g., skin fibroblasts) are harvested from a patient and expanded in culture. Cells are exposed to reprogramming transcriptional factors, in the form of cell permeant peptides and modified mRNA. The resulting iPSC colonies are differentiated into vascular progenitor cells, that are administered directly to patients with vascular disease, or which are incorporated into matrices as a biological conduit such as cylindrical bioengineered matrix or decellularized cadaveric vessels for surgical implantation. These bioengineered conduits would serve to replace autologous saphenous vein in patients that have insufficient or diseased veins [41].

6.4 Engineering Blood Vessels from Stem Cell-Derived Endothelial Cells: Recent Advances and Applications

In the last three sections, we introduced the structure of blood vessels, important cell signaling molecules in vasculogenesis/angiogenesis, and different cell sources for ECs. Now, we will describe the tissue engineering approaches available for making macrovessels and microvessels.

6.4.1 Approaches to Macrovesel Tissue Engineering (e.g., Heart Valve)

The approaches to engineer macrovessels can be divided into several distinct categories, although there may be some overlapping features. Successful application of these approaches, either individually or in combination, is expected to enhance therapeutic opportunities by building functional tissue and organ systems for regenerative medicine.

1. Formation of a tissue *in vitro* by seeding cells on a biodegradable scaffold and maturing a tissue (to be implanted *in vivo*) in a bioreactor.
2. Cell-seeded natural biodegradable scaffolds.
3. Guided tissue regeneration via implanted degradable tissue that is remodeled by endogenous cells.
4. Implantation of decellularized valvular material.
5. Other approaches such as microfabrication techniques and scaffold-free approaches.

In all of the mentioned approaches, choosing the right cell among the spectrum of stem cells to differentiated cells and also the right scaffold is of utmost importance [42]. The scaffold should provide the initial requisite mechanical strength to withstand *in vivo* hemodynamic forces until vascular SMCs and fibroblasts reinforce the ECM of the vessel wall. Hence, the choice of scaffold is crucial for providing guidance cues to the cells to behave in the required manner to produce tissues and organs of the desired shape and size. Several types of scaffolds have been used for the reconstruction of blood vessels. They can be broadly classified as biological scaffolds, decellularized matrices, and polymeric biodegradable scaffolds. A review written by Pankajakhshan et al. focuses on the different types of scaffolds that have been designed, developed, and tested for tissue engineering of blood vessels [43].

6.4.1.1 Bioreactor Approach

The bioreactor approach should provide a desirable physiological, metabolic, and mechanical environment for blood vessel formation *in vitro*. To develop well-developed and effective construct for implantation and remodeling one approach would be to optimize the cellular component, the scaffolds, and the *in vitro* process conditions. Novel scaffolds are also under investigation. Multiple studies have emphasized that dynamic conditioning using bioreactors that provide a flow regime that mimics that of the intended application enhances construct tissue properties [44, 45]. Oxygen tension might be a key parameter for the achievement of sufficient tissue quality and mechanical integrity in tissue-engineered heart valves [46, 47]. A mesenchymal stem cell-seeded, valve-shaped construct has been assembled from layered collagenous scaffolds. Autologous fibrin-based engineered heart valves showed favorable results both *in vitro* and *in vivo* [48, 49]. Culturing vascular cells on polymer scaffolds and subjecting the scaffold to pulsating flow is another approach that is studied by Niklason et al. [50]. In fact, they seeded bovine aortic SMCs into hollow tubular polyglycolic acid (PGA) scaffolds and then injected bovine aortic ECs into the lumen. Compared with native arteries, the engineered arteries demonstrate similarities in wall thickness and collagen content after eight weeks of culture in a bioreactor. A key issue moving forward will be the real-time noninvasive and nondestructive assessment of mechanical properties of engineered heart valves both *in vitro* and utilization of such techniques *in vivo* to ensure quality.

6.4.1.2 Decellularized Vascular Material

Removal of all viable cells while preserving the ECM integrity is the goal in producing decellularized xenogeneic tissue. This method provides valuable material for heart valve tissue engineering. Decellularized materials have the advantage of preserving ECM components that may support cell adhesion and molecular sequestering, as well as desirable mechanical properties. However, ECM disruption by the decellularization process and immunogenicity are concerns inherent in the use of decellularized ECMs. For instance, decellularization resulted in substantial microscopic disruption of the ECM, which may negatively impact the durability of heart valve leaflets [51]. Moreover, evaluation of the relative immune responses of different valve components of decellularized porcine aortic valve compared with native and glutaraldehyde fixed valves showed that collagen I elicited a strong response but elastin induced a minimal response [52]. Recellularization of these valves has been reported in an aortic valve replacement model in juvenile pigs [53]. Another study investigated the function, histological changes, potential of *in vivo* re-endothelialization of decellularized aortic valve allografts in orthotopic position in sheep. The valves exhibited trivial regurgitation and normal morphology with no signs of graft dilatation, degeneration, or rejection [54]. Toxicity that is introduced to scaffold by the chemicals used in the decellularization process is another concern in decellularized natural ECMs. A clinical study investigated the safety and

effectiveness of the Ross procedure (pulmonary to aortic valve autograft) using a decellularized, fibronectin-coated pulmonary valve allograft or xenograft seeded with autologous vascular ECs from a forearm or saphenous vein to reconstruct the right ventricular outflow tract. These valves showed excellent hemodynamic performance during midterm follow-up [55]. In contrast, recurrent right-sided heart failure after the Ross procedure was reported in a study done by Hiemann et al. [56].

6.4.1.3 Cell-Seeded Natural Biodegradable Scaffold

The cell-seeded natural biodegradable scaffold approach involves isolating and growing ECs on polymer scaffolds *in vitro*, followed by *in vivo* implantation. This method has been tested in an ovine model, where expanded pulmonary arterial cells were grown on polyglactin/poly (lactic-co-glycolic acid) tubular scaffolds for one week before transplantation into pulmonary arteries of lamb. Over a period of 24 weeks, the vascular grafts showed growth and development of endothelial lining and the production of ECM components, such as collagen and elastin fibers [57].

6.4.1.4 Microfabrication Technique

Another approach for the *in vitro* induction of endothelial networks in engineered tissue constructs is to prefabricate scaffolds to include channels that later could be lined with ECs. Microfabrication techniques are currently under way to engineer such network structures that will mimic the capillary network, expanding from a main vessel (like arteries), and merging back to a single vessel (like veins). In such systems, endothelial cells are seeded into the channel network and their attachment and behavior under flow are analyzed. Inkjet printing can be used to pattern cells into tubular structures. This technique, as well as other cell-printing techniques such as laser-guided direct writing, could be used in the future for the assembly of complex vascularized tissues. In one such approach, Tien and coworkers developed a method to prefabricate hollow channels within collagen gels. ECs were then seeded along the interior of the channel such that they formed a vessel-like structure that permitted flow of solution through the tube lumen. The authors demonstrated endothelial barrier function and appropriate barrier breakdown upon exposure to inflammatory cytokines [58].

6.4.1.5 Cell-Synthesized ECM-Scaffold-Free Approach

Although biomaterials-based solutions are promising, there are challenges that need to be solved. Some of the key issues that may affect the long-term behavior of the engineered tissue construct, and directly interfere with its primary biological function, are scaffold choice, immunogenicity, degradation rate, toxicity of degradation products, host inflammatory responses, fibrous tissue formation due to

scaffold degradation, and mechanical mismatch with the surrounding tissue. To address these problems, fabrication techniques for production of scaffold-free engineered tissue constructs have recently emerged. Norotte et al. reported a fully biological self-assembly approach, which was implemented through a rapid prototyping bioprinting method for scaffold-free small-diameter vascular reconstruction. Various vascular cell types, including SMCs and fibroblasts, were aggregated into discrete units, either multicellular spheroids or cylinders of controllable diameter (300–500 μm). These were printed layer-by-layer concomitantly with agarose rods, used as a molding template. A unique aspect of the method is the ability to engineer vessels of distinct shapes and hierarchical trees that combine tubes of distinct diameters. The technique is rapid and scalable [59].

In another study done by L'Heureux et al. the SMCs and fibroblasts were cultured in medium containing sodium ascorbate for increased ECM deposition. After 1 month of *in vitro* culture, the sheet of SMCs in their own ECM was wrapped around a tube, covered with a sheet of fibroblasts in their own ECM, and then, the luminal surface was seeded with ECs. This construct reportedly had burst strength of over 2,000 mm Hg. In addition, the SMCs expressed desmin, and the ECs strongly inhibited platelet adhesion *in vitro*. However, when these grafts were implanted in dogs as a canine femoral arterial interposition graft, they had a patency rate of approximately 50 %. In addition, the grafts required 3 months for production. This approach has been further tested in three patients undergoing hemodialysis. The vessels constructed from autologous dermal fibroblasts and ECs were implanted as arteriovenous fistulas for dialysis access and were allowed to mature *in vivo* before use. During five months of implantation, no failures were observed, and the grafts functioned well. Although the results are encouraging, this approach requires long culture and maturation periods that would limit the application of these vessels in urgent cases [60, 61].

6.4.2 Approaches to Microvessel Tissue Engineering (e.g., Capillaries)

Incorporation of a microcirculation into engineered tissues presents multiple challenges, including the formation of microscale vascular conduits for blood flow, a functional endothelium that regulates vascular activity, and specialized cell types that perform the physiological function of the tissue of interest. Several approaches have been developed to address these challenges, including the following:

1. Incorporation of biomolecular cues within the material.
2. Seeding of vascular or vascular-inducing cells in the scaffold.
3. Use of microfabrication technologies to engineer branched microfluidic channels within biocompatible materials.

Here, we discuss each of the above-mentioned approaches in more detail.

6.4.2.1 Incorporation of Biomolecular Cues Within the Material

Growth factor incorporation in three-dimensional (3D) engineered tissues is crucial for angiogenesis and vascularization. In order to establish a functional microvascular network, coordinated delivery of several key factors such as VEGF, FGFs, PDGFs, TGFs, angiopoietins, ephrins, placental growth factors and various chemokines are beneficial. Presentation of a single factor such as VEGF is not typically sufficient to form functional conduits and can, in contrast, lead to induction of tortuous and leaky vessels. Thus, spatial and temporal regulation of growth factor signaling may help ensure accurate vessel growth and remodeling [62, 63].

The need for materials that could be chemically and mechanically tailored to incorporate and release bioactive molecule, while meeting biocompatibility and biodegradability standards, has led to further use of hydrogels as scaffolds for engineered tissue constructs. Hydrogels are hydrated materials made from a cross-linked network of hydrophilic polymers. The integration of factors that induce rapid endothelial cell ingrowth and that stabilize the vascular network as it forms could support the success of these hydrogels [6]. We discuss growth factor-releasing hydrogels and protease-sensitive hydrogels in [Tissue Engineering Approaches to Deliver Growth Factors](#) and [Protease-Sensitive Hydrogels](#), respectively. ECM peptides that induce vasculogenesis/angiogenesis in hydrogels are discussed in [ECM Peptides Used in the Hydrogel Backbone to Induce Angiogenesis and Vasculogenesis](#). These discussions are followed by the effect of hydrogel stiffness and porosity on angiogenesis/vasculogenesis ([Hydrogel Stiffness and Porosity](#)).

Tissue Engineering Approaches to Deliver Growth Factors

Strategies for biomaterial presentation of growth factors in tissue engineering can be conceptually divided into two areas:

1. Chemical immobilization (covalent or noncovalent) of the growth factor into or onto the matrix; and
2. Physical encapsulation of growth factors in the delivery system.

The first approach typically involves chemical binding or affinity interaction between the growth factor-containing polymer and a cell or a tissue. The second approach is achieved by the encapsulation, diffusion, and pre-programmed release of growth factor from substrate into the surrounding tissue. There are several methods for each approach that are described in detail in a review by Mooney and coworkers [64].

Investigators have developed a wide range of ECM-mimicking biomaterials to immobilize growth factors or growth factor mimics, including hydrogels containing ligands from fibronectin, laminin, collagen, elastin or the GAGs heparin

sulfate, chondroitin sulfate, hyaluronic acid, or a variety of synthetic hydrogels [64]. In a study by Hubble and coworkers, a rationally designed combinatorial approach was used to discover a sulfated tetra-peptide that binds to VEGF. SY(SO₃)DY(SO₃) was identified as the top binder to VEGF, which mimics heparin binding to VEGF as a potential improvement over natural heparin [65]. Koch et al. similarly used a synthetic homo-bifunctional polymer cross-linker, disuccinimidyl disuccinate poly (ethylene glycol), to attach VEGF to collagen matrices [66]. PEG-ephrinA1 immobilized to hydrogel surfaces induced endothelial cell tubulogenesis with luminal diameters in the range of 5–30 μm , creating structures resembling early-stage capillaries [67]. In another study, PEG-VEGF not only increased endothelial cell tubulogenesis, but also increased endothelial cell motility 14-fold and cell–cell connections 3-fold in a three-dimensional, biodegradable hydrogel [68].

Saik et al. developed MMP-sensitive PEGDA hydrogels immobilized with ephrin A1 ligands, which stimulate a wide range of receptors that induce vascularization. The efficacy of ephrin A1 ligand conjugation was demonstrated 14 days after implantation, by comparing vascular network parameters such as vessel density, branch points of MMP-sensitive, PDGF-BB-containing PEGDA hydrogels with or without immobilized ligand. The biodegradable, bioactive hydrogels immobilized with ephrin A1 ligand produced a denser vasculature in the mouse cornea pocket relative to the nonligand-containing scaffold [69].

Transfecting cells to overexpress angiogenic growth factor genes is another way to promote prolonged, local growth factor delivery [70, 71]. In one example, mononuclear cells, which give rise to endothelial progenitor cells, were transfected to overexpress VEGF. Transfection with a VEGF-encoding gene stimulated their differentiation into ECs for vasculogenesis, while also enhancing local angiogenesis [70]. Myoblasts have also been transfected to express VEGF and bFGF to improve vascularity in engineered muscle tissue [72].

Protease-Sensitive Hydrogels

Cell-induced proteolysis is often required for 3D cell migration and invasion, because the porosity of the ECM may lead to barrier function and thus inhibit migration [73]. Whereas many synthetic biomaterials have been designed to degrade by ester hydrolysis, such nonenzymatic hydrolysis of matrices is not cell mediated and is less directly responsive to cell-mediated remodeling and tissue morphogenesis. Cell-induced proteolysis is a reciprocal interaction between ECM and the cells, as the ECM stimulates the cells and the cellular proteases remodel the ECM and release associated bioactive components from it. For example, Phelps et al. seeded NIH3T3 fibroblasts in poly (ethylene glycol)-diacrylate (PEGDA)-based degradable scaffold and incorporated some responsive elements, such as protease-labile cross-links, cell adhesive peptides, and conjugated VEGF. They demonstrated that both adhesive ligands and MMP-degradable sites were necessary for cells to spread. Furthermore, implantation of VEGF-conjugated

scaffolds into a mouse model of hindlimb ischemia resulted in rapid vascularization of the biomaterial that remained stable for at least 4 weeks [74].

Exciting progress has been made in mimicking the proteolytic recognition of natural ECMs in synthetic polymer gels. Protease-sensitive peptides can be categorized in two main general groups: Plasmin-sensitive peptides and MMP-sensitive peptides. For example, a fibrinogen-derived (R chain, residues L⁹⁴I¹¹⁹) peptide sequence that is combined with RGD cell adhesion site is a plasmin-sensitive peptide. (LRGDFSSANNR ↓ DNTYNR ↓ VSEDLRSRI, ↓ indicating the plasmin cleavage site) [75]. Alison et al. evaluated plasmin substrate sites reported in fibrinogen as potential substrate sites in the cross-linker peptide. After considering solubility and hydrophobicity and some other practical parameters, they came up with the engineered peptide sequence CYKNRDC. Because of a negative influence of the aspartate (D) residue on the reactivity of the cysteine © thiol toward vinyl-sulfone, this residue was eliminated from the final cross-linking peptide design [71].

Sequence (GGGPQG ↓ IWGQGK) is an MMP-sensitive peptide that can be incorporated in the backbone of the PEG block polymers with acrylate terminal groups, which allows cross-linking of precursors into networks. GGGPQG ↓ IWGQGK is a mutated version of $\alpha 1(I)$ collagen chain for increased degradation kinetics with various MMPs [76]. Anseth and coworkers incorporated a cysteine-containing bifunctional peptide, CPE ↓ NFFRGD into PEG hydrogels by thiol-acrylate photopolymerization. This peptide has the RGD motif for cell adhesion and the sequence of PENFF for MMP-13-sensitive cleavage [77]. The resulting hydrogels provided a platform that mimics the native upregulation and downregulation of cell adhesive proteins by the cell-secreted enzymes in the ECM for differentiating human mesenchymal stem cells (hMSCs). A review written by Zhu provides more information about other enzyme-sensitive peptides that have been used in the proteolytically degradable PEG hydrogel [78].

ECM Peptides Used in the Hydrogel Backbone to Induce Angiogenesis and Vasculogenesis

Cell adhesion to traditional biomaterials, such as polyethylene, polytetrafluoroethylene or silicone rubber, is based upon nonspecific adsorption of proteins from the body fluids to the material surface. A subset of these adsorbed proteins, including fibronectin, fibrinogen, and vitronectin, promote cell adhesion by interacting with the corresponding adhesion receptors on the cell surface. To achieve similar cell adhesion in a more well-defined synthetic context, several investigators have tested ECM protein-derived cell adhesive peptides as a component of biomaterials. These peptides are based on the primary amino acid sequence or structure of the receptor-binding domains of proteins such as fibronectin and laminin. Early work demonstrated an important possible advantage of working with short adhesion peptides, rather than the complete parent protein, as

the peptides could be displayed in a manner that enhanced peptide availability to cell-surface receptors [63]. Cell adhesive peptides are mainly derived from four ECM proteins, including fibronectin (FN) (e.g., RGD, KQAGDV, REDV and PHSRN), laminin (LN) (e.g., YIGSR, LGTIPG, IKVAV, PDGSR, LRE, LRGDN and IKLLI), collagen (e.g., DGEA and GFOGER), and elastin (e.g., VAPG). RGD is the most commonly used cell adhesive peptide, perhaps due to its long history of use and its effectiveness in promoting cell adhesion. RGD peptides are typically used in either linear (RGD) or cyclic (cRGD) form. Research has demonstrated that cRGD peptides have the advantage of increasing the affinity to integrin $\alpha_v\beta_3$ and enhancing biological activity up to 240 times in comparison with linear RGD analogues [79]. This enhanced effectiveness of cRGD is biomimetic, as the RGD sequence in the cell-binding domain of FN is exposed at the tip of a loop with a spatial constraint that results in increased affinity for cell binding. Thus, incorporation of cRGD peptides into PEGDA hydrogels can better mimic the native RGD loop structure and benefit cell adhesion [80].

In another study, Hubble et al. showed that within the adhesion protein fibronectin, the tetra-peptide REDV is a more specific ligand for integrin receptor $\alpha_4\beta_1$, which is present on the endothelial cell but not the blood platelet. It would be beneficial to use this specificity to develop vascular grafts that support endothelial cell adhesion and migration, while rejecting the adhesion of blood platelets [63].

Hydrogel Stiffness and Porosity

The physical properties of hydrogels can be regulated by the chemistry of the polymeric backbone, its hydrophilicity, polymer concentration, and cross-linking density. Increasing the cross-linking density and/or monomer concentration generally results in increased stiffness and reduced degradation rates because of a larger number of bonds that need to be cleaved during degradation of the material. The stiffness of hydrogels can be adjusted by varying the percentage of polymer used in the solution before the cross-linking procedure and can be controlled by adjusting the cross-linking agent and the cross-linking density during hydrogel formation. Increasing the number of bonds in the polymer also limits the ability of water molecules to diffuse in and out of the material. Thus, the degree of cross-linking of polymer networks can be used to tailor both the structural stability and the porosity of the material [81]. As a result, the degree of cross-linking is an important aspect in regulating the transport of solutes through hydrogel structures [82]. A recent study by West and colleagues showed that hydrogel stiffness affects the degree of endothelial tubule formation. In stiffer hydrogels, tubule formation was reduced and cell clusters remained short and rudimentary, as cells failed to migrate as much as they do in softer matrices [62]. Ghajar et al. studied the effect of matrix density on the regulation of 3D capillary morphogenesis and demonstrated a key role for both matrix stiffness and ligand density [83].

6.4.2.2 Seeding of Vascular or Vascular-Inducing Cells in the Scaffold

Encapsulation of ECs and supporting cells within biomaterials are common strategies that have attracted a great deal of attention. This encapsulation strategy benefits from cell signaling, differentiation, and migration as well as the dynamic interactions between cells that provide the biochemical environment beneficial for the ensuing tissue remodeling. For example, to mimic skin tissue vascularization, Black et al. co-cultured HUVECs, human-derived fibroblasts and keratinocytes (skin cells) housed within a collagen-based scaffold [84]. Biochemical coordination between the ECM generated by the fibroblasts and growth factors such as VEGF and TGF- β secreted by neighboring cells in the presence of HUVECs promoted the development of a vascular network both *in vitro* and in a mouse model [85, 86]. Furthermore, recent studies highlight the benefits gained from the addition of epithelial cells—those that line the body cavities such the gut and lungs—to stabilize and regulate the size and formation of capillaries within the vascularized model. Thus, various cell types can play complementary roles in tailoring vascularization.

The idea of implanting a co-culture of ECs with ECM-forming fibroblasts or bone-forming osteoblasts *in vivo* was validated by Alajati et al. HUVECs and osteoblasts were encapsulated within a scaffolding material composed of VEGF and FGF-2 in Matrigel (a murine tumor-derived ECM), fibrin, and thrombin, and the biomaterial was implanted subcutaneously in a severe combined immunodeficiency (SCID) mouse model for up to 20 days. The result was a durable perfused vascular network *in vivo* [87]. In another study, HUVECs were used to promote the human MSC differentiation into an endothelial lineage, promoting the formation of 3D vascular structures for up to 2 weeks in a Matrigel-based ECM [88]. A mature vascular network was also formed by combining HUVECs and human MSCs in a polymeric scaffold *in vivo* 4–7 days after implantation, thus accelerating the functional remodeling of the implant when used as a bone graft [89].

All in all, the scaffold is a crucial component that regulates the dynamic vascularization process. Scaffolds used in this area are either natural biodegradable materials, such as collagen and Matrigel, or synthetic biodegradable scaffolds, such as poly-L-lactic acid (PLLA) or poly-D,L-lactic-co-glycolic acid (PLGA). However, because of shortcomings seen in their mechanical strength, durability, immunogenicity, and other application-specific requirements, researchers continue to develop more suitable scaffolds for endothelial-cell-based vascularization for specific applications.

6.4.2.3 Use of Microfabrication Technologies to Engineer Branched Microfluidic Channels Within Biocompatible Materials

Microengineered scaffolds containing channels can be used to seed ECs to form a confluent endothelium on the walls of the vascular channels [90]. Microengineering techniques can be categorized into two different groups based on the

dimensionality of the produced structures: (1) *techniques that produce planar structure* such as photolithography and molding; and (2) *techniques that produce 3D structure* such as direct ink writing and omnidirectional printing. Photolithography is a process that uses light illumination through a mask to generate structures from light-sensitive materials, while molding is a process that uses a hollowed-out pattern to which a deposited material conforms. Photolithography and molding are both planar. A 3D structure can result from stacked 2D structures that comprise channels with rectangular cross sections instead of channels with circular cross sections [6]. Raghavan et al. developed a novel approach to control endothelial tubulogenesis by spatially patterning cells within micromolded collagen gels. ECs cultured within microscale channels that were filled with collagen hydrogel organized into tubes with lumens within 24–48 h of seeding. These tubes extended up to 1 cm in length and exhibited cell–cell junction formation characteristic of early-stage capillary vessels [91]. In another study, a 3D tissue construct composed of endothelialized hollow vascular structures was produced using a self-assembled monolayer (SAM)-based cell deposition technique and a hydrogel photocross-linking method to provide a robust hydrogel-based scaffold for endothelial cell attachment [92].

Direct ink writing and omnidirectional printing within a gel reservoir can create 3D vascular structures in vitro. In a recent study by Chen et al., a printing approach was used to generate a micropatterned sugar-based sacrificial layer around which cell-laden hydrogels could be built. The sugar-based layer was then dissolved, creating a 3D microarchitecture consisting of microvascular networks. Moreover, Chrobak et al. validated the hypothesis that the existent flow and shear conditions within such microscale channels are favorable for endothelium sustainability [58].

Zheng and co-workers created microvessels that replicated some aspects of angiogenesis using silicone molds together with casting gels made out of collagen. The researchers report that the microvessels were lined with continuous endothelium and did not leak. Moreover, when activated with appropriate biochemical signals, the vessels produced new branches and recruited mural cells, which normally associate with blood vessels and affect their functions. As such, the device not only allows the researchers to shape the network, but also permits the biological elements (cells and their products) to reshape or remodel the system dynamically [90]. Despite these substantial advances, new technologies are required to more accurately recreate the complexity of native tissues and enable formation of robust, functional microcapillary networks [93].

6.4.3 Mechanisms for Connecting MicroVessels to MacroVessels

The in vitro formation of mature vessel networks ready to anastomose with the host vasculature shortly after implantation has the potential to dramatically improve the rate of oxygen and nutrient delivery and waste product removal and

thus increases the viability of larger implanted tissues. Rapid (~ 1 day) anastomosis of engineered vessels with host vasculature is likely necessary for the survival and function of tissue specific cells, especially for oxygen-sensitive cells such as cardiomyocytes, hepatocytes, and various stem cells, all of which are of tremendous interest in the field of regenerative medicine [94]. Limited studies suggest that during embryonic vasculogenesis and angiogenesis, anastomosis is accomplished via connection of extended cellular processes followed by lumen propagation through intracellular and intercellular vacuole fusion, with macrophages playing an accessory role. However, it is not known whether this is the only mechanism for connecting vessels. Without a basic understanding of the cellular mechanisms of anastomosis, it is difficult to develop strategies for accelerating this critical step for perfusing engrafted tissues [95]. This section will describe the different mechanisms that are involved in anastomosis, based on a limited range of insights published to date in this area.

6.4.3.1 Engineered Blood Vessel Networks Connect to Host Vasculature via Wrapping-and-Tapping Anastomosis

Cheng et al. showed that implanted vascular networks anastomose with host vessels through a previously unidentified process of “wrapping and tapping” between the engrafted ECs and the host vasculature. At the host-implant interface, implanted ECs first wrap around nearby host vessels and then cause BM and pericyte reorganization and localized displacement of the underlying host endothelium. In this way, the implanted ECs replace segments of host vessels to divert blood flow to the developing implanted vascular network. The process is facilitated by high levels of matrix metalloproteinase-14 and matrix metalloproteinase-9 expressed by the wrapping ECs. These findings open the door to new strategies for improving perfusion of tissue grafts and may have implications for other physiological and pathological processes involving postnatal vasculogenesis. They found that tip cell connections and vacuole fusion were not integrally involved in host-implant vascular anastomosis, but instead, the engrafted endothelial networks wrapped around host vessels at the host-implant interface and then replaced sections of the underlying vessel wall to tap into the host blood supply [95].

6.4.3.2 Tensional Forces in the Collagen Matrix Control Directional Capillary Sprouting and Anastomosis

Formation of capillary anastomoses is associated with tensional remodeling of the collagen matrix and directional sprouting of outgrowing capillaries toward each other. To analyze whether directional sprouting is dependent on cytokine gradients or on endothelial-cell-derived traction forces transduced through the ECM, Korff and Augustin designed a matrix tension generator that enables the application of defined tensional forces on the ECM. Using this matrix tension generator, causal

evidence is presented that tensional forces on a fibrillar ECM such as type I collagen, but not fibrin, were sufficient to guide directional outgrowth of endothelial cells [96].

6.4.3.3 High Density of Co-transplanted Fibroblasts Promote Rapid Anastomosis of Endothelial Progenitor Cell-Derived Vessels with Host Vasculature

Chen et al. have shown that both endothelial progenitor cell-derived endothelial cells (EPC–ECs) and a high density of fibroblasts significantly accelerate the rate of functional anastomosis, and that pre-vascularizing an engineered tissue may be an effective strategy to enhance transport of nutrients *in vivo*. In this study, Chen et al. developed three-dimensional engineered vessel networks *in vitro* by co-culture of ECs and fibroblasts in a fibrin gel for 7 days. Vessels formed by cord blood EPC–ECs in the presence of a high density of fibroblasts created an interconnected tubular network within 4 days, compared with 5–7 days in the presence of a low density of fibroblasts. Vessels derived from human umbilical vein ECs (HUVECs) *in vitro* showed similar kinetics. Implantation of the pre-vascularized tissues into immune-compromised mice, however, revealed a dramatic difference in the ability of EPC–ECs and HUVECs to form anastomoses with the host vasculature. Vascular beds derived from EPC–ECs were perfused within 1 day of implantation, whereas no HUVEC vessels were perfused at day 1. Further, while almost 90 % of EPC–EC-derived vascular beds were perfused at day 3, only one-third of HUVEC-derived vascular beds were perfused. In both cases, a high density of fibroblasts accelerated anastomosis by 2–3 days [94]. This study and others described above emphasize the critical need to select suitable cell types and engineer surrounding microenvironments that optimize vascular network formation and anastomosis with the host *in vivo*.

6.5 Challenges for Future Translation of Engineered Tissue Vessels to the Clinic

Balloon angioplasty, stent placement, graft bypass surgery, and use of pharmacological agents are current treatment options for vascular diseases. Vascular grafts that are being used in patients can be divided into three categories, in order of decreasing diameter. Large- and medium-caliber synthetic grafts are used in the thoracic and abdominal cavities with good long-term outcomes. Almost 1,200,000 small-caliber grafts (<6 mm) are used every year for vascular access, to relieve lower limb ischemia and for coronary bypass surgery. Autologous veins or arteries are being used to replace small-caliber arteries, but in 30–40 % of patients these are not available due to prior harvesting or preexisting conditions. Using synthetic

grafts, which provide poor outcomes, is often the only option left for those patients. It is reported that $\sim 50\%$ of these synthetic grafts will occlude within 5 years, potentially leading to amputation [97].

Considering the need for vascular graft that is been estimated to be about 1.4 million in the US alone [98], there is a need for engineered blood vessels that are nonthrombogenic, withstand adequate burst pressure, show appropriate remodeling responses and are vasoactive [99]. Thus, for successful clinical translation of biomaterials that we discussed in Sect. 6.4, it is essential that researchers identify parameters that can be controlled to promote and regulate angiogenesis and vasculogenesis. The long-term in vivo function of various engineered vascular networks and tissue-engineered vessels still need to be further investigated.

Moreover, it is important that the engineered tissue vessels elicit the least inflammatory response. Ideally, a tissue-engineered vessel should not be immunogenic, nor should it induce thromboembolic complications or excessive and prolonged inflammation. Unfortunately, few biomaterials exist which can be considered biologically inert. For example, Teflon[®] (expanded polytetrafluoroethylene; ePTFE) and Dacron (polyethylene terephthalate—PET) vascular grafts function well in large-diameter graft applications without endothelial cell coverage but when used in peripheral applications, one half of these grafts occlude within the first five years of implantation [52, 97]. Moreover, preexisting pathology or existing risk factors could affect the long-term success of the implants. For example, implantation of a vascular graft in an atherosclerosis-prone patient results in decreased patency. So designing new approaches that account for the pathological status of the tissue, organ, or patient on the engineered tissue vessel could increase the rate of translational success of tissue-engineered vessels [97, 100].

It is also important to keep in mind efforts to link in vivo with in vitro research successfully in tissue engineering. In vitro culture of tissues and vascular cells provides the basis for our understanding of endothelial cell biology, cell-shape regulation, and blood vessel responses to physical forces. However, most in vitro models lack the three-dimensional complexity, blood flow, cell–cell interactions, and proper extracellular (matrix) environment that are typical of living tissues [101]. In vitro systems that more faithfully mimic the “context” of the native vasculature may lead to more informative in vitro studies.

After an initial period of hype and hope, we are now closer to clinical application. The prospects of using scaffolds, cells, and biochemical or biomechanical stimuli to create functional tissues such as valves and arteries are a power previously unimaginable. However, critical challenges remain for translation of blood vessel tissue engineering strategies. While the field continues to address these challenges, and to further understand the intricate biology of the endothelium, novel biomaterials and cell sources will be critical. In view of emerging advances in biomaterials synthesis/design and stem cell biology, tissue-engineered blood vessels at both the macroscale and the microscale may soon impact thousands of patients in need of tissue regeneration and repair.

References

1. Carmeliet P (2000) Mechanisms of angiogenesis and arteriogenesis. *Nat Med* 6(4):389–395
2. Jain RK (2003) Molecular regulation of vessel maturation. *Nat Med* 9(6):685–693
3. Maton A (1994) *Human biology and health*, 3rd edn. Englewood Cliffs, Prentice Hall, New Jersey
4. Ruoslahti E, Engvall E (1997) Integrins and vascular extracellular matrix assembly. *J Clin Invest* 99(6):1149–1152
5. Kelleher CM, McLean SE, Mecham RP (2004) Vascular extracellular matrix and aortic development. *Curr Top Dev Biol* 62:153–188
6. Bae H, Puranik AS, Gauvin R et al (2012) Building vascular networks. *Sci Transl Med* 4(160):160ps23
7. Herbert SP, Stainier DY (2011) Molecular control of endothelial cell behaviour during blood vessel morphogenesis. *Nat Rev Mol Cell Biol* 12(9):551–564
8. Holderfield MT, Hughes CCW (2008) Crosstalk between vascular endothelial growth factor, notch, and transforming growth factor- β in vascular morphogenesis. *Circ Res* 102(6):637–652
9. Sainson RC, Aoto J, Nakatsu MN et al (2005) Cell-autonomous notch signaling regulates endothelial cell branching and proliferation during vascular tubulogenesis. *FASEB J* 19(8):1027–1029
10. Cao L, Arany PR, Wang Y-S et al (2009) Promoting angiogenesis via manipulation of VEGF responsiveness with notch signaling. *Biomaterials* 30(25):4085–4093
11. Carmeliet P, Jain RK (2011) Molecular mechanisms and clinical applications of angiogenesis. *Nat* 473(7347):298–307
12. Adams RH, Alitalo K (2007) Molecular regulation of angiogenesis and lymphangiogenesis. *Nat Rev Mol Cell Biol* 8(6):464–478
13. Gaengel K, Genové G, Armulik A et al (2009) Endothelial-mural cell signaling in vascular development and angiogenesis. *Arterioscler Thromb Vasc Biol* 29(5):630–638
14. Allende ML, Yamashita T, Proia RL (2003) G-protein-coupled receptor S1P1 acts within endothelial cells to regulate vascular maturation. *Blood* 102(10):3665–3667
15. Augustin HG, Koh GY, Thurston G et al (2009) Control of vascular morphogenesis and homeostasis through the angiopoietin-Tie system. *Nat Rev Mol Cell Biol* 10(3):165–177
16. Bix G, Iozzo RV (2008) Novel interactions of perlecan: unraveling perlecan's role in angiogenesis. *J MRT* 71(5):339–348
17. Hallmann R, Horn N, Selg M et al (2005) Expression and function of laminins in the embryonic and mature vasculature. *Physiol Rev* 85(3):979–1000
18. Hayashi K (1992) Endothelial cells interact with the core protein of basement membrane perlecan through beta 1 and beta 3 integrins: an adhesion modulated by glycosaminoglycan. *J Cell Biol* 119(4):945–959
19. Davis GE (2005) Endothelial extracellular matrix: biosynthesis, remodeling, and functions during vascular morphogenesis and neovessel stabilization. *Cir Res* 97(11):1093–1107
20. Stratman AN, Davis GE (2011) Endothelial cell-pericyte interactions stimulate basement membrane matrix assembly: influence on vascular tube remodeling, maturation, and stabilization. *Microsc Microanal* 18(01):68–80
21. Saunders WB, Bohnsack BL, Faske JB et al (2006) Coregulation of vascular tube stabilization by endothelial cell TIMP-2 and pericyte TIMP-3. *J Cell Biol* 175(1):179–191
22. Risau W, Sariola H, Zerwes HG et al (1988) Vasculogenesis and angiogenesis in embryonic-stem-cell-derived embryoid bodies. *Development* 102(3):471–478
23. Vittet D, Prandini MH, Berthier R et al (1996) Embryonic stem cells differentiate in vitro to endothelial cells through successive maturation steps. *Blood* 88(9):3424–3431
24. Choi K, Chung YS, Zhang WJ (2005) Hematopoietic and endothelial development of mouse embryonic stem cells in culture. *Methods Mol Med* 105:359–368

25. Levenberg S (2002) Endothelial cells derived from human embryonic stem cells. *Proc Natl Acad Sci* 99(7):4391–4396
26. Levenberg S (2005) Engineering blood vessels from stem cells: recent advances and applications. *Curr Opin Biotechnol* 16(5):516–523
27. Gerecht-Nir S, Dazard J-E, Golan-Mashiach M et al (2005) Vascular gene expression and phenotypic correlation during differentiation of human embryonic stem cells. *Dev Dyn* 232(2):487–497
28. Rafii S, Lyden D (2003) Therapeutic stem and progenitor cell transplantation for organ vascularization and regeneration. *Nat Med* 9(6):702–712
29. Yamashita J, Itoh H, Hirashima M et al (2000) Flk1-positive cells derived from embryonic stem cells serve as vascular progenitors. *Nature* 408(6808):92–96
30. Iida M, Heike T, Yoshimoto M et al (2005) Identification of cardiac stem cells with FLK1, CD31, and VE-cadherin expression during embryonic stem cell differentiation. *FASEB J* 19(3):371–378
31. Gerecht-Nir S, Ziskind A, Cohen S et al (2003) Human embryonic stem cells as an in vitro model for human vascular development and the induction of vascular differentiation. *Lab Invest* 83(12):1811–1820
32. Kaufman DS (2001) Hematopoietic colony-forming cells derived from human embryonic stem cells. *Proc Natl Acad of Sci* 98(19):10716–10721
33. Asahara T (1997) Isolation of putative progenitor endothelial cells for angiogenesis. *Science* 275(5302):964–966
34. Kawamoto A, Gwon H-C, Iwaguro H et al (2001) Therapeutic potential of ex vivo expanded endothelial progenitor cells for Myocardial Ischemia. *Circulation* 103(5):634–637
35. Kocher AA, Schuster MD, Szabolcs MJ et al (2001) Neovascularization of ischemic myocardium by human bone-marrow-derived angioblasts prevents cardiomyocyte apoptosis, reduces remodeling and improves cardiac function. *Nat Med* 7(4):430–436
36. Stamm C, Westphal B, Kleine H-D et al (2003) Autologous bone-marrow stem-cell transplantation for myocardial regeneration. *Lancet* 361(9351):45–46
37. Ingram DA, Mead LE, Tanaka H et al (2004) Identification of a novel hierarchy of endothelial progenitor cells using human peripheral and umbilical cord blood. *Blood* 104(9):2752–2760
38. Narazaki G, Uosaki H, Teranishi M et al (2008) Directed and systematic differentiation of cardiovascular cells from mouse induced pluripotent stem cells. *Circulation* 118(5):498–506
39. Rufaihah AJ, Huang NF, Jamé S et al (2011) Endothelial cells derived from human iPSCs increase capillary density and improve perfusion in a mouse model of peripheral arterial disease. *Arterioscler Thromb Vasc Biol* 31(11):e72–79
40. Rufaihah AJ, Huang NF, Kim J et al (2013) Human induced pluripotent stem cell-derived endothelial cells exhibit functional heterogeneity. *Am J Transl Res* 5(1):21–35
41. Volz KS, Miljan E, Khoo A et al (2012) Development of pluripotent stem cells for vascular therapy. *Vasc Pharmacol* 56(5–6):288–296
42. Schoen FJ (2011) Heart valve tissue engineering: quo vadis? *Curr Opin Biotechnol* 22(5):698–705
43. Pankajakshan D, Agrawal DK (2010) Scaffolds in tissue engineering of blood vessels. *Can J Physiol Pharmacol* 88(9):855–873
44. Vismara R, Soncini M, Talò G et al (2010) A bioreactor with compliance monitoring for heart valve grafts. *Ann Biomed Eng* 38(1):100–108
45. Rubbens MP, Driessen-Mol A, Boerboom RA et al (2009) Quantification of the temporal evolution of collagen orientation in mechanically conditioned engineered cardiovascular tissues. *Ann Biomed Eng* 37(7):1263–1272
46. Balguid A, Mol A, Van Vlimmeren MA et al (2009) Hypoxia induces near-native mechanical properties in engineered heart valve tissue. *Circulation* 119(2):290–297
47. Wang L, Wilshaw S-P, Korossis S et al (2009) Factors influencing the oxygen consumption rate of aortic valve interstitial cells: application to tissue engineering. *Tissue Eng Part C Methods* 15(3):355–363

48. Robinson PS, Johnson SL, Evans MC et al (2008) Functional tissue-engineered valves from cell-remodeled fibrin with commissural alignment of cell-produced collagen. *Tissue Eng Part A* 14(1):83–95
49. Flanagan TC, Sachweh JS, Frese J et al (2009) In vivo remodeling and structural characterization of fibrin-based tissue-engineered heart valves in the adult sheep model. *Tissue Eng Part A* 15(10):2965–2976
50. Niklason LE (1999) Functional arteries grown in vitro. *Science* 284(5413):489–493
51. Liao J, Joyce EM, Sacks MS (2008) Effects of decellularization on the mechanical and structural properties of the porcine aortic valve leaflet. *Biomaterials* 29(8):1065–1074
52. Bayrak A, Tyralla M, Ladhoff J et al (2010) Human immune responses to porcine xenogeneic matrices and their extracellular matrix constituents in vitro. *Biomaterials* 31(14):3793–3803
53. Honge JL, Funder J, Hansen E et al (2011) Recellularization of aortic valves in pigs. *Eur J Cardiothorac Surg* 39(6):829–834
54. Baraki H, Tudorache I, Braun M et al (2009) Orthotopic replacement of the aortic valve with decellularized allograft in a sheep model. *Biomaterials* 30(31):6240–6246
55. Dohmen PM, Lembcke A, Holinski S et al (2007) Midterm clinical results using a tissue-engineered pulmonary valve to reconstruct the right ventricular outflow tract during the Ross procedure. *Ann Thorac Surg* 84(3):729–736
56. Hiemann NE, Mani M, Huebler M et al (2010) Complete destruction of a tissue-engineered porcine xenograft in pulmonary valve position after the Ross procedure. *J Thorac Cardiovasc Surg* 139(4):e67–68
57. Shinoka T, Shum-Tim D, Ma PX et al (1998) Creation of viable pulmonary artery autografts through tissue engineering. *J Thorac Cardiovasc Surg* 115(3):536–546
58. Chrobak KM, Potter DR, Tien J (2006) Formation of perfused, functional microvascular tubes in vitro. *Microvasc Res* 71(3):185–196
59. Norotte C, Marga FS, Niklason LE et al (2009) Scaffold-free vascular tissue engineering using bioprinting. *Biomaterials* 30(30):5910–5917
60. L'heureux N, Pâquet S, Labbé R et al (1998) A completely biological tissue-engineered human blood vessel. *FASEB J*. 12(1):47–56
61. L'Heureux N, Dussere N, Marini A et al (2007) Technology Insight: the evolution of tissue-engineered vascular grafts—from research to clinical practice. *Nat Clin Pract Cardiovasc Med* 4(7):389–395
62. Saik JE, McHale MK, West JL (2012) Biofunctional materials for directing vascular development. *Curr Vasc Pharmacol* 10(3):331–341
63. Hubbell JA (1999) Bioactive biomaterials. *Curr Opin Biotechnol* 10(2):123–129
64. Lee K, Silva EA, Mooney DJ (2011) Growth factor delivery-based tissue engineering: general approaches and a review of recent developments. *J R Soc Interface* 8(55):153–170
65. Maynard HD, Hubbell JA (2005) Discovery of a sulfated tetrapeptide that binds to vascular endothelial growth factor. *Acta Biomater* 1(4):451–459
66. Koch S, Yao C, Grieb G et al (2006) Enhancing angiogenesis in collagen matrices by covalent incorporation of VEGF. *J Mater Sci Mater Med* 17(8):735–741
67. Moon JJ, Lee S-H, West JL (2007) Synthetic biomimetic hydrogels incorporated with Ephrin-A1 for therapeutic angiogenesis. *Biomacromolecules* 8(1):42–49
68. Leslie-Barbick JE, Moon JJ, West JL (2009) Covalently-immobilized vascular endothelial growth factor promotes endothelial cell tubulogenesis in poly(ethylene glycol) diacrylate hydrogels. *J Biomater Sci Polym Ed* 20(12):1763–1779
69. Saik JE, Gould DJ, Keswani AH et al (2011) Biomimetic hydrogels with immobilized Ephrin-A1 for therapeutic angiogenesis. *Biomacromolecules* 12(7):2715–2722
70. Ikeda Y, Fukuda N, Wada M et al (2004) Development of angiogenic cell and gene therapy by transplantation of umbilical cord blood with vascular endothelial growth factor gene. *Hypertens Res* 27(2):119–128
71. Pratt AB, Weber FE, Schmoekel HG et al (2004) Synthetic extracellular matrices for in situ tissue engineering. *Biotechnol Bioeng* 86(1):27–36

72. Rinsch C, Quinodoz P, Pittet B et al (2001) Delivery of FGF-2 but not VEGF by encapsulated genetically engineered myoblasts improves survival and vascularization in a model of acute skin flap ischemia. *Gene Ther* 8(7):523–533
73. Lutolf MP, Hubbell JA (2005) Synthetic biomaterials as instructive extracellular microenvironments for morphogenesis in tissue engineering. *Nat Biotechnol* 23(1):47–55
74. Phelps EA, Landázuri N, Thulé PM et al (2010) Bioartificial matrices for therapeutic vascularization. *Proc Natl Acad Sci* 107(8):3323–3328
75. Halstenberg S, Panitch A, Rizzi S et al (2002) Biologically engineered protein-graft-poly(ethylene glycol) hydrogels: a cell adhesive and plasmin-degradable biosynthetic material for tissue repair. *Biomacromolecules* 3(4):710–723
76. Moon JJ, Saik JE, Poché RA et al (2010) Biomimetic hydrogels with pro-angiogenic properties. *Biomaterials* 31(14):3840–3847
77. Salinas CN, Anseth KS (2008) The enhancement of chondrogenic differentiation of human mesenchymal stem cells by enzymatically regulated RGD functionalities. *Biomaterials* 29(15):2370–2377
78. Zhu J (2010) Bioactive modification of poly(ethylene glycol) hydrogels for tissue engineering. *Biomaterials* 31(17):4639–4656
79. Xiao Y, Truskey GA (1996) Effect of receptor-ligand affinity on the strength of endothelial cell adhesion. *Biophys J* 71(5):2869–2884
80. Wacker BK, Alford SK, Scott EA et al (2008) Endothelial cell migration on RGD-Peptide-containing PEG hydrogels in the presence of Sphingosine 1-Phosphate. *Biophys J* 94(1):273–285
81. Papavasiliou G, Sokic S, Turturro M (2012) Synthetic PEG hydrogels as extracellular matrix mimics for tissue engineering applications. In: *Biotechnology—molecular studies and novel applications for improved quality of human life*, Prof. Sammour R (ed), ISBN: 978-953-51-0151-2, InTech, doi: [10.5772/31695](https://doi.org/10.5772/31695). Available from: <http://www.intechopen.com/books/biotechnology-molecular-studies-and-novel-applications-for-improved-quality-of-human-life/synthetic-peg-hydrogels-as-extracellular-matrix-mimics-for-tissue-engineering-applications>
82. Gauvin R, Parenteau-Bareil R, Dokmeci MR et al (2012) Hydrogels and microtechnologies for engineering the cellular microenvironment. *Wiley Interdiscip Rev Nanomed Nanobiotechnol* 4(3):235–246
83. Ghajar CM, Chen X, Harris JW et al (2008) The effect of matrix density on the regulation of 3-D capillary morphogenesis. *Biophys J* 94(5):1930–1941
84. Black AF, Berthod F, L'heureux N et al (1998) In vitro reconstruction of a human capillary-like network in a tissue-engineered skin equivalent. *FASEB J* 12(13):1331–1340
85. Hudon V, Berthod F, Black AF et al (2003) A tissue-engineered endothelialized dermis to study the modulation of angiogenic and angiostatic molecules on capillary-like tube formation in vitro. *Br J Dermatol* 148(6):1094–1104
86. Tremblay P-L, Hudon V, Berthod F et al (2005) Inosculation of tissue-engineered capillaries with the host's vasculature in a reconstructed skin transplanted on mice. *Am J Transplant* 5(5):1002–1010
87. Alajati A, Laib AM, Weber H et al (2008) Spheroid-based engineering of a human vasculature in mice. *Nat Methods* 5(5):439–445
88. Sorrell JM, Baber MA, Caplan AI (2009) Influence of adult mesenchymal stem cells on in vitro vascular formation. *Tissue Eng Part A* 15(7):1751–1761
89. Tsigkou O, Pomerantseva I, Spencer JA et al (2010) Engineered vascularized bone grafts. *Proc Natl Acad Sci* 107(8):3311–3316
90. Zheng Y, Chen J, Craven M et al (2012) In vitro microvessels for the study of angiogenesis and thrombosis. *Proc Natl Acad Sci* 109(24):9342–9347
91. Raghavan S, Nelson CM, Baranski JD et al (2010) Geometrically controlled endothelial tubulogenesis in micropatterned gels. *Tissue Eng Part A* 16(7):2255–2263
92. Sadr N, Zhu M, Osaki T et al (2011) SAM-based cell transfer to photopatterned hydrogels for microengineering vascular-like structures. *Biomaterials* 32(30):7479–7490

93. Miller JS, Stevens KR, Yang MT et al (2012) Rapid casting of patterned vascular networks for perfusable engineered three-dimensional tissues. *Nat Mater* 11(9):768–774
94. Chen X, Aledia AS, Popson SA et al (2010) Rapid anastomosis of endothelial progenitor cell-derived vessels with host vasculature is promoted by a high density of co-transplanted fibroblasts. *Tissue Eng Part A* 16(2):585–594
95. Cheng G, Liao S, Wong HK et al (2011) Engineered blood vessel networks connect to host vasculature via wrapping-and-tapping anastomosis. *Blood* 118(17):4740–4749
96. Korff T, Augustin HG (1999) Tensional forces in fibrillar extracellular matrices control directional capillary sprouting. *J Cell Sci* 112(19):3249–3258
97. Simionescu A, Schulte JB, Fercana G et al (2011) Inflammation in cardiovascular tissue engineering: the challenge to a promise: a minireview. *Int J Inflam* 2011:1–11
98. Niklason LE, Langer RS (1997) Advances in tissue engineering of blood vessels and other tissues. *Transpl Immunol* 5(4):303–306
99. Patel A, Fine B, Sandig M et al (2006) Elastin biosynthesis: the missing link in tissue-engineered blood vessels. *Cardiovasc Res* 71(1):40–49
100. Singh SK, Desai ND, Petroff SD et al (2008) The impact of diabetic status on coronary artery bypass graft patency: insights from the radial artery patency study. *Circulation* 118(14 Suppl):S222–225
101. Franco C, Gerhardt H (2012) Tissue engineering: blood vessels on a chip. *Nature* 488(7412):465–466

Chapter 7

Engineering Gene-Activated Matrices for the Repair of Articular Cartilage Defect

Junfeng Zhang and Zhen Huang

Abbreviations

AAV	Adenovirus-associated virus
BMP	Bone morphogenetic protein
FGF	Fibroblast growth factor
GAM	Gene-activated matrix
IGF	Insulin-like growth factor
iPS	Induced pluripotent stem cells
MSC	Marrow mesenchymal stem cells
PEI	Polyethyleneimine
PLGA	Poly(lactic-co-glycolic acid)
TGF- β	Transforming growth factor- β
3D	Three dimensional

7.1 Introduction

Cartilage is a slightly elastic connective tissue unique to humans and vertebrates, which is mainly present in the articular surface of bones, costal cartilage, the trachea, the ear, spinal disks, etc. [1]. Cartilage tissue is widely distributed in fetuses and young children, and it is gradually replaced by bone tissue over time. Cartilage is composed of chondrocytes, fibers, and a matrix. Depending on the matrix, cartilage can be categorized into hyaline cartilage, elastic cartilage, or fibrocartilage [2]. Articular cartilage is a type of hyaline cartilage that covers the surfaces of moving joints and disperses the load exerted on the subchondral bone by acting as a buffer. Articular cartilage mainly consists of thick and large

J. Zhang (✉) · Z. Huang
State Key Laboratory of Pharmaceutical Biotechnology, School of Life Sciences,
Nanjing University, Nanjing 210093, China
e-mail: jfzhang@nju.edu.cn

chondrocytes and a rich cartilage matrix, and it does not contain blood vessels, lymphatic vessels, or nerves [3]. No structure can be observed in articular cartilage under a light microscope. The main components of the cartilage matrix are water, proteoglycan, and collagen; other components include fat, protein, inorganic salts. Water and small molecules can flow freely within the cartilage matrix, imparting elasticity and compressibility to the cartilage. Exerting a load on a joint compresses the articular cartilage, initiating water flow to provide nutrition to the articular cartilage. Articular cartilage is a highly specialized tissue that can protect the bones in the joint area from the effects of load and impact, such that activities can be performed without friction between the articular surfaces [4].

Articular cartilage, especially in moving joints, can be damaged by various causes, such as physical injury or osteoarthritis [5, 6]. Cartilage defects often cause joint swelling and pain and limit activity, producing symptoms similar to those of meniscal tear. Cartilage damage can be classified in terms of the extent of the damage: matrix damage, partial cartilage defects, and full-layer cartilage defects [7]. Following body tissue or organ damage, the newly formed cells and matrix in the surrounding area recover and replace the defect cells and the matrix. The repair process for damaged cartilage tissue is similar to that for other tissues, but cartilage has poor repair ability, and its original cartilage structure and function are not restored in most cases [8–11]. The histological and biological characteristics of cartilage limit its response to damage for the following reasons: (1) Cartilage tissue does not have undifferentiated cells to repair damage and defects; (2) unlike other tissues, cartilage defect sites other than full-layer cartilage defects do not contain blood vessels, making it difficult for undifferentiated mesenchymal cells to enter the damaged site and enable the healing process; and (3) the chondrocytes embedded in the dense collagen—proteoglycan matrix hinder the proliferation and migration of cells. For all of these reasons, articular cartilage damage is a common clinical disease. More than 400,000 articular cartilage repair surgeries were performed in the United States in 2007 alone, at a total cost of \$50 to \$60 million [12].

Traditional articular cartilage defect repair methods can be divided into two main categories: articular surface reconstruction and biological grafting. The first category mainly consists of arthroscopic grinding, drilling into the articular surface, and microfracture. Microfracture is an extremely important method that is used to repair a full-layer defect by puncturing the subchondral bone [13–16]. Bone marrow and blood ooze from the hole and form blood clots. The clots provide a scaffold into which bone marrow mesenchymal stem cells can migrate and differentiate into chondrocytes and bone cells. The body itself responds to microfracture as a damage event and produces a new alternative cartilage for patients. However, the limitation of this surgery is that the efficacy depends on the patient's age and weight and the size of the defect [17]. In addition, studies have shown that the microfracture technique does not completely heal the cartilage damage because the resulting cartilage is fibrocartilage rather than hyaline cartilage [18]. Fibrocartilage has less mechanical strength and is denser than hyaline cartilage; therefore, it breaks more easily under the pressure of repeated daily activities [19]. Biological grafting mainly includes osteochondral transplantation, periosteal/cartilage membrane

transplantation, and bone cell transplantation. Autologous chondrocyte transplantation is currently the most commonly used biological grafting technique. This technique has been increasingly attracting attention since its initial introduction by Brittberg because the transplanted chondrocytes can secrete and synthesize a new extracellular matrix at the defect site, which has the potential to form hyaline cartilage tissue [20]. Autologous chondrocyte transplantation is mostly applied to local traumatic articular cartilage defects. The transplanted chondrocytes proliferate, thereby further regulating the repair process via signal transduction. Follow-up results have shown that autologous chondrocyte transplantation has been able to repair cartilage defects completely for most patients [21, 22]. The drawback of the technique is that the treatment results are sensitive to joint mechanical instability, excessive loads, and the patient's age [23]. The technique also needs to be developed further to ensure that the transplanted chondrocytes are confined to the defect site for matrix secretion.

7.2 Application of Tissue Engineering to Cartilage Repair

Developments in tissue engineering have advanced cartilage construction techniques [24]. Tissue-engineered cartilage is constructed as follows. Seed cells are extracted, isolated, and cultured *in vitro* [25]. Growth factor(s) are added to induce considerable proliferation. The seed cells are then transplanted onto biocompatible, biodegradable, and resorbable tissue engineering scaffolds to form a cell—scaffold complex, which is subsequently transplanted into the body at the joint defect sites. As the cells grow and proliferate, an extracellular matrix is formed and the scaffold is degraded and absorbed; until finally, new tissue with cartilage function forms to repair the tissue structure and restore its function. Developments in modern biology have spurred the increasing use of growth factors to treat articular cartilage defects [26, 27]. Studies have shown that various growth factors, such as transforming growth factor- β (TGF- β), insulin-like growth factor (IGF), fibroblast growth factor (FGF), and bone morphogenetic protein (BMP), promote articular cartilage repair [28–31].

The combined use of cell culture, biomaterials, and growth factors in tissue-engineered cartilage has been experimentally successful [32]. Tissue engineering techniques for repairing tissue defects use an ideal matrix scaffold with two components: a growth factor release carrier and a scaffolding structure for cell proliferation and repair, which effectively reconstructs the tissue. Many studies have shown that an appropriate growth factor can be used for chondrocytes that are cultured *in vitro* to promote chondrocyte proliferation and maintain the cell phenotype; a three-dimensional (3D) scaffold provides the structure for chondrocyte proliferation [33, 34]. The growth factor must be continuously present over the requisite time period to facilitate tissue reconstruction [35]. Therefore, the growth factor is embedded in a biodegradable 3D scaffold and is continuously released as

the scaffold gradually degrades. Lee et al. embedded TGF- β 1-coated microspheres in a scaffold, which effectively controlled the growth factor release to enhance cartilage formation in an in vitro culture [36]. Holland et al. studied the release rate of a TGF- β 1 composite scaffold for repairing human articular cartilage damage in a simulated environment [37]. The results showed that the TGF- β 1 complexed with an acidic gel under normal pH conditions in the body. The complex disappeared under acidic conditions (which would prevail in cases of tissue damage and inflammation, for example), significantly accelerating the release rate of the uncoated TGF- β 1. This phenomenon can be prevented by combining the growth factor with a scaffold in experiments to release TGF- β 1 at a specified constant rate. The cross-linking reaction time and the degree of cross linking of the 3D scaffold can be controlled to form scaffolds with different pore diameters and therefore release different rates of the embedded growth factor. All of these results show the considerable application potential of the growth factor composite scaffold in the application of tissue engineering techniques to repair cartilage defects. However, considerations of the large molecular weight of the growth factor and its short half-life in the body have continued to delay practical clinical studies on the application of the recombinant growth factor composite scaffold [38, 39]. The process of coating the growth factor onto microspheres requires a large amount of organic reagent, surfactants, and a high-temperature reaction [40, 41]. These conditions can degrade the growth factor, ultimately reducing its biological activity and increasing its immunogenicity instead. In addition, the difficulty in controlling the growth factor dose has also limited the use of the growth factor in clinical trials.

7.3 Gene-Activated Matrix

Several research initiatives are currently dedicated to developing a controlled release system to directly transfer the growth factor; however, a simpler technique is to convert the seed cells at the production site of the related proteins using gene transfer technology. A biological matrix containing genetic components is called a gene-activated matrix (GAM). A GAM combines the advantage tissue engineering and gene therapy to act as a cell growth scaffold in tissue engineering, provide a site and space for the growth and proliferation of seed cells, and act as a gene transfer carrier itself. A GAM can also enable the local transfer of a therapeutic gene [42]. In the defect area, the seed cells or cells in the tissue surrounding the GAM can capture the released genetic components or adhere to the matrix surface that has adsorbed the plasmid DNA. The therapeutic gene fragment is then obtained via endocytosis, such that the aforementioned cells act as local bioreactors for the expression and synthesis of the growth factors, which play autocrine and paracrine roles for the surrounding cells to ultimately realize the repair of the defect site.

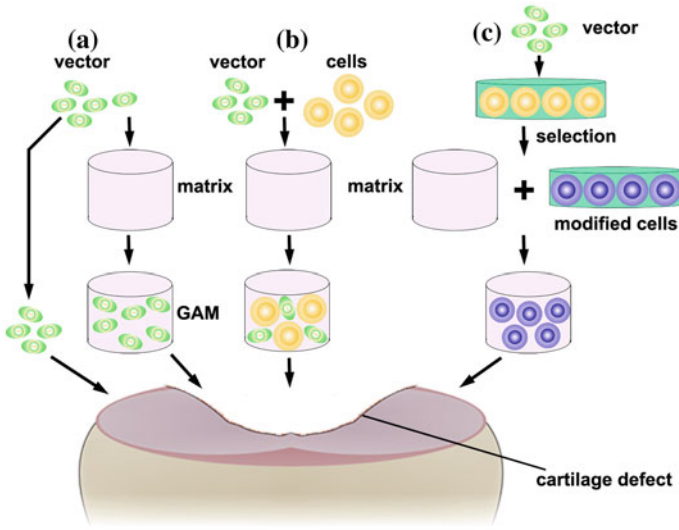


Fig. 7.1 Two different modes for gene transfer in articular cartilage regeneration: the direct in vivo method and the indirect ex vivo method

7.3.1 Gene Transfer Method to Repair Articular Cartilage

There are two main modes for gene transfer in articular cartilage repair, (as shown in Fig. 7.1): the direct in vivo method and the indirect ex vivo method. In the in vivo method, the gene vector (Fig. 7.1a) or the gene vector and the cells (Fig. 7.1b) are directly injected into the joint cavity; in the ex vivo method, the gene modification of seed cells is carried out in vitro, and these cells are then retransplanted into the body (Fig. 7.1c). Selecting one of the methods depends on many conditions including the gene and vector to be used. Recently, the ex vivo method has been most commonly used: The genetically modified cells are cultured on an in vitro matrix or embedded in a gel matrix, before being transferred to the cartilage defects for in situ repair [43]. This method can increase the cellular structure of the defect site; the gene is only transferred in situ, away from other non-specific tissues, thereby reducing edge effects.

7.3.2 Vector Types for Cartilage Gene Transfer

7.3.2.1 Viral Vectors

In recent years, viral vectors and non-viral vectors have been commonly used for cartilage gene transfer. The adenovirus vector is most commonly used for its high

transfection efficiency [44]. This vector can facilitate the stable and efficient transfection of a variety of cells but has a high immunogenicity in *in vivo* repair. The adenovirus vector also exhibits high toxicity at high doses. The toxicity of the adenovirus-associated virus (AAV) is milder than that of the adenovirus and has not been found to cause disease in humans thus far [45]. There is no viral protein expression in infected cells, but the transfection efficiency is not ideal. Adachi et al. used a retrovirus to transfect chondrocytes and stem cells *in vitro*, which were then embedded in a type I collagen gel and transplanted into the cartilage defect [46]. After 4 weeks, good histological results were obtained for the tissue repair in both groups. Nixon et al. used an adenovirus to transfect an IGF-1 gene that promotes secretion of a cartilage matrix into chondrocytes, bone marrow stem cells, and synovial cells, which were then filled into an articular cartilage defect [47]. The results showed that the aforementioned cells successfully prolonged the IGF-1 gene expression time and promoted the secretion of the cartilage matrix; however, a high initial virus titer was required, which had adverse long-term effects on the cartilage tissue. Note that in the aforementioned studies, all of the vectors used for gene transfection were viral vectors, which were chosen for their high transfection efficiency and ease of manipulation; however, the high immunogenicity of the viral vectors is as yet unresolved, which has limited their application to the clinical cartilage gene transfer system [48].

7.3.2.2 Non-viral Vectors

A technique has been developed that successfully uses non-viral vectors to elucidate gene structure, function, and expression. The preparation of a safe and efficient non-viral vector can profoundly impact the future development of gene therapy and biotechnology. Several polymers have been used for DNA transfer since the early 1970s; liposome is the most remarkable example of these polymers [49]. In 1987, Felgner et al. synthesized a cationic liposome, lipofectin [50]. The lipofectin/DNA complex is easy to manipulate and was the first vector used for *in vivo* chemical gene transfer. The peptide vector, in the form of the polylysine peptide vector, also has a strong affinity to DNA [50]. Consequently, the polylysine peptide vector/DNA complex can enhance the rate of cellular uptake. Polyethyleneimine (PEI) can inhibit lysosomes; in the acidic environment of endocytosis, PEI is protonated with an increased positive charge, which provides greater protection for DNA and facilitates plasmid escape from the lysosomes [51]. Consequently, PEI is widely used as a DNA transfer vector. Non-viral vectors are easy to manipulate for transfection and have a low immunogenicity and a high safety level; however, these vectors have a low transfection efficiency, and the target gene is only transiently expressed (typically for less than a week) [52]. Therefore, non-viral vectors are generally used only for *in vitro* mesenchymal stem cell differentiation and are difficult to use *in vivo*. Currently, an improved approach is being used in which the scaffold itself serves as a plasmid DNA transfer vector. The application of GAMs was developed to improve the poor efficiency of

non-viral vector via maintaining the high local gene concentration and sustainingly delivering therapeutic DNA to surrounding cells. The first report to be described for bone used scaffold comprising a collagen sponge impregnated with plasmid DNA encoding for the BMP-4 gene with or without another plasmid encoding a portion of the parathyroid hormone gene, PTH1-34. It was designed to deliver DNA to infiltrating reparative cells when implanted into an osseous defect. By expressing the transgene, the infiltrating cells generate an autocrine and paracrine osteogenic environment. Satisfactory therapeutic effect was observed in experimental defect models in rats and dogs [53, 54].

Another example is that poly-cationic polymers (chitosan and gelatin) can bind to the negatively charged plasmid DNA; this matrix is itself biodegradable, and its degradation products can form complexes and coat plasmid components to form a DNA/polymer complex. Meanwhile, the plasmid DNA attached to the matrix surface is also continuously released as the matrix degrades, thereby improving the transfection efficiency and ensuring the continuous expression of the target growth factors. Guo et al. prepared a gene-activated chitosan/gelatin scaffold embedded with a TGF- β 1 plasmid to effectively promote the proliferation of rabbit articular chondrocytes in vitro while maintaining the cartilage phenotype [55]. This gene-activated scaffold has the potential to become a new cartilage repair scaffold. Building Guo et al. work, Diao et al. transplanted bone marrow mesenchymal stem cells into the aforementioned scaffold to promote the differentiation of directional mesenchymal stem cells and the synthesis of a cartilage extracellular matrix; the active cartilage repair matrix, which had been constructed in vitro, was then transplanted into rabbit articular cartilage defects to repair the cartilage defects in vivo; favorable therapeutic results were obtained [56].

Chen et al. used two plasmids, TGF- β 1 and BMP-2, together for the bidirectional differentiation of bone marrow mesenchymal stem cells into chondrocytes and osteoblasts; an osteochondral transplantation complex was constructed on the same scaffold. The authors simulated a bone and cartilage-like tissue for both bone repair and cartilage function in vitro, which was subsequently used to repair a full-layer osteochondral defect; the tissue in the surface hyaline cartilage and the subchondral bone were simultaneously repaired successfully [57]. The schematic diagrams of constructing the bilayered GAM and the therapeutic effect are shown in Fig. 7.2.

7.3.3 Cell Types in the GAM

The cells used with a GAM for cartilage repair must have a stable source and a specified tissue repair potential. Currently used cells include adult chondrocytes, bone marrow mesenchymal stem cells, embryonic stem cells, newly discovered inducible pluripotent stem cells.

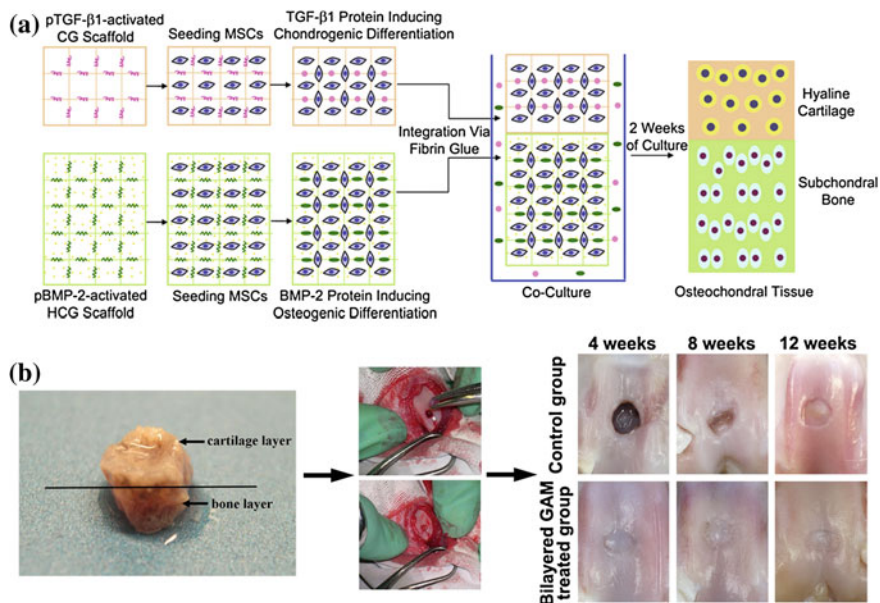


Fig. 7.2 **a** Diagrammatic representation of the procedures for the construction of the bilayered gene-activated composite osteochondral graft using mesenchymal stem cells loaded into TGF- β 1-activated CG scaffold layer and BMP-2-activated HCG scaffold layer. pTGF- β 1 plasmid TGF- β 1; pBMP-2, plasmid BMP-2; MSC mesenchymal stem cell; CG chitosan–gelatin; HCG hydroxy-apatite/chitosan–gelatin. **b** Osteochondral defects were created in the middle of each patellar groove of adult rabbits with a cylindrical drill. The bilayered gene-activated composite osteochondral graft was filled in the contralateral defect. Macrophotographs of the osteochondral repair in vivo were taken at 4, 8, and 12 weeks after the operation. Reproduced from [57]

7.3.3.1 Adult Chondrocytes

Adult chondrocytes are relatively simple to isolate and cultivate; these cells can be used to directly synthesize a cartilage-specific extracellular matrix [58]. A primary monolayer culture of chondrocytes can express a specific extracellular matrix, such as type II collagen and proteoglycans, which can be maintained for several weeks after passage. However, there is a limited source of adult chondrocytes, which tend to lose their phenotypes after multiple passages and culturing in vitro and to differentiate into fibroblasts, which cannot secrete a cartilage matrix. Consequently, the synthesis and secretion of type I and type III collagen increase, and the adult chondrocytes gradually lose their originally well-differentiated phenotypes, i.e., the tendency to dedifferentiate. The loss of phenotype has limited the large-scale in vitro proliferation of chondrocytes, making it difficult to obtain cartilage tissue with normal function after in vivo transplantation. Adult chondrocytes are usually used in conjunction with a scaffold or cell carrier, the surface features of which are used to maintain the normal matrix-secreting function of the chondrocytes. Autologous chondrocyte transplantation has been successfully carried out in clinical practice,

and satisfactory early treatment results have been obtained [59]. Animal experiments have shown that transplanting a chondrocyte/scaffold complex, which has been constructed *in vitro*, into large rabbit cartilage defects can promote the processes of repair and reconstruction [60]. The emergence and development of a 3D culture technique have enabled an extracellular matrix microenvironment to be simulated in the body. Chondrocytes, which have been cultured *in vitro*, can maintain a stable phenotype with a well-differentiated state and can even transform dedifferentiated chondrocytes in a monolayer culture into a well-differentiated state.

7.3.3.2 Bone Marrow Mesenchymal Stem Cells

Bone marrow mesenchymal stem cells (MSCs) are precursors to various mesenchymal cells such as osteoblasts, chondroblasts, and bone marrow stromal fibroblasts [61]. MSCs have a multi-directional differentiation potential with a high degree of evolutionary conservation. For over two decades, studies on the growth and differentiation of bone marrow MSCs have shown broad applications for stem cells that have been isolated and cultured from bone marrow by cartilage tissue engineering [62]. Currently, the isolation and application of MSCs is an important research subject in tissue engineering worldwide; experiments have shown that MSCs have a strong *in vitro* proliferative capacity and can be induced to differentiate into chondrocytes and form cartilage tissue *in vivo*. MSCs can be easily obtained via a simple bone marrow puncture: A couple dozen millimeters are sufficient to extract the number of cells needed in clinical trials. MSCs can be introduced into cartilage defects by two methods. The first method is the direct transplantation of MSCs into joints. Wakitani et al. were the first to transplant a complex of autologous bone marrow MSCs (which were cultured *in vitro*) and a type I collagen gel to repair rabbit articular cartilage full-layer defects [63]. The hyaline cartilage formed after only 2 weeks; by week 24, the articular cartilage and the subchondral bone defects were repaired, but the repaired tissue was thinner than the healthy tissue, and there was a gap between the repaired tissue and the healthy cartilage tissue. In the second method, chondrocytes that are induced *in vitro* or genetically modified chondrocytes are retransplanted into the defect area. Butnariu-Ephrat et al. used a high-density *in vitro* culture to induce MSCs into chondrocytes, which then formed a chondrocyte/2 % high molecular weight hyaluronic acid complex that was autologously transplanted to repair sheep articular cartilage defects [64]. A hyaline cartilage-like tissue similar to the normal articular cartilage structure formed after only 3 months.

7.3.3.3 Embryonic Stem Cells

Embryonic stem cells have an unlimited proliferative capacity and versatile differentiation; consequently, embryonic stem cells have a higher potential than adult stem cells to become new tissue engineering seed cells [65]. Embryonic stem cells

have been successfully induced to differentiate into chondrocytes *in vitro* and have even been used in attempts to construct cartilage tissue [66]. However, embryonic stem cell lines are difficult to obtain and establish. There are many challenges associated with the use of embryonic stem cell lines including safety, ethical, and immune rejection issues [67]. Therefore, there is currently only limited application of embryonic stem cells in tissue engineering.

7.3.3.4 Induced Pluripotent Stem Cells

Induced pluripotent stem (iPS) cells is a newly developed stem cell technology in which differentiated adult cells (such as skin cells) are introduced into a series of genes (Oct-3, Sox2, c-Myc, Klf4, and Nanog) and are then re-encoded into stem cells with multi-directional differentiation potential [68]. In this technique, isolated autologous adult differentiated cells are first re-encoded into stem cells, which differentiate into specific tissue cells under certain culture conditions. The specific tissue cells are then used for tissue engineering. All of the methods for obtaining induced pluripotent stem cells reported before March 2009 used a virus to transplant various genes into skin cells to promote cell transformation [69]. Both the viral vector and the transplanted gene pose cancer risks, which has greatly limited iPS application. Recently, breakthroughs have continued to be made with the iPS technique, such as bypassing the use of dangerous viral vectors to reduce the number of types of introduced genes and clean up the transplanted genes after the “usage time,” thereby avoiding the various risks introduced by foreign genes [70]. It has been reported that iPS has been successfully induced in chondrocytes [71]. Thus, a series of dangerous or potentially dangerous risks has been circumvented, and we anticipate that the unlimited potential of iPS will be tapped for cartilage damage repair.

7.3.4 Cartilage Tissue Engineering Scaffold

An ideal scaffold is crucial for the successful construction of tissue-engineered cartilage. An ideal scaffold should meet the following criteria: (1) Good biocompatibility, which is required for seed cell adhesion, proliferation, growth, and differentiation; (2) A 3D structure with an optimal porosity of over 90 %; (3) Good biodegradability, with non-toxic degradation products that can be absorbed by the human body; (4) An effective matrix–cell interface for cell adhesion and growth, which, more importantly, can activate cell-specific gene expression and maintain the normal cell phenotype; (5) Plasticity and a prescribed mechanical strength to support new tissue. According to different sources, biologically active materials in tissue engineering can be classified into natural and synthetic materials. Natural biological materials generally have cell signal recognition capabilities; can promote cell adhesion, proliferation, and differentiation; generally have no toxic side effects; and possess good biocompatibility and biodegradability [72]. Polysaccharides and

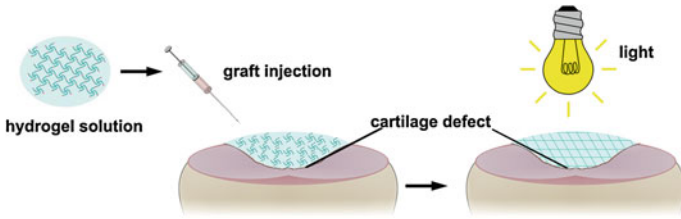


Fig. 7.3 The hydrogel solution is injected into the cartilage defect and photopolymerized in situ with light.

protein materials are commonly used because they are the main components of the extracellular matrix and can effectively simulate the microenvironment necessary for cell growth. Common natural polysaccharide materials include chitosan, chitin, chondroitin sulfate, and hyaluronic acid [73]. The proteins used as biological materials mainly include collagen, gelatin, and fibrin. These materials offer the advantage of carrying considerable biological information that enables cells to produce or maintain various functions [74]. These materials are directly derived from plants and animals and thus have good biocompatibility. The microstructure, the mechanical properties, and the degradation time of synthetic polymer materials can be predesigned and controlled [75]. Currently, poly(lactic-co-glycolic acid) (PLGA), which exhibits good biocompatibility, controlled degradation ability, etc., has been approved by the United States. FDA is a tissue engineering scaffold and is widely used [76]. However, PLGA also has many disadvantages for practical applications, such as insufficient hydrophilicity, weak cell adhesion, and the potential for inflammatory reactions of the acidic degradation products [77]. Composite materials are currently being intensively researched in tissue engineering: Two or more types of biological materials with complementary characteristics are combined in specified proportions following a particular method to produce a 3D material with an optimal structure and properties that compensate for the drawbacks of the individual materials themselves. Continuing advances in molecular biology, material science, and other disciplines have produced new materials such as electroplating chitosan/polyethylene oxide ethylene, fibrin polyurethane, and fiber bacterial cellulose. Experiments have shown that these scaffolds can act as artificial cartilage scaffold [78]. However, an ideal material has not been found thus far, and the search continues for a scaffold with enhanced cell compatibility, a controllable degradation rate, and a prescribed mechanical strength that can be used in current articular cartilage tissue engineering.

7.3.5 GAM Advantages for Cartilage Repair

GAMs offer several advantages for cartilage repair. (1) A GAM can be directly applied inside the articular cavity, which prevents excessive degradation of the genetic components by nucleic acid enzymes in the body's circulatory system; the

resulting locally high DNA concentration enhances the transfection efficiency. Local application also avoids ectopic transfection and is therefore safer. (2) The GAM functions as a targeted drug delivery system by directly acting on and targeting the cartilage repair cells; therefore, gene drug delivery into the joint cavity is maximized, and the genetic components are concentrated in the target area to several times or even hundreds of times the concentration of the systemic administration [79]. Huang et al. complexed BMP-4 plasmid and PEI, and the nanocomplex was encapsulated in a PLG scaffold. Researchers observed that this delivery strategy allows gene expression for periods of up to 18 weeks and achieved better therapeutic effect than blank scaffolds in a rat critical-sized defect [79, 80]. Therefore, the interaction between the DNA and the target cells is prolonged, thereby significantly improving the treatment results and reducing the amount of DNA used in the body and the rate of ectopic transfection. A GAM functions efficiently at low toxicity and therefore promotes safety. (3) The articular cartilage tissue cannot easily access large doses of cytokines from the blood circulation system, and it is therefore especially important to maintain a suitable concentration of cytokines in the defect area. In addition to facilitating the adhesion, proliferation, and differentiation of chondrocytes, the genetic components carried by the GAM can be locally expressed to secrete highly active therapeutic agents and promote repair. (4) The cartilage repair process consists of a single stage and does not require the long-term expression of the gene product. The DNA in the GAM has specific release kinetics to meet the requirements of the treatment window of the growth factor, thus avoiding excessive DNA dosing [81]. (5) A GAM may be incorporated into a 3D scaffold to provide filling support for the cartilage defect area; the scaffold is not affected by the range, size, and depth of the defect area and can be cut into any desired shape for direct injection into the articular cavity. Injectable *in situ* cross-linkable gels are highly desirable clinically as they can be performed using an arthroscopy, a convenient and less invasive procedure (Fig. 7.3). A recent study demonstrated that an alginate hydrogel containing BMP-2 plasmid and MSC could secrete biologically active BMP-2 protein 6 weeks after implantation. The protein levels were effective in inducing osteogenic differentiation as demonstrated by the production of collagen I and osteocalcin [82]. Injectable hydrogels containing plasmid encoding growth factors appear to be a promising new strategy for minimal-invasive delivery of growth factors in cartilage regeneration. (6) A variety of therapeutic genes can be composited together to synergistically affect cartilage defect repair. Our studies using gene therapy for cartilage repair applications have utilized growth factors such as TGF- β and BMP-2, which can promote the regeneration of both cartilage and subchondral bone [57]. From the results of H&E staining and immunohistochemical staining of collagen I and Alcian blue staining in Fig. 7.4, it is observed that the GAMs containing TGF- β or BMP-2 alone showed weakness in the repair of either subchondral bone or cartilage and need more wound healing time. Another study reported a combination of anabolic (IGF-1) and catabolic (IL-1 antagonist) to regulate tissue homeostasis using gene therapy. The catabolic proteins inhibit expression of genes related to catabolic tissue response, while

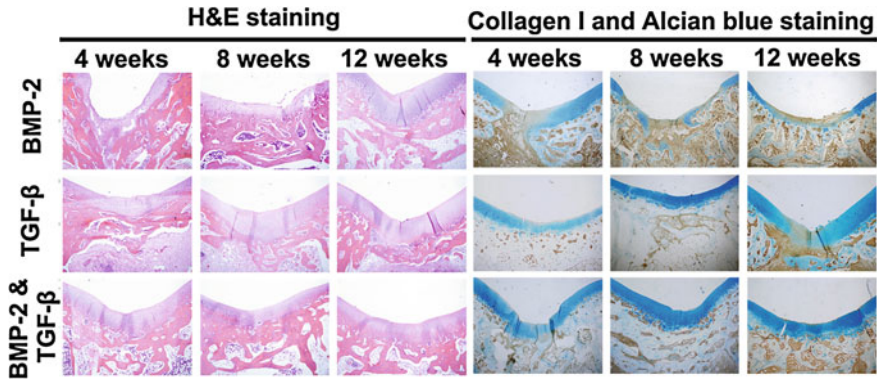


Fig. 7.4 H&E staining and immunohistochemical staining of collagen I and Alcian blue staining for hyaline cartilage at the indicated times during the osteochondral repair. Reproduced from [57]

anabolic proteins stimulate matrix production [83]. These studies indicate that multiple gene therapies have great potential in cartilage defect repair applications.

7.3.6 Issues in Using a GAM to Treat Cartilage Damage

GAMs have broad applications in the treatment of cartilage damage, but several challenges still remain. (1) Safety considerations show that both viral vectors and non-viral vectors pose risks of possible insertional mutations during the transfection process, which may cause cancer and auxiliary virus production. Conducting research and development to identify a safe vector without side effects is a daunting task in gene therapy. (2) The target gene has a low transfection efficiency and a short in vivo expression time. (3) Gene therapy for cartilage repair should develop in the direction of multi-gene transfection. Existing gene therapy studies mainly focus on single-gene diseases, whereas the complex pathological mechanism of cartilage damage is often a synergy of multiple factors. (4) Excessive and insufficient gene expressions are both harmful; therefore, further research is required to regulate gene expression such that the target gene products are expressed at an appropriate concentration and at an appropriate time and site.

7.4 The Prospects

Currently, many studies have demonstrated the effectiveness and feasibility of using GAMs for repairing tissue damage. Further development of these studies on the pathological mechanisms of tissue damage and the eventual resolution of the aforementioned issues can enable the GAM technique to become an effective and important method in the clinical treatment of orthopedic tissue damage.

References

1. Buckwalter JA, Mankin HJ (1998) Articular cartilage: degeneration and osteoarthritis, repair, regeneration, and transplantation. *Instr Course Lect* 47:487–504
2. Sophia Fox AJ, Bedi A, Rodeo SA (2009) The basic science of articular cartilage: structure, composition, and function. *Sports health* 1(6):461–468. doi:[10.1177/1941738109350438](https://doi.org/10.1177/1941738109350438)
3. Bhosale AM, Richardson JB (2008) Articular cartilage: structure, injuries and review of management. *Br Med Bull* 87:77–95. doi:[10.1093/bmb/ldn025](https://doi.org/10.1093/bmb/ldn025)
4. Eckstein F, Hudelmaier M, Putz R (2006) The effects of exercise on human articular cartilage. *J Anat* 208(4):491–512. doi:[10.1111/j.1469-7580.2006.00546.x](https://doi.org/10.1111/j.1469-7580.2006.00546.x)
5. Detterline AJ, Goldberg S, Bach BR, Jr., Cole BJ (2005) Treatment options for articular cartilage defects of the knee. *Orthop Nurs* 24 (5):361–366; quiz 367–368
6. Hunziker EB (2002) Articular cartilage repair: basic science and clinical progress. A review of the current status and prospects. *Osteoarthritis Cartilage* 10(6):432–463. doi:[10.1053/joca.2002.0801](https://doi.org/10.1053/joca.2002.0801)
7. Temenoff JS, Mikos AG (2000) Review: tissue engineering for regeneration of articular cartilage. *Biomaterials* 21(5):431–440
8. Buckwalter JA, Mankin HJ (1998) Articular cartilage: tissue design and chondrocyte-matrix interactions. *Instr Course Lect* 47:477–486
9. Hunziker EB (1999) Articular cartilage repair: are the intrinsic biological constraints undermining this process insuperable? *Osteoarthritis and cartilage/OARS, Osteoarthritis Cartilage* 7(1):15–28. doi:[10.1053/joca.1998.0159](https://doi.org/10.1053/joca.1998.0159)
10. Buckwalter JA (1998) Articular cartilage: injuries and potential for healing. *J Orthop Sports Phys Ther* 28(4):192–202
11. Hunziker EB, Kapfinger E (1998) Removal of proteoglycans from the surface of defects in articular cartilage transiently enhances coverage by repair cells. *J Bone Joint Surg Br* volume 80(1):144–150
12. McNickle AG, Provencher MT, Cole BJ (2008) Overview of existing cartilage repair technology. *Sports Med Arthrosc* 16(4):196–201. doi:[10.1097/JSA.0b013e31818c8db82](https://doi.org/10.1097/JSA.0b013e31818c8db82)
13. Elias DA, White LM (2004) Imaging of patellofemoral disorders. *Clin Radiol* 59(7):543–557. doi:[10.1016/j.crad.2004.01.004](https://doi.org/10.1016/j.crad.2004.01.004)
14. Dzioba RB (1988) The classification and treatment of acute articular cartilage lesions. *Arthroscopy* 4(2):72–80
15. Kim HK, Moran ME, Salter RB (1991) The potential for regeneration of articular cartilage in defects created by chondral shaving and subchondral abrasion. An experimental investigation in rabbits. *J Bone Joint Surg Am* 73(9):1301–1315
16. Falah M, Nierenberg G, Soudry M, Hayden M, Volpin G (2010) Treatment of articular cartilage lesions of the knee. *Int Orthop* 34(5):621–630. doi:[10.1007/s00264-010-0959-y](https://doi.org/10.1007/s00264-010-0959-y)
17. Mithoefer K, McAdams T, Williams RJ, Kreuz PC, Mandelbaum BR (2009) Clinical efficacy of the microfracture technique for articular cartilage repair in the knee: an evidence-based systematic analysis. *Am J Sports Med* 37(10):2053–2063. doi:[10.1177/0363546508328414](https://doi.org/10.1177/0363546508328414)
18. Ahlers J (2008) Treatment options for cartilage damage in the knee joint. *Am J Sports Med* 60(3):114–117
19. Krych AJ, Harnly HW, Rodeo SA, Williams RJ 3rd (2012) Activity levels are higher after osteochondral autograft transfer mosaicplasty than after microfracture for articular cartilage defects of the knee: a retrospective comparative study. *J Bone Joint Surg Am* 94(11):971–978. doi:[10.2106/JBJS.K.00815](https://doi.org/10.2106/JBJS.K.00815)
20. Brittberg M, Nilsson A, Lindahl A, Ohlsson C, Peterson L (1996) Rabbit articular cartilage defects treated with autologous cultured chondrocytes. *Clin Orthop Relat Res* 326:270–283
21. McPherson JM, Tubo R, Barone L (1997) Chondrocyte transplantation. *Arthroscopy* 13(4):541–547

22. Brittberg M, Lindahl A, Nilsson A, Ohlsson C, Isaksson O, Peterson L (1994) Treatment of deep cartilage defects in the knee with autologous chondrocyte transplantation. *N Engl J Med* 331(14):889–895. doi:[10.1056/NEJM199410063311401](https://doi.org/10.1056/NEJM199410063311401)
23. Messner K, Gillquist J (1996) Cartilage repair. A critical review. *Acta Orthop Scand* 67(5):523–529
24. Tuli R, Li WJ, Tuan RS (2003) Current state of cartilage tissue engineering. *Arthritis Res Ther* 5(5):235–238. doi:[10.1186/ar991](https://doi.org/10.1186/ar991)
25. Vunjak-Novakovic G, Obradovic B, Martin I, Bursac PM, Langer R, Freed LE (1998) Dynamic cell seeding of polymer scaffolds for cartilage tissue engineering. *Biotechnol Prog* 14(2):193–202. doi:[10.1021/bp970120j](https://doi.org/10.1021/bp970120j)
26. van Osch GJ, Mandl EW, Marijnissen WJ, van der Veen SW, Verwoerd-Verhoef HL, Verhaar JA (2002) Growth factors in cartilage tissue engineering. *Biorheology* 39(1–2):215–220
27. Loeser RF, Chubinskaya S, Pacione C, Im HJ (2005) Basic fibroblast growth factor inhibits the anabolic activity of insulin-like growth factor 1 and osteogenic protein 1 in adult human articular chondrocytes. *Arthritis Rheum* 52(12):3910–3917. doi:[10.1002/art.21472](https://doi.org/10.1002/art.21472)
28. Cals FL, Hellingman CA, Koevoet W, Baatenburg de Jong RJ, van Osch GJ (2012) Effects of transforming growth factor-beta subtypes on in vitro cartilage production and mineralization of human bone marrow stromal-derived mesenchymal stem cells. *J Tissue Eng Regen Med* 6(1):68–76. doi:[10.1002/term.399](https://doi.org/10.1002/term.399)
29. Fortier LA, Lust G, Mohammed HO, Nixon AJ (1999) Coordinate upregulation of cartilage matrix synthesis in fibrin cultures supplemented with exogenous insulin-like growth factor-I. *J Orthop Res* 17(4):467–474. doi:[10.1002/jor.1100170403](https://doi.org/10.1002/jor.1100170403)
30. Ma Z, Gao C, Gong Y, Shen J (2005) Cartilage tissue engineering PLLA scaffold with surface immobilized collagen and basic fibroblast growth factor. *Biomaterials* 26(11):1253–1259. doi:[10.1016/j.biomaterials.2004.04.031](https://doi.org/10.1016/j.biomaterials.2004.04.031)
31. Bessa PC, Casal M, Reis RL (2008) Bone morphogenetic proteins in tissue engineering: the road from laboratory to clinic, part II (BMP delivery). *J Tissue Eng Regen Med* 2(2–3):81–96. doi:[10.1002/term.74](https://doi.org/10.1002/term.74)
32. Kessler MW, Grande DA (2008) Tissue engineering and cartilage. *Organogenesis* 4(1):28–32
33. Blunk T, Sieminski AL, Gooch KJ, Courter DL, Hollander AP, Nahir AM, Langer R, Vunjak-Novakovic G, Freed LE (2002) Differential effects of growth factors on tissue-engineered cartilage. *Tissue Eng* 8(1):73–84. doi:[10.1089/107632702753503072](https://doi.org/10.1089/107632702753503072)
34. Kock L, van Donkelaar CC, Ito K (2012) Tissue engineering of functional articular cartilage: the current status. *Cell Tissue Res* 347(3):613–627. doi:[10.1007/s00441-011-1243-1](https://doi.org/10.1007/s00441-011-1243-1)
35. Yamamoto M, Ikada Y, Tabata Y (2001) Controlled release of growth factors based on biodegradation of gelatin hydrogel. *J Biomater Sci Polym Ed* 12(1):77–88
36. Lee JE, Kim KE, Kwon IC, Ahn HJ, Lee SH, Cho H, Kim HJ, Seong SC, Lee MC (2004) Effects of the controlled-released TGF-beta 1 from chitosan microspheres on chondrocytes cultured in a collagen/chitosan/glycosaminoglycan scaffold. *Biomaterials* 25(18):4163–4173. doi:[10.1016/j.biomaterials.2003.10.057](https://doi.org/10.1016/j.biomaterials.2003.10.057)
37. Holland TA, Tessmar JK, Tabata Y, Mikos AG (2004) Transforming growth factor-beta 1 release from oligo(poly(ethylene glycol) fumarate) hydrogels in conditions that model the cartilage wound healing environment. *J Control Release* 94(1):101–114
38. Langer R (1998) Drug delivery and targeting. *Nature* 392(6679 Suppl):5–10
39. Fu K, Klibanov AM, Langer R (2000) Protein stability in controlled-release systems. *Nat Biotechnol* 18(1):24–25. doi:[10.1038/71875](https://doi.org/10.1038/71875)
40. Bartus RT, Tracy MA, Emerich DF, Zale SE (1998) Sustained delivery of proteins for novel therapeutic agents. *Science* 281(5380):1161–1162
41. Zhu G, Mallery SR, Schwendeman SP (2000) Stabilization of proteins encapsulated in injectable poly (lactide-co-glycolide). *Nat Biotechnol* 18(1):52–57. doi:[10.1038/71916](https://doi.org/10.1038/71916)
42. De Laporte L, Shea LD (2007) Matrices and scaffolds for DNA delivery in tissue engineering. *Adv Drug Deliv Rev* 59(4–5):292–307. doi:[10.1016/j.addr.2007.03.017](https://doi.org/10.1016/j.addr.2007.03.017)

43. Nugent AE, Reiter DA, Fishbein KW, McBurney DL, Murray T, Bartusik D, Ramaswamy S, Spencer RG, Horton WE Jr (2010) Characterization of ex vivo-generated bovine and human cartilage by immunohistochemical, biochemical, and magnetic resonance imaging analyses. *Tissue Eng Part A* 16(7):2183–2196. doi:[10.1089/ten.TEA.2009.0717](https://doi.org/10.1089/ten.TEA.2009.0717)
44. Ulrich-Vinther M (2007) Gene therapy methods in bone and joint disorders. Evaluation of the adeno-associated virus vector in experimental models of articular cartilage disorders, periprosthetic osteolysis and bone healing. *Acta Orthop Suppl* 78(325):1–64
45. Vorburger SA, Hunt KK (2002) Adenoviral gene therapy. *Oncologist* 7(1):46–59
46. Adachi N, Sato K, Usas A, Fu FH, Ochi M, Han CW, Niyibizi C, Huard J (2002) Muscle derived, cell based ex vivo gene therapy for treatment of full thickness articular cartilage defects. *J Rheumatol* 29(9):1920–1930
47. Nixon AJ, Brower-Toland BD, Bent SJ, Saxer RA, Wilke MJ, Robbins PD, Evans CH (2000) Insulinlike growth factor-I gene therapy applications for cartilage repair. *Clin Orthop Relat Res* (379 Suppl):S201–213
48. Evans CH, Ghivizzani SC, Smith P, Shuler FD, Mi Z, Robbins PD (2000) Using gene therapy to protect and restore cartilage. *Clin Orthop Relat Res* (379):S214–219
49. Xiong F, Mi Z, Gu N (2011) Cationic liposomes as gene delivery system: transfection efficiency and new application. *Pharmazie* 66(3):158–164
50. Felgner PL, Gadek TR, Holm M, Roman R, Chan HW, Wenz M, Northrop JP, Ringold GM, Danielsen M (1987) Lipofection: a highly efficient, lipid-mediated DNA-transfection procedure. *Proc Natl Acad Sci U S A* 84(21):7413–7417
51. Mintzer MA, Simanek EE (2009) Nonviral vectors for gene delivery. *Chem Rev* 109(2):259–302. doi:[10.1021/cr800409e](https://doi.org/10.1021/cr800409e)
52. Godbey WT, Wu KK, Hirasaki GJ, Mikos AG (1999) Improved packing of poly(ethylenimine)/DNA complexes increases transfection efficiency. *Gene Ther* 6(8):1380–1388. doi:[10.1038/sj.gt.3300976](https://doi.org/10.1038/sj.gt.3300976)
53. Fang J, Zhu YY, Smiley E, Bonadio J, Rouleau JP, Goldstein SA, McCauley LK, Davidson BL, Roessler BJ (1996) Stimulation of new bone formation by direct transfer of osteogenic plasmid genes. *Proc Natl Acad Sci U S A* 93(12):5753–5758
54. Bonadio J, Smiley E, Patil P, Goldstein S (1999) Localized, direct plasmid gene delivery in vivo: prolonged therapy results in reproducible tissue regeneration. *Nat Med* 5(7):753–759. doi:[10.1038/10473](https://doi.org/10.1038/10473)
55. Guo T, Zhao J, Chang J, Ding Z, Hong H, Chen J, Zhang J (2006) Porous chitosan-gelatin scaffold containing plasmid DNA encoding transforming growth factor-beta1 for chondrocytes proliferation. *Biomaterials* 27(7):1095–1103. doi:[10.1016/j.biomaterials.2005.08.015](https://doi.org/10.1016/j.biomaterials.2005.08.015)
56. Diao H, Wang J, Shen C, Xia S, Guo T, Dong L, Zhang C, Chen J, Zhao J, Zhang J (2009) Improved cartilage regeneration utilizing mesenchymal stem cells in TGF-beta1 gene-activated scaffolds. *Tissue Eng Part A* 15(9):2687–2698. doi:[10.1089/ten.TEA.2008.0621](https://doi.org/10.1089/ten.TEA.2008.0621)
57. Chen J, Chen H, Li P, Diao H, Zhu S, Dong L, Wang R, Guo T, Zhao J, Zhang J (2011) Simultaneous regeneration of articular cartilage and subchondral bone in vivo using MSCs induced by a spatially controlled gene delivery system in bilayered integrated scaffolds. *Biomaterials* 32(21):4793–4805. doi:[10.1016/j.biomaterials.2011.03.041](https://doi.org/10.1016/j.biomaterials.2011.03.041)
58. Freyria AM, Mallein-Gerin F (2012) Chondrocytes or adult stem cells for cartilage repair: the indisputable role of growth factors. *Injury* 43(3):259–265. doi:[10.1016/j.injury.2011.05.035](https://doi.org/10.1016/j.injury.2011.05.035)
59. Marlovits S, Zeller P, Singer P, Resinger C, Vecsei V (2006) Cartilage repair: generations of autologous chondrocyte transplantation. *Eur J Radiol* 57(1):24–31. doi:[10.1016/j.ejrad.2005.08.009](https://doi.org/10.1016/j.ejrad.2005.08.009)
60. Raghunath J, Rollo J, Sales KM, Butler PE, Seifalian AM (2007) Biomaterials and scaffold design: key to tissue-engineering cartilage. *Biotechnol Appl Biochem* 46(Pt 2):73–84. doi:[10.1042/BA20060134](https://doi.org/10.1042/BA20060134)
61. Ringe J, Kaps C, Schmitt B, Buscher K, Bartel J, Smolian H, Schultz O, Burmester GR, Haupt T, Sittinger M (2002) Porcine mesenchymal stem cells. Induction of distinct mesenchymal cell lineages. *Cell Tissue Res* 307(3):321–327. doi:[10.1007/s00441-002-0525-z](https://doi.org/10.1007/s00441-002-0525-z)

62. Ballock RT, Reddi AH (1994) Thyroxine is the serum factor that regulates morphogenesis of columnar cartilage from isolated chondrocytes in chemically defined medium. *J Cell Biol* 126(5):1311–1318
63. Wakitani S, Yamamoto T (2002) Response of the donor and recipient cells in mesenchymal cell transplantation to cartilage defect. *Microsc Res Tech* 58(1):14–18. doi:[10.1002/jemt.10111](https://doi.org/10.1002/jemt.10111)
64. Butnariu-Ephrat M, Robinson D, Mendes DG, Halperin N, Nevo Z (1996) Resurfacing of goat articular cartilage by chondrocytes derived from bone marrow. *Clin Orthop Relat Res* 330:234–243
65. Vats A, Tolley NS, Bishop AE, Polak JM (2005) Embryonic stem cells and tissue engineering: delivering stem cells to the clinic. *J R Soc Med* 98(8):346–350. doi:[10.1258/jrsm.98.8.346](https://doi.org/10.1258/jrsm.98.8.346)
66. Lind M, Larsen A, Clausen C, Osther K, Everland H (2008) Cartilage repair with chondrocytes in fibrin hydrogel and MPEG poly(lactide) scaffold: an in vivo study in goats. *Knee Surg Sports Traumatol Arthrosc* 16(7):690–698. doi:[10.1007/s00167-008-0522-1](https://doi.org/10.1007/s00167-008-0522-1)
67. Thomson JA, Itskovitz-Eldor J, Shapiro SS, Waknitz MA, Swiergiel JJ, Marshall VS, Jones JM (1998) Embryonic stem cell lines derived from human blastocysts. *Science* 282(5391):1145–1147
68. Yamanaka S (2012) Induced pluripotent stem cells: past, present, and future. *Cell Stem Cell* 10(6):678–684. doi:[10.1016/j.stem.2012.05.005](https://doi.org/10.1016/j.stem.2012.05.005)
69. Liang G, Zhang Y (2013) Embryonic stem cell and induced pluripotent stem cell: an epigenetic perspective. *Cell Res* 23(1):49–69. doi:[10.1038/cr.2012.175](https://doi.org/10.1038/cr.2012.175)
70. Wu SM, Hochedlinger K (2011) Harnessing the potential of induced pluripotent stem cells for regenerative medicine. *Nat Cell Biol* 13(5):497–505. doi:[10.1038/ncb0511-497](https://doi.org/10.1038/ncb0511-497)
71. Diekman BO, Christoforou N, Willard VP, Sun H, Sanchez-Adams J, Leong KW, Guilak F (2012) Cartilage tissue engineering using differentiated and purified induced pluripotent stem cells. *Proc Natl Acad Sci U S A* 109(47):19172–19177. doi:[10.1073/pnas.1210422109](https://doi.org/10.1073/pnas.1210422109)
72. Ge Z, Li C, Heng BC, Cao G, Yang Z (2012) Functional biomaterials for cartilage regeneration. *J Biomed Mater Res A* 100(9):2526–2536. doi:[10.1002/jbm.a.34147](https://doi.org/10.1002/jbm.a.34147)
73. Iwasaki N, Yamane ST, Majima T, Kasahara Y, Minami A, Harada K, Nonaka S, Maekawa N, Tamura H, Tokura S, Shiono M, Monde K, Nishimura S (2004) Feasibility of polysaccharide hybrid materials for scaffolds in cartilage tissue engineering: evaluation of chondrocyte adhesion to polyion complex fibers prepared from alginate and chitosan. *Biomacromolecules* 5(3):828–833. doi:[10.1021/bm0400067](https://doi.org/10.1021/bm0400067)
74. Mafi P, Hindocha S, Mafi R, Khan WS (2012) Evaluation of biological protein-based collagen scaffolds in cartilage and musculoskeletal tissue engineering—a systematic review of the literature. *Curr Stem Cell Res Ther* 7(4):302–309
75. Lu L, Zhu X, Valenzuela RG, Currier BL, Yaszemski MJ (2001) Biodegradable polymer scaffolds for cartilage tissue engineering. *Clin Orthop Relat Res* (391):S251–270
76. Jeon YH, Choi JH, Sung JK, Kim TK, Cho BC, Chung HY (2007) Different effects of PLGA and chitosan scaffolds on human cartilage tissue engineering. *J Craniofac Surg* 18(6):1249–1258. doi:[10.1097/scs.0b013e3181577b55](https://doi.org/10.1097/scs.0b013e3181577b55)
77. Chan BP, Leong KW (2008) Scaffolding in tissue engineering: general approaches and tissue-specific considerations. *Eur Spine J* 17(Suppl 4):467–479. doi:[10.1007/s00586-008-0745-3](https://doi.org/10.1007/s00586-008-0745-3)
78. Bandt SK, Anderson D, Biller J (2008) Deep brain stimulation as an effective treatment option for post-midbrain infarction-related tremor as it presents with Benedikt syndrome. *J Neurosurg* 109(4):635–639. doi:[10.3171/JNS/2008/109/10/0635](https://doi.org/10.3171/JNS/2008/109/10/0635)
79. Huang YC, Simmons C, Kaigler D, Rice KG, Mooney DJ (2005) Bone regeneration in a rat cranial defect with delivery of PEI-condensed plasmid DNA encoding for bone morphogenetic protein-4 (BMP-4). *Gene Ther* 12(5):418–426. doi:[10.1038/sj.gt.3302439](https://doi.org/10.1038/sj.gt.3302439)
80. Huang YC, Riddle K, Rice KG, Mooney DJ (2005) Long-term in vivo gene expression via delivery of PEI-DNA condensates from porous polymer scaffolds. *Hum Gene Ther* 16(5):609–617. doi:[10.1089/hum.2005.16.609](https://doi.org/10.1089/hum.2005.16.609)

81. Storrie H, Mooney DJ (2006) Sustained delivery of plasmid DNA from polymeric scaffolds for tissue engineering. *Adv Drug Deliv Rev* 58(4):500–514. doi:[10.1016/j.addr.2006.03.004](https://doi.org/10.1016/j.addr.2006.03.004)
82. Wegman F, Bijenhof A, Schuijff L, Oner FC, Dhert WJ, Alblas J (2011) Osteogenic differentiation as a result of BMP-2 plasmid DNA based gene therapy in vitro and in vivo. *Eur Cell Mater* 21:230–242; discussion 242
83. Haupt JL, Frisbie DD, McIlwraith CW, Robbins PD, Ghivizzani S, Evans CH, Nixon AJ (2005) Dual transduction of insulin-like growth factor-I and interleukin-1 receptor antagonist protein controls cartilage degradation in an osteoarthritic culture model. *J Orthop Res* 23(1):118–126. doi:[10.1016/j.orthres.2004.06.020](https://doi.org/10.1016/j.orthres.2004.06.020)

Part II
Genetic and Protein Engineering

Chapter 8

Engineering Luciferases for Assays and Imaging

Andreas M. Loening and Zachary F. Walls

8.1 Introduction

Luciferases are a group of oxidizing enzymes that produce light as a by-product of the chemical reaction that they catalyze. This phenomenon has been observed throughout history, with Aristotle (384–332 BC) writing the first detailed descriptions of bioluminescence (or “cold light”) arising from both marine sources and insects [1]. Within the last several decades, bioluminescence has gained rapid prominence in biomedical experimentation. Luciferases have enabled scientists to shed light (both literally and figuratively) on fundamental biological processes and design analytical tests for a host of salient molecules [2]. However, due to the evolution of luciferases to suit specific applications in the natural world, their properties are not always synchronous with the needs imposed by biomedical research. Two of the most prevalent applications of luciferase, pyrosequencing and molecular imaging, require luciferases that are thermostable and emit redshifted wavelengths, respectively. The vast majority of wild-type luciferases, though, does not possess these attributes, and has thus been subject to modification. Due to their utility in biomedical applications, a substantial amount of effort has been spent within the scientific community to manipulate these and other properties of luciferases through protein engineering. What follows is an attempt to introduce the motivation for modifying luciferases, various techniques used for engineering of these enzymes, and highlights on the most relevant successes.

A. M. Loening
Department of Radiology, Stanford University School of Medicine, Stanford,
CA, USA

Z. F. Walls (✉)
Department of Pharmaceutical Sciences, East Tennessee State University,
Johnson City, TN, USA
e-mail: wallsz@etsu.edu

8.2 Major Categories of Luciferases

A comprehensive review of luciferases is outside the scope of this chapter. What follows is an abbreviated discussion of classes of luciferases and specific luciferases that are currently commercially available and/or have undergone significant protein engineering. The most salient details for these enzymes are collected in Table 8.1. For more extensive reviews of luciferases in general, please see any one of the several excellent reviews [3, 4].

8.2.1 Beetle Luciferases

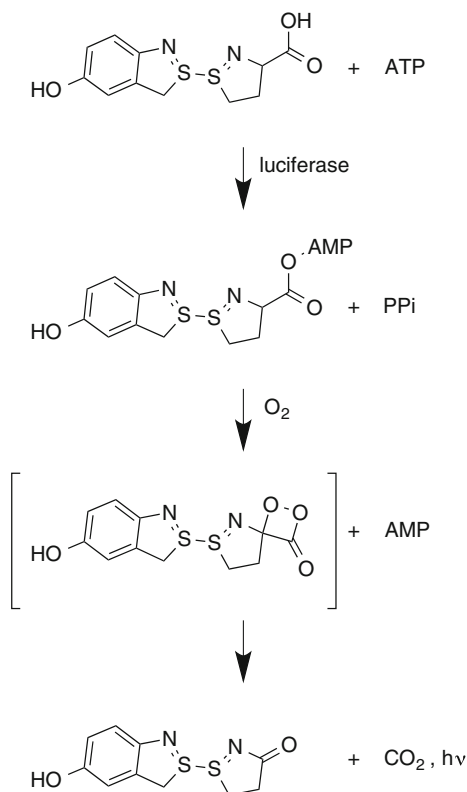
Terrestrial organisms have included luciferases in their evolutionary trajectory for a wide variety of applications, including defense, courtship, and the attraction of prey. Within the terrestrial luciferases, the best studied and by far the most commonly used in biomedical applications are the “beetle luciferases” found in organisms within the order *Elateroidea*. Although many beetle luciferases have been identified, including those from the click beetle (*Pyrophorus plagiophthalmus*) and the railroad worm (*Phrixothrix hirtus*), the most well-known and widely studied is that from the North American firefly, *Photinus pyralis*. The *P. pyralis* luciferase (generally referred to as firefly luciferase = FLuc) is a 62-kDa globular protein and can be thought of as the prototype for the beetle luciferases. The beetle luciferases are homologous, consistent with them evolving only once during the history of this planet. They all catalyze the identical enzymatic reaction, producing light by oxidizing their substrate D-luciferin in the presence of cofactors Mg^{2+} , O_2 , and ATP, but they can demonstrate slight differences in their emission wavelength. The beetle luciferases have been the focus of many engineering pursuits, mainly due to their earlier discovery, relatively redshifted emission compared to other well-studied luciferases, and their necessity for ATP, a central element in cellular metabolism, as a cofactor.

The oxidation of D-luciferin by beetle luciferases is a two-step enzymatic process (Fig. 8.1) [5]. The first step involves the reaction of luciferin and ATP to form luciferyl-adenylate. This step is similar to the one performed by many fatty acyl-CoA synthetases, and some evidence suggests that beetle luciferases are evolutionarily connected to these enzymes [6]. The second step of the reaction involves oxidation of luciferyl-adenylate by molecular oxygen to form an intermediate structure, which spontaneously breaks down into oxyluciferin and carbon dioxide. The energy released by the destruction of the chemical bond takes the form of a photon, and thus bioluminescence is produced.

Table 8.1 The most widely used luciferases in biomedical research are listed below according to their species of origin

Species	Peak wavelength (nm)	Size (kDa)	Native substrate	Co-factors	Native subcellular localization	Reference
<i>Photinus pyralis</i>	560	62	D-luciferin	ATP, O ₂	Intracellular (peroxisomes)	[91]
<i>Phrixothrix hirtus</i>	622	61	D-luciferin	ATP, O ₂	Intracellular (peroxisomes)	[92]
<i>Pyrophorus plagiophthalmus</i>	593	60	D-luciferin	ATP, O ₂	Intracellular (peroxisomes)	[93]
<i>Renilla reniformis</i>	480	36	Coelenterazine	O ₂	Intracellular (lumisomes)	[94]
<i>Gaussia princeps</i>	470	20	Coelenterazine	O ₂	Secreted	[95]
<i>Metridia longa</i>	480	24	Coelenterazine	O ₂	Secreted	[96]
<i>Oplophorus gracilirostris</i>	455	106 (heterotetramer)	Coelenterazine	O ₂	Secreted	[97]
<i>Vargula hilgendorffii</i>	460	68	Cypridina luciferin	O ₂	Secreted	[98]
<i>Cypridina noctiluca</i>	465	61	Cypridina luciferin	O ₂	Secreted	[18]
<i>Pyrocystis lunula</i>	474	140	Dinoflagellate luciferin	ATP, O ₂	Intracellular (microsources)	[19]
<i>Vibrio harveyi</i>	490	77 (heterodimer)	RCHO	FMNH ₂ , O ₂	Intracellular	[20]

Fig. 8.1 The oxidation of luciferin by beetle luciferases is a two-step process that is initiated by the formation of a luciferyl-adenylate intermediate. This chemical is then oxidized in the presence of molecular oxygen and light is generated as a by-product



8.2.2 *Coelenterazine Luciferases*

A variety of luciferin/luciferase systems also exist in marine environments. These marine luciferases most commonly emit light with a blue wavelength peak (~480 nm), likely reflecting the end result of selective pressure originating from the preferential transmittance of blue light by ocean water [7]. Within the marine luciferases, the best studied and the only ones in widespread biomedical utilization are those that utilize the substrate coelenterazine (or analogs of coelenterazine).

Coelenterazine is an imidazolopyrazine common in the marine food chain. In contrast to the beetle luciferases, coelenterazine-utilizing luciferases have evolved multiple times from a variety of different precursor enzymes to utilize this same substrate. This likely reflects the relatively simple chemistry and low kinetic barrier of the coelenterazine degradation scheme in comparison to D-luciferin. Although some specific coelenterazine luciferases may require cofactors, in general, these luciferases require only coelenterazine and oxygen, producing coelenteramide, carbon dioxide, and a blue wavelength photon of light. The ease with which a new enzyme can arise that catalyzes this reaction is exemplified by the observation that even albumin catalyzes the degradation of coelenterazine at a low

level [8]. This multiplicity is advantageous for protein engineering as there exists a number of very different starting points for developing novel luciferases.

The well-known coelenterazine luciferases can be categorized into three classes, luciferases from the genus *Renilla* (e.g., *Renilla reniformis* luciferase), copepod luciferases such as those from the family *Metridinidae* (e.g., *Gaussia princeps*, *Metridia longa*), and more recently the luciferase from the decapod *Oplophorus gracilirostris*. These different luciferases also demonstrate variable levels of specificity to coelenterazine versus analogs of coelenterazine, with *G. princeps* luciferase being the most specific, and *O. gracilirostris* luciferase being the least [9].

The coelenterazine luciferase most widely studied is that from the soft coral *R. reniformis*. This luciferase is often simply called “*Renilla* luciferase” (RLuc), although there are other species within the *Renilla* genus that have had their luciferases isolated (e.g., *Renilla mülleri* luciferase). *Renilla* luciferase is a 36-kDa intracellular monomeric protein that is efficiently expressed in a variety of bacterial and mammalian expression systems [10].

The second most studied coelenterazine luciferase is the luciferase from the copepod *G. princeps*, generally referred to simply as *Gaussia* luciferase (GLuc). GLuc is a 20-kDa protein, and similarly to the other copepod luciferases, is a secreted protein that harbors multiple disulfide bonds. These disulfide bonds have made copepod luciferases challenging to express in functional form in bacterial expression systems, although success has been obtained with insect [11] and cell-free systems [12]. The primary sequence of copepod luciferases contains two similar functional domains [13]. In the case of GLuc, these domains have demonstrated an ability to catalyze coelenterazine degradation independently, albeit with greatly decreased activity [14]. A potential limitation of the copepod luciferases to keep in mind is that their enzymatic action appears to be cooperative [15] and therefore light output is nonlinearly related to substrate concentration. However, in most assays, substrate concentration is relatively constant and luciferase concentration is the variable being measured, so this positive cooperative effect is rarely noticeable.

The coelenterazine luciferase from the decapod *O. gracilirostris* (OLuc) is a secreted enzyme complex, consisting of a heteromeric structure containing two 35-kDa and two 19-kDa catalytic subunits [16]. This complexity has previously limited its application to biomedical research. Recently, a monomeric luciferase (termed NanoLuc) has been derived by protein engineering from the 19-kDa OLuc catalytic subunit [17]. This OLuc variant should be more applicable to biomedical applications and is described in more detail later in this chapter.

8.2.3 Other Marine Luciferases

Additional marine luciferases have been studied, but have found much more limited use in biological assays and have not been extensively engineered. Two luciferases from Cypridina ostracods have been cloned, one from *Vargula*

hilgendorffii, and one from *Cypridina noctiluca*. These *Cypridina* luciferases emit blue light when degrading their substrate Vargulin. Given their unique substrate, they can be multiplexed in experimental use with D-luciferin and/or coelenterazine-utilizing luciferases. Although highly stable, these proteins are relatively large (61 kDa), are secreted enzymes, contain a total of 17 disulfide bonds [18], and their substrate vargulin is relatively unstable, all factors that would make the *Cypridina* luciferases a more challenging starting point for protein engineering than the coelenterazine or Beetle luciferases.

Several marine dinoflagellates express a luciferase, most likely used for quorum sensing. This luciferase is relatively large at ~ 140 kDa, and emits blue wavelengths. These properties have prevented a wide adoption of this luciferase, but its unique substrate provides the possibility for multiplexing with other luciferases. A 46-kDa active fragment of dinoflagellate luciferase has been developed and utilized as a reporter in mammalian cells [19]. This truncated dinoflagellate luciferase could be combined with firefly and *Renilla* luciferases, for example, to monitor the expression of three different genes.

8.2.4 Bacterial Luciferase

Luciferase-expressing bacteria can be found in a variety of ecosystems. Most possess symbiotic relationships with other organisms, providing a means for communication, attraction of prey, or defense to the host in exchange for nutrients. The bacterial luciferase is actually a cassette of five genes, two of which are responsible for substrate oxidation leading to bioluminescence, and three that synthesize the substrate from common biomolecules. Due to this level of complexity, the bacterial luciferase is seldom used in biomedical research, although efforts have been made to adapt it for the creation of autonomously luminescent cells [20]. This achievement is attractive for certain longitudinal studies of specific cellular populations because it obviates the necessity for repeated administration of exogenous luciferase substrate.

8.3 Current Biomedical Uses

Due to the intrinsic difficulties of translating optical technologies into a clinical setting (i.e., suboptimal wavelengths, necessity for exogenous genetic/proteinaceous material), luciferases have a limited role in the medical setting. They are widely used, however, in biomedical research, and are gaining ground in the area of diagnostic testing. One technique in particular named luciferase immunoprecipitation system (LIPS) has demonstrated considerable advantages over similar systems that use fluorescent or colorimetric indicators. The LIPS procedure is very similar to enzyme-linked immunosorbent assay (ELISA), with the exception that

an antibody-luciferase fusion protein is used for the detection of antigens in assays. Compared to similar immunodetection procedures, LIPS has proven to be more sensitive and specific [21]. As with other applications that will be discussed below, the use of luciferases for immunodiagnostics requires that the enzymes maintain stability over time and in some cases at elevated temperatures. Thus, engineering thermostable luciferases is crucial for the success of these techniques.

One of the biggest commercial successes of the beetle luciferases is pyrosequencing. This is a DNA sequencing technique that is predicated on three enzymatic reactions. The first reaction occurs during *de novo* DNA synthesis by DNA polymerase. This reaction produces an inorganic pyrophosphate molecule, which can then be converted into ATP by ATP sulfurylase (the second reaction). The final reaction is described in more detail in the previous section and involves the use of this ATP molecule by a beetle luciferase to produce a bioluminescent signal. Therefore, each nucleotide successfully integrated into the growing complementary chain of the template DNA can be quantitatively detected by light emission. Pyrosequencing has been shown to be quicker and simpler than other sequencing techniques and has become the method of choice for many sequencing needs [22]. As DNA polymerization is generally optimal at elevated temperatures, thermostable luciferases are absolutely necessary for this application, and many luciferase engineering studies have been performed to produce more pyrosequencing-friendly beetle luciferase variants.

Additionally, luciferases are used extensively in basic laboratory biomedical research as reporter genes. Traditionally, certain genes whose protein products are detectable by an optical or radiological device (e.g., green fluorescent protein, beta-galactosidase, thymidine kinase) have been used as surrogates to report on a genetic activity of interest. Often this takes the form of driving the expression of a reporter gene with the promoter of the gene of interest. In this manner, the transcriptional activation of a gene can be interrogated using convenient and fast readouts. Luciferases have proven to hold a special niche in this regard as they are often more sensitive than other reporter genes and generally translate better to small-animal *in vivo* studies. Moreover, due to the technique known as split-protein complementation, discussed in greater detail in a subsequent section, luciferases have been engineered to report on much more than gene expression. Recent studies have seen the design of luciferases that can report on small molecule kinase inhibition, DNA methylation, and caspase activity [23–25]. These studies require luciferases that have been specially engineered to only produce bioluminescence after these molecular events have occurred and demonstrate the degree of creativity and ingenuity currently being applied to luciferase engineering.

Small-animal *in vivo* imaging represents the final main application of engineered luciferases. This application is in many ways an extension of reporter gene assays, but imposes additional constraints upon the characteristics of the luciferase used. It generally favors the use of luciferases whose wavelengths have been shifted toward the red end of the electromagnetic spectrum due to the optical window of mammalian tissue (discussed in greater detail in a subsequent section).

These engineered luciferases have contributed greatly to our ability to translate cellular studies into more physiologically relevant models and have provided a potent tool for interrogating biological processes in a living system.

8.4 Rationale for Protein Engineering of Luciferases

Although there are a number of reasons for performing luciferase protein engineering, a common reason is that the native luciferin/luciferase system is not sufficiently robust for consistent use in a variety of laboratory solutions, cellular compartments, or temperatures. Each luciferin/luciferase system has evolved under the selective pressures of its native environment. For instance, *Renilla* luciferase evolved to work in a salt water creature, in small membrane-bound particles called lumisomes, associated with a green fluorescent protein, and at ocean temperatures [26]. Thus, it stands to reason that mutations could be readily identified to improve its performance and stability as a monomeric protein in laboratory solutions at room or mammalian body temperature.

Additionally, luciferases are relatively “easy” to engineer compared to other enzymes because their functional properties make mutants readily identifiable. Large-scale assays can be performed utilizing common bioluminescence imaging systems, or even the human eye for sufficiently bright luciferases [27].

8.5 Designing Selection Strategies for Protein Engineering of Luciferases

An important philosophical point in the protein engineering of luciferases is the definition of what constitutes “better.” Much as beauty is in the eye of the beholder, what constitutes a “better” luciferase is entirely dependent on the end application goal. Most comparisons between luciferases in the literature are made with respect to which is “brighter” in a particular assay condition, with little or no consideration given for the robustness of the improvement when the assay is performed in different solutions/cellular compartments/temperatures or the actual enzyme kinetics. For instance, a kinetically slow enzyme could look “better” than a fast enzyme if the fast enzyme degrades the majority of the applied luciferin before brightness is measured. A secreted luciferase may perform “better” than a nonsecreted luciferase in the context of a cell culture when the entire cell culture dish including media is assessed, but the loss of association between the cell of origin and the location of bioluminescence will limit utility of a secreted luciferase in small-animal bioluminescence imaging.

A closely related point is that many comparisons are based on assays (such as cell culture assays) in which the bioluminescence signal is not normalized to the

total amount of luciferase. This gives an advantage to luciferases that are more stable, as more of the luciferase will accumulate over the course of the experiment, and the experimental condition utilizing the more stable luciferase will appear to be “brighter” even though both luciferases may have the same light output per enzyme. Given the end goal of the assay, this stability may or may not be desired. Increased luciferase stability impedes the ability of an assay to monitor transient fluctuations in luciferase expression, and it takes longer to reach a steady state of luciferase activity within the cell. As discussed in a following section, some luciferase engineering has been directed into making the luciferase mRNA and/or protein less stable for this very reason.

This all leads to the first law of directed evolution: “you get what you select for.” The improved luciferase/luciferin combinations derived under artificial selective forces in the laboratory are being improved with respect to activity in a specific test. Screens must be designed carefully, or contain controls, to ensure that the mutations picked up are being selected for the desired end application goals. As an example, consider a random mutagenesis screen of a luciferase in *E. coli*. If the selection method is simply which colonies are brightest the screen will select for a number of different properties: increased thermostability at the incubation temperature, improved codon utilization for bacterial expression, removal of bacterial protease sites, improved folding in the bacterial expression system, better matching of the emission spectrum to the sensitivity profile of the detector, etc. Some of these “improvements” may be detrimental if the luciferase is utilized in a different system such as mammalian cells. If a more targeted goal is desired, such as faster enzyme kinetics, a more sophisticated screening system must be employed.

8.6 Methods for Protein Engineering of Luciferases

The techniques and theories driving luciferase engineering are not substantially different from those used to modify any other protein, but luciferase’s functional capacity has made it a facile model for experimentation, and its prominence in biomedical research has made it an attractive target.

Luciferase engineering can be broadly divided into two categories. The first category is similar to canonical protein engineering, in which changes made to the primary sequence affect the enzyme’s intrinsic properties (e.g., specific activity, thermostability, emission wavelength).

The second category is more prominent, although not exclusive, to reporter proteins such as the luciferases, and involves the dissection or interruption of the protein’s primary sequence into two distinct domains. The purpose of alterations in this second category is to prevent the enzyme from oxidizing its substrate in the absence of some other biomolecule, thus serving as an analyte detector.

Within each category, various strategies have been employed to introduce mutations. Random mutagenesis has been applied to luciferase engineering with

substantial success [28–33]. Different techniques have been used to induce random mutations, although the most common is error-prone PCR. In theory, this approach yields an unbiased distribution of mutants across the coding region of the protein, effectively maximizing the variable space. In practice, certain codons are more susceptible to mutagenesis than others, and the altered residues are often less randomly distributed than expected. Nevertheless, this technique yields a prodigious number of mutated enzymes that can be subjected to high throughput screens. In the case of luciferase engineering, the screens generally take the form of bioluminescent output under various constraints. For example, one screen used by several investigators to identify thermostable variants involves the incubation of luciferase-expressing bacterial colonies at an elevated temperature followed by application of the luminescent substrate and identification of the brightest colonies. Constructs are then sequenced to identify the mutations contributing to the new phenotype.

The other main technique for introducing mutations into luciferase is site-directed mutagenesis. Unlike random mutagenesis, this method is usually based on a specific hypothesis regarding how a certain mutation or mutation site will affect the enzyme's properties [10]. Site-directed mutations are most often initiated by structural or sequence analysis and can be far more efficient than random approaches. For instance, in the generation of the RLuc variant RLuc8 [10], only ~30 single-mutation RLuc variants were screened to generate a variant that was fourfold brighter and two orders of magnitude more stable.

Combinatorial mutagenesis is a variation on both of these methods for introducing mutations. This semi-rational method entails the random incorporation of a subset of site-specific mutations. Although this method has been used sparingly for luciferase engineering [28], its results are encouraging and may see wider use in the future.

8.6.1 Structure-Based Versus Sequence-Based

Sequence homology between the luciferase proteins of various species has driven many of the studies that seek to enhance these enzymes' properties. This has been a motivating impulse for those seeking to induce bathochromatic shifts in the beetle luciferases, as well as groups interested in improving protein stability in both beetle and coelenterazine luciferases, although the precise rationale in each case is slightly different. To provoke changes in peak wavelength of the beetle luciferases, sequence homology is often assessed in an attempt to graft the attributes of one luciferase onto another.

Sequence homology has also been used with great success for the creation of more stable luciferase enzymes [10, 34, 35], although for this application, homology is assessed between multiple species. One of the guiding principles of protein evolution is that conservation is driven either by stability or function. By selectively mutating residues within a luciferase so that they conform to a

consensus sequence, one is choosing candidate mutations that have already been screened by nature to be tolerated or even preferred within the context of the proteins' fold and are much less likely to be deleterious to the protein than a residue picked at random. This consensus mutagenesis approach requires that a number of homologous proteins already exist in the sequence database that, while being similar enough to allow a valid alignment, are evolutionarily distinct enough that a bias toward stabilizing mutations can be identified.

Structural considerations have also played a role in luciferase engineering. Different tactics have been used in this respect, including mutagenesis of residues involved in the active site, introduction of cysteine residues to form disulfide bridges, and mutagenesis of solvent-exposed residues [28, 36–38]. These studies use publicly available crystal structures of a handful of luciferases to develop biochemical hypotheses regarding the contribution of individual amino acids to stability and wavelength emission.

8.6.2 Codon Optimization

Although not strictly protein engineering as the primary sequence of the protein is conserved, evaluation of codon usage is often a useful initial step in improving expression levels of luciferase proteins. Several studies have generated codon-optimized luciferase genes, primarily for mammalian expression, to help improve transcriptional activity and mRNA stability [39–42]. This procedure is not specific for luciferases and is generally performed when attempting to generate robust expression of a nonmammalian gene in a mammalian system.

8.6.3 Protein Truncation/Extension

Certain studies have manipulated the stability or intracellular compartmentalization of luciferases by truncating or appending additional residues to the primary sequence. Again, this technique is not specific to luciferase engineering and has been applied to many other proteins.

In general, these modifications are used to alter properties of the luciferase that are of importance when used as a reporter gene (discussed in further detail later). Adding the PEST sequence or ubiquitinylation-prone sequences to the luciferase protein has the general effect of reporting on cellular dynamics and intracellular protein transport [43–45]. Removal of N-terminal signal peptide sequences or adding transmembrane domains have been utilized to maintain association of a normally secreted protein to its cell of origin [41, 46].

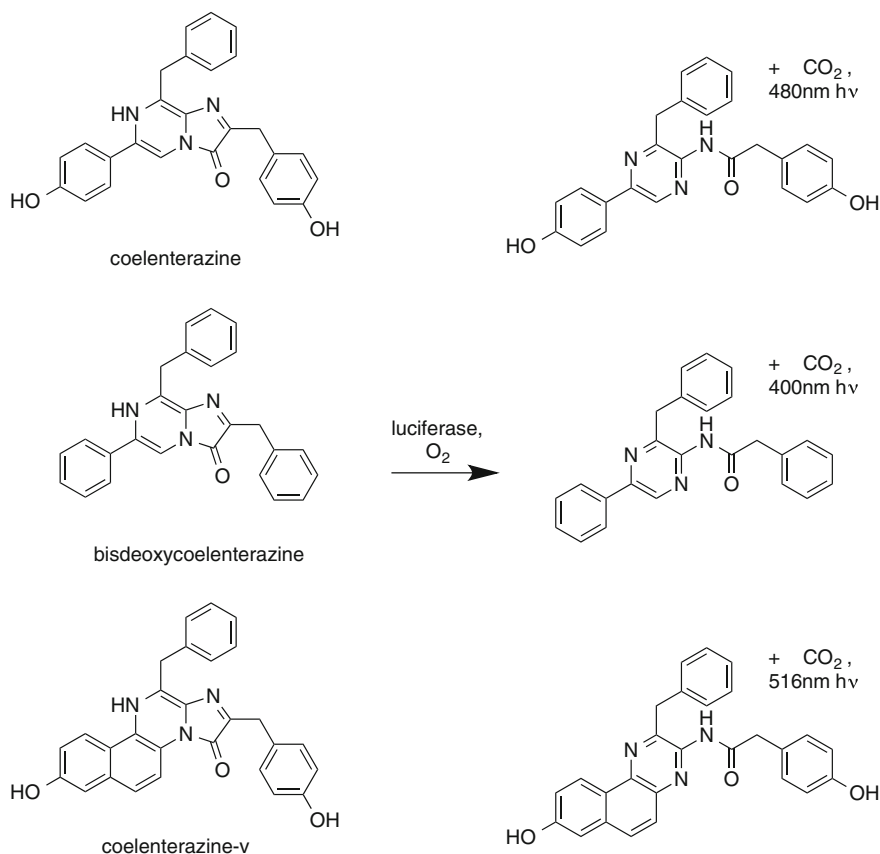


Fig. 8.2 Native coelenterazine (*top*) and two derivatives, bisdeoxycoelenterazine (*middle*) and coelenterazine-v (*bottom*), are all oxidized by *Renilla* luciferase. The wavelengths of the light produced by the oxidation of each substrate, however, are significantly different [27, 28, 88–90]

8.6.4 Substrate Alteration

An in-depth discussion of chemical modifications to luciferase substrates, chiefly D-luciferin and coelenterazine, is beyond the scope of a chapter focused on protein engineering of luciferases. However, it is important to note that an equally large body of work has reported on the successful design of modified luciferase substrates that have the potential to alter emission wavelength when oxidized, or prevent oxidation prior to conversion by a molecule of interest. Thus, equivalent results in terms of red shifts and molecular-sensing have been achieved by engineering of the luciferase substrates rather than the luciferases themselves [28, 47, 48].

It bears mentioning, that a factor to consider when comparing between different substrates is the autoluminescence rate of the luciferin under the assay conditions employed. For instance, the coelenterazine analog coelenterazine-v (Fig. 8.2)

generates an order of magnitude higher background autoluminescence than coelenterazine [47]. Even if a luciferase is brighter with coelenterazine-v, the increase in brightness is unlikely to make up for the order of magnitude decrease in sensitivity for conditions in which very small amounts of luciferase are present.

8.7 Examples of Luciferase Protein Engineering

8.7.1 Intensity Improvements

Although only a single study in the literature has specifically sought to enhance the intensity of beetle luciferase, many mutants have demonstrated increased light output as a result of stabilizing or color-shifting mutations. Further complicating the issue of comparing mutants between studies is the number of variables involved in measuring luminescent output (e.g., luciferin concentration, ATP concentration, acquisition time, photomultiplier tube wavelength sensitivity). For the purposes of this chapter, activity values relative to the mutant's parenteral luciferase are reported when possible, as this accounts for variations in luminescence measurements. Using this metric, the brightest, or most intense, mutant described to date is a triple mutant of the *P. pyralis* luciferase (I423L, D436G, L530R), which demonstrated a 12-fold increase in intensity over wild type [32]. Each mutation was discovered independently by random mutagenesis coupled with screening of bacterial cell lysates, and then all three mutations were combined to produce the final version. Also of note in this category of engineered luciferases is a report of a double mutant of the *P. hirtus* luciferase (I212L, N351K), yielding a 9.8-fold improvement in intensity over wild type [34]. These amino acid alterations were introduced by site-specific mutagenesis based on sequence homology to stabilizing mutations previously characterized in the luciferases of *Luciola cruciata* and *P. pyralis*. While even this mutant is much less bright compared to its compatriots in the luciferase gallery due to the low intrinsic activity of wild-type *P. hirtus*, this study is of particular interest because of the long peak emission wavelength of *P. hirtus*, an attribute which is examined in the following section.

Similar to the case for beetle luciferases, while a number of studies have generated "improved" coelenterazine luciferases, improvements in light output have generally been due to improvements in stability and therefore the amount of functional protein, rather than mutations that improve the quantum yield or kinetics of the enzyme. Utilizing a consensus sequence approach, an M185V mutation was identified for *Renilla* luciferase that led to a threefold increase in light output arising from improvements in both quantum yield and kinetics [10]. A random mutagenesis screen identified the mutations K189V and V267I that led to a threefold to fourfold improvement in light output compared to native *Renilla* luciferase [49]. These improvements were attributed to a combination of improved stability, improved kinetics, and decreased levels of substrate inhibition. These

mutation sites had previously been studied with other amino acid substitutions based either on a consensus mutation approach (V267) or due to their proximity to the active pocket (K189), but these other substitutions at the same sites did not yield improvements [27].

For the copepod luciferases, recognition that the N-terminal domain of *M. longa* was not homologous to *Gaussia* luciferase led to an N-terminal-truncated *M. longa* variant that demonstrated sixfold to tenfold improvements in light output compared to the native luciferase, albeit with decreased thermal stability [50]. A semi-rational mutagenesis strategy was performed on *Gaussia* luciferase by targeting hydrophobic regions presumed to constitute the enzymatic pocket, and substituting in other hydrophobic amino acids [51]. Screening of the resultant single-mutation variants and combining the beneficial mutations, led to a 4-mutation variant termed “Monsta” that exhibited ~six-fold greater light output than GLuc, with this improvement due to improved folding, turnover rate and quantum yield.

8.7.2 Stability Alterations

One of the major biomedical applications of the beetle luciferases is pyrosequencing. This technology is predicated on the necessity for ATP in order for beetle luciferases to oxidize D-luciferin. However, like most proteins produced by mesophilic organisms, beetle luciferases are unstable at elevated temperatures. Thus, a need exists for this particular application (among others) for the production of thermostable beetle luciferase mutants. A number of different groups have tackled this problem with varying techniques and results. Similar to the discussion of evaluating luciferase intensity, it is often difficult to compare reports of luciferase stability from one study to the next for two reasons: (1) the enzyme’s activity is highly dependent on environmental (i.e., buffer) conditions, and (2) different studies report stability at different temperatures (thus, a mutant that is highly stable at 37 °C may degrade quickly at 50 °C, but conversely, a mutant with good stability at 50 °C may not be as robust as others at 37 °C). What follows is a brief discussion of some of the most stable mutants described for discrete temperatures, and the methods used to engineer them.

One of the earliest, and still among the most successful, attempts at creating a thermostable beetle luciferase was carried out by Hall and colleagues on the luciferase from *Photuris pennsylvanica* [52]. This study used error-prone PCR to create random mutations in the luciferase gene, followed by cloning into a bacterial expression vector. Transformed bacteria were then plated and exposed to elevated temperatures prior to treatment with D-luciferin. Bioluminescent capture of the bacterial plates revealed individual colonies that expressed luciferase with stabilizing mutations. Remarkably, they were able to identify one mutant that retained activity after 5 h at 65 °C. The exact mutations of this enzyme, however, are unknown to the general scientific community, as this mutant remains a proprietary entity. A highly stable variant of the *P. pyralis* luciferase has been

described with a half-life at 37 °C of 11.5 h (T214A, A215L, I232A, F295L, E354K) [53, 54]. These mutations were discovered independently by random mutagenesis and screens similar to the one described above, with the site-directed combination of all 5 producing a synergistic effect. Of the reported mutants evaluated at 42 °C, an octuple mutant of the luciferase from *Luciola mingrelica* (S118C, C146S, R211L, T213S, A217V, E356K, S364C) has a half-life at that temperature of nearly 10 h [31]. This mutant was discovered by directed evolution, in which 4 rounds of random mutagenesis were employed, using the most thermostable mutant identified from each round as the basis for further mutagenesis. In contrast to the studies described above, a structure-based approach was used to engineer a double mutant of *L. mingrelica* luciferase (G216N, A217L) with a greater than 4.5 h half-life at 45 °C [35]. Using the known stabilizing, but activity-compromising, mutation A217L, these investigators altered residues with spatial proximity to 217 according to the crystal structure of the protein, in the hopes of producing a mutant that was both stable and highly active.

This subset of luciferase engineering has seen the use of several methods that are not as widely used as those previously discussed. Of note is one study that identified an undecuple mutant of the *P. pyralis* luciferase (F14A, L35Q, M118L, N138G, V182K, A215L, F295L, E354R, V366A, S420T, F465R) with a half-life of more than 72 h at 40 °C using combinatorial consensus mutagenesis [55]. This technique involves construction of a consensus sequence by aligning multiple proteins (in this case, all sequenced beetle luciferases) and identifying the residues at which the sequence of interest deviates from the consensus. Primers are then designed to mutate the wild-type sequence to the consensus sequence. In contrast to more canonical site-directed mutagenesis, however, combinatorial consensus mutagenesis incorporates these selected mutations at random, and then a screen is employed to select for mutants possessing the desired property (in this case thermostability).

Another unique method of engineering thermostability into a beetle luciferase was accomplished by creating disulfide bonds by mutating certain residues to cysteines. This attempt was made based on the observations that most proteins exposed to harsh extracellular conditions contain at least one disulfide bond. Using the crystal structure of the luciferase from *P. pyralis* and in silico analysis of putative disulfide sites, several mutations were made by site-directed mutagenesis [56]. Although the most stable mutant identified (A296C, A326C) is not as robust as some of the others discussed in this section, this study warrants mention as an alternative method for luciferase engineering with respect to thermostability [57].

One final technique that deserves inclusion in a discussion of engineering beetle luciferase thermostability is a site-directed mutagenesis of trypsin-cleavable sites within the primary sequence of the luciferase from *P. pyralis* [58]. The sites selected for mutagenesis were chosen from previous empirical studies coupled with interspecies luciferase sequence homology to exclude from alteration residues thought to be necessary for enzymatic activity. The most successful mutant, R337Q, demonstrated substantial resistance to trypsin hydrolysis and improved thermodynamic stability over wild type.

Several publications have focused on improving the stability of *Renilla* luciferase (RLuc). An early publication examining the effects of cysteines on stability for a secreted form of RLuc found that a C124A mutation was \sim six-fold more resistant to inactivation in their assay [59]. Although the authors postulated this was due to reduced inadvertent disulfide bond formation, the stability improvement could also be explained based on C124A being a mutation toward the consensus sequence [27]. A later publication performing a consensus-sequence-based approach on this RLuc/C124A variant identified an additional six stabilizing mutations that when combined generated an RLuc variant (RLuc8) that was 200-fold more resistant to inactivation in murine serum than the native luciferase and four-fold brighter on a per-enzyme basis [10]. Little attention has been paid to increasing the stability of the secreted copepod luciferases, as these already demonstrate impressive stability to pH conditions and heat shock [60].

8.7.3 Emission Wavelength Shifts

In the field of small-animal bioluminescence imaging, wavelengths in the visible red region of the electromagnetic spectrum reign supreme. This is due to the relative optical window for mammalian tissue that exists between 600 nm (below which wavelengths are absorbed predominantly by hemoglobin) and 1,200 nm (above which wavelengths are absorbed by water). For luciferase-based imaging, this means that despite the greater activity of the *P. pyralis* luciferase (557-nm peak wavelength), the number of photons that reach the surface of the subject being imaged could be fewer than those emanating from less active, but more redshifted luciferase such as *P. hirtus* (623-nm peak wavelength). Unfortunately, the *P. hirtus* luciferase is especially heat-labile and enzymatically slow, making it a poor choice for most molecular imaging applications.

Among the most successful attempts at engineering redshifted beetle luciferase enzymes is a single mutant of the luciferase from *Lampyrus turkestanicus* (S284T) that emitted a peak wavelength of 618 nm (compared to 555 nm of the wild-type enzyme) [61]. This mutation was based on sequence homology to a redshifted mutant of *P. pyralis* (S284T) with a similarly impressive bathochromatic shift (615-nm peak wavelength) identified by random mutagenesis [62]. The most redshifted variant of the *P. pyralis* luciferase described to date is a nonuple mutant referred to as Ppy RE9 (T214A, A215L, I232A, S284T, F295L, R330G, I351V, E354I, and F465R, 617-nm peak wavelength) that also uses the redshifted single-mutant S284T as a point of departure [40]. Ppy RE9 was designed by incorporating the stabilizing mutations T214A, I232A, and F295L, identified by random mutagenesis [63], A215L, based on homology to a stabilized mutant of the *L. cruciata* luciferase identified by random mutagenesis [64], the stabilizing mutation E354I, identified by random mutagenesis [29], and stabilizing mutations I351V and F465R, identified by selective mutagenesis of solvent-exposed amino acid residues determined by crystal structure analysis [38]. The redshifted mutation R330G was

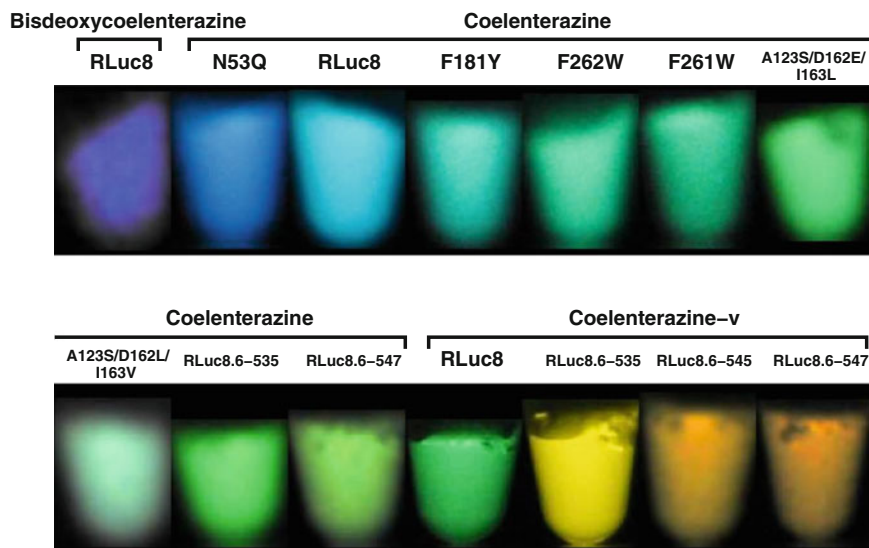


Fig. 8.3 A range of emission spectra can be achieved with *Renilla* luciferase via mutation of the luciferase and/or alteration of the substrate. The specific mutations utilized here have been previously published in the literature [10, 27, 28]

identified by performing random mutagenesis on this stabilized mutant and highlights the interconnectivity of luciferase attributes. A consistent theme running throughout the luciferase engineering literature is that mutations that enhance one attribute of the enzyme often come at the cost of another. Case in point, the authors of the Ppy RE9 study describe how the incorporation of the R330G mutation in a less stable version of the *P. pyralis* luciferase had significantly destabilizing effects.

While the most successful examples of shifting the peak wavelengths of beetle luciferases have been achieved by random mutagenesis as described above, similarly encouraging studies have resulted from site-directed mutagenesis based on sequence homology to red light-emitting luciferases such as *P. hirtus*. Such studies have yielded a 608-nm-emitting *P. pyralis* luciferase (K356 insertion [65]) and a 616-nm-emitting *L. turkestanicus* (R353 insertion [66]).

An extensive study performed on *Renilla* luciferase variants utilizing a combination of random mutagenesis with screening for color shifts and structural-based semi-rational mutagenesis, led to *Renilla* luciferase variants with redshifts up to 66 nm from the native luciferase (Fig. 8.3) [28]. The variant titled RLuc8.6-535 was felt to be the most useful by the authors and demonstrated improved properties compared to their previously described RLuc8 variant, with comparable stability to RLuc8, as well as a sixfold increased light output on a per-enzyme basis and a 49-nm redshift in comparison to RLuc. When combined with the redshifted substrate analog coelenterazine-v, the redshifts were found to be additive, with the combined total redshift being 89 nm in comparison to the native

luciferase/native substrate combination. A subsequent protein engineering study was performed to generate a redshifted RLuc variant without the increased stability that would be more appropriate for assessing transient changes in gene expression [67]. The result, RLuc7–521, demonstrated equivalent stability to the native luciferase, a 60 % improvement in light output on a per-enzyme basis, and a 40-nm redshift. When combined with coelenterazine-v, a total redshift of 73 nm was achieved with respect to the native luciferase/native substrate combination. Comparable mutations to those utilized to generate RLuc8.6–535 have been incorporated into *R. mulleri* luciferase to yield equivalent redshifts in its emission spectrum [47].

No studies have been performed on copepod luciferases to specifically alter the emission spectrum, but the 4-mutation variant of *Gaussia* luciferase Monsta (previously discussed in the intensity section) was found to have a 33-nm redshift with respect to native GLuc [51].

8.7.4 Codon Optimization

As mentioned previously, although codon optimization is not technically protein engineering, it is such a common first step for improving protein expression that we have included examples of codon optimization here. Although these optimizations are targeted toward improved protein expression in mammalian systems, the resultant codon utilization is generally improved for bacterial expression as well.

The firefly luciferase sequences that are most widely used have been extensively modified with respect to their codon utilization. One of the first and most notable changes to the gene's nucleotide sequence resulted in a codon usage profile specific for mammalian expression and the removal of a peroxisome-targeting sequence present in the wild-type luciferase sequence [68]. This version, known as luc+, was further improved by changing the gene's sequence to remove transcription factor binding sites and renamed luc2 [69]. This version of the firefly luciferase gene is present in Promega's widely used pGL4 reporter gene vectors.

Similar to the case for firefly luciferase, the most commonly used marine luciferases have also undergone codon optimization, and these codon-optimized forms have been used as the genetic starting point for most protein engineering that has followed. Alterations of the DNA sequence of *Renilla* luciferase for improved mammalian codon utilization and removal of binding sites for mammalian transcription factors resulted in 10- to 100-fold signal improvements in signal in a mammalian expression assay [42]. Alteration of the DNA sequence of *Gaussia* luciferase (GLuc) for improved mammalian codon utilization reported a 1,000-fold improvement in signal for a mammalian expression assay [41].

8.7.5 Cellular Localization

Adding intracellular localization signals to luciferases has been performed to alter their intracellular kinetics. Versions of firefly luciferase, *Renilla* luciferase, and NanoLuc have all been generated as fusion proteins with the 41 amino acid PEST degradation sequence to shorten intracellular half-life. In the case of FLuc, this reduces the intracellular half-life from 3.5 h to 0.8 h [45]. Similarly, this modification reduces the intracellular half-life of NanoLuc from >6 h to 20 min [17].

As discussed previously, secreted luciferases are problematic for small-animal bioluminescence imaging due to the decoupling of bioluminescence signal from the location of protein expression, and work has been performed to transform these secreted luciferases into forms that will remain in proximity to their cell of origin. While removal of the signal peptide of *Gaussia* luciferase decreased levels of secreted luciferase, it did not increase levels of cellular-associated luciferase [41]. Addition of a KDEL sequence to GLuc in an attempt to divert transit of the expressed protein to the endoplasmic reticulum resulted in increased luminescence in cell lysates, but did not alter the cell-associated signal in unlysed cells [41]. Addition of a CD8 transmembrane domain to the C-terminus of GLuc, to generate a variant termed extGLuc, was successful in retaining the expressed luciferase to the cell surface [46]. This approach has an advantage compared to the use of a cytoplasmically retained luciferase (such as RLuc), in that an extracellular luciferase obviates the need for the substrate to traverse the cell membrane and therefore removes confounding effects caused by MDR1 P-glycoprotein-mediated efflux of coelenterazine [70]. However, a carefully performed *in vivo* comparison experiment between FLuc, RLuc, and extGLuc involving viral luciferase expression in the mouse liver found extGLuc signal to be undetectable [71]. This finding reiterates the concern for a lack of robustness in many engineered luciferases and the need to confirm the applicability of a given luciferase for each specific biomedical use.

8.7.6 Luciferase-GFP Fusions

In nature, *Renilla* luciferase is normally associated with a green fluorescent protein (*Renilla* GFP). In this context, the energy released from substrate degradation is not directly released as a photon of light from the luciferase, but in a process termed bioluminescence resonance energy transfer (BRET), the energy is used instead to excite the adjacent fluorescent protein and then released as a photon of light from the fluorophore. In *Renilla*, the combination of luciferase and GFP leads to improved light output/quantum yield compared to the luciferase on its own [72]. In a similar manner, enhanced yellow fluorescent protein (EYFP) was combined as a fusion protein with RLuc8 to generate a luminescent protein (eBAF-Y) that was 26-fold brighter than RLuc in mammalian cell culture conditions [73].

In this fashion, Saito et al. generated a *Renilla* luciferase-fluorescent protein fusion protein with even greater light output [74]. They first subjected RLuc8 to a random mutagenesis screen and identified an S257G mutation that yielded a small improvement in activity (note though that S257G has previously been described as a destabilizing mutation in the context of native RLuc [10]). They then combined this new luciferase with the yellow fluorescent protein variant “Venus,” to generate a luminescent protein they termed “Nanolantern.” Nanolantern demonstrated a ~five-fold improvement in light output compared to RLuc8, a ~three-fold improvement in light output compared to eBAF-Y, and a redshifted emission spectrum (peak ~530 nm) consistent with the principle light emitter in Nanolantern being the fluorescent protein. This improvement in light output may arise from improved quantum yield of the BRET system compared to the luciferase, and/or fluorescent protein-induced conformational changes to the luciferase that improve the enzymatic properties of the luciferase. The authors went on to demonstrate the utility of Nanolantern for imaging intracellular structures in living cells, for video-rate bioluminescence imaging in a small-animal model, and for the construction of Ca²⁺ and ATP sensors.

8.7.7 *NanoLuc*

As a prime example and excellent summary of many of the techniques stated above, Hall and colleagues performed extensive mutagenesis and protein engineering on the secreted decapod luciferase from the deep-sea shrimp *O. gracilirostris* (OLuc), turning it into a small, highly active, monomeric, intracellular luciferase called NanoLuc [17]. OLuc is a heterotetramer containing two 35-kDa and two 19-kDa subunits, with the luciferase activity associated with the smaller 19-kDa subunits. A consensus approach to semi-rational mutagenesis was not available due to the lack of similar proteins in the protein databases. Based on fold homology to intracellular lipid binding proteins, an N166R mutation was introduced into the smaller 19-kDa subunit that led to ~three-fold increased luminescence intensity. They then performed a single round of random mutagenesis, uncovering eight additional beneficial mutations that, when combined, led to a 30,000-fold increase in light output in their assay. Random mutagenesis was then performed on this 9-mutation variant of the 19-kDa OLuc subunit and the variants were subjected to a library of coelenterazine analogs. From this screen, they identified a number of additional beneficial mutations, as well as a coelenterazine analog (titled furimazine) that showed both decreased background autoluminescence and increased luminescence relative to coelenterazine in the presence of their variants. They combined these beneficial mutations into a 14-mutation variant and then performed another random mutagenesis screen with furimazine as the substrate. Incorporating the additional beneficial mutations, the final product was a 16-mutation variant of the 19-kDa OLuc subunit that the authors termed “NanoLuc.” In a final step, they performed codon optimization for mammalian

cell expression. Based on western blot analysis, the superiority of NanoLuc compared to OLuc was credited to improved stability and protein expression, rather than enzymatic improvements in the luciferase. Gel permeation chromatography demonstrated the monomeric nature of NanoLuc, and thermal and pH stability were confirmed. NanoLuc (with furimazine) demonstrated ~ 150 -fold more luminescence per enzyme than either FLuc (with D-luciferin) or RLuc (with coelenterazine) under glow-type assay conditions. Given NanoLuc's recent development at the time of this publication, its robustness has yet to be confirmed in the scientific literature, but it appears quite promising for cell culture experiments. Given its narrow blueshifted emission peak (460 nm) compared to RLuc and FLuc, very few photons will be generated within the optical window for mammalian tissue (above 600 nm). As such, its suitability of bioluminescence imaging in small-animal models remains to be determined.

8.7.8 *Split-Lucs*

As alluded to previously, a prominent area of luciferase engineering is related to a technique known as split-protein complementation. This phenomenon has been described in only a handful of other enzymes (of which the fluorescent protein GFP is probably the most prominent). It revolves around the observation that the luciferase can be split into two separate polypeptides, which by themselves possess little to no luminescent activity, but when sufficiently colocalized, can perform the bioluminescent reaction without reestablishing a covalent peptide bond between the two entities. This property has been exploited extensively to image protein-protein interactions, most commonly by creating gene fusion constructs between the split halves and a pair of interacting proteins. It has been adapted to encompass imaging of protein-DNA, protein-RNA, and DNA-DNA interactions, as well as protein phosphorylation, small molecule inhibition, nutrient sensing, viral pathogenesis, and protease activity.

As it applies to the discussion of luciferase engineering, a handful of studies have attempted to determine the most optimal split site within the luciferase enzyme. For most applications, this entails choosing a site that renders two fragments with little to no activity, but retain the ability to reconstitute as much of the intact enzyme's bioluminescence as possible when colocalized. The first report of split luciferase complementation, and the one which has served as a basis for almost all subsequent investigations on split beetle luciferases, used the crystal structure of the *P. pyralis* luciferase to estimate the most optimal split site [75]. The investigators split the protein within the flexible linker connecting the disparate N- and C-terminal domains (437/438). This split site was used as a starting point for a different approach performed several years later. In the subsequent study, a library of semi-random, and frequently overlapping, luciferase fragments were fused to the rapamycin-inducible interacting protein pair of FRB (rapamycin-binding domain of mTOR) and FKBP (FK506-binding protein 12) and

then expressed in bacteria [76]. When the bacteria were exposed to rapamycin, FRB and FKBP were induced to interact with one another, bringing the split luciferase halves into proximity with one another and facilitating luciferin oxidation. This experimental design allowed the authors to both screen against self-complementing pairs by omitting colonies that luminesced in the absence of rapamycin, and screen for pairs whose complementation resulted in the highest levels of photon emission by selecting the brightest colonies in the presence of rapamycin. The study revealed slightly overlapping luciferase halves (416/398) with more favorable properties than the original split luciferases. Another study using a similar experimental design but a different library revealed a potentially more favorable split site of 398/394 [77].

In contrast to the intermolecular interaction screen discussed above, a split site for the *P. plagiophthalmus* luciferase was determined by intramolecular inducible folding [78]. The split luciferases in this study were evaluated by inserting the androgen receptor ligand binding domain and its dihydrotestosterone (DHT)-inducible peptide-binding partner at various sites with the luciferase gene. Then, in a fashion similar to the previous studies, individual colonies were screened in the presence and absence of DHT to determine the most optimal split site (439/440). A split site for the luciferase from *Pyrearinus termitilluminans* (415/394) was found using a semirational approach in which overlapping fragments were systematically evaluated by altering the split site with single amino acid resolution [79]. While the strategy employed for this evaluation was similar to the ones described above, the study represents the first time that a luciferase split site had been so rigorously characterized.

A number of split coelenterazine luciferases appropriate for protein complementation assays have also been developed. Split *Renilla* luciferases were initially developed without structural information to guide split selection sites [80, 81], but more recent publications have selected split sites derived from homology-based [82] or crystallographic structural information [83]. A number of split *Gaussia* luciferases have also been developed. Due to an absence of homology or structural information for the copepod luciferases, these split GLuc have been developed by primary sequence analysis including predictions of unstructured regions [84] and hydrophobicity [85].

8.7.9 Chemical Sensitivity/Altered Substrate Specificity

Independent of the luciferases engineered for sensitivity to small molecules via split-protein complementation design, several variants have been constructed that have intrinsic sensitivity to various chemicals due to mutations in their primary sequence. Often, this involves altering the enzymatic specificity of luciferase. Due to the extensive investigations of luciferase enzymology and the availability of high resolution crystal structures, the engineering of luciferase with altered chemical sensitivities is generally a very rational endeavor. Aminoluciferin is a

derivative of D-luciferin in which the hydroxyl group of luciferin is replaced with an amino group. This enables more facile functionalization of the substrate and is often used as a starting material for substrate engineering studies. However as a synthetic substrate, beetle luciferases do not oxidize aminoluciferin as efficiently as they do D-luciferin. This problem was rectified by performing saturation mutagenesis on active site residues of the luciferase from *P. pyralis*, as determined by the crystal structure, followed by screening bacterial lysates in the presence of aminoluciferin and its derivatives [86]. A library of mutants with improved specificity for a variety of aminoluciferin derivatives were discovered.

A random approach was taken for engineering the luciferase from *L. lateralis* to be less sensitive to the detergent benzalkonium chloride (BAC). BAC is used in certain protocols for the extraction of intracellular ATP from mammalian cells. Since ATP is a necessary cofactor of luciferase, it can be quantified by bioluminescence detection. Unfortunately, BAC can interfere with luciferin oxidation, so a random mutagenesis approach was taken, followed by a screen of bacterial lysates, to identify a BAC-resistant double mutant (A217L, E490K) [87].

8.8 Conclusion

The field of luciferase engineering has seen a wave of extraordinary advances in recent years, though by no means has it reached its apogee. Because of its functional capacity, altering the properties of luciferase is a relatively straightforward endeavor. Thus, luciferase engineering will remain a topic of interest to those concerned not only with the native proteins' biochemistry, but also to investigators seeking to synthesize biomolecules with novel capacities. As we tried to demonstrate in this chapter, luciferase engineering is limited largely by the creativity and effectiveness of the screen. Similar to other fields such as phage display and catalytic RNA, in which a large pool of variants must be sifted through to find the most beneficial changes, luciferase engineering has few procedural bounds and relies on the cleverness of the investigator to produce appreciable results.

Due to this fundamental reliance on the screen, however, the results of luciferase engineering are not necessarily transferable from one application to another. The selection of a luciferase remains an unavoidably empirical exercise. The luciferase that proves to be optimal for detecting bacterial contamination in the field may demonstrate little utility when assessing lymphocyte activation in a living animal and vice versa. Therefore, the reader should be cautioned not to assume that the examples cited herein can serve every need. And though several of the mutants described above may perform well across many platforms, we hope that the studies enumerated in this chapter can serve as guideposts for the development of a panoply of new mutants, each exquisitely tuned for a precise application.

References

1. Lee J (2008) Bioluminescence: the first 3000 years. *J Siberian Federal Univ Biol* 1(3):194–205
2. Prescher JA, Contag CH (2010) Guided by the light: visualizing biomolecular processes in living animals with bioluminescence. *Curr Opin Chem Biol* 14(1):80–89. doi:S1367-5931(09)00183-5 [pii] [10.1016/j.cbpa.2009.11.001](https://doi.org/10.1016/j.cbpa.2009.11.001)
3. Widder EA (2010) Bioluminescence in the ocean: origins of biological, chemical, and ecological diversity. *Science* 328(5979):704–708. doi:[10.1126/science.1174269](https://doi.org/10.1126/science.1174269)
4. Viviani VR (2002) The origin, diversity, and structure function relationships of insect luciferases. *Cell Mol Life Sci* 59(11):1833–1850
5. Fraga H, Fernandes D, Fontes R, Esteves da Silva JC (2005) Coenzyme A affects firefly luciferase luminescence because it acts as a substrate and not as an allosteric effector. *FEBS J* 272(20):5206–5216. doi:[10.1111/j.1742-4658.2005.04895.x](https://doi.org/10.1111/j.1742-4658.2005.04895.x)
6. Inouye S (2010) Firefly luciferase: an adenylate-forming enzyme for multicatalytic functions. *Cell Mol Life Sci* 67(3):387–404. doi:[10.1007/s00018-009-0170-8](https://doi.org/10.1007/s00018-009-0170-8)
7. Haddock SHD, Case JF (1999) Bioluminescence spectra of shallow and deep-sea gelatinous zooplankton: ctenophores, medusae and siphonophores. *Mar Biol* 133(3):571–582
8. Vassel N, Cox CD, Naseem R, Morse V, Evans RT, Power RL, Brancale A, Wann KT, Campbell AK (2012) Enzymatic activity of albumin shown by coelenterazine chemiluminescence. *Lumin J Biol Chem Lumin* 27(3):234–241. doi:[10.1002/bio.2357](https://doi.org/10.1002/bio.2357)
9. Inouye S, Sahara-Miura Y, Sato J, Iimori R, Yoshida S, Hosoya T (2013) Expression, purification and luminescence properties of coelenterazine-utilizing luciferases from *Renilla*, *Oplophorus* and *Gaussia*: comparison of substrate specificity for C2-modified coelenterazines. *Protein Expr Purif* 88(1):150–156. doi:[10.1016/j.pep.2012.12.006](https://doi.org/10.1016/j.pep.2012.12.006)
10. Loening AM, Fenn TD, Wu AM, Gambhir SS (2006) Consensus guided mutagenesis of *Renilla* luciferase yields enhanced stability and light output. *Protein Eng Des Sel* 19(9):391–400. doi:[10.1093/protein/gz1023](https://doi.org/10.1093/protein/gz1023)
11. Stepanyuk GA, Xu H, Wu CK, Markova SV, Lee J, Vysotski ES, Wang BC (2008) Expression, purification and characterization of the secreted luciferase of the copepod *Metridia longa* from Sf9 insect cells. *Protein Expr Purif* 61(2):142–148. doi:[10.1016/j.pep.2008.05.013](https://doi.org/10.1016/j.pep.2008.05.013)
12. Goerke AR, Loening AM, Gambhir SS, Swartz JR (2008) Cell-free metabolic engineering promotes high-level production of bioactive *Gaussia* princeps luciferase. *Metab Eng* 10(3–4):187–200. doi:[10.1016/j.ymben.2008.04.001](https://doi.org/10.1016/j.ymben.2008.04.001)
13. Takenaka Y, Yamaguchi A, Tsuruoka N, Torimura M, Gojobori T, Shigeri Y (2012) Evolution of bioluminescence in marine planktonic copepods. *Mol Biol Evol* 29(6):1669–1681. doi:[10.1093/molbev/mss009](https://doi.org/10.1093/molbev/mss009)
14. Inouye S, Sahara Y (2008) Identification of two catalytic domains in a luciferase secreted by the copepod *Gaussia* princeps. *Biochem Biophys Res Commun* 365(1):96–101. doi:[10.1016/j.bbrc.2007.10.152](https://doi.org/10.1016/j.bbrc.2007.10.152)
15. Tzertzinis G, Schildkraut E, Schildkraut I (2012) Substrate cooperativity in marine luciferases. *PLoS ONE* 7(6):e40099. doi:[10.1371/journal.pone.0040099](https://doi.org/10.1371/journal.pone.0040099)
16. Inouye S, Sasaki S (2007) Overexpression, purification and characterization of the catalytic component of *Oplophorus* luciferase in the deep-sea shrimp *Oplophorus gracilirostris*. *Protein Expr Purif* 56(2):261–268. doi:[10.1016/j.pep.2007.08.002](https://doi.org/10.1016/j.pep.2007.08.002)
17. Hall MP, Unch J, Binkowski BF, Valley MP, Butler BL, Wood MG, Otto P, Zimmerman K, Vidugiris G, Machleidt T, Robers MB, Benink HA, Eggers CT, Slater MR, Meisenheimer PL, Klauert DH, Fan F, Encell LP, Wood KV (2012) Engineered luciferase reporter from a deep sea shrimp utilizing a novel imidazopyrazinone substrate. *ACS Chem Biol* 7(11):1848–1857. doi:[10.1021/cb3002478](https://doi.org/10.1021/cb3002478)

18. Nakajima Y, Kobayashi K, Yamagishi K, Enomoto T, Ohmiya Y (2004) cDNA cloning and characterization of a secreted luciferase from the luminous Japanese ostracod *Cypridina noctiluca*. *Biosci Biotechnol Biochem* 68(3):565–570
19. Suzuki C, Nakajima Y, Akimoto H, Wu C, Ohmiya Y (2005) A new additional reporter enzyme, dinoflagellate luciferase, for monitoring of gene expression in mammalian cells. *Gene* 344:61–66. doi:[10.1016/j.gene.2004.09.028](https://doi.org/10.1016/j.gene.2004.09.028)
20. Close DM, Patterson SS, Ripp S, Baek SJ, Sanseverino J, Sayler GS (2010) Autonomous bioluminescent expression of the bacterial luciferase gene cassette (*lux*) in a mammalian cell line. *PLoS ONE* 5(8):e12441. doi:[10.1371/journal.pone.0012441](https://doi.org/10.1371/journal.pone.0012441)
21. Ramanathan R, Burbelo PD, Groot S, Iadarola MJ, Neva FA, Nutman TB (2008) A luciferase immunoprecipitation systems assay enhances the sensitivity and specificity of diagnosis of *Strongyloides stercoralis* infection. *J Infect Dis* 198(3):444–451. doi:[10.1086/589718](https://doi.org/10.1086/589718)
22. Ronaghi M (2001) Pyrosequencing sheds light on DNA sequencing. *Genome Res* 11(1):3–11
23. Badran AH, Furman JL, Ma AS, Comi TJ, Porter JR, Ghosh I (2011) Evaluating the global CpG methylation status of native DNA utilizing a bipartite split-luciferase sensor. *Anal Chem* 83(18):7151–7157. doi:[10.1021/ac2015239](https://doi.org/10.1021/ac2015239)
24. Jester BW, Gaj A, Shomin CD, Cox KJ, Ghosh I (2012) Testing the promiscuity of commercial kinase inhibitors against the AGC kinase group using a split-luciferase screen. *J Med Chem* 55(4):1526–1537. doi:[10.1021/jm201265f](https://doi.org/10.1021/jm201265f)
25. Shekhawat SS, Campbell ST, Ghosh I (2011) A comprehensive panel of turn-on caspase biosensors for investigating caspase specificity and caspase activation pathways. *Chem Biochem* 12(15):2353–2364. doi:[10.1002/cbic.201100372](https://doi.org/10.1002/cbic.201100372)
26. Anderson JM, Cormier MJ (1976) Transductive coupling in bioluminescence: effects of monovalent cations and ionophores on the calcium-triggered luminescence of *Renilla lumisomes*. *Biochem Biophys Res Commun* 68(4):1234–1241
27. Loening AM, Gambhir SS (2006) Technologies for imaging with bioluminescently labeled probes. Thesis (Ph D), Stanford University
28. Loening AM, Wu AM, Gambhir SS (2007) Red-shifted *Renilla reniformis* luciferase variants for imaging in living subjects. *Nat Methods* 4(8):641–643. doi:[10.1038/nmeth1070](https://doi.org/10.1038/nmeth1070)
29. White PJ, Squirrell DJ, Arnaud P, Lowe CR, Murray JA (1996) Improved thermostability of the North American firefly luciferase: saturation mutagenesis at position 354. *Biochem J* 319(2):343–350
30. Shapiro E, Lu C, Baneyx F (2005) A set of multicolored *Photinus pyralis* luciferase mutants for in vivo bioluminescence applications. *Protein Eng Des Sel* 18(12):581–587. doi:[gzi066](https://doi.org/10.1093/protein/gzi066) [pii] [10.1093/protein/gzi066](https://doi.org/10.1093/protein/gzi066)
31. Koksharov MI, Ugarova NN (2011) Thermostabilization of firefly luciferase by in vivo directed evolution. *Protein Eng Des Sel* 24(11):835–844. doi:[10.1093/protein/gzr044](https://doi.org/10.1093/protein/gzr044)
32. Fujii H, Noda K, Asami Y, Kuroda A, Sakata M, Tokida A (2007) Increase in bioluminescence intensity of firefly luciferase using genetic modification. *Anal Biochem* 366(2):131–136. doi:[10.1016/j.ab.2007.04.018](https://doi.org/10.1016/j.ab.2007.04.018)
33. Koksharov MI, Ugarova NN (2008) Random mutagenesis of *Luciola mingrelica* firefly luciferase. Mutant enzymes with bioluminescence spectra showing low pH sensitivity. *Biochemistry (Mosc)* 73(8):862–869
34. Li X, Nakajima Y, Niwa K, Viviani VR, Ohmiya Y (2010) Enhanced red-emitting railroad worm luciferase for bioassays and bioimaging. *Protein Sci* 19(1):26–33. doi:[10.1002/pro.279](https://doi.org/10.1002/pro.279)
35. Koksharov MI, Ugarova NN (2011) Triple substitution G216N/A217L/S398M leads to the active and thermostable *Luciola mingrelica* firefly luciferase. *Photochem Photobiol Sci* 10(6):931–938. doi:[10.1039/c0pp00318b](https://doi.org/10.1039/c0pp00318b)
36. Branchini BR, Southworth TL, Murtiashaw MH, Boije H, Fleet SE (2003) A mutagenesis study of the putative luciferin binding site residues of firefly luciferase. *Biochemistry* 42(35):10429–10436. doi:[10.1021/bi030099x](https://doi.org/10.1021/bi030099x)
37. Nazari M, Hosseinkhani S (2011) Design of disulfide bridge as an alternative mechanism for color shift in firefly luciferase and development of secreted luciferase. *Photochem Photobiol Sci* 10(7):1203–1215. doi:[10.1039/c1pp05012e](https://doi.org/10.1039/c1pp05012e)

38. Law GH, Gandelman OA, Tisi LC, Lowe CR, Murray JA (2006) Mutagenesis of solvent-exposed amino acids in *Photinus pyralis* luciferase improves thermostability and pH-tolerance. *Biochem J* 397(2):305–312. doi:[10.1042/BJ20051847](https://doi.org/10.1042/BJ20051847)
39. Maguire CA, van der Mijl JC, Degeling MH, Morse D, Tannous BA (2011) Codon-optimized *Luciola italica* luciferase variants for mammalian gene expression in culture and in vivo. *Mol Imaging*. doi:[10.2310/7290.2011.00022](https://doi.org/10.2310/7290.2011.00022)
40. Branchini BR, Ablamsky DM, Davis AL, Southworth TL, Butler B, Fan F, Jathoul AP, Pule MA (2010) Red-emitting luciferases for bioluminescence reporter and imaging applications. *Anal Biochem* 396(2):290–297. doi:[10.1016/j.ab.2009.09.009](https://doi.org/10.1016/j.ab.2009.09.009)
41. Tannous BA, Kim DE, Fernandez JL, Weissleder R, Breakefield XO (2005) Codon-optimized *Gussia* luciferase cDNA for mammalian gene expression in culture and in vivo. *Mol Ther J Am Soc Gene Ther* 11(3):435–443. doi:[10.1016/j.ymthe.2004.10.016](https://doi.org/10.1016/j.ymthe.2004.10.016)
42. Zhuang Y, Butler B, Hawkins E, Paguio A, Orr L, Wood MG, Wood KV (2001) New synthetic *Renilla* gene and assay system increase expression, reliability and sensitivity. *Promega Notes*, vol 79
43. Kanno A, Yamanaka Y, Hirano H, Umezawa Y, Ozawa T (2007) Cyclic luciferase for real-time sensing of caspase-3 activities in living mammals. *Angew Chem Int Ed Engl* 46(40):7595–7599. doi:[10.1002/anie.200700538](https://doi.org/10.1002/anie.200700538)
44. Worley CK, Ling R, Callis J (1998) Engineering in vivo instability of firefly luciferase and *Escherichia coli* beta-glucuronidase in higher plants using recognition elements from the ubiquitin pathway. *Plant Mol Biol* 37(2):337–347
45. Leclerc GM, Boockfor FR, Faught WJ, Frawley LS (2000) Development of a destabilized firefly luciferase enzyme for measurement of gene expression. *Biotechniques* 29(3):590–591, 594–596, 598 passim
46. Santos EB, Yeh R, Lee J, Nikhamin Y, Punzalan B, Punzalan B, La Perle K, Larson SM, Sadelain M, Brentjens RJ (2009) Sensitive in vivo imaging of T cells using a membrane-bound *Gussia princeps* luciferase. *Nat Med* 15(3):338–344. doi:[10.1038/nm.1930](https://doi.org/10.1038/nm.1930)
47. Stepanyuk GA, Unch J, Malikova NP, Markova SV, Lee J, Vysotski ES (2010) Coelenterazine-v ligated to Ca²⁺-triggered coelenterazine-binding protein is a stable and efficient substrate of the red-shifted mutant of *Renilla muelleri* luciferase. *Anal Bioanal Chem* 398(4):1809–1817. doi:[10.1007/s00216-010-4106-9](https://doi.org/10.1007/s00216-010-4106-9)
48. Cali JJ, Niles A, Valley MP, O'Brien MA, Riss TL, Shultz J (2008) Bioluminescent assays for ADMET. *Expert Opin Drug Metab Toxicol* 4(1):103–120. doi:[10.1517/17425255.4.1.103](https://doi.org/10.1517/17425255.4.1.103)
49. Woo J, Howell MH, von Arnim AG (2008) Structure-function studies on the active site of the coelenterazine-dependent luciferase from *Renilla*. *Protein Sci* 17(4):725–735. doi:[10.1110/ps.073355508](https://doi.org/10.1110/ps.073355508)
50. Markova SV, Burakova LP, Vysotski ES (2012) High-active truncated luciferase of copepod *Metridia longa*. *Biochem Biophys Res Commun* 417(1):98–103. doi:[10.1016/j.bbrc.2011.11.063](https://doi.org/10.1016/j.bbrc.2011.11.063)
51. Kim SB, Suzuki H, Sato M, Tao H (2011) Superluminescent variants of marine luciferases for bioassays. *Anal Chem* 83(22):8732–8740. doi:[10.1021/ac2021882](https://doi.org/10.1021/ac2021882)
52. Hall M, Gruber M, Hannah RR, Jennens-Clough ML, Wood KV (1998) Stabilization of firefly luciferase using directed evolution. In: Roda A, Pazzagli M, Kricka L, Stanley P (eds) *Bioluminescence and Chemiluminescence: Perspectives for the 21st Century*. Wiley, Chichester, UK
53. Branchini BR, Ablamsky DM, Murtiashaw MH, Uzasci L, Fraga H, Southworth TL (2007) Thermostable red and green light-producing firefly luciferase mutants for bioluminescent reporter applications. *Anal Biochem* 361(2):253–262. doi:[10.1016/j.ab.2006.10.043](https://doi.org/10.1016/j.ab.2006.10.043)
54. Baggett B, Roy R, Momen S, Morgan S, Tisi L, Morse D, Gillies RJ (2004) Thermostability of firefly luciferases affects efficiency of detection by in vivo bioluminescence. *Mol Imaging* 3(4):324–332. doi:[10.1162/1535350042973553](https://doi.org/10.1162/1535350042973553)
55. Walls ZF (2008) Molecular imaging of gene expression at the level of RNA in living animals

56. Imani M, Hosseinkhani S, Ahmadian S, Nazari M (2010) Design and introduction of a disulfide bridge in firefly luciferase: increase of thermostability and decrease of pH sensitivity. *Photochem Photobiol Sci* 9(8):1167–1177. doi:[10.1039/c0pp00105h](https://doi.org/10.1039/c0pp00105h)
57. Nazari M, Hosseinkhani S, Hassani L (2012) Step-wise addition of disulfide bridge in firefly luciferase controls color shift through a flexible loop: a thermodynamic perspective. *Photochem Photobiol Sci*. doi:[10.1039/c2pp25140j](https://doi.org/10.1039/c2pp25140j)
58. Riahi-Madvar A, Hosseinkhani S (2009) Design and characterization of novel trypsin-resistant firefly luciferases by site-directed mutagenesis. *Protein Eng Des Sel* 22(11):655–663. doi:[10.1093/protein/gzp047](https://doi.org/10.1093/protein/gzp047)
59. Liu J, Escher A (1999) Improved assay sensitivity of an engineered secreted Renilla luciferase. *Gene* 237(1):153–159
60. Wiles S, Ferguson K, Stefanidou M, Young DB, Robertson BD (2005) Alternative luciferase for monitoring bacterial cells under adverse conditions. *Appl Environ Microbiol* 71(7):3427–3432. doi:[10.1128/AEM.71.7.3427-3432.2005](https://doi.org/10.1128/AEM.71.7.3427-3432.2005)
61. Tafreshi NKH, Sadeghizadeh M, Emamzadeh R, Ranjbar B, Naderi-Manesh H, Hosseinkhani S (2008) Site-directed mutagenesis of firefly luciferase: implication of conserved residue(s) in bioluminescence emission spectra among firefly luciferases. *Biochem J* 412(1):27–33. doi:[10.1042/BJ20070733](https://doi.org/10.1042/BJ20070733) [pii]
62. Branchini BR, Southworth TL, Khattak NF, Michelini E, Roda A (2005) Red- and green-emitting firefly luciferase mutants for bioluminescent reporter applications. *Anal Biochem* 345(1):140–148. doi:[10.1016/j.ab.2005.07.015](https://doi.org/10.1016/j.ab.2005.07.015)
63. Tisi LC, White PJ, Squirrell DJ, Murphy MJ, Lowe CR, Murray JA (2002) Development of a thermostable firefly luciferase. *Anal Chim Acta* 457(1):115–123
64. Kajiyama N, Nakano E (1993) Thermostabilization of firefly luciferase by a single amino acid substitution at position 217. *Biochemistry* 32(50):13795–13799
65. Moradi A, Hosseinkhani S, Naderi-Manesh H, Sadeghizadeh M, Alipour BS (2009) Effect of charge distribution in a flexible loop on the bioluminescence color of firefly luciferases. *Biochemistry* 48(3):575–582. doi:[10.1021/bi802057w](https://doi.org/10.1021/bi802057w)
66. Tafreshi NKH, Hosseinkhani S, Sadeghizadeh M, Sadeghi M, Ranjbar B, Naderi-Manesh H (2007) The influence of insertion of a critical residue (Arg356) in structure and bioluminescence spectra of firefly luciferase. *J Biol Chem* 282(12):8641–8647. doi:[10.1074/jbc.M609271200](https://doi.org/10.1074/jbc.M609271200)
67. Loening AM, Dragulescu-Andrasi A, Gambhir SS (2010) A red-shifted Renilla luciferase for transient reporter-gene expression. *Nat Methods* 7(1):5–6. doi:[10.1038/nmeth0110-05](https://doi.org/10.1038/nmeth0110-05)
68. Sherf BA, Wood KV (1994) Firefly luciferase engineered for improved genetic reporting. *Promega Notes*, vol 49
69. Paguio A, Almond B, Fan F, Stecha PF, Garvin D, Wood MG, Wood KV (2005) pGL4 vectors: a new generation of luciferase reporter vectors. *Promega Notes*, vol 89
70. Pichler A, Prior JL, Piwnicka-Worms D (2004) Imaging reversal of multidrug resistance in living mice with bioluminescence: MDR1 P-glycoprotein transports coelenterazine. *Proc Natl Acad Sci USA* 101(6):1702–1707. doi:[10.1073/pnas.0304326101](https://doi.org/10.1073/pnas.0304326101)
71. Gil JS, Machado HB, Herschman HR (2012) A method to rapidly and accurately compare the relative efficacies of non-invasive imaging reporter genes in a mouse model and its application to luciferase reporters. *Mol Imaging Biol* 14(4):462–471. doi:[10.1007/s11307-011-0515-1](https://doi.org/10.1007/s11307-011-0515-1)
72. Ward WW, Cormier MJ (1979) An energy transfer protein in coelenterate bioluminescence. Characterization of the Renilla green-fluorescent protein. *J Biol Chem* 254(3):781–788
73. Hoshino H, Nakajima Y, Ohmiya Y (2007) Luciferase-YFP fusion tag with enhanced emission for single-cell luminescence imaging. *Nat Methods* 4(8):637–639. doi:[10.1038/nmeth1069](https://doi.org/10.1038/nmeth1069)
74. Saito K, Chang YF, Horikawa K, Hatsugai N, Higuchi Y, Hashida M, Yoshida Y, Matsuda T, Arai Y, Nagai T (2012) Luminescent proteins for high-speed single-cell and whole-body imaging. *Nat Commun* 3:1262. doi:[10.1038/ncomms2248](https://doi.org/10.1038/ncomms2248)

75. Ozawa T, Kaihara A, Sato M, Tachihara K, Umezawa Y (2001) Split luciferase as an optical probe for detecting protein-protein interactions in mammalian cells based on protein splicing. *Anal Chem* 73(11):2516–2521
76. Luker KE, Smith MC, Luker GD, Gammon ST, Piwnica-Worms H, Piwnica-Worms D (2004) Kinetics of regulated protein-protein interactions revealed with firefly luciferase complementation imaging in cells and living animals. *Proc Natl Acad Sci USA* 101(33):12288–12293. doi:[10.1073/pnas.0404041101](https://doi.org/10.1073/pnas.0404041101)
77. Paulmurugan R, Gambhir SS (2007) Combinatorial library screening for developing an improved split-firefly luciferase fragment-assisted complementation system for studying protein-protein interactions. *Anal Chem* 79(6):2346–2353. doi:[10.1021/ac062053q](https://doi.org/10.1021/ac062053q)
78. Kim SB, Otani Y, Umezawa Y, Tao H (2007) Bioluminescent indicator for determining protein-protein interactions using intramolecular complementation of split click beetle luciferase. *Anal Chem* 79(13):4820–4826. doi:[10.1021/ac0621571](https://doi.org/10.1021/ac0621571)
79. Misawa N, Kafi AK, Hattori M, Miura K, Masuda K, Ozawa T (2010) Rapid and high-sensitivity cell-based assays of protein-protein interactions using split click beetle luciferase complementation: an approach to the study of G-protein-coupled receptors. *Anal Chem* 82(6):2552–2560. doi:[10.1021/ac100104q](https://doi.org/10.1021/ac100104q)
80. Paulmurugan R, Gambhir SS (2003) Monitoring protein-protein interactions using split synthetic Renilla luciferase protein-fragment-assisted complementation. *Anal Chem* 75(7):1584–1589
81. Kaihara A, Kawai Y, Sato M, Ozawa T, Umezawa Y (2003) Locating a protein-protein interaction in living cells via split Renilla luciferase complementation. *Anal Chem* 75(16):4176–4181
82. Stefan E, Aquin S, Berger N, Landry CR, Nyfeler B, Bouvier M, Michnick SW (2007) Quantification of dynamic protein complexes using Renilla luciferase fragment complementation applied to protein kinase A activities in vivo. *Proc Natl Acad Sci USA* 104(43):16916–16921. doi:[10.1073/pnas.0704257104](https://doi.org/10.1073/pnas.0704257104)
83. Ishikawa H, Meng F, Kondo N, Iwamoto A, Matsuda Z (2012) Generation of a dual-functional split-reporter protein for monitoring membrane fusion using self-associating split GFP. *Protein Eng Des Sel* 25(12):813–820. doi:[10.1093/protein/gzs051](https://doi.org/10.1093/protein/gzs051)
84. Remy I, Michnick SW (2006) A highly sensitive protein-protein interaction assay based on Gaussia luciferase. *Nat Methods* 3(12):977–979. doi:[10.1038/nmeth979](https://doi.org/10.1038/nmeth979)
85. Kim SB, Sato M, Tao H (2009) Split Gaussia luciferase-based bioluminescence template for tracing protein dynamics in living cells. *Anal Chem* 81(1):67–74. doi:[10.1021/ac801658y](https://doi.org/10.1021/ac801658y)
86. Harwood KR, Mofford DM, Reddy GR, Miller SC (2011) Identification of mutant firefly luciferases that efficiently utilize aminoluciferins. *Chem Biol* 18(12):1649–1657. doi:[10.1016/j.chembiol.2011.09.019](https://doi.org/10.1016/j.chembiol.2011.09.019)
87. Hattori N, Kajiyama N, Maeda M, Murakami S (2002) Mutant luciferase enzymes from fireflies with increased resistance to benzalkonium chloride. *Biosci Biotechnol Biochem* 66(12):2587–2593
88. Hart RC, Matthews JC, Hori K, Cormier MJ (1979) Renilla reniformis bioluminescence: luciferase-catalyzed production of nonradiating excited states from luciferin analogues and elucidation of the excited state species involved in energy transfer to Renilla green fluorescent protein. *Biochemistry* 18(11):2204–2210
89. Matthews JC, Hori K, Cormier MJ (1977) Purification and properties of Renilla reniformis luciferase. *Biochemistry* 16(1):85–91
90. Inouye S, Shimomura O (1997) The use of Renilla luciferase, Oplophorus luciferase, and apoaequorin as bioluminescent reporter protein in the presence of coelenterazine analogues as substrate. *Biochem Biophys Res Commun* 233(2):349–353. doi:[10.1006/bbrc.1997.6452](https://doi.org/10.1006/bbrc.1997.6452)
91. de Wet JR, Wood KV, Helinski DR, DeLuca M (1985) Cloning of firefly luciferase cDNA and the expression of active luciferase in Escherichia coli. *Proc Natl Acad Sci USA* 82(23):7870–7873

92. Viviani VR, Bechara EJ, Ohmiya Y (1999) Cloning, sequence analysis, and expression of active *Phrixothrix* railroad-worms luciferases: relationship between bioluminescence spectra and primary structures. *Biochemistry* 38(26):8271–8279. doi:[10.1021/bi9900830](https://doi.org/10.1021/bi9900830)
93. Wood KV, Lam YA, Seliger HH, McElroy WD (1989) Complementary DNA coding click beetle luciferases can elicit bioluminescence of different colors. *Science* 244(4905):700–702
94. Lorenz WW, McCann RO, Longiaru M, Cormier MJ (1991) Isolation and expression of a cDNA encoding *Renilla reniformis* luciferase. *Proc Natl Acad Sci USA* 88(10):4438–4442
95. Verhaegent M, Christopoulos TK (2002) Recombinant *Gaussia* luciferase. Overexpression, purification, and analytical application of a bioluminescent reporter for DNA hybridization. *Anal Chem* 74(17):4378–4385
96. Markova SV, Golz S, Frank LA, Kalthof B, Vysotski ES (2004) Cloning and expression of cDNA for a luciferase from the marine copepod *Metridia longa*. A novel secreted bioluminescent reporter enzyme. *J Biol Chem* 279(5):3212–3217. doi:[10.1074/jbc.M309639200](https://doi.org/10.1074/jbc.M309639200)
97. Inouye S, Watanabe K, Nakamura H, Shimomura O (2000) Secretional luciferase of the luminous shrimp *Oplophorus gracilirostris*: cDNA cloning of a novel imidazopyrazinone luciferase(1). *FEBS Lett* 481(1):19–25
98. Thompson EM, Nagata S, Tsuji FI (1989) Cloning and expression of cDNA for the luciferase from the marine ostracod *Vargula hilgendorfii*. *Proc Natl Acad Sci USA* 86(17):6567–6571

Chapter 9

Engineered Split Reporter Systems for Molecular Imaging of Protein–Protein Interactions in Living Subjects

Tarik F. Massoud and Ramasamy Paulmurugan

9.1 Significance of Protein–Protein Interactions

Proteins perform cellular functions primarily as components of complexes. We now appreciate that the cell is not a simple aqueous solution, but instead a dense gel of interacting proteins forming the basis of phenomena at almost every level of cell function, in the structure of sub-cellular organelles, the transport machinery across biological membranes, packaging of chromatin, the network of sub-membrane filaments, muscle contraction, signal transduction, and regulation of gene expression, to name a few [1, 2]. Other interacting protein complexes work as components of cellular machines, such as ribosomes that read genetic information and synthesize proteins. Indeed, a frequent theme pervading biological investigation is that the great majority of proteins generally operate as constituents of complexes that contain other macromolecules, and together, carry out specific biological functions and that networks of such interactions (interactomes) connect multiple, different cellular processes [3].

Protein–protein interactions (PPIs) have been the object of intense research for many years because of their importance in development and disease. Many human diseases can be traced to aberrant PPIs either through the loss of an essential interaction or through the formation of an abnormal protein complex at an

T. F. Massoud (✉)

Department of Radiology, Section of Neuroradiology, Laboratory of Experimental and Molecular Neuroimaging (LEMNI), Molecular Imaging Program at Stanford (MIPS), and Bio-X, Stanford University School of Medicine and Medical Center, 300 Pasteur Drive, Grant S-047A, Stanford, CA 94305-5105, USA
e-mail: tmassoud@stanford.edu

R. Paulmurugan

Department of Radiology, Cellular Pathway Imaging Laboratory (CPIL), Molecular Imaging Program at Stanford (MIPS), and Bio-X, Stanford University School of Medicine and Canary Center, 1501 S. California Avenue, Stanford, CA 94304, USA
e-mail: paulmur8@stanford.edu

inappropriate time or location involving endogenous proteins, proteins from pathogens, or both [4].

A meticulous characterization of PPIs is necessary for a thorough understanding of cell function. This characterization includes, but is by no means limited to, the determination of the three-dimensional structures of these molecules [5]. Examples of the structures of a few protein interaction motifs involved in cell signaling provide an idea of the beauty and diversity of protein structure. In addition to structural considerations, the dynamic and energetic properties of these systems reveal the exquisite subtlety involved in biological specificity and control [5]. Noninvasive molecular imaging of PPIs in living subjects offers another dimension for investigating and characterizing these all important intracellular events.

9.2 Methods to Study Protein–Protein Interactions

It is useful to generate many different classes of information about proteins [6]. For any given protein, these classes of knowledge would include the following: (1) structure and sequence, (2) evolutionary history and conservation pattern, (3) expression profile, (4) intracellular localization, (5) forms of post-translational regulation to which a protein is subject, and (6) the other cellular proteins with which the protein associates. All the first five points together contribute to the determination of the sixth, and determination of the profile of PPIs is an extremely important step toward the ultimate goal of identifying the functional significance of the activity of any given protein in a cell [6].

Techniques to provide classes of information regarding PPIs fall into three categories [6]: first, there are techniques to identify every possible interacting set of proteins for a given protein of interest. Current research aims to isolate and structurally characterize all the proteins that exist in the cell. Importantly, PPIs are now considered to be so vital to cellular function that one of the first experiments performed on a protein may be a search for its interaction partners [2]. As of May 2013, 42,737 out of 83,860 proteins in the Protein Data Bank were of known protein–protein complexes; this being up from 26,069 out of 49,279 proteins in October 2008, from a variety organisms, of assemblies involving two or more protein chains. Just how many complexes exist in a particular proteome is not easy to deduce because of the different component types (e.g., proteins, nucleic acids, nucleotides, and metal ions) and the varying life spans of the protein complexes (e.g., transient PPIs, such as those involved in signaling, and stable interactions, such as in the ribosome). Until recently, the most comprehensive information about PPIs was available for the yeast proteome, consisting of approximately 6,200 proteins [7, 8]. In yeast, there are about nine protein partners per protein, although not necessarily all direct or interacting at the same time. The human proteome may have an order of magnitude more complexes than the yeast cell [7, 9].

The second set of techniques is used in circumstances where interacting proteins have been defined, and the goal is to detail the biological function and impact

of their interactions, i.e., to establish physiological significance [6]. In this case, it is essential to be able to study the interaction under conditions that correspond as closely as possible to the endogenous situation. In its current role, noninvasive strategies for molecular imaging of PPIs in living subjects fit within this second category of techniques, and the advantages of these approaches are discussed below. Finally, there are techniques to devise high-throughput methodologies to identify agents that modulate a known and well-characterized interaction in desirable ways [10].

Several technologies, grouped together under the term “proteomics” (a term introduced in 1995 by Wasinger et al. [11]), have emerged with the common objective of studying protein function at the scale of an entire pathway, a whole cell, or even a whole organism. Proteomic analyses encompass large-scale studies of PPIs or complexes to establish comprehensive protein interactomes, the global examination of protein expression profiles and, more recently, of protein post-translational modifications [12]. Many experimental techniques, e.g., co-immunoprecipitation, bimolecular fluorescence complementation, fluorescence resonance energy transfer, label transfer, yeast two-hybrid screen, in vivo crosslinking of protein complexes using photo-reactive amino acid analogs, tandem affinity purification, chemical crosslinking, quantitative immunoprecipitation combined with knock-down, dual polarization interferometry, protein–protein docking, static light scattering, MALDI mass spectrometry, strep–protein interaction experiments, surface plasmon resonance, fluorescence correlation spectroscopy (many of these techniques are reviewed elsewhere [1, 13] have been developed and studied using intact cells and cell extracts to study PPIs and to facilitate these proteomic endeavors. Each of these analytical systems has its own merits and demerits, as reviewed previously [13, 14]. Clearly, one aim of proteomics is to identify which proteins interact. While the molecular imaging and study of individual PPIs (that have already been identified as such) might appear to fall outside the scope of proteomic endeavors, it is also important to note their complementary roles. Indeed, a prime challenge in the future is to conduct targeted studies of proteins of interest (including noninvasive molecular imaging analysis) while considering the larger context of whole organismal function and conversely to carefully validate systematic large-scale models of organismal function through individual test cases [6].

9.3 Advantages of Noninvasive Molecular Imaging of Protein–Protein Interactions

The overall modification of existing in vitro and cell culture-based experimental assays to study PPIs in living small animal models of disease is dependent on the challenging task of adapting them so that signals can be noninvasively detected from the exterior of living subjects upon the cellular or sub-cellular interaction of two proteins of interest. Only over the last decade has it been possible to develop

such methods as a result of the true explosion in availability of noninvasive small animal imaging technologies and the rapidly expanding field of molecular imaging, allowing signal detection from deep tissues within a living subject. We previously reviewed in detail the many advantages afforded by molecular imaging in living subjects (such as assessment of whole-body phenomena, repeatability, functionality, and quantification) [15]. One subset of molecular imaging techniques comprises reporter gene expression imaging. This represents an “indirect” imaging method involving multiple components, entailing the use of a pre-targeting molecule (an imaging reporter gene) that is subsequently activated upon occurrence of a specific molecular event. Following this, a molecular probe (a substrate or a ligand) specific for the activated pre-targeting molecule (an enzyme or receptor) is often needed (but not for fluorescent reporter proteins) and used to image its activation [16]. An important feature of reporter gene imaging techniques is their particular versatility, which allows them to be adapted for imaging diverse PPIs in intact living subjects, as outlined below, and as also reviewed by our group [14, 17, 18], and others [19–27].

The ability to noninvasively image PPIs has important implications for a wide variety of biological research endeavors, drug discovery, and molecular medicine. In particular, the visual representation, characterization, quantification, and timing of these biological processes in living subjects could create unprecedented opportunities to complement available *in vitro* or cell culture methodologies, in order: 1) to accelerate the evaluation in living subjects of novel drugs that promote or inhibit active homodimeric, heterodimeric, or multimeric protein assembly, and 2) to characterize more fully known PPIs (e.g., the reasons for, and the factors that drive their association) in the context of whole-body physiologically authentic environments [28].

9.4 Split Reporter Gene Imaging of Protein–Protein Interactions

The three general methods currently available for imaging protein–protein interactions in living subjects using reporter genes are as follows: a modified mammalian two-hybrid system, a bioluminescence resonance energy transfer (BRET) system, and split reporter protein complementation and reconstitution strategies. Table 9.1 outlines the chronological developments of molecular imaging strategies for the detection of PPIs in living animals to date.

Several areas of investigation are required to further refine the use of the modified mammalian two-hybrid system for noninvasive imaging of PPIs confined to the nucleus. As well as further quantitative and kinetic evaluations (e.g., characterizing the ability to follow interactions over time based on the half-life of the reporter protein(s) that are transactivated), studies are needed to optimize the choice of transactivator as well as the choice of promoters and levels of fusion

Table 9.1 Showing chronological developments of molecular imaging strategies for detection of protein–protein interactions in living animals

Years	Authors	Area of PPI study	Imaging assay	Reporter used	References used
2002	Ray et al.	Development of new assay	Two-hybrid system	Fluc	[68]
2002	Luker et al.	Development of new assay	Two-hybrid system	TK and Fluc	[69]
2002	Paulmurugan et al.	Development of new assay	Split reporter complementation and reconstitution	Fluc	[31]
2003	Luker et al.	PPI between p53 and large T antigen of SV40 virus	Two-hybrid system	TK and Fluc	[70]
2004	Paulmurugan et al.	Rapamycin modulation of FRB and FKBP12 PPI	Split reporter complementation	Rluc	[55]
2004	Massoud et al.	Homodimeric PPIs	Split reporter complementation	Rluc	[28]
2004	Kim et al.	Protein nuclear transport	Split reporter reconstitution	Rluc	[45]
2004	Luker et al.	Development and applications of new split reporter fragments	Split reporter complementation	Fluc	[22]
2005	Paulmurugan et al.	Development of self-complementing split reporter fragments	Split reporter complementation	Fluc	[54]
2005	Paulmurugan et al.	Development of a fusion protein approach to image drug modulation of PPIs	Split reporter complementation	Rluc	[58]
2005	De et al.	Development of a new assay	BRET	Rluc (and GFP variant)	[71]
2005	Kim et al.	Detection of stress-related corticosterone level increases	Split reporter reconstitution	Rluc	[46]
2006	Kanno et al.	Detection of protein release from mitochondria to cytosol	Split reporter reconstitution	Rluc	[47]
2007	De et al.	Further developments of an assay	BRET	Rluc (and GFP variant)	[72]
2007	Zhang et al.	Detection of Akt kinase activity	Split reporter complementation	Fluc	[52]
2007	Paulmurugan et al.	Detection of mutiprotein PPIs	Split reporter complementation	Fluc and Rluc	in text
2008	Choi et al.	PPI between HIF-1 alpha and VHL	Split reporter complementation	Fluc	[50]

(continued)

Table 9.1 (continued)

Years	Authors	Area of PPI study	Imaging assay	Reporter used	References
2008	Chan et al.	Detection of HSP90 inhibitors	Split reporter complementation	Rluc	[59]
2008	Zhang et al.	Enhanced detection of Akt kinase activity	Split reporter complementation	Fluc	[53]
2008	Luker et al.	Activation of the chemokine receptor CXCR4	Split reporter complementation	Fluc	[73]
2008	Pichler et al.	Development of a universal transgenic reporter mouse for PPI detection	Two-hybrid system	Fluc	[74]
2009	De et al.	Further developments of an assay	BRET	Rluc (and GFP variant)	[75]
2009	Chan et al.	Detection of protein phosphorylation mediated by protein kinases	Split reporter complementation	Fluc	[51]
2010	Pan et al.	Monitoring of rapamycin pharmacodynamics	Two-hybrid system	Fluc	[76]
2010	Massoud et al.	Development of a PET-based split reporter	Split reporter complementation	TK	[65]
2011	Dragulescu-Andrasi et al.	Detection of deep seated PPIs	BRET	Rluc	[77]

Fluc Firefly luciferase

Rluc Renilla luciferase

TK Herpes simplex virus type-1 thymidine kinase

GFP Green fluorescent protein

FRB FK506-binding protein (FKBP12) rapamycin-binding domain

FKBP12 FK506-binding protein

PPI Protein-protein interaction

BRET bioluminescence resonance energy transfer

HIF-1alpha hypoxia-inducible factor-1alpha

VHL von Hippel-Lindau tumor suppressor

HSP90 Heat shock protein 90

Akt Enzymes that are members of the serine/threonine-specific protein kinase family. Akt was originally identified as the oncogene in the transforming retrovirus, AKT8

proteins. This strategy will not be discussed further in this chapter; and a separate chapter dedicated to BRET imaging can be found elsewhere in this book.

In certain circumstances, functional proteins can assemble from one or more polypeptide fragments, with the occurrence and efficiency of assembly commandeered into a strategy to measure real-time PPIs. Indeed, synthetically separated fragments of some enzymes can reconstitute functionally active protein particularly if the interaction is helped along by fusion of the enzyme fragments to

strongly interacting moieties. Thus, in the “split protein” strategy, a single reporter protein/enzyme is cleaved into N-terminal and C-terminal segments; each segment is fused to one of two interacting proteins (X and Y). Physical interactions between the two proteins X and Y reconstitutes the functional reporter protein leading to signal generation that can be measured. This split protein strategy can work either through protein-fragment complementation assays (PCA), or intein-mediated reconstitution assays. In the former, noncovalent assembly of the reporter protein occurs, and in the latter case, reconstitution of the full reporter protein occurs through covalent bonding. To date, several reporter proteins (e.g., β -lactamase, β -galactosidase, ubiquitin, dihydrofolate reductase, firefly luciferase [Fluc], Renilla luciferase [Rluc], Gaussia luciferase [GLuc], Click beetle luciferase [CBLuc], green fluorescent protein) have been adapted for split protein strategies by finding various split sites for each reporter protein [29–32]. If a full-length reporter can be imaged in living subjects, and this reporter can be appropriately split, then the split reporter assay could possibly be used to noninvasively image PPIs. The appropriate split point should lead to two fragments that do not have significant affinity for each other and yet when brought together (through interaction of the two proteins being studied for their mutual affinity) lead to detectable signal.

The principle of the PCA strategy for detecting PPIs was first demonstrated by Pelletier et al. using the enzyme dihydrofolate reductase (DHFR) [33], following inspiration from a 1994 paper by Johnsson and Varshavsky [34] describing what they called the “ubiquitin split protein sensor.” In all PCAs, splitting a specific reporter protein into two distinct fragments abolishes its function. Bringing the two fragments back together in a controlled manner then restores functional activity [35]. Selected fragments of many proteins can associate to produce functional bimolecular complexes [36]; the PCA system can therefore be generalized for a number of enzymes for the detection of PPIs, examples including DHFR, glycylamide ribonucleotide (GAR) transformylase, aminoglycoside, and hygromycin B phosphotransferases, all reviewed by Michnick et al. [35], *Escherichia coli* TEM-1 β -lactamase [29, 37], green fluorescent protein and its variants [36], and the molecular imaging reporters Fluc [31] and Rluc [30, 38]. A review of this subject was also published recently by Shekhawat and Gosh [39].

9.4.1 *Intein-mediated Reconstitution Assays*

These assays are based on the restoration of the full reporter protein through covalent bonding. Inteins have been defined as protein sequences embedded in-frame within a precursor protein sequence and excised during a maturation process termed protein splicing [40]. Protein splicing is a post-translational event involving precise excision of the intein sequence and concomitant ligation of the flanking sequences (N- and C-exteins) by a normal peptide bond [41]. Inteins are intervening DNA sequences that are not present in the mature gene product as a result of splicing at the protein level instead of at the RNA level. In 1998, it was

discovered that the gene for the catalytic α subunit of the replicative DNA polymerase III from *Synechocystis* sp. PCC6803 (*Ssp*) is encoded in two segments *dnaE-n* and *dnaE-c* [42]. Inteins represent a potentially powerful means of protein manipulation, because two peptide bonds are broken, and a new peptide bond is formed during the protein splicing process. Protein splicing is an exceedingly complex self-catalyzed process that requires neither cofactors nor auxiliary enzymes. It requires no source of metabolic energy and therefore involves bond rearrangements rather than bond cleavage followed by re-synthesis. The elucidation of the reaction steps involved in protein splicing has made it possible to modulate the reactions by mutations and to design proteins that can undergo highly specific self-cleavage and protein ligation reactions. An intein can be viewed as an enzyme whose substrate is the adjacent amino acid residues in the two exteins to which it is linked.

Ozawa et al. [43] initially demonstrated that *Fluc* can be split between amino acid positions 437 and 438 and used with inteins (*DnaE*) in a reconstitution strategy to detect insulin-induced interaction of phosphorylated insulin receptor substrate 1 (*IRS-1*) and its target N-terminal SH2 domain of phosphoinositide-3 kinase (*PI-3 K*) in a cell culture assay. Upon interaction of the two proteins, the two *DnaE* fragments are brought close enough to fold together and initiate splicing and linking of the two *Fluc* halves with a peptide bond. The *Fluc* gene has to be rationally dissected so that each half of *Fluc* is inactive. After ligating the *Fluc* fragments together, the resultant mature *Fluc* recovers its bioluminescence activity [44].

We subsequently reasoned that it may be possible to split *Fluc* and use split reporter complementation *without* inteins. We therefore studied PCA and intein-mediated reconstitution of *Fluc* fragments and found that a complementation strategy was as sensitive as the intein-mediated reconstitution strategy under the conditions tested [31]. Thus, we demonstrated for the first time the feasibility of imaging PPIs using split reporters in small living animals. We studied a PCA based on split *Fluc* (cleaved into two fragments n*Fluc*: residues 1–437; and c*Fluc*: residues 438–550), using the interaction of *Id* and *MyoD* as test proteins [31].

Subsequently, Kim et al. [45] developed a genetically encoded bioluminescence indicator for monitoring and imaging the nuclear trafficking of target proteins *in vitro* and *in vivo*. The principle is based on reconstitution of split fragments of *Rluc* by protein splicing with a *DnaE* intein. A target cytosolic protein fused to the N-terminal half of *Rluc* is expressed in mammalian cells. If the protein translocates into the nucleus, the *Rluc* moiety meets the C-terminal half of *Rluc*, and full-length *Rluc* is reconstituted by protein splicing. They demonstrated quantitative cell-based *in vitro* sensing and *in vivo* imaging of ligand-induced translocation of androgen receptor, which allowed high-throughput screening of exogenous and endogenous agonists and antagonists of this receptor.

The same authors used a similar approach to noninvasive molecular imaging of physical and emotional stress by developing a method for detecting physiological increases in the endogenous corticosterone caused by exo- and endogenous stress in living animals [46]. They constructed a pair of genetically encoded indicators composed of cDNAs of glucocorticoid receptor (*GR*), split *Rluc*, and a *DnaE*

intein. The GR fused with C-terminal halves of Rluc and DnaE was localized in the cytosol, whereas a fusion protein of N-terminal halves of Rluc and DnaE was localized in the nucleus. If corticosterone induces GR translocation into the nucleus, the C-terminal Rluc meets the N-terminal one in the nucleus, and full-length Rluc is reconstituted by protein splicing with DnaE. Cell-based methods provided a quantitative bioluminescence assay of the extent of GR translocation into the nucleus. The authors further demonstrated that the indicator enabled noninvasive imaging in mice subjected to two different types of imposed stress: a forced swimming and metabolic perturbation caused by 2-deoxy-D-glucose. This stress indicator should be valuable for screening pharmacological compounds and in studying mechanisms of physiological stress.

Kanno et al. [47] also developed a genetically encoded bioluminescence indicator for monitoring the release of proteins from the mitochondria in living cells. The principle of this method is based on reconstitution of split Rluc fragments by protein splicing with a DnaE intein. A target mitochondrial protein connected with an N-terminal fragment of Rluc and an N-terminal fragment of DnaE is expressed in mammalian cells. If the target protein is released from the mitochondria toward the cytosol upon stimulation with a specific chemical, the N-terminal Rluc meets the C-terminal Rluc connected with C-terminal DnaE in the cytosol, and thereby, the full-length Rluc is reconstituted by protein splicing. The extent of release of the target fusion protein was evaluated by measuring activities of the reconstituted Rluc. To test the feasibility of this method, the authors monitored the release of Smac/DIABLO protein from mitochondria during apoptosis in living cells and mice. Their method allowed high-throughput screening of an apoptosis-inducing reagent, staurosporine, and imaging of the Smac/DIABLO release in cells and in living mice. This rapid analysis may be used for screening and assaying chemicals that would increase or inhibit the release of mitochondrial proteins in living cells and animals.

The split-intein system generally suffers from slow kinetic response rates posing problems for quantitative interrogation of reversible biochemical reactions, drug-induced protein associations, or shifts in equilibrium states of interacting proteins. The truly important aspects of studying PPIs in living cells or animals lie in the ability to do so in real time. The inevitable delay in the ability to detect an interaction using the split-intein strategy can be attributed to the time required for the splicing reaction. While this may not be a factor for slow reactions occurring over long time frames, numerous drugs, chemicals, and natural ligands exert their effects in seconds to minutes. The system also exhibits a high false-positive rate on account of the split-intein fragments being so small that at times it is believed they act merely as simple linker proteins, thus limiting the quantification of protein interactions.

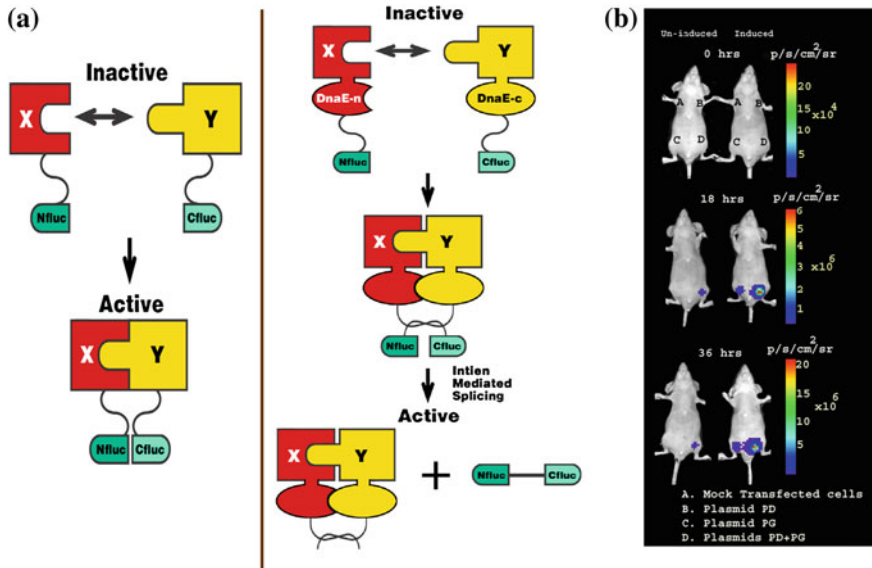


Fig. 9.1 Schematic diagram of the split reporter-based complementation strategy used to optically image PPIs in living mice. The N-terminal half of firefly luciferase is attached to protein X through a short peptide linker FFAGYC, and the C-terminal half firefly luciferase is connected to protein Y through the peptide linker CLKS. Interaction of proteins X and Y recovers Fluc activity through protein complementation (Fig. 9.1a). In vivo optical cooled CCD camera imaging of mice carrying transiently cotransfected 293T cells for the induction of the complementation-based split-luciferase system. All images shown are the visible light image superimposed on the optical CCD bioluminescence image with a scale in $\text{p/sec/cm}^2/\text{sr}$. Mice were imaged in a supine position after IP injection of D-Luciferin. (Fig. 9.1b). A set of nude mice was repetitively imaged after subcutaneous implantation of 293T cells transiently cotransfected with various plasmids as described in Paulmurugan et al. [31]. One group of mice was induced with $\text{TNF-}\alpha$, and the other group was not induced. The images were one representative mouse from each group immediately after implanting cells (0 h), and 18 and 36 h after $\text{TNF-}\alpha$ induction. The induced mouse showed higher Fluc signal at site D (where interacting proteins result in reporter protein complementation) when compared with the mouse not receiving $\text{TNF-}\alpha$. The Fluc signal significantly increases after receiving $\text{TNF-}\alpha$. Reproduced with permission from Paulmurugan et al. [31]

9.4.2 Protein-Fragment Complementation Assays Using Split Firefly Luciferase

The most commonly used bioluminescence reporter gene for research purposes has been the luciferase from the North American Firefly (*Photinus pyralis*; *Fluc*). Fluc (61 kDa) catalyzes the transformation of its substrate D-Luciferin into oxyluciferin in a process dependent on ATP, Mg^{++} , and O_2 , leading to self-emission of light from green to yellow wavelengths (560–610 nm, peak emission at 562 nm). In 2002, we demonstrated for the first time the feasibility of imaging PPIs using split

reporters in small living animals [31]. We studied a PCA based on split Fluc (cleaved into two fragments, nFluc: residues 1–437; and cFluc: residues 438–550), using the interaction of Id and MyoD as test proteins (Fig. 9.1).

Subsequently, Luker et al. [48] described a systematic truncation library yielding alternative complementary N- and C-fragments of Fluc (nFluc: residues 2-416; and cFluc: residues 398-550). These fragments were used to monitor rapamycin-mediated interaction of rapamycin-binding proteins FRB and FKBP12. We similarly used the Fluc fragments previously tested with Id and MyoD to study rapamycin-mediated interactions and found the complementation to be too weak for optical imaging in living animals using the CCD camera (unpublished data).

Further studies on reporter complementation assays for imaging of PPIs in living subjects led us to use a combinatorial strategy to identify a novel split site for Fluc with improved imaging characteristics over previously published split sites [49]. A combination of fragments with greater absolute signal and near-zero background signal was achieved by screening 115 different combinations. The identified fragments were further characterized by using five different interacting protein partners and an intramolecular folding strategy (see below). Cell culture studies and imaging in living mice were performed to validate the new split sites. In addition, the signal generated by the newly identified combination of fragments (nFluc 398/cFluc 394) was compared with different split-luciferase fragments then in use for studying PPIs and was shown to be markedly superior with a lower self-complementation signal and equal or higher post-interaction absolute signal. This study also identified many different combinations of nonoverlapping and overlapping Fluc fragments that can be used for studying different cellular events such as sub-cellular localization of proteins, cell–cell fusion, and evaluating cell delivery vehicles, in addition to PPIs, both in cells and small living animals.

The developed split Fluc system was used to study the crucial role of tumor hypoxia in tumorigenesis [50]. Under hypoxia, hypoxia-inducible factor 1 alpha (HIF-1 alpha) regulates activation of genes promoting malignant progression. Under normoxia, HIF-1 alpha is hydroxylated on prolines 402 and 564 and is targeted for ubiquitin-mediated degradation by interacting with the von Hippel-Lindau protein complex (pVHL). We developed a novel method of studying the interaction between HIF-1 alpha and pVHL using the split Fluc complementation-based bioluminescence system in which HIF-1 alpha and pVHL are fused to amino-terminal and carboxy-terminal fragments of the luciferase, respectively. We demonstrated that hydroxylation-dependent interaction between the HIF-1 alpha and pVHL leads to complementation of the two luciferase fragments, resulting in bioluminescence in vitro and in vivo. Complementation-based bioluminescence is diminished when mutant pVHLs with decreased affinity for binding HIF-1 alpha are used. This method represents a new approach for studying interaction of proteins involved in the regulation of protein degradation.

In another application, protein phosphorylation mediated by protein kinases was studied using a genetically encoded, generalizable split Fluc-assisted complementation system [51]. This was developed for noninvasive monitoring of phosphorylation events and efficacies of kinase inhibitors in cell culture and in

small living subjects by optical bioluminescence imaging. The serine/threonine kinase Akt mediates mitogenic and anti-apoptotic responses that result from activation of multiple signaling cascades. It is considered a key determinant of tumor aggressiveness and is a major target for anticancer drug development. An Akt sensor (AST) was constructed to monitor Akt phosphorylation and the effect of different PI-3 K and Akt inhibitors. Specificity of AST was determined using a nonphosphorylatable mutant sensor containing an alanine substitution (ASA). It was found that the PI-3 K inhibitor LY294002 and Akt kinase inhibitor perifosine led to temporal- and dose-dependent increases in complemented Fluc activities in 293T human kidney cancer cells stably expressing AST (293T/AST) but not in 293T/ASA cells. Inhibition of endogenous Akt phosphorylation and kinase activities by perifosine also correlated with increase in complemented Fluc activities in 293T/AST cells but not in 293T/ASA cells. Treatment of nude mice bearing 293T/AST xenografts with perifosine led to a twofold increase in complemented Fluc activities compared with that of 293T/ASA xenografts. Our system was used to screen a small chemical library for novel modulators of Akt kinase activity. It is foreseen that this generalizable approach for noninvasive monitoring of phosphorylation events will accelerate the discovery and validation of novel kinase inhibitors and modulators of phosphorylation events.

Zhang et al. [52] have also described a new reporter molecule whose bioluminescence activity within live cells and in mice can be used to measure Akt activity. Akt activity in cultured cells, and tumor xenografts was monitored quantitatively and dynamically in response to activation or inhibition of receptor tyrosine kinase, inhibition of PI-3 K, or direct inhibition of Akt. The results provided unique insights into the pharmacokinetics and pharmacodynamics of agents that modulate Akt activity, revealing the usefulness of this reporter for rapid dose and schedule optimization in the drug development process. Having constructed a genetically engineered hybrid bioluminescent Akt reporter (BAR) molecule that reports on Akt serine/threonine kinase activity (containing an Akt consensus substrate peptide, consisting of a domain that binds phosphorylated amino acid residues (FHA2) flanked by nFluc and cFluc reporter domains), the same authors subsequently described a modified version of this reporter molecule (myristoylated and palmitoylated bioluminescent Akt reporter [MyrPalm-BAR]), which is membrane bound and the bioluminescence activity of which can be used to monitor Akt activity at the cell membrane [53]. This was based on the fact that Akt is recruited to the plasma membrane upon activation. Using changes in Akt activation status with small molecule inhibitors of Akt, they demonstrated that the membrane-targeted Akt reporter was more sensitive and quantitative. In addition, inhibition of upstream signaling kinases such as epidermal growth factor receptor and phosphatidylinositol 3-kinase activity resulted in changes in Akt activity that was quantitatively monitored by bioluminescence imaging. Based on these results, the authors proposed that the membrane-associated Akt reporter may be better suited for high-throughput screening and identification of novel compounds that modulate the Akt pathway.

In a slight variation on the theme of imaging PPIs, we identified different fragments of *Fluc* based on the crystal structure of Fluc; these split reporter genes, which encode fragments distinctly different from those currently used for studying PPIs, can *self*-complement and provide Fluc enzyme activity in different cell lines in culture and in living mice [54]. The comparison of the fragment complementation associated recovery of Fluc activity with intact Fluc was estimated for different fragment combinations and ranged from 0.01 to 4 % of the full Fluc activity. Using a cooled optical charge-coupled device camera, the analysis of Fluc fragment complementation in transiently transfected subcutaneous 293T cell implants in living mice showed significant detectable enzyme activity upon injecting D-Luciferin, especially from the combinations of fragments identified (nFluc and cFluc are the N and C fragments of Fluc, respectively): nFluc (1–475)/cFluc (245–550), nFluc (1–475)/cFluc (265–550), and nFluc (1–475)/cFluc (300–550). The cFluc (265–550) fragment, upon expression with the nuclear localization signal (NLS) peptide of SV40, showed reduced enzyme activity when the cells were cotransfected with the nFluc (1–475) fragment expressed without NLS. We also proved in this study, by delivering TAT-cFluc (265–550) to cells stably expressing nFluc (1–475) and recovering signal, that the complementing fragments could be efficiently used for screening macromolecule delivery vehicles. These complementing fragments should be useful for many reporter-based assays including intracellular localization of proteins, studying cellular macromolecule delivery vehicles, studying cell–cell fusions, and also developing intracellular phosphorylation sensors based on fragment complementation.

9.4.3 Protein-Fragment Complementation Assays Using Split *Renilla luciferase*

The enzyme Rluc (or the synthetically mutated humanized version, hRluc), is a 311-residue, 36-kDa monomeric bioluminescence imaging reporter protein, being the smallest optical reporter protein identified to date for studying PPIs in a PCA strategy [30, 38]. This PCA strategy, using N- and C-terminal halves of split Rluc functions in both cell culture and in living animals, and has been demonstrated with several different protein partners. We used fragments generated by splitting between residues 229 and 230 to study rapamycin-induced interaction of the human proteins FRB and FKBP12 [55]. Moreover, protein interaction between IRS1 and the SH2 domain of PI3 K in the insulin-signaling pathway was located in living mammalian cells using Rluc split between residues 91 and 92 [30].

Rluc is capable of generating a flash of blue light (460–490 nm, peak emission at 482 nm) upon reaction with its substrate coelenterazine. One limitation associated with the use of Rluc is its relatively rapid reaction kinetics, requiring early time-point measurements [56]. Nevertheless, this split reporter system appears highly suitable for studying PPIs in cells and in living animals owing to its optical

bioluminescence nature, and its signal that is amplifiable through an enzymatic process. Further, the complementation strategies based on Rluc fragments, with smaller fragment size than Fluc, have less hindrance with interacting protein partners, and work more efficiently with different imaging assays. Another clear advantage of using the split Rluc system when compared to the split Fluc is that the former's enzymatic reaction is ATP independent and therefore could be used in specific situations where the PPI under study itself requires ATP, e.g., the binding of Hsp90 to the co-chaperone protein p23. Unfortunately, several coelenterazines have been found to be substrates for the efflux transporter *MDR1* P-glycoprotein, including coelenterazine f, h, and hcp [57]. This raises some general concern for the indiscriminant use of coelenterazine and Rluc reporters in live cell assays and noninvasive whole-animal imaging. The photon output of the reporter can be impacted by changes in P-glycoprotein transport activity that alter substrate availability within the cells, thereby introducing signal artifacts not related to the biological process under investigation, that is, PPIs. Furthermore, coelenterazine cannot be used in experimentation involving transport across the blood–brain barrier because brain capillaries are rich in outwardly directed P-glycoprotein, effectively excluding coelenterazine from the central nervous system.

To date, the split Rluc system has been used in several molecular imaging applications, including PPIs, small molecule-induced PPIs, small molecule-mediated inhibition of PPIs, and protein homodimerization. More recently, we developed a novel fusion protein approach for studying rapamycin-mediated interaction of fused FRB and FKBP12 with either split hRluc or split enhanced GFP, to achieve a system with greater sensitivity for detecting lower levels of drug-mediated PPIs in vivo [58]. These applications are described more fully below.

Networks of protein interactions mediate cellular responses to environmental stimuli and direct the execution of many different cellular functional pathways. Small molecules synthesized within cells or recruited from the external environment mediate many protein interactions. The study of small molecule-mediated interactions of proteins is important to understand abnormal signal transduction pathways in cancer and in drug development and validation. In one study, we used split hRluc protein-fragment-assisted complementation to evaluate heterodimerization of the human proteins FRB and FKBP12 mediated by the small molecule rapamycin [55] (Fig. 9.2). The concentration of rapamycin required for efficient dimerization and that of its competitive binder ascomycin required for dimerization inhibition were studied in cell lines. The system was dually modulated in cell culture at the transcription level, by controlling nuclear factor kappaB promoter/enhancer elements using tumor necrosis factor alpha, and at the interaction level, by controlling the concentration of the dimerizer rapamycin. The rapamycin-mediated dimerization of FRB and FKBP12 also was studied in living mice by locating, quantifying, and timing the hRluc complementation-based bioluminescence imaging signal using a cooled charge-coupled device camera. It was found that this split reporter system can be used to efficiently screen small molecule drugs that modulate PPIs and also to assess drugs in living animals. Both are

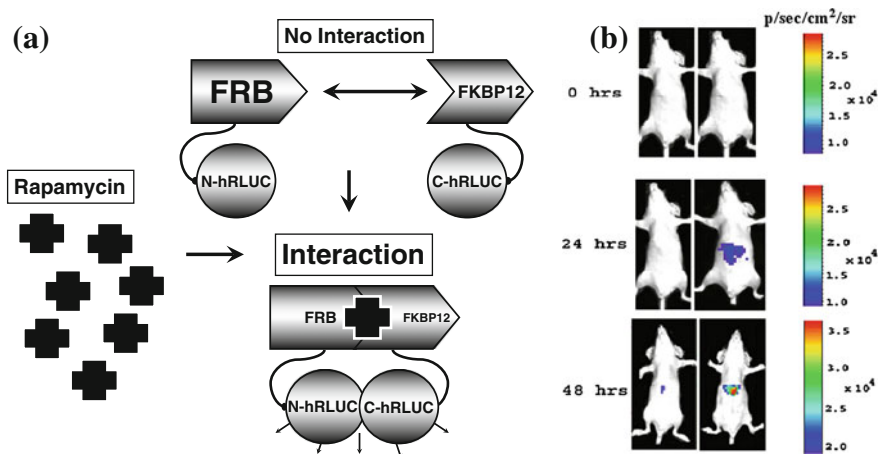


Fig. 9.2 Schematic diagram of rapamycin-mediated synthetic Renilla luciferase (hRLuc) protein-fragment-assisted complementation strategy. In this strategy (Fig. 9.2a) N-terminal and C-terminal portions of hRLuc fragments are attached to proteins FRB and FKBP12, respectively, through a short peptide linker GGGGSGGGGS. The N- and C-portions of hRLuc fragments are closely approximated by the dimerization of proteins FRB and FKBP12 only in the presence of the small molecule rapamycin, and this, in turn, leads to recover the activity of the hRLuc protein. Optical CCD camera imaging of living mice carrying IV injected 293T cells transiently cotransfected with NhrLuc-FRB and FKBP12-Chrluc (Fig. 9.2b). The animals not receiving rapamycin showed only a mean background signal of $4 \pm 1 \times 10^3$ p/s/cm²/sr at all of the four time points studied. The animals receiving repeated injections of rapamycin emitted signals in the region of abdomen that were three fold (mean, 1.6×10^4 p/s/cm²/sr) and five-fold (mean, 3.0×10^4 p/s/cm²/sr) higher than background ($p < 0.05$) at 24 and 48 h after the injection of rapamycin, respectively. (left-sided animals did not receive rapamycin; right-sided animals received rapamycin). Reproduced with permission from Paulmurugan et al. [54]

essential steps in the preclinical evaluation of candidate pharmaceutical agents targeting PPIs, including signaling pathways in cancer cells.

In another study adopting a different strategy, we evaluated the rapamycin-mediated interaction of the human proteins FK506-binding protein (FKBP12) rapamycin-binding domain (FRB) and FKBP12 by constructing a fusion of these proteins with a split-Rluc or a split enhanced green fluorescent protein (split-EGFP) such that complementation of the reporter fragments occurs in the presence of rapamycin [58]. Different linker peptides in the fusion protein were evaluated for the efficient maintenance of complemented reporter activity. This system was studied in both cell culture and xenografts in living animals. We found that peptide linkers with two or four EAAAR amino acid repeats showed higher PPI-mediated signal with lower background signal compared with having no linker or linkers with amino acid sequences GGGGSGGGGS, ACGSLSCGSF, and ACGSLSCGSFACGSLSCGSF. A $9 \pm$ twofold increase in signal intensity both in cell culture and in living mice was seen compared with a system that expresses both reporter fragments and the interacting proteins separately. In this fusion system,

rapamycin-induced heterodimerization of the FRB and FKBP12 moieties occurred rapidly even at very lower concentrations (0.00001 nmol/L) of rapamycin. For a similar fusion system employing split-EGFP, flow cytometry analysis showed significant level of rapamycin-induced complementation.

We also evaluated small molecule-mediated inhibition of PPIs [59]. Heat shock protein 90 alpha (Hsp90 alpha)/p23 and Hsp90 beta/p23 interactions are crucial for proper folding of proteins involved in cancer and neurodegenerative diseases. Small molecule Hsp90 inhibitors block Hsp90 alpha/p23 and Hsp90 beta/p23 interactions in part by preventing ATP binding to Hsp90. The importance of isoform-selective Hsp90 alpha/p23 and Hsp90 beta/p23 interactions in determining the sensitivity to Hsp90 was examined using 293T human kidney cancer cells stably expressing split Rluc reporters. Interactions between Hsp90 alpha/p23 and Hsp90 beta/p23 in the split Rluc reporters led to complementation of Rluc activity, which was determined by bioluminescence imaging of intact cells in cell culture and living mice using a cooled charge-coupled device camera. The three geldanamycin-based and seven purine-scaffold Hsp90 inhibitors led to different levels of inhibition of complemented Rluc activities (10–70 %). However, there was no isoform selectivity to either class of Hsp90 inhibitors in cell culture conditions. The most potent Hsp90 inhibitor, PU-H71, however, led to a 60 and 30 % decrease in Rluc activity (14 h) in 293T xenografts expressing Hsp90 alpha/p23 and Hsp90 beta/p23 split reporters, respectively, relative to carrier control-treated mice. Molecular imaging of isoform-specific Hsp90 alpha/p23 and Hsp90 beta/p23 interactions and efficacy of different classes of Hsp90 inhibitors in living subjects have been achieved with a novel genetically encoded reporter gene strategy that should help in accelerating development of potent and isoform-selective Hsp90 inhibitors.

Homodimeric protein interactions are potent regulators of cellular functions but are particularly challenging to study *in vivo*. We also used a split hRluc complementation-based bioluminescence assay to study homodimerization of herpes simplex virus type 1 thymidine kinase (TK) in mammalian cells and in living mice [28]. We quantified and imaged homodimerization of TK chimeras containing N-terminal (n-hRluc) or C-terminal (c-hRluc) fragments of hRluc in the upstream and downstream positions, respectively, (tail-to-head homodimer). This was monitored using luminometry (68-fold increase, and was significantly [$P < 0.01$] above background light emission) and by CCD camera imaging of living mice implanted with *ex vivo* transfected 293T cells (2.7-fold increase and was significantly [$P < 0.01$] above background light emission). We also made a mutant-TK to generate n-hRluc mutant TK and mutant TK-c-hRluc by changing a single amino acid at position 318 from arginine to cysteine, a key site that has previously been reported to be essential for TK homo-dimerization, to support the specificity of the hRluc complementation signal from TK homodimerization. *Ex vivo* substrate (8-3H Penciclovir) accumulation assays in 293T cells expressing the TK protein chimeras showed active TK enzyme. We also devised an experimental strategy by constructing variant TK chimeras (possessing extra n-hRluc or c-hRluc ‘spacers’) to monitor incremental lack of association of the tail-to-head TK

homodimer. Application of this potentially generalizable assay to screen for molecules that promote or disrupt ubiquitous homodimeric PPIs could serve not only as an invaluable tool to understand biological networks but could also be applied to drug discovery and validation in living subjects.

As an offshoot to our designing of strategies for PPI imaging, we used the split Renilla system to help devise newer approaches to high-throughput analysis of interactions between various hormones and drugs with the estrogen receptor (ER) [60]. These are crucial for accelerating the understanding of ER biology and pharmacology. Through the careful analyses of the crystal structures of the human ER (hER) ligand-binding domain (hER-LBD) in complex with different ligands, we hypothesized that the hER-LBD intramolecular folding pattern could be used to distinguish ER agonists from selective ER modulators and pure antiestrogens. We therefore constructed and validated intramolecular folding sensors encoding various hER-LBD fusion proteins that could lead to split Rluc/Fluc reporter complementation in the presence of the appropriate ligands. A mutant hER-LBD with low affinity for circulating estradiol was also identified for imaging in living subjects. Cells stably expressing the intramolecular folding sensors expressing wild-type and mutant hER-LBD were used for imaging ligand-induced intramolecular folding in living mice. This is the first hER-LBD intramolecular folding sensor suited for high-throughput quantitative analysis of interactions between hER with hormones and drugs using cell lysates, intact cells, and molecular imaging of small living subjects. The strategies developed can also be extended to study and image other important protein intramolecular folding systems. A subsequent further development of this system allowed for *in vivo* molecular imaging of ER α and ER β homo- and heterodimerization using split Fluc or Rluc [61].

In an interesting combined application of both split Fluc and split Rluc systems, we demonstrated the feasibility of imaging ER-ligand-modulated multiprotein interactions [human estrogen receptors (ER-alpha/beta), p53 tumor suppressor protein and the human equivalent of mouse double minute 2 (HDM2)] [R Paulmurugan and SS Gambhir: Imaging ER-ligand-modulated multiprotein interactions [(human estrogen receptors (ER-alpha/beta), p53 tumor suppressor protein and the human equivalent of mouse double minute 2 (HDM2)] with a split-luciferase system. Presented at the Joint Molecular Imaging Conference, Providence, Rhode Island, September 2007]. The background impetus to this arises from knowledge that cancers develop when accumulated genetic defects cause cells to proliferate unchecked and escape from programmed cell-death. p53, HDM2, and ERs are a few among several prime targets that generate genetic abnormalities that lead to cancer. These proteins function independently and interact together by forming a ternary complex that regulates the expression level of different proteins required for normal cell death/growth. The advantages of these targets over other proteins are that they can be controlled by small-molecule ligands that bind to any one of these three (p53/HDM2/ER) to modulate the functional role of all three proteins. The authors showed for the first time simultaneous interaction of these multiproteins and their modulation in response to different ER-ligands. Plasmids expressing fusion-proteins nFluc-ER-alpha/beta-chRluc, p53-cFluc and nhRluc-HDM2 were transiently

cotransfected in 293T cells and complemented Fluc (ER/p53-interaction) and Rluc (p53/HDM2-interaction) activities were determined before and after exposure to 13-different ligands that bind to ER. The results showed significant levels of modulation by ER-ligands for the Fluc signals (ER/p53-interaction). There was no significant change in the Rluc signal (p53/HDM2-interaction). Studies with both ER-alpha and beta showed similar levels of interaction with p53. The system with the ER/p53 interaction showed significant levels of reversibility upon removal of the ligand. These results demonstrated that the interaction between ER and p53 was ligand-dependent. Studying this multiprotein interaction system with ligands specific to p53 or/to HDM2, in the presence and the absence of ER-ligands, may further identify the complexity behind the interactions between these three proteins. This was the first demonstration of multiprotein-interactions studied with multiple-split-reporters and this strategy should be useful for also studying other similar types of complex interactions.

Of note, the split protein strategies described previously are based on absolute stereospecific and regiospecific requirements for complex formation among interacting sequences. Although no head-to-head comparison is available, this strategy would therefore appear more specific than the modified yeast two-hybrid system, which suffers from many false-positive outcomes, at least in its standard (nonimaging) laboratory use. Moreover, the split protein strategies can be used to image interacting proteins anywhere in the cell.

9.4.4 Protein-Fragment Complementation Assays Using Other Split Reporters, and Other Reporter Complementation Strategies

Although not yet at a stage of application in living subjects, Kim et al. [62] have recently evaluated the Click beetle luciferase (CBluc) and its luminescence signal as a bioanalytical index reporting the magnitude of a signal transduction of interest. CBluc is insensitive to pH, temperature, and heavy metals, and emits a stable, highly tissue-transparent red light with luciferin in physiological circumstances. They validated a single-molecule-format complementation system of split CBluc to study signal-controlled PPIs. First, they generated 10 pairs of N- and C-terminal fragments of CBluc to examine, respectively, whether a significant recovery of the activity occurs through intramolecular complementation. The ligand binding domain of androgen receptor (AR LBD) was connected to a functional peptide sequence through a flexible linker. The fusion protein was then sandwiched between the dissected N- and C-terminal fragments of CBluc. Androgen induces the association between AR LBD and a functional peptide and the subsequent complementation of N- and C-terminal fragments of split CBluc inside the single-molecule-format probe, which restores the activities of CBluc.

The examination about the split sites of CBluc revealed that the dissection positions next to the amino acids D412 and I439 can admit a stable recovery of CBluc activity through an intramolecular complementation. The ligand sensitivity and kinetics of the single molecular probe with split CBluc were studied in various cell lines and in different protein-peptide binding models. The probe may be applicable to developing biotherapeutic agents relevant to AR signaling and for screening adverse chemicals that possibly influence the signal transduction of proteins in living cells or animals, although the latter setting is yet to be verified.

Gaussia Luciferase (GLuc) is another high-sensitive optical reporter protein of 19.9 kDa (185 amino acids) that emits blue light (at a peak of 480nm) and uses the substrate coelenterazine. Optimal split sites identified between amino acids Gly93 and Glu94 by screening a library of N- and C-terminal fragments using a rapamycin-mediated FRB/FKBP12 interaction system were successfully evaluated for leucine zipper interaction and TGF β -mediated interaction of serine-threonine kinase PKB/Akt and the transcriptional activator Smad3 [63]. Later, Kim et al. in 2009 [64], identified fragments generated by a split site between amino acids 105 and 106 can successfully reconstitute enzymatic activity through PPIs driven by calcium (calmodulin and M13 peptide interaction) in cell cultures. Even though GLuc is highly sensitive, the secretory nature of this protein limits its application for in vivo studies.

Importantly, there is a pressing need to develop better techniques for noninvasive imaging of PPIs using split reporters. We recently described the molecular engineering rationale and construction of a novel positron emission tomography (PET)-based reporter (the herpes simplex virus type 1 thymidine kinase [TK]) split into two fragments between Thr-265 and Ala-266 after demonstration of preserved enzymatic activity (85.2 %, as compared to intact TK) in a circularly permuted variant based on this cleavage site [65]. We used this split TK in a PCA to quantitatively measure PPIs in mammalian 293T cells using an in vitro [8-³H]Penciclovir cell uptake assay. We showed a greater extent of TK fragment complementation when using FRB/FKBP12 than Id/MyoD as test proteins. We determined that co-expression of nTK-FRB together with FKBP12-cTK gave the optimal orientation of chimeras for evaluation in this PCA assay. We also demonstrated the use of this split TK in a PCA to quantitatively microPET image PPIs in 293T cells subcutaneously implanted in living mice. For this, we prepared 293T cells stably expressing nTK-FRB and FKBP12-cTK in a single vector. Cell uptake studies using these stably transfected cells demonstrated that the competitive inhibitor ascomycin (FK506) prevented rapamycin-induced TK activity in a dose-dependent manner. Prior to imaging we also established that adequate levels of protein expression were present by western blot. The designing of this novel split TK reporter and its application in an in vivo PET-based PCA potentially allows for the first time a more precise fully quantitative and tomographic localization of cytosolic or nuclear PPIs in pre-clinical small and large animal models of disease than has been possible to date.

9.5 Future Outlook and Conclusions

We have reviewed the main methods currently available for imaging PPIs in living subjects based on use of the split reporter systems. Unlike fluorescence microscopy-based techniques, studies of the kinetics of PPIs, including analysis of complementation reversibility, are not possible at present, although this will be an area of future active investigation. These future experiments will also require assessment in several cell lines, as well as with a greater variety of protein partners of different sizes and interaction affinities (weak transient to strong obligate), to establish the general widespread applicability of this technique.

The opportunity to measure two different protein interactions at the same time by spectrally unmixing output colors will be useful in attempts to multiplex image protein interaction networks [66]. Recent advances in processing of two color imaging now allows for the total spectral deconvolution of multicolored bioluminescent images, assuming the spectra are different enough to reliably calculate the contribution of each individual emitter within each detection window, based on their published spectra. Simultaneous imaging of multiple interactions should allow deconvolution of complex protein interactions and, eventually, protein interactomes.

The high sensitivity of these assays for detecting, locating, and quantifying PPIs, combined with the advantages of doing so in a living subject environment, should make them of potential value in many areas of biological investigation and future clinical molecular medicine applications (especially with the now available PET-based split TK PCA system). Indeed, endpoints in molecular imaging of PPIs can be quantified and therefore are particularly useful for translational research. Ultimately, we foresee innovative molecular imaging tools, such as the one presented, enhancing our appreciation of entire biological pathway systems and their pharmacological regulation, and accelerating the achievement of a 'systems biology' understanding of biological complexity [67].

References

1. Droit A, Poirier GG, Hunter JM (2005) Experimental and bioinformatic approaches for interrogating protein-protein interactions to determine protein function. *J Mol Endocrinol* 34:263–280
2. Mayer BJ (2006) Protein-protein interactions in signalling cascades. *Methods Mol Biol* 332:79–99
3. Cusick ME, Klitgord N, Vidal M, Hill DE (2005) Interactome: gateway into systems biology. *Hum Mol Genet* 14:R171–R181
4. Ryan DP, Matthews JM (2005) Protein-protein interactions in human disease. *Curr Opin Struct Biol* 15:441–446
5. Royer C (2004) Protein-protein interactions. Available from: <http://www.biophysics.org/education/croyer.pdf>

6. Golemis E (2002) Toward an understanding of protein interactions. In: Golemis E (ed) Protein-protein interactions: a molecular cloning manual. Cold Spring Harbor Laboratory Press, Woodbury, pp 1–6
7. Russell RB, Alber F, Aloy P, Davis FP, Korkin D, Pichaud M, Topf M, Sali A (2004) A structural perspective on protein–protein interactions. *Curr Opin Struct Biol* 14:313–324
8. Ho Y, Gruhler A, Heilbut A, Bader GD, Moore L, Adams SL, Millar A, Taylor P, Bennett K, Boutillier K et al (2002) Systematic identification of protein complexes in *Saccharomyces cerevisiae* by mass spectrometry. *Nature* 415:180–183
9. Abbott A (2002) Proteomics: the society of proteins. *Nature* 417:894–896
10. Gentleman R, Huber W (2007) Making the most of high-throughput protein-interaction data. *Genome Biol* 8:112
11. Wasinger VC, Cordwell SJ, Cerpa-Poljak A, Yan JX, Gooley AA, Wilkins MR, Duncan MW, Harris R, Williams KL, Humphrey-Smith I (1995) Progress with gene-product mapping of the mollusc: *Mycoplasma genitalium*. *Electrophoresis* 16:1090–1094
12. Colland F, Daviet L (2004) Integrating a functional proteomic approach into the target discovery process. *Biochimie* 86:625–632
13. Golemis E (2002) Protein-protein interactions: a molecular cloning manual. Cold Spring Harbor Laboratory Press, Woodbury
14. Paulmurugan R, Ray P, De A, Chan CT, Gambhir SS (2005) Imaging protein–protein interactions in living subjects. *Trends Anal Chem* 24:446–458
15. Massoud TF, Gambhir SS (2003) Molecular imaging in living subjects: seeing fundamental biological processes in a new light. *Genes Dev* 17:545–580
16. Gambhir SS, Barrio JR, Herschman HR, Phelps ME (1999) Assays for noninvasive imaging of reporter gene expression. *Nucl Med Biol* 26:481–490
17. Massoud TF, Paulmurugan R, De A, Ray P, Gambhir SS (2007) Reporter gene imaging of protein–protein interactions in living subjects. *Curr Opin Biotechnol* 18:31–37
18. Paulmurugan R, Ray P, De A, Chan CT, Gambhir SS (2006) Split luciferase complementation assay for studying interaction of proteins x and y in cells. *CSH Protoc* 6: doi: [10.1101/pdb.prot4596](https://doi.org/10.1101/pdb.prot4596)
19. De A (2011) The new era of bioluminescence resonance energy transfer technology. *Curr Pharm Biotechnol* 12:558–568
20. Haberkorn U, Altmann A (2003) Noninvasive imaging of protein–protein interactions in living organisms. *Trends Biotechnol* 21:241–243
21. Luker GD, Sharma V, Piwnica-Worms D (2003) Visualizing protein–protein interactions in living animals. *Methods* 29:110–122
22. Luker KE, Piwnica-Worms D (2004) Optimizing luciferase protein fragment complementation for bioluminescent imaging of protein–protein interactions in live cells and animals. *Methods Enzymol* 385:349–360
23. Ozawa T (2006) Designing split reporter proteins for analytical tools. *Anal Chimica Acta* 556:58–68
24. Takeuchi M, Ozawa T (2007) Methods for imaging and analyses of intracellular organelles using fluorescent and luminescent proteins. *Anal Sci* 23:25–29
25. Umezawa Y (2003) Seeing what was unseen: new analytical methods for molecular imaging. *Chem Rec* 3:22–28
26. Umezawa Y (2005) Genetically encoded optical probes for imaging cellular signaling pathways. *Biosens Bioelectron* 20:2504–2511
27. Villalobos V, Naik S, Piwnica-Worms D (2007) Current state of imaging protein–protein interactions in vivo with genetically encoded reporters. *Annu Rev Biomed Eng* 9:321–349
28. Massoud TF, Paulmurugan R, Gambhir SS (2004) Molecular imaging of homodimeric protein–protein interactions in living subjects. *FASEB J* 18:1105–1107
29. Galarneau A, Primeau M, Trudeau LE, Michnick SW (2002) Beta-lactamase protein fragment complementation assays as in vivo and in vitro sensors of protein–protein interactions. *Nat Biotechnol* 20:619–622

30. Kaihara A, Kawai Y, Sato M, Ozawa T, Umezawa Y (2003) Locating a protein–protein interaction in living cells via split Renilla luciferase complementation. *Anal Chem* 75:4176–4181
31. Paulmurugan R, Umezawa Y, Gambhir SS (2002) Noninvasive imaging of protein–protein interactions in living subjects by using reporter protein complementation and reconstitution strategies. *Proc Natl Acad Sci U S A* 99:15608–15613
32. Wehrman T, Kleaveland B, Her JH, Balint RF, Blau HM (2002) Protein–protein interactions monitored in mammalian cells via complementation of beta-lactamase enzyme fragments. *Proc Natl Acad Sci U S A* 99:3469–3474
33. Pelletier JN, Campbell-Valois F, Michnick SW (1998) Oligomerization domain-directed reassembly of active dihydrofolate reductase from rationally designed fragments. *Proc Natl Acad Sci U S A* 95:12141–12146
34. Johnson N, Varshavsky A (1994) Split ubiquitin as a sensor of protein interactions in vivo. *Proc Natl Acad Sci U S A* 91:10340–10344
35. Michnick SW, Remy I, Campbell-Valois FX, Vallee-Balisle A, Pelletier JN (2000) Detection of protein–protein interactions by protein fragment complementation strategies. *Methods Enzymol* 328:208–230
36. Hu CD, Kerppola TK (2003) Simultaneous visualization of multiple protein interactions in living cells using multicolor fluorescence complementation analysis. *Nat Biotech* 21:539–545
37. Spotts JM, Dolmetsch RE, Greenberg ME (2002) Time-lapse imaging of a dynamic phosphorylation-dependent protein–protein interaction in mammalian cells. *Proc Natl Acad Sci U S A* 99:15142–15147
38. Paulmurugan R, Gambhir SS (2003) Monitoring protein–protein interactions using split synthetic renilla luciferase protein-fragment-assisted complementation. *Anal Chem* 75:1584–1589
39. Shekhawat SS, Ghosh I (2011) Split-protein systems: beyond binary protein–protein interactions. *Curr Opin Chem Biol* 15:789–797
40. Martin DD, Xu MQ, Evans TC Jr (2001) Characterization of a naturally occurring trans-splicing intein from *Synechocystis* sp. PCC6803. *Biochemistry* 40:1393–1402
41. Paulus H (2000) Protein splicing and related forms of protein autoprocessing. *Annu Rev Biochem* 69:447–96
42. Wu H, Hu Z, Liu XQ (1998) Protein trans-splicing by a split intein encoded in a split DnaE gene of *Synechocystis* sp. PCC6803. *Proc Natl Acad Sci U S A* 95:9226–9231
43. Ozawa T, Kaihara A, Sato M, Tachihara K, Umezawa Y (2001) Split luciferase as an optical probe for detecting protein–protein interactions in mammalian cells based on protein splicing. *Anal Chem* 73:2516–2521
44. Ozawa T, Umezawa Y (2001) Detection of protein–protein interactions in vivo based on protein splicing. *Curr Opin Chem Biol* 5:578–583
45. Kim SB, Ozawa T, Watanabe S, Umezawa Y (2004) High-throughput sensing and noninvasive imaging of protein nuclear transport by using reconstitution of split renilla luciferase. *Proc Natl Acad Sci USA* 101:11542–11547
46. Kim SB, Ozawa T, Umezawa Y (2005) Genetically encoded stress indicator for noninvasively imaging endogenous corticosterone in living mice. *Anal Chem* 77:6588–6593
47. Kanno A, Ozawa T, Umezawa Y (2006) Genetically encoded optical probe for detecting release of proteins from mitochondria toward cytosol in living cells and mammals. *Anal Chem* 78:8076–8081
48. Luker KE, Smith MC, Luker GD, Gammon ST, Piwnica-Worms H, Piwnica-Worms D (2004) Kinetics of regulated protein–protein interactions revealed with firefly luciferase complementation imaging in cells and living animals. *Proc Natl Acad Sci USA* 101:12288–12293
49. Paulmurugan R, Gambhir SS (2007) Combinatorial library screening for developing an improved split-firefly luciferase fragment-assisted complementation system for studying protein–protein interactions. *Anal Chem* 79:2346–2353

50. Choi CY, Chan DA, Paulmurugan R, Sutphin PD, Le QT, Koong AC, Zundel W, Gambhir SS, Giaccia AJ (2008) Molecular imaging of hypoxia-inducible factor 1 alpha and von hippel-lindau interaction in mice. *Mol Imaging* 7:139–146
51. Chan CT, Paulmurugan R, Reeves RE, Solow-Cordero D, Gambhir SS (2009) Molecular imaging of phosphorylation events for drug development. *Mol Imaging Biol* 11:144–158
52. Zhang L, Lee KC, Bhojani MS, Khan AP, Shilman A, Holland EC, Ross BD, Rehemtulla A (2007) Molecular imaging of Akt kinase activity. *Nat Med* 13:1114–1119
53. Zhang L, Bhojani MS, Ross BD, Rehemtulla A (2008) Enhancing Akt imaging through targeted reporter expression. *Mol Imaging* 7:168–174
54. Paulmurugan R, Gambhir SS (2005) Firefly luciferase enzyme fragment complementation for imaging in cells and living animals. *Anal Chem* 77:1295–1302
55. Paulmurugan R, Massoud TF, Huang J, Gambhir SS (2004) Molecular imaging of drug-modulated protein–protein interactions in living subjects. *Cancer Res* 64:2113–2119
56. Bhaumik S, Gambhir SS (2002) Optical imaging of Renilla luciferase reporter gene expression in living mice. *Proc Natl Acad Sci U S A* 99:377–382
57. Pichler A, Prior J, Piwnica-Worms D (2004) Imaging reversal of multidrug resistance in living mice with bioluminescence: *MDR1* P-glycoprotein transports coelenterazine. *Proc Natl Acad Sci USA* 101:1702–1707
58. Paulmurugan R, Gambhir SS (2005) Novel fusion protein approach for efficient high-throughput screening of small molecule-mediating protein–protein interactions in cells and living animals. *Cancer Res* 65:7413–7420
59. Chan CT, Paulmurugan R, Gheysens OS, Kim J, Chiosis G, Gambhir SS (2008) Molecular imaging of the efficacy of heat shock protein 90 inhibitors in living subjects. *Cancer Res* 68:216–226
60. Paulmurugan R, Gambhir SS (2006) An intramolecular folding sensor for imaging estrogen receptor-ligand interactions. *Proc Natl Acad Sci U S A* 103:15883–15888
61. Paulmurugan R, Tamrazi A, Massoud TF, Katzenellenbogen JA, Gambhir SS (2011) In vitro and in vivo molecular imaging of estrogen receptor α and β homo- and heterodimerization: exploration of new modes of receptor regulation. *Mol Endocrinol* 25:2029–2040
62. Kim SB, Otani Y, Umezawa Y, Tao H (2007) Bioluminescent indicator for determining protein–protein interactions using intramolecular complementation of split click beetle luciferase. *Anal Chem* 79:4820–4826
63. Remy I, Michnick SW (2006) A highly sensitive protein–protein interaction assay based on Gaussia luciferase. *Nat Methods* 3:977–979
64. Kim SB, Sato M, Tao H (2009) Split Gaussia luciferase-based bioluminescence template for tracing protein dynamics in living cells. *Anal Chem* 81:67–74
65. Massoud TF, Paulmurugan R, Gambhir SS (2010) A molecularly engineered split reporter for imaging protein–protein interactions with positron emission tomography. *Nat Med* 16:921–926
66. Gammon ST, Leevy WM, Gross S, Gokel GW, Piwnica-Worms D (2006) Spectral unmixing of multicolored bioluminescence emitted from heterogeneous biological sources. *Anal Chem* 78:1520–1527
67. Massoud TF, Gambhir SS (2007) Integrating noninvasive molecular imaging into molecular medicine: an evolving paradigm. *Trends Mol Med* 13:183–191
68. Ray P, Pimenta H, Paulmurugan R, Berger F, Phelps ME, Iyer M, Gambhir SS (2002) Noninvasive quantitative imaging of protein–protein interactions in living subjects. *Proc Natl Acad Sci U S A* 99:3105–3110
69. Luker GD, Sharma V, Pica CM, Dahlheimer JL, Li W, Ochesky J, Ryan CE, Piwnica-Worms H, Piwnica-Worms D (2002) Noninvasive imaging of protein–protein interactions in living animals. *Proc Natl Acad Sci USA* 99:6961–6966
70. Luker GD, Sharma V, Pica CM, Prior JL, Li W, Piwnica-Worms D (2003) Molecular imaging of protein–protein interactions: controlled expression of p53 and large T-antigen fusion proteins in vivo. *Cancer Res* 63:1780–1788

71. De A, Gambhir SS (2005) Noninvasive imaging of protein–protein interactions from live cells and living subjects using bioluminescence resonance energy transfer. *FASEB J* 19:2017–2019
72. De A, Loening AM, Gambhir SS (2007) An improved bioluminescence resonance energy transfer strategy for imaging intracellular events in single cells and living subjects. *Cancer Res* 67:7175–7183
73. Luker KE, Gupta M, Luker GD (2008) Imaging CXCR4 signaling with firefly luciferase complementation. *Anal Chem* 80:5565–5573
74. Pichler A, Prior JL, Luker GD, Piwnica-Worms D (2008) Generation of a highly inducible Gal4/Fluc universal reporter mouse for in vivo bioluminescence imaging. *Proc Natl Acad Sci U S A* 105:15932–15937
75. De A, Ray P, Loening AM, Gambhir SS (2009) BRET3: a red-shifted bioluminescence resonance energy transfer (BRET) based integrated platform for imaging protein–protein interactions from single live cell and living animals. *FASEB J* 23:2702–2709
76. Pan MH, Lin J, Prior JL, Piwnica-Worms D (2010) Monitoring molecular-specific pharmacodynamics of rapamycin in vivo with inducible Gal4- > Fluc transgenic reporter mice. *Mol Cancer Ther* 9:2752–2760
77. Dragulescu-Andrasi A, Chan CT, De A, Massoud TF, Gambhir SS (2011) Bioluminescence resonance energy transfer (BRET) imaging of protein–protein interactions within deep tissues of living subjects. *Proc Natl Acad Sci U S A* 108:12060–12065

Chapter 10

Engineering Aspects of Bioluminescence Resonance Energy Transfer Systems

Abhijit De, Rohit Arora and Akshi Jasani

Abbreviations

PPI/PPIs	Protein–protein interaction(s)
ELISA	Enzyme-linked Immunosorbent Assay
Y2H	Yeast two-hybrid assay
IY2H	Induced Yeast two-hybrid assay
PCAs	Protein-fragment complementation assays
FRET	Fluorescence resonance energy transfer
BRET	Bioluminescence resonance energy transfer
BL	Bioluminescence
RLuc	<i>Renilla</i> luciferase
FLuc	Firefly luciferase
ATP	Adenosine triphosphate
LH ₂	D-Luciferin substrate for FLuc
AMP	Adenosine monophosphate
CO ₂	Carbon dioxide
Em _{max}	Emission maximum
Clz	Coelenterazine
RET	Resonance energy transfer
E _{RET}	Efficiency of resonance energy transfer
FP/FPs	Fluorescent protein(s)
GFP	Green fluorescent protein
EYFP	Enhanced yellow fluorescent protein
Ex _{max}	Excitation maximum
C _f	Correction factor
Clz- <i>h</i>	Coelenterazine- <i>h</i>

A. De (✉) · R. Arora · A. Jasani
Molecular Functional Imaging Lab, ACTREC, Tata Memorial Centre, Sector 22, Kharghar,
Navi Mumbai, Maharashtra 410210, India
e-mail: ade@actrec.gov.in

R. Arora
e-mail: rohit0288@gmail.com

A. Jasani
e-mail: akshi.aj@gmail.com

RFP	Red fluorescent protein
Clz- <i>v</i>	Coelenterazine- <i>v</i>
CBP	Coelenterazine-binding protein
RLuc-m	<i>Renilla muelleri</i> luciferase
BLI	Bioluminescence imaging
MLuc	<i>Metridia</i> luciferase
OLuc	<i>Oplophorus</i> luciferase
CBG	Click beetle green luciferase
GLuc	<i>Gaussia</i> luciferase
VLuc	<i>Vargula</i> luciferase
NLuc	NanoLuc TM
OLuc-19	19-kDa catalytic domain of OLuc
OLuc-35	35-kDa stabilizing domain of OLuc
wtGFP	Wild-type green fluorescent protein
avGFP	Green fluorescent protein from <i>Aequorea victoria</i>
EGFP	Enhanced green fluorescent protein
RFP	Red fluorescent protein
SRET	Sequential resonance energy transfer
BiFC-BRET	Bimolecular fluorescence complementation-bioluminescence resonance energy transfer
CODA-RET	Complemented donor-acceptor resonance energy transfer
BiLC-BiFC	Bimolecular luminescence complementation-bimolecular fluorescence complementation
NST	Nocistatin
N/OFQ	Nociceptin/Orphanin FQ
HIV	Human immunodeficiency virus
PR	Protease
HTS	High-throughput screening
FCV	Feline calicivirus
RG	Arginine-glycine peptide
CRET	Chemiluminescence resonance energy transfer
tdTA	tdTomato-aequorin system
CaM	Calmodulin
cpVenus	Circularly permuted Venus
cpFPs	Circularly permuted fluorescent proteins
FKBP12	FK506-binding protein 12
FRB	FKBP12-Rapamycin-binding domain
mTOR	Mammalian target of rapamycin
GPCR	G protein-coupled receptor
CB ₁ R	Cannabinoid-1 receptor
D ₂ R	Dopamine D ₂ receptor
A _{2A} R	Adenosine A _{2A} receptor
SH2	Src homology 2 domain
OS-BLIA	Open sandwich bioluminescent assay

V _H	Variable heavy chain of antibody
V _L	Variable light chain of antibody
Trx	Thioredoxin
RT-PCR	Reverse-transcriptase polymerase chain reaction
ARM	Arginine-rich motifs
BIV	Bovine immunodeficiency virus
JDV	Jembrana deficiency virus
NIR	Near-infrared
QD/QDs	Quantum dot(s)
MMP-2	Matrix metalloproteinase-2
MMP-7	Matrix metalloproteinase-7
uPA	Urokinase-type plasminogen activator
CLuc	<i>Cypridina</i> luciferase
FBP	Far-red bioluminescent protein
Dlk-1	Delta-like protein-1
C-60	Carbon-60/Fullerene
PMT	Photomultiplier tube
BLM	Bioluminescence microscopy
CCD	Charge-coupled device
EB-CCD	Electron bombarded charged coupled device
EMCCD	Electron multiplying cooled charge-coupled
DR	Double ratio

10.1 Introduction

In this era of rapid expansion in scientific technology, scientists are keen on solving the mysteries of a variety of diseases. With more and more genomic data piling up, there is an urgent need to develop techniques that utilize this data to understand their phenotypic implications. Different biological processes are mediated by a plethora of specific protein-protein interactions (PPIs). Any anomalies in the genome will be manifested in the form of altered proteins and their functions. So, the study of these PPIs in normal and diseased cells becomes pivotal in the understanding of diseases and developing a suitable therapy. Conventional biochemical assays like coimmunoprecipitation [1, 2], gel-filtration chromatography [3], sandwich enzyme-linked immunosorbent assay (ELISA) [4], etc. have long been used in the investigation of PPIs. These assays, though successful, are essentially endpoint, in vitro measurements and thus fail to provide spatiotemporal information on specific PPIs occurring within live cells. Furthermore, they also require mechanical-, chaotropic-, or detergent-based cell lyses, which can alter native PPIs in some cases [5, 6]. Moreover, such techniques are insensitive to transient interactions that may affect cellular processes. To overcome these limitations, various non-invasive approaches using genetic reporter genes

have been developed over the last two decades, which allow the study of PPIs in their native environment [6]. Of the various techniques developed, the yeast two-hybrid (Y2H) system [7], inducible yeast two-hybrid (IY2H) system [8], split reporter complementation assays or protein-fragment complementation assays (PCAs) [9], fluorescence resonance energy transfer (FRET), and bioluminescence resonance energy transfer (BRET) [6, 10] are prominent in the field. The Y2H uses a bait protein linked to a DNA-binding domain and is used to find a prey protein that is connected to a transcription activation domain. With a similar underlying principle, IY2H indicates an *in vivo* interaction under the influence of an external stimulus (e.g., cytokine, growth factor, etc.). The PCAs/split reporter complementation assays are based on the detection of a positive signal gain upon the reconstitution of the two functional halves of a reporter gene, usually an enzyme-like luciferase or β -lactamase, each of which are fused to potential protein partners of interest [6]. In contrast, BRET and FRET are biophysical techniques guided by the Förster Resonance Energy Transfer principle. In this chapter, we will be describing bioluminescence resonance energy transfer (BRET) principle in detail, highlighting various engineering aspects related to its assay design, customized development of various BRET-based sensors and ingenious advances in this technique in the recent past.

10.2 Biophysical Basis of BRET

10.2.1 Bioluminescence Light Emission

Bioluminescence (BL), which is a naturally occurring phenomenon in many living organisms, has been used in the life sciences for several decades. Luminescence relies on an enzyme-based chemical reaction occurring within the specimen, and this enzyme–substrate catalysis results in the emission of a specific wavelength of light. This independent mechanism of light production has evolved in many organisms (especially in deep-sea organisms) to support their defense mechanism, distract predators, or even demonstrate sexual behavior [11].

The luciferases widely used in BRET are *Renilla* luciferase (RLuc) from the sea pansy *Renilla reniformis* and firefly luciferase (FLuc) from the firefly *Photinus pyralis*. Other luciferases that have been introduced as candidates for BRET include *Gaussia*, *Metridia*, and *Vargula* luciferases (discussed later in this chapter). The exact mechanism for bioluminescence reactions differs from species to species. However, they are broadly categorized into two groups as ATP-dependent and ATP-independent reactions. The first group comprising of beetle firefly luciferases (FLuc) requires ATP and Mg^{2+} for the catalytic reaction. During this reaction, FLuc enzyme catalyzes the production of luciferyl adenylate (LH_2 -AMP) from the substrate D-luciferin (LH_2) in the presence of ATP. Then, LH_2 -AMP is oxidized by molecular oxygen to yield excited-state oxyluciferin and CO_2 .

The excited-state oxyluciferin relaxes to its ground state with the emission of yellowish green light (emission maximum or $E_{m_{\max}}$ 562 nm) and AMP [12–15]. This ATP dependency has been widely used as a method to determine the cellular ATP levels in bacteria and blood [16].

On the other hand, luciferases such as RLuc that use imidazopyrazinone-type substrate called coelenterazine (Clz) function in an ATP-independent mechanism that employs a simple oxygenation reaction, wherein O_2 is incorporated into the RLuc substrate to form an excited state intermediate dioxetane derivative that releases CO_2 , followed by the formation of an excited coelenteramide anion that ultimately yields a photonic blue light emission ($E_{m_{\max}}$ 480 nm) [14, 17].

10.2.2 Fluorescence Light Emission

In a fluorescence emission, electrons in the fluorophore get excited upon illumination by an excitation light source in the UV or visible range. In this excited state, the electrons dissipate some of their excess energy through collisions with other molecules. The fluorophore then relaxes back to its ground-state energy level by emitting low-energy photons at a wavelength longer than the excitation photons [18]. Different fluorophores have distinct excitation and emission spectra which can be detected using specific filter sets of appropriate wavelength range.

10.2.3 Förster Resonance Energy Transfer

Resonance energy transfer (RET) is a principle that was first described by the German scientist Theodor Förster in 1948 to describe the quantum-mechanical behavior of the transfer of electronic excitation energy between two molecules. Basically, RET is a phenomenon occurring between two closely spaced chromophores (color-producing compounds) when the emission spectrum of one (the donor) overlaps with the excitation spectrum of the other (the acceptor). Following donor excitation, part of the electronic excitation energy of the donor is dissipated due to random collisions with other molecules, while the remaining electronic relaxation energy is transferred to the acceptor molecule through non-radiative dipole-dipole coupling [19]. It is important to understand here that transfer of resonance energy between the donor and acceptor does not take place in the form of a physical entity like photons. It is simply an electrodynamic interaction or non-radiative energy which occurs between the electric fields of the transient dipoles of the donor and the acceptor [20]. Upon excitation, the acceptor molecule now acts as a normal fluorophore and emits its photonic energy at its characteristic wavelength (Fig. 10.1). This results in a decrease in donor emission paralleled by an increase in acceptor emission [10]. Thus, the secondary emission by the acceptor molecule is the outcome of the energy transfer only and not from any external light source.

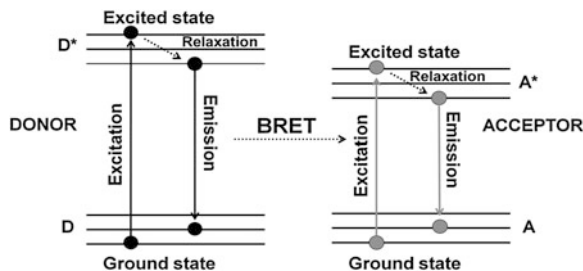


Fig. 10.1 Jablonski diagram to illustrate the electronic changes occurring in the donor and acceptor molecules during a BRET process. The donor (D) molecule is normally in its ground state energy level. Upon substrate oxidation, it is elevated to a higher energy state (D^*). Then, the excited donor loses some of its energy as vibrational relaxation energy. A part of the remaining energy is either emitted out as donor luminescence or is transferred to the nearby acceptor in a non-radiative manner. The acceptor fluorophore now gets excited (A^*) and then relaxes back to its ground state by releasing photons at its characteristic wavelength, completing a BRET process

10.2.4 Factors Controlling Energy Transfer in RET

Several variables affect the efficiency of energy transfer between the two chromophore groups. First, the distance between the donor and acceptor molecule which is inversely proportional to the extent of energy transfer; the energy transfer gradually decreases when the distance between the donor and acceptor increases. The optimal distance for Förster resonance energy transfer is 1–10 nm. This is because the efficiency of energy transfer (E_{RET}) is inversely proportional to the sixth power of the distance (R) between donor and acceptor molecules, Eq. 10.1.

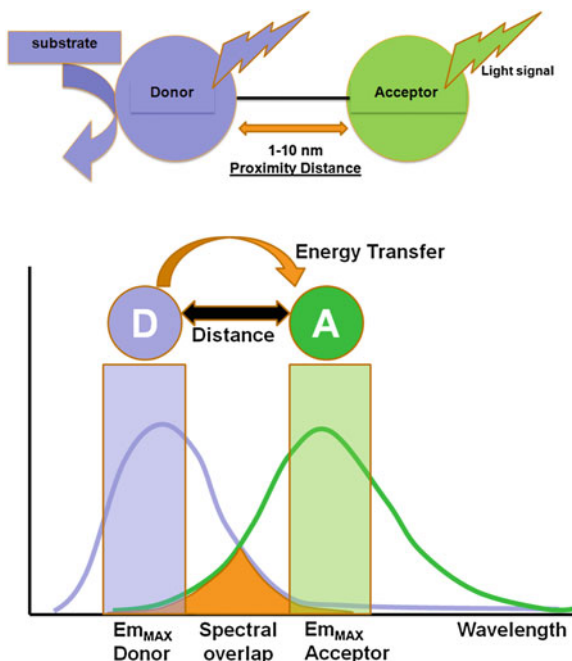
$$E_{RET} = \frac{1}{1 + \frac{R^6}{R_0^6}} \quad (10.1)$$

where R_0 is the distance for 50 % energy transfer from the donor to the acceptor, which is about 5 nm [10, 21, 22]. Now, the Förster distance of a pair depends on the overlap integral of the donor emission spectrum with the acceptor absorption spectrum and their mutual molecular orientation and is calculated based on the Eq. 10.2.

$$R_0 = 2.11 \times 10^{-2} \times [\kappa^2 \times J(\lambda) \times \eta^{-4} \times Q_D]^{1/6} \quad (10.2)$$

where κ^2 is the dipole orientation factor, η is the refractive index of the medium, $J(\lambda)$ is the spectral overlap integral, and Q_D denotes the donor quantum yield in the absence of acceptor. Because of the sixth-root dependence in the calculation of R_0 , small changes in the value of Q_D should not have a large effect on the overall BRET efficiency [23, 24]. Second, the orientation angle between donor and acceptor molecules affects RET efficiency since energy transfer will take place only if the transient dipoles of the interacting molecules are aligned in a position suitable for this transfer. Third, the degree of spectral overlap between donor emission and acceptor absorbance is also a significant factor. Higher the spectral overlap, the better the energy transfer [22]. Fourth, the quantum yield of the donor

Fig. 10.2 Schematic illustration of the basic elements involved in a typical BRET system. In the presence of its specific substrate, the donor luciferase gets excited and emits light at its characteristic wavelength. Within the proximity distance of 1–10 nm, resonance energy transfer occurs to a suitable fluorescence acceptor, leading to the photon emission at its characteristic wavelength. Light signal obtained from both donor and acceptor emission can be measured using suitable band-pass filters, and BRET ratio can be judged as a measure of the distance between the donor and acceptor pair



should be high, since the energy cannot be transferred if it is lost too quickly through non-radiative decay [6].

In the RET-based PPI assay, i.e., BRET or FRET, the two chromophores are genetically tagged to two proteins whose interaction is to be investigated. The strict dependence of RET on the inter-chromophoric distance (1–10 nm) makes it an appropriate “molecular yardstick” for determining PPIs. This is true, since the average protein radius is ~ 5 nm, which means that a positive RET signal will only take place if the two proteins come within ~ 10 nm of each other, a distance that is an indicator of direct interaction between the two proteins [21].

10.2.5 Bioluminescence Resonance Energy Transfer

BRET exploits non-radiative (dipole–dipole) energy transfer occurring between a luminescent luciferase donor (instead of a fluorescent donor as in FRET) and a compatible fluorescent protein (FP) acceptor in order to study PPIs between two proteins fused to these donor and acceptor moieties (Fig. 10.2). The detection of a positive BRET signal means that the two proteins are situated within the BRET-permissive distance of 10 nm, thereby positively affirming their interaction [25, 26]. However, absence of a BRET signal does not necessarily mean that the two target proteins do not interact with each other. Lack of a signal can be accounted for by an unfavorable orientation between the donor and acceptor dipoles [27]. To nullify this

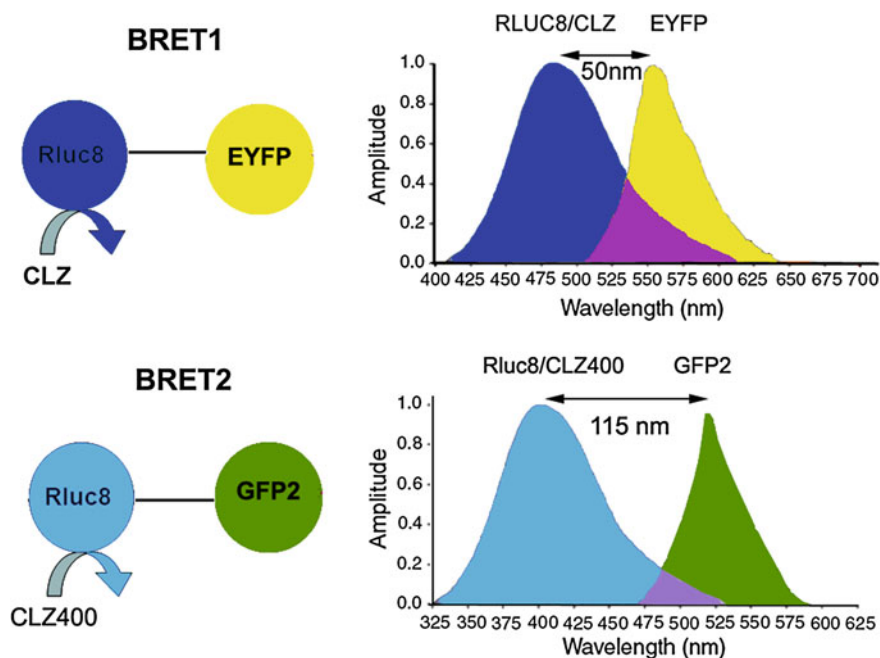


Fig. 10.3 Schematic representations of BRET¹ and BRET² assays showing all the essential components in each. While both BRET¹ and BRET² use RLuc donor, they use different coelenterazine analogs such as Clz and Clz400 as indicated. Note the change in donor emission maximum in case of BRET². In general, an 18-amino-acid linker is placed between the donor and acceptor proteins. Spectral resolution of each system is marked as a bidirectional arrow and spectral overlap region is marked with purple-color zone at the intersection of the donor and acceptor emission. Note, the donor and acceptor emission spans and intensities are thematic (not normalized)

issue, both N- and C-terminus fusions using flexible peptide linkers (6–18 amino acids) must be tested. Such design can reduce steric hindrance and improve the orientation. Normally, the linker sequence comprises of GGGGS or (GGGGS) × 2 residues where glycine–serine combinations confer flexibility, allowing the fusion proteins to fold to their optimal conformation [28, 29] and achieve the proximity distance between donor and acceptor.

BRET is an intrinsic phenomena occurring in the organisms *Renilla reniformis* and *Aequorea victoria*. In *Aequorea victoria*, a Ca²⁺-dependent photoprotein called aequorin releases flashes of blue light, which is transduced by a green fluorescent protein (GFP) to emit green light. Exploiting the underlying principle of BRET from *Aequorea victoria*, Xu et al. developed a BRET system in 1999 to study the interactions of circadian clock proteins in bacteria [25]. This BRET system termed as BRET¹ uses *Renilla* luciferase (RLuc) as the donor moiety and enhanced yellow fluorescent protein (EYFP) as the acceptor ($E_{m_{max}} \sim 530$ nm) moiety. The spectral resolution (separation of peak donor and acceptor emission spectra) achieved in BRET¹ is ~ 50 nm only (Fig. 10.3) [23, 30].

Another BRET system, designated as BRET² was developed that combined RLuc with a UV-excitable GFP variant called GFP² [31, 32]. In this case, the substrate for RLuc was a coelenterazine analog DeepBlueCTM (also known as coelenterazine 400a/Clz400, bisdeoxycoelenterazine), which is similar to the native substrate in being cell permeable and non-toxic but shifts the Em_{max} to 400 nm. GFP² excites at a maximum (Ex_{max}) of 396 nm and emits photons at 510 nm. This yields a much larger spectral resolution of 110 nm (Fig. 10.3), which allows the use of wideband filters and minimizes bleed-through signal (residual emission of RLuc detected by the acceptor filter or vice versa). On the other hand, possible disadvantages associated with the use of the Clz400 substrate are poor substrate utilization, reduced quantum yield (~ 100 fold lower than Clz), and rapid decay in serum [23, 27]. Seeing the above two examples, it becomes clear that the balance between quantum yield and spectral resolution is of critical importance while choosing an appropriate BRET pair for in vivo applications. One should bear in mind that the same factors that affect the efficiency of RET are also applicable in BRET. To design the required BRET fusion proteins, the cDNA of the target proteins is inserted in frame into a suitable expression vector (by placing an appropriate linker as mentioned before) that has either the donor or acceptor gene. The stop codon of the amino terminus protein of the fusion partner should be removed by mutagenesis, and it should only be present in frame at the end of the carboxyl terminal protein so that the fusion protein can be expressed. One can design both C- and N- terminal protein fusions to assess their efficacy. Once the required fusion proteins are verified by expressing in mammalian cells, the BRET signal can be measured using suitable filter sets as explained later in this chapter. The BRET ratio [33] can be calculated as per Eqs. 10.3 and 10.4.

$$\text{BRET} = \frac{\text{BL}_{\text{emission}}(\text{Acceptor}) - C_f \times \text{BL}_{\text{emission}}(\text{Donor})}{\text{BL}_{\text{emission}}(\text{Donor})} \quad (10.3)$$

where

$$C_f = \frac{\text{BL}_{\text{emission}}(\text{Acceptor})_{\text{donor-only}}}{\text{BL}_{\text{emission}}(\text{Donor})_{\text{donor-only}}} \quad (10.4)$$

In Eq. 10.4, the correction factor (C_f) represents the BRET signal detected from cells transfected only with the donor protein. Subtracting this factor from the overall BRET ratio can give us an idea of the dynamic range for a particular BRET pair. Moreover, since BRET-based assays can be performed on live cells, under normal culture conditions and the indicative result being ratiometric, any variability due to assay volume or cell number variation is nullified.

10.3 Engineering the BRET Components

So far, we have just begun to understand the basic principles underlying the BRET technique. In order to explore the engineering aspects of BRET, we need to delve deeper into four main facets viz., the donor components i.e., the luciferase protein and its substrate, the acceptor fluorescent protein as well as detection devices (discussed in Sect. 10.5).

10.3.1 Bioluminescence Donor

As indicated before, to date, the luciferase enzyme from *Renilla* sp. has been predominantly used as the donor protein for the BRET systems in use, but in the recent years, several other luciferases from various other sources have also been engineered and used as BRET donors. We will now discuss various aspects of protein engineering that have been applied to each of them. Simultaneously, where applies, their respective engineered substrate is also discussed.

10.3.1.1 *Renilla* Luciferase and Coelenterazine

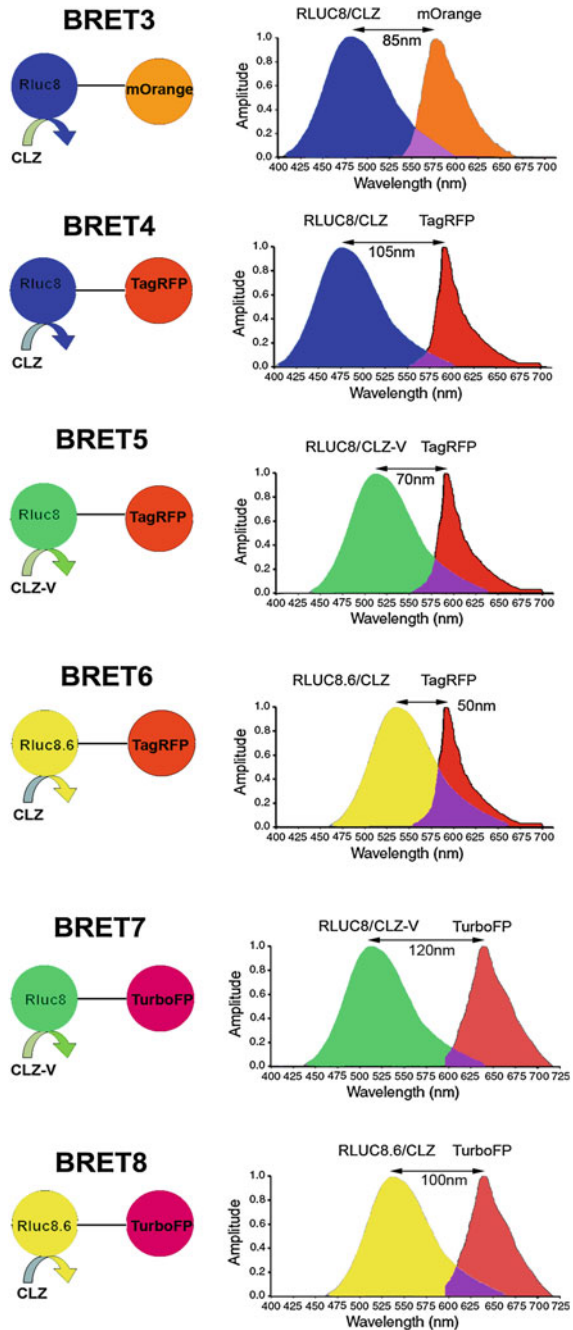
The main strength of a BRET signal is primarily dependent upon the efficiency of the luciferase enzyme to yield a high photon output upon the oxidation of its substrate. The 35-kDa RLuc protein typically emits light in the blue-green region ($E_{m_{max}}$ 480 nm). To further increase the donor quantum output, Angers et al. used coelenterazine-h (Clz-h) as a substrate for RLuc, which has the same $E_{m_{max}}$ as native Clz, but has a higher luminescence capacity than the latter [34]. For usage of this luciferase enzyme in mammalian systems, predominantly human cell lines, several commercial sources have developed a codon-optimized version hRLuc (BioSignal Packard) or hRL (Promega) that display improved bioluminescence than the native protein. However, a major limitation of hRLuc is its poor stability in serum (half-life of ~ 0.5 – 1 h in murine serum) which impedes bioluminescence or BRET imaging in animals for a sustained time period. To correct this problem, Loening et al. adopted a consensus-guided mutagenesis approach (for details, refer to Chap. 8) to identify beneficial mutations in hRLuc that render increased stability to the enzyme [35]. In the process of doing so, they also pinpointed mutations that showed increased quantum output. Upon introducing various point mutations, RLuc2 (C124A, M185V) and an eight mutation form of RLuc i.e., RLuc8 (A55T, C124A, S130A, K136R, A143M, M185V, M253L, and S287L) were developed that displayed greatly improved characteristics suitable for developing new BRET partners. Compared with the native enzyme, RLuc8 exhibited an intracellular half-life >50 h, a fourfold increment in quantum output, and a 5-nm wavelength shift in the emission spectrum [35]. The successful utilization of these mutations in

improving BRET² assay sensitivity with expanded dynamic range was demonstrated by us [24]. Later, by combining RLuc8 with the monomeric red FP variant mOrange ($E_{m_{max}}$ 564 nm), the BRET3 system was also developed (Fig. 10.4). On addition of Clz substrate, BRET3 provides a spectral resolution of ~ 85 nm [30]. Further, RLuc8 has shown to transfer adequate energy over a spectral distance of 100 nm when we combine RLuc8 donor with TagRFP ($E_{m_{max}}$ 584 nm) [36].

Another obstacle to the use of RLuc and its variants in BRET imaging was the blue-green light emission that greatly attenuated the signal in animal tissues, as pigments like myoglobin and hemoglobin strongly absorb photons from the blue-green region. Thus, use of RLuc for BRET detection from deeper tissues was severely limited [30, 37]. In the field of in vivo imaging, it is well known that light emitted above 600 nm can be better detected from deeper tissues of small animals. To achieve red-shifted light emission from RLuc, efforts have been made in two possible ways, i.e., genetic engineering of luciferase protein itself and chemical engineering of Clz substrate. Applying the genetic engineering approach to produce more red-shifted RLuc, Loening et al. [38] identified several mutants of which RLuc8.6 with an $E_{m_{max}}$ 535 nm (A123S, D154M, E155G, D162E, I163L, V185L point mutations in RLuc8) showed significant promise in live cells as well as animals. In 2010, Loening et al. [39] created another variant i.e., RLuc7 ($E_{m_{max}}$ 521 nm) with a rapid turnover and a half-life (~ 6.8 h) similar to the native RLuc in order to detect transient changes in gene expression. RLuc7 exhibited a twofold increase in the signal output compared to RLuc. Depending on the experimental requirements, one can decrease the stability of the luciferase enzyme without any mutagenesis by simply appending a signaling sequence at the 5' or 3' termini of the protein to direct the protein to early degradation. One such sequence is the PEST (Pro-Glu-Ser-Thr) sequence that has been frequently used to produce destabilized luciferases [40, 41].

Another remarkable finding is that the utilization of coelenterazine analog Clz-*v* with any of the RLuc variants has an additive effect as it further shifts the $E_{m_{max}}$ to the right by 35 nm. As shown, by using Clz-*v* in combination with RLuc8.6 protein, one can obtain an $E_{m_{max}}$ at 570 nm [36]. However, this substrate is not commercially available because of its problematic purification process possibly owing to sensitivity under chromatographic conditions, and it exhibits an order of magnitude increase in background auto-chemiluminescence [39]. Stepanyuk et al. ligated Clz-*v* to the coelenterazine binding protein (CBP) from the organism *Renilla muelleri* which acts as a 'protector' for Clz-*v* that results in a marked improvement in the stability of this conjugated Clz-*v* at 37 °C in addition to a higher bioluminescence signal output (twofold) in comparison with the native Clz-*v* when used with a *R. muelleri* luciferase (RLuc-m) mutant [42]. Taking advantage of these mutated RLuc donor and Clz analogs, several new combinations of BRET using red and far-red FPs have also been made as summarized in Fig. 10.4, expanding the scope of multiplexed BRET imaging. Of these new assays developed, BRET8 displaying a spectral resolution of 100 nm was used to image live cells and animals in the far-red region of the visible spectra [36]. Point to be mentioned, in Fig. 10.4, we have renamed some of the recently developed

Fig. 10.4 Schematic representation of the expanded BRET fusion constructs developed using *Renilla* luciferase donor. The bioluminescence spectra illustrate the emission spectra of the RLuc mutants used as donor and the emission of the red fluorescent acceptor proteins. For all constructs, an 18-amino-acid linker is used between the donor and acceptor proteins. Luciferase substrates used in each case are indicated as either CLZ or CLZ-v. Spectral resolution of each system is marked as a bidirectional arrow. Spectral overlap region is also marked with a purple-color zone at the intersection of the emission spectrum. Note, the donor and acceptor emission spans and intensities are thematic (not normalized). Figure adapted with modifications as permitted by PNAS [36]



BRET vectors, such as BRET4.1, BRET5, and BRET6 as BRET5, BRET6, and BRET8, respectively, while eliminating some others reported such as BRET3.1 or BRET6.1 as their low spectral resolution may impede spectral separation for BRET imaging application.

Efforts continued further on synthesis of new coelenterazine analogs with better bathochromic emission shifts. Recently, Giuliani et al. [43] developed a new series of red-shifted coelenterazine analogs and a novel approach to alter the photochemical properties of the light-emitter intermediates. By insertion of a C-8-bonded S atom, the substrate molecules favor the emergence of lower energy emitters in coelenteramide. This bathochromic effect was evident in the presence of either the phenyl or the phenol ring in C-6, indicating that the red-shift can occur regardless of whether the main emitter is the neutral or the amide–anion form of the molecule.

One problem associated with coelenterazine and its derivatives was its quick decay upon auto-oxidation in the presence of aqueous media of cultured cells. For instance, Clz reduces in concentration by 50 % within 17 min of its addition to cell media. This decay not only reduces the availability of Clz molecules in the media, but also increases the background signal, thereby decreasing the assay sensitivity. Moreover, this limits its use in BRET assays to cell lysates only and fails to empower BRET applications to catch the live cell dynamics. This is equally true for other Clz analogs including Clz400. To solve this problem, Levi et al. [44] reported a clever approach to protect the putative oxygenation sites of Clz400 substrate and demonstrated that depending on the protection modifications, long-term BRET² monitoring is achievable. Similarly, another commercial source has developed two substrates EnduRenTM and ViviRenTM that can be used specifically for live cell imaging [45]. These are protected forms of coelenterazine that have esters or oxymethyl ethers added at the site of substrate oxidation. The intracellular esterases and lipases yield the active Clz-*h* upon hydrolytic cleavage of the protected forms. The absence of active Clz-*h* in the media significantly reduces the background signal due to auto-oxidation, and the half-life of Clz-*h* increases. EnduRenTM and ViviRenTM substrates have been designed to display different kinetics. EnduRenTM shows a slow but gradual increase in bioluminescence. It reaches its maximum photon output at 90 min and then emits a constant signal for over 24 h (Fig. 10.5). In contrast, ViviRenTM can generate a threefold brighter signal which is instantaneous but short-lived. Pflieger et al. [46] demonstrated the use of EnduRenTM in monitoring the agonist-induced interaction of GPCRs in real time over a period of several hours. This was the first successful step in the direction of real-time BRET assays, as previously, the short half-life of Clz-*h* hampered the monitoring of PPIs in live cells. This modified BRET system was designated as extended BRET (eBRET), which is a superior approach for dynamic monitoring of PPI kinetics in their native cellular environment.

10.3.1.2 Firefly Luciferase and D-Luciferin

Another commonly used luciferase is the North American firefly luciferase (FLuc) from *Photinus pyralis*. It is a 61-kDa protein that emits orange light at an $E_{m_{max}}$

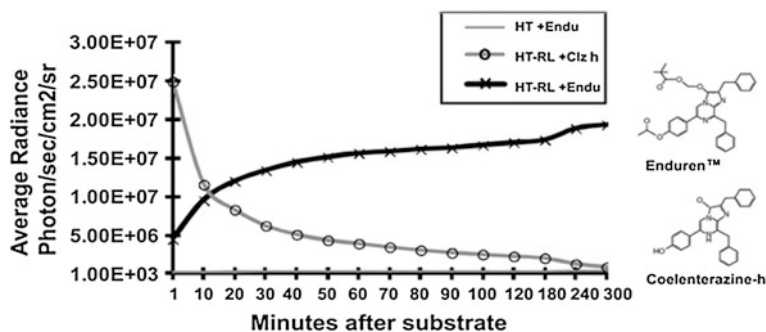


Fig. 10.5 Chart represents time kinetics of the light output after addition of normal coelenterazine-*h* substrate or protected coelenterazine-*h* substrate i.e., EnduRenTM [45]. Plain HT1080 mammalian cells (HT) or HT1080 cells overexpressing RLuc8 protein (HT-RL) were used for measuring the photon output as marked. Note the difference of time kinetics, where Clz-*h* substrate activity diminishes quickly within an hour; EnduRenTM substrate activity shows gradual increase till 90 min and remains maintained till the end point of measurement. Also note the y-axis scale bar representing a log scale. Note changes in the chemical structures that convert the Clz-*h* substrate into EnduRenTM

562 nm [47, 48]. The emission of orange bioluminescence is a positive feature for bioluminescence imaging (BLI); however, its use in BRET is limited thus far, owing to its bulky size and low photon output. Moreover, the obligate dependence of FLuc on Mg²⁺ and ATP as its cofactors also diminishes its worth as a BRET donor. Nonetheless, FLuc has been employed in several BRET applications in combination with red- and far-red-shifted FPs such as DsRed [49] and mKate variant [50], respectively, as well as non-protein fluorophores [51]. For example, Arai et al. reported the use of the coral red fluorescent protein (DsRed) ($E_{x,max}$ 558 nm; $E_{m,max}$ 583 nm) as acceptor in combination with FLuc [49]. However, the use of DsRed is not preferred owing to its propensity to tetramerize, and the FLuc-DsRed system will have a spectral resolution of <20 nm which is highly unfavorable due to substantial overlap between FLuc and DsRed emission peak, thus necessitating the use of signal correction factor. Recently, BRET comprising a thermostable mutant form of firefly luciferase from *Photinus pyralis* (Ppy WT-TS; $E_{m,max}$ 565 nm) along with a variant of mKate (S158A) ($E_{m,max}$ 610 nm) was developed by Branchini et al. [52]. In the literature, Cy3 and Cy3.5 fluorophores have been attempted to be combined with FLuc as BRET partners [51]. However, the main drawback of using a non-protein fluorophore is that it has to be chemically linked with the donor and must be efficiently delivered within the cell for signal detection. Taking all these factors into account, the use of FLuc in BRET systems still needs to be optimized. Similar to RLuc, the codon-optimized version of FLuc (hFLuc) for use in mammalian cells has been created by commercial sources. Caysa et al. [37] have developed a red-shifted mutant of hFLuc ($E_{m,max}$ 615 nm) by introducing a single point mutation S284T. Even though the light output of the mutant FLuc drops to 25 % of the native FLuc, the signal output detected from whole animals is considerably higher (threefold) than its native

counterpart, possibly due to the reduced tissue attenuation attributed to the red-shift in emission to above 600 nm. Branchini et al. [53] have also developed several FLuc mutants Ppy GR-TS and Ppy RE-TS that possess an Em_{max} of 546 and 610 nm, respectively, and Ppy RE8 and Ppy RE9 that show an Em_{max} of 617 nm, with Ppy RE9 being the superior luciferase. However, to the best of our knowledge, these mutant forms have so far not been recruited in any BRET system. In the D-luciferin molecule, N- and S-heteroatoms exist in a particular electron-rich configuration, which may play a fundamental role in the formation of multiple oxyluciferin excited states, resulting in a relatively broad emission spectrum [54]. Furthermore, the relatively slower and stable emission kinetics makes it naturally suitable for kinetic measurements from live environment without chemical modifications to its structure.

10.3.1.3 Other Luciferases

A range of other luciferases are now available from organisms like *Metridia longa*, *Metridia pacifica*, *Cypridina noctiluca*, *Oplophorus gracilirostris*, click beetle, railroad tapeworm (*Phrixothrix hirtus*), *Vargula hilgendorffii*, *Gaussia princeps*, etc., most of which are marine organisms. Some of them are popularly used as reporter genes for BLI, but have limited applicability in BRET due to their undesirable characteristics. For instance, *Metridia* luciferases (MLuc) are secretory in nature [55, 56], while *Oplophorus* luciferase (OLuc) is a 106-kDa secretory protein composed of a dimeric repeat [57] which is too bulky for use in BRET. Some luciferases show promising features and have successfully been exploited in the development of functional BRET systems. These comprise of click beetle green luciferase (CBG) [58], *Gaussia* luciferase (GLuc) [59], and *Vargula* luciferase (VLuc) [60].

Gammon et al. [58] reported a new combination of click beetle green (CBG) luciferase as donor and tdTomato as acceptor. *Gaussia* luciferase (GLuc) is a 19.9-kDa secretory protein with an Em_{max} 480 nm that extends till 600 nm. A codon-optimized version of GLuc (hGLuc) offers several advantages over other luciferases. In addition to its small size, hGLuc is highly heat stable, strongly resistant to acidic and basic conditions, and generates a ~ 100 -fold higher intracellular signal compared to FLuc and hRLuc. Furthermore, unlike hRLuc or FLuc, it can be used either as a secretory or as an intracellular reporter depending on the experimental needs [61]. These features can contribute to the robustness of GLuc-based BRET systems. Li et al. reported the development of GLuc-EGFP BRET assay for protease activity sensing in vitro [59]. Like GLuc, *Vargula* luciferase (VLuc) is a secretory protein, but of higher size (62 kDa) [62] with an Em_{max} 460 nm. The VLuc-EGFP combination has been reported by Otsuji et al. [60]. Irrespective of its bulky size, this system offers similar benefits in terms of applicability as in GLuc.

NanoLucTM (NLuc) is a mutant form obtained from the deep-sea shrimp *Oplophorus* luciferase (OLuc). OLuc is a heteromeric structure composed of two

19-kDa catalytic subunits (OLuc-19) and two 35-kDa subunits (OLuc-35) that provide stability to the 19-kDa subunits. When Inouye et al. attempted to use the isolated OLuc-19 as a luciferase, they found that it was highly unstable and poorly expressed in the absence of its 35-kDa counterpart [57]. Hall et al. envisaged the creation of a variant of this OLuc-19 that ultimately led to the generation of NLuc. To achieve this, OLuc-19 was subjected to site-directed and random mutagenesis in order to obtain a stable variant. Further, through a single round of random mutagenesis, they generated a variant C1A4E with eight mutations (A4E, Q11R, A33K, V44I, A54F, P115E, Q124K, and Y138I). In the next phase, several coelenterazine derivatives were screened in order to create a superior substrate for optimal bioluminescence. Twenty-four coelenterazine analogs were developed and then screened against a library of C1A4E variants. Of these, the C1A4E variant (Q18L, F54I, F68Y, L72Q, M75K, and I90V) showed a ~ 10 -fold higher stability over C1A4E at 37 °C with the coelenterazine derivative 2-furanylmethyl-deoxy-coelenterazine (Furimazine). In the final phase of optimization, they used furimazine to screen for other beneficial mutations in OLuc-19 variants. These mutations (L27V, K33N, K43R, and Y68D) were then combined with the previous mutations to produce NanoLucTM. In total, 16 amino acid substitutions of the wild-type OLuc-19 resulted in NLuc, having $E_{m_{max}}$ 460 nm and an intracellular half-life of >15 h at 37 °C. Using furimazine as its substrate exhibits a >150 -fold higher light output than both RLuc and FLuc, which makes it a very attractive candidate for BRET multiplexing. Despite the emission maxima of NLuc in the blue-green region, its sufficiently high quantum output with furimazine can be used to couple it with any of the available BRET acceptors currently used with RLuc8.

10.3.2 Fluorescence Acceptor

The other component of a BRET system is a fluorescent protein that can be compatibly partnered with the luciferase in use. A good FP entails several characteristics. First, it should express efficiently in a system without invoking any cellular toxicity. Second, it should produce a high signal-to-noise ratio. Third, the FP should have sufficient photostability so as to be imaged for the duration of the experiment. Fourth, if the FP is to be fused to another protein of interest, then it should not have a tendency to oligomerize. Finally, it should be resistant to environmental conditions like pH and temperature [63].

Having realized the versatility of FPs in a variety of biological applications such as imaging and FRET, wild-type GFP from the organism *Aequorea victoria* (also known as wtGFP or avGFP) isolated by Shimomura et al. was cloned by Prasher et al. in 1992 [64]. Thus began the era of “GFP-technology”. The chromophore of wtGFP consists of Ser/Thr65-Tyr66-Gly67, which is protected by a shell consisting of 11 strands of β -barrels and one α -helix. The N- and C-termini of GFP are flexible, whereas the β -barrel shell is well structured and rigid, which protects the chromophore group from the external environment [65]. However, it

does not fold efficiently at 37 °C since the optimal temperature for its maturation is 28 °C [66], and it forms weak dimers that may result in the formation of artifacts [65]. Thus, several GFP variants have been created, of which EGFP (Enhanced GFP from Clontech), AcGFP (Clontech), TurboGFP (Evrogen), and Emerald (Invitrogen) have overcome some of the limitations of GFP.

Yellow fluorescent proteins (YFPs) provide an edge over GFPs as their emission maxima lies in the 500–550 nm range. The original enhanced yellow fluorescent protein (EYFP) was derived from wtGFP and is now obsolete owing to its high sensitivity to chloride ions and slower maturation at 37 °C. Overcoming this problem, several successors of EYFP are now available such as citrine and its monomeric version mCitrine [67], Venus [68], and YPet [69]. Of these, YPet displays the brightest signal and so provides an advantage over its competitors [69].

As discussed above, a major shortcoming of using GFPs or YFPs used in early generation of BRET assays is their photon attenuation in mammalian tissues. To fulfill this demand of FPs emitting at red and far-red range, screening of various animal resources was initiated. A major breakthrough was the isolation of DsRed—a red fluorescent protein (RFP) from coral *Discosoma striata*. The excitation and emission maxima of DsRed are at 558 and 583 nm, respectively [70]. Moreover, it exhibits several positive features such as elevated extinction coefficient, high quantum yield, resistance to pH variations, and resistance to photobleaching. DsRed, however, tends to form tetramers [71], which often results in the poor localization as well as artificial oligomerization that may consequently impair the functions of proteins to which it is tagged. Furthermore, this chromophore matures very slowly, often taking days for the protein to convert from the premature greenish to the mature red emission. Monomeric RFP1 (mRFP1) [72] obtained after multiple rounds of mutagenesis (33 mutations in the parental DsRed) was the first true monomeric RFP with distinct improvements over previous versions of DsRed, namely DsRed2, T1 [73] and dimer2 [72], such as faster maturation and a 25-nm wavelength shift in excitation and emission. However, mRFP1 failed to acquire images with high spatial and temporal resolution due to its much lower quantum yield and extinction coefficient and a poor photostability [72]. Overcoming these limitations, Shaner et al. [74] and Wang et al. [75] reported a wide range of monomeric ‘fruit’ FPs named after fruits, representing the color similar to their emission such as mHoneydew, mBanana, mOrange, mTangerine, mStrawberry, mCherry [74], mRaspberry, and mPlum [75], as well as a tandem dimeric FP tdTomato, all with relatively long excitation and emission wavelengths (Table 10.1).

Another group, Merzlyak et al. [76], developed RFP variants from a red eqFP578 protein isolated from the sea anemone *Entacmea quadricolor*. Dimeric eqFP578 again underwent several rounds of random mutagenesis that consequently produced an enhanced dimeric FP called TurboRFP with Em_{max} 574 nm. TurboRFP displayed superior qualities over DsRed2 such as greater pH stability, faster maturation at 37 °C, and higher extinction coefficient and quantum yield. Despite being a dimer, TurboRFP does not form aggregates in cell. It was further subjected to site-directed mutagenesis (R162E, Q166D, S180N, F198V, and F200Y) that contribute to the dimeric nature of TurboRFP as well as random

Table 10.1 The key properties of various classes of fluorescent proteins

Class	Fluorescent protein	Ex _{max} (nm)	Em _{max} (nm)	Oligomerization	Reference
Green	GFP	395/475	508/503	w.d.	[80]
	EGFP	488	507	w.d.	[80]
	Emerald	487	509	w.d.	[80]
Yellow	EYFP	514	527	w.d.	[63]
	Venus	515	528	w.d.	[68]
	mCitrine	516	529	m.m.	[67]
Orange	YPet	517	530	w.d.	[69]
	mBanana	540	553	m.m.	[74]
	mKO	548	559	m.m.	[81]
Red and Far-red	mOrange	548	562	m.m.	[74]
	TurboRFP	553	574	d.m.	[76]
	tdTomato	554	581	t.d.	[74]
	DsRed	558	583	t.m.	[70]
	TagRFP	555	584	m.m.	[76]
	mTangerine	568	585	m.m.	[74]
	mStrawberry	574	596	m.m.	[74]
	mCherry	587	610	m.m.	[74]
	mRaspberry	598	625	m.m.	[75]
	mKate2	588	633	m.m.	[78]
	mKate	588	635	m.m.	[77]
	TurboFP635/ Katushka	588	635	d.m.	[77]
	mPlum	590	649	m.m.	[75]
TagRFP657	611	657	m.m.	[79]	

w.d. weak dimer, *d.m.* dimer, *m.m.* monomer, *t.d.* tandem dimer, *t.m.* tetramer

mutagenesis to stabilize the monomeric form. The final product obtained was TagRFP which is a monomer and has a 10-nm shift in its Em_{max}. In addition, it is almost 2–3 folds brighter than mCherry, with a good maturation rate and a very high pH stability (pK_a = 4), making it suitable for use in acidic organelles as well. Furthermore, Shcherbo et al. [77] succeeded in generating a dimeric RFP called Katushka or TurboFP635, with excitation and emission peaks at 588 nm and 635 nm, respectively. It is characterized by fast maturation rate, high pH stability (pK_a = 5.5), low toxicity in mammalian cells, and superior brightness in comparison with its counterparts in the 650–800 nm optical window. However, since Katushka was dimeric in nature, Shcherbo et al. also targeted to develop monomeric Katushka, called mKate. They used monomeric TagRFP as the starting template and modified the residues surrounding its chromophores group to resemble that of Katushka. Thus, mKate has similar spectral characteristics as Katushka, albeit with slightly lowered quantum yield and pH stability. Shcherbo et al. [78] further optimized mKate and developed mKate2. Adding the mutation S165A to mKate, which converted its crystal structure from the *trans* to the *cis* form, resulted in an mKate variant with higher brightness and lower pH dependence. They also added two beneficial mutations V48A and K238R, developing

the final product mKate2 with enhanced brightness and improved pH stability, photostability, and maturation rate. It is threefold brighter than mKate and 10-fold brighter than mPlum. Morozova et al. [79] have also recently succeeded in developing an even further red-shifted variant of mKate called TagRFP657 with $E_{x_{max}}$ and $E_{m_{max}}$ at 611 and 657 nm, respectively.

10.4 Engineering BRET Sensors for Functional Measurement

Unlike many other assays such as PCA, BRET system provides unique opportunity to readily adapt the newly evolved donor and acceptor proteins with preferred characteristics. This feature of BRET led to the rapid expansion and growth in identifying new BRET formats which eventually widened the BRET applicability. In this section, we will focus on engineering efforts that have expanded the scope of BRET applications. To do this, we can categorize reports under two major subheadings i.e., genetic BRET systems and synthetic BRET systems and discuss various applications that they have been tested for.

10.4.1 Genetic BRET Systems

As stated above, several genetically encoded BRET systems comprising of different combinations of luminescent and FP variants have been developed over the last decade. Due to attenuation of photons below 600 nm wavelengths in biological tissues, the BRET¹ and BRET² systems are suboptimal for small animal imaging use. To overcome their short falls, many variants of BRET systems utilizing *Renilla* luciferase mutants (RLuc8 or RLuc8.6) with mOrange ($E_{m_{max}}$ 564 nm), TagRFP ($E_{m_{max}}$ 584 nm), or TurboFP635 ($E_{m_{max}}$ 635 nm) FPs were rapidly developed by us as described in the previous section (Table 10.2). All these efforts were made with the goal of finding an optimal BRET assay that is most suitable for animal imaging applications. Together, these systems also give an edge in performing multiplexed BRET assays in live environment. Many of these systems can now serve as a unified format for in vitro measurements as well as physiologically relevant BRET experiments using live cells and mice models.

To date, the advancement in the field of multiplexed approach for detecting higher-order complexes has been facilitated by creative approaches like sequential RET (SRET) [82, 83], bimolecular fluorescence complementation-BRET (BiFC-BRET) [84, 85], complemented donor-acceptor resonance energy transfer (CODA-RET) [86], and bimolecular luminescence complementation-bimolecular fluorescence complementation (BiLC-BiFC) [26, 87]. We will briefly describe the SRET development here, while others are discussed later in the chapter. In the SRET technique, three potentially interacting complex-forming proteins are each

Table 10.2 Comprehensive chart featuring key characteristics of the BRET assays developed using *Renilla* luciferase

Assay	Donor	Acceptor	Substrate	Important features ^a
BRET ¹	RLuc 480 nm (Improved version using RLuc2/RLuc8)	YFP/EYFP 535 nm	Clz/EnduRen TM	1 Efficient BRET • Spectral resolution 55 nm • Small dynamic range
BRET ²	RLuc 400 nm (Improved version using RLuc2/RLuc8)	GFP ² 515 nm	Clz400/protected Clz400	2 Efficient BRET • Spectral resolution 115 nm • Very large dynamic range
BRET ³	RLuc8 480 nm	mOrange 564 nm	Clz/EnduRen TM	3 Efficient BRET • Spectral resolution 85 nm • Large dynamic range
BRET ⁴	RLuc8 480 nm	TagRFP 584 nm	Clz/EnduRen TM	4 Very efficient BRET • Spectral resolution 104 nm • Large dynamic range
BRET ⁵	RLuc8 515 nm	TagRFP 584 nm	Clz- ν	5 Less efficient BRET • Spectral resolution 70 nm • Moderate dynamic range
BRET ⁶	RLuc8.6 535 nm	TagRFP 584 nm	Clz/EnduRen TM	6 Very efficient BRET • Spectral resolution 50 nm • Large dynamic range
BRET ⁷	RLuc8 480 nm	TurboFP 635 nm	Clz- ν	• Less efficient BRET • Spectral resolution 155 nm • Small dynamic range
BRET ⁸	RLuc8.6 535 nm	TurboFP 635 nm	Clz/EnduRen TM	7 Efficient BRET • Spectral resolution 100 nm • Moderate dynamic range

^a BRET efficiencies are categorized as less efficient, efficient, or very efficient. Dynamic ranges are categorized as small, moderate, large, or very large. Table adapted with modifications as permitted by Bentham Science [23]

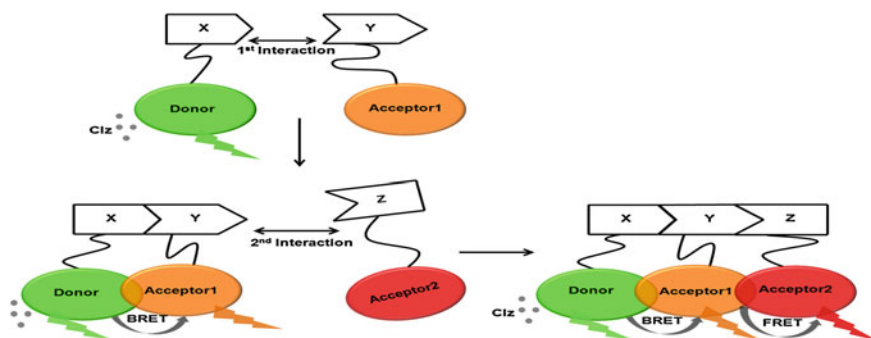


Fig. 10.6 Schematic representations illustrating an application of sequential RET (SRET). In this scheme, three target proteins whose interaction is to be investigated are fused to either a donor or one of the two fluorescent acceptors. If donor-tagged protein X interacts with Acceptor 1-tagged protein Y, it results in a BRET process accompanied by acceptor emission upon substrate addition. If this XY dimer now interacts with a third protein Z fused to the second acceptor (Acceptor 2), a FRET process will occur between Acceptor 1 and Acceptor 2, without additional light/substrate inputs. Thus, only when all the three proteins, X, Y, and Z form a complex, both BRET and FRET signals can be seen

fused to either a donor luciferase or two acceptor FPs. Upon interaction between the donor and the first FP, the light emitted by the BRET process will fuel a FRET process between the two FPs in a sequential manner (Fig. 10.6). The development of SRET¹ (RLuc-YFP-DsRed) and SRET² (RLuc-GFP²-YFP) utilizing Clz-*h* and Clz400 substrates, respectively, were reported in the literature for the first time. In SRET¹, RLuc emits at 480 nm which excites the primary BRET acceptor YFP. YFP, in turn, emits at 530 nm, which then excites a secondary acceptor DsRed through a FRET process, leading to its peak emission at ~580 nm. But, the major constraint in the utilization of SRET¹ system is that DsRed is tetrameric in nature, which may enhance the signal output from DsRed and can consequently give an unnaturally high SRET ratio. This downside of SRET¹ system can be addressed by using a monomeric red FP. On the other hand, the use of GFP and EYFP as FRET partners in the SRET² system is highly undesirable due to a low spectral resolution of only ~20 nm. Ideally, for a SRET platform to work efficiently, the three SRET partners should be so chosen, that their spectral overlap is sufficient only to ensure an optimal RET process, without having to rectify for a high signal bleed-through. Thus, this technique, though very promising, still calls for the design of more efficient SRET systems for multiplexing approaches [82].

In a broad sense, the BRET technique has so far been applied in four main areas, namely as sensors for protease, ion influx, protein–protein interactions (especially dimerization studies), and protein phosphorylation (Fig. 10.7). Taking examples from each category, we will now explain them in detail.

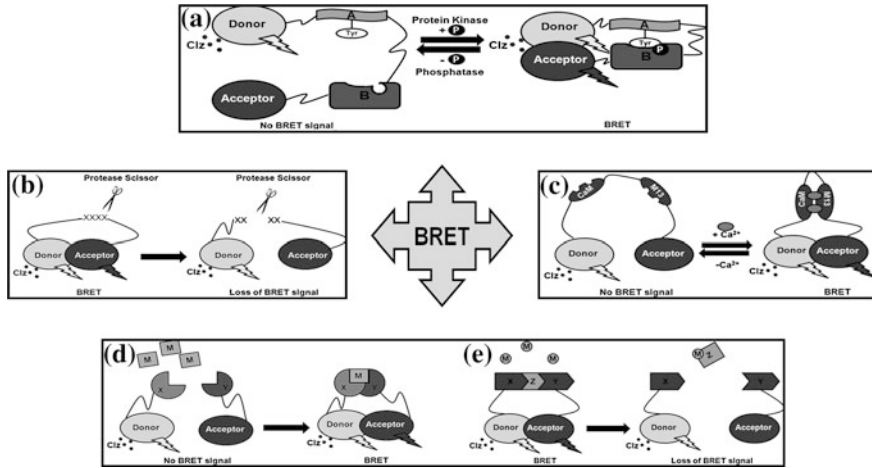


Fig. 10.7 Schematic representations illustrating various applications of BRET. **a** BRET-based biosensor for monitoring the phosphorylation or dephosphorylation. The sensor can be designed using a substrate peptide (*A*) containing phosphorylation-specific tyrosine (*Tyr*) residue and the substrate recognition domain (*B*) such as SH2, which brings about a conformational change upon phosphorylation bringing the donor and acceptor within proximity; gain in BRET signal will be observed in case of phosphorylation or vice versa in case of dephosphorylation. **b** BRET-based probe for protease detection is shown. In this case, the protease recognition domain is situated in the linker region, and upon proteolytic cleavage, BRET signal will be lost. **c** BRET-based probe for Ca²⁺ ion sensing. Ca²⁺-sensing domain calmodulin (*CaM*) and M13 are present between the donor and acceptor. In calcium-deficient state, CaM-M13 complex has extended conformation (*left*). Increase in BRET signal will be seen when Ca²⁺ brings CaM and M13 close to each other (*right*). **d** BRET-based sensor to monitor positive modulator (*M*) activity, which mediates the dimerization of two proteins (*X* and *Y*); BRET signal will only be observed in the presence of the modulator (*right*). **e** BRET-based sensor to monitor negative modulator (*M*) activity. In the absence of modulator, a BRET signal will be observed (*left*); addition of modulator brings conformational change in the bridging protein (*Z*), disrupting the interaction of *X* and *Y*, leading to loss of BRET signal (*right*)

10.4.1.1 Sensor for Protease Activity Measurement

Post-translational modification by proteolytic processing plays a crucial role in cellular functions such as peptide generation, cell cycle, and apoptosis. Such a process is also implicated in diseased conditions such as tumor metastasis, HIV, and Alzheimer's diseases. BRET can be applied to assess real-time proteolysis in living cells. In a study, a BRET-based protease sensor was developed to study peptide processing of nocistatin (NST) and nociceptin/orphanin FQ (N/OFQ) by using a novel VLuc-EYFP system [60]. As VLuc is secretory in nature, direct measurements of protease activity from the spent media make it an attractive system. To design the sensor, the NST/Noc peptide sequence was sandwiched between the VLuc-EYFP BRET probes. This peptide is bridged by a proteolytic cleavage motif of Lys-Arg. A similar RLuc-GFP BRET probe with NST/Noc propeptide was also prepared for the comparison of BRET performance. Upon

protease induction, it was found that the level of BRET activity in the spent media had decreased significantly.

To measure human immunodeficiency virus type-1 protease (HIV-1 PR) activity, a sensor was developed using BRET² system [88] by placing the HIV-1 Gag-p2/Gag-p7 protease sites in between GFP² and hRLuc. The vector comprising hRLuc-p2/p7-GFP² was coexpressed with HIV-1 codon-optimized PR + and PR- Gag/Pol expressor, resulting in a reduction or no change in BRET² signal, respectively. Such a biosensor can be adapted to high-throughput screening (HTS) assays for screening new HIV-1 protease inhibitors and/or study of viral maturation. Similarly, a BRET² biosensor for detection of feline calicivirus (FCV) was also developed [89]. By incorporating a functional or truncated FCV protease site within the BRET² biosensor, they created BRET²-FCV-Cut or BRET²-FCV-Uncut, respectively, and tested in feline cells. BRET assays can detect very low quantities of protease or protease inhibitor, making it ideal for an HTS platform.

Similarly, in another study, a thrombin protease target peptide was used to monitor the thrombin protease activity [90]. In this study, the RLuc molecule was inserted either at the N-terminal or C-terminal of GFP², producing RLuc-RG-GFP² and GFP²-RG-RLuc fusions, respectively, where RG refers to the Arg-Gly cleavage site specific for recognition by the thrombin protease. In line with the results reported by other groups, the GFP² at the N-terminus of the fusion protein yields better signal. Further, in this study, a direct quantitative comparison was made between BRET¹ and BRET² systems and contrary to previous findings, BRET² appears to be a better system which can be further improvised by the use of mutant donors such as RLuc2 [24].

10.4.1.2 Sensor for Ion Influx Measurement

Calcium sensors—Ca²⁺ is a ubiquitous second messenger molecule that plays a pivotal role in important cellular and physiological functions such as neurotransmission, muscular contraction, hormone secretion, etc. Determining the dynamic changes in intracellular concentration of Ca²⁺ has always been an area of exploration as even a slight disturbance in the Ca²⁺ homeostasis can contribute to the manifestation of cardiac and neuronal functions. There are, however, certain limiting factors in the determination of intracellular Ca²⁺ levels. For instance, the rise and fall in Ca²⁺ are very fast, and that change is restricted to a narrow time frame (microseconds) and concentration (100 nM–100 μM). Aequorin [91], which functionally behaves as a luciferase, has three binding sites for Ca²⁺. Ca²⁺ binding stimulates a conformational change in aequorin that ultimately results in the oxidation of Clz [92] and light emission (Em_{max} 470 nm). However, aequorin has a poor quantum yield; so, in such sensors, it is generally coupled to GFP or other FPs to produce chimeric proteins, wherein GFP acts as an amplifier of the photon signal from aequorin through chemiluminescence resonance energy transfer (CRET) and then emits at 510 nm. The advantage of using aequorin in the detection of Ca²⁺ is that it exclusively binds to only Ca²⁺. In addition, it is non-toxic, relatively

pH-insensitive [93], and does not affect the intracellular Ca^{2+} concentration due to its low affinity for Ca^{2+} ($K_d = 10 \mu\text{M}$) [92], which allows for the detection of $[\text{Ca}]^{2+}$ from 10^{-7} to 10^{-3} M. It can also be targeted to different subcellular compartments [93], such as the mitochondrial matrix. Bakayan et al. [93] fused several RFPs with aequorin, of which tdTomato was reported to be the best acceptor, owing to its high quantum output and wide absorbance spectra that has allowed Ca^{2+} imaging from live animals as well. The tdTomato-Aequorin (tdTA) system could successfully image K^+ -induced voltage-gated Ca^{2+} ion channels upon membrane depolarization in primary culture of mouse neurons as a time-dependent function. In addition, the tdTA system could also monitor the intracellular Ca^{2+} oscillations in cells in response to extracellular agonists.

In an alternative approach, the use of the affinity of calmodulin (CaM) for Ca^{2+} has been reported. This approach is shown to be more useful over the conventional aequorin-based system when long-term imaging of Ca^{2+} is required. Interaction of CaM to its target peptide M13 is mediated via the binding of Ca^{2+} ion (Fig. 10.7c). This principle is made use of in a wide variety of FRET-based Ca^{2+} sensors [94–96]. Saito et al. [97] developed a similar BRET-based Ca^{2+} sensor using RLuc8 and different versions of Venus. The donor and the acceptor are joined to either CaM or M13. The binding of Ca^{2+} to the CaM domain is reversible, and this induces a conformational change in the CaM-M13 fusion protein, making it either extended or compact, thereby changing the BRET signal. In an attempt to further optimize the BRET output, Saito et al. tried out different versions of Venus including several circularly permuted Venus (cpVenus) proteins in opposite orientations with RLuc8. In some FPs such as EGFP or ECFP, it has been observed that their fluorescence remains unaffected upon cleavage at specific points within their amino acid backbone, especially at site 144, if their C-terminal and N-terminal are linked together by a short peptide linker. Such modified FPs are called circularly permuted FPs or cpFPs and are conferred with greater sensitivity to pH and temperature. Venus-CaM-M13-RLuc8 shows the highest dynamic range (60 %), followed by RLuc8-CaM-M13-Venus, RLuc8-CaM-M13-cp157Venus, and cp229Venus-CaM-M13-RLuc8, each of which had a 30 % dynamic range. This quantitative Ca^{2+} probe could successfully visualize the intracellular Ca^{2+} dynamics at the single-cell level in plant and mammalian cells [97].

10.4.1.3 Sensor for Protein Dimerization Measurement

One of the most straightforward applications of BRET technology has been in the study of protein dimerization particularly in the context of GPCR/receptor oligomerization studies, ligand–receptor binding studies, and drug screening assays. Exhaustive work has been done over the last decade in these areas. Covering every aspect of BRET studies in GPCRs is not the purpose of this chapter, and thus a comprehensive summary of some of the important strategies are discussed here.

To explain the concept of protein dimerization, we will be discussing the frequently used model example of rapamycin-mediated heterodimerization of FRB

and FKBP12 domains, which has been a standard proof of principle system to establish the validity of new BRET systems developed during the past decade [30, 98]. Rapamycin is a small macrolide antibiotic known for its anti-fungal and immunosuppressive activities. It targets the 12-kDa receptor immunophilin FK506-binding protein (FKBP12) in cells. Together, this rapamycin–FKBP12 complex can bind to the 11-kDa FKBP12–rapamycin-binding domain (FRB) that inhibits the kinase activity of mammalian target of rapamycin (mTOR) protein [99]. To validate a BRET system, one can design two fusion tags, the donor and acceptor, each of which is genetically fused to either FRB or FKBP12. For instance, while validating the improved BRET² using RLuc mutants or new BRET systems developed such as BRET3 to BRET6, FRB and FKBP12 model has been used to demonstrate the power of each. In all of these studies, FRB and FKBP12 are inserted in between the respective donor and acceptor pair used. Even though flexible linker amino acids were not used in the fusion protein sequence, rapamycin could induce the heterodimerization of FRB and FKBP12 and as indicated by control equivalent BRET ratio was observed. Moreover, the magnitude of the BRET signal was shown to be Rapamycin dosage dependent (Fig. 10.8). Further, in an independent experiment, it has been shown that engineered cells overexpressing the GFP²-FRB-FKBP12-RLuc8 biosensor show a BRET signal gain or loss in the presence or absence of rapamycin mediator in the culture media, respectively. These studies together suggest that using this approach, HTS drug screening platforms can be designed, wherein the candidate drugs are added to live cell environment directly to measure their modulatory effects on the target protein interactions [24, 30].

As mentioned earlier, BRET-based GPCR studies were conducted to answer questions like whether a particular receptor subtype has a tendency to homodimerize or heterodimerize or both, the effect of a receptor agonist/antagonist on the dimerization state and activity of the receptor, the interaction of a receptor with other enzymes like kinases or regulators, and to understand whether the active form of a receptor is monomeric or oligomeric [34, 100–102]. In a typical GPCR study, the receptor is fused to both the donor and the acceptor at either N-terminus or C-terminus to verify the best possible orientation. The orientation that demonstrates the best BRET signal is then taken forward for the detection of the receptor oligomerization state in the presence or absence of the receptor agonist/antagonist [103]. Further advancement was exemplified by Carriba et al. who studied the heteromeric complexes of more than two neurotransmitter receptors [82]. Using SRET, they identified complexes of cannabinoid CB₁ receptor (CB₁R), dopamine D₂ receptor (D₂R), and adenosine A_{2A} receptor (A_{2A}R) in living cells.

To study the interaction between Ca²⁺-binding proteins CaM, A_{2A}, and D₂ receptors Navarro et al. used SRET² system described before, which provides evidence for the CaM-A_{2A}-D₂ oligomerization [83]. This model has utility in basal ganglion disorder, since A_{2A}-D₂R receptor heteromers are considered as potent target for anti-parkinson's agent. Thus, these systems were indicated for use as multi-drug screening platform.

Another approach to study the CB₁R, D₂R, and A_{2A}R employs the bimolecular fluorescence complementation coupled with BRET (BiFC-BRET), which was

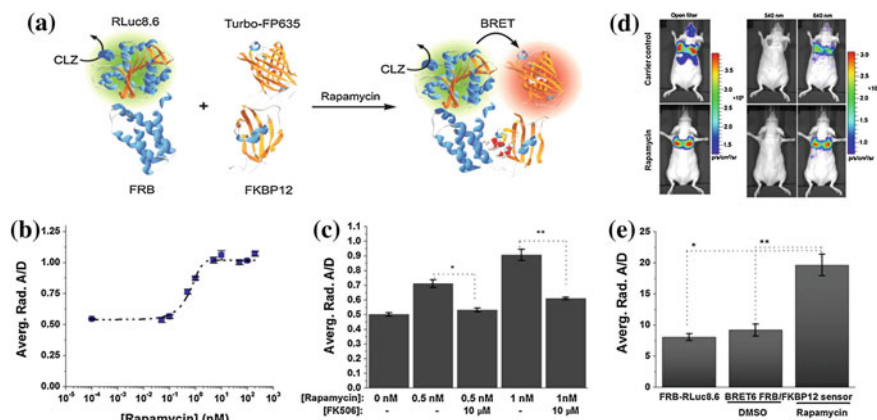


Fig. 10.8 Characterization of the genetically encoded FRB-FKBP12 BRET6 sensor. **a** Schematic illustration of the BRET6 (TurboFP₆₃₅-RLuc8.6) sensor for monitoring the rapamycin induced FRB-FKBP12 association. **b** Rapamycin dose response curve for live HT1080 cells expressing BRET6 FRB-FKBP12 sensor. HT1080 cells (1×10^5) expressing both FRB-RLuc8.6 and FKBP12-TurboFP635 sensor components were plated in black well plates, incubated with increasing concentrations of rapamycin and imaged spectrally using IVIS-200 at 6 h. The data were fitted to a sigmoidal curve fitting ($EC_{50} = 0.7 \pm 0.2$ nM); error bars represent standard deviation. **c** Inhibition of rapamycin-induced FRB-FKBP12 association by FK506. HT1080 cells were incubated for 6 h with rapamycin (0, 0.5, and 1 nM) and with and without FK506 (10 μ M), followed by imaging as described above. **d** Representative bioluminescence images of HT1080 cells stably expressing FRB-FKBP12 BRET6 sensor accumulated in the lungs of nude mice. Cells (3×10^6 in 150 μ L PBS) were injected through the tail vein, resulting in significant trapping in the lungs. One group of mice ($n = 8$) was injected 2 h after cell injection with 40 μ g rapamycin dissolved in 20 μ L DMSO and further diluted in 130 μ L PBS administered through the tail vein. The control group of mice ($n = 8$) was injected with DMSO (20 μ L in 130 μ L PBS). Two hours after cells injection, the mice were injected with Clz substrate intravenously and sequentially imaged using open/donor/acceptor filters. **e** Average A/D values for BRET6 FRB-FKBP12 sensor (rapamycin and DMSO-treated groups) and donor-only FRB-RLuc8.6 calculated from mice lung-trapping model imaging experiments; error bars represent the SEM. *Note that BRET6 is now renamed as BRET8 in this chapter.* Figure represented with permission from PNAS [36]

developed by Navarro et al. [85]. In this system, they used the truncated forms of YFP fluorophore, the N-terminal truncated as Nyfp, and C-terminal truncated as cYFP. The truncated nYFP and cYFP were tagged with CB₁R and A_{2A}R, respectively. When CB₁RnYFP and A_{2A}RcYFP receptors were cotransfected, the fluorescence was observed at 530 nm. No fluorescence was detected when cells were cotransfected with A_{2A}RcYFP and nYFP or with CB₁RnYFP and cYFP. The dopamine D₂ and D₄ receptors were tagged with RLuc to form D₂RLuc and D₄RLuc which serve as positive and negative controls, respectively. When D₂RLuc was cotransfected with A_{2A}RcYFP and CB₁RnYFP, the BRET signal was specific and was assessed by the energy transfer from donor to the complemented bimolecular fluorophore (by the interaction of A_{2A}RcYFP and CB₁RnYFP). This approach has a distinct advantage over SRET. In SRET, since all the interacting partners are tagged to distinct donor or acceptors, chances of increase in

spatiotemporal change in the tagged proteins due to steric hindrance is likely. On the other hand, in BiFC-BRET, the donor is tagged to one protein, while the other two proteins are tagged to complementable fluorophores which significantly reduce the steric forces.

Urizar et al. developed the complemented donor–acceptor resonance energy transfer (CODA-RET) [86], where complementation of donor subunits tagged with dopamine D₁ and D₂ receptors constitute the luminescence signal, which further transfer resonance energy to an FP tagged with G-protein subunit. These systems have the potency to be used with agonist/antagonist-induced receptor heteromerization studies and as a tool to screen drugs and its pharmacological analysis.

Guo et al. combined luminescence and fluorescence complementation to study resonance energy transfer (BiLC-BiFC) [87]. To study the maximum receptor oligomerization with minimal tagging, split luciferase (RLuc8) was tagged to dopamine receptor D₂ (D₂-L₁ and D₂-L₂), and split fluorophore (mVenus) was also tagged to dopamine receptor D₂ (D₂-V₁ and D₂-V₂). The tetramerization of D₂-L₁-D₂-L₂-D₂-V₁-D₂-V₂ was studied. A major bottleneck in the utilization of any of the above-mentioned complementation approaches is the severe loss of signal when split luciferases or split fluorophores are used. With suitable engineering to improve the split reporter performance and the use of more sensitive detection instruments, this approach might be feasible in the future.

10.4.1.4 Sensor for Phosphorylation Measurement

Protein phosphorylation is an important post-translational modification that controls many aspects of cellular signaling in multicellular organisms. Protein kinases phosphorylate the protein at specific serine, threonine, or tyrosine residues by the addition of covalently bound phosphate group. Upon phosphorylation, substrate proteins are subjected to conformational changes due to the negative charge of the phosphate groups, which subsequently triggers their enzymatic activation and interaction with target proteins. Ideally, interactions of phosphorylated proteins should be studied in the physiological context and in real-time, and thus, a BRET-based method provides an advantage. To study protein phosphorylation using BRET technology, two basic types of phosphorylation sensors can be designed. In the first approach, a tandem fusion of substrate domain and phosphorylation recognition domain is sandwiched between donor–acceptor pair (Fig. 10.7a). In the second approach, a sensor to study the formation of homo- or heterodimers of receptor tyrosine kinases [104, 105] or its downstream effector proteins [106] can be designed.

The Src homology 2 (SH2) domain is the most prevalent of substrate recognition modules and plays a central role in tyrosine kinase signaling pathways. The human genome contains a total of 120 such SH2 domains in 110 distinct proteins. SH2 domain is relatively small (~100 amino acids) and can fold independently; hence, the isolated domain can be expressed independently and used for direct binding assays. The SH2 domains also differ in their binding preferences for specific phosphorylated ligands, resulting in specificity in signal transduction.

Using such strategy, though FRET-based direct phosphorylation sensing was demonstrated [107], BRET applications are yet to come. The only BRET-based study that demonstrated the existence of the preassociated STAT3 molecules in the cytoplasm of live cells as dimers or multimers is by Schröder et al. They questioned the belief of activation-induced STAT3 dimerization in cytoplasm and provided an alternative hypothesis [108]. Thus, the reconsideration of STAT3 activation pathway was addressed using BRET¹.

10.4.1.5 Miscellaneous Sensors

While most of the work done using BRET technology represents the categories mentioned above, there are some very unique BRET sensors developed that are worth mentioning and have raised the applicability of BRET to the next level. Arai et al. [109] designed an immunoassay platform that can detect the presence of an antigen in a solution using BRET. Coined as open sandwich bioluminescent immunoassay (OS-BLIA), this assay comprises of the variable heavy and light chains of an antibody against the hen egg lysozyme fused to the donor (RLuc) and acceptor (EYFP) proteins, respectively. The only prerequisite for the assay to work is that the antibody variable region should have a negligibly weak V_H - V_L interaction in the absence of its antigen followed by the formation of a stabilized association upon the addition of the bridging antigen. The V_H and V_L proteins are both conjugated to thioredoxin (Trx) which has been shown to enhance the binding efficiency of these proteins to the antigen [109]. This sensor showed an antigen-dependent increase in BRET signal output, with signal saturation at an antigen concentration above 100 $\mu\text{g/mL}$. Although the dynamic range of this assay is miniscule (~ 0.14 only), this assay is one of its kind and opens up a new avenue in BRET-based assays. Moreover, its requirement for only a single antibody provides a definite advantage and obviates the need for a second antibody (against another epitope on the antigen) as in the case of sandwich ELISA. With further optimization, this assay might prove promising as antigen detection kits.

Another novel application of BRET technology is in the detection of specific RNA sequences that may again be used to develop RNA detection kits. In this area, two different studies have successfully designed suitable BRET-based assay. The first technique was pioneered by Walls et al. [110], which comprised of a dual probe system. The first probe consisted of a 20-mer oligonucleotide complementary to a specific RNA sequence (in this case the FLuc cDNA/mRNA) and conjugated at its 5' terminal to RLuc8. The second probe consisted of another 20-mer oligonucleotide (which is again complementary to the same target RNA but at a different locus than the previous one) and conjugated at its 3' terminal to GFP². The biotinylated target mRNA which is immobilized on a streptavidin-coated 96-well black plate acts as a "scaffold" on which the two probes can bind. The successful hybridization of the probes with the target RNA brings the BRET partners in close proximity to each other, consequently leading to a positive BRET signal upon substrate addition. The BRET signal was optimal when the binding sites of the two

probes were 10 nucleotides apart (lesser distance increased steric hindrance, while greater distance reduced RET efficiency). The attractive features of this technique are its high specificity upon the use of two probes, rapid results, and the ease with which this system can be customized for every new target mRNA without affecting its efficiency. However, obstacles like low sensitivity (can detect only up to 1 μg , while RT-PCR can detect as low as 100 ng RNA) need to be minimized before its commercial diagnostic application.

Recently, Andou et al. [111] reported another RNA detection system that made use of the arginine-rich motifs (ARM) derived from RNA-viruses and flanked by hRLuc and EYFP on its either side. The ARM peptide can recognize and bind to specific RNA sequences upon which, it undergoes a conformational change which is reflected as a change in the BRET signal. Additionally, different flexible [(GGGS)₅] and rigid linkers [(EAAAK)₄ or (EAAAK)₅] of varying lengths were also added adjacent to the ARM peptide to monitor their effect on the BRET signal. Of the three viral ARM peptides used, namely Human Immunodeficiency Virus Rev peptide (Rev), Bovine Immunodeficiency Virus (BIV Tat), and Jembrana Deficiency Virus Tat peptide (JDV Tat), BIV Tat peptide and modified JDV Tat peptide, which are both specific for TAR RNA, adopt a β -hairpin conformation upon successful binding to the TAR RNA and show the maximum change in BRET signal, thus establishing the validity of this assay design. However, this is just a prototype and developing a uniform diagnostic platform based on this model for a diverse range of target RNAs has a long way to go.

10.4.2 Synthetic BRET Probes

Recently, some high-throughput BRET systems were developed that harness the power of synthetic chemistry. As near-infrared (NIR)-emitting FPs are rare or the ones available and generally suffer from either poor stability, low excitation coefficient, or low quantum output, which are important determinants for an acceptor molecule, they have a limited use in BRET assay system development. In complementation to genetic BRET reporter systems, synthetic BRET probes viz., quantum dots (QDs) and fluorescent dyes have surfaced to overcome the limitations of genetic BRET systems.

10.4.2.1 BRET Using Quantum Dots

A remarkable development of QD as BRET probes has provided a new tool for resonance energy transfer systems [112]. QDs are colloidal nanocrystalline semiconductors possessing unique properties such as large stoke shift, broad excitation and narrow size-tunable emission spectra, negligible photobleaching, and high photochemical stability, which make them highly suitable fluorophores for use as a BRET acceptor (Fig. 10.9). The surface of QDs has a crucial effect on

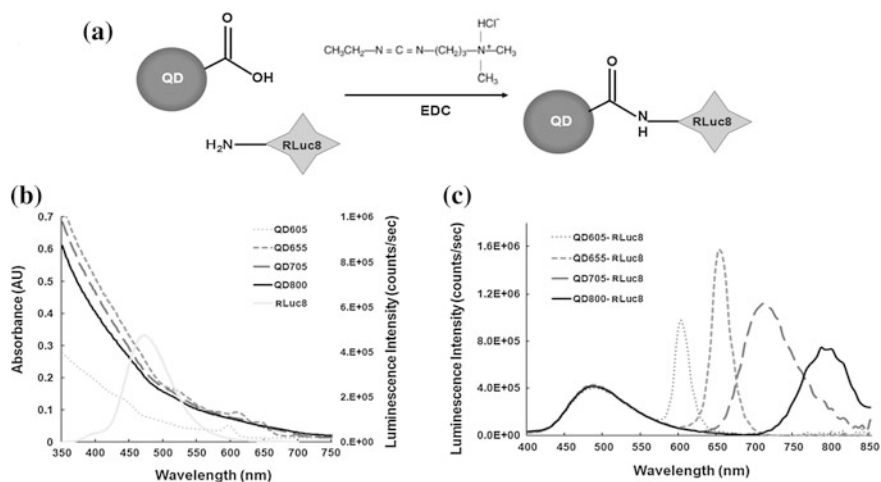


Fig. 10.9 Schematic illustration of QD BRET assay system. **a** QDs are linked to a bioluminescent *Renilla* luciferase mutant protein (RLuc8) by chemical bonding. It is possible to link up to six RLuc8 protein molecules on each QD surface and insert various linker sequences (such as protease recognition sequence) to develop biosensor probe. **b** Chart showing absorbance curves of selected color variant QDs which basically vary by their sizes. The chart is superimposed with RLuc8 luminescence emission curve (luminescence scale bar on z-axis), indicating that RLuc8 protein can be used as donor for all the size variant QD's to obtain BRET-based QD emission. **c** Chart showing luminescence intensity versus wavelength curves captured by exposing the color variant QD-RLuc8 molecules to coelenterazine substrate, providing multiplexing opportunity for spectral imaging. Figure adapted with modifications as permitted by NPG [112]

photoluminescence. This can be understood by the concept of trap states, which are caused by structural defects, such as atomic vacancies, local lattice mismatches, dangling bonds, or adsorbates at the surface. Excited electrons or holes can be trapped by these trap states, leading to non-radiative recombination. Surface passivation by overcoating the QDs with CdSe coated with ZnS (such semiconductors provide a wider band gap) can be used to minimize this trapping. This increases the photostability of the core, and hence, the quantum yield, making these core-shell-structured QDs more favorable for fluorescence-based applications [113].

A pioneering study reporting the development of QD-BRET system comprises the *Renilla* luciferase mutant (RLuc8) conjugated to the polymer-coated CdSe/ZnS core-shell QD655 ($E_{m,max}$ 655 nm) through coupling of amino groups on RLuc8 to the carboxylated group presented on QDs [112]. Gel electrophoresis can confirm the conjugation of QD655-RLuc8. The hydrodynamic diameter of QD655-RLuc8 was estimated to be ~ 2 nm larger than that of QD655. Each QD655-RLuc8 conjugate was estimated to contain on an average six RLuc8 molecules as donor. On addition of Clz to QD655-RLuc8, in addition to the RLuc8 emission at 480 nm, a strong peak at 655 nm was detected, indicating non-radiative energy transfer to the QD655. By applying synthetic chemistry, distance-dependent variation in the BRET ratio was tested. Further, the QD655-RLuc8 BRET probe stability has been

tested *in vitro* in mouse serum. The multiplexing approach has also been demonstrated, utilizing QD605, QD655, QD705, and QD800 tagging with the same RLuc8 protein yielding BRET ratios of 0.70, 1.20, 2.30, and 1.32, respectively. The spectrally distinct emission of these four conjugates can enable multiplexed BLI. Such multiplexing opportunities are unique amongst all the BRET probes designed so far, which provides an option for the user to choose the size of QD based on their intended use in cell-based or animal imaging.

Since the conjugation of QD and luciferase is random, the orientation of both the moieties can influence the sensitivity of the BRET protease assay. An intein-mediated chemical method can be recruited which specifically controls their relative orientation as well as restrict the number of conjugated RLuc8 moieties to one. Intein is a polypeptide sequence inside a protein that is able to excise itself and rejoins the remaining portion with a peptide bond. Further, QD-BRET systems were adopted to detect the cellular protease activity. A series of QD-BRET biosensors were synthesized for detection of MMP-2, MMP-7, and urokinase-type plasminogen activator (uPA) activity. These sensors having varied sensitivity can easily detect protease in serum [114]. QD655-MMP7-RLuc8 BRET was assayed with increasing amount of MMP-7 protease. Since the protease specifically cleaves off the peptide between the QD655 and RLuc8, the signal at 575–650 nm emission filter decreases and so will the BRET ratio. A similar decrease in BRET signal was observed for QD655-MMP2-RLuc8 and QD655-uPA-RLuc8 sensor when incubated with the MMP-2 and uPA proteases in buffer and serum. Simultaneous detection of MMP-2 and uPA proteases by spectrally resolved QD655-MMP-2-RLuc8 and QD705-uPA-RLuc8 was performed. The multiplexing ability of varied QD-BRET systems can provide a useful tool for the detection of many proteases/targets in a sample. A QD-BRET approach has also been demonstrated for nucleic acid detection [115].

10.4.2.2 BRET Using Fluorescent Dyes

As the use of QD-BRET is limited due to bulky size and toxicity of QD itself, fluorescent dyes having low molecular weight, extended absorption spectra, high stability, and high photon output may offer advantages as synthetic BRET probes. In a recent literature, conjugation of the luciferase protein CLuc (*Cypridina* luciferase) with a far-red fluorescent dye Indocyanine via a glycol chain was reported to form a far-red bioluminescent protein “FBP” [116]. CLuc oxidizes *Cypridina* luciferin to yield a light emission peak at 460 nm. A biotinylated FBP was tagged with a monoclonal antibody against human delta-like protein-1(Dlk-1) using a biotin–avidin interaction. This probe was used in the BLI of cancer cells *in vitro* and *in vivo*. The use of a self-illuminating probe eliminates the need of external illumination; rather, it is readily detectable upon substrate addition.

As reported in literatures, modification at cysteine and lysine residues of luciferase by chemical methods severely impairs their bioluminescence activity.

Branchini et al. [117] reported a firefly luciferase variant having point mutations to incorporate two cysteine residues, which permits the binding of dyes to the luciferase without destroying the native cysteine residues and preserving the bioluminescence activity of luciferase. BRET-based probes emitting in NIR region were developed by coupling an FLuc mutant (as donor; $E_{m_{max}}$ 617 nm) to Alexa Fluor[®] 680 ($E_{m_{max}}$ 705 nm) or Alexa Fluor[®] 750 ($E_{m_{max}}$ 750 nm) as acceptor. Branchini et al. [52] further reported the design of a single soluble probe based on the SRET principle. This probe comprises of a thermostable firefly luciferase ($E_{m_{max}}$ 560 nm) linked via different proteolytic target peptide sites to an mKate variant ($E_{m_{max}}$ 620 nm) covalently labeled with two Alexa Fluor[®] 680 ($E_{m_{max}}$ 705 nm). These probes enable the detection of protease activity in NIR, making it an attractive system for animal imaging.

10.4.2.3 BRET Using Carbon-60

Utilizing the luminescence quenching and free radicals scavenging properties of carbon-60 fullerene (C_{60}) derivatives, a novel BRET system was constructed for protease detection in combination with hGLuc [118]. The free radical quenching property of C_{60} is attributed to the delocalized π bond, curvature of its surface, and electron deficiency. Here, two different fullerene derivatives, carboxyl C_{60} ($C_{60}[C(COOH)_2]_3$) and amino hydroxyl C_{60} ($C_{60}(NH_2)_x(OH)_y$), have been examined to see whether they have any special effects on hGLuc luminescence. The strong absorption of C_{60} -COOH in the wavelength range of 425 nm to 525 nm indicates that C_{60} -COOH could be a good quencher not only for hGLuc but also for other luciferases, therefore providing a good acceptor in BRET assays. This assay works on the principle of attenuation of bioluminescence from hGLuc by C_{60} . As the peptide joining hGLuc and C_{60} is severed off, gain in bioluminescence signal is detected. The high sensitivity obtained for detection of a thrombin protease demonstrated that C_{60} -COOH- $(Ni)^{+2}$ -hGLuc system is an efficient system and can facilitate the testing of longer peptide linkers for many other protease assays in the future.

10.5 Engineering BRET Measurement Equipments

10.5.1 Microplate Reader

Since its inception in biological research, BRET signal is quantitatively measured using photomultiplier tube (PMT)-based microplate reader equipments. Scanning spectroscopy or a suitable plate reader capable of sequential or simultaneous detection of the two distinct wavelength ranges can be quantified for determining BRET efficiencies. Microplate measurements of BRET signal has so far been limited by its association with substrate injection before signal measurement from

each well of a multi-well plate. As discussed in the previous section, an important landmark development in live cell BRET measurement was achieved by the introduction of live cell substrate e.g., EnduRenTM which greatly stabilizes the RLuc flash kinetics. Availability of live cell Clz-*h* or Clz400 substrates would definitely help further automation toward developing a high-throughput screening methodology using BRET. In the following sections, we will address the issue of validating the BRET assay to compensate for the false-positive results.

While counting photons using plate reader in BRET PPIs studies, especially for the receptor oligomerization studies, there is a very high probability of artifacts if the concentration of the expressed receptor is high. In such a situation, the increased abundance of receptors means that there is a greater chance of two receptors being within the BRET-permissive distance of each other, leading to random collisions and consequently non-specific BRET, a phenomenon known as bystander BRET [101]. To distinguish between the genuine and random BRET interactions, appropriate controls must be recruited. As an appropriate negative control in the BRET assay, the acceptor FP without fusing it to another protein can be used. Alternatively, when receptors are being studied, one can also make use of a protein that is expressed at a similar level to the target receptor, but which does not interact with the other target protein [27]. A suitable positive control to use in conjunction with the BRET assay is the donor and acceptor molecules fused to each other through a flexible linker [27]. This can give us an indication of the highest possible BRET signal that can be achieved for a particular BRET pair.

10.5.1.1 BRET Dilution Assay

In this assay, the concentrations of both the donor and the acceptor fusion proteins are gradually diluted till the bystander BRET can be sufficiently eliminated. Theoretically, the BRET signal can be denoted by Eq. 10.5.

$$\text{BRET} = \text{BRET}_0 + k([D] = [A]) \quad (10.5)$$

where $[D]$ and $[A]$ are donor and acceptor concentrations, respectively. By simultaneously lowering the concentration of both receptors (dilution) at a constant $[A]/[D]$ ratio, the BRET signal decreases toward BRET_0 , which is the real oligomerization signal. This assay can then be used to set the optimal donor and acceptor concentrations for BRET saturation assays [26].

10.5.1.2 BRET Saturation Assay

This assay involves coexpressing a constant amount of donor fusion protein with a gradually increasing concentration of acceptor-tagged protein. The concentration of the donor protein is determined to be the minimum concentration of donor which gives a reliable and detectable signal output (as previously determined by the dilution

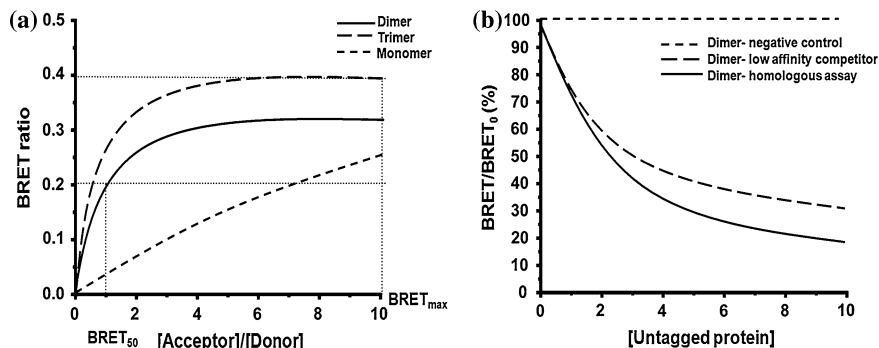


Fig. 10.10 Chart illustrating various assay parameters that validate the BRET assay. **a** The expected BRET saturation curves obtained as a function of the ratio of concentration of acceptor- and donor-tagged receptor molecules. The sigmoidal curve represents a true BRET event, while a linear plot is seen due to bystander BRET. The saturation in BRET signal is denoted by $BRET_{max}$ which is the highest possible BRET activity. Note that receptor trimerization can achieve a faster saturation compared to dimers, as can be seen by a lower $BRET_{50}$ value which is the $[A]/[D]$ ratio required to obtain a 50 % $BRET_{max}$. **b** Hypothetical BRET competition assay as a function of the untagged competitor molecule concentration. As the concentration of untagged receptor increases, it will compete with the tagged receptors to form dimers. In the negative control, a non-competing protein is used, where the BRET activity of the target receptors remains unaffected. In the homologous assay, the same kind of receptor as the target receptor is taken as the competitor that will maximally affect the receptor oligomerization of the BRET partners; while in the other case, a different receptor type with lowered binding affinity to the receptors is used as the competitor

assay). In this case, the BRET signal will increase till all acceptor molecules are interacting with the available donor molecules and a $BRET_{max}$ signal is achieved. Beyond this, an increase in acceptor concentration will not affect the BRET signal [26]. The higher the oligomerization state of the receptor, the faster the saturation can be achieved (Fig. 10.10a). Thus, if the experimental data can be fitted to match these theoretical curves, it reflects the specificity of receptor interactions [103]. Moreover, by comparing the $BRET_{50}$ values (the receptor concentration at which the BRET signal is 50 % of its maximum value) for homodimers and heterodimers, a saturation assay can help evaluate the relative affinity for their formation.

10.5.1.3 BRET Competition Assay

In this assay, the donor- and acceptor-tagged proteins are coexpressed with constant or increasing concentrations of untagged proteins which will compete with the tagged proteins for binding with the other tagged proteins. The decrease in the BRET output due to competitive inhibition provides evidence for the specificity of protein–protein interactions (Fig. 10.10b).

10.5.2 BRET Imaging Microscope

The ability to identify the subcellular location of interacting proteins and quantitative assessment of the changes undergoing therein provide a clear advantage over spectrophotometric BRET analysis from cell populations using a microplate reader. Bioluminescence microscopy (BLM), as its name suggests, uses luminescence rather than fluorescence. Like fluorescence imaging, BLM enables the visualization of genetic expression and physiological processes at the molecular level in living tissues. Imaging cells by exploiting luminescence reaction has several advantages over fluorescence. First, repeated exposure of living cells or tissues to fluorescence excitation wavelengths can photodamage the cells or photobleach the fluorophore, while bioluminescence is not burdened by such phototoxic or photobleaching effects. Also, unlike fluorescence, bioluminescence imaging typically does not suffer from auto-fluorescence background signal. The resulting high signal-to-background ratio allows more straightforward signal quantification and more sensitive signal detection. Furthermore, only viable cells emit luminescence signals, and thus measurements are absolute and directly quantitative, making live cell imaging much more suitable for long-term imaging. However, despite these advantages, applications for luminescence in live cell imaging have been limited until now, primarily due to the lack of sensitive detection device which can resolve low photon emission from micron-size space. Because luminescence is much dimmer than fluorescence, it requires longer capture time. Though the optics components required for luminescence detection are simpler, the availability and cost of the detection devices like intensely cooled charge-coupled device (CCD) cameras were the main constraint until a few years back. Furthermore, it is difficult to resolve spatial information with the subcellular, ultra-structural details as is possible with fluorescence microscopy today. Therefore, most systems in use have been built specifically by the researchers using components that are best suitable for their experimental requirements [106]. For instance, Xu et al. [119] used a microscope equipped with a modified electron bombarded charge-coupled device (EB-CCD) camera and a dual-view microimager attached directly to a 4x microscopic objective. Later on, Coulon et al. [120] demonstrated subcellular measurement of BRET signal using a modified version of inverted microscope equipped with electron-multiplying cooled charge-coupled device (EMCCD) camera. Recently, we have also demonstrated live cell imaging using BRET3 assay and a commercial luminescence microscope [30].

10.5.3 Macroscopic BRET Imaging

The ability to non-invasively image PPIs from their natural physiological environments has an important implication on a wide variety of biological research endeavors, such as drug discovery, molecular medicine, etc. With the introduction

of the intensely cooled CCD camera-based optical imaging instrumentation, the ability to detect very dim photon signals from live cells in culture or from animal or plant tissues has become possible. To detect signals with detectors placed outside the animal subjects, the cells of interest present at a depth within the subject must produce detectable signal. Here, the use of red and NIR light signals is favored as they have better tissue penetration capacity. Therefore, overall modification of existing assays to adapt them for non-invasive monitoring is a challenging task. Approaching the development of a single-format imaging assay that can serve to measure PPIs from isolated single cells as well as physiologically relevant animal/plant models, both BRET¹ and BRET² strategies, display some form of confinements. Therefore, while attempting live animal BRET assays, we have conducted serial experiments to identify an optimal BRET assay showing satisfactory performance as a single-format assay [24, 30, 98]. By now, we have ample variety of the red-light-emitting BRET vectors (as mentioned in Table 10.2) developed, many of which undoubtedly show superior performance over the previous assays used. By withdrawing the traditional method of BRET measurement using a microplate reader, we adapted a method for spectral separation of donor and acceptor signal by using a black-box cooled CCD camera macroimager [98]. An important parameter to successfully adapt this imaging method was the use of the BRET formats with relatively large spectral resolution, which allows the selection of wide band-pass emission filters in the device. Unlike the plate reader, the CCD camera-based macroimaging instrument can measure BRET signals from lysed or live cells placed in multi-well plates. The same instrument can then be used for BRET measurement from whole organisms as well. Point worth noting here is that BRET imaging from animal tissue is further complicated by the consideration of tissue attenuation factor. To address this, a double ratio (DR) which provides a depth-independent measure of the BRET signal in animal experiment was defined [36].

The main bottleneck of extending FRET strategy in small animal evaluation is associated with the auto-fluorescence correction method. As light travels in and out from animal tissues, the resulting photon attenuation complicates the FRET ratio calculations. In this context, the exclusion of an external photon input makes BRET-based technologies more acquiescent for macroscale imaging. We have also done proof of principle studies by confirming the detection of the rapamycin-dependent interaction of FKBP12 and FRB from living animals [24, 30, 36] (Fig. 10.8). Following the successful BRET imaging from small animal model, macroimaging of plant tissue was also reported [119]. Visualization of the COP1 (a plant light signaling regulator protein) homodimerization using RLuc-EYFP BRET assay was demonstrated in the rootlet and cotyledons of tobacco seedlings. Considering careful validation of the PPIs in systematic, large-scale models using individual test cases, the molecular imaging assays like BRET appear promising in the current proteomic developments.

10.6 Future Prospects and Concluding Remarks

Tremendous developments in the field of protein interaction analysis have been fueled by current efforts in the life sciences to dissect cellular protein function. A full understanding of how the proteins function and contribute to the signaling networks in the cell requires approaches to study protein interactions from different perspectives. Once the specific and relevant interactions have been identified, in-depth characterization of the molecular and biophysical parameters such as the kinetic rate constants, the oligomeric state of the interaction partners, and the stoichiometric ratio in the complex will follow. For this part of subjective analysis of a known pair of interactors, purified and well-characterized proteins are required. However, when one has to identify the protein interaction partners and gather a detailed understanding of protein interactions at the molecular and cellular context, screening techniques that can operate in live cell environment are required. Therefore, for a thorough understanding of PPIs in normal and diseased biology, need of technologies that offer options for both in vitro as well as in vivo assessment will speed up this epic task. With the huge expansion and adjustment made as described in this chapter, bioengineered BRET systems will continue to expand and fuel this area in future. The ability to tag endogenous proteins of interest with donor and acceptor molecule within live cell environment is a challenging task, and perhaps technology will develop in future to enhance our ability to achieve that as well.

Acknowledgments Funding support to AD from DBT Bioengineering, New Delhi and ACT-REC, TMC, India is gratefully acknowledged.

References

1. Selbach M, Mann M (2006) Protein interaction screening by quantitative immunoprecipitation combined with knockdown (QUICK). *Nat Methods* 3(12):981–983. doi:[10.1038/nmeth972](https://doi.org/10.1038/nmeth972)
2. Williams NE (2000) Immunoprecipitation procedures. *Methods Cell Biol* 62:449–453. doi:[10.1016%2FS0091-679X%2808%2961549-6](https://doi.org/10.1016%2FS0091-679X%2808%2961549-6)
3. Phizicky EM, Fields S (1995) Protein-protein interactions: methods for detection and analysis. *Microbiol Rev* 59(1):94–123
4. Rediger A, Tarnow P, Bickenbach A, Schaefer M, Krude H, Gruters A, Biebermann H (2009) Heterodimerization of hypothalamic G-protein-coupled receptors involved in weight regulation. *Obes Facts* 2(2):80–86. doi:[10.1159/000209862](https://doi.org/10.1159/000209862)
5. Ciruela F (2008) Fluorescence-based methods in the study of protein–protein interactions in living cells. *Curr Opin Biotechnol* 19(4):338–343. doi:[10.1016/j.copbio.2008.06.003](https://doi.org/10.1016/j.copbio.2008.06.003)
6. Ciruela F, Vilardaga JP, Fernandez-Duenas V (2010) Lighting up multiprotein complexes: lessons from GPCR oligomerization. *Trends Biotechnol* 28(8):407–415. doi:[10.1016/j.tibtech.2010.05.002](https://doi.org/10.1016/j.tibtech.2010.05.002)
7. Fields S, Song O (1989) A novel genetic system to detect protein–protein interactions. *Nature* 340(6230):245–246. doi:[10.1038/340245a0](https://doi.org/10.1038/340245a0)

8. Ray P, Pimenta H, Paulmurugan R, Berger F, Phelps ME, Iyer M, Gambhir SS (2002) Noninvasive quantitative imaging of protein–protein interactions in living subjects. *Proc Natl Acad Sci USA* 99(5):3105–3110. doi:[10.1073/pnas.052710999](https://doi.org/10.1073/pnas.052710999)
9. Mohler WA, Blau HM (1996) Gene expression and cell fusion analyzed by lacZ complementation in mammalian cells. *Proc Natl Acad Sci USA* 93(22):12423–12427
10. Piehler J (2005) New methodologies for measuring protein interactions in vivo and in vitro. *Curr Opin Struct Biol* 15(1):4–14. doi:[10.1016/j.sbi.2005.01.008](https://doi.org/10.1016/j.sbi.2005.01.008)
11. Widder EA (2010) Bioluminescence in the ocean: origins of biological, chemical, and ecological diversity. *Science* 328(5979):704–708. doi:[10.1126/science.1174269](https://doi.org/10.1126/science.1174269)
12. Seliger HH, Mc EW (1960) Spectral emission and quantum yield of firefly bioluminescence. *Arch Biochem Biophys* 88:136–141
13. Koo JA, Schmidt SP, Schuster GB (1978) Bioluminescence of the firefly: key steps in the formation of the electronically excited state for model systems. *Proc Natl Acad Sci USA* 75(1):30–33
14. Hoshino H (2009) Current advanced bioluminescence technology in drug discovery. *Expert Opin Drug Discov* 4(4):373–389. doi:[10.1517/17460440902804372](https://doi.org/10.1517/17460440902804372)
15. Ohmiya Y (2005) Basic and applied aspects of color tuning of bioluminescence systems. *Jpn J Appl Phys* 44 (9A):6368–6379. doi:[10.1143/jjap.44.6368](https://doi.org/10.1143/jjap.44.6368)
16. Beutler E, Baluda MC (1964) Simplified determination of blood adenosine triphosphate using the firefly system. *Blood* 23:688–698
17. Shimomura O, Johnson FH (1978) Peroxidized coelenterazine, the active group in the photoprotein aequorin. *Proc Natl Acad Sci USA* 75(6):2611–2615
18. van Roessel P, Brand AH (2002) Imaging into the future: visualizing gene expression and protein interaction interactions with fluorescent proteins. *Nat Cell Biol* 4(1):E15–E20. doi:[10.1038/ncb0102-e15](https://doi.org/10.1038/ncb0102-e15)
19. Forster T (1948) Zwischenmolekulare Energiewanderung und Fluoreszenz. *Ann Phys* 2:54–75
20. Clegg RM (1992) Fluorescence resonance energy transfer and nucleic acids. *Methods Enzymol* 211:353–388
21. Wu P, Brand L (1994) Resonance energy transfer: methods and applications. *Anal Biochem* 218(1):1–13
22. Stryer L, Haugland RP (1967) Energy transfer: a spectroscopic ruler. *Proc Natl Acad Sci USA* 58(2):719–726
23. De A (2011) The new era of bioluminescence resonance energy transfer technology. *Curr Pharm Biotechnol* 12(4):558–568
24. De A, Loening AM, Gambhir SS (2007) An improved bioluminescence resonance energy transfer strategy for imaging intracellular events in single cells and living subjects. *Cancer Res* 67(15):7175–7183. doi:[10.1158/0008-5472.CAN-06-4623](https://doi.org/10.1158/0008-5472.CAN-06-4623)
25. Xu Y, Piston DW, Johnson CH (1999) A bioluminescence resonance energy transfer (BRET) system: application to interacting circadian clock proteins. *Proc Natl Acad Sci USA* 96(1):151–156
26. Drinovec L, Kubale V, Nohr Larsen J, Vrecl M (2012) Mathematical models for quantitative assessment of bioluminescence resonance energy transfer: application to seven transmembrane receptors oligomerization. *Front Endocrinol* 3:104. doi:[10.3389/fendo.2012.00104](https://doi.org/10.3389/fendo.2012.00104)
27. Pflieger KD, Eidne KA (2006) Illuminating insights into protein–protein interactions using bioluminescence resonance energy transfer (BRET). *Nat Methods* 3(3):165–174. doi:[10.1038/nmeth841](https://doi.org/10.1038/nmeth841)
28. Bacart J, Corbel C, Jockers R, Bach S, Couturier C (2008) The BRET technology and its application to screening assays. *Biotechnol J* 3(3):311–324. doi:[10.1002/biot.200700222](https://doi.org/10.1002/biot.200700222)
29. Hamdan FF, Percherancier Y, Breton B, Bouvier M (2006) Monitoring protein–protein interactions in living cells by bioluminescence resonance energy transfer (BRET). In: *Curr Protoc Neurosci*. 2008/04/23 edn. Wiley, pp 5.23.21–25.23.20. doi:[10.1002/0471142301.ns0523s34](https://doi.org/10.1002/0471142301.ns0523s34)

30. De A, Ray P, Loening AM, Gambhir SS (2009) BRET3: a red-shifted bioluminescence resonance energy transfer (BRET)-based integrated platform for imaging protein–protein interactions from single live cells and living animals. *FASEB J* 23(8):2702–2709. doi:[10.1096/fj.08-118919](https://doi.org/10.1096/fj.08-118919)
31. Dionne P, Mireille C, Labonte A, Carter-Allen K, Houle B, Joly E, Taylor SC, Menard L (2002) BRET2: efficient energy transfer from Renilla Luciferase to GFP2 to measure protein–protein interactions and intracellular signaling events in live cells. In: van Dyke K, van Dyke C, Woodfork K (eds) *Luminescence biotechnology: instruments and applications*. CRC Press, pp 539–555
32. Bertrand L, Parent S, Caron M, Legault M, Joly E, Angers S, Bouvier M, Brown M, Houle B, Menard L (2002) The BRET2/arrestin assay in stable recombinant cells: a platform to screen for compounds that interact with G protein-coupled receptors (GPCRS). *J Recept Signal Transduct Res* 22(1–4):533–541. doi:[10.1081/RRS-120014619](https://doi.org/10.1081/RRS-120014619)
33. Eidne KA, Kroeger KM, Hanyaloglu AC (2002) Applications of novel resonance energy transfer techniques to study dynamic hormone receptor interactions in living cells. *Trends Endocrinol Metab* 13(10):415–421
34. Angers S, Salahpour A, Joly E, Hilairat S, Chelsky D, Dennis M, Bouvier M (2000) Detection of beta 2-adrenergic receptor dimerization in living cells using bioluminescence resonance energy transfer (BRET). *Proc Natl Acad Sci USA* 97(7):3684–3689. doi:[10.1073/pnas.060590697](https://doi.org/10.1073/pnas.060590697)
35. Loening AM, Fenn TD, Wu AM, Gambhir SS (2006) Consensus guided mutagenesis of Renilla luciferase yields enhanced stability and light output. *Protein Eng Des Sel* 19(9):391–400. doi:[10.1093/protein/gzl023](https://doi.org/10.1093/protein/gzl023)
36. Dragulescu-Andrasi A, Chan CT, De A, Massoud TF, Gambhir SS (2011) Bioluminescence resonance energy transfer (BRET) imaging of protein–protein interactions within deep tissues of living subjects. *Proc Natl Acad Sci USA* 108(29):12060–12065. doi:[10.1073/pnas.1100923108](https://doi.org/10.1073/pnas.1100923108)
37. Caysa H, Jacob R, Muther N, Branchini B, Messerle M, Soling A (2009) A red-shifted codon-optimized firefly luciferase is a sensitive reporter for bioluminescence imaging. *Photochem Photobiol Sci* 8(1):52–56. doi:[10.1039/b814566k](https://doi.org/10.1039/b814566k)
38. Loening AM, Wu AM, Gambhir SS (2007) Red-shifted Renilla reniformis luciferase variants for imaging in living subjects. *Nat Methods* 4(8):641–643. doi:[10.1038/nmeth1070](https://doi.org/10.1038/nmeth1070)
39. Loening AM, Dragulescu-Andrasi A, Gambhir SS (2010) A red-shifted Renilla luciferase for transient reporter-gene expression. *Nat Methods* 7(1):5–6. doi:[10.1038/nmeth0110-05](https://doi.org/10.1038/nmeth0110-05)
40. Fan F, Wood KV (2007) Bioluminescent assays for high-throughput screening. *Assay Drug Dev Technol* 5(1):127–136. doi:[10.1089/adt.2006.053](https://doi.org/10.1089/adt.2006.053)
41. Hall MP, Unch J, Binkowski BF, Valley MP, Butler BL, Wood MG, Otto P, Zimmerman K, Vidugiris G, Machleidt T, Robers MB, Benink HA, Eggers CT, Slater MR, Meisenheimer PL, Klaubert DH, Fan F, Encell LP, Wood KV (2012) Engineered luciferase reporter from a deep sea shrimp utilizing a novel imidazopyrazinone substrate. *ACS Chem Biol* 7(11):1848–1857. doi:[10.1021/cb3002478](https://doi.org/10.1021/cb3002478)
42. Stepanyuk GA, Unch J, Malikova NP, Markova SV, Lee J, Vysotski ES (2010) Coelenterazine-*v* ligated to Ca²⁺-triggered coelenterazine-binding protein is a stable and efficient substrate of the red-shifted mutant of Renilla muelleri luciferase. *Anal Bioanal Chem* 398(4):1809–1817. doi:[10.1007/s00216-010-4106-9](https://doi.org/10.1007/s00216-010-4106-9)
43. Giuliani G, Molinari P, Ferretti G, Cappelli A, Anzini M, Vomero S, Costa T (2012) New red-shifted coelenterazine analogues with an extended electronic conjugation. *Tetrahedron Lett* 53(38):5114–5118. doi:[10.1016/j.tetlet.2012.07.041](https://doi.org/10.1016/j.tetlet.2012.07.041)
44. Levi J, De A, Cheng Z, Gambhir SS (2007) Bisdeoxycoelenterazine derivatives for improvement of bioluminescence resonance energy transfer assays. *J Am Chem Soc* 129(39):11900–11901. doi:[10.1021/ja073936h](https://doi.org/10.1021/ja073936h)
45. Otto-Duessel M, Khankaldyyan V, Gonzalez-Gomez I, Jensen MC, Laug WE, Rosol M (2006) In vivo testing of Renilla luciferase substrate analogs in an orthotopic murine model of human glioblastoma. *Mol Imaging* 5(2):57–64. doi:[10.2310/7290.2006.00006](https://doi.org/10.2310/7290.2006.00006)

46. Pfeleger KD, Dromey JR, Dalrymple MB, Lim EM, Thomas WG, Eidne KA (2006) Extended bioluminescence resonance energy transfer (eBRET) for monitoring prolonged protein–protein interactions in live cells. *Cell Signal* 18(10):1664–1670. doi:[10.1016/j.cellsig.2006.01.004](https://doi.org/10.1016/j.cellsig.2006.01.004)
47. Green AA, McElroy WD (1956) Crystalline firefly luciferase. *Biochim Biophys Acta* 20(1):170–176
48. Chiu NH, Christopoulos TK (1999) Two-site expression immunoassay using a firefly luciferase-coding DNA label. *Clin Chem* 45(11):1954–1959
49. Arai R, Nakagawa H, Kitayama A, Ueda H, Nagamune T (2002) Detection of protein–protein interaction by bioluminescence resonance energy transfer from firefly luciferase to red fluorescent protein. *J Biosci Bioeng* 94(4):362–364. doi:[10.1263/jbb.94.362](https://doi.org/10.1263/jbb.94.362)
50. Branchini BR, Rosenberg JC, Ablamsky DM, Taylor KP, Southworth TL, Linder SJ (2011) Sequential bioluminescence resonance energy transfer–fluorescence resonance energy transfer-based ratiometric protease assays with fusion proteins of firefly luciferase and red fluorescent protein. *Anal Biochem* 414(2):239–245. doi:[10.1016/j.ab.2011.03.031](https://doi.org/10.1016/j.ab.2011.03.031)
51. Yamakawa Y, Ueda H, Kitayama A, Nagamune T (2002) Rapid homogeneous immunoassay of peptides based on bioluminescence resonance energy transfer from firefly luciferase. *J Biosci Bioeng* 93(6):537–542. doi:[10.1016/S1389-1723\(02\)80234-1](https://doi.org/10.1016/S1389-1723(02)80234-1)
52. Branchini BR, Rosenberg JC, Ablamsky DM, Taylor KP, Southworth TL, Linder SJ (2011) Sequential bioluminescence resonance energy transfer–fluorescence resonance energy transfer-based ratiometric protease assays with fusion proteins of firefly luciferase and red fluorescent protein. *Anal Biochem* 414(2):239–245. doi:[10.1016/j.ab.2011.03.031](https://doi.org/10.1016/j.ab.2011.03.031)
53. Branchini BR, Ablamsky DM, Davis AL, Southworth TL, Butler B, Fan F, Jathoul AP, Pule MA (2010) Red-emitting luciferases for bioluminescence reporter and imaging applications. *Anal Biochem* 396(2):290–297. doi:[10.1016/j.ab.2009.09.009](https://doi.org/10.1016/j.ab.2009.09.009)
54. Naumov P, Ozawa Y, Ohkubo K, Fukuzumi S (2009) Structure and spectroscopy of oxyluciferin, the light emitter of the firefly bioluminescence. *J Am Chem Soc* 131(32):11590–11605. doi:[10.1021/ja904309q](https://doi.org/10.1021/ja904309q)
55. Takenaka Y, Masuda H, Yamaguchi A, Nishikawa S, Shigeri Y, Yoshida Y, Mizuno H (2008) Two forms of secreted and thermostable luciferases from the marine copepod crustacean. *Metridia pacifica Gene* 425(1–2):28–35. doi:[10.1016/j.gene.2008.07.041](https://doi.org/10.1016/j.gene.2008.07.041)
56. Markova SV, Burakova LP, Vysotski ES (2012) High-active truncated luciferase of copepod *Metridia longa*. *Biochem Biophys Res Commun* 417(1):98–103. doi:[10.1016/j.bbrc.2011.11.063](https://doi.org/10.1016/j.bbrc.2011.11.063)
57. Inouye S, Watanabe K, Nakamura H, Shimomura O (2000) Secretional luciferase of the luminous shrimp *Oplophorus gracilirostris*: cDNA cloning of a novel imidazopyrazinone luciferase(1). *FEBS Lett* 481(1):19–25
58. Gammon ST, Villalobos VM, Roshal M, Samrakandi M, Piwnica-Worms D (2009) Rational design of novel red-shifted BRET pairs: platforms for real-time single-chain protease biosensors. *Biotechnol Prog* 25(2):559–569. doi:[10.1002/btpr.144](https://doi.org/10.1002/btpr.144)
59. Li F, Yu J, Zhang Z, Cui Z, Wang D, Wei H, Zhang XE (2012) Buffer enhanced bioluminescence resonance energy transfer sensor based on *Gussia* luciferase for in vitro detection of protease. *Anal Chim Acta* 724:104–110. doi:[10.1016/j.aca.2012.02.047](https://doi.org/10.1016/j.aca.2012.02.047)
60. Otsuji T, Okuda-Ashitaka E, Kojima S, Akiyama H, Ito S, Ohmiya Y (2004) Monitoring for dynamic biological processing by intramolecular bioluminescence resonance energy transfer system using secreted luciferase. *Anal Biochem* 329(2):230–237. doi:[10.1016/j.ab.2004.03.010](https://doi.org/10.1016/j.ab.2004.03.010)
61. Tannous BA, Kim DE, Fernandez JL, Weissleder R, Breakefield XO (2005) Codon-optimized *Gussia* luciferase cDNA for mammalian gene expression in culture and in vivo. *Mol Ther* 11(3):435–443. doi:[10.1016/j.ymthe.2004.10.016](https://doi.org/10.1016/j.ymthe.2004.10.016)
62. Thompson EM, Nagata S, Tsuji FI (1989) Cloning and expression of cDNA for the luciferase from the marine ostracod *Vargula hilgendorfii*. *Proc Natl Acad Sci USA* 86(17):6567–6571

63. Shaner NC, Steinbach PA, Tsien RY (2005) A guide to choosing fluorescent proteins. *Nat Methods* 2(12):905–909. doi:[10.1038/nmeth819](https://doi.org/10.1038/nmeth819)
64. Prasher DC, Eckenrode VK, Ward WW, Prendergast FG, Cormier MJ (1992) Primary structure of the *Aequorea victoria* green-fluorescent protein. *Gene* 111(2):229–233
65. Wang Y, Shyy JY, Chien S (2008) Fluorescence proteins, live-cell imaging, and mechanobiology: seeing is believing. *Annu Rev Biomed Eng* 10:1–38. doi:[10.1146/annurev.bioeng.010308.161731](https://doi.org/10.1146/annurev.bioeng.010308.161731)
66. Muller-Taubenberger A, Anderson KI (2007) Recent advances using green and red fluorescent protein variants. *Appl Microbiol Biotechnol* 77(1):1–12. doi:[10.1007/s00253-007-1131-5](https://doi.org/10.1007/s00253-007-1131-5)
67. Griesbeck O, Baird GS, Campbell RE, Zacharias DA, Tsien RY (2001) Reducing the environmental sensitivity of yellow fluorescent protein. Mechanism and applications. *J Biol Chem* 276(31):29188–29194. doi:[10.1074/jbc.M102815200](https://doi.org/10.1074/jbc.M102815200)
68. Nagai T, Ibata K, Park ES, Kubota M, Mikoshiba K, Miyawaki A (2002) A variant of yellow fluorescent protein with fast and efficient maturation for cell-biological applications. *Nat Biotechnol* 20(1):87–90. doi:[10.1038/nbt0102-87](https://doi.org/10.1038/nbt0102-87)
69. Nguyen AW, Daugherty PS (2005) Evolutionary optimization of fluorescent proteins for intracellular FRET. *Nat Biotechnol* 23(3):355–360. doi:[10.1038/nbt1066](https://doi.org/10.1038/nbt1066)
70. Matz MV, Fradkov AF, Labas YA, Savitsky AP, Zaraisky AG, Markelov ML, Lukyanov SA (1999) Fluorescent proteins from nonbioluminescent Anthozoa species. *Nat Biotechnol* 17(10):969–973. doi:[10.1038/13657](https://doi.org/10.1038/13657)
71. Baird GS, Zacharias DA, Tsien RY (2000) Biochemistry, mutagenesis, and oligomerization of DsRed, a red fluorescent protein from coral. *Proc Natl Acad Sci USA* 97(22):11984–11989. doi:[10.1073/pnas.97.22.11984](https://doi.org/10.1073/pnas.97.22.11984)
72. Campbell RE, Tour O, Palmer AE, Steinbach PA, Baird GS, Zacharias DA, Tsien RY (2002) A monomeric red fluorescent protein. *Proc Natl Acad Sci USA* 99(12):7877–7882. doi:[10.1073/pnas.082243699](https://doi.org/10.1073/pnas.082243699)
73. Bevis BJ, Glick BS (2002) Rapidly maturing variants of the *Discosoma* red fluorescent protein (DsRed). *Nat Biotechnol* 20(1):83–87. doi:[10.1038/nbt0102-83](https://doi.org/10.1038/nbt0102-83)
74. Shaner NC, Campbell RE, Steinbach PA, Giepmans BN, Palmer AE, Tsien RY (2004) Improved monomeric red, orange and yellow fluorescent proteins derived from *Discosoma* sp. red fluorescent protein. *Nat Biotechnol* 22(12):1567–1572. doi:[10.1038/nbt1037](https://doi.org/10.1038/nbt1037)
75. Wang L, Jackson WC, Steinbach PA, Tsien RY (2004) Evolution of new nonantibody proteins via iterative somatic hypermutation. *Proc Natl Acad Sci USA* 101(48):16745–16749. doi:[10.1073/pnas.0407752101](https://doi.org/10.1073/pnas.0407752101)
76. Merzlyak EM, Goedhart J, Shcherbo D, Bulina ME, Shcheglov AS, Fradkov AF, Gaintzeva A, Lukyanov KA, Lukyanov S, Gadella TW, Chudakov DM (2007) Bright monomeric red fluorescent protein with an extended fluorescence lifetime. *Nat Methods* 4(7):555–557. doi:[10.1038/nmeth1062](https://doi.org/10.1038/nmeth1062)
77. Shcherbo D, Merzlyak EM, Chepurnykh TV, Fradkov AF, Ermakova GV, Solovieva EA, Lukyanov KA, Bogdanova EA, Zaraisky AG, Lukyanov S, Chudakov DM (2007) Bright far-red fluorescent protein for whole-body imaging. *Nat Methods* 4(9):741–746. doi:[10.1038/nmeth1083](https://doi.org/10.1038/nmeth1083)
78. Shcherbo D, Murphy CS, Ermakova GV, Solovieva EA, Chepurnykh TV, Shcheglov AS, Verkhusha VV, Pletnev VZ, Hazelwood KL, Roche PM, Lukyanov S, Zaraisky AG, Davidson MW, Chudakov DM (2009) Far-red fluorescent tags for protein imaging in living tissues. *Biochem J* 418(3):567–574. doi:[10.1042/BJ20081949](https://doi.org/10.1042/BJ20081949)
79. Morozova KS, Piatkevich KD, Gould TJ, Zhang J, Bewersdorf J, Verkhusha VV (2010) Far-red fluorescent protein excitable with red lasers for flow cytometry and superresolution STED nanoscopy. *Biophys J* 99(2):L13–L15. doi:[10.1016/j.bpj.2010.04.025](https://doi.org/10.1016/j.bpj.2010.04.025)
80. Tsien RY (1998) The green fluorescent protein. *Annu Rev Biochem* 67:509–544. doi:[10.1146/annurev.biochem.67.1.509](https://doi.org/10.1146/annurev.biochem.67.1.509)

81. Karasawa S, Araki T, Nagai T, Mizuno H, Miyawaki A (2004) Cyan-emitting and orange-emitting fluorescent proteins as a donor/acceptor pair for fluorescence resonance energy transfer. *Biochem J* 381(Pt 1):307–312. doi:[10.1042/BJ20040321](https://doi.org/10.1042/BJ20040321)
82. Carriba P, Navarro G, Ciruela F, Ferre S, Casado V, Agnati L, Cortes A, Mallol J, Fuxe K, Canela EI, Lluís C, Franco R (2008) Detection of heteromerization of more than two proteins by sequential BRET-FRET. *Nat Methods* 5(8):727–733. doi:[10.1038/nmeth.1229](https://doi.org/10.1038/nmeth.1229)
83. Navarro G, Aymerich MS, Marcellino D, Cortes A, Casado V, Mallol J, Canela EI, Agnati L, Woods AS, Fuxe K, Lluís C, Lanciego JL, Ferre S, Franco R (2009) Interactions between calmodulin, adenosine A2A, and dopamine D2 receptors. *J Biol Chem* 284(41):28058–28068. doi:[10.1074/jbc.M109.034231](https://doi.org/10.1074/jbc.M109.034231)
84. Heroux M, Hogue M, Lemieux S, Bouvier M (2007) Functional calcitonin gene-related peptide receptors are formed by the asymmetric assembly of a calcitonin receptor-like receptor homo-oligomer and a monomer of receptor activity-modifying protein-1. *J Biol Chem* 282(43):31610–31620. doi:[10.1074/jbc.M701790200](https://doi.org/10.1074/jbc.M701790200)
85. Navarro G, Carriba P, Gandia J, Ciruela F, Casado V, Cortes A, Mallol J, Canela EI, Lluís C, Franco R (2008) Detection of heteromers formed by cannabinoid CB1, dopamine D2, and adenosine A2A G-protein-coupled receptors by combining bimolecular fluorescence complementation and bioluminescence energy transfer. *Sci World J* 8:1088–1097. doi:[10.1100/tsw.2008.136](https://doi.org/10.1100/tsw.2008.136)
86. Urizar E, Yano H, Kolster R, Gales C, Lambert N, Javitch JA (2011) CODA-RET reveals functional selectivity as a result of GPCR heteromerization. *Nat Chem Biol* 7(9):624–630. doi:[10.1038/nchembio.623](https://doi.org/10.1038/nchembio.623)
87. Guo W, Urizar E, Kralikova M, Mobarec JC, Shi L, Filizola M, Javitch JA (2008) Dopamine D2 receptors form higher order oligomers at physiological expression levels. *EMBO J* 27(17):2293–2304. doi:[10.1038/emboj.2008.153](https://doi.org/10.1038/emboj.2008.153)
88. Hu K, Clement JF, Abrahamyan L, Strebel K, Bouvier M, Kleiman L, Mouland AJ (2005) A human immunodeficiency virus type 1 protease biosensor assay using bioluminescence resonance energy transfer. *J Virol Methods* 128(1–2):93–103. doi:[10.1016/j.jviromet.2005.04.012](https://doi.org/10.1016/j.jviromet.2005.04.012)
89. Oka T, Takagi H, Tohya Y, Murakami K, Takeda N, Wakita T, Katayama K (2011) Bioluminescence technologies to detect calicivirus protease activity in cell-free system and in infected cells. *Antiviral Res* 90(1):9–16. doi:[10.1016/j.antiviral.2011.02.002](https://doi.org/10.1016/j.antiviral.2011.02.002)
90. Dacres H, Dumancic MM, Horne I, Trowell SC (2009) Direct comparison of bioluminescence-based resonance energy transfer methods for monitoring of proteolytic cleavage. *Anal Biochem* 385(2):194–202. doi:[10.1016/j.ab.2008.10.040](https://doi.org/10.1016/j.ab.2008.10.040)
91. Rogers KL, Picaud S, Roncali E, Boisgard R, Colasante C, Stinnakre J, Tavittian B, Brulet P (2007) Non-invasive in vivo imaging of calcium signaling in mice. *PLoS ONE* 2(10):e974. doi:[10.1371/journal.pone.0000974](https://doi.org/10.1371/journal.pone.0000974)
92. Baubet V, Le Mouelliec H, Campbell AK, Lucas-Meunier E, Fossier P, Brulet P (2000) Chimeric green fluorescent protein-aequorin as bioluminescent Ca²⁺ reporters at the single-cell level. *Proc Natl Acad Sci USA* 97(13):7260–7265. doi:[10.1073/pnas.97.13.7260](https://doi.org/10.1073/pnas.97.13.7260)
93. Bakayan A, Vaquero CF, Picazo F, Llopis J (2011) Red fluorescent protein-aequorin fusions as improved bioluminescent Ca²⁺ reporters in single cells and mice. *PLoS ONE* 6(5):e19520. doi:[10.1371/journal.pone.0019520](https://doi.org/10.1371/journal.pone.0019520)
94. Miyawaki A, Llopis J, Heim R, McCaffery JM, Adams JA, Ikura M, Tsien RY (1997) Fluorescent indicators for Ca²⁺ based on green fluorescent proteins and calmodulin. *Nature* 388(6645):882–887. doi:[10.1038/42264](https://doi.org/10.1038/42264)
95. Miyawaki A, Griesbeck O, Heim R, Tsien RY (1999) Dynamic and quantitative Ca²⁺ measurements using improved cameleons. *Proc Natl Acad Sci USA* 96(5):2135–2140
96. Romoser VA, Hinkle PM, Persechini A (1997) Detection in living cells of Ca²⁺-dependent changes in the fluorescence emission of an indicator composed of two green fluorescent protein variants linked by a calmodulin-binding sequence. A new class of fluorescent indicators. *J Biol Chem* 272(20):13270–13274

97. Saito K, Hatsugai N, Horikawa K, Kobayashi K, Matsu-Ura T, Mikoshiba K, Nagai T (2010) Auto-luminescent genetically-encoded ratiometric indicator for real-time Ca²⁺ imaging at the single cell level. *PLoS ONE* 5(4):e9935. doi:[10.1371/journal.pone.0009935](https://doi.org/10.1371/journal.pone.0009935)
98. De A, Gambhir SS (2005) Noninvasive imaging of protein–protein interactions from live cells and living subjects using bioluminescence resonance energy transfer. *FASEB J* 19(14):2017–2019. doi:[10.1096/fj.05-4628fje](https://doi.org/10.1096/fj.05-4628fje)
99. Bjornsti MA, Houghton PJ (2004) The TOR pathway: a target for cancer therapy. *Nat Rev Cancer* 4(5):335–348. doi:[10.1038/nrc1362](https://doi.org/10.1038/nrc1362)
100. Kroeger KM, Hanyaloglu AC, Seeber RM, Miles LE, Eidne KA (2001) Constitutive and agonist-dependent homo-oligomerization of the thyrotropin-releasing hormone receptor. Detection in living cells using bioluminescence resonance energy transfer. *J Biol Chem* 276(16):12736–12743. doi:[10.1074/jbc.M011311200](https://doi.org/10.1074/jbc.M011311200)
101. Mercier JF, Salahpour A, Angers S, Breit A, Bouvier M (2002) Quantitative assessment of beta 1- and beta 2-adrenergic receptor homo- and heterodimerization by bioluminescence resonance energy transfer. *J Biol Chem* 277(47):44925–44931. doi:[10.1074/jbc.M205767200](https://doi.org/10.1074/jbc.M205767200)
102. Ayoub MA, Couturier C, Lucas-Meunier E, Angers S, Fossier P, Bouvier M, Jockers R (2002) Monitoring of ligand-independent dimerization and ligand-induced conformational changes of melatonin receptors in living cells by bioluminescence resonance energy transfer. *J Biol Chem* 277(24):21522–21528. doi:[10.1074/jbc.M200729200](https://doi.org/10.1074/jbc.M200729200)
103. Pflieger KD, Eidne KA (2005) Monitoring the formation of dynamic G-protein-coupled receptor-protein complexes in living cells. *Biochem J* 385(Pt 3):625–637. doi:[10.1042/BJ20041361](https://doi.org/10.1042/BJ20041361)
104. Boute N, Pernet K, Issad T (2001) Monitoring the activation state of the insulin receptor using bioluminescence resonance energy transfer. *Mol Pharmacol* 60(4):640–645
105. Issad T, Blanquart C, Gonzalez-Yanes C (2007) The use of bioluminescence resonance energy transfer for the study of therapeutic targets: application to tyrosine kinase receptors. *Exp Opin Ther Targets* 11(4):541–556. doi:[10.1517/14728222.11.4.541](https://doi.org/10.1517/14728222.11.4.541)
106. Tan PK, Wang J, Littler PL, Wong KK, Sweetnam TA, Keefe W, Nash NR, Reding EC, Piu F, Brann MR, Schiffer HH (2007) Monitoring interactions between receptor tyrosine kinases and their downstream effector proteins in living cells using bioluminescence resonance energy transfer. *Mol Pharmacol* 72(6):1440–1446. doi:[10.1124/mol.107.039636](https://doi.org/10.1124/mol.107.039636)
107. Sato M, Ozawa T, Inukai K, Asano T, Umezawa Y (2002) Fluorescent indicators for imaging protein phosphorylation in single living cells. *Nat Biotechnol* 20(3):287–294
108. Schroder M, Kroeger KM, Volk HD, Eidne KA, Grutz G (2004) Preassociation of nonactivated STAT3 molecules demonstrated in living cells using bioluminescence resonance energy transfer: a new model of STAT activation? *J Leukoc Biol* 75(5):792–797. doi:[10.1189/jlb.1003496](https://doi.org/10.1189/jlb.1003496)
109. Arai R, Nakagawa H, Tsumoto K, Mahoney W, Kumagai I, Ueda H, Nagamune T (2001) Demonstration of a homogeneous noncompetitive immunoassay based on bioluminescence resonance energy transfer. *Anal Biochem* 289(1):77–81. doi:[10.1006/abio.2000.4924](https://doi.org/10.1006/abio.2000.4924)
110. Walls ZF, Gambhir SS (2008) BRET-based method for detection of specific RNA species. *Bioconjug Chem* 19(1):178–184. doi:[10.1021/bc700278n](https://doi.org/10.1021/bc700278n)
111. Andou T, Endoh T, Mie M, Kobatake E (2011) Development of an RNA detection system using bioluminescence resonance energy transfer. *Sensor Actuat B Chem* 152(2):277–284. doi:[10.1016/j.snb.2010.12.020](https://doi.org/10.1016/j.snb.2010.12.020)
112. So MK, Xu C, Loening AM, Gambhir SS, Rao J (2006) Self-illuminating quantum dot conjugates for in vivo imaging. *Nat Biotechnol* 24(3):339–343. doi:[10.1038/nbt1188](https://doi.org/10.1038/nbt1188)
113. Frasco MF, Chaniotakis N (2009) Semiconductor quantum dots in chemical sensors and biosensors. *Sensors* 9(9):7266–7286. doi:[10.3390/s90907266](https://doi.org/10.3390/s90907266)
114. Xia Z, Xing Y, So MK, Koh AL, Sinclair R, Rao J (2008) Multiplex detection of protease activity with quantum dot nanosensors prepared by intein-mediated specific bioconjugation. *Anal Chem* 80(22):8649–8655. doi:[10.1021/ac801562f](https://doi.org/10.1021/ac801562f)

115. Kumar M, Zhang D, Broyles D, Deo SK (2011) A rapid, sensitive, and selective bioluminescence resonance energy transfer (BRET)-based nucleic acid sensing system. *Biosens Bioelectron* 30(1):133–139. doi:[10.1016/j.bios.2011.08.043](https://doi.org/10.1016/j.bios.2011.08.043)
116. Wu C, Mino K, Akimoto H, Kawabata M, Nakamura K, Ozaki M, Ohmiya Y (2009) In vivo far-red luminescence imaging of a biomarker based on BRET from *Cypridina* bioluminescence to an organic dye. *Proc Natl Acad Sci USA* 106(37):15599–15603. doi:[10.1073/pnas.0908594106](https://doi.org/10.1073/pnas.0908594106)
117. Branchini BR, Ablamsky DM, Rosenberg JC (2010) Chemically modified firefly luciferase is an efficient source of near-infrared light. *Bioconjug Chem* 21(11):2023–2030. doi:[10.1021/bc100256d](https://doi.org/10.1021/bc100256d)
118. Yu J, Guan M, Li F, Zhang Z, Wang C, Shu C, Wei H, Zhang XE (2012) Effects of fullerene derivatives on bioluminescence and application for protease detection. *Chem Commun* 48(89):11011–11013. doi:[10.1039/c2cc36099c](https://doi.org/10.1039/c2cc36099c)
119. Xu X, Soutto M, Xie Q, Servick S, Subramanian C, von Arnim AG, Johnson CH (2007) Imaging protein interactions with bioluminescence resonance energy transfer (BRET) in plant and mammalian cells and tissues. *Proc Natl Acad Sci USA* 104(24):10264–10269. doi:[10.1073/pnas.0701987104](https://doi.org/10.1073/pnas.0701987104)
120. Coulon V, Audet M, Homburger V, Bockaert J, Fagni L, Bouvier M, Perroy J (2008) Subcellular imaging of dynamic protein interactions by bioluminescence resonance energy transfer. *Biophys J* 94(3):1001–1009. doi:[10.1529/biophysj.107.117275](https://doi.org/10.1529/biophysj.107.117275)

Chapter 11

Antibody Engineering in Translational Medicine

Eliane Fischer

11.1 Introduction

Antibodies (Abs), also known as immunoglobulins (Igs), are an important component of the immune system [1]. They are produced by specialized B-cells, which secrete them into the blood stream. Abs recognize and bind to foreign antigen (e.g., bacteria, viruses, or toxins), but they also recruit additional components of the immune system to eliminate the antigen from the body. These effector functions include antibody-dependent cellular cytotoxicity (ADCC), antibody-dependent cellular phagocytosis (ADCP), and complement-dependent cellular cytotoxicity (CDC). ADCC and ADCP are mediated by interaction of cell-bound Ab with Fc gamma receptors (Fc γ R) and CDC through interaction with a series of soluble blood proteins, the so-called complement. An almost unlimited variety of Abs with different antigen specificity can potentially be generated in the human body by random combination of a set of gene segments and by somatic hypermutation [2, 3].

Due to the unique properties of this class of molecules, i.e., the combination of highly specific binding with defined effector functions, Abs have entered the clinics as a promising class of potent therapeutics. Concomitantly, the field of Ab engineering has emerged to tailor Abs for defined medical applications [4]. Given the complex structure and function of Abs, there are many different ways in which an Ab can be engineered to further improve its efficacy for therapy or diagnosis.

E. Fischer (✉)
Paul Scherrer Institute (PSI), 5232 Villigen, Switzerland
e-mail: eliane.fischer@psi.ch

11.1.1 Medical Applications of Antibodies

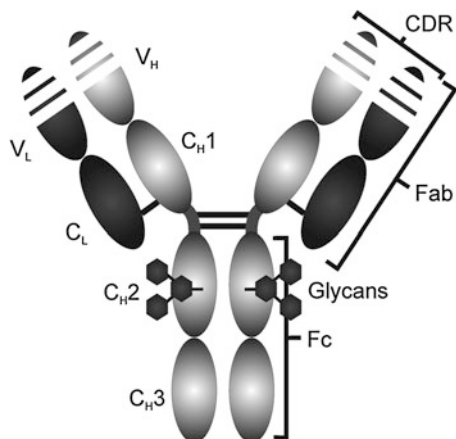
Abs are a fast-growing class of therapeutics, and there are currently about 350 Abs in clinical development [5]. Therapeutic Abs usually have only one single specificity. They are derived from a cell clone and are therefore named monoclonal antibodies (mAbs). Most mAbs in clinical trials are being evaluated as cancer therapeutics, followed by immunological disorders, such as rheumatoid arthritis, psoriasis, or Crohn disease. Therapeutic mAbs can act through various mechanisms. In cancer therapy, they often bind to cell surface antigens that are over-expressed on cancer cells and have an implication in disease progression. By binding to their targets, mAbs may block interaction of growth factors with their receptors, affect cellular signaling, or mediate cytotoxicity by ADCC. However, very often Abs are not curative as single-agent therapeutics. One of the major goals of antibody engineering is therefore the empowerment of Abs with more potent cytotoxic entities or the enhancement of their intrinsic effector functions. As a result of these strategies, only about 50 % of the Abs in clinical development for cancer therapy are nowadays canonical Abs [6]. The other half consists of engineered Abs which are conjugated to drugs or radionuclides or otherwise engineered for enhanced efficacy.

11.1.2 Antibodies: Structure and Function

Abs consist of two heavy and two light chains, which are connected by disulfide bridges (Fig. 11.1). The light chains comprise a variable and a constant domain, while the heavy chains consist of a variable and three constant domains. The variable region of the Ab is responsible for antigen binding. Within each of the variable domains are three hyper-variable regions complementarity determining regions (CDRs), which account for most of the diversity among the antibody sequences. The CDRs are flanked by more conserved sequences of the variable domains, the framework regions. It is the diversity in the CDRs that ultimately leads to the specificity and affinity of an Ab for its target antigen. In contrast, the constant region of the heavy chain defines the Ab isotype and is responsible for the effector functions and the half-life in blood. Upon enzymatic digestion with papain, three fragments of similar size are obtained: two fragments antigen-binding (Fab) and a fragment crystallizable (Fc).

Most therapeutic mAbs are of the γ -immunoglobulin (IgG) isotype. IgG has a particularly long half-life in serum, due to a recycling mechanism based on the interaction with the neonatal Fc receptor (FcRn). Endocytosed IgG binds with its Fc part to the FcRn at pH 6.0–6.5 in the endosomes and recycles to the blood serum. IgG contain a single *N*-glycosylation site in the constant region of each heavy chain. The attached glycans have been shown to play a crucial role for some of the effector functions, but also contribute to the stability of the Ab. There are

Fig. 11.1 Structure of an antibody (IgG1). IgG1 consists of two heavy chains (*gray*) and two light chains (*black*) which are connected by disulfide bonds. The heavy chain contains three constant domains (C_{H1} – C_{H3}), a variable domain (V_H), and a hinge region between C_{H1} and C_{H2} . The light chain contains a constant (C_L) and a variable (V_L) domain



four different subtypes of IgG in humans (IgG1–IgG4), which have different structural features and biological properties.

11.2 Reducing Immunogenicity of Therapeutic Antibodies

Rodent Abs The *in vitro* production of murine mAbs from hybridoma cell lines first made it possible to use this class of molecules as therapeutics [7]. However, murine mAbs (suffix: -omab) are immunogenic in humans and induce human anti-mouse Abs (HAMA) [8]. This precludes repeated administration of murine mAbs and therefore long-term therapy. In addition, the half-life of murine mAbs in humans is relatively short, and they are not efficient in recruiting effector functions. Despite these difficulties, several murine mAbs have been approved by the FDA, primarily for diagnostic use.

Chimeric Abs A first attempt to reduce the immunogenicity of murine mAbs was the design of chimeric mouse–human Abs (suffix: -ximab). The variable regions of rodent heavy and light chains were grafted onto the constant regions of human IgG1 by recombinant DNA techniques [9–11]. Chimeric mAbs exhibited a longer half-life in humans and were less immunogenic than murine mAbs. In addition, the isotype relevant to the desired biological function of the mAb, typically IgG1, could be chosen by the chimerization technique. Several chimeric mAbs have been approved as therapeutics, for example, cetuximab, rituximab, or infliximab. However, about 33 % of the sequence is still of mouse origin and induce the human anti-chimeric antibody (HACA) response [12].

Humanized Abs To confine the potential immunogenicity of therapeutic mAbs, further reduction of the mouse sequences was approached by various methods. Humanized Abs (suffix: -zumab) obtained by *CDR-grafting* contain only the hypervariable regions from the original mouse mAb [13]. This method often

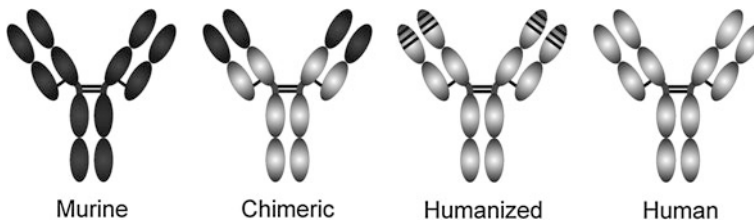


Fig. 11.2 Monoclonal antibody types. Murine sequences are shown in *dark*, human sequences in *light gray*

requires the introduction of some amino acids from the original mouse sequence into the framework regions of the variable domains, in order to retain the binding properties of the original Ab in a process termed *reshaping* [14]. CDR grafting results in humanized Abs with about 95 % of the sequence of human origin (Fig. 11.2).

Further reduction of the murine sequences can be achieved by *SDR transfer* instead of CDR grafting. Only 20–33 % of the CDR residues have been found to participate in antigen binding. These “specificity determining residues” (SDR) were successfully grafted to human Ab sequences with “abbreviated CDRs” [15]. Alternatively, in a process termed *veneering* or *resurfacing*, only the surface residues of the framework regions of murine variable domains are replaced with human residues [16, 17], while the remaining sequences, including CDRs and buried amino acids, remain murine.

DeImmunization Deimmunization is a technique by which potential linear T cell epitopes in Ab sequences are predicted by bioinformatic approaches [18]. Specifically, known human HLA class I or class II epitopes are identified *in silico*. Potential T cell epitopes can then be altered by appropriate amino acid substitution. A similar approach aims at the removal of both T and B cell epitopes using human string content (HSC) [19].

Human Abs Fully human Abs (suffix: -umab) can be generated by *in vitro* display techniques, including phage display [20–22] or yeast display [23]. Phage display libraries consist of a large diversity ($>10^9$) of filamentous bacteriophage, each expressing a different Ab fragment. Typically, Fab fragments or single-chain variable fragments (scFv) are presented on the phage. The diversity of such *in vitro* libraries can either be derived from a human antibody repertoire or generated synthetically. The library is screened against the target antigen to enrich for target-binding Ab fragments. This procedure usually requires several rounds of selection to obtain high-affinity Ab fragments. *In vitro* selection of Abs allows close control over stringency and specificity. For example, it is possible to include steps into the selection strategy that allow enrichment of Abs that cross-react with the rodent variant of the antigen or to deselect Abs that cross-react with homologous proteins.

Alternatively, fully human mAbs can be generated in transgenic mouse strains with inactivated mouse immunoglobulin genes which have been replaced with the corresponding human gene sequences [24–27]. Many different transgenic mouse

platforms have been developed and yielded human mAbs for clinical development. Today, human mAbs are the fastest growing category of mAb therapeutics entering clinical studies [28].

11.3 Engineering Pharmacokinetics

IgG have a relatively long half-life in blood, ranging from 7 to more than 16 days. One major goal of Ab engineering is to further prolong the half-life of therapeutic mAbs in circulation, in order to maintain therapeutic mAb levels and to allow for less frequent dosing. On the other hand, a shorter half-life may be of interest for radiolabeled Abs, for example, to control toxicity or to reduce background radiation in imaging. Mutations have been introduced in the Fc part of IgG1 in order to increase binding to FcRn under acidic conditions. These mutations lead to an optimized recycling of the engineered mAb through FcRn binding in endosomes and thus to a longer half-life [29, 30]. Further, the fast-clearing isotypes IgG2, IgG3, and IgG4 have been engineered in their Fc part to improve half-life and stability in blood [31–33].

A variable that contributes to the non-specific clearance of mAbs is their isoelectric point (pI). Non-specific clearance is a result of pinocytosis of Ab into the endosomes and subsequent lysosomal degradation of the non-FcRn-bound Ab [34]. A higher pI generally results in a faster clearance of the mAb [35]. Lowering the pI by engineering the variable region is therefore a promising approach to increase the half-life of some mAbs [36]. In addition to mutagenesis, chemical modification has been used to improve the pharmacokinetics by altering the pI [37].

Finally, antigen-mediated clearance may contribute to the clearance rate of an mAb. Similar to the FcRn binding described above, Abs have been engineered for pH-dependent antigen binding [38]. These Abs maintain high binding affinity at neutral pH, but dissociate rapidly from their target in the acidic environment of the endosomes. The antibody then recycles back to the cell surface and is rescued from lysosomal degradation [39, 40].

11.4 Enhancing Therapeutic Efficacy

Monoclonal antibodies are an important class of cancer therapeutics and widely used in the clinics today. However, they often are not sufficiently effective as monotherapies and need to be combined with chemotherapeutics. Hence, Abs have been engineered to become more potent cytotoxic drugs. There are several strategies that aim at the generation of more cytotoxic Ab constructs. These include engineering to enhance intrinsic effector functions or the introduction of an additional cytotoxic moiety attached to the Ab. In the latter cases, the Ab's effector

functions play a subordinate role as does the biological significance of the target for disease development. The Ab simply becomes a vehicle which delivers cytotoxic payload to the tumor cells.

11.4.1 Fc Engineering to Enhance Effector Functions

IgG are able to induce ADCC by interaction with the Fc γ R which is expressed on cytotoxic T lymphocytes and natural killer cells. Improving the binding of the IgG to Fc γ R could therefore improve the therapeutic efficacy of mAbs where these effector functions are the mechanism of action to destroy the target cells.

The Asn297-linked glycans of an IgG play an important role in the interaction with the Fc γ R. It has been demonstrated that engineering of the glycan structure by the presence of a bisecting N-acetylglucosamine or the absence of fucose enhances the binding to the Fc γ RIII and consequently improves ADCC [41, 42]. The glycoengineered Abs are obtained from mutant CHO cell lines which are expressing or lacking the corresponding sugar-modifying enzymes.

Mutagenesis of amino acids close to the hinge region of the C_H2 domain has been shown to improve binding to Fc γ R. Several of these mutants exhibited enhanced ADCC in vitro [43, 44]. Both Fc and glycoengineered Abs are currently being evaluated in clinical trials.

11.4.2 Antibody–Drug Conjugates

Antibody–drug conjugates (ADCs) combine the specificity and targeting properties of an mAb with the potency of a cytotoxic drug [45]. Typically, a cytotoxic small molecule is chemically linked to an mAb which binds to an antigen expressed on the cell membrane of cancer cells. Upon binding, the ADC–antigen complex is internalized into the cell and transported along the endosomal–lysosomal pathway. The attached drug is eventually released from the ADC and becomes active within the cell by interfering with vital cellular processes. It is a prerequisite that the cytotoxic drug is extremely potent and exhibits its cytotoxic potential at low concentrations. While early ADCs employed classical chemotherapeutics as drugs such as vinblastine, doxorubicin, or methotrexate, typical drugs now include highly potent microtubule-targeting agents (auristatins, maytansinoids) or DNA-damaging drugs (calicheamicins, duocarmycins). Due to their high systemic toxicity and lack of specificity for cancer cells, these drugs cannot be used as single-agent therapeutics.

To ensure controlled release of the drug within the target cells, a linker has to be introduced between the mAb and the cytotoxic drug [46]. These linkers have to be stable in circulation to prevent spontaneous release of the drug and consequential damage to non-targeted tissue. Current linker strategies include the following:

- Acid-labile hydrazone linkers, which are cleaved in the low-pH environment of the endosomes (pH 5.0–6.5) and lysosomes (pH 4.5–5.0), but relatively stable in the bloodstream (pH 7.3–7.5).
- Disulfide-based linkers, which are cleaved in the reducing environment of the cytosol.
- Non-cleavable thioether linkers, which depend on the degradation of the mAb in the lysosome and result in the release of drug still attached to the linker and the amino acid (usually lysine) to which the drug has been attached [47].
- Linkers that are cleaved by specific enzymes of the lysosomes (e.g., cathepsin B or β -glucuronidase). These include dipeptide linkers (e.g., citrulline–valine or phenylalanine–lysine) [48, 49].

Dipeptide and thioether linkers are more stable in circulation than the chemically cleavable hydrazone or disulfide-based linkers. However, the cytotoxic metabolite resulting from the cleavage of thioether-linked ADCs is charged and has been shown to be less cytotoxic on neighboring cells than the corresponding product from a cleavable linker.

Wyeth's Mylotarg (anti-CD33 humanized IgG4 mAb conjugated to a calicheamicin by a hydrazone linker) was the first ADC to reach the market [50]. It was withdrawn by Pfizer in 2010 because of limited clinical benefits and safety concerns. Adectris (Brentuximab Vedotin) and anti-CD30 chimeric mAb conjugated to auristatin E (MMAE) received FDA approval in 2011 [51] for the treatment of Hodgkin lymphoma and anaplastic large-cell lymphoma. Recently, FDA approved the maytansinoid-based ADC Trastuzumab emtansine (T-DM1, Roche/Genentech) for breast cancer [52]. The three ADCs that have reached the market so far are different in linker strategy, target antigen, and drug (Table 11.1). Many ADCs are now in early-stage clinical testing [45]. Future developments address new highly potent drugs, more uniform production of ADCs, and the better penetration of solid tumors by ADCs, for example, by using antibody fragments or non-IgG scaffolds.

One of the difficulties associated with ADC production is the resulting heterogeneous mixtures after chemical conjugation of cytotoxic drugs. In principle, each of the ADC species in the mixture can come with a different pharmacokinetic, therapeutic, and safety profile [53]. Recently, various strategies have been described to generate more homogeneous ADC, both regarding the sites to which the drugs are attached and the number of drugs that are loaded on an Ab. Generally, a drug-to-antibody ratio of about 2–4 is desirable. Coupling fewer drugs per antibody would compromise efficacy of the ADC. On the other hand, a higher drug load may negatively affect stability, circulation half-life, or binding to the target.

One example of a strategy that yields homogeneous ADCs are THIOMABs, in which the drugs are linked to defined, engineered cysteine residues [54]. Other approaches include enzymatic modification by transglutaminase of deglycosylated mAbs [55] or introduction of non-natural amino acids into the mAb constant regions for subsequent chemical modification [56].

Table 11.1 Antibody–drug conjugates that reached the market by 2013

ADC		Status	Antigen	Linker	Drug
Mylotarg	Gemtuzumab ozogamicin	Withdrawn	CD33	Hydrazone	Calicheamicin
Adectris	Brentuximab vedotin	Approved	CD30	Citrulline-valine	MMAE
T-DM1	Trastuzumab emtansine	Approved	HER2	Thioether	Maytansinoid

11.4.3 Radioimmunoconjugates

Radioimmunoconjugates are a special class of antibody conjugates with enhanced toxicity. The concept of empowering an mAb with cytotoxic radiation is similar to the ADCs described above. However, the unique properties of radioactive decay entail several special features of radioimmunoconjugates.

Unlike cytotoxic drugs, the radionuclide attached to the antibody does not need to be cleaved from the antibody to become activated. Radioactivity does not only affect the target cell, but also affect neighboring antigen-negative cells. This so-called “cross-fire” effect is one of the attractive features of radioimmunotherapy, especially for tumors with heterogenous antigen expression.

Radionuclides which emit α or β^- radiation are most suitable for radioimmunotherapy because of their short range in tissue (Table 11.2). The radiolabeled antibody accumulates at the tumor site, and the energy from the emitted radiation is deposited near the tumor cells. Depending on the type of radiation, single cells, small clusters of cells, or small tumors can be efficiently irradiated [57]. Auger electrons are a third type of radiation which is potentially useful to eradicate single cells. However, due to the very short range in tissue, Auger electrons have to be brought close to the nucleus of the cell to introduce enough DNA damage for efficient cytotoxicity [58]. Therapeutic radionuclides in current clinical trials include primarily the β^- emitters ^{90}Y , ^{177}Lu , and ^{131}I [59]. The choice of a suitable radionuclide is not only dependent on the range of the radiation in tissue, but also dependent on the radiochemistry, the physical half-life of the radionuclide, and the availability of the radionuclide. While iodination can be achieved by direct modification of tyrosine residues of an Ab, radiometals have to be attached to proteins using a chelating agent. Two radioimmunoconjugates have been approved for the treatment of non-Hodgkin’s lymphoma, both targeting CD20: ^{131}I -tositumomab (Bexxar) and ^{90}Y -ibritumomab (Zevalin).

One of the problems associated with radioimmunotherapy is hematological toxicity. Due to the long circulation times of mAbs in blood, the bone marrow is continuously exposed to irradiation. Attempts to reduce the half-lives of mAbs in circulation, including the use of antibody fragments, generally lead to significantly lower tumor uptake and retention, which again impairs their therapeutic value.

Pretargeting is a strategy to decouple the slow pharmacokinetics of mAbs from the radioactive moiety [60]. Briefly, a tumor-targeting mAb derivative with high affinity for the radioactive moiety is injected first. The mAb is allowed to accumulate at the target site, which usually reaches highest uptake after about two days. In a second step, the small radioactive molecule is administered. It is crucial

Table 11.2 Examples of radionuclides suitable for radioimmunotherapy

Radionuclide	Half-life	Radiation	Maximum range in tissue
^{177}Lu	6.6 days	β^-	2 mm
^{90}Y	2.7 days	β^-	12 mm
^{131}I	8.0 days	β^-	2 mm
^{225}Ac	10 days	α^{-1}	50–100 μm
^{211}At	7.2 h	α	50–100 μm
^{125}I	59.4 days	Auger electrons	<10 μm
^{67}Ga	3.3 days	Auger electrons	<10 μm

for pretargeting approaches that the antibody does not internalize completely into the target cells, because it needs to remain accessible for the radioactive moiety. One of the pretargeting strategies uses antibody–(strept) avidin constructs and a biotinylated chelating agent containing the radionuclide [61], which has a very fast blood clearance. While the pretargeting approach worked in principle, there were several issues associated with this system, including the immunogenicity of streptavidin. Other pretargeting strategies focus on bispecific Ab constructs targeting both tumor antigen and a small molecule or peptide containing the radionuclide [62]. Pretargeting strategies usually result in excellent biodistributions with very high tumor-to-blood ratios of the radionuclide.

Because of their ability to bind antigen with high affinity and specificity, radiolabeled Abs are useful tools for *in vivo* molecular imaging. To this aim, Abs can be labeled with diagnostic radionuclides, for example, for positron emission tomography (PET) or single-photon emission computed tomography (SPECT) [63]. In contrast to therapeutic agents, a long half-life in blood is not desired for imaging probes, because it leads to a high background. Further, accumulation at the tumor site by mAbs is slow, and radiolabeling with short-lived radioisotopes is not feasible. Instead, suitable radionuclides for PET or SPECT imaging include radionuclides with physical half-lives of >10 h (Table 11.3).

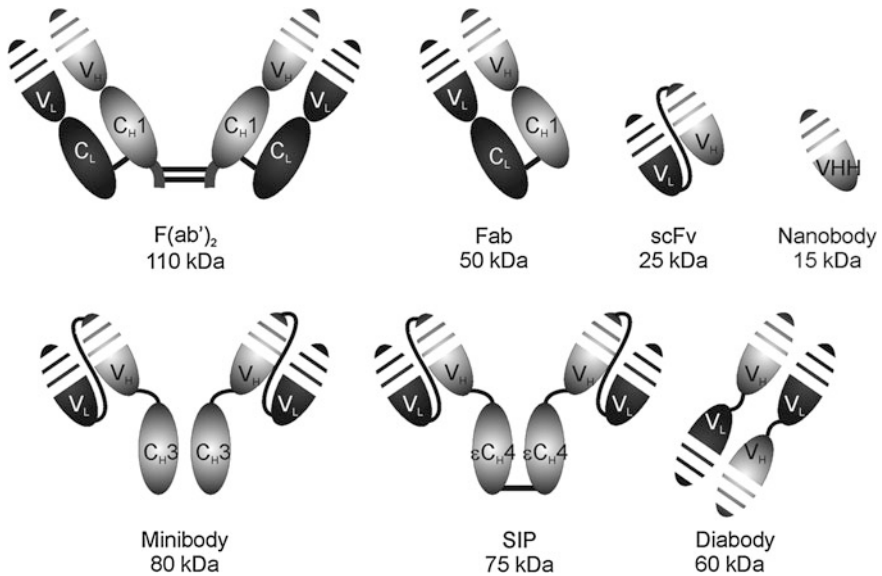
11.5 Engineered Antibody Fragments

For a range of applications, but especially for imaging, smaller Ab fragments including Fab, scFv, or single-domain Abs (Fig. 11.3) are often preferred to full-length IgG because of their faster accumulation and blood clearance and better tissue penetration [64]. To retain avidity, many different bivalent Ab formats have been developed, including $\text{F}(\text{ab}')_2$ fragments, diabodies, SIPs, and minibodies [65].

Many of these engineered Ab fragments can be easily expressed in prokaryotes. This is another advantage over IgGs, which have to be produced in mammalian cells. Because the fragment Fv consisting of V_H and V_L , is not stable, single-chain variable fragments (scFv) have been developed. In this format, a linker connects V_H and V_L . By choosing a shorter linker, a bivalent diabody forms [66]. Other

Table 11.3 Radionuclides for immuno-PET or immuno-SPECT

Radionuclide	Half-life	Imaging modality
^{64}Cu	12.7 h	PET
^{89}Zr	3.3 days	PET
^{111}In	2.8 days	SPECT
^{67}Ga	3.3 days	SPECT

**Fig. 11.3** Examples of different antibody formats and engineered antibody fragments

formats use the C_H3 domain (Minibody [67]) or the C_H4 domain from IgE (small immunoprotein, SIP [68]) to form bivalent molecules from scFv. Single-domain Abs are even smaller, with a molecular weight of only about 15 kDa. While single-domain Abs (V_H) from human or mouse origin are not stable, other species, including sharks and camelids, have stable variable domains, V_{HH}, because these Abs lack light chains [69]. Nanobodies from llama are the most widely used single-domain Ab fragments. These molecules are easy to express in bacteria and have exceptional thermal and conformational stability.

11.6 Bispecific Antibodies

Bispecific Abs are engineered Ab-based molecules that bind two target epitopes. Many different formats have been described [70]. Some of them consist of tandem antibody fragments or bispecific diabodies, and others attach an additional binding

fragment to full-length IgGs. Bispecific Ab constructs are either obtained by genetic engineering or by chemical conjugation to native IgGs. However, many of these formats have unfavorable pharmacokinetic or physicochemical properties. Closest to a native antibody are bispecific IgGs in which each Fab arm has a different specificity. Controlled production of these asymmetric molecules for clinical use is challenging because the correct assembly of heavy and light chains needs to be established.

Bispecific IgGs were first obtained from hybrid hybridomas (quadromas), which produce two different heavy and light chains within one cell [71]. Because the assembly of heavy and light chains is stochastic, this leads to the formation of side products due to wrong pairing of heavy and light chains. The resulting IgGs have to be purified by two-step affinity chromatography. Various strategies have been followed to produce more uniform bispecific Abs. The “Knobs-into-holes” technology [72] introduces two different mutations into the C_{H3} domains of the heavy chains of either specificity. A bulky amino acid residue (“knob”) on one heavy chain and a small amino acid residue (“hole”) on the other. This technique significantly favors the heterodimeric pairing of heavy chains. Similarly, electrostatic steering [73] introduces negative charge on one heavy chain and positive charge on the other to yield a higher fraction of heterodimeric IgG. Both approaches have the limitation that the light chains are still randomly paired with the heterodimeric heavy chains. To overcome this limitation, invariant light chains, which do not participate in antigen binding, have been employed with these constructs [74]. In CrossMabs technology [75], domains between heavy and light chains are swapped in one arm of the antibody, leading to correct pairing of heavy and light chains. Combining CrossMab technology with Knobs-into-holes, uniform bispecific IgGs can be produced. Controlled Fab arm exchange [76] allows the formation of bispecific Abs from two different parental IgG under controlled reducing conditions *in vitro*. Again, matched point mutations in the C_{H3} domains are required to form stable heterodimers. A totally different approach to obtain mAbs with specificity for two epitopes is the selection of so-called two-in-one Abs [77]. Here, the sequences of the light chain CDRs of an existing mAb were mutated, and mAbs with dual specificity were selected by phage display.

Bispecific Abs can be used as therapeutics which simultaneously bind to two different disease-specific targets, thereby potentially enhancing specificity or efficacy. A very promising use of bispecific Abs is retargeting. Thereby, one arm of the Ab binds to a disease-specific target, and the other recruits a cytotoxic entity. Most prominently, CD3 on T cells or CD16 on natural killer cells are recognized by bispecific mAbs to recruit these immune cells to the diseased tissue. Catumaxomab [78], binding to EpCAM and CD3, was approved in Europe in 2009 for treatment of malignant ascites. Further, bispecific Abs are widely used in pretargeting strategies, as described in Sect. 11.4.3.

Finally, bispecific Abs have been designed for delivery into the brain [79]. A bispecific Ab which binds to the transferrin receptor (TfR) and the enzyme β -secretase has been developed for treatment of Alzheimer’s disease. This bispecific

Ab is able to cross the blood brain barrier in preclinical studies by low-affinity binding to the TfR and subsequent receptor-mediated transcytosis [80].

11.7 Conclusion

More than 25 years after the approval of the first murine mAb for therapeutic use, mAb-based therapeutics have become diverse in shape and function. The field of Ab engineering continues to develop strategies that empower Abs with novel mechanisms of action or further enhance their intrinsic properties as excellent targeting molecules.

References

1. Owen JA, Punt J, Stranford SA, Jones PP, Kuby J (2013) Kuby immunology, 7th edn. W.H Freeman, New York
2. Market E, Papavasiliou FN (2003) V(D)J recombination and the evolution of the adaptive immune system. *PLoS Biol* 1(1):E16
3. Diaz M, Casali P (2002) Somatic immunoglobulin hypermutation. *Curr Opin Immunol* 14(2):235–240
4. Buss NA, Henderson SJ, McFarlane M, Shenton JM, de Haan L (2012) Monoclonal antibody therapeutics: history and future. *Curr Opin Pharmacol* 12(5):615–622
5. Reichert JM (2013) Which are the antibodies to watch in 2013? *MABs* 5(1):1–4
6. Reichert JM, Dhimolea E (2012) The future of antibodies as cancer drugs. *Drug Discov Today* 17(17–18):954–963
7. Köhler G, Milstein C (1975) Continuous cultures of fused cells secreting antibody of predefined specificity. *Nature* 256(5517):495–497
8. Mirick GR, Bradt BM, Denardo SJ, Denardo GL (2004) A review of human anti-globulin antibody (HAGA, HAMA, HACA, HAHA) responses to monoclonal antibodies. Not four letter words. *Q J Nucl Med Mol Imaging* 48(4):251–257
9. Morrison SL, Johnson MJ, Herzenberg LA, Oi VT (1984) Chimeric human antibody molecules: mouse antigen-binding domains with human constant region domains. *Proc Natl Acad Sci USA* 81(21):6851–6855
10. Boulianne GL, Hozumi N, Shulman MJ (1984) Production of functional chimaeric mouse/human antibody. *Nature* 312(5995):643–646
11. Neuberger MS, Williams GT, Mitchell EB, Jouhal SS, Flanagan JG, Rabbitts TH (1985) A hapten-specific chimaeric IgE antibody with human physiological effector function. *Nature* 314(6008):268–270
12. Brüggemann M, Winter G, Waldmann H, Neuberger MS (1989) The immunogenicity of chimeric antibodies. *J Exp Med* 170(6):2153–2157
13. Jones PT, Dear PH, Foote J, Neuberger MS, Winter G (1986) Replacing the complementarity-determining regions in a human antibody with those from a mouse. *Nature* 321(6069):522–525
14. Riechmann L, Clark M, Waldmann H, Winter G (1988) Reshaping human antibodies for therapy. *Nature* 332(6162):323–327
15. Padlan EA, Abergel C, Tipper JP (1995) Identification of specificity-determining residues in antibodies. *FASEB J* 9(1):133–139

16. Padlan EA (1991) A possible procedure for reducing the immunogenicity of antibody variable domains while preserving their ligand-binding properties. *Mol Immunol* 28(4–5):489–498
17. Pedersen JT, Henry AH, Searle SJ, Guild BC, Roguska M, Rees AR (1994) Comparison of surface accessible residues in human and murine immunoglobulin Fv domains. Implication for humanization of murine antibodies. *J Mol Biol* 235(3):959–973
18. Baker MP, Jones TD (2007) Identification and removal of immunogenicity in therapeutic proteins. *Curr Opin Drug Discov Devel* 10(2):219–227
19. Lazar GA, Desjarlais JR, Jacinto J, Karki S, Hammond PW (2007) A molecular immunology approach to antibody humanization and functional optimization. *Mol Immunol* 44(8):1986–1998
20. McCafferty J, Griffiths AD, Winter G, Chiswell DJ (1990) Phage antibodies: filamentous phage displaying antibody variable domains. *Nature* 348(6301):552–554
21. Clackson T, Hoogenboom HR, Griffiths AD, Winter G (1991) Making antibody fragments using phage display libraries. *Nature* 352(6336):624–628
22. Vaughan TJ, Williams AJ, Pritchard K, Osbourn JK, Pope AR, Earnshaw JC, McCafferty J, Hodits RA, Wilton J, Johnson KS (1996) Human antibodies with sub-nanomolar affinities isolated from a large non-immunized phage display library. *Nat Biotechnol* 14(3):309–314
23. Boder ET, Wittrup KD (1997) Yeast surface display for screening combinatorial polypeptide libraries. *Nat Biotechnol* 15(6):553–557
24. Green LL (1999) Antibody engineering via genetic engineering of the mouse: XenoMouse strains are a vehicle for the facile generation of therapeutic human monoclonal antibodies. *J Immunol Methods* 231(1–2):11–23
25. Green LL, Hardy MC, Maynard-Currie CE, Tsuda H, Louie DM, Mendez MJ, Abderrahim H, Noguchi M, Smith DH, Zeng Y, David NE, Sasai H, Garza D, Brenner DG, Hales JF, McGuinness RP, Capon DJ, Klapholz S, Jakobovits A (1994) Antigen-specific human monoclonal antibodies from mice engineered with human Ig heavy and light chain YACs. *Nat Genet* 7(1):13–21
26. Lonberg N (2005) Human antibodies from transgenic animals. *Nat Biotechnol* 23(9):1117–1125
27. Lonberg N, Taylor LD, Harding FA, Trounstein M, Higgins KM, Schramm SR, Kuo CC, Mashayekh R, Wymore K, McCabe JG et al (1994) Antigen-specific human antibodies from mice comprising four distinct genetic modifications. *Nature* 368(6474):856–859
28. Nelson AL, Dhimolea E, Reichert JM (2010) Development trends for human monoclonal antibody therapeutics. *Nat Rev Drug Discov* 9(10):767–774
29. Dall'Acqua WF, Kiener PA, Wu H (2006) Properties of human IgG1 s engineered for enhanced binding to the neonatal Fc receptor (FcRn). *J Biol Chem* 281(33):23514–23524
30. Zalevsky J, Chamberlain AK, Horton HM, Karki S, Leung IW, Sproule TJ, Lazar GA, Roopenian DC, Desjarlais JR (2010) Enhanced antibody half-life improves in vivo activity. *Nat Biotechnol* 28(2):157–159
31. Stapleton NM, Andersen JT, Stemerding AM, Bjarnarson SP, Verheul RC, Gerritsen J, Zhao Y, Kleijer M, Sandlie I, de Haas M, Jonsdottir I, van der Schoot CE, Vidarsson G (2011) Competition for FcRn-mediated transport gives rise to short half-life of human IgG3 and offers therapeutic potential. *Nat Commun* 2:599
32. Lu Y, Harding SE, Rowe AJ, Davis KG, Fish B, Varley P, Gee C, Mulot S (2008) The effect of a point mutation on the stability of IgG4 as monitored by analytical ultracentrifugation. *J Pharm Sci* 97(2):960–969
33. Vaccaro C, Zhou J, Ober RJ, Ward ES (2005) Engineering the Fc region of immunoglobulin G to modulate in vivo antibody levels. *Nat Biotechnol* 23(10):1283–1288
34. Lobo ED, Hansen RJ, Balthasar JP (2004) Antibody pharmacokinetics and pharmacodynamics. *J Pharm Sci* 93(11):2645–2668
35. Boswell CA, Tesar DB, Mukhyala K, Theil FP, Fielder PJ, Khawli LA (2010) Effects of charge on antibody tissue distribution and pharmacokinetics. *Bioconjug Chem* 21(12):2153–2163

36. Igawa T, Tsunoda H, Tachibana T, Maeda A, Mimoto F, Moriyama C, Nanami M, Sekimori Y, Nabuchi Y, Aso Y, Hattori K (2010) Reduced elimination of IgG antibodies by engineering the variable region. *Protein Eng Des Sel* 23(5):385–392
37. Sharifi J, Khawli LA, Hornick JL, Epstein AL (1998) Improving monoclonal antibody pharmacokinetics via chemical modification. *Q J Nucl Med* 42(4):242–249
38. Vincent KJ, Zurini M (2012) Current strategies in antibody engineering: Fc engineering and pH-dependent antigen binding, bispecific antibodies and antibody drug conjugates. *Biotechnol J* 7(12):1444–1450
39. Igawa T, Ishii S, Tachibana T, Maeda A, Higuchi Y, Shimaoka S, Moriyama C, Watanabe T, Takubo R, Doi Y, Wakabayashi T, Hayasaka A, Kadono S, Miyazaki T, Haraya K, Sekimori Y, Kojima T, Nabuchi Y, Aso Y, Kawabe Y, Hattori K (2010) Antibody recycling by engineered pH-dependent antigen binding improves the duration of antigen neutralization. *Nat Biotechnol* 28(11):1203–1207
40. Chaparro-Riggers J, Liang H, DeVay RM, Bai L, Sutton JE, Chen W, Geng T, Lindquist K, Casas MG, Boustany LM, Brown CL, Chabot J, Gomes B, Garzone P, Rossi A, Strop P, Shelton D, Pons J, Rajpal A (2012) Increasing serum half-life and extending cholesterol lowering in vivo by engineering antibody with pH-sensitive binding to PCSK9. *J Biol Chem* 287(14):11090–11097
41. Shields RL, Lai J, Keck R, O'Connell LY, Hong K, Meng YG, Weikert SH, Presta LG (2002) Lack of fucose on human IgG1 N-linked oligosaccharide improves binding to human FcγRIII and antibody-dependent cellular toxicity. *J Biol Chem* 277(30):26733–26740
42. Umana P, Jean-Mairet J, Moudry R, Amstutz H, Bailey JE (1999) Engineered glycoforms of an antineuroblastoma IgG1 with optimized antibody-dependent cellular cytotoxic activity. *Nat Biotechnol* 17(2):176–180
43. Lazar GA, Dang W, Karki S, Vafa O, Peng JS, Hyun L, Chan C, Chung HS, Eivazi A, Yoder SC, Vielmetter J, Carmichael DF, Hayes RJ, Dahiyat BI (2006) Engineered antibody Fc variants with enhanced effector function. *Proc Natl Acad Sci USA* 103(11):4005–4010
44. Shields RL, Namenuk AK, Hong K, Meng YG, Rae J, Briggs J, Xie D, Lai J, Stadlen A, Li B, Fox JA, Presta LG (2001) High resolution mapping of the binding site on human IgG1 for FcγRI, FcγRII, FcγRIII, and FcγRn and design of IgG1 variants with improved binding to the FcγRIII. *J Biol Chem* 276(9):6591–6604
45. Sievers EL, Senter PD (2013) Antibody-drug conjugates in cancer therapy. *Annu Rev Med* 64:15–29
46. Ducry L, Stump B (2010) Antibody-drug conjugates: linking cytotoxic payloads to monoclonal antibodies. *Bioconjug Chem* 21(1):5–13
47. Erickson HK, Park PU, Widdison WC, Kovtun YV, Garrett LM, Hoffman K, Lutz RJ, Goldmacher VS, Blattler WA (2006) Antibody-maytansinoid conjugates are activated in targeted cancer cells by lysosomal degradation and linker-dependent intracellular processing. *Cancer Res* 66(8):4426–4433
48. Doronina SO, Toki BE, Torgov MY, Mendelsohn BA, Cerveny CG, Chace DF, DeBlanc RL, Gearing RP, Bovee TD, Siegall CB, Francisco JA, Wahl AF, Meyer DL, Senter PD (2003) Development of potent monoclonal antibody auristatin conjugates for cancer therapy. *Nat Biotechnol* 21(7):778–784
49. Doronina SO, Bovee TD, Meyer DW, Miyamoto JB, Anderson ME, Morris-Tilden CA, Senter PD (2008) Novel peptide linkers for highly potent antibody-auristatin conjugate. *Bioconjug Chem* 19(10):1960–1963
50. Bross PF, Beitz J, Chen G, Chen XH, Duffy E, Kieffer L, Roy S, Sridhara R, Rahman A, Williams G, Pazdur R (2001) Approval summary: gemtuzumab ozogamicin in relapsed acute myeloid leukemia. *Clin Cancer Res* 7(6):1490–1496
51. Katz J, Janik JE, Younes A (2011) Brentuximab Vedotin (SGN-35). *Clin Cancer Res* 17(20):6428–6436
52. Lewis Phillips GD, Li G, Dugger DL, Crocker LM, Parsons KL, Mai E, Blattler WA, Lambert JM, Chari RV, Lutz RJ, Wong WL, Jacobson FS, Koeppen H, Schwall RH, Kenkare-Mitra SR, Spencer SD, Sliwkowski MX (2008) Targeting HER2-positive breast

- cancer with trastuzumab-DM1, an antibody–cytotoxic drug conjugate. *Cancer Res* 68(22):9280–9290
53. Hamblett KJ, Senter PD, Chace DF, Sun MM, Lenox J, Cerveny CG, Kissler KM, Bernhardt SX, Kopcha AK, Zabinski RF, Meyer DL, Francisco JA (2004) Effects of drug loading on the antitumor activity of a monoclonal antibody drug conjugate. *Clin Cancer Res* 10(20):7063–7070
 54. Junutula JR, Flagella KM, Graham RA, Parsons KL, Ha E, Raab H, Bhakta S, Nguyen T, Dugger DL, Li G, Mai E, Lewis Phillips GD, Hilaragi H, Fuji RN, Tibbitts J, Vandlen R, Spencer SD, Scheller RH, Polakis P, Sliwkowski MX (2010) Engineered thio-trastuzumab-DM1 conjugate with an improved therapeutic index to target human epidermal growth factor receptor 2-positive breast cancer. *Clin Cancer Res* 16(19):4769–4778
 55. Jeger S, Zimmermann K, Blanc A, Grunberg J, Honer M, Hunziker P, Struthers H, Schibli R (2010) Site-specific and stoichiometric modification of antibodies by bacterial transglutaminase. *Angew Chem Int Ed Engl* 49(51):9995–9997
 56. Axup JY, Bajjuri KM, Ritland M, Hutchins BM, Kim CH, Kazane SA, Halder R, Forsyth JS, Santidrian AF, Stafin K, Lu Y, Tran H, Seller AJ, Biroc SL, Szydlak A, Pinkstaff JK, Tian F, Sinha SC, Felding-Habermann B, Smider VV, Schultz PG (2012) Synthesis of site-specific antibody-drug conjugates using unnatural amino acids. *Proc Natl Acad Sci, USA*
 57. Koppe MJ, Postema EJ, Aarts F, Oyen WJ, Bleichrodt RP, Boerman OC (2005) Antibody-guided radiation therapy of cancer. *Cancer Metastasis Rev* 24(4):539–567
 58. Cornelissen B, Vallis KA (2010) Targeting the nucleus: an overview of Auger-electron radionuclide therapy. *Curr Drug Discov Technol* 7(4):263–279
 59. Steiner M, Neri D (2011) Antibody-radionuclide conjugates for cancer therapy: historical considerations and new trends. *Clin Cancer Res* 17(20):6406–6416
 60. Goldenberg DM, Chang CH, Rossi EA, McBride JW, Sharkey RM (2012) Pretargeted molecular imaging and radioimmunotherapy. *Theranostics* 2(5):523–540
 61. Hnatowich DJ, Virzi F, Ruszkowski M (1987) Investigations of avidin and biotin for imaging applications. *J Nucl Med* 28(8):1294–1302
 62. Goldenberg DM, Chatal JF, Barbet J, Boerman O, Sharkey RM (2007) Cancer imaging and therapy with bispecific antibody pretargeting. *Update Cancer Ther* 2(1):19–31
 63. Pecking AP, Bellet D, Alberini JL (2012) Immuno-SPET/CT and immuno-PET/CT: a step ahead to translational imaging. *Clin Exp Metastasis* 29(7):847–852
 64. Yokota T, Milenic DE, Whitlow M, Schlom J (1992) Rapid tumor penetration of a single-chain Fv and comparison with other immunoglobulin forms. *Cancer Res* 52(12):3402–3408
 65. Holliger P, Hudson PJ (2005) Engineered antibody fragments and the rise of single domains. *Nat Biotechnol* 23(9):1126–1136
 66. Holliger P, Prospero T, Winter G (1993) “Diabodies”: small bivalent and bispecific antibody fragments. *Proc Natl Acad Sci USA* 90(14):6444–6448
 67. Hu S, Shively L, Raubitschek A, Sherman M, Williams LE, Wong JY, Shively JE, Wu AM (1996) Minibody: a novel engineered anti-carcinoembryonic antigen antibody fragment (single-chain Fv-CH3) which exhibits rapid, high-level targeting of xenografts. *Cancer Res* 56(13):3055–3061
 68. Borsi L, Balza E, Bestagno M, Castellani P, Carnemolla B, Biro A, Leprini A, Sepulveda J, Burrone O, Neri D, Zardi L (2002) Selective targeting of tumoral vasculature: comparison of different formats of an antibody (L19) to the ED-B domain of fibronectin. *Int J Cancer* 102(1):75–85
 69. Hamers-Casterman C, Atarhouch T, Muyldermans S, Robinson G, Hamers C, Songa EB, Bendahman N, Hamers R (1993) Naturally occurring antibodies devoid of light chains. *Nature* 363(6428):446–448
 70. Kontermann R (2012) Dual targeting strategies with bispecific antibodies. *MAbs* 4(2):182–197
 71. Karawajew L, Micheel B, Behrsing O, Gaestel M (1987) Bispecific antibody-producing hybrid hybridomas selected by a fluorescence activated cell sorter. *J Immunol Methods* 96(2):265–270

72. Ridgway JB, Presta LG, Carter P (1996) 'Knobs-into-holes' engineering of antibody CH3 domains for heavy chain heterodimerization. *Protein Eng* 9(7):617–621
73. Gunasekaran K, Pentony M, Shen M, Garrett L, Forte C, Woodward A, Ng SB, Born T, Retter M, Manchulenko K, Sweet H, Foltz IN, Wittekind M, Yan W (2010) Enhancing antibody Fc heterodimer formation through electrostatic steering effects: applications to bispecific molecules and monovalent IgG. *J Biol Chem* 285(25):19637–19646
74. Merchant AM, Zhu Z, Yuan JQ, Goddard A, Adams CW, Presta LG, Carter P (1998) An efficient route to human bispecific IgG. *Nat Biotechnol* 16(7):677–681
75. Schaefer W, Regula JT, Bahner M, Schanzer J, Croasdale R, Durr H, Gassner C, Georges G, Kettenberger H, Imhof-Jung S, Schwaiger M, Stubenrauch KG, Sustmann C, Thomas M, Scheuer W, Klein C (2011) Immunoglobulin domain crossover as a generic approach for the production of bispecific IgG antibodies. *Proc Natl Acad Sci USA* 108(27):11187–11192
76. Labrijn AF, Meesters JI, de Goeij BE, van den Bremer ET, Neijssen J, van Kampen MD, Strumane K, Verploegen S, Kundu A, Gramer MJ, van Berkel PH, van de Winkel JG, Schuurman J, Parren PW (2013) Efficient generation of stable bispecific IgG1 by controlled Fab-arm exchange. *Proc Natl Acad Sci U S A* 110(13):5145–5150
77. Bostrom J, Yu SF, Kan D, Appleton BA, Lee CV, Billeci K, Man W, Peale F, Ross S, Wiesmann C, Fuh G (2009) Variants of the antibody herceptin that interact with HER2 and VEGF at the antigen binding site. *Science* 323(5921):1610–1614
78. Linke R, Klein A, Seimetz D (2010) Catumaxomab: clinical development and future directions. *MAbs* 2(2):129–136
79. Watts RJ, Dennis MS (2013) Bispecific antibodies for delivery into the brain. *Curr Opin Chem Biol*
80. Yu YJ, Zhang Y, Kenrick M, Hoyte K, Luk W, Lu Y, Atwal J, Elliott JM, Prabhu S, Watts RJ, Dennis MS (2011) Boosting brain uptake of a therapeutic antibody by reducing its affinity for a transcytosis target. *Sci Transl Med* 3(84):84ra44

Chapter 12

Engineered Affibodies in Translational Medicine

Xiang Hu, Hongguang Liu and Zhen Cheng

12.1 Introduction

Translational medicine is a medical practice that integrates research from the basic sciences, social sciences, and political sciences to optimize patient care and clinical medicine. It encourages collaborations among different disciplines. Translational medicine could be facilitated by connecting basic scientists with the reality of human disease and making translational research more than an interesting concept. The purpose of translational medicine is to develop novel diagnostic and therapeutic strategies for humans through experimentation, with the aim of solving public health problems and improving the longevity of the world's populations. Translational medicine is based on translational research, and it leads scientists to focus their efforts on linking bench-based discoveries to the area of clinical investigation, such as drug development, clinical assistance techniques, and clinical practice.

Novel molecular imaging and targeted therapy techniques, which are important branches of disease diagnosis and therapy, play important roles in translational medicine. In molecular imaging, for example, the visualization, characterization, and quantification of a disease target, such as a cell-surface receptor, can provide an overview of all tumor sites and metastatic lesions in the body and can be a valuable tool for diseases diagnosis and prognosis for targeted therapy in patients. For both diagnostic imaging and targeted radionuclide therapy, it is essential that the accumulation of radioactivity at a targeted site be much higher than the accumulation in adjacent normal healthy tissues. Therefore, molecular binders or ligands that can recognize different molecular targets are widely used in the field of molecular imaging and therapy.

X. Hu · H. Liu · Z. Cheng (✉)

Molecular Imaging Program at Stanford, Department of Radiology, Stanford University,
1201 Welch Road, Lucas Expansion, P095, Stanford, CA 94305, USA

e-mail: zcheng@stanford.edu

Affibody proteins are an emerging class of protein scaffold-based affinity reagents. This group of small (7 kDa) affinity proteins was first reported 10 years ago and has since been developed to bind to a variety of targets [1]. Affibody proteins were originally produced from staphylococcal protein A (SPA), which is also related to immunotechnology [2]. Several native and recombinant variants of SPA have been used to detect and purify antibodies [2]. In addition, five known highly homologous Ig-binding domains are contained in the SPA gene [3]. These domains were used as affinity gene fusion partners to produce and purify recombinant fusion proteins (such as for IgG-affinity chromatography) [4, 5]. Z-domain, an engineered variant of an SPA domain (Domain B), has been used as an Affibody-binding protein scaffold. During the engineering of the Z-domain, a few modifications were made to enhance the affinity of both the gene fragment and successive protein scaffold toward hydroxylamine through a Gly to Ala substitution [6, 7].

An Affibody protein is a three-helix-bundle Z-protein of 58 amino acids. It consists of a single polypeptide subunit, which makes it capable of independent and rapid folding, and is devoid of cysteine residues [8, 9]. Consequently, Affibody proteins have a native high-affinity interaction with binding targets through a set of surface-located residues and can be translated into soluble and stable forms when needed for cell imaging or therapy [1]. Based on the development of protein library technology and unexpected frustration from the prokaryotic production of several cloned antibody-derived constructs, researchers have raised the question of whether the advantageous features of the Z-domain could be used to generate a novel type of affinity reagents [10] (Fig. 12.1). The native specific binding site for Fc of IgG on the face of the small protein could be modified to bind to other targets of interest through amino acid substitutions while simultaneously retaining most of the advantageous properties of the Z-protein scaffold [1, 10].

Affibody-binding proteins have no Ig origin and were functionally selected as a protein scaffold from libraries of a small and cysteine-free three-helix-bundle Z-domain [11]. Since Affibodies were first described, high-affinity Affibody proteins have been selected to bind assorted targets for various applications, such as bioseparation, functional inhibition, drug development, viral targeting, and *in vivo* targeted diagnostics and therapeutics [11]. With 13 amino acids as a binding sequence, Affibody proteins could potentially provide high-affinity binding proteins against different targets via protein engineering, and the small size of Affibody binders has been found to be advantageous for further modification, such as site-specific labeling and chelators' conjugation.

12.2 Affibody Molecules Selection and Preparation

In recent years, numerous studies have examined the selection of Affibody proteins for molecular targeting. Currently, phage display technology has been introduced for all reported *de novo* selections of Affibody-binding proteins [12]. This technology was based on selection protocols and standard phage mid vectors. Other

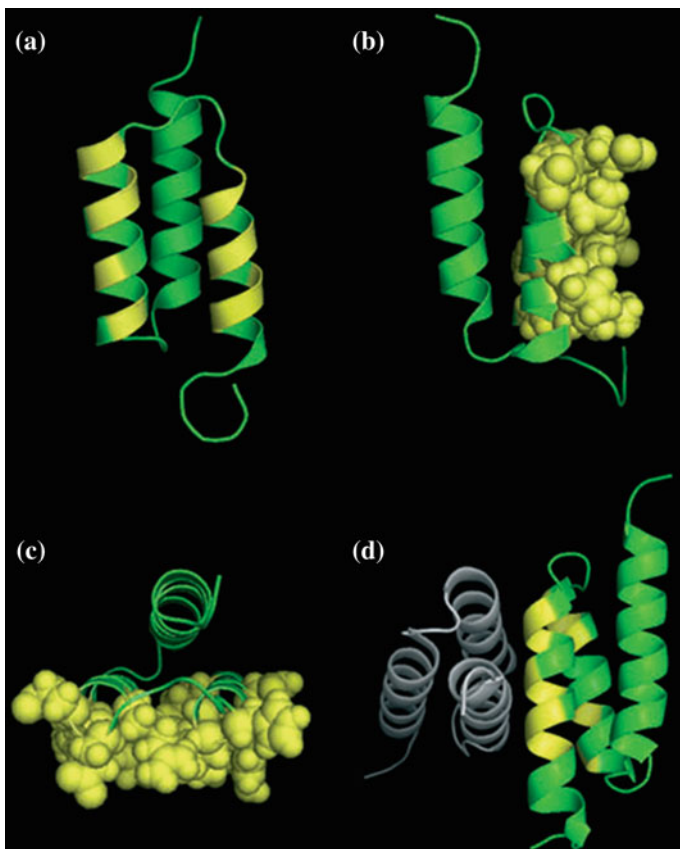


Fig. 12.1 Affibody-binding proteins: library and target binding. Illustration of the three-helix bundle affibody protein scaffold Z in band representation (green), with the 13 positions randomized during affibody protein library constructions highlighted (yellow) **a**. Side views **b** and **top views c** of the affibody protein scaffold showing the 13 surface-located positions in helices 1 and 2 employed for library constructions. **d** The structure of the complex between affibody proteins selected for binding to Taq DNA polymerase (ZTaq; white) and its anti-idiotypic affibody protein (anti-ZTaq; green with randomized positions in yellow). (Reproduced with permission from Ref. [10]. Copyright 2008 FEBS)

selection systems are also being investigated as alternative methods, including staphylococcal display, ribosomal display, microbead display, and b-lactamase-based protein fragment complementation [13]. The affinities obtained from Affibody proteins for different targets are similar to the affinities of antibody fragments or alternative scaffolds from similar native libraries. Different target structure characteristics and library complexity resulted in different dissociation constants (K_D), ranging from micromolar to low picomolar. For example, the highest affinity for an Affibody target to the breast cancer marker ErbB2 was recently reported as only 22 pM [14]. The epidermal growth factor receptor (EGFR)-binding Affibody

molecules with moderate affinity have also been isolated using phase-display selection technology. A study found that the molecules bind specifically to EGFR on EGFR-expressing cells in biosensors [15, 16]. Protein scaffolds can be prepared using either chemical or biological methods. For some small protein scaffolds, both methods can be used. After display selection, high-affinity scaffold molecules can be well established from the bulk of regular DNA templates. These DNA templates are produced using regular recombinant techniques. The high-affinity molecules exhibited high specificity and targeting capacity in protein engineering. For example, Affibodies can be prepared in *E. coli*, which makes the procedure easy and inexpensive compared with antibody production [17, 18]. In purification using a nickel column, a His-6 tag is typically added to the sequence of a scaffold protein when it is denatured [19]. This added His-6 can not only help purification but also achieve site-specific labeling with radionuclide ^{99m}Tc . More complicated post-transcription modifications can be either a disadvantage or advantage as is the case with glycosylation [19].

Small Affibody molecules can also be prepared directly by solid-phase peptide synthesis (SPPS), which is a desirable way to produce Affibody molecules with function groups for site-specifically labeling with a variety of reporters such as fluorophores, radionuclides, and nanoparticles [20, 21]. Synthesis of Affibodies using SPPS provides the freedom to label the protein with more than one reporter, and it facilitates the isolation of a homogeneous product when compared to recombinant production [21]. Furthermore, this approach could avoid the biological contaminants which largely exist in recombinant production. However, a limitation on this chemical approach is that the synthetic efficiency highly depends on the sequence and length of the Affibody proteins [22]. But the yield in organic synthesis of small proteins could be improved using a approach which involves the parallel synthesis of fragments and then assembling of them [23]. Importantly, it is feasible to perform chemical synthesis of the scaffold proteins without affecting the active amino acids or other functional group (Fig. 12.2) [20]. Manual modifications have been extensively applied to the synthetic Affibody proteins. For example, the resin-bound proteins have been manually modified by the introduction of thiol and biotin groups for surface immobilization (Fig. 12.2) [20].

For the promotion the applications of Affibody, in addition to SPPS, combinatorial assembled Affibody molecules have been designed and prepared by native chemical ligation (NCL) [21, 22]. In Affibody molecules, the amino acids located in the N-terminal part of the protein (helices 1 and 2) determine the target-binding ability and specificity, whereas the C-terminal part (the third helix and its flanking regions) is preserved in all variants [24]. The distinct division of the protein sequence between variable and constant segment makes Affibody high tolerance toward scaffold modification. And then it makes a fragment condensation strategy very appealing. Thus, the concept of combinatorial assembling has been introduced for the synthesis of three different Affibody molecules. Specifically, the helice 3 of Affibody containing a cysteine residue located at the site of ligation is prepared and can be used for directed immobilization, and it has no unintentional interference to the function groups of the investigated proteins. Moreover, different

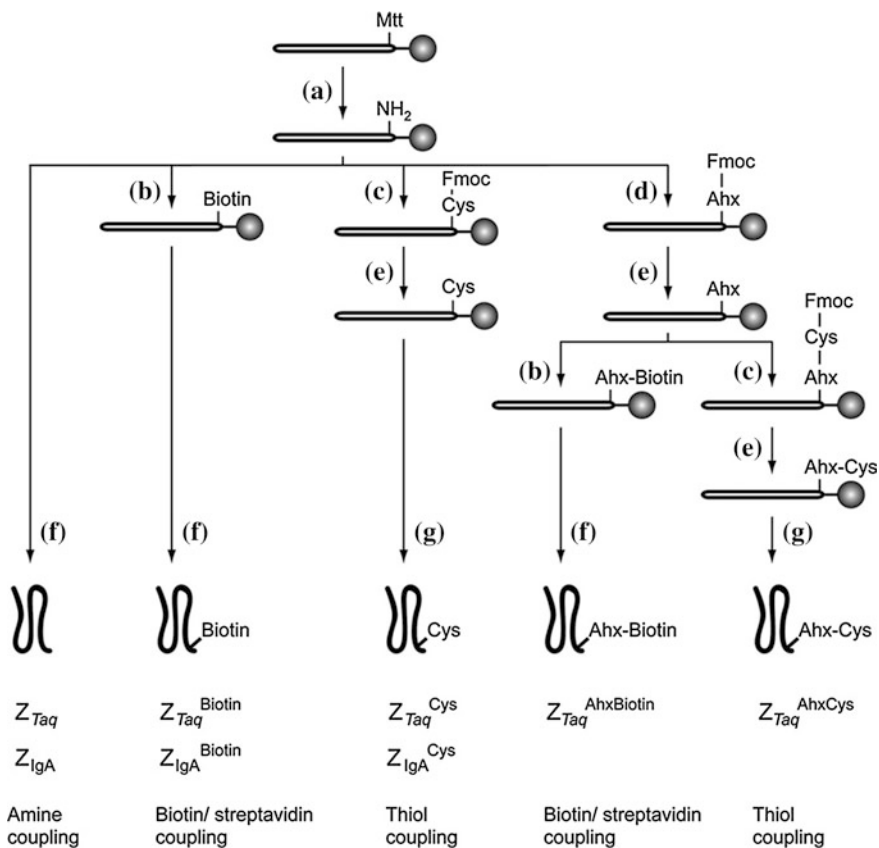


Fig. 12.2 Synthetic scheme for the preparation of five different Affibody variants: (a) TFA:TIS:DCM (1:5:94); (b) D-biotin, HBTU, HOBt, DIEA in NMP; (c) Fmoc-Cys(Trt)-OH, HBTU, HOBt, DIEA in NMP; (d) Fmoc-Ahx-OH, HBTU, HOBt, DIEA in NMP; (e) 20 % piperidine–NMP; (f) TFA:TIS:H₂O (95:2.5:2.5); (g) TFA:TIS:EDT:H₂O (94:1:2.5:2.5). (Reproduced with permission from Ref. [20]. Copyright 2005 Elsevier Inc.)

C-terminal modifications to helix 3 are performed to improve yield in preparation of Affibody proteins [24]. Three different 2-helix Affibodies with specificity for IgG, insulin, or human epidermal growth factor receptor 2 (HER2) can then be coupled with helix 3 by NCL to produce the full Affibodies (Fig. 12.3) [23].

12.3 Modification of Affibodies with Radionuclides

The most widely used molecular imaging agents in translational medicine are based on the radiolabeled molecules. It is very important to use appropriate labeling chemistry and find suitable radionuclides when developing protein based

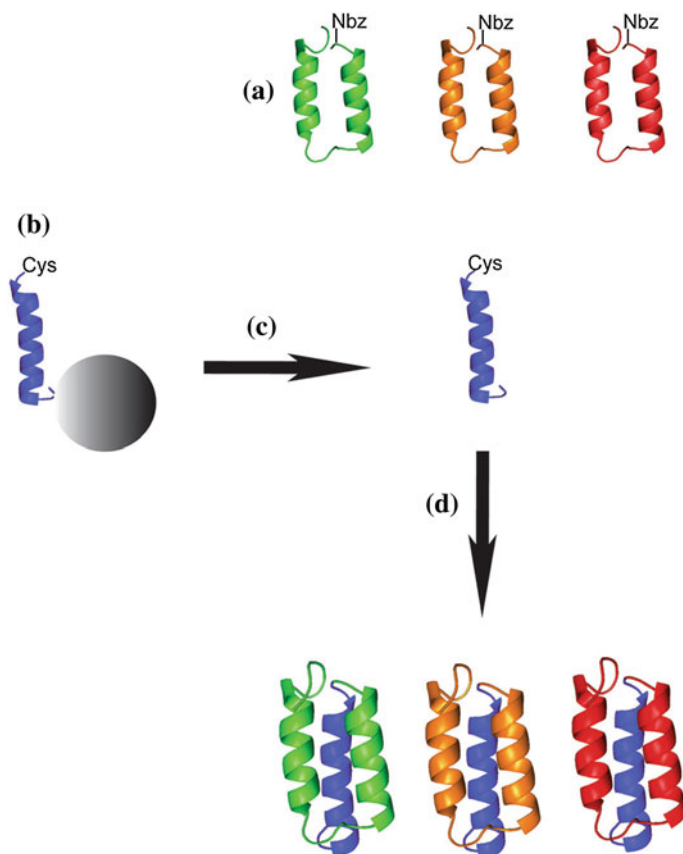


Fig. 12.3 Schematic overview of the combinatorial assembly approach by NCL for preparation of Affibody molecules (a): Selected Affibody molecules are determined by the N-terminal amino acid sequence that comprises helices 1 and 2. The C-terminal part contains helix 3 (b), and is constant in all Affibody molecules. Peptides are cleaved from the solid support (c), and NCL is used to yield the full-length Affibody molecules (d). (Reproduced with permission from Ref. [23]. Copyright 2012 Wiley-VCH Verlag GmbH & Co. KGaA, Weinheim)

imaging probes or radiotherapeutics. Labeling chemistry, chosen for different radionuclides, is one of the most important factors in the successful engineering of new diagnostic or therapeutic proteins. It plays a substantial role in efficient radiolabeling and maintains the bioactivity of the molecules. For example, radionuclides can be used to label proteins and molecules directly by in situ oxidation [25–27]. This method is straightforward and typically results in efficient labeling. However, the function groups such as tyrosines may be critical for binding, and the directly labeling could result in low-binding affinity and targeting efficiency [26–28]. In some reports, anti-HER2 Affibody molecules labeled with radionuclides directly indeed show a loss of binding capacity in relation to the

tyrosine modification in binding sites [25]. The inactivation of the HER2 Affibody molecule could be prevented using indirect labeling methods, such as site-specific modification with chelator or other moieties. Indirect labeling methods can consequently avoid the direct oxidization of protein and reduce the modification to the active amino groups of lysines and cisterns [25, 29]. Radionuclides selected for diagnosis and therapy highly depend on the properties of the targeting agent and its application. Physical half-life, the energy type of the emitted radiation, and the availability and cost of the nuclide must be considered. In addition, the requirements for matching the binder's biological properties and targeting mechanisms with radionuclide's physical properties should be considered. Different applications also require different radiation. For example, ^{18}F , ^{11}C , ^{13}N , and ^{15}O are the most common radionuclides for PET, whereas $^{99\text{m}}\text{Tc}$ and ^{111}In are most often used for single-photon emission computed tomography (SPECT) [30, 31]. In these radionuclides, the physical half-lives of ^{11}C , ^{13}N , and ^{15}O are too short to label peptides and proteins. Radionuclides with relatively longer half-lives, such as ^{68}Ga and ^{89}Zr , are used for PET imaging for targeted peptide or protein radiopharmaceuticals.

The cellular uptake and retention of radiolabeled molecules by cells and excretory organs are important to consider for the optimal design of an imaging probe. Different radionuclides (such as ^{125}I and ^{111}In) could impact targeting efficacy, imaging contrast, cellular protein degradation, and catabolism [30, 31]. For radio halogen-labeled biomolecules, after lysosomal degradation radionuclide catabolites are often quickly released from cells as uncharged lipophilic molecules. In contrast, radionuclides trapped in chelators are positively charged and typically hydrophilic and stay in cytoplasm for a long time. In addition, catabolism may occur in blood, excretory organs and even in tumor sites. As a result, the radio catabolites could re-enter the circulation and be redistributed [32]. This non-specific radioactivity would contribute to a high image background. Thus, the properties of radio catabolites should be considered when selecting a radionuclide for translational medicine engineering. Depending on their chemical nature, radio catabolites accumulated in the liver may be trapped inside hepatocytes or excreted into bile. This hepatobiliary excretion results in an increased background in the lower abdomen. Consequently, the behavior of a radiolabeled probe in excretory organs plays an important role in clinical performance and contributes to different imaging and therapy applications [33]. Increased uptake in the excretory organs generally indicates an undesirable elevated intake in healthy tissues. It has also been shown those labeled molecules smaller than 60 kDa are associated with high tumor retention of radioactivity but accompanied by a high accumulation of radioactivity in kidneys, because 60 kDa is the cutoff for glomerular filtration, and smaller proteins are mostly reabsorbed by the kidney [34, 35].

12.4 Affibody-based Molecular Imaging Techniques

12.4.1 Radionuclide Imaging

Two types of radionuclide imaging are in current use. One type is single-photon imaging, which includes SPECT and planar γ -camera imaging, and the other type is PET. Both planar imaging and SPECT are based on a γ camera, but in SPECT, the γ camera rotates around the target, avoiding the interfering radioactivity between the area of interest and the target [9, 36]. The molecular agents, which are clinically used for cancer imaging, are labeled with radionuclides such as ^{99m}Tc and ^{111}In and imaged using a γ camera. PET imaging has developed rapidly in recent years. It enables better resolution and more accurate quantification compared with single-photon detection [36]. PET utilizes randomized detection of the pair of photons formed after positron annihilation and emitted by radionuclides. PET combined with computed tomography (CT) or magnetic resonance imaging (MRI) provides multimodality information and detailed anatomical fusion images with a higher degree of accuracy for both bone and soft tissue. The most frequently used PET probe is ^{18}F -fluorodeoxyglucose (^{18}F -FDG), which is used to assess glucose metabolism, e.g., in the brain and heart. Tumors often have a high metabolic activity and ^{18}F -FDG uptake, which promotes tumor imaging using this probe [37, 38]. It has been reported that ^{18}F -FDG-PET provides valuable diagnostic information and helps in the staging of lung cancer [37]. A limitation is the non-specific uptake in inflammatory sites, which may create a false-positive result [39]. In summary, PET imaging is superior to γ camera in terms of the imaging properties of resolution, sensitivity, and quantification. However, SPECT may currently be the most widely used molecular imaging technique because of the greater availability of SPECT diagnostic devices and the lower cost of the radiotracers [9].

Protein scaffolds have been used as a platform for molecular probe development for various imaging modalities, especially for SPECT and PET. Currently, Affibody molecules are the dominant protein scaffolds used in imaging translation. Affibody scaffolds typically exhibit high serum stability, fast and good uptake in target tissues, low uptake in other normal tissues and kidney clearance. A variety of HER2 Affibody (Z_{HER2}) molecules constituted a large Affibody family have been reported [2, 40]. They have been labeled with ^{99m}Tc and ^{111}In and used for planar scintigraphy and SPECT imaging. Several radiolabeled Affibody proteins, such as ^{99m}Tc - $Z_{\text{HER2}:2395}\text{-C}$, ^{99m}Tc -maEEE- $Z_{\text{HER2}:342}$, and ^{111}In - CHX - A00 - DTPA - $Z_{\text{HER2}:2395}\text{c}$, provide easy radiolabeling and high serum stability. High-imaging contrast at 1 h post-injection (pi) was also demonstrated in vivo in a SKOV3 tumor model [40–42]. Among the numerous HER2 Affibody-based probes, ^{99m}Tc - $Z_{\text{HER2}:2395}\text{-C}$ has the highest tumor-to-blood ratio, high kidney accumulation, moderate liver retention, and low uptakes in all other organs [42]. In a LS174T colon cancer tumor model with moderate HER2 expression compared to

SKOV3 tumor model, ^{99m}Tc -Z_{HER2:2395}-C still exhibits good imaging properties in terms of the tumor-to-blood ratio (121 ± 24 at 4 h after injection) [42].

^{18}F -FBO-Z_{HER2:477} and ^{18}F -FBEM-Z_{HER2:342}, the ^{18}F -labeled HER2 targeting Affibody molecules, have also been labeled with site-specific methods [15]. These probes offer rapid uptake and high and specific accumulation as demonstrated by biodistribution and small animal PET imaging studies in HER2 overexpressing SKOV3 tumors. In addition, ^{18}F -FBO-Z_{HER2:477} shows significantly higher tumor-to-normal tissue (blood, muscle, liver, and lung) ratios than ^{18}F -FBO-(Z_{HER2:477})₂ at all the time points investigated in SKOV3 tumor-bearing mice. At 3 h after injection, the tumor-to-blood and tumor-to-muscle ratios of ^{18}F -FBO-Z_{HER2:477} are 12.72 ± 2.94 and 28.03 ± 8.28 , respectively [37]. Relatively fast clearance from the kidneys has also been observed in these probes, demonstrating that ^{18}F -labeled HER2 targeting Affibody molecules are promising new type of HER2 PET probe. More importantly, one of the HER2-targeting Affibody molecules, ^{18}F -FBZM-Z_{HER2:342} can detect and quantify HER2 expression changes through PET imaging. ^{18}F -FBZM-Z_{HER2:342} enhanced the accuracy of HER2 targeted probes in tumor molecular imaging [43]. Other HER2-targeting probes, such as ^{124}I -, ^{64}Cu -labeled Z_{HER2}, and optical dye (such as Alexa-750)-labeled Z_{HER2-ABD} fusion proteins, have also been evaluated for PET imaging in a SKOV3 tumor model [43, 44]. The imaging contrast is excellent for tumors observed at 6–24 h pi, and most of probe is cleared out by 24 h pi except from the kidney [44].

The EGFR-targeted Affibody molecules (Z_{EGFR}) have also been developed for molecular imaging. ^{111}In -Bz-DTPA-Z_{EGFR:1907} and ^{111}In -Bz-DTPA-(Z_{EGFR:1907})₂ have exhibited significantly higher contrast in EGFR-positive tumors than in negative ones [45]. More interestingly, ^{111}In -Bz-DTPA-Z_{EGFR:1907} presents results similar to those of radiolabeled HER2 Affibody-based probes in vivo, such as quick tumor uptake, specific targeting, and high accumulations and rapid clearance from the kidneys [45, 46]. ^{64}Cu -labeled Z_{EGFR:1907} has also been evaluated with PET in an A431 tumor model. This probe exhibits good contrast in tumors with target-positive expression, and it displays fast clearance through the liver and kidneys at an early time point p.i. Another more clinical relevant probe, ^{18}F -labeled Ac-Cys-Z_{EGFR:1907} has been developed and this novel protein scaffold-based PET probes able to image EGFR overexpressing tumors. It can also differentiate tumors with high and low EGFR expression in vivo and hold high promise for future clinical translation (Fig. 12.4a) [47]. Lastly, therapeutic agent, ^{177}Lu -DO3A-HSA-Z_{EGFR:1907}, has been prepared and show as a potential radiopharmaceutical for radionuclide therapy of EGFR-expressing head and neck carcinomas (Fig. 12.4b) [48].

12.4.2 Optical Imaging

SPECT and PET involve the use of highly ionizing materials for imaging, and the imaging systems are also expensive and complicated to use. In addition, production of some short half-life PET radionuclides such as ^{18}F requires a cyclotron.

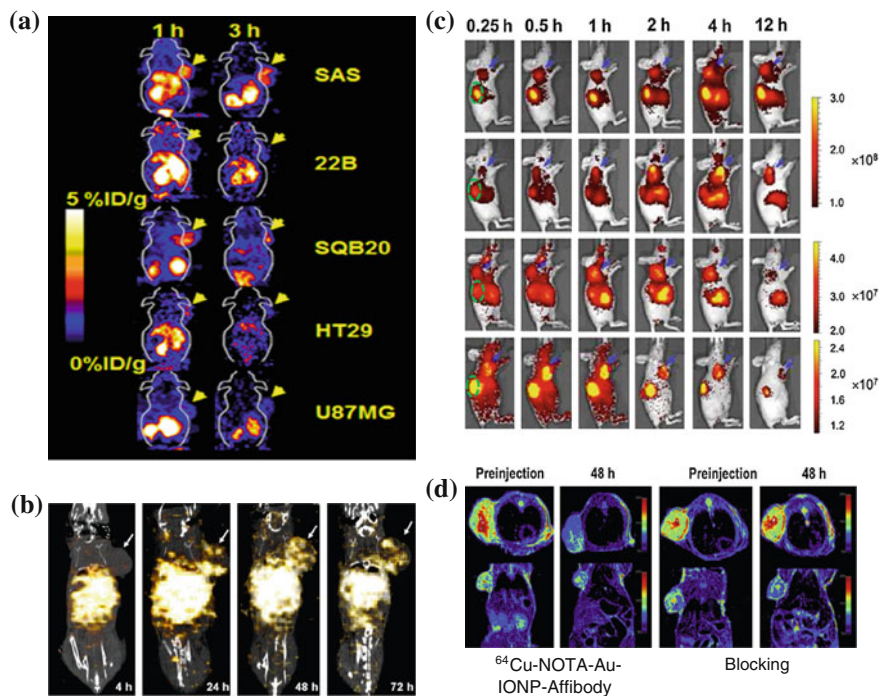


Fig. 12.4 Representative multimodality imaging using Affibody-based probes. **a** ^{18}F -FBEM-Cys- $Z_{\text{EGFR}:1907}$ PET of EGFR overexpression xenograft models. **b** SPECT/CT imaging of a mouse bearing SAS tumor xenograft at 4, 24, 48, and 72 h after administration of ^{177}Lu -DO3A-HSA- $Z_{\text{EGFR}:1907}$. Arrows indicate the location of tumors. White color indicates the highest radioactivity accumulation. **c** In vivo fluorescence imaging of subcutaneous A431 tumor-bearing nude mice at 0.25, 0.5, 1, 2, 4, and 12 h after injection of 0.5 nmol Cy5.5- $Z_{\text{EGFR}:1907}$ (1), Alexa680- $Z_{\text{EGFR}:1907}$ (2), SR680- $Z_{\text{EGFR}:1907}$ (3), or 800CW- $Z_{\text{EGFR}:1907}$ (4). Arrows in blue color and ovals in green color indicate the location of tumors and kidneys, respectively. **d** In vivo T2-weighted MR images of A431 tumor-bearing mice acquired before and at 48 h after injection of ^{64}Cu -NOTA-Au-IONP-Affibody and blocking dose of Affibody. (Reproduced with permission from (a) [47] copyright 2012 Society of Nuclear Medicine and Molecular Imaging, Inc. (b) [48] copyright 2012 SBIC (c) [53] copyright 2012 American Chemical Society (d) Ref [55]. Copyright 2013 Elsevier Ltd)

Therefore, nuclear imaging can usually only be set up in large clinical or research facilities. In contrast, optical imaging is simple to set up, safe, and does not require dedicated instruments. Optical imaging uses charge coupled device (CCD) cameras to collect the signals originating from fluorescent and bioluminescent probes [49–51]. Because of its many favorable properties including cheap, wide availability, non-ionization and minimal invasiveness, optical imaging presents an attractive option for tumors imaging and therapeutic monitoring. Recently, an Affibody-based, HER2-specific fluorescence probe was introduced to monitor the change of the target signal in the process of treatment in vivo of the receptors [52].

Subcutaneous tumor xenografts, which express different levels of HER2, were imaged with a NIR fluorescence small animal imaging system and linearly depends on HER2 expression as measured by an ELISA assay *ex vivo* for the same tumor, at several times post-injection of the probe [52]. This work suggests that optical imaging, combined with mathematical modeling, may monitor the molecular expression and then further allow non-invasive monitoring of HER2 expression *in vivo* using an Affibody-based optical probe. Moreover, several $Z_{\text{EGFR}:1907}$ based Affibody optical probes have been prepared through conjugation the $Z_{\text{EGFR}:1907}$ with different optical dyes. EGFR-positive tumors can be clearly delineated using these four probes [53] (Fig. 12.4c). These works have laid down solid foundation for using Affibody-based probes for tumor optical imaging and image-guided surgery.

12.4.3 MRI

MRI provides high spatial resolution and excellent soft-tissue contrast without any radiation when compared with PET and SPECT, making it one of the best modalities for soft-tissue imaging and tumor diagnosis. MRI can be further combined with appropriate imaging contrast agents for certain molecular targeted diagnosis. It also provides multiplane capabilities and high-quality 3D anatomic data. A nanoparticle combining the biotinylated anti-HER2 Affibody molecules and streptavidin functionalized super paramagnetic iron oxide (SPIO) has been reported to image HER2-positive SKOV-3 tumor [54]. The nanoparticles bind specifically to HER2 after the administration of the nanoconstruct, and the tumor could be clearly imaged using a gradient-echo sequence on MRI [54]. In another report, ^{64}Cu -NOTA-Au-IONP- $Z_{\text{EGFR}:1907}$ has been used for EGFR-targeted MRI imaging when the Affibody molecules combined with gold iron oxide nanoparticle [55] (Fig. 12.4d). These studies demonstrate that combined Affibody-IO can be used for targeted *in vivo* tumor MRI.

12.5 Application of Affibodies in Biomedical Research

12.5.1 Affibody Molecule-based Tumor Imaging

The use of molecular imaging in clinics depends on its accuracy, which includes the sensitivity and specificity of the imaging agent. A good imaging agent should be sensitive to the target. The transport path, such as blood circulation or local diffusion in tissues, is also important and contributes to accumulation or retention in the target tissue [8, 56]. The sensitivity of the molecular imaging agent is mainly

determined by the contrast between the radioactivity concentration in the tumor and normal healthy tissues. Therefore, an imaging agent is desired to be of small size and soluble to allow for rapid tumor tissue penetration and accumulation, and it should also bind specifically to a molecular target with minimal non-specific binding. Moreover, molecular targeted agents should be cleared quickly from the blood and other background organs by kidney excretion [56–58]. Rapid clearance is important in providing a good imaging contrast in a short period of time and minimizing clinical protocols. Other factors influencing the accuracy of imaging agents are the target expression level, the binding and retention of the probe to the target, the vascularization of tumor, and the device used to optimize resolution and sensitivity [56, 58]. Affibody-based probes possess many desirable features and thus have been extensively studied for imaging several important tumor targets in pre-clinical and clinical studies.

ErbB receptors are involved in the development of many human cancers, such as breast, prostate, head and neck and colon cancer [59, 60]. It has been further reported that alterations of ErbB receptors showed more aggressive disease with a poor prognosis in patients [60–62]. EGFR (also known as ErbB1 or HER1), ErbB2 (or HER2), ErbB3 (or HER3), and ErbB4 (or HER4) are four members of the ErbB family of Receptor Tyrosine Kinases (RTKs) [16, 63–65]. All ErbB receptors have three common parts: an extracellular ligand-binding domain, a single membrane—spanning region and a cytoplasmic protein TK (tyrosine kinase) domain [16, 63–65]. The expression of the ErbB receptor can be found in epithelial, mesenchymal and neuronal origin, and the expression of the ligands physiologically controls the activation of the ErbB receptors [66]. Importantly, it has been found that the expression of RTKs, EGFR, and HER2 is up-regulated in various solid tumors. These biomarkers usually correlate with the tumor cells proliferation and metastasis and therefore serve as important targets for tumor molecular imaging. Monitoring their expression could potentially facilitate targeted therapy or monitor the therapeutic response [67].

12.5.1.1 HER2

The HER2 receptor has been widely investigated for cancer targeted therapy. A humanized IgG1mAb, herceptin (trastuzumab), has been widely used for the treatment of metastatic breast cancer patients who showed over-expressed HER2 [68–72]. It thus important to develop HER2 imaging agent for the purpose of patient prognosis and stratification for personalized therapy. Anti-HER2 antibody derivatives have been used for HER2 targeted imaging using the modality of PET [73] and a gamma-camera [73]. However, it requires long time (days) to achieve good imaging contrast. High-affinity Affibody molecules have been extensively explored for HER2 targeting in many pre-clinical studies and a pilot clinical study [14]. Particularly, one of anti-HER2 Affibody variants, Z_{HER2:342}, exhibit several

beneficial properties, including high stability and affinity, good solubility, and good tumor uptake, making it a promising protein for further development. Orlova et al. describe that ^{125}I -labelled $Z_{\text{HER2}:342}$ exhibit a tumor uptake of approximately 9 % ID/g at 4 h pi and a ratio (tumor/muscle) of 38:1 in SKOV-3 tumor models in vivo [74]. It also exhibits higher contrast in tumors 6 h pi in γ -camera imaging. For SPECT imaging, ^{111}In -benzyl-DTPA- $Z_{\text{HER2}:342}$ exhibits specificity to the HER2-positive-expressing cell line SKOV-3 [75, 76]. High tumor uptake has been found at 4 h after the injection of ^{111}In -benzyl-DTPA- $Z_{\text{HER2}:342}$ SKOV-3 tumors in vivo [75, 76]. Moreover, it can be cleared out quickly from blood, and the tumor/blood ratio is approximately 100:1 at 4 h pi. High uptake is observed in the kidneys and ascribed to the properties of ^{111}In [41].

$^{99\text{m}}\text{Tc}$ is one of the most commonly used radionuclides in the clinic. $Z_{\text{HER2}:342}$ is conjugated with a chelator and coupled with $^{99\text{m}}\text{Tc}$ [31]. $^{99\text{m}}\text{Tc}$ -maGGG- $Z_{\text{HER2}:342}$ (in which maGGG is the chelator with a sequence of merc-aptoacetyl-glycyl-glycyl-glycyl) exhibits specific targeting in HER2-positive tumors in mice and high tumor-to-non-tumor ratios based on imaging results and biodistribution studies [21]. However, this probe displays predominantly hepatobiliary clearance, which causes high radioactivity in the intestine, hindering the detection of abdominal tumors. To address this limitation, chelators with a more hydrophilic character have been applied. When compared with the more hydrophilic $^{99\text{m}}\text{Tc}$ -maEEE- $Z_{\text{HER2}:342}$ (E: glutamic acid), $^{99\text{m}}\text{Tc}$ -maGGG- $Z_{\text{HER2}:342}$ lead to a tenfold decrease of radioactivity in the intestine, accompanied by an increased kidney uptake [21, 31]. In addition, a set of serine and glutamic acids in the chelator is modified to the Affibody molecules. For example, the glutamic acid in $^{99\text{m}}\text{Tc}$ -maEEE- $Z_{\text{HER2}:342}$ are altered with serine to produce $^{99\text{m}}\text{Tc}$ -maESE- $Z_{\text{HER2}:342}$. This modification results in lower uptake in the intestinal tract compared with the original form, and the renal retention of radioactivity is reduced by one-third. In addition, several ^{18}F -labeled Z_{HER2} have been reported. For example, ^{18}F -NOTA- $Z_{\text{HER2}:2395}$ is developed to minimize the re-absorption of Affibody molecules by the kidney [77].

Despite there are many advantages of HER2-targeting imaging and therapy with Affibody molecules, a few potential limitations also need to be considered. First, HER2-targeted imaging may be interfered by free HER2, which is released by HER2-overexpressing tumors to the circulation and may bind to Affibody probes [44, 78]. In many pre-clinical studies, it has been proved that high contrast imaging can still be achieved for HER2-overexpressing tumors even in the presence of shed HER2 [79, 80]. But the impact of this interference to clinical imaging remains to be carefully studied. Second, the re-absorption of Affibody molecules by the kidneys may result in high un-intended accumulation in kidney of the probes [15, 44, 79, 81–83]. Thus, the visualization of tumor lesions located adjacent to the kidney may be interfered, though the metastasis of the tumors to kidney is rare and not a major problem [43, 84–86].

12.5.1.2 EGFR

EGFR is a transmembrane protein belonging to the ErbB receptor kinase family, and it is the first cellular surface receptor identified that is linked directly to human tumors [67]. Many tumors are regarded to be developed by EGFR activation and the mutation of the receptor. It has been known that in many cancer cells, the gene amplification leads to EGFR overexpression for EGFR stimulation through autocrine loops [87, 88]. Interestingly, the overexpression and over activation of EGFR are shown in many cancers, such as head and neck, ovary, colon, breast, and prostate cancer [89–91]. Furthermore, EGFR expression level is a strong prognostic indicator for head and neck, ovarian, cervical, bladder, and esophageal cancer and has moderate prognosis value for breast cancer, colon cancer, gastric, and endometrial cancers [62, 92]. A variety of small molecules or antibody-based drugs, such as Cetuximab, Gefitinib, Erlotinib, and Lapatinib, have been developed and shown clinical benefits to many cancer patients by targeting overexpressed/activated EGFR [93–95]. Molecular imaging of EGFR are thus expected to find many important applications including prognosis of cancer patients, evaluation anti-tumor drug effect, stratification cancer patient for EGFR-targeted therapy [96].

Recently, anti-EGFR Affibody proteins (Z_{EGFR}) have been designed as agents both for diagnosis and for the treatment of diseases. Affibody molecules have been demonstrated to be useful for SPECT, PET, and NIR imaging. Specifically, Z_{EGFR} -based molecular probes, ^{111}In - $Z_{EGFR:1907}$, ^{64}Cu -DOTA-Cys- $Z_{EGFR:1907}$, and Cy5.5-Cys- $Z_{EGFR:1907}$ were successfully prepared and found to show rapid tumor targeting ability and good tumor-imaging contrast at even 1 h pi in the EGFR expression A431 tumor xenograft model [16, 32, 35, 97–99]. All these probes are also predominately cleared through kidney. Interestingly, it has been found that improved tumor-imaging quality in small animal models can be achieved using the probes spiked with small amount of $Z_{EGFR:1907}$ (e.g., 50 μg), but co-injection of the probes with large amount of $Z_{EGFR:1907}$ (e.g. 500 μg) significantly reduce the tumor uptake. Moreover, the $Z_{EGFR:1907}$ has been labeled with several different NIR dyes for in vivo optical imaging, all with retained specificity and affinity [53]. Lastly, as discussed above, ^{18}F -FBEM-Cys- $Z_{EGFR:1907}$ has been prepared and evaluated in a variety of tumor models (A431, SAS, SQ20B, 22B, U87MG, and HT29) to study whether the PET probe can be used for imaging of EGFR-positive tumors and quantitative PET imaging of EGFR expression in vivo. The results demonstrate that ^{18}F -FBEM-Cys- $Z_{EGFR:1907}$ rapidly accumulates in the tumor and cleared from the most of normal organs except liver and kidneys at 3 h p.i., allowing excellent tumor-to-normal tissue contrast to be obtained. Similar as other Z_{EGFR} probes, co-injection of the PET probe with small amount of 45 μg of $Z_{EGFR:1907}$ improves the tumor uptake (3.9 vs. 8.1 %ID/g, at 3 h p.i.) and tumor-imaging contrast, while co-injection with 500 μg of $Z_{EGFR:1907}$ successfully blocks the tumor uptake significantly (8.1 vs. 1.0 %ID/g, at 3 h p.i., 88 % inhibition <0.05). Mostly, importantly, moderate correlation has been found between the tumor ^{18}F -FBEM-Cys- $Z_{EGFR:1907}$ uptakes at 3 h p.i. quantified by PET and EGFR expression levels measured by western blot assay ($P = 0.007$, $R = 0.59$).

All these studies highlight that Z_{EGFR} molecules are a promising new class of cancer targeting ligands with high clinical translation ability and thus worthy of further investigation to develop probes to image EGFR with different modalities.

12.5.1.3 IGF-1R

ErbB receptor network has also been reported cross-talk with many other signal pathways including insulin-like growth factor 1 receptor (IGF-1R) [59, 87]. IGF-1R has been reported involved in a number of neoplastic diseases, including several common carcinomas. IGF-1R appears to be an attractive target for many transforming agents (genetic, viral, and chemical) in tumor molecular imaging and therapy. The tumorigenic potential of IGF-1R is mediated through its anti-apoptotic and transforming signaling pathway as well as pro-metastatic pathways. Down-regulation of IGF-1R is showed to reverse the neoplastic phenotype and sensitized cells to antitumor treatments in pre-clinical studies. IGF-1R-binding Affibody molecule $Z_{\text{IGF1R:4551}}$ has also been reported recently. It was site specifically conjugated with DOTA to the C-terminal cysteine and labeled with ^{111}In [100]. The binding of radiolabeled $Z_{\text{IGF1R:4551}}$ to IGF-1R-expressing cells was evaluated in vitro and in vivo. It showed the potential for imaging and treatment of prostate cancer [100].

12.5.2 Affibody Molecules for Imaging in the Clinic

Radiolabeled $Z_{\text{HER2:342}}$ has been evaluated in a pilot clinical trial recently [101]. This trial marks the first clinical administration of the Affibody molecule. $Z_{\text{HER2:342}}$ was conjugated with DOTA and then labeled ^{111}In (^{111}In -DOTA- $Z_{\text{HER2:342}}$) and studied in limited-recurrent breast cancer patients [101]. Less than 100 μg of ^{111}In -DOTA- $Z_{\text{HER2:342}}$ were administered, and it resulted in high-quality SPECT imaging. This dose enabled the detection of 12- to 14-mm lesions, even at 2 h p.i [101]. The probe was also shown to effectively monitor Herceptin treatment. Moreover, three patients were also imaged with ^{111}In or ^{68}Ga -labeled DOTA⁰- $Z_{\text{HER2:342}}$ -pep2 (ABY-002), and the SPECT or PET/CT imaging results were compared with ^{18}F -FDG PET/CT results in breast cancer patients. The pilot clinical study reveals that radiolabeled ABY-002 can be well tolerated. More interestingly, radiolabeled ABY-002 can detect 9 of 11 ^{18}F -FDG-positive metastases as early as 2–3 h p.i. (Fig. 12.5) [102]. This first report on clinical imaging of Affibody-based scaffold protein highlights that molecular imaging using ^{111}In or ^{68}Ga -labeled ABY-002 has the potential to localize metastatic lesions in vivo, and this novel imaging technique may provide qualitative information of HER2 status in tumor metastases.

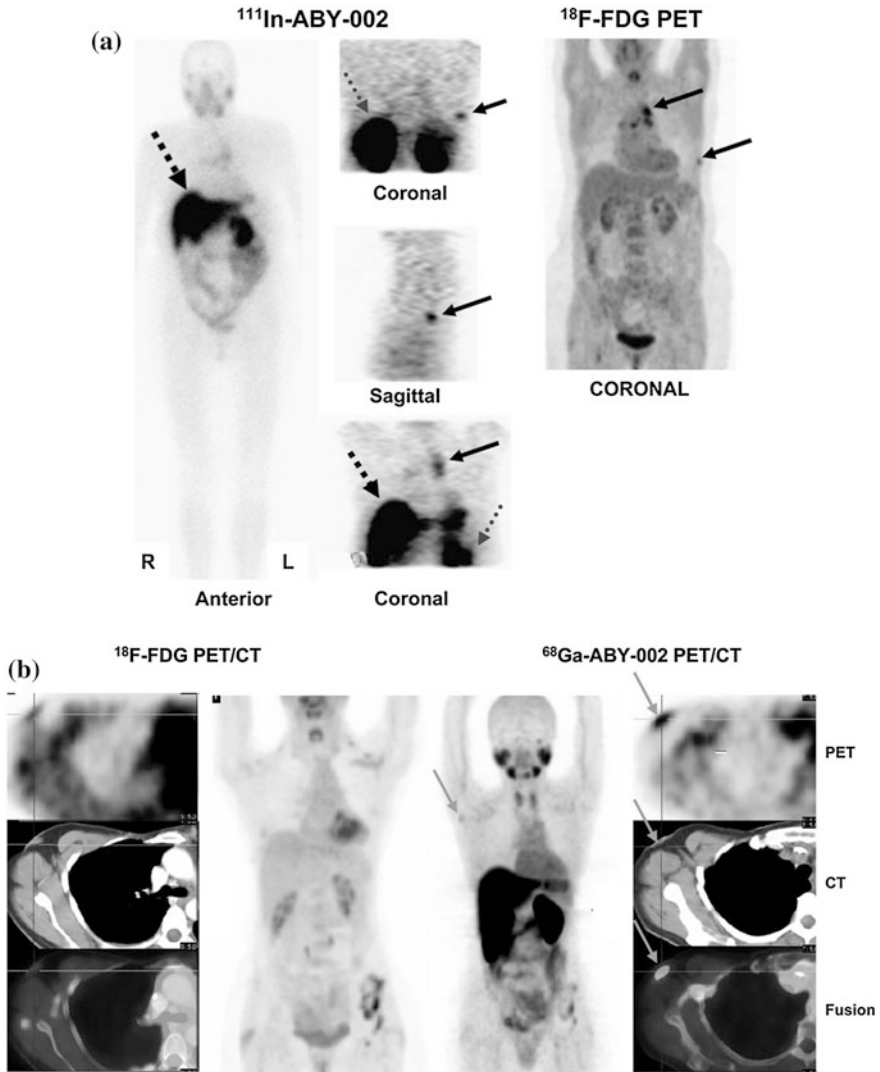


Fig. 12.5 **a** γ -camera imaging was performed after administration of $^{111}\text{In-ABY-002}$ in breast cancer patient. Images showing localization of metastases (*solid arrows*), kidney (*dotted arrows*), and liver (*dashed arrows*). *Left*: Whole-body scan 4 h after injection shows uptake predominantly in liver and kidney, with additional uptake in parotid and submandibular glands, thorax, and gastrointestinal tract. SPECT images 3 h after injection (*middle*) show the localization of thoracic wall metastasis (*upper coronal image and sagittal image*) and mediastinal lymph node metastases (*lower*). *Right*: PET was performed after intravenous injection of $^{18}\text{F-FDG}$. Localization of thoracic wall metastasis and mediastinal lymph node metastases was showed. **b** Potential metastasis (*arrows*) in chest wall near the axilla is seen with $^{68}\text{Ga-ABY-002}$ on transverse PET (*top*), CT (*middle*), and PET/CT (*bottom*) images and on coronal maximum-intensity projection images (in between). This metastasis was not visible with $^{18}\text{F-FDG}$ in a representative breast cancer patient. Reprinted by permission from [102] of Society of Nuclear Medicine and Molecular Imaging

12.5.3 Affibody Molecules in Radionuclide Therapy

Systemic treatment is always required in disseminated disease. In this case, chemotherapy plays an important role; however, it lacks specificity and causes unintended toxicity to untargeted organs [33]. To address this problem, cytotoxic substances, such as radionuclide, can be delivered to the tumor cells over-expressing molecular targets while with low or absent levels in normal tissues [103]. Two radionuclide-labeled therapeutic antibodies, Bexxar (^{131}I) and Zevalin (^{90}Y), are currently approved to treat non-Hodgkin's lymphoma [104, 105]. However, radionuclide-based therapy using MAb has not achieved a breakthrough in solid tumors. Two major issues that are the properties of the agents do not allow an adequate radioactive dose to accumulate in the target tumor and accumulations are far lower than the therapeutic dose in the critical organs [106]. These issues are also relevant for the most commonly used targeting agents, intact immunoglobulins. They could be delivered to the tumors but without delivering enough high doses in many cases. In addition, slow blood clearance and insufficient tumor penetration are also limiting factors for immunoglobulin-based agents, resulting in low-efficiency targeted therapy [106]. Some smaller targeting agents, such as antibody derivatives and peptides, have been considered in radionuclide therapy. These agents were designed to provide better tumor penetration, fast blood clearance, and enhanced permeability and retention, leading to an increased tumor-to-muscle ratio and improved tumor accumulations [45, 48]. Small molecules still have some limitations. With their small size, the fast blood clearance could lead to non-specific and insufficient tumor uptake at doses that are too low to treat malignant cells [45, 48]. Thus, the effects of size modulation on agents and their interaction with other proteins are also considered when upgrading targeted therapy.

As has been discussed previously, small Affibody molecules exhibited high kidney uptake of radioactivity and specific accumulation in target tumors; thus, they need to be modified for targeted radiotherapy [4]. Recently, it was shown that the fast clearance and high kidney uptake of radioactivity in Affibody targeting can be suppressed by modifications with a 46-amino acid albumin-binding domain (ABD) [103]. This modification was used to achieve a reversible interaction with human serum albumin and prolong the circulation in the blood system. As in the literature, DOTA-conjugated $Z_{\text{HER2}:342}$ was stably labeled with the low-energy β -radiation emitter ^{177}Lu and the high-energy β -radiation emitter ^{90}Y without losing HER2-binding specificity [48, 107]. The biodistribution of the ^{177}Lu -labelled anti-HER2 Affibody in normal nude mice exhibited a high uptake in the kidneys, a low uptake in most other organs, and rapid clearance from the blood system. These findings indicate that this radiolabeled Affibody could accumulate considerable radioactivity in bladder carcinomas, contributing to its potential application as a targeting agent for local bladder cancer treatment [107]. On the other hand, the biodistribution of ^{177}Lu -CHX-A-DTPA-ABD-($Z_{\text{HER2}:342}$)₂ in normal mice demonstrated a substantially prolonged half-life and a 25-fold

reduced uptake in kidney than ^{177}Lu labeled Affibody without ABD modification [48, 107]. Biodistribution of ^{177}Lu -CHX-A-DTPA-ABD-($Z_{\text{HER2:342}}$)₂ in SKOV-3 tumor-bearing nude mice exhibited high tumor uptake (19 ± 7 ID/g) at 24 h pi. For the radionuclide therapy study, when 17.4 MBq ^{177}Lu -CHX-A-DTPA-ABD-($Z_{\text{HER2:342}}$)₂ was administered to SKOV-3 tumor-bearing nude mice, it resulted in the complete prevention of tumor formation [48, 107]. These results clearly suggest that the fusion of an ABD to an anti-HER Affibody can be a promising agent for targeted tumor treatment.

Given their highly affinity and specificity to HER2-overexpressed tissues, anti-HER2 Affibodies may also be used in local treatment. For example, EGFR is overexpressed in bladder cancer, and some normal healthy organs such as the liver or skin will reduce the accumulation of Affibodies in the targeted bladder cancer [62]. The unintended accumulation of radioactivity in normal organs will thus decrease the efficacy of systemic treatment for EGFR-expressing tumors and metastases. In addition, to achieve high doses in target tumors, the administration dose will have to be much higher than the patient can tolerate. The local treatment of EGFR-targeting molecules such as Affibody in patients after tumor surgical resection becomes a potential application that could be used to remove micro tumors in case of any remains. Studies have described the use of intracavity radionuclide therapy as a promising strategy for the postoperative treatment in glioblastomas [108]. The small anti-EGFR-specific Affibody molecule could attach to and eradicate migrating glioma cells [108]. Intravesical treatment could also be a local administration option for urinary bladder cancer [62].

12.5.4 Affibody Molecules for Alternative Therapeutic Application

An alternative strategy to radionuclide-mediated tumor therapy is the application of receptor targeting ability of agents in cell signal transduction to prevent tumor progression. Several targeting agents have been described, such as mAbs and small molecules. Interference with membrane receptor signaling using a small molecule or Affibody molecule would affect the cell progression, even inside the cellular compartment. Anti-HER Affibody molecules could target and retain the HER receptor and then down-regulate cell-surface HER2 receptors and subsequent cell growth in the endoplasmic reticulum [81, 109, 110]. Proteins in the immune system are another group of potential targets for Affibodies in tumor cell killing when targeted to natural immune effector cells, as in the application of bispecific targeting Affibody molecules in cytotoxic T-lymphocytes and NK cells [111–113]. Affibody molecules can be synthesized as multidomain or multitargeted agents, such as dimeric Affibody molecules, ABD-fused Affibody molecules, and Fc-fused Affibody molecules [81, 114–116]. These molecules can be potentially used as bi- or multispecific targeting agents. For example ($Z_{\text{EGFR:1907}}$)₂ is a dimeric Affibody molecule with high affinity to the extracellular EGFR. Cytotoxic effects

of (Z_{EGFR:1907})₂ combining with external radiation and the possible inhibitory effects are showed in the EGFR signaling pathways in the colon cancer cell lines HT-29 and HCT116. It indicates the potential application in molecular therapy [45].

12.5.5 Affibody Enhances the Targeting Efficacy in Human Adenoviruses Vectors

Human adenoviruses have a high potential as anticancer vector to improve the targeted therapy. One strategy to improve their molecular specificity and silence/overexpression efficacy on tumor inhibition is to anchor targeting ligands in the viral capsid. This can be achieved by fusing multitargeting ligands with the minor capsid protein IX [117]. Previous research suggested the inefficient release of protein IX-fused ligands from their cognate receptors in the endosome, contribution to the limitation of protein IX-mediated targeting [118]. Affibody molecules have currently been investigated to augment the targeted transduction of tumor cells when bind to protein IX anchor in cathepsin-cleavage site [117]. Viral particles enhance the cleavable protein IX-ligand fusion in capsid-transduced HER2/neu-positive SKOV-3 ovarian carcinoma cells. It showed the increased efficiency in vitro. In accordance, different growth with or without Affibody-assisted cathepsin transduction was showed in chorioallantoic membrane of embryonated chicken eggs [117]. These data demonstrated that inclusion of a cathepsin-cleavage sequence between protein IX and a high-affinity Affibody-targeting ligand enhances targeted transduction [117]. This modification further augments the applicability of Affibody as an enhanced molecule for targeting ligands. Affibody molecules have also been implicated in studies of gene therapy viral vectors because of its cell-binding specificities. Cellular-specific targeting is very important for effective and safe gene therapy [119, 120]. In virus-mediated gene therapy engineering, specific cell-binding to a target is a limitation in terms of entering the mammalian cell cytoplasm, where the viral particles originating from HER2 receptors have been successfully retargeted in an adenovirus that was incorporated into the use of anti-HER2-specific Affibody molecules [119].

12.6 Conclusion

In summary, Affibody molecules have favorable properties for the development of novel diagnostic imaging and therapeutic agents for biotechnological applications. The first clinical trials indicate safety and efficacy of anti-HER2 Affibody imaging agents. Affibody molecules are thus highly promising in clinical translation medicine. More Affibody agents are needed to be developed for different imaging modalities and different molecular targets.

References

1. Lofblom J, Feldwisch J, Tolmachev V, Carlsson J, Stahl S, Frejd FY (2010) Affibody molecules: engineered proteins for therapeutic, diagnostic and biotechnological applications. *FEBS Lett* 584(12):2670–2680
2. Friedman M, Stahl S (2009) Engineered affinity proteins for tumour-targeting applications. *Biotechnol Appl Biochem* 53(Pt 1):1–29
3. Nilsson B, Moks T, Jansson B, Abrahmsen L, Elmlblad A, Holmgren E, Henrichson C, Jones TA, Uhlen M (1987) A synthetic IgG-binding domain based on staphylococcal protein A. *Protein Eng* 1(2):107–113
4. Tolmachev V, Orlova A, Nilsson FY, Feldwisch J, Wennborg A, Abrahmsen L (2007) Affibody molecules: potential for in vivo imaging of molecular targets for cancer therapy. *Expert Opin Biol Ther* 7(4):555–568
5. Binz HK, Amstutz P, Pluckthun A (2005) Engineering novel binding proteins from nonimmunoglobulin domains. *Nat Biotechnol* 23(10):1257–1268
6. Nilsson FY, Tolmachev V (2007) Affibody molecules: new protein domains for molecular imaging and targeted tumor therapy. *Curr Opin Drug Discov Devel* 10(2):167–175
7. Stahl S, Nygren PA (1997) The use of gene fusions to protein A and protein G in immunology and biotechnology. *Pathol Biol (Paris)* 45(1):66–76
8. Tolmachev V, Tran TA, Rosik D, Sjoberg A, Abrahmsen L, Orlova A (2012) Tumor targeting using affibody molecules: interplay of affinity, target expression level, and binding site composition. *J Nucl Med* 53(6):953–960
9. Miao Z, Levi J, Cheng Z (2011) Protein scaffold-based molecular probes for cancer molecular imaging. *Amino Acids* 41(5):1037–1047
10. Nygren PA (2008) Alternative binding proteins: affibody binding proteins developed from a small three-helix bundle scaffold. *FEBS J* 275(11):2668–2676
11. Skerra A (2007) Alternative non-antibody scaffolds for molecular recognition. *Curr Opin Biotechnol* 18(4):295–304
12. Tolcher AW, Sweeney CJ, Papadopoulos K, Patnaik A, Chiorean EG, Mita AC, Sankhala K, Furfine E, Gokemeijer J, Iacono L, Eaton C, Silver BA, Mita M (2011) Phase I and pharmacokinetic study of CT-322 (BMS-844203), a targeted Adnectin inhibitor of VEGFR-2 based on a domain of human fibronectin. *Clin Cancer Res* 17(2):363–371
13. Lofdahl PA, Nygren PA (2010) Affinity maturation of a TNF α -binding affibody molecule by Darwinian survival selection. *Biotechnol Appl Biochem* 55(3):111–120
14. Orlova A, Magnusson M, Eriksson TL, Nilsson M, Larsson B, Hoiden-Guthenberg I, Widstrom C, Carlsson J, Tolmachev V, Stahl S, Nilsson FY (2006) Tumor imaging using a picomolar affinity HER2 binding affibody molecule. *Cancer Res* 66(8):4339–4348
15. Orlova A, Jonsson A, Rosik D, Lundqvist H, Lindborg M, Abrahmsen L, Ekblad C, Frejd FY, Tolmachev V (2013) Site-Specific Radiometal Labeling and Improved Biodistribution Using ABY-027, a Novel HER2-targeting affibody molecule-albumin-binding domain fusion protein. *J Nucl Med* 54(6):961–968
16. Tolmachev V, Rosik D, Wallberg H, Sjoberg A, Sandstrom M, Hansson M, Wennborg A, Orlova A (2010) Imaging of EGFR expression in murine xenografts using site-specifically labelled anti-EGFR ^{111}In -DOTA-Z_{EGFR:2377} Affibody molecule: aspect of the injected tracer amount. *Eur J Nucl Med Mol Imaging* 37(3):613–622
17. Mattes MJ, Griffiths GL, Diril H, Goldenberg DM, Ong GL, Shih LB (1994) Processing of antibody-radioisotope conjugates after binding to the surface of tumor cells. *Cancer* 73(3 Suppl):787–793
18. Shih LB, Thorpe SR, Griffiths GL, Diril H, Ong GL, Hansen HJ, Goldenberg DM, Mattes MJ (1994) The processing and fate of antibodies and their radiolabels bound to the surface of tumor cells in vitro: a comparison of nine radiolabels. *J Nucl Med* 35(5):899–908

19. Ahlgren S, Orlova A, Rosik D, Sandstrom M, Sjoberg A, Baastrup B, Widmark O, Fant G, Feldwisch J, Tolmachev V (2008) Evaluation of maleimide derivative of DOTA for site-specific labeling of recombinant affibody molecules. *Bioconjug Chem* 19(1):235–243
20. Renberg B, Shiroyama I, Engfeldt T, Nygren PK, Karlstrom AE (2005) Affibody protein capture microarrays: synthesis and evaluation of random and directed immobilization of affibody molecules. *Anal Biochem* 341(2):334–343
21. Ekblad T, Orlova A, Feldwisch J, Wennborg A, Karlstrom AE, Tolmachev V (2009) Positioning of 99 mTc-chelators influences radiolabeling, stability and biodistribution of Affibody molecules. *Bioorg Med Chem Lett* 19(14):3912–3914
22. Engfeldt T, Renberg B, Brumer H, Nygren PA, Karlstrom AE (2005) Chemical synthesis of triple-labelled three-helix bundle binding proteins for specific fluorescent detection of unlabelled protein. *ChemBioChem* 6(6):1043–1050
23. Lindgren J, Ekblad C, Abrahamson L, Eriksson Karlstrom A (2012) A native chemical ligation approach for combinatorial assembly of affibody molecules. *ChemBioChem* 13(7):1024–1031
24. Feldwisch J, Tolmachev V, Lendel C, Herne N, Sjoberg A, Larsson B, Rosik D, Lindqvist E, Fant G, Hoiden-Guthenberg I, Galli J, Jonasson P, Abrahamson L (2010) Design of an optimized scaffold for affibody molecules. *J Mol Biol* 398(2):232–247
25. Namavari M, Padilla De Jesus O, Cheng Z, De A, Kovacs E, Levi J, Zhang R, Hoerner JK, Grade H, Syud FA, Gambhir SS (2008) Direct site-specific radiolabeling of an Affibody protein with 4-[¹⁸F] fluorobenzaldehyde via oxime chemistry. *Mol Imaging Biol* 10(4):177–181
26. Wilbur DS (1992) Radiohalogenation of proteins: an overview of radionuclides, labeling methods, and reagents for conjugate labeling. *Bioconjug Chem* 3(6):433–470
27. Laverman P, D'Souza CA, Eek A, McBride WJ, Sharkey RM, Oyen WJ, Goldenberg DM, Boerman OC (2012) Optimized labeling of NOTA-conjugated octreotide with F-18. *Tumour Biol* 33(2):427–434
28. Tolmachev V, Carlsson J, Lundqvist H (2004) A limiting factor for the progress of radionuclide-based cancer diagnostics and therapy—availability of suitable radionuclides. *Acta Oncol* 43(3):264–275
29. Wallberg H, Lofdahl PK, Tschapalda K, Uhlen M, Tolmachev V, Nygren PK, Stahl S (2011) Affinity recovery of eight HER2-binding affibody variants using an anti-idiotypic affibody molecule as capture ligand. *Protein Expr Purif* 76(1):127–135
30. Orlova A, Wallberg H, Stone-Elander S, Tolmachev V (2009) On the selection of a tracer for PET imaging of HER2-expressing tumors: direct comparison of a ¹²⁴I-labeled affibody molecule and trastuzumab in a murine xenograft model. *J Nucl Med* 50(3):417–425
31. Tran T, Engfeldt T, Orlova A, Sandstrom M, Feldwisch J, Abrahamson L, Wennborg A, Tolmachev V, Karlstrom AE (2007) ^{99m}Tc-maEEE-Z_{HER2:342}, an Affibody molecule-based tracer for the detection of HER2 expression in malignant tumors. *Bioconjug Chem* 18(6):1956–1964
32. Miao Z, Ren G, Liu H, Jiang L, Cheng Z (2010) Small-animal PET imaging of human epidermal growth factor receptor positive tumor with a ⁶⁴Cu labeled affibody protein. *Bioconjug Chem* 21(5):947–954
33. Hoppmann S, Miao Z, Liu S, Liu H, Ren G, Bao A, Cheng Z (2011) Radiolabeled affibody-albumin bioconjugates for HER2-positive cancer targeting. *Bioconjug Chem* 22(3):413–421
34. Ekblad T, Tolmachev V, Orlova A, Lendel C, Abrahamson L, Karlstrom AE (2009) Synthesis and chemoselective intramolecular crosslinking of a HER2-binding affibody. *Biopolymers* 92(2):116–123
35. Tolmachev V, Friedman M, Sandstrom M, Eriksson TL, Rosik D, Hodik M, Stahl S, Frejd FY, Orlova A (2009) Affibody molecules for epidermal growth factor receptor targeting in vivo: aspects of dimerization and labeling chemistry. *J Nucl Med* 50(2):274–283
36. Rahmim A, Zaidi H (2008) PET versus SPECT: strengths, limitations and challenges. *Nucl Med Commun* 29(3):193–207

37. Cheng Z, De Jesus OP, Namavari M, De A, Levi J, Webster JM, Zhang R, Lee B, Syud FA, Gambhir SS (2008) Small-animal PET imaging of human epidermal growth factor receptor type 2 expression with site-specific ^{18}F -labeled protein scaffold molecules. *J Nucl Med* 49(5):804–813
38. Miao Z, Ren G, Jiang L, Liu H, Webster JM, Zhang R, Namavari M, Gambhir SS, Syud F, Cheng Z (2011) A novel ^{18}F -labeled two-helix scaffold protein for PET imaging of HER2-positive tumor. *Eur J Nucl Med Mol Imaging* 38(11):1977–1984
39. Xu XY, Borghi A, Nchimi A, Leung J, Gomez P, Cheng Z, Defraigne JO, Sakalihasan N (2010) High levels of ^{18}F -FDG uptake in aortic aneurysm wall are associated with high wall stress. *Eur J Vasc Endovasc Surg* 39(3):295–301
40. Lindberg H, Hofstrom C, Altai M, Honorvar H, Wallberg H, Orlova A, Stahl S, Graslund T, Tolmachev V (2012) Evaluation of a HER2-targeting affibody molecule combining an N-terminal HEHEHE-tag with a GGGC chelator for $^{99\text{m}}\text{Tc}$ -labelling at the C terminus. *Tumour Biol* 33(3):641–651
41. Orlova A, Rosik D, Sandstrom M, Lundqvist H, Einarsson L, Tolmachev V (2007) Evaluation of [$^{111/114}\text{m In}$]CHX-A-DTPA- $\text{Z}_{\text{HER2}:342}$, an affibody ligand conjugate for targeting of HER2-expressing malignant tumors. *Q J Nucl Med Mol Imaging* 51(4):314–323
42. Engfeldt T, Tran T, Orlova A, Widstrom C, Feldwisch J, Abrahmsen L, Wennborg A, Karlstrom AE, Tolmachev V (2007) $^{99\text{m}}\text{Tc}$ -chelator engineering to improve tumour targeting properties of a HER2-specific Affibody molecule. *Eur J Nucl Med Mol Imaging* 34(11):1843–1853
43. Kramer-Marek G, Bernardo M, Kiesewetter DO, Bagci U, Kuban M, Aras O, Zielinski R, Seidel J, Choyke P, Capala J (2012) PET of HER2-positive pulmonary metastases with ^{18}F - $\text{Z}_{\text{HER2}:342}$ affibody in a murine model of breast cancer: comparison with ^{18}F -FDG. *J Nucl Med* 53(6):939–946
44. Altai M, Varasteh Z, Andersson K, Eek A, Boerman O, Orlova A (2013) In vivo and in vitro studies on renal uptake of radiolabeled affibody molecules for imaging of HER2 expression in tumors. *Cancer Biother Radiopharm* 28(3):187–195
45. Haggblad Sahlberg S, Spiegelberg D, Lennartsson J, Nygren P, Glimelius B, Stenerlow B (2012) The effect of a dimeric Affibody molecule (ZEGFR: 1907) 2 targeting EGFR in combination with radiation in colon cancer cell lines. *Int J Oncol* 40(1):176–184
46. Vernet E, Lundberg E, Friedman M, Rigamonti N, Klausning S, Nygren PA, Graslund T (2009) Affibody-mediated retention of the epidermal growth factor receptor in the secretory compartments leads to inhibition of phosphorylation in the kinase domain. *N Biotechnol* 25(6):417–423
47. Miao Z, Ren G, Liu H, Qi S, Wu S, Cheng Z (2012) PET of EGFR expression with an ^{18}F -labeled affibody molecule. *J Nucl Med* 53(7):1110–1118
48. Hoppmann S, Qi S, Miao Z, Liu H, Jiang H, Cutler CS, Bao A, Cheng Z (2012) ^{177}Lu -DO3A-HSA- $\text{Z}_{\text{EGFR}:1907}$ characterization as a potential radiopharmaceutical for radionuclide therapy of EGFR-expressing head and neck carcinomas. *J Biol Inorg Chem* 17(5):709–718
49. Becker A, Hessenius C, Licha K, Ebert B, Sukowski U, Semmler W, Wiedenmann B, Grotzinger C (2001) Receptor-targeted optical imaging of tumors with near-infrared fluorescent ligands. *Nat Biotechnol* 19(4):327–331
50. Bugaj JE, Achilefu S, Dorshow RB, Rajagopalan R (2001) Novel fluorescent contrast agents for optical imaging of in vivo tumors based on a receptor-targeted dye-peptide conjugate platform. *J Biomed Opt* 6(2):122–133
51. Engelbrecht CJ, Johnston RS, Seibel EJ, Helmchen F (2008) Ultra-compact fiber-optic two-photon microscope for functional fluorescence imaging in vivo. *Opt Express* 16(8):5556–5564
52. Lee SB, Hassan M, Fisher R, Chertov O, Chernomordik V, Kramer-Marek G, Gandjbakhche A, Capala J (2008) Affibody molecules for in vivo characterization of HER2-positive tumors by near-infrared imaging. *Clin Cancer Res* 14(12):3840–3849

53. Qi S, Miao Z, Liu H, Xu Y, Feng Y, Cheng Z (2012) Evaluation of four Affibody-based near-infrared fluorescent probes for optical imaging of epidermal growth factor receptor positive tumors. *Bioconjug Chem*, 23(6):1149–1156
54. Kinoshita M, Yoshioka Y, Okita Y, Hashimoto N, Yoshimine T (2010) MR molecular imaging of HER-2 in a murine tumor xenograft by SPIO labeling of anti-HER-2 affibody. *Contrast Media Mol Imaging* 5(1):18–22
55. Yang M, Cheng K, Qi S, Liu H, Jiang Y, Jiang H, Li J, Chen K, Zhang H, Cheng Z (2013) Affibody modified and radiolabeled gold-Iron oxide hetero-nanostructures for tumor PET, optical and MR imaging. *Biomaterials* 34(11):2796–2806
56. Wahlberg E, Lendel C, Helgstrand M, Allard P, Dincbas-Renqvist V, Hedqvist A, Berglund H, Nygren PA, Hard T (2003) An affibody in complex with a target protein: structure and coupled folding. *Proc Natl Acad Sci USA* 100(6):3185–3190
57. Lundberg E, Hoiden-Guthenberg I, Larsson B, Uhlen M, Graslund T (2007) Site-specifically conjugated anti-HER2 Affibody molecules as one-step reagents for target expression analyses on cells and xenograft samples. *J Immunol Methods* 319(1–2):53–63
58. Lendel C, Wahlberg E, Berglund H, Eklund M, Nygren PA, Hard T (2002) ^1H , ^{13}C and ^{15}N resonance assignments of an affibody-target complex. *J Biomol NMR* 24(3):271–272
59. Yarden Y, Sliwkowski MX (2001) Untangling the ErbB signalling network. *Nat Rev Mol Cell Biol* 2(2):127–137
60. Holbro T, Civenni G, Hynes NE (2003) The ErbB receptors and their role in cancer progression. *Exp Cell Res* 284(1):99–110
61. Arteaga CL (2002) Epidermal growth factor receptor dependence in human tumors: more than just expression? *Oncologist* 7(Suppl 4):31–39
62. Nicholson RI, Gee JM, Harper ME (2001) EGFR and cancer prognosis. *Eur J Cancer* 37(Suppl 4):S9–S15
63. Nordberg E, Ekerljung L, Sahlberg SH, Carlsson J, Lennartsson J, Glimelius B (2010) Effects of an EGFR-binding affibody molecule on intracellular signaling pathways. *Int J Oncol* 36(4):967–972
64. Gostring L, Chew MT, Orlova A, Hoiden-Guthenberg I, Wennborg A, Carlsson J, Frejd FY (2010) Quantification of internalization of EGFR-binding Affibody molecules: Methodological aspects. *Int J Oncol* 36(4):757–763
65. Friedman M, Lindstrom S, Ekerljung L, Andersson-Svahn H, Carlsson J, Brismar H, Gedda L, Frejd FY, Stahl S (2009) Engineering and characterization of a bispecific HER2 \times EGFR-binding affibody molecule. *Biotechnol Appl Biochem* 54(2):121–131
66. Burden S, Yarden Y (1997) Neuregulins and their receptors: a versatile signaling module in organogenesis and oncogenesis. *Neuron* 18(6):847–855
67. Beuttler J, Rothdiener M, Muller D, Frejd FY, Kontermann RE (2009) Targeting of epidermal growth factor receptor (EGFR)-expressing tumor cells with sterically stabilized affibody liposomes (SAL). *Bioconjug Chem* 20(6):1201–1208
68. Khasraw M, Bell R (2012) Primary systemic therapy in HER2-amplified breast cancer: a clinical review. *Expert Rev Anticancer Ther* 12(8):1005–1013
69. Infante JR, Yardley DA, Burris HA 3rd, Greco FA, Farley CP, Webb C, Spigel DR, Hainsworth JD (2009) Phase II trial of weekly docetaxel, vinorelbine, and trastuzumab in the first-line treatment of patients with HER2-positive metastatic breast cancer. *Clin Breast Cancer* 9(1):23–28
70. Tokudome N, Ito Y, Hatake K, Toi M, Sano M, Iwata H, Sato Y, Saeki T, Aogi K, Takashima S (2008) Trastuzumab and vinorelbine as first-line therapy for HER2-overexpressing metastatic breast cancer: multicenter phase II and pharmacokinetic study in Japan. *Anticancer Drugs* 19(7):753–759
71. Burstein HJ, Harris LN, Marcom PK, Lambert-Falls R, Havlin K, Overmoyer B, Friedlander RJ Jr, Gargiulo J, Strenger R, Vogel CL, Ryan PD, Ellis MJ, Nunes RA, Bunnell CA, Campos SM, Hallor M, Gelman R, Winer EP (2003) Trastuzumab and vinorelbine as first-line therapy for HER2-overexpressing metastatic breast cancer: multicenter phase II trial

- with clinical outcomes, analysis of serum tumor markers as predictive factors, and cardiac surveillance algorithm. *J Clin Oncol* 21(15):2889–2895
72. Arteaga CL (2003) Trastuzumab, an appropriate first-line single-agent therapy for HER2-overexpressing metastatic breast cancer. *Breast Cancer Res* 5(2):96–100
 73. Tang Y, Wang J, Scollard DA, Mondal H, Holloway C, Kahn HJ, Reilly RM (2005) Imaging of HER2/neu-positive BT-474 human breast cancer xenografts in athymic mice using ^{111}In -trastuzumab (Herceptin) Fab fragments. *Nucl Med Biol* 32(1):51–58
 74. Orlova A, Nilsson FY, Wikman M, Widstrom C, Stahl S, Carlsson J, Tolmachev V (2006) Comparative in vivo evaluation of technetium and iodine labels on an anti-HER2 affibody for single-photon imaging of HER2 expression in tumors. *J Nucl Med* 47(3):512–519
 75. Tran T, Orlova A, Sivaev I, Sandstrom M, Tolmachev V (2007) Comparison of benzoate- and dodecaborate-based linkers for attachment of radioiodine to HER2-targeting Affibody ligand. *Int J Mol Med* 19(3):485–493
 76. Tolmachev V, Nilsson FY, Widstrom C, Andersson K, Rosik D, Gedda L, Wennborg A, Orlova A (2006) ^{111}In -benzyl-DTPA- $Z_{\text{HER2}:342}$, an affibody-based conjugate for in vivo imaging of HER2 expression in malignant tumors. *J Nucl Med* 47(5):846–853
 77. Heskamp S, Laverman P, Rosik D, Boschetti F, van der Graaf WT, Oyen WJ, van Laarhoven HW, Tolmachev V, Boerman OC (2012) Imaging of human epidermal growth factor receptor type 2 expression with ^{18}F -labeled affibody molecule $Z_{\text{HER2}:2395}$ in a mouse model for ovarian cancer. *J Nucl Med* 53(1):146–153
 78. Ekerljung L, Lennartsson J, Gedda L (2012) The HER2-binding affibody molecule ($Z_{\text{HER2}:342}$)₂ increases radiosensitivity in SKBR-3 cells. *PLoS ONE* 7(11):e49579
 79. Ekerljung L, Steffen AC, Carlsson J, Lennartsson J (2006) Effects of HER2-binding affibody molecules on intracellular signaling pathways. *Tumour Biol* 27(4):201–210
 80. Wikman M, Steffen AC, Gunneriusson E, Tolmachev V, Adams GP, Carlsson J, Stahl S (2004) Selection and characterization of HER2/neu-binding affibody ligands. *Protein Eng Des Sel* 17(5):455–462
 81. Tolmachev V, Orlova A, Pehrson R, Galli J, Baastrup B, Andersson K, Sandstrom M, Rosik D, Carlsson J, Lundqvist H, Wennborg A, Nilsson FY (2007) Radionuclide therapy of HER2-positive microxenografts using a ^{177}Lu -labeled HER2-specific Affibody molecule. *Cancer Res* 67(6):2773–2782
 82. Orlova A, Tolmachev V, Pehrson R, Lindborg M, Tran T, Sandstrom M, Nilsson FY, Wennborg A, Abrahamson L, Feldwisch J (2007) Synthetic affibody molecules: a novel class of affinity ligands for molecular imaging of HER2-expressing malignant tumors. *Cancer Res* 67(5):2178–2186
 83. Engfeldt T, Orlova A, Tran T, Bruskin A, Widstrom C, Karlstrom AE, Tolmachev V (2007) Imaging of HER2-expressing tumours using a synthetic Affibody molecule containing the $^{99\text{m}}\text{Tc}$ -chelating mercaptoacetyl-glycyl-glycyl-glycyl (MAG3) sequence. *Eur J Nucl Med Mol Imaging* 34(5):722–733
 84. Nishimura Y, Ishii J, Okazaki F, Ogino C, Kondo A (2012) Complex carriers of affibody-displaying bio-nanocapsules and composition-varied liposomes for HER2-expressing breast cancer cell-specific protein delivery. *J Drug Target* 20(10):897–905
 85. van de Ven SM, Elias SG, Chan CT, Miao Z, Cheng Z, De A, Gambhir SS (2012) Optical imaging with HER2-targeted affibody molecules can monitor hsp90 treatment response in a breast cancer xenograft mouse model. *Clin Cancer Res* 18(4):1073–1081
 86. Qvarnstrom OF, Simonsson M, Carlsson J, Tran TA (2011) Effects of affinity on binding of HER2-targeting Affibody molecules: model experiments in breast cancer spheroids. *Int J Oncol* 39(2):353–359
 87. Hynes NE, Lane HA (2005) ERBB receptors and cancer: the complexity of targeted inhibitors. *Nat Rev Cancer* 5(5):341–354
 88. Burgess AW, Cho HS, Eigenbrot C, Ferguson KM, Garrett TP, Leahy DJ, Lemmon MA, Sliwkowski MX, Ward CW, Yokoyama S (2003) An open-and-shut case? Recent insights into the activation of EGF/ErbB receptors. *Mol Cell* 12(3):541–552

89. Harari PM (2004) Epidermal growth factor receptor inhibition strategies in oncology. *Endocr Relat Cancer* 11(4):689–708
90. Perez-Soler R (2004) HER1/EGFR targeting: refining the strategy. *Oncologist* 9(1):58–67
91. Rocha-Lima CM, Soares HP, Raez LE, Singal R (2007) EGFR targeting of solid tumors. *Cancer Control* 14(3):295–304
92. DiGiovanna MP, Stern DF, Edgerton SM, Whalen SG, Moore D 2nd, Thor AD (2005) Relationship of epidermal growth factor receptor expression to ErbB-2 signaling activity and prognosis in breast cancer patients. *J Clin Oncol* 23(6):1152–1160
93. Burris HA 3rd (2004) Dual kinase inhibition in the treatment of breast cancer: initial experience with the EGFR/ErbB-2 inhibitor lapatinib. *Oncologist* 9(Suppl 3):10–15
94. Geyer CE, Forster J, Lindquist D, Chan S, Romieu CG, Pienkowski T, Jagiello-Gruszfeld A, Crown J, Chan A, Kaufman B, Skarlos D, Campone M, Davidson N, Berger M, Oliva C, Rubin SD, Stein S, Cameron D (2006) Lapatinib plus capecitabine for HER2-positive advanced breast cancer. *N Engl J Med* 355(26):2733–2743
95. Jones HE, Goddard L, Gee JM, Hiscox S, Rubini M, Barrow D, Knowlden JM, Williams S, Wakeling AE, Nicholson RI (2004) Insulin-like growth factor-I receptor signalling and acquired resistance to gefitinib (ZD1839; Iressa) in human breast and prostate cancer cells. *Endocr Relat Cancer* 11(4):793–814
96. Pantaleo MA, Nannini M, Maleddu A, Fanti S, Nanni C, Boschi S, Lodi F, Nicoletti G, Landuzzi L, Lollini PL, Biasco G (2009) Experimental results and related clinical implications of PET detection of epidermal growth factor receptor (EGFR) in cancer. *Ann Oncol* 20(2):213–226
97. Miao Z, Ren G, Liu H, Jiang L, Cheng Z (2010) Cy5.5-labeled Affibody molecule for near-infrared fluorescent optical imaging of epidermal growth factor receptor positive tumors. *J Biomed Opt* 15(3):036007
98. Friedman M, Orlova A, Johansson E, Eriksson TL, Hoiden-Guthenberg I, Tolmachev V, Nilsson FY, Stahl S (2008) Directed evolution to low nanomolar affinity of a tumor-targeting epidermal growth factor receptor-binding affibody molecule. *J Mol Biol* 376(5):1388–1402
99. Nordberg E, Orlova A, Friedman M, Tolmachev V, Stahl S, Nilsson FY, Glimelius B, Carlsson J (2008) In vivo and in vitro uptake of ^{111}In , delivered with the affibody molecule (ZEGFR: 955) 2 in EGFR expressing tumour cells. *Oncol Rep* 19(4):853–857
100. Tolmachev V, Malmberg J, Hofstrom C, Abrahmsen L, Bergman T, Sjoberg A, Sandstrom M, Graslund T, Orlova A (2012) Imaging of insulinlike growth factor type 1 receptor in prostate cancer xenografts using the affibody molecule ^{111}In -DOTA-Z_{IGF1R:4551}. *J Nucl Med* 53(1):90–97
101. Wallberg H, Orlova A (2008) Slow internalization of anti-HER2 synthetic affibody monomer ^{111}In -DOTA-Z_{HER2:342-pep2}: implications for development of labeled tracers. *Cancer Biother Radiopharm* 23(4):435–442
102. Baum RP, Prasad V, Muller D, Schuchardt C, Orlova A, Wennborg A, Tolmachev V, Feldwisch J (2010) Molecular imaging of HER2-expressing malignant tumors in breast cancer patients using synthetic ^{111}In - or ^{68}Ga -labeled affibody molecules. *J Nucl Med* 51(6):892–897
103. Orlova A, Feldwisch J, Abrahmsen L, Tolmachev V (2007) Update: affibody molecules for molecular imaging and therapy for cancer. *Cancer Biother Radiopharm* 22(5):573–584
104. Tomblyn M (2012) Radioimmunotherapy for B-cell non-hodgkin lymphomas. *Cancer Control* 19(3):196–203
105. Morschhauser F, Radford J, Van Hoof A, Botto B, Rohatiner AZ, Salles G, Soubeyran P, Tilly H, Bischof-Delaloye A, van Putten WL, Kylastra JW, Hagenbeek A (2013) 90 Yttrium-Ibritumomab Tiuxetan consolidation of first remission in advanced-stage follicular non-Hodgkin lymphoma: updated results after a median follow-up of 7.3 Years from the international, randomized, phase III First-Line Indolent Trial. *J Clin Oncol* 31(16):1977–1983

106. Behr TM, Goldenberg DM, Becker W (1998) Reducing the renal uptake of radiolabeled antibody fragments and peptides for diagnosis and therapy: present status, future prospects and limitations. *Eur J Nucl Med* 25(2):201–212
107. Fortin MA, Orlova A, Malmstrom PU, Tolmachev V (2007) Labelling chemistry and characterization of [⁹⁰Y/¹⁷⁷Lu]-DOTA-Z_{HER2:342-3} Affibody molecule, a candidate agent for locoregional treatment of urinary bladder carcinoma. *Int J Mol Med* 19(2):285–291
108. Carlsson J, Ren ZP, Wester K, Sundberg AL, Heldin NE, Hesselager G, Persson M, Gedda L, Tolmachev V, Lundqvist H, Blomquist E, Nister M (2006) Planning for intracavitary anti-EGFR radionuclide therapy of gliomas, literature review and data on EGFR expression. *J Neurooncol* 77(1):33–45
109. Orlova A, Tran TA, Ekblad T, Karlstrom AE, Tolmachev V (2010) ¹⁸⁶Re-maSGS-Z_(HER2:342), a potential Affibody conjugate for systemic therapy of HER2-expressing tumours. *Eur J Nucl Med Mol Imaging* 37(2):260–269
110. Tolmachev V, Wallberg H, Andersson K, Wennborg A, Lundqvist H, Orlova A (2009) The influence of Bz-DOTA and CHX-A''-DTPA on the biodistribution of ABD-fused anti-HER2 Affibody molecules: implications for ^{114m}In-mediated targeting therapy. *Eur J Nucl Med Mol Imaging* 36(9):1460–1468
111. Hammond SA, Lutterbuese R, Roff S, Lutterbuese P, Schlereth B, Bruckheimer E, Kinch MS, Coats S, Baeuerle PA, Kufer P, Kiener PA (2007) Selective targeting and potent control of tumor growth using an EphA2/CD3-Bispecific single-chain antibody construct. *Cancer Res* 67(8):3927–3935
112. Reusch U, Sundaram M, Davol PA, Olson SD, Davis JB, Demel K, Nissim J, Rathore R, Liu PY, Lum LG (2006) Anti-CD3 x anti-epidermal growth factor receptor (EGFR) bispecific antibody redirects T-cell cytolytic activity to EGFR-positive cancers in vitro and in an animal model. *Clin Cancer Res* 12(1):183–190
113. Kipriyanov SM, Cochlovius B, Schafer HJ, Moldenhauer G, Bahre A, Le Gall F, Knackmuss S, Little M (2002) Synergistic antitumor effect of bispecific CD19 x CD3 and CD19 x CD16 diabodies in a preclinical model of non-Hodgkin's lymphoma. *J Immunol* 169(1):137–144
114. Friedman M, Nordberg E, Hoiden-Guthenberg I, Brismar H, Adams GP, Nilsson FY, Carlsson J, Stahl S (2007) Phage display selection of Affibody molecules with specific binding to the extracellular domain of the epidermal growth factor receptor. *Protein Eng Des Sel* 20(4):189–199
115. Steffen AC, Wikman M, Tolmachev V, Adams GP, Nilsson FY, Stahl S, Carlsson J (2005) In vitro characterization of a bivalent anti-HER-2 affibody with potential for radionuclide-based diagnostics. *Cancer Biother Radiopharm* 20(3):239–248
116. Ronnmark J, Hansson M, Nguyen T, Uhlen M, Robert A, Stahl S, Nygren PA (2002) Construction and characterization of affibody-Fc chimeras produced in *Escherichia coli*. *J Immunol Methods* 261(1–2):199–211
117. de Vrij J, Dautzenberg IJ, van den Hengel SK, Magnusson MK, Uil TG, Cramer SJ, Vellinga J, Verissimo CS, Lindholm L, Koppers-Lalic D, Hoeben RC (2012) A cathepsin-cleavage site between the adenovirus capsid protein IX and a tumor-targeting ligand improves targeted transduction. *Gene Ther* 19(9):899–906
118. Zatovicova M, Jelenska L, Hulikova A, Csaderova L, Ditte Z, Ditte P, Goliasova T, Pastorek J, Pastorekova S (2010) Carbonic anhydrase IX as an anticancer therapy target: preclinical evaluation of internalizing monoclonal antibody directed to catalytic domain. *Curr Pharm Des* 16(29):3255–3263
119. Magnusson MK, Kraaij R, Leadley RM, De Ridder CM, van Weerden WM, Van Schie KA, Van der Kroeg M, Hoeben RC, Maitland NJ, Lindholm L (2012) A transductionally retargeted adenoviral vector for virotherapy of HER2/neu-expressing prostate cancer. *Hum Gene Ther* 23(1):70–82
120. Myhre S, Henning P, Friedman M, Stahl S, Lindholm L, Magnusson MK (2009) Re-targeted adenovirus vectors with dual specificity; binding specificities conferred by two different Affibody molecules in the fiber. *Gene Ther* 16(2):252–261

Chapter 13

Alternative Protein Scaffolds for Molecular Imaging and Therapy

Benjamin J. Hackel

13.1 Introduction

Molecular targeting can improve the sensitivity and specificity of diagnosis and treatment for a multitude of diseases including cancers, cardiovascular disease, and immune disorders. Nature's most frequent general solution to molecular recognition is the antibody, which has resultantly become the most common laboratory solution as well. The capacity for high-affinity, specific binding in a modestly stable, reasonably bioavailable construct has yielded multiple clinical successes with the antibody [1]. Yet, a multitude of shortcomings renders the antibody as suboptimal for many applications. Large size (150 kDa for immunoglobulin G) limits permeability and diffusion to hinder physiological distribution [2, 3]. In concert with neonatal Fc receptor binding, large size also results in slow plasma clearance for elevated background targeting. Structural complexity hinders protein fusion such as for bispecific formats or immunotoxins. Glycosylation, disulfide bonds, and multi-domain architecture necessitate mammalian cell culture for precise production. Disulfide bonds generally preclude intracellular use and complicate thiol-based site-specific conjugation of drugs, detection moieties, or additional effectors. Antibodies also have moderate instability that can impact efficacy and immunogenicity. Lastly, the complex intellectual property landscape for antibodies is often a hindrance to commercial development.

As a result of these limitations, alternatives to antibodies have emerged in the last decade and a half for scientific, biotechnological, and clinical applications [4, 5]. These alternative protein scaffolds comprise a diversified binding paratope and a conserved structural framework that imparts biophysical benefits relative to the multi-domain immunoglobulin construct. The aforementioned antibody limitations are addressed to varying degrees by different scaffolds but generally comprise

B. J. Hackel (✉)

Department of Chemical Engineering and Materials Science, University of Minnesota,
421 Washington Avenue SE, Minneapolis, MN 55455, USA
e-mail: hackel@umn.edu

Table 13.1 Protein scaffolds

Name	Amino acids	Topology	Typical paratope	Stability (T_m , °C)	
				Parental	Binders
Knottin	20–50	Knotted 3-disulfide core	Loop 1	~100	N.d.
Affibody	58	Triple α -helical bundle	13 amino acids on surface of helices 1 and 2	72	37–65 (46)
Fibronectin	94	β sandwich	BC + FG (+DE) loops	86	42–73 (57)
DARPin	130–200	4–6 repeats of: β turn + two α helices	Select amino acids in β turn and first α helix	>90	66–85 (79)
Anticalin	150–185	β barrel	12–20 amino acids near “top” of β barrel; dependent on target	79	53–73 (68)

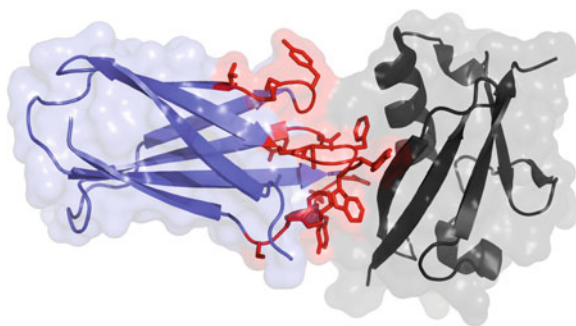
small, disulfide-free, stable, single domains capable of evolution to specific, high-affinity binding to various targets. This is achieved with a diverse array of protein topologies including helical bundles (affibodies [6]) and beta sandwiches (fibronectin domains [7]), repeats of antiparallel alpha helices with a beta turn (designed ankyrin repeat proteins (DARPins) [8]), beta barrels (anticalin [9]), cystine knots (knottins [10]), and many others (Table 13.1). Clearly, there are multiple topological solutions to the molecular recognition challenge. Each offers its own advantages and disadvantages. Rather than aiming to identify the ultimate scaffold in general, efficacy would benefit from selecting the appropriate scaffold for the task at hand. Identification and enhancement of binding ligands based on these scaffolds is most commonly achieved by directed evolution using genotype–phenotype linked display technologies, including phage display, yeast surface display, and mRNA display, that empower high-throughput search of protein sequence space [11].

The multitude of scientific, industrial, and in vitro applications empowered by these scaffolds, as well as the optimization of their evolution, has been reviewed [5, 12]. This chapter will provide biophysical information on each scaffold and then focus on the translation of these scaffolds to clinical use in patients; thus, experimental work in animal models and clinical trials are highlighted. Also, at an admitted cost of timeliness, the focus is placed on peer-reviewed published research.

13.2 Fibronectin Domains

The tenth type III domain of human fibronectin (also known as monobody or Adnectin) is a 94-amino-acid (10 kDa) beta sandwich with high thermal stability ($T_m = 86$ °C) (Fig. 13.1) [13]. The scaffold is tolerant to mutations within the loop

Fig. 13.1 Fibronectin domain (*blue and red*) in complex with human small ubiquitin-like modifier 1 (*black*); PDB: 3RZW. The residues commonly mutated in scaffold evolution are shown in *red* with side chains



regions connecting the beta strands, particularly the adjacent loops connecting the BC, DE, and FG strands [14]. Diversification within one to three of these loops has enabled discovery and evolution of specific, high-affinity binding ligands to cell surface receptors, intracellular targets, and extracellular proteins. Affinities typically range from mid-nanomolar to low picomolar [7]. Destabilization due to diversification yields proteins with T_m values of 42–73 °C (median 57 °C) [13, 15–17]. It should be noted that incorporation of stability bias in the naïve library elevated the average T_m of engineered clones by 10 °C [17]. The scaffold is stable to moderate acidity [18] and devoid of natural cysteines; thus, it is appropriate for use in various intracellular locales. A single thiol can be genetically introduced for site-specific chemistry, or primary amines (N-terminus and lysine at position 63 distal to the paratope) can also be used.

13.2.1 CT-322

The fibronectin molecule that has advanced the furthest clinically is CT-322 (BMS-844203, pegdinetanib), a vascular endothelial growth factor receptor 2 binder (VEGFR2) developed by Adnexus Therapeutics (Bristol-Myers Squibb). The lead molecule was discovered by mRNA display [15] and affinity matured for human and mouse cross-reactivity [19]. The evolved protein was modified in several ways as follows: (a) seven amino acids at the N-terminal end, VSDVPRD, were removed; (b) the natural seven-amino-acid linker following the tenth type III domain, EIDKPSQ, was introduced; (c) the serine in the C-terminal tail was mutated to cysteine; and (d) the unique cysteine introduced at the penultimate residue was conjugated to a 40-kDa branched poly (ethylene glycol) (PEG). The resultant molecule has 11 nM affinity for VEGFR2 and negligible cross-reactivity for VEGFR1 or VEGFR3 [20]. PEGylation slows the plasma clearance from a terminal half-time of 4 ± 2 h for native protein to 17 ± 2 h with 20-kDa PEG and 50 ± 20 h with 40-kDa PEG.

In the initial publication of *in vivo* results for CT-322, the molecule reduced the growth of orthotopic MiaPaCa-xenografted tumors by 42 % in nude mice [21].

Physiological manifestations included increased apoptosis, reduced microvessel density, and reduced VEGF-activated blood vessels. However, metastases were still observed at the same frequency as control treatment. Conversely, in a syngeneic Pan02 xenograft model in immunocompetent mice, CT-322 eliminated metastases although the 23 % reduction in primary tumor size was not statistically significant. Combination therapy with gemcitabine elevated efficacy to a 65 % reduction in tumor size, further validating the therapeutic potential of the evolved scaffold.

Evaluation in a glioblastoma xenograft model in nude mice demonstrated a 45 % reduction in tumor growth [20]. Increasing the dose to 30 mg/kg every other day yielded inhibition of tumor growth and microvessel generation equivalent to anti-VEGFR2 antibody DC101. CT-322 was also compared to small-molecule receptor tyrosine kinase inhibitors. Colo-205 xenograft growth inhibition by CT-322 (30 mg/kg biweekly) was comparable to sorafenib and sunitinib but with reduced skin rash, weight loss, and death. Vascular growth was significantly inhibited [22]. CT-322 (60 mg/kg thrice weekly) was comparable to mTor inhibitor temsirolimus, and the benefits were partially additive. Also, in a separate model, the incidence of breast cancer metastasis was inhibited 64 % by CT-322.

Evaluation of CT-322 in an intracranial glioblastoma murine model further validated its efficacy [23]. Monotherapy decreased U87 xenograft tumor size and increased survival from 19 to 29 days. Moreover, CT-322 boosts therapeutic efficacy of the DNA-alkylating agent temozolomide by further decreasing tumor size and extending survival from 32 to 47 days. Immunohistochemical staining demonstrates inhibited microvessel formation, increased apoptosis, and decreased proliferation.

Therapeutic efficacy in multiple murine models with concomitant validation of physiological mechanisms motivated further clinical translation of CT-322. Toxicology studies indicated no adverse effects at 5 and 10 mg/kg in rats and monkeys [24], further supporting human trials. A phase I trial identified a maximum tolerated dose of 2 mg/kg intravenously weekly or biweekly, which yielded a lack of severe toxicity and a clearance half-time of 71–98 h [24]. 82 % of patients developed anti-drug antibodies that were shown to bind to the engineered loops of CT-322, which are of synthetic, non-human origin. Nevertheless, the response did not impact CT-322 or VEGF-A concentrations. Of the 34 patients available for therapeutic evaluation, 68 % had stable disease and 12 % demonstrated a reduction in tumor size.

In a phase II study for first-line treatment of advanced non-small-cell lung cancer, patients received paclitaxel/carboplatin plus either CT-322 or bevacizumab (antibody targeting VEGF-A) [25]. Progression-free survival (5.6 months vs. 6.8 months; CT-322 vs. bevacizumab), overall survival (12.5 months vs. 15.2 months), and response rate (25 % vs. 33 %) were all lower with CT-322 than with bevacizumab. Thrombocytopenia and grade ≥ 3 hypertension increased with CT-322. The efficacy of CT-322 in other clinical indications awaits further study.

13.2.2 Additional Therapeutic Fibronectins

An additional growth factor receptor antagonist, a type I insulin-like growth factor receptor (IGF1R) binder with 110 pM affinity, has been studied [26]. This molecule, PEGylated akin to CT-322, reduced vascular surface area by 59 % and reduced tumor growth by 37 % in a xenograft mouse model of Ewing's sarcoma. Combination treatment with CT-322 did not yield statistically significant gains in tumor inhibition.

This agent was also genetically fused to an epidermal growth factor receptor (EGFR)-targeted fibronectin [27]. PEGylation reduced the affinity of both components 10–20 fold though strong parental affinity yielded 1 and 10 nM final affinity for IGF1R and EGFR. The bispecific agent inhibits H292 lung cancer xenografted tumors in mice compared to EGFR-targeted panitumumab. More notably, the bispecific fibronectin construct inhibits RH41 pediatric rhabdomyosarcoma xenografted tumors, which are not effectively treated by panitumumab. In BxPC3 xenografted tumors, the bispecific yielded greater tumor growth inhibition than EGFR-targeted cetuximab or even a mixture of monospecific fibronectin domains. Thus, bispecific agents may provide benefits over multi-agent treatment approaches. Notably, the fibronectin-based bispecific agent was a simple genetic fusion with a (GS)₁₀ linker and was stable ($T_m = 58\text{ }^\circ\text{C}$) and monomeric. ¹⁴C labeling of the domain along with whole-body autoradiography delineated physiological distribution including variable tumor uptake (1–3 %ID/g in RH41 vs. 6–11 %ID/g in H292) [28].

Research on an alternative multi-specific agent provides data on one possible mechanism for improved efficacy relative to monospecific agents. An antibody–fibronectin construct targeting three independent EGFR epitopes clusters receptors, yielding downregulation of surface EGFR. This construct dramatically reduced the growth of BRAF and KRAS xenografted tumors in mice [29].

13.2.3 Diagnostics

On the diagnostic front, the fibronectin domain has demonstrated effective imaging in molecular positron emission tomography (PET). A fibronectin domain engineered for binding EGFR was radiolabeled with ⁶⁴Cu using a 1,4,7,10-tetra-azacyclododecane-1,4,7,10-tetraacetic acid (DOTA) chelator [30]. The resultant molecule is stable in mouse and human serum for at least 24 h. Molecular PET exhibits EGFR-specific tumor uptake within ~20 min and rapid clearance from blood (half-time = 2.1 min) and healthy tissue. $3.4 \pm 1.0\text{ }\%ID/g$ was achieved in tumor at 1 h post-injection with a 9:1 tumor:background ratio. The primary limitation of the molecule is high renal uptake and retention although the 2.1 mGy/MBq renal dose is still only 2 % of the maximum tolerated dose. Moreover, preliminary work indicates that using an ¹⁸F-labeling approach substantially reduces renal signal. The higher positron yield and more rapid radioactive decay (half-life = 1.8 h) make ¹⁸F a

preferable isotope for clinical use. The impact of protein scaffold hydrophilicity and charge on physiological distribution was elucidated using molecular PET to analyze delivery of fibronectin mutants [31]. Renal retention was reduced by selective removal of charged residues. Hydrophilicity reduces hepatic retention but elevates renal retention.

13.2.4 Future Outlook for Fibronectin

Fibronectin domains have been effectively used as monovalent antagonists, multi-specific fusions, immunotoxins in cell culture [32], and molecular PET diagnostics. A PEGylated fibronectin has proven safe and biologically active in patients. Additional study will continue to identify the efficacy of this compound and others relative to alternative therapeutic molecules in various indications including cardiovascular disease [33]. The small size and rapid clearance of non-PEGylated fibronectins are well suited for molecular imaging, which has demonstrated preclinical efficacy. Efficacy in both therapy and imaging coupled with robust, efficient evolution of stable, high affinity binders to a multitude of targets poise the fibronectin scaffold for continued successful development.

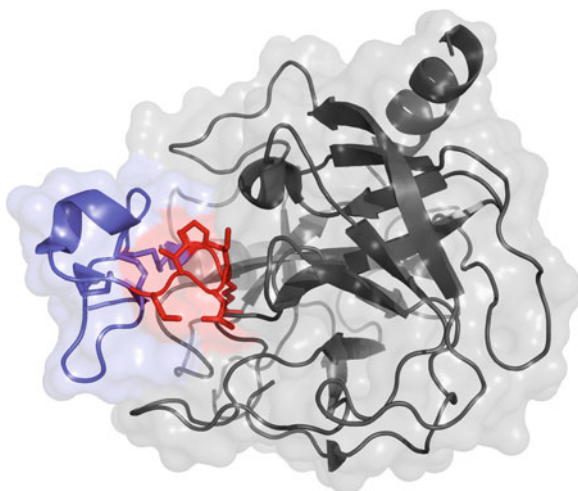
13.3 Knottins

Knottins are polypeptides, typically 25–50 amino acids in length, with at least three disulfide bonds that result in a knotted structure (Fig. 13.2). An additional subset of knottins, called cyclotides, have connected N- and C-termini to yield cyclic knots. The knotted core provides exceptional stability, including the ability to withstand near-boiling temperatures and denaturants [34]. Knottins have demonstrated stability to gastric proteases and provide potential for oral delivery [35]. The small size is well suited to rapid, efficient physiological distribution. The molecule can be prepared recombinantly, typically in the methylotropic yeast *Pichia pastoris* [36], or synthetically, in which the complex knotted structure requires careful refolding. The knotted structure yields several solvent-accessible loops between cysteine residues; these loops exhibit sequence and length variability across the multitude of knottins [37]. Appropriate sequences within one or two of these loops can provide binding to a host of targets.

13.3.1 Natural Knottins

Several natural knottins have been explored for clinical use. For example, ziconotide, isolated from the cone snail, is an N-type calcium channel antagonist. It is approved by the United States Food and Drug Administration (FDA) as an

Fig. 13.2 Knottin peptide (blue and red) in complex with trypsin (black); PDB: 1H9I. The residues commonly mutated in scaffold evolution of loop 1 are shown in red with side chains



analgesic for severe chronic pain. It has also demonstrated 44 % reduction in ischemic cerebral damage in a rabbit model [38]. In mouse models of cachexia, a 50-amino-acid portion of agouti-related peptide (AgRP) targeting melanocortin receptor has effectively inhibited appetite suppression and weight loss induced by radiation or tumor growth [39]. The 36-amino-acid chlorotoxin targets annexin A2, resulting in preferential binding to multiple malignant cell types relative to healthy tissue. Conjugation with ^{131}I enables single-photon emission computed tomography (SPECT) imaging of glioma in human patients [40] and has completed phase I and II trials for radiotherapy [41, 42]. Conjugation of the near-infrared fluorophore Cy5.5 has enabled fluorescence molecular imaging of xenografted glioma, spontaneous medulloblastoma, primary prostate tumors, and lung metastases in mice [43]. Decoration of superparamagnetic iron oxide nanoparticles with chlorotoxin permits molecular magnetic resonance imaging [44].

13.3.2 Synthetic Knottins

Synthetic knottins have been engineered by grafting binding motifs into knottin loops and evolving the grafted peptides. Thrombopoietin peptide mimics were grafted into knottin frameworks based on AgRP or *Ecbalium elaterium* trypsin inhibitor II (EETI-II) and crosslinked [45]. The resultant dimers stimulated proliferation of megakaryoblasts. A 200 ng dose of an EETI-II-based dimer was able to double the platelet count in a mouse model.

The Cochran lab in conjunction with the Cheng and Gambhir labs has performed extensive murine studies on knottins for molecular imaging of integrins. The RGD tripeptide motif was inserted into loop 1 of the EETI-II scaffold, and

directed evolution with yeast surface display was used to identify clones with ~ 20 nM affinity for integrin $\alpha_v\beta_3$ [46]. These clones were then used for development of molecular imaging agents. Conjugation with Cy5.5 or ^{64}Cu enabled near-infrared fluorescence imaging or PET of xenografted U87 tumors in nude mice [47]. At 4 h post-injection, 4 %ID/g tumor and a 20:1 tumor:muscle ratio were achieved for the radiolabeled agent. Simultaneous labeling with the fluorophore and radioisotope was also achieved while retaining activity [48]. To better match the rapid biodistribution and clearance of the 4-kDa knottin, clone 2.5D was radiolabeled with ^{18}F using N-succinimidyl-4-fluorobenzoate chemistry [49]. Effective tumor imaging was retained although tumor uptake (2.6 ± 0.7 %ID/g at 0.5 h, 1.5 ± 0.4 %ID/g at 1 h), and specificity (5:1 tumor:muscle at 0.5 h, 3:1 tumor:muscle at 1 h) reduced slightly. ^{64}Cu -labeled clone 2.5F exhibited superior specificity relative to ^{18}F -fluorodeoxyglucose for imaging nascent lung nodules in a transgenic mouse model (6.0 ± 0.6 tumor:background for ^{64}Cu -knottin vs. 4.4 ± 0.7 for ^{18}F -fluorodeoxyglucose) [50]. The 2.5D clone was also used for molecular ultrasound [51]. Conjugation to perfluorocarbon-filled microbubbles yielded specific detection of integrin $\alpha_v\beta_3$ -expressing tumors in murine models. Targeting was superior to microbubbles labeled with integrin $\alpha_v\beta_3$ antibodies or cyclic RGD peptides and was molecularly specific as verified by blocking and cellular control studies.

The diversity of the knottin family was also demonstrated as the AgRP scaffold was used to engineer nanomolar affinity binders to integrin $\alpha_v\beta_3$ [52] and label them with ^{64}Cu for PET [53]. Imaging of xenografted U87 tumors in nude mice was effective although tumor uptake was slightly lower (2.7 ± 1.1 %ID/g at 1 h vs. 4.6 ± 0.6 %ID/g) and renal signal much higher (60 ± 18 %ID/g vs. 4 ± 1 %ID/g) than with EETI-II. ^{111}In labeling reduced renal signal to 34 ± 8 %ID/g but hindered tumor retention [54]. ^{18}F labeling using 4-nitrophenyl-2-fluoropropionate reduced renal signal to 20 %ID/g [55]. Evolution of an additional scaffold, the *Momordica cochinchinensis* trypsin inhibitor-II (MCoTI-II), further substantiated the breadth of the knottin scaffold, including application to a new integrin target, $\alpha_v\beta_6$ [56]. Clones with low nanomolar affinity were evolved by loop grafting and directed evolution with yeast surface display. Ligands were labeled with ^{64}Cu for molecular PET of nude mice with subcutaneous or orthotopic xenografted pancreatic cancers. The original, arginine-rich scaffold yielded 5 ± 1 %ID/g tumor with an 8 ± 2 tumor:background ratio at 1 h post-injection albeit with 75 ± 5 %ID/g kidney. Transfer of the evolved loop sequence to a serine-rich scaffold decreased renal uptake to 18 ± 3 %ID/g but also decreased tumor uptake to 1.8 ± 0.4 %ID/g. Renal retention was substantially reduced with ^{18}F radiolabeling using N-succinimidyl-4-fluorobenzoate chemistry (9 ± 3 %ID/g kidney) albeit with slight tumor reduction (2.3 ± 0.6 %ID/g) [57].

Radiolabeled knottins were also evaluated for radiotherapy. ^{177}Lu -labeled integrin $\alpha_v\beta_3$ binders 2.5D and 2.5F were administered to mice bearing U87 tumor xenografts [58]. 61 mGy/mCi absorbed dose was achieved in the tumor with 18 mGy/mCi in the kidneys and < 2 mGy/mCi elsewhere.

13.3.3 Future Outlook for Knottins

Natural knottins have demonstrated efficacy in a range of applications but are limited to targeting their native binding partners. Loop grafting and evolution in multiple knottin frameworks have proven highly efficacious for integrin targeting in a variety of murine models, primarily across multiple modalities of molecular imaging but also for radiotherapy. The breadth of impact for the knottin family will depend on the ability to robustly and efficiently develop high-affinity binders to a multitude of targets. To aid in affinity, an integrin binding motif was simultaneously grafted into two loops of the EETI-II scaffold, which enhanced binding and maintained effective molecular PET [59]. Looking to expand the evolutionary capacity of the scaffolds beyond integrins, the EETI-II scaffold has been evolved for binding to seven different targets albeit with limited affinity evaluation [60]. If high affinity can be readily achieved from naïve libraries without grafted motifs, the stable, small knottin family of scaffolds has tremendous potential for molecularly targeted imaging and therapy.

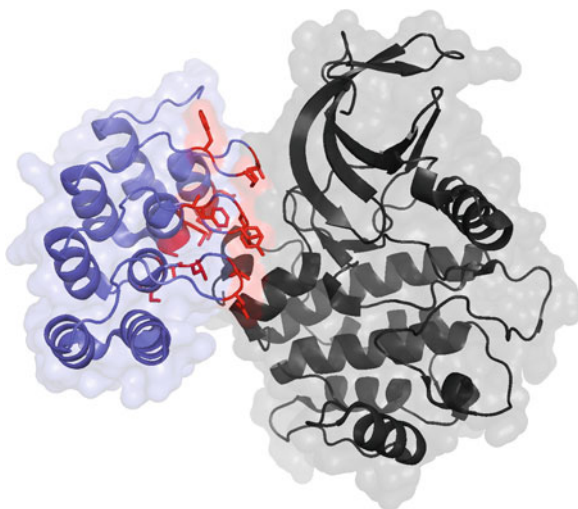
13.4 DARPinS

DARPins comprise ankyrin repeat domains, typically four to six repeats each of which has a beta turn and two antiparallel alpha helices [8] (Fig. 13.3). A tight hydrophobic core, improved by consensus design, imparts tremendous stability. This is evidenced by robustness to boiling and guanidine hydrochloride and tremendously slow amide proton exchange. While the sequence is fully non-human, immunogenicity is expected to be limited as the inherent stability limits degradation. Molecular size (~ 15 kDa depending on the number of repeats) provides reasonable permeability and diffusion along with rapid plasma clearance. DARPins are very well expressed in the soluble phase of bacterial culture (≥ 100 mg/L in shake flask and ≥ 1 g/L in a fermenter). Diversification in the beta turn and the first alpha helix presents a rigid potential paratope with extensive surface area. Ligands with nanomolar to picomolar affinities for many targets have been evolved.

13.4.1 Applications of DARPins

DARPins have demonstrated efficacy in a variety of applications. A DARPin was evolved by ribosome display to achieve 90 pM affinity for human epidermal growth factor receptor 2 (HER2) [61]. The ligand was labeled with ^{99m}Tc and yielded effective localization of a murine tumor xenograft via SPECT/CT [62]. Biodistribution quantitation indicated 9 ± 2 %ID/g tumor with 13 ± 3 tumor:blood at 1 h;

Fig. 13.3 DARPIn (blue and red) in complex with polo-like kinase 1 domain (black); PDB: 2V5Q. The residues commonly mutated in scaffold evolution are shown in red with side chains. C-terminal capping domain has been omitted



8 ± 3 %ID/g tumor, 27 ± 15 tumor:blood at 4 h; and 8 ± 2 %ID/g tumor, 62 ± 28 tumor:blood at 24 h. Kidney and liver backgrounds were 239 ± 33 %ID/g and 7.3 ± 1.0 %ID/g, respectively, at 4 h. Extensive characterization was performed to quantify the impacts of affinity and size. While protein dimerization had a nearly negligible impact on plasma clearance (half-time of ~ 3 min), PEGylation drastically slowed clearance (half-time = 19 h for 20 kDa PEG; 50 h for 40 and 60 kDa PEG). This pharmacokinetic modulation decreased tumor:blood ratio from 13 ± 3 , 27 ± 15 , and 72 ± 27 tumor:blood at 1, 4, and 24 h post-injection for native protein to 0.2 ± 0.1 , 0.6 ± 0.3 , and 4.7 ± 3.1 for the PEGylated protein. Tumor uptake correlated with affinity for (a) the 14.5 kDa native proteins from 1 to 48 h and (b) the PEGylated constructs at later time points.

The 90 pM HER2 binder was also efficacious for *in vitro* diagnostics. The DARPIn exhibited superior sensitivity and specificity relative to a validated antibody in immunohistochemistry of breast cancer tissue microarrays [63]. Picomolar affinity was critical to success as a DARPIn mutant with 1 nM affinity was significantly less effective.

HER2 DARPins were also effective in viral targeting. Fusion of a hemagglutinin mutant with an anti-HER2 DARPIn enabled molecular targeting of lentiviral vectors [64]. Vector particles were systemically administered into mice with subcutaneous tumor xenografts of HER2-positive (SKOV3) or HER2-negative (U87MG) tumors. Using a luciferase reporter, HER2-specific viral targeting was evident within 3 days and was retained for at least 14 days. Oncolytic recombinant measles virus was also effectively targeted with an anti-HER2 DARPIn [65]. Tumor inhibition following intratumoral injection of a DARPIn-targeted virus was superior to an antibody-targeted virus; inhibition was comparable to untargeted virus, but without associated toxic side effects. Also, a dual-targeted (HER2 and

epithelial cell adhesion molecule (EpCAM)) bispecific virus demonstrated improved resistance to tumor modulation in cell culture.

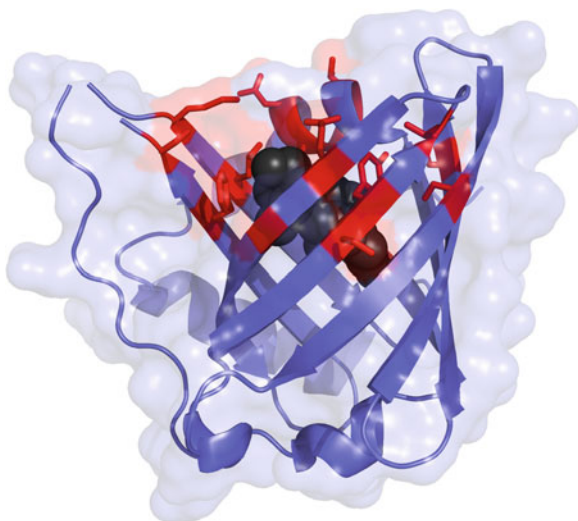
The EpCAM DARPIn was also effective in the construction of an immunotoxin [66]. Fusion to *Pseudomonas aeruginosa* toxin A generated an immunotoxin with an in vitro IC_{50} of 5 fM. The fusion protein readily accumulated in subcutaneous HT29 tumor xenografts in nude mice following intravenous injection and reduced tumor growth by $\sim 90\%$ relative to saline injection or untargeted immunotoxin. Slower growing W2 small-cell lung carcinoma xenografts were inhibited by 67%. Despite the inherent potency of toxin A, body weight and liver transaminase activity were comparable for DARPIn immunotoxin and saline control, indicative of the safety of the targeted approach.

Moreover, stand-alone DARPins have been demonstrated as effective antagonists. A VEGF antagonist named MP0112 (Molecular Partners) is under clinical study for ocular indications. MP0112 underwent a phase I/II study in treatment-naïve patients (aged >50 years) with wet age-related macular degeneration [67]. The DARPIn was safe and well tolerated; resolvable sterile inflammation was the only adverse effect. All patients had stable or improved visual acuity at 16-week follow-up. Quarterly dosing is considered a potential option. Phase I/II study for diabetic macular edema demonstrated maintenance of aqueous concentrations above the IC_{50} for 8–12 weeks following a single injection [68]. 0.15-mg and 0.40-mg dose cohorts demonstrated reductions in mean central subfield thickness and improvements in visual acuity. However, ocular inflammation was observed in 11 of 18 patients with one severe case. High-resolution chromatography identified contaminant proteins, likely bacterial host proteins, that likely caused the inflammation. Purification has been improved for ongoing trials.

13.4.2 Future Outlook for DARPins

DARPins have been broadly effective in a range of applications. The relative rigidity and size of the modular paratope promote evolvability of novel binding function to very high affinities. The combination of stability and facile recombinant production make them especially attractive for clinical in vitro diagnostics. Their efficient coupling via genetic fusion and chemical conjugation bolsters further study for targeted delivery and dual-activity constructs. The tolerability (upon purification), efficacy, and extended duration in ocular applications warrant further study for therapeutic uses across many indications both as direct agents (agonists or antagonists) and for targeted delivery.

Fig. 13.4 Anticalin (*blue* and *red*) in complex with digoxigenin (*black*); PDB: 1LKE. The residues commonly mutated in scaffold evolution are shown in *red* with side chains



13.5 Anticalins

Lipocalins are ~ 20 -kDa proteins with a beta-barrel structure with eight antiparallel beta strands and an exterior alpha helix [9] (Fig. 13.4). A hydrophobic core exists in the center of the barrel and is shielded by relatively short loops on one end of the barrel. This structure is conserved in the 12 human lipocalins although sequence homology is minimal and natural ligand specificity is varied. The opposite end of the barrel is especially diverse in sequence and conformation and is amenable to diversification to engender the scaffold with binding capabilities for different targets. The evolution of human lipocalins as scaffolds, known as anticalins, for molecular recognition has been led by the laboratory of Arne Skerra [9]. Different library designs have been used for different classes of molecular target. Randomization of 12 residues within the concave binding pocket is used to bind small molecules [69], whereas randomization of 20 residues within the loops enables binding to protein targets [70]. Both natural and synthetically evolved lipocalins have been developed for clinical applications.

13.5.1 Natural Lipocalins

A saliva protein from the soft tick *Ornithodoros moubata* binds complement C5 with nanomolar affinity [71]. The recombinant form (rEV576) prevented neuronal damage and perisynaptic Schwann cell injury in a murine model of Miller Fisher syndrome [72]. rEV576 demonstrated efficacy in a rat model of myasthenia gravis [73]. The molecule also reduced thrombus formation and tissue factor activity in a

murine model of anti-phospholipid-mediated cytotoxicity [74]. A lipocalin from the tick *Rhipicephalus appendiculatus* binds histamine with high affinity. In a murine model of allergic asthma, the recombinant form (rEV131) was highly active: 70 % reduction in airway hyperreactivity and elimination of cytokine secretion, peri-bronchial inflammation, and pulmonary eosinophilia [75]. Intranasal delivery of rEV131 was effective to combat acute respiratory distress syndrome induced by inhaled lipopolysaccharide in a mouse model [76]. Bronchoconstriction and TNF- α secretion were reduced in a dose-dependent manner. Neutrophil recruitment was reduced by rEV131 comparably to treatment with the glucocorticosteroid budesonide. However, clinical translation has stalled as a phase II trial of rEV131 failed to demonstrate any significant difference between rEV131 and placebo for treatment of allergic rhinitis (hay fever). Current lipocalin development focuses on synthetically evolved lipocalins.

13.5.2 Synthetic Anticalins

Digoxin has a narrow therapeutic window for the treatment of ventricular tachyarrhythmias and congestive heart failure [77]; thus, availability of an effective antidote for toxic overdose is needed. An anticalin (DigiA16(H86 N), DigiCal) evolved from the bilin-binding protein using phage display to bind digoxin with subnanomolar affinity completely reversed toxic effects of an otherwise lethal digoxin dose in a guinea pig model [78]. In a rat model, digoxin was administered intravenously followed by a bolus injection of DigiCal [79]. Within 1 min, the concentration of free digoxin in plasma dropped by 35 % (1 mg dose) to 98 % (20 mg dose). Resultantly, rats exhibited dose-dependent delay in time to arrhythmia, heart rate decrease, arterial pressure drop, and, ultimately, death. The anticalin effects were dynamic rather than fully protective because free digoxin concentration in plasma increased within minutes after the initial precipitous decline; this likely occurred due to intravasation of digoxin from tissue coincident with rapid clearance of the small (~ 20 kDa) anticalin.

Antagonism of the T-cell regulator cytotoxic T-lymphocyte-associated antigen 4 (CTLA-4) has been validated in multiple indications including FDA approval of ipilimumab for metastatic melanoma. An anticalin with 3 nM affinity for CTLA-4 was conjugated site-specifically with 30-kDa PEG and tested in a mouse model of parasite infection. *L. donovani*-infected mice were treated with PEGylated anticalin (PRS-010, 30 mg/kg i.p. daily for 2 weeks) or anti-CTLA4 antibody (4 mg/kg once). At 4 weeks, the anticalin-treated mice had a 51 ± 4 % reduction in parasite burden relative to non-targeted lipocalin control. This result was essentially equivalent to the antibody approach, which further validates the anticalin technology.

The most clinically advanced anticalin, named PRS-050 or AngioCal (Pieris), has nanomolar affinity for VEGF. This PEGylated anticalin has demonstrated antagonism in mouse tumor xenograft models and a rabbit model of age-related

macular degeneration [80]. The phase I trial examined safety, pharmacokinetics, and pharmacodynamics in 26 patients with solid tumors [81]. Alteration of administration to include appropriate premedication (steroids, antipyretics, H1/H2 blockers, or antihypertensives) and slow infusion resulted in good tolerance. No maximum tolerated dose was identified, and a 6 mg/kg dose every 2 weeks was recommended. A terminal half-life of 6 days was observed. At 10 weeks, no anti-PRS-050 antibodies were detected. Stable disease was achieved in nine patients although there were no objective responses. Evidence of desired action exists as anticalin-VEGF-A complex was detectable in all patients for up to 3 weeks and both matrix metalloprotease levels and dynamic contrast enhanced magnetic resonance imaging suggest physiological activity.

Anticalins have also been used in fusion proteins for pretargeting applications. Single-chain antibody variable fragments (scFvs) were fused to both the N- and C-termini of a fluorescein-binding anticalin. The scFvs were specific for the EDA domain of fibronectin, which is a marker for tumor angiogenesis. The fusion construct was administered to mice with subcutaneous tumor xenografts and allowed to distribute for 24 h. Mice were then injected intravenously with a fluorescein-IRDye750 molecule, which rapidly distributes due to small size. Near-infrared fluorescent imaging to detect the IRDye750 specifically identified tumor, whereas mice injected with an IRDye750 molecule without fluorescein did not localize to tumor [82].

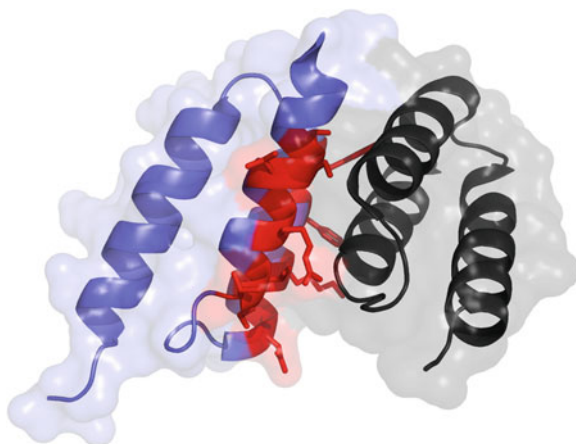
13.5.3 Future Outlook for Anticalins

Among the prevalent non-immunoglobulin scaffolds, the concave binding pocket of the beta barrel topology renders anticalins as especially effective at binding small molecules and convex epitopes on protein targets. This poises the scaffold for efficacy in a variety of applications including the demonstrated success in antidotes and pretargeting. Patient tolerance of natural and synthetic lipocalins has been demonstrated. These constructs are now poised for further assessment of clinical efficacy.

13.6 Affibodies

The affibody scaffold is based on the 58-amino-acid, three-helix bundle of a single domain of staphylococcal protein A (Fig. 13.5). Diversification of 13 residues on one face of helices 1 and 2 can generate novel binding activity toward a multitude of molecular targets. Affinities range from low picomolar to high nanomolar. Destabilization due to diversification yields proteins with T_m values of 37–65 °C (median 46 °C) [83–88] although unfolding is generally reversible. An optimized version has been engineered for improved stability and chemical synthesis with

Fig. 13.5 Affibody (*blue* and *red*) in complex with protein Z domain (*black*); PDB: 1LP1. The residues commonly mutated in scaffold evolution are shown in *red* with side chains



reduced immunoglobulin binding and retained hydrophilicity and binding capacity [84]. In addition, a two-helix version has been evaluated [89–91] but would benefit from improved balance of stability and affinity.

13.6.1 Applications of Affibodies

The highlights of this scaffold will be provided only briefly as more details can be found in another chapter in this volume. Affibodies have been implemented in a variety of applications, though the dominant use has been in molecular imaging for oncology. Effective tumor imaging in mouse models has been demonstrated for multiple targets using ^{99m}Tc and ^{111}In for SPECT, ^{124}I , ^{68}Ga , ^{64}Cu , ^{18}F for PET, and near-infrared fluorophores for optical imaging [92, 93]. Trimodality gold-iron oxide heteronanostructures targeted with affibodies have recently been developed and validated in subcutaneous tumor xenograft models in mice for magnetic resonance imaging, positron emission tomography, and optical imaging [94]. Clinical trials with ^{68}Ga and ^{111}In affibodies showed utility for HER2 imaging of metastatic breast cancer [95].

In addition to imaging, therapeutic applications have been explored including affibody–toxin fusions [96], radiotherapy with ^{177}Lu [97] and ^{211}At [98], and targeted viruses [99].

13.7 Other Scaffolds

A 60-amino-acid protein derived from a Kunitz domain in human tissue factor pathway inhibitor has been evolved by phage display to inhibit plasma kallikrein

Table 13.2 Protein scaffolds in applications

Name	Clinical	Imaging	Therapy	Immunotoxin	Bispecific	Other
Knottin	Natural: approved; synthetic: preclinical	Natural: SPECT (human), fluor. (mouse); synthetic: PET, fluor., US (mouse)	Natural: pain, oncology; synthetic: oncology	No	No	Radiotherapy
Affibody	Phase I/II	SPECT, PET (human), PET, SPECT, fluor., MRI (mouse)	Oncology (mouse)	Yes (mouse)	Bivalent, monospecific	Radiotherapy, targeted viruses
Fibronectin	Phase II	PET (mouse)	Oncology (human, mouse)	Yes (in vitro)	Yes (mouse)	–
DARPin	Phase I/II	SPECT (mouse)	Ocular (human), oncology (mouse)	Yes (mouse)	Yes (in vitro)	Viral targeting
Anticalin	Natural: phase II; synthetic: phase I	Fluorescence (mouse)	Oncology (human), antidote (rat), infection (mouse)	No	Anticalin—scFv (mouse)	–

[100]. The protein, named ecallantide, is FDA approved for acute hereditary angioedema [101]. Another scaffold, the avimer, comprises linked multimers of small receptor domains that promote strong binding by an avidity effect. An avimer that binds interleukin-6 with an IC_{50} of 0.8 pM effectively reduced serum levels of the target in mouse models [102].

Antibody fragments and reformatted domains have also been extensively explored [103]. These constructs include monovalent heavy-chain variable domains (V_HH , nanobody), scFvs, and antigen-binding fragments (Fabs) as well as bivalent scFv dimers (diabodies) and scFvs dimerized by CH_3 (minibodies). As with the non-immunoglobulin scaffolds, different formats address the shortcomings of full intact immunoglobulins to different degrees of success.

13.8 Conclusions

The manifold applications for molecular recognition ligands entail significantly different demands for performance. As the protein sequence–structure–function relationships are elucidated and protein engineering technologies improve, researchers can identify ligands within more precise biophysical and physiological constraints. As such, the highlighted scaffolds (Table 13.2) will continue to evolve for improved performance and additional topologies will certainly be introduced. The evolution of the field is away from the one-size-(and shape, valency, affinity, stability, solubility, etc.)-fits-all antibody approach; rather the optimal scaffold may be unique to the task at hand as the requisite parameters are differentially balanced for each application. Continued scientific, preclinical, and clinical development of a diverse array of scaffolds will empower researchers with the flexibility to select the most effective molecule. To this end, the field will benefit greatly from standardized evaluations of efficacy as well as direct comparisons of alternative scaffolds in a multitude of applications.

References

1. Scott AM, Wolchok JD, Old LJ (2012) Antibody therapy of cancer. *Nat Rev Cancer* 12:278–287. doi:[10.1038/nrc3236](https://doi.org/10.1038/nrc3236)
2. Yuan F, Dellian M, Fukumura D et al (1995) Vascular permeability in a human tumor xenograft: molecular size dependence and cutoff size. *Cancer Res* 55:3752–3756
3. Schmidt MM, Wittrup KD (2009) A modeling analysis of the effects of molecular size and binding affinity on tumor targeting. *Mol Cancer Ther* 8:2861–2871. doi:[10.1158/1535-7163.MCT-09-0195](https://doi.org/10.1158/1535-7163.MCT-09-0195)
4. Binz HK, Amstutz P, Plückthun A (2005) Engineering novel binding proteins from nonimmunoglobulin domains. *Nat Biotechnol* 23:1257–1268. doi:[10.1038/nbt1127](https://doi.org/10.1038/nbt1127)
5. Löfblom J, Frejd FY, Ståhl S (2011) Non-immunoglobulin based protein scaffolds. *Curr Opin Biotechnol*. doi:[10.1016/j.copbio.2011.06.002](https://doi.org/10.1016/j.copbio.2011.06.002)

6. Löfblom J, Feldwisch J, Tolmachev V et al (2010) Affibody molecules: engineered proteins for therapeutic, diagnostic and biotechnological applications. *FEBS Lett* 584:2670–2680. doi:[10.1016/j.febslet.2010.04.014](https://doi.org/10.1016/j.febslet.2010.04.014)
7. Lipovsek D (2011) Adnectins: engineered target-binding protein therapeutics. *Protein Eng Des Sel* 24:3–9. doi:[10.1093/protein/gzq097](https://doi.org/10.1093/protein/gzq097)
8. Tamaskovic R, Simon M, Stefan N et al (2012) Designed ankyrin repeat proteins (DARPin)s from research to therapy. *Meth Enzymol* 503:101–134. doi:[10.1016/B978-0-12-396962-0.00005-7](https://doi.org/10.1016/B978-0-12-396962-0.00005-7)
9. Gebauer M, Skerra A (2012) Anticalins small engineered binding proteins based on the lipocalin scaffold. *Meth Enzymol* 503:157–188. doi:[10.1016/B978-0-12-396962-0.00007-0](https://doi.org/10.1016/B978-0-12-396962-0.00007-0)
10. Moore SJ, Leung CL, Cochran JR (2012) Knottins: disulfide-bonded therapeutic and diagnostic peptides. *Drug Discov Today: Technol* 9:e3–e11. doi:[10.1016/j.ddtec.2011.07.003](https://doi.org/10.1016/j.ddtec.2011.07.003)
11. Ståhl S, Kronqvist N, Jonsson A, Löfblom J (2012) Affinity proteins and their generation. *J Chem Technol Biotechnol* 88:25–38. doi:[10.1002/jctb.3929](https://doi.org/10.1002/jctb.3929)
12. Gebauer M, Skerra A (2009) Engineered protein scaffolds as next-generation antibody therapeutics. *Curr Opin Chem Biol* 13:245–255. doi:[10.1016/j.cbpa.2009.04.627](https://doi.org/10.1016/j.cbpa.2009.04.627)
13. Hackel BJ, Kapila A, Wittrup KD (2008) Picomolar affinity fibronectin domains engineered utilizing loop length diversity, recursive mutagenesis, and loop shuffling. *J Mol Biol* 381:1238–1252. doi:[10.1016/j.jmb.2008.06.051](https://doi.org/10.1016/j.jmb.2008.06.051)
14. Batori V, Koide A, Koide S (2002) Exploring the potential of the monobody scaffold: effects of loop elongation on the stability of a fibronectin type III domain. *Protein Eng* 15:1015–1020
15. Parker MH, Chen Y, Danehy F et al (2005) Antibody mimics based on human fibronectin type three domain engineered for thermostability and high-affinity binding to vascular endothelial growth factor receptor two. *Protein Eng Des Sel* 18:435–444. doi:[10.1093/protein/gzi050](https://doi.org/10.1093/protein/gzi050)
16. Hackel BJ, Wittrup KD (2010) The full amino acid repertoire is superior to serine/tyrosine for selection of high affinity immunoglobulin G binders from the fibronectin scaffold. *Protein Eng Des Sel* 23:211–219. doi:[10.1093/protein/gzp083](https://doi.org/10.1093/protein/gzp083)
17. Hackel BJ, Ackerman ME, Howland SW, Wittrup KD (2010) Stability and CDR composition biases enrich binder functionality landscapes. *J Mol Biol* 401:84–96. doi:[10.1016/j.jmb.2010.06.004](https://doi.org/10.1016/j.jmb.2010.06.004)
18. Koide A, Jordan MR, Horner SR et al (2001) Stabilization of a fibronectin type III domain by the removal of unfavorable electrostatic interactions on the protein surface. *Biochemistry* 40:10326–10333
19. Getmanova EV, Chen Y, Bloom L et al (2006) Antagonists to human and mouse vascular endothelial growth factor receptor 2 generated by directed protein evolution in vitro. *Chem Biol* 13:549–556. doi:[10.1016/j.chembiol.2005.12.009](https://doi.org/10.1016/j.chembiol.2005.12.009)
20. Mamluk R, Carvajal IM, Morse BA et al (2010) Anti-tumor effect of CT-322 as an adnectin inhibitor of vascular endothelial growth factor receptor-2. *mAbs*, vol 2, pp 199–208
21. Dineen SP, Sullivan LA, Beck AW et al (2008) The Adnectin CT-322 is a novel VEGF receptor 2 inhibitor that decreases tumor burden in an orthotopic mouse model of pancreatic cancer. *BMC Cancer* 8:352. doi:[10.1186/1471-2407-8-352](https://doi.org/10.1186/1471-2407-8-352)
22. Ackermann M, Carvajal IM, Morse BA et al (2011) Adnectin CT-322 inhibits tumor growth and affects microvascular architecture and function in Colo205 tumor xenografts. *Int J Oncol* 38:71–80. doi:[10.3892/ijo_00000825](https://doi.org/10.3892/ijo_00000825)
23. Waters JD, Sanchez C, Sahin A et al (2012) CT322, a VEGFR-2 antagonist, demonstrates anti-glioma efficacy in orthotopic brain tumor model as a single agent or in combination with temozolomide and radiation therapy. *J Neurooncol* 110:37–48. doi:[10.1007/s11060-012-0948-7](https://doi.org/10.1007/s11060-012-0948-7)
24. Tolcher AW, Sweeney CJ, Papadopoulos K et al (2011) Phase I and pharmacokinetic study of CT-322 (BMS-844203), a targeted Adnectin inhibitor of VEGFR-2 based on a domain of human fibronectin. *Clin Cancer Res* 17:363–371. doi:[10.1158/1078-0432.CCR-10-1411](https://doi.org/10.1158/1078-0432.CCR-10-1411)

25. Paschold EH, Mazieres J, Lena H et al (2012) A randomized, double-blinded, phase II study of paclitaxel/carboplatin (PC) plus CT-322 versus PC plus bevacizumab (Bev) as first-line treatment for advanced nonsquamous non-small cell lung cancer (NSCLC). *J Clin Oncol* 30:a7584
26. Ackermann M, Morse BA, Delventhal V et al (2012) Anti-VEGFR2 and anti-IGF-1R-Adnectins inhibit Ewing's sarcoma A673-xenograft growth and normalize tumor vascular architecture. *Angiogenesis* 15:685–695. doi:[10.1007/s10456-012-9294-9](https://doi.org/10.1007/s10456-012-9294-9)
27. Emanuel SL, Engle LJ, Chao G et al. (2011) A fibronectin scaffold approach to bispecific inhibitors of epidermal growth factor receptor and insulin-like growth factor-1 receptor. *mAbs* vol 3, pp 38–48
28. Wang H, Wang L, Cao K et al (2012) Development of a carbon-14 labeling approach to support disposition studies with a pegylated biologic. *Drug Metab Dispos* 40:1677–1685. doi:[10.1124/dmd.112.044792](https://doi.org/10.1124/dmd.112.044792)
29. Spangler JB, Manzari MT, Rosalia EK et al (2012) Triepitopic antibody fusions inhibit cetuximab-resistant BRAF and KRAS mutant tumors via EGFR signal repression. *J Mol Biol* 422:532–544. doi:[10.1016/j.jmb.2012.06.014](https://doi.org/10.1016/j.jmb.2012.06.014)
30. Hackel BJ, Kimura RH, Gambhir SS (2012) Use of ⁶⁴Cu-labeled fibronectin domain with EGFR-overexpressing tumor xenograft: molecular imaging. *Radiology* 263:179–188. doi:[10.1148/radiol.12111504](https://doi.org/10.1148/radiol.12111504)
31. Hackel BJ, Sathirachinda A, Gambhir SS (2012) Designed hydrophilic and charge mutations of the fibronectin domain: towards tailored protein biodistribution. *Protein Eng Des Sel* 25:639–647. doi:[10.1093/protein/gzs036](https://doi.org/10.1093/protein/gzs036)
32. Pirie CM, Hackel BJ, Rosenblum MG, Witttrup KD (2011) Convergent potency of internalized gelonin immunotoxins across varied cell lines, antigens, and targeting moieties. *J Biol Chem* 286:4165–4172. doi:[10.1074/jbc.M110.186973](https://doi.org/10.1074/jbc.M110.186973)
33. Brautbar A, Ballantyne CM (2011) Pharmacological strategies for lowering LDL cholesterol: statins and beyond. *Nat Rev Cardiol* 8:253–265. doi:[10.1038/nrcardio.2011.2](https://doi.org/10.1038/nrcardio.2011.2)
34. Colgrave ML, Craik DJ (2004) Thermal, chemical, and enzymatic stability of the cyclotide kalata B1: the importance of the cyclic cystine knot. *Biochemistry* 43:5965–5975. doi:[10.1021/bi049711q](https://doi.org/10.1021/bi049711q)
35. Werle M, Schmitz T, Huang H-L et al (2006) The potential of cystine-knot microproteins as novel pharmacophoric scaffolds in oral peptide drug delivery. *J Drug Target* 14:137–146. doi:[10.1080/10611860600648254](https://doi.org/10.1080/10611860600648254)
36. Moore SJ, Cochran JR (2012) Engineering knottins as novel binding agents. *Meth Enzymol* 503:223–251. doi:[10.1016/B978-0-12-396962-0.00009-4](https://doi.org/10.1016/B978-0-12-396962-0.00009-4)
37. Gracy J, Le-Nguyen D, Gelly J-C et al (2008) KNOTTIN: the knottin or inhibitor cystine knot scaffold in 2007. *Nucleic Acids Res* 36:D314–D319. doi:[10.1093/nar/gkm939](https://doi.org/10.1093/nar/gkm939)
38. Perez-Pinzon MA, Yenari MA, Sun GH et al (1997) SNX-111, a novel, presynaptic N-type calcium channel antagonist, is neuroprotective against focal cerebral ischemia in rabbits. *J Neurol Sci* 153:25–31
39. Joppa MA, Gogas KR, Foster AC, Markison S (2007) Central infusion of the melanocortin receptor antagonist agouti-related peptide (AgRP(83-132)) prevents cachexia-related symptoms induced by radiation and colon-26 tumors in mice. *Peptides* 28:636–642. doi:[10.1016/j.peptides.2006.11.021](https://doi.org/10.1016/j.peptides.2006.11.021)
40. Hockaday DC, Shen S, Fiveash J et al (2005) Imaging glioma extent with ¹³¹I-TM-601. *J Nucl Med* 46:580–586
41. Mamelak AN (2006) Phase I single-dose study of intracavitary-administered iodine-131-TM-601 in adults with recurrent high-grade glioma. *J Clin Oncol* 24:3644–3650. doi:[10.1200/JCO.2005.05.4569](https://doi.org/10.1200/JCO.2005.05.4569)
42. Mrugala MM, Adair JE, Kiem H-P (2012) Outside the box—novel therapeutic strategies for glioblastoma. *Cancer J* 18:51–58. doi:[10.1097/PPO.0b013e318243f785](https://doi.org/10.1097/PPO.0b013e318243f785)
43. Vieseh M, Gabikian P, Bahrami S-B et al (2007) Tumor paint: a chlorotoxin: Cy5.5 bioconjugate for intraoperative visualization of cancer foci. *Cancer Res* 67:6882–6888. doi:[10.1158/0008-5472.CAN-06-3948](https://doi.org/10.1158/0008-5472.CAN-06-3948)

44. Sun C, Veiseh O, Gunn J et al (2008) In vivo MRI detection of gliomas by chlorotoxin-conjugated superparamagnetic nanoprobe. *Small* 4:372–379. doi:[10.1002/sml.200700784](https://doi.org/10.1002/sml.200700784)
45. Krause S, Schmoldt H-U, Wentzel A et al (2007) Grafting of thrombopoietin-mimetic peptides into cystine knot miniproteins yields high-affinity thrombopoietin antagonists and agonists. *FEBS J* 274:86–95. doi:[10.1111/j.1742-4658.2006.05567.x](https://doi.org/10.1111/j.1742-4658.2006.05567.x)
46. Kimura RH, Levin AM, Cochran FV, Cochran JR (2009) Engineered cystine knot peptides that bind $\alpha v \beta 3$, $\alpha v \beta 5$, and $\alpha 5 \beta 1$ integrins with low-nanomolar affinity. *Proteins* 77:359–369. doi:[10.1002/prot.22441](https://doi.org/10.1002/prot.22441)
47. Kimura RH, Cheng Z, Gambhir SS, Cochran JR (2009) Engineered knottin peptides: a new class of agents for imaging integrin expression in living subjects. *Cancer Res* 69:2435–2442. doi:[10.1158/0008-5472.CAN-08-2495](https://doi.org/10.1158/0008-5472.CAN-08-2495)
48. Kimura RH, Miao Z, Cheng Z et al (2010) A dual-labeled knottin peptide for PET and near-infrared fluorescence imaging of integrin expression in living subjects. *Bioconjug Chem* 21:436–444. doi:[10.1021/bc9003102](https://doi.org/10.1021/bc9003102)
49. Miao Z, Ren G, HHongguang L (2009) An engineered knottin peptide labeled with ^{18}F for PET imaging of integrin expression. *Bioconjug Chem* 20:2342–2347. doi:[10.1021/bc900361g](https://doi.org/10.1021/bc900361g)
50. Nielsen CH, Kimura RH, Withofs N et al (2010) PET imaging of tumor neovascularization in a transgenic mouse model with a novel ^{64}Cu -DOTA-knottin peptide. *Cancer Res* 70:9022–9030. doi:[10.1158/0008-5472.CAN-10-1338](https://doi.org/10.1158/0008-5472.CAN-10-1338)
51. Willmann JK, Kimura RH, Deshpande N et al (2010) Targeted contrast-enhanced ultrasound imaging of tumor angiogenesis with contrast microbubbles conjugated to integrin-binding knottin peptides. *J Nucl Med* 51:433–440. doi:[10.2967/jnumed.109.068007](https://doi.org/10.2967/jnumed.109.068007)
52. Silverman AP, Levin AM, Lahti JL, Cochran JR (2009) Engineered cystine-knot peptides that bind $\alpha v \beta 3$ integrin with antibody-like affinities. *J Mol Biol* 385:1064–1075. doi:[10.1016/j.jmb.2008.11.004](https://doi.org/10.1016/j.jmb.2008.11.004)
53. Jiang L, Kimura RH, Miao Z et al (2010) Evaluation of a (^{64}Cu) -labeled cystine-knot peptide based on agouti-related protein for PET of tumors expressing $\alpha v \beta 3$ integrin. *J Nucl Med* 51:251–258. doi:[10.2967/jnumed.109.069831](https://doi.org/10.2967/jnumed.109.069831)
54. Jiang L, Miao Z, Kimura RH et al (2012) ^{111}In -labeled cystine-knot peptides based on the agouti-related protein for targeting tumor angiogenesis. *J Biomed Biotechnol* 2012:1–8. doi:[10.1002/ijc.23575](https://doi.org/10.1002/ijc.23575)
55. Jiang H, Moore SJ, Liu S et al (2013) A novel radiofluorinated agouti-related protein for tumor angiogenesis imaging. *Amino Acids* 44:673–681. doi:[10.1007/s00726-012-1391-y](https://doi.org/10.1007/s00726-012-1391-y)
56. Kimura RH, Teed R, Hackel BJ et al (2012) Pharmacokinetically stabilized cystine knot peptides that bind $\alpha v \beta 6$ integrin with single-digit nanomolar affinities for detection of pancreatic cancer. *Clin Cancer Res* 18:839–849. doi:[10.1158/1078-0432.CCR-11-1116](https://doi.org/10.1158/1078-0432.CCR-11-1116)
57. Hackel BJ, Kimura RH, Miao Z et al (2013) ^{18}F -labeled cystine knot peptides for PET imaging of integrin $\alpha v \beta 6$. *J Nucl Med* 54(7):1101–1105
58. Jiang L, Miao Z, Kimura RH et al (2011) Preliminary evaluation of (^{177}Lu) -labeled knottin peptides for integrin receptor-targeted radionuclide therapy. *Eur J Nucl Med Mol Imaging* 38:613–622. doi:[10.1007/s00259-010-1684-x](https://doi.org/10.1007/s00259-010-1684-x)
59. Kimura RH, Jones DS, Jiang L et al (2011) Functional mutation of multiple solvent-exposed loops in the Ecballium elaterium trypsin inhibitor-II cystine knot miniprotein. *PLoS ONE* 6:e16112. doi:[10.1371/journal.pone.0016112](https://doi.org/10.1371/journal.pone.0016112)
60. Souriau C, Chiche L, Irving R, Hudson P (2005) New binding specificities derived from Min-23, a small cystine-stabilized peptidic scaffold. *Biochemistry* 44:7143–7155. doi:[10.1021/bi0481592](https://doi.org/10.1021/bi0481592)
61. Zahnd C, Wyler E, Schwenk JM et al (2007) A designed ankyrin repeat protein evolved to picomolar affinity to Her2. *J Mol Biol* 369:1015–1028. doi:[10.1016/j.jmb.2007.03.028](https://doi.org/10.1016/j.jmb.2007.03.028)
62. Zahnd C, Kawe M, Stumpp MT et al (2010) Efficient tumor targeting with high-affinity designed ankyrin repeat proteins: effects of affinity and molecular size. *Cancer Res* 70:1595–1605. doi:[10.1158/0008-5472.CAN-09-2724](https://doi.org/10.1158/0008-5472.CAN-09-2724)

63. Theurillat J-P, Dreier B, Nagy-Davidescu G et al (2010) Designed ankyrin repeat proteins: a novel tool for testing epidermal growth factor receptor 2 expression in breast cancer. *Mod Pathol* 23:1289–1297. doi:[10.1038/modpathol.2010.103](https://doi.org/10.1038/modpathol.2010.103)
64. Münch RC, Mühlebach MD, Schaser T et al (2011) DARPin: an efficient targeting domain for lentiviral vectors. *Mol Ther* 19:686–693. doi:[10.1038/mt.2010.298](https://doi.org/10.1038/mt.2010.298)
65. Friedrich K, Hanauer JR, Prüfer S et al (2013) DARPin-targeting of measles virus: unique bispecificity, effective oncolysis, and enhanced safety. *Mol Ther*. doi:[10.1038/mt.2013.16](https://doi.org/10.1038/mt.2013.16)
66. Martin-Killias P, Patricia M-K, Stefan N et al (2011) A novel fusion toxin derived from an EpCAM-specific designed ankyrin repeat protein has potent antitumor activity. *Clin Cancer Res* 17:100–110. doi:[10.1158/1078-0432.CCR-10-1303](https://doi.org/10.1158/1078-0432.CCR-10-1303)
67. Wolf S, Souied EH, Mauget-Faysse M et al (2011) Phase I MP0112 wet AMD study: results of a single escalating dose study with DARPin MP0112 in wet AMD. 2011 annual meeting of the association for research in vision and ophthalmology, vol 1655
68. Campochiaro PA, Channa R, Berger BB et al (2013) Treatment of diabetic macular edema with a designed ankyrin repeat protein that binds vascular endothelial growth factor: a phase I/II study. *Am J Ophthalmol* 155(697–704):e2. doi:[10.1016/j.ajo.2012.09.032](https://doi.org/10.1016/j.ajo.2012.09.032)
69. Kim HJ, Eichinger A, Skerra A (2009) High-affinity recognition of lanthanide (III) chelate complexes by a reprogrammed human lipocalin 2. *J Am Chem Soc* 131:3565–3576. doi:[10.1021/ja806857r](https://doi.org/10.1021/ja806857r)
70. Schönfeld D, Matschiner G, Chatwell L et al (2009) An engineered lipocalin specific for CTLA-4 reveals a combining site with structural and conformational features similar to antibodies. *Proc Natl Acad Sci* 106:8198–8203. doi:[10.1073/pnas.0813399106](https://doi.org/10.1073/pnas.0813399106)
71. Nunn MA, Sharma A, Paesen GC et al (2005) Complement inhibitor of C5 activation from the soft tick *Ornithodoros moubata*. *J Immunol* 174:2084–2091
72. Halstead SK, Humphreys PD, Zitman FMP et al (2008) C5 inhibitor rEV576 protects against neural injury in an in vitro mouse model of Miller Fisher syndrome. *J Peripher Nerv Syst* 13:228–235. doi:[10.1111/j.1529-8027.2008.00181.x](https://doi.org/10.1111/j.1529-8027.2008.00181.x)
73. Soltys J, Kusner LL, Young A et al (2009) Novel complement inhibitor limits severity of experimentally myasthenia gravis. *Ann Neurol* 65:67–75. doi:[10.1002/ana.21536](https://doi.org/10.1002/ana.21536)
74. Carrera-Marin AL, Romay-Penabad Z, Machin S et al (2011) C5 inhibitor rEV576 ameliorates in vivo effects of antiphospholipid antibodies. *Arthritis and Rheumatism* 63:S5–S5
75. Couillin I, Maillet I, Vargaftig BB et al (2004) Arthropod-derived histamine-binding protein prevents murine allergic asthma. *J Immunol* 173:3281–3286
76. Ryffel B, Couillin I, Maillet I et al (2005) Histamine scavenging attenuates endotoxin-induced acute lung injury. *Ann N Y Acad Sci* 1056:197–205. doi:[10.1196/annals.1352.034](https://doi.org/10.1196/annals.1352.034)
77. Hauptman PJ, Kelly RA (1999) Digitalis. *Circulation* 99:1265–1270
78. Schlehner S, Skerra A (2005) Lipocalins in drug discovery: from natural ligand-binding proteins to “anticalins”. *Drug Discov Today* 10:23–33. doi:[10.1016/S1359-6446\(04\)03294-5](https://doi.org/10.1016/S1359-6446(04)03294-5)
79. Eyer F, Steimer W, Nitzsche T et al (2012) Intravenous application of an anticalin dramatically lowers plasma digoxin levels and reduces its toxic effects in rats. *Toxicol Appl Pharmacol* 263:352–359. doi:[10.1016/j.taap.2012.07.009](https://doi.org/10.1016/j.taap.2012.07.009)
80. Wurch T, Pierré A, Depil S (2012) Novel protein scaffolds as emerging therapeutic proteins: from discovery to clinical proof-of-concept. *Trends Biotechnol* 30:575–582. doi:[10.1016/j.tibtech.2012.07.006](https://doi.org/10.1016/j.tibtech.2012.07.006)
81. Mross K, Fischer R, Richly H et al (2011) Abstract A212: first in human phase I study of PRS-050 (Angiocal), a VEGF-A targeting anticalin, in patients with advanced solid tumors: results of a dose escalation study. *Mol Cancer Ther* 10:A212–A212. doi:[10.1158/1535-7163.TARG-11-A212](https://doi.org/10.1158/1535-7163.TARG-11-A212)
82. Steiner M, Gutbrodt K, Krall N, Neri D (2013) Tumor-targeting antibody-anticalin fusion proteins for in vivo pretargeting applications. *Bioconjug Chem* 24:234–241. doi:[10.1021/bc300567a](https://doi.org/10.1021/bc300567a)
83. Lendel C, Dincbas-Renqvist V, Flores A et al (2004) Biophysical characterization of Z(SPA-1)–a phage-display selected binder to protein A. *Protein Sci* 13:2078–2088. doi:[10.1110/ps.04728604](https://doi.org/10.1110/ps.04728604)

84. Feldwisch J, Tolmachev V, Lendel C et al (2010) Design of an optimized scaffold for affibody molecules. *J Mol Biol* 398:232–247. doi:[10.1016/j.jmb.2010.03.002](https://doi.org/10.1016/j.jmb.2010.03.002)
85. Lundberg E, Brismar H, Gråslund T (2009) Selection and characterization of Affibody ligands to the transcription factor c-Jun. *Biotechnol Appl Biochem* 52:17–27. doi:[10.1042/BA20070178](https://doi.org/10.1042/BA20070178)
86. Nygren P-Å (2008) Alternative binding proteins: affibody binding proteins developed from a small three-helix bundle scaffold. *FEBS J* 275:2668–2676. doi:[10.1111/j.1742-4658.2008.06438.x](https://doi.org/10.1111/j.1742-4658.2008.06438.x)
87. Lindborg M, Cortez E, Höidén-Guthenberg I et al (2011) Engineered high-affinity affibody molecules targeting platelet-derived growth factor receptor β in vivo. *J Mol Biol* 407:298–315. doi:[10.1016/j.jmb.2011.01.033](https://doi.org/10.1016/j.jmb.2011.01.033)
88. Kronqvist N, Malm M, Göstring L et al (2011) Combining phage and staphylococcal surface display for generation of ErbB3-specific Affibody molecules
89. Webster JM, Zhang R, Gambhir SS et al (2009) Engineered two-helix small proteins for molecular recognition. *ChemBioChem* 10:1293–1296. doi:[10.1002/cbic.200900062](https://doi.org/10.1002/cbic.200900062)
90. Ren G, Zhang R, Liu Z et al (2009) A 2-helix small protein labeled with ^{68}Ga for PET imaging of HER2 expression. *J Nucl Med* 50:1492–1499. doi:[10.2967/jnumed.109.064287](https://doi.org/10.2967/jnumed.109.064287)
91. Miao Z, Ren G, Jiang L et al (2011) A novel (18)F-labeled two-helix scaffold protein for PET imaging of HER2-positive tumor. *Eur J Nucl Med Mol Imaging*. doi:[10.1007/s00259-011-1879-9](https://doi.org/10.1007/s00259-011-1879-9)
92. Ahlgren S, Tolmachev V (2010) Radionuclide molecular imaging using Affibody molecules. *Curr Pharm Biotechnol* 11:581–589
93. Miao Z, Levi J, Cheng Z (2010) Protein scaffold-based molecular probes for cancer molecular imaging. *Amino Acids*. doi:[10.1007/s00726-010-0503-9](https://doi.org/10.1007/s00726-010-0503-9)
94. Yang M, Cheng K, Qi S et al (2013) Affibody modified and radiolabeled gold-Iron oxide hetero-nanostructures for tumor PET, optical and MR imaging. *Biomaterials* 34:2796–2806. doi:[10.1016/j.biomaterials.2013.01.014](https://doi.org/10.1016/j.biomaterials.2013.01.014)
95. Baum RP, Prasad V, Müller D et al (2010) Molecular imaging of HER2-expressing malignant tumors in breast cancer patients using synthetic ^{111}In - or ^{68}Ga -labeled affibody molecules. *J Nucl Med* 51:892–897. doi:[10.2967/jnumed.109.073239](https://doi.org/10.2967/jnumed.109.073239)
96. Zielinski R, Lyakhov I, Hassan M et al (2011) HER2-affitoxin: a potent therapeutic agent for the treatment of HER2-overexpressing tumors. *Clin Cancer Res* 17:5071–5081. doi:[10.1158/1078-0432.CCR-10-2887](https://doi.org/10.1158/1078-0432.CCR-10-2887)
97. Andersen JT, Pehrson R, Tolmachev V et al (2011) Extending half-life by indirect targeting of the neonatal Fc receptor (FcRn) using a minimal albumin binding domain. *J Biol Chem* 286:5234–5241. doi:[10.1074/jbc.M110.164848](https://doi.org/10.1074/jbc.M110.164848)
98. Steffen A-C, Almqvist Y, Chyan M-K et al (2007) Biodistribution of ^{211}At labeled HER-2 binding affibody molecules in mice. *Oncol Rep* 17:1141–1147
99. Myhre S, Henning P, Friedman M et al (2009) Re-targeted adenovirus vectors with dual specificity; binding specificities conferred by two different Affibody molecules in the fiber. *Gene Ther* 16:252–261. doi:[10.1038/gt.2008.160](https://doi.org/10.1038/gt.2008.160)
100. Lehmann A (2008) Ecallantide (DX-88), a plasma kallikrein inhibitor for the treatment of hereditary angioedema and the prevention of blood loss in on-pump cardiothoracic surgery. *Expert Opin Biol Ther* 8:1187–1199. doi:[10.1517/14712598.8.8.1187](https://doi.org/10.1517/14712598.8.8.1187)
101. Zuraw B, Yasothan U, Kirkpatrick P (2010) Ecallantide. *Nat Rev Drug Discov* 9:189–190. doi:[10.1038/nrd3125](https://doi.org/10.1038/nrd3125)
102. Silverman J, Liu Q, Lu Q et al (2005) Multivalent avimer proteins evolved by exon shuffling of a family of human receptor domains. *Nat Biotechnol* 23:1556–1561. doi:[10.1038/nbt1166](https://doi.org/10.1038/nbt1166)
103. Hudson PJ, Souriau C (2003) Engineered antibodies. *Nat Med* 9:129–134. doi:[10.1038/nm0103-129](https://doi.org/10.1038/nm0103-129)

Chapter 14

Engineering Multivalent and Multispecific Protein Therapeutics

Cassie J. Liu and Jennifer R. Cochran

14.1 Biomedical Applications of Multivalent and Multispecific Proteins

Proteins have attracted great interest as therapeutic agents due to their high-binding affinity and specificity to clinical targets of interest [1]. The last several decades have witnessed a surge in our ability to engineer protein drug candidates, from improved algorithms for rational design [2, 3] to new platforms for directed evolution [4–7]. In parallel, multivalent or multispecific proteins have shown great therapeutic potential compared with their monospecific protein counterparts due to increased efficacy or enhanced selectivity toward sites of disease [8–11]. Nature commonly exploits multivalency and multispecificity to regulate numerous physiological processes [12, 13]; applying these concepts to protein drug discovery offers exciting new avenues for clinical development. A thorough understanding of the thermodynamic and kinetic principles underlying multivalency and multispecificity is essential to develop therapeutic proteins that promote these improved biological effects. In addition, this understanding allows researchers to effectively affirm or challenge proposed molecular mechanisms for existing protein therapeutics. This chapter will present the underlying principles of multivalent or multispecific protein therapeutics as outlined below, where each concept will be accompanied with example case studies from literature:

14.2 Multivalency and Binding Avidity.

14.3 Tuning Selectivity through Multivalency and Multispecificity.

14.4 Biological Principles for Multivalent and Multispecific Protein Design.

J. R. Cochran (✉)

Departments of Chemical Engineering and Bioengineering, Stanford University,
Stanford, CA, USA

e-mail: jennifer.cochran@stanford.edu

C. J. Liu

Department of Chemical Engineering, Stanford University, Stanford, CA, USA

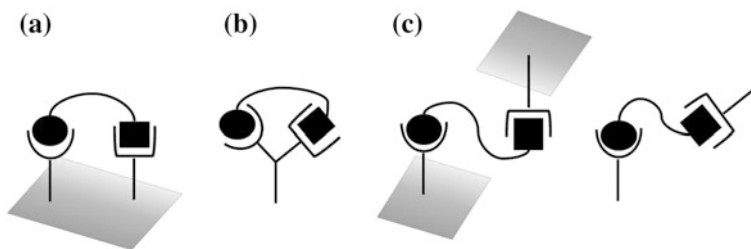


Fig. 14.1 Targeting strategies for multivalent and multispecific proteins. *Circles* and *squares* represent individual binding sites that can be either identical (monospecific) or different (bispecific). Ligand can simultaneously bind: **a** two receptors on the same cell surface; **b** two epitopes on the same receptor; and **c** two receptors on separate surfaces or in solution

14.2 Multivalency and Binding Avidity

Before considering the design and engineering of proteins for clinical applications, one must first have a clear understanding of the underlying concepts behind binding affinity and avidity effects stemming from *multivalency* and *multispecificity*. We refer to a molecule as multivalent if it contains multiple binding sites, and refer to it as multispecific if the sites bind to different targets, or different epitopes within a target. The reader should note that multivalency by definition encompasses multispecificity; that is, a molecule with more than one binding site will always be multivalent, but not necessarily multispecific. A multispecific protein is, however, always multivalent. Figure 14.1 shows examples of how the two binding sites of bivalent molecules can interact in different ways with their respective targets. For our discussion, a target is a biomolecule, such as a receptor, that has clinical relevance and whose biological activity mediates disease pathology.

In this section, we present the basic kinetic and thermodynamic models for ligand–receptor binding, beginning with a monovalent interaction and expand these models to include multivalency. More detailed analyses are offered in various textbooks and reviews as cited; this introduction should give the reader a sense of the physical factors contributing to the advantageous properties of multivalent proteins, and how information from these models can guide the design and engineering of protein therapeutics.

14.2.1 Equilibrium Binding Constant, K_D

A monovalent binding interaction between a therapeutic protein, which we call ligand (L), and the target molecule, which we call receptor (R), is described by the following equation:



where LR represents the 1:1 complex of L and R , and k_{on} and k_{off} are the rate constants for association and dissociation, respectively. The association and dissociation rates are defined as follows:

$$r_{\text{association}} = k_{\text{on}}[L][R] \quad (14.2)$$

$$r_{\text{dissociation}} = k_{\text{off}}[LR] \quad (14.3)$$

At some time after the start of the reaction, the system reaches equilibrium concentrations of L , R , and LR , reflecting the relative values of k_{on} , k_{off} , and the initial concentrations of L and R : $\frac{d[L]}{dt} = \frac{d[R]}{dt} = \frac{d[LR]}{dt} = 0$. The concentrations of free L and R , and LR remain in a dynamic equilibrium, in that $r_{\text{association}} = r_{\text{dissociation}}$. We can therefore say that:

$$k_{\text{on}}[L]_{\text{eq}}[R]_{\text{eq}} = k_{\text{off}}[LR]_{\text{eq}} \quad (14.4)$$

which can be rearranged to:

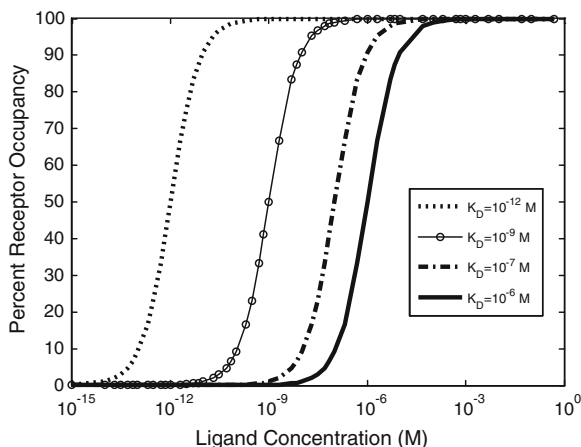
$$\frac{k_{\text{off}}}{k_{\text{on}}} = \frac{[L]_{\text{eq}}[R]_{\text{eq}}}{[LR]_{\text{eq}}} \quad (14.5)$$

The subscript “eq” indicates that the concentrations are at equilibrium. The ratio of k_{off} over k_{on} describes the strength of the interaction and is defined as the equilibrium binding constant (K_D) of L and R .

$$K_D = \frac{k_{\text{off}}}{k_{\text{on}}} [=] \text{mole}/L \quad (14.6)$$

As shown in Eqs. 14.5 and 14.6, the K_D represents the ratio of the individual concentrations of L and R to the concentration of the LR complex at equilibrium. From this definition, a lower K_D corresponds to stronger binding affinity, while a higher K_D corresponds to weaker binding affinity. Measurements of K_D , k_{on} , and k_{off} provide common metrics for describing the binding affinity and kinetic binding parameters of a molecular interaction. These properties can play a direct role in the biological efficacy of a protein therapeutic [14–16]. Thus, there has been great interest in determining the relationships between binding affinity and biological function, and how alterations in these parameters can be leveraged in protein engineering to direct a biological outcome. Figure 14.2 illustrates the effect of K_D on the percent of R converted to LR at equilibrium, for a range of L concentrations. Typical K_D values range from μM for enzyme–substrate interactions, to nM and pM for cell surface receptor binding events, and even fM in rare cases such as biotin–streptavidin, underscoring how nature has optimized binding affinities for different biological contexts.

Fig. 14.2 Ligand–receptor binding for a range of K_D values



14.2.2 Thermodynamic Considerations in Binding

The laws of thermodynamics dictate protein biophysical properties, including folding, structure, and binding energetics. Our discussion on thermodynamics will be centered around the Gibbs free energy (ΔG) of binding, which can be thought of as the energy (kcal/mol) gained from or lost to the environment in a binding event. Studies of protein–protein interactions often explore how altering amino acid sequence and protein structure affects ΔG , consequently identifying important molecular contributions to binding affinity. The following equation relates the Gibbs free energy to the K_D :

$$\Delta G = RT \ln(K_D) \quad (14.7)$$

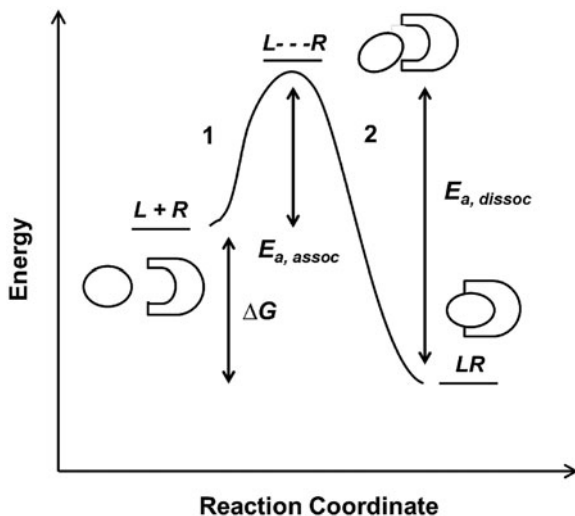
where R is the ideal gas constant, with units of kcal/(mol * K). The same equation can be rearranged to obtain:

$$K_D = e^{\frac{\Delta G}{RT}} \quad (14.8)$$

The implication of Eqs. 14.7 and 14.8 is that the binding affinity is dependent on the energetics of binding as well as temperature. Here, a negative ΔG indicates an energetically favorable binding reaction that will spontaneously proceed in the forward direction, and a positive ΔG indicates an unfavorable one. The simplest way to understand the relationship between energetics and kinetics is through a reaction coordinate diagram, as shown in Fig. 14.3.

On the reaction coordinate, the relative energies of free L and R and the complex LR are measured as ΔG . The LR complex state must be lower in energy than the free states in order for the binding interaction to be favorable. This corresponds to a negative sign for ΔG if defined as $G_{\text{complex}} - G_{\text{free}}$. The curve represents the reaction pathway and is indicative of the equilibrium amounts of L , R , and LR as defined by the K_D value. In this case, the binding event is comprised of two steps. The first step (1), which requires some starting energy $E_{a,\text{assoc}}$,

Fig. 14.3 Reaction coordinate diagram of a monovalent binding interaction



arranges the ligand and receptor an optimal position and conformation for binding. The starting energy $E_{a,assoc}$ arises from thermal fluctuation of the molecules in solution. In the second step (2), the LR complex formation releases an energy that drives the binding interaction forward. The same principles drive the dissociation reaction (with an $E_{a,dissoc} = E_{a,assoc} + \Delta G$), until the system reaches equilibrium between the two states. The relative amount of energy $E_{a,assoc}$ or $E_{a,dissoc}$ required for association or dissociation, respectively, determines the probability of the molecules to successfully move forward or backward on the coordinate diagram. This probability is reflected in the rate constants, and hence K_D . In reality, protein–protein interactions are often more complicated than the simple curve and two-step reaction illustrated above; for example, a reaction mechanism may contain multiple intermediate steps or require cofactors to facilitate ligand–receptor binding. However, the reaction coordinate provides good intuitive understanding of binding energetics and kinetics.

We can now further describe ΔG of binding in more physical terms, namely ΔH (enthalpy), temperature, and ΔS (entropy) of binding. Note that both ΔH and ΔS are state functions, meaning that regardless of the simplicity or complexity of the reaction mechanism, their values depend only on the relative energies between the free (initial) and complexed (final) states.

$$\Delta G = \Delta H - T\Delta S \quad (14.9)$$

Formally, enthalpy is defined as the sum of internal energy of a system (energy required to create the system) and the work the system exerts on its surroundings. In the context of protein–protein interactions, we can think of enthalpy as a measure of the electrostatic and geometric complementarity between two proteins. Enthalpic contributions consist of molecular interactions of both binding partners that facilitate stronger noncovalent binding, as well as molecular interactions between the

proteins and the surrounding environment. A negative ΔH value indicates an exothermic reaction (binding releases energy) while a positive ΔH value indicates an endothermic reaction (binding requires energy). Since a favorable binding event necessitates a negative ΔG value, a larger negative ΔH value correlates with better complementarity between the two binding partners.

Entropic contributions describe changes in the degrees of freedom of movement of L , R , and their surrounding solvent upon binding. In order to form an LR complex, L and R must adopt optimal conformations relative to each other, reducing the entropy of both proteins ($S_{\text{final}} - S_{\text{initial}} < 0$); from Eq. 14.9, we see that this results in a negative ΔS value, leading to a more positive, and therefore less favorable ΔG value. To better explain entropy, we divide ΔS into more specific subtypes [17–20]:

$$\Delta S = \Delta S_{\text{translation}} + \Delta S_{\text{rotation}} + \Delta S_{\text{conformation}} + \Delta S_{\text{solvation}} \quad (14.10)$$

Translational and rotational entropy describes the protein's ability to move in three-dimensional space. In nature, the reduction of translational degrees of freedom is necessary for facilitating many biological processes; a canonical example is the movement of proteins along DNA [21]. In our monovalent binding example, LR complex formation restricts the movement of ligand L to a particular volume occupied by the receptor R , and vice versa. Conformational entropy describes the protein's thermal fluctuations around its native state. This idea is based on the prevalent view that free ligand and receptor are able to sample a range of orientations around their primary native states, which are optimal for binding to each other. In the context of Fig. 14.3, one could imagine many slightly different free protein conformations at various energies, with an average energy as indicated by the horizontal line at $L + R$. Upon binding, the primary conformations of both ligand and receptor are stabilized, greatly reducing their accessibilities to the initial range of conformations. Solvation entropy refers to the energy required to arrange water molecules around each other and around a protein. Upon protein binding, formation of the binding interface reduces the surface area between protein and water. Given that water molecules experience the greatest entropy when they are allowed to arrange around each other, protein binding results in a positive change in solvation entropy.

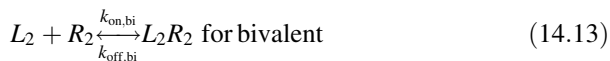
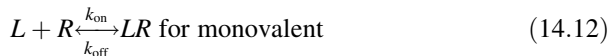
Using Eq. 14.9, we can rewrite Eq. 14.8 as:

$$K_D = e^{\left(\frac{\Delta H}{RT} - \frac{\Delta S}{R}\right)} \quad (14.11)$$

This representation shows that manipulations of enthalpy and entropy alter the free energy, and hence the binding affinity, of a given protein toward its intended target molecule [22, 23]. To enhance enthalpic contributions one might, for example, mutate amino acid residues within a binding interface to increase the charge or size complementarity. However, these effects are difficult to predict *a priori* using rational design; changes in the enthalpy of a protein–protein interaction often have unintended effects on entropy, and vice versa, all of which influence the K_D value [19, 24].

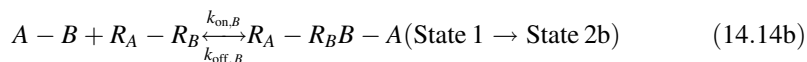
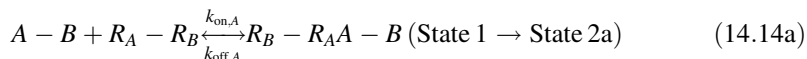
14.2.3 Binding Avidity

We now extend the kinetic model to the case of a bivalent protein ligand; models describing proteins of higher order valency will follow the same principles outlined below. Bivalency increases the complexity of ligand–receptor binding kinetics through the physical tethering of one binding site in close proximity to another. The ligand is now a molecule containing two binding sites, each binding to one receptor molecule on a cell surface. Hence, the binding equation is altered as follows:



where $k_{\text{on,bi}}$ and $k_{\text{off,bi}}$ are the *apparent* rate constants of the bivalent ligand to the receptor. The term *apparent* is used to indicate empirically determined parameters that cannot distinguish between the individual receptor binding events of each ligand component. Often, there is an increase in the apparent affinity of a bivalent protein compared with the affinities of its monovalent components, a phenomenon known as *avidity*. To illustrate this point, we introduce the sequential binding reactions shown in Fig. 14.4, a concept originally proposed by Jencks [25]. In this schematic, ligands A , B , and $A-B$ are free-floating, while their receptors are constrained to a surface (i.e., cell membrane) at a certain density. A and B can be identical (monospecific ligand) or different (bispecific ligand); the analysis is the same regardless of their identities. First consider Fig. 14.4a, where the binding sites A and B are untethered. In this case, the receptor binding events are independent monovalent interactions that can be described by Eq. 14.12. Hence, the interactions of A and B with their receptors are defined by their affinities $K_{D,A}$ and $K_{D,B}$, respectively.

Now, we consider the more complex scenario in Fig. 14.4b, where A and B are tethered. The binding of the first site, whether it be A or B , to its target receptor follows the same monovalent binding kinetics as in Fig. 14.4a (State 1) and assumes that the binding events are independent. Below we present the binding equations of State 1 going to State 2:



In Eqs. 14.14a and 14.14b, the receptors are represented as $R_A - R_B$ to indicate that they are on the same cell surface. In State 2, one ligand binding site is bound to a receptor, and thus, the cell surface, while the other is brought to the surface but still unbound. The second binding site is thus constrained to a volume defined by

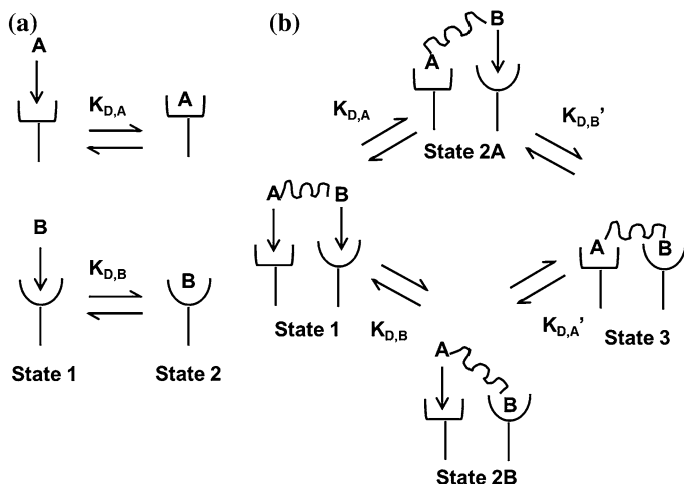


Fig. 14.4 Binding schematic of ligands A and B with their respective receptors. **a** Untethered A and B bind receptors independent of each other with affinities $K_{D,A}$ and $K_{D,B}$. **b** Tethered A — B binds receptors in multiple states. State 1: both binding sites are unattached. State 2a,b: either A or B binds independent of the other with affinities $K_{D,A}$ and $K_{D,B}$. State 3: second binding event depends on the first. Either A or B binds with affinities $K_{D,A'}$ and $K_{D,B'}$. Figure adapted from Jencks [25]

the space available to the linker joining A and B (State 2a and 2b). Although only one of the binding sites is bound to a receptor, the second binding site is more favorably placed near its receptor, increasing its probability of undergoing a binding interaction. In effect, we have transitioned from an intermolecular binding event to an intramolecular binding event [18, 26] as described by Eqs. 14.15a and 14.15b.



How do the apparent affinities $K_{D,A'}$ and $K_{D,B'}$ differ from the monovalent affinities $K_{D,A}$ and $K_{D,B}$? If we look at the binding events that occur from State 2 to State 3, we see that the effective concentration of the second binding site around free receptors has dramatically increased (Fig 14.5). It is important to recognize that this effective concentration can be orders of magnitude greater than the concentration of free ligand in solution, to the point where $K_{D,A'} \ll K_{D,A}$ and $K_{D,B'} \ll K_{D,B}$. In other words, at equilibrium, the dominant species in solution are those in 14.15a and 14.15b representing State 2 and State 3. This phenomenon explains the avidity effect: *when the effective concentration of the second ligand is so large that it drives the subsequent association reaction forward, the rate of*

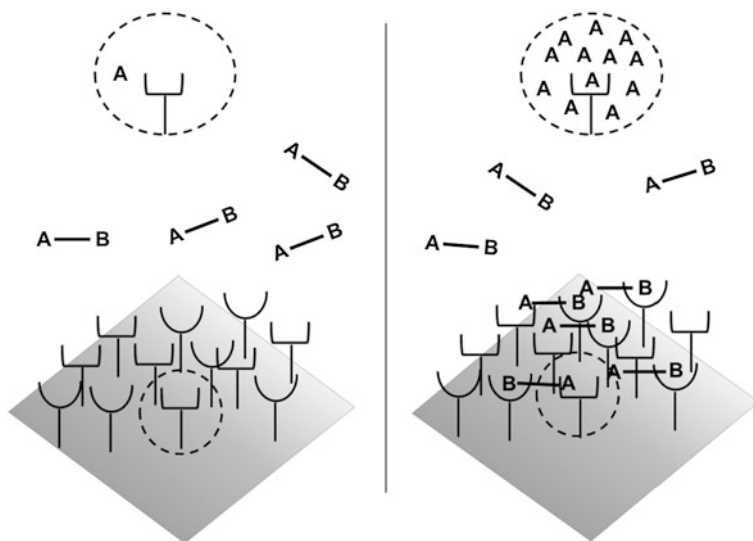


Fig. 14.5 Avidity effects due to increased effective concentration. *Left:* Before binding, the concentration of binding sites as seen by a cell surface receptor is equivalent to the ligand concentration in solution. *Right:* Upon monovalent binding of site B, the effective concentration of binding site A seen by the receptor is vastly increased, driving the association reaction forward

complete dissociation of the ligand from the cell surface is greatly reduced compared with that of monovalent binding interactions.

Now, we relate increased effective concentration to increased overall affinity due to bivalency. C_{eff} is a term describing the enhancement of effective concentration of either A or B due to their tethering [19, 26]. We define C_{eff} as the ratio of the ligand–receptor affinity of the monovalent binding event compared with their apparent affinity in a bivalent binding event:

$$C_{\text{eff}} = \frac{K_{D,A}}{K_{D,A'}} = \frac{K_{D,B}}{K_{D,B'}} \quad (14.16)$$

If $C_{\text{eff}} > 1$ M, the bivalent protein has an increased apparent affinity to the cell surface due to avidity effects. This sequential binding event can be represented by an overall affinity $K_{D,AB,\text{bi}}$:

$$K_{D,AB,\text{bi}} = K_{D,A} * K_{D,B'} = K_{D,B} * K_{D,A'} \quad (14.17)$$

Since the reaction going from State 2 to State 3 is unimolecular, $K_{D,A'}$ and $K_{D,B'}$ are unitless. $K_{D,AB,\text{bi}}$ therefore has units of M.

Avidity can increase the apparent affinity of a multivalent ligand to be orders of magnitude greater compared with that of its monovalent components. As such, multivalency is a common phenomenon exploited by nature to enhance the affinities of protein ligands to their binding partners, eliminating the need to

produce large amounts of monovalent protein or to evolve a single binding domain with high affinity. As examples, many growth factors utilize multivalency to achieve overall binding affinities in the nM–pM range. Vascular endothelial growth factor (VEGF) is a disulfide-linked homodimer that binds to two VEGF-receptor 2 (VEGFR2) molecules on the cell surface and induces their dimerization, stimulating downstream cell-signaling pathways [27, 28]. The strong affinity of VEGF for its receptor is in part due to its bivalent binding properties; when one VEGFR2-binding site was eliminated through directed mutagenesis, the affinity of VEGF was reduced by two orders of magnitude [28]. Hepatocyte growth factor (HGF) is a multidomain-soluble ligand that also binds to and dimerizes its cognate receptor (c-MET) with pM affinity [29]. Recent studies have shown that individual domains of HGF contribute weakly to c-MET binding, resulting in overall avidity effects when all domains are present [30, 31]. As a further demonstration of avidity effects in this system, a truncated HGF fragment termed NK1, despite its ability to dimerize the receptor, binds c-MET with a reduced affinity (nM) and is orders of magnitude less efficacious in inducing c-MET activation compared to HGF [30, 32]. In the context of protein therapeutics, the most well-studied natural multivalent protein is the antibody. Antibodies are modular, containing a constant (Fc) domain that mediates immune system activity, and two identical antigen-binding regions consisting of heavy and light variable chains. Natural antibodies are bivalent, but monospecific, in that these two antigen binding sites interact with the same target. Antibodies have been specifically evolved, either by nature or in the laboratory, for high-affinity recognition of a wide range of antigen targets and thus are applicable across a broad spectrum of medical problems [9, 10, 33].

14.2.4 Linkers and Avidity

Designing multivalent proteins with the desired kinetic properties can be carried out by: (1) engineering the binding sites themselves, (2) optimizing the linker that tethers the monovalent components, if applicable, or (3) both. Methods for altering protein–protein interactions have been extensively reviewed, and include both rational design and directed evolution [2–7]. In addition, much effort has gone into linker development, as optimal flexibilities and length requirements differ among systems [34, 35]. Linkers can strongly influence the avidity of multivalent protein interactions through entropic effects, and thus, their optimization is essential for achieving desired levels of therapeutic efficacy. In this subsection, we will describe the relationship between linker entropy and ligand-binding kinetics.

To introduce linker thermodynamics, we will use a polymer chain as an example of a model linker. Linkers can assume many different geometries and chemical compositions but are often linear peptide chains of varying length [36]. Entropy demands that the linker exist in random orientations in solution; this randomness is caused by thermal fluctuations. However, there is a deformation cost to bending that opposes entropy. This property, which depends on linker

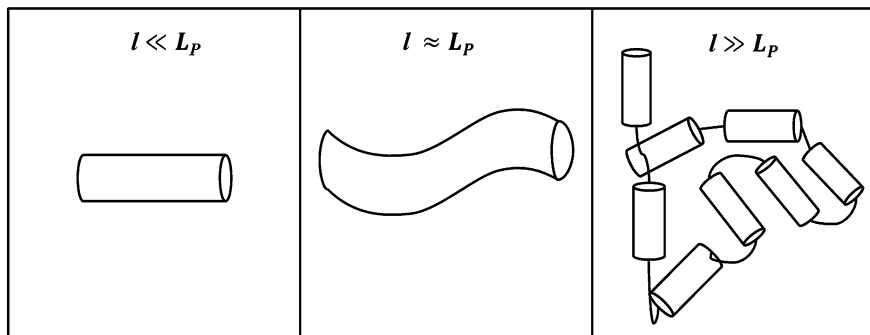


Fig. 14.6 Polymer chain at three different length scales. As l increases, deformation of the chain by thermal fluctuations randomizes the orientation

composition, is referred to as its elasticity. To illustrate this concept, we introduce a parameter called the persistence length L_P , whose informal definition is the length over which a polymer strand is relatively straight, and is a measure of the strand's elasticity or rigidity. Formally, it is the ratio of the linker's elastic energy over thermal energy. A small L_P indicates a flexible strand since the deformation cost is easily overcome by thermal fluctuations. Similarly, a large L_P indicates a rigid strand, since the deformation cost is large, and the strand is not easily bent to different conformations. In Fig. 14.6, we present three different views of a polymer strand: at length $l \ll L_P$, the strand looks perfectly straight; at $l \approx L_P$, the polymer is still relatively straight, but one sees the initial deformation of the strand; at $l \gg L_P$, the linker can now be seen as a collection of rigid segments of length L_P where the hinges allow each segment freedom of translation and rotation, and linker orientation can be approximated as a random walk in three dimensions.

To understand the mechanism of how linkers influence binding affinity, we will explore avidity effects in the context of thermodynamics. The binding of the first site in Fig. 14.4b (State 1) lowers the translational, rotational, and conformational freedom of both molecules in the complex, represented by ΔS (see Eq. 14.10). As a result, the effective concentrations of the other ligand-binding sites are increased; in other words, the translational and rotational space that the tethered sites can sample is restricted to a smaller volume around their receptors. Thus, the entropic penalty for constraining any tethered binding site and its receptor in proximity with each other is paid to an extent by the binding of the first ligand. The ΔG of binding is therefore decreased for any subsequent interaction, lowering the apparent K_D for a multivalent ligand compared with that of a monovalent ligand. The requirement for avidity is thus $\Delta G_{\text{multi},N} < \Delta G_{1,\text{mono}} + \Delta G_{2,\text{mono}} + \dots + \Delta G_{N,\text{mono}}$ [18], where $\Delta G_{\text{multi},N}$ is the total energy loss upon binding of the multivalent ligand with valency N , and $\Delta G_{J,\text{mono}}$ is the total energy loss upon binding of an independent monovalent site J . Linker length and elasticity determines the magnitude of entropy loss for each binding event between a multivalent ligand and

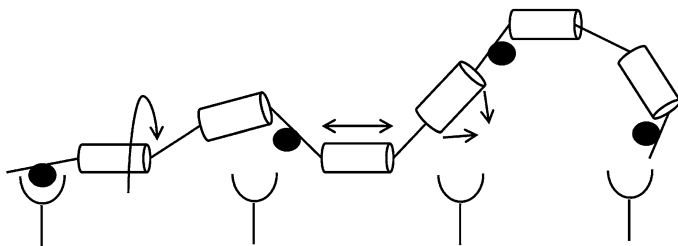


Fig. 14.7 Entropy losses from constraint of a flexible linker. Circles (●) represent ligand-binding sites, while cylinders represent rigid segments of a flexible linker. Arrows indicate degrees of freedom of movement for the polymer chain; each segment can undergo rotation (*left*), extension (*middle*), and bending (*right*)

receptors on a surface. On the simplest level, the longer and more flexible the linker is, the greater the entropic penalty paid for each subsequent binding event. To illustrate this concept, we expand our polymer chain model to include identical ligand-binding sites (represented by ●) interspersed along a chain of length $l \gg L_p$ (Fig. 14.7). Each chain segment has several degrees of freedom from the translational, rotational, and conformational contributions to entropy. Therefore, each binding event results in an entropy loss for the linker as well as for the ligand binding site and receptor. In Fig. 14.7, the first binding event on the left pays the majority of the entropic penalty and localizes the entire ligand in proximity to other receptors. Although subsequent binding interactions will also incur entropy losses for the linker and ligand-binding sites, these losses decrease for each additional binding event. If these entropic losses are less than the energy necessary to bring each monovalent binding site from solution to the receptor, the overall $\Delta G_{\text{multi},N}$ is still lower than the sum of N separate $\Delta G_{\bullet, \text{mono}}$ and there will be an avidity effect. However, if the linker is too elastic or too long, the overall entropic penalty for binding the entire ligand increases, as would $\Delta G_{\text{multi},N}$. In this case, avidity would decrease, resulting in a weaker binding affinity. If the overall entropic penalty increases to the point where $\Delta G_{\text{multi},N} = N\Delta G_{\bullet, \text{mono}}$, then no avidity effect will be observed.

In the case of an idealized multivalent protein, there is no entropy loss upon the interaction of subsequent binding sites, and the apparent affinity is thus the theoretical maximum; that is, the linker is perfectly designed so that the first binding event essentially places all remaining binding sites in an optimal orientation relative to their respective binding partners. A classic example of using linkers that maximize avidity is the binding of trivalent vancomycin and trivalent D-Ala-D-Ala [37]. The monovalent affinity between the vancomycin and D-Ala-D-Ala monomers is $\sim 1 \mu\text{M}$; by trimerizing both receptor and ligand, an overall affinity of sub-fM binding was achieved, an increase of eleven orders of magnitude. The key to optimizing avidity in this case was selecting linkers rigid enough to minimize entropy loss during intermolecular binding.

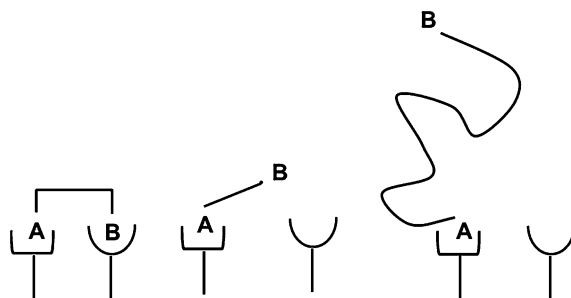


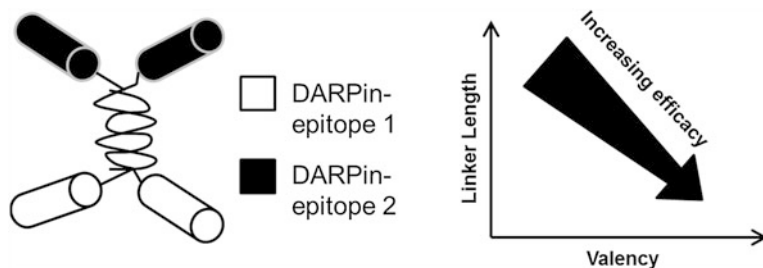
Fig. 14.8 Linker effects on binding. *Left:* Idealized case. Linker length and elasticity is theoretically optimal for constraining *B* in proximity to its receptor upon binding of *A*. *Middle:* Linker length is too short/inelastic, such that the limited volume sampled by *B* does not permit its binding to its receptor. *Right:* Linker length is too long/elastic such that the volume sampled by *B* is similar to free *B* in solution, resulting in negligible avidity effects

Despite this elegant example of a “perfect” multivalent interaction, in the majority of cases avidity effects will fall below the theoretical maximum. In practice, even with an optimized linker, entropic penalties can still occur. In the vancomycin/D-Ala-D-Ala example above, both interacting molecules were soluble and presented to each other as pre-formed trimers, minimizing the entropy loss upon binding compared with physiological protein–protein interactions that require conformational changes or receptor clustering to effectively bind. Linker design is ultimately a balance between elasticity and minimizing entropy loss. In cases where receptor spatial orientation is well characterized, a rigid linker that positions the binding sites at the exact distances between receptors is desirable. This arrangement minimizes the loss of entropy upon binding of each site and approaches the optimal affinity possible for the multivalent construct (Fig. 14.8, left). In contrast, a short and/or rigid linker that cannot span two receptors results in monovalent binding (Fig. 14.8, middle). Alternatively, the entropic costs conferred by a long, elastic linker (Fig. 14.8, right) can be large enough to where avidity effects are negligible. For more detailed information about linker effects on receptor binding, the reader is referred to texts from Krishnamurthy et al. [19] and Zhou [26].

A wide variety of linkers have been used for tethering multiple binding sites. While chemical linkers of varying composition have been used to conjugate proteins [38–40], challenges often arise with heterogeneous product formation and purification; thus, these linkers are often used to tether peptides and small molecules produced through synthetic methods. Peptide-based linkers, which can be expressed as genetic fusions between proteins, have generated great interest as alternatives [41]. Common elastic linkers include combinations of glycine and serine, while inelastic linkers tend to include conformationally constrained amino acids such as proline, or residues that form stable α -helices [36]. Natural protein domains have also been exploited as tethers and provide geometrical rigidity to restrain the binding sites of a multivalent protein [42]. The most well-studied

example in protein therapeutics is again the antibody. The two variable regions of an antibody are fused to a constant domain that fixes the spatial distance between the antigen-binding sites. Antibodies have therefore been used as robust molecular scaffolds to create more than 35 different fusion proteins, spanning a broad range of multivalent and multispecific protein architectures [8, 9, 43]. Several such antibodies have advanced to clinic trials, underscoring the adoption of multivalency and multispecificity in novel protein design [43]. More recently, multivalency and multispecificity have been engineered into single-domain proteins, providing a novel method to constrain the orientation and topological arrangement of binding sites [44–46].

Example 14.1: *Tuning Protein Valency and Linker Design for Improved Biological Potency.*



Epidermal growth factor receptor (EGFR) overexpression is associated with many cancers, thus there has been great interest in designing protein therapeutics that inhibit the receptor and its downstream cell-signaling pathways. In Boersma et al. [47], designed ankyrin repeat proteins (DARPins) were evolved to bind distinct EGFR epitopes with sub-nM affinities. The authors then used these engineered DARPins to create bispecific/bivalent, as well as bispecific/tetravalent fusions, with the goal of improving biological efficacy.

A trend of increased efficacy, as measured by cell growth inhibition, was observed with increased valency. Furthermore, the engineered molecules demonstrated varying degrees of inhibition in cell culture models depending on linker length, linker elasticity, and monomer orientation. Specifically, a bispecific/tetravalent DARPin fusion was created by tethering individual monomeric subunits to a rigid leucine zipper, via different elastic glycine or glycine-serine linkers (inset). In this study, the shortest linkers, namely Gly₄ and Gly₂Ser₂, resulted in multivalent proteins with the highest levels of biological inhibition. These results demonstrate that valency and linker length can be tuned to improve biological potency.

14.3 Tuning Selectivity Through Multivalency and Multispecificity

In Sect. 14.2, we introduced fundamental biophysical principles underlying protein–protein interactions and discussed how these concepts explain avidity effects in the case of multivalent proteins. The examples in the previous section used multivalency and multispecificity as tools to engineer proteins with higher affinity to a target of interest. We now consider protein therapeutics in a physiological context, with the critical question: How can we use the properties of multivalency and multispecificity to effectively distinguish between receptor targets that are associated with disease versus those that are necessary for normal biological processes? The goal of any protein therapeutic is to target specific cells and/or specific biological pathways involved in disease pathology. Protein therapeutics that bind a target receptor with high affinity and specificity can be effective in cases where the target receptor is expressed at high levels within a disease site, or if disease is caused by a mutated receptor that is distinct from the natural one. Challenges arise, however, when there is not a marked difference between “target” and “non-target” states. The inability of a protein therapeutic to distinguish between these two states can lead to undesired off-target effects and toxicity [48]. In this section, we will explore how target receptor selectivity can be increased with multivalent and multispecific proteins, namely by preferentially targeting diseased cells with higher numbers of receptors, or by targeting two different receptors on diseased cells (Fig 14.9).

First, we will define *specificity* and *selectivity* in the context of this chapter. Specificity refers to the ability of a protein therapeutic to distinguish between its target receptor and all other biomolecules; namely, by having a higher binding affinity to this target. Selectivity refers to the ability of a protein therapeutic to bind with greater affinity to target receptors on diseased cells. Mathematically, it can be represented as:

$$\text{Selectivity} = \frac{\text{\#ligand bound to target cells}}{\text{\#ligand bound to non-target cells}} \quad (14.18)$$

Specificity is usually required for, but does not guarantee, selectivity. Therapeutic efficacy is determined in part by selectivity, and whether a drug is able to carry out its intended function without off-target effects.

As stated above, the important criteria for an effective protein therapeutic is tight binding to target cells and weak to no binding to non-target cells. This translates to the expression: $K_{D,\text{target}} \ll K_{D,\text{non-target}}$, which should be familiar to readers as it is similar to our description of avidity. In Sect. 14.2.3, we defined parameters for avidity where any subsequent binding event for a multivalent protein has a stronger apparent affinity than that for a monovalent binding event ($K_{D,A'} \ll K_{D,A}$ and $K_{D,B'} \ll K_{D,B}$). When considering a protein therapeutic that has specificity toward receptors on both target and non-target cells, *to achieve selectivity for target cells, it must bind these cells with an apparent affinity*

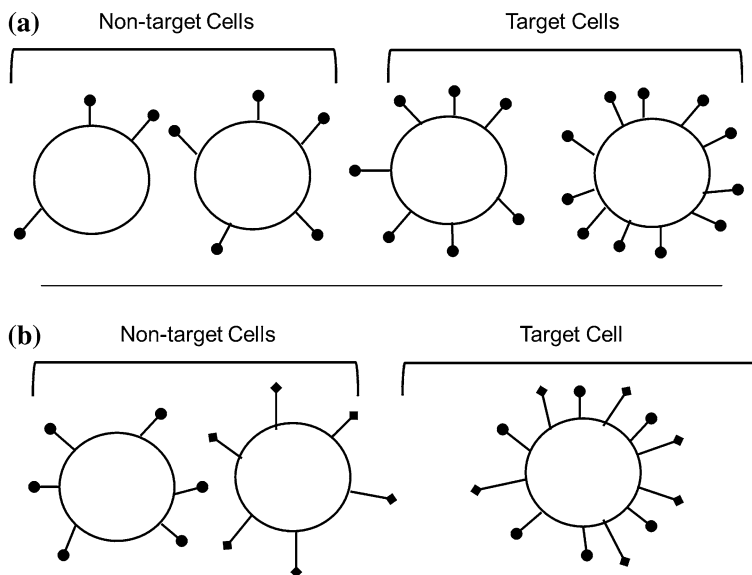


Fig. 14.9 Two scenarios that can be exploited with multivalent and multispecific proteins to preferentially distinguish between target and non-target cells. **a** Non-target and target cells both express the same receptors (●), with target cells expressing receptors at a slightly higher density. **b** Target cells express two receptor types abundant on non-target cells (●, ■). Non-target cells only exclusively express one receptor type

bolstered by avidity, while binding non-target cells at a weak, characteristically monovalent affinity. Thus, by engineering a protein therapeutic to be multivalent and/or multispecific, one can achieve this difference in apparent affinity. The optimal therapeutic needs to strike a delicate balance: while the overall affinity for the target cell should be strong, the individual affinities of each binding interaction must be relatively weak. This is the key to selectivity.

Using the scenarios in Fig. 14.9 as model systems, we will demonstrate how multivalency and multispecificity can lead to selectivity. More detailed analyses of these models can be found in Caplan and Rosca [49], which is our main source for this discussion. Each model will be complemented by an example from literature that uses the concepts of multivalency and multispecificity to achieve high selectivity in targeting a diseased state; these models can serve to inform the design of protein therapeutics with improved efficacy and safety profiles.

14.3.1 Model 1: Selectivity Based on Receptor Density

For an intuitive understanding of selectivity, we will analyze the behavior of monovalent, bivalent, and higher order multivalent ligands in a mixture of target and non-target cells that differ in receptor density (Fig. 14.10).

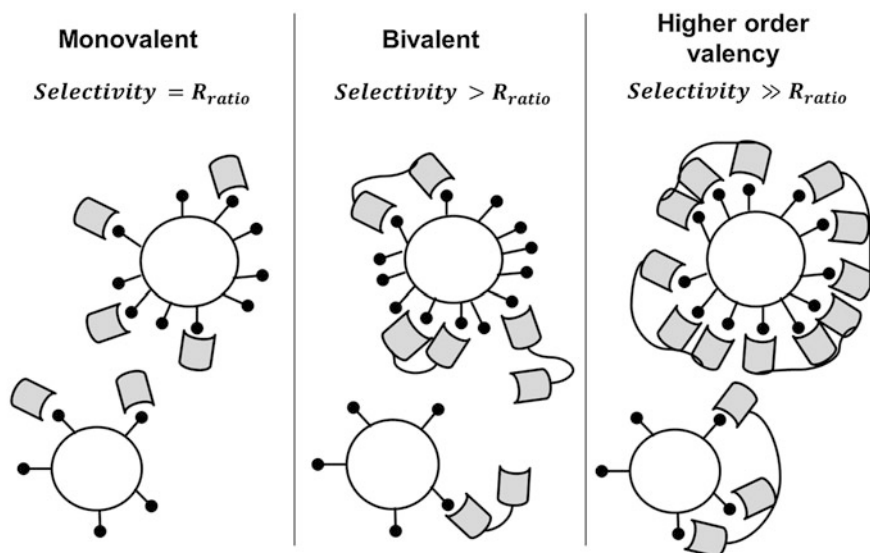


Fig. 14.10 Selectivity increases with valency. R_{ratio} is defined as the receptor density ratio of target over non-target cells. In this scenario, $R_{ratio} = 2$

Suppose diseased cells express twice as many receptors as normal cells, as in Fig. 14.10. Let us begin by considering the case of a monovalent ligand, as shown in the left panel. The affinity of the ligand for receptor is the same for both cell types, and thus, the number of bound ligands on the cell surface is directly proportional to the receptor density. In this example, the selectivity of the monovalent ligand is simply 2:1 for diseased cells to normal cells; to make a general statement, selectivity is equal to the receptor density ratio. Now, we will consider how a bivalent ligand would behave. The schematic in the middle panel suggests that selectivity is enhanced, and the relative number of bound ligands is greater than the receptor density ratio. We can understand this phenomenon from the principle of avidity. The first binding event has the same kinetics as that for the monovalent ligand, but the increase in C_{eff} of the second binding site dramatically drives further ligand–receptor association (Eq. 14.16). However, this increase in C_{eff} is useful for increasing the apparent affinity only when there is an appropriately large receptor density on the cell surface to participate in the second binding event. This means that for a bivalent ligand, the apparent K_D on cells with low receptor density is similar to that of the monovalent ligand. In contrast, on cells with high receptor density, avidity results in an apparent K_D value that is much tighter than that for the monovalent ligand. This difference in apparent affinity is the basis for a multivalent protein’s selectivity for cells with higher receptor density. With this idea in mind, since greater valency can lead to greater avidity, the selectivity must also increase with valency as seen in the right panel. Thus, to design a selective protein, one must determine both the degree of valency necessary, as well as the

Fig. 14.11 Desired selectivity for distinguishing between target and non-target cells with slightly different receptor densities. The two peaks represent two overlapping cell populations. The *dark curve* is the number of ligand bound for a range of receptor densities

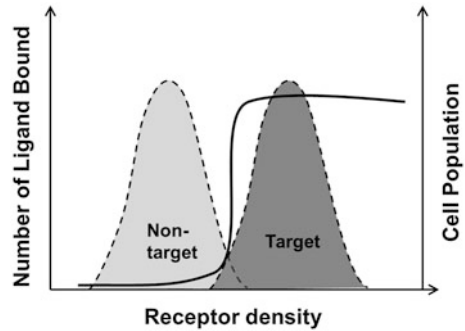
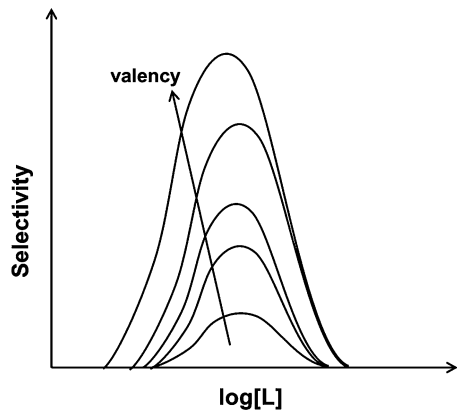


Fig. 14.12 Increased selectivity is observed between cell types with a fixed number of target and non-target receptor densities as ligand valency increases. Selectivity peaks at intermediate levels of ligand concentration and decreases at low and high concentrations of ligand. Figured adapted from Perelson [50]

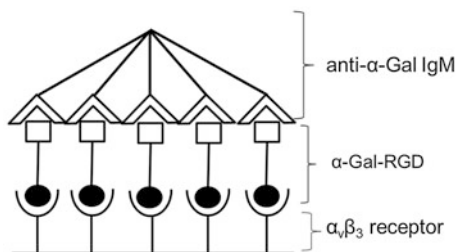


optimal binding affinity of each individual binding domain. A general strategy for maximizing selectivity is to incorporate individual binding sites with weak affinity to eliminate substantial binding to non-target cells with low receptor density, while increasing valency such that strong affinity is achieved toward target cells with higher receptor density. Figure 14.11 provides a graphical representation of the selectivity depicted in Fig. 14.10 for a multivalent ligand. Note that even for cell types with slight differences in receptor densities, one can in principle design protein therapeutics to discriminate between target and non-target cells effectively.

At fixed target and non-target cell receptor densities, the selectivity phenomenon in Fig. 14.11 depends highly on ligand concentration. In Fig. 14.12, we see that the selectivity of multivalent ligands can be described by bell-shaped curves. In the case where ligand concentration is very low, selectivity is reduced since the ligands form very few complexes on both target and non-target cells. At intermediate levels of ligand concentration, selectivity reaches a peak and multivalent ligands will display enhanced selectivity, as they have more opportunities to form multiple binding interactions with receptors on the cell surface. Proteins with high order valency have increased apparent affinity to target cells compared with

non-target cells, which results in increased selectivity. As the ligand concentration increases, the selectivity is again reduced, as the ligand is in great excess and will bind receptors on both cell types primarily through monovalent interactions. In other words, a high number of ligand molecules are competing for a limited number of receptor sites, such that at equilibrium relatively few are able to bind multivalently to the cell surface.

Example 14.2: *Directing An Immune Response Against Cells that Express High Levels of $\alpha_v\beta_3$ Integrin.*



$\alpha_v\beta_3$ integrin is a cell surface receptor that is expressed at high levels on many tumor cells and their vasculature. In Carlson et al. [51], $\alpha_v\beta_3$ integrin served as a model receptor to test the selectivity of a tumor-targeting agent. In this study, a modular multispecific agent was constructed by conjugating a peptide, containing an integrin-binding Arg-Gly-Asp (RGD) motif, to a highly immunogenic trisaccharide Gal α (1-3)Gal β (1-4)Glc (α -Gal). The α -Gal-RGD conjugate (inset) relies on the binding of pentameric human anti- α -Gal IgM to the α -Gal moiety to recruit the complement system and stimulate cell death. Anti- α -Gal IgM binds to α -Gal through weak multivalent interactions: each of its five binding sites has a K_D value in the μ M range, while the overall apparent K_D to an array of α -Gal is in the fM range. Drawing from the model introduced above, the anti- α -Gal IgM should bind weakly to cells with a low $\alpha_v\beta_3$ integrin density, and strongly to cells with a high $\alpha_v\beta_3$ integrin density.

The results showed that the multivalent strategy of cell targeting was highly selective and discriminated between several cancer cell lines with varying densities of $\alpha_v\beta_3$ integrin. The α -Gal-RGD conjugate only induced death in cells with receptor numbers above a certain threshold; cells with receptor numbers below this threshold remained viable. While this study took advantage of the selectivity inherent in the immune system, one can imagine using similar concepts to design other multivalent proteins that mimic this recognition strategy.

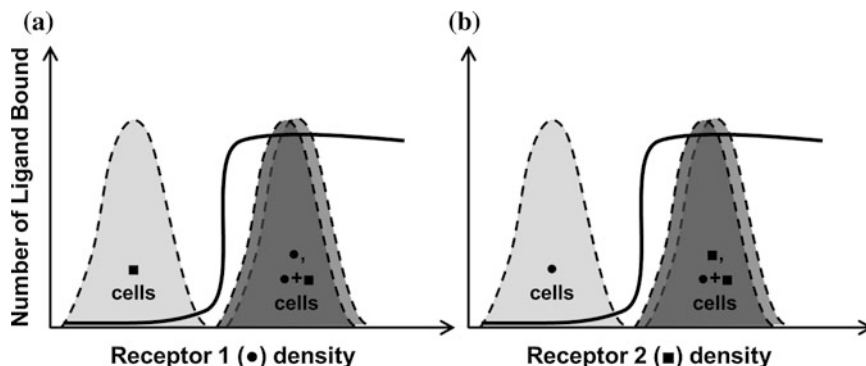


Fig. 14.13 Monospecific ligands from Model 1 do not discriminate between target cells (● + ■) and non-target cells (● only, ■ only). **a** Selectivity of a ligand specific for Receptor 1 (●). **b** Selectivity of a ligand specific for Receptor 2 (■)

14.3.2 Model 2: Specificity Based on Receptor Type

We now describe a second, more complex model where effective targeting is not achieved with the monospecific, multivalent proteins described above but instead requires a different strategy. Suppose we have three cell types, two normal and one diseased. The two normal cell types each express a different receptor (Receptor 1 or 2), while the diseased type expresses both receptor types (Fig. 14.9b). There is no difference in receptor density between the normal and diseased cell types for either receptor. If we create two monospecific, multivalent ligands, one that is specific for Receptor 1 and another that is specific for Receptor 2, either ligand will effectively bind the target cells, but will also have significant off-target binding effects (Fig. 14.13). It is clear that neither a monovalent nor a monospecific, multivalent ligand will confer selectivity in this scenario.

In this example, only a multispecific ligand will confer selectivity; it will bind with monovalent affinity to either of the normal cells and will exhibit substantially increased affinity for the diseased cells where multivalent ligand–receptor complexes are possible (Fig. 14.14). As with the first model in Fig. 14.12, a similar bell-shaped curve is seen in response to ligand concentration on both diseased and normal cells. Consequently, multispecific protein therapeutics are often necessary to effectively target one cell type over another and as such have generated great interest for protein-based drug design [52].

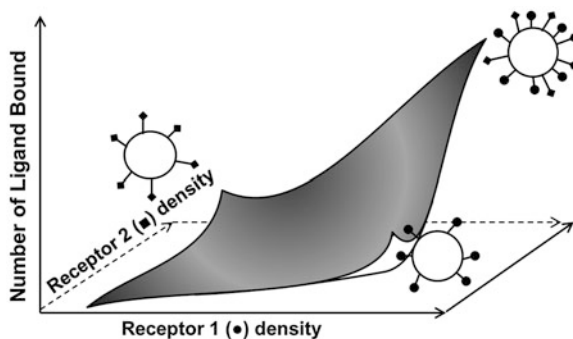
Example 14.3: Bispecific Antibody Fragments Optimized for Tumor Targeting



In this example, the target cells express two particular receptors that are also individually abundant in non-target cells. Robinson et al. [53] engineered a bi-specific single-chain Fv antibody (bs-scFv) whose variable regions bind to ErbB3 and human epidermal growth factor 2 (HER2) with affinities of 160 and 1.6 nM, respectively, as measured by surface plasmon resonance. Despite this measured ErbB3 affinity, the bs-scFv did not exhibit appreciable binding to an ErbB3⁺HER2⁻ cell line, even at concentrations of 1 μ M. The selectivity of the bs-scFv to ErbB3⁺HER2⁺ cells over ErbB3⁻HER2⁺ cells was determined using flow cytometry, with the goal of binding to cells expressing both receptors while excluding cells that express one receptor. The results mirrored our description of Model 2: at high antibody concentration, there was no discrimination between the two cell types, most likely due to monovalent binding of the bs-scFv. As the concentration of bs-scFv decreased, however, the selectivity gradually increased. At 100 pM, there were ten bound ErbB3⁺HER2⁺ cells for every one ErbB3⁻HER2⁺ cell bound. These data were confirmed in an in vivo experiment, where the bs-scFv accumulated in tumors expressing both receptors to a significantly greater extent compared with tumors expressing only one of the receptors. Thus, a combination of multispecificity and low-affinity monovalent interactions between ligand and receptor led to optimal targeting of a particular cancer cell type.

The above examples describe several points of consideration for improving the selectivity of a protein therapeutic. Ideally, the target cell should be distinguished from non-target cells in some way, typically by a unique receptor fingerprint. Multivalency or multispecificity can be exploited to improve selectivity; however, receptor expression patterns and affinities of individual binding sites should be carefully considered to optimize selectivity for target versus non-target cells. One can often turn to nature for inspiration when designing protein therapeutics based on these concepts; several reviews provide good examples where multivalency and multispecificity are key to achieving a desired biological effect [12, 18].

Fig. 14.14 Three-dimensional portrayal of multispecific ligand selectivity over a range of receptor densities. The multispecific ligand will bind with monovalent affinity to non-target cells expressing individual receptors (●) and (■), and with multivalent affinity to target cells that express both receptor types (● + ■)



14.4 Biological Principles for Multivalent and Multispecific Protein Design

In [Sect. 14.2](#), we saw that avidity effects from multivalency increase the overall affinity of an interaction, and in [Sect. 14.3](#), we saw that multivalency and multispecificity can be used to confer selectivity. We will now discuss ways in which these concepts can be partnered with knowledge of underlying biological principles to design effective protein therapeutics. Some questions to consider at the outset are the following:

1. What is the desired biological outcome, and what input signals should be targeted?
2. What is the goal for the multivalent or multispecific protein? To increase affinity? To increase selectivity? Or to control the oligomerization state of the target?
3. Is affinity and selectivity enough to counter the effects of competing ligands and the complexity of biochemical pathways?

In practice, it is sometimes difficult to predict the physiological response elicited by a protein therapeutic. In particular, the biological consequences of simultaneously modulating multiple biomedical targets is often unknown and can have unintended effects [54]. However, examples of carefully designed multivalent and multispecific proteins that have achieved a desired therapeutic outcome are growing [55], with several candidates moving through the clinical pipeline [43]. In this section, we will present three complex biological problems and provide examples of how multivalent and multispecific protein therapeutics can be used to address them.

14.4.1 Complexity of Cell-Signaling Pathways: Receptor Crosstalk and Biological Redundancies

Physiological responses are regulated by a complex network of cell-signaling pathways. Receptor crosstalk, where multiple biochemical inputs modulate the activity of one another (Fig. 14.15), occurs in both healthy and diseased states [56–59]. In the context of oncology, receptor crosstalk has limited the efficacy of traditional monospecific protein inhibitors, as alternative cell-signaling networks can compensate for the effects of the inhibited pathway [60–62]. Nature has also evolved mechanisms of biological redundancy where multiple ligands and receptors carry out similar effects, thus inhibiting only one ligand/receptor interaction with a monospecific protein may limit therapeutic efficacy [59]. In contrast, multiple cell-signaling pathways often need to be engaged to stimulate effective tissue regeneration, which is difficult to achieve with a monospecific protein [63].

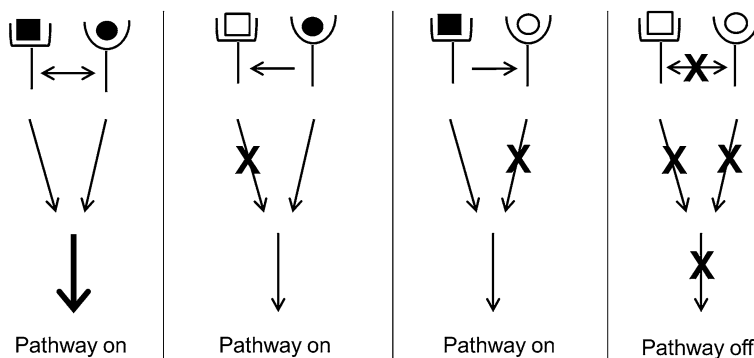


Fig. 14.15 Schematics representing receptor crosstalk. *Black-filled shapes* represent agonists (■, ●) while *white-filled shapes* represent antagonists (□, ○). Two receptors may exhibit crosstalk by stimulating the same pathway in parallel, or by affecting each other. Targeting one receptor (second, third panels) incompletely effects the pathway. Only by stimulating or antagonizing both receptors (first, fourth panels) is the pathway completely activated or inhibited

Receptor crosstalk can be achieved through several mechanisms: cells may alter their expression of non-target receptors, stimulating the target pathway through alternate means, or non-target receptors may amplify or inhibit the signaling of the target receptor to the point where even a high fraction of bound therapeutic does not result in a significant physiological effect [64] (Fig. 14.15). Thus, mechanisms for modulating the effects of multiple receptors are often sought to achieve increased control over a biological system. Accordingly, combination therapy can be more efficacious compared to treatment with individual monospecific agents, particularly in oncology indications [64, 65]. However, potential drawbacks to combination therapy are increased risk of toxicity from off-target effects, and increased cost [54, 65]. Multispecific protein therapeutics, in which each component binding site interacts with and inhibits a distinct receptor, have generated much interest for addressing these concerns. Simultaneous inhibition or stimulation of pathway inputs can greatly improve efficacy through additive or synergistic effects, often at lower doses compared with monospecific agents [11, 66].

Example 14.4: *A Bispecific Protein is More Potent Compared to Monospecific Agents*



VEGFR2 and $\alpha_v\beta_3$ integrin have been implicated in tumor-associated blood vessel formation, a process known as angiogenesis. Due to compelling evidence for crosstalk between VEGFR2 and $\alpha_v\beta_3$ integrin and their cell-signaling pathways

[67], there has been great interest in developing multispecific proteins that inhibit both of these receptors, with the goal of developing therapeutics that can effectively block tumor neovascularization.

Papo et al. [45] used the native VEGF ligand as a molecular scaffold to create a bispecific protein that bound to both VEGFR2 and $\alpha_v\beta_3$ integrin with high affinity. The receptor-binding sites of a VEGF homodimer are located on opposite poles of the protein. To create the bispecific molecule, VEGFR2 binding at one end of the protein was abolished and replaced with a new epitope that conferred binding to $\alpha_v\beta_3$ integrin (inset). Monospecific variants of these proteins that bound VEGFR2 or $\alpha_v\beta_3$ integrin alone were created for direct comparison. The bispecific protein was able to simultaneously engage both VEGFR2 and $\alpha_v\beta_3$ integrin, and more strongly inhibited receptor-mediated angiogenic processes *in vitro* and *in vivo* compared to monospecific agents, which were only marginally effective. These results demonstrate that antagonizing two receptors using a multispecific protein can have synergistic or additive effects on biological potency.

14.4.2 Receptor Trafficking

Attenuation of cell signaling can occur through ligand-induced receptor internalization or receptor desensitization [68]. Consequently, protein therapeutics that alter cell surface receptor densities have the potential to affect disease pathologies associated with receptor-mediated cell-signaling pathways. An intimate knowledge of receptor internalization and trafficking dynamics is required to design protein therapeutics that achieve this goal. Figure 14.16a shows a typical model for receptor trafficking. Upon activation or clustering, a receptor is endocytosed into the cell where it is sorted either for degradation or recycling back to the cell surface. It is the relative rates of synthesis, endocytosis, recycling, and degradation that determine the steady-state receptor density on the cell surface. For a detailed analysis regarding mathematical models for receptor trafficking refer to Lauffenburger and Linderman [69]. Each of these rates is a potential target that could be altered to regulate cell signaling through downstream pathways. For example, if inhibition of receptor activity is desired, one might engineer a ligand that increases endocytosis and degradation rates. If cell stimulation is desired, then one might engineer a ligand that increases the recycling rate (Fig. 14.16b).

Thermodynamic principles play a large role in regulating receptor trafficking, by directing receptor clustering and cell-signaling events. A major consideration is therefore how to geometrically constrain a certain density of receptor (which requires a large loss of entropy), while maintaining high affinity to the target cell (low ΔG of binding). A multivalent and multispecific protein therapeutic works particularly well in meeting these criteria. Optimization of linkers and binding site orientation within these protein fusions can drastically reduce the entropy of forming multiple ligand/receptor complexes on the cell surface.

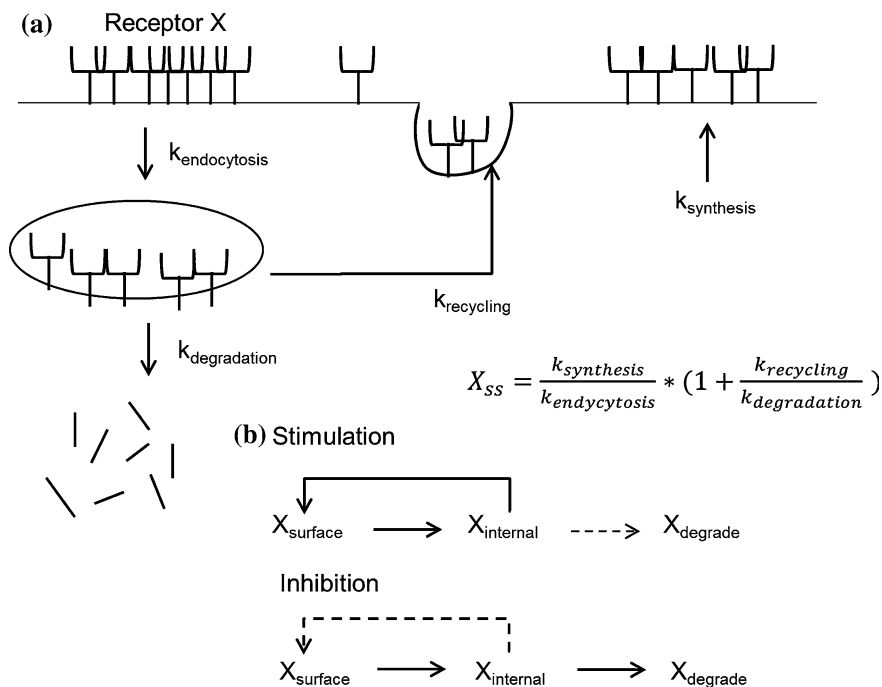
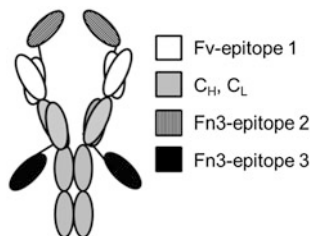


Fig. 14.16 Schematic of receptor trafficking. **a** Trafficking of receptor X can be summed up by the processes of synthesis, endocytosis, degradation and recycling. X_{SS} is the steady-state concentration of X on the cell surface. **b** Strategies for stimulating or inhibiting receptor X . Solid arrows indicate increase in rate, dashed arrows indicated a decrease in rate. A mathematical description of the concepts illustrated here is described in Lauffenburger and Linderman [69]

Example 14.5: Multivalent and Multispecific Therapeutic Proteins That Induce Receptor Clustering and Downregulation



Multivalent and multispecific proteins targeting different epitopes of the same receptor can have an inhibitory effect [70], with the notion that receptor clustering through noncompetitive binding increases internalization and/or degradation rates, resulting in signal attenuation. Recently, Spangler et al. [71] created a hexavalent, trispecific protein that ablated cell signaling through ligand competition, receptor

clustering, and recruitment of immune system effector functions. Through competitive and noncompetitive receptor binding, affinity was enhanced and the target receptors were oriented in a specific spatial arrangement to promote receptor downregulation. Toward this goal, multivalent/multispecific constructs were created by linking an EGFR-specific antibody (cetuximab) to two engineered protein domains (Fn3) that bind distinct EGFR epitopes. Constructs with Fn3 domains attached at various locations on the antibody were tested for their ability to induce EGFR downregulation. A fusion protein which has one EGFR-specific Fn3 domain linked to the N-terminus of the heavy chain and another to the C-terminus of the light chain (inset) was shown to have optimal efficacy and induced robust EGFR clustering and internalization, consequently inhibiting downstream signaling events. Interestingly, molecules with the same valencies and specificities, but different orientations, were less effective; the superiority of a particular topology underscores the relevance of antibody fusion geometry in eliciting optimum receptor downregulation. In addition, this hexavalent, trispecific protein demonstrated a remarkable ability to inhibit tumor growth in cetuximab-resistant BRAF and KRAS mutant cancers. Finally, it was shown that the hexavalent, trispecific fusion protein downregulates EGFR through both increased endocytosis and decreased recycling. In comparison, combination monospecific therapy did not increase endocytosis rates above baseline levels [72]. These experiments showed that the topological arrangement and orientation of receptor-binding domains strongly influenced apparent binding affinity, as well as the observed biological effects.

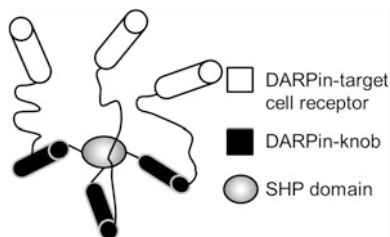
14.4.3 Multispecific Proteins for Recruitment and Delivery Applications

So far, we have seen applications where multispecific proteins target receptors on the same cell surface. In medicine, there are many instances in which two different cells, or a cell and a therapeutic moiety, need to be brought in close proximity for a therapeutic effect (Fig. 14.1). In these cases, the multispecific protein is an adaptor, rather than the actual therapeutic agent. Prime examples are bispecific antibody fragments engineered to recruit immune system effector cells to tumors [73]. In these constructs, one arm of the bispecific binds an overexpressed receptor on the tumor surface, while the other arm binds a receptor unique to the effector cell. More recently, there have been examples of adaptor bispecific proteins that bring viruses or nanoparticles with a gene or drug payload to diseased cells [74, 75], as well as bispecific proteins that bridge stem cells to injured tissue during tissue regeneration [76].

Cell recruitment and therapeutic delivery present interesting applications for multispecific proteins. One can consider these scenarios as a series of smaller protein engineering problems where the protein ligand requires separate affinity

and selectivity optimization for each of its binding targets. Ineffective interactions with target cells or therapeutic moieties may result in low efficacy or off-target effects. In addition, the linker that bridges the components of a multispecific protein adaptor may be instrumental in dictating the relative spatial distance and orientation of the target cell or therapeutic entity necessary to promote the desired biological effect. Thus, even if the multispecific protein does not directly serve as a therapeutic agent and instead acts as an adaptor, its design still needs to follow thermodynamic and kinetic principles as outline above.

Example 14.6: *Engineered Hexavalent, Bispecific Proteins for Targeted Gene Delivery*



Targeted gene therapy has been a long-standing goal for a number of genetic diseases. Dreier et al. [77] developed a modular, multispecific protein adaptor that links adenoviruses (gene carriers) to target cells. For drug/gene delivery applications, the essential characteristic of a protein adaptor is extremely high affinity to the therapeutic payload, in this case the adenovirus. Specifically, the dissociation rate as determined by k_{off} of the adaptor should be slower than the time needed to deliver the therapeutic to target cells. This is important for both toxicity and efficacy, as without an attached targeting moiety the therapeutic may act indiscriminately on non-target cells. To accomplish this goal, the authors used the capsid-stabilizing protein of lambdaoid phage 21 (SHP domain) to create a trimer of a designed ankyrin repeat protein (DARPin), evolved to bind a receptor recognition knob protein on adenovirus. The DARPin trimer was then genetically linked to three identical DARPins, engineered to bind receptor targets expressed on cancer cells (inset). Adenovirus complexed through the multispecific DARPin adaptor was tested for transduction efficiency against several target cancer cell lines.

First, SHP domain-mediated trimeric adaptors outperformed monovalent and bivalent adaptor constructs in binding adenovirus knob protein. This suggests that the additional valency of the trimer presented avidity effects that allowed strong binding between adaptor and adenovirus. Second, spatial arrangement as well as valency contributed to affinity. In one experiment, an adaptor construct with linearly arranged knob-specific DARPins dissociated from adenovirus within one day and could not initiate target cell transduction. In contrast, a construct where the knob-specific DARPins formed a triangular arrangement around the central SHP

domain was able to stay attached to adenovirus and maintain unchanged transduction efficiency for at least ten days. In this case, entropic effects from the linkers had a large effect on avidity and proved to be an integral part of protein design. In final experiments, the hexavalent, bispecific adaptor successfully led to selective transduction of cell lines depending on the specificity of the receptor-binding DARPins attached to the knob-binding trimer. As this study shows, an effective adaptor for targeted gene delivery can be created by tuning valency and binding orientation.

14.5 Conclusion

In this chapter, we present the biophysical principles underlying binding affinity, avidity, and selectivity and provide examples of their considerations for the design and engineering of protein therapeutics. Nature has long exploited the concepts of multivalency and multispecificity for optimal control of biological processes. Inspired by these examples, biomolecular engineers have begun to create elegant protein-based molecular architectures that more effectively address complex medical challenges.

Acknowledgments The authors thank Mihalis Kariolis, Cheuk Lun (Alan) Leung, and Shiven Kapur for valuable insight and feedback on the manuscript.

References

1. Jones DS, Silverman AP, Cochran JR (2008) Developing therapeutic proteins by engineering ligand–receptor interactions. *Trends Biotechnol* 26:498–505. doi:[10.1016/j.tibtech.2008.05.009](https://doi.org/10.1016/j.tibtech.2008.05.009)
2. Kiss G, Çelebi-Ölçüm N, Moretti R et al (2013) Computational enzyme design. *Angew Chem Int Ed* 52:2–28. doi:[10.1002/anie.201204077](https://doi.org/10.1002/anie.201204077)
3. Karanicolas J, Kuhlman B (2009) Computational design of affinity and specificity at protein–protein interfaces. *Curr Opin Struct Biol* 19:458–463. doi:[10.1016/j.sbi.2009.07.005](https://doi.org/10.1016/j.sbi.2009.07.005)
4. Gai SA, Wittrup KD (2007) Yeast surface display for protein engineering and characterization. *Curr Opin Struct Biol* 17:467–473. doi:[10.1016/j.sbi.2007.08.012](https://doi.org/10.1016/j.sbi.2007.08.012)
5. Löfblom J (2011) Bacterial display in combinatorial protein engineering. *Biotechnol J* 6:1115–1129. doi:[10.1002/biot.201100129](https://doi.org/10.1002/biot.201100129)
6. Sidhu SS, Koide S (2007) Phage display for engineering and analyzing protein interaction interfaces. *Curr Opin Struct Biol* 17:481–487. doi:[10.1016/j.sbi.2007.08.007](https://doi.org/10.1016/j.sbi.2007.08.007)
7. Hanes J, Plückthun A (1997) In vitro selection and evolution of functional proteins by using ribosome display. *Proc Natl Acad Sci USA* 94:4937–4942
8. Cuesta AM, Sainz-Pastor N, Bonet J et al (2010) Multivalent antibodies: when design surpasses evolution. *Trends Biotechnol* 28:355–362. doi:[10.1016/j.tibtech.2010.03.007](https://doi.org/10.1016/j.tibtech.2010.03.007)
9. Fitzgerald J, Lugovskoy A (2011) Rational engineering of antibody therapeutics targeting multiple oncogene pathways. *MAbs* 3:299–309. doi:[10.4161/mabs.3.3.15299](https://doi.org/10.4161/mabs.3.3.15299)

10. Kufer P, Lutterbüse R, Baeuerle PA (2004) A revival of bispecific antibodies. *Trends Biotechnol* 22:238–244. doi:[10.1016/j.tibtech.2004.03.006](https://doi.org/10.1016/j.tibtech.2004.03.006)
11. Schaefer G, Haber L, Crocker LM et al (2011) A two-in-one antibody against HER3 and EGFR has superior inhibitory activity compared with monospecific antibodies. *Cancer Cell* 20:472–486. doi:[10.1016/j.ccr.2011.09.003](https://doi.org/10.1016/j.ccr.2011.09.003)
12. Erijman A, Aizner Y, Shifman JM (2011) Multispecific recognition: mechanism, evolution, and design. *Biochemistry* 50:602–611. doi:[10.1021/bi101563v](https://doi.org/10.1021/bi101563v)
13. Alarcón B, Swamy M, Van Santen HM, Schamel WWA (2006) T-cell antigen-receptor stoichiometry: pre-clustering for sensitivity. *EMBO Rep* 7:490–495. doi:[10.1038/sj.embor.7400682](https://doi.org/10.1038/sj.embor.7400682)
14. Tummino PJ, Copeland RA (2008) Residence time of receptor–ligand complexes and its effect on biological function. *Biochemistry* 47:5481–5492. doi:[10.1021/bi8002023](https://doi.org/10.1021/bi8002023)
15. Davda JP, Hansen RJ (2010) Properties of a general PK/PD model of antibody–ligand interactions for therapeutic antibodies that bind to soluble endogenous targets. *MABs* 2:576–588. doi:[10.4161/mabs.2.5.12833](https://doi.org/10.4161/mabs.2.5.12833)
16. Aston PJ, Derks G, Raji A et al (2011) Mathematical analysis of the pharmacokinetic–pharmacodynamic (PKPD) behaviour of monoclonal antibodies: predicting in vivo potency. *J Theor Biol* 281:113–121. doi:[10.1016/j.jtbi.2011.04.030](https://doi.org/10.1016/j.jtbi.2011.04.030)
17. Handl HL, Vagner J, Han H et al (2004) Hitting multiple targets with multimeric ligands. *Expert Opin Ther Targets* 8:565–586. doi:[10.1517/14728222.8.6.565](https://doi.org/10.1517/14728222.8.6.565)
18. Mammen M, Choi S-K, Whitesides GM (1998) Polyvalent interactions in biological systems: implications for design and use of multivalent ligands and inhibitors. *Angew Chem Int Ed* 37:2754–2794. doi:[10.1002/chin.199909293](https://doi.org/10.1002/chin.199909293)
19. Krishnamurthy VM, Estroff LA, Whitesides GM (2006) Multivalency in ligand design. In: Jahnke W, Erlanson DA (eds) *Fragment-based Approaches in Drug Discovery*. WILEY-VCH Verlag GmbH & Co., Weinheim, pp 11–53
20. Brady GP, Sharp KA (1997) Entropy in protein folding and in protein–protein interactions. *Curr Opin Struct Biol* 7:215–221. doi:[0959-440X-007-00215](https://doi.org/10.1016/S0959-440X(007-00215)
21. Gorman J, Greene EC (2008) Visualizing one-dimensional diffusion of proteins along DNA. *Nat Struct Mol Biol* 15:768–774. doi:[10.1038/nsmb.1441](https://doi.org/10.1038/nsmb.1441)
22. Lippow SM, Tidor B (2007) Progress in computational protein design. *Curr Opin Biotechnol* 18:305–311. doi:[10.1016/j.copbio.2007.04.009](https://doi.org/10.1016/j.copbio.2007.04.009)
23. Huggins DJ, Sherman W, Tidor B (2012) Rational approaches to improving selectivity in drug design. *J Med Chem* 55:1424–1444. doi:[10.1021/jm2010332](https://doi.org/10.1021/jm2010332)
24. Williams DH, Stephens E, O'Brien DP, Zhou M (2004) Understanding noncovalent interactions: ligand binding energy and catalytic efficiency from ligand-induced reductions in motion within receptors and enzymes. *Angew Chem Int Ed* 43:6596–6616. doi:[10.1002/anie.200300644](https://doi.org/10.1002/anie.200300644)
25. Jencks WP (1981) On the attribution and additivity of binding energies. *Proc Natl Acad Sci USA* 78:4046–4050. doi:[10.1038/386671a0](https://doi.org/10.1038/386671a0)
26. Zhou H-X (2003) Quantitative account of the enhanced affinity of two linked scFvs specific for different epitopes on the same antigen. *J Mol Biol* 329:1–8. doi:[10.1016/S0022-2836\(03\)00372-3](https://doi.org/10.1016/S0022-2836(03)00372-3)
27. Risau W (1997) Mechanisms of Angiogenesis. *Nature* 386:671–674
28. Fuh G, Li B, Crowley C et al (1998) Requirements for binding and signaling of the kinase domain receptor for vascular endothelial growth factor. *J Biol Chem* 273:11197–11204
29. Nakamura T, Mizuno S (2010) The discovery of hepatocyte growth factor (HGF) and its significance for cell biology, life sciences and clinical medicine. *Proc Jpn Acad Ser B* 86:588–610. doi:[10.2183/pjab.86.588](https://doi.org/10.2183/pjab.86.588)
30. Holmes O, Pillozzi S, Deakin JA et al (2007) Insights into the structure/function of hepatocyte growth factor/scatter factor from studies with individual domains. *J Mol Biol* 367:395–408. doi:[10.1016/j.jmb.2006.12.061](https://doi.org/10.1016/j.jmb.2006.12.061)

31. Stamos J, Lazarus RA, Yao X et al (2004) Crystal structure of the HGF beta-chain in complex with the sema domain of the Met receptor. *EMBO J* 23:2325–2335. doi:[10.1038/sj.emboj.7600243](https://doi.org/10.1038/sj.emboj.7600243)
32. Jakubczak JL, Larochelle WJ, Merlino G (1998) NK1, a natural splice variant of hepatocyte growth factor/scatter factor, is a partial agonist in vivo. *Mol Cell Biol* 18:1275–1283
33. Hudson PJ, Souriau C (2003) Engineered antibodies. *Nature* 9:129–134
34. Duan J, Wu J, Valencia CA, Liu R (2007) Fibronectin type III domain based monobody with high avidity. *Biochemistry* 46:12656–12664. doi:[10.1021/bi701215e](https://doi.org/10.1021/bi701215e)
35. Ekerljung L, Wällberg H, Sohrabian A et al (2012) Generation and evaluation of bispecific affibody molecules for simultaneous targeting of EGFR and HER2. *Bioconjugate Chem* 23:1802–1811. doi:[10.1021/bc3000645](https://doi.org/10.1021/bc3000645)
36. Chen X, Zaro JL, Shen W-C (2012) Fusion protein linkers: property, design and functionality. *Adv Drug Deliv Rev*. doi:[10.1016/j.addr.2012.09.039](https://doi.org/10.1016/j.addr.2012.09.039)
37. Rao J (1998) A trivalent system from vancomycin-d-Ala-d-Ala with higher affinity than avidin-biotin. *Science* 280:708–711. doi:[10.1126/science.280.5364.708](https://doi.org/10.1126/science.280.5364.708)
38. Chaudri ZN, Bartlett-jones M, Panayotou G et al (1999) Dual specificity antibodies using a double-stranded oligonucleotide bridge. *FEBS Lett* 450:14–16
39. Glennie MJ, McBride HM, Worth AT, Stevenson GT (1987) Preparation and performance of bispecific F(ab' gamma)2 antibody containing thioether-linked Fab' gamma fragments. *J Immunol* 139:2367–2375
40. Jung G, Freimann U, Von Marschall Z et al (1991) Target cell-induced T cell activation with bi- and trisppecific antibody fragments. *Eur J Immunol* 21:2431–2435. doi:[10.1002/eji.1830211020](https://doi.org/10.1002/eji.1830211020)
41. Argos P (1990) An investigation of oligopeptides linking domains in protein tertiary structures and possible candidates for general gene fusion. *J Mol Biol* 211:943–958. doi:[10.1016/0022-2836\(90\)90085-Z](https://doi.org/10.1016/0022-2836(90)90085-Z)
42. Kipriyanov SM, Little M, Kropshofer H et al (1996) Affinity enhancement of a recombinant antibody: formation of complexes with multiple valency by a single-chain Fv fragment-core streptavidin fusion. *Protein Eng* 9:203–211
43. Kontermann RE (2012) Dual targeting strategies with bispecific antibodies. *MAbs* 4:182–197
44. Lee C-H, Park K-J, Kim SJ et al (2011) Generation of bivalent and bispecific kringle single domains by loop grafting as potent agonists against death receptors 4 and 5. *J Mol Biol* 411:201–219. doi:[10.1016/j.jmb.2011.05.040](https://doi.org/10.1016/j.jmb.2011.05.040)
45. Papo N, Silverman AP, Lahti JL, Cochran JR (2011) Antagonistic VEGF variants engineered to simultaneously bind to and inhibit VEGFR2 and alphavbeta3 integrin. *Proc Natl Acad Sci USA* 108:14067–14072. doi:[10.1073/pnas.1016635108](https://doi.org/10.1073/pnas.1016635108)
46. Nilvebrant J, Alm T, Hober S, Lofblom J (2011) Engineering bispecificity into a single albumin-binding domain. *PLoS ONE* 6:e25791. doi:[10.1371/Citation](https://doi.org/10.1371/Citation)
47. Boersma YL, Chao G, Steiner D et al (2011) Bispecific designed ankyrin repeat proteins (DARPin)s targeting epidermal growth factor receptor inhibit A431 cell proliferation and receptor recycling. *J Biol Chem* 286:41273–41285. doi:[10.1074/jbc.M111.293266](https://doi.org/10.1074/jbc.M111.293266)
48. Kelly RJ, Billemont B, Rixe O (2009) Renal toxicity of targeted therapies. *Targ Oncol* 4:121–133. doi:[10.1007/s11523-009-0109-x](https://doi.org/10.1007/s11523-009-0109-x)
49. Caplan MR, Rosca EV (2005) Targeting drugs to combinations of receptors: a modeling analysis of potential specificity. *Ann Biomed Eng* 33:1113–1124. doi:[10.1007/s10439-005-5779-1](https://doi.org/10.1007/s10439-005-5779-1)
50. Perelson AS (1981) Receptor clustering on a cell surface. III. Theory of receptor cross-linking by multivalent ligands: description by ligand states. *Math Biosci* 53:1–39
51. Carlson CB, Mowery P, Owen RM et al (2007) Selective tumor cell targeting using low-affinity, multivalent interactions. *ACS Chem Biol* 2:119–127. doi:[10.1021/cb6003788](https://doi.org/10.1021/cb6003788)
52. Cochran JR (2010) Engineered proteins pull double duty. *Sci Transl Med*. doi:[10.1126/scitranslmed.3000276](https://doi.org/10.1126/scitranslmed.3000276)

53. Robinson MK, Hodge KM, Horak E et al (2008) Targeting ErbB2 and ErbB3 with a bispecific single-chain Fv enhances targeting selectivity and induces a therapeutic effect in vitro. *Br J Cancer* 99:1415–1425. doi:[10.1038/sj.bjc.6604700](https://doi.org/10.1038/sj.bjc.6604700)
54. Punt CJA, Tol J (2009) More is less—combining targeted therapies in metastatic colorectal cancer. *Nat Rev Clin Oncol* 6:731–733. doi:[10.1038/nrclinonc.2009.168](https://doi.org/10.1038/nrclinonc.2009.168)
55. Kariolis MS, Kapur S, Cochran JR (2013) Beyond antibodies: using biological principles to guide the development of next-generation protein therapeutics. *Curr Opin Biotechnol* 1–6. doi: [10.1016/j.copbio.2013.03.017](https://doi.org/10.1016/j.copbio.2013.03.017)
56. Hill SM (1998) Receptor crosstalk: communication through cell signaling pathways. *Anat Rec (New Anat)* 253:42–48. doi:[10.1002/\(SICI\)1097-0185\(199804\)253:2<42::AID-AR7>3.0.CO;2-G](https://doi.org/10.1002/(SICI)1097-0185(199804)253:2<42::AID-AR7>3.0.CO;2-G)
57. Eliceiri BP (2001) Integrin and growth factor receptor crosstalk. *Circ Res* 89:1104–1110. doi:[10.1161/hh2401.101084](https://doi.org/10.1161/hh2401.101084)
58. Margadant C, Sonnenberg A (2010) Integrin-TGF-beta crosstalk in fibrosis, cancer and wound healing. *EMBO Rep* 11:97–105. doi:[10.1038/embor.2009.276](https://doi.org/10.1038/embor.2009.276)
59. Lai AZ, Abella JV, Park M (2009) Crosstalk in Met receptor oncogenesis. *Trends Cell Biol* 19:542–551. doi: [10.1016/j.tcb.2009.07.002](https://doi.org/10.1016/j.tcb.2009.07.002)
60. Gusenbauer S, Vlaicu P, Ullrich A (2012) HGF induces novel EGFR functions involved in resistance formation to tyrosine kinase inhibitors. *Oncogene* 1–11. doi: [10.1038/onc.2012.396](https://doi.org/10.1038/onc.2012.396)
61. Zhang Z, Lee JC, Lin L et al (2012) Activation of the AXL kinase causes resistance to EGFR-targeted therapy in lung cancer. *Nat Genet* 44:852–860. doi:[10.1038/ng.2330](https://doi.org/10.1038/ng.2330)
62. Wheeler DL, Iida M, Kruser TJ et al (2009) Epidermal growth factor receptor cooperates with Src family kinases in acquired resistance to cetuximab. *Cancer Biol Ther* 8:696–703
63. McNeill H, Woodgett JR (2010) When pathways collide: collaboration and connivance among signalling proteins in development. *Nat Rev Mol Cell Biol* 11:404–413. doi:[10.1038/nrm2902](https://doi.org/10.1038/nrm2902)
64. Stommel JM, Kimmelman AC, Ying H et al (2007) Coactivation of receptor tyrosine kinases affects the response of tumor cells to targeted therapies. *Science* 318:287–290. doi:[10.1126/science.1142946](https://doi.org/10.1126/science.1142946)
65. Kummur S, Chen HX, Wright J et al (2010) Utilizing targeted cancer therapeutic agents in combination: novel approaches and urgent requirements. *Nat Rev Drug Discovery* 9:843–856. doi:[10.1038/nrd3216](https://doi.org/10.1038/nrd3216)
66. Dong J, Sereno A, Snyder WB et al (2011) Stable IgG-like bispecific antibodies directed toward the type I insulin-like growth factor receptor demonstrate enhanced ligand blockade and anti-tumor activity. *J Biol Chem* 286:4703–4717. doi:[10.1074/jbc.M110.184317](https://doi.org/10.1074/jbc.M110.184317)
67. Somanath PR, Malinin NL, Byzova TV (2009) Cooperation between integrin alphavbeta3 and VEGFR2 in angiogenesis. *Angiogenesis* 12:177–185. doi:[10.1007/s10456-009-9141-9](https://doi.org/10.1007/s10456-009-9141-9)
68. Shankaran H, Wiley HS, Resat H (2007) Receptor downregulation and desensitization enhance the information processing ability of signalling receptors. *BMC Syst Biol* 1:48. doi:[10.1186/1752-0509-1-48](https://doi.org/10.1186/1752-0509-1-48)
69. Lauffenburger DA, Linderman JJ (1993) Receptors: models for binding, trafficking, and signaling. Oxford University Press, New York
70. Boersma YL, Plückthun A (2011) DARPins and other repeat protein scaffolds: advances in engineering and applications. *Curr Opin Biotechnol* 22:849–857. doi:[10.1016/j.copbio.2011.06.004](https://doi.org/10.1016/j.copbio.2011.06.004)
71. Spangler JB, Manzari MT, Rosalia EK et al (2012) Triepitopic antibody fusions inhibit cetuximab-resistant BRAF and KRAS mutant tumors via EGFR signal repression. *J Mol Biol* 422:532–544. doi:[10.1016/j.jmb.2012.06.014](https://doi.org/10.1016/j.jmb.2012.06.014)
72. Spangler JB, Neil JR, Abramovitch S et al (2010) Combination antibody treatment down-regulates epidermal growth factor receptor by inhibiting endosomal recycling. *Proc Natl Acad Sci USA* 107:13252–13257. doi:[10.1073/pnas.0913476107](https://doi.org/10.1073/pnas.0913476107)
73. Frankel SR, Baeuerle PA (2013) Targeting T cells to tumor cells using bispecific antibodies. *Curr Opin Chem Biol* 17:1–8. doi:[10.1016/j.cbpa.2013.03.029](https://doi.org/10.1016/j.cbpa.2013.03.029)

74. Schneider B, Grote M, John M et al (2012) Targeted siRNA delivery and mRNA knockdown mediated by bispecific digoxigenin-binding antibodies. *Mol Ther Nucleic Acids* 1:e46. doi:[10.1038/mtna.2012.39](https://doi.org/10.1038/mtna.2012.39)
75. Baek H, Uchida H, Jun K et al (2011) Bispecific adapter-mediated retargeting of a receptor-restricted HSV-1 vector to CEA-bearing tumor cells. *Mol Ther* 19:507–514. doi:[10.1038/mt.2010.207](https://doi.org/10.1038/mt.2010.207)
76. Lee RJ, Fang Q, Davol PA et al (2007) Antibody targeting of stem cells to infarcted myocardium. *Stem cells* 25:712–717. doi:[10.1634/stemcells.2005-0602](https://doi.org/10.1634/stemcells.2005-0602)
77. Dreier B, Honegger A, Hess C et al (2013) Development of a generic adenovirus delivery system based on structure-guided design of bispecific trimeric DARPin adapters. *Proc Natl Acad Sci USA* 110:E869–E877. doi:[10.1073/pnas.1213653110](https://doi.org/10.1073/pnas.1213653110)

Chapter 15

Engineering Aptamers for Biomedical Applications: Part I

Ya Cao and Genxi Li

15.1 Introduction

Since the discovery of ribozyme, an increasing number of functional nucleic acids, which possess unique functions beyond carrying and passing genetic information, have been found in nature or isolated from random oligonucleotides libraries [1]. Aptamer is one kind of man-made functional nucleic acids that can bind to target with high affinity and specificity. The first aptamers were reported by different groups in 1990 using the “systematic evolution of ligands by exponential enrichment (SELEX)” technique [2, 3]. After the past 20 years, aptamers have been selected against various types of target molecules, ranging from small ions [4] to large molecular weight proteins [5] or even supramolecular complexes (e.g., cells [6]).

Several characteristics inherent to aptamers may make them attractive for biomedical applications. On the one hand, aptamers show a high affinity for their targets. The dissociation constants (K_d) of aptamer-target complexes typically range from the picomolars to nanomolars, comparable to other recognition molecules [7]. Aptamers also possess extremely high target specificity. For example, the L-arginine aptamer has a selectivity of 12,000-fold higher for the L-arginine than that for D-arginine [8]. Because of these merits, aptamers have become ideal molecular recognition elements for diagnosis [9], targeted drug delivery [10] and bioimaging [11]. On the other hand, some aptamers can bind to a specific protein and further inhibit its function or protein–protein interactions [12]. As a consequence, aptamers hold great potential as therapeutics in clinical studies [13, 14].

Y. Cao · G. Li (✉)

Laboratory of Biosensing Technology, School of Life Sciences, Shanghai University,
Shanghai 200444, China
e-mail: genxili@nju.edu.cn

G. Li

Department of Biochemistry and State Key Laboratory of Pharmaceutical
Biotechnology, Nanjing University, Nanjing 210093, China

In addition, the small molecular weight of aptamer allows cost-effective chemical synthesis, fast tissue penetration, low immunogenicity, and toxicity [15], which may further promote the biomedical applications of aptamers.

Despite the list of advantages and potential applications, aptamers also suffer from some shortcomings. High susceptibility to nuclease-mediated degradation is the main drawback to applying aptamers in biological fluids [16]. In terms of biosensor, which is a simple-to-operate analytical device that leads to a number of biomedical applications (e.g., glucose monitoring) [17, 18], the lack of intrinsic property to transduce the binding event into measurable signal [19–21] may discourage the application of aptamers in this field. Fortunately, because of their oligonucleotide nature, aptamers can be modified with chemical groups, linkers, and reporter molecules or can be combined with other functional nucleic acids [22]. Such molecular engineering may facilitate the utilization of aptamers for a wide range of biomedical applications. In this chapter, we will give an introduction to the SELEX process, detail the methods for aptamer engineering, and highlight recent developments, particularly in the field of biosensor with a focus on engineered aptamers.

15.2 Aptamer Selection by SELEX

15.2.1 *Standard SELEX*

Aptamers are typically selected via the SELEX procedure. Figure 15.1 shows a traditional SELEX process that involves repeating cycles of three steps [23]. The first step is the generation of a random oligonucleotide library, typically containing 10^{15} – 10^{16} single-stranded DNA or RNA molecules. The sequence of these oligonucleotides is comprised of a variable region flanked on both sides with constant primers. The second step is initiated by exposing the library to a target of interest. The few nucleic acids that bind to the target are subsequently separated from nonbinding molecules by filtration (for protein target) or by affinity chromatography (for small molecules target) [24]. After separation, the nucleic acids bound to the target are eluted and amplified by the polymerase chain reaction (PCR) in the final step, generating a smaller library enriched in target-binding sequences for next cycle. To yield an aptamer with ideal affinity, 8–15 cycles are usually required [25].

15.2.2 *Improved SELEX*

Along with the continuous development, a series of improving methods for SELEX have been developed, with the purpose of enhancing the efficiency of the selection or increasing the universality of aptamers [26, 27].

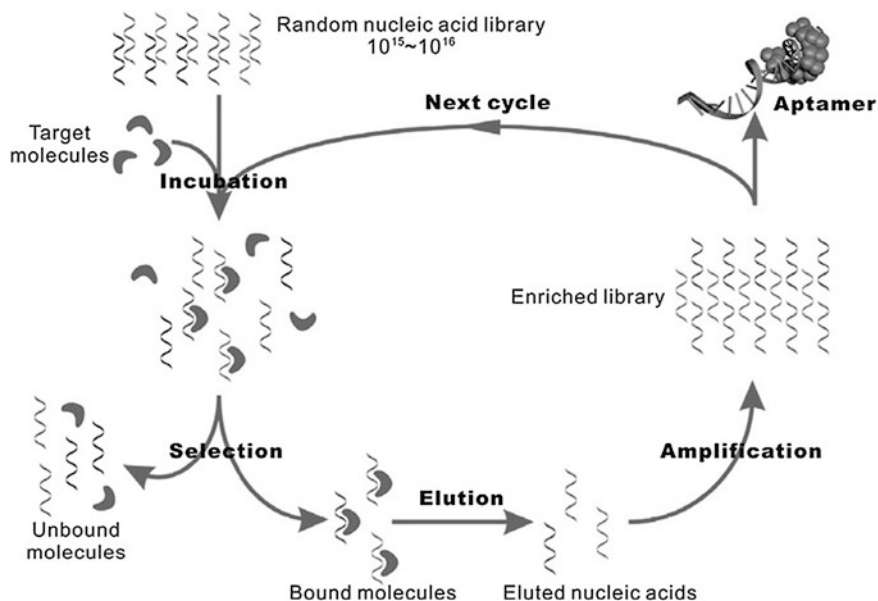


Fig. 15.1 The general procedure for systematic evolution of ligands by exponential enrichment (SELEX). Recreated with kind permission of Elsevier Ltd [100]

The most critical step of SELEX is to separate the binding sequences from the unbound ones, which can affect the quality of aptamers and the speed of selection. In pursuit of an efficient selection system, a number of separation techniques, beyond conventionally used filtration and affinity chromatography, have been tested in recent years, such as capillary electrophoresis (CE) [28], deoxyribonuclease digestion [29], surface plasmon resonance (SPR) [30], and atomic force microscopy (AFM) [31]. A particularly interesting technology is the CE-SELEX that can offer great efficiency and isolate aptamers with low dissociation constants. The first use of CE-SELEX was reported by Mendonsa and Bowser [28]. With the method, they obtained a human immunoglobulin E (IgE) aptamer by four selection rounds, with the affinity only a bit lower than that of the aptamer gained from conventional SELEX after 15 cycles. Till now, CE-SELEX has been successfully used to isolate high-affinity aptamers for large quantities of targets, such as neuropeptide Y [32] and ricin toxin [33]. Microfluidic SELEX (M-SELEX) technology may provide another valuable way to enhance the selection efficiency, considering their advantages of low cost, good reproducibility, and automation [34, 35]. By combining the magnetic bead-based separation with the microfluidic technology, Soh and coworkers have proposed a highly effective M-SELEX method [36]. In the screening process of the improved method, picomolar amounts of target protein conjugated to magnetic beads is first incubated with a random nucleic acid pool. Then, any bead-bound nucleic acids are partitioned in a disposable microfluidic chip by applying a magnetic field. After bead elution, the captured nucleic acids are

amplified via PCR and used for the next cycle of selection. As a proof of principle, an aptamer against streptavidin has been generated in only three selection rounds with dissociation constants ranging from 25 to 65 nM.

Apart from purified molecules, complex targets have been increasingly adopted for the selection of aptamers. Cell-SELEX is a newly developed strategy using whole living cells as targets, which can be performed without prior knowledge of cell surface molecules [37]. As a result, a variety of aptamers capable of recognizing specific types of cells have been discovered [38–40]. Moreover, molecules on the cell membrane will keep their natural structures and contain possible posttranslational modifications throughout the Cell-SELEX process. Thus, aptamers selected using the Cell-SELEX process will be able to identify their targets with native conformations [16]. Tissues have also been used as targets for aptamer screen. Very recently, Liu et al. [41] reported a use of SELEX system to isolate aptamers specific for adipose tissue, which is considered as an important therapeutic target for obesity and related metabolic disorders.

15.3 Engineering Aptamers for Biosensor Development

A biosensor is commonly composed of at least three components, that is, a bio-recognition element, a signal-transduction system, and a physical readout instrument. Up to now, various recognition elements, including antibodies [42], receptors [43], small molecules [44], and enzymes [45], have been extensively studied and utilized for sensing. Among them, antibodies are the most commonly used ligands owing to their special high affinity and selectivity upon interacting with target molecules. However, having been developed for about 70 years, antibodies still exhibit many limitations in bioanalytical applications, such as pH and temperature sensitivity, laborious and expensive producing process, easy degradation [46]. Aptamers, which are chemically stable and cost-effective, can be promising alternatives to antibodies in the fields of biosensors. More importantly, aptamers may offer remarkable flexibility and convenience in engineering, which would further improve their properties and make them easily incorporated into novel bioassays.

15.3.1 *Engineering to Improve the Bioavailability of Aptamers*

Aptamers are selected in buffer systems and built from four natural DNA or RNA bases that are easily degraded by nucleases. The resulting short half-life and low binding affinity of aptamers in biological fluids would severely restrict the practical clinical application of aptamer-based biosensors (aptasensors). To overcome

these problems, many efforts have been made to engineer aptamers with enhanced bioavailability [47].

Chemical modifications have been firstly introduced to different parts of aptamers to produce nuclease-resistant oligonucleotides. Inspired by nature that RNAs can be protected by methylation of the 2'-hydroxyl groups, researchers have introduced several modifications into aptamer at the 2'- position of ribose moiety, including 2'-methoxy [48], 2'-fluoro [49] and 2'-amino [50], by solid-phase-based chemical synthesis. These modifications have shown to effectively increase the stability of aptamers in complex biological fluids. Locked nucleic acids (LNAs), in which the 2'-oxygen of ribose and the 4'-carbon is bridged by a methylene group, are a novel class of modified nucleotides. Incorporation of LNAs into aptamer can provide enhanced thermal stability and good resistance against nuclease hydrolysis, without affecting the binding capability to the target. Successful applications of LNAs have been reported to a number of known aptamers, such as thrombin-binding aptamer [51] and Tenascin-C-binding aptamer [52].

From another viewpoint, the C5 position on thymine or uracil is the most permissive sites for modifications accepted by polymerases [53], laying the foundation for efficient SELEX with 5'-modified bases. In a recent study, Shoji et al. screened a thalidomide-binding aptamer from a library of non-natural DNA prepared with 5-*N*-(6-aminoethyl) carbamoylmethyl-2'-deoxyuridine triphosphate instead of thiamine triphosphate [54]. The obtained modified DNA aptamer can be stable against several nucleases and show high enantioselectivity for the (*R*)-form thalidomide with a K_d of 1.0 μM . In contrast to post-SELEX modifications of existing aptamers, performing SELEX on a library containing modified nucleotides may not only enhance nuclease resistance but also increase target affinity [55].

Modifications have also been introduced to the phosphodiester backbone [56]. Gorenstein and coworkers have obtained a modified DNA aptamer specific to the nuclear factor for human IL6 from a fully substituted phosphorothioate library [57]. Detailed experimental studies reveal that the modified aptamer can possess reduced nuclease activity and bind at least 5-fold tighter to the target than the normal backbone aptamer.

Another important set of modifications is performed at 3'-termini or 5'-termini of aptamers. The capping of oligonucleotide terminus has been demonstrated capable of increasing the resistance of aptamers to exonucleases. For example, an inverted thymidine cap can make the RNA aptamer against coagulation factor IXa stable in human plasma for at least 5 h [58]. Similar phenomenon may also happen to a keratinocyte growth factor aptamer modified with 2'-fluorides, 2'-O-methyl groups, and 3'-capping by inverted thymidine [59].

Other than chemical modification, multiple aptamer assembly offers an alternative way to enhance the bioavailability of aptamers through polyvalent interactions [60, 61]. Thrombin is a multifunctional serine protease with pro-coagulant and anticoagulant activities. Several aptamers have been selected against the enzyme [62–64]. One of the most intensively used aptamers is the 15-base

thrombin aptamer (TBA₁₅), which binds to the fibrinogen-binding exosite to inactivate the enzyme. Although being functional, the practical application of TBA₁₅ is usually restricted by relatively low binding affinity. To increase the activity of TBA₁₅, a series of methods have been proposed by engineering assemblies of TBA₁₅ with other thrombin aptamers [65, 66]. For instance, by using a poly-dT linker, Ikebukuro and coworkers have connected the TBA₁₅ with a 29-base aptamer (TBA₂₉), which may recognize a different exosite of thrombin with high affinity [67]. The aptamer dimer can have a K_d value of 0.15 nM, much lower than those of the individual precursor aptamers (3.5 nM for TBA₂₉ and 20.2 nM for TBA₁₅).

Another possible way to achieve polyvalent interactions relies on the use of nanomaterial–aptamer conjugates. One typical work conducted by Hsu et al. [68] is to covalently link the TBA₁₅ and TBA₂₉ to gold nanoparticles (AuNPs) through disulfide bonds together with sulfated galactose acid (sulf-Gal). Experimental results reveal that the 15-TBA₁₅/TBA₂₉/sulf-Gal–AuNPs conjugates can be stable in human plasma for at least 48 h and exhibit ultrahigh affinity toward thrombin ($K_d = 3.4 \times 10^{-12}$ M). In another work, Au–Ag nanorods are utilized for multiple attachments of aptamers selected for CCRE-CEM cells [69]. Simultaneous immobilization of 80 aptamers can result in ~ 26 -fold enhanced binding affinity compared to that of single aptamer molecule. Apart from the enhanced binding affinity, nanomaterial–aptamer conjugates can also protect the aptamer against nuclease-mediated degradation. For example, Lin and coworkers have reported an ATP biosensor that can be directly used in living cells by preparing an aptamer/graphene oxide nanocomplex [70]. Another example is a thiol-modified aptamer attached with methylene blue that is chemisorbed on AuNPs through gold–thiol bond [71]. The resulting AuNPs–aptamer conjugates can exhibit high stability during exposing to complex biofluids, proving that the immobilized aptamer is sufficiently robust for clinical diagnostic applications. Above examples clearly show that nanomaterial–aptamer conjugates are effective for fabricating aptasensors for diagnostics of biological samples [72]. With advances in nanotechnology and aptamer selection, a significant progress in this direction can be highly expected.

15.3.2 Engineering to Generate Detectable Signals

The application of aptamers in the field of biosensor mainly relies on their acting as recognition molecules with high binding affinity and specificity. However, like most other biomolecules, aptamers do not respond in any readily measurable way upon target binding [19–21]. Therefore, rational engineering of aptamers, such as incorporation with other functional nucleic acids or modification with molecular reporters, which can provide potentially solutions to the problem, may promote the development of aptasensors.

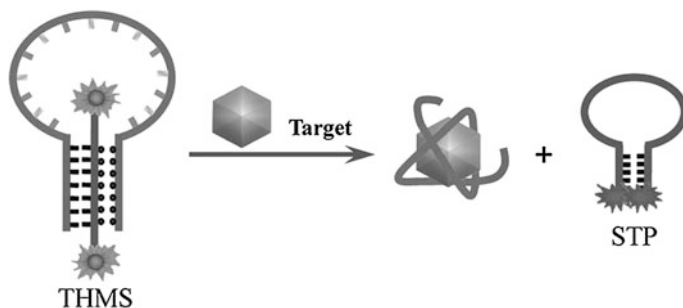


Fig. 15.2 An aptamer-based sensing platform using a triple helix molecular switch (*THMS*). Recreated with kind permission of American Chemical Society [82]

15.3.2.1 Signal Generation Incorporating Functional Nucleic Acids

Since the first report in 1996 [73], molecular beacons, defined as “nucleic acid probes able to undergo spontaneous conformational change after hybridizing their complementary strands,” have become a new kind of DNA probes that are widely used in DNA/RNA studies [74–76]. Engineering aptamers into molecular aptamer beacons (MABs) might efficiently combine the binding affinity of aptamers with the signal generation mechanism of molecular beacons. A common strategy to design MABs has been proposed by Stanton and coworkers [77], which can be used for the engineering of many aptamers. For instance, a thrombin aptamer has been engineered into a MAB by adding nucleotides to its 5′-end, complementary to a small sequence at the 3′-end of the aptamer. The hairpin structure formed in the absence of the target is then broken by the addition of thrombin, generating an increased fluorescence signal. Similar approaches have also been used to construct sensors for potassium ion [78], IgE [79], interferon- γ [80], and CCRF-CEM cells [81]. Very recently, Tan and coworkers reported a new type of MABs, named as triple helix molecular switch (THMS) [82]. The THMS consists of a dual-labeled signal-transduction probe (STP) and a central aptamer sequence that is extended with two arm segments. In the absence of target, the two arm segments of the aptamer are hybridized with the loop sequence of STP, enforcing the STP to hold an “open” configuration. However, upon target binding, the aptamer motif forms a complex with target, resulting in the release of the STP, which leads to new signal readout (Fig. 15.2). Based on this strategy, thrombin, ATP, and L-argininamide can be sensitively detected.

Catalytic nucleic acids (DNAzymes or ribozymes) are a class of nucleic acid-based biocatalysts capable of performing chemical transformations [83]. Coupling of aptamers with catalytic nucleic acids may result in novel functional nucleic acids that can be applied for both molecular recognition and signal generation in sensors. A simple way to engineer aptamers in combination with catalytic nucleic acids is to make the catalytic activity to be aptamer-target dependent [84, 85]. For instance, in a work reported by Achenbach et al. [86], an ATP aptamer is directly

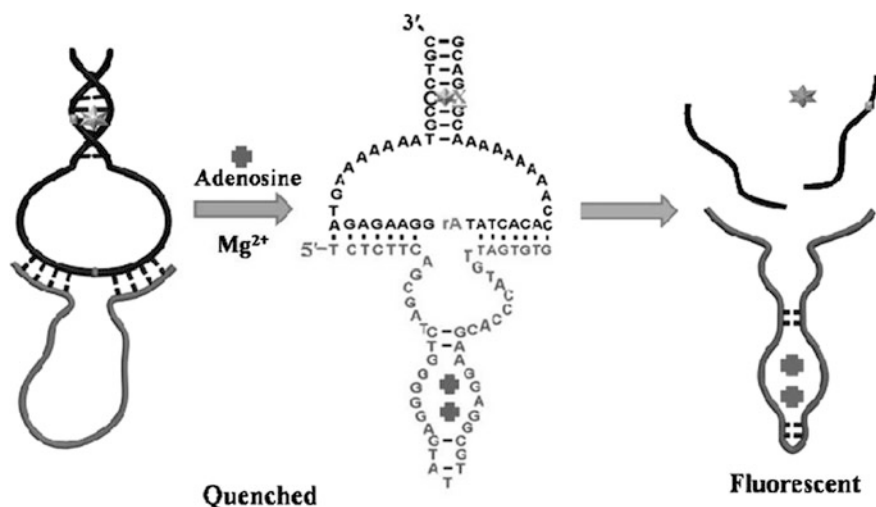


Fig. 15.3 A fluorescent aptasensor for adenosine on the basis of an aptamer–DNAzyme junction. Recreated with kind permission of American Chemical Society [87]

linked to a RNA-cleaving DNAzyme. A blocker strand is used to inhibit the catalytic activity by annealing with the aptamer–DNAzyme junction. Upon addition of ATP, however, the blocker strand could be liberated, consequently triggering the action of the DNAzyme. In a different approach, an adenosine aptamer is engineered to be embedded in the catalytic core of an Mg^{2+} -dependent 10–23 DNAzyme [87]. The sequence of the whole DNA strand is designed to avoid forming active structure to perform cleavage of the substrate in the absence of target. However, binding of adenosine could induce a structural change of the aptamer region, activating the DNAzyme and resulting in an increased signal (Fig. 15.3).

Besides engineering aptamers in conjugation with molecular beacons and catalytic nucleic acids, rationally designed aptamer cooperativities have also been used for biosensor development [88, 89]. Recognition and signal-transduction mechanism of such aptamer assemblies is that target binding of the recognition aptamer will induce weakening or enhancement of the binding ability of the reporting aptamer, which may subsequently generate detectable signals [24]. On the basis of positive cooperativities, Stojanovic et al. have reported a label-free fluorescent biosensor by using the aptamer against malachite green (MG) dye as a reporting element and the ATP aptamer as a recognition element [90]. Target binding by the ATP aptamer will increase the affinity and possibility for MG to bind to the reporting aptamer and exhibit high fluorescence intensity. Negative cooperativities have also been used for preparing such aptamer assemblies. For example, Wang et al. have proposed a bifunctional aptamer that contains an anti-thrombin region and a hemin–aptamer region [91]. Interestingly, the two functional regions share six crucial bases, thus making thrombin binding inhibited by hemin.

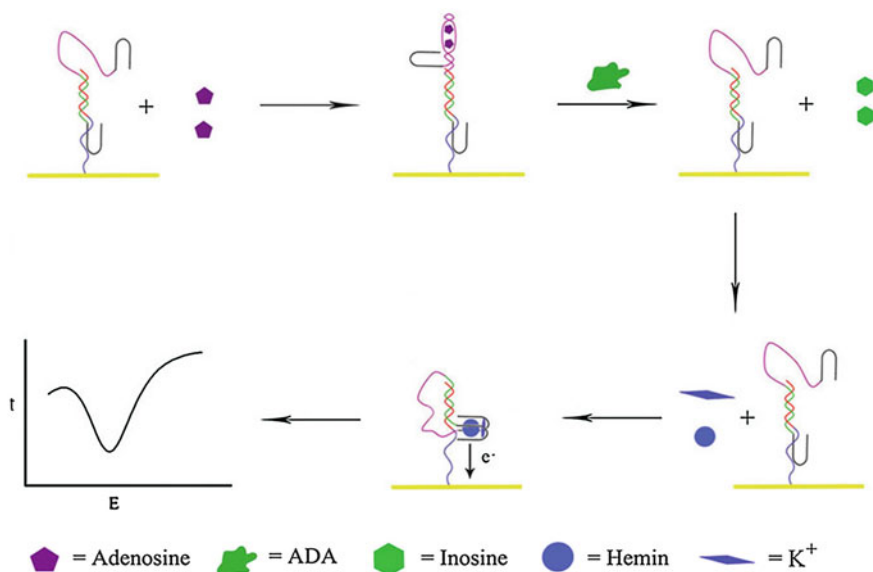


Fig. 15.4 An electrochemical sensor based on negative aptamer cooperativities. Recreated with kind permission of American Chemical Society [92]

In another work, the hemin–aptamer is split in two parts and fused with an adenosine aptamer and a linker sequence [92]. Binding of adenosine can force the two split of hemin–aptamer away from one another. However, once the adenosine deaminase (ADA)-catalyzed deamination process takes place, adenosine will be converted to inosine and released from the electrode, enabling the hemin–aptamer complex to be formed on the electrode surface to give an electrochemical response (Fig. 15.4). Based on this biosensor, the authors are able to assay the ADA activity with a detect limit of 0.2 U ml^{-1} .

15.3.2.2 Signal Generation Using Molecular Reporters

Through engineering aptamers with molecular reporters, the binding events can be simply converted into measurable signals. In fact, almost all sorts of reporters, including fluorophores [93], redox-active reporting units [94], proteins [95] and nanomaterials [96] can be covalently linked to aptamers. The development of reporter-linked aptamers is mainly focused on the design of different signaling strategies, so we will give an introduction on molecular reporters in the viewpoint of assay formats in this section.

In 1996, Drolet et al. detailed the first reporter-linked aptamer assay for detecting human vascular endothelial growth factor (VEGF) [97]. In this approach, a capture monoclonal antibody was immobilized on the microtiter plate surface and a VEGF aptamer was labeled on the 5'-terminus with a fluorescein moiety. In

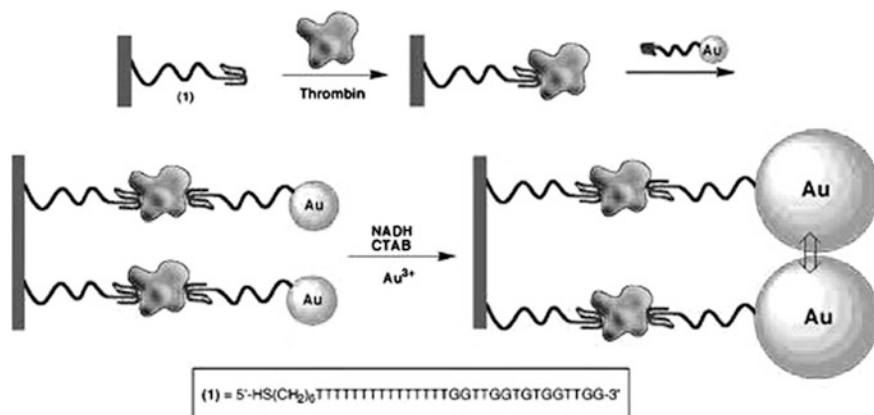


Fig. 15.5 A sandwich-type AuNP-conjugated aptamer-based colorimetric sensor for thrombin. Recreated with kind permission of American Chemical Society [99]

the presence of the target protein, the analyte would be captured by the antibody and the aptamer, forming a sandwich structure. Subsequently, an alkaline phosphatase-conjugated anti fluorescein FAB fragment was added to bind fluorescein and generate chemiluminescence signals, which were directly concerned with the concentration of VEGF. Ever since then, sandwich designs based on reporter-linked aptamers have been widely used for biosensing, while thrombin [62, 63] and platelet-derived growth factor (PDGF) [98] that include two binding sites for the aptamers are often utilized as model targets. Figure 15.5 shows a typical work for thrombin assay. Specifically, the thrombin aptamer is covalently attached to a maleimide-functionalized siloxane monolayer. After capturing thrombin to the surface by the aptamer, AuNP-conjugated thrombin aptamer is then added to bind to the other site on thrombin [99]. The resulting AuNP seeds on the glass slides are then enlarged in the growth solution. Therefore, absorbance spectra of the functionalized surfaces can be monitored upon analyzing different concentrations of thrombin, and a detection limit of 2 nM can be achieved.

Sandwich structure strategy offers a feasible way to utilize reporter-linked aptamers for constructing biosensing systems with high sensitivity and specificity. However, since the assays based on sandwich structure rely on the possibility that two or more recognition molecules including aptamer can simultaneously bind to one target molecular without mutual interference, it can hardly be applied to the assays of all kinds of targets. For example, small molecules, which are usually buried within the small binding pocket of aptamer structures, usually leaving little room for the interaction with a second recognition element [100, 101], would unlikely be assayed in this format. On the other hand, proteins have complex spatial structures and they can interact with aptamers in different ways, offering a variety of possibilities for biosensor design. However, unfortunately, only a few proteins possess two recognition sites to make the recognition molecules including

aptamer bind to two different epitopes [102]. So the sandwich approach based on the use of reporter-linked aptamers is mainly confined to the detection of a few kinds of proteins, such as thrombin [103, 104], PDGF [105, 106], and IgE [107].

It has been known that some aptamers will fold their flexible, single-stranded chains into unique secondary or tertiary structures when interacting with their targets. Provided the aptamers are engineered with reporter molecules, this behavior would leave the reporter moieties away from or in close proximity to quenchers for fluorescent detection, or electrodes for electrochemical detection, resulting in a detectable signal change. Therefore, the structural change of reporter-linked aptamers upon target binding has also been developed as an efficient strategy for signal generation. Fluorescence is a popular method used in this strategy. By attaching two pyrene molecules to both ends of a PDGF aptamer, Tan and coworkers have proposed a fluorescent biosensor to monitor the target protein in complex biological fluids [108]. In the absence of PDGF, the two ends of the aptamer are far away. Nevertheless, when the target exists, the target–aptamer interaction will induce aptamer conformation re-arrangement, causing the two pyrene molecules close to each other. Consequently, the fluorescence emission of the aptamer is switched from 400 to 485 nm. Such a shift in emission wavelength can solve the significant problem of background signal, allowing direct detection of PDGF in complex biological fluids.

Electrochemical means have also received increasing attentions in recent years for the use in this strategy as signal readout technique. Compared with optical assays, the sensing systems based on the fundamental of electrochemistry may be more stable, more cost-effective, easier to miniaturize, and less sensitive to contaminants [109, 110]. Therefore, emerging efforts have been made to combine the target-induced structural change of reporter-linked aptamers with different kinds of modified electrodes for biosensing. One typical example is the work conducted by Xiao et al., which is based on the fact that the thrombin aptamer will undergo a structural re-arrangement upon target binding [111]. The biosensor is constructed by covalently attaching a thrombin aptamer, dually labeled with thiol and methylene blue at either end, to a gold electrode. In the initial state, the aptamer adopts a flexible, unfolded configuration, enabling the electrical communication of methylene blue with the electrode. After interaction with thrombin, the aptamer is driven to fold into a G-quadruplex structure to make the electrochemical label away from the electrode surface, shielding the electron transfer, so the analytical signal is diminished. In a similar manner, potassium ion has also been detected with specificity [112]. In the meantime, since this sensing design has a critical disadvantage of negative signal, several “signal-on” approaches are proposed. One approach is based on the frequency tuning of the voltammetric measurements [113]. By appropriately changing the scan pulse frequency of square-wave voltammetry, the difference in the structure of target-free and target-bound aptamers can be read out electrochemically, resulting in successful “signal-on” assay of thrombin and cocaine [114]. In another approach, the interaction between the labeled aptamer and its target is rationally designed to shorten the distance of the electroactive labels from the electrode, thereby increasing the redox current. In a

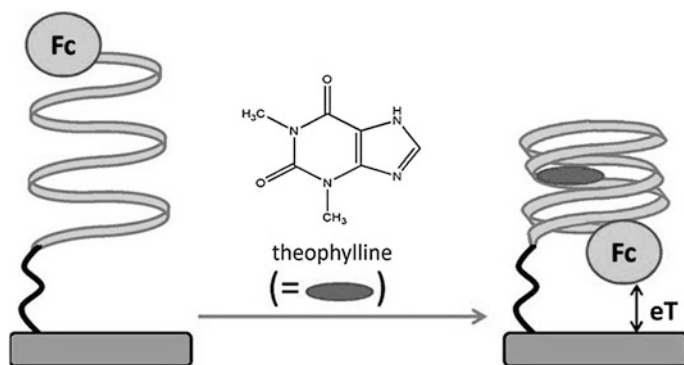


Fig. 15.6 A signal-on electrochemical aptasensor for theophylline detection by making use of the target-induced structural change of Fc-linked aptamer. Recreated with kind permission of American Chemical Society [115]

typical work, an anti-theophylline RNA aptamer with a terminal electroactive ferrocene (Fc) group as the redox reporter is immobilized on gold electrode (Fig. 15.6) [115]. In the absence of the analyte, the aptamer stays in a relatively open conformation, and the Fc moiety will be in various distant positions relative to the electrode surface. However, binding of theophylline will completely fold the aptamer, placing the Fc units in close proximity to the electrode surface, and thereby enhances the electron transfer efficiency, producing an increasing electrochemical current. To date, the same principle has also been applied to design sensors for the detection of thrombin [116], cocaine [117], VEGF [118], and potassium ion [119].

Besides the target-induced structural change strategy, rationally engineering reporter-linked aptamers into split fragments has brought a new direction for developing sensing devices. Typically, the aptamer is divided into two subunits that cannot interact with one another in the absence of the target; the specific ligand may induce self-assembly of aptamer fragments into supramolecular structures, generating a detectable signal. For the assays based on split-type strategy, small molecules are the common detection targets. Such small molecules include cocaine [120–122], ATP [123], and adenosine [124]. In addition to the small molecules, some proteins can also be assayed by using the split-type strategy [125, 126]. For instance, in a work conducted by Liu et al., an anti-thrombin aptamer is divided into two halves. While one part is immobilized on a gold electrode surface via S–Au reaction, the other is functionalized with Ru(bpy)₃²⁺-doped silica nanoparticles (Ru-SNPs) [127]. The target-directed assembly of the two fragments will make the concentration of Ru-SNPs at the electrode surface to be increased. By monitoring the electrochemiluminescence signal, thrombin can be selectively detected with a detection limit of 0.2 pM.

In the two assay strategies mentioned above, knowledge of the secondary structure of aptamers is crucial for either sensor design or split engineering.

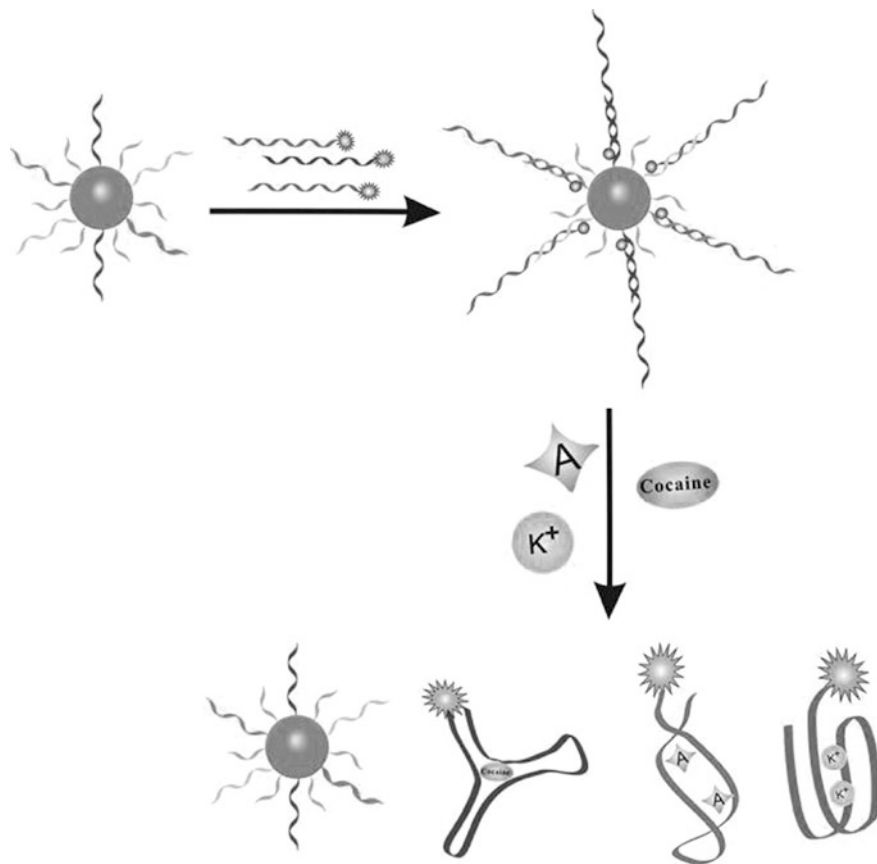


Fig. 15.7 A multicolor aptasensor based on the structure switching from an aptamer/DNA duplex to an aptamer/target complex. Recreated with kind permission of Wiley-VCH [130]

However, many aptamers cannot have an easily determined secondary structure [128]. To overcome this problem, numerous efforts have been devoted to establish alternative strategies. For instance, since aptamers can associate either with complementary DNA (cDNA) strands or with target analytes, the structure switching from an aptamer/DNA duplex to an aptamer/target complex may offer a feasible way to develop biosensors that have little restrictions on the knowledge of the secondary structure of aptamers. A representative assay conducted by Mei et al. is to use a fluorophore-linked aptamer [129]. In the resting state, fluorescence is quenched by the quencher-modified cDNA. The introduction of the target will force the departure of the cDNA strand from the aptamer, resulting in a fluorescence recovery. Using AuNPs as the quencher, Fan and coworkers have proposed a multicolor sensor, which can be used to simultaneously detect adenosine, potassium ion, and cocaine (Fig. 15.7) [130]. This strategy has also been extended to fabricate electrochemical biosensors based on the design that redox-tagged

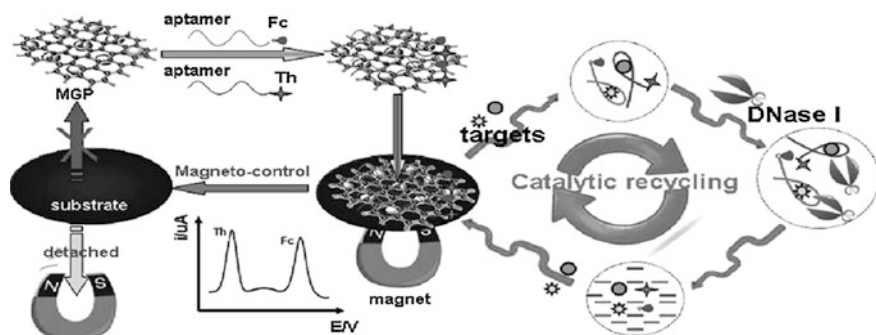


Fig. 15.8 Ultrasensitive aptamer-based multiplexed electrochemical detection with the aid of magnetic graphene nanosheets and DNase I. Recreated with kind permission of American Chemical Society [143]

aptamer hybridizes with its complementary sequence which is immobilized on an electrode surface [131, 132]. Since the presence of the target will release the aptamer strand from the electrode, electrochemical signals are thereby changed. Of note, such electrochemical biosensors will present signal-off results, largely precluding their further development. Recently, Chen and coworkers have reported a signal-on platform for adenosine detection based on the quenching of Ru-SNPs electrochemiluminescence by ferrocene [133], which may provide a promising method to overcome the shortcoming of the signal-off methodology.

Single-stranded aptamer has been demonstrated to adsorb stably on the surface of nanomaterials, e.g., AuNPs [134], single-wall carbon nanotubes [135] and graphene oxides [136]. Interestingly, when the target is present, the aptamers will interact with their targets and be released from the nanomaterials [137–139]. On the basis of this feature, a series of aptamer sensing approaches have been generated [140–142]. Figure 15.8 shows a classical assay strategy [143]. The redox-tagged aptamers are initially bound onto the surface of magnetic graphene nanosheets (MGPs) that are adsorbed on an electrode surface. However, the interaction between the aptamer and MGPs can be easily disturbed by the formation of aptamer-target complexes. Therefore, in the presence of the targets, the redox-tagged aptamers are released from the electrode surface, resulting in decreased electrochemical signals. Through coupling DNase I-based catalytic recycling of the analytes, low detection limits (0.1 pM for ATP and 1.5 pM for cocaine) can be obtained.

15.3.3 Engineering to Achieve Signal Amplification

In some cases, the sensitivity of aptamer-based assays is not satisfactory because of the low abundance of target biomolecules in complex biofluids. For this reason, signal amplification strategies, such as nucleic acid amplification, catalytic signal

amplification, and nanomaterial-mediated amplification, have been incorporated into aptasensors. Since several excellent and comprehensive reviews on signal amplification using functional nanomaterials have already been published [144, 145], only an introduction on the first two strategies is offered here.

15.3.3.1 Nucleic Acid Amplification

The chemical nature of oligonucleotides makes aptamers readily engineered to trigger nucleic acid amplification processes. As a result, a variety of sequence amplification methods, including PCR, rolling circle amplification (RCA), nicking endonuclease (NEase) or exonuclease-assisted amplification approaches, have been used in aptasensors fabrication.

PCR is one of the most powerful DNA amplification techniques and thus has been widely used in molecular diagnostic research [146, 147]. Making use of PCR can amplify a single or a few copies of a piece of DNA across several orders of magnitude, significantly improving assay sensitivity [148]. Figure 15.9 shows the utilization of PCR for IgG detection by using PCR template tethered aptamer. Firstly, the target molecules are captured on a surface, and the IgG aptamer is subjected to coupling with a double-stranded PCR template [149]. Then, direct monitoring of the PCR products may enable the fluorescent detection of the target protein with a greatly enhanced sensitivity. In another work, Landegren and coworkers have developed a novel aptamer and PCR-based strategy for protein detection, termed as proximity ligation assay (PLA) [150]. In this study, aptamers specific for PDGF are extended at both ends to be a pair of proximity probes. Upon simultaneous recognition of the same target, the extensions of such probes efficiently hybridize to a connector oligonucleotide, which is followed by the ligation of oligonucleotides and real-time PCR amplification. Given the sensitivity of the assay, PLA has also been adapted to detect other targets [151, 152].

Different from PCR, RCA is an isothermal DNA amplification method that uses a short DNA primer and a circular, single-stranded template [153]. In a RCA process, DNA polymerase continuously replicates around the template and displaces the synthesized fragment, forming a long concatemeric DNA product with repeated units that are complementary to the template. Because of the needless of thermal cycling and the nuclease resistance of circular template, RCA is often employed as a signal amplification technique in clinical diagnostics [154, 155]. Adaptation of aptamers to RCA has yielded a series of sensitive sensors [156, 157]. For example, Ellington and coworkers have prepared a novel conformation-switching aptamer-based biosensor for PDGF detection [158]. Since the presence of protein target can induce circularization of the aptamer, triggering the subsequent RCA process, by monitoring the generated fluorescence signal, down to 0.4-nM PDGF can be detected.

NEases are a class of restriction endonucleases that recognize specific nucleotide sequences in double-stranded DNA but cleave only one of the strands at a fixed position [159]. The unique cleaving feature of NEase makes it favorable for

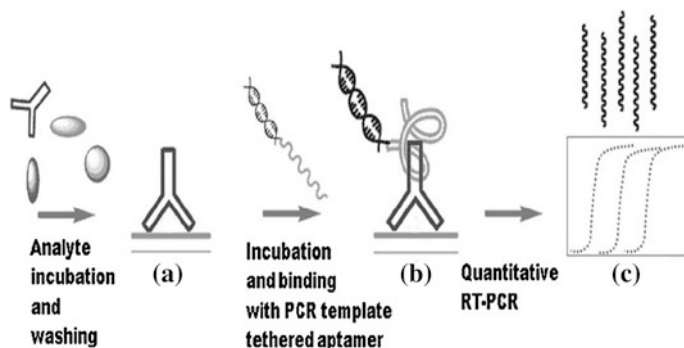


Fig. 15.9 Schematic representation of PCR-based signal amplification. Recreated with kind permission of American Chemical Society [149]

performing isothermal target recycling, which enables the development of ultra-sensitive detection of nucleic acids [160, 161]. In the past few years, NEase-assisted amplification has been often utilized for conducting aptamer-based assays [162, 163]. Figure 15.10a shows a typical work conducted by Zhu et al. [164]. In this system, the potassium-binding aptamer is designed to hybridize with a linker, forming two complete recognition sites for NEase. The subsequent nicking process may generate a cycle of nicking–dissociation–hybridization, resulting in the cleavage of many linkers. On the contrary, in the presence of potassium ions, the aptamer will bind with the ions, leading to the silence of NEase and the accumulation of linker molecules. By coupling the NEases-assisted amplification with probe DNA-functionalized AuNPs, potassium ion can be sensitively detected with a detection limit of ~ 0.1 mM. However, the above assay may hardly be extended to other analytes, due to the requirement of a NEase recognition site in the aptamer sequence. Recently, Qu and coworkers have reported a more universal strategy on the basis of a structurally engineered aptamer [165]. In this study, Qu et al. have used two hairpin structures, one of which is a MAB that contains an IgE aptamer and a trigger sequence, while another one is complementary to the trigger. Since recognition of the target will open the hairpin structure of the MAB, exposing the trigger sequence, a complete recognition site for NEase is formed, activating the autonomous nicking–dissociation–hybridization process (Fig. 15.10b). By monitoring the increase in fluorescence intensity, a detection limit of 5 pM can be achieved for IgE detection.

Besides NEases, other nucleic acid-cleaving enzymes, especially exonucleases, have also been employed for signal amplification [166]. Exonuclease III (Exo III) is an enzyme of the 3'-5' exonuclease family, catalyzing the stepwise removal of mononucleotides from 3'-hydroxyl termini of double-stranded DNA [167]. Previous studies have demonstrated the effectiveness of Exo III for amplified DNA detection [168, 169]. Using Exo III for regenerating analytes, Willner and coworkers have proposed a sensitive aptasensor for ATP detection [170]. The assay system involves the use of an engineered aptamer that, upon binding the

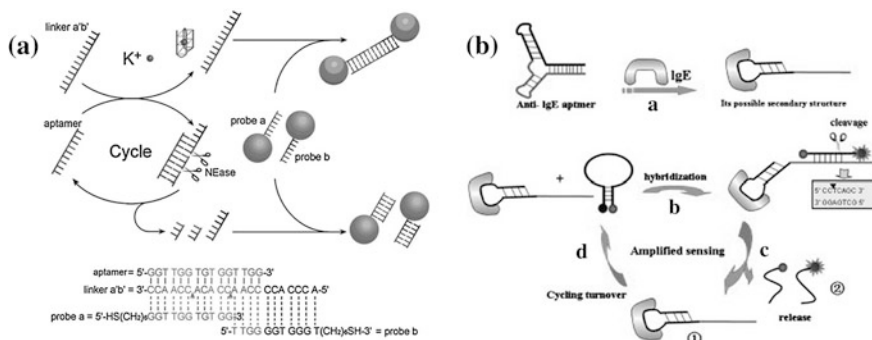


Fig. 15.10 Nicking endonuclease-assisted signal amplification (NESA): **a** NESA process is activated by the formation of aptamer/linker duplex. The presence of target will break the duplex, thereby inhibiting the NESA process. Recreated with kind permission of American Chemical Society [164]. **b** Binding of target induces the structural change of the engineered aptamer, triggering the autonomous enzyme-mediated signal amplification. Recreated with kind permission of Elsevier Ltd [165]

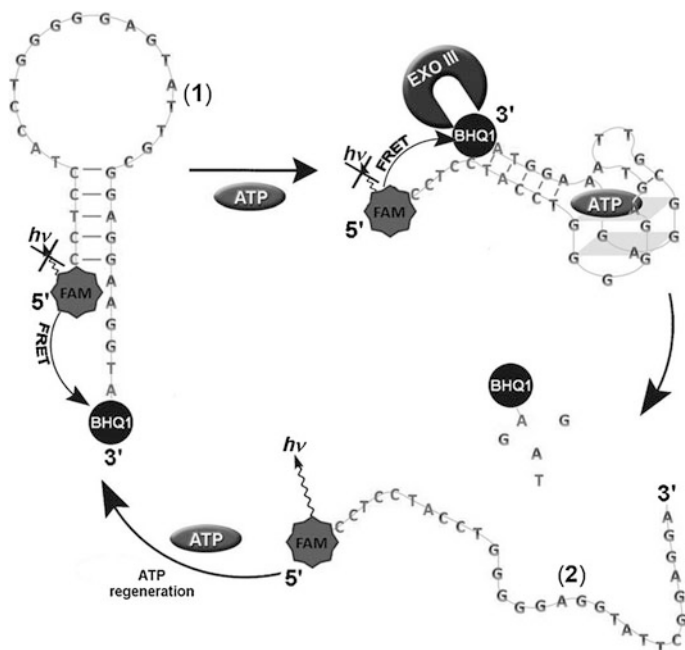


Fig. 15.11 An amplified fluorescence aptasensor using Exonuclease III-aided target recycling. Recreated with kind permission of Wiley-VCH [170]

target, may trigger the Exo III-catalyzed digestion of aptamer and the recycling of the analyte (Fig. 15.11). In theory, one ATP molecule can eventually result in the digestion of numerous aptamers, thus the detection system can yield ultrahigh

sensitivity. In another aptasensor for Ochratoxin A detection, RecJ_f exonuclease that degrades single-stranded DNA in the direction of 5′–3′ is utilized by Tong et al. [171]. For the fabrication of this sensor, Ochratoxin A aptamer is initially engineered with three bases addition at the 5′ end to make it able to be recognized by the exonuclease upon target binding. Signal amplification is achieved through the formation of aptamer–target complex and the subsequent RecJ_f exonuclease-catalyzed target recycling. Due to the signal amplification approach, sensitive detection of Ochratoxin A can be achieved.

15.3.3.2 Catalytic Signal Amplification

The ability to catalyze many cycles of conversions of substrates into products makes a catalyst an ideal signal amplifier [172]. Based on the association of aptamers with catalytic labels, the sensitivity of the fabricated biosensors can be markedly improved. Enzymes are the most commonly used catalysts in aptasensors. For instance, Zhu et al. have engineered an enzyme–aptamer conjugate by coupling the horseradish peroxidase (HRP) with mucin 1 (MUC1) aptamer using a bifunctional cross-linker [173]. As shown in Fig. 15.12a, dual-recognition between the aptamers and MUC1-overexpressed breast cancer cells can fabricate the formation of sandwich architecture and bring enzyme–aptamer conjugates to the electrode surface. Since the attached HRP can efficiently catalyze the reduction of hydrogen peroxide (H₂O₂), sensitive signal readout can be obtained. As a result, down to 100 cells can be detected with this sensor.

In addition to enzymes, some nanomaterials are reported to be able to act as effective catalysts [174–176], so they have been incorporated with aptamers for constructing biosensors. For example, the electrocatalytic behavior of platinum nanoparticles (Pt NPs) has been employed for the amplified electrochemical detection of cocaine with a detection limit of 10 μM [177]. In the meanwhile, a colorimetric thrombin biosensor has been developed by using aptamer-conjugated AuNPs as catalytic labels [178]. The analytical procedure of the biosensor consists of the interaction of target with aptamer-functionalized magnetic particles, followed by binding the second aptamer-conjugated AuNPs. The resulting sandwich-type complex is then collected by magnetic field and utilized to catalyze the decolorization of organic dyes, which may lead to significant decreases in absorbance. Benefited from AuNP-based catalytic signal amplification, this biosensor can be applied for thrombin detection with very high sensitivity and selectivity.

As described in Sect. 15.3.2.1, catalytic nucleic acids have been introduced into different aptasensors as signaling moiety. However, in most of these designs, the enzymatic reaction is only single turnover, which will greatly limit the sensitivity of the fabricated biosensor [179]. In 1998, G-quadruplex structures were reported to exhibit peroxidase mimetic activity after binding with hemin [180]. In the presence of H₂O₂/luminol or 2, 2′-azino-bis(3-ethylbenzothiazoline-6-sulfonic acid) (ABTS²⁻), the resulting HRP-mimicking DNAzyme can catalyze multiple turnover reactions. Recent studies have also demonstrated the excellent electrocatalytic activity of the

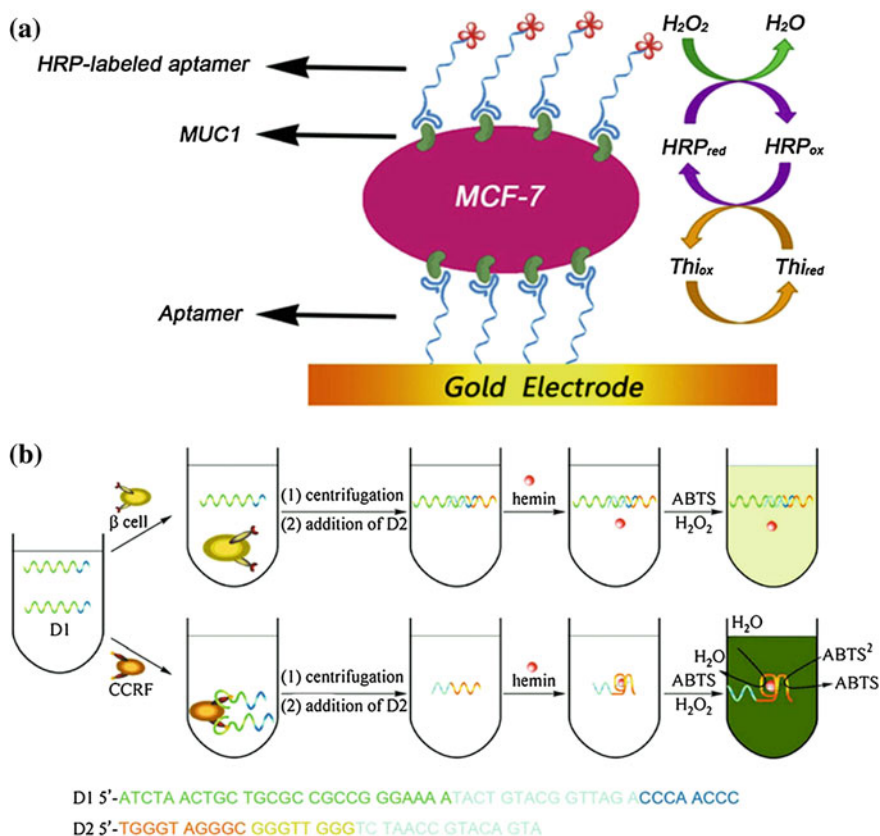


Fig. 15.12 Aptasensors with catalytic signal amplification. **a** Horseradish peroxidase–aptamer conjugates were employed to catalyze the electrochemical reduction of H_2O_2 and enabled the sensitive detection of target cells. Recreated with kind permission of Elsevier Ltd [173]. **b** The presence of target cell induced the formation of hemin-contained DNAzyme, catalyzing multiple turnover reactions. Recreated with kind permission of Springer [187]

DNAzyme [181–183], as well as new functions that may mimic NADH oxidase and NADH peroxidase activities [184]. Given these unique properties, the hemin-G-quadruplex complex is regarded as an ideal catalyst, and the incorporation of the complex in aptasensors is expanding rapidly [185, 186]. As an example, Zhu et al. have developed an optical sensor for the detection of human leukemic lymphoblasts (CCRF-CEM cells) by adapting the DNAzyme and an aptamer that is extended with a linker sequence for targeting CCRF-CEM cells [187]. In the absence of target cells, the extended aptamer will hybridize with the base sequence that can fold into G-quadruplex structure, consequently inhibiting the formation of hemin-contained DNAzyme. However, the presence of CCRF-CEM cells will induce the dissociation of the duplex, activating the formation of the DNAzyme, which can catalyze the oxidation of ABTS^{2-} to give a detectable signal (Fig. 15.12b).

15.4 Conclusion

The information presented in this chapter clearly shows that significant progress has been made in engineering aptamers and applying them for developing aptasensors. However, the clinical use of aptasensors is still limited. One issue is that most aptasensors are conducted and optimized in buffer solution, leading to poor performance in biological fluids. Another fatal problem is the limited number of aptamers that used in the development of aptasensors. As counted by Mascini and coworkers, almost 60 % studies on aptamer-based assays in the past 10 years are dominated by only eight well-known aptamers [102]. In addition, some post-SELEX aptamer engineering methods may affect the affinity and specificity of the original aptamers, which will restrict their practical applications. However, considering the enormous and great efforts of biologists, chemists, and engineers, it is believed that rationally engineered aptamer-based biosensors will become real valuable tools for clinical application in the near future.

References

1. Navani N, Li Y (2006) Nucleic acid aptamers and enzymes as sensors. *Curr Opin Chem Biol* 10(3):272–281. doi:10.1016/j.cbpa.2006.04.003
2. Ellington AD, Szostak JW (1990) In vitro selection of RNA molecules that bind specific ligands. *Nature* 346(6287):818–822. doi:10.1038/346818a0
3. Tuerk C, Gold L (1990) Systematic evolution of ligands by exponential enrichment: RNA ligands to bacteriophage T4 DNA polymerase. *Science* 249(4968):505–510. doi:10.1126/science.2200121
4. Ciesiolka J, Gorski J, Yarus M (1995) Selection of an RNA domain that binds Zn²⁺. *RNA* 1(5):538–550
5. Li N, Wang Y, Pothukuchy A, Syrett A, Husain N, Gopalakrishna S, Kosaraju P, Ellington AD (2008) Aptamers that recognize drug-resistant HIV-1 reverse transcriptase. *Nucleic Acids Res* 36(21):6739–6751. doi:10.1093/nar/gkn775
6. Shangguan D, Meng L, Cao ZC, Xiao Z, Fang X, Li Y, Cardona D, Witek RP, Liu C, Tan W (2008) Identification of liver cancer-specific aptamers using whole live cells. *Anal Chem* 80(3):721–728. doi:10.1021/ac701962v
7. Mairal T, Cengiz Özalp V, Lozano Sánchez P, Mir M, Katakis I, O’Sullivan CK (2007) Aptamers: molecular tools for analytical applications. *Anal Bioanal Chem* 390(4):989–1007. doi:10.1007/s00216-007-1346-4
8. Geiger A, Burgstaller P, von der Eltz H, Roeder A, Famulok M (1996) RNA aptamers that bind L-arginine with sub-micromolar dissociation constants and high enantioselectivity. *Nucleic Acids Res* 24(6):1029–1036. doi:10.1093/nar/24.6.1029
9. Hong P, Li W, Li J (2012) Applications of aptasensors in clinical diagnostics. *Sensors* 12(12):1181–1193. doi:10.3390/s120201181
10. Tan W, Wang H, Chen Y, Zhang X, Zhu H, Yang C, Yang R, Liu C (2011) Molecular aptamers for drug delivery. *Trends Biotechnol* 29(12):634–640. doi:10.1016/j.tibtech.2011.06.009
11. Iliuk AB, Hu L, Tao WA (2011) Aptamer in bioanalytical applications. *Anal Chem* 83(12):4440–4452. doi:10.1021/ac201057w

12. Keefe AD, Pai S, Ellington A (2010) Aptamers as therapeutics. *Nat Rev Drug Discov* 9(7):537–550. doi:[10.1038/nrd3141](https://doi.org/10.1038/nrd3141)
13. Meyer C, Hahn U, Rentmeister A (2011) Cell-specific aptamers as emerging therapeutics. *J Nucleic Acids* 2011:1–18. doi:[10.4061/2011/904750](https://doi.org/10.4061/2011/904750)
14. Zhu G, Ye M, Donovan MJ, Song E, Zhao Z, Tan W (2012) Nucleic acid aptamers: an emerging frontier in cancer therapy. *Chem Commun* 48(85):10472. doi:[10.1039/c2cc35042d](https://doi.org/10.1039/c2cc35042d)
15. Esposito CL, Catuogno S, de Francisisci V, Cerchia L (2011) New insight into clinical development of nucleic acid aptamers. *Discov Med* 11(61):487–496
16. Wang J, Li G (2011) Aptamers against cell surface receptors: selection, modification and application. *Curr Med Chem* 18(27):4107–4116. doi:[10.2174/092986711797189628](https://doi.org/10.2174/092986711797189628)
17. Hirsch IB, Armstrong D, Bergenstal RM, Buckingham B, Childs BP, Clarke WL, Peters A, Wolpert H (2008) Clinical application of emerging sensor technologies in diabetes management: consensus guidelines for continuous glucose monitoring (CGM). *Diabetes Technol Ther* 10(4):232–244. doi:[10.1089/dia.2008.0016](https://doi.org/10.1089/dia.2008.0016) quiz 245–236
18. Deisingh AK (2006) Aptamer-based biosensors: biomedical applications. *Handb Exp Pharmacol* 173:341–357. doi:[10.1007/3-540-27262-3_17](https://doi.org/10.1007/3-540-27262-3_17)
19. Citartan M, Gopinath SC, Tominaga J, Tan SC, Tang TH (2012) Assays for aptamer-based platforms. *Biosens Bioelectron* 34(1):1–11. doi:[10.1016/j.bios.2012.01.002](https://doi.org/10.1016/j.bios.2012.01.002)
20. Vallée-Bélisle A, Plaxco KW (2010) Structure-switching biosensors: inspired by nature. *Curr Opin Struc Biol* 20(4):518–526. doi:[10.1016/j.sbi.2010.05.001](https://doi.org/10.1016/j.sbi.2010.05.001)
21. Lubin AA, Plaxco KW (2010) Folding-based electrochemical biosensors: the case for responsive nucleic acid architectures. *Acc Chem Res* 43(4):496–505. doi:[10.1021/ar900165x](https://doi.org/10.1021/ar900165x)
22. You M, Chen Y, Peng L, Han D, Yin B, Ye B, Tan W (2011) Engineering DNA aptamers for novel analytical and biomedical applications. *Chem Sci* 2(6):1003. doi:[10.1039/c0sc00647e](https://doi.org/10.1039/c0sc00647e)
23. Song K-M, Lee S, Ban C (2012) Aptamers and their biological applications. *Sensors* 12(12):612–631. doi:[10.3390/s120100612](https://doi.org/10.3390/s120100612)
24. Liu J, Cao Z, Lu Y (2009) Functional nucleic acid sensors. *Chem Rev* 109(5):1948–1998. doi:[10.1021/cr030183i](https://doi.org/10.1021/cr030183i)
25. Tombelli S, Minunni M, Mascini M (2005) Analytical applications of aptamers. *Biosens Bioelectron* 20(12):2424–2434. doi:[10.1016/j.bios.2004.11.006](https://doi.org/10.1016/j.bios.2004.11.006)
26. Wang W, Jia L-Y (2009) Progress in aptamer screening methods. *Chinese J Anal Chem* 37(3):454–460. doi:[10.1016/s1872-2040\(08\)60092-4](https://doi.org/10.1016/s1872-2040(08)60092-4)
27. Gopinath SCB (2006) Methods developed for SELEX. *Anal Bioanal Chem* 387(1):171–182. doi:[10.1007/s00216-006-0826-2](https://doi.org/10.1007/s00216-006-0826-2)
28. Mendonsa SD, Bowser MT (2004) In vitro evolution of functional DNA using capillary electrophoresis. *J Am Chem Soc* 126(1):20–21. doi:[10.1021/ja037832s](https://doi.org/10.1021/ja037832s)
29. Liu Y, Wang C, Li F, Shen S, Tyrell DLJ, Le XC, Li X-F (2012) DNase-mediated single-cycle selection of aptamers for proteins blotted on a membrane. *Anal Chem* 84(18):7603–7606. doi:[10.1021/ac302047e](https://doi.org/10.1021/ac302047e)
30. Misono TS, Kumar PKR (2005) Selection of RNA aptamers against human influenza virus hemagglutinin using surface plasmon resonance. *Anal Biochem* 342(2):312–317. doi:[10.1016/j.ab.2005.04.013](https://doi.org/10.1016/j.ab.2005.04.013)
31. Miyachi Y, Shimizu N, Ogino C, Kondo A (2009) Selection of DNA aptamers using atomic force microscopy. *Nucleic Acids Res* 38(4):e21–e21. doi:[10.1093/nar/gkp1101](https://doi.org/10.1093/nar/gkp1101)
32. Mendonsa SD, Bowser MT (2005) In vitro selection of aptamers with affinity for neuropeptide Y using capillary electrophoresis. *J Am Chem Soc* 127(26):9382–9383. doi:[10.1021/ja052406n](https://doi.org/10.1021/ja052406n)
33. Tang J, Xie J, Shao N, Yan Y (2006) The DNA aptamers that specifically recognize ricin toxin are selected by two in vitro selection methods. *Electrophoresis* 27(7):1303–1311. doi:[10.1002/elps.200500489](https://doi.org/10.1002/elps.200500489)

34. Lou X, Qian J, Xiao Y, Viel L, Gerdon AE, Lagally ET, Atzberger P, Tarasow TM, Heeger AJ, Soh HT (2009) Micromagnetic selection of aptamers in microfluidic channels. *Proc Natl Acad Sci USA* 106(9):2989–2994. doi:[10.1073/pnas.0813135106](https://doi.org/10.1073/pnas.0813135106)
35. Weng C-H, Huang C-J, Lee G-B (2012) Screening of aptamers on microfluidic systems for clinical applications. *Sensors* 12(12):9514–9529. doi:[10.3390/s120709514](https://doi.org/10.3390/s120709514)
36. Qian J, Lou X, Zhang Y, Xiao Y, Soh HT (2009) Generation of highly specific aptamers via micromagnetic selection. *Anal Chem* 81(13):5490–5495. doi:[10.1021/ac900759k](https://doi.org/10.1021/ac900759k)
37. Fang X, Tan W (2010) Aptamers generated from cell-SELEX for molecular medicine: a chemical biology approach. *Acc Chem Res* 43(1):48–57. doi:[10.1021/ar900101s](https://doi.org/10.1021/ar900101s)
38. Shangguan D, Li Y, Tang Z, Cao ZC, Chen HW, Mallikaratchy P, Sefah K, Yang CJ, Tan W (2006) From the cover: aptamers evolved from live cells as effective molecular probes for cancer study. *Proc Natl Acad Sci USA* 103(32):11838–11843. doi:[10.1073/pnas.0602615103](https://doi.org/10.1073/pnas.0602615103)
39. Tang Z, Parekh P, Turner P, Moyer RW, Tan W (2009) Generating aptamers for recognition of virus-infected cells. *Clin Chem* 55(4):813–822. doi:[10.1373/clinchem.2008.113514](https://doi.org/10.1373/clinchem.2008.113514)
40. Kunii T, S-i Ogura, Mie M, Kobatake E (2011) Selection of DNA aptamers recognizing small cell lung cancer using living cell-SELEX. *Analyst* 136(7):1310. doi:[10.1039/c0an00962h](https://doi.org/10.1039/c0an00962h)
41. Liu J, Liu H, Sefah K, Liu B, Pu Y, Van Simaey D, Tan W (2012) Selection of aptamers specific for adipose tissue. *PLoS ONE* 7(5):e37789. doi:[10.1371/journal.pone.0037789](https://doi.org/10.1371/journal.pone.0037789)
42. Thielges MC, Zimmermann J, Yu W, Oda M, Romesberg FE (2008) Exploring the energy landscape of antibody-antigen complexes: protein dynamics, flexibility, and molecular recognition. *Biochemistry* 47(27):7237–7247. doi:[10.1021/bi800374q](https://doi.org/10.1021/bi800374q)
43. Liu L, Zhu X, Zhang D, Huang J, Li G (2007) An electrochemical method to detect folate receptor positive tumor cells. *Electrochem Commun* 9(10):2547–2550. doi:[10.1016/j.elecom.2007.07.032](https://doi.org/10.1016/j.elecom.2007.07.032)
44. Cao Y, Zhu S, Yu J, Zhu X, Yin Y, Li G (2012) Protein detection based on small molecule-linked DNA. *Anal Chem* 84(10):4314–4320. doi:[10.1021/ac203401h](https://doi.org/10.1021/ac203401h)
45. Wang J, Shen M, Cao Y, Li G (2010) Switchable “on–off” electrochemical technique for detection of phosphorylation. *Biosens Bioelectron* 26(2):638–642. doi:[10.1016/j.bios.2010.07.006](https://doi.org/10.1016/j.bios.2010.07.006)
46. Xu Y, Cheng G, He P, Fang Y (2009) A review: electrochemical aptasensors with various detection strategies. *Electroanalysis* 21(11):1251–1259. doi:[10.1002/elan.200804561](https://doi.org/10.1002/elan.200804561)
47. Tolle F, Mayer G (2013) Dressed for success—applying chemistry to modulate aptamer functionality. *Chem Sci* 4(1):60. doi:[10.1039/c2sc21510a](https://doi.org/10.1039/c2sc21510a)
48. Burmeister PE, Lewis SD, Silva RF, Preiss JR, Horwitz LR, Pendergrast PS, McCauley TG, Kurz JC, Epstein DM, Wilson C, Keefe AD (2005) Direct in vitro selection of a 2'-O-methyl aptamer to VEGF. *Chem Biol* 12(1):25–33. doi:[10.1016/j.chembiol.2004.10.017](https://doi.org/10.1016/j.chembiol.2004.10.017)
49. Sekiya S, Noda K, Nishikawa F, Yokoyama T, Kumar PK, Nishikawa S (2006) Characterization and application of a novel RNA aptamer against the mouse prion protein. *J Biochem* 139(3):383–390. doi:[10.1093/jb/mvj046](https://doi.org/10.1093/jb/mvj046)
50. Lin Y, Nieuwlandt D, Magallanez A, Feistner B, Jayasena SD (1996) High-affinity and specific recognition of human thyroid stimulating hormone (hTSH) by in vitro-selected 2'-amino-modified RNA. *Nucleic Acids Res* 24(17):3407–3414. doi:[10.1093/nar/24.17.3407](https://doi.org/10.1093/nar/24.17.3407)
51. Virno A, Randazzo A, Giancola C, Bucci M, Cirino G, Mayol L (2007) A novel thrombin binding aptamer containing a G-LNA residue. *Bioorgan Med Chem* 15(17):5710–5718. doi:[10.1016/j.bmc.2007.06.008](https://doi.org/10.1016/j.bmc.2007.06.008)
52. Schmidt KS (2004) Application of locked nucleic acids to improve aptamer in vivo stability and targeting function. *Nucleic Acids Res* 32(19):5757–5765. doi:[10.1093/nar/gkh862](https://doi.org/10.1093/nar/gkh862)
53. Kuwahara M, Sugimoto N (2010) Molecular evolution of functional nucleic acids with chemical modifications. *Molecules* 15(8):5423–5444. doi:[10.3390/molecules15085423](https://doi.org/10.3390/molecules15085423)
54. Shoji A, Kuwahara M, Ozaki H, Sawai H (2007) Modified DNA aptamer that binds the (R)-isomer of a thalidomide derivative with high enantioselectivity. *J Am Chem Soc* 129(5):1456–1464. doi:[10.1021/ja067098n](https://doi.org/10.1021/ja067098n)

55. Keefe AD, Cload ST (2008) SELEX with modified nucleotides. *Curr Opin Chem Biol* 12(4):448–456. doi:[10.1016/j.cbpa.2008.06.028](https://doi.org/10.1016/j.cbpa.2008.06.028)
56. King DJ, Bassett SE, Li X, Fennewald SA, Herzog NK, Luxon BA, Shope R, Gorenstein DG (2002) Combinatorial selection and binding of phosphorothioate aptamers targeting human NF-kappa B RelA(p65) and p50. *Biochemistry* 41(30):9696–9706. doi:[10.1021/bi020220k](https://doi.org/10.1021/bi020220k)
57. King DJ, Ventura DA, Brasier AR, Gorenstein DG (1998) Novel combinatorial selection of phosphorothioate oligonucleotide aptamers. *Biochemistry* 37(47):16489–16493. doi:[10.1021/bi981780f](https://doi.org/10.1021/bi981780f)
58. Du H, Rosbash M (2002) The U1 snRNP protein U1C recognizes the 5' splice site in the absence of base pairing. *Nature* 419(6902):86–90. doi:[10.1038/nature00947](https://doi.org/10.1038/nature00947)
59. Pagratis NC, Bell C, Chang YF, Jennings S, Fitzwater T, Jellinek D, Dang C (1997) Potent 2'-amino-, and 2'-fluoro-2'-deoxyribonucleotide RNA inhibitors of keratinocyte growth factor. *Nat Biotechnol* 15(1):68–73. doi:[10.1038/nbt0197-68](https://doi.org/10.1038/nbt0197-68)
60. Musumeci D, Montesarchio D (2012) Polyvalent nucleic acid aptamers and modulation of their activity: a focus on the thrombin binding aptamer. *Pharmacol Therapeut* 136(2):202–215. doi:[10.1016/j.pharmthera.2012.07.011](https://doi.org/10.1016/j.pharmthera.2012.07.011)
61. Dollins CM, Nair S, Boczkowski D, Lee J, Layzer JM, Gilboa E, Sullenger BA (2008) Assembling OX40 aptamers on a molecular scaffold to create a receptor-activating aptamer. *Chem Biol* 15(7):675–682. doi:[10.1016/j.chembiol.2008.05.016](https://doi.org/10.1016/j.chembiol.2008.05.016)
62. Tasset DM, Kubik MF, Steiner W (1997) Oligonucleotide inhibitors of human thrombin that bind distinct epitopes. *J Mol Biol* 272(5):688–698. doi:[10.1006/jmbi.1997.1275](https://doi.org/10.1006/jmbi.1997.1275)
63. Padmanabhan K, Padmanabhan KP, Ferrara JD, Sadler JE, Tulinsky A (1993) The structure of alpha-thrombin inhibited by a 15-mer single-stranded DNA aptamer. *J Biol Chem* 268(24):17651–17654
64. Bock LC, Griffin LC, Latham JA, Vermaas EH, Toole JJ (1992) Selection of single-stranded DNA molecules that bind and inhibit human thrombin. *Nature* 355(6360):564–566. doi:[10.1038/355564a0](https://doi.org/10.1038/355564a0)
65. Müller J, Wulffen B, Pöttsch B, Mayer G (2007) Multidomain targeting generates a high-affinity thrombin-inhibiting bivalent aptamer. *ChemBioChem* 8(18):2223–2226. doi:[10.1002/cbic.200700535](https://doi.org/10.1002/cbic.200700535)
66. Kim Y, Dennis DM, Morey T, Yang L, Tan W (2010) Engineering dendritic aptamer assemblies as superior inhibitors of protein function. *Chem Asian J* 5(1):56–59. doi:[10.1002/asia.200900421](https://doi.org/10.1002/asia.200900421)
67. Hasegawa H, Taira K, Sode K, Ikebukuro K (2008) Improvement of aptamer affinity by dimerization. *Sensors* 8:1090–1098. doi:[10.3390/s8021090](https://doi.org/10.3390/s8021090)
68. Hsu C-L, Chang H-T, Chen C-T, Wei S-C, Shiang Y-C, Huang C-C (2011) Highly efficient control of thrombin activity by multivalent nanoparticles. *Chem Eur J* 17(39):10994–11000. doi:[10.1002/chem.201101081](https://doi.org/10.1002/chem.201101081)
69. Huang YF, Chang HT, Tan W (2008) Cancer cell targeting using multiple aptamers conjugated on nanorods. *Anal Chem* 80(3):567–572. doi:[10.1021/ac702322j](https://doi.org/10.1021/ac702322j)
70. Wang Y, Li Z, Hu D, Lin CT, Li J, Lin Y (2010) Aptamer/graphene oxide nanocomplex for in situ molecular probing in living cells. *J Am Chem Soc* 132(27):9274–9276. doi:[10.1021/ja103169v](https://doi.org/10.1021/ja103169v)
71. Cho H, Baker BR, Wachsmann-Hogiu S, Pagba CV, Laurence TA, Lane SM, Lee LP, Tok JB (2008) Aptamer-based SERRS sensor for thrombin detection. *Nano Lett* 8(12):4386–4390. doi:[10.1021/nl802245w](https://doi.org/10.1021/nl802245w)
72. Xing H, Wong NY, Xiang Y, Lu Y (2012) DNA aptamer functionalized nanomaterials for intracellular analysis, cancer cell imaging and drug delivery. *Curr Opin Chem Biol* 16(3–4):429–435. doi:[10.1016/j.cbpa.2012.03.016](https://doi.org/10.1016/j.cbpa.2012.03.016)
73. Tyagi S, Kramer FR (1996) Molecular beacons: probes that fluoresce upon hybridization. *Nat Biotechnol* 14(3):303–308. doi:[10.1038/nbt0396-303](https://doi.org/10.1038/nbt0396-303)

74. Tan W, Fang X, Li J, Liu X (2000) Molecular beacons: a novel DNA probe for nucleic acid and protein studies. *Chemistry* 6(7):1107–1111. doi:[10.1002/\(SICI\)1521-3765\(20000403\)6:7<1107:AID-CHEM1107>3.0.CO;2-9](https://doi.org/10.1002/(SICI)1521-3765(20000403)6:7<1107:AID-CHEM1107>3.0.CO;2-9)
75. Wang K, Tang Z, Yang CJ, Kim Y, Fang X, Li W, Wu Y, Medley CD, Cao Z, Li J, Colon P, Lin H, Tan W (2009) Molecular engineering of DNA: molecular beacons. *Angew Chem Int Ed* 48(5):856–870. doi:[10.1002/anie.200800370](https://doi.org/10.1002/anie.200800370)
76. Song S, Liang Z, Zhang J, Wang L, Li G, Fan C (2009) Gold-nanoparticle-based multicolor nanobeacons for sequence-specific DNA analysis. *Angew Chem Int Ed* 48(46):8670–8674. doi:[10.1002/anie.200901887](https://doi.org/10.1002/anie.200901887)
77. Hamaguchi N, Ellington A, Stanton M (2001) Aptamer beacons for the direct detection of proteins. *Anal Biochem* 294(2):126–131. doi:[10.1006/abio.2001.5169](https://doi.org/10.1006/abio.2001.5169)
78. Kim B, Jung IH, Kang M, Shim H-K, Woo HY (2012) Cationic conjugated polyelectrolytes-triggered conformational change of molecular beacon aptamer for highly sensitive and selective potassium ion detection. *J Am Chem Soc* 134(6):3133–3138. doi:[10.1021/ja210360v](https://doi.org/10.1021/ja210360v)
79. Wu Z-S, Zheng F, Shen G-L, Yu R-Q (2009) A hairpin aptamer-based electrochemical biosensing platform for the sensitive detection of proteins. *Biomaterials* 30(15):2950–2955. doi:[10.1016/j.biomaterials.2009.02.017](https://doi.org/10.1016/j.biomaterials.2009.02.017)
80. Liu Y, Tuleouva N, Ramanculov E, Revzin A (2010) Aptamer-based electrochemical biosensor for interferon gamma detection. *Anal Chem* 82(19):8131–8136. doi:[10.1021/ac101409t](https://doi.org/10.1021/ac101409t)
81. Shi H, He X, Wang K, Wu X, Ye X, Guo Q, Tan W, Qing Z, Yang X, Zhou B (2011) Activatable aptamer probe for contrast-enhanced in vivo cancer imaging based on cell membrane protein-triggered conformation alteration. *Proc Natl Acad Sci USA* 108(10):3900–3905. doi:[10.1073/pnas.1016197108](https://doi.org/10.1073/pnas.1016197108)
82. Zheng J, Li J, Jiang Y, Jin J, Wang K, Yang R, Tan W (2011) Design of aptamer-based sensing platform using triple-helix molecular switch. *Anal Chem* 83(17):6586–6592. doi:[10.1021/ac201314y](https://doi.org/10.1021/ac201314y)
83. Lu Y, Liu J (2006) Functional DNA nanotechnology: emerging applications of DNAszymes and aptamers. *Curr Opin Biotech* 17(6):580–588. doi:[10.1016/j.copbio.2006.10.004](https://doi.org/10.1016/j.copbio.2006.10.004)
84. Cho EJ, Yang L, Levy M, Ellington AD (2005) Using a deoxyribozyme ligase and rolling circle amplification to detect a non-nucleic acid analyte, ATP. *J Am Chem Soc* 127(7):2022–2023. doi:[10.1021/ja043490u](https://doi.org/10.1021/ja043490u)
85. Lu L-M, Zhang X-B, Kong R-M, Yang B, Tan W (2011) A ligation-triggered DNAszyme cascade for amplified fluorescence detection of biological small molecules with zero-background signal. *J Am Chem Soc* 133(30):11686–11691. doi:[10.1021/ja203693b](https://doi.org/10.1021/ja203693b)
86. Achenbach JC, Nutiu R, Li Y (2005) Structure-switching allosteric deoxyribozymes. *Anal Chim Acta* 534(1):41–51. doi:[10.1016/j.aca.2004.03.080](https://doi.org/10.1016/j.aca.2004.03.080)
87. Song P, Xiang Y, Xing H, Zhou Z, Tong A, Lu Y (2012) Label-free catalytic and molecular beacon containing an abasic site for sensitive fluorescent detection of small inorganic and organic molecules. *Anal Chem* 84(6):2916–2922. doi:[10.1021/ac203488p](https://doi.org/10.1021/ac203488p)
88. Sook Bang G, Cho S, Lee N, Lee B-R, Kim J-H, Kim B-G (2013) Rational design of modular allosteric aptamer sensor for label-free protein detection. *Biosens Bioelectron* 39(1):44–50. doi:[10.1016/j.bios.2012.06.038](https://doi.org/10.1016/j.bios.2012.06.038)
89. Yoshida W, Sode K, Ikebukuro K (2006) Aptameric enzyme subunit for biosensing based on enzymatic activity measurement. *Anal Chem* 78(10):3296–3303. doi:[10.1021/ac060254o](https://doi.org/10.1021/ac060254o)
90. Stojanovic MN, Kolpashchikov DM (2004) Modular aptameric sensors. *J Am Chem Soc* 126(30):9266–9270. doi:[10.1021/ja032013t](https://doi.org/10.1021/ja032013t)
91. Wang J, Cao Y, Chen G, Li G (2009) Regulation of thrombin activity with a bifunctional aptamer and hemin: development of a new anticoagulant and antidote pair. *ChemBioChem* 10(13):2171–2176. doi:[10.1002/cbic.200900408](https://doi.org/10.1002/cbic.200900408)
92. Zhang K, Zhu X, Wang J, Xu L, Li G (2010) Strategy to fabricate an electrochemical aptasensor: application to the assay of adenosine deaminase activity. *Anal Chem* 82(8):3207–3211. doi:[10.1021/ac902771k](https://doi.org/10.1021/ac902771k)

93. Wang J, Liu B (2009) Fluorescence resonance energy transfer between an anionic conjugated polymer and a dye-labeled lysozyme aptamer for specific lysozyme detection. *Chem Commun* 17:2284. doi:[10.1039/b820001g](https://doi.org/10.1039/b820001g)
94. Zuo X, Song S, Zhang J, Pan D, Wang L, Fan C (2007) A target-responsive electrochemical aptamer switch (TREAS) for reagentless detection of nanomolar ATP. *J Am Chem Soc* 129(5):1042–1043. doi:[10.1021/ja067024b](https://doi.org/10.1021/ja067024b)
95. Shlyahovsky B, Li D, Katz E, Willner I (2007) Proteins modified with DNazymes or aptamers act as biosensors or biosensor labels. *Biosens Bioelectron* 22(11):2570–2576. doi:[10.1016/j.bios.2006.10.009](https://doi.org/10.1016/j.bios.2006.10.009)
96. Chen Y, O'Donoghue MB, Huang YF, Kang H, Phillips JA, Chen X, Estevez MC, Yang CJ, Tan W (2010) A surface energy transfer nanoruler for measuring binding site distances on live cell surfaces. *J Am Chem Soc* 132(46):16559–16570. doi:[10.1021/ja106360v](https://doi.org/10.1021/ja106360v)
97. Drolet DW, Moon-McDermott L, Romig TS (1996) An enzyme-linked oligonucleotide assay. *Nat Biotechnol* 14(8):1021–1025. doi:[10.1038/nbt0896-1021](https://doi.org/10.1038/nbt0896-1021)
98. Green LS, Jellinek D, Jenison R, Ostman A, Heldin CH, Janjic N (1996) Inhibitory DNA ligands to platelet-derived growth factor B-chain. *Biochemistry* 35(45):14413–14424. doi:[10.1021/bi961544+](https://doi.org/10.1021/bi961544+)
99. Pavlov V, Xiao Y, Shlyahovsky B, Willner I (2004) Aptamer-functionalized Au nanoparticles for the amplified optical detection of thrombin. *J Am Chem Soc* 126(38):11768–11769. doi:[10.1021/ja046970u](https://doi.org/10.1021/ja046970u)
100. Song S, Wang L, Li J, Fan C, Zhao J (2008) Aptamer-based biosensors. *TrAC-Trend. Anal Chem* 27(2):108–117. doi:[10.1016/j.trac.2007.12.004](https://doi.org/10.1016/j.trac.2007.12.004)
101. Han K, Liang Z, Zhou N (2010) Design strategies for aptamer-based biosensors. *Sensors* 10(5):4541–4557. doi:[10.3390/s100504541](https://doi.org/10.3390/s100504541)
102. Mascini M, Palchetti I, Tombelli S (2012) Nucleic acid and peptide aptamers: fundamentals and bioanalytical aspects. *Angew Chem Int Ed* 51(6):1316–1332. doi:[10.1002/anie.201006630](https://doi.org/10.1002/anie.201006630)
103. Numnuam A, Chumbimuni-Torres KY, Xiang Y, Bash R, Thavarungkul P, Kanatharana P, Pretsch E, Wang J, Bakker E (2008) Aptamer-based potentiometric measurements of proteins using ion-selective microelectrodes. *Anal Chem* 80(3):707–712. doi:[10.1021/ac701910r](https://doi.org/10.1021/ac701910r)
104. Wang J, Meng W, Zheng X, Liu S, Li G (2009) Combination of aptamer with gold nanoparticles for electrochemical signal amplification: application to sensitive detection of platelet-derived growth factor. *Biosens Bioelectron* 24(6):1598–1602. doi:[10.1016/j.bios.2008.08.030](https://doi.org/10.1016/j.bios.2008.08.030)
105. Bai L, Yuan R, Chai Y, Zhuo Y, Yuan Y, Wang Y (2012) Simultaneous electrochemical detection of multiple analytes based on dual signal amplification of single-walled carbon nanotubes and multi-labeled graphene sheets. *Biomaterials* 33(4):1090–1096. doi:[10.1016/j.biomaterials.2011.10.012](https://doi.org/10.1016/j.biomaterials.2011.10.012)
106. Zhang YL, Huang Y, Jiang JH, Shen GL, Yu RQ (2007) Electrochemical aptasensor based on proximity-dependent surface hybridization assay for single-step, reusable, sensitive protein detection. *J Am Chem Soc* 129(50):15448–15449. doi:[10.1021/ja0773047](https://doi.org/10.1021/ja0773047)
107. Wang J, Munir A, Li Z, Zhou HS (2009) Aptamer–Au NPs conjugates-enhanced SPR sensing for the ultrasensitive sandwich immunoassay. *Biosens Bioelectron* 25(1):124–129. doi:[10.1016/j.bios.2009.06.016](https://doi.org/10.1016/j.bios.2009.06.016)
108. Yang CJ, Jockusch S, Vicens M, Turro NJ, Tan WH (2005) Light-switching excimer probes for rapid protein monitoring in complex biological fluids. *Proc Natl Acad Sci USA* 102(48):17278–17283. doi:[10.1073/pnas.0508821102](https://doi.org/10.1073/pnas.0508821102)
109. Mok W, Li Y (2008) Recent progress in nucleic acid aptamer-based biosensors and bioassays. *Sensors* 8(11):7050–7084. doi:[10.3390/s8117050](https://doi.org/10.3390/s8117050)
110. Willner I, Zayats M (2007) Electronic aptamer-based sensors. *Angew Chem Int Ed* 46(34):6408–6418. doi:[10.1002/anie.200604524](https://doi.org/10.1002/anie.200604524)

111. Xiao Y, Lubin AA, Heeger AJ, Plaxco KW (2005) Label-free electronic detection of thrombin in blood serum by using an aptamer-based sensor. *Angew Chem Int Ed* 44(34):5456–5459. doi:[10.1002/anie.200500989](https://doi.org/10.1002/anie.200500989)
112. Wu Z-S, Chen C-R, Shen G-L, Yu R-Q (2008) Reversible electronic nanoswitch based on DNA G-quadruplex conformation: a platform for single-step, reagentless potassium detection. *Biomaterials* 29(17):2689–2696. doi:[10.1016/j.biomaterials.2008.02.024](https://doi.org/10.1016/j.biomaterials.2008.02.024)
113. Li H, Cao Y, Wu X, Ye Z, Li G (2012) Peptide-based electrochemical biosensor for amyloid β 1–42 soluble oligomer assay. *Talanta* 93:358–363. doi:[10.1016/j.talanta.2012.02.055](https://doi.org/10.1016/j.talanta.2012.02.055)
114. White RJ, Plaxco KW (2010) Exploiting binding-induced changes in probe flexibility for the optimization of electrochemical biosensors. *Anal Chem* 82(1):73–76. doi:[10.1021/ac902595f](https://doi.org/10.1021/ac902595f)
115. Ferapontova EE, Olsen EM, Gothelf KV (2008) An RNA aptamer-based electrochemical biosensor for detection of theophylline in serum. *J Am Chem Soc* 130(13):4256–4258. doi:[10.1021/ja711326b](https://doi.org/10.1021/ja711326b)
116. Radi AE, Acero Sanchez JL, Baldrich E, O'Sullivan CK (2006) Reagentless, reusable, ultrasensitive electrochemical molecular beacon aptasensor. *J Am Chem Soc* 128(1):117–124. doi:[10.1021/ja053121d](https://doi.org/10.1021/ja053121d)
117. Baker BR, Lai RY, Wood MS, Doctor EH, Heeger AJ, Plaxco KW (2006) An electronic, aptamer-based small-molecule sensor for the rapid, label-free detection of cocaine in adulterated samples and biological fluids. *J Am Chem Soc* 128(10):3138–3139. doi:[10.1021/ja056957p](https://doi.org/10.1021/ja056957p)
118. Zhao S, Yang W, Lai RY (2011) A folding-based electrochemical aptasensor for detection of vascular endothelial growth factor in human whole blood. *Biosens Bioelectron* 26(5):2442–2447. doi:[10.1016/j.bios.2010.10.029](https://doi.org/10.1016/j.bios.2010.10.029)
119. Radi A-E, O'Sullivan CK (2006) Aptamer conformational switch as sensitive electrochemical biosensor for potassium ion recognition. *Chem Commun* 32:3432. doi:[10.1039/b606804a](https://doi.org/10.1039/b606804a)
120. Zuo X, Xiao Y, Plaxco KW (2009) High specificity, electrochemical sandwich assays based on single aptamer sequences and suitable for the direct detection of small-molecule targets in blood and other complex matrices. *J Am Chem Soc* 131(20):6944–6945. doi:[10.1021/ja901315w](https://doi.org/10.1021/ja901315w)
121. Sharma AK, Kent AD, Heemstra JM (2012) Enzyme-linked small-molecule detection using split aptamer ligation. *Anal Chem* 84(14):6104–6109. doi:[10.1021/ac300997q](https://doi.org/10.1021/ac300997q)
122. Freeman R, Sharon E, Tel-Vered R, Willner I (2009) Supramolecular cocaine-aptamer complexes activate biocatalytic cascades. *J Am Chem Soc* 131(14):5028–5029. doi:[10.1021/ja809496n](https://doi.org/10.1021/ja809496n)
123. Kashefi-Kheyraadi L, Mehrgardi MA (2012) Aptamer-conjugated silver nanoparticles for electrochemical detection of adenosine triphosphate. *Biosens Bioelectron* 37(1):94–98. doi:[10.1016/j.bios.2012.04.045](https://doi.org/10.1016/j.bios.2012.04.045)
124. Dave N, Liu J (2012) Biomimetic sensing based on chemically induced assembly of a signaling DNA aptamer on a fluid bilayer membrane. *Chem Commun* 48(31):3718. doi:[10.1039/c2cc00070a](https://doi.org/10.1039/c2cc00070a)
125. Freeman R, Girsh J, Fang-ju Jou A, Ho JAA, Hug T, Dervede J, Willner I (2012) Optical aptasensors for the analysis of the vascular endothelial growth factor (VEGF). *Anal Chem* 84(14):6192–6198. doi:[10.1021/ac3011473](https://doi.org/10.1021/ac3011473)
126. Yamamoto-Fujita R, Kumar PK (2005) Aptamer-derived nucleic acid oligos: applications to develop nucleic acid chips to analyze proteins and small ligands. *Anal Chem* 77(17):5460–5466. doi:[10.1021/ac050364f](https://doi.org/10.1021/ac050364f)
127. Lin Z, Chen L, Zhu X, Qiu B, Chen G (2010) Signal-on electrochemiluminescence biosensor for thrombin based on target-induced conjunction of split aptamer fragments. *Chem Commun* 46(30):5563. doi:[10.1039/c0cc00932f](https://doi.org/10.1039/c0cc00932f)
128. Nutiu R, Li Y (2003) Structure-switching signaling aptamers. *J Am Chem Soc* 125(16):4771–4778. doi:[10.1021/ja028962o](https://doi.org/10.1021/ja028962o)

129. Mei H, Bing T, Yang X, Qi C, Chang T, Liu X, Cao Z, Shangguan D (2012) Functional-group specific aptamers indirectly recognizing compounds with alkyl amino group. *Anal Chem* 84(17):7323–7329. doi:[10.1021/ac300281u](https://doi.org/10.1021/ac300281u)
130. Zhang J, Wang L, Zhang H, Boey F, Song S, Fan C (2010) Aptamer-based multicolor fluorescent gold nanoprobe for multiplex detection in homogeneous solution. *Small* 6(2):201–204. doi:[10.1002/smll.200901012](https://doi.org/10.1002/smll.200901012)
131. Yoshizumi J, Kumamoto S, Nakamura M, Yamana K (2008) Target-induced strand release (TISR) from aptamer–DNA duplex: a general strategy for electronic detection of biomolecules ranging from a small molecule to a large protein. *Analyst* 133(3):323. doi:[10.1039/b719089c](https://doi.org/10.1039/b719089c)
132. Wu ZS, Guo MM, Zhang SB, Chen CR, Jiang JH, Shen GL, Yu RQ (2007) Reusable electrochemical sensing platform for highly sensitive detection of small molecules based on structure-switching signaling aptamers. *Anal Chem* 79(7):2933–2939. doi:[10.1021/ac0622936](https://doi.org/10.1021/ac0622936)
133. Chen L, Cai Q, Luo F, Chen X, Zhu X, Qiu B, Lin Z, Chen G (2010) A sensitive aptasensor for adenosine based on the quenching of Ru(bpy)₃²⁺-doped silica nanoparticle ECL by ferrocene. *Chem Commun* 46(41):7751. doi:[10.1039/c0cc03225e](https://doi.org/10.1039/c0cc03225e)
134. Li H, Rothberg L (2004) Colorimetric detection of DNA sequences based on electrostatic interactions with unmodified gold nanoparticles. *Proc Natl Acad Sci USA* 101(39):14036–14039. doi:[10.1073/pnas.0406115101](https://doi.org/10.1073/pnas.0406115101)
135. Zheng M, Jagota A, Semke ED, Diner BA, McLean RS, Lustig SR, Richardson RE, Tassi NG (2003) DNA-assisted dispersion and separation of carbon nanotubes. *Nat Mater* 2(5):338–342. doi:[10.1038/nmat877](https://doi.org/10.1038/nmat877)
136. Lu C-H, Yang H-H, Zhu C-L, Chen X, Chen G-N (2009) A graphene platform for sensing biomolecules. *Angew Chem Int Ed* 48(26):4785–4787. doi:[10.1002/anie.200901479](https://doi.org/10.1002/anie.200901479)
137. Yang R, Tang Z, Yan J, Kang H, Kim Y, Zhu Z, Tan W (2008) Noncovalent assembly of carbon nanotubes and single-stranded DNA: an effective sensing platform for probing biomolecular interactions. *Anal Chem* 80(19):7408–7413. doi:[10.1021/ac801118p](https://doi.org/10.1021/ac801118p)
138. Zhao J, Chen G, Zhu L, Li G (2011) Graphene quantum dots-based platform for the fabrication of electrochemical biosensors. *Electrochem Commun* 13(1):31–33. doi:[10.1016/j.elecom.2010.11.005](https://doi.org/10.1016/j.elecom.2010.11.005)
139. Wang J, Wang L, Liu X, Liang Z, Song S, Li W, Li G, Fan C (2007) A gold nanoparticle-based aptamer target binding readout for ATP assay. *Adv Mater* 19(22):3943–3946. doi:[10.1002/adma.200602256](https://doi.org/10.1002/adma.200602256)
140. Wang W, Chen C, Qian M, Zhao XS (2008) Aptamer biosensor for protein detection using gold nanoparticles. *Anal Biochem* 373(2):213–219. doi:[10.1016/j.ab.2007.11.013](https://doi.org/10.1016/j.ab.2007.11.013)
141. Wang L, Zhu J, Han L, Jin L, Zhu C, Wang E, Dong S (2012) Graphene-based aptamer logic gates and their application to multiplex detection. *ACS Nano* 6(8):6659–6666. doi:[10.1021/nn300997f](https://doi.org/10.1021/nn300997f)
142. Zhu Z, Tang Z, Phillips JA, Yang R, Wang H, Tan W (2008) Regulation of singlet oxygen generation using single-walled carbon nanotubes. *J Am Chem Soc* 130(33):10856–10857. doi:[10.1021/ja802913f](https://doi.org/10.1021/ja802913f)
143. Tang D, Tang J, Li Q, Su B, Chen G (2011) Ultrasensitive aptamer-based multiplexed electrochemical detection by coupling distinguishable signal tags with catalytic recycling of DNase I. *Anal Chem* 83(19):7255–7259. doi:[10.1021/ac201891w](https://doi.org/10.1021/ac201891w)
144. Lei J, Ju H (2012) Signal amplification using functional nanomaterials for biosensing. *Chem Soc Rev* 41(6):2122. doi:[10.1039/c1cs15274b](https://doi.org/10.1039/c1cs15274b)
145. Chiu T-C, Huang C-C (2009) Aptamer-functionalized nano-biosensors. *Sensors* 9(12):10356–10388. doi:[10.3390/s91210356](https://doi.org/10.3390/s91210356)
146. Moore P (2005) PCR: replicating success. *Nature* 435(7039):235–238. doi:[10.1038/435235a](https://doi.org/10.1038/435235a)
147. Kim J, Easley CJ (2011) Isothermal DNA amplification in bioanalysis: strategies and applications. *Bioanalysis* 3(2):227–239. doi:[10.4155/bio.10.172](https://doi.org/10.4155/bio.10.172)

148. Eisenstein BI (1990) The polymerase chain reaction. A new method of using molecular genetics for medical diagnosis. *N Engl J Med* 322(3):178–183. doi:[10.1056/NEJM199001183220307](https://doi.org/10.1056/NEJM199001183220307)
149. Liao S, Liu Y, Zeng J, Li X, Shao N, Mao A, Wang L, Ma J, Cen H, Wang Y, Zhang X, Zhang R, Wei Z, Wang X (2010) Aptamer-based sensitive detection of target molecules via RT-PCR signal amplification. *Bioconjug Chem* 21(12):2183–2189. doi:[10.1021/bc100032v](https://doi.org/10.1021/bc100032v)
150. Fredriksson S, Gullberg M, Jarvius J, Olsson C, Pietras K, Gustafsdottir SM, Ostman A, Landegren U (2002) Protein detection using proximity-dependent DNA ligation assays. *Nat Biotechnol* 20(5):473–477. doi:[10.1038/nbt0502-473](https://doi.org/10.1038/nbt0502-473)
151. Pai SS, Ellington AD (2009) Using RNA aptamers and the proximity ligation assay for the detection of cell surface antigens. *Methods Mol Biol* 504:385–398. doi:[10.1007/978-1-60327-569-9_21](https://doi.org/10.1007/978-1-60327-569-9_21)
152. Kim J, Hu J, Sollie RS, Easley CJ (2010) Improvement of sensitivity and dynamic range in proximity ligation assays by asymmetric connector hybridization. *Anal Chem* 82(16):6976–6982. doi:[10.1021/ac101762m](https://doi.org/10.1021/ac101762m)
153. Lizardi PM, Huang X, Zhu Z, Bray-Ward P, Thomas DC, Ward DC (1998) Mutation detection and single-molecule counting using isothermal rolling-circle amplification. *Nat Genet* 19(3):225–232. doi:[10.1038/898](https://doi.org/10.1038/898)
154. Miao P, Ning L, Li X, Li P, Li G (2012) Electrochemical strategy for sensing protein phosphorylation. *Bioconjugate Chem* 23(1):141–145. doi:[10.1021/bc200523p](https://doi.org/10.1021/bc200523p)
155. Zhao W, Ali MM, Brook MA, Li Y (2008) Rolling circle amplification: applications in nanotechnology and biodetection with functional nucleic acids. *Angew Chem Int Ed* 47(34):6330–6337. doi:[10.1002/anie.200705982](https://doi.org/10.1002/anie.200705982)
156. Lee J, Icoz K, Roberts A, Ellington AD, Savran CA (2010) Diffractometric detection of proteins using microbead-based rolling circle amplification. *Anal Chem* 82(1):197–202. doi:[10.1021/ac901716d](https://doi.org/10.1021/ac901716d)
157. Cho EJ, Lee J-W, Ellington AD (2009) Applications of aptamers as sensors. *Annu Rev Anal Chem* 2(1):241–264. doi:[10.1146/annurev.anchem.1.031207.112851](https://doi.org/10.1146/annurev.anchem.1.031207.112851)
158. Yang L, Fung CW, Cho EJ, Ellington AD (2007) Real-time rolling circle amplification for protein detection. *Anal Chem* 79(9):3320–3329. doi:[10.1021/ac062186b](https://doi.org/10.1021/ac062186b)
159. Xu Y, Lunnen KD, Kong H (2001) Engineering a nicking endonuclease N. AlwI by domain swapping. *Proc Natl Acad Sci USA* 98(23):12990–12995. doi:[10.1073/pnas.241215698](https://doi.org/10.1073/pnas.241215698)
160. Xu W, Xue X, Li T, Zeng H, Liu X (2009) Ultrasensitive and selective colorimetric DNA detection by nicking endonuclease assisted nanoparticle amplification. *Angew Chem Int Ed* 48(37):6849–6852. doi:[10.1002/anie.200901772](https://doi.org/10.1002/anie.200901772)
161. Liu Z, Zhang W, Zhu S, Zhang L, Hu L, Parveen S, Xu G (2011) Ultrasensitive signal-on DNA biosensor based on nicking endonuclease assisted electrochemistry signal amplification. *Biosens Bioelectron* 29(1):215–218. doi:[10.1016/j.bios.2011.07.076](https://doi.org/10.1016/j.bios.2011.07.076)
162. Li J, Fu H-E, Wu L-J, Zheng A-X, Chen G-N, Yang H-H (2012) General colorimetric detection of proteins and small molecules based on cyclic enzymatic signal amplification and hairpin aptamer probe. *Anal Chem* 84(12):5309–5315. doi:[10.1021/ac3006186](https://doi.org/10.1021/ac3006186)
163. Jie G, Wang L, Yuan J, Zhang S (2011) Versatile electrochemiluminescence assays for cancer cells based on dendrimer/CdSe–ZnS–quantum dot nanoclusters. *Anal Chem* 83(10):3873–3880. doi:[10.1021/ac200383z](https://doi.org/10.1021/ac200383z)
164. Zhu X, Zhao J, Wu Y, Shen Z, Li G (2011) Fabrication of a highly sensitive aptasensor for potassium with a nicking endonuclease-assisted signal amplification strategy. *Anal Chem* 83(11):4085–4089. doi:[10.1021/ac200058r](https://doi.org/10.1021/ac200058r)
165. Feng K, Kong R, Wang H, Zhang S, Qu F (2012) A universal amplified strategy for aptasensors: enhancing sensitivity through allostery-triggered enzymatic recycling amplification. *Biosens Bioelectron* 38(1):121–125. doi:[10.1016/j.bios.2012.05.008](https://doi.org/10.1016/j.bios.2012.05.008)
166. Zhang H, Li F, Dever B, Li X-F, Le XC (2012) DNA-mediated homogeneous binding assays for nucleic acids and proteins. *Chem Rev*. doi:[10.1021/cr300340p](https://doi.org/10.1021/cr300340p)

167. Fan Q, Zhao J, Li H, Zhu L, Li G (2012) Exonuclease III-based and gold nanoparticle-assisted DNA detection with dual signal amplification. *Biosens Bioelectron* 33(1):211–215. doi:[10.1016/j.bios.2012.01.003](https://doi.org/10.1016/j.bios.2012.01.003)
168. Zuo X, Xia F, Xiao Y, Plaxco KW (2010) Sensitive and selective amplified fluorescence DNA detection based on exonuclease III-aided target recycling. *J Am Chem Soc* 132(6):1816–1818. doi:[10.1021/ja909551b](https://doi.org/10.1021/ja909551b)
169. Xuan F, Luo X, Hsing IM (2012) Ultrasensitive solution-phase electrochemical molecular beacon-based DNA detection with signal amplification by exonuclease III-assisted target recycling. *Anal Chem* 84(12):5216–5220. doi:[10.1021/ac301033w](https://doi.org/10.1021/ac301033w)
170. Liu X, Freeman R, Willner I (2012) Amplified fluorescence aptamer-based sensors using exonuclease III for the regeneration of the analyte. *Chem Eur J* 18(8):2207–2211. doi:[10.1002/chem.2011103342](https://doi.org/10.1002/chem.2011103342)
171. Tong P, Zhang L, Xu J-J, Chen H-Y (2011) Simply amplified electrochemical aptasensor of ochratoxin A based on exonuclease-catalyzed target recycling. *Biosens Bioelectron* 29(1):97–101. doi:[10.1016/j.bios.2011.07.075](https://doi.org/10.1016/j.bios.2011.07.075)
172. Scrimin P, Prins LJ (2011) Sensing through signal amplification. *Chem Soc Rev* 40(9):4488. doi:[10.1039/c1cs15024c](https://doi.org/10.1039/c1cs15024c)
173. Zhu X, Yang J, Liu M, Wu Y, Shen Z, Li G (2013) Sensitive detection of human breast cancer cells based on aptamer–cell–aptamer sandwich architecture. *Anal Chim Acta* 764:59–63. doi:[10.1016/j.aca.2012.12.024](https://doi.org/10.1016/j.aca.2012.12.024)
174. Cao Y, Wang J, Xu Y, Li G (2010) Combination of enzyme catalysis and electrocatalysis for biosensor fabrication: Application to assay the activity of indoleamine 2,3-dioxygenase. *Biosens Bioelectron* 26(1):87–91. doi:[10.1016/j.bios.2010.05.019](https://doi.org/10.1016/j.bios.2010.05.019)
175. Song Y, Qu K, Zhao C, Ren J, Qu X (2010) Graphene oxide: intrinsic peroxidase catalytic activity and its application to glucose detection. *Adv Mater* 22(19):2206–2210. doi:[10.1002/adma.200903783](https://doi.org/10.1002/adma.200903783)
176. Gao L, Zhuang J, Nie L, Zhang J, Zhang Y, Gu N, Wang T, Feng J, Yang D, Perrett S, Yan X (2007) Intrinsic peroxidase-like activity of ferromagnetic nanoparticles. *Nat Nanotechnol* 2(9):577–583. doi:[10.1038/nnano.2007.260](https://doi.org/10.1038/nnano.2007.260)
177. Golub E, Pelosof G, Freeman R, Zhang H, Willner I (2009) Electrochemical, photoelectrochemical, and surface plasmon resonance detection of cocaine using supramolecular aptamer complexes and metallic or semiconductor nanoparticles. *Anal Chem* 81(22):9291–9298. doi:[10.1021/ac901551q](https://doi.org/10.1021/ac901551q)
178. Li W, Li J, Qiang W, Xu J, Xu D (2013) Enzyme-free colorimetric bioassay based on gold nanoparticle-catalyzed dye decolorization. *Analyst* 138(3):760. doi:[10.1039/c2an36374g](https://doi.org/10.1039/c2an36374g)
179. Zhang XB, Wang Z, Xing H, Xiang Y, Lu Y (2010) Catalytic and molecular beacons for amplified detection of metal ions and organic molecules with high sensitivity. *Anal Chem* 82(12):5005–5011. doi:[10.1021/ac1009047](https://doi.org/10.1021/ac1009047)
180. Vinkenborg JL, Karnowski N, Famulok M (2011) Aptamers for allosteric regulation. *Nat Chem Biol* 7(8):519–527. doi:[10.1038/nchembio.609](https://doi.org/10.1038/nchembio.609)
181. Yang Q, Nie Y, Zhu X, Liu X, Li G (2009) Study on the electrocatalytic activity of human telomere G-quadruplex–hemin complex and its interaction with small molecular ligands. *Electrochim Acta* 55(1):276–280. doi:[10.1016/j.electacta.2009.08.050](https://doi.org/10.1016/j.electacta.2009.08.050)
182. Zhu X, Zhang W, Xiao H, Huang J, Li G (2008) Electrochemical study of a hemin–DNA complex and its activity as a ligand binder. *Electrochim Acta* 53(13):4407–4413. doi:[10.1016/j.electacta.2008.01.042](https://doi.org/10.1016/j.electacta.2008.01.042)
183. Pelosof G, Tel-Vered R, Elbaz J, Willner I (2010) Amplified biosensing using the horseradish peroxidase-mimicking DNAzyme as an electrocatalyst. *Anal Chem* 82(11):4396–4402. doi:[10.1021/ac100095u](https://doi.org/10.1021/ac100095u)
184. Golub E, Freeman R, Willner I (2011) A hemin/G-quadruplex acts as an NADH oxidase and NADH peroxidase mimicking DNAzyme. *Angew Chem Int Ed* 50(49):11710–11714. doi:[10.1002/anie.201103853](https://doi.org/10.1002/anie.201103853)

185. Tang L, Liu Y, Ali MM, Kang DK, Zhao W, Li J (2012) Colorimetric and ultrasensitive bioassay based on a dual-amplification system using aptamer and DNAzyme. *Anal Chem* 84(11):4711–4717. doi:[10.1021/ac203274k](https://doi.org/10.1021/ac203274k)
186. Yuan Y, Yuan R, Chai Y, Zhuo Y, Ye X, Gan X, Bai L (2012) Hemin/G-quadruplex simultaneously acts as NADH oxidase and HRP-mimicking DNAzyme for simple, sensitive pseudobioenzyme electrochemical detection of thrombin. *Chem Commun* 48(38): 4621–4623. doi:[10.1039/c2cc31423a](https://doi.org/10.1039/c2cc31423a)
187. Zhu X, Cao Y, Liang Z, Li G (2010) Aptamer-based and DNAzyme-linked colorimetric detection of cancer cells. *Protein Cell* 1(9):842–846. doi:[10.1007/s13238-010-0110-2](https://doi.org/10.1007/s13238-010-0110-2)

Chapter 16

Engineering Aptamers for Biomedical Applications: Part II

Laura Cerchia, Luciano Cellai and Vittorio de Franciscis

16.1 Introduction

The last decade has witnessed an enormous advance in the identification of disease-associated molecular targets for the development of new therapeutic and imaging agents. Indeed, the development of high-affinity reagents to selectively target affected tissues and organs has led to substantial advantages in combating important life-threatening diseases, including cancer. Major hurdles are represented by the lack of efficient, safe, and specific delivery systems able to selectively target the diseased tissue or organs. Until now, monoclonal antibodies are considered to be the molecules of choice predominantly used for cell-specific targeting. Nucleic acid aptamers have been recently shown to represent a valuable alternative to antibodies because they couple the advantages of their chemical nature to the high specific binding of antibodies to their proper targets. Indeed, aptamers have similar binding affinities as monoclonal antibodies, and like antibodies, they can be used for the recognition and sometimes the inhibition of disease-associated proteins [1, 2]. On the other hand, aptamers have a number of unique properties that make them particularly interesting for diverse areas, not just as alternatives to antibodies, but as main tools of medical and analytical strategies. They are produced chemically in a readily scalable process, thus avoiding the use of animal cells and assuring an easy, relatively inexpensive, and rapid production with high batch fidelity. At difference of protein-based reagents that undergo irreversible denaturation, functional aptamers, once denatured, can be regenerated

L. Cerchia (✉) · V. de Franciscis
Istituto per l'Endocrinologia e l'Oncologia Sperimentale del CNR "G. Salvatore",
via Pansini 5 80131 Naples, Italy
e-mail: cerchia@unina.it

V. de Franciscis
e-mail: defranci@unina.it

L. Cellai
Istituto di Cristallografia, CNR 00015 Monterotondo Stazione, Rome, Italy

easily within minutes. Aptamers have shown no or low immunogenicity and are generally non-toxic [3, 4], which is an important advantage in comparison with antibodies for clinical applications requiring long period treatments.

Aptamers are short, structured single-stranded DNA or RNA able to bind, due to their specific three-dimensional shapes, with high affinity and specificity to a multitude of targets ranging from small chemical compounds to cells and tissues [1, 5–8]. They can be developed against almost any target protein through iterative cycles of *in vitro* screening of a combinatorial oligonucleotide library for target binding by a process named systematic evolution of ligands by exponential enrichment (SELEX) [9, 10]. Aptamers have a small size (ca. 15 kDa) which allows easy membrane penetration and short blood residence and can have been chemically modified to enhance their stability, bioavailability, and pharmacokinetics [11–13]. Furthermore, introduction of functional groups during the chemical synthesis of aptamers allows their subsequent derivatization with other molecules (nanocarriers, tracers for imaging, drugs). Aptamers can then perform therapeutic functions both acting as direct therapeutic agents and upon conjugation, as drug-targeting vectors, addressing drugs onto specific aptamer-sensitive targets [6, 7].

16.2 Aptamers Against Cell Surface Proteins as Delivery Systems: The Goal of Specificity

A great promise in developing specific molecular probes for disease biomarker discovery and for diagnostic and therapeutic applications is represented by the cell-SELEX strategy that allows us to select aptamers against even rare antigens if specifically expressed on living cells used as target for selection [6, 14–16]. This approach permits to select aptamers against cell surface transmembrane proteins, including receptor tyrosine kinase, in a physiological context, and can be carried out even when the purification of the target protein in native conformations can be difficult [17–22]. Furthermore, cell-SELEX can be developed without prior knowledge of the multiple proteins exposed on the surface of the target cells allowing the selection of aptamer ligands that specifically recognize a surface molecular signature specific of the cells.

As recently shown, when applied to cancer cell lines, cell-SELEX consents to select a set of aptamers that, by binding, distinguish with high accuracy even close tumor types in terms of malignancy, therapeutic response, metastatic potential, proliferation, and apoptotic rate, thus representing an ideal tool for supporting a more specific and selective antitumor therapy [6, 16, 18].

It has been reported that several aptamers by binding cell surface proteins are transported through the plasma membrane, thus acting as specific delivery agents for a variety of imaging and therapeutic agents including RNAs (siRNAs, miRNAs, antagomiRs) whose activity depends on their effective delivery to intracellular compartments [6, 23–26]. This approach combines the cell-type-specific

expression of proteins, as targets of therapeutic value, on the surface of cell populations, to the high affinity and specificity of aptamers versus such proteins. This means that aptamers may function as specific recognition ligands for targeted proteins exposed on the surface of the targeted cell type. Thus, aptamers can permit that conjugated reagents impart their therapeutic effect onto a specific subset of cells. Since non-targeted cells should not be exposed to the conjugated reagent, the risk of unwanted side effects is largely reduced.

The ability of aptamers to penetrate from outside the target cell to the cytosol, thus assisting the tissue-specific internalization of transported molecules, becomes crucial when an effective delivery strategy for those molecules is still lacking, as in the case of therapeutic antisense, siRNA or miRNA (ONs). Indeed, while the therapeutic value of sequence-specific gene silencing with small ncRNA is being evaluated in preclinical and clinical trials, the highly negatively charged RNA has the problem of requiring transport across cell membranes to the cytosol. Consequently, the development of vectors for specific ncRNA delivery is one of the key hurdles to overcome before RNA-based therapeutics can achieve widespread clinical use. A variety of natural and synthetic nanocarriers, including liposomes, micelles, exosomes, synthetic organic polymers, and inorganic materials, have been developed for the delivery of short ncRNAs, and some of them have entered clinical evaluation. However, these carriers are unable to specifically target a given cell or tissue unless driven by a recognition moiety as MoAbs or aptamers.

Several variants of the SELEX approach have been recently used by us and others to generate aptamers as specific ligands of membrane-bound receptors [19, 20, 27–31] or to select aptamers for cell-specific internalization [22]. These aptamers have been shown to be invaluable reagents for cell-specific targeting able to distinguish target cells both grown *in vitro* and in mouse xenograft *in vivo*. Some aptamers revealed as potent antagonist of the transmembrane receptor targets, and more recently, cell-specific aptamers have proved to mediate specific targeting of nanoparticles, anticancer drugs, toxins, enzymes, radionuclides, virus, and siRNAs (Fig. 16.1). The cargoes are attached to the aptamers either by direct conjugation or by using delivery carrier nanoparticles for loading [25].

16.3 The Conjugation of Aptamers

Biomolecules can be conjugated with other biomolecules, forming bioconjugates, and with chemical entities of a different nature, giving rise to assemblies endowed with new properties. In the field of medicinal chemistry, the goal of conjugation is, for example, the enhancement of drug potency, a more precise and effective targeting, an improvement in absorption, distribution, metabolism, elimination, and toxicity, the development of new therapeutic systems, the development of novel diagnostics and biosensors. Common components of conjugates are small molecules, such as drugs, biotin, fluorescent dyes, and larger molecules, such as proteins, oligosaccharides, nucleic acids, synthetic polymers, and also nanomaterials.

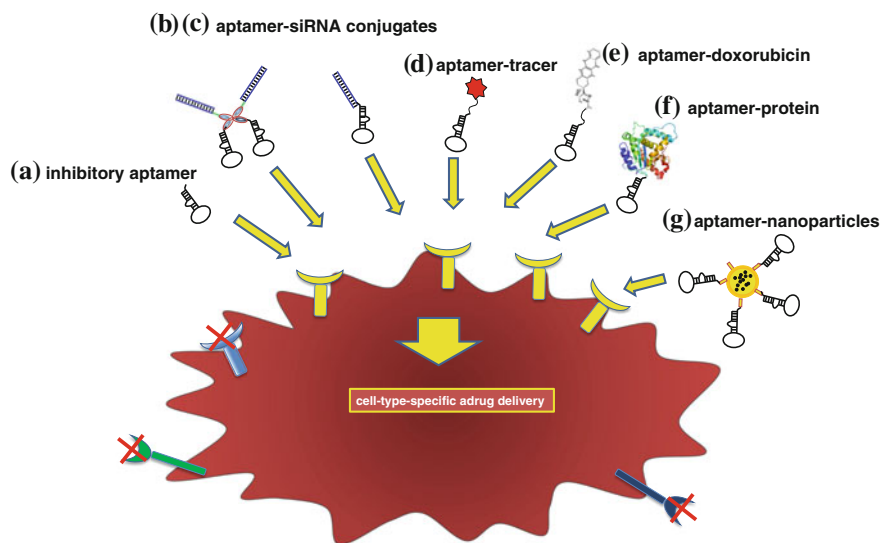


Fig. 16.1 Aptamers against cell surface proteins. Aptamers can act both as direct antagonist of the transmembrane receptor targets **a** and as delivery agents (**b–g**). **b** Aptamer–streptavidin–siRNA conjugates; **c** aptamer–siRNA chimeras; **d** aptamer–radionuclide/fluorescent agent conjugates; **e** aptamer–doxorubicin; **f** aptamer–protein conjugates; **g** aptamer–nanoparticles–drug conjugates

Aptamers are commonly synthesized by solid-phase chemical synthesis; therefore, chemical conjugation is possible at any position in the molecule, differently from proteins and peptides that can accept conjugation only on specific residues.

Common strategies for the post-synthesis, covalent bioconjugation of aptamers exploit the coupling of a terminal group like an amino group with a reactive succinimidyl ester or of a sulfhydryl group with a reactive maleimide.

Common strategies for the post-synthesis, non-covalent bioconjugation of aptamers are mainly based on interactions regulating nucleic acids and proteins structural assembly and association, involving the use of post-synthetic linkers, of sticky ends, or similar ways.

16.3.1 Conjugation of Aptamers with siRNA/miRNA

Because of their nucleic acid nature, the rational design of structured conjugates of aptamers with siRNA, with miRNAs, or even with larger therapeutic RNA-based molecules is greatly simplified. Recently, different groups have constructed distinct aptamer–siRNA conjugates for successful delivery of siRNA into target cells by employing diverse strategies to realize the chimeric molecules. Since aptamers

are commonly prepared by automated synthesis, they can be directly fused with their partner component in the chimeric molecule by the design and synthesis of single longer molecules. Additionally, particular labels, like many dyes or biotin, can be directly added as labeled phosphoramidite within the same process. In addition, aptamers and siRNA molecules can be assembled via a protein connector, or alternatively, completely RNA-based chimeric molecules can be generated by means of several approaches (see below).

16.3.1.1 Streptavidin–Aptamer–siRNA Conjugates

One of the first studies on the development of aptamer–siRNA conjugates involved the non-covalent conjugation of a 27-mer siRNA-targeting laminin A/C and GAPDH genes with the antiprostate-specific membrane antigen (PSMA) A9 RNA aptamer via a streptavidin bridge [32]. The siRNA aptamer and the RNA aptamer were chemically conjugated with biotin. Further, to enhance siRNA release in the cytoplasm, a reducible disulfide linker was designed between the sense strand of siRNA and the biotin group. In cell-based assays, the resulting conjugates were efficacious in silencing target genes at levels comparable with what observed with conventional lipid-based reagents.

16.3.1.2 Aptamer–siRNA/MiRNA Conjugates Consisting Only of RNA Components

Research has gone beyond with the aim to develop completely RNA-based delivery methods, thus reducing the various side effects associated with reagents such as proteins. The first report of a delivery system consisting only of RNA components was by McNamara et al. [33]. They described an approach in which the anti-PSMA A10 aptamer was covalently conjugated at the 3' end to the 21-mer sequence complementary to the antisense strand of the siRNA and the chimeras were formed by annealing to the siRNA antisense strand. The resulting aptamer–siRNA molecules were shown to be selectively internalized into PSMA-positive cells and to effectively target the tumor survival genes polo-like kinase 1 and BCL-2. Further developments, including truncation of the aptamer portion, swapping of the sense and antisense strands of the siRNA portion, and addition to the chimera of a two-nucleotide 3'-overhang and of a PEG tail, produced analogous chimeric RNAs displaying enhanced silencing activity and specificity, and optimized in vivo kinetics [34]. By applying the same approach, PSMA aptamer–siRNA fusions were generated to target two key components of the nonsense-mediated mRNA decay (NMD) [35]. Tumor-targeted NMD inhibition forms the basis of a clinically feasible approach to enhance the antigenicity of disseminated tumors leading to their immune recognition and rejection.

Again by using the anti-PSMA A10 aptamer as a vector, Wullner et al. succeeded in generating bivalent aptamer–siRNA constructs in which the siRNA

against the eukaryotic elongation factor was used as a linker to join the two aptamers, or alternatively, the siRNAs were appended onto the 3' ends of each aptamer [36].

Most work in the generation of aptamer–siRNA chimeric molecules has been performed by the group of Rossi JJ by using the 2'-F-modified RNA aptamer targeting the HIV-1 envelope glycoprotein gp120 as a vector. The gp-120 aptamer was covalently linked to siRNAs that target the HIV-1 *tat/rev* common exon, thus generating a novel anti-gp120 aptamer–siRNA chimera in which both components function as anti-HIV agents, thus showing a dual inhibitory function [37]. Further, a highly versatile approach was developed by the same group by using a G-C-rich dsRNA of 16 nucleotides “stick” as the scaffold to link the aptamer and the siRNAs. The two complementary sticky sequences were chemically conjugated at the 3' end of the aptamer and of one of the two siRNA strands, thereby allowing the aptamer and siRNA portions to be non-covalently conjugated via Watson–Crick base-pairing by simple mixing. Both aptamer and siRNA were separated from each sticky strand by a flexible seven-unit three-carbon linker. The assembly proved efficacious both *in vitro* and *in vivo* [38, 39]. The functional assembly “aptamer–stick–siRNA” displayed a great versatility offering the possibility to easily combine different siRNAs to the vector aptamer, thus envisaging the possibility of using these chimeras for an antiretroviral siRNA combinatorial therapy [26, 40].

Recently, by using the delivery stick approach, we have generated completely RNA-based chimeric molecules containing internalizing aptamers coupled to therapeutic miRNAs that are down-regulated in human tumors and whose expression results in selective tumor growth inhibition. We have shown that when applied to cells expressing the specific aptamer target, the chimeric molecules are internalized and processed by Dicer, thus increasing miRNA cellular level and inhibiting miRNA target protein (our personal communication).

Two approaches have been reported to generate RNA-based chimeric molecules by directly fusing the aptamer with its partner component in a single longer molecule. In the first construct, Ni et al. [41] linked a short hairpin RNA against the DNA-activated protein kinase to a truncated A10 aptamer generating a single intact nuclease-stabilized molecule. The 3'-terminus of the A10 aptamer was conjugated to the passenger (sense) strand, followed by a 10-mer loop sequence and then by the guide or silencing (antisense) strand of the siRNA. In the second construct, chimeric molecules containing internalizing antimucin 1 (MUC1) aptamer fused to therapeutic miR-29b palindromic sequence were generated by direct synthesis. Applied to cells expressing the specific aptamer target, the chimeric molecules proved to be internalized and to increase miRNA cellular level [42].

With the increasing development of the conjugation strategies, the list of aptamers against surface epitopes that are being used as delivery agents for siRNA/miRNA is growing rapidly and now includes, in addition to PSMA and gp120 aptamers, those against CD4 [43], epidermal growth factor receptor 2 (HER2) [22], MUC 1 [30, 42], B cell-activating factor (BAFF) receptor (BAFF-R) [44], transferrin receptor [45], (see Table 16.1).

Table 16.1 Aptamers as delivery agents for siRNA/miRNA

Aptamer composition	Target	siRNA/miRNA delivery	References
RNA, 2'-F-Py	PSMA	siRNA	[32–36, 41]
RNA, 2'-F-Py	PSMA	miRNA	[51]
RNA, 2'-F-Py	gp120	siRNA	[37–40]
RNA, 2'-F-Py	CD4	siRNA	[43]
RNA, 2'-F-Py	HER2	siRNA	[22]
DNA	Mucin 1	miRNA	[30, 42]
RNA, 2'-F-Py	TfR	siRNA	[45]
RNA, 2'-F-Py	BAFF-R	siRNA	[44]

16.3.2 Covalent Conjugation of Aptamers with Drugs

Conjugation of aptamers with drugs can be used as a tool favoring specific cell targeting and internalization, in particular for drugs like antitumor drugs, which often lack cell specificity and produce life-threatening toxic side effects in patients.

Doxorubicin is the most utilized anticancer drug against neoplasms including acute lymphoblastic and myeloblastic leukemias, and malignant lymphomas, although producing heavy side effects among which cumulative cardiac damage. In order to improve its therapeutic potential, doxorubicin was covalently conjugated to DNA aptamer Sgc8c [46], selected for human T cell ALL CCRF-CEM cell lines, that can act as a drug carrier, targeting protein tyrosine kinase 7 (PTK7), a transmembrane receptor highly expressed in CCRF-CEM cells. To this aim, doxorubicin was reacted with N-(ϵ -maleimidocaproic acid) hydrazide to yield the C-13 (6-maleimidocaproyl) hydrazone derivative and then combined with the 5'-thiol-modified sgc8c DNA, prepared by automated synthesis. The linked sgc8c aptamer prevents the non-specific uptake of doxorubicin and decreases cellular toxicity to non-target cells.

However, despite the fact that anti-CEM/PTK7 aptamer has been reported to bind specifically to leukemia cell lines thus indicating PTK7 as a new biomarker specific for leukemia cells, Li et al. by examining how the aptamer performed with additional cell lines, which were not of hematopoietic origin, showed that it is possible that the aptamer instead of a specific binding to PTK7 may identify a propensity for adherence, thus needing further investigation [47].

16.3.3 Conjugation of Aptamers with Synthetic Polymers

Conjugation of biomolecules to synthetic polymers, such as polyethylene glycol (PEG), is used to increase the hydrodynamic volume to molecular weight ratio and thus improve their performance as therapeutics influencing their permanence in the body. Aptamers are relatively small, and charged molecules subject to rapid renal elimination and PEGylation of aptamers can overcome this potential limitation.

PEG shows low toxicity, non-immunogenicity, and high solubility in water and is commercially available in various configurations (linear, branched, or comb-shaped) and molecular weights and with a large variety of terminal functional groups suitable for conjugation.

PEGylated aptamers have been prepared by coupling the activated polymer to amino-modified aptamers [48]. In addition, comb polymers of PEG acrylate containing a pyridyl disulfide terminus have been reversibly conjugated to siRNAs [49].

As an example of more recent PEGylation chemistry, a 3'-thiol-modified (disulfide protected) 25-nucleotide DNA aptamer, selected against the protein core of MUC1 glycoprotein, was successfully conjugated via a maleimide–thiol reaction to a range of maleimide-activated PEGs. The affinity of the PEG–aptamer conjugate for the target resulted to vary according to the structure and conformation of the synthetic polymer [50].

PEG was also used as a spacer and linker for a second polymer, polyamidoamine (PAMAM), to construct a multicomponent, multifunction aptamer conjugate. PAMAM, due to the positively charged amino groups present on its surface, can bind, transport, and deliver therapeutic nucleic acids like siRNA and miRNA. The multicomponent conjugate was accomplished by combining first PEG with PAMAM and then adding aptamer A10-3.2, a shortened version (39 nucleotides) of PSMA-specific aptamer A10, more easily synthesized, more stable, and more efficient than A10 itself. In details, PAMAM dendrimer was reacted with α -maleimidyl- ω -N-hydroxysuccinimidyl polyethylene glycol to give PAMAM/PEG conjugate further reacted with sulfhydryl A10-3.2. The conjugate PAMAM/PEG/ aptamer was used as a vehicle for the safe and effective target delivery of miR-15a and miR-16-1, identified as tumor suppressor genes in prostate cancer. These miRNA/PAMAM/PEG/aptamer conjugates proved ca. fivefold more active than miRNA/PAMAM/PEG conjugates, lacking the aptamer, in viability assays on PSMA-positive human prostate adenocarcinoma (LNCaP) cells [51].

16.3.4 Conjugation of Aptamers with Nanoparticles

The integration of cell-type-specific aptamers with nanocarriers like liposomes, micelles, synthetic polymer nanoparticles, carbon nanotubes, quantum dots (QDs), and other nanoparticles can produce new, versatile, and multifunctional specific delivery vehicles. Aptamer-functionalized nanoparticles have a size in the mid-nanometer range, allowing preferential accumulation in target tissues and organs through an enhanced permeability and retention effect, facilitating cellular entry by endocytosis. Conjugation with nanocarriers can also reduce renal clearance and improve circulation half-life and biodistribution in vivo [26].

16.3.4.1 Conjugation of Aptamers with Synthetic Polymer Nanoparticles

Aptamer–nanoparticles were prepared by first synthesizing a poly(lactic acid) (PLA)-block-PEG copolymer, with a terminal carboxylic acid functional group (PLAPEG-COOH), by ring-opening polymerization of the D,L-lactic acid dimeric lactide and OH-PEG3400-COOH. Nanoparticles were then prepared using the water-in-oil-in-water solvent evaporation procedure (double-emulsion method). These nanoparticles ($M_n = 10,500$) carry carboxylic acid groups available for covalent conjugation to amino-modified aptamers, forming a negative charge surface, which may minimize non-specific interactions with the negatively charged aptamers. The presence of PEG on particle surface enhances circulating half-life. The nanoparticles were conjugated with 3'-NH₂-modified A10 RNA aptamer-targeting PSMA and the resulting bioconjugates proved to efficiently target and take up by PSMA-expressing prostate LNCaP cells [52].

16.3.4.2 Conjugation of Aptamers to Drug Carrier Synthetic Polymer Nanoparticles

An aptamer–nanoparticles-based delivery system, targeting the transmembrane MUC1 protein, overexpressed in most malignant adenocarcinomas, has been realized for delivering the anticancer drug paclitaxel to MUC1-positive tumor cells. To this aim, the S2.2, 25-nucleotide MUC1 aptamer was synthesized as chimeric ON with a 3'-NH₂-modified 73-nucleotide spacer and covalently conjugated to a nanoparticle made of poly(lactic-co-glycolic-acid) (PLGA, 50:50, MW = 16,000). The paclitaxel–Apt–NP assembly was realized using the emulsion/evaporation method. The MUC1 Apt–NP system proved to enhance the delivery of paclitaxel to MUC1-positive MCF-7 cells in vitro [53].

16.3.4.3 Conjugation of Aptamers to Self-assembling Nanoparticles

Self-assembling nanoparticles, able to deliver siRNA and other therapeutics to targeted cells, can be obtained by fusion with the packaging phi29 motor RNA (pRNA). For example, a CD4 aptamer and a siRNA against survivin were covalently fused with pRNA and assembled into dimers that proved to specifically bind to CD4-expressing cells and to be internalized, knocking down the target transcripts [54].

16.3.4.4 Conjugation of Aptamers to Form Micelles

An amphiphilic block copolymer made of a hydrophilic oligonucleotide and a hydrophobic polymer, in aqueous solution, can self-assemble into a spherical or a

nanorod-like micelle. An aptamer with a hydrophobic polymeric tail attached to its end can form a highly ordered micelle-like structure, in which the aptamer not only acts as the building block for the nanostructure, but also performs the recognition of its specific target. Furthermore, the dense packing of the aptamer in the micelle can greatly improve binding affinity to its specific targets. Micelles are also considered to be dynamic and soft materials, which may interact with the dynamic lipid bilayer of the cell membrane favoring drug delivery.

Aptamer TDO5, specific to Ramos cells (a B-cell lymphoma cell line), generated by automated synthesis, has been directly fused to a PEG linker carrying a diacyl lipid tail. This TDO5 amphiphilic conjugate self-assembled into a spherical micelle structure, as demonstrated by transmission electron microscopy (TEM). The average diameter of TDO5–micelles, estimated to contain 1,000 copies of conjugate unit, resulted 68 ± 13 nm, consistent with the hydrodynamic diameter of 67.22 nm measured by dynamic light scattering. The TDO5–micelles demonstrated extremely rapid recognition of the target cells, were found to enhance the binding capability of otherwise low-affinity TDO5 aptamer at physiological temperature, and helped cell internalization. Additionally, the aptamer–micelles displayed low k_{off} once on the cell membrane, high sensitivity, low critical micelle concentration values, great dynamic specificity in flow channel systems that mimic drug delivery in a flowing system, thereby appearing to function as an efficient detection/delivery vehicle in the biological living system [55].

16.3.4.5 Conjugation of Aptamers with Liposomes

Liposomes can be loaded with pharmaceuticals, in particular highly toxic or poorly soluble chemotherapeutics. A therapeutic aptamer–liposome (100 nm diameter) drug delivery system was molecularly engineered by assembling hydrogenated soy phosphatidylcholine, cholesterol, methoxy poly-(ethylene glycol)-distearoyl-phosphatidyl-ethanolamine and maleimide-terminated poly-(ethylene glycol)-distearoyl-phosphatidyl-ethanolamine, in a second step covalently linked to 3'-thiol-modified sgc8 aptamer, which has high binding affinity toward leukemia CEM-CCRF cells. The liposome system proved stabilized by PEG coating and able to bind target cells and deliver a model drug [56].

16.3.4.6 Conjugation of Aptamers with Gold Nanoparticles

Gold nanoparticles (AuNPs) hold great promise for biological and medicinal applications. AuNPs can be synthesized by reducing tetrachloroauric acid with trisodium citrate. AuNPs can be characterized by UV–vis spectroscopy and TEM. The concentration of the AuNPs can be calculated according to Beer's law using an extinction coefficient of $2.4 \times 10^8 \text{ M}^{-1} \text{ cm}^{-1}$ at 520 nm for the 12 nm AuNPs [57].

They have unique colorimetric, conductivity, and nonlinear optical properties, easy surface conjugation with biological entities, high stability, biological compatibility, controllable morphology, and size dispersion. On the basis of their unique surface plasmon resonance (SPR) property, dispersed AuNPs appear red, whereas their aggregates appear purple allowing target-induced colorimetric assays generally based on their assembly or disassembly associated with target recognition [58].

Detection methods relying on the conjugation of ONs with AuNPs show more sensitivity than conventional assays based on ONs probes, so that AuNPs functionalized in particular with an aptamer (Apt) provide a powerful platform for targeted delivery, detection, and therapy. Some tests based on Apt-AuNPs have been commercialized [59].

AuNPs can be directly functionalized with thiolated aptamers and other thiolated ONs by chemisorption. With the introduction of the Apt-AuNPs platform, many kinds of analytes have been monitored on the basis of different mechanisms.

According to a bridging mechanism, AuNPs modified with aptamers for platelet-derived growth factors (PDGFs) produced a highly specific sensing system with detection limits of 3.2 nM [60]. Aggregation and redispersion of AuNPs connected to specific color changes can be achieved by inducing loss or screening of surface charges [61]. Assays based on the process of AuNPs disassembly can be performed with ODNs-AuNPs first cross-linked by an aptamer sequence to form aggregates that are forced to dissociate upon binding of a specific target [62].

Aptamers linked to the surface of solid AuNPs can result hindered in assuming the functional conformation with respect to free solution, and their target recognition ability can result impaired. To overcome this problem, AuNPs have been assembled with ONs complementary (cON) to a non-functional part of the aptamer sequence, allowing the subsequent hybridization of the aptamer, in this way leaving the functional part more exposed to solution and free to assume the appropriate conformation [63]. Taking advantage of the highly efficient fluorescence quenching properties of AuNPs for proximately fluorescent dyes through energy transfer processes (FRET) [64], this method of bioconjugation was applied to perform the multiplex detection of small molecules (adenosine, potassium, and cocaine) through the utilization of aptamer-based multicolor fluorescent AuNPs probes.

The strategy exploiting a 3'-FAM-Apt:cON-AuNPs probe has been applied to the monitoring of a protein, on the basis of the hybrid disruption and release of the aptamer from the Apt:cON-AuNPs assembly upon binding by its target protein. Upon hybridization, the fluorescence of the 3'-FAM-Apt is quenched through FRET by the AuNP, while in the presence of the target protein, the aptamer is induced to fold, fitting to its target and disrupting the hybrid, which causes 3'-FAM-Apt to be released and the generation of a fluorescence signal.

Recombinant human erythropoietin- α (rHuEPO- α) has been monitored by a simple signal transduction system made of 3'-FAM-modified aptamer (35 nt) hybridized to a partially complementary ON linked to AuNPs through a 5'-thiol linker. This simple method has shown high selectivity. It was observed that the

cON length and composition should be optimized; the average cON loading attached to each AuNPs can be estimated [65]; the Apt:cODN-AuNPs probe should be equilibrated in solution with, for example, BSA for preventing non-specific binding with any possible interfering proteins.

16.3.4.7 Conjugation of Aptamers to Quantum Dot Nanoparticles

Among aptamer–siRNA chimeric delivery systems, those based on inorganic nanoparticles are positively charged; consequently, negatively charged aptamer–siRNA may collapse onto their cationic carriers, thus affecting aptamer conformation and selective binding. To overcome this problem, aptamer–siRNA chimeras were linked onto quantum dot (QD) nanoparticles following a two-step approach. siRNA molecules (targeting eGFP), modified with a thiol reactive group, were first adsorbed onto polyethylene imine (PEI)-coated nanoparticles, and then, thiol-modified aptamers (targeting PSMA) were added to form aptamer–siRNA chimeras through the thiol-disulfide exchange reaction. The non-covalent adsorption facilitates the release of siRNA from the nanocarrier inside cells; additionally, neutralizing some of the positive charges on the nanoparticle surface, their interaction with aptamers is weakened, thus helping to retain aptamer properties [66]. Highly stable, water-soluble QDs were prepared by molecular self-assembly of hydrophobic QDs with amphiphilic copolymers poly (maleic anhydride-alt-1-tetradecene). Adding carbodiimide-activated QDs to polyethyl-eneimine yields single non-aggregated PEI-QDs. QDs excellent photoluminescent properties allows real-time monitoring.

Aptamer–siRNA chimeras directly adsorbed in one step onto nanoparticles elicited only ca. 8 % improvement in selective gene silencing with respect to non-targeted nanoparticle siRNA complexes, while the two-step approach produced 34 % more silenced cells.

16.3.4.8 Conjugation of Aptamers to Magnetic Nanoparticles

Biocompatible aptamer-conjugated magnetic nanoparticles (ACMNPs) have been prepared by conjugating streptavidin-coated iron oxide nanoparticles with biotin-labeled aptamers and used for cancer cell detection and pattern recognition [67]. In fact, binding of the aptamer to target cells produces an aggregation of dispersed ACMNPs and this variation determines a decrease in spin–spin relaxation time (T_2) of adjacent water protons that can be measured by an NMR analyzer. The ACMNPs can detect as few as 10 cancer cells in a 250 μ L sample; their specificity and sensitivity are maintained also in complex biological samples. Since cell lines more abundant in receptors produce comparatively larger T_2 variations, distinct recognition patterns can be associated with different levels of receptor expression in different cell lines. ACMNPs can be arranged in arrays able to recognize patterns of different types of cancer cells.

A nanosurgeon system was prepared by modifying the surface of commercially available carboxylated dextran-coated MNPs, with a diameter of 200 ± 50 nm, through conjugation, via the carbodiimide chemistry, with a 5'-NH₂-modified GB-10 aptamer, specifically targeting human glioblastoma cell lines. Aptamer-conjugated magnetic nanoparticles, controlled by an externally applied three-dimensional rotational magnetic field, proved able to perform selective surgical actions on target cells in in vitro studies [68].

16.3.4.9 Conjugation of Aptamers to Silica-Coated Magnetic Nanoparticles

ACNPs made of silica-coated magnetic (MNPs) and fluorophore-doped silica nanoparticles (FNPs) have been conjugated to highly selective aptamers to detect and extract targeted cells in a variety of matrices, according to dual nanoparticles-based assays. Following to an accurate process of optimization, the best performing ACNPs proved to be the 60 nm MNPs, with the most efficient capacity of extraction, and the tetramethylrhodamine-doped FNPs, showing the greatest signal-to-background ratio. The use of multiple aptamer sequences on the NPs increased sensitivity without impacting selectivity, allowing us to reach a theoretical limit of detection of 6.6 cells. This approach can be adapted for different types of cancer cells [69].

16.3.5 Conjugation of Aptamers with ^{99m}Tc for Single-Photon Emission Computed Tomography

Despite the fact that to date only a few aptamers have been developed as targeting agents in imaging modalities, very promising examples indicate their great potential in this field. Among them, the TTA1 aptamer directed against tenascin-C (TN-C) [70] has been extensively modified for performing single-photon emission computed tomography (SPECT), an imaging technique using gamma rays that allows for visualization of tumors at a spatial resolution in the submillimeter range. Indeed, to improve aptamer in vivo stability and guarantee a good blood persistence leading to sufficient signal-to-noise ratios for imaging, aptamer backbone (2'-F-Py containing RNA, 39 mer) has been further modified with the addition of 2'-OMe purine substitutions, a thymidine cap at the 3' end and locked nucleic acids (LNA) in not binding critical stem [71]. The TTA1 derivative has been conjugated with mercapto-acetyl diglycine (MAG2) chelate via a hexyl-aminolinker at the 5' end, labeled with ^{99m}Tc and administrated by intravenous injection in murine xenograft models of glioblastoma and breast cancer [48]. Data showed a rapid renal and hepatobiliary clearance, 0.2 and 1.5 %ID/g at 3 h, respectively, and a rapid tumor penetration (6 % injected dose at 60 min). Tumor retention was

urable (2.7 % injected dose at 60 min), and the tumor-to-blood signal was significantly high, thus enabling clear tumor imaging.

Also, DNA aptamers that target MUC1 have been labeled with ^{99m}Tc [72]. Four types of chelating agents have been coupled to the aptamer to generate novel complexes for diagnostic imaging: MetCyc, MAG3, DOTA, and porphyrin. Different from the monomeric Tc-MetCyc-Apt and Tc-MAG3-Apt, the tetrameric compounds, DOTA and porphyrin, conjugated with ^{99m}Tc were able to grab four aptamer molecules modified at 5' by inserting amine groups to facilitate coupling with the ligands carboxylic terminations and at 3' ends to protect against nuclease degradation. Despite the fact that the tetrameric complexes showed improved tumor retention and pharmacokinetic properties compared to the monomeric compounds, biodistribution studies have shown the presence of free Tc in the stomach and large intestine highlighting some kind of lack in the Tc-aptamer binding [73]. In another study by Pieve et al. [74], anti-MUC1 aptamers have been successfully conjugated to MAG2 chelator and labeled with ^{99m}Tc to analyze biodistribution of the aptamer in MCF7 xenograft-bearing nude mice. Even if the radiolabeled aptamers demonstrate good tumor uptake and clearance, they require further optimization before diagnostic use.

16.4 Modifications of Aptamers

RNA aptamers resulting from the SELEX process are single-stranded oligoribonucleotides composed in the average of ca. 80 bases. In general, they are not utilized as such but could be truncated to the minimal target-binding domain, usually down to 25–50 ribonucleotides, in order to reduce the risk of unwanted interactions. The reduction in the aptamer length, combined with different modifications (Fig. 16.2), may allow to first increase their stability in the biological media of application and second to render their chemical synthesis easier and more convenient in terms of final yield and accordingly also of economic cost.

It is well known that RNA aptamers, siRNAs, miRNAs, and other synthetic RNAs exposed to cells or tissues for performing therapeutic, diagnostic, or therapeutic functions must be generally protected to overcome degradation by ribonucleases, with the consequent loss of their potential activity. In order to enhance resistance to nuclease attack, chemical modifications at position 2' of ribonucleotides can be exploited with success, since ribonucleases utilize the 2'-OH group for the cleavage of the adjacent phosphodiester bond. In particular, substitution at the 2' position of ribonucleotides with 2'-amino (2'-NH₂), 2'-fluoro (2'-F), or a variety of 2'-O-alkyl moieties has proven to lend resistance preventing degradation [75].

The most used chemical modification for the development of RNA aptamers stable in animal serum is the substitution of 2'-OH with 2'-F in pyrimidines. Such RNA can also be efficiently transcribed *in vitro* with a mutant viral RNA polymerase, thus facilitating its use in the SELEX process [9, 10, 75]. However, the

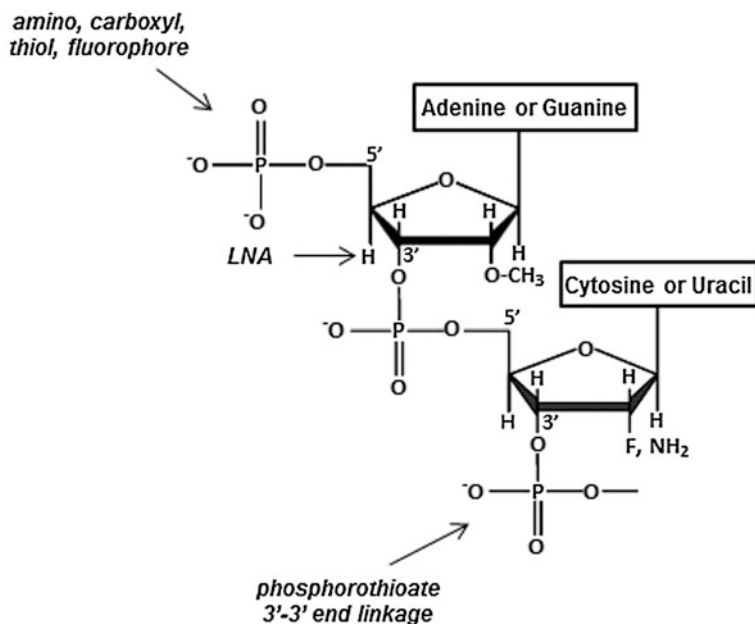


Fig. 16.2 Possible chemical modifications of aptamers

stability of RNA modified with 2'-fluoro-modified pyrimidines in the different contexts has not yet been well assessed.

It is noteworthy to mention that in culture media contaminated by mycoplasma, there are multiple mycoplasma-derived ribonucleases that can readily degrade also RNA modified with either 2'-F or 2'-O-methyl-modified pyrimidines [76].

Comparing the modification of aptamers with either 2'-NH₂ or 2'-F pyrimidines, it was concluded that (1) 2'-NH₂ modification decreases the thermal stability of model DNA/DNA, RNA/RNA, and RNA/DNA duplexes [77, 78] that, on the contrary, is increased by substitution with 2'-F [79–81]; (2) 2'-NH₂ groups increase in general the conformational flexibility of ODNs, and this may limit the binding affinity of 2'-NH₂-pyrimidine-modified aptamers, while 2'-F-pyrimidine-modified aptamers may adopt more rigid conformations and, thus, may exhibit higher binding affinities for their targets; (3) the chemical synthesis of 2'-F-pyrimidine-modified aptamers is more economical, i.e., the coupling efficiency of 2'-F-pyrimidine phosphoramidites during automated synthesis is greater than that of 2'-NH₂-pyrimidine phosphoramidites and the 2'-F groups do not require protection/deprotection steps [82].

Another way to make ONs resistant to nucleases is the transformation of the phosphodiester backbone into a phosphorothioate backbone, with the substitution of non-bonding oxygen of the bridging phosphate group with a sulfur atom, by the use of sulfurizing agents directly within the automated synthesis of the ONs. Analogously, resistance can be acquired by the synthesis of ONs as LNAs, by the use of the

appropriate phosphoramidites (Exiqon A/S), in which the ribose moiety is modified with an extra bridge connecting the 2' oxygen and 4' carbon [83]. The substitution of RNAs with LNAs leads to nuclease insensitivity and higher melting temperatures. For example, the introduction of LNA modifications in the TN-C aptamer significantly improved its plasma stability and enhanced its tumor uptake [71].

A challenging approach to enhance stability of aptamers is based on the selection of RNA aptamers binding to the mirror image of an intended target molecule (e.g., an unnatural D-amino acid peptide), followed by the chemical synthesis of the mirror images of the selected sequences, named Spiegelmers [84]. Since they are enantiomers of natural nucleic acids, they are not recognized by nucleases. Two Spiegelmers, NOX-A12 and NOX-E36, are in clinical trials for the treatment of type 2 diabetes and hematologic tumors, respectively [reviewed in 7, 8].

In order to render the chemical synthesis of RNA aptamers more efficient and less costly, systematic studies are usually carried out with the aim of defining the minimal length of the aptamer compatible with an acceptable binding affinity for the target. In fact, the chemistry at the basis of the oligoribonucleotide synthesis is such that the shorter is the sequence to synthesize, the higher is the final yield and the lower is the cost. A type of refinement consists in the screening of the single bases along the natural sequence that must/can be kept as unmodified ribonucleosides. A further refinement consists in protecting the 3' end of the oligoribonucleotide from degradation by replacing a number of phosphodiester bonds with phosphorothioate bonds and to introduce an initial 3'-3' oligodesoxynucleotidic capping junction.

With the support of computational programs, able to predict the conformational structure of the aptamer of interest, tracts can be identified along the sequence that can be substituted with non-nucleosidic bridges, like (CH₂CH₂O) units, thus improving stability and final yield, while reducing the cost.

16.5 Conclusions

In the last decade, researches in the field of aptamer have generated great interest because of their high potential as targeting agents. They discriminate between closely related targets and are characterized by high specificity and low toxicity, thus representing a valid alternative to antibodies for *in vivo* cell recognition. Further, due to their relatively simple chemistry, aptamers have several advantages that make this class of molecules as highly promising for their use in clinic. Development of new effective selection methodologies as, for example, whole-cell-SELEX, has recently offered the possibility to generate aptamers able to internalize into the cell in a receptor-mediated manner and thus molecules of choice for the cell-specific delivery of nucleic acid-based therapeutics. The increasing knowledge gathered in the last decade of the molecular mechanisms of RNA interference has boosted the interest in this class of molecules, including siRNAs, microRNAs, antisense oligonucleotides, and ribozymes as safe and

highly selective therapeutics. In this respect, because of their chemical nature, aptamers are more easier than antibodies to accept functional groups needed to create conjugates with nanoparticles or other macromolecules. Therefore, the combined advantages of cell-specific aptamers with those of nanoparticles and RNAi-based therapeutic agents provide now a very attractive and flexible new approach for selective delivery in the desired cells or tissue.

Acknowledgements This work was supported by funds from CNR, AICR No 11-0075 (L. Cerchia), MIUR grant, MERIT RBNE08YFN3_001 (VdF), AICR No 13345 (VdF), AICR No 11781 (L.Cerchia), by the Juvenile Diabetes Research Foundation International (JDRF, 5-2011-330), by the Compagnia di San Paolo, and from the Italian Ministry of Economy and Finance to the CNR for the Project FaReBio di Qualità.

References

1. Famulok M, Hartig JS, Mayer G (2007) Functional aptamers and aptazymes in biotechnology, diagnostics, and therapy. *Chem Rev* 107:3715–3743
2. Eaton BE, Gold L, Zichi DA (1995) Let's get specific: the relationship between specificity and affinity. *Chem Biol* 2:633–638
3. Foy JWD, Rittenhouse K, Modi M, Patel M (2007) Local tolerance and systemic safety of pegaptanib sodium in the dog and rabbit. *J Ocul Pharmacol Ther* 23:452–466
4. Yu D, Wang D, Zhu FG, Bhagat L, Dai M, Kandimalla ER, Agrawal S (2009) Modifications incorporated in CpG motifs of oligodeoxynucleotides lead to antagonist activity of toll-like receptors 7 and 9. *J Med Chem* 52:5108–5114
5. Mayer G (2009) The chemical biology of aptamers. *Angew Chem Int Ed Engl* 48:2672–2689
6. Cerchia L, de Franciscis V (2010) Targeting cell surface with nucleic acid-aptamers: the specific recognition of cancer cells. *Trends Biotechnol* 28(10):517–525
7. Keefe AD, Pai S, Ellington A (2010) Aptamers as therapeutics. *Nat Rev Drug Discov* 9:537–550
8. Esposito CL, Catuogno S, de Franciscis V, Cerchia L (2011) New insight into clinical development of nucleic acid aptamers. *Discov Med* 11:487–496
9. Ellington AD, Szostak JW (1990) In vitro selection of RNA molecules that bind specific ligands. *Nature* 346(6287):818–822
10. Tuerk C, Gold L (1990) Systematic evolution of ligands by exponential enrichment: RNA ligands to bacteriophage T4 DNA polymerase. *Science* 249:505–510
11. Keefe AD, Cload ST (2008) SELEX with modified nucleotides. *Curr Opin Chem Biol* 12:448–456
12. Chelliserrykattil J, Ellington AD (2004) Evolution of a T7 RNA polymerase variant that transcribes 2'-O-methyl RNA. *Nat Biotechnol* 22:1155–1160
13. Burmeister PE, Lewis SD, Silva RF, Preiss JR, Horwitz LR, Pendergrast PS, Mccauley TG, Kurz JC, Epstein DM, Wilson C et al (2005) Direct in vitro selection of a 2-O-methyl aptamer to VEGF. *Chem Biol* 12:25–33
14. Morris KN, Jensen KB, Julin CM, Weil M, Gold L (1998) High affinity ligands from in vitro selection: complex targets. *Proc Natl Acad Sci U S A* 95:2902–2907
15. Shanguan D, Li Y, Tang Z, Cao ZC, Chen HW et al (2006) Aptamers evolved from live cells as effective molecular probes for cancer study. *Proc Natl Acad Sci USA* 103:11838–11843
16. Chen HW, Medley CD, Sefah K, Shanguan D, Tang Z et al (2008) Molecular recognition of small-cell lung cancer cells using aptamers. *ChemMedChem* 3(6):991–1001

17. Cerchia L, Duconge F, Pestourie C, Boulay J, Aissouni Y et al (2005) Neutralizing aptamers from whole-cell SELEX inhibit the RET receptor tyrosine kinase. *PLoS Biol* 3:e123
18. Cerchia L, Esposito CL, Jacobs AH, Tavitian B, de Franciscis V (2009) Differential SELEX in human glioma cell lines. *PLoS ONE* 4(11):e7971
19. Esposito CL, Passaro D, Longobardo I, Condorelli G, Marotta P, Affuso A, de Franciscis V, Cerchia L (2011) A neutralizing RNA aptamer against EGFR causes selective apoptotic cell death. *PLoS ONE* 6(9):e24071
20. Cerchia L, Esposito CL, Camorani S, Rienzo A, Stasio L, Insabato L, Affuso A, de Franciscis V (2012) Targeting Ax1 with an high-affinity inhibitory aptamer. *Mol Ther* 20(12):2291–2303
21. Xiao Z, Shangguan D, Cao Z, Fang X, Tan W (2008) Cell-specific internalization study of an aptamer from whole cell selection. *Chemistry* 14(6):1769–1775
22. Thiel KW, Hernandez LI, Dassie JP, Thiel WH, Liu X, Stockdale KR, Rothman AM, Hernandez FJ, McNamara JO 2nd, Giangrande PH (2012) Delivery of chemo-sensitizing siRNAs to HER2+ breast cancer cells using RNA aptamers. *Nucleic Acids Res* 40(13):6319–6337
23. Cerchia L, Esposito CL, Camorani S, Catuogno S, de Franciscis V (2011) Coupling aptamers to short interfering RNAs as therapeutics. *Pharmaceuticals* 4:1434–1449
24. Thiel KW, Giangrande PH (2010) Intracellular delivery of RNA-based therapeutics using aptamers. *Thera Deliv* 1(6):849–861
25. Zhou J, Rossi JJ (2011) Cell-specific aptamer-mediated targeted drug delivery. *Oligonucleotides* 1:1–10
26. Zhou J, Rossi JJ (2013) Aptamer-Mediated siRNA Targeting. In: Howard KA (ed) *RNA Interference from biology to therapeutics*. Advances in delivery science and technology
27. Li N, Nguyen HH, Byrom M, Ellington AD (2011) Inhibition of cell proliferation by an anti-EGFR aptamer. *PLoS ONE* 6(6):e20299
28. Lupold SE, Hicke BJ, Lin Y, Coffey DS (2002) Identification and characterization of nuclease-stabilized RNA molecules that bind human prostate cancer cells via the prostate-specific membrane antigen. *Cancer Res* 62:4029–4033
29. Li N, Larson T, Nguyen HH, Sokolov KV, Ellington AD (2010) Directed evolution of gold nanoparticle delivery to cells. *Chem Commun (Camb)* 46:392–394
30. Liu N, Zhou C, Zhao J, Chen Y (2012) Reversal of paclitaxel resistance in epithelial ovarian carcinoma cells by a MUC1 aptamer-let-7i chimera. *Cancer Invest* 8:577–582
31. Ye M, Hu J, Peng M, Liu J, Liu J, Liu H, Zhao X, Tan W (2012) Generating aptamers by cell-SELEX for applications in molecular medicine. *Int J Mol Sci* 13(3):3341–3353
32. Chu TC, Twu KY, Ellington AD, Levy M (2006) Aptamer mediated siRNA delivery. *Nucleic Acids Res* 34(10):e73
33. McNamara JO 2nd, Andrechek ER, Wang Y, Viles KD, Rempel RE, Gilboa E, Sullenger BA, Giangrande PH (2006) Cell type-specific delivery of siRNAs with aptamer-siRNA chimeras. *Nat Biotechnol* 24:1005–1115
34. Dassie JP, Liu XY, Thomas GS, Whitaker RM, Thiel KW, Stockdale KR, Meyerholz DK, McCaffrey AP, McNamara JO 2nd, Giangrande PH (2009) Systemic administration of optimized aptamer-siRNA chimeras promotes regression of PSMA-expressing tumors. *Nat Biotechnol* 27(9):839–849
35. Pastor F, Kolonias D, Giangrande PH, Gilboa E (2010) Induction of tumour immunity by targeted inhibition of nonsense-mediated mRNA decoy. *Nature* 465:227–230
36. Wullner U, Neef I, Eller A, Kleines M, Tur MK, Barth S (2008) Cell-specific induction of apoptosis by rationally designed bivalent aptamer-siRNA transcripts silencing eukaryotic elongation factor 2. *Curr Cancer Drug Targets* 8:554–565
37. Zhou J, Li H, Li S, Zaia J, Rossi JJ (2008) Novel dual inhibitory function aptamer-siRNA delivery system for HIV-1 therapy. *Mol Ther* 16:1481–1489
38. Zhou J, Swiderski P, Li H, Zhang J, Neff CP, Akkina R, Rossi JJ (2009) Selection, characterization and application of new RNA HIV gp 120 aptamers for facile delivery of dicer substrate siRNAs into HIV infected cells. *Nucleic Acids Res* 37:3094–3109

39. Neff CP, Zhou J, Remling L, Kuruvilla J, Zhang J, Li H, Smith DD, Swiderski P, Rossi JJ, Akkina R (2011) An aptamer-siRNA chimera suppresses HIV-1 viral loads and protects from helper CD4(+) T cell decline in humanized mice. *Sci Transl Med* 3(66):66ra6. doi: [10.1126/scitranslmed.3001581](https://doi.org/10.1126/scitranslmed.3001581)
40. Zhou J, Neff CP, Swiderski P, Li H, Smith DD, Aboellail T, Remling-Mulder L, Akkina R, Rossi JJ (2013) Functional in vivo delivery of multiplexed anti- HIV-1 siRNAs via a chemically synthesized aptamer with a sticky bridge. *Mol Ther* 21:192–200
41. Ni X, Zhang Y, Ribas J, Chowdhury WH, Castanares M, Zhang Z, Laiho M, DeWeese TL, Lupold SE (2011) Prostate-targeted radiosensitization via aptamer-shRNA chimeras in human tumor xenografts. *J Clin Invest* 121:2383–2390
42. Dai F, Zhang Y, Zhu X, Shan N, Chen Y (2012) Anticancer role of MUC1 aptamer-miR-29b chimera in epithelial ovarian carcinoma cells through regulation of PTEN methylation. *Target Oncol* 7:217–225
43. Wheeler LA, Trifonova R, Vrbancac V, Basar E, McKernan S, Xu Z, Seung E, Deruaz M, Dudek T, Einarsson JI, Yang L, Allen TM, Luster AD, Tager AM, Dykxhoorn DM, Lieberman J (2011) Inhibition of HIV transmission in human cervicovaginal explants and humanized mice using CD4 aptamer-siRNA chimeras. *J Clin Invest* 121(6):2401–2412
44. Zhou J, Tiemann K, Chomchan P, Alluin J, Swiderski P, Burnett J, Zhang X, Forman S, Chen R, Rossi J (2013) Dual functional BAFF receptor aptamers inhibit ligand-induced proliferation and deliver siRNAs to NHL cells. *Nucleic Acids Res* [Epub ahead of print]
45. Wilner SE, Wengerter B, Maier K, de Lourdes Borba Magalhães M, Del Amo DS, Pai S, Opazo F, Rizzoli SO, Yan A, Levy M (2012) An RNA alternative to human transferrin: a new tool for targeting human cells, *Mol Ther Nucleic Acids* 1:e21. doi: [10.1038/mtna.2012.14](https://doi.org/10.1038/mtna.2012.14)
46. Huang YF, Shangguan D, Liu H, Phillips JA, Zhang X, Chen Y, Tan W (2009) Molecular assembly of an aptamer–drug conjugate for targeted drug delivery to tumor cells. *ChemBioChem* 10:862–868
47. Li N, Ebright JN, Stovall GM, Chen X, Nguyen HH, Singh A, Syrett A, Ellington AD (2009) Technical and biological issues relevant to cell typing with aptamers. *J Proteome Res* 8(5):2438–2448
48. Hicke BJ, Stephens AW, Gould T, Chang Y-F, Lynott K, Heil J, Borkowski S, Hilger C-S, Cook G, Warren S, Schmidt P (2006) Tumor targeting by an aptamer. *J Nucl Med* 47:668–678
49. Heredia KL, Nguyen TH, Chang CW, Bulmus V, Davis TP, Maynard HD (2008) Reversible siRNA polymer conjugates by RAFT polymerization. *Chem Commun* 28:3245–3247
50. Da Pieve C, Williams P, Haddleton DM, Palmer RMJ, Missailidis S (2010) Modification of thiol functionalized aptamers by conjugation of synthetic polymers. *Bioconjugate Chem* 21:169–174
51. Wu X, Ding B, Gao J, Wang H, Fan W, Wang X, Zhang W, Wang X, Ye L, Zhang M, Ding X, Liu J, Zhu Q, Gao S (2011) Second-generation aptamer-conjugated PSMA-targeted delivery system for prostate cancer therapy. *Int J Nanomed* 6:1747–1756
52. Farokhzad OC, Jon S, Khademhosseini A, Tran T-NT, LaVan DA, Langer R (2004) Nanoparticle-aptamer bioconjugates a new approach for targeting prostate cancer cells. *Cancer Res* 64:7668–7672
53. Yu C, Hu Y, Duan J, Yuan W, Wang C, Xu H, Yang X-D (2011) Novel aptamer-nanoparticle bioconjugates enhances delivery of anticancer drug to MUC1-positive cancer cells in vitro. *PLoS ONE* 6:e24077
54. Shu Y, Cinier M, Shu D, Guo P (2011) Assembly of multifunctional phi29 pRNA nanoparticles for specific delivery of siRNA and other therapeutics to targeted cells. *Methods* 154:204–214
55. Wua Y, Sefaha K, Liua H, Wanga R, Tan W (2010) DNA aptamer-micelle as an efficient detection/delivery vehicle toward cancer cells. *PNAS* 107:5–10
56. Kang H, O'Donoghue MB, Liu H, Tan W (2011) A liposome-based nanostructure for aptamer directed delivery. *Chem Commun* 6:249–251

57. Sun J, Guo A, Zhang Z, Guo L, Xie J (2011) A conjugated aptamer-gold nanoparticle fluorescent probe for highly sensitive detection of rHuEPO- α . *Sensors* 11:10490–10501
58. Yang L, Zhang X, Ye M, Jiang J, Yang R, Fu T, Chen Y, Wang K, Tan W (2011) Aptamer-conjugated nanomaterials and their applications. *Adv Drug Deliv Rev* 63:1361–1370
59. Giljohann DA, Seferos DS, Daniel WL, Massich MD, Patel PC, Mirkin CA (2010) In vitro selection of structure-switching signaling aptamers. *Angew Chem Int Ed* 49:3280–3294
60. Huang C, Huang Y, Cao Z, Tan W, Chang H (2005) Aptamer-modified gold nanoparticles for colorimetric determination of platelet-derived growth factors and their receptors. *Anal Chem* 77:5735–5741
61. Zhao W, Chiuman W, Lam JC, McManus SA, Chen W, Cui Y, Pelton R, Brook MA, Li Y (2008) DNA aptamer folding on gold nanoparticles: from colloid chemistry to biosensors. *J Am Chem Soc* 130(11):3610–3618
62. Liu J, Lu Y (2006) Preparation of aptamer-linked gold nanoparticle purple aggregates for colorimetric sensing of analytes. *Nat Protoc* 1:246–252
63. Zhang J, Wang L, Zhang H, Boey F, Song S, Fan C (2010) Aptamer-based multicolor fluorescent gold nanoprobe for multiplex detection in homogeneous solution. *Small* 6:201–204
64. Dubertret B, Calame M, Libchaber AJ (2001) Single-mismatch detection using gold-quenched fluorescent oligonucleotides. *Nat Biotechnol* 19:365–370
65. Zhang Z, Guo L, Guo AT, Xu H, Tang JJ, Guo XJ, Xie JW (2010) In vitro lectin-mediated selection and characterization of rHuEPO- α -binding ssDNA aptamers. *Bioorg Med Chem* 18:8016–8025
66. Bagalkot V, Gao X (2011) siRNA-aptamer chimeras on nanoparticles: Preserving targeting functionality for effective gene silencing. *ACSNano* 5:8131–8139
67. Bamrungsap S, Chen T, Shukoor MI, Chen Z, Sefah K, Chen Y, Tan W (2012) Pattern recognition of cancer cells using Aptamer-conjugated magnetic nanoparticles. *ACSNano.org* 6:3974–3981
68. Nair BG, Nagaoka Y, Morimoto H, Yoshida Y, Maekawa T, Kumar DS (2010) Aptamer conjugated magnetic nanoparticles as nanosurgeons. *Nanotechnology* 21:455102. doi:[10.1088/0957-4484/21/45/455102](https://doi.org/10.1088/0957-4484/21/45/455102)
69. Medley CD, Bamrungsap S, Tan W, Smith JE (2011) Aptamer-conjugated nanoparticles for cancer cell detection. *Anal Chem* 83(3):727–734
70. Hicke BJ, Marion C, Chang YF, Gould T, Lynott CK, Parma D, Schmidt PG, Warren S (2001) Tenascin-C aptamers are generated using tumor cells and purified protein. *J Biol Chem* 276(52):48644–48654
71. Schmidt KS, Borkowski S, Kurreck J, Stephens AW, Bald R, Hecht M, Friebe M, Dinkelborg L, Erdmann VA (2004) Application of locked nucleic acids to improve aptamer in vivo stability and targeting function. *Nucleic Acids Res* 32(19):5757–5765
72. Ferreira CS, Matthews CS, Missailidis S (2006) DNA aptamers that bind to MUC1 tumour marker: design and characterization of MUC1-binding single-stranded DNA aptamers. *Tumour Biol* 27(6):289–301
73. Borbas KE, Ferreira CS, Perkins A, Bruce JI, Missailidis S (2007) Design and synthesis of mono and multimeric targeted radiopharmaceuticals based on novel cyclen ligands coupled to anti-MUC1 aptamers for the diagnostic imaging and targeted radiotherapy of cancer. *Bioconjug Chem* 18:1205–1212
74. Pieve CD, Perkins AC, Missailidis S (2009) Anti-MUC1 aptamers: radiolabelling with (99 m)Tc and biodistribution in MCF-7 tumour-bearing mice. *Nucl Med Biol* 36:703–710
75. Pieken WA, Olsen DB, Benseler F, Aurup H, Eckstein F (1991) Kinetic characterization of ribonuclease-resistant 2'-modified hammerhead ribozymes. *Science* 253:314–317
76. Hernandez FJ, Stockdale KR, Huang L, Horswill AR, Behlke MA, McNamara JO (2012) Degradation of nuclease-stabilized RNA oligonucleotides in mycoplasma-contaminated cell culture media. *Nucleic Acid Ther* 22(1):58–68

77. Aurup H, Tuschl T, Benseler F, Ludwig J, Eckstein F (1994) Oligonucleotide duplexes containing 2'-amino-2'-deoxycytidines: thermal stability and chemical reactivity. *Nucleic Acids Res* 22:20–24
78. Lin Y, Qiu Q, Gill SC, Jayasena SD (1994) Modified RNA sequence pools for in vitro selection. *Nucleic Acids Res* 22(24):5229–5234
79. Cummins LL, Owens SR, Risen LM, Lesnik EA, Freler SM, McGee D, Guinosso CJ, Cook PD (1995) Characterization of fully 2'-modified oligoribonucleotide hetero- and homoduplex hybridization and nuclease sensitivity. *Nucleic Acids Res* 23:2019–2024
80. Lesnik EA, Guinosso CJ, Kawasaki AM, Sasmor H, Zounes M, Cummins LL, Ecker DJ, Cook PD, Freier SM (1993) Oligodeoxynucleotides containing 2'-O-modified adenosine: synthesis and effects on stability of DNA:RNA duplexes. *Biochemistry* 32:7832–7838
81. Kawasaki AM, Casper MD, Freier SM, Lesnik EA, Zounes MC, Cummins LL, Gonzalez C, Cook PD (1993) Uniformly modified 2'-deoxy-2'-fluoro phosphorothioate oligonucleotides as nuclease-resistant antisense compounds with high affinity and specificity for RNA targets. *J Med Chem* 36(7):831–841
82. Ruckman J, Green LS, Beeson J, Waugh S, Gillette WL, Henninger DD, Claesson-Welsh L, Janjić N (1998) 2'-Fluoropyrimidine RNA-based aptamers to the 165-amino acid form of vascular endothelial growth factor (VEGF165). *J Biol Chem* 273(32):20556–205567
83. Petersen M, Wengel J (2003) LNA: a versatile tool for therapeutics and genomics. *Trends Biotechnol* 21(2):74–81
84. Eulberg D, Klusmann S (2003) Spiegelmers: biostable aptamers. *ChemBioChem* 4(10):979–983

Chapter 17

Engineering DNA Vaccines for Cancer Therapy

Brian M. Olson and Douglas G. McNeel

Abbreviations

APC	Antigen-presenting cell
CMV IE	Cytomegalovirus immediate-early
CTL	Cytotoxic T lymphocyte
DC	Dendritic cell
ER	Endoplasmic reticulum
GM-CSF	Granulocyte-macrophage colony-stimulating factor
HIV	Human immunodeficiency virus
HRPC	Hormone-refractory prostate cancer
HPV	Human papillomavirus
HSP	Heat-shock protein
IL	Interleukin
MHC	Major histocompatibility antigen
NK	Natural killer
PAP	Prostatic acid phosphatase
Poly-A	Poly-adenylation
PSA	Prostate-specific antigen
PSMA	Prostate-specific membrane antigen
T _H	T helper cell

17.1 Introduction

Cancer is one of the central public health problems across the globe, with more than 1.5 million new diagnoses and more than half a million cancer deaths in the United States alone [1]. Despite its pernicious impact throughout society, medical research

B. M. Olson · D. G. McNeel (✉)

Department of Medicine, Wisconsin Institutes for Medical Research, University of Wisconsin, Room 7007, 1111 Highland Avenue, Madison, WI 53705, USA
e-mail: dm3@medicine.wisc.edu

has made significant advances in the treatment of patients with disease. While these therapies have provided options to help control or even cure some malignancies, they are also often associated with significant side effects. For example, chemotherapy (treatment utilizing cytotoxic anti-neoplastic agents) can be used to specifically target rapidly dividing cells, which is one of the main characteristics of tumor cells. However, many other cell types also undergo rapid cell division (such as blood cells and hair follicles), and as such are also targets of these chemotherapeutic agents, leading to side effects such as immunosuppression and hair loss. As such, research has sought to identify alternative therapeutic modalities that can be used to therapies that can provide clinical efficacy without the life-altering side effects.

The relationship between the immune system and cancer has been studied for more than a century, with research showing that the immune system has the ability to recognize and eliminate tumor cells. While preexisting anti-tumor immune responses are nearly always insufficient to elicit tumor regression, tumor immunologists have sought to take advantage of the potential of these responses by designing therapies aimed at enhancing the quantity and quality of anti-tumor immune responses. The development of such tumor immunotherapies has seen several exciting advances in recent years, with the approval of a vaccine for advanced prostate cancer (sipuleucel-T [2]) and an effective treatment for metastatic melanoma (ipilimumab [3]). However, even before the approval of these treatments, the first vaccine approved in the US for the treatment of cancer was a DNA vaccine for canine melanoma [4–6]. A DNA vaccine is a circular DNA plasmid that (in the case of anti-tumor vaccines) encodes the cDNA of a specific protein antigen that is expressed by tumor cells, and when given to patients can augment antigen-specific immune responses. In this chapter, we will be reviewing the use of DNA vaccines for the treatment of cancer, focusing on how these vaccines are designed and characterized. Furthermore, we discuss ways in which DNA vaccines are being engineered to enhance their immune and anti-tumor efficacy.

17.1.1 Tumor Immunology

The immune system is composed of many different cell types whose basic function is to recognize and distinguish foreign and self-antigens and help eliminate infected or other potentially harmful cells (such as tumor cells) from the body. The immune system is broadly divided into two subgroups with innate and adaptive components. Innate immunity is the body's first line of defense, in which cells such as macrophages, dendritic cells (DCs), and natural killer (NK) cells provide an immediate, nonspecific immune response. In addition, the innate immune response helps activate adaptive immunity by both serving as antigen-presenting cells (APCs) as well as providing the inflammatory signals necessary to recruit and activate the lymphocytes that mediate adaptive immunity.

The adaptive immune system is designed to recognize and target specific protein antigens that the immune system recognizes as nonself. The adaptive (or acquired)

immune system further subdivided into two branches, humoral (B-cell) and cellular (T-cell) immunity. Humoral immunity is mediated primarily by antibody production, which occurs after bone marrow-derived B cells encounter their specific extracellular antigen, which triggers the production of antigen-specific immunoglobulin that can neutralize these antigens. Alternatively, cellular immunity is composed of T cells, both CD4+ T helper (T_H) cells and CD8+ cytotoxic T lymphocytes (CTL). T cells are generated by progenitors in the bone marrow and undergo a complex process of differentiation and maturation in the thymus. T cells recognize specific peptide antigens in the context of major histocompatibility complexes (MHC, also known as human leukocyte antigens (HLA) in humans). In the case of CD4+ T cells, these T_H cells recognize peptides (12–18 residues) that are presented on the surface of professional APCs bound to MHC class II. When T_H cells are activated, they can secrete cytokines that help activate and direct the adaptive immune responses toward a cellular (Th1) or humoral (Th2)-type phenotype. Alternatively, CD8+ T cells recognize smaller, usually nonameric, peptides that are derived from intracellular antigens and are presented on the surface of all nucleated nongerm cells bound to MHC class I. When CD8+ T cells encounter a cell displaying their specific antigen and receive proper co-stimulation from APCs, they become activated and can differentiate and exponentially proliferate into effector CTL that have the same peptide-specificity as the original T cell. These activated CTL can then go back into circulation, searching for other cells that are displaying the same peptide, which they can bind to and lyse using a variety of effector mechanisms. This ability to directly lyse target cells has led cellular immunity to play a central role in immune-mediated tumor recognition and rejection.

Our understanding of the immune system's ability to recognize and eliminate tumor cells has undergone considerable evolution since the seminal work of Paul Ehrlich in 1909 (and Thomas and Burnet half a century later), in which he first proposed that the immune system can help prevent the outgrowth of malignant tumor cells [7–9]. Specific changes to this “immune surveillance hypothesis” have been based on our improved understanding of the immune system and cancer biology, including findings such as:

- Case reports of immune-mediated spontaneous tumor regression, particularly melanoma and neuroblastomas [10].
- Increased lymphocyte infiltration of tumors is associated with enhanced prognosis and is a predictor of enhanced prognosis in a variety of malignancies [11–16].
- Immunosuppressed patients (such as patients with AIDS or transplant recipients) have higher cancer occurrences than patients with normal immune function [17–21].
- Increased incidences of cancer in elderly patients have been shown to be correlated with a decrease in immune function, especially cellular immunity [1, 22–24].
- Tumor antigen-specific antibodies and T cells have been observed in patients with several types of tumors [25–32].

These observations show that the immune system is capable of recognizing and eliminating tumor cells. However, the tumor in turn is able to recognize these immune responses and undergoes a process of “immunoediting”, where the tumor undergoes changes to avoid immune detection. This can include decreasing the expression of MHC class I molecules or the antigen being targeted, increasing the expression of factors that can inhibit immune responses (including surface molecules such as PD-L1 and PD-L2 as well as secreted factors such as indoleamine 2, 3-dioxygenase), or other mechanisms [33–41]. However, while this is clearly an imperfect system, it provides a clear rationale for therapies directed at augmenting the immunogenicity of tumors or anti-tumor immune responses themselves.

17.1.2 Tumor Immunotherapy

The goal of tumor immunotherapy is to harness the immune system to generate or augment productive anti-tumor immune responses. Cancer immunotherapeutics are divided into two subtypes: passive and active immunotherapy. Passive immunotherapy involves the transfer of immunological mediators (such as tumor-specific antibodies or autologous T cells) into tumor-bearing hosts, where the transferred immune agents are able to direct an anti-tumor response without augmenting the host’s own immune system. Alternatively, active immunotherapy (including immunotherapeutic vaccines) is designed to utilize vaccines to elicit and/or augment the host’s own intrinsic anti-tumor immune responses. These active immunotherapeutics are also subdivided into either antigen-specific or antigen-nonspecific vaccines. Antigen-nonspecific vaccines are designed to elicit an anti-tumor immune response to any and all antigens displayed by tumor cells. Common examples of this type of vaccine are irradiated tumor cell vaccines, such as the GVAX vaccine for prostate cancer [42, 43].

As opposed to nonspecific vaccines, antigen-specific vaccines are designed to elicit an anti-tumor immune response against one particular antigen that is made and displayed by tumor cells. To utilize antigen-specific vaccines, one first needs to identify an appropriate antigen to target. There are several considerations to take into account when selecting an appropriate tumor antigen to target; in fact, the National Cancer Institute convened a panel of some of the nation’s top tumor immunologists to narrow down the innumerable factors that go into antigen selection and prioritize a list of characteristics that can be used to identify a potentially ideal vaccine target antigen [27]. The top antigen characteristic this panel identified was the therapeutic activity of a vaccine targeting this antigen, ideally in clinical trials or in preclinical studies. This panel identified antigen immunogenicity as being the second most important attribute; whether the antigen is naturally recognized by antibody or T-cell responses in individuals with cancer. The next antigen characteristic was oncogenicity; whether the antigen contributes to the proliferation of tumor cells. This is an often overlooked characteristic; however, it can have an important impact on the ultimate success of antigen-specific vaccines. As stated above, tumor cells can

decrease their expression of the target antigen to avoid anti-tumor immune responses. However, if the targeted antigen plays a critical role in oncogenicity, decreasing expression of this antigen will result in the selection of tumor cell variants with potentially decreased proliferative capacity. Specificity was another characteristic that was identified as being important to a vaccine target antigen—whether an antigen is only expressed in cancer cells, or whether it is overexpressed or has other modifications that make its expression unique to tumor cells. The expression level of the antigen was also identified by this NCI panel, both in terms of the frequency and amplitude of expression. Other factors include whether the antigen is expressed by stem cells, the number of patients that express the antigen of interest, the number of immunogenic epitopes contained within that antigen, and the cellular location of expression. By carefully considering the biological mechanisms that contribute to a particular cancer type, it is possible to engineer antigen-specific vaccines that target antigens with many of these characteristics.

In addition to selecting an appropriate antigen to target, another important consideration is the type of vaccination approach to utilize. There are several classes of vaccines that have been used extensively, including peptide or protein vaccines, antigen-pulsed APCs vaccines, viral vaccines, bacterial vaccines, and DNA vaccines. Each of these approaches has been and is currently being characterized in clinical trials, and each has advantages and disadvantages associated with the particular means of delivery. Peptide and protein vaccines have the benefit of using a highly purified vaccine delivered without extraneous antigens, as is the case with antigen-presenting cell, viral, and bacterial vaccines. In particular, several peptide vaccines targeting specific tumor antigen-derived epitopes have been evaluated clinically, including peptides targeting antigens such as prostate-specific antigen (PSA) in prostate cancer or HER2/neu in breast cancer [44–48]. However, since these vaccines are delivered as extracellular antigens, they elicit predominantly Th2-type (humoral) immune responses, which are largely ineffective against intracellular tumor antigens [49, 50]. Furthermore, peptide vaccines (which target specific peptide epitopes derived from tumor antigens) are limited by the MHC specificity of the peptide, restricting the potential patient population. Antigen-pulsed APC vaccines are used to deliver autologous, antigen-loaded APCs to patients, where they are designed to activate the host's intrinsic antigen-specific T-cell responses [2, 51–53]. These vaccines have been tested extensively in preclinical models and clinical trials where they have been shown to provide a modest clinical benefit. The best example of this type of vaccine approach is sipuleucel-T, a vaccine which takes a patient's APCs and pulses them with a fusion protein comprised of prostatic acid phosphatase (PAP, a prostate tumor-associated antigen) and granulocyte-macrophage colony-stimulating factor (GM-CSF, an immunostimulatory cytokine). In a randomized phase III clinical trial, this vaccine was shown to provide a significant increase in overall survival in immunized patients, leading to its approval for the treatment of patients with castrate-resistant prostate cancer [2]. However, while these vaccines have shown some efficacy in clinical trials, they require autologous APCs and as such have to

be specifically created and tailored for each individual patient, making it very costly and cumbersome in terms of production, storage, and delivery.

An alternative approach to protein and APC-based vaccines are genetic vaccines, such as viral, bacterial, or DNA vaccines, which are designed to deliver cDNA encoding the antigen of interest to host APCs. These APCs can then express the encoded antigen, which is naturally processed and presented via MHC class I to circulating CD8+ T cells [54, 55]. Alternatively, these vectors can also be taken up by non-APCs at the injection site (by cells such as keratinocytes or monocytes), and via cross-presentation can be displayed on the surface of APCs bound to MHC class II [54, 55]. As a result, these vaccines are able to elicit both humoral and cellular antigen-specific immunity, a characteristic that sets genetic vaccines apart from most other types of active immunotherapy [54, 55]. Viral vaccines employ a viral vector that also encodes the cDNA of the antigen of interest and are able to utilize the viral vector to efficiently enter host APCs at the injection site [56, 57]. An example of a viral vaccine is PROSTVAC, which is a viral vaccine encoding PSA. This vaccine was shown to provide an increase in overall survival in a randomized phase II clinical trial [58]. However, this vaccine also illustrates some of the challenges associated with viral constructs. In this immunization schema, the first vaccination is a vaccinia virus encoding PSA, and all subsequent booster vaccinations are fowlpox virus encoding PSA. This is required because patients can generate potent immune responses to the virus itself, which can compromise the response against the encoded antigen. Bacterial vaccines are similar to viral vaccines in that they use an immunogenic pathogen as a vector to deliver the gene of interest to host APCs [59]. A prime example of bacterial vaccines is CRS-207, which is a live-attenuated strain of *Listeria monocytogenes* that is engineered to encode mesothelin [60]. This vaccine has been studied in multiple phase I trials in patients with mesothelin-expressing cancers, including pancreatic cancer, and has been shown to activate mesothelin-specific immune responses and is currently in being evaluated in later-stage clinical trials [60]. However, bacterial vectors also suffer from deleterious and potentially harmful responses to the bacterial vector itself. Alternatively, DNA vaccines are nonpathogenic vectors that are easy to create, modify, store, and transport, and have been shown to elicit potent antigen-specific immune responses against several malignancies (including cancer) in both preclinical models as well as clinical trials [61–64].

17.2 DNA Vaccines

The use of DNA vaccines to treat cancer dates back to research conducted by Wolff and colleagues at the University of Wisconsin, who found that if naked DNA is injected into recipients, host cells can take up this DNA and express the encoded antigen [65]. Later research has shown that DNA vaccines can directly transfect APCs, which can then express the encoded antigen and subsequently present antigen-derived peptides bound to MHC complexes or can transfect host

cells such as melanocytes or keratinocytes, which can subsequently be cross-presented on host APCs to activate an immune response [61]. This was first translated into a vaccine targeting influenza in studies which showed that immunization with a DNA vaccine encoding an influenza nucleoprotein could elicit protective immunity [66]. This has since been translated into several different malignancies, including several types of solid tumors (such as melanoma, prostate, and breast cancer), which have shown that immunization with DNA vaccines can elicit potent antigen-specific immune responses [61–64].

DNA vaccines have several benefits compared to other immunization approaches. As opposed to passive immunotherapies or protein/APC vaccine approaches, DNA vaccines can activate both arms of the adaptive immune system, eliciting CD4+ and CD8+ cellular immunity in addition to humoral responses as well. And while viral and bacterial vaccines are also able to stimulate both humoral and cellular immunity, DNA vaccines have the benefit of not being associated with any other pathogens, preventing deleterious and potentially harmful responses to vector-specific antigens. Additionally, by incorporating immunostimulatory CpG motifs in the backbone of the DNA plasmid itself, DNA vaccines are also able to stimulate innate immune responses [67, 68]. As opposed to APC vaccines, DNA vaccines are an “off-the-shelf” vaccine option, which can be easily stored, transported, and administered (making global immunization approaches much more feasible). Furthermore, DNA vaccines are convenient in that in addition to being able to target a specific antigen (or multiple antigens in the same vector), they can be easily modified to incorporate additional antigens or co-stimulatory molecules and can be rapidly produced for large-scale production.

Given these attractive qualities, several groups have investigated the use of DNA vaccines to treat a variety of diseases. This includes viral infections, such as human immunodeficiency virus (HIV), influenza, human papillomavirus (HPV), measles, and ebola, as well as other infectious diseases such as malaria [61, 69–72]. Additionally, DNA vaccines have also been used for a variety of other conditions, including allergies or autoimmune diseases such as multiple sclerosis [61, 73–76]. And while many of these vaccines are currently in preclinical and early-stage clinical trials, several DNA vaccines have been approved for the treatment of various animal diseases, including canine melanoma [4–6], equine West Nile virus [77], and infectious hematopoietic necrosis in salmon [78].

However, DNA vaccines have been most heavily studied in the field of cancer, where they have entered clinical trials for more than a dozen malignancies [61–64]. DNA vaccines (as is the case with most immunotherapies) have been most heavily studied in patients with melanoma, where vaccines have been tested in phase I clinical trials targeting antigens such as gp100, tyrosinase, and other melanoma differentiation antigens [79–83]. One of these trials was conducted by Wolchok and colleagues, in which patients with stage III/IV melanoma were immunized with both human and mouse tyrosinase [81]. By immunizing with DNA vaccines encoding both the human protein as well as the highly homologous mouse tyrosinase protein, the authors sought to take advantage of targeting both the endogenous antigen as well as a highly homologous xenoantigen, thus eliciting stronger immune

responses against the native tyrosinase antigen. In this trial, patients were immunized intramuscularly every three weeks with 100–1,500 µg of plasmid DNA encoding either human or mouse tyrosinase. Following three immunizations with one construct, the patients then crossed over and received three immunizations with the DNA vaccine from the other species. In this trial, the authors found that nearly half of the patients (7/17) developed antigen-specific T-cell responses, and patients were found to have a median survival of greater than 42 months (whereas median survival of patients with this stage of disease is 36 months [81]). In another trial targeting patients with stage III/IV melanoma, patients were immunized with a DNA vaccine encoding seven MHC class I-restricted epitopes from a variety of melanoma tumor-associated antigens (tyrosinase, melan-A, MAGE-1, MAGE-3, and NY-ESO; [83, 84]). In this trial, patients received either two or four DNA immunizations (composed of 2,000 or 4,000 µg DNA per immunization) every three weeks, followed by up to four booster immunizations using an Ankara virus encoding these same antigens. In this trial, 22/31 patients were found to develop antigen-specific T-cell responses, and 8/41 patients had a radiographic clinical benefit by response evaluation criteria in solid tumors (RECIST) [83, 84].

Prostate cancer has also shown itself to be a disease particularly suitable to immunotherapeutic intervention, with DNA vaccines targeting antigens such as PAP, PSA, and prostate-specific membrane antigen (PSMA) being evaluated in clinical trials [85–90]. In one of the earliest prostate cancer DNA vaccine clinical trials, patients with hormone-refractory prostate cancer (HRPC) were immunized five times every four weeks with a DNA vaccine encoding PSA [87, 88]. In this trial, 2/8 patients developed antigen-specific immune responses shortly following immunization, and 4/8 patients developed immune responses in long-term follow-up [87, 88]. Furthermore, patients with PSA-specific immune responses were also found to have decreases in serum PSA values (a serum biomarker of disease). Another phase I/II vaccine trial targeting PSMA, where HRPC patients were immunized five times with a PSMA DNA vaccine, delivered either intramuscularly or via electroporation (a technique that utilizes electrical currents to increase gene transfection [90, 91]). In this trial, 29/30 patients developed a CD4+ T-cell responses, 16/30 patients developed an epitope-specific CD8+ T-cell response, and 14/24 patients had an increase in PSA doubling-time (a potential marker of clinical efficacy in prostate cancer) at any point during the study [90, 91]. Finally, in a phase I clinical trial evaluating a DNA vaccine targeting PAP in prostate cancer patients (who were immunized intradermally up to six times biweekly), it was found that 10/22 patients developed antigen-specific immune responses two weeks following immunization, and 8/22 patients had long-term antigen-specific immune responses 3–12 months following the final immunization [85]. Interestingly, it was these long-term immune responses that were found to correlate with a favorable change in PSA doubling-time, highlighting the importance of comprehensive immune monitoring when evaluating the efficacy of DNA vaccines [86].

While DNA vaccines have shown an ability to generate antigen-specific immune responses in immunized individuals, there have not been resounding clinical responses in these (albeit underpowered) clinical trials. Therefore, efforts are being

Table 17.1 Modifications to enhance the immune and anti-tumor efficacy of DNA vaccines

Class of modification	Modification to plasmid backbone	Resultant alterations	References
<i>Increasing antigen expression</i>			
	Gene promoter	Increased transcription	[92–94]
	Intronic sequence	Increased transcription	[95–97]
	Enhancer/transactivator	Increased transcription	[62, 99, 100]
	Polyadenylation sequences	Increased transcription termination efficiency	[62, 93, 101]
	Multiple stop codons	Increased transcription termination efficiency	[62]
	Kozak sequence	Increased translation initiation	[93, 102, 103]
	Codon optimization	Increased translation efficiency	[93, 104–108]
<i>Increasing antigen processing and presentation</i>			
	Ubiquitination fusion	Increased degradation	[110–115]
	PEST sequence	Increased ubiquitination and subsequent degradation	[116–118]
	Amino-terminal residue	Increased degradation	[119–121]
	Induced protein misfolding	Increased degradation	[103, 122]
	Signal sequence	Increased MHC class I presentation of minigenes	[123–126]
	HSPs	Increased MHC I and II presentation, increased MHC expression	[127–134]
	Target to endosome/lysosome	Increased MHC II processing and presentation	[108, 135]
<i>Intrinsic immunogenicity</i>			
	CpG motifs and other DNA sensor motifs	Activation of innate immune responses	[136–143]
	T _H epitopes	Activation of CD4 + T cells, and subsequent production of immunostimulatory cytokines	[54, 90, 91, 144–146]
	Cytokines/chemokines	Enhanced T-cell activation	[147]
	Co-stimulatory molecules	Enhance antigen-presentation capacity of APCs that take up plasmid	[147]

undertaken to determine methods that can be used to engineer DNA vaccines to increase their immune and anti-tumor efficacy. Many investigations are seeking to determine whether methods of delivery can be optimized to improve the efficacy of DNA vaccines, as well as altered schedules of administration, ideal patient populations to immunize, and exogenous adjuvants. However, the remainder of this review will focus on molecular modifications to plasmid DNA itself that have been pursued to enhance the immune and anti-tumor efficacy of DNA vaccines. Specifically, we will focus on previous efforts to engineer specific elements into DNA vaccines to increase their antigen expression, increase antigen processing and presentation, and enhance their intrinsic immunogenicity, as outlined in Table 17.1.

17.3 Engineering DNA Vaccines to Enhance Their Immune and Anti-tumor Efficacy

17.3.1 Increasing Antigen Expression

DNA vaccines are composed of a circular bacterial plasmid that normally contains a minimum of two components: the antigen expression unit (composed of promoter/enhancer sequences followed by the coding sequence for the targeted antigen) and the bacterial production unit (composed of bacterial sequences necessary for plasmid amplification and selection). The construction of bacterial plasmids with vaccine inserts is accomplished using recombinant DNA technology, where the cDNA of the tumor antigen is cloned into a bacterial DNA plasmid backbone under the expression of a eukaryotic promoter. Once constructed, the vaccine plasmid is transformed into bacteria, where bacterial growth produces multiple plasmid copies. The plasmid DNA is then purified from the bacteria by separating the circular plasmid from the much larger bacterial DNA and other bacterial impurities and then used for immunization studies. However, while this is the base construct for a DNA vaccine, several elements can be incorporated into this DNA backbone to enhance the expression of the encoded antigen when delivered to recipient APCs, and this increased expression can result in stronger antigen-specific immune responses.

17.3.1.1 Promoters and Transcriptional Enhancer Elements

While early DNA plasmids were designed to drive gene expression using strong promoters from oncogenic viruses such as SV40 or RSV, the vaccines that have been translated into human studies have predominantly utilized promoters from nononcogenic sources, such as the human cytomegalovirus immediate-early (CMV IE) promoter [92, 93]. Alternatively, groups have investigated the use of tissue-specific promoters to drive antigen expression in specific cell types, to both specifically target the cell of interest as well as avoiding potentially detrimental effects of antigen expression in irrelevant cell types. This technique has been used to specifically target myocytes or keratinocytes and could also be used to specifically drive antigen expression within dendritic cells, B cells, or macrophages, selectively targeting host APCs for expression of the antigen of interest [93, 94].

In connection with the promoter of interest, gene expression can be enhanced by including an intronic sequence. For example, when using the CMV IE promoter, the CMV intron A sequence is commonly incorporated into the plasmid backbone. Inclusion of introns has been shown to result in increased gene expression, which occurs due to increased gene transcription [95–97]. Similarly, the incorporation of various enhancer, transactivator, and leader sequences can further enhance gene transcription. One commonly used element is the human T-cell leukemia virus (HTLV) 5' long terminal repeat (LTR), which can enhance

transcription and the inclusion of which has been shown to enhance immune responses following DNA vaccination [62, 98]. Additionally, in studies evaluating an HIV DNA vaccine, the incorporation of an IgE leader sequence enhanced the immunogenicity of this vaccine [99, 100].

17.3.1.2 Transcription Termination Signals

While the use of strong promoters incorporated into DNA vaccines can help drive expression of the encoded antigen, the termination of gene transcription is also a process that needs to be enhanced to ensure that there is not a bottleneck that slows the overall gene expression process. Therefore, DNA vaccines commonly incorporate polyadenylation (poly-A) sequences downstream of the encoded antigen that can enhance the efficiency of transcription termination and export of mRNA from the nucleus. The selection of an appropriate poly-A signal is an important factor in the construction of an appropriate DNA vaccine backbone, as it can have a significant impact on the efficiency of the promoter in driving gene expression [101]. Commonly used poly-A sequences are from SV40, rabbit β -globulin, and especially bovine growth hormone, which has a synergistic effect on gene transcription when combined with the CMV promoter [62, 93, 101]. Another important method of ensuring efficient termination of transcription is including a second stop codon to the 3' end of the gene of interest. This can prevent read through by RNA polymerase, which can potentially result in mRNA products that are the incorrect size and lead to RNA secondary structures which can decrease mRNA stability and impede efficient translation.

17.3.1.3 Kozak Sequence

In addition to adding DNA elements that can enhance the transcription of the encoded antigen, DNA vaccines can also be engineered to include factors that can drive translation of the gene transcript. One of these elements is a Kozak sequence, a small consensus sequence (GCCGCC(A/G)CC) located immediately upstream to the ATG start site that can serve as a eukaryotic ribosomal initiation sequence, slowing the rate of scanning by the ribosome and increasing the chance of recognition of the AUG start site [93, 102]. Interestingly, we have found that inclusion of this sequence can be required for efficient translation of a gene product encoded by a DNA vaccine [103 and Olson and McNeel, unpublished observations].

17.3.1.4 Codon Optimization

Another important factor that can affect the efficiency of protein translation is codon usage. All species have different ideal codon usage; therefore, optimizing the specific codons used can have a direct impact on how efficiently these codons

are translated into protein. Doing so will optimize the transcribed product to the tRNAs that are most commonly available in the host organism, as well as avoiding secondary RNA structures that can have a detrimental impact on RNA stability. The impact of codon optimization has been shown in DNA vaccines for a variety of diseases, including studies using DNA vaccines encoding bacterial and parasite epitopes where the natural sequences were altered to encode optimized codons for expression in mammals, which led to enhanced expression and immune responses [93, 104, 105]. Codon optimization has also been shown to impact the immune and anti-tumor efficacy of DNA vaccines for cancer. In preclinical studies using a DNA vaccine targeting the oncogenic protein E7 from HPV16, a codon-optimized construct was able to induce protein expression several fold higher than the native codons, induced a stronger immune response, and protected immunize animals from tumor growth [106–108].

17.3.2 Increasing Antigen Processing and Presentation

After DNA vaccines are taken up by host APCs and the encoded gene is transcribed and translated, the next step in the antigen-presentation pathway is that the newly translated protein is degraded by the proteasome into small peptide fragments. These peptides are then shuttled to the endoplasmic reticulum (ER), where they bind to MHC class I molecules and are then sent to the surface of the cell and presented to circulating CD8+ T cells. Alternatively, for presentation on MHC class II molecules, an extracellular antigen (either the protein itself or a non-APC that has taken up the DNA plasmid and expressed the antigen) is taken up by professional APCs, and the antigen-containing endosome then degrades this antigen into short peptide fragments. Meanwhile, MHC class II molecules are synthesized in the ER and then secreted, where they will then fuse with antigen-containing endosomes. As a result, the antigen-derived peptides can bind to MHC class II and are then shuttled to the surface of the cell and presented to circulating CD4+ T cells. As this processing and presentation pathway plays a central role in the development of antigen-specific immunity, research has focused on engineering sequences into the plasmid DNA that can increase antigen degradation, processing, and presentation (reviewed in [109]).

17.3.2.1 Increasing Antigen Degradation

To enhance antigens being presented through the MHC class I pathway, a variety of approaches have been taken to increase the degradation of vaccine-encoded antigens by the proteasome. Some of this research has focused on increasing protein ubiquitination (ubiquitin being a post-translational modification that triggers transport to the proteasome) by directly fusing an ubiquitin moiety to the gene of interest, which can serve as a base for subsequent polyubiquitination (which is

required for efficient proteasomal degradation [110]). This has been shown to enhance the proteasomal degradation of antigens encoded by DNA vaccines, as well as inducing stronger antigen-specific immune responses, in several disease models including cancer [111–115].

In addition to directly fusing ubiquitin moieties to the encoded antigen, increased protein degradation can be induced by incorporating specific sequences that target proteins for proteasomal degradation, such as a PEST sequence. A PEST sequence is a short region of amino acids rich in proline (P), glutamic acid (E), serine (S), and threonine (T) and are associated with decreased protein half-life [116]. This has been translated to studies using DNA vaccines in several disease models, including HIV and cancer [117, 118]. In a study evaluating immune responses to the tumor-associated antigen E7 from HPV16, it was found that a PEST sequence associated with the gene of interest was required for maximal immune and anti-tumor efficacy [117]. In addition to PEST sequences, increased protein degradation can be induced simply by altering the amino acid that is encoded at the amino terminus of the protein. This so-called N-end rule has shown that the amino acid that is exposed at the amino terminus following the removal of the initiating methionine can have a direct impact on the half-life of the protein [119]. This has been incorporated into DNA vaccines, where proteins whose amino termini are engineered to have shorter half-lives have been shown to induce stronger antigen-specific immune responses [120, 121].

In addition to these specific mechanisms to increase proteasomal degradation of encoded antigens, other characteristics of the antigen of interest can be engineered to enhanced protein degradation. For example, misfolded proteins are rapidly ubiquitinated and degraded by the proteasome. This can be utilized in DNA vaccines by incorporating protein sequences that trigger protein misfolding, which has been shown to increase the generation of MHC class I-restricted peptides [122]. Alternatively, misfolding can be induced by altering the sequence of the encoded antigen (for example, putting the carboxy terminal domain at the 5' end of the coding sequence). We have observed increased proteasomal degradation in our own studies evaluating a DNA vaccine targeting a domain of the androgen receptor, which is quickly degraded via the proteasome [103 and Olson and McNeel, unpublished observations].

17.3.2.2 Increasing Antigen Presentation

While generating increased frequencies of MHC-restricted peptides can result in enhanced immune responses, it is necessary that these peptides are appropriately presented on MHC class I molecules on the surface of cells. This presentation process can be enhanced in a number of ways. One technique that is used to enhance the presentation of DNA vaccines encoding minigenes (specific T-cell epitopes, rather than the full-length protein) is to incorporate a signal sequence proximal to the 5' end of the coding sequence. This triggers the gene product to enter the secretory pathway, first being transported to the ER, where it can

subsequently bind to MHC class I and be presented on the surface of cells [123]. This has been shown to enhance antigen-specific T-cell responses and can increase the anti-tumor efficacy of vaccines [124–126].

In addition to directly routing peptides to the ER, another method that has been shown to increase antigen presentation is incorporating heat shock proteins (HSPs) into antigen-specific vaccines. These HSPs induce antigen-specific immune responses using a variety of mechanisms: HSP-derived peptides have been shown to be immunologically recognized, activating innate immunity by acting as a danger signal, increasing MHC class I expression, and triggering expression of immunostimulatory cytokines [127–130]. In addition, HSPs have been suggested to directly increase the presentation of antigen-derived peptides by facilitating their transport to the ER or to other APCs, and DNA vaccines fusing antigen to HSPs have been shown to increase antigen presentation and induce enhanced immune responses [131–134].

17.3.2.3 Increasing MHC Class II Antigen Processing and Presentation

While engineering DNA vaccines to enhance the degradation and presentation of intracellular antigens is useful when one is trying to elicit a CD8+ T-cell response against an intracellular antigen, sometimes it is desirable to focus on enhancing MHC class II-restricted immune responses. Some of the previously described methods, in particular fusion constructs encoding both the antigen of interest and HSPs, as well as the incorporation of signal sequences upstream of full-length antigens, can be used to enhance cross-presentation of antigens encoded by DNA vaccines. However, there are specific modifications that can be engineered into DNA vaccines that can enhance antigen presentation on MHC class II molecules. One such modification is to direct the antigen of interest to be trafficked to the endosomal/lysosomal pathway. This is commonly achieved by fusing the gene of interest to the cytoplasmic domain of lysosome-associated membrane protein 1 (LAMP-1), which contains an amino acid sequence that targets antigens to the endosomal/lysosomal pathway. This has been used in the context of DNA vaccines, where a vaccine targeting HPV16 E7 fused to this region of LAMP-1 enhanced the immune and anti-tumor efficacy of this vaccine [108, 135].

17.3.3 Intrinsic Immunogenicity of DNA Vaccines

While the primary goal of DNA vaccines for the treatment of cancer is to elicit and/or augment an antigen-specific immune response to a particular tumor-associated antigen, enhancing this antigen-specific response does not solely focus on making changes to the antigen of interest. Other antigen-nonspecific elements can be engineered into DNA vaccines that can activate innate and adaptive immunity, which can subsequently enhance the immune response directed against the antigen of interest.

17.3.3.1 CpG Motifs

While DNA vaccines are designed to elicit immune responses to the encoded antigen, plasmid DNA itself has been shown to be immunogenic. This is largely through the incorporation of Immunostimulatory sequences (ISS), which contain cytosine-guanine (CpG) nucleotide repeats. These repeats are unmethylated when the DNA plasmid is produced in bacteria, and this unmethylated DNA is then recognized as foreign when injected into mammals. As a result, these CpG repeats have been shown to activate innate immune responses (in part through signaling via TLR9) and can enhance the immune efficacy of DNA vaccines through the recruitment of immune populations and increased expression of immunostimulatory cytokines [136–139]. Additionally, other DNA sensors can recognize plasmid DNA and can lead to the activation of innate immune responses [140–143].

17.3.3.2 Fusion to Immunostimulatory Molecules

While many efforts to enhance the immunogenicity of DNA vaccines have focused on mechanisms to enhance the expression, processing, and presentation of the encoded antigen, groups have also investigated enhancing the efficacy of these vaccines by encoding other immunostimulatory molecules into the vaccine construct that can have an antigen-nonspecific effect on enhancing the immune response. One mechanism that has been pursued is incorporating strong T_H epitopes into the vaccine construct. These T_H epitopes can recruit and engage CD4+ T cells at the vaccine site, which can help nonspecifically enhance the immune response against the encoded antigen. These T_H epitopes have been evaluated in preclinical models as well as clinical trials, including epitopes from tetanus toxoid, viral proteins, other bacteria, and other pathogens, where they have been shown to enhance antigen-specific immune responses in vivo [54, 90, 91, 144–146].

In addition to encoding specific epitopes to enhance T-cell responses, tumor immunologists have also investigated incorporating other adjuvants into the vaccine backbone to increase the immune and anti-tumor efficacy of these vaccines. This has included the expression of various cytokines, such as IL-2, IL-12, IFN γ , GM-CSF, and IL-15, as well as various chemokines [147]. In addition, groups have investigated including various other co-stimulatory molecules, such as CD80, CD86, CD40, or CD40L, which have been shown to enhance immune responses to DNA vaccines in vivo [147].

17.4 Concluding Remarks

The development of DNA vaccines for the treatment of cancer has seen significant advances since their inception nearly 20 years ago. However, despite their safe administration in clinical trials, significant hurdles remain before these vaccines can be fully implemented into clinical practice. Research into optimal methods of

delivery should continue to be investigated, as well as combinatorial therapies combining vaccination with other immunotherapeutic agents or standard therapies with known immunomodulatory effects. Furthermore, in addition to selecting the appropriate antigens to target, DNA vaccines should be optimized by engineering specific components into the DNA backbone that can enhance the immune response against the antigen of interest. Given the facile nature of incorporating and evaluating these specific elements within the context of a DNA plasmid, DNA vaccines serve as an ideal platform to evaluate the effects of these specific elements, and how they can act in concert to affect anti-tumor immunity. By identifying the ideal combination of elements within a DNA vaccine, it will be possible to generate vaccines that can provide an effective therapeutic option for patients with cancer.

References

1. Siegel R, Naishadham D, Jemal A (2013) Cancer statistics. *CA Cancer J Clin* 63(1):11–30
2. Kantoff PW et al (2010) Sipuleucel-T immunotherapy for castration-resistant prostate cancer. *N Engl J of Med* 363(5):411–422
3. Hodi FS et al. (2010) Improved survival with ipilimumab in patients with metastatic melanoma. *N Engl J Med*, 363(8):711–723
4. USDA licenses DNA vaccine for treatment of melanoma in dogs (2010). *J Am Vet Med Assoc*, 236(5):495
5. Bergman PJ, Camps-Palau MA, McKnight JA, Leibman NF, Craft DM, Leung C, Liao J, Riviere I, Sadelain M, Hohenhaus AE, Gregor P, Houghton AN, Perales MA, Wolchok JD (2006) Development of a xenogeneic DNA vaccine program for canine malignant melanoma at the animal med center. *Vaccine* 24(21):4582–4585
6. Bergman PJ, McKnight J, Novosad A, Charney S, Farrelly J, Craft D, Wulderk M, Jeffers Y, Sadelain M, Hohenhaus AE, Segal N, Gregor P, Engelhorn M, Riviere I, Houghton AN, Wolchok JD (2003) Long-term survival of dogs with advanced malignant melanoma after DNA vaccination with xenogeneic human tyrosinase: a phase I trial. *Clin Cancer Res* 9(4):1284–1290
7. Ehrlich P (1909) Über den jetzigen stand der karzinomforschung. *Ned Tijdschr Geneesk* 5(1):273–290
8. Thomas L (1959) Discussion of cellular and humoral aspects of the hypersensitive states. In: Lawrence HS (ed) *Cellular and humoral aspects of the hypersensitive states*. Hoeber-Harper, New York, pp 529–532
9. Burnet FM (1967) Immunological aspects of malignant disease. *Lancet* 1:1171
10. Challis GB, Stam HJ (1990) The spontaneous regression of cancer. A review of cases from 1900 to 1987. *Acta oncologica (Stockholm, Sweden)* 29(5):545–550
11. Pages F, Galon J, Dieu-Nosjean MC, Tartour E, Sautes-Fridman C, Fridman WH (2009) Immune infiltration in human tumors: a prognostic factor that should not be ignored. *Oncogene* 29 (8):1093–1102
12. Vesalainen S, Lipponen P, Talja M, Syrjanen K (1994) Histological grade, perineural infiltration, tumour-infiltrating lymphocytes and apoptosis as determinants of long-term prognosis in prostatic adenocarcinoma. *Eur J Cancer* 30A(12):1797–1803
13. Mihm MC Jr, Clemente CG, Cascinelli N (1996) Tumor infiltrating lymphocytes in lymph node melanoma metastases: a histopathologic prognostic indicator and an expression of local immune response. *Lab Invest* 74(1):43–47

14. Gooden MJ, de Bock GH, Leffers N, Daemen T, Nijman HW (2011) The prognostic influence of tumour-infiltrating lymphocytes in cancer: a systematic review with meta-analysis. *Br J Cancer* 105(1):93–103
15. Jochems C, Schlom J (2011) Tumor-infiltrating immune cells and prognosis: the potential link between conventional cancer therapy and immunity. *Exp Biol Med* (Maywood, NJ) 236(5):567–579
16. Naito Y, Saito K, Shiiba K, Ohuchi A, Saigenji K, Nagura H, Ohtani H (1998) CD8+ T cells infiltrated within cancer cell nests as a prognostic factor in human colorectal cancer. *Cancer Res* 58(16):3491–3494
17. Berkow R, Beers M (1997) Cancer and the immune system. In: *The merck manual of medical information*. Merck Research Laboratories, Whitehouse Station, NJ, pp 792–794
18. Penn I (1970) *Malignant tumors in organ transplant recipients, recent results in cancer research series*. Springer-Verlag, LLC, New York
19. Gatti RA, Good RA (1971) Occurrence of malignancy in immunodeficiency diseases, a literature review. *Cancer* 28(1):89–98
20. Boshoff C, Weiss R (2002) AIDS-related malignancies. *Nat Rev Cancer* 2(5):373–382
21. Sheil AG (1986) Cancer after transplantation. *World J Surg* 10(3):389–396
22. Derhovanessian E, Solana R, Larbi A, Pawelec G (2008) Immunity, ageing and cancer. *Immun Ageing* 5:11
23. Borek D, Butcher D, Hassanein K, Holmes F (1990) Relationship of age to histologic grade in prostate cancer. *Prostate* 16(4):305–311
24. Leibovitz A, Baumoehl Y, Segal R (2004) Increased incidence of pathological and clinical prostate cancer with age: age related alterations of local immune surveillance. *J Urol* 172(2):435–437
25. Olson BM, McNeel DG (2007) Antibody and T-cell responses specific for the androgen receptor in patients with prostate cancer. *Prostate* 67(16):1729–1739
26. Zarour H, DeLeo A, Finn O, Storkus W (2003) Cancer Med 6: tumor antigens. *Cancer Med*
27. Cheever MA, Allison JP, Ferris AS, Finn OJ, Hastings BM, Hecht TT, Mellman I, Prindiville SA, Viner JL, Weiner LM, Matrisian LM (2009) The prioritization of cancer antigens: a national cancer institute pilot project for the acceleration of translational research. *Clin Cancer Res* 15(17):5323–5337
28. Disis M, Calenoff E, McLaughlin G, Murphy A, Chen W, Groner B, Jeschke M, Lydon N, McGlynn E, Livingston R (1994) Existent T-cell and antibody immunity to HER-2/neu protein in patients with breast cancer. *Cancer Res* 54(1):16–20
29. Hirohashi Y, Torigoe T, Inoda S, Kobayasi J, Nakatsugawa M, Mori T, Hara I, Sato N (2009) The functioning antigens: beyond just as the immunological targets. *Cancer Sci* 100(5):798–806
30. Olson BM, McNeel DG (2011) CD8+ T cells specific for the androgen receptor are common in patients with prostate cancer and are able to lyse prostate tumor cells. *Cancer Immunol Immunother* 60:781–792
31. Olson BM, Frye TP, Johnson LE, Fong L, Knutson KL, Disis ML, McNeel DG (2010) HLA-A2-restricted T-cell epitopes specific for prostatic acid phosphatase. *Cancer Immunol Immunother* 59(6):943–953
32. Rentzsch C, Kayser S, Stumm S, Watermann I, Walter S, Stevanovic S, Wallwiener D, Guckel B (2003) Evaluation of pre-existent immunity in patients with primary breast cancer: molecular and cellular assays to quantify antigen-specific T lymphocytes in peripheral blood mononuclear cells. *Clin Cancer Res* 9(12):4376–4386
33. Godin-Ethier J, Hanafi LA, Piccirillo CA, Lapointe R (2011) Indoleamine 2, 3-dioxygenase expression in human cancers: clinical and immunologic perspectives. *Clin Cancer Res* 17(22):6985–6991
34. Schreiber H, Wu TH, Nachman J, Kast WM (2002) Immunodominance and tumor escape. *Semin in Cancer Biol* 12(1):25–31
35. Khong HT, Restifo NP (2002) Natural selection of tumor variants in the generation of “tumor escape” phenotypes. *Nat Immunol* 3(11):999–1005

36. Gajewski TF (2006) Identifying and overcoming immune resistance mechanisms in the melanoma tumor microenvironment. *Clin Cancer Res* 12(7 Pt 2):2326s–2330s
37. Willimsky G, Blankenstein T (2005) Sporadic immunogenic tumours avoid destruction by inducing T-cell tolerance. *Nat* 437(7055):141–146
38. DuPage M, Mazumdar C, Schmidt LM, Cheung AF, Jacks T (2012) Expression of tumour-specific antigens underlies cancer immunoediting. *Nat* 482(7385):405–409
39. Ahmad M, Rees RC, Ali SA (2004) Escape from immunotherapy: possible mechanisms that influence tumor regression/progression. *Cancer Immunol Immunother* 53(10):844–854
40. Nagaraj S, Gupta K, Pisarev V, Kinarsky L, Sherman S, Kang L, Herber DL, Schneck J, Gibrilovich DI (2007) Altered recognition of antigen is a mechanism of CD8+ T cell tolerance in cancer. *Nat Med* 13(7):828–835. doi:[10.1038/nm1609](https://doi.org/10.1038/nm1609)
41. Topalian SL, Drake CG, Pardoll DM (2012) Targeting the PD-1/B7-H1(PD-L1) pathway to activate anti-tumor immunity. *Curr Opin Immunol* 24(2):207–212
42. Higano CS, Corman JM, Smith DC, Centeno AS, Steidle CP, Gittleman M, Simons JW, Sacks N, Aimi J, Small EJ (2008) Phase 1/2 dose-escalation study of a GM-CSF-secreting, allogeneic, cellular immunotherapy for metastatic hormone-refractory prostate cancer. *Cancer* 113(5):975–984
43. Emens LA (2009) GM-CSF-secreting vaccines for solid tumors. *Curr Opin Investig Drugs* 10(12):1315–1324
44. Kouivaskaia DV, Berard CA, Datena E, Hussain A, Dawson N, Klyushnenkova EN, Alexander RB (2009) Vaccination with agonist peptide PSA: 154–163 (155L) derived from prostate specific antigen induced CD8 T-cell response to the native peptide PSA: 154–163 but failed to induce the reactivity against tumor targets expressing PSA: a phase 2 study in patients with recurrent prostate cancer. *J Immunother* 32(6):655–666
45. Disis ML, Wallace DR, Gooley TA, Dang Y, Slota M, Lu H, Coveler AL, Childs JS, Higgins DM, Fintak PA, dela Rosa C, Tietje K, Link J, Waisman J, Salazar LG (2009) Concurrent trastuzumab and HER2/neu-specific vaccination in patients with metastatic breast cancer. *J Clin Oncol* 27 (28):4685–4692
46. Perez SA, von Hofe E, Kallinteris NL, Gritzapis AD, Peoples GE, Papamichail M, Baxevanis CN (2010) A new era in anticancer peptide vaccines. *Cancer* 116 (9):2071–2080
47. Noguchi M, Kakuma T, Uemura H, Nasu Y, Kumon H, Hirao Y, Moriya F, Suekane S, Matsuoka K, Komatsu N, Shichijo S, Yamada A, Itoh K (2010) A randomized phase II trial of personalized peptide vaccine plus low dose estramustine phosphate (EMP) versus standard dose EMP in patients with castration resistant prostate cancer. *Cancer Immunol Immunother* 59(7):1001–1009
48. Bolonaki I et al (2007) Vaccination of patients with advanced non-small-cell lung cancer with an optimized cryptic human telomerase reverse transcriptase peptide. *J Clin Oncol* 25(19):2727–2734
49. Perez SA, von Hofe E, Kallinteris NL, Gritzapis AD, Peoples GE, Papamichail M, Baxevanis CN (2010) A new era in anticancer peptide vaccines. *Cancer* 116 (9):2071–2080
50. Koths K (1995) Recombinant proteins for medical use: the attractions and challenges. *Curr Opin in Biotechnol* 6(6):681–687
51. Fujii S, Takayama T, Asakura M, Aki K, Fujimoto K, Shimizu K (2009) Dendritic cell-based cancer immunotherapies. *Archivum Immunologiae et Therapiae Experimentalis* 57(3):189–198
52. Ilett EJ, Prestwich RJ, Melcher AA (2010) The evolving role of dendritic cells in cancer therapy. *Expert Opin Biol Ther* 10 (3):369–379
53. Su Z, Dannull J, Yang BK, Dahm P, Coleman D, Yancey D, Sichi S, Niedzwiecki D, Boczkowski D, Gilboa E, Vieweg J (2005) Telomerase mRNA-transfected dendritic cells stimulate antigen-specific CD8+ and CD4+ T cell responses in patients with metastatic prostate cancer. *J Immunol* 174(6):3798–3807
54. Rice J, Ottensmeier CH, Stevenson FK (2008) DNA vaccines: precision tools for activating effective immunity against cancer. *Nat Rev Cancer* 8(2):108–120

55. Anderson RJ, Schneider J (2007) Plasmid DNA and viral vector-based vaccines for the treatment of cancer. *Vaccine* 25(Suppl 2):B24–B34
56. Collins SA, Guinn BA, Harrison PT, Scallan MF, O'Sullivan GC, Tangney M (2008) Viral vectors in cancer immunotherapy: which vector for which strategy? *Curr Gene Ther* 8(2):66–78
57. Woo CY, Osada T, Clay TM, Lysterly HK, Morse MA (2006) Recent clinical progress in virus-based therapies for cancer. *Expert Opin Biol Ther* 6(11):1123–1134
58. Kantoff PW, Schuetz TJ, Blumenstein BA, Glode LM, Billhartz DL, Wyand M, Manson K, Panicali DL, Laus R, Schlom J, Dahut WL, Arlen PM, Gulley JL, Godfrey WR (2010) Overall survival analysis of a phase II randomized controlled trial of a Poxviral-based PSA-targeted immunotherapy in metastatic castration-resistant prostate cancer. *J Clin Oncol* 28(7):1099–1105
59. Brockstedt DG, Dubensky TW (2008) Promises and challenges for the development of Listeria monocytogenes-based immunotherapies. *Expert Rev Vaccines* 7(7):1069–1084
60. Le DT et al (2012) A live-attenuated Listeria vaccine (ANZ-100) and a live-attenuated Listeria vaccine expressing mesothelin (CRS-207) for advanced cancers: phase I studies of safety and immune induction. *Clin Cancer Res* 18(3):858–868
61. Liu MA (2011) DNA vaccines: an historical perspective and view to the future. *Immunol Rev* 239(1):62–84
62. Kutzler MA, Weiner DB (2008) DNA vaccines: ready for prime time? *Nat Rev Genet* 9(10):776–788
63. Nabel GJ, Kaslow DC, Ulmer JB, Liu MA (2009) DNA vaccines. In: Levine M (ed) *N Generation Vaccines*, 4th edn
64. Liu MA, Ulmer JB (2005) Hum clinical trials of plasmid DNA vaccines. *Adv Genet* 55:25–40
65. Wolff JA, Malone RW, Williams P, Chong W, Acsadi G, Jani A, Felgner PL (1990) Direct gene transfer into mouse muscle in vivo. *Sci* 247(4949 Pt 1):1465–1468
66. Ulmer JB, Donnelly JJ, Parker SE, Rhodes GH, Felgner PL, Dworki VJ, Gromkowski SH, Deck RR, DeWitt CM, Friedman A et al (1993) Heterologous protection against influenza by injection of DNA encoding a viral protein. *Sci* 259(5102):1745–1749
67. Krieg AM, Yi AK, Schorr J, Davis HL (1998) The role of CpG dinucleotides in DNA vaccines. *Trends Microbiol* 6(1):23–27
68. Klinman DM, Yamshchikov G, Ishigatsubo Y (1997) Contribution of CpG motifs to the immunogenicity of DNA vaccines. *J Immunol* 158(8):3635–3639
69. Garcia F, Leon A, Gatell JM, Plana M, Gallart T (2012) Therapeutic vaccines against HIV infection. *Hum Vaccines and Immunotherapeutics* 8(5):569–581
70. Choo AY, Broderick KE, Kim JJ, Sardesai NY (2010) DNA-based influenza vaccines: evaluating their potential to provide universal protection. *IDrugs* 13(10):707–712
71. Griffin DE, Pan CH (2009) Measles: old vaccines, new vaccines. *Curr topics in microbiology and immunol* 330:191–212
72. Grant-Klein RJ, Altamura LA, Schmaljohn CS (2011) Progress in recombinant DNA-derived vaccines for Lassa virus and filoviruses. *Virus Res* 162(1–2):148–161
73. Fissolo N, Montalban X, Comabella M (2012) DNA-based vaccines for multiple sclerosis: current status and future directions. *Clin Immunol* 142(1):76–83
74. Chua KY, Kuo IC, Huang CH (2009) DNA vaccines for the prevention and treatment of allergy. *Curr Opin in Allergy and Clinical Immunol* 9(1):50–54
75. Shimamura M, Sato N, Morishita R (2011) Experimental and clinical application of plasmid DNA in the field of central nervous diseases. *Curr Gene Ther* 11(6):491–500
76. Tabira T (2010) Immunization therapy for Alzheimer disease: a comprehensive review of active immunization strategies. *The Tohoku J Exp Med* 220(2):95–106
77. Davidson AH, Traub-Dargatz JL, Rodeheaver RM, Ostlund EN, Pedersen DD, Moorhead RG, Stricklin JB, Dewell RD, Roach SD, Long RE, Albers SJ, Callan RJ, Salman MD (2005) Immunologic responses to West Nile virus in vaccinated and clinically affected horses. *J Am Vet Med Assoc*, 226 (2):240–245

78. Garver KA, LaPatra SE, Kurath G (2005) Efficacy of an infectious hematopoietic necrosis (IHN) virus DNA vaccine in Chinook *Oncorhynchus tshawytscha* and sockeye *O. nerka* salmon. *Diseases of Aquatic Org* 64 (1):13–22
79. Yuan J, Ku GY, Gallardo HF, Orlandi F, Manukian G, Rasalan TS, Xu Y, Li H, Vyas S, Mu Z, Chapman PB, Krown SE, Panageas K, Terzulli SL, Old LJ, Houghton AN, Wolchok JD (2009) Safety and immunogenicity of a human and mouse gp100 DNA vaccine in a phase I trial of patients with melanoma. *Cancer Immun* 9:5
80. Ginsberg BA, Gallardo HF, Rasalan TS, Adamow M, Mu Z, Tandon S, Bewkes BB, Roman RA, Chapman PB, Schwartz GK, Carvajal RD, Panageas KS, Terzulli SL, Houghton AN, Yuan JD, Wolchok JD (2010) Immunologic response to xenogeneic gp100 DNA in melanoma patients: comparison of particle-mediated epidermal delivery with intramuscular injection. *Clin Cancer Res* 16(15):4057–4065
81. Wolchok JD, Yuan J, Houghton AN, Gallardo HF, Rasalan TS, Wang J, Zhang Y, Ranganathan R, Chapman PB, Krown SE, Livingston PO, Heywood M, Riviere I, Panageas KS, Terzulli SL, Perales MA (2007) Safety and immunogenicity of tyrosinase DNA vaccines in patients with melanoma. *Mol Ther* 15(11):2044–2050
82. Weber J, Boswell W, Smith J, Hersh E, Snively J, Diaz M, Miles S, Liu X, Obrocea M, Qiu Z, Bot A (2008) Phase I trial of intranodal injection of a Melan-A/MART-1 DNA plasmid vaccine in patients with stage IV melanoma. *J Immunother* 31(2):215–223
83. Dangoor A, Lorigan P, Keilholz U, Schadendorf D, Harris A, Ottensmeier C, Smyth J, Hoffmann K, Anderson R, Cripps M, Schneider J, Hawkins R (2010) Clinical and immunological responses in metastatic melanoma patients vaccinated with a high-dose poly-epitope vaccine. *Cancer Immunol Immunother* 59(6):863–873. doi:10.1007/s00262-009-0811-7
84. Smith CL, Dunbar PR, Mirza F, Palmowski MJ, Shepherd D, Gilbert SC, Coulie P, Schneider J, Hoffman E, Hawkins R, Harris AL, Cerundolo V (2005) Recombinant modified vaccinia Ankara primes functionally activated CTL specific for a melanoma tumor antigen epitope in melanoma patients with a high risk of disease recurrence. *Int J Cancer* 113(2):259–266
85. McNeel DG, Dunphy EJ, Davies JG, Frye TP, Johnson LE, Staab MJ, Horvath DL, Straus J, Alberti D, Marmochia R, Liu G, Eickhoff JC, Wilding G (2009) Safety and immunological efficacy of a DNA vaccine encoding prostatic acid phosphatase in patients with stage D0 prostate cancer. *J Clin Oncol* 27(25):4047–4054
86. Becker JT, Olson BM, Johnson LE, Davies JG, Dunphy EJ, McNeel DG (2010) DNA vaccine encoding prostatic acid phosphatase (PAP) elicits long-term T-cell responses in patients with recurrent prostate cancer. *J Immunother* 33(6):639–647
87. Pavlenko M, Roos AK, Lundqvist A, Palmberg A, Miller AM, Ozenci V, Bergman B, Egevad L, Hellstrom M, Kiessling R, Masucci G, Wersall P, Nilsson S, Pisa P (2004) A phase I trial of DNA vaccination with a plasmid expressing prostate-specific antigen in patients with hormone-refractory prostate cancer. *Br J Cancer* 91(4):688–694
88. Miller AM, Ozenci V, Kiessling R, Pisa P (2005) Immune monitoring in a phase I trial of a PSA DNA vaccine in patients with hormone-refractory prostate cancer. *J Immunother* 28(4):389–395
89. Todorova K, Ignatova I, Tchakarov S, Altankova I, Zoubak S, Kyurkchiev S, Mincheff M (2005) Humoral immune response in prostate cancer patients after immunization with gene-based vaccines that encode for a protein that is proteasomally degraded. *Cancer Immun* 5:1
90. Low L, Mander A, McCann K, Dearnaley D, Tjelle T, Mathiesen I, Stevenson F, Ottensmeier CH (2009) DNA vaccination with electroporation induces increased antibody responses in patients with prostate cancer. *Hum Gene Ther* 20(11):1269–1278
91. Chudley L, McCann K, Mander A, Tjelle T, Campos-Perez J, Godeseth R, Creak A, Dobbyn J, Johnson B, Bass P, Heath C, Kerr P, Mathiesen I, Dearnaley D, Stevenson F, Ottensmeier C (2012) DNA fusion-gene vaccination in patients with prostate cancer induces high-frequency CD8(+) T-cell responses and increases PSA doubling time. *Cancer Immunol Immunother* 61(11):2161–2170. doi:10.1007/s00262-012-1270-0

92. Boshart M, Weber F, Jahn G, Dorsch-Hasler K, Fleckenstein B, Schaffner W (1985) A very strong enhancer is located upstream of an immediate early gene of human cytomegalovirus. *Cell* 41(2):521–530
93. Garmory HS, Brown KA, Titball RW (2003) DNA vaccines: improving expression of antigens. *Genet Vaccines Ther* 1(1):2
94. Weeratna RD, Wu T, Efler SM, Zhang L, Davis HL (2001) Designing gene therapy vectors: avoiding immune responses by using tissue-specific promoters. *Gene Ther* 8(24):1872–1878
95. Chapman BS, Thayer RM, Vincent KA, Haigwood NL (1991) Effect of intron A from human cytomegalovirus (Towne) immediate-early gene on heterologous expression in mammalian cells. *Nucleic Acids Res* 19(14):3979–3986
96. Huang MT, Gorman CM (1990) Intervening sequences increase efficiency of RNA 3' processing and accumulation of cytoplasmic RNA. *Nucleic Acids Res* 18(4):937–947
97. Le Hir H, Nott A, Moore MJ (2003) How introns influence and enhance eukaryotic gene expression. *Trends Biochem Sci* 28(4):215–220
98. Barouch DH, Yang ZY, Kong WP, Koriath-Schmitz B, Sumida SM, Truitt DM, Kishko MG, Arthur JC, Miura A, Mascola JR, Letvin NL, Nabel GJ (2005) A human T-cell leukemia virus type 1 regulatory element enhances the immunogenicity of human immunodeficiency virus type 1 DNA vaccines in mice and nonhuman primates. *J Virol* 79(14):8828–8834
99. Bodles-Brakhop AM, Draghia-Akli R (2008) DNA vaccination and gene therapy: optimization and delivery for cancer therapy. *Expert Rev Vaccines* 7(7):1085–1101
100. Hirao LA, Wu L, Khan AS, Hokey DA, Yan J, Dai A, Betts MR, Draghia-Akli R, Weiner DB (2008) Combined effects of IL-12 and electroporation enhances the potency of DNA vaccination in macaques. *Vaccine* 26(25):3112–3120
101. Tejada-Mansir A, Montesinos RM (2008) Upstream processing of plasmid DNA for vaccine and gene therapy applications. *Recent Patents on Biotechnol* 2(3):156–172
102. Kozak M (1987) At least six nucleotides preceding the AUG initiator codon enhance translation in mammalian cells. *J Mol Biol* 196(4):947–950
103. Olson BM, Johnson LE, McNeel DG (2012) The androgen receptor: a biologically relevant vaccine target for the treatment of prostate cancer. *Cancer Immunol Immunother*
104. Uchijima M, Yoshida A, Nagata T, Koide Y (1998) Optimization of codon usage of plasmid DNA vaccine is required for the effective MHC class I-restricted T cell responses against an intracellular bacterium. *J Immunol* 161(10):5594–5599
105. Nagata T, Uchijima M, Yoshida A, Kawashima M, Koide Y (1999) Codon optimization effect on translational efficiency of DNA vaccine in mammalian cells: analysis of plasmid DNA encoding a CTL epitope derived from microorganisms. *Biochem and Biophys Res comm* 261(2):445–451
106. Cid-Arregui A, Juarez V, zur Hausen H (2003) A synthetic E7 gene of human papillomavirus type 16 that yields enhanced expression of the protein in mammalian cells and is useful for DNA immunization studies. *J Virol*, 77 (8):4928–4937
107. Cheung YK, Cheng SC, Sin FW, Xie Y (2004) Plasmid encoding papillomavirus Type 16 (HPV16) DNA constructed with codon optimization improved the immunogenicity against HPV infection. *Vaccine* 23(5):629–638
108. Kim MS, Sin JI (2005) Both antigen optimization and lysosomal targeting are required for enhanced anti-tumour protective immunity in a human papillomavirus E7-expressing animal tumour model. *Immunol* 116(2):255–266
109. Leifert JA, Rodriguez-Carreno MP, Rodriguez F, Whitton JL (2004) Targeting plasmid-encoded proteins to the antigen presentation pathways. *Immunol Rev* 199:40–53
110. Rodriguez F, An LL, Harkins S, Zhang J, Yokoyama M, Widera G, Fuller JT, Kincaid C, Campbell IL, Whitton JL (1998) DNA immunization with minigenes: low frequency of memory cytotoxic T lymphocytes and inefficient antiviral protection are rectified by ubiquitination. *J Virol* 72(6):5174–5181
111. Rodriguez F, Zhang J, Whitton JL (1997) DNA immunization: ubiquitination of a viral protein enhances cytotoxic T-lymphocyte induction and antiviral protection but abrogates antibody induction. *J Virol* 71(11):8497–8503

112. Barry MA, Lai WC, Johnston SA (1995) Protection against mycoplasma infection using expression-library immunization. *Nat 377*(6550):632–635
113. Delogu G, Howard A, Collins FM, Morris SL (2000) DNA vaccination against tuberculosis: expression of a ubiquitin-conjugated tuberculosis protein enhances antimycobacterial immunity. *Infection and Imm* 68(6):3097–3102
114. Xiang R, Lode HN, Chao TH, Ruehlmann JM, Dolman CS, Rodriguez F, Whitton JL, Overwijk WW, Restifo NP, Reisfeld RA (2000) An autologous oral DNA vaccine protects against murine melanoma. *Proc Natl Acad Sci USA* 97(10):5492–5497
115. Leachman SA, Shylankevich M, Slade MD, Levine D, Sundaram RK, Xiao W, Bryan M, Zelterman D, Tiegelaar RE, Brandsma JL (2002) Ubiquitin-fused and/or multiple early genes from cottontail rabbit papillomavirus as DNA vaccines. *J Virol* 76(15):7616–7624
116. Rogers S, Wells R, Rechsteiner M (1986) Amino acid sequences common to rapidly degraded proteins: the PEST hypothesis. *Sci* 234(4774):364–368
117. Sewell DA, Shahabi V, Gunn GR 3rd, Pan ZK, Dominiacki ME, Paterson Y (2004) Recombinant *Listeria* vaccines containing PEST sequences are potent immune adjuvants for the tumor-associated antigen human papillomavirus-16 E7. *Cancer Res* 64(24):8821–8825
118. Starodubova ES, Boberg A, Litvina M, Morozov A, Petrakova NV, Timofeev A, Latshev O, Tunitskaya V, Wahren B, Isagulians MG, Karpov VL (2008) HIV-1 reverse transcriptase artificially targeted for proteasomal degradation induces a mixed Th1/Th2-type immune response. *Vaccine* 26(40):5170–5176
119. Varshavsky A (1996) The N-end rule: functions, mysteries, uses. *Proc Natl Acad Sci USA* 93(22):12142–12149
120. Tobery T, Siliciano RF (1999) Cutting edge: induction of enhanced CTL-dependent protective immunity in vivo by N-end rule targeting of a model tumor antigen. *J Immunol* 162(2):639–642
121. Wu Y, Kipps TJ (1997) Deoxyribonucleic acid vaccines encoding antigens with rapid proteasome-dependent degradation are highly efficient inducers of cytolytic T lymphocytes. *J Immunol* 159(12):6037–6043
122. Anton LC, Schubert U, Bacik I, Princiotta MF, Wearsch PA, Gibbs J, Day PM, Realini C, Rechsteiner MC, Bennink JR, Yewdell JW (1999) Intracellular localization of proteasomal degradation of a viral antigen. *J Cell Biol* 146(1):113–124
123. Anderson K, Cresswell P, Gammon M, Hermes J, Williamson A, Zweerink H (1991) Endogenously synthesized peptide with an endoplasmic reticulum signal sequence sensitizes antigen processing mutant cells to class I-restricted cell-mediated lysis. *J Exp Med* 174(2):489–492
124. Bacik I, Cox JH, Anderson R, Yewdell JW, Bennink JR (1994) TAP (transporter associated with antigen processing)-independent presentation of endogenously synthesized peptides is enhanced by endoplasmic reticulum insertion sequences located at the amino- but not carboxyl-terminus of the peptide. *J Immunol* 152(2):381–387
125. Ciernik IF, Berzofsky JA, Carbone DP (1996) Induction of cytotoxic T lymphocytes and antitumor immunity with DNA vaccines expressing single T cell epitopes. *J Immunol* 156(7):2369–2375
126. Rice J, King CA, Spellerberg MB, Fairweather N, Stevenson FK (1999) Manipulation of pathogen-derived genes to influence antigen presentation via DNA vaccines. *Vaccine* 17(23–24):3030–3038
127. Wallin RP, Lundqvist A, More SH, von Bonin A, Kiessling R, Ljunggren HG (2002) Heat-shock proteins as activators of the innate immune system. *Trends in Immunol* 23(3):130–135
128. Gallucci S, Matzinger P (2001) Danger signals: SOS to the immune system. *Curr Opin Immunol* 13(1):114–119
129. Wells AD, Rai SK, Salvato MS, Band H, Malkovsky M (1998) Hsp72-mediated augmentation of MHC class I surface expression and endogenous antigen presentation. *Int Immunol* 10(5):609–617

130. Wells AD, Malkovsky M (2000) Heat shock proteins, tumor immunogenicity and antigen presentation: an integrated view. *Immunol Today* 21(3):129–132
131. Suzue K, Zhou X, Eisen HN, Young RA (1997) Heat shock fusion proteins as vehicles for antigen delivery into the major histocompatibility complex class I presentation pathway. *Proc Natl Acad Sci USA* 94(24):13146–13151
132. Chu NR, Wu HB, Wu T, Boux LJ, Siegel MI, Mizzen LA (2000) Immunotherapy of a human papillomavirus (HPV) type 16 E7-expressing tumour by administration of fusion protein comprising *Mycobacterium bovis* bacille Calmette-Guerin (BCG) hsp65 and HPV16 E7. *Clin and Exp Immunol* 121(2):216–225
133. Geng H, Zhang GM, Xiao H, Yuan Y, Li D, Zhang H, Qiu H, He YF, Feng ZH (2006) HSP70 vaccine in combination with gene therapy with plasmid DNA encoding sPD-1 overcomes immune resistance and suppresses the progression of pulmonary metastatic melanoma. *Int J Cancer* 118(11):2657–2664
134. Chen CH, Wang TL, Hung CF, Yang Y, Young RA, Pardoll DM, Wu TC (2000) Enhancement of DNA vaccine potency by linkage of antigen gene to an HSP70 gene. *Cancer Res* 60(4):1035–1042
135. Ji H, Wang TL, Chen CH, Pai SI, Hung CF, Lin KY, Kurman RJ, Pardoll DM, Wu TC (1999) Targeting human papillomavirus type 16 E7 to the endosomal/lysosomal compartment enhances the antitumor immunity of DNA vaccines against murine human papillomavirus type 16 E7-expressing tumors. *Hum Gene Ther* 10(17):2727–2740
136. Williams JA, Carnes AE, Hodgson CP (2009) Plasmid DNA vaccine vector design: impact on efficacy, safety and upstream production. *Biotechnol Adv* 27(4):353–370
137. Sato Y, Roman M, Tighe H, Lee D, Corr M, Nguyen MD, Silverman GJ, Lotz M, Carson DA, Raz E (1996) Immunostimulatory DNA sequences necessary for effective intradermal gene immunization. *Sci* 273(5273):352–354
138. Schneeberger A, Wagner C, Zemann A, Luhrs P, Kutil R, Goos M, Stingl G, Wagner SN (2004) CpG motifs are efficient adjuvants for DNA cancer vaccines. *J invest Derm* 123(2):371–379
139. McCluskie MJ, Weeratna RD, Davis HL (2000) The role of CpG in DNA vaccines. *Springer Semin Immunopathology* 22(1–2):125–132
140. Barber GN (2011) Innate immune DNA sensing pathways: STING, AIMII and the regulation of interferon production and inflammatory responses. *Curr Opin Immunol* 23(1):10–20
141. Vilaysane A, Muruve DA (2009) The innate immune response to DNA. *Semin Immunol* 21(4):208–214
142. Sharma S, Fitzgerald KA (2011) Innate immune sensing of DNA. *PLoS Pathog* 7(4):e1001310
143. Herrada AA, Rojas-Colonelli N, Gonzalez-Figueroa P, Roco J, Oyarce C, Ligtnerberg MA, Lladser A (2012) Harnessing DNA-induced immune responses for improving cancer vaccines. *Hum Vaccines Immunother* 8(11):1682–1693
144. Engelhorn ME, Guevara-Patino JA, Merghoub T, Liu C, Ferrone CR, Rizzuto GA, Cymerman DH, Posnett DN, Houghton AN, Wolchok JD (2008) Mechanisms of immunization against cancer using chimeric antigens. *Mol Ther* 16(4):773–781
145. Staff C, Mozaffari F, Haller BK, Wahren B, Liljefors M (2011) A Phase I safety study of plasmid DNA immunization targeting carcinoembryonic antigen in colorectal cancer patients. *Vaccine* 29(39):6817–6822
146. Conry RM, Curiel DT, Strong TV, Moore SE, Allen KO, Barlow DL, Shaw DR, LoBuglio AF (2002) Safety and immunogenicity of a DNA vaccine encoding carcinoembryonic antigen and hepatitis B surface antigen in colorectal carcinoma patients. *Clin Cancer Res* 8(9):2782–2787
147. Saade F, Petrovsky N (2012) Technologies for enhanced efficacy of DNA vaccines. *Expert Rev Vaccines* 11(2):189–209

Part III
Nanoengineering

Chapter 18

Multifunctional Nanoscale Delivery Systems for Nucleic Acids

Richard Conroy and Belinda Seto

18.1 Introduction

The ability to deliver nucleic acids to specific sites within the body is a significant engineering problem, but one that, when fully addressed, will radically change how diseases and conditions are treated. Only a small fraction of the discoveries made in the laboratory have progressed to clinical trials because of challenges in developing efficient, sensitive, and specific delivery systems. Ideally, a delivery system is taken up only by the targeted cells and does not cause unwanted side effects, the nucleic acid cargo is not degraded before reaching its intracellular target, and there is sufficient delivery to produce a sustained therapeutic effect. However, in a complex, heterogeneous human population, all of these characteristics are hard to achieve reproducibility.

Of the more than 1,800 gene therapy clinical trials started by the end of 2012, more than two-thirds have used viral vectors, but fewer than 5 % have progressed beyond the equivalent of phase II of the US Food and Drug Administration (FDA) regulatory process. Two-thirds of the studies have been carried out in the United States and a similar fraction has focused on cancer-related indications [1]. The number of small interfering ribonucleic acids (siRNA) clinical trials is more modest at around 30 studies, although for this type of nucleic acid, the use of synthetic vectors outnumbers the use of viral vectors [2].

Synthetic and viral delivery systems offer contrasting advantages. In general terms, viral vectors promise excellent performance characteristics and make better use of multiple biological systems but have significant safety concerns, whereas synthetic vectors have better safety profiles, but much lower efficiency. Much of the work over the past two decades has focused on addressing these safety and efficacy concerns and optimizing one or two steps of what is a multi-step delivery process.

R. Conroy · B. Seto (✉)
National Institute of Biomedical Imaging and Bioengineering,
National Institutes of Health, 6707 Democracy Blvd, Suite 200,
Bethesda, MD 20892, USA
e-mail: setob@mail.nih.gov

However, beyond discovery-driven research and individual step optimization, it is clear that by taking a systems approach to delivery, there are multiple paths to more widespread clinical reality with safe and effective multifunctional nanoscale delivery systems tailored to individual conditions and therapeutic agents.

Delivery systems are not absolutely required for deoxyribonucleic acid (DNA) to generate a therapeutic effect *in vivo*. Local delivery of naked DNA into skeletal muscle [3], heart muscle [4], and into tumors [5] is sufficient to induce a response. Indeed, naked or plasmid DNAs (pDNA) are the third most common delivery approach used in gene therapy clinical trials and are three times more common than liposome systems [1]. However, for RNA interference (RNAi) therapies, nucleases will degrade up to 70 % of naked siRNA molecules within minutes of systemic administration [6], requiring chemical modification or a protective carrier for efficient use. To increase their efficiency and effectiveness, they need to be protected from capture and degradation before reaching their target, to have their anionic backbone shielded for efficient cell uptake, and to be targeted to cells of interest without provoking an immune response or increasing systemic clearance. Although at a very early stage, the potential to rationally design and engineer multifunctional vectors is particularly exciting and a step toward making nucleic-acid-based therapy a routine clinical tool.

The growing availability of tools to engineer delivery systems at the nanometer level, commensurate with the persistence length of nucleic acids, has led to a deeper understanding of how the unique properties of matter can be exploited in this size range, as well as enhancing *in vivo* delivery. The size, shape, charge, composition, mechanical stiffness, and surface functionalization of delivery systems influence both the physiological and cellular barriers to delivery. For example, particles above 200 nm in size are susceptible to phagocytosis in the reticular endothelial system, and particles below 100 nm can get caught in Kupffer cells, while particles below 5 nm are removed by glomerular filtration. Particles below 40 nm can freely diffuse in a cell's cytoplasm, while below 5 nm, they can cross the capillary endothelium and particles below 1 nm in size can translocate the cell membrane. Most nanoscale delivery systems fall in the 5–200 nm range and, after systemic administration, circulate in the blood stream until cleared or moved into the extracellular space. If they come in contact with a target cell, they can enter the cell through a number of mechanisms. For example, if they enter by endocytosis, the nucleic acids need to make a timely escape before degradation in a lysosome.

All of these interactions can be tuned by engineering the delivery system's physical, chemical, and biological characteristics. An ideal multifunctional nanoscale delivery system efficiently delivers its nucleic acid cargo to the desired site and effectively releases the cargo at the desired time, while performing additional functions, such as simultaneous drug delivery, providing imaging contrast, or environmental sensing. For efficient and effective delivery, the system should include site-specific targeting and the ability to disrupt the normal cell pathways to deliver its nucleic acid payload. While doing this, the delivery system and payload must be carefully tuned not to stimulate the immune system, create toxicity, or be

captured or degraded by the circulatory system. In this chapter, we will review recent research developments in both viral and nonviral vectors, focusing on progress toward the clinical application of these nanoscale delivery systems.

18.2 Delivery Systems

The delivery of nucleic acids *in vivo* requires a safe, stable, sensitive, and specific approach. In order to prevent degradation, to reduce side effects, and promote efficient delivery, nucleic acids can be encapsulated, bound, or complexed into nanometer-sized constructs. The physical and chemical properties of these constructs can be tuned to change clearance rates, uptake processes, and intracellular fate and to account for delivery method. Although systemic injection is the most common delivery method, physical methods such as stereotactic injection and ballistic delivery as well as the use of optical, magnetic, electric, and ultrasound fields to generate force and disrupt the cell membrane can be used to enhance uptake. Effective delivery of nucleic acids can also be achieved by topical administration [7], nasal delivery [8], and direct injection into the brain [9].

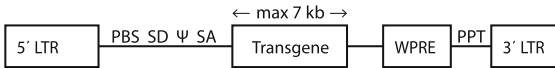
18.2.1 Viral Delivery Systems for Nucleic Acids

Viruses are efficient vehicles for delivering nucleic acids to a wide range of organisms. Viruses have evolved natural mechanisms to enter their host cells and are capable of delivering kilobase-long nucleic acid sequences to a wide range of target cells. These are major advantages *in vivo*, where the goal is to deliver the nucleic acids to specific targets without causing significant harm to the host. As such, viral vectors have been designed to be stable, achieve efficient transduction, and have high viral titer and sustained expression of the heterologous nucleic acids of interest (transgenes). Figure 18.1 illustrates general schemes for the design of three commonly used viral vectors. Despite the many advantages of viral delivery vectors, they are known to be capable of producing several adverse effects, which include immune reactions, oncogene activation, and nonspecific cellular tropism [10].

18.2.1.1 Retroviral Vectors

Retroviruses are enveloped RNA viruses of 80–130 nm in diameter with a genome size of 8–11 kilobases (kb) [11]. Retroviral genomes are made up of *gag*, *pol*, *env*, and 5' and 3' long terminal repeats (LTR). Retroviral vectors are rendered replication defective by deleting the structural, envelope, and enzymatic genes, and instead, the desired transgenes are inserted [12]. These replication-defective vectors, or proviruses, are incapable of continuing to spread after the initial infection of

Gammaretroviral vector



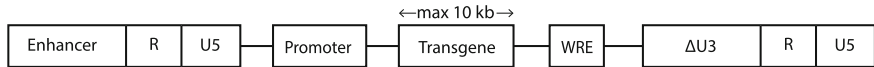
Ψ: packaging signal
 PBS: tRNA binding site
 LTR: long terminal repeats
 WPRE: woodchuck hepatitis post-transcriptional regulatory element

Helper plasmid

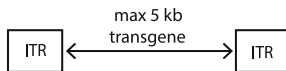


prom: promoter
 gag: structural proteins
 pol: replication enzymes
 pA: poly A signal

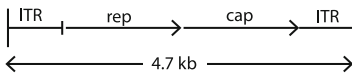
Lentiviral Vectors



AAV Vectors



AAV Genome



rep: replication proteins
 cap: capsid proteins, VP1, VP2, VP3
 ITR: inverted terminal repeats, replication origin, and packaging signal

Fig. 18.1 Viral vector designs

the target cells. The initial round of vector replication is dependent on several *cis* acting elements from the viral genome, including a promoter and polyadenylation signal, reverse transcription signal, transfer RNA (tRNA), primer binding site (PBS), and a polyurine tract, to initiate complementary DNA (cDNA) synthesis. Cellular tRNA binds to the PBS to initiate reverse transcription. Vectors containing the transgene are then packaged into viral particles as directed by a packaging signal (Ψ), PBS, and LTRs. Helper viruses, or plasmids, that carry the viral genes *gag/pol* and *env*, but lacking the packaging signal ψ [13], are required to express the viral proteins needed to produce vector-containing infectious viral particles. The helper function can also be provided by transfecting helper plasmids into cell cultures to produce helper cells [14]. The process of expressing the transgene in the retroviral vectors and delivering them to the target cells is called transduction [13].

Entry of the viral vectors into targeted cells is an essential first step in viral-vector-based gene delivery. Gaining entry into cells involves the interaction of the viral envelope with the host cell receptor. For lentiviral vectors, which are derived from human immunodeficiency virus type 1 (HIV1) [15], this involves a two-stage process [16]. Initially, the glycoprotein 120 (gp120) subunit of the envelope protein interacts with the target cell receptor CD4. The resulting conformational changes in gp120 allow binding with the co-receptors CXCR4 or CCR5, which belong to the chemokine family [17, 18]. Subsequently, another envelope protein subunit, gp41, signals fusion that is then followed by the release of viral capsid into the cytoplasm of the target cells. In addition to viral entry, the envelope plays an important role in determining cellular tropism by a technique called pseudotyping, where a viral vector is combined with foreign envelope proteins. Cellular tropism enhances the range of susceptible cells for the viral vectors. The lentiviral vector envelope can be substituted by the vesicular stomatitis virus G glycoprotein (VSV-G). This pseudotyping strategy has been shown not only to increase the range of possible target cell types, but also to improve stability and increase viral titers [13, 19]. Gammaretroviral vectors, e.g., murine leukemia viral vectors, transduce only dividing cells [20] and have a narrow range of cells that can have genetic material transferred to them. However, these vectors have ready access to the host genome because the nuclear membrane is removed during cell division. In contrast, lentiviral vectors transduce a wide variety of cell types, both dividing and nondividing cells such as neurons and B and T cells, albeit with varying degree of transduction efficiency [19, 21, 22].

A distinguishing feature of retroviruses is their ability to integrate into the host genome, resulting in sustained expression of the transgene. However, integration presents challenges in vector design if the vector is inserted at a site where the regulatory elements in the vector result in transcriptional activation of oncogenes [23]. Such insertional mutagenesis was the underlying cause for the adverse events in an early human gene transfer trial involving patients with severe combined immunodeficiency defect (SCID) [24]. Some patients involved in this trial subsequently developed T-cell leukemia. For lentiviral vectors, the risk of insertional mutagenesis can be reduced by designing self-inactivation (SIN) vectors that lack the viral transcriptional control elements, promoter/enhancer, and, thus, reduce the possibility of activating an oncogene located adjacent to the vector integration site [25]. Strategies have also been developed to target specific chromosomal insertion sites for the transgenes [26]. Research has also led to approaches to avoid integration. Because integration requires integrase attachment on the LTRs, mutating the integrase gene or modifying the attachment sequences of the LTRs may eliminate integration [27]. The transgene can also be expressed as episomal DNA without integration into the host genome. Such expression can occur for a relatively long duration in nondividing cells, such as retina cells [28, 29], or transiently in dividing cells.

Gammaretroviral vectors can accommodate up to 7 kb sequences [30, 31], while lentiviral vectors can accommodate larger transgenes, up to 10 kb [25]. In addition to the length of the inserted sequences, vector design must also consider stability issues. Retroviral vectors have half-lives of a few hours at 37 °C

and up to a few months at -80°C . A contributing factor to the instability is the loss of function of the envelope protein. Another factor to consider is viral titer. Lentiviral vectors can be produced at 10^7 transducing units/ml. The titer can be increased to 10^9 – 10^{10} transducing units/ml by ultracentrifugation [25]. However, titers may decrease when larger transgenes are inserted.

The first human gene transfer was conducted in 1989, as an immunotherapy to treat patients with advanced melanoma, using retroviral vectors and tumor-infiltrating lymphocytes [32, 33]. Targeted gene therapy began in 1990 with the adenosine deaminase gene for treatment of SCID [34]. Since then, numerous disorders have been treated by gene therapy [35]. They include inherited genetic disorders that involve autosomal X-linked recessive single genes or some autosomal dominant genes, and some acquired diseases, such as cancer, vascular diseases, neurodegenerative disorders, and inflammatory diseases. The first clinical trial using lentiviral vectors was approved in 2002 [36]. Currently several clinical trials are underway in which lentiviral vectors have been used to: (1) treat HIV infection, (2) transduce neuronal cells of the central nervous system for the treatment of Parkinson's disease [37], and (3) deliver beta-globin gene for beta-thalassemia treatment [38].

There are safety concerns with the use of retroviral vectors for gene delivery. Both gammaretroviral and lentiviral vectors have the potential to illicit an immune response from the host. Immune reactions toward the viral vector result in rejection of all expressing cells. However, it should be noted that immune response is a beneficial outcome if lentiviral vectors are used to deliver genetic vaccines to treat HIV infection. Another serious safety issue is homologous recombination, which occurs when the packaging virus recombines with the vector to produce replication competent viruses. These viruses can produce harmful infections, and additionally gammaretroviruses can also cause cancer if an oncogene is activated by insertional mutagenesis [39]. In contrast, there is no evidence that lentiviral vectors result in oncogene activation through insertional mutagenesis. Another concern is the spread of the vector beyond the intended target tissue, which may cause persistent unwanted biological activity or unpredictable responses. All of these concerns have increased caution in the use of retroviral vectors although their advantages can be overwhelmingly attractive.

18.2.1.2 Adeno-Associated Viral Vectors

Adeno-associated virus (AAV) is a small, single-stranded DNA virus of 4,681 nucleotides (nt). The wild-type (wt) genome is made up of two genes, *rep* and *cap*, that encode four replication proteins and three capsid proteins, respectively. The three capsid proteins, Vp1, Vp2, and Vp3, are produced from the same open reading frame, but from differential splicing (Vp1) and alternative translational start sites (Vp2 and Vp3, respectively) [40]. Vp3 is the most abundant subunit in the virion and interacts with the host cell receptor. Recognition of Vp3 by the receptor determines cellular tropism of the virus. A phospholipase domain, essential for viral

infectivity, has been identified in the unique N-terminus of Vp1 [41, 42]. The functional significance of Vp2 remains to be resolved. The viral genome is flanked on either side by 145-bp inverted terminal repeats (ITR) [43]. With the deletion of most of the viral genes, transgenes can be inserted into the *cis* 145-bp ITRs, to create a recombinant AAV (rAAV). The transgene can be expressed in the transduced cells without integration into the host cell genome and persists as episomal DNA [44]. The small genome size poses a limitation for AAV vector in delivering large transgenes. However, recent studies have shown delivery of genomes up to 6 kb, although delivery of these larger payloads was less efficient [43, 45]. Typically, transgenes of up to 5 kb are delivered. Strategies have been developed to improve efficiency, for example by splitting the vectors, with each vector containing approximately half of the transgene within the same cell. This approach, however, is still limited by viral packaging capacity. Additionally, cells have to be infected with different viral particles to achieve full transgene expression.

Transcapsidation is an approach to improve the packaging capacity, increase tissue tropisms, and transduction efficiency, where more than 100 different capsids from different serotypes can be exchanged to produce dozens of rAAV containing the same genome [45]. AAV serotype 2 is the best-studied AAV and was the first one used for gene transfer. However, vectors derived from alternative serotypes, e.g., 1, 4, 5, and 6 have been packaged with the same vector genome, but different viral capsids to improve efficiency and tropisms [46, 47].

rAAVs have been used in gene therapies in human muscle, liver, lung, central nervous system [48], and recently in the retina [49]. In a gene therapy trial of Parkinson's patients, there was an improvement in the Unified Parkinson's Disease Rating Scale (UPDRS) after 6 months for patients who received the glutamic acid decarboxylase (GAD) gene carried by an AAV2 vector that was delivered to the subthalamic nucleus [50]. rAAV2 vector carrying the gene encoding retinal pigment epithelium-specific 65-kilodalton protein (RPE65) has been used in a gene therapy trial to treat severe retinal dystrophy [51]. These results show promise, but further clinical trials are needed to demonstrate clinical significance.

18.2.2 Nonviral Delivery Systems

There has been a four-decade long history of nonviral delivery system development, prompted by on-going safety concerns associated with viral vectors. DNA transfection protocols emerged in the late 1970s, and liposome-based gene delivery strategies were first reported in the 1980s, though the field really took off in the late 1990s with the discovery of siRNA which required the use of a delivery system *in vivo*. Nonviral delivery systems are attractive because they typically have lower immunogenicity, lower toxicity, and their production can be easily scaled for widespread clinical use; but they also have disadvantages. These disadvantages lead to lower efficiency at each stage of the delivery process, with an overall efficiency <0.1 %.

There are a number of basic engineering considerations in the design of all synthetic vectors. They should be nontoxic, nonimmunogenic, and biodegradable, protect their nucleic acid cargo against degradation, and efficiently deliver their cargo to both the cells of interest and the desired intracellular target. Optimizing the efficiency of nonviral delivery has been the focus of much research, which includes understanding the best targeting approach for selecting the cells of interest, how the stability of formulations change after administration, and how to get efficient endosomal release. Some of the barriers to delivery are illustrated in Fig. 18.2 and include: (1) formation of nucleic acid complex, (2) entry of the complex into the cells of interest, (3) endosomal escape of the nucleic acids, (4) dissociation of the complex, and (5) transport of the nucleic acid to site of action [52]. In contrast to viral vectors, synthetic vectors are poorly optimized to take advantage of existing cellular architecture. In particular, they cannot control endosomal release, have low diffusion rate, and are unable to take advantage of active transport mechanisms. Ideally for DNA, delivery is perinuclear, and for siRNA, it is targeting of the RNA-induced silencing complex (RISC). However, the rate-limiting steps of delivery are not fully understood, and there is not a good mechanistic understanding of how to rationally optimize loading rate.

A further challenge has been that the optimization of synthetic vectors for efficient *in vitro* cell culture delivery rarely translates to similar *in vivo* results. Monolayers of selected cells, in a carefully controlled environment, are not representative of the complex *in vivo* environment. The *in vivo* environment is a three-dimensional heterogeneous structure in an extracellular matrix, complete with enzymes, different cell morphologies, and a circulatory and immune system that cannot be easily replicated *in vitro*. In the worst case, some parameters can be optimized *in vitro* based on misleading effects which do not occur *in vivo*. In cell culture, size can be an advantage due to sedimentation efficiency, but *in vivo* smaller (less than 40 nm) particles are favored because of faster diffusion rates [53]. Another example is that positively charged vectors are beneficial *in vitro* for binding nucleic acids and enhancing uptake by interacting with the negatively charged cell membrane. However *in vivo*, negatively charged serum will bind to the vector, significantly reducing effectiveness. Some of the common designs for synthetic nanoscale delivery systems are illustrated in Fig. 18.3 and described in more detail in the following sections.

18.2.2.1 Bioconjugation

Bioconjugation is a technique for improving delivery by covalently linking nucleic acids to bioactive targeting agents. Bioconjugation to lipids, sugars, polyethylene glycol (PEG), and peptides is in principle more attractive than delivery with cationic liposomes and cationic polymers due to the advantages of smaller-size and enhanced pharmacokinetics. They easily clear systemic circulation and, thus, can be useful for targeting oligonucleotides to cells that are not in direct contact with the vasculature such as hepatocytes. Bioconjugates of oligonucleotides have

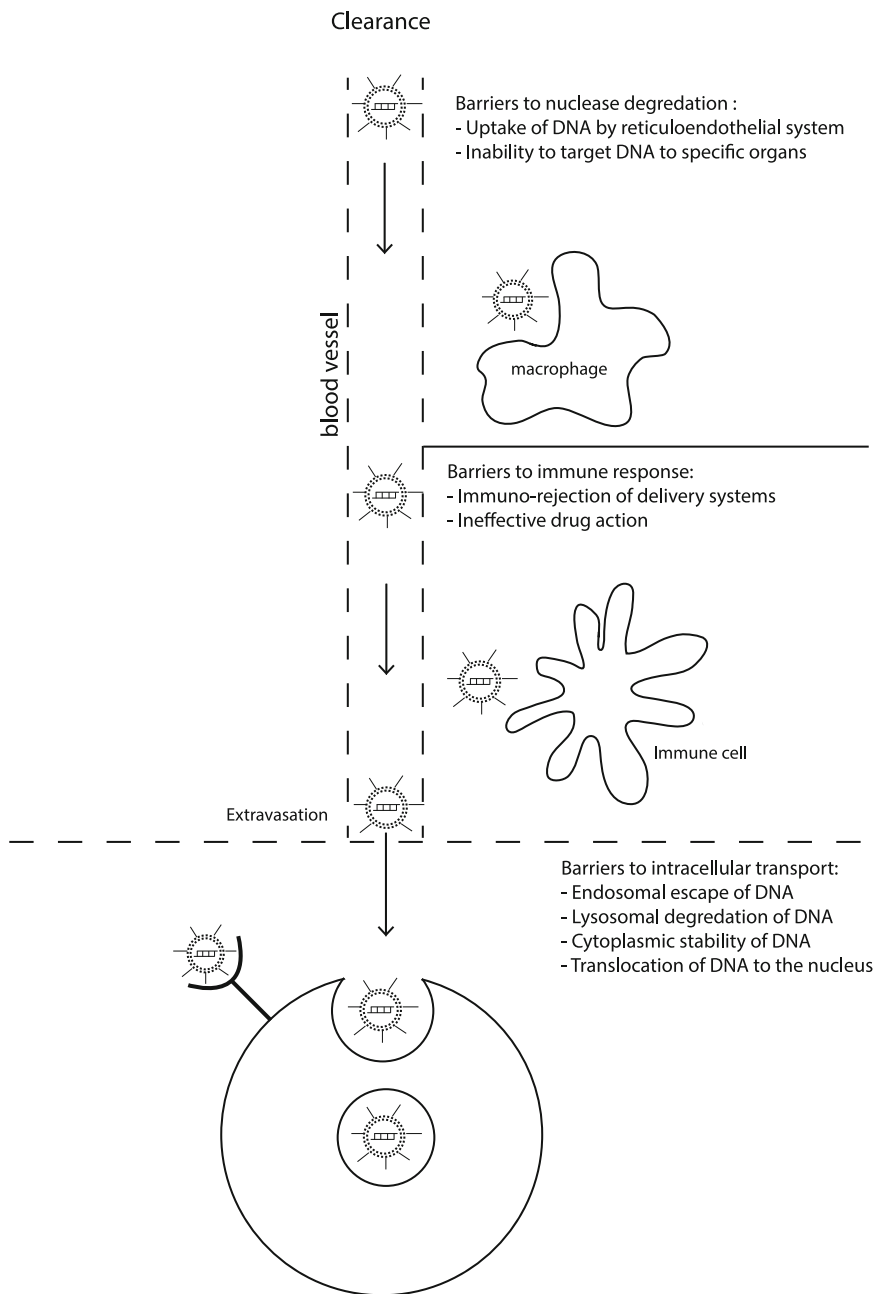


Fig. 18.2 Systemic and cellular barriers to delivery in vivo

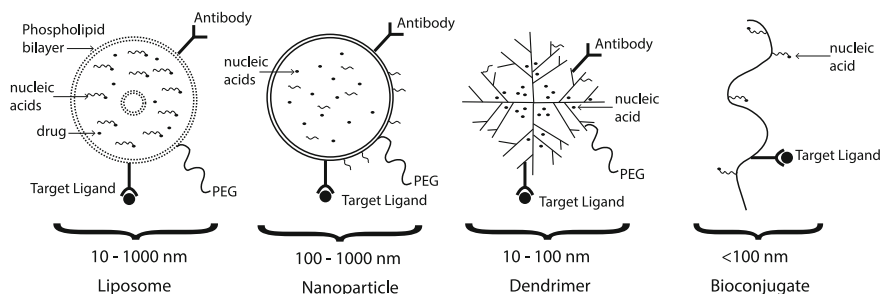


Fig. 18.3 Synthetic delivery system designs

been used to deliver oligonucleotides to treat liver fibrosis [54]. Lipids, which are common targeting agents, have also been conjugated with nucleic acids for delivery of DNA, antisense oligonucleotides, and siRNA. Development of bioconjugated therapeutic drugs is more advanced; for example, site-specific anticancer drugs have been designed to consist of the hydrophobic drug linked to the nucleoside analog to form an amphiphilic bioconjugate. After cell uptake, the inactive bioconjugates or prodrugs are activated only at the target site by pH change or enzymatic cleavage.

18.2.2.2 Cell-Penetrating Peptides

Cell-penetrating peptides (CPP) are short peptides, typically arginine or lysine rich, that enhance cell uptake of an attached cargo [55]. Because of their cationic nature, they bind to the anionic glycan moieties of the extracellular matrix through electrostatic interactions [56]. Their ability to penetrate the cell membrane has been exploited to deliver large molecules, such as drugs, into cells. The positively charged CPPs are also useful for delivering negatively charged DNA or siRNA via electrostatic interactions. However, electrostatic interactions require excess CPPs, in approximately a 10:1 ratio, to maintain an overall positive charge in order to bind to glycans. A major shortcoming of CPPs as a drug delivery vehicle is their lack of specificity, but approaches have been developed to overcome this shortcoming and enhance target cell specificity. For neutral molecules, such as antisense oligomers and peptide nucleic acids (PNA), CPPs can be used as a delivery vehicle by covalent chemical conjugation. There are inherent disadvantages to using this conjugation process because the cargo may be altered as a result. Alternatively, as a way to combat this disadvantage, CPPs can form a complex with PNA, via complementary sequence hybridization, and the resulting conjugate is then used to deliver antisense oligomers to the cells.

Major families of CPPs studied in the published literature to date include: (1) penetratin, a drosophila antennapedia-derived peptide, (2) Tat peptide derived from HIV, and (3) transportan peptides [57]. These CPPs have been used to deliver

therapeutic peptides that target tumor tissues by receptor-mediated endocytosis [58]. For example, the N-terminus of elastin-like polypeptides that are responsive to thermal control can be fused to CPPs. Tumor cells are specifically and selectively heated to 40–43 °C by microwave, radio-frequency, or high-intensity focused ultrasound. At these elevated temperatures, the thermally responsive elastin-like polypeptide delivery complex along with the therapeutic peptides and are taken up by tumor cells.

18.2.2.3 Liposomes

Liposomes are artificial vesicles composed of a lipid bilayer, typically in the size range of 50 nm to several microns, which self-assemble to entrap a liquid core. The surface chemistry, size, and charge of the liposome can be easily tuned through different preparation methods, and in general, they have good biocompatibility and pharmacokinetic profiles for a range of cargos. Liposomes can be fabricated with multiple concentric bilayers, with a single bilayer enclosing a liquid core, or they can form a solid or a nanostructured lipid nanoparticle [59]. Lipid nanoparticles can be fabricated down to 50 nm in size, and, as long as the formation of a crystalline structure is prevented through a blend of liquid and solid phases, there is efficient cargo loading and improved stability. However, the lipophilic core of solid particles is in general not attractive for the delivery of nucleic acids alone.

Liposomes have gained the most attention among the nonviral delivery systems because of their flexibility, biocompatibility, and tunability as well as their low toxicity, immunogenicity, and biodegradability *in vivo*. Two major engineering advances have helped push liposomal drug delivery products to commercial and clinical success: (1) the modification of lipids to bypass the reticular endothelial system and promote targeting, and (2) efficient cargo loading processes.

Since their first use for delivery of nucleic acids, many different types of liposomes have been developed and tested, with cationic lipids emerging as a preferred choice, often in combination with other “helper” lipids. The positively charged head groups of cationic lipids form lipoplexes with negatively charged nucleic acids, giving up to 100 % loading efficiency under the right concentrations and ratios. Endosomal escape is also primarily mediated by the cationic lipids that are believed to destabilize the endosome by forming cationic–anionic pairs with anionic lipids of the endosome membrane. This process can be enhanced by engineering the geometry of the cationic lipids and the choice of helper lipids [60].

Liposome-based delivery systems have a number of advantages, including the ability to transport large pieces of DNA, and a degree of enzyme protection in the lipoplex. Other advantages include low immunogenicity, they can be modified easily to target specific cells and their production can be scaled easily and relatively inexpensively. These advantages are offset by a number of limitations, including low overall delivery efficiency, challenges in encapsulating mixed cargos, burst release of cargo rather than controlled release, poor storage stability, and lack of controlled release in the intracellular region of interest. For DNA

delivery, ideally, this release is in the perinuclear space and the DNA can be trafficked across the nuclear envelope for efficient delivery, while for siRNA it would be close to the RISC.

Engineering of the liposome surface or the encapsulated space can address some of these limitations and increase functionality. Surface modification with PEG can provide a degree of stealth and increase circulation half-life [61], while incorporating antibodies, peptides, aptamers, affibodies, and vitamins can increase targeting efficiency [62], though it remains to be seen whether targeting robustly results in improved efficiency in humans. Mixing in helper lipids can improve fusogenicity by promoting fusion and by causing membrane destabilization [63]. Furthermore, the use of environmental triggers can increase control [64]. For example, lyso-lecithin formulations, which are thermosensitive, have progressed to clinical trials for treatment of breast and liver cancer. Photosensitive liposomes are being tested in animals and magnetosensitive liposomes are in preliminary development [59]. Environmental sensitivity can be added through enzyme-cleavable lipids and pH-sensitive lipids, both of which destabilize the liposome. Use of bioactive lipids, such as ceramide, has also been explored for tumor targeting in murine models [65]. A recent review covers many of the challenges and opportunities related to the surface chemistry of liposomes [59].

Despite nearly 50 years of research, attractive properties and many *in vivo* demonstrations, few liposome delivery systems have reached the market. To illustrate this point, liposomes have great potential as vehicles for DNA and peptide-based vaccines because their formulation can be adapted to protect multiple cargoes, target specific tissues, perform an immunostimulating and adjuvant role, and tuned for both humoral and cellular immune responses [66]. However, liposomes are weaker on commercially significant parameters like shelf-stability, cost-effectiveness, and the ability to scale up production reproducibly. Solid and nanostructured lipid particles that compose different lipids potentially do not share all of these weaknesses, but introduce other concerns like aggregation or coagulation.

Several engineering challenges remain for the more widespread use of liposomal delivery. Many of the studies to optimize delivery have been based on empirical observations; however, with the increasing availability of proteomic tools to understand the arrangement of transportation complexes and super-resolution microscopy to study trafficking events, a more mechanistic understanding is increasingly possible [67].

18.2.2.4 Polymers

Polymer nanoparticles can be synthesized easily in a wide range of sizes from 10 nm to several microns, and in a range of designs, including spherical and core-shell structures. Many families of polymers have been explored for nucleic acid delivery, including synthetic and natural polymers [68]. In principle, there are three ways in which polymer nanoparticles can be used for delivery: (1) by direct conjugation of the therapeutic agent with the polymer, (2) associating the agent

with polymer through an electrostatic or hydrophobic interaction, or (3) by encapsulation of the agent. The most common route for nucleic acid delivery is by the formation of association complexes between the anionic backbone of the nucleic acid and a cationic polymer. The use of high buffering capacity moieties like polyanimes, so-called proton sponges, or the use of pH-sensitive components in the range pH 5–7 can also be used to aid endosomal escape to increase efficiency once captured. Furthermore, the addition of hydrophilic polymers like PEG can provide steric stability and minimize interactions in the physiological environment and reduce immune stimulation. This has driven researchers to explore heteropolymers and polymer-liposome complexes to identify efficient nonimmunogenic formations and has led to more than 35 combinations being tested so far *in vivo* [68].

The low molecular weight polycationic polymers, such as the polyethylene imines (PEI), are among the most commonly studied because of their small size, good association with nucleic acids, their high buffering capacity, and well-controlled chemistry. PEI/nucleic acid complexes (polyplexes) have good stability and can complex well with both siRNA and DNA, but their unmodified use is limited by stability and toxicity issues [69]. Polyarginine [70] and polylysine [71] are both lower toxicity alternatives but require additional modification for efficient *in vivo* use.

Naturally occurring polymers including albumin, collagen, gelatin, and chitosan have also been considered as delivery vehicles [72]. The degradation of these polymers in the presence of particular enzymes makes them attractive for controlled release. Chitosan is among the best studied and, with modification, may be attractive for oral delivery [73].

Advances in polymer chemistry have led to a number of designs incorporating functional components for enhancing efficiency and functionality, including redoxable di-sulfides, pH labile linkers, polythioketals sensitive to reactive oxygen species, and pH-sensitive hydrazone linkers [68]. The sensitivity of these smart polymers is likely to broaden over the next decade to include a wider range of physicochemical characteristics and biological processes. For controlled release of multiple therapeutic agents, the porosity of polymer nanoparticles can be tuned by formulation and manufacturing and has led to a resurgence of interest in biodegradable polymers like the synthetic copolymer polylactide–polyglycolide (PLGA), which can be mixed with PEI for delivery of siRNA *in vivo* [74]. Polymeric micelles, hydrogel nanoparticles, and other protein-based nanoparticles have also been explored for drug delivery [75] and when used in combination with cationic polymers may offer some advantages for multifunctional delivery.

18.2.2.5 Dendrimers

Dendrimers are highly branched three-dimensional synthetic macromolecules, which can be produced with well-defined sizes in the range of 1–10 nm and with low dispersity. Higher generations of dendrimers resulting in the size range of

5–20 nm are favored for *in vivo* work because of efficient kidney filtering below 5 nm and high positive charge densities potentially creating toxicity issues and endocytosis efficiency drops as the size approaches 100 nm [76]. Their globular structure allows loading of nucleic acids and other cargos onto the outside surface via covalent bonding or electrostatic interactions to form dendriplexes, often through the use of amino groups grafted onto the end of the dendrimer branches. Poly(amidoamine) (PAMAM) dendrimers are the best studied, although they require chemical modification to reduce toxicity *in vivo* [77].

The small size of dendrimers makes them attractive for targeting the brain and deep tissues [76]. There have been some demonstrations of their use to deliver DNA [78] and siRNA [79] *in vivo*, although *in vivo* performance does not always match *in vitro* promise. By optimizing the choice of generation and surface chemistry, dendrimers do offer a potentially interesting route to cross the blood–brain barrier and deliver nucleic acid therapies to the brain.

18.2.2.6 Nanoparticles

The unique properties of materials in the nanometer to micron size range have provoked a lot of interest among physical and life scientists. For life scientists in particular, five broad classes of particles have emerged as the most studied because of their properties: (1) small particles of iron oxide, (2) quantum dots, (3) silica particles, (4) gold particles, and (5) carbon nanoparticles. The ability to design and engineer these particles to modulate their interactions with biological molecules, to carry a therapeutic cargo, and to possess characteristics favorable for imaging have led to optimism that nanometer-sized platforms can be used as multifunctional theranostics [80]. However, concerns about cytotoxicity and organ accumulation have dampened enthusiasm for the *in vivo* use of some of these materials.

Nucleic acids can be electrostatically immobilized on the surface of nanoparticles and protected from enzyme degradation using cationic polymers, such as the polyethylenimines or polyallylamines functionalized onto the surface of the particle. Functionalization with a mixture of polymers can also provide a degree of biocompatibility and stability *in vivo*. Much of the research work so far on nanoparticles has focused on *in vitro* and rodent studies, although to progress to human studies will require a more judicious choice of surface decoration and a better understanding of the kinetics of these particles and their nucleic acid cargoes. Some of the multifunctional imaging and delivery combinations for nanoparticles are illustrated in Table 18.1 and described in more detail in the following sections.

Small Particles of Iron Oxide Nanoparticles

Small particles of iron oxide nanoparticles (SPIONs) are nanometer-sized particles of superparamagnetic magnetite and maghemite. These properties make them

Table 18.1 Some of the imaging and therapeutic combinations for nanoparticle-based multifunctional delivery systems

Nanoparticle	Imaging methods	Delivery methods
SPIONs	Optical imaging	siRNA delivery
	MRI imaging	pDNA delivery
	PET/SPECT imaging	Drug delivery
	Electron microscopy/X-ray imaging	Hyperthermia
Quantum dots	Photoacoustic/ultrasound imaging	
	Optical imaging	siRNA delivery
	PET/SPECT imaging	pDNA delivery
	Electron microscopy/X-ray imaging	Drug delivery
Silica	Photoacoustic/ultrasound imaging	
	Optical imaging	siRNA delivery
	PET/SPECT imaging	pDNA delivery
		Drug delivery
Gold		Phototherapy
	Optical imaging	siRNA delivery
	PET/SPECT imaging	pDNA delivery
	Electron microscopy/X-ray imaging	Drug delivery
Carbon	Photoacoustic/ultrasound imaging	Hyperthermia
	Optical imaging	Phototherapy
	PET/SPECT imaging	siRNA delivery
	Photoacoustic/ultrasound imaging	pDNA delivery
	Drug delivery	Hyperthermia
		Phototherapy

attractive for T₂ magnetic resonance imaging (MRI), for targeting using a magnetic field and for hyperthermia. The biocompatibility and excellent in vivo imaging characteristics have led to widespread use of SPIONs for diagnostic imaging and for decorating them with different moieties, such as dyes, polymers, and peptides. Although there have been concerns about the off-target impact of these particles, a noteworthy study compared uptake of SPIONs decorated with a near-infrared dye, siRNA, and membrane translocation peptides in a mice tumor model using in vivo MRI and ex vivo optical imaging and found that there was no indication of an inflammation or cytotoxicity response [81]. Plasma DNA can also be delivered in vivo using SPIONs and imaged using MRI, fluorescence, and transmission electron microscopy (TEM) [82]. The multifunctional nature of SPIONs and their flexible surface chemistry has enabled target refinement and improvements in stability, leading to higher efficiency, as well as the delivery of a combination of anticancer drugs and siRNA in vivo [83].

Quantum Dots

At nanometer scales, semiconductor materials can possess very attractive photo-physical properties, including tunable fluorescence, resistance to photobleaching, and long-term stability. The hydrophobic surface can be functionalized with polymers and decorated with peptides for targeted nucleic acid delivery in live cells [84]. Concerns about toxicity and efficiency and challenges to image deep tissues have hindered progress toward more routine use of quantum dots *in vivo*. *In vivo* work with quantum dots has focused on conjugation with antibodies for diagnostic purposes and for drug delivery [85, 86], but there may be a resurgence of interest with smaller, less toxic polymer quantum dot hybrids [87].

Silica Particles

In contrast to the other nanoparticles, silica does not offer unique imaging characteristics in the nanometer-size range, but does have excellent biocompatibility, stability and can be fabricated inexpensively into a range of shapes with different porosities, providing both interior and surface space to carry a therapeutic cargo. Some recent examples of progress in this field include a demonstration that second-generation polyamidoamine dendrimers covalently attached to the surface of 250 nm mesoporous silica particles provide protection for complexed pDNA and can successfully transfect HeLa cells *in vitro* [88]. Silica particles decorated with the cationic polymer polyethylenimine and loaded with siRNA have also been used to knock down EGFP expression in PANC-1 cells *in vitro* [89]. The porous region has been used to extend functionality beyond nucleic acid delivery to include chemotherapy agents [90], and anti-malarials [91]. The use of mesoporous silica particles to co-deliver of doxorubicin and siRNA to silence P-glycoprotein exporters in a xenograft breast cancer mouse model has recently been shown to provide synergistic tumor growth inhibition [92].

Gold Nanoparticles

The excellent chemical, physical, and optical properties of gold in the nanometer range, as well as easy synthesis of a variety of shapes and configurations has led to a long interest in gold-based synthetic vectors. Cationic polymers covalently attached to gold particles were found to be an efficient vehicle for pDNA transfection of COS-7 cells *in vitro* [93], and knockdown enhanced green fluorescence protein in endothelial cells *in vitro* using antisense oligonucleotides [94]. Increasingly, complicated designs have been developed to enhance efficiency and prolong effectiveness of siRNA using multiple layers [95], giving 70 % gene silencing of glyceraldehyde 3-phosphate dehydrogenase (GAPDH) in a mouse model for more than 10 days post-injection [96].

Carbon Nanoparticles

Carbon has many unusual physical and chemical properties in the nanometer range and can form several different structures which are of interest as delivery vehicles. Three of these structures, nanodiamonds, carbon nanotubes (CNT), and graphene sheets have attractive features and have been explored as synthetic vectors over the past decade.

The increasing availability, innate photoluminescence, characteristic Raman signal, and good biocompatibility of nanometer-sized (~ 5 nm) diamonds makes them attractive for gene delivery [97–99]. In vitro delivery of siRNA into Ewing sarcoma cells has been demonstrated [99] and the attractive optical properties had led to early in vivo studies in *Caenorhabditis elegans* [100], although the kinetics of the functionalized nanodiamonds have not yet been fully characterized in vivo.

CNT have the ability to enter a range of cell types by passive diffusion and act as a vector [101]. A lot of effort has gone into optimizing surface modification of the CNT to enhance efficiency and biocompatibility. Hybrid cationic polymer-CNT have been demonstrated to be effective for delivering siRNA in mice at doses of <1 mg/kg with relatively high clearance [102].

Graphene sheets have high surface area and mechanical strength as well as exceptional conductivity and attractive functionalization chemistry. Oxidizing graphene followed by functionalization has emerged as an early solution to its hydrophobic nature and has been used as a siRNA vector for in vitro experiments [98]. The strong near-infrared absorption of graphene oxide has been used to demonstrate a photothermal effect in a mouse tumor model [103], and it has been used for delivery of doxorubicin in vivo [104], though more data are required to understand cellular uptake mechanisms, biodistribution, and toxicity.

18.2.3 Directed Delivery

Complementary to the carrier-mediated viral and nonviral systems described previously, delivery of nucleic acids can be enhanced locally using a range of forces, or delivered locally using a number of noninvasive and minimally invasive techniques. Local delivery or the use of fields to target regions is attractive to avoid initial systemic clearance processes, enhance cargo concentration in the region of the cells of interest, and avoid side effects associated with large doses. However, disruption of the normal physiology of the local region because of these delivery methods may have unintended consequences, including generating an inflammatory response, altering lymphatic flow and perturbation of physiological functions. Ideally, the goal for directed delivery is to combine both regional and cell-specific delivery, to minimize disturbance of neighboring cells.

18.2.3.1 Hydrodynamic Delivery

Hydrodynamic delivery, or the use of a rapid injection of fluid to deliver force in a noncompressible environment, can disrupt physical barriers, such as endothelial layers and cell membranes, to enable efficient delivery to parenchymal cells. In less than a decade, this technique progressed from first demonstration in a mouse model to use in a human clinical trial, in part because it is a simple, effective, and versatile approach and can be repeated multiple times [105]. This approach has been used for both DNA and RNA delivery to a range of tissues including liver, kidney, skeletal muscle, and myocardium, as well as tumors, through veins, arteries, and ducts. While effective in rodents, scaling hydrodynamic delivery to humans has been challenging because of concerns about the induction of irregularities in cardiac function, localized increase in blood pressure, expansion in organ size, and structural deformation, with the effects lasting up to several days in animals [105]. A number of refinements have been developed including the use of catheters, balloons, computer-controlled injectors [106], and image-guidance [107], which may address some of these challenges.

18.2.3.2 Ballistic Delivery

The ballistic delivery of nucleic acids attached to dense particles is an attractive approach for dermal targets because it is more efficient and less invasive than injection. Gene guns, using a burst of helium to give nucleic-acid-coated gold or tungsten particles enough momentum to penetrate physical barriers, emerged in the 1980s as an alternative transfection tool. For *in vivo* applications, the particles have enough momentum to breach the stratum corneum of the skin and have been used for vaccine delivery, but have also been used to deliver pDNA to mouse skeletal muscle cells [108]. The approach has a number of challenges, which include the risk of inflammation and damage in the target region, limited particle choices, limited nucleic acid loading capacity, indiscriminate and poor uniformity of the delivery, and sensitivity to a wide range of environmental factors. Although particle-mediated vaccine delivery systems have been tested in humans [109], it remains unclear whether cost and complexity will be barriers to wider use. However, engineering advances such as contoured shock tubes and better vaccine preservation techniques, and the lure of dose-sparing and more controlled immune response are continuing to drive interest beyond clinical studies toward regulatory approval [110]. Two other dermal delivery methods have emerged for vaccine delivery, microneedles and liquid jet injectors, both of which are reviewed in detail by Kis et al. [110].

18.2.3.3 Electric Field-Assisted Delivery

Electroporation is an extremely effective and simple technique for increasing the permeability of cells for nucleic acid delivery that has been used for more than 30 years. A number of techniques have been developed for electroporation *in vivo* and this technique has been used to successfully transfect liver, skin, tumor, and skeletal muscle cells [108]. Electroporation has been commonly used in DNA vaccine studies and enhanced efficacy up to 1,000-fold over naked DNA intramuscular injections in animal models [111]. At least 10 phase I or phase II human clinical studies have been conducted with promising results [112], though with some significant adverse effects also reported that include subjects reporting pain and bleeding at the injection site [113]. At an earlier stage of development are minimally invasive electroporation devices for transdermal delivery [114] and multifunctional systems [115] that have the potential to address some of the concerns with naked DNA delivery by intramuscular injection and invasive electroporation.

18.2.3.4 Ultrasound-Assisted Delivery

Ultrasound is routinely used for *in vivo* imaging, although it is also known to have a therapeutic effect at higher intensities because of mechanical stimulation or disruption. Microbubbles of gas can also undergo oscillations under ultrasound stimulation disrupting the membrane and increasing the permeability of neighboring cells. This sonoporation approach has been studied for more than 25 years although all the mechanisms involved in internalization and other effects on the cell are not well used. To avoid tissue damage, relatively high frequencies (~ 1 MHz) and low-to-moderate mechanical indices are used, which is sufficient to cause stable cavitation of the bubbles at lower intensities and inertial cavitation at higher intensities. The 500–5,000 nm bubbles are typically composed of gas cores of a high molecular weight hydrophobic gas and a shell containing phospholipids, surfactants, targeting moieties, and nucleic acids. *In vivo* delivery studies have focused on organs routinely imaged by ultrasound, including successful delivery in heart, skeletal muscle, and kidney, as well as the pancreas, liver, and the central nervous system, either through direct injection into the organ or into the blood stream [116]. Both siRNA [117] and pDNA [118] have been delivered *in vivo* with delivery limited to the focal region of the noninvasive ultrasound. Ultrasound-mediated delivery bypasses the endocytic pathway, although there is little to no control about where the nucleic acids will enter the cell. Some concerns have been raised about efficiency [119] and that microbubbles may exacerbate underlying hypotensive reactions in some patients [120], suggesting that further optimization is required to move beyond early animal studies [121].

18.2.3.5 Magnetic Field-Assisted Delivery

The magnitude and gradient of external magnetic fields can be used to target superparamagnetic particles *in vivo*, as well as provide a basis for MRI, spectroscopy, and hysteretic heating. However, achieving strong enough field gradients to generate sufficient force on submicron particles is very challenging in regions other than the extremities. A local magnetizable structure can enhance the field gradient, such as implantable stents [122]. Much of the *in vivo* work with magnetic targeting has focused on drug and cell delivery work, although more generally solid, lipid-based, and microbubble magnetic vectors have been used to deliver DNA [123] and siRNA [81]. Some of the challenges to be addressed include concerns about toxicity, particularly at higher concentrations, aggregation of the particles, and overall efficiency of the nucleic acid delivery to target cells. A recent review has comprehensively described the progress and prospects for magnetically enhanced delivery [124].

18.2.3.6 Optically Assisted Delivery

Arguably, the least developed method for membrane pore generation is the use of optical fields, although it was first demonstrated nearly 30 years ago. An optical field can generate a pore through thermal heating with continuous wave lasers, while at femtosecond timescales, disruption can occur through the generation of low-density plasma and intermediate pulses can generate bubbles and thermoelastic stresses [125]. Experimental results suggest that shorter pulses result in better viability, though not necessarily an improvement in efficiency, and they have been used to deliver DNA [126] and messenger RNA (mRNA) [127] *in vitro*. *In vivo* studies are more challenging by the need for local optical access; however, two approaches have been demonstrated: (1) the transfection of zebrafish blastomeres with pDNA [128] and (2) a microendoscope with an axicon tip [129]. Other optical properties have also been explored for nucleic acid delivery. Particles driven by laser-induced plasma jets have been demonstrated [130], however many engineering challenges still exist and scientists have yet to find an efficient, effective and reproducible way to deliver nucleic acids *in vivo* using optical fields.

18.3 Therapeutic Components

Nucleic acids and their analogs have been increasingly used as therapeutic agents over the past 40 years. The development of a host of tools for engineering monomers as well as polymeric sequences that have favorable physical, chemical, or biological characteristics has helped drive nucleic acid therapies toward being practical and reproducible in the clinic. The desired type of therapeutic effect drives the choice of nucleic acid, which along with delivery considerations

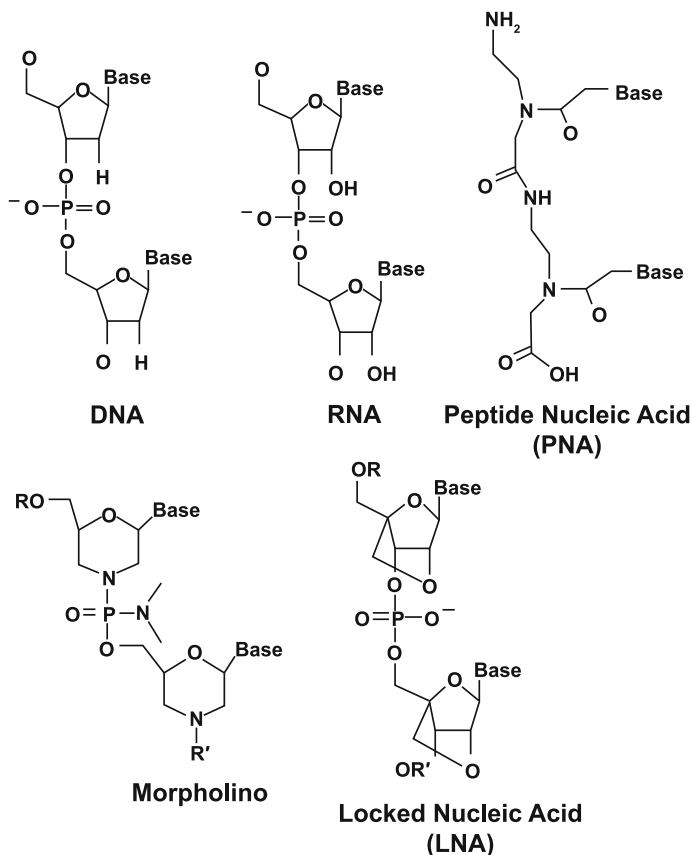


Fig. 18.4 Nucleic acids and analogs

narrows down the choice of analog. DNA, RNA, and nucleic acid analogs have all been explored extensively as therapeutic cargos for nanoscale delivery systems. The chemical structure of DNA, RNA, and three of analogs are illustrated in Fig. 18.4 and described in more detail in the following sections.

18.3.1 DNA-Based Therapeutics

pDNA have been used extensively as a therapeutic agent and delivered in a large number of different ways. pDNA can be systemically delivered with low uptake efficiency, or by a number of physical mechanisms, including electroporation, gene gun transfer, ultrasound, or by forming chemical complexes with cationic polymers and lipids [131, 132]. Uptake is thought to be primarily accomplished by endocytosis [133] and once inside, pDNA escapes from lysosomal degradation.

For treatment of muscle diseases, naked pDNA containing the transgenes can be delivered to muscles by either intramuscular injection [134] or intravascular injection by a procedure known as hydrodynamic limb vein injection [135, 136]. This procedure involves the use of a tourniquet to temporarily isolate an area in a peripheral vein or artery of a limb from normal blood flow. This is followed by injection of the pDNA into the vessel in the anterograde direction. The pDNA is delivered in a large volume of saline so as to facilitate extravasation of the pDNA from the vasculature into the muscle tissue. Naked pDNA is susceptible to nuclease degradation, which limits the serum half-life to approximately 10 min [137]. The rapid clearance is mitigated by delivering an excessively high number of copies of the transgene. Transgene expression in a plasmid is achieved by placing it under transcriptional control of an appropriate promoter/enhancer. The expression is not as efficient as viral vectors that are integrated into the host genome. However, in nondividing cells, pDNA transgene expression has been shown to persist for years after direct intramuscular injection [134, 138]. A major advantage of naked pDNA over viral delivery of transgene is that the former is nonimmunogenic.

In addition to injection, pDNA can also be delivered using bacteria. Production of pDNA in bacteria involves the use of specific selection markers, such as an antibiotic resistance gene to identify bacterial colonies that are transfected. However, given the safety concerns with antibiotic-resistant bacterial strains, alternative antibiotic-free strategies have been developed which may be a more practical way of delivering pDNA in humans [139].

18.3.2 RNA-Based Therapeutics and Delivery Systems

This section describes a range of RNA molecules that can be used as research tools in drug discovery or therapeutic application: aptamers, ribozymes, antisense, and siRNA. These are powerful tools to silence gene expression, but they have to get into the cells and bind to the complementary genes for silencing. For in vivo use, these therapeutics must overcome barriers of limited stability, poor cellular uptake, unfavorable subcellular trafficking, lack of targeting, nonspecific tissue distribution, and susceptibility to nuclease degradation.

18.3.2.1 Aptamers

Aptamers are single-stranded DNA or RNA oligonucleotides of 20–80 bases that are generated in vitro from random libraries of nucleic acids [140]. Because they are single-strand, they exist in many three-dimensional shapes including hairpin-like monomers, duplexes, triplexes, or quadruplexes [141–145]. The basic technology for screening and selecting aptamers was developed two decades ago. This process is called Systematic Evolution of Ligands by Exponential enrichment

(SELEX) [146–148]. However, it was soon discovered that aptamer specificity and binding affinity can be improved with modification of the basic SELEX screening. For example, procedures involving the immobilization of fluorescence-labeled targets (FlyMag-SELEX) or the oligonucleotides (Capture-SELEX) on magnetic beads have been developed to improve selection of aptamers that target organic molecules or pharmaceuticals [149, 150]. Highly specific aptamers have been selected with the modified SELEX for use in biosensors and assays for detecting drug targets, antibiotic, or pharmaceuticals. Aptamers have also been isolated by a Cell-SELEX procedure that target cell surface markers for therapeutic and diagnostic purposes.

Aptamers are versatile molecules and can bind to a range of targets including small molecules such as adenosine triphosphate (ATP) or macromolecules such as proteins or microorganisms [151, 152]. Aptamer binding has been likened to antibodies in that they are highly specific and bind with high affinity. For these reasons, aptamers have been used in basic research to investigate protein interactions and in clinical applications as therapeutics or as vehicles to deliver drugs. Aptamer-mediated drug delivery holds promise as it minimizes off-target side effects. In clinical applications, aptamers have the added advantages of low immunogenicity in contrast to antibodies and storage stability. Intracellular stability against nuclease activities can be achieved by chemical modifications involving primarily the sugar moieties, the nitrogenous base, and replacing the phosphate backbone with phosphorothionate [153]. The 2'-ribose can be modified by adding methyl- or amino groups [154, 155]. The nitrogenous base can also be substituted with uracil derivatives and other pyrimidines [156].

Currently, there are six RNA-based aptamers that have been clinically evaluated. A vascular epithelial growth factor (VEGF)-specific RNA-modified aptamer (Macugen by Pfizer/Eyetech) has been approved by the FDA for treating age-related macular degeneration [157–160]. A clinical trial sponsored by Regado Bioscience is evaluating REG1 as part of a dual-aptamer therapy for acute coronary syndrome [161]. Kang and his colleagues identified two aptamers that specifically recognize cell surface membrane proteins expressed on glioblastoma cell lines. These results suggest that aptamers may be promising cancer therapeutics.

18.3.2.2 Ribozymes

The seminal research of Thomas Cech showed that RNA is capable of enzymatic activities for which he was awarded the Nobel Prize in 1989 [162]. The term ribozyme refers to antisense RNA molecules that have catalytic activity. Biologically active ribozymes share either the “hammerhead” or “hairpin” motifs that reflect their secondary structures. Most ribozymes self-catalyze as evidenced by splicing of introns and subsequent ligation [163]. They recognize specific nucleotide sequences in the catalytic sites. Hammerhead ribozymes cleave RNA at UA, UC, or UU whereas hairpin ribozymes cleave CUG sequences [164, 165]. Ribozymes have been engineered and synthesized to improve site-specific enzymatic activities and

stability while maintaining the hammerhead and hairpin motifs. Automated solid-phase RNA synthesis [166] has been successfully used to produce synthetic ribozyme analogs that are more stable and are amenable to labeling with fluorescent tags, radioisotopes (for NMR studies), and other groups to improve biological activity and resistance to RNase degradation. The scope, utility, and intracellular stability can be enhanced by increasing the secondary structure such as stem-loop on either side of the ribozymes. Chemically modified ribozymes have been produced that act as riboswitches in biosensor technology [167, 168].

Clinical applications of ribozymes include use as antivirals or gene therapies. Studies with HeLa cells transfected with hammerhead ribozymes targeting the *gag* transcripts showed reduced *gag* expression [169, 170]. Similarly, a hammerhead ribozyme targeting the 5' leader sequence showed reduced HIV1 replication in T-cell lines [169]. Targeting the leader sequence (with either hammerhead or hairpin ribozymes) has been demonstrated to prevent HIV1 from establishing infection [170–172]. The latter approach is promising for vaccine development. Immunotherapies for infectious diseases, such as HIV1 infection, have been developed by using the infected individuals own immune cells such as CD4, CD8, CD34, or antigen presenting cells that were transduced with ribozyme carried on a murine retroviral vector [173]. However, the use of ribozymes for HIV1 gene therapy is challenging because the virus mutates at a high rate such that the cleavage sequences could be disrupted.

18.3.2.3 Small Interfering RNA

siRNA was discovered by Professors Andrew Fire and Craig Mello who were awarded the Nobel prize in 1996 for their seminal research [174]. They discovered that long, double-stranded RNA, introduced into cells either by viral pathogens, such as HIV1 or jumping genes, can be cut into short 20–25 nucleotide pieces by an enzyme called Dicer. These short double-stranded RNAs bind to several proteins to form the RISC. The RISC contains a helicase module that unwinds the two strands of siRNA to form the single-stranded short RNA or siRNA. The siRNA binds to the complementary mRNA, which is cleaved by the endonuclease activity in RISC and silenced from protein expression [158]. The sequence-specific binding of siRNA to turn off or turn down gene expression is a powerful approach to: (1) identify gene function, (2) regulate gene expression, (3) determine drug targets, and (4) develop therapeutics for disease. Despite these promising approaches, siRNA development for therapeutic purposes is fraught with challenges. The full therapeutic potential of siRNA has yet to be fully realized because of the barriers to delivery and creating a sustained therapeutic effect, including shielding the negatively charged backbone, preventing nuclease degradation, promoting uptake only by cells of interest, and ensuring endosomal escape at the optimum time. The susceptibility of siRNA to nuclease degradation [175, 176] limits their serum half-life [137]. The intracellular stability can be improved with

chemical modification of the oligonucleotides. Another challenge with therapeutic uses is that the intracellular siRNA concentration decreases with each cell division.

siRNA delivery systems have been an active area of research. Various nanotechnology approaches have been used to improve delivery to tumor cells in animal models. For example, Cho et al. reported an innovative nanoparticle construct that expresses siRNA *in vivo* by conjugating to the particle surface target ligands and double-stranded DNA nanocassettes containing a promoter and a shRNA gene [177]. Other approaches include the use of plasmids and viral vectors to deliver siRNA into both dividing and nondividing cells, stem cells, zygotes, and their differentiating progeny [178]. Another delivery option is Lipofectamine 2000, which is a cationic liposome, that has been used in a complex with siRNA to transfect mammalian cells [55, 179]. However, its toxicity and low transfection efficiency in certain types of cells limited its usefulness. Other approaches include nanodelivery systems and CCP, as discussed earlier.

It is a little more than a decade since the first demonstration of RNA interference *in vivo* [180] and great strides have been made in understanding and optimizing delivery. siRNA for silencing disease-associated mRNA transcripts has been successfully used as an antiviral for HIV1 susceptible cells [181, 182]. siRNA has also been shown to be capable of knocking down targets relevant to many diseases, including ovarian cancer [183], cirrhosis [184], and hypercholesterolemia [185]. siRNA therapeutics have progressed rapidly into clinical trials, with more than 14 diseases being targeted by more than 20 therapeutics in more than 30 clinical trials. A review, in 2011, noted that 8 of 9 intravenous siRNA therapeutics used a synthetic carrier: four were composed of cationic liposomes, one of anionic liposomes, two were polymeric, and one was naked siRNA [2]. Furthermore, localized delivery of siRNA by intravitreal injection, intralesional injection, and topical application has been tested in clinical trials as well as one study on oral delivery of *E coli*, which produce shRNA for treatment of familial adenomatous polyposis. There have also been three trials studying autologous cell therapy using siRNA.

18.3.3 Nucleic Acid Analogs

The modification of the phosphodiester backbone, sugar ring, or nucleobase can introduce new functions or enhance the performance of nucleic acids. Over the past two decades, an increasing variety of analogs have been synthesized to complement the dideoxynucleotides used in sequencing. The most widely studied are the backbone analogs, including PNA, locked nucleic acids (LNA), and morpholinos, as well as fluorescent base analogs such as 2-animopurine (2-AP). Differences in the conformational structure, as a result of these analog bases, such as the sugar ring pucker, can result in very different antisense activity [186] and have led to expanding interest in engineering modified oligonucleotides for gene silencing *in vivo* [187].

18.3.3.1 Peptide Nucleic Acids

PNAs are stable, neutral charge DNA analogs first developed in the 1980s with a peptide-based backbone, but maintaining the nucleobases to preserve base-pairing rules. They bind DNA and RNA with high affinity and have a number of interesting properties, including resistance to enzyme degradation, double-stranded DNA invasion, triplex formation, and act via a translation inhibition mechanism [187]. With charge neutrality, water solubility is length-dependent and there is much stronger binding to DNA/RNA because of the lack of charge repulsion, as well as the potential for co-delivery with hydrophobic drugs. PNA can persist in the cytoplasm for at least 48 h and binds more quickly to negatively supercoiled DNA, making it attractive for *in vivo* therapeutic use. Recently, PGLA nanoparticles were used to systemically delivery PNA and DNA to human cells in non-obese diabetic (NOD) mice and demonstrate site-specific gene editing [188]. Site-specific intradermal delivery of PNA, coupled to a cell penetration peptide, to keratinocytes has also been demonstrated [189]. PNA is also attractive for fluorescence *in situ* hybridization (FISH) because it can bind under unfavorable conditions. It also has been incorporated into FDA-approved *in vitro* molecular diagnostic tools, and coupled to imaging agents to investigate mRNA expression *in vivo* [190], suggesting a route to multifunctional delivery *in vivo*.

18.3.3.2 Locked Nucleic Acids

LNA is a chemically modified RNA analog first described in 1998 with high affinity for complementary RNA or DNA and has been used to improve *in vitro* methods including microarray profiling, allele-specific polymerase chain reaction (PCR) and FISH [191]. The nucleosides are locked in a North sugar confirmation, making them useful in anti-miRNA, antisense, and siRNA applications, while having improved nuclease resistance and potentially lower immuno-stimulation [187]. Several derivatives of LNA have been developed to further improve performance and enable further chemical modification, and two LNA-based therapeutics have progressed to human clinical trials [192]. The exclusive licensing of LNA to Exiqon A/S and nontrivial synthesis may be barriers to more widespread research and development of LNA-based multifunctional approaches.

18.3.3.3 Morpholinos

Morpholinos are modified oligonucleotides with an uncharged substitute for the phosphodiester linkages and the furanose sugars, developed in the mid-1980s. Their preparation is a more cost-effective transformation of ribonucleosides, and assembly efficiency is high through the morpholine nitrogen. They show similar or increased affinity and nuclease resistance and can be used as translational inhibitors [187]. Antisense morpholino oligonucleotides have been delivered *in vivo* to a

splice-reporter mouse model using a dendritic transporter resulting in the expression of splice-corrected GFP [193]. Some concerns have been raised about off-target effects and the assessment of efficacy [194], although these are addressable through well-conceived control experiments.

18.4 Challenges and Opportunities for Multifunctional Delivery in Vivo

The broad challenge for multifunctional nanoscale delivery systems is identification of the most robust method to deliver a targeted therapeutic dose of nucleic acids and other components efficiently in vivo with minimal invasiveness, while minimizing side effects and maximizing clinically actionable information.

Table 18.2 highlights some of the challenges and solutions that have identified so far. However, many challenges remain, as highlighted in the previous sections of this chapter. Each of the components, carrier, nucleic acid cargo, and functional components can be optimized independently and readily developed under in vitro circumstances, although it is challenging to make the leap to system optimization for the complex and less predictable environment of human therapies.

One ongoing area of intense work is the optimization of vectors. For synthetic vectors, the primary challenge is to enhance uptake efficiency and control intracellular fate through the use of ligands to activate signaling cascades and nuclear targeting, without increasing immunogenicity. This will require a deeper understanding of the mechanisms underlying the RISC, nuclear transport, active transport of particles in the cytoplasm, routes to deep tissue penetration, such as the exosome pathways. While viral vectors have much higher efficiency, their challenges are around reducing side effects, such as oncogene activation, immunogenicity, adequate viral titers, production, length of the transgene, and the range of cell targets. These challenges are active areas of research and understanding the the virology underpinning these vectors has been crucial in overcoming the barriers.

Another area where there is still room for development is the optimization of the composition of vectors during development of nanoscale delivery systems by utilizing realistic three-dimensional heterogeneous microenvironments. A better understanding of the physical and chemical environments in living organs, combined with the engineering of cell culture, using microfabricated structures, has enabled the generation of complex microenvironments that more closely mimic the physiological environment in vivo beyond the conventional two-dimensional culture systems [195].

A third area where there is a need for deep understanding is the dynamic interaction of the delivery systems with the entry site, the extracellular matrix, and circulatory system, as well as how these interactions modify the therapeutic effect in a heterogeneous human population. Viral vectors enter cells via membrane

Table 18.2 Some challenges and solutions in nucleic acid delivery systems

Problems	Mechanisms	Solutions	
Short-lived expression	Loss of plasmids	Episomal replication	
	Promoter shutdown	Site-specific integration	
	CpG motifs	Alternative promoters: transcriptional targeting	
	Degradation	Minimize GC content DNA topology	
Toxicity	Interaction with cell membrane	M_w Charge	
	Interaction with cell components	Amphiphiles Biodegradability Natural compounds	
	Heterogeneity of expression	Cell cycle	Active nuclear uptake strategies
		Cell type	Receptor-mediated uptake Targeting
Low efficiency	Aggregation	Shielding (PEG)	
	Poor uptake	Stabilized particles	
	Degradation	Size	
	Inefficient intracellular processing		Condensing agents Membrane-penetrating agents Microtubule-mediated transport
			Endosomal escape strategies
			Active nuclear uptake strategies

receptors and therefore serve as experimental systems because mutations can be introduced in the receptors leading to altered downstream intracellular events. The emergence of molecular imaging is a promising direction for helping to unravel these interactions using MRI, positron emission tomography (PET), single-photon emission computed tomography (SPECT), ultrasound (US), or optical imaging moieties (some of which were described earlier in this chapter) and enables imaging theranostics as a process for achieving precision medicine [196]. In vivo imaging agents that are sensitive to their environment, bioswitches that turn on/off the delivery of payloads, and biomarker analysis, will help provide new methods for characterizing toxicity, reduce off-target effects, and minimize immune stimulation, as well as optimize deep tissue delivery and circulation time. More detailed analysis of the overall in vivo efficiency across multiple model systems is required to understand the kinetics of circulation, degradation, internalization, and intracellular fate of nucleic acid therapies, and the relative contributions of helper ligands.

A final area where engineering will play a significant role is in the development of targeted delivery of nanoscale systems. The use of minimally invasive delivery systems and fields to localize delivery are likely to grow to address challenges like sustained delivery, off-target effects, and maximizing therapeutic effect with minimizing dose.

The most challenging question is the long-term impact of multifunctional nanoscale delivery systems on clinical care. With naked nucleic acid delivery and simple delivery systems already in clinical trials, the value proposition for multifunctional delivery systems in current clinical practice is unclear, particularly if the multifunctional components are designed for real-time monitoring and optimization of care. The current clinical workflow model is based on quality control and careful planning of treatment in advance to minimize errors, but also limiting personalized analysis to static or slowly varying biomarkers. This makes it very difficult to detect immune responses and off-target effects or to modify dose based on whether a therapeutic response is observed. Building information from the increased functionality of these nanoscale delivery systems into the clinical workflow will help protect and improve health as well as expand the knowledge based in medical and associated sciences.

Acknowledgments The authors are indebted to Drs. William Heetderks and Antonio Sastre for their critical review and to Ms. Christine Rogers for her assistance with preparing the manuscript. Figure 26.4 Used with permission and modified from *Biochimica et Biophysica Acta (BBA)—Proteins and Proteomics*, 1697, Yoon S. Cho-Chung, Antisense protein kinase A RI α -induced tumor reversion: portrait of a microarray, 71–79, Copyright 2004, with permission from Elsevier.

Conflict of Interest The authors declare that they have no conflict of interests.

References

1. Edelstein M (2012) Gene therapy clinical trials worldwide. *J Gene Med*. <http://www.abedia.com/wiley/vectors.php>. Accessed 21 Jan 2013
2. Burnett JC, Rossi JJ, Tiemann K (2011) Current progress of siRNA/shRNA therapeutics in clinical trials. *Biotechnol J* 6:1130–1146. doi:10.1002/biot.201100054
3. Jiao S, Williams P, Berg R et al (1992) Direct gene transfer into nonhuman primate myofibers in vivo. *Hum Gene Ther* 3:21–33. doi:10.1089/hum.1992.3.1-21
4. Ardehali A, Fyfe A, Laks H et al (1995) Direct gene transfer into donor hearts at the time of harvest. *J Thorac Cardiovasc Surg* 109:716–720. doi:10.1016/S0022-5223(95)70353-5
5. Vile R, Hart I (1993) In vitro and in vivo targeting of gene expression to melanoma cells. *Cancer Res* 53:962–967
6. Khatri N, Rathi M, Baradia D et al (2012) In vivo delivery aspects of miRNA, shRNA and siRNA. *Crit Rev Ther Drug Carrier Syst* 29:487–527
7. Inoue T, Sugimoto M, Sakurai T et al (2007) Modulation of scratching behavior by silencing an endogenous cyclooxygenase-1 gene in the skin through the administration of siRNA. *J Gene Med* 9:994–1001. doi:10.1002/jgm.1091
8. Bitko V, Musiyenko A, Shulyayeva O, Barik S (2005) Inhibition of respiratory viruses by nasally administered siRNA. *Nat Med* 11:50–55. doi:10.1038/nm1164
9. DiFiglia M, Sena-Esteves M, Chase K et al (2007) Therapeutic silencing of mutant huntingtin with siRNA attenuates striatal and cortical neuropathology and behavioral deficits. *Proc Natl Acad Sci USA* 104:17204–17209. doi:10.1073/pnas.0708285104
10. Sinn PL, Anthony RM, McCray PB Jr (2011) Genetic therapies for cystic fibrosis lung disease. *Hum Mol Genet* 20:R79–R86. doi:10.1093/hmg/ddr104

11. Kamimura K, Suda T, Zhang G, Liu D (2011) Advances in gene delivery systems. *Pharmaceut Med* 25:293–306. doi:[10.2165/11594020-000000000-00000](https://doi.org/10.2165/11594020-000000000-00000)
12. Maetzig T, Galla M, Baum C, Schambach A (2011) Gammaretroviral vectors: biology, technology and application. *Viruses* 3:677–713. doi:[10.3390/v3060677](https://doi.org/10.3390/v3060677)
13. Coffin JM, Hughes SH, Varmus HE (1997) *Retroviruses*. Cold Spring Harbor Laboratory Press, Cold Spring Harbor
14. Hu WS, Pathak VK (2000) Design of retroviral vectors and helper cells for gene therapy. *Pharmacol Rev* 52:493–511
15. Lewis P, Hensel M, Emerman M (1992) Human immunodeficiency virus infection of cells arrested in the cell cycle. *EMBO J* 11:3053–3058
16. Lee C-L, Dang J, Joo K-I, Wang P (2011) Engineered lentiviral vectors pseudotyped with a CD4 receptor and a fusogenic protein can target cells expressing HIV-1 envelope proteins. *Virus Res* 160:340–350. doi:[10.1016/j.virusres.2011.07.010](https://doi.org/10.1016/j.virusres.2011.07.010)
17. Dimitrov DS (1997) How do viruses enter cells? The HIV coreceptors teach us a lesson of complexity. *Cell* 91:721–730
18. Moore JP (1997) Coreceptors: implications for HIV pathogenesis and therapy. *Science* 276:51–52
19. Cockrell AS, Kafri T (2007) Gene delivery by lentivirus vectors. *Mol Biotechnol* 36:184–204
20. Miller DG, Adam MA, Miller AD (1990) Gene transfer by retrovirus vectors occurs only in cells that are actively replicating at the time of infection. *Mol Cell Biol* 10:4239–4242
21. Durand S, Cimarelli A (2011) The inside out of lentiviral vectors. *Viruses* 3:132–159. doi:[10.3390/v3020132](https://doi.org/10.3390/v3020132)
22. Pfeifer A, Ikawa M, Dayn Y, Verma IM (2002) Transgenesis by lentiviral vectors: lack of gene silencing in mammalian embryonic stem cells and preimplantation embryos. *Proc Natl Acad Sci USA* 99:2140–2145. doi:[10.1073/pnas.251682798](https://doi.org/10.1073/pnas.251682798)
23. Bahrami S, Pedersen FS (2009) Viral technology for delivery of nucleic acids. In: Jorgensen L, Nielsen HM (eds) *Delivery technologies for biopharmaceuticals*. Wiley, Chichester, pp 93–112
24. Cavazzana-Calvo M (2000) Gene therapy of human severe combined immunodeficiency (SCID)-X1 disease. *Science* 288:669–672. doi:[10.1126/science.288.5466.669](https://doi.org/10.1126/science.288.5466.669)
25. Mátrai J, Chuah MKL, VandenDriessche T (2010) Recent advances in lentiviral vector development and applications. *Mol Ther* 18:477–490. doi:[10.1038/mt.2009.319](https://doi.org/10.1038/mt.2009.319)
26. Izmiryan A, Basmaciogullari S, Henry A et al (2011) Efficient gene targeting mediated by a lentiviral vector-associated meganuclease. *Nucleic Acids Res* 39:7610–7619. doi:[10.1093/nar/gkr524](https://doi.org/10.1093/nar/gkr524)
27. Sarkis C, Philippe S, Mallet J, Serguera C (2008) Non-integrating lentiviral vectors. *Curr Gene Ther* 8:430–437
28. Nightingale SJ, Hollis RP, Pepper KA et al (2006) Transient gene expression by nonintegrating lentiviral vectors. *Mol Ther* 13:1121–1132. doi:[10.1016/j.ymthe.2006.01.008](https://doi.org/10.1016/j.ymthe.2006.01.008)
29. Yáñez-Muñoz RJ, Balagán KS, MacNeil A et al (2006) Effective gene therapy with nonintegrating lentiviral vectors. *Nat Med* 12:348–353. doi:[10.1038/nm1365](https://doi.org/10.1038/nm1365)
30. Barquinero J, Eixarch H, Pérez-Melgosa M (2004) Retroviral vectors: new applications for an old tool. *Gene Ther* 11(Suppl 1):S3–S9. doi:[10.1038/sj.gt.3302363](https://doi.org/10.1038/sj.gt.3302363)
31. Daniel R, Smith JA (2008) Integration site selection by retroviral vectors: molecular mechanism and clinical consequences. *Hum Gene Ther* 19:557–568. doi:[10.1089/hum.2007.148](https://doi.org/10.1089/hum.2007.148)
32. Culver K, Cornetta K, Morgan R et al (1991) Lymphocytes as cellular vehicles for gene therapy in mouse and man. *Proc Natl Acad Sci USA* 88:3155–3159
33. Rosenberg SA, Aebersold P, Cornetta K et al (1990) Gene transfer into humans—immunotherapy of patients with advanced melanoma, using tumor-infiltrating lymphocytes modified by retroviral gene transduction. *N Engl J Med* 323:570–578. doi:[10.1056/NEJM199008303230904](https://doi.org/10.1056/NEJM199008303230904)

34. Blaese RM, Culver KW, Miller AD et al (1995) T lymphocyte-directed gene therapy for ADA-SCID: initial trial results after 4 years. *Science* 270:475–480
35. Stone D (2010) Novel viral vector systems for gene therapy. *Viruses* 2:1002–1007. doi:[10.3390/v2041002](https://doi.org/10.3390/v2041002)
36. D’Costa J, Mansfield SG, Humeau LM (2009) Lentiviral vectors in clinical trials: current status. *Curr Opin Mol Ther* 11:554–564
37. Schambach A, Baum C (2008) Clinical application of lentiviral vectors: concepts and practice. *Curr Gene Ther* 8:474–482
38. Bank A, Dorazio R, Leboulch P (2005) A phase I/II clinical trial of beta-globin gene therapy for beta-thalassemia. *Ann N Y Acad Sci* 1054:308–316. doi:[10.1196/annals.1345.007](https://doi.org/10.1196/annals.1345.007)
39. Pedersen FS, Pyrz M, Duch M (2011) Retroviral replication. *Encyclopedia of Life Sciences*. doi:[10.1002/9780470015902.a0000430.pub3](https://doi.org/10.1002/9780470015902.a0000430.pub3)
40. Muralidhar S, Becerra SP, Rose JA (1994) Site-directed mutagenesis of adeno-associated virus type 2 structural protein initiation codons: effects on regulation of synthesis and biological activity. *J Virol* 68:170–176
41. Girod A, Wobus CE, Zádori Z et al (2002) The VP1 capsid protein of adeno-associated virus type 2 is carrying a phospholipase A2 domain required for virus infectivity. *J Gen Virol* 83:973–978
42. Zádori Z, Szelei J, Lacoste MC et al (2001) A viral phospholipase A2 is required for parvovirus infectivity. *Dev Cell* 1:291–302
43. Grieger JC, Samulski RJ (2005) Packaging capacity of adeno-associated virus serotypes: impact of larger genomes on infectivity and postentry steps. *J Virol* 79:9933–9944. doi:[10.1128/JVI.79.15.9933-9944.2005](https://doi.org/10.1128/JVI.79.15.9933-9944.2005)
44. McCarty DM, Young SM Jr, Samulski RJ (2004) Integration of adeno-associated virus (AAV) and recombinant AAV vectors. *Annu Rev Genet* 38:819–845. doi:[10.1146/annurev.genet.37.110801.143717](https://doi.org/10.1146/annurev.genet.37.110801.143717)
45. Allocca M, Doria M, Petrillo M et al (2008) Serotype-dependent packaging of large genes in adeno-associated viral vectors results in effective gene delivery in mice. *J Clin Invest* 118:1955–1964. doi:[10.1172/JCI34316](https://doi.org/10.1172/JCI34316)
46. Gao G, Vandenberghe LH, Wilson JM (2005) New recombinant serotypes of AAV vectors. *Curr Gene Ther* 5:285–297
47. Taymans J-M, Vandenberghe LH, Haute CVD et al (2007) Comparative analysis of adeno-associated viral vector serotypes 1, 2, 5, 7, and 8 in mouse brain. *Hum Gene Ther* 18:195–206. doi:[10.1089/hum.2006.178](https://doi.org/10.1089/hum.2006.178)
48. Carter BJ (2005) Adeno-associated virus vectors in clinical trials. *Hum Gene Ther* 16:541–550. doi:[10.1089/hum.2005.16.541](https://doi.org/10.1089/hum.2005.16.541)
49. Bennett J (2006) Commentary: an aye for eye gene therapy. *Hum Gene Ther* 17:177–179. doi:[10.1089/hum.2006.17.177](https://doi.org/10.1089/hum.2006.17.177)
50. LeWitt PA, Rezai AR, Leehey MA et al (2011) AAV2-GAD gene therapy for advanced Parkinson’s disease: a double-blind, sham-surgery controlled, randomised trial. *Lancet Neurol* 10:309–319. doi:[10.1016/S1474-4422\(11\)70039-4](https://doi.org/10.1016/S1474-4422(11)70039-4)
51. Bainbridge JWB, Smith AJ, Barker SS et al (2008) Effect of gene therapy on visual function in Leber’s congenital amaurosis. *N Engl J Med* 358:2231–2239. doi:[10.1056/NEJMoa0802268](https://doi.org/10.1056/NEJMoa0802268)
52. Zabner J, Fasbender AJ, Moninger T et al (1995) Cellular and molecular barriers to gene transfer by a cationic lipid. *J Biol Chem* 270:18997–19007
53. Ng CP, Pun SH (2008) A perfusable 3D cell-matrix tissue culture chamber for in situ evaluation of nanoparticle vehicle penetration and transport. *Biotechnol Bioeng* 99:1490–1501. doi:[10.1002/bit.21698](https://doi.org/10.1002/bit.21698)
54. Ye Z, Houssein HSH, Mahato RI (2007) Bioconjugation of oligonucleotides for treating liver fibrosis. *Oligonucleotides* 17:349–404. doi:[10.1089/oli.2007.0097](https://doi.org/10.1089/oli.2007.0097)
55. Mo RH, Zaro JL, Shen W-C (2012) Comparison of cationic and amphipathic cell penetrating peptides for siRNA delivery and efficacy. *Mol Pharm* 9:299–309. doi:[10.1021/mp200481g](https://doi.org/10.1021/mp200481g)

56. Shiraishi T, Nielsen PE (2011) Peptide nucleic acid (PNA) cell penetrating peptide (CPP) conjugates as carriers for cellular delivery of antisense oligomers. *Artif DNA PNA XNA* 2:90–99
57. Sanders WS, Johnston CI, Bridges SM et al (2011) Prediction of cell penetrating peptides by support vector machines. *PLoS Comput Biol* 7:e1002101. doi:[10.1371/journal.pcbi.1002101](https://doi.org/10.1371/journal.pcbi.1002101)
58. Bidwell GL 3rd, Raucher D (2010) Cell penetrating elastin-like polypeptides for therapeutic peptide delivery. *Adv Drug Deliv Rev* 62:1486–1496. doi:[10.1016/j.addr.2010.05.003](https://doi.org/10.1016/j.addr.2010.05.003)
59. Puri A, Loomis K, Smith B et al (2009) Lipid-based nanoparticles as pharmaceutical drug carriers: from concepts to clinic. *Crit Rev Ther Drug Carrier Syst* 26:523–580
60. Semple SC, Akinc A, Chen J et al (2010) Rational design of cationic lipids for siRNA delivery. *Nat Biotechnol* 28:172–176. doi:[10.1038/nbt.1602](https://doi.org/10.1038/nbt.1602)
61. Chapter 17—Engineering cationic liposome s... [Methods Enzymol 464:343–454 (2009). doi:[10.1016/S0076-6879\(09\)64017-9](https://doi.org/10.1016/S0076-6879(09)64017-9)—PubMed—NCBI. <http://www.ncbi.nlm.nih.gov/pubmed/19903563>. Accessed 4 Feb 2013
62. Kenjo E, Asai T, Yonenaga N et al (2013) Systemic delivery of small interfering RNA by use of targeted polycation liposomes for cancer therapy. *Biol Pharm Bull* 36:287–291
63. Zuhorn IS, Bakowsky U, Polushkin E et al (2005) Nonbilayer phase of lipoplex-membrane mixture determines endosomal escape of genetic cargo and transfection efficiency. *Mol Ther* 11:801–810. doi:[10.1016/j.ymthe.2004.12.018](https://doi.org/10.1016/j.ymthe.2004.12.018)
64. Guo X, Szoka FC Jr (2003) Chemical approaches to triggerable lipid vesicles for drug and gene delivery. *Acc Chem Res* 36:335–341. doi:[10.1021/ar9703241](https://doi.org/10.1021/ar9703241)
65. Stover TC, Sharma A, Robertson GP, Kester M (2005) Systemic delivery of liposomal short-chain ceramide limits solid tumor growth in murine models of breast adenocarcinoma. *Clin Cancer Res* 11:3465–3474. doi:[10.1158/1078-0432.CCR-04-1770](https://doi.org/10.1158/1078-0432.CCR-04-1770)
66. Giddam AK, Zaman M, Skwarczynski M, Toth I (2012) Liposome-based delivery system for vaccine candidates: constructing an effective formulation. *Nanomedicine (Lond)* 7:1877–1893. doi:[10.2217/nnm.12.157](https://doi.org/10.2217/nnm.12.157)
67. Lam AP, Dean DA (2010) Progress and prospects: nuclear import of nonviral vectors. *Gene Ther* 17:439–447. doi:[10.1038/gt.2010.31](https://doi.org/10.1038/gt.2010.31)
68. Wu Z-W, Chien C-T, Liu C-Y et al (2012) Recent progress in copolymer-mediated siRNA delivery. *J Drug Target* 20:551–560. doi:[10.3109/1061186X.2012.699057](https://doi.org/10.3109/1061186X.2012.699057)
69. Lee S-Y, Huh MS, Lee S et al (2010) Stability and cellular uptake of polymerized siRNA (poly-siRNA)/polyethylenimine (PEI) complexes for efficient gene silencing. *J Control Release* 141:339–346. doi:[10.1016/j.jconrel.2009.10.007](https://doi.org/10.1016/j.jconrel.2009.10.007)
70. Kim SW, Kim NY, Choi YB et al (2010) RNA interference in vitro and in vivo using an arginine peptide/siRNA complex system. *J Control Release* 143:335–343. doi:[10.1016/j.jconrel.2010.01.009](https://doi.org/10.1016/j.jconrel.2010.01.009)
71. Guo J, Cheng WP, Gu J et al (2012) Systemic delivery of therapeutic small interfering RNA using a pH-triggered amphiphilic poly-l-lysine nanocarrier to suppress prostate cancer growth in mice. *Eur J Pharm Sci* 45:521–532. doi:[10.1016/j.ejps.2011.11.024](https://doi.org/10.1016/j.ejps.2011.11.024)
72. Panyam J, Labhasetwar V (2003) Biodegradable nanoparticles for drug and gene delivery to cells and tissue. *Adv Drug Deliv Rev* 55:329–347
73. He C, Yin L, Tang C, Yin C (2013) Multifunctional polymeric nanoparticles for oral delivery of TNF- α siRNA to macrophages. *Biomaterials*. doi:[10.1016/j.biomaterials.2013.01.033](https://doi.org/10.1016/j.biomaterials.2013.01.033)
74. Woodrow KA, Cu Y, Booth CJ et al (2009) Intravaginal gene silencing using biodegradable polymer nanoparticles densely loaded with small-interfering RNA. *Nat Mater* 8:526–533. doi:[10.1038/nmat2444](https://doi.org/10.1038/nmat2444)
75. Bamrungsap S, Zhao Z, Chen T et al (2012) Nanotechnology in therapeutics: a focus on nanoparticles as a drug delivery system. *Nanomedicine (Lond)* 7:1253–1271. doi:[10.2217/nnm.12.87](https://doi.org/10.2217/nnm.12.87)
76. Pérez-Martínez FC, Ocaña AV, Pérez-Carrión MD, Ceña V (2012) Dendrimers as vectors for genetic material delivery to the nervous system. *Curr Med Chem* 19:5101–5108

77. Albertazzi L, Gherardini L, Brondi M et al (2013) In vivo distribution and toxicity of PAMAM dendrimers in the central nervous system depend on their surface chemistry. *Mol Pharm* 10:249–260. doi:[10.1021/mp300391v](https://doi.org/10.1021/mp300391v)
78. Liu Y, Huang R, Han L et al (2009) Brain-targeting gene delivery and cellular internalization mechanisms for modified rabies virus glycoprotein RVG29 nanoparticles. *Biomaterials* 30:4195–4202. doi:[10.1016/j.biomaterials.2009.02.051](https://doi.org/10.1016/j.biomaterials.2009.02.051)
79. Yu T, Liu X, Bolcato-Bellemin A-L et al (2012) An amphiphilic dendrimer for effective delivery of small interfering RNA and gene silencing in vitro and in vivo. *Angew Chem Int Ed Engl* 51:8478–8484. doi:[10.1002/anie.201203920](https://doi.org/10.1002/anie.201203920)
80. Xie J, Lee S, Chen X (2010) Nanoparticle-based theranostic agents. *Adv Drug Deliv Rev* 62:1064–1079. doi:[10.1016/j.addr.2010.07.009](https://doi.org/10.1016/j.addr.2010.07.009)
81. Medarova Z, Pham W, Farrar C et al (2007) In vivo imaging of siRNA delivery and silencing in tumors. *Nat Med* 13:372–377. doi:[10.1038/nm1486](https://doi.org/10.1038/nm1486)
82. Cormode DP, Skajaa GO, Delshad A et al (2011) A versatile and tunable coating strategy allows control of nanocrystal delivery to cell types in the liver. *Bioconjug Chem* 22:353–361. doi:[10.1021/bc1003179](https://doi.org/10.1021/bc1003179)
83. Taratula O, Garbuzenko O, Savla R et al (2011) Multifunctional nanomedicine platform for cancer specific delivery of siRNA by superparamagnetic iron oxide nanoparticles-dendrimer complexes. *Curr Drug Deliv* 8:59–69
84. Derfus AM, Chen AA, Min D-H et al (2007) Targeted quantum dot conjugates for siRNA delivery. *Bioconjug Chem* 18:1391–1396. doi:[10.1021/bc060367e](https://doi.org/10.1021/bc060367e)
85. Gao X, Cui Y, Levenson RM et al (2004) In vivo cancer targeting and imaging with semiconductor quantum dots. *Nat Biotechnol* 22:969–976. doi:[10.1038/nbt994](https://doi.org/10.1038/nbt994)
86. Zrazhevskiy P, Sena M, Gao X (2010) Designing multifunctional quantum dots for bioimaging, detection, and drug delivery. *Chem Soc Rev* 39:4326–4354. doi:[10.1039/b915139g](https://doi.org/10.1039/b915139g)
87. Zhang P, Liu W (2010) ZnO QD@PMAA-co-PDMAEMA nonviral vector for plasmid DNA delivery and bioimaging. *Biomaterials* 31:3087–3094. doi:[10.1016/j.biomaterials.2010.01.007](https://doi.org/10.1016/j.biomaterials.2010.01.007)
88. Radu DR, Lai C-Y, Jeftinija K et al (2004) A polyamidoamine dendrimer-capped mesoporous silica nanosphere-based gene transfection reagent. *J Am Chem Soc* 126:13216–13217. doi:[10.1021/ja046275m](https://doi.org/10.1021/ja046275m)
89. Hom C, Lu J, Liang M et al (2010) Mesoporous silica nanoparticles facilitate delivery of siRNA to shutdown signaling pathways in mammalian cells. *Small* 6:1185–1190. doi:[10.1002/sml.200901966](https://doi.org/10.1002/sml.200901966)
90. Meng H, Liang M, Xia T et al (2010) Engineered design of mesoporous silica nanoparticles to deliver doxorubicin and P-glycoprotein siRNA to overcome drug resistance in a cancer cell line. *ACS Nano* 4:4539–4550. doi:[10.1021/nn100690m](https://doi.org/10.1021/nn100690m)
91. Bhattarai SR, Muthuswamy E, Wani A et al (2010) Enhanced gene and siRNA delivery by polycation-modified mesoporous silica nanoparticles loaded with chloroquine. *Pharm Res* 27:2556–2568. doi:[10.1007/s11095-010-0245-0](https://doi.org/10.1007/s11095-010-0245-0)
92. Meng H, Mai WX, Zhang H et al (2013) Codelivery of an optimal drug/siRNA combination using mesoporous silica nanoparticles to overcome drug resistance in breast cancer in vitro and in vivo. *ACS Nano*. doi:[10.1021/nn3044066](https://doi.org/10.1021/nn3044066)
93. Thomas M, Klibanov AM (2003) Conjugation to gold nanoparticles enhances polyethylenimine's transfer of plasmid DNA into mammalian cells. *Proc Natl Acad Sci USA* 100:9138–9143. doi:[10.1073/pnas.1233634100](https://doi.org/10.1073/pnas.1233634100)
94. Rosi NL, Giljohann DA, Thaxton CS et al (2006) Oligonucleotide-modified gold nanoparticles for intracellular gene regulation. *Science* 312:1027–1030. doi:[10.1126/science.1125559](https://doi.org/10.1126/science.1125559)
95. Guo S, Huang Y, Jiang Q et al (2010) Enhanced gene delivery and siRNA silencing by gold nanoparticles coated with charge-reversal polyelectrolyte. *ACS Nano* 4:5505–5511. doi:[10.1021/nn101638u](https://doi.org/10.1021/nn101638u)

96. Bonoiu AC, Bergey EJ, Ding H et al (2011) Gold nanorod–siRNA induces efficient in vivo gene silencing in the rat hippocampus. *Nanomedicine (Lond)* 6:617–630. doi:[10.2217/nmm.11.20](https://doi.org/10.2217/nmm.11.20)
97. Zhang X-Q, Chen M, Lam R et al (2009) Polymer-functionalized nanodiamond platforms as vehicles for gene delivery. *ACS Nano* 3:2609–2616. doi:[10.1021/nn900865g](https://doi.org/10.1021/nn900865g)
98. Zhang L, Lu Z, Zhao Q et al (2011) Enhanced chemotherapy efficacy by sequential delivery of siRNA and anticancer drugs using PEI-grafted graphene oxide. *Small* 7:460–464. doi:[10.1002/smll.201001522](https://doi.org/10.1002/smll.201001522)
99. Alhaddad A, Adam M-P, Botsoa J et al (2011) Nanodiamond as a vector for siRNA delivery to Ewing sarcoma cells. *Small* 7:3087–3095. doi:[10.1002/smll.201101193](https://doi.org/10.1002/smll.201101193)
100. Mohan N, Chen C-S, Hsieh H-H et al (2010) In vivo imaging and toxicity assessments of fluorescent nanodiamonds in *Caenorhabditis elegans*. *Nano Lett* 10:3692–3699. doi:[10.1021/nl1021909](https://doi.org/10.1021/nl1021909)
101. Pantarotto D, Singh R, McCarthy D et al (2004) Functionalized carbon nanotubes for plasmid DNA gene delivery. *Angew Chem Int Ed Engl* 43:5242–5246. doi:[10.1002/anie.200460437](https://doi.org/10.1002/anie.200460437)
102. McCarrroll J, Baigude H, Yang C-S, Rana TM (2010) Nanotubes functionalized with lipids and natural amino acid dendrimers: a new strategy to create nanomaterials for delivering systemic RNAi. *Bioconjug Chem* 21:56–63. doi:[10.1021/bc900296z](https://doi.org/10.1021/bc900296z)
103. Yang K, Zhang S, Zhang G et al (2010) Graphene in mice: ultrahigh in vivo tumor uptake and efficient photothermal therapy. *Nano Lett* 10:3318–3323. doi:[10.1021/nl100996u](https://doi.org/10.1021/nl100996u)
104. Zhang W, Guo Z, Huang D et al (2011) Synergistic effect of chemo-photothermal therapy using PEGylated graphene oxide. *Biomaterials* 32:8555–8561. doi:[10.1016/j.biomaterials.2011.07.071](https://doi.org/10.1016/j.biomaterials.2011.07.071)
105. Suda T, Liu D (2007) Hydrodynamic gene delivery: its principles and applications. *Mol Ther* 15:2063–2069. doi:[10.1038/sj.mt.6300314](https://doi.org/10.1038/sj.mt.6300314)
106. Suda T, Suda K, Liu D (2008) Computer-assisted hydrodynamic gene delivery. *Mol Ther* 16:1098–1104. doi:[10.1038/mt.2008.66](https://doi.org/10.1038/mt.2008.66)
107. Kamimura K, Zhang G, Liu D (2010) Image-guided, intravascular hydrodynamic gene delivery to skeletal muscle in pigs. *Mol Ther* 18:93–100. doi:[10.1038/mt.2009.206](https://doi.org/10.1038/mt.2009.206)
108. Mellott AJ, Forrest ML, Detamore MS (2012) Physical non-viral gene delivery methods for tissue engineering. *Ann Biomed Eng*. doi:[10.1007/s10439-012-0678-1](https://doi.org/10.1007/s10439-012-0678-1)
109. Fuller DH, Loudon P, Schmaljohn C (2006) Preclinical and clinical progress of particle-mediated DNA vaccines for infectious diseases. *Methods* 40:86–97. doi:[10.1016/j.ymeth.2006.05.022](https://doi.org/10.1016/j.ymeth.2006.05.022)
110. Kis EE, Winter G, Myschik J (2012) Devices for intradermal vaccination. *Vaccine* 30:523–538. doi:[10.1016/j.vaccine.2011.11.020](https://doi.org/10.1016/j.vaccine.2011.11.020)
111. Sardesai NY, Weiner DB (2011) Electroporation delivery of DNA vaccines: prospects for success. *Curr Opin Immunol* 23:421–429. doi:[10.1016/j.coi.2011.03.008](https://doi.org/10.1016/j.coi.2011.03.008)
112. Littel-van Van Drunen, den Hurk S, Hannaman D (2010) Electroporation for DNA immunization: clinical application. *Expert Rev Vaccines* 9:503–517. doi:[10.1586/erv.10.42](https://doi.org/10.1586/erv.10.42)
113. Daud AI, DeConti RC, Andrews S et al (2008) Phase I trial of interleukin-12 plasmid electroporation in patients with metastatic melanoma. *J Clin Oncol* 26:5896–5903. doi:[10.1200/JCO.2007.15.6794](https://doi.org/10.1200/JCO.2007.15.6794)
114. Broderick KE, Shen X, Soderholm J et al (2011) Prototype development and preclinical immunogenicity analysis of a novel minimally invasive electroporation device. *Gene Ther* 18:258–265. doi:[10.1038/gt.2010.137](https://doi.org/10.1038/gt.2010.137)
115. Yamaoka A, Guan X, Takemoto S et al (2010) Development of a novel Hsp70-based DNA vaccine as a multifunctional antigen delivery system. *J Control Release* 142:411–415. doi:[10.1016/j.jconrel.2009.11.005](https://doi.org/10.1016/j.jconrel.2009.11.005)
116. Suzuki R, Oda Y, Utoguchi N, Maruyama K (2011) Progress in the development of ultrasound-mediated gene delivery systems utilizing nano- and microbubbles. *J Control Release* 149:36–41. doi:[10.1016/j.jconrel.2010.05.009](https://doi.org/10.1016/j.jconrel.2010.05.009)

117. He Y, Bi Y, Hua Y et al (2011) Ultrasound microbubble-mediated delivery of the siRNAs targeting MDR1 reduces drug resistance of yolk sac carcinoma L2 cells. *J Exp Clin Cancer Res* 30:104. doi:[10.1186/1756-9966-30-104](https://doi.org/10.1186/1756-9966-30-104)
118. Raju BI, Leyvi E, Seip R et al (2013) Enhanced gene expression of systemically administered plasmid DNA in the liver with therapeutic ultrasound and microbubbles. *IEEE Trans Ultrason Ferroelectr Freq Control* 60:88–96
119. Liu Y, Yan J, Prausnitz MR (2012) Can ultrasound enable efficient intracellular uptake of molecules? A retrospective literature review and analysis. *Ultrasound Med Biol* 38:876–888. doi:[10.1016/j.ultrasmedbio.2012.01.006](https://doi.org/10.1016/j.ultrasmedbio.2012.01.006)
120. Cosgrove D, Harvey C (2009) Clinical uses of microbubbles in diagnosis and treatment. *Med Biol Eng Comput* 47:813–826. doi:[10.1007/s11517-009-0434-3](https://doi.org/10.1007/s11517-009-0434-3)
121. Alzarraa A, Gravante G, Chung WY et al (2012) Targeted microbubbles in the experimental and clinical setting. *Am J Surg* 204:355–366. doi:[10.1016/j.amjsurg.2011.10.024](https://doi.org/10.1016/j.amjsurg.2011.10.024)
122. Chorny M, Fishbein I, Yellen BB et al (2010) Targeting stents with local delivery of paclitaxel-loaded magnetic nanoparticles using uniform fields. *Proc Natl Acad Sci USA* 107:8346–8351. doi:[10.1073/pnas.0909506107](https://doi.org/10.1073/pnas.0909506107)
123. Zheng X, Lu J, Deng L et al (2009) Preparation and characterization of magnetic cationic liposome in gene delivery. *Int J Pharm* 366:211–217. doi:[10.1016/j.ijpharm.2008.09.019](https://doi.org/10.1016/j.ijpharm.2008.09.019)
124. Plank C, Zelphati O, Mykhaylyk O (2011) Magnetically enhanced nucleic acid delivery. Ten years of magnetofection—progress and prospects. *Adv Drug Deliv Rev* 63:1300–1331. doi:[10.1016/j.addr.2011.08.002](https://doi.org/10.1016/j.addr.2011.08.002)
125. Vogel A, Noack J, Hüttman G, Paltauf G (2005) Mechanisms of femtosecond laser nanosurgery of cells and tissues. *Applied Physics B* 81:1015–1047. doi:[10.1007/s00340-005-2036-6](https://doi.org/10.1007/s00340-005-2036-6)
126. Tirlapur UK, König K (2002) Cell biology: Targeted transfection by femtosecond laser. *Nature* 418:290–291. doi:[10.1038/418290a](https://doi.org/10.1038/418290a)
127. Barrett LE, Sul J-Y, Takano H et al (2006) Region-directed phototransfection reveals the functional significance of a dendritically synthesized transcription factor. *Nat Methods* 3:455–460. doi:[10.1038/nmeth885](https://doi.org/10.1038/nmeth885)
128. Kohli V, Robles V, Cancela ML et al (2007) An alternative method for delivering exogenous material into developing zebrafish embryos. *Biotechnol Bioeng* 98:1230–1241. doi:[10.1002/bit.21564](https://doi.org/10.1002/bit.21564)
129. Tsampoula X, Taguchi K, Cizmár T et al (2008) Fibre based cellular transfection. *Opt Express* 16:17007. doi:[10.1364/OE.16.017007](https://doi.org/10.1364/OE.16.017007)
130. Menezes V, Mathew Y, Takayama K et al (2012) Laser plasma jet driven microparticles for DNA/drug delivery. *PLoS ONE* 7:e50823. doi:[10.1371/journal.pone.0050823](https://doi.org/10.1371/journal.pone.0050823)
131. Kawakami S, Higuchi Y, Hashida M (2008) Nonviral approaches for targeted delivery of plasmid DNA and oligonucleotide. *J Pharm Sci* 97:726–745. doi:[10.1002/jps.21024](https://doi.org/10.1002/jps.21024)
132. Passineau MJ, Zourelias L, Machen L et al (2010) Ultrasound-assisted non-viral gene transfer to the salivary glands. *Gene Ther* 17:1318–1324. doi:[10.1038/gt.2010.86](https://doi.org/10.1038/gt.2010.86)
133. Al-Dosari MS, Gao X (2009) Nonviral gene delivery: principle, limitations, and recent progress. *AAPS J* 11:671–681. doi:[10.1208/s12248-009-9143-y](https://doi.org/10.1208/s12248-009-9143-y)
134. Wolff JA, Ludtke JJ, Acsadi G et al (1992) Long-term persistence of plasmid DNA and foreign gene expression in mouse muscle. *Hum Mol Genet* 1:363–369
135. Hagstrom JE, Hegge J, Zhang G et al (2004) A facile nonviral method for delivering genes and siRNAs to skeletal muscle of mammalian limbs. *Mol Ther* 10:386–398. doi:[10.1016/j.ymthe.2004.05.004](https://doi.org/10.1016/j.ymthe.2004.05.004)
136. Sebestyén MG, Hegge JO, Noble MA et al (2007) Progress toward a nonviral gene therapy protocol for the treatment of anemia. *Hum Gene Ther* 18:269–285. doi:[10.1089/hum.2006.186](https://doi.org/10.1089/hum.2006.186)
137. Kawabata K, Takakura Y, Hashida M (1995) The fate of plasmid DNA after intravenous injection in mice: involvement of scavenger receptors in its hepatic uptake. *Pharm Res* 12:825–830

138. Wang M, Orsini C, Casanova D et al (2001) MUSEAP, a novel reporter gene for the study of long-term gene expression in immunocompetent mice. *Gene* 279:99–108
139. Vandermeulen G, Marie C, Scherman D, Pr at V (2011) New generation of plasmid backbones devoid of antibiotic resistance marker for gene therapy trials. *Mol Ther* 19:1942–1949. doi:[10.1038/mt.2011.182](https://doi.org/10.1038/mt.2011.182)
140. Kanwar JR, Roy K, Kanwar RK (2011) Chimeric aptamers in cancer cell-targeted drug delivery. *Crit Rev Biochem Mol Biol* 46:459–477. doi:[10.3109/10409238.2011.614592](https://doi.org/10.3109/10409238.2011.614592)
141. Bouchard PR, Hutabarat RM, Thompson KM (2010) Discovery and development of therapeutic aptamers. *Annu Rev Pharmacol Toxicol* 50:237–257. doi:[10.1146/annurev.pharmtox.010909.105547](https://doi.org/10.1146/annurev.pharmtox.010909.105547)
142. Huang D-B, Vu D, Cassiday LA et al (2003) Crystal structure of NF-kappaB (p50)2 complexed to a high-affinity RNA aptamer. *Proc Natl Acad Sci USA* 100:9268–9273. doi:[10.1073/pnas.1632011100](https://doi.org/10.1073/pnas.1632011100)
143. Mashima T, Matsugami A, Nishikawa F et al (2009) Unique quadruplex structure and interaction of an RNA aptamer against bovine prion protein. *Nucleic Acids Res* 37:6249–6258. doi:[10.1093/nar/gkp647](https://doi.org/10.1093/nar/gkp647)
144. Phan AT, Kuryavyi V, Darnell JC et al (2011) Structure-function studies of FMRP RGG peptide recognition of an RNA duplex-quadruplex junction. *Nat Struct Mol Biol* 18:796–804. doi:[10.1038/nsmb.2064](https://doi.org/10.1038/nsmb.2064)
145. Sussman D, Wilson C (2000) A water channel in the core of the vitamin B(12) RNA aptamer. *Structure* 8:719–727
146. Ellington AD, Szostak JW (1990) In vitro selection of RNA molecules that bind specific ligands. *Nature* 346:818–822. doi:[10.1038/346818a0](https://doi.org/10.1038/346818a0)
147. Ellington AD, Szostak JW (1992) Selection in vitro of single-stranded DNA molecules that fold into specific ligand-binding structures. *Nature* 355:850–852. doi:[10.1038/355850a0](https://doi.org/10.1038/355850a0)
148. Tuerk C, Gold L (1990) Systematic evolution of ligands by exponential enrichment: RNA ligands to bacteriophage T4 DNA polymerase. *Science* 249:505–510
149. Nutiu R, Li Y (2005) In vitro selection of structure-switching signaling aptamers. *Angew Chem Int Ed Engl* 44:1061–1065. doi:[10.1002/anie.200461848](https://doi.org/10.1002/anie.200461848)
150. Stoltenburg R, Nikolaus N, Strehlitz B (2012) Capture-SELEX: selection of DNA aptamers for aminoglycoside antibiotics. *J Anal Methods Chem* 2012:415697. doi:[10.1155/2012/415697](https://doi.org/10.1155/2012/415697)
151. Binning JM, Leung DW, Amarasinghe GK (2012) Aptamers in virology: recent advances and challenges. *Front Microbiol* 3:29. doi:[10.3389/fmicb.2012.00029](https://doi.org/10.3389/fmicb.2012.00029)
152. Kang D, Wang J, Zhang W et al (2012) Selection of DNA aptamers against glioblastoma cells with high affinity and specificity. *PLoS ONE* 7:e42731. doi:[10.1371/journal.pone.0042731](https://doi.org/10.1371/journal.pone.0042731)
153. Eckstein F, Gish G (1989) Phosphorothioates in molecular biology. *Trends Biochem Sci* 14:97–100
154. Green LS, Jellinek D, Bell C et al (1995) Nuclease-resistant nucleic acid ligands to vascular permeability factor/vascular endothelial growth factor. *Chem Biol* 2:683–695
155. Ruckman J, Green LS, Beeson J et al (1998) 2'-Fluoropyrimidine RNA-based aptamers to the 165-amino acid form of vascular endothelial growth factor (VEGF165). Inhibition of receptor binding and VEGF-induced vascular permeability through interactions requiring the exon 7-encoded domain. *J Biol Chem* 273:20556–20567
156. Lin Y, Nieuwlandt D, Magallanez A et al (1996) High-affinity and specific recognition of human thyroid stimulating hormone (hTSH) by in vitro-selected 2'-amino-modified RNA. *Nucleic Acids Res* 24:3407–3414
157. Keefe AD, Pai S, Ellington A (2010) Aptamers as therapeutics. *Nat Rev Drug Discov* 9:537–550. doi:[10.1038/nrd3141](https://doi.org/10.1038/nrd3141)
158. Khar RK, Jain GK, Warsi MH et al (2010) Nano-vectors for the ocular delivery of nucleic acid-based therapeutics. *Indian J Pharm Sci* 72:675–688. doi:[10.4103/0250-474X.84575](https://doi.org/10.4103/0250-474X.84575)
159. Sanghvi YS (2011) A status update of modified oligonucleotides for chemotherapeutics applications. *Curr Protoc Nucleic Acid Chem* Chap 4: Unit 4.1.1–22. Doi: [10.1002/0471142700.nc0401s46](https://doi.org/10.1002/0471142700.nc0401s46)

160. Thiel KW, Giangrande PH (2009) Therapeutic applications of DNA and RNA aptamers. *Oligonucleotides* 19:209–222. doi:[10.1089/oli.2009.0199](https://doi.org/10.1089/oli.2009.0199)
161. Cohen MG, Purdy DA, Rossi JS et al (2010) First clinical application of an actively reversible direct factor IXa inhibitor as an anticoagulation strategy in patients undergoing percutaneous coronary intervention. *Circulation* 122:614–622. doi:[10.1161/CIRCULATIONAHA.109.927756](https://doi.org/10.1161/CIRCULATIONAHA.109.927756)
162. Altman S, Cech TR (2013) The nobel prize in chemistry 1989. http://www.nobelprize.org/nobel_prizes/chemistry/laureates/1989/. Accessed 4 Apr 2013
163. Scherer LJ, Rossi JJ (2003) Approaches for the sequence-specific knockdown of mRNA. *Nat Biotechnol* 21:1457–1465. doi:[10.1038/nbt915](https://doi.org/10.1038/nbt915)
164. Burke JM (1996) Hairpin ribozyme: current status and future prospects. *Biochem Soc Trans* 24:608–615
165. Usman N, Beigelman L, McSwiggen JA (1996) Hammerhead ribozyme engineering. *Curr Opin Struct Biol* 6:527–533
166. El-Sagheer AH, Brown T (2010) New strategy for the synthesis of chemically modified RNA constructs exemplified by hairpin and hammerhead ribozymes. *Proc Natl Acad Sci USA* 107:15329–15334. doi:[10.1073/pnas.1006447107](https://doi.org/10.1073/pnas.1006447107)
167. Liang JC, Bloom RJ, Smolke CD (2011) Engineering biological systems with synthetic RNA molecules. *Mol Cell* 43:915–926. doi:[10.1016/j.molcel.2011.08.023](https://doi.org/10.1016/j.molcel.2011.08.023)
168. Wieland M, Berschneider B, Erlacher MD, Hartig JS (2010) Aptazyme-mediated regulation of 16S ribosomal RNA. *Chem Biol* 17:236–242. doi:[10.1016/j.chembiol.2010.02.012](https://doi.org/10.1016/j.chembiol.2010.02.012)
169. Sarver N, Cantin EM, Chang PS et al (1990) Ribozymes as potential anti-HIV-1 therapeutic agents. *Science* 247:1222–1225
170. Yu M, Ojwang J, Yamada O et al (1993) A hairpin ribozyme inhibits expression of diverse strains of human immunodeficiency virus type 1. *Proc Natl Acad Sci USA* 90:6340–6344
171. Dropulić B, Lin NH, Martin MA, Jeang KT (1992) Functional characterization of a U5 ribozyme: intracellular suppression of human immunodeficiency virus type 1 expression. *J Virol* 66:1432–1441
172. Ojwang JO, Hampel A, Looney DJ et al (1992) Inhibition of human immunodeficiency virus type 1 expression by a hairpin ribozyme. *Proc Natl Acad Sci USA* 89:10802–10806
173. Wong-Staal F, Poeschla EM, Looney DJ (1998) A controlled, phase 1 clinical trial to evaluate the safety and effects in HIV-1 infected humans of autologous lymphocytes transduced with a ribozyme that cleaves HIV-1 RNA. *Hum Gene Ther* 9:2407–2425. doi:[10.1089/hum.1998.9.16-2407](https://doi.org/10.1089/hum.1998.9.16-2407)
174. (2013) Press release: the 2006 nobel prize in physiology or medicine. http://www.nobelprize.org/nobel_prizes/medicine/laureates/2006/press.html. Accessed 12 Apr 2013
175. Pecot CV, Calin GA, Coleman RL et al (2011) RNA interference in the clinic: challenges and future directions. *Nat Rev Cancer* 11:59–67. doi:[10.1038/nrc2966](https://doi.org/10.1038/nrc2966)
176. Sibley CR, Seow Y, Wood MJA (2010) Novel RNA-based strategies for therapeutic gene silencing. *Mol Ther* 18:466–476. doi:[10.1038/mt.2009.306](https://doi.org/10.1038/mt.2009.306)
177. Cho Y-S, Lee GY, Sajja HK et al (2013) Targeted delivery of siRNA-generating DNA nanocassettes using multifunctional nanoparticles. *Small*. doi:[10.1002/smll.201201973](https://doi.org/10.1002/smll.201201973)
178. Wall NR, Shi Y (2003) Small RNA: can RNA interference be exploited for therapy? *Lancet* 362:1401–1403. doi:[10.1016/S0140-6736\(03\)14637-5](https://doi.org/10.1016/S0140-6736(03)14637-5)
179. Dalby B, Cates S, Harris A et al (2004) Advanced transfection with Lipofectamine 2000 reagent: primary neurons, siRNA, and high-throughput applications. *Methods* 33:95–103. doi:[10.1016/j.ymeth.2003.11.023](https://doi.org/10.1016/j.ymeth.2003.11.023)
180. McCaffrey AP, Meuse L, Pham T-TT et al (2002) RNA interference in adult mice. *Nature* 418:38–39. doi:[10.1038/418038a](https://doi.org/10.1038/418038a)
181. Liu YP, Vink MA, Westerink J-T et al (2010) Titers of lentiviral vectors encoding shRNAs and miRNAs are reduced by different mechanisms that require distinct repair strategies. *RNA* 16:1328–1339. doi:[10.1261/ma.1887910](https://doi.org/10.1261/ma.1887910)

182. Van den Haute C, Eggermont K, Nuttin B et al (2003) Lentiviral vector-mediated delivery of short hairpin RNA results in persistent knockdown of gene expression in mouse brain. *Hum Gene Ther* 14:1799–1807. doi:[10.1089/104303403322611809](https://doi.org/10.1089/104303403322611809)
183. Halder J, Kamat AA, Landen CN Jr et al (2006) Focal adhesion kinase targeting using in vivo short interfering RNA delivery in neutral liposomes for ovarian carcinoma therapy. *Clin Cancer Res* 12:4916–4924. doi:[10.1158/1078-0432.CCR-06-0021](https://doi.org/10.1158/1078-0432.CCR-06-0021)
184. Sato Y, Murase K, Kato J et al (2008) Resolution of liver cirrhosis using vitamin A-coupled liposomes to deliver siRNA against a collagen-specific chaperone. *Nat Biotechnol* 26:431–442. doi:[10.1038/nbt1396](https://doi.org/10.1038/nbt1396)
185. Frank-Kamenetsky M, Grefhorst A, Anderson NN et al (2008) Therapeutic RNAi targeting PCSK9 acutely lowers plasma cholesterol in rodents and LDL cholesterol in nonhuman primates. *Proc Natl Acad Sci USA* 105:11915–11920. doi:[10.1073/pnas.0805434105](https://doi.org/10.1073/pnas.0805434105)
186. Marquez VE, Siddiqui MA, Ezzitouni A et al (1996) Nucleosides with a twist. Can fixed forms of sugar ring pucker influence biological activity in nucleosides and oligonucleotides? *J Med Chem* 39:3739–3747. doi:[10.1021/jm960306+](https://doi.org/10.1021/jm960306+)
187. Deleavey GF, Damha MJ (2012) Designing chemically modified oligonucleotides for targeted gene silencing. *Chem Biol* 19:937–954. doi:[10.1016/j.chembiol.2012.07.011](https://doi.org/10.1016/j.chembiol.2012.07.011)
188. McNeer NA, Schleifman EB, Cuthbert A et al (2012) Systemic delivery of triplex-forming PNA and donor DNA by nanoparticles mediates site-specific genome editing of human hematopoietic cells in vivo. *Gene Ther*. doi:[10.1038/gt.2012.82](https://doi.org/10.1038/gt.2012.82)
189. Rogers FA, Hu R-H, Milstone LM (2013) Local delivery of gene-modifying triplex-forming molecules to the epidermis. *J Invest Dermatol* 133:685–691. doi:[10.1038/jid.2012.351](https://doi.org/10.1038/jid.2012.351)
190. Chakrabarti A, Zhang K, Aruva MR et al (2007) Radiohybridization PET imaging of KRAS G12D mRNA expression in human pancreas cancer xenografts with [(64)Cu]DO3A-peptide nucleic acid-peptide nanoparticles. *Cancer Biol Ther* 6:948–956
191. Karkare S, Bhatnagar D (2006) Promising nucleic acid analogs and mimics: characteristic features and applications of PNA, LNA, and morpholino. *Appl Microbiol Biotechnol* 71:575–586. doi:[10.1007/s00253-006-0434-2](https://doi.org/10.1007/s00253-006-0434-2)
192. Campbell MA, Wengel J (2011) Locked vs. unlocked nucleic acids (LNA vs. UNA): contrasting structures work towards common therapeutic goals. *Chem Soc Rev* 40:5680–5689. doi:[10.1039/c1cs15048k](https://doi.org/10.1039/c1cs15048k)
193. Li Y-F, Morcos PA (2008) Design and synthesis of dendritic molecular transporter that achieves efficient in vivo delivery of morpholino antisense oligo. *Bioconjug Chem* 19:1464–1470. doi:[10.1021/bc8001437](https://doi.org/10.1021/bc8001437)
194. Eisen JS, Smith JC (2008) Controlling morpholino experiments: don't stop making antisense. *Development* 135:1735–1743. doi:[10.1242/dev.001115](https://doi.org/10.1242/dev.001115)
195. Huh D, Hamilton GA, Ingber DE (2011) From 3D cell culture to organs-on-chips. *Trends Cell Biol* 21:745–754. doi:[10.1016/j.tcb.2011.09.005](https://doi.org/10.1016/j.tcb.2011.09.005)
196. Kelkar SS, Reineke TM (2011) Theranostics: combining imaging and therapy. *Bioconjug Chem* 22:1879–1903. doi:[10.1021/bc200151q](https://doi.org/10.1021/bc200151q)

Chapter 19

Engineering Nanomaterials for Biosensors and Therapeutics

Tse-Ying Liu, Chun-Liang Lo, Chih-Chia Huang, Syue-Liang Lin and C. Allen Chang

19.1 Introduction

Nanotechnology, an interdisciplinary technology, has seen huge developments in the last decade with applications in the fields of electronics, medicine, and industry and is of great potential for economic development. Nanomaterials have an important role in nanotechnology and can be classified into two types: (a) nanophase: a material with a nanoscaled size that can also be defined as a nanoparticle (NP); (b) nanostructure: a nanoscaled or bulk material with nanosized microstructures. Recently, inorganic NPs, including Au, Ag, Pt, Pd, quantum dots (QDs) (e.g., CdSe, CdS, and ZnS), TiO₂, ZnO, SiO₂, hydroxyapatite, and magnetic compounds (e.g., Fe₃O₄ and

T.-Y. Liu

Department of Biomedical Engineering, National Yang Ming University,
7923, No. 155, Sec. 2, Li-Nong Street, Taipei 112, Taiwan, ROC
e-mail: tyliu5@ym.edu.tw

C.-L. Lo

Department of Biomedical Engineering, National Yang Ming University,
7914, No. 155, Sec. 2, Li-Nong Street, Taipei 112, Taiwan, ROC
e-mail: cllo@ym.edu.tw

C.-C. Huang

Institute of Biophotonics, National Yang Ming University, 7959, No. 155,
Sec. 2, Li-Nong Street, Taipei 112, Taiwan, ROC
e-mail: huang.chihchia@gmail.com

S.-L. Lin

Department of Biotechnology and Laboratory Science in Medicine,
National Yang Ming University, 5540, No. 155, Sec. 2,
Li-Nong Street, Taipei 112, Taiwan, ROC
e-mail: g39919041@ym.edu.tw

C. A. Chang (✉)

Department of Biomedical Imaging and Radiological Sciences,
National Yang Ming University, 7199, No. 155, Sec. 2,
Li-Nong Street, Taipei 112, Taiwan, ROC
e-mail: cachang@ym.edu.tw

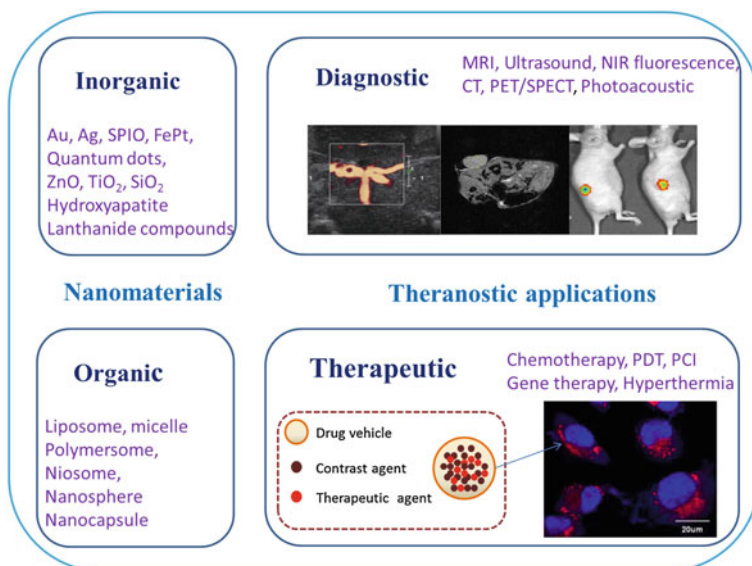


Fig. 19.1 Nanomaterials employed for theranostic applications

FePt), have received considerable attention in the field of biomedical materials research due to their unique properties such as photoluminescence, photocatalysis, and superparamagnetism. These NPs with differing morphologies (nanoparticle, nanorod, nanowire, quantum well, quantum dot, and nanoporous) and hybrid structures (core-shell, inorganic-inorganic hybrid crystal, and inorganic-organic hybrid structure) have been applied in theranostic applications including imaging, labeling, and tracking agents as well as drug carriers, vectors for gene therapy, and agents for hyperthermia treatments. This chapter reviews the synthesis of nanoparticulate raw materials, polymer surface modifications, surface-modified nanosensors and nanotheranostic agents used in the biomedical field (Fig. 19.1).

19.2 Synthesis of Nanoparticulate Raw Materials

19.2.1 Nobel Metal Nanoparticles

19.2.1.1 Gold

Gold and its compounds have long been used as medicinal agents, and their use can be tracked to ancient Egypt and China [1]. The Egyptians added gold to certain foods for spiritual and bodily purification 5,000 years ago. In 2500 BC, red colloidal gold was included in Chinese remedies for longer life. During the last century, gold has

also been used to treat arthritis. Recently, gold nanoparticles (GNPs) have become an important biomedical material for cancer research due to their inert properties and non-toxic nature, ease of synthesis and functionalization, tunable size via synthetic parameters, and the surface plasma resonance (SPR) effect [2–6].

In general, well-dispersed GNPs can be prepared by reducing gold salts in the presence of appropriate reductants and stabilizing agents, a process that has been applied for over 50 years. The size and shape of the GNPs can be manipulated by varying temperature, concentration of the precursor, the type and concentration of the reductant, and the type and concentration of the stabilizing agents [5]. Well-dispersed gold colloids have been applied in bio-sensing, bio-labeling, targeted imaging, and photoacoustic imaging [7]. In order to achieve the targeting, sensing, and delivering functions, delivery systems based on GNPs-bearing functional moieties with thiol linkers have been developed. In the most common procedure for preparing GNPs, AuCl_4^- salts are reduced with NaBH_4 in the presence of the desired thiol-based capping agents. The size of the particles can be tuned from 1.5 to 6 nm by adjusting the stoichiometry of the thiol–gold reaction [8]. On the other hand, for some biomedical applications, such as photoacoustic imaging, gold nanorods, are required [9]. Gold nanorods can be synthesized by using the seed-mediated growth method. Jana et al. prepared colloidal gold nanorods by firstly forming citrate-capped gold seeds, which were subsequently added to a growth solution obtained by using ascorbic acid to reduce HAuCl_4 in the presence of the surfactant cetyltrimethylammonium bromide (CTAB) and silver ions [10]. This method was modified by Nikoobakht et al. [11] in which the seed solution was obtained by using NaBH_4 to reduce HAuCl_4 in the presence of CTAB in an ice bath. This seed solution was then added to the Au growth solution obtained by using ascorbic acid to reduce HAuCl_4 in the presence of CTAB and treated with AgNO_3 prior to the mixing to facilitate the nanorod growth and to tune the aspect ratio.

19.2.1.2 Silver

Silver has been used as an antimicrobial agent for thousands of years. Recently, silver nanoparticles have received considerable attention because of their SPR phenomenon, surface enhanced Raman scattering (SERS) effect, and catalytic property, in addition to antimicrobial activity [12, 13]. These properties of silver nanoparticles vary with their shape, size and formulation [14] which can be manipulated by a variety of synthetic methodologies using photo-, thermo-, sono-, wet-, bio- and electro-chemical principles [12]. For example, electrochemistry has been employed to prepare Ag nanowires, nanorods, nanocubes, and nanoplates by tuning parameters such as current density and Ag salt concentration. In order to further manipulate the nucleation and growth kinetics during the synthetic process, ultrasonication was employed to enhance mass transport and organic capping agents were used to selectively inhibit crystal growth in specific crystallographic planes. Organic capping reagents, such as the non-toxic poly(vinyl pyrrolidone) (PVP), are widely used in the shape-selective synthesis of NPs.

19.2.2 Quantum Dots: CdSe and CdTe

In general, QDs are defined as nanometer-sized crystals that demonstrate a quantum confinement effect when the nanoparticle radius is smaller than the Bohr radius of the electron, hole, and exciton. Typically, QD sizes range between 2 and 10 nm [15]. Recently, QDs have been intensively investigated because their photoluminescence properties are size-dependent and stable compared with those of organic fluorescent molecules, which are advantageous for bio-sensing, bio-labeling, and imaging [16]. However, most QDs without further surface modification are toxic, which limits their application for medical use (*vide infra*).

CdSe and CdTe are the most common QDs studied because their quantum confinement region covers the entire visible light spectrum range. The main cause of the toxicity of Cd-based QDs is the ability of released Cd^{2+} ions to bind to thiol groups in mitochondria, followed by considerable stress and damage that causes cell death. Hence, a variety of surface coatings have been developed to reduce the release of Cd^{2+} ions. One of the most common coating layers used is the amorphous SiO_2 shell, which can be prepared by using a silica precursor, such as tetraethylorthosilicate (TEOS). The silica shell can further conjugate with other molecules or polymers to construct a hydrophilic, well-dispersed, and functionalized colloid system [17].

CdSe QDs can be prepared by the pyrolysis of organometallic precursors of Cd (e.g., dimethyl cadmium, CdMe_2) and Se in trioctylphosphine (TOP) at 230–300 °C. Size-selective precipitation is employed to obtain mono-sized nanoparticles. This method was later modified because of the volatile, pyrophoric, and toxic nature of CdMe_2 . Alternative Cd precursors such as cadmium oxide and cadmium acetate have been used [18]. The QDs obtained through the thermal decomposition route are usually hydrophobic because the precursors are decomposed and reacted with capping agents in an oil-phase state. However, in most cases, hydrophilic, colloidal QDs dispersed in aqueous solution are preferred for intravascular, extravascular, and intracellular delivery. Therefore, many methods have been developed to synthesize hydrophilic QDs [19, 20]. In one method, the hydrophobic ligands are replaced with bifunctional molecules containing a soft acidic group (e.g., thioglycolic acid, TGA) and hydrophilic groups (e.g., $-\text{COOH}$ or $-\text{NH}_2$) to improve the colloid stability [21]. On the other hand, TGA has been used as a hydrophilic capping agent to synthesize CdTe QDs directly. In this process, first, aluminum telluride is mixed with a dilute sulfuric acid solution under N_2 atmosphere to prepare H_2Te . The resulting H_2Te gas and an aqueous solution of cadmium perchlorate hexahydrate are then reacted in the presence of TGA at 100 °C and pH 11.5 to produce CdTe QDs.

19.2.3 Magnetic Nanoparticles: Fe_3O_4

Superparamagnetic iron oxide nanoparticles (SPIONs) have been used for a number of biomedical applications such as separation of biomolecules, biosensing, targeted drug delivery, hyperthermia, magnetic-triggered release, and as

magnetic resonance imaging (MRI) contrast agents. Several synthetic methods have been developed to prepare SPIONs employing microemulsions, sol–gel syntheses, sonochemical reactions, hydrothermal reactions, hydrolysis, and thermolysis of precursors [22–24].

The coprecipitation method is the simplest way to prepare Fe_3O_4 (magnetite) nanoparticles in which an aqueous mixture of Fe(II) and Fe(III) chloride at a 1:2 molar ratio is added a base in a non-oxidizing oxygen environment at pH 9–14. For example, highly monodisperse SPIONs can be synthesized by utilizing water-in-oil microemulsions in which the aqueous core of aerosol-OT (AOT)/n-hexane reverse micelles is formed to dissolve hydrophilic precursors in a deoxygenated sodium hydroxide solution. Chemical precipitation occurs in the reverse micelles (i.e., nanoreactors), which leads to the formation of SPIONs with diameter less than 15 nm.

On the other hand, iron organic precursors, such as $\text{Fe}(\text{CO})_5$ and $\text{Fe}(\text{acac})_3$, have been used to prepare mono-sized and well-dispersed nanoparticles in octyl ether and oleic acid at high temperature. In another process, $\text{Fe}(\text{CO})_5$ is decomposed at 100 °C in the presence of oleic acid and then aged at 300 °C to yield high crystallinity monodisperse maghemite ($\gamma\text{-Fe}_2\text{O}_3$) in oil phase. These high temperature thermolysis reactions are normally carried out under sonication to generate high temperature hot spot, i.e., ultrasound-induced cavitation. For example, an aqueous solution of $\text{Fe}(\text{CO})_5$ mixed with sodium dodecyl sulfate under sonication yielded amorphous Fe_3O_4 nanoparticles.

19.2.4 Bioactive Nanoparticles: Hydroxyapatite

Nanomaterials can also be found in animals. For example, bone is composed of calcium phosphate (with nanosized crystals) and collagen (with nanosized structure) by which the high strength/weight ratio can be achieved to mechanically protect and support the body. Hydroxyapatite (HAp) is one type of calcium phosphate and the major inorganic component of bone mineral [25]. The calcium-deficient apatitic structure (Ca-deficient hydroxyapatite, CDHA) is also an essential component of natural bone mineral. CDHA is compositionally similar to tricalcium phosphates ($\text{Ca/P} = 1.5$) and structurally similar to stoichiometric hydroxyapatite ($\text{Ca/P} = 1.67$) [26]. Therefore, HA and CDHA are considered to be candidate materials for orthopedic applications with respect to both mechanical reinforcement and biological activity [27]. In the human body, the nanosized HAp crystals (generally 30–50 nm in length, 15–30 nm in width, and 2–10 nm in thickness) play an important role in the strength (resistance to deformation) and toughness (resistance to flaw propagation) of the bone. In addition, nanosized HAp crystals act as Ca and P reservoirs for many metabolic processes in the human body.

Many synthetic routes have been developed to prepare HAp nanoparticles including sol–gel, co-precipitation and hydrothermal methods [28, 29]. Among these methods, co-precipitation is the most common wet-chemical method to

prepare HAp nanoparticles [30]. In this method, HAp nanoparticles are obtained by mixing aqueous solutions of a number of precursor compounds containing Ca^{2+} [e.g., CaCl_2 , $\text{Ca}(\text{NO}_3)_2$, $\text{Ca}(\text{OH})_2$, CaCO_3 , $\text{CaSO}_4 \cdot 2\text{H}_2\text{O}$, and $\text{Ca}(\text{CH}_3\text{COO})_2$] and PO_4^{3-} [e.g., H_3PO_4 , $\text{NH}_4\text{H}_2\text{PO}_4$, $(\text{NH}_4)_2\text{HPO}_4$, Na_3PO_4 , and K_3PO_4] ions at a Ca/P ratio of 1.67 and pH values of 7–14. The pH of the reaction solution is one of the most important parameters affecting the morphology and crystallinity of HA nanoparticles by changing the rate and extent of the precursor hydrolysis reaction which can be adjusted by adding ammonia gas, NH_4OH , or NaOH . In addition to pH, other parameters such as the concentrations of the precursor salts, mixing sequence and rate, reaction temperature, and aging time all affect the morphology and crystallinity of HA nanoparticles. To further manipulate the morphology of HA nanoparticles, the synthetic reaction could be restricted in nanosized reaction vessels, such as reverse micelles, microemulsions, and vesicles. For example, poly(allylamine hydrochloride)/ PO_4^{3-} complex was employed as spatial reaction vessels and a source of phosphate anions to capture calcium cations to synthesize HAp.

19.3 Polymer-Based Nanoparticles

19.3.1 *The Physiological Itinerary of Nanoparticles*

The use of nanoparticles efficiently to deliver to targeted tissues for diagnosis or therapy requires to fulfill three major concerns that are associated with physiological conditions. The first is to prolong the circulation half-life of the nanoparticles, to which the main barriers are believed to be the interactions with blood components, filtration by the kidney, recognition by the reticuloendothelial system (RES) in the liver, spleen, and lung [31], as well as clearance by the monophagocytic system (MPs) [32]. It is known that both physical properties (e.g., particle size, morphology, shape, and hydrophobicity) and chemical properties (e.g., surface chemistries such as charges and modifications) of the nanoparticles can affect directly their absorption of plasma proteins, recognition by the RES and elimination from the blood [33–35]. For example, microparticles with diameters 1–10 μm could be directly captured by liver's Kupffer cells, whereas nanoparticles below 100 nm were recognized for extravasation from blood into targeted tissues [36, 37]. For the effect of shape on circulation, cylindrical particles showed negligible phagocytosis and prolonged circulation as compared with spherical particles under the same volume [38]. However, by surface-chemical modification, gold nanorods in combination with various polymer grafting levels exhibited different biodistribution results in liver, lung, and spleen [39]. Zhang et al. evaluated the effect of particle size (45–90 nm) on the in vivo pharmacokinetics and biodistribution [40]. Their results demonstrated that 90 nm particles were taken up more rapidly than 45 and 60 nm particles by RES cells.

The second concern is to deliver nanoparticles from blood through permeation to targeted tumor tissues and accumulate there. The accumulation of nanoparticles in tumors can be achieved by the microvascular hyperpermeability due to vast angiogenesis and localized leaky vasculature, called the “enhanced permeability and retention (EPR) effect” [41, 42]. The pore cutoff size in most solid tumors studied is in general in the range 380–780 nm, beyond which the nanoparticles cannot be accumulated in the tumor tissue [43]. Perrault et al. reported the effect of nanoparticle size from 10 to 100 nm on the passive targeting onto tumors and found that PEG-modified GNPs having 40–100 nm diameter would provide excellent tumor accumulation [44]. Normally, smaller nanoparticles had relatively higher permeation rate from vasculature to tumors and vice versa for their clearance. If the goal is to deliver a nanoparticulate contrast agent to tumors, Perrault et al. suggested that moderate sized particles having a final diameter of 60–100 nm after mPEG modification would be preferred. However, if nanoparticles were to be used as drug carriers for cancer therapy for which longer localization within the tumor mass is important, it is better to use an active tumor targeting process. This can be achieved by chemically modifying ligands on the surfaces of nanoparticles to allow selective binding to receptors that are specifically expressed on the membranes of cancer cells.

The third concern is the uptake of nanoparticles by the cancer cells following accumulation, if nanoparticles are designed for intracellular delivery. In general, the internalization of nanoparticles into cells could be done by either pinocytosis or receptor-mediated endocytosis. Unlike receptor-mediated endocytosis which uptakes nanoparticles via the interaction of ligands with specific receptors on the cellular membrane, pinocytosis is a low efficiency and non-specific transport pathway. In addition to cell type, nanoparticle surface properties such as ligands modification, particle size and charge all influence the rate and accumulated efficiency of cellular uptake. Many studies of intracellular accumulation suggest that GNPs with diameters of approximately 40–60 nm exert the fastest wrapping time and moderate exocytosis and therefore accumulate the most in cancer cells [45–49]. It is known that positively charged nanoparticles activate a compensatory endocytosis pathway that also enhances the accumulation of nanoparticles in cells [50]. These results all suggest that the physical and chemical properties of nanoparticles strongly influence the circulation half-life, biodistribution, tumor accumulation, and cellular internalization.

19.3.2 Polymers in Nanoparticles Modification

The most direct method to alter the physical and chemical properties of nanoparticles to enhance the accumulation in targeted cells is to modify them by hydrophilic polymers (i.e., passive targeting) and decorated with specific targeting ligands (i.e., active targeting). GNPs could be used as a model system for describing the biodistribution of particles, vasculature permeation, and cell

internalization for polymer modification. De Jong et al. [51] studied the particle size dependence on the distribution in organs of intravenously injected GNPs. Their results revealed that naked GNPs of sizes 10, 50, 100, and 250 nm were all present in the liver and spleen. However, the smallest (10 nm) nanoparticles were also widely distributed in various other organs, including kidney, testis, thymus, heart, lung, and brain which might create problems if specific targeting to tumors is desired. Lipka et al. [52] showed that modifying 5 nm GNPs with PEG affected their pharmacokinetics, especially prolonging their circulation time and reducing their uptake by the liver, spleen, and other organs. Similar to GNPs, single-walled carbon nanotubes (SWNTs) coated with PEG showed relatively long circulation time and low RES uptake, as compared with un-modified SWNTs [53]. Also, dextran-coated iron oxide nanoparticles with PEG and chimeric L6 antibody modification exhibited long circulation time and ability to exit from blood vessels and access the cancer cells [54].

Besides directly changing the biodistribution and organ accumulation, nanoparticles modified by biocompatible hydrophilic polymers can also decrease their cellular cytotoxicity which is also of prime concern if these materials are to be used clinically. For example, CdSe QDs have been used for a number of animal in vivo imaging studies before extensive cytotoxicity studies, however, bare CdSe QDs undergo surface oxidation when incubated with cells and induce the release of Cd(II) ions, which is known to damage mitochondrial and lead to cell death [55]. One method to prevent Cd(II) ions releasing from CdSe QDs is to coat an inner ZnS shell onto their surface together with a polymer (e.g., PEG) outer layer. Another example to reduce cytotoxicity is to use the hydrophilic pullulan (Pn) polymer to modify the surface of SPIONs [56]. It has been reported that naked SPIONs may promote cell apoptosis and lead to low cell viability. With Pn-coating, the modified SPIONs exhibit significantly lower cytotoxicity than naked particles.

The biocompatible hydrophilic polymers used for nanoparticle surface modification include PEG, dextran, and chitosan. PEG is the most important and widely used hydrophilic and water soluble polymer so far. It has been approved by FDA for parenteral applications because of its better understood biocompatibility and safety properties. The molecular weights of PEG for safe parenteral administration range from 1 to 20 kDa. Several reports have showed the use of PEG on inorganic nanoparticles to increase the biocompatibility and blood circulation time [57–59]. In addition to PEG, dextran is a hydrophilic polysaccharide also often used for polymer coating with a well-known history of safe applications. For example, dextran has been used to coat SPIONs (e.g., Ferridex[®], a FDA approved MRI contrast agent) to enhance particle stability and to prolong blood circulation time [60]. On the other hand, chitosan is a non-toxic, biocompatible, biodegradable, and muco-adhesive polymer. The use of chitosan-modified magnetic nanoparticles has generated some research interests [61, 62]. For example, chitosan encapsulating nanoparticles comprising both CdSe-ZnS QDs and GdDTPA have been reported as potential dual-modality fluorescent biomarkers and MRI contrast agents [63]. These kinds of multifunctional nano-medicines are considered as promising candidates for future biomedical applications.

19.3.3 Surface Engineering of Inorganic Nanoparticles by Polymers

For surface modification of nanoparticles, direct linkage of polymers by covalent coupling and coating polymers by non-covalent immobilization are two major used strategies. Non-covalent immobilization is also known as physical adsorption which results from molecular interactions by Van der Waals and/or electrostatic forces, molecular affinity, and polymer crosslinking after adsorption. Polycyclic aromatic compounds could be immobilized onto the surface of carbon nanotubes through Van der Waals forces [64]. An electrostatic interaction has been used to link positively charged enzymes and negatively charged CdTe QDs [65]. Molecules such as glutathione with disulfide bonds and PEG derivatives with thiol functional groups have been conjugated directly to gold surfaces by their strong affinities to gold atoms [44, 66]. Such interactions between thiols and metal atoms are also called semi-covalent interaction.

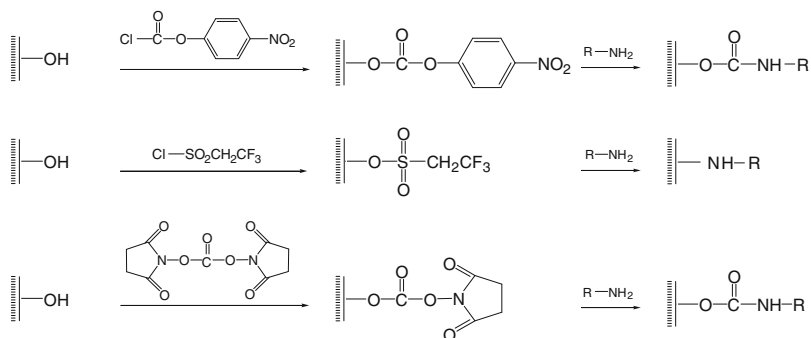
For covalent binding of polymer on inert solid nanoparticles, the surface must firstly be chemically treated to provide reactive function groups (e.g., hydroxyl (–OH), amine (–NH₂), carboxyl (–COOH), etc.) for the subsequent immobilization steps. These surface functional groups can be generated by oxidation, hydrolysis, and radiation. After the surface pretreatment, polymer immobilization on nanoparticles by covalent coupling can be performed through peptide, ester or other bond formation. Scheme 19.1 illustrates some examples of covalent surface modification. For example, the hydroxyl end-capped group can react with aminosilane, trisylchloride, cyanogen bromide or p-nitrophenyl chloroformate to form an active intermediate. Thionyl chloride, phosgene, butanediol, or bis(2,5-dioxopyrrolidin-1-yl) carbonate can be used to prepare active intermediates with an end-capped amine group. For the carboxyl group, the active intermediate can be synthesized with thionyl chloride or N-hydroxysuccinimide. The immobilization of polymer on nanoparticles can then be performed by appropriate specific reaction with the active intermediate.

19.4 Surface-Modified Nano-Biosensors

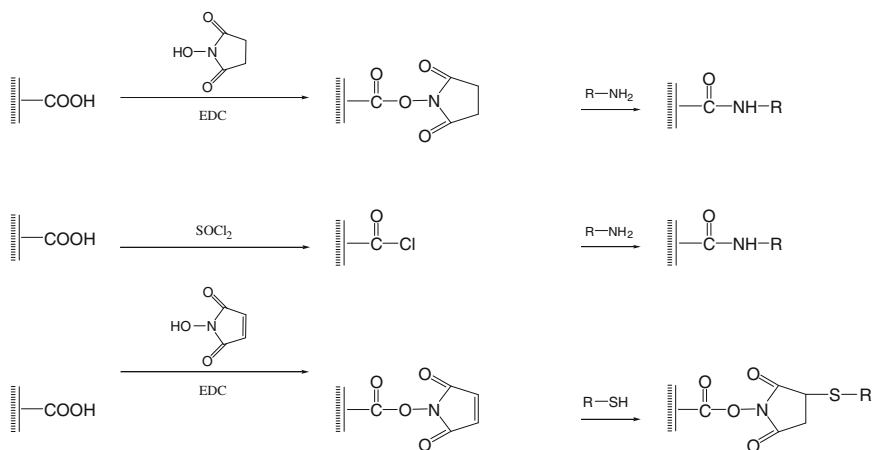
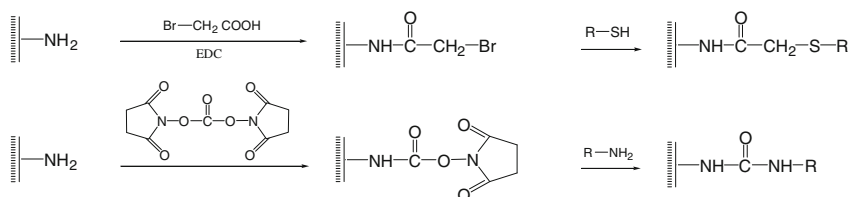
19.4.1 Surface-Modified Gold Nanoparticle-Based Colorimetric Biosensing

Over the past several decades, the modulation of Au nanomaterials through dispersion-aggregation conversion process has been developed as a colorimetric sensing platform for rapid and cost-effective bioanalysis and environmental monitoring. Spherical Au nanoparticles exerted localized SPR absorption [67]. For example, 13-nm-sized Au nanoparticles have strong and single SPR peak at

Activation of -OH



Activation of -COOH

Activation of -NH₂**Scheme 19.1** Covalent surface modification of solid nanoparticles

520 nm with high extinction coefficient ($2.7 \times 10^8 \text{ M}^{-1} \text{ cm}^{-1}$). The dispersed colloidal solution of Au nanoparticles has a red color with over 100 time greater intensity than most organic dyes. In the presence of specific analyte molecules of interest, the Au nanoparticles could aggregate and the red color converts to purple due to shifting of SPR band maximum to longer wavelength [67, 68].

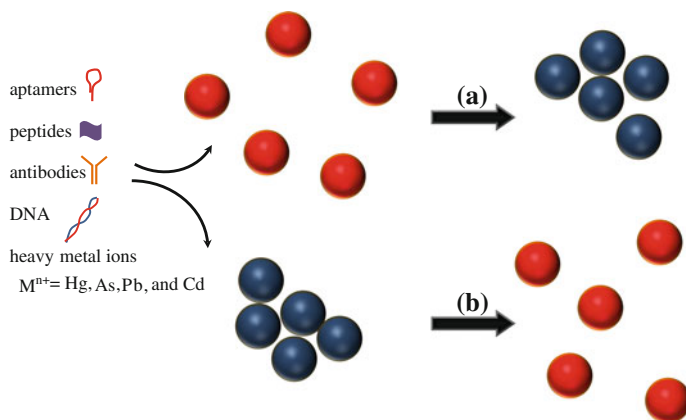


Fig. 19.2 Schematic illustration of analytes sensing principle based on the **a** light-on (Au aggregation), and **b** light-off (Au dispersion) strategies by manipulating the degree of dispersion-aggregation conversion of the Au nanoparticles in the presence of different analytes

The degree of dispersion and/or aggregation process of the Au nanomaterials can be successfully manipulated by using similar or different sizes and/or shapes of Au nanoparticles in the form of nanospheres, nanorods, and nanosphere/nanorod mixtures which self-assemble in the presence of analyte molecules (Fig. 19.2) [69–78]. For this reason, specific analyte molecules could be determined by different colors resulted from this manipulation. In 1997, Mirkin and co-workers firstly reported the detection of specific polynucleotides through the hybridization of their Au nanoparticle derivatives with known-sequence DNA-modified Au nanoparticles [71]. The Thiol (–SH) functional groups on the polynucleotides have good affinity to immobilize on the Au nanoparticle surfaces by the formation of Au–S bonds. A significant color change from red to blue-purple was found when the polynucleotides hybridize with the known-sequence DNA molecules. The color change was reversible if the surrounding temperature was increased to the melting temperature of the polynucleotide-DNA hybrid. This method is more sensitive compared with the traditional one based on the DNA absorption intensity changes at 260 nm.

The detection of low concentration prostate-specific antigen (PSA) in sera is a very important issue for early diagnosis of breast cancer. After many continuous research works, the same group developed an ultrasensitive test for PSA by means of a bio-bar-code assay using a similar Au colorimetric nanotechnology [71, 72]. This PSA-capture assay was designed through the hybridization of oligonucleotide-coated Au nanoparticles, PSA, and anti-PSA monoclonal antibody-functionalized iron oxide microbeads, leading to the formation of sandwich structured complex and resulted in SPR red shift. This method allowed the detection of PSA at a concentration as low as 30 aM.

Many other different strategies for the selective detections of aptamers [73, 74], peptides [75, 76], antibodies [77, 78], and DNA molecules [79, 80] have also been reported. On the other hand, DNA modifications on the surfaces of Au nanoparticles have been used most successfully for the determination of nucleic acids, drugs, various biomolecules, and heavy metal ions. In particular, when coupled with enzymatic reactions, many substrates could be determined at relatively low concentrations [69, 72, 79–86].

It is noted that the above-mentioned DNA-based nano-assemblies not only can be used for real-time analyses and biomonitoring, they can also be fabricated for the preparation of complicated nanostructures. These novel nanomaterials could further be applied for multimodal optical analyses and to improve detection limits, sensitivity, and selectivity. For example, a satellite-like nanostructure was prepared by the DNA template-assisted assembly of 8 nm GNPs on the surfaces of 31 nm GNPs [87]. This allowed the coupling of the SPR bands of different sized Au nanoparticles and resulted in a band broadening and red shift from 524 to 543 nm. As another example, Irudayaraj and co-workers reported an aptamer–protein-binding strategy to generate Au nanorod–Au nanoparticle junctions. The resulted close packings gave rise to enhanced surface Raman scattering and allowed highly sensitive detection of proteins [88].

In a different approach, Su et al. were able to determine estrogen receptor α (ER α , a transcription factor) by allowing it to react with a double-stranded DNA (dsDNA) conjugated Au nanoparticles [89]. Two groups of Au nanoparticles were prepared, and one group is modified with oligonucleotides that are capable of interacting with ER α , the other with the complimentary oligonucleotides. In the absence of ER α , the two groups of Au nanoparticles form various aggregates showing blue color. However, in the presence of ER α , the strong binding between the oligonucleotides and ER α destroys the aggregates and results in a red color.

A method for the determination of ascorbic acid without nanoparticle modification was reported by Chen et al. utilizing mesoporous silica-coated Au nanorods (Au@SiO₂ nanorods) [90]. By adding AgNO₃ into the solution of Au@SiO₂ nanorods and ascorbic acid, the Ag⁺ ions were reduced to Ag atoms and deposited over the Au@SiO₂ surface causing the absorption band to blue-shift. The amount of blue-shifted wavelength varies with ascorbic acid concentration in the linear range 0.1–2.5 μ m, and a detection limit of 49 nM could be achieved. This method was quite selective for ascorbic acid with little interferences by other species, such as urea, oxalic acid, citrate acid, glycine, and cysteine. It is also comparable with other currently used methods via fluorometric, electrochemical, chemiluminescence, and chromatographic techniques; however, the latter required expensive instruments.

The US Environmental Protection Agency and World Health Organization have defined a guideline for acceptable concentrations as low as in the ppb level for several heavy metal ions in drinking water. Plasmonic Au nanoparticles integrated with different surface functional molecules have been developed to recognize specific heavy metal ions and used as colorimetric nanosensors which are highly sensitive even in the nM or ppb concentration level. For examples, a number of

biomolecules such as glutathione [91], gallic acid [92], peptide [93], DNAzyme [94], and DNA [95] have been employed on the surface of Au nanoparticles to track lead ions based on metal–ligand chelation reactions. Specifically, glutathione and gallic acid-modified Au nanoparticles could be used to determine Pb^{2+} ion down to 4.8 pM and 10 nM, respectively. In another case, Pb^{2+} ion could be determined, when it is present with a highly Pb^{2+} -specific DNAzyme to cleave its recognized substrate strands at the ribonucleic acid adenosine (rA) sites in a self-assembly of Au nanoparticles by dsDNA hybridization [94]. As a result, the initial purple DNA-mediated Au nanoparticles assembly turned to free-standing ones in red. The detection limit for the Pb^{2+} ion was 100 nM.

The Flg-A3 peptide (-Asp-Tyr-Lys-Asp-Asp-Asp-Asp-Lys-Pro-Ala-Tyr-Ser-Ser-Gly-Pro-Ala-Pro-Pro-Met-Pro-Pro-Phe-) has been found to exhibit optical signatures when functionalized on gold nanoparticles (PFNs) and interacts with various metal ions [96]. The PFNs without metal ions has a SPR peak maximum at 524 nm, upon binding metal ions it shifts to 593 nm for Co^{2+} , 580 nm for Hg^{2+} , 614 nm for Pb^{2+} , 617 nm for Pd^{2+} , 542 nm for Pt^{2+} at various metal ion concentrations from 23 to 242 nM. This peptide might be applicable for rapid and selective multiple metal ion determinations.

19.4.2 Carbon and Magnetic Nanomaterials for H_2O_2 -Based Colorimetric Sensor

Carbon-based nanotubes, nanodots, and graphene can catalyze the redox reaction between H_2O_2 and 3,3',5,5'-tetramethylbenzidine (TMB) and convert the colorless TMB into a deep blue diimine product. Because H_2O_2 is an intermediate of glucose oxidation by O_2 , the combined reaction in the presence of glucose oxidase could be applied for a sensitive and selective colorimetric determination of blood glucose with a linear range of 0.001–0.50 mM [97–99]. Dong and co-workers reported that further modification of the graphene nanosheets through the π - π interactions with hemin (iron protoporphyrin) resulted in much higher peroxidase-like activity, and therefore, lower detection limit which was ascribed to the presence of Fe(II) ion in the protoporphyrin [100]. It is interesting to note that the classical Fenton reagent (i.e., Fe(II)- H_2O_2) has a similar redox process leading to the decomposition of H_2O_2 to water molecule and hydroxyl radical [101, 102]. Unfortunately, free Fe(II) ions in solution are disadvantageous for applications in normal physiological environment because they are stable only at low pH conditions. Recently, Yan et al. discovered that 30 nm-sized Fe_3O_4 nanoparticles can function in neutral solutions with a peroxidase-like activity which could be used to determine H_2O_2 with a sensitivity 40 times better than that by using conventional horseradish peroxidase catalyzed reaction method [103]. Other iron oxides [e.g., haematite (α - Fe_2O_3), maghemite (γ - Fe_2O_3), wüstite (FeO), magnetite (Fe_3O_4), and amorphous iron oxide] [103–105] and manganese oxides [106] were also

investigated in this heterogeneous catalytic reaction of H_2O_2 and TMB for colorimetric H_2O_2 biosensing. Liao et al. reported that the poly(allylamine hydrochloride) coated $\text{Mn}_x\text{Fe}_{3-x}\text{O}_4$ (e.g., $x = 1.4$ or 2.5) nanomaterial accelerated the H_2O_2 decomposition reaction, however, the mechanism of which remained to be explored in detail [107].

19.5 Nano-Therapeutics

Nanoparticles have been tested as *in vivo* diagnostics and to treat various diseases particularly cancer. It is known that cancer is one of the most serious diseases worldwide and constitutes one-fourth of the death rate. The traditional ways such as radiation, chemotherapy and surgery for cancer therapy have their inherited problems including lack of specificity, drug resistance, and many side effects. Within the last decade, several targeted drugs including small molecules and antibodies have been developed which successfully improve cancer treatment with reduced side effects. These drugs were designed based on either overexpressed biomarkers by cancerous cells [108] or enhanced permeability of cancer tissues and retention of macromolecules by EPR [109, 110]. For example, the drug substances of Iressa and Tarceva are small molecules targeting epidermal growth factor receptor (EGFR), and Avastin and Erbitux are antibodies targeting vascular endothelial growth factor receptor (VEGFR) and EGFR, respectively. However, these drugs are cytostatic and tumors can still develop drug resistance and escape from treatment via different cancer hallmarks. Thus, other highly specific cancer treatments with fewer side effects are still in needs. Both hyperthermia and photodynamic therapy (PDT) involving the use of therapeutic nanoparticles are briefly discussed below.

19.5.1 Hyperthermia

19.5.1.1 Photothermal Therapy

Photothermal therapy employs visible or infrared (IR) light to illuminate skin tissues and produce heat to kill cancer cells due to their inferior heat tolerance as compared to normal cells. Because of the shallow penetration depth of the visible and IR light, photothermal therapy has been applied mainly to treat cancers on skin surface. However, recent study indicates that the composite material with Au nanoparticles coating on the surface of a magnetic core of iron oxide (Fe_3O_4) can be used to absorb deeper-penetrating near IR (NIR) light and overcome the shallow penetration problem [111]. If these superparamagnetic nano-probes are linked with targeting ligands, the targeted cells could be separated and purified in the presence of a magnetic field selectively.

19.5.1.2 Magnetic Hyperthermia

SPIONs could be targeted to tumor cells through surface modification with specific cancer cell markers and generate heat in the presence of an alternating magnetic field (i.e., electromagnetic heating) to kill cancer cells [112]. A recent study showed that 15 nm magnetic nanoparticles could be targeted to head and neck tumor cells in an animal mode and heated in a 7T alternating magnetic field for 5–10 min to 40 °C to kill cancerous cells and reduce tumor volume as well as increase survival rate [113].

19.5.2 Photodynamic Therapy

PDT uses non-toxic photosensitizers and non-ionizing radiation to generate reactive oxygen species (ROS) such as free radicals or the cytotoxic singlet oxygen and kill tumor cells by inducing apoptosis and necrosis [114]. Current clinical applications of photodynamic therapy are mainly for the treatment of acne, psoriasis, and skin melanoma and are limited by shallow penetration depth of tissue, in addition to the lack of specificity for tumor targeting of photosensitizer used.

19.5.2.1 Photodynamic Therapy Using Upconversion Nanoparticles

Newly developed upconversion nanoparticles (UCNPs) can absorb long wavelength light (e.g., near infrared light) and emit short wavelength light (e.g., visible light) [115]. These UCNPs are chemically quite stable and unlike those organic fluorescent dyes, they normally do not have photobleach. If lanthanide elements are involved, their fluorescence properties are not affected by local biological or chemical environment. The advantages of using these UCNPs for in vitro (cell) and in vivo (animal) imaging and therapeutic studies are their abilities to avoid the interferences of auto-fluorescence by other biomolecules and to obtain signals with high signal-to-noise ratio. Particularly, if cancer biomarker–modified UCNPs are excited by NIR light (wavelength range 700–1,000 nm), their penetration depths could be increased without tissue re-absorption and scattering [116]. In addition, these UCNPs could be easily surface modified with polymers, photosensitizers and targeting molecules to form bioconjugates for tumor treatment. For example, 20 nm NaYF₄:Yb,Er nanoparticles can be synthesized by a thermal decomposition method and surface modified with folic acid and a photosensitizer. Irradiation with 980 nm NIR light on tumor cells in situ as well as in animal models containing these UCNPs could effectively kill tumor cells [117, 118]. Comparisons of direct irradiation with 660 nm laser light and indirect upconversion irradiation at 980 nm employing UCNPs-Zinc(II) phthalocyanine (ZnPc) showed 77 and 66 % suppression of tumor growth, respectively. However, if a piece of 1-cm-thick tissue is placed on top of the tumor cells, the respective suppression rates reduced to 18 and 50 %. This

evidence clearly demonstrated that PDT with UCNP photosensitive nanocomposites could penetrate deeper into the tumor tissues and is potentially more efficacious in cancer treatment as compared to traditional PDT treatment [119].

19.5.2.2 X-ray-Induced Photodynamic Therapy

Another possible way to solve the penetration depth problem in PDT is to use an excitation source such as X-ray with greater penetration depth and appropriate photosensitizers. In this regard, scintillator materials that have been used widely in computed tomography as scintillator phosphors panel materials could be used to convert X-ray into visible or NIR light [120]. If nanoscintillator materials can be prepared with low toxicity and easily modified with biomarkers and photosensitizers, these materials might be promising for use in X-ray-induced PDT. Indeed, a photosensitive nanocomposite comprising 12 nm Y_2O_3 nanoscintillator bioconjugated with psoralen can be excited by X-ray and emits 370 nm UV light to kill tumor cells *in vitro* more effectively than using Y_2O_3 alone [121].

19.6 Conclusion and Future Perspective

The field of nanotechnology has become increasingly complex from an interdisciplinary point of view, including chemistry, physics, materials, life and medical sciences. During the last decade, the development of nanotechnology together with many groundbreaking research results in genomics, proteomics and stem cell biology provide many novel and effective solutions and possibilities for medical theranostic applications. New synthetic methodologies to prepare nanomaterials with various sizes, shapes, chemical, physical, surface, and biological properties will continue to be discovered, including composites and polymer-coated nanomaterials. These are required because, for example, for *in vivo* biomedical applications the nanomaterials must be biocompatible with adjustable blood circulation time, better selectivity, safety and efficacy for disease diagnosis and therapy.

For *in vitro* applications, several biosensor and assay systems by using optical methods with gold, carbon, and magnetic nanomaterials have been demonstrated for the determination of a variety of biomolecules with better selectivity and detection limits. However, their practical applications await real samples to be tested such as those in complex environment, blood and intracellular matrices with significant interferences. Adequate formulations to preserve colloidal stabilities for these nanomaterial products are also needed. On the other hand, nanomaterials modified with hydrophilic polymers, appropriate photosensitizers and targeting biomarkers have been proven useful in animal disease model studies, which are potential drug substance candidates to improve treatment efficacy for photodynamic therapy with NIR and/or X-ray irradiation and hyperthermia in alternating magnetic field against deep tumor tissues.

Last but not least, to make use of all the innovative ideas and demonstrative prove-of-principles of nanomaterials for both in vitro and in vivo practical biomedical applications, it is absolutely necessary to emphasize and expand efforts on their translational research and development, including preclinical and clinical studies, chemistry, materials and control (CMC) and large-scale manufacturing of these novel engineered nanomaterials. Needless to say, the impact of nanomaterials on long term human health, environment and ecology must also be seriously investigated in an integrated and interdisciplinary approach.

Acknowledgments We would like to thank the National Science Council (grant no. NSC 101-2627-E-010-001 and NSC 101-2113-M-010-002-MY2) and the Ministry of Education of Taiwan for financial support of the integrated research in the nanotechnology and biomedical science and engineering areas.

References

1. Patra CR, Bhattacharya R, Mukhopadhyay D, Mukherjee P (2010) Fabrication of gold nanoparticles for targeted therapy in pancreatic cancer. *Adv Drug Deliv Rev* 62(3):346–361
2. Nguyen DT, Kim D-J, Kim K-S (2011) Controlled synthesis and biomolecular probe application of gold nanoparticles. *Micron* 42(3):207–227
3. Zhao P, Li N, Astruc D (2013) State of the art in gold nanoparticle synthesis. *Coord Chem Rev* 257(3):638–665
4. Ghosh P, Han G, De M, Kim CK, Rotello VM (2008) Gold nanoparticles in delivery applications. *Adv Drug Deliv Rev* 60(11):1307–1315
5. Murphy CJ, Thompson LB, Chernak DJ, Yang JA, Sivapalan ST, Boulos SP et al (2011) Gold nanorod crystal growth: from seed-mediated synthesis to nanoscale sculpting. *Curr Opin Colloid Interface Sci* 16(2):128–134
6. Lu F, Doane TL, Zhu J-J, Burda C (2012) Gold nanoparticles for diagnostic sensing and therapy. *Inorg Chim Acta* 393:142–153
7. Lu W, Huang Q, Ku G, Wen X, Zhou M, Guzatov D et al (2010) Photoacoustic imaging of living mouse brain vasculature using hollow gold nanospheres. *Biomaterials* 31(9):2617–2626
8. Patra CR, Bhattacharya R, Mukhopadhyay D, Mukherjee P (2010) Fabrication of gold nanoparticles for targeted therapy in pancreatic cancer. *Adv Drug Deliv Rev* 62(3):346–361
9. Pérez-Juste J, Pastoriza-Santos I, Liz-Marzán LM, Mulvaney P (2005) Gold nanorods: Synthesis, characterization and applications. *Coord Chem Rev* 249(17–18):1870–1901
10. Orendorff CJ, Gearheart L, Jana NR, Murphy CJ (2006) Aspect ratio dependence on surface enhanced Raman scattering using silver and gold nanorod substrates. *Phys Chem Chem Phys* 8(1):165–170
11. Nikoobakht B, Burda C, Braun M, Hun M, El-Sayed MA (2002) The quenching of CdSe quantum dots photoluminescence by gold nanoparticles in solution. *Photochem Photobiol* 75(6):591–597
12. Meng XK, Tang SC, Vongehr S (2010) A review on diverse silver nanostructures. *J Mater Sci Tech* 26(6):487–522
13. Kalishwaralal K, BarathManiKanth S, Pandian SRK, Deepak V, Gurunathan S (2010) Silver nano—a trove for retinal therapies. *J Controlled Release* 145(2):76–90
14. Besinis A, Peralta TD, Handy RD (2012) The antibacterial effects of silver, titanium dioxide and silica dioxide nanoparticles compared to the dental disinfectant chlorhexidine on *Streptococcus mutans* using a suite of bioassays. *Nanotoxicology* Nov 15. (Epub ahead of print)

15. Drbohlavova J, Adam V, Kizek R, Hubalek J (2009) Quantum dots—characterization, preparation and usage in biological systems. *Int Mol Sci* 10(2):656–673
16. Byers RJ, Hitchman ER (2011) Quantum dots brighten biological imaging. *Prog Histochem Cytochem* 45(4):201–237
17. Durgadas CV, Sreenivasan K, Sharma CP (2012) Bright blue emitting CuSe/ZnSe/silica core/shell/shell quantum dots and their biocompatibility. *Biomaterials* 33(27):6420–6429
18. Peng ZA, Peng X (2001) Formation of high-quality CdTe, CdSe, and CdS nanocrystals using CdO as precursor. *J Am Chem Soc* 123(1):183–184
19. Aldana J, Wang YA, Peng X (2001) Photochemical instability of CdSe nanocrystals coated by hydrophilic thiols. *J Am Chem Soc* 123(36):8844–8850
20. Weng J, Song X, Li L, Qian H, Chen K, Xu X et al (2006) Highly luminescent CdTe quantum dots prepared in aqueous phase as an alternative fluorescent probe for cell imaging. *Talanta* 70(2):397–402
21. Yu WW (2008) Semiconductor quantum dots: synthesis and water-solubilization for biomedical applications. *Expert Opin Biol Ther* 8(10):1571–1581
22. Mahmoudi M, Sant S, Wang B, Laurent S, Sen T (2011) Superparamagnetic iron oxide nanoparticles (SPIOs): Development, surface modification and applications in chemotherapy. *Adv Drug Deliv Rev* 63(1–2):24–46
23. Gupta AK, Gupta M (2005) Synthesis and surface engineering of iron oxide nanoparticles for biomedical applications. *Biomaterials* 26(18):3995–4021
24. Mandel K, Hutter F, Gellermann C, Sendl G (2011) Synthesis and stabilisation of superparamagnetic iron oxide nanoparticle dispersions. *Colloids Surf A* 390(1–3):173–178
25. Dorozhkin SV (2010) Nanosized and nanocrystalline calcium orthophosphates. *Acta Biomater* 6(3):715–734
26. Liu TY, Chen SY, Liu DM, Liou SC (2005) On the study of BSA-loaded calcium-deficient hydroxyapatite nano-carriers for controlled drug delivery. *J Controlled Release* 107(1):112–121
27. Liu TY, Chen SY, Liu DM (2004) Influence of the aspect ratio of bioactive nanofillers on rheological behavior of PMMA-based orthopedic materials. *J Biomed Mater Res B Appl Biomater* 71(1):116–122
28. Alves Cardoso D, Jansen JA, Leeuwenburgh SC (2012) Synthesis and application of nanostructured calcium phosphate ceramics for bone regeneration. *J Biomed Mater Res B Appl Biomater* 100(8):2316–2326
29. Liu DM, Troczynski T, Tseng WJ (2001) Water-based sol gel synthesis of hydroxyapatite: process development. *Biomaterials* 22(13):1721–1730
30. Liu TY, Chen SY, Li JH, Liu DM (2006) Study on drug release behaviour of CDHA/chitosan nanocomposites—effect of CDHA nanoparticles. *J Controlled Release* 112(1):88–95
31. Nishiyama N, Kataoka K (2006) Nanostructured devices based on block copolymer assemblies for drug delivery: designing structures for enhanced drug function. *Adv Polym Sci* 193:67–101
32. Dunn SE, Brindley A, Davis SS, Davies MC, Illum L (1994) The effect of PEG surface density on the in vitro cell interaction and in vitro biodistribution. *Pharm Res* 11:1016–1022
33. Stolnik S, Illum L, Davis SS (1995) Long circulating microparticulate drug carriers. *Adv Drug Deliv Rev* 16:195–214
34. Mosquera VCF, Legrand P, Gulik A, Bourdon O, Gref R, Labarre D, Barratt G (2001) Relationship between complement activation, cellular uptake and surface physicochemical aspects of novel PEG-modified nanocapsules. *Biomaterials* 22:2967–2979
35. Aggarwal P, Hall JB, McLeland CB, Dobrovolskaia MA, McNeil SE (2009) Nanoparticles interaction with plasma proteins as it relates to particle biodistribution, biocompatibility and therapeutic efficacy. *Adv Drug Deliv Rev* 61:428–437
36. Alexis F, Prud'homme E, Molnar LK, Farokhzad OC (2008) Factors affecting the clearance and biodistribution of polymeric nanoparticles. *Mol Pharmacol* 5:505–515
37. Geng Y, Dalhaimer P, Cai S, Tsai R, Tewari M, Minko T, Discher DE (2007) Shape effects of filaments versus spherical particles in flow and drug delivery. *Nat Nanotech* 2:249–255

38. Akiyama Y, Mori T, Katayama Y, Niidome T (2009) The effects of PEG grafting level and injection dose on gold nanorod biodistribution in the tumor-bearing mice. *J Controlled Release* 139:81–84
39. Zhang G, Yang Z, Lu W, Zhang R, Huang Q, Tian M, Li L, Liang D, Li C (2009) Influence of anchoring ligands and particle size on the colloidal stability and in vivo biodistribution of polyethylene glycol-coated gold nanoparticles in tumor-xenografted mice. *Biomaterials* 30:1928–1936
40. Matsumura Y, Maeda H (1986) A new concept for macromolecular therapeutics in cancer chemotherapy: mechanism of tumorotropic accumulation of proteins and the antitumor agent smancs. *Cancer Res* 46:6387–6392
41. Maeda H (2001) SMANCS and polymer-conjugated macromolecular drugs: advantages in cancer chemotherapy. *Adv Drug Deliv Rev* 46:169–185
42. Hobbs SK, Monsky WL, Yuan F, Gregory Roberts W, Griffith L, Torchilin VP, Jain RK (1998) Regulation of transport pathways in tumor vessels: role of tumor type and microenvironment. *Proc Natl Acad Sci USA* 95:4607–4612
43. Perrault SD, Walkey C, Jennings T, Fischer HC, Chan WCW (2009) Mediating tumor targeting efficiency of nanoparticles through design. *Nano Lett* 9:1909–1915
44. Gao H, Shi W, Freund LB (2005) Mechanics of receptor-mediated endocytosis. *Proc Natl Acad Sci USA* 102:9469–9474
45. Bao G, Bao XR (2005) Shedding light on the dynamics of endocytosis and viral budding. *Proc Natl Acad Sci USA* 102:9997–9998
46. Chithrani BD, Ghazani AA, Chan WCW (2006) Determining the size and shape dependence of gold nanoparticle uptake into mammalian cells. *Nano Lett* 6:662–668
47. Chithrani BD, Chan WCW (2007) Elucidating the mechanism of cellular uptake and removal of protein-coated gold nanoparticles of different sizes and shapes. *Nano Lett* 7:1542–1550
48. Jiang W, Kim BYS, Rutka JT, Chan WCW (2008) Nanoparticle-mediated cellular response is size-dependent. *Nat Nanotech* 3:145–150
49. Harush-Frenkel O, Debotton N, Benita S, Altschuler Y (2007) Targeting of nanoparticles to the clathrin-mediated endocytic pathway. *Biochem Biophys Res Commun* 353:26–32
50. Zhang LW, Monteiro-Riviere NA (2009) Mechanisms of quantum dot nanoparticle cellular uptake. *Toxicol Sci* 110:138–155
51. De Jong WH, Hagens WI, Krystek P, Burger MC, Sips AJAM, Geertsma RE (2008) Particles size-dependent organ distribution of gold nanoparticles after intravenous administration. *Biomaterials* 29:1912–1919
52. Lipka J, Semmler-Behnke M, Sperling RA, Wenk A, Takenaka S, Schleh C, Kissel T, Parak WJ, Kreyling WG (2010) Biodistribution of PEG-modified gold nanoparticles following intratracheal instillation and intravenous injection. *Biomaterials* 31:6574–6581
53. Liu Z, Cai W, He L, Nakayama N, Chen K, Sun X, Chen X, Dai H (2007) In vivo biodistribution and highly efficient tumour targeting of carbon nanotubes in mice. *Nat Nanotechnol* 2:47–52
54. DeNardo SJ, DeNardo GL, Natarajan A, Miers LA, Foreman AR, Gruettner C, Adamson GN, Ivkov R (2007) Thermal dosimetry predictive of efficacy of ¹¹¹In-ChL6 nanoparticle AMF-induced thermoablative therapy for human breast cancer in mice. *J Nucl Med* 48:437–444
55. Derfus AM, Chan WCW, Bhatia SN (2004) Probing the cytotoxicity of semiconductor quantum dots. *Nano Lett* 4:11–18
56. Gupta AK, Gupta M (2005) Cytotoxicity suppression and cellular uptake enhancement of surface modified magnetic nanoparticles. *Biomaterials* 26:1565–1573
57. Paul KG, Frigo TB, Groman JY, Groman EV (2004) Synthesis of ultrasmall superparamagnetic iron oxides using reduced polysaccharides. *Bioconjug Chem* 15:394–401
58. Tiefenauer LX, Tschirky A, Kühne G, Andres RY (1996) In vivo evaluation of magnetite nanoparticles for use as a tumor contrast agent in MRI. *Magn Reson Imaging* 14:391–402

59. Moghimi SM, Hunter AC, Murray JC (2001) Long-circulating and target-specific nanoparticles: theory to practice. *Pharmacol Rev* 53:283–318
60. Massia SP, Stark J, Letbetter DS (2000) Surface-immobilized dextran limits cell adhesion and spreading. *Biomaterials* 21:2253–2261
61. Jia Z, Yujun W, Yangcheng L, Jingyu M, Guangsheng L (2006) In situ preparation of magnetic chitosan/Fe₃O₄ composite nanoparticles in tiny pools of water-in-oil microemulsion. *React Funct Polym* 66:1552–1558
62. Sipos P, Berkesi O, Tombacz E, St. Pierre TG, Webb J (2003) Formation of spherical iron(III) oxyhydroxide nanoparticles sterically stabilized by chitosan in aqueous solutions. *J Inorg Biochem* 95:55–63
63. Tan WB, Zhang Y (2005) Multifunctional quantum-dot-based magnetic chitosan nanobeads. *Adv Mater* 17:2375–2380
64. Star A, Han TR, Gabriel JCP, Bradley K, Gruner G (2003) Interaction of aromatic compounds with carbon nanotubes: correlation to the Hammett parameter of the substituent and measured carbon nanotube FET response. *Nano Lett* 3:1421–1423
65. Lin Z, Cui S, Zhang H, Chen Q, Yang B, Su X, Zhang J, Jin Q (2003) Studies on quantum dots synthesized in aqueous solution for biological labeling via electrostatic interaction. *Anal Biochem* 319:239–243
66. Schaaff TG, Knight G, Shafiqullin MN, Borkman RF, Whetten RL (1998) Isolation and selected properties of a 10.4 kDa gold: glutathione cluster compound. *J Phys Chem B* 102:10643–10646
67. Ghosh SK, Pal T (2007) Interparticle Coupling Effect on the Surface Plasmon Resonance of Gold Nanoparticles: From Theory to Applications. *Chem Rev* 107:4797–4862
68. Daniel MC, Astruc D (2004) Gold nanoparticles: assembly, supramolecular chemistry, quantum-size-related properties, and applications toward biology, catalysis, and nanotechnology. *Chem Rev* 104:293–346
69. Elghanian R, Storhoff JJ, Mucic RC et al (1997) Selective colorimetric detection of polynucleotides based on the distance-dependent optical properties of gold nanoparticles. *Science* 277:1078–1081
70. Storhoff JJ, Elghanian R, Mucic RC et al (1998) One-pot colorimetric differentiation of polynucleotides with single base imperfections using gold nanoparticle probes. *J Am Chem Soc* 120:1959–1964
71. Nam JM, Thaxton CS, Mirkin CA (2003) Nanoparticle-based bio-bar codes for the ultrasensitive detection of proteins. *Science* 301:1884–1886
72. Stoeva SI, Lee JS, Smith JE et al (2006) Multiplexed detection of protein cancer markers with biobarcode nanoparticle probes. *J Am Chem Soc* 128:8378–8379
73. Chen SJ, Huang YF, Huang CC et al (2008) Colorimetric determination of urinary adenosine using aptamer-modified gold nanoparticles. *Biosens Bioelectron* 23:1749–1753
74. Huang CC, Huang YF, Cao ZT et al (2005) Aptamer-modified gold nanoparticles for colorimetric determination of platelet-derived growth factors and their receptors. *Anal Chem* 77:5735–5741
75. Aili D, Selegard R, Baltzer L et al (2009) Colorimetric protein sensing by controlled assembly of gold nanoparticles functionalized with synthetic receptors. *Small* 5:2445–24512
76. Guarise C, Pasquato L, Filippis V et al (2006) Gold nanoparticles-based protease assay. *Proc Natl Acad Sci USA* 103:3978–3982
77. Hirsch LR, Jackson JB, Lee A et al (2003) A whole blood immunoassay using gold nanoshells. *Anal Chem* 75:2377–2381
78. Liu X, Dai Q, Austin L et al (2008) A one-step homogeneous immunoassay for cancer biomarker detection using gold nanoparticle probes coupled with dynamic light scattering. *J Am Chem Soc* 130:2780–2782
79. Thompson DG, Enright A, Faulds K et al (2008) Ultrasensitive DNA detection using oligonucleotide – silver nanoparticle conjugates. *Anal Chem* 80:2805–2810

80. Liu SH, Zhang ZH, Han MY et al (2005) Gram-scale synthesis and biofunctionalization of silica-coated silver nanoparticles for fast colorimetric DNA detection. *Anal Chem* 77:2595–2600
81. Zhao W, Brook MA (2008) Design of gold nanoparticle-based colorimetric biosensing assays. *Chem Bio Chem* 9:2363–2371
82. Lee JS, Ulmann PA, Han MS et al (2008) A DNA-gold nanoparticle-based colorimetric competition assay for the detection of cysteine. *Nano Lett* 8:529–533
83. Hurst SJ, Han MS, Lytton-Jean AKR et al (2007) Screening the sequence selectivity of DNA-binding molecules using a gold nanoparticle-based colorimetric approach. *Anal Chem* 79:7201–7205
84. Han MS, Lytton-Jean AKR, Oh BK et al (2006) Colorimetric screening of DNA-binding molecules with gold nanoparticle probes. *Angew Chem Int Ed* 45:1807–1810
85. Lee JS, Han MS, Mirkin CA (2007) Colorimetric detection of mercuric ion (Hg_2^+) in aqueous media using DNA-functionalized gold nanoparticles. *Angew Chem Int Ed* 46:4093–4096
86. Xu X, Han MS, Mirkin CA (2007) A gold-nanoparticle-based real-time colorimetric screening method for endonuclease activity and inhibition. *Angew Chem Int Ed* 46:3468–3470
87. Mucic RC, Storhoff JJ, Mirkin DA (1998) DNA-directed synthesis of binary nanoparticle network materials. *J Am Chem Soc* 120:12674–12675
88. Wang Y, Lee K, Irudayaraj J (2010) SERS aptasensor from nanorod–nanoparticle junction for protein detection. *Chem Commun* 46:613–615
89. Tan YN, Su X, Zhu Y et al (2010) Sensing of transcription factor through controlled-assembly of metal nanoparticles modified with segmented DNA elements. *ACS Nano* 4:5101–5110
90. Wang G, Chen Z, Chen L (2011) Mesoporous silica-coated gold nanorods: towards sensitive colorimetric sensing of ascorbic acid via target-induced silver overcoating. *Nanoscale* 3:1756–1759
91. Chai F, Wang CG, Wang TT, Li L et al (2010) Colorimetric detection of Pb^{2+} using glutathione a functionalized gold nanoparticles. *ACS Appl Mater Interfaces* 2:1466–1470
92. Huang KW, Yu CJ, Tseng WL (2010) Sensitivity enhancement in the colorimetric detection of lead(II) ion using gallic acid–capped gold nanoparticles: Improving size distribution and minimizing interparticle. *Biosens Bioelectron* 25:984–989
93. Slocik JM, Zabinski JS, Phillips DM et al (2008) Colorimetric response of peptide-functionalized gold nanoparticles to metal ions. *Small* 4:548–551
94. Liu JW, Lu Y (2003) A colorimetric lead biosensor using DNAzyme-directed assembly of gold nanoparticles. *J Am Chem Soc* 125:6642–6643
95. Wang B, Zhu Q, Liaoa D (2011) Perylene probe induced gold nanoparticles aggregation. *J Mater Chem* 21:4821–4826
96. Slocik JM, Zabinski JS Jr, Phillips DM et al (2008) Colorimetric response of peptide-functionalized gold nanoparticles to metal ions. *Small* 4:548–551
97. Song Y, Qu K, Zhao C et al (2010) Molten salt synthesis and high rate performance of the “Desert-Rose” form of $LiCoO_2$. *Adv Mater* 22:2206–2210
98. Song Y, Wang X, Zhao C et al (2010) Label-free colorimetric detection of single nucleotide polymorphism by using single-walled carbon nanotube intrinsic peroxidase-like activity. *Chem Eur J* 16:3617–3621
99. Shi W, Wang Q, Long Y et al (2011) Carbon nanodots as peroxidase mimetics and their applications to glucose detection. *Chem Commun* 47:6695–6697
100. Guo Y, Deng L, Li J et al (2011) Hemin – graphene hybrid nanosheets with intrinsic peroxidase-like activity for label-free colorimetric detection of single-nucleotide polymorphism. *ACS Nano* 5:1282–1290
101. Giraldi TR, Arruda CC, Costa GMD et al (2009) Heterogeneous Fenton reactants: a study of the behavior of iron oxide nanoparticles obtained by the polymeric precursor method. *J Sol-Gel Sci Technol* 52:299–303

102. Gromboni CF, Kamogawa MY, Ferreira AG et al (2007) Microwave-assisted photo-Fenton decomposition of chlorfenvinphos and cypermethrin in residual water. *J Photochem Photobiol* 185:32–37
103. Gao L, Zhuang J, Nie L et al (2007) Intrinsic peroxidase-like activity of ferromagnetic nanoparticles. *Nat Nanotechnol* 2:577–583
104. Hermanek M, Hermankova P, Pechousek J (2010) Quasi-isothermal decomposition: a way to nanocrystalline mesoporous-like Fe₂O₃ catalyst for rapid heterogeneous decomposition of hydrogen peroxide. *J Mater Chem* 20:3709–3715
105. Huang HH, Lu MC, Chen JN (2001) Catalytic Decomposition of Hydrogen Peroxide and 2-chlorophenol with iron oxides. *Water Res* 35:2291–2299
106. Park JN, Shon JK, Jin M et al (2010) Highly ordered mesoporous α -Mn₂O₃ for catalytic decomposition of H₂O₂ at low temperatures. *Chem Lett* 39:493–495
107. Liao MY, Huang CC, Chang MC et al (2011) Synthesis of magnetic hollow nanotubes based on the Kirkendall effect for MR contrast agent and colorimetric hydrogen peroxide sensor. *J Mater Chem* 21:7974–7981
108. Wang RE, Niu Y, Wu H, Hu Y, Cai J (2012) Development of NGR-based anti-cancer agents for targeted therapeutics and imaging. *Anticancer Agents Med Chem* 2:76–86
109. Maeda H, Wu J, Sawa T, Matsumura Y, Hori K (2000) Tumor vascular permeability and the EPR effect in macromolecular therapeutics: a review. *J Controlled Release* 65:271–284
110. Bolhassani A, Safaiyari S, Rafati S (2011) Improvement of different vaccine delivery systems for cancer therapy. *Mol Cancer* 10:3
111. Fan Z et al (2012) Multifunctional plasmonic shell–magnetic core nanoparticles for targeted diagnostics, isolation, and photothermal destruction of tumor cells. *ACS Nano* 6(2):1065–1073
112. Hirsch LR et al (2003) Nanoshell-mediated near-infrared thermal therapy of tumors under magnetic resonance guidance. *Proc Natl Acad Sci USA* 100(23):13549–13554
113. Zhao Q, Wang L, Cheng R, Mao L, Arnold RD, Howerth EW, Chen ZG, Platt S (2012) Magnetic nanoparticle-based hyperthermia for head & neck cancer in mouse models. *Theranostics* 2(1):113–121
114. Babilas P, Schreml S, Landthaler M, Szeimies RM (2010) Photodynamic therapy in dermatology: state-of-the-art. *Photodermatol Photoimmunol Photomed* 26(3):118–132
115. Haase M, Schäfer H (2011) Upconverting nanoparticles. *Angew Chem Int Ed* 50(26):5808–5829
116. Wang LV, Wu HI (2007) *Biomedical optics*. Wiley
117. Liu K et al (2012) Covalently assembled NIR nanoplatfor for simultaneous fluorescence imaging and photodynamic therapy of cancer cells. *ACS Nano* 6(5):4054–4062
118. Idris NM et al (2012) In vivo photodynamic therapy using upconversion nanoparticles as remote-controlled nanotransducers. *Nat Med* 18(10):1580–1585
119. Cui S et al (2012) In vivo targeted deep-tissue photodynamic therapy based on near-infrared light triggered upconversion nanoconstruct. *ACS Nano* 7(1):676–688
120. Duclos SJ (1998) Scintillator phosphors for medical imaging. *Electrochem Soc Interface Summer* 34–38
121. Scaffidi JP et al (2011) Activity of psoralen-functionalized nanoscintillators against cancer cells upon X-ray excitation. *ACS Nano* 5(6):4679–4687

Chapter 20

Engineering Fluorescent Nanoparticles for Biomedical Applications

Oscar F. Silvestre and Xiaoyuan Chen

20.1 Introduction

Nanotechnology has been defined as the “intentional design, characterization, production, and applications of materials, structures, devices, and systems by controlling their size and shape in the nanoscale range (1–100 nm)” [1]. Furthermore, nanomedicine can be described as the medical application of nanotechnology for treatment, diagnosis, monitoring, and control of biological systems [2]; it is expected to result in important developments to enhance and improve human healthcare. Engineering nanoparticles (NPs) represents an important part of this field; these have been designed with different materials and architectures for a multitude of functions and to be detected with different imaging modalities [3–5]. Examples of relevant NP biomedical imaging modalities include: ultrasound, computed tomography (CT), magnetic resonance imaging (MRI), and positron emission tomography (PET), on the present chapter we are going to focus on fluorescent NPs.

Through this chapter, we are going to use the general term “fluorescence” to refer to the emission of light from a probe upon external excitation. Although in reality dependent on the material or transition phenomena, this may not be the absolute scientifically precise terminology, for example the electron–hole recombination in semiconductor quantum dots (QDs) should be correctly termed photoluminescence [6].

A search on the Thomson Reuters Web of Knowledge database for the term “fluorescence AND nanoparticles” returned approximately 12,457 recorded publications in the last 5 years. Adding the term “biomedical” reduced the results to around 514 records. This simple reveals the high number of studies related to this

O. F. Silvestre · X. Chen (✉)

Laboratory of Molecular Imaging and Nanomedicine (LOMIN), National Institute of Biomedical Imaging and Bioengineering (NIBIB), National Institutes of Health (NIH), Bethesda, MD 20892, USA
e-mail: shawn.chen@nih.gov

field. Most of the fluorescent NPs described applications were related to imaging technologies, with special emphasis on cancer research for *in vivo* imaging of tumors. Although NPs have been extensively used *in vitro* [7] and in biosensing detection systems [8], in this chapter, we are going to focus exclusively on their *in vivo* applications.

Fluorescent theranostics NPs represent a powerful new development; these NPs are designed with a therapy component to act as nanocarriers for drug delivery combined with the fluorescence component. This makes them capable of diagnosis, drug delivery, and monitoring of therapeutic response through optical imaging, these NPs were recently review [9–12].

Considering the extensively diversity of fluorescent NPs described in the literature and that a significant part of these studies claim that the studied NPs have “potential” biomedical or clinical use *in vivo*. In this chapter, we focus only on selected fluorescent NPs types, which are already on track or have been widely described to have substantial potential for clinical applications. The main emphasis of this chapter is in the translational relevance of the NPs for human use. The initial sections would provide an overview of some important NPs design parameters for their *in vivo* application and discuss the fluorescence imaging technology status in the clinic. In this chapter, we will mainly focus on three different types of fluorescent NPs: QDs, fluorescent dye-loaded inorganic and organic NPs. For each, we will briefly highlight their characteristics, advantages, limitations, and engineering strategies employed to enhance their *in vivo* use and describe some examples of preclinical studies. We will emphasize translational work and when applicable describe examples of NPs that were translated to human studies. Finally, we would provide a perspective of the fluorescent NPs advances needed for future human application.

20.2 Fluorescent Nanoparticles Parameters

Studies involving NPs, most of the time adhere to an overall pattern. Synthesized or constructed NPs with specific design properties (e.g., size, shape, internal and surface chemistry/coating) are evaluated using *in vitro* or more relevant *in vivo* biological systems. These studies draw correlations between NPs design variations and specific biological responses parameters (e.g., higher circulation time, enhanced tumor accumulation, increase in fluorescent signal) [13]. Some parameters are in general common to any type of NPs design, independent if is only a drug nanocarrier or includes an optical or magnetic detection, while other NPs properties are directly related to the imaging modality, which is relevant for this chapter fluorescence. A brief overview of some of those parameters is described next.

20.2.1 General Nanoparticle Design Parameters for In Vivo Applications

Several NPs properties such as size, shape, internal and surface chemistry/coating, architecture, conjugation with labels and/or therapeutics can be engineered to obtain desired biological responses on live animals relevant to their biomedical application, and these include the following.

20.2.1.1 Blood Circulation Time

This is an important parameter that is mainly affected by the NPs size, shape, and surface chemistry/coating. The intravenous injection of large NPs (above 200 nm) results in accumulation at the spleen and liver, while small NPs (less than 6 nm) can be eliminated quickly from the body [13, 14]. Rod-shaped NPs have been shown to increase circulation time up to ten times compared to spherical NPs [15]. Serum proteins are absorbed to the NPs after injection into circulation, and this dictates their biodistribution, clearance, and also toxicity [16]. Here, the external NP chemistry plays an important role, for example positive NPs absorb proteins that promote their quick removal by the reticuloendothelial system. A widespread strategy to increase biocompatibility is the coating of NPs with long-chain polymers (e.g., polyethylene glycol (PEG)). This prevents aggregation and cell interaction and decreases serum protein absorption, prolonging NPs blood circulation time [16].

20.2.1.2 Biodistribution and Tumor Delivery Efficiency

This is probably one of the most critical issues with any type of NPs in vivo. Normally, only a small fraction (1–10 %) of the injected NPs are actually delivered to the tumor [13]. So, it is imperative to maximize delivery/accumulation in the tumor and minimize NPs retention in other organs. The delivery mechanisms can be divided into passive delivery and active targeting, and this latter involves adding bimolecular ligands on the NPs coating with affinity to specific markers overexpressed on the target tissues or tumor cells, with the aim to enhance delivery. Passive delivery uses the enhanced permeation and retention (EPR) effect, where leakier tumor blood vessels combined with a poor lymphatic drainage, leads to the accumulation of NPs with long circulation time in the tumor site. Studies showed that by changing the size of the NPs, it was possible to control accumulation and penetration depth into the tumor [17]. Active targeting seems to change the NPs location in the tumor site and improves their cell internalization [18], but there are contradicting reports on how effective targeting is on promoting tumor accumulation [13, 18], and sometimes the extra nanoformulation complexity of the targeting may not be justified for clinical NPs [19]. Shape or even the

architecture of NPs seems to also play a role, recently chains of spherical connected active targeted NPs (~ 100 nm width) provided higher tumors detection due to enhanced contact with the blood vessels wall [20]. Also, an additional strategy would be to actually “normalize” the abnormal blood vessels in tumors by making them less leaky, and this could provide deeper NPs penetration in the tumor [14]; recently, it was calculated that the NPs ideal size to maximize penetration should be of around 12 nm [21].

20.2.1.3 Biocompatibility, Clearance, and Toxicity

These are interconnected aspects and possible the most important factors in the translation of any NPs to human use. Most of the injected NPs, if not eliminated in the short-term, accumulate not in the target tissue/tumor but in the spleen, liver, and other organs, with low degradation/clearance, where their long-term toxicity and induced biological perturbations are largely unknown [13, 22]. Although the external coating makes them biocompatible and nontoxic, this is only a temporary effect, has the coating of the accumulated NPs would eventually be degraded exposing biological reactive surfaces or releasing potential toxic materials. QDs coated with PEG initially present good biocompatibility in vivo, but studies show that they accumulate in the body and after prolonged tissue residence the internal core/shell presents visible signs of degradation [23]. Here, NPs chemistry/composition is a critical factor, NPs should be constructed with nontoxic materials, with the exception of the therapeutic agent, or their toxicity should be manageable and limited on time. After their intended application, they should be degraded and/or cleared from the body rapidly without inducing further biological perturbations. For example, silica-based NPs where engineered to self-destroy after cell internalization in vivo into smaller components that could than be easily cleared from the body [24, 25].

20.2.2 Fluorescent Relevant Parameters

Fluorescent NPs for either theranostic or imaging have to be designed to present ideal properties for fluorescence optical imaging. The ratio between fluorescent probe signal and background (autofluorescence) noise is one of the major issues for fluorescent imaging. In deep tissues, the natural absorption and scattering of light acts to greatly attenuate and “blur” the emitted fluorescence light [26] or any other photon originating or travelling through the tissue or organism [27]. Also, probes developed for dynamic in vivo fluorescence imaging have to remain stable enough to allow repetitive time points acquisitions, inside the tissue of whole animal hosts. Overall, relevant parameters of the probe or in this case the fluorescent NPs include the following.

20.2.2.1 Quantum Yield

This is an important parameter that is defined as the ratio of the number of photons emitted to the number of photons absorbed [28]. A high quantum yield is a clear advantage especially to overcome signal/noise interference and allow easy detection of the fluorescent signal. For example, engineered semiconductor QDs present a quite high quantum yield value of up to 50 % [29].

20.2.2.2 Photostability

Repetitive or/and high-intensity illumination conditions can that lead to the photochemical destruction (photobleaching) of the probe, undermining the fluorescent signal readouts [28].

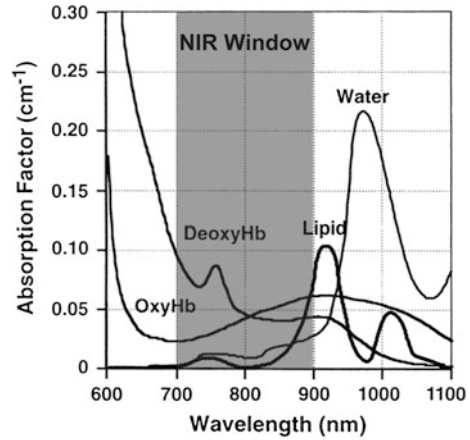
20.2.2.3 Biostability

This is related to the stability of the probe in biological environments. Fluorescent probes may be degraded or metabolized by cells/tissues, or the biological environment may modify their optical properties to different degrees. Also, the fluorescent probe could be inherently toxic due its chemical composition (or its metabolites) or yield a phototoxic effect, usually associated with the production of oxygen free radicals [26]. Here, the addition of external coating in the case of QDs [30–32] or the encapsulation of fluorescent dyes inside NPs [33, 34] represents a strategy to minimize biological degradation and/or toxic effects to a certain point.

20.2.2.4 Wavelengths

A key strategy for in vivo imaging is the use of the near-infrared (NIR) light window (Fig. 20.1), around 700–900 nm. This is because hemoglobin (the principal absorber of visible light) plus water and lipids (the principal absorbers of infrared light) have their lowest absorption coefficients in the NIR region. Imaging in this region provides deeper tissue penetration and lower absorption, scatters, and minimizes tissue autofluorescence, which further improves the signal/noise ratio [35–38].

Fig. 20.1 Near-infrared (NIR) window tissue absorption coefficients. Between the wavelengths of approximately 700–900 nm, the oxygenated hemoglobin (OxyHb), deoxygenated hemoglobin (DeoxyHb), water, and lipid absorption spectra reach a minimum; this makes this window ideal for in vivo imaging. “Recreated with kind permission of [Elsevier] [38]”



20.3 Fluorescence Imaging Technologies in the Clinic: Advantages and Limitations

Fluorescence imaging is by far the most widely used technology for in vitro and in vivo micro-/macro-imaging research. Where preclinical whole-body NIR fluorescence imaging is extensively used, its main advantages include being easy to use, safe, low cost, and highly versatile. Nevertheless, NIR fluorescence imaging contrary to other modalities, such as ultrasound, CT, MRI, and PET, is still lagging behind widespread human use in the clinic. However, NIR fluorescence imaging has revealed growing potential in this field, recently reviewed [39–42].

Briefly, NIR fluorescence has been associated with fiber-optic endoscopy techniques, namely in the diagnosis of suspected lesions and assisted target intervention, in gastrointestinal [43] and lung cancer [44]. Endoscopy is already an established optical-based technology that only needs to be upgraded with the fluorescent component, which represents a major advantage for its clinical translation [41, 42].

Additionally, NIR fluorescence imaging using contrast probes can provide real-time image data for tumor guided resection [45], sentinel lymph node mapping [38, 40, 46], provide contrast to identify critical structures such as nerves [47] and blood vessels in reconstructive surgery [48]. Nevertheless, there are several technical aspects that require improvements for the above applications, namely for sentinel lymph node mapping or any open surgery application. NIR light is invisible to the human eye, so besides the excitation source and acquisition camera, the imaging systems need a display for the surgeon to visualize the fluorescent signal. Also, these procedures traditionally require the fluorescent acquisition to be performed in the dark; to minimize interference from the environment light, these factors may restrict surgical performance.

Recent studies proposed new imaging systems for the application of this technology on the surgical room [40]. These included the fluorescence-assisted resection and exploration (FLARE) a specialized intraoperative NIR fluorescence imaging system which easily allowed seeing the surgical anatomy with 3 image views: color, NIR fluorescence, and color-NIR merged [38, 49]. Furthermore, the integration of fluorescence imaging with minimally invasive robotic surgery, such as the da Vinci surgical system [50] could represent a powerful approach. Recently, this system was tested with the NIR dye (indocyanine green (ICG)) in a human study, to visualize the biliary anatomy during a cholecystectomy [51], identify renal vasculature, and differentiate renal tumors from normal tissue during a nephrectomy [52].

20.4 Semiconductor Quantum Dots

Semiconductor nanocrystal QDs have been one of most intensely studied fluorescent NPs for biomedical nanomedicine applications; especially in cancer research, extensive reviews are available [29, 53–58].

20.4.1 *Quantum Dots Characteristics and Advantages*

These nanocrystals present different light emission properties than traditional chemically synthesized dyes or fluorescent proteins. Briefly, the absorption of a photon with energy above the semiconductor bandgap energy results in the creation of an electron–hole pair (or exciton). The radiative decay of the exciton results in photon emission with wavelengths corresponding to the semiconductor's bandgap. The absorption has an increased probability at higher energies (i.e., shorter wavelengths) and results in a broadband absorption spectrum [56].

The advantages of using QDs in the place of other traditional organic dyes have been widely reported [59, 60]. The unique optical properties of QDs include high absorbance, high quantum yield, low photobleaching, narrow emission bands, and large Stokes' shifts. QDs are more chemically stable and are not so easily metabolized or degraded by the cells compared to fluorescent dyes. The emission spectra of QDs can be tuned across a wide range by changing the size and composition of the QD core, where the narrower emissions allow to resolve more wavelength peaks than possible with standard fluorescent dyes [61].

20.4.2 Quantum Dots Engineering Strategies for In Vivo Applications

QDs were first illustrated by Alivisatos et al. [62], and their potential for ultra-sensitive biological detection was unraveled by Chan and Nie [63]. Since the first reports describing this type of materials, engineering strategies have been employed to improve and tailor QDs physical, chemical, and optical properties to enable them to be used in biological systems. These include development of the size and chemical composition of the QDs core, shell, and hydrophilic coating structure, including conjugation with biomolecular ligands [29, 64].

Today, term “QDs” can be applied to a wide range of nanoparticle types with different compositions, but typically semiconductor QDs have a core/shell structure of 2–8 nm in diameter; normally, the core is composed of heavy metal semiconductor crystalline compounds such as cadmium selenide (CdSe), cadmium telluride (CdTe), indium arsenide (InAs), or lead selenide (PbSe) and a shell made of zinc sulfide (ZnS). The introduction of a shell made of a larger bandgap material such as ZnS was a major design advance. The shell confines the exciton to the core and passivates dangling bonds. This greatly enhances the QD, improves photostability, and provides resistance against environmental photooxidation [7]. Additionally, the bare QDs are not soluble in water or biocompatible as such, so another important design development that enabled their use in biological systems was the coating with a hydrophilic layer that ensured compatibility with physiological media and provided extra protection for the core [29, 56, 65]. Several strategies and different types of hydrophilic coating molecules have been described in the literature [7, 29, 64]. One of the most extensively used is the coating with PEG or other polymers; besides water solubility, it greatly reduced nonspecific cellular uptake of QDs [66–68]. The QDs surface was also functionalized with targeting biomolecular ligands, such as antibodies, peptides, or small molecules, used to target specific cells/tissues, and importantly tumor sites, NPs tumors targeting strategies have been recently reviewed [69–71].

20.4.3 Quantum Dots Toxicity In Vivo

The QDs main drawbacks are related to biocompatibility, clearance, and long-term toxicity issues. QDs injected intravenously in mice even when targeted to tumor accumulate in the body. They have been detected in the kidney, liver, lymph nodes, and bone marrow [72, 73], in some cases up to two years after injection, with a blue shift of the emission spectra due to NPs degradation [23]. The extent of degradation of the shell/coating is critical for toxicity, since they shield the release of highly toxic Cd from the core. The release of free Cd and other heavy metals compounds is one of the main safety issues raised regarding to use of QDs in humans [22].

Also, QDs are highly reactive and are subject to photooxidation and air oxidation, with the formation of free radicals, another mechanism of toxicity [74]. The QDs toxicity issues have been extensively reviewed elsewhere [9, 75, 76]. Several engineering strategies to try to minimize this aspect have been described; some examples include the use of Cd-free QDs [77, 78]. Some works studied developments to maximize integrity on the shell/coating [30–32], and this should be effective only as long as the coating remains intact. Other strategies focus on enhancing clearance from the body, and low-sized QDs functionalized with tumor-specific small molecular ligands were tested in a mice model and shown to be cleared from the kidneys if the hydrodynamic diameter was less than 5.5 nm [79].

20.4.4 Quantum Dots Preclinical In Vivo Applications

The potential of QDs for preclinical tumor imaging and detection, including theranostics applications, has been recently reviewed [53, 54, 73, 80]. Examples of relevant studies include the following.

20.4.4.1 Sentinel Lymph Node Mapping

This was performed with NIR QDs in different types of animal tumors models, such as bladder [81], breast [82], esophageal [83], gastrointestinal [84], and lung [38, 85]. Relatively to traditional techniques (e.g., fluorescent dyes), QDs due to their high quantum yield present greater emission light penetration through thick tissues and superior signal to noise, minimizing the interference of autofluorescence tissue background [86]. In addition, for this technique size matters, as injections in the tumor of small NPs (<5 nm) can pass through multiple lymph nodes giving up false positives, QDs offer the possibility for precise engineered size to enable optimal location on the sentinel lymph nodes [86].

20.4.4.2 Primary Tumors Guided Surgery

QDs passive accumulation in the tumor or conjugation with specific biomolecular ligands to target tumor cells, offer the possibility to help surgeons to delineate tumor margins, identify metastatic sites, and evaluate whether the tumor has been completely removed [87–90].

20.4.4.3 Theranostics

QDs have been engineered to be also nanocarriers of therapeutics, combining drug delivery with imaging for monitoring the pharmacodynamics of the drugs and the effectiveness of the treatment. For example, a recent study described a pH-responsive QD–mucin1 aptamer–doxorubicin conjugate tested on an ovarian tumor mice model. Mucin1 represented the tumor-targeting ligand and doxorubicin was attached to the QD, quenching the fluorescent signal, through a pH-sensitive hydrazone bond. Inside the cells, the acidic environment promoted the release of the drug with the subsequent recovery of the fluorescent signal that could be detected [91]. Other studies employed QDs to track siRNA delivery and interference [92–96], although these were only tested *in vitro* with cultured cells, but reveal some potential for *in vivo* use.

Overall, despite the notable number of preclinical research performed with QDs and their high potential for biomedical clinical applications, there are no records of any intended or performed human clinical trials. Safety concerns related to their *in vivo* behavior represent by far the major limitation for their clinical use.

20.5 Fluorescent Dyes: Indocyanine Green Clinical Applications and Advantages of Dye-Loaded Nanoparticles

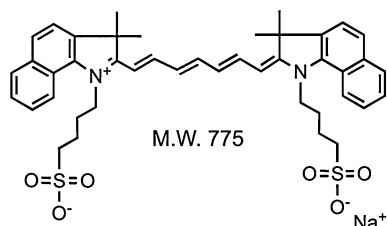
As described previously for *in vivo* imaging, the NIR window (~ 700 – 900 nm) of the spectrum provides higher penetration and lower host tissue interference with the light. For preclinical research, there are a vast selection of NIR organic dyes available [97–99] and other types of molecules (e.g., fluorescent proteins) [98]. Some examples include cyanine-based lipophilic dyes such as DiD (ex.644 nm; em.665) [100], DiR (ex.750 nm; em.782 nm) [101], hydrophilic dyes such as Cy5 (ex.650 nm; em.670 nm), Cy7 (ex.743 nm; em.767 nm) [102], and far-red engineered proteins such as the eqFP650 (ex.592 nm; em.650 nm) [103].

20.5.1 *Indocyanine Green and other Clinically Relevant Dyes*

Relatively to clinical applications very few dyes have been employed in human studies. Indocyanine green (ICG) is a 775-Da (Fig. 20.2) cyanine derivative dye (ex.760–785 nm; em.820–840 nm), first FDA approved in 1958 for indicator dilution studies [40].

Today, ICG is still the only NIR dye approved by the FDA for human clinical use. One of its major applications is in sentinel lymph node mapping for image

Fig. 20.2 Indocyanine green (ICG) molecular structure. “Recreated with kind permission of [Elsevier] [38]”



guided surgery following injection at the tumor site [40, 46]. ICG has also been used in reconstructive surgery, ophthalmic angiography, to evaluate cardiac output, hepatic function, and liver blood flow [40, 48, 104]. When injected intravenously ICG presents a very short lifetime in the blood, with a half-life of approximately 3–4 min [105]. ICG main issues are its weak fluorescent properties and low stability compared to other NIR dyes employed in preclinical studies [104]. Other clinical significant dyes include methylene blue [39, 106] and omocyanine [107, 108], although these two were only approved to be use in selected clinical trials.

20.5.2 Advantages of Dye-Loaded Nanoparticles

Direct application of ICG or any other type of low molecular weight dyes *in vivo* can be limited by several factors. These include rapid clearance from the body and relative fast degradation of the dye with the correspondent loss of the fluorescent signal.

The use of engineered nanoplatfroms where the dye is encapsulated or attached on the surface of the NPs represents an interesting strategy. This approach presents several advantages for tumor studies. These include: first, a versatile NP of controlled size and structure where is possible to include different probes for multi-modal imaging and/or sensing, with the option to also include therapeutic agents [9–12]. Second, specify coating of the NPs is to increase the body circulation time, enhancing the passive accumulation in the tumor site and with the option to decorate the NPs external coating with tumor/tissue targeting ligands. Third, the association with the NPs material stabilizes and decreases the dye biological degradation. Fourth, because the dye is concentrated in the particle, there is an increase in brightness; although to high concentrations, it may produce the opposite effect due to self-quenching.

There are a number of different compounds and strategies described in the literature to produce NPs with incorporated dyes or other fluorescent components [3, 10, 109–113]. In the next sections, we will describe some of those subdivided into inorganic materials (calcium phosphate and silica) and organic complexes (polymeric and liposome based) (Fig. 20.3).

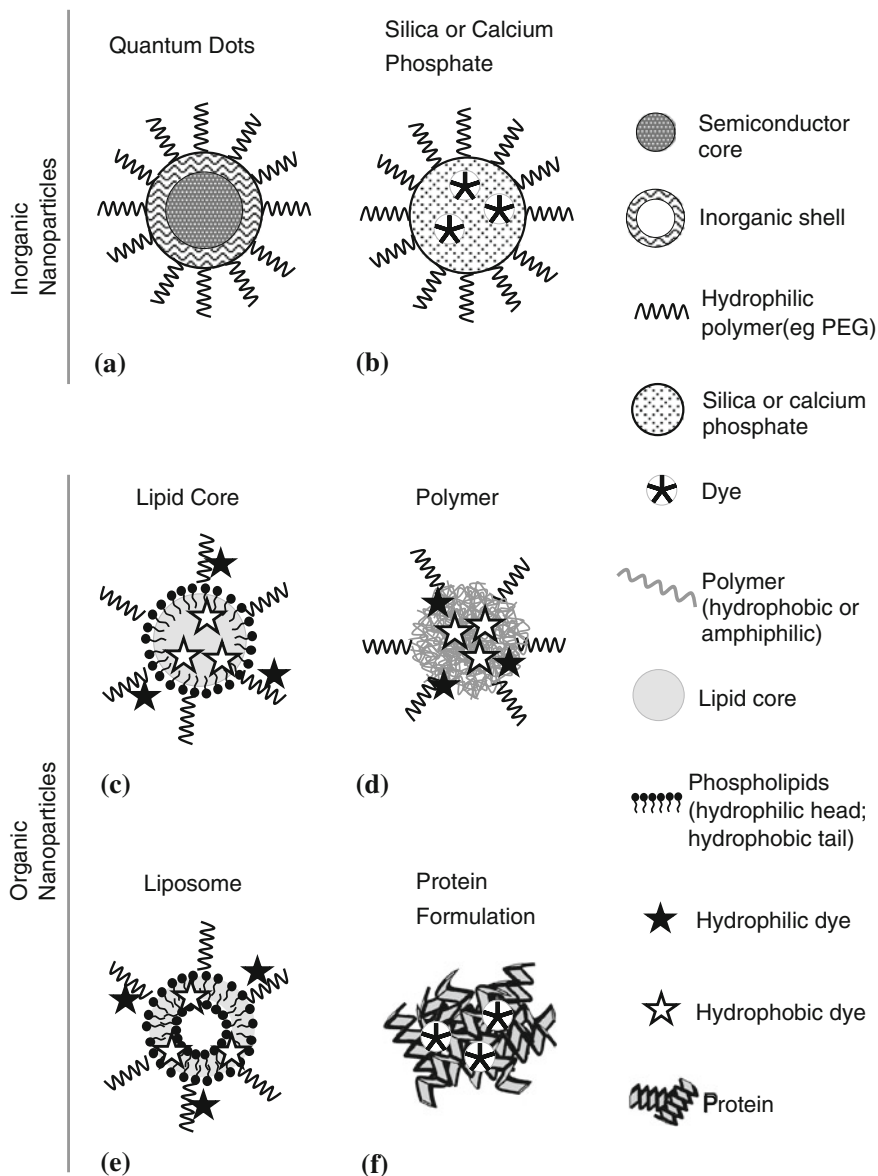


Fig. 20.3 Schematic representation depicting some types of fluorescent nanoparticles designs. Inorganic nanoparticles: **a** semiconductor quantum dots and **b** calcium phosphate or silica matrix loaded with organic dye and coated with a hydrophilic polymer. Organic nanoparticles loaded with dye, lipid or polymer based, with **c** lipid core, **e** liposome, **d** polymer self-assemble architectures, and **f** protein dye absorbed nanoparticles. Hydrophobic organic dyes can be loaded in the lipid core (**c**) or the phospholipid bilayer “shell” (**e**) and also within the polymer hydrophobic “core” groups (**d**), while hydrophilic organic dye can be conjugated to the polymers backbone (**c**, **d**, **e**). “Adapted with kind permission from [MDPI] [109]”

20.6 Inorganic Nanoparticles Loaded with Dyes

Generally, these NPs are composed of fluorescent dyes incorporated on an inorganic matrix (Fig. 20.3b). Several types of material can be included in these categories; many times, these are multimodal NPs where beside the dyes, other types of materials (e.g., gold, iron oxide, gadolinium, and carbon particles) can be incorporated or linked to the inorganic matrix [114–118]. For the purpose of the present section, we will discuss two prevalent types of fluorescent inorganic NPs, calcium phosphate, and silica.

20.6.1 Calcium Phosphate Fluorescent Nanoparticles

Calcium phosphate is one of the most widely known agents for in vitro nonviral DNA/RNA delivery [119–121]. The precipitate NPs display a pH-dependent solubility profile and relatively low toxicity, are highly biocompatible and biodegradable, and therefore have been studied for imaging and therapeutic application with encapsulated oligonucleotides, but also drugs and dyes [122].

An important drawback for in vivo use is that calcium phosphate particles are unstable and present variable size, but engineering design refinements in the synthesis protocols and polymer coating (e.g., PEG) helped stabilize the structure [123, 124].

The potential for application in small animals imaging have been described using ICG-loaded calcium phosphate [125–127]. Despite the translational potential, relatively low toxicity and the fact that some injectable derivate products are already FDA approved for medical use (e.g., bone synthetic cement graph) [128], so far there are no records of calcium phosphate nanoparticle-based clinical trials.

20.6.2 Silica Fluorescent Nanoparticles

20.6.2.1 Characteristics and Advantages

Silica- or silicon-based NPs main design advantages for biomedical applications are related to their high surface area, large pore volume, uniform porosity, and stable aqueous dispersion, together with good in vivo biocompatibility and biodegradability [24, 129].

20.6.2.2 Engineering Strategies for In Vivo Application

Silica NPs represent a versatile nanoplatform where fluorescent dyes and other functional molecules can be loaded inside the pores or covalently attached to the particles [130]. Importantly, the loaded dyes fluorescence properties remain quite stable in the silica matrix [34, 131–133], and this represents a major advantage for in vivo applications. Considering that these particles normally do not contain heavy metal components, in contrast to QDs, toxicity of silica NPs in the body is normally associated with mechanical vasculature obstruction of the organs that leads to blocking and organ failure [134]. It was demonstrated that both silica toxicity and biodistribution are influenced significantly by NPs porosity and surface characteristics, and the capacity for particles being able to be degraded and excreted out of the body by urinary and hepatobiliary routes [129].

Recent works described an interesting engineering strategy applied to fluorescence porous silica NPs loaded with anticancer drug doxorubicin, these could self-destruct in vivo into smaller components releasing the drug and be cleared out of the body within a relatively short period of time reducing the risk of causing damage to normal organs [24, 25].

20.6.2.3 Preclinical In Vivo Applications and Human Clinical Trials

There are a number of biological studies, recently reviewed [113, 130, 135, 136], performed with these types of particles, where silica NPs were successfully employed for small animal drug/gene delivery and imaging [114, 115, 137–141], commonly using a multimodal strategies [114–116, 118].

Most significantly, the so-called silica C-dots [133, 142] represent one of the first times an inorganic particle was approved to be used as a platform for both diagnostics and staging in advanced melanoma tumors in human clinical trials [143]. The C-dots were labeled with a radioactive probe and injected in the tumor site for PET detection of the surrounding lymph nodes. Although in the previous study the probe used was radioactive iodine, animal studies with Cy5-loaded C-dots also demonstrated the advantages of using NIR imaging for the localization of superficial lymph nodes [5]. This opens up the possibility for in the future being able to use already FDA approved NIR fluorescent dyes with these NPs. For example, other silica NPs loaded with ICG have already been described in several animal imaging studies [116, 117, 141, 144].

20.7 Organic Nanoparticles Loaded with Dyes

In these types of NPs, the dye is incorporated by either just adsorption or through a covalent bond to an organic structure; an extensive range of different organic materials and designs have been described [4, 145]. Also similar to the inorganic

NPs, many times, these particles can incorporate other materials for multimodal imaging (e.g., PET, MRI) and/or a therapeutic component [4, 146, 147].

Organic NPs in general demonstrated effective properties as an *in vivo* nanocarrier, giving rise to several clinical contract agent conjugates and drug nanoformulation used in humans. Making them the most successful group of NPs to be translated to the clinic, this aspect has been recently reviewed [110, 145]. Two examples are as follows: Doxil, the first FDA approved nanoformulation in 1995 for AIDS-related Kaposi's syndrome, which resulted from the incorporation of doxorubicin, within liposomes [148], and Abraxane, approved in 2005, is based on an albumin-bound formulation with paclitaxel, developed to treat metastatic breast cancer [149].

20.7.1 General Advantages and Issues

The main advantages of organic-based NPs include the capacity to enhance drugs efficiency without the need to alter the drug compound, improvement in the access to the target tissue/cells due to higher biological barriers crossing capacity, and importantly, they have proved to be safe for human use [4, 145]. This is because these particles are constituted by synthetic or natural occurring organic molecules, some of those already present in the human body, making them highly biocompatible and biodegradable.

The main issues are related to the organic NPs heterogeneity, namely in obtaining and maintaining reproducible NPs proprieties such as size, drug/dye load, structural architecture, and also their stability during storage and under physiological conditions. They normally are classified based on their composition/structure; we will briefly discuss two examples: lipid- and polymeric-based NPs.

20.7.2 Lipid Fluorescent Nanoparticles

20.7.2.1 Characteristics, Advantages, and Issues

Lipid NPs result from ensembles of lipophilic and/or amphiphilic lipids in small artificial vesicles of spherical shape (Fig. 20.3e and c), with a general diameter 50–300 nm [150, 151]. Different compositions and structures of lipid NPs have been described for imaging and therapy, such as nanoemulsions [152], nanocapsules [153, 154], solid lipid NPs [155], and liposomes [151, 156]. Due to their nature, they can for example be used to incorporate negative charged nucleic acid through electrostatic interactions with the positive charge phospholipids [156] and different lipophilic cargo, where drugs represent a major application [145].

The main issue of this type of particles is related to their colloidal stability; especially on living systems, they are relatively less stable than for example polymeric NPs [151].

20.7.2.2 Engineering Strategies for In Vivo Application

There are different strategies to improve stability, and this includes conjugation with polymeric moieties, such as PEG [147]. Another example involved the use of a complex mixture of different types of lipids (long-chain mono-, di-, and triglycerides) and other surfactants (phospholipids and PEG-stearate) to stabilize the NPs [152]. An important feature of lipid NPs is the option to encapsulate different dyes such as DiD, DiR [153, 154, 157], and ICG [105, 158, 159] to obtain bright fluorescent NPs.

20.7.2.3 Preclinical In Vivo Applications

The engineering strategies used to improve the general particle stability also contribute to improving their fluorescence properties and decreasing the dye degradation. For example, in the case of nanoemulsions or nanocapsules, lipophilic dyes can be homogeneously incorporated in the lipid core in high concentration (Fig. 20.3c) providing excellent brightness [150, 153]. Self-quenching phenomena, due to high dye loading, have to be monitored, and dye leakage can be a greater issue on the lipid NPs, compared to more stable dye-loaded inorganic or polymeric NPs [33]. Nevertheless, there were some recent studies with lipid NPs, termed Lipidots, composed of DiD-loaded lipid core that claimed comparable results to commercial QDs with much lower toxicity, when used as a fluorescent contrast agent for lymph node mapping in mice [109, 150]. Other preclinical studies on small animal have been performed to demonstrate the application of ICG-loaded lipid NPs for sentinel lymph node mapping [160] and general tumor imaging [161, 162]. Despite some lipid nanoformulations already in use in the clinic [145, 148], there are no records of human approved fluorescent lipid NPs.

20.7.3 Polymeric Fluorescent Nanoparticles

20.7.3.1 Characteristics and Advantages

Polymeric NPs present a variety of structural arrangements and are formulated with different polymer constituents. The different structures are related to the self-assembly of the hydrophobic/hydrophilic polymer subunits and can include other compounds, such as dyes [109] and therapeutic drugs, extensively reviewed elsewhere [111, 145]. Relevant examples of NPs architectures have been

described, and this included polymeric micelles [163], dendrimers [164], and polymer capsules [165]. Some examples of prominent synthetic polymer constituents used on the design of these NPs are PEG, poly(lactic acid) (PLA), poly(D,L-lactic-co-glycolide) (PLGA), and poly(caprolactone) (PCL). Other important described constituents are natural occurring polymers such as poly(glutamic acid) (PGA), poly(lysine), saccharides (dextran and chitosan) and body present polymers (hyaluronic acid and human serum albumin) [109, 145].

The common advantages of these polymers are their high biocompatibility and/or biodegradable properties, plus being relatively safe. Several studies described polymer-based NPs used as nonviral gene delivery system [166–168], but the vast majority of works with these NPs are related to their use as a nanocarrier for therapeutic drug delivery [111, 165, 169] where these particles presented greater clinical success [145]. It is also common for these particles to be loaded or conjugated with fluorescent dyes for imaging [110] or distinct theranostic applications [170].

20.7.3.2 Engineering Strategies for In Vivo Application

Some of main advantages and associated engineering rational in the development of these NPs are related to the increase in drug solubility and in turn bioavailability, controlled delivery with accumulation on target locations, maintenance of systemic drug concentration (i.e., increasing serum half-life) and demonstrated safety for human use [111, 145]. For example, PEG is one of the most widely used polymers to increase circulation time on NPs and has been approved for human use [169]. Similar to the previously described lipid NPs, different polymer compositions/designs provide efficient loading and delivery of the drugs or/and fluorescent dyes, enable degradation and excretion from the body, but importantly should reveal lower toxicity [171].

Polymer NPs are high versatile allowing for different designs and the conjugation with diverse materials (e.g., gold, iron oxide, carbon particles) resulting in multifunctional/multimodal NPs [4, 10, 146, 147].

Highly relevant for optical imaging is the incorporation of fluorescent dyes. Different approaches have been described; for example, NIR lipophilic dyes such as DiD and DiR [172] can be incorporated on the polymer hydrophobic “core.” While hydrophilic dyes, such as Cy5.5, can be covalently conjugated to the polymers backbone (Fig. 20.3d), this improved stability and reduced dye leaking from the NPs [170, 173, 174]. Hyaluronic acid (HA) is a polysaccharide present in the extracellular matrix and synovial fluids of the body, making it extremely biocompatibility and biodegradable [175]. HA-based self-assemble NPs represent an interesting versatile platform where is possible to load hydrophobic drugs/dyes in the hydrophobic “cores” or covalently attach them to the polymer backbone. Furthermore, they revealed specific targeting to tumor sites, due to strong receptor-binding affinity to CD44, overexpressed in most tumor cells [176]. The covalently attached Cy5.5-dye-labeled HA NPs demonstrated to be relatively stable under physiological

conditions and presented good fluorescence properties. They have been successfully used for tumor imaging [177–179] and theranostic applications [170, 180].

20.7.3.3 Preclinical In Vivo Applications and Human Clinical Trials

For example, recently HA-based NPs were engineered as a theranostic system combining early tumor detection with targeted tumor therapy and evaluated on a colon cancer mice model [170]. The diagnostic consisted of Cy5.5 chemically conjugated to the HA that successfully allowed fluorescence imaging detection of small-sized colon tumors as well as liver-implanted colon tumors on live mice. The target therapy part consisted of the anticancer drug irinotecan encapsulated into the hydrophobic HA cores, that was effective on suppressing tumor growth, and this response was also possible to be monitored through fluorescence imaging [170].

Several researchers used the clinically significant ICG dye to perform pre-clinical studies. The dye was encapsulated on polymeric NPs such as PLGA [181, 182] and PEG-folate-conjugated ring-opening metathesis polymerization-based copolymers [183] for mice tumor imaging. Concretely sentinel lymph node mapping was demonstrated with ICG-loaded PGA [184] and HA NPs [185, 186].

Importantly, ICG has been noncovalently absorbed/complexed with human serum albumin in a NP formulation (Fig. 20.3f), revealing a hydrodynamic diameter of around 7 nm, which improved the optical properties, resulting in quantum yield enhancement, compared to free ICG [187, 188]. Most significantly, both ICG individually and albumin-related drug complexes, such as Abraxane [149], are already approved for human use. This may help explain why albumin–ICG was one of only polymeric fluorescent NPs approved for human clinical trials so far [40].

Invasive tumors spread from their original site through the lymph channels to regional nodes, and the injection of a contrast agent at the tumor site allows the surgeon to easily identify and take biopsy of the first or sentinel lymph nodes which the cancer encounters. If the analysis of the sentinel lymph node reveals that is free of tumor cells there is high probability all the lymph nodes in the region are also free, this spares the patient from unnecessary greater surgical procedure to remove all the lymph nodes. Albumin–ICG NPs were used on human clinical trials for sentinel lymph node mapping in breast [189], cervical [190], head and neck cancer [191], and vulvar [192] (Fig. 20.4) cancers. All these human trials were performed using the mini-FLARE imaging system [49]. But the da Vinci minimally invasive robotic surgery system was used recently with ICG to image human biliary anatomy [193], and there are ongoing clinical trials for endometrial cancer sentinel node mapping [194] and to help identify renal cortical tumors [195].

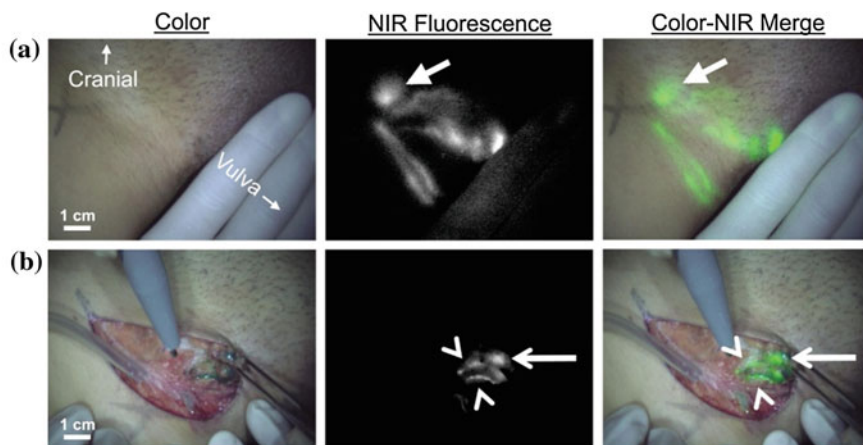


Fig. 20.4 Sentinel lymph node (SNL) mapping using near-infrared (NIR) fluorescence imaging FLARE system in a human patient with vulvar cancer. **a** Peritumoral injection of 1.6 mL of 500 μ M indocyanine green human serum albumin (ICG:HSA), injection site covered by hand, identifies lymphatic channels, which converge in a SLN (arrow) that can be seen percutaneously (top row). **b** Identification of the SLN (arrow) and 2 afferent lymphatic channels (arrowheads) is demonstrated using NIR fluorescence imaging 17 min after injection of ICG:HSA (bottom row). Scale bars represent 1 cm. “Recreated with kind permission of [Elsevier] [192]”

20.8 Conclusion and Future Perspectives

20.8.1 Fluorescence Imaging Technologies in the Clinic

Despite fluorescence imaging widespread use in preclinical research with NPs and other probes, this has not yet translated to the clinic, where others technologies (i.e., ultrasound, CT, MRI, and PET) are already well established. Nevertheless, there is a growing potential in this field [39–42].

For example, fluorescent endoscopy represents a potential application without the need for major technological adaptation [41, 42], and other fluorescence technologies, such as intraoperative imaging systems, are being evaluated for the translation to the surgical environment [48].

In our perspective, we believe that specialized intraoperative NIR fluorescence imaging systems, such as the FLARE [38, 49], and more recently, minimally invasive robotic surgery [50] technologies represent important developments that could potentiate the use of fluorescent NPs in the clinic. Minimally invasive robotic surgery systems combined with fluorescence imaging are especially interesting, as the surgeon performs all the procedure through a display video system, they can more easily engage surgery on both color and fluorescence modes, providing an excellent interplay between the “normal” tissue color view and fluorescence imaging. Although this system at this moment is highly specialized and not common, this could contribute to bringing fluorescence imaging to routine use in the clinic.

20.8.2 Quantum Dots in the Clinic

QDs have been one of the most widely studied NPs in preclinical *in vivo* research, because of their unique photophysical properties, namely broad excitation, narrow emission, and high quantum yield. However, safety concerns related to their use *in vivo* represent by far the major limitation for their clinical application in humans [9, 75, 76].

Although some design strategies were tested to minimize toxicity, the fact is that practically all QDs are composed of potentially toxic heavy metals components. Some reports described Cd-free QDs [77, 78], but still the safety of these materials needs to be clarified. Nevertheless, despite their heavy metal content, *in vivo* studies with Cd-based QDs in rodents [196, 197] and recently on nonhuman primates [198] showed no adverse toxic effects at certain doses within the examined biological parameters.

Therefore, from our perspective, these studies confirm the need to perform specialized assays to evaluate QDs toxicity at the molecular level and critically examine any biological perturbations. We suggest that future studies should probe genotoxic/epigenetic perturbations. Recent works described this at the *in vitro* cellular level [199], but it is critical to study QDs long-term effects in full living systems. A suggested approach would be to follow previous described methodologies used to evaluate the biological perturbation of free heavy metals on the body [200, 201]. Overall, we believe that with the current knowledge, the possibility of human clinical use of QDs is highly improbable.

20.8.3 Dye-Loaded Nanoparticles in the Clinic

Calcium phosphate and silica NPs seem much more biocompatible than QDs; also, there were already clinical trials with silica NPs, although not using fluorescence imaging.

Nevertheless, lipid and in particular polymeric-based nanoformulations are the most successfully examples of human tested or actually approved NPs for clinical use [145]. They are largely applied for drug delivery, where NPs formulated with polymers already naturally present on the human body, such as human serum albumin, represent currently the most relevant examples [145]. Within this class of nanoformulations, there are very few clinical trials with fluorescent NPs. To our knowledge, albumin-ICG NPs for sentinel lymph node mapping represents the only example [189–192]. Although the low number of fluorescent NPs may be explained in part due to the “low demand” of these on the clinical environment. Considering the overwhelming output of published preclinical NPs on this category, there is a significant “bottleneck” in the translation of fluorescent NPs to the clinic.

Therefore, our opinion on the immediate advancements in the development of fluorescent NPs would be to incorporate ICG dye into engineered NPs designed with polymers already present on the body or with nanoformulations already on clinical

trials/approved for other purposes (i.e., drug delivery). Additionally, we believe that an important limitation on this field is related to the fluorescence performance and the low number of actually available FDA approved probes, where ICG approved more than 50 years ago is in essence the only option at the moment.

20.8.4 Final Remarks

Fluorescence imaging and the advent of nanotechnology brought the promise of a major impact in the clinic. Despite the overwhelming number of fluorescent NPs published in the literature in the last years, and considerable progress for research applications and preclinical studies, the fact is that only very few potential NPs have ever reach clinical phase trials.

Analyzing the discussed NPs design characteristics correlated with the clinical application outcome, it seems that in general, the NPs do not necessary need to have the “best” fluorescent properties, as long they are showed to be relatively safe for human use and present significant clinical advantages compared to other probes or procedures.

Overall, this chapter demonstrates the need to critically address the NPs design and safety concerns within an integrated engineering strategy, to advance the translation of already studied or newly developed fluorescence NPs into the clinic.

Acknowledgments The authors would like to acknowledge the NIH Fellows Editorial Board for proofreading the manuscript and the NIH–NIBIB intramural funding. Oscar F. Silvestre is supported by an AXA Research Fund Postdoctoral Fellowship.

References

1. The appropriateness of existing methodologies to assess the potential risks associated with engineered and adventitious products (2005). European commission health and consumer protection directorate-general
2. Moghimi SM, Hunter AC, Murray JC (2005) Nanomedicine: current status and future prospects. *Faseb J* 19(3):311–330. doi:10.1096/fj.04-2747rev
3. Lee DE, Koo H, Sun IC, Ryu JH, Kim K, Kwon IC (2012) Multifunctional nanoparticles for multimodal imaging and theragnosis. *Chem Soc Rev* 41(7):2656–2672. doi:10.1039/c2cs15261d
4. Rabanel JM, Aoun V, Elkin I, Mokhtar M, Hildgen P (2012) Drug-loaded nanocarriers: passive targeting and crossing of biological barriers. *Curr Med Chem* 19(19):3070–3102
5. Benezra M, Penate-Medina O, Zanzonico PB, Schaer D, Ow H, Burns A, DeStanchina E, Longo V, Herz E, Iyer S, Wolchok J, Larson SM, Wiesner U, Bradbury MS (2011) Multimodal silica nanoparticles are effective cancer-targeted probes in a model of human melanoma. *J Clin Invest* 121(7):2768–2780. doi:10.1172/jci45600
6. Valeur B, Berberan-Santos MN (2011) A brief history of fluorescence and phosphorescence before the emergence of quantum theory. *J Chem Educ* 88(6):731–738. doi:10.1021/ed100182h
7. Delehanty JB, Susumu K, Manthe RL, Algar WR, Medintz IL (2012) Active cellular sensing with quantum dots: transitioning from research tool to reality; a review. *Anal Chim Acta* 750:63–81. doi:10.1016/j.aca.2012.05.032

8. Vendrell M, Zhai DT, Er JC, Chang YT (2012) Combinatorial strategies in fluorescent probe development. *Chem Rev* 112(8):4391–4420. doi:[10.1021/cr200355j](https://doi.org/10.1021/cr200355j)
9. Xie J, Lee S, Chen XY (2010) Nanoparticle-based theranostic agents. *Adv Drug Deliv Rev* 62(11):1064–1079. doi:[10.1016/j.addr.2010.07.009](https://doi.org/10.1016/j.addr.2010.07.009)
10. Choi KY, Liu G, Lee S, Chen XY (2012) Theranostic nanoplatforams for simultaneous cancer imaging and therapy: current approaches and future perspectives. *Nanoscale* 4(2):330–342. doi:[10.1039/c1nr11277e](https://doi.org/10.1039/c1nr11277e)
11. Chen X, Gambhir SS, Cheon J (2011) Theranostic nanomedicine. *Acc Chem Res* 44(10):841. doi:[10.1021/ar200231d](https://doi.org/10.1021/ar200231d)
12. Ahmed N, Fessi H, Elaissari A (2012) Theranostic applications of nanoparticles in cancer. *Drug Discov Today* 17(17–18):928–934. doi:[10.1016/j.drudis.2012.03.010](https://doi.org/10.1016/j.drudis.2012.03.010)
13. Albanese A, Tang PS, Chan WCW (2012) The effect of nanoparticle size, shape, and surface chemistry on biological systems. In: Yarmush ML (ed) *Annual review of biomedical engineering*, annual reviews, Palo Alto, vol 14, pp 1–16. doi:[10.1146/annurev-bioeng-071811-150124](https://doi.org/10.1146/annurev-bioeng-071811-150124)
14. Jain RK, Stylianopoulos T (2010) Delivering nanomedicine to solid tumors. *Nat Rev Clin Oncol* 7(11):653–664. doi:[10.1038/nrclinonc.2010.139](https://doi.org/10.1038/nrclinonc.2010.139)
15. Geng Y, Dalhaimer P, Cai SS, Tsai R, Tewari M, Minko T, Discher DE (2007) Shape effects of filaments versus spherical particles in flow and drug delivery. *Nat Nanotechnol* 2(4):249–255. doi:[10.1038/nnano.2007.70](https://doi.org/10.1038/nnano.2007.70)
16. Karmali PP, Simberg D (2011) Interactions of nanoparticles with plasma proteins: implication on clearance and toxicity of drug delivery systems. *Expert Opin Drug Deliv* 8(3):343–357. doi:[10.1517/17425247.2011.554818](https://doi.org/10.1517/17425247.2011.554818)
17. Perrault SD, Walkey C, Jennings T, Fischer HC, Chan WCW (2009) Mediating tumor targeting efficiency of nanoparticles through design. *Nano Lett* 9(5):1909–1915. doi:[10.1021/nl900031y](https://doi.org/10.1021/nl900031y)
18. Lee H, Fonge H, Hoang B, Reilly RM, Allen C (2010) The effects of particle size and molecular targeting on the intratumoral and subcellular distribution of polymeric nanoparticles. *Mol Pharm* 7(4):1195–1208. doi:[10.1021/mp100038h](https://doi.org/10.1021/mp100038h)
19. Cheng ZL, Al Zaki A, Hui JZ, Muzykantov VR, Tsourkas A (2012) Multifunctional nanoparticles: cost versus benefit of adding targeting and imaging capabilities. *Science* 338(6109):903–910. doi:[10.1126/science.1226338](https://doi.org/10.1126/science.1226338)
20. Peiris PM, Toy R, Doolittle E, Pansky J, Abramowski A, Tam M, Vicente P, Tran E, Hayden E, Camann A, Mayer A, Erokwu BO, Berman Z, Wilson D, Baskaran H, Flask CA, Keri RA, Karathanasis E (2012) Imaging metastasis using an integrin-targeting chain-shaped nanoparticle. *ACS Nano* 6(10):8783–8795. doi:[10.1021/nn303833p](https://doi.org/10.1021/nn303833p)
21. Chauhan VP, Stylianopoulos T, Martin JD, Popovic Z, Chen O, Kamoun WS, Bawendi MG, Fukumura D, Jain RK (2012) Normalization of tumour blood vessels improves the delivery of nanomedicines in a size-dependent manner. *Nat Nanotechnol* 7(6):383–388. doi:[10.1038/nnano.2012.45](https://doi.org/10.1038/nnano.2012.45)
22. Rzigalinski BA, Strobl JS (2009) Cadmium-containing nanoparticles: perspectives on pharmacology and toxicology of quantum dots. *Toxicol Appl Pharmacol* 238(3):280–288. doi:[10.1016/j.taap.2009.04.010](https://doi.org/10.1016/j.taap.2009.04.010)
23. Fitzpatrick JAJ, Andreko SK, Ernst LA, Waggoner AS, Ballou B, Bruchez MP (2009) Long-term persistence and spectral blue shifting of quantum dots in vivo. *Nano Lett* 9(7):2736–2741. doi:[10.1021/nl901534q](https://doi.org/10.1021/nl901534q)
24. Park JH, Gu L, von Maltzahn G, Ruoslahti E, Bhatia SN, Sailor MJ (2009) Biodegradable luminescent porous silicon nanoparticles for in vivo applications. *Nat Mater* 8(4):331–336. doi:[10.1038/nmat2398](https://doi.org/10.1038/nmat2398)
25. Singh N, Karambelkar A, Gu L, Lin K, Miller JS, Chen CS, Sailor MJ, Bhatia SN (2011) Bioresponsive mesoporous silica nanoparticles for triggered drug release. *J Am Chem Soc* 133(49):19582–19585. doi:[10.1021/ja206998x](https://doi.org/10.1021/ja206998x)
26. Ballou B, Ernst LA, Waggoner AS (2005) Fluorescence imaging of tumors in vivo. *Curr Med Chem* 12(7):795–805

27. Ntziachristos V (2006) Fluorescence molecular imaging. *Annu Rev Biomed Eng* 8(1):1–33
28. White NS, Errington RJ (2005) Fluorescence techniques for drug delivery research: theory and practice. *Adv Drug Deliv Rev* 57(1):17–42
29. Zrazhevskiy P, Sena M, Gao XH (2010) Designing multifunctional quantum dots for bioimaging, detection, and drug delivery. *Chem Soc Rev* 39(11):4326–4354. doi:[10.1039/b915139g](https://doi.org/10.1039/b915139g)
30. Ryman-Rasmussen JP, Riviere JE, Monteiro-Riviere NA (2007) Surface coatings determine cytotoxicity and irritation potential of quantum dot nanoparticles in epidermal keratinocytes. *J Invest Dermatol* 127(1):143–153. doi:[10.1038/sj.jid.5700508](https://doi.org/10.1038/sj.jid.5700508)
31. Zhang TT, Stilwell JL, Gerion D, Ding LH, Elboudwarej O, Cooke PA, Gray JW, Alivisatos AP, Chen FF (2006) Cellular effect of high doses of silica-coated quantum dot profiled with high throughput gene expression analysis and high content cellomics measurements. *Nano Lett* 6(4):800–808. doi:[10.1021/nl0603350](https://doi.org/10.1021/nl0603350)
32. Ballou B, Lagerholm BC, Ernst LA, Bruchez MP, Waggoner AS (2004) Noninvasive imaging of quantum dots in mice. *Bioconjug Chem* 15(1):79–86. doi:[10.1021/bc034153y](https://doi.org/10.1021/bc034153y)
33. Klymchenko AS, Roger E, Anton N, Anton H, Shulov I, Vermot J, Mely Y, Vandamme TF (2012) Highly lipophilic fluorescent dyes in nano-emulsions: towards bright non-leaking nano-droplets. *RSC Adv* 2(31):11876–11886. doi:[10.1039/c2ra21544f](https://doi.org/10.1039/c2ra21544f)
34. Chen GW, Song FL, Wang X, Sun SG, Fan JL, Peng XJ (2012) Bright and stable Cy3-encapsulated fluorescent silica nanoparticles with a large Stokes shift. *Dyes Pigm* 93(1–3):1532–1537. doi:[10.1016/j.dyepig.2011.09.002](https://doi.org/10.1016/j.dyepig.2011.09.002)
35. Weissleder R, Ntziachristos V (2003) Shedding light onto live molecular targets. *Nat Med* 9(1):123–128
36. Wagnieres GA, Star WM, Wilson BC (1998) In vivo fluorescence spectroscopy and imaging for oncological applications. *Photochem Photobiol* 68(5):603–632
37. Kobayashi H, Ogawa M, Alford R, Choyke PL, Urano Y (2010) New strategies for fluorescent probe design in medical diagnostic imaging. *Chem Rev* 110(5):2620–2640. doi:[10.1021/cr900263j](https://doi.org/10.1021/cr900263j)
38. Khullar O, Frangioni JV, Grinstaff M, Colson YL (2009) Image-guided sentinel lymph node mapping and nanotechnology-based nodal treatment in lung cancer using invisible near-infrared fluorescent light. *Semin Thorac Cardiovasc Surg* 21(4):309–315
39. Gioux S, Choi HS, Frangioni JV (2010) Image-guided surgery using invisible near-infrared light: fundamentals of clinical translation. *Mol Imaging* 9(5):237–255. doi:[10.2310/7290.2010.00034](https://doi.org/10.2310/7290.2010.00034)
40. Polom K, Murawa D, Rho YS, Nowaczyk P, Hunerbein M, Murawa P (2011) Current trends and emerging future of indocyanine green usage in surgery and oncology a literature review. *Cancer* 117(21):4812–4822. doi:[10.1002/cncr.26087](https://doi.org/10.1002/cncr.26087)
41. Kosaka N, Ogawa M, Choyke PL, Kobayashi H (2009) Clinical implications of near-infrared fluorescence imaging in cancer. *Future Oncol* 5(9):1501–1511. doi:[10.2217/fo.09.109](https://doi.org/10.2217/fo.09.109)
42. Taruttis A, Ntziachristos V (2012) Translational optical imaging. *Am J Roentgenol* 199(2):263–271. doi:[10.2214/ajr.11.8431](https://doi.org/10.2214/ajr.11.8431)
43. Piyawattanametha W, Ra H, Qiu Z, Friedland S, Liu JTC, Loewke K, Kino GS, Solgaard O, Wang TD, Mandella MJ, Contag CH (2012) In vivo near-infrared dual-axis confocal microendoscopy in the human lower gastrointestinal tract. *J Biomed Opt* 17(2). doi:[10.1117/1.jbo.17.2.021102](https://doi.org/10.1117/1.jbo.17.2.021102)
44. El-Bayoumi E, Silvestri GA (2008) Bronchoscopy for the diagnosis and staging of lung cancer. *Semin Respir Crit Care Med* 29(3):261–270. doi:[10.1055/s-2008-1076746](https://doi.org/10.1055/s-2008-1076746)
45. Winer JH, Choi HS, Gibbs-Strauss SL, Ashitate Y, Colson YL, Frangioni JV (2010) Intraoperative localization of insulinoma and normal pancreas using invisible near-infrared fluorescent light. *Ann Surg Oncol* 17(4):1094–1100. doi:[10.1245/s10434-009-0868-8](https://doi.org/10.1245/s10434-009-0868-8)
46. Miyashiro I, Miyoshi N, Hiratsuka M, Kishi K, Yamada T, Ohue M, Ohigashi H, Yano M, Ishikawa O, Imaoka S (2008) Detection of sentinel node in gastric cancer surgery by

- indocyanine green fluorescence imaging: comparison with infrared imaging. *Ann Surg Oncol* 15(6):1640–1643. doi:[10.1245/s10434-008-9872-7](https://doi.org/10.1245/s10434-008-9872-7)
47. Gibbs-Strauss SL, Nasr KA, Fish KM, Khullar O, Ashitate Y, Siclován TM, Johnson BF, Barnhardt NE, Hehir CAT, Frangioni JV (2011) Nerve-highlighting fluorescent contrast agents for image-guided surgery. *Mol Imaging* 10(2):91–101. doi:[10.2310/7290.2010.00026](https://doi.org/10.2310/7290.2010.00026)
 48. Lee BT, Hutteman M, Gioux S, Stockdale A, Lin SJ, Ngo LH, Frangioni JV (2010) The FLARE intraoperative near-infrared fluorescence imaging system: a first-in-human clinical trial in perforator flap breast reconstruction. *Plast Reconstr Surg* 126(5):1472–1481. doi:[10.1097/PRS.0b013e3181f059c7](https://doi.org/10.1097/PRS.0b013e3181f059c7)
 49. Troyan SL, Kianzad V, Gibbs-Strauss SL, Gioux S, Matsui A, Oketokoun R, Ngo L, Khamene A, Azar F, Frangioni JV (2009) The FLARE((TM)) intraoperative near-infrared fluorescence imaging system: a first-in-human clinical trial in breast cancer sentinel lymph node mapping. *Ann Surg Oncol* 16(10):2943–2952. doi:[10.1245/s10434-009-0594-2](https://doi.org/10.1245/s10434-009-0594-2)
 50. Yu HY, Friedlander DF, Patel S, Hu JC (2013) The current status of robotic oncologic surgery. *CA-Cancer J Clin* 63(1):45–56. doi:[10.3322/caac.21160](https://doi.org/10.3322/caac.21160)
 51. Buchs NC, Hagen ME, Pugin F, Volonte F, Bucher P, Schiffer E, Morel P (2012) Intraoperative fluorescent cholangiography using indocyanin green during robotic single site cholecystectomy. *Int J Med Robot Comput Assist Surg* 8(4):436–440. doi:[10.1002/rcs.1437](https://doi.org/10.1002/rcs.1437)
 52. Tobis S, Knopf J, Silvers C, Yao J, Rashid H, Wu G, Golijanin D (2011) Near infrared fluorescence imaging with robotic assisted laparoscopic partial nephrectomy: initial clinical experience for renal cortical tumors. *J Urol* 186(1):47–52. doi:[10.1016/j.juro.2011.02.2701](https://doi.org/10.1016/j.juro.2011.02.2701)
 53. Chen C, Peng J, Sun SR, Peng CW, Li Y, Pang DW (2012) Tapping the potential of quantum dots for personalized oncology: current status and future perspectives. *Nanomedicine* 7(3):411–428. doi:[10.2217/nmm.12.9](https://doi.org/10.2217/nmm.12.9)
 54. Luo GP, Long J, Zhang B, Liu C, Ji SR, Xu J, Yu XJ, Ni QX (2012) Quantum dots in cancer therapy. *Expert Opin Drug Deliv* 9(1):47–58. doi:[10.1517/17425247.2012.638624](https://doi.org/10.1517/17425247.2012.638624)
 55. Ho YP, Leong KW (2010) Quantum dot-based theranostics. *Nanoscale* 2(1):60–68. doi:[10.1039/b9nr00178f](https://doi.org/10.1039/b9nr00178f)
 56. Michalet X, Pinaud FF, Bentolila LA, Tsay JM, Doose S, Li JJ, Sundaresan G, Wu AM, Gambhir SS, Weiss S (2005) Quantum dots for live cells, in vivo imaging, and diagnostics. *Science* 307(5709):538–544. doi:[10.1126/science.1104274](https://doi.org/10.1126/science.1104274)
 57. Gao XH, Cui YY, Levenson RM, Chung LWK, Nie SM (2004) In vivo cancer targeting and imaging with semiconductor quantum dots. *Nat Biotechnol* 22(8):969–976
 58. Cai WB, Hsu AR, Li ZB, Chen XY (2007) Are quantum dots ready for in vivo imaging in human subjects? *Nanoscale Res Lett* 2(6):265–281. doi:[10.1007/s11671-007-9061-9](https://doi.org/10.1007/s11671-007-9061-9)
 59. Resch-Genger U, Grabolle M, Cavaliere-Jaricot S, Nitschke R, Nann T (2008) Quantum dots versus organic dyes as fluorescent labels. *Nat Methods* 5(9):763–775. doi:[10.1038/nmeth.1248](https://doi.org/10.1038/nmeth.1248)
 60. Jaiswal JK, Simon SM (2004) Potentials and pitfalls of fluorescent quantum dots for biological imaging. *Trends Cell Biol* 14(9):497–504. doi:[10.1016/j.tcb.2004.07.012](https://doi.org/10.1016/j.tcb.2004.07.012)
 61. Kosaka N, Ogawa M, Sato N, Choyke PL, Kobayashi H (2009) In vivo real-time, multicolor, quantum dot lymphatic imaging. *J Invest Dermatol* 129(12):2818–2822. doi:[10.1038/jid.2009.161](https://doi.org/10.1038/jid.2009.161)
 62. Alivisatos AP (1996) Semiconductor clusters, nanocrystals, and quantum dots. *Science* 271(5251):933–937
 63. Chan WCW, Nie SM (1998) Quantum dot bioconjugates for ultrasensitive nonisotopic detection. *Science* 281(5385):2016–2018
 64. Wang YQ, Chen LX (2011) Quantum dots, lighting up the research and development of nanomedicine. *Nanomed-Nanotechnol Biol Med* 7(4):385–402. doi:[10.1016/j.nano.2010.12.006](https://doi.org/10.1016/j.nano.2010.12.006)
 65. Frasco MF, Chaniotakis N (2010) Bioconjugated quantum dots as fluorescent probes for bioanalytical applications. *Anal Bioanal Chem* 396(1):229–240. doi:[10.1007/s00216-009-3033-0](https://doi.org/10.1007/s00216-009-3033-0)
 66. Mei BC, Susumu K, Medintz IL, Mattoussi H (2009) Polyethylene glycol-based bidentate ligands to enhance quantum dot and gold nanoparticle stability in biological media. *Nat Protoc* 4(3):412–423. doi:[10.1038/nprot.2008.243](https://doi.org/10.1038/nprot.2008.243)

67. Schipper ML, Iyer G, Koh AL, Cheng Z, Ebenstein Y, Aharoni A, Keren S, Bentolila LA, Li JQ, Rao JH, Chen XY, Banin U, Wu AM, Sinclair R, Weiss S, Gambhir SS (2009) Particle size, surface coating, and PEGylation influence the biodistribution of quantum dots in living mice. *Small* 5(1):126–134. doi:[10.1002/smll.200800003](https://doi.org/10.1002/smll.200800003)
68. Maldiney T, Richard C, Seguin J, Wattier N, Bessodes M, Scherman D (2011) Effect of core diameter, surface coating, and PEG chain length on the biodistribution of persistent luminescence nanoparticles in mice. *ACS Nano* 5(2):854–862. doi:[10.1021/nn101937h](https://doi.org/10.1021/nn101937h)
69. Wang M, Thanou M (2010) Targeting nanoparticles to cancer. *Pharmacol Res* 62(2):90–99. doi:[10.1016/j.phrs.2010.03.005](https://doi.org/10.1016/j.phrs.2010.03.005)
70. Yu MK, Park J, Jon S (2012) Targeting strategies for multifunctional nanoparticles in cancer imaging and therapy. *Theranostics* 2(1):3–44. doi:[10.7150/thno.3463](https://doi.org/10.7150/thno.3463)
71. Wang AZ, Langer R, Farokhzad OC (2012) Nanoparticle Delivery of Cancer Drugs. In: Caskey CT, Austin CP, Hoxie JA (eds) Annual review of medicine, annual reviews, Palo Alto, vol 63, pp 185–198. doi:[10.1146/annurev-med-040210-162544](https://doi.org/10.1146/annurev-med-040210-162544)
72. Yang RH, Chang LW, Wu JP, Tsai MH, Wang HJ, Kuo YC, Yeh TK, Yang CS, Lin P (2007) Persistent tissue kinetics and redistribution of nanoparticles, quantum dot 705, in mice: ICP-MS quantitative assessment. *Environ Health Perspect* 115(9):1339–1343. doi:[10.1289/ehp.10290](https://doi.org/10.1289/ehp.10290)
73. Pericleous P, Gazouli M, Lyberopoulou A, Rizos S, Nikiteas N, Efstathopoulos EP (2012) Quantum dots hold promise for early cancer imaging and detection. *Int J Cancer* 131(3):519–528. doi:[10.1002/ijc.27528](https://doi.org/10.1002/ijc.27528)
74. King-Heiden TC, Wicinski PN, Mangham AN, Metz KM, Nesbit D, Pedersen JA, Hamers RJ, Heideman W, Peterson RE (2009) Quantum dot nanotoxicity assessment using the zebrafish embryo. *Environ Sci Technol* 43(5):1605–1611. doi:[10.1021/es801925c](https://doi.org/10.1021/es801925c)
75. Lewinski N, Colvin V, Drezek R (2008) Cytotoxicity of nanoparticles. *Small* 4(1):26–49. doi:[10.1002/smll.200700595](https://doi.org/10.1002/smll.200700595)
76. Yong KT, Law WC, Hu R, Ye L, Liu LW, Swihart MT, Prasad PN (2013) Nanotoxicity assessment of quantum dots: from cellular to primate studies. *Chem Soc Rev* 42(3):1236–1250. doi:[10.1039/c2cs35392j](https://doi.org/10.1039/c2cs35392j)
77. Xie RG, Chen K, Chen XY, Peng XG (2008) InAs/InP/ZnSe core/shell/shell quantum dots as near-infrared emitters: bright, narrow-band, non-cadmium containing, and biocompatible. *Nano Res* 1(6):457–464. doi:[10.1007/s12274-008-8048-x](https://doi.org/10.1007/s12274-008-8048-x)
78. Gao JH, Chen K, Xie RG, Xie J, Lee S, Cheng Z, Peng XG, Chen XY (2010) Ultrasmall near-infrared non-cadmium quantum dots for in vivo tumor imaging. *Small* 6(2):256–261. doi:[10.1002/smll.200901672](https://doi.org/10.1002/smll.200901672)
79. Choi HS, Liu WH, Liu FB, Nasr K, Misra P, Bawendi MG, Frangioni JV (2010) Design considerations for tumour-targeted nanoparticles. *Nat Nanotechnol* 5(1):42–47. doi:[10.1038/nnano.2009.314](https://doi.org/10.1038/nnano.2009.314)
80. Samir TM, Mansour MMH, Kazmierczak SC, Azzazy HME (2012) Quantum dots: heralding a brighter future for clinical diagnostics. *Nanomedicine* 7(11):1755–1769. doi:[10.2217/nmm.12.147](https://doi.org/10.2217/nmm.12.147)
81. Knapp DW, Adams LG, DeGrand AM, Niles JD, Ramos-Vara JA, Weil AB, O'Donnell MA, Lucroy MD, Frangioni JV (2007) Sentinel lymph node mapping of invasive urinary bladder cancer in animal models using invisible light. *Eur Urol* 52(6):1700–1709. doi:[10.1016/j.eururo.2007.07.007](https://doi.org/10.1016/j.eururo.2007.07.007)
82. Hama Y, Koyama Y, Urano Y, Choyke PL, Kobayashi H (2007) Simultaneous two-color spectral fluorescence lymphangiography with near infrared quantum dots to map two lymphatic flows from the breast and the upper extremity. *Breast Cancer Res Treat* 103(1):23–28. doi:[10.1007/s10549-006-9347-0](https://doi.org/10.1007/s10549-006-9347-0)
83. Parungo CP, Ohnishi S, Kim SW, Kim S, Laurence RG, Soltesz EG, Chen FY, Colson YL, Cohn LH, Bawendi MG, Frangioni JV (2005) Intraoperative identification of esophageal sentinel lymph nodes with near-infrared fluorescence imaging. *J Thorac Cardiovasc Surg* 129(4):844–850. doi:[10.1016/j.jtcvs.2004.08.001](https://doi.org/10.1016/j.jtcvs.2004.08.001)

84. Soltesz EG, Kim S, Kim SW, Laurence RG, De Grand AM, Parungo CP, Cohn LH, Bawendi MG, Frangioni JV (2006) Sentinel lymph node mapping of the gastrointestinal tract by using invisible light. *Ann Surg Oncol* 13(3):386–396. doi:[10.1245/aso.2006.04.025](https://doi.org/10.1245/aso.2006.04.025)
85. Soltesz EG, Kim S, Laurence RG, DeGrand AM, Parungo CP, Dor DM, Cohn LH, Bawendi MG, Frangioni JV, Mihaljevic T (2005) Intraoperative sentinel lymph node mapping of the lung using near-infrared fluorescent quantum dots. *Ann Thorac Surg* 79(1):269–277. doi:[10.1016/j.athoracsur.2004.06.055](https://doi.org/10.1016/j.athoracsur.2004.06.055)
86. Tanaka E, Choi HS, Fujii H, Bawendi MG, Frangioni JV (2006) Image-guided oncologic surgery using invisible light: completed pre-clinical development for sentinel lymph node mapping. *Ann Surg Oncol* 13(12):1671–1681. doi:[10.1245/s10434-006-9194-6](https://doi.org/10.1245/s10434-006-9194-6)
87. Arndt-Jovin DJ, Kantelhardt SR, Carls W, de Vries AHB, Giese A, Jovin TM (2009) Tumor-targeted quantum dots can help surgeons find tumor boundaries. *IEEE Trans Nanobiosci* 8(1):65–71. doi:[10.1109/tmb.2009.2016548](https://doi.org/10.1109/tmb.2009.2016548)
88. Cai WB, Shin DW, Chen K, Gheysens O, Cao QZ, Wang SX, Gambhir SS, Chen XY (2006) Peptide-labeled near-infrared quantum dots for imaging tumor vasculature in living subjects. *Nano Lett* 6(4):669–676. doi:[10.1021/nl052405t](https://doi.org/10.1021/nl052405t)
89. Cai WB, Chen XY (2008) Preparation of peptide-conjugated quantum dots for tumor vasculature-targeted imaging. *Nat Protoc* 3(1):89–96. doi:[10.1038/nprot.2007.478](https://doi.org/10.1038/nprot.2007.478)
90. Li Y, Li Z, Wang XH, Liu FJ, Cheng YS, Zhang BB, Shi DL (2012) In vivo cancer targeting and imaging-guided surgery with near infrared-emitting quantum dot bioconjugates. *Theranostics* 2(8):769–776. doi:[10.7150/thno.4690](https://doi.org/10.7150/thno.4690)
91. Savla R, Taratula O, Garbuzenko O, Minko T (2011) Tumor targeted quantum dot-mucin 1 aptamer-doxorubicin conjugate for imaging and treatment of cancer. *J Control Release* 153(1):16–22. doi:[10.1016/j.jconrel.2011.02.015](https://doi.org/10.1016/j.jconrel.2011.02.015)
92. Li JM, Zhao MX, Su H, Wang YY, Tan CP, Ji LN, Mao ZW (2011) Multifunctional quantum-dot-based siRNA delivery for HPV18 E6 gene silence and intracellular imaging. *Biomaterials* 32(31):7978–7987. doi:[10.1016/j.biomaterials.2011.07.011](https://doi.org/10.1016/j.biomaterials.2011.07.011)
93. Li JM, Wang YY, Zhao MX, Tan CP, Li YQ, Le XY, Ji LN, Mao ZW (2012) Multifunctional QD-based co-delivery of siRNA and doxorubicin to HeLa cells for reversal of multidrug resistance and real-time tracking. *Biomaterials* 33(9):2780–2790. doi:[10.1016/j.biomaterials.2011.12.035](https://doi.org/10.1016/j.biomaterials.2011.12.035)
94. Qi LF, Shao WJ, Shi DL (2013) JAM-2 siRNA intracellular delivery and real-time imaging by proton-sponge coated quantum dots. *J Mater Chem B* 1(5):654–660. doi:[10.1039/c2tb00027j](https://doi.org/10.1039/c2tb00027j)
95. Tan WB, Jiang S, Zhang Y (2007) Quantum-dot based nanoparticles for targeted silencing of HER2/neu gene via RNA interference. *Biomaterials* 28(8):1565–1571. doi:[10.1016/j.biomaterials.2006.11.018](https://doi.org/10.1016/j.biomaterials.2006.11.018)
96. Yezhelyev MV, Qi LF, O'Regan RM, Nie S, Gao XH (2008) Proton-sponge coated quantum dots for siRNA delivery and intracellular imaging. *J Am Chem Soc* 130(28):9006–9012. doi:[10.1021/ja800086u](https://doi.org/10.1021/ja800086u)
97. Fabian J, Nakazumi H, Matsuoka M (1992) Near-infrared absorbing dyes. *Chem Rev* 92(6):1197–1226. doi:[10.1021/cr00014a003](https://doi.org/10.1021/cr00014a003)
98. Dsouza RN, Pischel U, Nau WM (2011) Fluorescent dyes and their supramolecular host/guest complexes with macrocycles in aqueous solution. *Chem Rev* 111(12):7941–7980. doi:[10.1021/cr200213s](https://doi.org/10.1021/cr200213s)
99. Luo SL, Zhang EL, Su YP, Cheng TM, Shi CM (2011) A review of NIR dyes in cancer targeting and imaging. *Biomaterials* 32(29):7127–7138. doi:[10.1016/j.biomaterials.2011.06.024](https://doi.org/10.1016/j.biomaterials.2011.06.024)
100. Leung K (2009) DiD-labeled anti-EpCAM-directed NK-92-scFv (MOC31) zeta cells. In: molecular imaging and contrast agent database (MICAD). Bethesda MD, p Available from:<http://www.ncbi.nlm.nih.gov/books/NBK23559/>
101. Shan L (2009) Near-infrared fluorescence 1,1-dioctadecyl-3,3,3,3-tetramethylindotricarbocyanine iodide (DiR)-labeled macrophages for cell imaging. In: molecular imaging and contrast agent database (MICAD). Bethesda MD, p Available from:<http://www.ncbi.nlm.nih.gov/books/NBK23531/>

102. Mujumdar RB, Ernst LA, Mujumdar SR, Lewis CJ, Waggoner AS (1993) Cyanine dye labeling reagents—sulfoindocyanine succinimidyl esters. *Bioconjug Chem* 4(2):105–111. doi:[10.1021/bc00020a001](https://doi.org/10.1021/bc00020a001)
103. Shcherbo D, Shemiakina, II, Ryabova AV, Luker KE, Schmidt BT, Souslova EA, Gorodnicheva TV, Strukova L, Shidlovskiy KM, Britanova OV, Zaraisky AG, Lukyanov KA, Loschenov VB, Luker GD, Chudakov DM (2010) Near-infrared fluorescent proteins. *Nat Methods* 7(10):827–829. doi:[10.1038/nmeth.1501](https://doi.org/10.1038/nmeth.1501)
104. Sevick-Muraca EM (2012) Translation of near-infrared fluorescence imaging technologies: emerging clinical applications. In: Caskey CT, Austin CP, Hoxie JA (eds) *Annual review of medicine, annual reviews*, Palo Alto, vol 63, pp 217–231. doi:[10.1146/annurev-med-070910-083323](https://doi.org/10.1146/annurev-med-070910-083323)
105. Desmettre T, Devoisselle JM, Mordon S (2000) Fluorescence properties and metabolic features of indocyanine green (ICG) as related to angiography. *Surv Ophthalmol* 45(1):15–27. doi:[10.1016/s0039-6257\(00\)00123-5](https://doi.org/10.1016/s0039-6257(00)00123-5)
106. Matsui A, Tanaka E, Choi HS, Kianzad V, Gioux S, Lomnes SJ, Frangioni JV (2010) Real-time, near-infrared, fluorescence-guided identification of the ureters using methylene blue. *Surgery* 148(1):78–86. doi:[10.1016/j.surg.2009.12.003](https://doi.org/10.1016/j.surg.2009.12.003)
107. Poellinger A, Persigehl T, Mahler M, Bahner M, Ponder SL, Diekmann F, Bremer C, Moesta T (2011) Near-infrared imaging of the breast using omocianine as a fluorescent dye results of a placebo-controlled, clinical. *Multicenter Trial Invest Radiol* 46(11):697–704. doi:[10.1097/RLI.0b013e318229ff25](https://doi.org/10.1097/RLI.0b013e318229ff25)
108. van de Ven S, Wiethoff A, Nielsen T, Brendel B, van der Voort M, Nachabe R, Van der Mark M, Van Beek M, Bakker L, Fels L, Elias S, Luijten P, Mali W (2010) A novel fluorescent imaging agent for diffuse optical tomography of the breast: first clinical experience in patients. *Mol Imaging Biol* 12(3):343–348. doi:[10.1007/s11307-009-0269-1](https://doi.org/10.1007/s11307-009-0269-1)
109. Merian J, Gravier J, Navarro F, Texier I (2012) Fluorescent nanoprobe dedicated to in vivo imaging: from preclinical validations to clinical translation. *Molecules* 17(5):5564–5591. doi:[10.3390/molecules17055564](https://doi.org/10.3390/molecules17055564)
110. Vollrath A, Schubert S, Schubert US (2013) Fluorescence imaging of cancer tissue based on metal-free polymeric nanoparticles—a review. *J Mater Chem B* 1(15):1994–2007
111. Larson N, Ghandehari H (2012) Polymeric conjugates for drug delivery. *Chem Mat* 24(5):840–853. doi:[10.1021/cm2031569](https://doi.org/10.1021/cm2031569)
112. Vrignaud S, Benoit JP, Saulnier P (2011) Strategies for the nanoencapsulation of hydrophilic molecules in polymer-based nanoparticles. *Biomaterials* 32(33):8593–8604. doi:[10.1016/j.biomaterials.2011.07.057](https://doi.org/10.1016/j.biomaterials.2011.07.057)
113. Mai WX, Meng H (2013) Mesoporous silica nanoparticles: a multifunctional nano therapeutic system. *Integr Biol* 5(1):19–28. doi:[10.1039/c2ib20137b](https://doi.org/10.1039/c2ib20137b)
114. Kim J, Kim HS, Lee N, Kim T, Kim H, Yu T, Song IC, Moon WK, Hyeon T (2008) Multifunctional uniform nanoparticles composed of a magnetite nanocrystal core and a mesoporous silica shell for magnetic resonance and fluorescence imaging and for drug delivery. *Angew Chem-Int Edit* 47(44):8438–8441. doi:[10.1002/anie.200802469](https://doi.org/10.1002/anie.200802469)
115. Kumar R, Roy I, Ohulchanskyy TY, Vathy LA, Bergey EJ, Sajjad M, Prasad PN (2010) In vivo biodistribution and clearance studies using multimodal organically modified silica nanoparticles. *ACS Nano* 4(2):699–708. doi:[10.1021/nn901146y](https://doi.org/10.1021/nn901146y)
116. Li JG, Jiang H, Yu ZQ, Xia HY, Zou G, Zhang QJ, Yu Y (2013) Multifunctional uniform core-shell Fe₃O₄@mSiO₂ mesoporous nanoparticles for bimodal imaging and photothermal therapy. *Chem-Asian J* 8(2):385–391. doi:[10.1002/asia.201201033](https://doi.org/10.1002/asia.201201033)
117. Luo T, Huang P, Gao G, Shen GX, Fu S, Cui DX, Zhou CQ, Ren QS (2011) Mesoporous silica-coated gold nanorods with embedded indocyanine green for dual mode X-ray CT and NIR fluorescence imaging. *Opt Express* 19(18):17030–17039
118. Sharma P, Bengtsson NE, Walter GA, Sohn HB, Zhou GY, Iwakuma N, Zeng HD, Grobmyer SR, Scott EW, Moudgil BM (2012) Gadolinium-doped silica nanoparticles encapsulating indocyanine green for near infrared and magnetic resonance imaging. *Small* 8(18):2856–2868. doi:[10.1002/sml.201200258](https://doi.org/10.1002/sml.201200258)

119. Kovtun A, Heumann R, Epple M (2009) Calcium phosphate nanoparticles for the transfection of cells. *Bio-Med Mater Eng* 19(2–3):241–247. doi:[10.3233/bme-2009-0586](https://doi.org/10.3233/bme-2009-0586)
120. Graham FL, Vandereb AJ (1973) New technique for assay of infectivity of human adenovirus 5 DNA. *Virology* 52(2):456–467. doi:[10.1016/0042-6822\(73\)90341-3](https://doi.org/10.1016/0042-6822(73)90341-3)
121. Chen C, Okayama H (1987) High-efficiency transformation of mammalian-cells by plasmid DNA. *Mol Cell Biol* 7(8):2745–2752
122. Tabakovic A, Kester M, Adair JH (2012) Calcium phosphate-based composite nanoparticles in bioimaging and therapeutic delivery applications. *Wiley Interdiscip Rev-Nanomed Nanobiotechnol* 4(1):96–112. doi:[10.1002/wnan.163](https://doi.org/10.1002/wnan.163)
123. Zhang MZ, Ishii A, Nishiyama N, Matsumoto S, Ishii T, Yamasaki Y, Kataoka K (2009) PEGylated calcium phosphate nanocomposites as smart environment-sensitive carriers for siRNA delivery. *Adv Mater* 21(34):3520–3525. doi:[10.1002/adma.200800448](https://doi.org/10.1002/adma.200800448)
124. Giger EV, Leroux JC, Allemann E (2012) Stabilization of calcium phosphate nanoparticles for transfection with nucleic acid drugs. ETH
125. Altinoglu EI, Russin TJ, Kaiser JM, Barth BM, Eklund PC, Kester M, Adair JH (2008) Near-Infrared Emitting Fluorophore-Doped Calcium Phosphate Nanoparticles for In Vivo Imaging of Human Breast Cancer. *ACS Nano* 2(10):2075–2084. doi:[10.1021/nl800448r](https://doi.org/10.1021/nl800448r)
126. Barth BM, Altinoglu EI, Shanmugavelandy SS, Kaiser JM, Crespo-Gonzalez D, DiVittore NA, McGovern C, Goff TM, Keasey NR, Adair JH, Loughran TP, Claxton DF, Kester M (2011) Targeted indocyanine-green-loaded calcium phosphosilicate nanoparticles for in vivo photodynamic therapy of leukemia. *ACS Nano* 5(7):5325–5337. doi:[10.1021/nn2005766](https://doi.org/10.1021/nn2005766)
127. Barth BM, Sharma R, Altinoglu EI, Morgan TT, Shanmugavelandy SS, Kaiser JM, McGovern C, Matters GL, Smith JP, Kester M, Adair JH (2010) Bioconjugation of calcium phosphosilicate composite nanoparticles for selective targeting of human breast and pancreatic cancers in vivo. *ACS Nano* 4(3):1279–1287. doi:[10.1021/nn901297q](https://doi.org/10.1021/nn901297q)
128. Dorozhkin SV (2009) Calcium orthophosphate cements and concretes. *Materials* 2(1):221–291. doi:[10.3390/ma2010221](https://doi.org/10.3390/ma2010221)
129. Yu T, Hubbard D, Ray A, Ghandehari H (2012) In vivo biodistribution and pharmacokinetics of silica nanoparticles as a function of geometry, porosity and surface characteristics. *J Control Release* 163(1):46–54. doi:[10.1016/j.jconrel.2012.05.046](https://doi.org/10.1016/j.jconrel.2012.05.046)
130. Yang PP, Gai SL, Lin J (2012) Functionalized mesoporous silica materials for controlled drug delivery. *Chem Soc Rev* 41(9):3679–3698. doi:[10.1039/c2cs15308d](https://doi.org/10.1039/c2cs15308d)
131. Huang XL, Teng X, Chen D, Tang FQ, He JQ (2010) The effect of the shape of mesoporous silica nanoparticles on cellular uptake and cell function. *Biomaterials* 31(3):438–448. doi:[10.1016/j.biomaterials.2009.09.060](https://doi.org/10.1016/j.biomaterials.2009.09.060)
132. Larson DR, Ow H, Vishwasrao HD, Heikal AA, Wiesner U, Webb WW (2008) Silica nanoparticle architecture determines radiative properties of encapsulated fluorophores. *Chem Mat* 20(8):2677–2684. doi:[10.1021/cm7026866](https://doi.org/10.1021/cm7026866)
133. Burns AA, Vider J, Ow H, Herz E, Penate-Medina O, Baumgart M, Larson SM, Wiesner U, Bradbury M (2009) Fluorescent silica nanoparticles with efficient urinary excretion for nanomedicine. *Nano Lett* 9(1):442–448. doi:[10.1021/nl803405h](https://doi.org/10.1021/nl803405h)
134. Yu T, Greish K, McGill LD, Ray A, Ghandehari H (2012) Influence of geometry, porosity, and surface characteristics of silica nanoparticles on acute toxicity: their vasculature effect and tolerance threshold. *ACS Nano* 6(3):2289–2301. doi:[10.1021/nn2043803](https://doi.org/10.1021/nn2043803)
135. Santos HA, Bimbo LM, Herranz B, Shahbazi MA, Hirvonen J, Salonen J (2013) Nanostructured porous silicon in preclinical imaging: Moving from bench to bedside. *J Mater Res* 28(2):152–164. doi:[10.1557/jmr.2012.271](https://doi.org/10.1557/jmr.2012.271)
136. Tang FQ, Li LL, Chen D (2012) Mesoporous silica nanoparticles: synthesis, biocompatibility and drug delivery. *Adv Mater* 24(12):1504–1534. doi:[10.1002/adma.201104763](https://doi.org/10.1002/adma.201104763)
137. Slowing II, Vivero-Escoto JL, Wu CW, Lin VSY (2008) Mesoporous silica nanoparticles as controlled release drug delivery and gene transfection carriers. *Adv Drug Deliv Rev* 60(11):1278–1288. doi:[10.1016/j.addr.2008.03.012](https://doi.org/10.1016/j.addr.2008.03.012)

138. Slowing I, Trewyn BG, Lin VSY (2006) Effect of surface functionalization of MCM-41-type mesoporous silica nanoparticles on the endocytosis by human cancer cells. *J Am Chem Soc* 128(46):14792–14793. doi:[10.1021/ja0645943](https://doi.org/10.1021/ja0645943)
139. Suma T, Miyata K, Anraku Y, Watanabe S, Christie RJ, Takemoto H, Shioyama M, Gouda N, Ishii T, Nishiyama N, Kataoka K (2012) Smart multilayered assembly for biocompatible siRNA delivery featuring dissolvable silica, endosome-disrupting polycation, and detachable PEG. *ACS Nano* 6(8):6693–6705. doi:[10.1021/nm301164a](https://doi.org/10.1021/nm301164a)
140. Gary-Bobo M, Mir Y, Rouxel C, Brevet D, Basile I, Maynadier M, Vaillant O, Mongin O, Blanchard-Desce M, Morere A, Garcia M, Durand JO, Raehm L (2011) Mannose-functionalized mesoporous silica nanoparticles for efficient two-photon photodynamic therapy of solid tumors. *Angew Chem-Int Edit* 50(48):11425–11429. doi:[10.1002/anie.201104765](https://doi.org/10.1002/anie.201104765)
141. Lee CH, Cheng SH, Wang YJ, Chen YC, Chen NT, Souris J, Chen CT, Mou CY, Yang CS, Lo LW (2009) Near-infrared mesoporous silica nanoparticles for optical imaging: characterization and in vivo biodistribution. *Adv Funct Mater* 19(2):215–222. doi:[10.1002/adfm.200800753](https://doi.org/10.1002/adfm.200800753)
142. Fuller JE, Zugates GT, Ferreira LS, Ow HS, Nguyen NN, Wiesner UB, Langer RS (2008) Intracellular delivery of core-shell fluorescent silica nanoparticles. *Biomaterials* 29(10):1526–1532. doi:[10.1016/j.biomaterials.2007.11.025](https://doi.org/10.1016/j.biomaterials.2007.11.025)
143. Friedman R (2011) Nano dot technology enters clinical trials. *J Natl Cancer Inst* 103(19):1428–1429. doi:[10.1093/jnci/djr400](https://doi.org/10.1093/jnci/djr400)
144. Quan B, Choi K, Kim YH, Kang KW, Chung DS (2012) Near infrared dye indocyanine green doped silica nanoparticles for biological imaging. *Talanta* 99:387–393. doi:[10.1016/j.talanta.2012.05.069](https://doi.org/10.1016/j.talanta.2012.05.069)
145. Kamaly N, Xiao ZY, Valencia PM, Radovic-Moreno AF, Farokhzad OC (2012) Targeted polymeric therapeutic nanoparticles: design, development and clinical translation. *Chem Soc Rev* 41(7):2971–3010. doi:[10.1039/c2cs15344k](https://doi.org/10.1039/c2cs15344k)
146. Graham MM, Menda Y (2011) Radiopeptide imaging and therapy in the United States. *J Nucl Med* 52:56S–63S. doi:[10.2967/jnumed.110.085746](https://doi.org/10.2967/jnumed.110.085746)
147. Sahoo SK, Parveen S, Panda JJ (2007) The present and future of nanotechnology in human health care. *Nanomed-Nanotechnol Biol Med* 3(1):20–31. doi:[10.1016/j.nano.2006.11.008](https://doi.org/10.1016/j.nano.2006.11.008)
148. Northfelt DW, Dezube BJ, Thommes JA, Miller BJ, Fischl MA, Friedman-Kien A, Kaplan LD, Du Mond C, Mamelok RD, Henry DH (1998) Pegylated-liposomal doxorubicin versus doxorubicin, bleomycin, and vincristine in the treatment of AIDS-related Kaposi's sarcoma: results of a randomized phase III clinical trial. *J Clin Oncol* 16(7):2445–2451
149. Gradishar WJ, Tjulandin S, Davidson N, Shaw H, Desai N, Bhar P, Hawkins M, O'Shaughnessy J (2005) Phase III trial of nanoparticle albumin-bound paclitaxel compared with polyethylated castor oil-based paclitaxel in women with breast cancer. *J Clin Oncol* 23(31):7794–7803. doi:[10.1200/jco.2005.04.937](https://doi.org/10.1200/jco.2005.04.937)
150. Gravier J, Navarro FP, Delmas T, Mittler F, Couffin AC, Vinet F, Texier I (2011) Lipidots: competitive organic alternative to quantum dots for in vivo fluorescence imaging. *J Biomed Opt* 16 (9). doi:096013 [10.1117/1.3625405](https://doi.org/10.1117/1.3625405)
151. Pinto-Alphandary H, Andreumont A, Couvreur P (2000) Targeted delivery of antibiotics using liposomes and nanoparticles: research and applications. *Int J Antimicrob Agents* 13(3):155–168. doi:[10.1016/s0924-8579\(99\)00121-1](https://doi.org/10.1016/s0924-8579(99)00121-1)
152. Delmas T, Piraux H, Couffin AC, Texier I, Vinet F, Poulin P, Cates ME, Bibette J (2011) How to prepare and stabilize very small nanoemulsions. *Langmuir* 27(5):1683–1692. doi:[10.1021/la104221q](https://doi.org/10.1021/la104221q)
153. Texier I, Goutayer M, Da Silva A, Guyon L, Djaker N, Jossierand V, Neumann E, Bibette J, Vinet F (2009) Cyanine-loaded lipid nanoparticles for improved in vivo fluorescence imaging. *J Biomed Opt* 14 (5). doi:054005 [10.1117/1.3213606](https://doi.org/10.1117/1.3213606)
154. David S, Carmoy N, Resnier P, Denis C, Misery L, Pitard B, Benoit JP, Passirani C, Montier T (2012) In vivo imaging of DNA lipid nanocapsules after systemic administration in a melanoma mouse model. *Int J Pharm* 423(1):108–115. doi:[10.1016/j.ijpharm.2011.06.031](https://doi.org/10.1016/j.ijpharm.2011.06.031)

155. Qi JP, Lu Y, Wu W (2012) Absorption, disposition and pharmacokinetics of solid lipid nanoparticles. *Curr Drug Metab* 13(4):418–428
156. Buyens K, De Smedt SC, Braeckmans K, Demeester J, Peeters L, van Grunsven LA, du Jeu XD, Sawant R, Torchilin V, Farkasova K, Ogris M, Sanders NN (2012) Liposome based systems for systemic siRNA delivery: stability in blood sets the requirements for optimal carrier design. *J Control Release* 158(3):362–370. doi:[10.1016/j.jconrel.2011.10.009](https://doi.org/10.1016/j.jconrel.2011.10.009)
157. Delmas T, Couffin AC, Bayle PA, de Crecy F, Neumann E, Vinet F, Bardet M, Bibette J, Texier I (2011) Preparation and characterization of highly stable lipid nanoparticles with amorphous core of tuneable viscosity. *J Colloid Interface Sci* 360(2):471–481. doi:[10.1016/j.jcis.2011.04.080](https://doi.org/10.1016/j.jcis.2011.04.080)
158. Navarro FP, Mittler F, Berger M, Josserand V, Gravier J, Vinet F, Texier I (2012) Cell tolerability and biodistribution in mice of indocyanine green-loaded lipid nanoparticles. *J Biomed Nanotechnol* 8(4):594–604. doi:[10.1166/jbn.2012.1422](https://doi.org/10.1166/jbn.2012.1422)
159. Zheng XH, Xing D, Zhou FF, Wu BY, Chen WR (2011) Indocyanine green-containing nanostructure as near infrared dual-functional targeting probes for optical imaging and photothermal therapy. *Mol Pharm* 8(2):447–456. doi:[10.1021/mp100301t](https://doi.org/10.1021/mp100301t)
160. Navarro FP, Berger M, Guillermet S, Josserand V, Guyon L, Neumann E, Vinet F, Texier I (2012) Lipid nanoparticle vectorization of indocyanine green improves fluorescence imaging for tumor diagnosis and lymph node resection. *J Biomed Nanotechnol* 8(5):730–741. doi:[10.1166/jbn.2012.1430](https://doi.org/10.1166/jbn.2012.1430)
161. Zheng CF, Zheng MB, Gong P, Jia DX, Zhang PF, Shi BH, Sheng ZH, Ma YF, Cai LT (2012) Indocyanine green-loaded biodegradable tumor targeting nanoprobe for in vitro and in vivo imaging. *Biomaterials* 33(22):5603–5609. doi:[10.1016/j.biomaterials.2012.04.044](https://doi.org/10.1016/j.biomaterials.2012.04.044)
162. Suganami A, Toyota T, Okazaki S, Saito K, Miyamoto K, Akutsu Y, Kawahira H, Aoki A, Muraki Y, Madono T, Hayashi H, Matsubara H, Omatsu T, Shirasawa H, Tamura Y (2012) Preparation and characterization of phospholipid-conjugated indocyanine green as a near-infrared probe. *Bioorg Med Chem Lett* 22(24):7481–7485. doi:[10.1016/j.bmcl.2012.10.044](https://doi.org/10.1016/j.bmcl.2012.10.044)
163. Kulthe SS, Choudhari YM, Inamdar NN, Mourya V (2012) Polymeric micelles: authoritative aspects for drug delivery. *Des Monomers Polym* 15(5):465–521. doi:[10.1080/1385772x.2012.688328](https://doi.org/10.1080/1385772x.2012.688328)
164. Gardikis K, Micha-Screttas M, Demetzos C, Steele BR (2012) Dendrimers and the development of new complex nanomaterials for biomedical applications. *Curr Med Chem* 19(29):4913–4928
165. De Koker S, Hoogenboom R, De Geest BG (2012) Polymeric multilayer capsules for drug delivery. *Chem Soc Rev* 41(7):2867–2884. doi:[10.1039/c2cs15296g](https://doi.org/10.1039/c2cs15296g)
166. Huh MS, Lee SY, Park S, Lee S, Chung H, Choi Y, Oh YK, Park JH, Jeong SY, Choi K, Kim K, Kwon IC (2010) Tumor-homing glycol chitosan/polyethylenimine nanoparticles for the systemic delivery of siRNA in tumor-bearing mice. *J Control Release* 144(2):134–143. doi:[10.1016/j.jconrel.2010.02.023](https://doi.org/10.1016/j.jconrel.2010.02.023)
167. Samal SK, Dash M, Van Vlierberghe S, Kaplan DL, Chiellini E, van Blitterswijk C, Moroni L, Dubruel P (2012) Cationic polymers and their therapeutic potential. *Chem Soc Rev* 41(21):7147–7194. doi:[10.1039/c2cs35094g](https://doi.org/10.1039/c2cs35094g)
168. Nimesh S, Gupta N, Chandra R (2011) Strategies and advances in nanomedicine for targeted siRNA delivery. *Nanomedicine* 6(4):729–746. doi:[10.2217/nmm.11.15](https://doi.org/10.2217/nmm.11.15)
169. Milla P, Dosio F, Cattel L (2012) PEGylation of proteins and liposomes: a powerful and flexible strategy to improve the drug delivery. *Curr Drug Metab* 13(1):105–119
170. Choi KY, Jeon EJ, Yoon HY, Lee BS, Na JH, Min KH, Kim SY, Myung SJ, Lee S, Chen XY, Kwon IC, Choi K, Jeong SY, Kim K, Park JH (2012) Theranostic nanoparticles based on PEGylated hyaluronic acid for the diagnosis, therapy and monitoring of colon cancer. *Biomaterials* 33(26):6186–6193. doi:[10.1016/j.biomaterials.2012.05.029](https://doi.org/10.1016/j.biomaterials.2012.05.029)
171. Markovsky E, Baabur-Cohen H, Eldar-Boock A, Omer L, Tiram G, Ferber S, Ofek P, Polyak D, Scamparin A, Satchi-Fainaro R (2012) Administration, distribution, metabolism and elimination of polymer therapeutics. *J Control Release* 161(2):446–460. doi:[10.1016/j.jconrel.2011.12.021](https://doi.org/10.1016/j.jconrel.2011.12.021)

172. Wagh A, Jyoti F, Mallik S, Qian S, Leclerc E, Law B (2013) Polymeric nanoparticles with sequential and multiple FRET cascade mechanisms for multicolor and multiplexed imaging. *Small*:n/a-n/a. doi:[10.1002/smll.201202655](https://doi.org/10.1002/smll.201202655)
173. Kim K, Kim JH, Park H, Kim YS, Park K, Nam H, Lee S, Park JH, Park RW, Kim IS, Choi K, Kim SY, Kwon IC (2010) Tumor-homing multifunctional nanoparticles for cancer theragnosis: simultaneous diagnosis, drug delivery, and therapeutic monitoring. *J Control Release* 146(2):219–227. doi:[10.1016/j.jconrel.2010.04.004](https://doi.org/10.1016/j.jconrel.2010.04.004)
174. Tong R, Coyle VJ, Tang L, Barger AM, Fan TM, Cheng JJ (2010) Polylactide nanoparticles containing stably incorporated cyanine dyes for in vitro and in vivo imaging applications. *Microsc Res Tech* 73(9):901–909. doi:[10.1002/jemt.20824](https://doi.org/10.1002/jemt.20824)
175. Lapcik L, De Smedt S, Demeester J, Chabreck P (1998) Hyaluronan: preparation, structure, properties, and applications. *Chem Rev* 98(8):2663–2684
176. Choi KY, Yoon HY, Kim JH, Bae SM, Park RW, Kang YM, Kim IS, Kwon IC, Choi K, Jeong SY, Kim K, Park JH (2011) Smart nanocarrier based on PEGylated hyaluronic acid for cancer therapy. *ACS Nano* 5(11):8591–8599. doi:[10.1021/nn202070n](https://doi.org/10.1021/nn202070n)
177. Choi KY, Chung H, Min KH, Yoon HY, Kim K, Park JH, Kwon IC, Jeong SY (2010) Self-assembled hyaluronic acid nanoparticles for active tumor targeting. *Biomaterials* 31(1):106–114. doi:[10.1016/j.biomaterials.2009.09.030](https://doi.org/10.1016/j.biomaterials.2009.09.030)
178. Choi KY, Min KH, Na JH, Choi K, Kim K, Park JH, Kwon IC, Jeong SY (2009) Self-assembled hyaluronic acid nanoparticles as a potential drug carrier for cancer therapy: synthesis, characterization, and in vivo biodistribution. *J Mater Chem* 19(24):4102–4107. doi:[10.1039/b900456d](https://doi.org/10.1039/b900456d)
179. Choi KY, Min KH, Yoon HY, Kim K, Park JH, Kwon IC, Choi K, Jeong SY (2011) PEGylation of hyaluronic acid nanoparticles improves tumor targetability in vivo. *Biomaterials* 32(7):1880–1889. doi:[10.1016/j.biomaterials.2010.11.010](https://doi.org/10.1016/j.biomaterials.2010.11.010)
180. Swierczewska M, Choi KY, Mertz EL, Huang XL, Zhang F, Zhu L, Yoon HY, Park JH, Bhirde A, Lee S, Chen XY (2012) A facile, one-step nanocarbon functionalization for biomedical applications. *Nano Lett* 12(7):3613–3620. doi:[10.1021/nl301309g](https://doi.org/10.1021/nl301309g)
181. Saxena V, Sadoqi M, Shao J (2006) Polymeric nanoparticulate delivery system for Indocyanine green: biodistribution in healthy mice. *Int J Pharm* 308(1–2):200–204. doi:[10.1016/j.ijpharm.2005.11.003](https://doi.org/10.1016/j.ijpharm.2005.11.003)
182. Ma Y, Sadoqi M, Shao J (2012) Biodistribution of indocyanine green-loaded nanoparticles with surface modifications of PEG and folic acid. *Int J Pharm* 436(1–2):25–31. doi:[10.1016/j.ijpharm.2012.06.007](https://doi.org/10.1016/j.ijpharm.2012.06.007)
183. Miki K, Oride K, Inoue S, Kuramochi Y, Nayak RR, Matsuoka H, Harada H, Hiraoka M, Ohe K (2010) Ring-opening metathesis polymerization-based synthesis of polymeric nanoparticles for enhanced tumor imaging in vivo: synergistic effect of folate-receptor targeting and PEGylation. *Biomaterials* 31(5):934–942. doi:[10.1016/j.biomaterials.2009.10.005](https://doi.org/10.1016/j.biomaterials.2009.10.005)
184. Noh YW, Park HS, Sung MH, Lim YT (2011) Enhancement of the photostability and retention time of indocyanine green in sentinel lymph node mapping by anionic polyelectrolytes. *Biomaterials* 32(27):6551–6557. doi:[10.1016/j.biomaterials.2011.05.039](https://doi.org/10.1016/j.biomaterials.2011.05.039)
185. Mok H, Jeong H, Kim SJ, Chung BH (2012) Indocyanine green encapsulated nanogels for hyaluronidase activatable and selective near infrared imaging of tumors and lymph nodes. *Chem Commun* 48(69):8628–8630. doi:[10.1039/c2cc33555g](https://doi.org/10.1039/c2cc33555g)
186. Park HS, Lee JE, Cho MY, Hong JH, Cho SH, Lim YT (2012) Hyaluronic acid/poly (ss-Amino Ester) polymer nanogels for cancer-cell-specific NIR fluorescence switch. *Macromol Rapid Commun* 33(18):1549–1555. doi:[10.1002/marc.201200246](https://doi.org/10.1002/marc.201200246)
187. Ohnishi S, Lomnes SJ, Laurence RG, Gogbashian A, Mariani G, Frangioni JV (2005) Organic alternatives to quantum dots for intraoperative near-infrared fluorescent sentinel lymph node mapping. *Mol Imaging* 4(3):172–181
188. Moody ED, Viskari PJ, Colyer CL (1999) Non-covalent labeling of human serum albumin with indocyanine green: a study by capillary electrophoresis with diode laser-induced fluorescence detection. *J Chromatogr B* 729(1–2):55–64. doi:[10.1016/s0378-4347\(99\)00121-8](https://doi.org/10.1016/s0378-4347(99)00121-8)

189. Mieog JSD, Troyan SL, Hutteman M, Donohoe KJ, van der Vorst JR, Stockdale A, Liefers GJ, Choi HS, Gibbs-Strauss SL, Putter H, Gioux S, Kuppen PJK, Ashitate Y, Lowik C, Smit V, Oketokoun R, Ngo LH, van de Velde CJH, Frangioni JV, Vahrmeijer AL (2011) Toward optimization of imaging system and lymphatic tracer for near-infrared fluorescent sentinel lymph node mapping in breast cancer. *Ann Surg Oncol* 18(9):2483–2491. doi:[10.1245/s10434-011-1566-x](https://doi.org/10.1245/s10434-011-1566-x)
190. van der Vorst JR, Hutteman M, Gaarenstroom KN, Peters AAW, Mieog JSD, Schaafsma BE, Kuppen PJK, Frangioni JV, van de Velde CJH, Vahrmeijer AL (2011) Optimization of near-infrared fluorescent sentinel lymph node mapping in cervical cancer patients. *Int J Gynecol Cancer* 21(8):1472–1478. doi:[10.1097/IGC.0b013e31822b451d](https://doi.org/10.1097/IGC.0b013e31822b451d)
191. van der Vorst JR, Schaafsma BE, Verbeek FPR, Keereweer S, Jansen JC, van der Velden LA, Langeveld APM, Hutteman M, Lowik C, van de Velde CJH, Frangioni JV, Vahrmeijer AL (2013) Near-infrared fluorescence sentinel lymph node mapping of the oral cavity in head and neck cancer patients. *Oral Oncol* 49(1):15–19. doi:[10.1016/j.oraloncology.2012.07.017](https://doi.org/10.1016/j.oraloncology.2012.07.017)
192. Hutteman M, van der Vorst JR, Gaarenstroom KN, Peters AAW, Mieog JSD, Schaafsma BE, Lowik C, Frangioni JV, van de Velde CJH, Vahrmeijer AL (2012) Optimization of near-infrared fluorescent sentinel lymph node mapping for vulvar cancer. *Am J Obstet Gynecol* 206(1). doi:89.e1 [10.1016/j.ajog.2011.07.039](https://doi.org/10.1016/j.ajog.2011.07.039)
193. Hospital SAeBeCAU (2011) A prospective investigation of the use of the fluorescence imaging on the da Vinci surgical system for intra-operative near infrared imaging of the biliary tree. ClinicalTrials. Gov, Bethesda (MD), National library of medicine (US). <http://www.clinicaltrials.gov/ct2/show/NCT01410734?term=da+Vinci+ICG&rank=1>
194. Center SM (2012) A prospective investigation of the use of fluorescence imaging on the da Vinci surgical system for ultrastaging of endometrial cancer by sentinel node assessment. ClinicalTrials. Gov, Bethesda (MD), National library of medicine (US). <http://www.clinicaltrials.gov/ct2/show/NCT01562106?term=da+Vinci+ICG&rank=3>
195. Center CoHM (2011) A prospective investigation of the use of the fluorescence imaging on the da Vinci surgical system for intraoperative near infrared imaging of renal cortical tumors. ClinicalTrials. Gov, Bethesda (MD), National library of medicine (US). <http://www.clinicaltrials.gov/ct2/show/NCT01281488?term=da+Vinci+ICG&rank=2>
196. Law WC, Yong KT, Roy I, Ding H, Hu R, Zhao WW, Prasad PN (2009) Aqueous-phase synthesis of highly luminescent CdTe/ZnTe core/shell quantum dots optimized for targeted bioimaging. *Small* 5(11):1302–1310. doi:[10.1002/smll.200801555](https://doi.org/10.1002/smll.200801555)
197. Hauck TS, Anderson RE, Fischer HC, Newbigging S, Chan WCW (2010) In vivo quantum-dot toxicity assessment. *Small* 6(1):138–144. doi:[10.1002/smll.200900626](https://doi.org/10.1002/smll.200900626)
198. Ye L, Yong KT, Liu LW, Roy I, Hu R, Zhu J, Cai HX, Law WC, Liu JW, Wang K, Liu J, Liu YQ, Hu YZ, Zhang XH, Swihart MT, Prasad PN (2012) A pilot study in non-human primates shows no adverse response to intravenous injection of quantum dots. *Nat Nanotechnol* 7(7):453–458. doi:[10.1038/nnano.2012.74](https://doi.org/10.1038/nnano.2012.74)
199. Bhirde AA, Kapoor A, Liu G, Iglesias-Bartolome R, Jin A, Zhang G, Xing R, Lee S, Leapman RD, Gutkind JS, Chen X (2012) Nuclear mapping of nanodrug delivery systems in dynamic cellular environments. *ACS Nano*. doi:[10.1021/nn300516g](https://doi.org/10.1021/nn300516g)
200. Wang B, Li Y, Shao C, Tan Y, Cai L (2012) Cadmium and its epigenetic effects. *Curr Med Chem* 19(16):2611–2620
201. Cheng TF, Choudhuri S, Muldoon-Jacobs K (2012) Epigenetic targets of some toxicologically relevant metals: a review of the literature. *J Appl Toxicol* 32(9):643–653. doi:[10.1002/jat.2717](https://doi.org/10.1002/jat.2717)

Chapter 21

Magnetic Nanoparticles for Biomedical Applications: From Diagnosis to Treatment to Regeneration

Yu Gao, Yi Liu and Chenjie Xu

21.1 Introduction

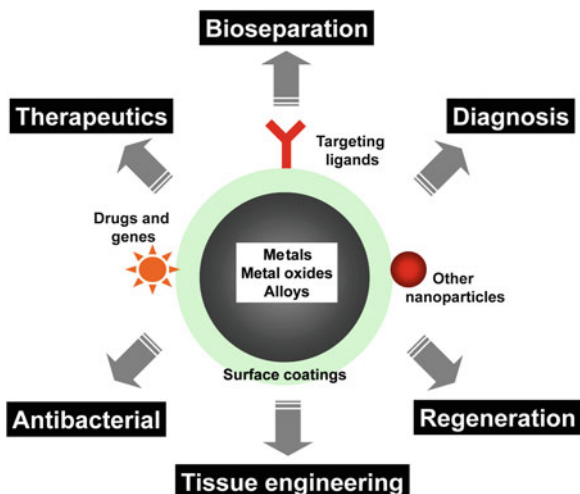
Today, nanotechnology is one of the fastest-growing research and development fields in the world. It brings marvelous technologies and leads revolutions in the fields of energy, electronics, data storage, food, and health care [1–4]. One exciting domain for development is the convergence of nanotechnology and medical applications, or so-called Biomedical Applications of Nanotechnology. By the year 2012, there have been at least 247 applications and products that were approved for clinical studies [5, 6]. The applications include but are not limited to in vitro diagnosis, in vivo imaging/diagnosis, device coating, implantable materials, surgery, drug delivery, and tissue engineering. Nano-dimensioned materials in those applications include liposomes, micelles, inorganic and organic nanoparticles (NPs). Each has its own unique set of properties presenting only in nanoscale, such as the tunable fluorescent emission of semiconductor nanocrystals and switchable magnetic properties of magnetic NPs (MNPs).

Among all nanomaterials, MNPs are one of the most frequently chosen systems for biomedical applications due to their nontoxicity, biocompatibility, and particularly their inducible magnetic moment that allows them to be directed to a defined location or heated with an external alternating current (AC) magnetic field [7–9]. MNPs of controlled composition, size, shape, and surface coating have been developed for specific applications. For example, to improve the magnetic moment and thus the sensitivity of magnetic resonance imaging, researchers have prepared NPs, composing transition metals (e.g., Fe, Co), alloys (e.g., FePt, CoPt, FeCo), and metal oxides (e.g., Fe_3O_4 , $\gamma\text{-Fe}_2\text{O}_3$, CoFe_2O_4) [10–12]. However, considering the stability and biocompatibility, commercialized MNPs for biomedical

Y. Gao · Y. Liu · C. Xu (✉)

Division of Bioengineering, School of Chemical and Biomedical Engineering, Nanyang Technological University, Building N1.3, Level B2, Room 06, 70 Nanyang Drive, Singapore 637457, Singapore
e-mail: cjxu@ntu.edu.sg

Fig. 21.1 Schematic illustrating the biomedical applications of MNPs



applications are mainly iron oxide-based NPs less than 100 nm, which are coated with either inorganic (e.g., gold, silica, hydroxyapatite) or organic (e.g., dextran, polyvinyl alcohol, polyethylene glycol) shells [7]. The coating prevents the particle aggregation caused by both hydrophobic interaction and ferromagnetic behavior. More importantly, NPs with a proper surface coating can be stealthy to immune system (such as reticuloendothelial system, RES) and stay longer in circulation [13]. In the following content, we will briefly overview the latest achievements in the biomedical applications of MNPs (Fig. 21.1).

21.2 Separation of Biological Samples

MNPs functionalized with biologically specific components such as antibodies offer a unique opportunity to control and extract biological samples from a mixture. For the separation of large biological samples such as cells (10–100 μm), magnetic microparticles (above 1 μm) can be used. However, to get close contact with biological entities with smaller size, such as virus (20–450 nm), proteins (5–50 nm), or genes (2 nm wide and 10–100 nm long), materials in the nanodimension (i.e., NPs) are preferred. Moreover, the high surface-to-volume ratio of NPs compared to microparticles allows a higher ratio of labeling with less non-specific binding [14]. Driven by these benefits, MNPs have been utilized to isolate and purify various different biological entities such as proteins, bacteria, and cells.

One of the earliest applications is the protein separation. In proteomics, the purification of native and recombinant proteins is always a time-consuming task. The job is usually performed using variety of chromatography, electrophoresis, ultrafiltration, precipitation, etc. Among them, affinity chromatography is one of the favorite techniques. However, this technique is unable to cope with samples

containing particulate materials, so it is not suitable for early stages of the purification process where suspended solid and fouling components are presented in the sample [15]. Therefore, magnetic separation is attractive because of simple handling, low cost, and high efficiency for crude samples. For example, FePt MNPs functionalized with Ni(II)-chelated nitrilotriacetic acid (NTA-Ni²⁺) showed tight binding to the 6-histidine-tagged proteins, through the 6 coordination sites of the nickel ion. The 6-histidine-tagged protein was easily and rapidly separated from the cell lysate without any pretreatment. Following analysis revealed a high binding capacity of 2–3 mg proteins/1 mg of MNPs, which was about 200 times higher than that of commercial magnetic microbeads [16–18].

Bacteria separation is another exciting application, which was first demonstrated by Gu et al. [19]. Specifically, FePt MNPs were conjugated with vancomycin (Van), which bound to the terminal D-Ala-D-Ala dipeptide of bacterial cell wall precursors. By mixing Van-FePt MNPs with a solution containing Van-sensitive bacteria for 10 min, bacteria–MNPs conjugates could be separated by magnet. The detection limit was 8 cfu/mL for *S. aureus*, 10 cfu/mL for *S. epidermidis* and 4 cfu/mL for coagulase-negative staphylococci, which was comparable to the standard but time-consuming polymerase chain reaction (PCR) assay [19].

The last but not least one is cell capture and isolation such as the isolation of circulating tumor cells (CTCs). CTCs are cancer cells which slough off cancerous tissue and move through the bloodstream to a new site. Thus, they are considered as seeds for metastasis [20]. The presence of CTCs in the peripheral blood has been shown to be associated with decreased progression-free survival and decreased overall survival in patients treated for metastatic breast, colorectal, or prostate cancer. And quantification of CTCs can be used for both the prognosis of cancer metastasis and the reliable surrogate marker of treatment response. One method for the CTC isolation and quantification is the CellSearch[®] system that can specifically and efficiently separate CTCs from other types of cells in blood samples [21]. Typically, blood sample is firstly placed in a tube and centrifuged to removal solid blood from plasma. Then, MNPs conjugated with CTC-specific antibodies (i.e., anti epithelial cell adhesion molecule antibody) are mixed with blood samples for a few minutes before being magnetically separated and washed with buffers. The isolated cells are further stained with cytokeratin monoclonal antibodies (stain CTCs), CD45 monoclonal antibodies (stained leukocytes which may contaminate the sample), and DAPI (stain nuclei of both CTCs and leukocytes). Finally, CTCs are identified with positive signals for both cytokeratin and DAPI [21].

21.3 Diagnosis

Early, accurate, and in-time diagnoses of diseases are critical to prevent the deterioration, to identify the effective and efficient treatment, to evaluate the efficacy of treatment, to improve the quality of patient life, and to reduce the cost of treatment. With functionalized MNPs, disease progression can be examined by

using *ex vivo* bioassays (colorimetric immunoassay and magnetic immunoassay) and/or *in vivo* imaging like magnetic resonance imaging (MRI).

21.3.1 Magnetic Immunoassay

Magnetic immunoassay (MIA) is a novel type of diagnostic assay, which utilizes MNPs as labels instead of conventional radioisotopes (radioimmunoassay), fluorescent dyes (fluorescent immunoassay), substrates and enzymes (enzyme-linked immunosorbent assay, ELISA). MNPs are usually conjugated with an antigen or antibody for the recognition of interested molecules. The binding between MNPs and interested molecules causes the clustering of MNPs, which results in an increase of magnetic moment for the detection [22, 23]. For example, Lee et al. [23] developed a handheld diagnostic magnetic resonance (DMR) system, which consisted of planar microcoils, microfluidic channels, and a portable magnet. It used T_2 relaxation time as detection signal, and could be performed in turbid samples (e.g., blood, urine, and sputum) with few or no preparation steps. In a recent report, they determined the accuracy of the DMR system by comparing its performance to a large benchtop NMR relaxometer. In addition to the smaller sample volume required (~ 5 μL for DMR vs. 300 μL for NMR relaxometer), the DMR system showed a mass detection limit improvement of two orders of magnitude (1 ng vs. 80 ng for avidin detection). This technology could also be extended for the detection of bacteria, cancer cells, and protein biomarkers with a high mass detection sensitivity (more than 800-fold improvement relative to a benchtop relaxometer). The sensitivity could be further improved by preparing new classes of water-soluble MNPs with higher magnetization [23].

21.3.2 Colorimetric Immunoassay

Colorimetric immunoassay quantifies the analytes through absorbance generated from a color reaction between substrates and enzymes. One of the most widely used enzymes is peroxidase, which catalyzes the oxidation of organic substrates and produces a color change for detection. Peroxidase enzymes and their mimics contain Fe^{2+} and Fe^{3+} in the reaction centers, which is essential for the catalytic activity. Although MNPs like Fe_3O_4 NPs have been conjugated with horseradish peroxidase (HRP) to introduce peroxidase activity in a number of applications including commercially available magnetic ELISA kits, their peroxidase-like activity has been ignored for a long time. Until recently, Fe_3O_4 NPs have been reported to possess intrinsic peroxidase-like activity. In the presence of H_2O_2 , all different sizes (30, 150, and 300 nm) of Fe_3O_4 MNPs catalyzed the reaction and produced a blue color for substrate 3,3',5,5'-tetramethylbenzidine (TMB), a brown color for diazoaminobenzene (DAB), and an orange color for *o*-phenylenediamine

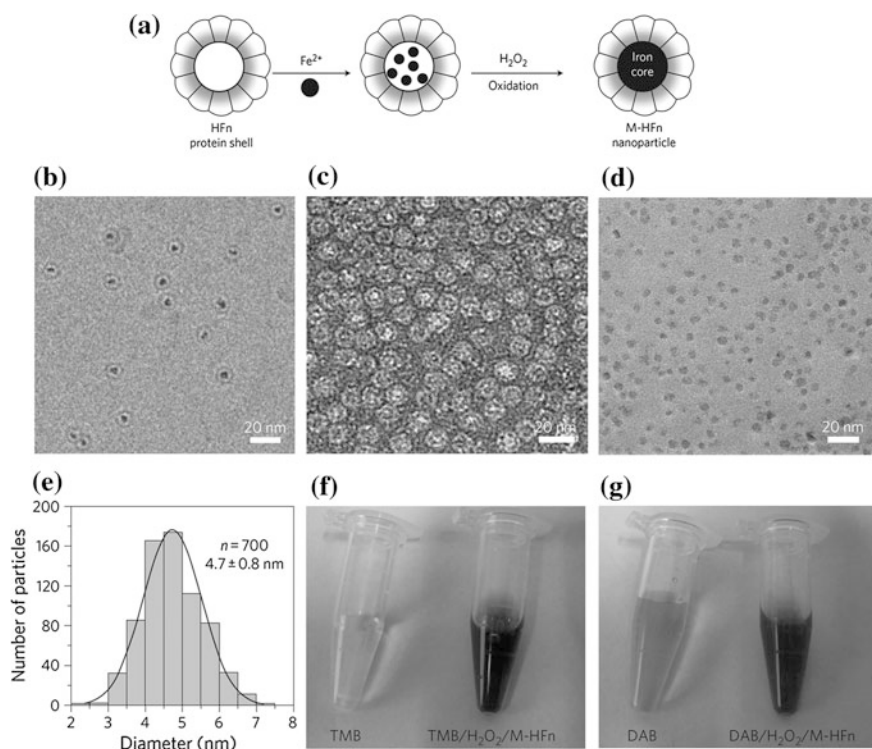
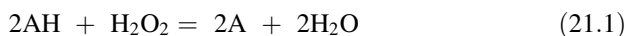


Fig. 21.2 Preparation and characterization of M-HFn NPs. **a** Schematic showing the preparation of M-HFn NPs and their structure. **b** CryoTEM image of M-HFn NPs. **c**, **d** TEM images of protein shells (**c**) and iron oxide cores (**d**). HFfn protein shells were negatively stained with uranyl acetate for TEM observations, and iron oxide cores in HFfn were unstained. **e** Size distribution of iron oxide cores, with a median diameter of 4.7 ± 0.8 nm. **f**, **g** Characterization of peroxidase activity of M-HFn NPs. M-HFn catalyzed the oxidation of peroxidase substrates TMB (**f**) and DAB (**g**) in the presence of H_2O_2 to give a colored product. Recreated with kind permission of (© 2012 Macmillan Publishers Limited) [25]

(OPD) [24]. If AH represents the substrate, which is a hydrogen donor, the mechanism of the catalytic reaction could be written as follow:



Through a series of studies, the peroxidase-like activity of Fe_3O_4 MNPs was found to be H_2O_2 , pH, and temperature dependent. Meanwhile, the reaction followed Michaelis–Menten kinetics. Two formats of immunoassay based on this concept have been performed to detect hepatitis B virus surface antigen and cardiac troponin I (a biomarker for myocardial infarction) [24].

More recently, the peroxidase-like activity of Fe_3O_4 MNPs was used for targeting and visualizing tumor tissues. Magnetoferritin (M-HFn) NPs were prepared by encapsulating iron oxide NPs inside a HFfn shell. The schematic process is shown in Fig. 21.2a. TEM images (Fig. 21.2b–d) are shown a core–shell structure

with a 4.7-nm core of iron oxide (Fig. 21.2e). The color reactions are shown in Fig. 21.2f, g. The HFn protein shell could specifically bind to tumor cells that overexpressed transferring receptor 1 (TfR1). These M-HFn NPs allowed to the visualization of the tumor tissue through the peroxidase-like activity of iron oxide core without any additional recognition ligands on their surface. This strategy simplified the modification process of conventional NPs and prevented nonspecific binding induced by an excess of ligands on the NP surface; 474 clinical specimens from patients with nine types of cancers were examined. They confirmed that M-HFn NPs could distinguish cancerous cells from normal cells with a sensitivity (positive/cases) of 98 % and a specificity (negative/cases) of 95 % [25].

21.3.3 Magnetic Resonance Imaging

MRI is a noninvasive imaging modality that has been widely used in clinical diagnosis [26]. This technique is based on the property that the magnetization of hydrogen protons in human body will be aligned around an applied external magnetic field. The presence of MNPs shortens the spin–spin relaxation time and thus produces a negative (decreased) signal in T_2 - and T_2^* -weighted MR images [27]. Therefore, by labeling the interested cells/tissues with MNPs, we can visualize them noninvasively. So far, MNPs have been applied as MRI contrast agents to improve the sensitivity of detection and diagnosis of major diseases including cancers, cardiovascular diseases, and diabetes which in total account for nearly 2 of every 3 deaths in the USA—close to 1.5 million people in the year 2001.

In cancer prognosis, the status of lymph node is an independent adverse prognostic factor. The enlargement of lymph node usually indicates the potential malignancy or metastasis [28]. Given that intravenously or subcutaneously injected MNPs would be taken up by lymph nodes by means of interstitial-lymphatic fluid transport, we can label lymph nodes with MNPs for cancer diagnosis with MRI. In 2003, 80 patients with presurgical clinical stages T1, T2, or T3 prostate cancer were examined by MRI before and 24 h after the intravenous administration of MNPs. The imaging results were correlated with histological findings; 71.4 % of nodes did not fulfill the usual imaging criteria for malignancy. MNPs have effectively identified small (with a diameter of 5–10 mm) and otherwise undetectable lymph node metastases in patients with prostate cancer [28].

Besides cancer, MNPs are also used in the diagnosis of the cardiovascular diseases such as myocardial injury, atherosclerosis, and vascular disease [29]. The wash-in kinetics of MNPs, which are normally confined to the intravascular space, can be used to demarcate the area of myocardium at risk. The hyperacute stage of myocardial injury increases the capillary permeability and hyperemia, which finally enhances the contrast of the injured areas [30]. To prevent the wash-out of MNPs from acutely injured myocardium, an active ligand binding which achieves specific targeted imaging is also highly promising [31]. Atherosclerosis is another cardiovascular condition in which an artery wall thickens as a result of the

accumulation of fatty materials and formation of multiple plaques within the arteries. Long-circulating MNPs are able to penetrate an atherosclerotic plaque and then taken up by the macrophage [32]. Thus, plaque macrophage content could be gauged by MRI for atherosclerosis diagnosis. In addition, MNPs labeled with linear peptides (screened by phage display) can specifically bind to the vascular adhesion molecule-1 (VCAM-1), which is expressed on vascular endothelium. These VCAM-1-targeted MNPs have been demonstrated as sensitive contrast agents for detection of VCAM-1 expression in the aortic roots of statin-treated mice [33].

Diabetes is another major health and development challenge of the twenty-first century. Worldwide, there are already more than 360 million people with diabetes and another 280 million at identifiably high risk of developing diabetes. One major type of diabetes is type 1 diabetes (3–5 % of diabetes globally) is an autoimmune disease that destroys the insulin-producing cells (beta cells) of the pancreas. The initial immune infiltration, termed insulinitis, starts many years before the development of type 1 diabetes (T1D) and progresses slowly until a critical mass of beta cells has been annihilated. In the progress of immune infiltration, lymphocytes migrate to the pancreas and destroy beta cells. Thus, pancreatic biopsy is one approach to diagnose insulinitis but has been resisted by patients due to its invasiveness. A more attractive alternative to biopsy is provided by noninvasive MRI imaging, in which microvascular leakage was taken as an indicator of inflammation [34]. Specifically, Denis and colleagues developed long-circulating magnetofluorescent NPs with half-lives of over 10 h in blood vessel for both fluorescent and MR imaging, which could follow the microvascular changes accompanying inflammation. Results from mouse showed a positive correlation in magnetofluorescent NPs accumulation in the pancreas and insulinitis aggressivity [34]. With this technology, the same group could predict the onset of diabetes (from 6 to 10 weeks) in nonobese diabetic (NOD) mice [35]. In general, MNPs-based imaging holds potential as a useful tool for performing long-term, longitudinal studies of the progression of diabetes in humans.

21.4 Therapeutics

21.4.1 MNPs as Carriers for Drugs and Genes

Targeted drug delivery using MNPs was first proposed in the late 1970s and has been one of the most desirable applications of MNPs for chemotherapy [14]. Following the early studies of Widder and Senyi, the efficacy of this approach was demonstrated in numerous small animal studies and even resulted in a small number of clinical trials. However, despite these efforts and achievements, this technique has yet to develop into a workable clinical application.

One of the reasons is the low payload capacity of existing MNPs because payload (i.e., drugs) can only be attached on the surface or embedded in the double-layer coating around MNPs. To address this issue, a novel platform of engineered Fe_3O_4 porous hollow NPs (HMNPs) was designed for the controlled release of cisplatin. Specifically, cisplatin was encapsulated in the interior cavities, and the targeting agent, Herceptin, was attached on the surface of MNPs. These NPs could then efficiently target and deliver cisplatin to ErbB2-/Neu-positive breast cancer cells (SK-BR-3). The percentage of loaded cisplatin was improved from 4.82 % of Fe_3O_4 MNPs to 24.8 % of Fe_3O_4 HMNPs. Meanwhile, the pores were subject to acid etching in low pH environment and subsequently facilitated cisplatin release. The amount of cisplatin released when $\text{pH} < 6$ was more than 3 times compared to a release in neutral physiological conditions. Once HMNPs were internalized to the endosomes/lysosomes, pH-sensitive pores were further opened up to accelerate the cisplatin release and finally kill the cancer cells [36].

Besides the effort of improving the drug loading efficiency, another focus is to integrate drug delivery and molecular imaging into the same system. For example, dumbbell-shaped Au- Fe_3O_4 NPs were synthesized (Fig. 21.3a, b) and conjugated with cisplatin complexes to serve as a multifunctional platform for targeted cisplatin delivery (Fe_3O_4 part) and optical imaging (Au part) [37, 38]. Herceptin was immobilized onto Fe_3O_4 through PEG3000-CONH-Herceptin to offer specific SK-BR-3 cell targeting ability. While cisplatin complexes were attached onto Au side by reacting with Au-S- $\text{CH}_2\text{CH}_2\text{N}(\text{CH}_2\text{COOH})_2$. Reflection images of SK-BR-3 and MCF-7 cells after incubation with the same concentration of cisplatin-Au- Fe_3O_4 -Herceptin NPs (Fig. 21.3d, e) showed the specificity and efficacy of these NPs. Au- Fe_3O_4 NPs did not inhibit cell growth at tested Fe concentration. However, once coupled with cisplatin, these NPs showed remarkable cytotoxicity with a low half-maximal inhibitory concentration (IC_{50}) toward SK-BR-3 cells of 1.76 $\mu\text{g}/\text{mL}$ of Pt (Fig. 21.3f) compared to free cisplatin needed (3.5 $\mu\text{g}/\text{mL}$ of Pt). This methodology was expected to have a great potential to function as nanovehicles for highly sensitive diagnostic and highly efficient therapeutic applications [38].

Finally, MNPs could also deliver peptide/protein, oligonucleotide, plasmid, etc. One example is magnetofection which uses magnetic field to concentrate MNPs containing nucleic acids into cells. MNPs can be incorporated into viral or nonviral platforms to facilitate gene delivery. Recently, recombinant adeno-associated virus 2 (rAAV) was conjugated onto MNPs to achieve therapeutic levels of transgene expression. This platform enhanced the transfection efficacy. The same level of transfection seen with free vector can be achieved using 1 % of vector conjugated MNPs [39]. For nonviral deliver systems, MNPs can be coated with polyethyleneimine (PEI) or polyethylene glycol-grafted PEI (to reduce cytotoxicity of PEI), which allows the efficient loading and protection of genes and holds a great potential for advanced gene delivery and therapy [40].

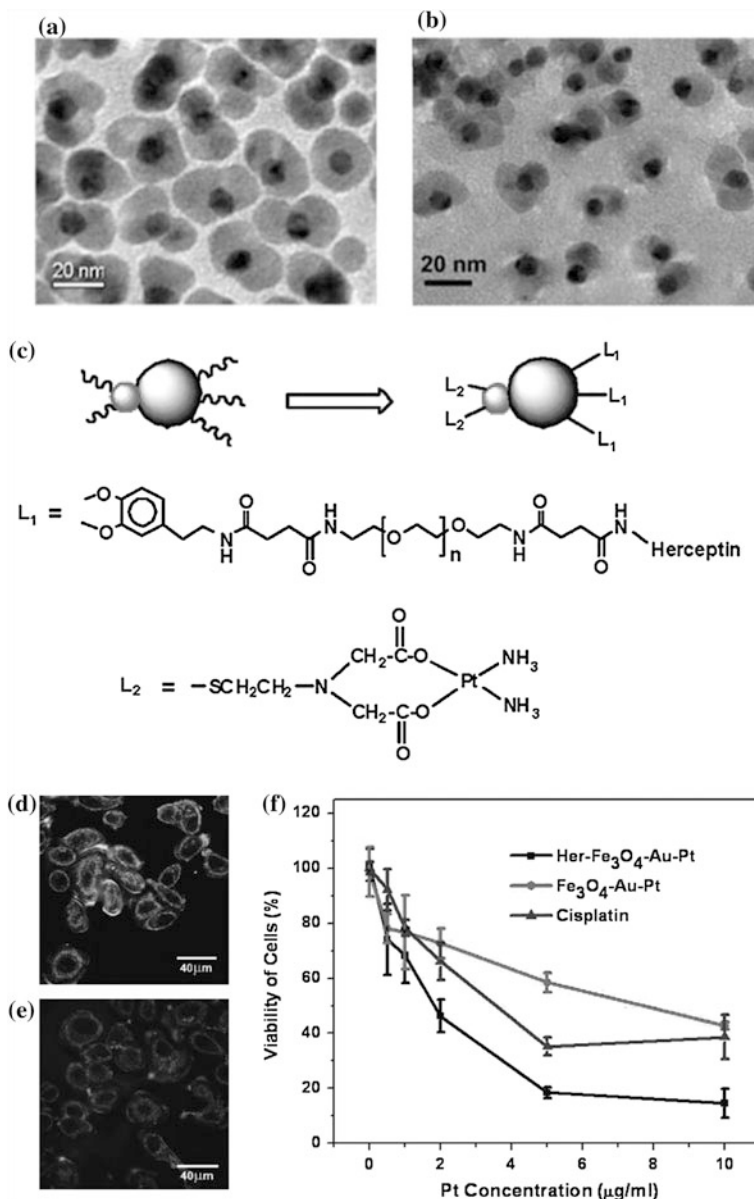


Fig. 21.3 **a, b** TEM images of the 8–20 nm dumbbell-like Au-Fe₃O₄ NPs before **(a)** and after **(b)** surface modification. **c** Schematic illustration of dumbbell-like NPs coupled with Herceptin and a cisplatin complex for target-specific cisplatin delivery. **d, e** Reflection images of SK-BR-3 **(d)** and MCF-7 cells **(e)** after incubation with the same concentration of cisplatin-Au-Fe₃O₄-Herceptin NPs. **f** Viability of Sk-Br3 cells after incubation with platinum-Au-Fe₃O₄ NPs, platinum-Au-Fe₃O₄-Herceptin NPs, and free cisplatin. Recreated with kind permission of (© 2008 Wiley-VCH Verlag GmbH and Co. KGaA, Weinheim), [37] and (© 2009 American Chemical Society) [38]

21.4.2 MNPs for Iron Deficiency

Deficiencies of iron (Fe) and zinc (Zn) are major health problems globally, affecting 2 billion populations [41]. Fe deficiency causes anemia, while Zn deficiency impairs the growth and immune function. As Fe and Zn deficiencies usually coexist, therapeutics containing two elements are suitable for both nutritional addition and anemia treatment [41].

Currently, the only iron powder recommended by World Health Organization (WHO) for anemia is electrolytic iron. However, the bioavailability still need to be further improved [42]. Reducing the size of low-solubility Fe-containing compounds to nanoscale is a promising way to improve their bioavailability. A type of poorly water-soluble nanosized Fe and Fe/Zn compounds (~ 11 nm) was made by scalable flame aerosol technology. They were demonstrated to be approximately 40–80 % more bioavailable than electrolytic iron in rat without tissue accumulation. Meanwhile, their low solubility reduces the unpleasant color and taste of conventional ferrous sulfate. The mixed Fe/Zn ratio could be further adjusted to meet the specific need of individual patients [42].

Another type of MNPs for the treatment of iron deficiency anemia is ferumoxytol, which is used in both Europe and the USA for the adult patients with chronic kidney disease (CKD). This intravenously administered drug was prepared by coating carbohydrate shell onto superparamagnetic iron oxide NPs. In a phase III clinical trails, ferumoxytol was more effective than oral iron in patients with CKD, with mild or moderate adverse effects. Local injection-site reactions were considered as the most common adverse effects, while serious hypersensitivity or hypotensive reactions were uncommon [43].

21.4.3 Hyperthermia with MNPs for Cancer Therapy

Hyperthermia is a method that uses heat to treat cancer. Cancer cells undergo apoptosis or necrosis after the heat treatment above 41 °C [44]. It has been demonstrated that cancer cells are more susceptible to heat due to their high metabolism rates. Hence, hyperthermia is very promising for cancer therapy [7].

MNPs can generate heat under an alternating magnetic filed based on Brown relaxation (friction generated from particle oscillation) and Neél relaxation (rotation of magnetic moment with each field oscillation) [45]. MNP-aided hyperthermia for cancer therapy is particular promising due to noninvasiveness and no limitation of penetration depth of magnetic field. This method also provides MR imaging for particle tracking and platform for combined chemotherapy (MNPs conjugated with other medicines). Numerous laboratory research works have been published in this field [45, 46].

In 2007, a clinical study of MNP-aided hyperthermia for glioblastoma multiforme therapy was conducted by Maier-Hauff and colleagues [47]. The aminosilane-coated superparamagnetic iron oxide (SPIO) NPs (diameter of 15 nm) were dispersed in water with an iron concentration of 112 mg/mL and then intratumorally injected to the tumor at doses of 0.1–0.7 mL per mL tumor volume. Then, patients received the heat treatment at magnetic field strengths of 3.8–13.5 kA/m using an alternating magnetic field applicator MFH[®] 300 F. MRI and computed tomography (CT) were used to calculate the heat distribution within the tumor accompanying applied magnetic field strength. All patients in this study could tolerate the injection of NPs without any complication. The researchers believed that deep cranial hyperthermia therapy using MNPs could be safely applied on glioblastoma multiforme patients [47].

21.5 Antibacterial Application

Medical device-related infections occur frequently and have raised deep concerns due to an increasing prevalence world widely. One cause is the formation of biofilm that is due to the adherence of bacteria onto medical devices followed by the formation of a matrix of proteins, DNA, and extra polysaccharide. The generation of biofilm protects pathogenic bacteria from antibiotics and causes chronic infections [48]. Ideal antibacterial agents must locally destroy bacteria without being toxic to the surrounding tissue. Silver NPs are recognized as promising antimicrobial agents due to their significant antibacterial activity. However, there are two drawbacks with these particles: their toxic effects on human cells and their low yield for penetration through the bacterial biofilms. Hence, researchers believe that using MNPs to carry antibacterial agents (such as TiO₂, ZnO, MgO, silver, and copper) will achieve targeted antibacterial (by external magnetic field) effect and eradication of bacterial biofilms.

Silver NPs are promising candidates to fight against resistant pathogens. Two types of core-shell NPs, Ag@Fe₃O₄, and γ -Fe₂O₃@Ag, were synthesized [49]. Both NPs exhibited significant antibacterial and antifungal activities, with minimum inhibition concentrations (MIC) from 15.6 mg/L to 125 mg/L against ten tested bacterial strains, and from 1.9 to 31.3 mg/L against four candida species. Moreover, the cytotoxicity against mice embryonic fibroblasts was relative low, with MIC of 430 mg/L for Ag@Fe₃O₄ and 292 mg/L for γ -Fe₂O₃@Ag. These NPs have been proposed for targeted magnetic delivery of silver NPs for disinfection applications. Recently, SPIO NPs conjugated with Fe, Zn, and Ag, respectively, through a chelation process (involving dimercaptosuccinic acid and metal ions) were found to reduce biofilm formation and planktonic growth [49]. Successful fighting against antibacterial resistance has also been demonstrated in an engineered nanocrystal comprising a magnetic core and a silver ring with a ligand gap [50].

21.6 Tissue Engineering

Organ shortage has been a growing problem globally due to the increasing incidences of organ failure and the scarcity of organ donors. Recent advances in tissue engineering (TE) provide a promising technology to overcome this problem for organ transplantations. TE strategy consists of multidisciplinary fields that integrate knowledge of engineering, biology, and medicine. It aims to replace, repair, restore diseased tissues, and improve the quality of lives of patients [51].

The idea of using MNPs for bone tissue engineering was first explored by Pareta et al. [52]. First, different MNPs with drug coatings were synthesized and injected into porous bone sites. The drug-coated MNPs were then directed to and attached on the bone tissue under an applied magnetic field. Results showed that γ - Fe_2O_3 NPs significantly promoted osteoblast density (cell per well) after five and eight days compared to Fe_3O_4 NPs and control groups. When coated with hydroxyapatite (HA, the main inorganic component of bone), γ - Fe_2O_3 NPs effectively promoted the osteoblast proliferation after 1 day [52]. Although the mechanism was still not well understood, the researchers believed that adsorption of some specific proteins (such as vitronectin and fibronectin) on nanoscale surfaces enhanced the adhesion of osteoblast, which might be essential for promoting cell functions.

To date, the main problem of tissue-engineered constructs is lack of structural complexity. In order to reproduce complex tissues with functional constructs, well-defined spatial cell organization is required. Although cell patterning methods such as microcontact printing and lithography have been developed, they need specialized surfaces and prolonged procedures. Consequently, using an external force such as electric field, optical trap, and magnetic field for spatial cell patterning may be an alternative and simple approach. Ino and colleagues labeled cells with 10 nm magnetite NPs using cationic liposomes as carriers. When steel plates placed on a magnet were positioned under a cell culture surface, the magnetically labeled cells aligned with the steel plates. Complex cell patterns (curved, parallel, or crossing patterns) were successfully fabricated, and human umbilical vein endothelial cells were patterned on matrigel, thereby forming patterned capillaries [53]. Based on the same concept, a three-dimensional multicellular assembly of tunable size and controlled geometry for tissue engineering was constructed using magnetic patterning. Human endothelial progenitor cells and mouse macrophages were labeled with anionic citrate-coated iron oxide NPs. By tuning the magnetic field gradient geometry and intensity, the magnetic cellular load, and the number of cells, they demonstrated that magnetic force-assisted cell seeding provided effective cell seeding into 3D porous scaffolds [54].

21.7 Regenerative Medicine

Stem cell-based cell therapy holds great promise for patients living with serious and currently incurable diseases including cancers, Alzheimer's disease, Parkinson's disease, and diabetes. These potentials of stem cells rely on their remarkable properties of self-renewal and differentiation into diverse specialized cells, offering hopes for the regeneration of tissues/organs for replacing diseased and damaged areas in the body. While preclinical results are promising, few treatments have been translated to humans due to conflicting results. It is in part due to the lack of a comprehensive understanding of the fate, distribution, and the function of transplanted stem cells in the local microenvironment [55]. Thus, noninvasive imaging methods are highly needed to monitor transplanted stem cells qualitatively and quantitatively.

The application of MNPs for regenerative medicine is based on the noninvasive nature of MRI for transplanted stem cells. MRI provides excellent soft tissue contrast with high resolution and can be used for visualization of single cells against a homogeneous background. Usually, iron oxide NPs were loaded into stem cells by passive internalization. The introduction of surface coatings or target ligands may further increase the uptake by cells. There are plenty of researches on stem cell tracking by MNP-aided MRI methodology [56, 57]. However, the main drawback of this technology is lack of information of cellular function after transplantation. This is common for all imaging techniques employing exogenous labeling agents that continue to display contrast when cells are dying. Hence, a nanosensor based on MNPs for detecting cellular function as well as tracking by MRI will be highly attractive.

21.8 Challenges

Although holding great promise of MNPs in biomedical applications, there are still problems should be addressed before translating into clinical settings. First, currently most magnetic controllers consist of a permanent magnet, which is placed near the target site. As reported, this method can only penetrate a tissue depth of 8–12 cm [58]. The development of new type of magnetic control system as well as synthesis of MNPs with high magnetic moment may solve this problem. To improve the magnetic moment, other metal ions (Mn^{2+} , Co^{2+} , or Ni^{2+}) are doped into the spinel structure of ferrite. High magnetic moment metallic MNPs (alloys) are also promising to achieve large magnetic moment. Second, clinical MRI diagnosis is restricted to its low resolution and sensitivity. Other NP components such as Au NPs and carbon nanotubes responsible for different imaging modalities should also be combined into one MNP unit to improve the sensitivity and accuracy of MRI. Third, to improve the therapeutic efficacy, hollow MNPs are designed to load more drugs both inside and outside the NPs. At last, before MNPs

can be used practically as probes or carriers for diagnostic and therapeutic applications, their biodistribution and metabolism need to be better understood. Once they complete the task, MNPs should be eliminated by biological system without any other bad effects. The long-term effect of MNPs on biological system should also be studied.

References

1. Rosi NL, Mirkin CA (2005) Nanostructures in biodiagnostics. *Chem Rev* 105(4):1547–1562. doi:[10.1021/cr030067f](https://doi.org/10.1021/cr030067f)
2. Heath JR, Kuekes PJ, Snider GS, Williams RS (1998) A defect-tolerant computer architecture: opportunities for nanotechnology. *Science* 280(5370):1716–1721. doi:[10.1126/science.280.5370.1716](https://doi.org/10.1126/science.280.5370.1716)
3. Peer D, Karp JM, Hong S, FaroKhazad OC, Margalit R, Langer R (2007) Nanocarriers as an emerging platform for cancer therapy. *Nat Nanotechnol* 2(12):751–760. doi:[10.1038/nnano.2007.387](https://doi.org/10.1038/nnano.2007.387)
4. Kamat PV (2008) Quantum dot solar cells. Semiconductor nanocrystals as light harvesters. *J Phys Chem C* 112(48):18737–18753. doi:[10.1021/jp806791s](https://doi.org/10.1021/jp806791s)
5. Etheridge ML, Campbell SA, Erdman AG, Haynes CL, Wolf SM, McCullough J (2013) The big picture on nanomedicine: the state of investigational and approved nanomedicine products. *Nanomed-Nanotechnol Biol Med* 9(1):1–14. doi:[10.1016/j.nano.2012.05.013](https://doi.org/10.1016/j.nano.2012.05.013)
6. Wagner V, Dullaart A, Bock AK, Zweck A (2006) The emerging nanomedicine landscape. *Nat Biotechnol* 24(10):1211–1217. doi:[10.1038/nbt1006/1211](https://doi.org/10.1038/nbt1006/1211)
7. Tran N, Webster TJ (2010) Magnetic nanoparticles: biomedical applications and challenges. *J Mater Chem* 20(40):8760–8767. doi:[10.1039/c0jm00994f](https://doi.org/10.1039/c0jm00994f)
8. Xu C, Sun S (2012) New forms of superparamagnetic nanoparticles for biomedical applications. *Adv Drug Deliv Rev*. doi:[10.1016/j.addr.2012.10.008](https://doi.org/10.1016/j.addr.2012.10.008)
9. Xu CJ, Sun SH (2009) Superparamagnetic nanoparticles as targeted probes for diagnostic and therapeutic applications. *Dalton Trans* 29:5583–5591. doi:[10.1039/b900272n](https://doi.org/10.1039/b900272n)
10. Hao R, Xing RJ, Xu ZC, Hou YL, Gao S, Sun SH (2010) Synthesis, functionalization, and biomedical applications of multifunctional magnetic nanoparticles. *Adv Mater* 22(25):2729–2742. doi:[10.1002/adma.201000260](https://doi.org/10.1002/adma.201000260)
11. Jun YW, Choi JS, Cheon J (2006) Shape control of semiconductor and metal oxide nanocrystals through nonhydrolytic colloidal routes. *Angew Chem-Int Edit* 45(21):3414–3439. doi:[10.1002/anie.200503821](https://doi.org/10.1002/anie.200503821)
12. Jun YW, Lee JH, Cheon J (2008) Chemical design of nanoparticle probes for high-performance magnetic resonance imaging. *Angew Chem-Int Edit* 47(28):5122–5135. doi:[10.1002/anie.200701674](https://doi.org/10.1002/anie.200701674)
13. Berry CC, Curtis ASG (2003) Functionalisation of magnetic nanoparticles for applications in biomedicine. *J Phys D-Appl Phys* 36(13):R198–R206. doi:[10.1088/0022-3727/36/13/203](https://doi.org/10.1088/0022-3727/36/13/203)
14. Pankhurst QA, Connolly J, Jones SK, Dobson J (2003) Applications of magnetic nanoparticles in biomedicine. *J Phys D-Appl Phys* 36(13):R167–R181. doi:[10.1088/0022-3727/36/13/201](https://doi.org/10.1088/0022-3727/36/13/201)
15. Safarik I, Safarikova M (2004) Magnetic techniques for the isolation and purification of proteins and peptides. *Biomagn Res Technol* 2(1):7
16. Gu HW, Xu KM, Xu CJ, Xu B (2006) Biofunctional magnetic nanoparticles for protein separation and pathogen detection. *Chem Commun* 9:941–949. doi:[10.1039/b514130c](https://doi.org/10.1039/b514130c)
17. Xu CJ, Xu KM, Gu HW, Zhong XF, Guo ZH, Zheng RK, Zhang XX, Xu B (2004) Nitrotri-acetic acid-modified magnetic nanoparticles as a general agent to bind histidine-tagged proteins. *J Am Chem Soc* 126(11):3392–3393. doi:[10.1021/ja031776d](https://doi.org/10.1021/ja031776d)

18. Xu CJ, Xu KM, Gu HW, Zheng RK, Liu H, Zhang XX, Guo ZH, Xu B (2004) Dopamine as a robust anchor to immobilize functional molecules on the iron oxide shell of magnetic nanoparticles. *J Am Chem Soc* 126(32):9938–9939. doi:[10.1021/ja0464802](https://doi.org/10.1021/ja0464802)
19. Gu HW, Ho PL, Tsang KWT, Wang L, Xu B (2003) Using biofunctional magnetic nanoparticles to capture vancomycin-resistant enterococci and other gram-positive bacteria at ultralow concentration. *J Am Chem Soc* 125(51):15702–15703. doi:[10.1021/ja0359310](https://doi.org/10.1021/ja0359310)
20. Williams SCP (2013) Circulating tumor cells. *Proc Natl Acad Sci USA* 110(13):4861. doi:[10.1073/pnas.1304186110](https://doi.org/10.1073/pnas.1304186110)
21. de Bono JS, Scher HI, Montgomery RB, Parker C, Miller MC, Tissing H, Doyle GV, Terstappen L, Pienta KJ, Raghavan D (2008) Circulating tumor cells predict survival benefit from treatment in metastatic castration-resistant prostate cancer. *Clin Cancer Res* 14(19):6302–6309. doi:[10.1158/1078-0432.ccr-08-0872](https://doi.org/10.1158/1078-0432.ccr-08-0872)
22. Nikitin MP, Torno M, Chen H, Rosengart A, Nikitin PI (2008) Quantitative real-time in vivo detection of magnetic nanoparticles by their nonlinear magnetization. *J Appl Phys* 103(7). doi:[10.1063/1.283094](https://doi.org/10.1063/1.283094)
23. Lee H, Sun E, Ham D, Weissleder R (2008) Chip-NMR biosensor for detection and molecular analysis of cells. *Nat Med* 14(8):869–874. doi:[10.1038/nm.1711](https://doi.org/10.1038/nm.1711)
24. Gao LZ, Zhuang J, Nie L, Zhang JB, Zhang Y, Gu N, Wang TH, Feng J, Yang DL, Perrett S, Yan X (2007) Intrinsic peroxidase-like activity of ferromagnetic nanoparticles. *Nat Nanotechnol* 2(9):577–583. doi:[10.1038/nnano.2007.260](https://doi.org/10.1038/nnano.2007.260)
25. Fan KL, Cao CQ, Pan YX, Lu D, Yang DL, Feng J, Song LN, Liang MM, Yan XY (2012) Magnetoferritin nanoparticles for targeting and visualizing tumour tissues. *Nat Nanotechnol* 7(7):459–464. doi:[10.1038/nnano.2012.90](https://doi.org/10.1038/nnano.2012.90)
26. Sun C, Lee JSH, Zhang MQ (2008) Magnetic nanoparticles in MR imaging and drug delivery. *Adv Drug Deliv Rev* 60(11):1252–1265. doi:[10.1016/j.addr.2008.03.018](https://doi.org/10.1016/j.addr.2008.03.018)
27. Xu C, Mu L, Roes I, Miranda-Nieves D, Nahrendorf M, Ankrum JA, Zhao W, Karp JM (2011) Nanoparticle-based monitoring of cell therapy. *Nanotechnology* 22(49):494001. doi:[10.1088/0957-4484/22/49/494001](https://doi.org/10.1088/0957-4484/22/49/494001)
28. Harisinghani MG, Barentsz J, Hahn PF, Deserno WM, Tabatabaei S, van de Kaa CH, de la Rosette J, Weissleder R (2003) Noninvasive detection of clinically occult lymph-node metastases in prostate cancer. *N Engl J Med* 348(25):2491–2495. doi:[10.1056/NEJMoa022749](https://doi.org/10.1056/NEJMoa022749)
29. Sosnovik DE, Nahrendorf M, Weissleder R (2007) Molecular magnetic resonance imaging in cardiovascular medicine. *Circulation* 115(15):2076–2086. doi:[10.1161/circulationaha.106.658930](https://doi.org/10.1161/circulationaha.106.658930)
30. Krombach GA, Wendland MF, Higgins CB, Saeed M (2002) MR imaging of spatial extent of microvascular injury in reperfused ischemically injured rat myocardium: value of blood pool ultrasmall superparamagnetic particles of iron oxide. *Radiology* 225(2):479–486. doi:[10.1148/radiol.2252011512](https://doi.org/10.1148/radiol.2252011512)
31. Sosnovik DE, Schellenberger EA, Nahrendorf M, Novikov MS, Matsui T, Dai G, Reynolds F, Grazette L, Rosenzweig A, Weissleder R, Josephson L (2005) Magnetic resonance imaging of cardiomyocyte apoptosis with a novel magneto-optical nanoparticle. *Magn Reson Med* 54(3):718–724. doi:[10.1002/mrm.20617](https://doi.org/10.1002/mrm.20617)
32. Jaffer FA, Libby P, Weissleder R (2006) Molecular and cellular imaging of atherosclerosis—Emerging applications. *J Am Coll Cardiol* 47(7):1328–1338. doi:[10.1016/j.jacc.2006.01.029](https://doi.org/10.1016/j.jacc.2006.01.029)
33. Nahrendorf M, Jaffer FA, Kelly KA, Sosnovik DE, Aikawa E, Libby P, Weissleder R (2006) Noninvasive vascular cell adhesion molecule-1 imaging identifies inflammatory activation of cells in atherosclerosis. *Circulation* 114(14):1504–1511. doi:[10.1161/circulationaha.106.646380](https://doi.org/10.1161/circulationaha.106.646380)
34. Denis MC, Mahmood U, Benoist C, Mathis D, Weissleder R (2004) Imaging inflammation of the pancreatic islets in type 1 diabetes. *Proc Natl Acad Sci USA* 101(34):12634–12639. doi:[10.1073/pnas.040437101](https://doi.org/10.1073/pnas.040437101)

35. Fu WX, Wojtkiewicz G, Weissleder R, Benoist C, Mathis D (2012) Early window of diabetes determinism in NOD mice, dependent on the complement receptor CR1g, identified by noninvasive imaging. *Nat Immunol* 13(4):361–368. doi:[10.1038/ni.2233](https://doi.org/10.1038/ni.2233)
36. Cheng K, Peng S, Xu CJ, Sun SH (2009) Porous hollow Fe₃O₄ nanoparticles for targeted delivery and controlled release of cisplatin. *J Am Chem Soc* 131(30):10637–10644. doi:[10.1021/ja903300f](https://doi.org/10.1021/ja903300f)
37. Xu C, Xie J, Ho D, Wang C, Kohler N, Walsh EG, Morgan JR, Chin YE, Sun S (2008) Au–Fe₃O₄ dumbbell nanoparticles as dual-functional probes. *Angew Chem-Int Edit* 47(1):173–176. doi:[10.1002/anie.200704392](https://doi.org/10.1002/anie.200704392)
38. Xu C, Wang B, Sun S (2009) Dumbbell-like Au-Fe₃O₄ Nanoparticles for target-specific platinum delivery. *J Am Chem Soc* 131(12):4216–4217. doi:[10.1021/ja900790v](https://doi.org/10.1021/ja900790v)
39. Mah C, Fraites TJ, Zolotukhin I, Song SH, Flotte TR, Dobson J, Batich C, Byrne BJ (2002) Improved method of recombinant AAV2 delivery for systemic targeted gene therapy. *Mol Ther* 6(1):106–112. doi:[10.1006/mthe.2001.0636](https://doi.org/10.1006/mthe.2001.0636)
40. Kievit FM, Veiseh O, Bhattarai N, Fang C, Gunn JW, Lee D, Ellenbogen RG, Olson JM, Zhang MQ (2009) PEI-PEG-chitosan-copolymer-coated iron oxide nanoparticles for safe gene delivery: synthesis, complexation, and transfection. *Adv Funct Mater* 19(14):2244–2251. doi:[10.1002/adfm.200801844](https://doi.org/10.1002/adfm.200801844)
41. Hilty FM, Teleki A, Krumeich F, Buchel R, Hurrell RF, Pratsinis SE, Zimmermann MB (2009) Development and optimization of iron- and zinc-containing nanostructured powders for nutritional applications. *Nanotechnology* 20(47). doi:[47510110.1088/0957-4484/20/47/475101](https://doi.org/47510110.1088/0957-4484/20/47/475101)
42. Hilty FM, Arnold M, Hilbe M, Teleki A, Knijnenburg JTN, Ehrensperger F, Hurrell RF, Pratsinis SE, Langhans W, Zimmermann MB (2010) Iron from nanocompounds containing iron and zinc is highly bioavailable in rats without tissue accumulation. *Nat Nanotechnol* 5(5):374–380. doi:[10.1038/nnano.2010.79](https://doi.org/10.1038/nnano.2010.79)
43. McCormack PL (2012) Ferumoxytol in iron deficiency anaemia in adults with chronic kidney disease. *Drugs* 72(15):2013–2022
44. Hildebrandt B, Wust P, Ahlers O, Dieing A, Sreenivasa G, Kerner T, Felix R, Riess H (2002) The cellular and molecular basis of hyperthermia. *Crit Rev Oncol/Hematol* 43(1):33–56. doi:[10.1016/s1040-8428\(01\)00179-2](https://doi.org/10.1016/s1040-8428(01)00179-2)
45. Cherukuri P, Glazer ES, Curley SA (2010) Targeted hyperthermia using metal nanoparticles. *Adv Drug Deliv Rev* 62(3):339–345. doi:[10.1016/j.addr.2009.11.006](https://doi.org/10.1016/j.addr.2009.11.006)
46. Pankhurst QA, Thanh NTK, Jones SK, Dobson J (2009) Progress in applications of magnetic nanoparticles in biomedicine. *J Phys D-Appl Phys* 42(22). doi:[22400110.1088/0022-3727/42/22/224001](https://doi.org/22400110.1088/0022-3727/42/22/224001)
47. Maier-Hauff K, Rothe R, Scholz R, Gneveckow U, Wust P, Thiesen B, Feussner A, von Deimling A, Waldoefner N, Felix R, Jordan A (2007) Intracranial thermotherapy using magnetic nanoparticles combined with external beam radiotherapy: results of a feasibility study on patients with glioblastoma multiforme. *J Neuro-Oncol* 81(1):53–60. doi:[10.1007/s11060-006-9195-0](https://doi.org/10.1007/s11060-006-9195-0)
48. Hajipour MJ, Fromm KM, Ashkarran AA, de Aberasturi DJ, de Larramendi IR, Rojo T, Serpooshan V, Parak WJ, Mahmoudi M (2012) Antibacterial properties of nanoparticles. *Trends Biotechnol* 30(10):499–511. doi:[10.1016/j.tibtech.2012.06.004](https://doi.org/10.1016/j.tibtech.2012.06.004)
49. Taylor EN, Kummer KM, Durmus NG, Leuba K, Tarquinio KM, Webster TJ (2012) Superparamagnetic iron oxide nanoparticles (SPION) for the treatment of antibiotic-resistant biofilms. *Small* 8(19):3016–3027. doi:[10.1002/sml.201200575](https://doi.org/10.1002/sml.201200575)
50. Mahmoudi M, Serpooshan V (2012) Silver-coated engineered magnetic nanoparticles are promising for the success in the fight against antibacterial resistance threat. *ACS Nano* 6(3):2656–2664. doi:[10.1021/nn300042m](https://doi.org/10.1021/nn300042m)
51. Khademhosseini A, Langer R, Borenstein J, Vacanti JP (2006) Microscale technologies for tissue engineering and biology. *Proc Natl Acad Sci USA* 103(8):2480–2487. doi:[10.1073/pnas.0507681102](https://doi.org/10.1073/pnas.0507681102)

52. Pareta RA, Taylor E, Webster TJ (2008) Increased osteoblast density in the presence of novel calcium phosphate coated magnetic nanoparticles. *Nanotechnology* 19(26). doi:[10.1088/0957-4484/19/26/265101](https://doi.org/10.1088/0957-4484/19/26/265101)
53. Ino K, Ito A, Honda H (2007) Cell patterning using magnetite nanoparticles and magnetic force. *Biotechnol Bioeng* 97(5):1309–1317. doi:[10.1002/bit.21322](https://doi.org/10.1002/bit.21322)
54. Frasca G, Gazeau F, Wilhelm C (2009) Formation of a three-dimensional multicellular assembly using magnetic patterning. *Langmuir* 25(4):2348–2354. doi:[10.1021/la8030792](https://doi.org/10.1021/la8030792)
55. Gao Y, Cui Y, Chan JK, Xu C (2013) Stem cell tracking with optically active nanoparticles. *Am J Nucl Med Mol Imaging* 3(3):232
56. Bulte JWM, Duncan ID, Frank JA (2002) In vivo magnetic resonance tracking of magnetically labeled cells after transplantation. *J Cereb Blood Flow Metab* 22(8):899–907
57. Bulte JWM, Kraitchman DL (2004) Iron oxide MR contrast agents for molecular and cellular imaging. *NMR Biomed* 17(7):484–499. doi:[10.1002/nbm.924](https://doi.org/10.1002/nbm.924)
58. Neuberger T, Schopf B, Hofmann H, Hofmann M, von Rechenberg B (2005) Superparamagnetic nanoparticles for biomedical applications: possibilities and limitations of a new drug delivery system. *J Magn Magn Mater* 293(1):483–496. doi:[10.1016/j.jmmm.2005.01.064](https://doi.org/10.1016/j.jmmm.2005.01.064)

Chapter 22

Engineering Upconversion Nanoparticles for Biomedical Imaging and Therapy

Feng Chen, Wenbo Bu, Weibo Cai and Jianlin Shi

22.1 Introduction

Upconversion nanoparticle (UCNP) has gained growing interests owing to their unique upconversion luminescence (UCL) features that are highly suitable for multimodal imaging in living subjects [1]. UCL is a unique process where low-energy continuous wave (CW) of near infrared (NIR) light is converted to higher energy light (emission bands ranging from ultraviolet [UV] to NIR region) through the sequential absorption of multiple photons or energy transfer [2]. After excitation using a 980 nm laser, UCNP could exhibit attractive optical features such as sharp emission lines [3], long lifetimes (\sim ms) [4], large anti-Stokes shift [3], superior photostability [5], high detection sensitivity [6], nonblinking and nonbleaching [5, 7], high tissue penetration depth [8], minimal photodamage [9], and extremely low auto-fluorescence [10]. Moreover, by doping with well-selected lanthanide ions of Gd^{3+} , Er^{3+}/Yb^{3+} and Tm^{3+}/Yb^{3+} (or combination of these ions) in suitable crystal hosts (e.g., $NaYF_4$), magnetic resonance (MR) and multicolor UCL imaging could be readily achieved [7, 11–13]. With the presence of heavy metal ions like Gd^{3+} , Yb^{3+} , and Lu^{3+} in $NaYF_4$ matrix, such UCNP has also been considered as an intrinsic computed tomography (CT) contrast agent recently [14–16]. Importantly, in comparison with traditional optical imaging agents, such as organic dyes and quantum dots (QDs), UCNP excludes the potential UV photodamage and has low imaging background, high tissue penetration depth, and relatively low toxicity [1, 17].

F. Chen · W. Bu · J. Shi (✉)

State Key Laboratory of High Performance Ceramics and Superfine Microstructure,
Shanghai Institute of Ceramics, Chinese Academy of Sciences, Shanghai 200050,
People's Republic of China
e-mail: jlshi@mail.sic.ac.cn

W. Bu

e-mail: wbbu@mail.sic.ac.cn

W. Cai

Departments of Radiology, University of Wisconsin, Madison, Wisconsin, USA

Besides using UCNP as molecular imaging agents, loading UCNP with certain anticancer drugs (e.g., doxorubicin [DOX]) or photosensitizers (PSs) could further render attractive imaging-integrated chemotherapy or improved photodynamic therapy [18, 19]. All of these have made UCNP one of the most promising nanoparticles for future cancer imaging and therapy.

Here, we summarized the recent advances in engineering of UCNP for controlled size and morphology, tunable optical and surface properties, well-designed multiple imaging modalities, and integrated therapeutic functionality. Particle size, shape, surface properties, optical features of UCNP are extremely important for biological applications. The traditional synthetic strategies for the synthesis and surface modifications of high-quality UCNP will be briefly covered with our focus on some newly developed strategies for synthesizing ultrasmall UCNP with excellent up-conversion property. Particularly, progress in engineering of UCNPs as multimodal molecular imaging probes will be reviewed in detail. We will also describe a few successful examples of *in vitro* and *in vivo* cancer therapy by using UCNP-based theranostic agents. Finally, we will discuss the present obstacles and future research directions in engineering of UCNP for biological imaging and therapy.

22.2 Engineering the Size and Morphology of UCNP

Uniform size and suitable morphology of UCNP could play a significant role in biological applications. So far, control and synthesis of UCNPs with tunable size (from sub-10 to over 100 nm) and various morphologies (such as nanospheres, nanocubes, nanorods, and nanoplates) have already been well-documented and are on longer a big challenge [1]. Oleic acid-assisted hydrothermal reaction and thermal decomposition are two of the most popular methods for the synthesis of various kinds of UCNPs with controlled size and morphology [20–22]. Recently, a user-friendly solvo thermal method has also been developed and been accepted as the most adopted strategy for not only single UCNP cores but core@multi-shell high-quality hexagonal-phase UCNPs [23, 24]. In this section, we focus our interest in reviewing newly developed strategies for synthesizing small UCNP with excellent UC properties.

Ultrasmall nanoparticle (<10 nm) with suitable surface modifications could become an attractive imaging probe which could not only target to tumor *in vivo*, but also potentially be cleared from kidney within reasonable time [25, 26]. Recent research showed that the absolute quantum yield (QY) of UCNP is relatively low and size-dependent [27]. Typically, 100 nm-sized UCNP could have a QY of about 0.3 %, and owing to the significantly increased surface defects in these ultrasmall UCNPs, it would suffer from a significant decrease to 0.005 % after decreasing the size down to ~ 10 nm [27].

Wang et al. have offered an interesting solution by introducing the co-doping of gadolinium (Gd^{3+}) ions in $NaYF_4:Er/Yb$ nanocrystals [28]. They demonstrated theoretically and experimentally that doping $NaYF_4:Er/Yb$ with defined amount of Gd^{3+} ion could simultaneously allow precise control over the phase (from cubic to

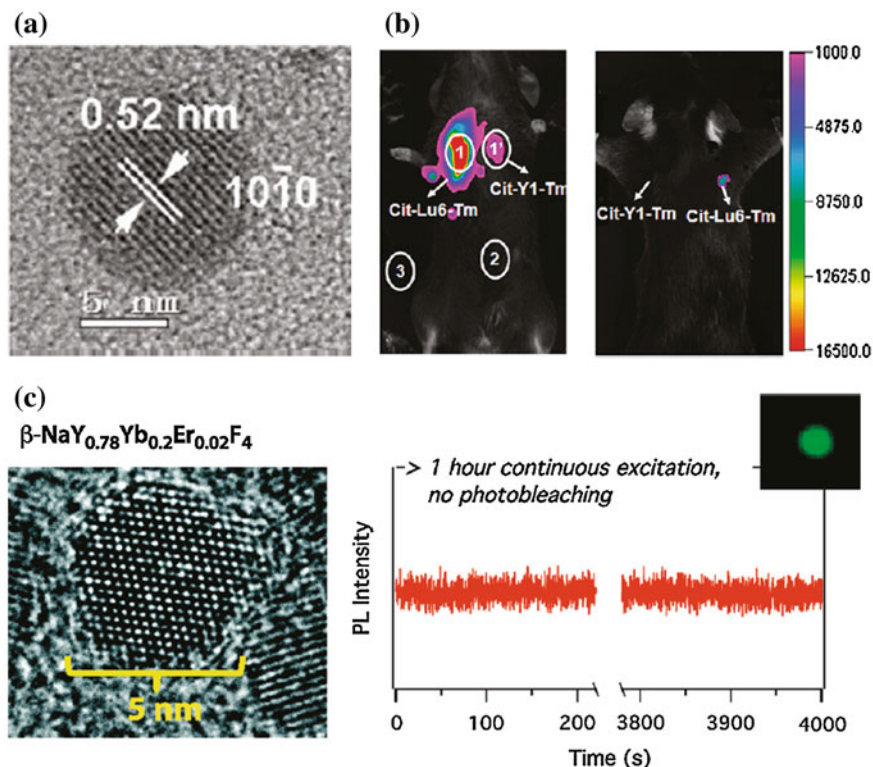


Fig. 22.1 **a** TEM image of ~ 8 nm-sized β -NaLuF₄:Gd/Yb/Tm. **b** In vivo imaging of a black mouse after subcutaneous injection of citric acid-modified sub-10 nm-sized β -NaLuF₄:Gd³⁺/Yb³⁺/Tm³⁺ and citric acid-modified β -NaYF₄:Yb/Tm when detected from the chest side (*left*) or the back side (*right*). **c** *Left* TEM image of β -NaYF₄:Yb/Er. *Right* The time trace of emission intensity from a single UCNP under continuous laser illumination for over 1 h (Recreated with kind permission of American Chemical Society [29, 46])

hexagonal), size (down to sub-10 nm), and UCL efficiency [28]. Inspired by this work, Liu et al. reported a greatly enhanced UCL efficiency in ~ 8 nm-sized β -NaLuF₄:Gd/Yb/Tm nanocrystals simply by replacing crystal host of NaYF₄ for NaLuF₄ (Fig. 22.1a) [29]. As-synthesized ultrasmall UCNP displayed bright UCL with a QY estimated to be 0.47 ± 0.06 %, which is even higher than the previously reported 100 nm-sized NaYF₄:Er/Yb (QY = 0.3 ± 0.1 %) [27]. The authors have further demonstrated an impressive in vivo deep tissue imaging (Fig. 22.1b) and attributed such greatly enhanced UCL in small UCNPs to the presence of hexagonal phase and successful suppression of nonradiative processes.

Besides improving the optical property of small UCNP either by altering the doping strategy or changing the crystal hosts, epitaxial growth of a protective shell represents the second technique for reducing the surface defects and improving the UCL property [30, 31]. However, successful synthesis of sub-10 nm-sized

core@shell-structured UCNP has not been achieved until very recently. By changing the concentration of basic surfactants, $Y^{3+}:F^{-}$ ratio and reaction temperature, Ostrowski et al. have succeeded in synthesizing core@shell-structured hexagonal-phase $NaYF_4:Yb/Er@NaYF_4$ with a diameter less than 10 nm [32]. As-synthesized smaller UCNP were extremely stable and exhibited no measurable photobleaching or blinking (Fig. 22.1c).

Although, the engineering of ultrasmall UCNPs for biological imaging and therapy is still at its early stage, they are expected to play a vital role in designing tumor-targeted imaging probe that could be efficiently cleared from body. To date, most of researchers are still interested in developing core@shell-structured UCNPs with particle size ranging from 10 to 50 nm for biological imaging applications.

22.3 Engineering of UCNP for Biological Imaging

22.3.1 Engineering the Surface for Water-Soluble UCNPs

With the superior UCL properties and suitable surface modification and functionalization, UCNP has been demonstrated as a promising candidate of traditional imaging agents (e.g., QDs and organic dyes). Surface engineering is the first and a vital step before any biological imaging of UCNP. Although oleic acid-assisted strategy could guarantee high-quality UCNPs with uniform size and morphology, as-synthesized UCNPs are always coated with a layer of oleic acid ligands, which makes UCNPs water insoluble. So far methods used for engineering water-soluble UCNPs include ligand exchange (or removal) [33, 34], ligand oxidation reaction [35], layer-by-layer method [36], hydrophobic–hydrophobic interaction [37], host-guest interaction [38], and silanization [39].

22.3.2 Homemade In Vivo Imaging System for UCNP

One of the obstacles in developing UCNP for biological imaging applications lies in the lack of 980 nm excitation source in nearly all of the commercially available confocal microscopes and in vivo imaging systems. To date, all of the in vitro and in vivo UCNP imaging researches are completed by using homemade (or modified) imaging systems [5, 6, 40].

Nyk et al. reported the first whole-body in vivo imaging of UCNP in mouse [40]. As-synthesized UCNPs (i.e., $NaYF_4:Tm/Yb$) were excited at 975 nm by a defocused emission from a fiber-coupled laser diode. An emission filter (cut off at 850 nm) was used to keep the 975 nm excitation light of the imaging CCD camera. Images were collected and processed by using Maestro GNIR FLEX fluorescence imaging system (CRI). After dosing the Balb-c mouse with

NaYF₄:Tm/Yb (200 μ L of 2 mg/mL in water with 5 % glucose), a high-contrast signal from UCNPs could successfully be detected both through the skin and after dissection of the animal (Fig. 22.2a).

In a separated study, Xiong et al. reported an improved UCNP in vivo imaging setup by adding two CW 980 nm lasers, Andor DU897 EMCCD and filters to a Kodak in vivo imaging system [10]. The successful in vivo UCNP imaging has been demonstrated in U87MG and MCF-7 tumors bearing nude mice. After intravenous (i.v.) injection of RGD-labeled NaYF₄:Er/Tm/Yb (\sim 50 μ g/mouse), the mice were illuminated with two beam-expanded 980 nm lasers. A cooled EMCCD camera was then used to record the 800 nm emission of UCNPs and images were processed using Kodak molecular imaging software. As shown in Fig. 22.2b, under excitation of 980 nm laser, intense UCL signal could be observed in the U87MG tumor, while no significant signal could be seen in the MCF-7 tumor, indicating the targeted tumor uptake of UCNPs in U87MG. A high signal-to-noise (\sim 24) between tumor and the background has been achieved in this study.

Besides modifying commercially available in vivo imaging systems by adding extra 980 nm laser and suitable filters, combining digital single-lens reflex (DSLR) camera and suitable optical filters might represent the simplest way to carry out an in vivo UCNP imaging experiment [41, 42]. Park et al. have built an in vivo UCNP imaging system by using a fiber-coupled 980 nm laser, a Nikon D90 DSLR camera, certain optical filters, and a dark box. The authors managed to image the tumor uptake of UCNP-Ce6 in nude mouse with their system [41]. Possibly because of the limited light coverage of 980 nm laser on mice, only signal from tumor site could be seen from the images (Fig. 22.2c). Also, since green light from UCNP could only have very limited tissue penetration depth, better in vivo images could be achieved by altering the system for detecting strong NIR (800 nm) or red (657 nm) emissions from UCNP.

22.3.3 Engineering of UCNP for Excellent NIR and Red Emissions

22.3.3.1 Strategies for Improving the NIR-Band Emission

Red and NIR light could have much deeper tissue penetration depth compared with UV and other visible light (e.g., blue and green light). Typically, UCL of UCNP is known to have multiple emission bands with various optical intensities after 980 nm excitation. For example, the emissions of NaYF₄:Er/Yb/Tm nanoparticles include UV (330–350 nm, 350–370 nm), blue (390–420 nm, 440–460 nm, 460–500 nm), green (510–530 nm, 530–570 nm), red (630–660 nm), and NIR (770–810 nm) bands [17]. Recently, there has been an increasing focus on the design and synthesis of UCNPs with tunable UC emission from UV to near-infrared (NIR) through

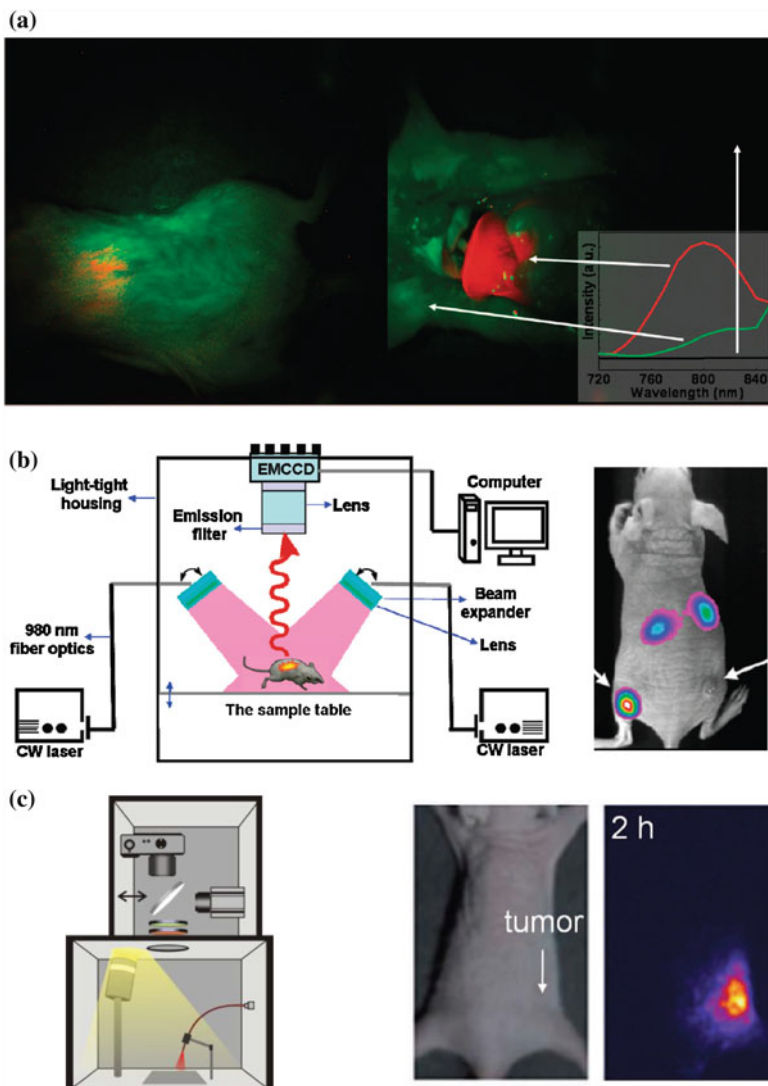


Fig. 22.2 Comparison of different homemade UCNP in vivo imaging systems. **a** In vivo whole body images of mouse injected with UCNP. Images were obtained in a modified Maestro GNIR FLEX fluorescence imaging system (CRI). (*left*) Intact mouse, (*right*) same mouse after dissection. **b** *Left* Schematic illustration of an in vivo UCNP imaging system based on modification of a Kodak in vivo imaging system. *Right* A representative images showing the in vivo tumor-targeted imaging of U87MG and MCF-7 tumors bearing mouse. **c** *Left* In vivo luminescence imaging setup which composed of a fiber-coupled 980 nm laser, a DSLR camera, optical filters, and a dark box. Middle: bright filed image of mouse. *Right* UCL image of the tumor site from mouse (Recreated with kind permission of American Chemical Society [10, 40] and Wiley-VCH Verlag GmbH & Co. KGaA [41])

various doping strategies or by introducing well-designed core@shell nanostructures [40, 43]. In particular, engineering of UCNPs with excellent NIR emission ($\lambda = \sim 800$ nm) or single-band red emission ($\lambda = \sim 650$ nm) could result in ideal optical biolabels for future deep tissue imaging and has become a new attractive topic currently [44].

The mostly used UCNP for achieving a NIR-to-NIR in vivo imaging is Tm^{3+} and Yb^{3+} co-doped $\beta\text{-NaYF}_4$, which, after 980 nm excitation, could give out strong NIR emission located at 800 nm, ideally for deep tissue imaging [8, 40]. Several interesting methods have been developed to improve the NIR emission intensity of $\text{NaYF}_4\text{:Tm/Yb}$ nanoparticles.

Increasing the concentration of Tm^{3+} ions in the host lattice is one of the simplest techniques to achieve the goal. Wang et al. demonstrated that $\text{NaYF}_4\text{:Tm/Yb}$ nanoparticles with Tm^{3+} doping fixed at 0.2 mol % could only have a weak emission at 800 nm, and increasing the Tm^{3+} concentration up to 2 mol % could result in a significant enhancement thanks to the enhanced $^3\text{H}_4$ level [45]. By further replacing all Y^{3+} in $\text{NaYF}_4\text{:Tm/Yb}$ to Yb^{3+} ions, Chen et al. have developed ultrasmall-sized (7–10 nm) $\text{NaYbF}_4\text{:Tm}$ (2 mol %) nanoparticles with 3.6-fold enhancement in total upconversion emission intensity in comparison with that of 25 nm-sized $\text{NaYF}_4\text{:Tm/Yb}$ (2/20 mol %) [46]. Such enhancement has been suggested to arise from the increased absorptions induced by the Yb^{3+} ions and the increased efficiency of energy transfer between Yb^{3+} and Tm^{3+} ions. In a followed-up study, Liu et al. reported a lutetium (Lu)-based UCNP with excellent NIR emission [29]. As-synthesized sub-10 nm-sized $\beta\text{-NaLuF}_4\text{:Gd/Yb/Tm}$ (24/20/1 mol %) displayed bright UCL with high QY estimated to be 0.47 ± 0.06 %. In comparison with 20 nm-sized $\text{NaYF}_4\text{:Tm/Yb}$ (1/20 mol %), approximately 11-fold enhancement in NIR emission could be achieved. The successful suppression of nonradiative process has been suggested as the main reason behind such enhancement.

Epitaxial growth of an inert protective shell over pre-prepared $\text{NaYF}_4\text{:Tm/Yb}$ core has been accepted as another useful strategy for minimizing the surface defects for preserving the optical integrity of UCNPs [30, 31]. Although cation-exchange and Ostwald ripening methods have been developed as alternative options recently [47, 48], seed-mediated growth still remains the most adopted technique for synthesis of such core@multi-shell structured UCNP [23]. By coating $\alpha\text{-NaYbF}_4\text{:Tm}$ (0.5 mol %) with a well-selected CaF_2 protective shell, Chen et al. have developed a novel and biocompatible $\alpha\text{-NaYbF}_4\text{:Tm}$ (0.5 mol %)/ Yb@CaF_2 with highly efficient NIR-to-NIR upconversion property (Fig. 22.3a) [49]. CaF_2 was chosen as the epitaxial shell due to its low lattice mismatch with $\alpha\text{-NaYbF}_4\text{:Tm}$, good optical transparency, high crystallizability, stability, and biocompatibility. As-design UCNP exhibited an impressive high QY of 0.6 ± 0.1 % under low power density excitation (0.3 W/cm^2). Thanks to the suppressing of surface quenching effects via hetero-epitaxial growth of CaF_2 shell, an approximately 35-fold enhancement in UCL intensity could be achieved in comparison to the noncoated $\alpha\text{-NaYbF}_4\text{:Tm}$ (Fig. 22.3b). The authors also demonstrated the possibility of imaging deep tissue by using $\alpha\text{-NaYbF}_4\text{:Tm}$ (0.5 mol %)/ Yb@CaF_2 nanoparticles. Clear NIR signal could be detected even through 3.2 cm pork tissue (Fig. 22.3c).

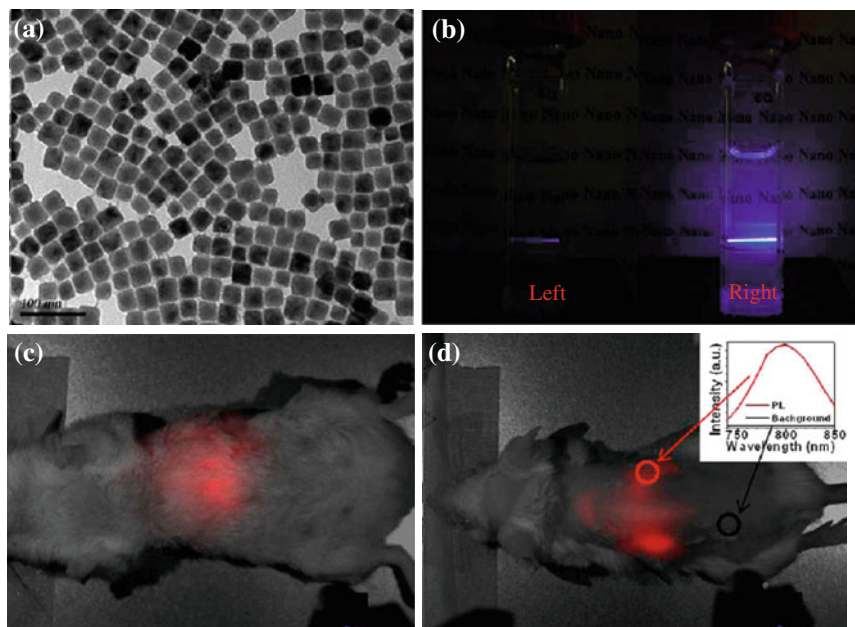


Fig. 22.3 **a** TEM image of ~ 27 nm-sized α -NaYbF₄:Tm(0.5 mol %)/Yb@CaF₂. **b** Photographic images of cuvettes with suspensions of the core (*left*) and the core/shell (*right*) nanoparticles under laser excitation at 975 nm. Whole-animal imaging of a BALB/c mouse injected via tail vein with the HA-coated α -NaYbF₄:Tm(0.5 mol %)/Yb@CaF₂ core/shell nanoparticles. Mice were imaged in the **c** belly and **d** back positions. Insert in **d** is the spectra of the NIR upconversion luminescence and background taken from the circled area (Recreated with kind permission of American Chemical Society [49])

22.3.3.2 Strategies for Improving the Red-Band Emission

UCNP with strong single-band red emission has been emerged as another interesting imaging probe for *in vivo* imaging. Recently, studies on Yb³⁺/Er³⁺ co-doped MnF₂ and KMnF₃ nanoparticles have demonstrated a substantially enhanced red-to-green (R/G) emission ratio owing to the energy transfer between the Er³⁺ and Mn²⁺ [50, 51]. Inspired by these, Wang et al. have developed cube-shaped KMnF₃:Yb/Er (18/2 mol %) with extremely high red emission and completely disappeared blue and green emissions (Fig. 22.4a, b) [44]. Such single-band up-conversion emission has been ascribed to nonradiative energy transfer from the ¹H_{9/2} and ⁴S_{3/2} levels of Er³⁺ to the ⁴T₁ level of Mn²⁺, followed by back-energy transfer to the ⁴F_{9/2} lever of Er³⁺. Pure NIR emission of KMnF₃:Yb/Tm (18/2 mol %) could also be achieved by applying the same idea (Fig. 22.4c). In a followed-up study, Tian et al. presented a hydrothermal synthesis of Mn²⁺-doped NaYF₄:Yb/Er nanoparticles with a strong single-band red emission [42].

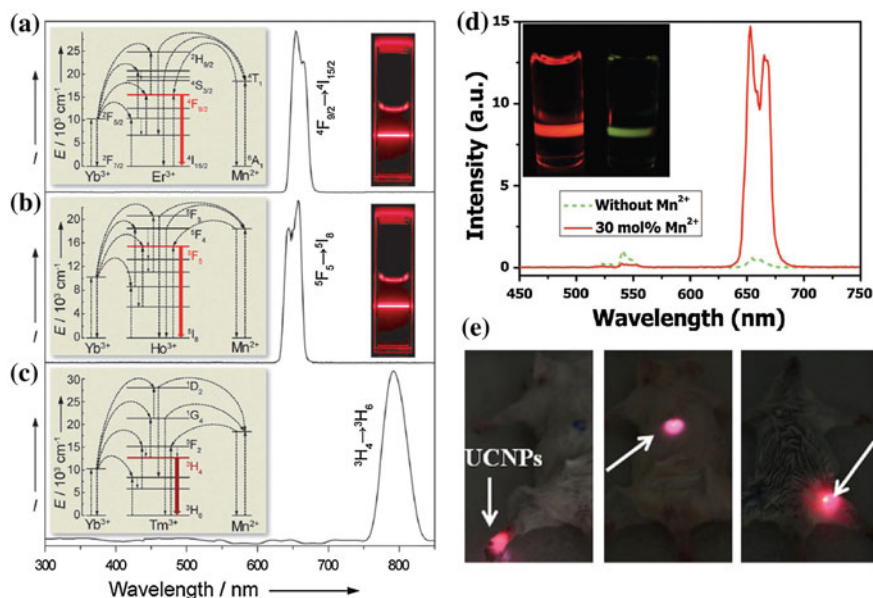


Fig. 22.4 Room-temperature upconversion emission spectra of **a** KMnF_3 :Yb/Er (18:2 mol %), **b** KMnF_3 :Yb/Ho (18:2 mol %), and **c** KMnF_3 :Yb/Tm (18:2 mol %) nanocrystals in cyclohexane (insets proposed energy transfer mechanisms and corresponding luminescent photos of the colloidal solutions). **d** Upconversion emission spectra of NaYF_4 :Yb/Er (18/2 mol %) nanocrystals with 0 and 30 mol % Mn^{2+} dopant ions dispersed in cyclohexane (1 mg/mL), respectively. (inset the corresponding luminescent photographs for intensity comparison). **e** In vivo upconversion luminescence imaging of PEG-UCNPs injected into translucent foot (left), skin of back (middle), and thin muscles of mice (right) (Recreated with kind permission of Wiley-VCH Verlag GmbH & Co. KGaA [42, 44])

Surprisingly, as-designed nanoparticles could have a R/G ratio of 163.78 after increasing the doping level of Mn^{2+} up to 30 mol %. The doping of Mn^{2+} also resulted in significant enhancement (about 15 times) in overall optical intensity in comparison with Mn-free sample (Fig. 22.4d). As a proof-of-concept experiment, the author injected water-soluble PEGylated NaYF_4 :Yb/Er/Mn at the foot, back, and upper leg regions of white Kunming mice and demonstrated a clear tissue penetration and high-contrast photoluminescent imaging of the red emission (Fig. 22.4e).

The engineering of UCNP nanostructures for excellent NIR- and red-band emissions by doping with suitable amount of Mn^{2+} ions will continue to attract increasing interests. More importantly, selectively doping UCNP with other lanthanide ions, such as Gd^{3+} , Lu^{3+} , Yb^{3+} , and $^{153}\text{Sm}^{3+}$ might endow UCNP with useful imaging modalities, such as magnetic resonance imaging (MRI), CT, and positron emission tomography (PET).

22.3.4 Engineering of UCNP for Multimodal Imaging

Each imaging modality has its strengths and weaknesses [52–55]. MRI provides excellent spatial resolution, exceptional anatomical information, and unlimited depth for in vivo imaging, but suffers from limited sensitivity. PET possesses remarkable detection sensitivity but only with a very limited spatial resolution (\sim mm). Photoluminescence imaging is capable of providing the highest spatial resolution and is the best modality for live cell imaging. However, it lacks the capability to obtain anatomical and physiological detail in vivo owing to limited penetration of light in tissues. Engineering of UCNP by suitable doping strategy could have a great possibility to achieve a multimodal imaging probe which holds balance in sensitivity, resolution, and penetration depth, enabling excellent visualizing (cancer) cells from the cellular scale to whole-body noninvasive imaging. In this section, we review the recent progress on how to engineer UCNP for in vivo multimodal imaging by lanthanide ions doping strategy.

22.3.4.1 Engineering of UCNP for UCL/MR Dual-modal Imaging

Although combination of super paramagnetic iron oxide nanoparticles (SPIONs) with UCNP could result in bimodal imaging probe with UCL and MR modalities [39, 56], doping paramagnetic Gd^{3+} ions (or Mn^{2+}) in UCNP crystal lattice should represent a better strategy for introducing MR contrast imaging capability without sacrificing the UCL intensities [11, 12]. Kumar et al. reported the first such example by doping Gd^{3+} ions into $NaYF_4$ and demonstrated the combination of UCL and MR bimodal imaging in one single nanocrystal [12]. The first in vivo demonstration of such bimodal UCL/MRI imaging was later achieved using hexagonal-phase carboxylic acid-functionalized $NaGdF_4:Tm^{3+}/Er^{3+}/Yb^{3+}$ nanoparticles [13]. However, because the majority of the Gd^{3+} ions are doped into the rigid crystal lattice and have limited chance to alter the relaxation time of surrounding water protons, only low MR sensitivity could be achieved in most of the previous reports [7, 12, 57]. The nanostructure re-engineering and relaxivity mechanism probing of the Gd^{3+} -doped UCNP might hold a great chance to enhance its MR sensitivity.

Recently, we have designed three different types of Gd^{3+} -doped UCNPs with various Gd^{3+} ion locations and surface densities to probe the roles of surface and bulk Gd^{3+} ions on shortening the T_1 -relaxation time of surrounding water molecules [11]. Our systematic research have demonstrated that it is only the surface Gd^{3+} ions in Gd^{3+} -doped UCNP are responsible for shortening the T_1 -relaxation time of water protons, and bulk Gd^{3+} ions could have little impact even with high concentration (Fig. 22.5). A remarkable increase in r_1 -relaxivity (up to $6.18 \text{ mM}^{-1}\text{s}^{-1}/Gd^{3+}$) has been achieved by further decreasing the $NaGdF_4$ shell thickness down to $<1 \text{ nm}$ [11]. By using ultrasmall $NaGdF_4$ nanocrystals as models, Johnson et al. have shown the similar observation of increased r_1 -

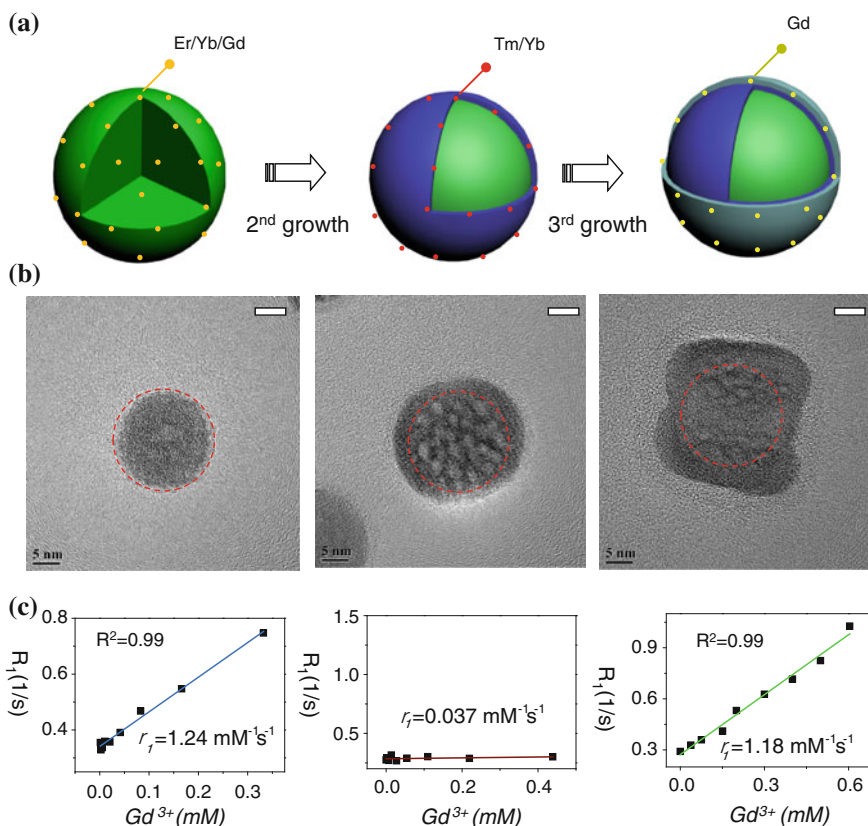


Fig. 22.5 **a** A schematic illustration showing the synthesis of core@multi-shell UCNPs. **b** HR-TEM images of highly crystalline NaYF₄:Er/Yb/Gd (left), NaYF₄:Er/Yb/Gd@NaYF₄:Tm/Yb (middle), NaYF₄:Er/Yb/Gd@NaYF₄:Tm/Yb@NaGdF₄ (right) nanoparticles. **c** Plots of longitudinal relaxation rate (R_1) versus Gd^{3+} concentration of three samples, (left) NaYF₄:Er/Yb/Gd@SiO₂ ($r_1 = 1.24 \text{ mM}^{-1}\text{s}^{-1}$), (middle) NaYF₄:Er/Yb/Gd@NaYF₄:Tm/Yb@SiO₂ ($r_1 = 0.037 \text{ mM}^{-1}\text{s}^{-1}$), and (right) NaYF₄:Er/Yb/Gd@NaYF₄:Tm/Yb@NaGdF₄@SiO₂ ($r_1 = 1.18 \text{ mM}^{-1}\text{s}^{-1}$) (Recreated with kind permission of Wiley-VCH Verlag GmbH & Co. KGaA [11])

relaxivity per Gd^{3+} ion (from 3.0 to 7.2 $\text{mM}^{-1}\text{s}^{-1}$) with decreased NaGdF₄ particle size (from 8 to 2.5 nm), again demonstrating the role of surface Gd^{3+} ions in relaxivity enhancement [58].

In an attempt to understand the relaxivity mechanism of Gd^{3+} -doped UCNP, we further introduced mesoporous and dense silica coatings for systematically investigating its possible relaxivity mechanisms [59]. A surface-dependent relaxivity mechanism has been proposed based on our results. Specifically, we showed a co-existing of inner- and outer-sphere r_1 -relaxivity mechanism in ligand-free Gd^{3+} -doped UCNP, while only main contribution of outer-sphere mechanism in silica-shielded probes. The origin of r_2 -relaxivity is inferred mainly from an outer-sphere mechanism with the r_2 value being surface state related. Also, key factors

for tuning r_2/r_1 ratio have been found to be highly dependent on the thickness of NaGdF₄ shell and surface modification strategy. Based on these, we showed a 105-fold enhancement in r_1 -relaxivity ($14.73 \text{ mM}^{-1}\text{s}^{-1}/\text{Gd}^{3+}$) in comparison with the first-reported same value ($0.14 \text{ mM}^{-1}\text{s}^{-1}/\text{Gd}^{3+}$). These new findings provide not only deeper insight into the origin of contrast enhancement of water-soluble Gd³⁺-doped UCNP, but also useful strategy for achieving both high MR sensitivity for future biological imaging applications.

22.3.4.2 Engineering of UCNP for UCL/MR/CT Triple-modal Imaging

With the presence of heavy metal ions like Gd³⁺, Yb³⁺, and Lu³⁺ in NaYF₄ matrix, lanthanide ions-doped UCNPs also have been considered as an inherent CT contrast agent recently [14–16, 60]. Ultrasmall NaGdF₄:Er/Yb nanocrystals have firstly been developed via an interesting two-phase system and been demonstrated as UCL/MR/CT triple-modal imaging contrast agent [14]. In a followed-up study, Liu et al. reported a Yb-based NaYbF₄:Er/Gd nanoparticles with improved CT contrast capabilities [15]. The doping of Gd³⁺ ions has been demonstrated vital to control both the morphology and R/G ratio of NaYbF₄:Er/Gd nanoparticles (Fig. 22.6a, b). As-synthesized water-soluble polyethylene glycol (PEG)-modified NaYbF₄:Er/Gd nanoparticles have been found to be the best CT contrast agents among iobitridol, Au-, Pt-, Bi-, and Ta-based nanoparticulate agents under the same testing conditions. In vivo imaging study demonstrated the capability of PEG-modified NaYbF₄:Er/Gd nanoparticles as an excellent CT contrast agent (Fig. 22.6c, d). Water-soluble NaLuF₄:Tm/Yb nanoparticles might represent the third type of inherent CT agents. After coating with iron oxide shell, or modified with Gd³⁺-complex, such modified NaLuF₄:Tm/Yb nanoparticles could also be probes with well-combined UCL/MR/CT triple modalities [16, 61, 62]. Although other matrixes, such as BaYbF₅ and BaGdF₅ [63, 64], have also been reported as inherent CT contrast agents, they might not be a good choice for efficient up-conversion optical imaging.

Another way for adding a CT contrast capability is by decorating Gd³⁺ ions-doped UCNP with CT contrast nanoparticles, such as tantalum oxide (TaO_x) and ultrasmall gold nanoparticles (Fig. 22.7) [60, 65]. Starting from NaYF₄:Yb/Er/Tm@NaGdF₄ nanocrystals, we recently demonstrated an efficiently way to add CT imaging modality by decorating with a fluorescence-transparent TaO_x shell [65]. As-design water-soluble litchi-shaped trimodal imaging probe showed an extraordinary high r_1 ($11.45 \text{ mM}^{-1}\text{s}^{-1}$) and r_2 ($147.3 \text{ mM}^{-1}\text{s}^{-1}$) values thanks to the ultrathin NaGdF₄ shell. An obvious CT contrast enhancement could be obtained by the combined effect of radiopaque TaO_x shell and UCNP itself. Both the in vitro and in vivo trimodal imaging have been demonstrated, providing us a new possibility for potential early cancer detection.

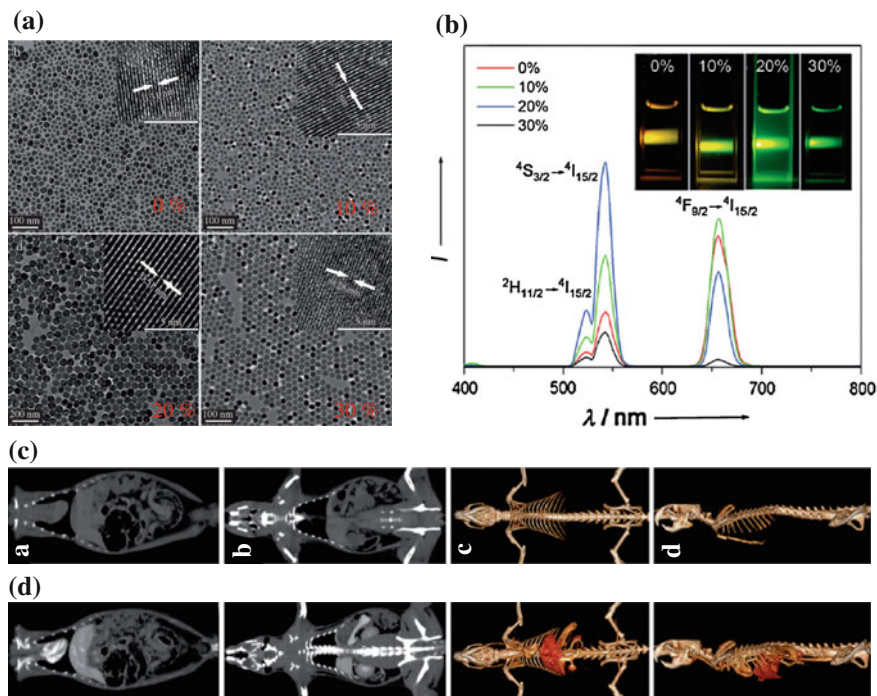


Fig. 22.6 **a** TEM image of Gd-doped $\text{NaYbF}_4:\text{Er}$ nanoparticles with various doping levels of Gd^{3+} ions and corresponding **b** room temperature NIR-to-Vis upconversion luminescence spectra. The inset in **b** shows the upconversion luminescence photograph of the Gd-doped $\text{NaYbF}_4:\text{Er}$ nanoparticles with different concentrations of Gd under excitation at 980 nm. In vivo CT coronal view images of a rat after intravenous injection of 1 mL PEG-UCNPs (70 mgYb/mL) solution at different time intervals. **c** Pre-injection, **d** 10 min postinjection (Recreated with kind permission of Wiley-VCH Verlag GmbH & Co. KGaA [15])

22.3.4.3 Engineering of Radiolabeled UCNP for PET/SPECT Imaging

Suitable surface engineering and isotopes labeling of UCNP could make it also a PET/SPECT (i.e. single-photon emission computed tomography) tracer. To date, research on synthesis and application of radioactive UCNP (*r*-UCNP) is still in its infancy. Two techniques have been developed for the synthesis of radioactive UCNP. They are surface ion reaction (or exchange) method and direct isotope(s) doping strategy.

^{18}F -labeled UCNP, synthesized via surface ion reaction between ^{18}F and rare-earth ions, is the first-reported *r*-UCNP [66–69]. Simply by incubating ^{18}F ions with nanoparticles that contain rare-earth ions [e.g., Y_2O_3 , NaYF_4 , $\text{NaYF}_4:\text{Yb/Tm}$, $\text{Y}(\text{OH})_3$ and $\text{Gd}(\text{OH})_3$], researchers from Li's group have demonstrated that the labeling of ^{18}F can be achieved impressively with an average yield of >90 % within only one minute [67]. The effectiveness of ^{18}F -labeled rare-earth nanoparticles was further evaluated by PET imaging of their in vivo distribution and

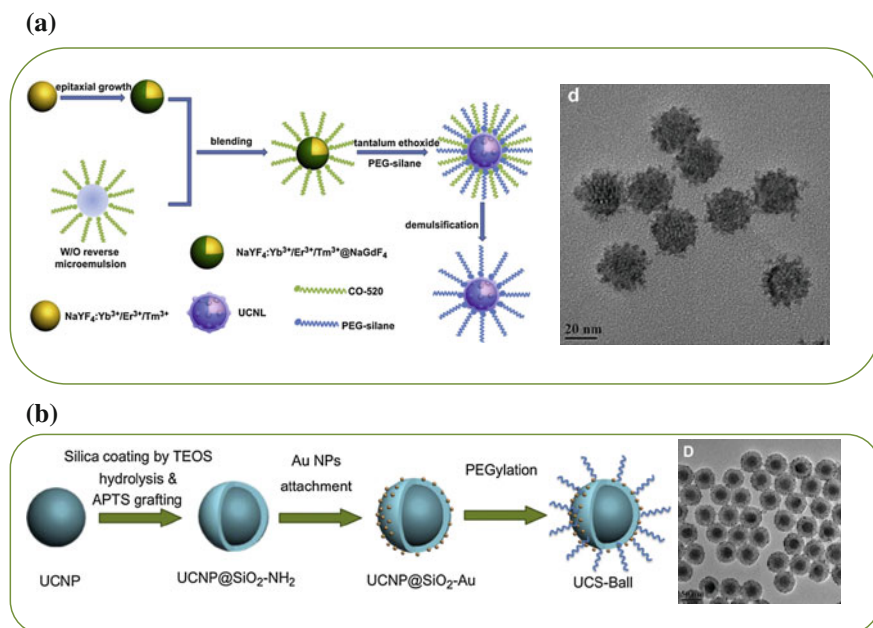


Fig. 22.7 Schematic illustration and TEM image of **a** TaO_x -decorated $\text{NaYF}_4:\text{Yb}/\text{Er}/\text{Tm}@\text{NaGdF}_4$ nanoparticles, **b** gold nanoparticles-decorated $\text{NaYF}_4:\text{Yb}/\text{Er}/\text{Tm}/\text{Gd}$ (Recreated with kind permission of Elsevier [60, 65])

application in lymph monitoring (Fig. 22.8). The same group later demonstrated that radioactive $^{153}\text{Sm}^{3+}$ could also be embedded into the UCNP matrix via a cation-exchange process, resulting in ^{153}Sm -labeled $\text{NaLuF}_4:\text{Yb}/\text{Gd}/\text{Tm}$ [70].

Simply by reacting slight amount of $^{153}\text{SmCl}_3$ with other normal precursors (e.g., oleic acid, sodium oleate, LuCl_3 , YbCl_3 and TmCl_3) at 160°C for 8 h, Li's group also reported a one-pot hydrothermal synthesis of $\text{NaLuF}_4:^{153}\text{Sm}/\text{Yb}/\text{Tm}$ nanocrystals as UCL/SPECT bimodal imaging agent [71]. Their results showed that the introduction of small amount of radioactive $^{153}\text{Sm}^{3+}$ showed little influence on the upconversion luminescence properties. Lower cytotoxicity and excellent in vitro and in vivo performance have also been demonstrated by using UCL/SPECT dual imaging modalities. Since NaLuF_4 nanoparticles have already been demonstrated as an excellent CT contrast agent [16, 61], and doping Gd^{3+} could not only enhance the UCL intensity of $\text{NaLuF}_4:\text{Tm}/\text{Yb}$, but also introduce MR imaging modality, water-soluble $\text{NaLuF}_4:^{153}\text{Sm}/\text{Gd}/\text{Tm}/\text{Yb}$ nanoparticle might represent one of the best multimodal imaging probes so far.

Of note, the above-mentioned rapid and efficient labeling of rare-earth nanoparticles with ^{18}F and ^{153}Sm may not represent a general strategy for labeling other PET/SPECT isotopes such as ^{11}C ($t_{1/2}:20.4$ min), ^{64}Cu ($t_{1/2}:12.7$ h), ^{68}Ga ($t_{1/2}:67.7$ min), ^{86}Y ($t_{1/2}:14.7$ h), ^{89}Zr ($t_{1/2}:3.3$ d), ^{124}I ($t_{1/2}:4.2$ d), $^{99\text{m}}\text{Tc}$ ($t_{1/2}:6.0$ h), ^{111}In ($t_{1/2}:2.8$ d). Postisotope labeling with the assistance of

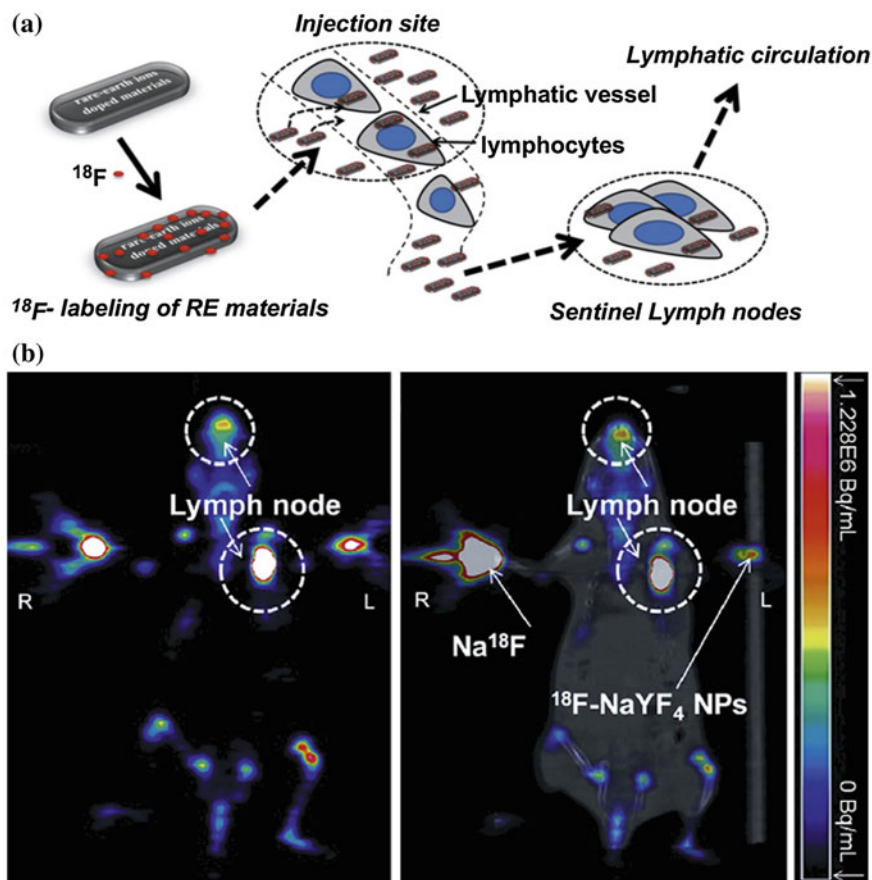


Fig. 22.8 **a** Schematic representation of preparation of ^{18}F -labeled rare-earth nanoparticles and lymph node imaging mechanism. **b** PET imaging (*left*) and PET/CT imaging (*right*) of lymph node 30 min after subcutaneous injection of ^{18}F -UCNPs (Recreated with kind permission of Elsevier [67])

certain chelators should be the best choice for labeling many different kinds of radioactive metal ions.

Over 10 years of efforts in engineering of UCNPs have made it a powerful imaging probe, which could also be a useful nanoplatform for integrating therapeutic capability. Although breakthrough in cancer-targeted imaging and therapy has not been achieved yet, developing of smart and efficient UCNPs-based theranostic nanosystems has still attracted growing interests recently [18, 19].

22.3.5 Engineering of UCNP for Integrating Therapeutic Functionality

To date, only limited progress has been achieved in regard to using UCNP as a drug delivery vehicle. How to improve the drug-loading capacity and in vivo tumor-targeted drug delivery of such UCNP-based theranostic nanosystems are still two of most obvious obstacles in this field. In this section, we will review some examples on design, synthesis, and application of theranostic nanosystems based on UCNPs.

Generally, loading small molecular anticancer drugs and PSs into surface-modified UCNPs are two of the main strategies for integrating therapeutic functionality. Smart hydrogels [72], mesoporous silica shell [18, 19, 73], dense silica shell [74–76], amphiphilic copolymer [77, 78], chitosan [79], polyethylene glycol (PEG) or PEG-phospholipids [80, 81], and poly(ethylene)imine (PEI) [82] have already been used for not only transferring UCNPs into water phase, but also loading DOX and many different kinds of PSs into the systems.

Loading DOX into mesoporous or polymer-coated UCNP to form theranostic agents has been reported [18, 80, 83]. Zhang et al. have developed novel magnetic upconversion fluoride nanorattles via an ion-exchange process [18]. Small molecular drug of DOX could be loaded into the free volume of the nanorattles with a high loading capacity of 32 wt %. With the SPION and UCNP together in the system, in vivo UCL imaging has been used to demonstrate the accumulation of nanocarriers in tumor site when applying a magnetic field near the tumor site. In vivo therapeutic investigation in marine hepatocarcinoma (H22) tumor-bearing mice showed a significant inhibition of tumor growth rate after injecting DOX-loaded nanorattles while applying with a magnetic field (Fig. 22.9). In another study, magnetic-guided thermal therapeutic effect could also be integrated in a UCNP nanoplatfrom by engineering the UCNP surface with ultrasmall Fe₃O₄ and gold nanoparticles through a layer-by-layer strategy [84].

By using the visible emission bands of UCNP for triggering the generation of singlet oxygen, researchers have developed many different versions of UCNP/PS nanocomposites for 980 nm laser-initiated photodynamic therapy (PDT). Owing to the advantage in deeper tissue penetration depth of 980 nm in comparison with the traditional visible light, such UCNP/PS-based PDT agents should hold better potential for treating deeper cancer using PDT. Since the first report on UCNP/M540 (i.e., Merocyanine-540)-based PDT agent [76], many other combinations of UCNP/PS have been reported and the quest for strategies to improve the PDT efficiency is continuing [19, 41, 72–75, 78, 81, 82, 85].

The first prototype of UCNP/PS-based PDT drug was constructed by encapsulating M540 into a silica matrix using traditional Stöber method [76]. Due to the electrostatic repulsion between negatively charged M540 and the tetraethyl orthosilicate (TEOS) precursor, the loading capacity of M540 was limited. We recently reported a new UCNP/PS-based PDT drug by using brighter Gd³⁺-doped

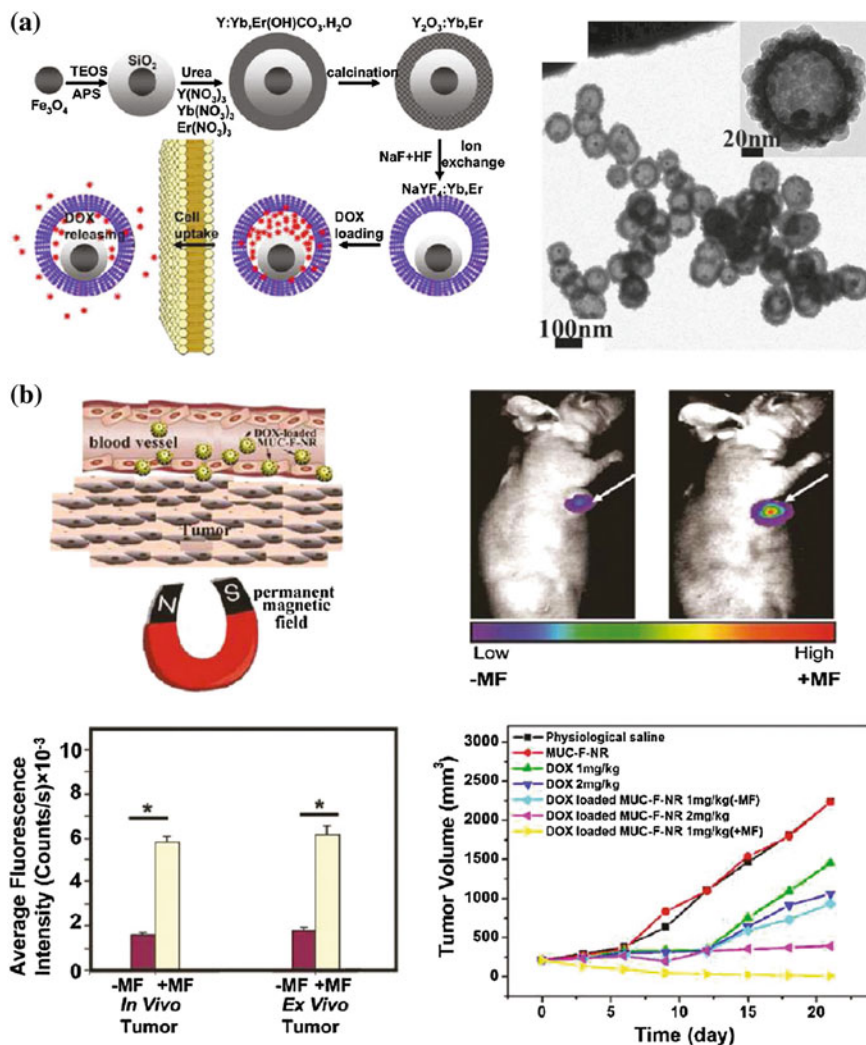


Fig. 22.9 **a** Synthetic procedure for the drug-loaded $\text{Fe}_3\text{O}_4@ \text{SiO}_2@ \alpha\text{-NaYF/Yb,Er}$ nanorattles (*left*) and TEM image of $\text{Fe}_3\text{O}_4@ \text{SiO}_2@ \alpha\text{-NaYF/Yb,Er}$ (*right*). **b** In vivo magnetic-guided chemotherapy of $\text{Fe}_3\text{O}_4@ \text{SiO}_2@ \alpha\text{-NaYF/Yb,Er}$ (Recreated with kind permission of American Chemical Society [87])

UCNP and water-soluble methylene blue (MB) [75]. Successful “trapping” of the positively charged MB within the negatively charged silica resulted in a core@-shell structure of $\text{UCNP}@ \text{SiO}_2(\text{MB})$ with attractive properties such as higher PS-loading capacity, zero-PS-prerelease, 980 nm laser on-demand $^1\text{O}_2$ release, and UCL/MR dual-modal imaging capabilities.

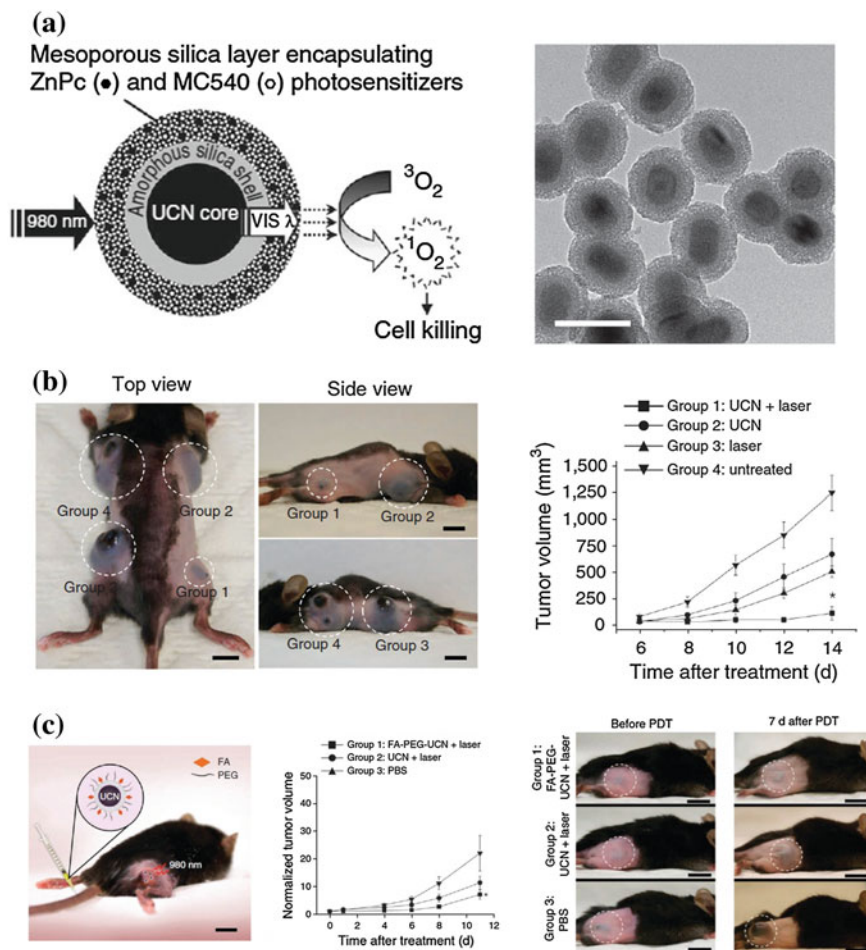


Fig. 22.10 a Schematic of mesoporous-silica-coated UCNP co-loaded with ZnPc and MC540 photosensitizers for PDT (left), and TEM image of mesoporous-silica-coated UCNP (right). b In vivo PDT of injected tumor cells prelabeled with UCNP. c Targeted in vivo PDT of a subcutaneous tumor model injected with FA-PEG-UCNP (Recreated with kind permission of Nature Publishing Group [19])

Although many different kinds of UCNP/PS systems have been developed most of the therapeutic studies were only limited to in vitro studies mainly because of the relatively low efficiency of as-designed PDT agent. By carefully selecting and loading two or more different kinds PSs into the system, PSs are able to completely utilize the emission bands of UCNP. Such multiple-PS-loading strategy might hold a better chance for further enhancing the PDT effect. Idris et al. recently demonstrated this idea by encapsulating two different PSs (ZnPc and MC540) into mesoporous-silica-coated NaYF₄:Er/Yb nanoparticles (Fig. 22.10a) [19]. In vitro

experiments demonstrated the higher generation of singlet oxygen and lower cell viability when shedding 980 nm light on co-loaded nanoparticles. To demonstrate the *in vivo* PDT effect, they injected B10-F0 melanoma cell pre-labeled with double-PS-loaded UCNP under the skin of C57BL/6 mice and then irradiated the injected site with a 980 nm laser. Successful inhibit of tumor growth rate has been observed in the positive group, while only continuous tumor growth could be seen in the control groups (Fig. 22.10b). However, in the case of injecting the drug intratumorally and intravenously, only slightly tumor growth inhibition could be achieve, indicating that *in vivo* PDT effect is still limited (Fig. 22.10c). Since the half-life of singlet oxygen is very short, on the order of microseconds, and can therefore act only on target structures that are in close proximity to it, in order to guarantee an effective PDT therapeutic outcome, sufficient amount of PDT agents should be able to internalize by the cells. Unfortunately, achieving this goal has long been considered as one of the biggest challenges in the war against cancer [86].

22.4 Conclusion and Future Perspectives

In conclusion, we summarized the very recent advances in engineering of UCNPs for cancer imaging and therapy applications. Engineering of ultrasmall-sized UCNP with excellent optical properties has attracted increasing interests and will potentially be used for designing a renal clearable UCNP-based imaging probe. Because of their advantages in imaging deeper tissue, UCNP with strong near-infrared emissions (or single red band) has also attracted growing interest recently. Doping suitable ions into UCNP crystal lattices has become one of the most unique and efficient techniques for integrating many clinical relevant imaging modalities (e.g., PET, MRI, SPECT, and CT) together in one single UCNP.

Despite recent progress in engineering of UCNP for tunable size and improve imaging capabilities, many challenges still remained for future cancer imaging and therapy of UCNP.

1. Improving the upconversion efficiency of ultrasmall UCNPs. Development and optimization of strategies for synthesis of ultrasmall UCNPs with high optical quality will be urgently needed in the coming years. Such UCNPs are expected to play a vital role in designing clinically translational tumor imaging probe which could targeted specifically to tumor and excreted through kidney within hours.
2. Perfection of NIR and red emission intensities of UCNPs. Owing to their high tissue penetration depth, UCNPs with excellent NIR emission or single-band red emission has been considered as the ideal probes for *in vivo* optical imaging applications. Strategies for further improving NIR- and red-band emission efficiency of UCNPs will become a new hot topic in this filed.

3. Developing imaging systems specifically for tracking UCNPs both in vitro and in vivo. Considering that most of the UCNP imaging systems are homemade by employing an additional 980 nm laser module, commercialization of in vivo imaging system which can be used for whole-body imaging of UCNP in small animals will be very helpful for speeding up the development and application of UCNPs.
4. Design of theranostic nanomedicines based on UCNP. So far, only small molecular anticancer drugs and photosensitizers have been loaded within surface-engineered UCNPs for simultaneous imaging and therapy. Although a few examples about integrated imaging and therapy have been reported, new strategies are still needed for achieving enhanced therapeutic efficiency.
5. Targeting UCNP to the tumor site. To date, in vivo tumor cell (or tumor vasculature) targeting based on UCNP is still a big challenge. Optimization of particle size, surface characteristics, as well as selecting the suitable targeting ligands to improve the targeting efficiency, should deserve more research efforts in the coming future.

References

1. Zhou J, Liu Z, Li F (2012) Upconversion nanophosphors for small-animal imaging. *Chem Soc Rev* 41(3):1323–1349. doi:[10.1039/c1cs15187h](https://doi.org/10.1039/c1cs15187h)
2. Auzel F (2004) Upconversion and anti-Stokes processes with f and d ions in solids. *Chem Rev* 104(1):139–173. doi:[10.1021/cr020357g](https://doi.org/10.1021/cr020357g)
3. Haase M, Schafer H (2011) Upconverting nanoparticles. *Angew Chem Int Ed* 50(26):5808–5829. doi:[10.1002/anie.201005159](https://doi.org/10.1002/anie.201005159)
4. Ju Q, Tu D, Liu Y, Li R, Zhu H, Chen J, Chen Z, Huang M, Chen X (2012) Amine-functionalized lanthanide-doped KGdF₄ nanocrystals as potential optical/magnetic multimodal bioprobes. *J Am Chem Soc* 134(2):1323–1330. doi:[10.1021/ja2102604](https://doi.org/10.1021/ja2102604)
5. Wu S, Han G, Milliron DJ, Aloni S, Altoe V, Talapin DV, Cohen BE, Schuck PJ (2009) Nonblinking and photostable upconverted luminescence from single lanthanide-doped nanocrystals. *Proc Natl Acad Sci U S A* 106(27):10917–10921. doi:[10.1073/pnas.0904792106](https://doi.org/10.1073/pnas.0904792106)
6. Cheng L, Wang C, Liu Z (2012) Upconversion nanoparticles and their composite nanostructures for biomedical imaging and cancer therapy. *Nanoscale* 5(1):23–37. doi:[10.1039/c2nr32311g](https://doi.org/10.1039/c2nr32311g)
7. Park YI, Kim JH, Lee KT, Jeon KS, Bin Na H, Yu JH, Kim HM, Lee N, Choi SH, Baik SI, Kim H, Park SP, Park BJ, Kim YW, Lee SH, Yoon SY, Song IC, Moon WK, Suh YD, Hyeon T (2009) Nonblinking and nonbleaching upconverting nanoparticles as an optical imaging nanoprobe and T1 magnetic resonance imaging contrast agent. *Adv Mater* 21 (44):4467. doi:[10.1002/adma.200901356](https://doi.org/10.1002/adma.200901356)
8. Chatterjee DK, Rufaihah AJ, Zhang Y (2008) Upconversion fluorescence imaging of cells and small animals using lanthanide doped nanocrystals. *Biomaterials* 29(7):937–943. doi:[10.1016/j.biomaterials.2007.10.051](https://doi.org/10.1016/j.biomaterials.2007.10.051)
9. Nam SH, Bae YM, Park YI, Kim JH, Kim HM, Choi JS, Lee KT, Hyeon T, Suh YD (2011) Long-term real-time tracking of lanthanide ion doped upconverting nanoparticles in living cells. *Angew Chem Int Ed* 50(27):6093–6097. doi:[10.1002/anie.201007979](https://doi.org/10.1002/anie.201007979)

10. Xiong L, Chen Z, Tian Q, Cao T, Xu C, Li F (2009) High contrast upconversion luminescence targeted imaging in vivo using peptide-labeled nanophosphors. *Anal Chem* 81(21):8687–8694. doi:[10.1021/ac901960d](https://doi.org/10.1021/ac901960d)
11. Chen F, Bu WB, Zhang SJ, Liu XH, Liu JN, Xing HY, Xiao QF, Zhou LP, Peng WJ, Wang LZ, Shi JL (2011) Positive and negative lattice shielding effects co-existing in Gd(III) ion doped bifunctional upconversion nanoprobos. *Adv Funct Mater* 21(22):4285–4294. doi:[10.1002/adfm.201101663](https://doi.org/10.1002/adfm.201101663)
12. Kumar R, Nyk M, Ohulchanskyy TY, Flask CA, Prasad PN (2009) Combined optical and MR bioimaging using rare earth ion doped NaYF₄ nanocrystals. *Adv Funct Mater* 19(6):853–859. doi:[10.1002/adfm.200800765](https://doi.org/10.1002/adfm.200800765)
13. Zhou J, Sun Y, Du X, Xiong L, Hu H, Li F (2010) Dual-modality in vivo imaging using rare-earth nanocrystals with near-infrared to near-infrared (NIR-to-NIR) upconversion luminescence and magnetic resonance properties. *Biomaterials* 31(12):3287–3295. doi:[10.1016/j.biomaterials.2010.01.040](https://doi.org/10.1016/j.biomaterials.2010.01.040)
14. He M, Huang P, Zhang CL, Hu HY, Bao CC, Gao G, He R, Cui DX (2011) Dual phase-controlled synthesis of uniform lanthanide-doped NaGdF₄ upconversion nanocrystals via an OA/Ionic Liquid Two-Phase System for in vivo dual-modality imaging. *Adv Funct Mater* 21(23):4470–4477. doi:[10.1002/adfm.201101040](https://doi.org/10.1002/adfm.201101040)
15. Liu Y, Ai K, Liu J, Yuan Q, He Y, Lu L (2012) A high-performance ytterbium-based nanoparticulate contrast agent for in vivo X-ray computed tomography imaging. *Angew Chem Int Ed* 51(6):1437–1442. doi:[10.1002/anie.201106686](https://doi.org/10.1002/anie.201106686)
16. Zhu X, Zhou J, Chen M, Shi M, Feng W, Li F (2012) Core-shell Fe₃O₄@NaLuF₄:Yb, Er/Tm nanostructure for MRI, CT and upconversion luminescence tri-modality imaging. *Biomaterials* 33(18):4618–4627. doi:[10.1016/j.biomaterials.2012.03.007](https://doi.org/10.1016/j.biomaterials.2012.03.007)
17. Wang F, Banerjee D, Liu Y, Chen X, Liu X (2010) Upconversion nanoparticles in biological labeling, imaging, and therapy. *Analyst* 135(8):1839–1854. doi:[10.1039/c0an00144a](https://doi.org/10.1039/c0an00144a)
18. Hong H, Yang K, Zhang Y, Engle JW, Feng L, Yang Y, Nayak TR, Goel S, Bean J, Theuer CP, Barnhart TE, Liu Z, Cai W (2012) In Vivo Targeting and Imaging of Tumor Vasculature with Radiolabeled, Antibody-Conjugated Nanographene. *ACS Nano* 6(3):2361–2370. doi:[10.1021/nn204625e](https://doi.org/10.1021/nn204625e)
19. Idris NM, Gnanasamandhan MK, Zhang J, Ho PC, Mahendran R, Zhang Y (2012) In vivo photodynamic therapy using upconversion nanoparticles as remote-controlled nanotransducers. *Nat Med* 18(10):1580–1585. doi:[10.1038/nm.2933](https://doi.org/10.1038/nm.2933)
20. Wang X, Zhuang J, Peng Q, Li Y (2005) A general strategy for nanocrystal synthesis. *Nature* 437(7055):121–124. doi:[10.1038/nature03968](https://doi.org/10.1038/nature03968)
21. Mai HX, Zhang YW, Si R, Yan ZG, Sun LD, You LP, Yan CH (2006) High-quality sodium rare-earth fluoride nanocrystals: controlled synthesis and optical properties. *J Am Chem Soc* 128(19):6426–6436. doi:[10.1021/ja060212h](https://doi.org/10.1021/ja060212h)
22. Boyer JC, Cuccia LA, Capobianco JA (2007) Synthesis of colloidal upconverting NaYF₄:Er³⁺/Yb³⁺ and Tm³⁺/Yb³⁺ monodisperse nanocrystals. *Nano Lett* 7(3):847–852. doi:[10.1021/nl070235+](https://doi.org/10.1021/nl070235+)
23. Qian HS, Zhang Y (2008) Synthesis of hexagonal-phase core-shell NaYF₄ nanocrystals with tunable upconversion fluorescence. *Langmuir* 24(21):12123–12125. doi:[10.1021/la802343f](https://doi.org/10.1021/la802343f)
24. Li Z, Zhang Y (2008) An efficient and user-friendly method for the synthesis of hexagonal-phase NaYF₄:Yb, Er/Tm nanocrystals with controllable shape and upconversion fluorescence. *Nanotechnology* 19(34):345606. doi:[10.1088/0957-4484/19/34/345606](https://doi.org/10.1088/0957-4484/19/34/345606)
25. Choi HS, Liu W, Liu F, Nasr K, Misra P, Bawendi MG, Frangioni JV (2010) Design considerations for tumour-targeted nanoparticles. *Nat Nanotechnol* 5(1):42–47. doi:[10.1038/nnano.2009.314](https://doi.org/10.1038/nnano.2009.314)
26. Choi HS, Liu W, Misra P, Tanaka E, Zimmer JP, Itty Ipe B, Bawendi MG, Frangioni JV (2007) Renal clearance of quantum dots. *Nat Biotechnol* 25(10):1165–1170. doi:[10.1038/nbt1340](https://doi.org/10.1038/nbt1340)

27. Boyer JC, van Veggel FC (2010) Absolute quantum yield measurements of colloidal NaYF₄:Er³⁺, Yb³⁺ upconverting nanoparticles. *Nanoscale* 2(8):1417–1419. doi:[10.1039/c0nr00253d](https://doi.org/10.1039/c0nr00253d)
28. Wang F, Han Y, Lim CS, Lu YH, Wang J, Xu J, Chen HY, Zhang C, Hong MH, Liu XG (2010) Simultaneous phase and size control of upconversion nanocrystals through lanthanide doping. *Nature* 463(7284):1061–1065. doi:[10.1038/Nature08777](https://doi.org/10.1038/Nature08777)
29. Liu Q, Sun Y, Yang T, Feng W, Li C, Li F (2011) Sub-10 nm hexagonal lanthanide-doped NaLuF₄ upconversion nanocrystals for sensitive bioimaging in vivo. *J Am Chem Soc* 133(43):17122–17125. doi:[10.1021/ja207078s](https://doi.org/10.1021/ja207078s)
30. Wang F, Wang J, Liu X (2010) Direct evidence of a surface quenching effect on size-dependent luminescence of upconversion nanoparticles. *Angew Chem Int Ed* 49(41):7456–7460. doi:[10.1002/anie.201003959](https://doi.org/10.1002/anie.201003959)
31. Chen Y, Gao Y, Chen H, Zeng D, Li Y, Zheng Y, Li F, Ji X, Wang X, Chen F, He Q, Zhang L, Shi J (2012) Engineering inorganic nanoemulsions/nanoliposomes by fluoride-silica chemistry for efficient delivery/co-delivery of hydrophobic agents. *Adv Funct Mater*:n/a-n/a. doi:[10.1002/adfm.201102052](https://doi.org/10.1002/adfm.201102052)
32. Ostrowski AD, Chan EM, Gargas DJ, Katz EM, Han G, Schuck PJ, Milliron DJ, Cohen BE (2012) Controlled synthesis and single-particle imaging of bright, sub-10 nm lanthanide-doped upconverting nanocrystals. *ACS Nano* 6(3):2686–2692. doi:[10.1021/nm3000737](https://doi.org/10.1021/nm3000737)
33. Bogdan N, Vetrone F, Ozin GA, Capobianco JA (2011) Synthesis of ligand-free collooidally stable water dispersible brightly luminescent lanthanide-doped upconverting nanoparticles. *Nano Lett* 11(2):835–840. doi:[10.1021/nl1041929](https://doi.org/10.1021/nl1041929)
34. Zhang T, Ge J, Hu Y, Yin Y (2007) A general approach for transferring hydrophobic nanocrystals into water. *Nano Lett* 7(10):3203–3207. doi:[10.1021/nl071928t](https://doi.org/10.1021/nl071928t)
35. Chen Z, Chen H, Hu H, Yu M, Li F, Zhang Q, Zhou Z, Yi T, Huang C (2008) Versatile synthesis strategy for carboxylic acid-functionalized upconverting nanophosphors as biological labels. *J Am Chem Soc* 130(10):3023–3029. doi:[10.1021/ja076151k](https://doi.org/10.1021/ja076151k)
36. Wang L, Yan R, Huo Z, Wang L, Zeng J, Bao J, Wang X, Peng Q, Li Y (2005) Fluorescence resonant energy transfer biosensor based on upconversion-luminescent nanoparticles. *Angew Chem Int Ed* 44(37):6054–6057. doi:[10.1002/anie.200501907](https://doi.org/10.1002/anie.200501907)
37. Li LL, Zhang R, Yin L, Zheng K, Qin W, Selvin PR, Lu Y (2012) Biomimetic surface engineering of lanthanide-doped upconversion nanoparticles as versatile bioprobes. *Angew Chem Int Ed* 51(25):6121–6125. doi:[10.1002/anie.201109156](https://doi.org/10.1002/anie.201109156)
38. Liu Q, Li C, Yang T, Yi T, Li F (2010) “Drawing” upconversion nanophosphors into water through host-guest interaction. *Chem Commun* 46(30):5551–5553. doi:[10.1039/c0cc01352h](https://doi.org/10.1039/c0cc01352h)
39. Chen F, Zhang S, Bu W, Liu X, Chen Y, He Q, Zhu M, Zhang L, Zhou L, Peng W, Shi J (2010) A “neck-formation” strategy for an anti-quenching magnetic/upconversion fluorescent bimodal cancer probe. *Chemistry* 16(37):11254–11260. doi:[10.1002/chem.201000525](https://doi.org/10.1002/chem.201000525)
40. Nyk M, Kumar R, Ohulchanskyy TY, Bergey EJ, Prasad PN (2008) High contrast in vitro and in vivo photoluminescence bioimaging using near infrared to near infrared up-conversion in Tm³⁺ and Yb³⁺ doped fluoride nanophosphors. *Nano Lett* 8(11):3834–3838
41. Park YI, Kim HM, Kim JH, Moon KC, Yoo B, Lee KT, Lee N, Choi Y, Park W, Ling D, Na K, Moon WK, Choi SH, Park HS, Yoon SY, Suh YD, Lee SH, Hyeon T (2012) Theranostic probe based on lanthanide-doped nanoparticles for simultaneous in vivo dual-modal imaging and photodynamic therapy. *Adv Mater* 24(42):5755–5761. doi:[10.1002/adma.201202433](https://doi.org/10.1002/adma.201202433)
42. Tian G, Gu Z, Zhou L, Yin W, Liu X, Yan L, Jin S, Ren W, Xing G, Li S, Zhao Y (2012) Mn²⁺ dopant-controlled synthesis of NaYF₄:Yb/Er upconversion nanoparticles for in vivo imaging and drug delivery. *Adv Mater* 24(9):1226–1231. doi:[10.1002/adma.201104741](https://doi.org/10.1002/adma.201104741)
43. Wang F, Deng R, Wang J, Wang Q, Han Y, Zhu H, Chen X, Liu X (2011) Tuning upconversion through energy migration in core-shell nanoparticles. *Nat Mater* 10(12):968–973. doi:[10.1038/nmat3149](https://doi.org/10.1038/nmat3149)
44. Wang J, Wang F, Wang C, Liu Z, Liu X (2011) Single-band upconversion emission in lanthanide-doped KMnF₃ nanocrystals. *Angew Chem Int Ed* 50(44):10369–10372. doi:[10.1002/anie.201104192](https://doi.org/10.1002/anie.201104192)

45. Wang F, Liu X (2008) Upconversion multicolor fine-tuning: visible to near-infrared emission from lanthanide-doped NaYF₄ nanoparticles. *J Am Chem Soc* 130(17):5642–5643. doi:[10.1021/ja800868a](https://doi.org/10.1021/ja800868a)
46. Chen G, Ohulchanskyy TY, Kumar R, Agren H, Prasad PN (2010) Ultrasmall monodisperse NaYF₄:Yb(3+)/Tm(3+) nanocrystals with enhanced near-infrared to near-infrared upconversion photoluminescence. *ACS Nano* 4(6):3163–3168. doi:[10.1021/nn100457j](https://doi.org/10.1021/nn100457j)
47. Dong C, Korinek A, Blasiak B, Tomanek B, van Veggel FCJM (2012) Cation exchange: a facile method to make NaYF₄:Yb, Tm-NaGdF₄Core-shell nanoparticles with a thin, tunable, and uniform shell. *Chem Mater* 24(7):1297–1305. doi:[10.1021/cm2036844](https://doi.org/10.1021/cm2036844)
48. Johnson NJ, Korinek A, Dong C, van Veggel FC (2012) Self-focusing by Ostwald ripening: a strategy for layer-by-layer epitaxial growth on upconverting nanocrystals. *J Am Chem Soc* 134(27):11068–11071. doi:[10.1021/ja302717u](https://doi.org/10.1021/ja302717u)
49. Chen G, Shen J, Ohulchanskyy TY, Patel NJ, Kutikov A, Li Z, Song J, Pandey RK, Agren H, Prasad PN, Han G (2012) (alpha-NaYbF₄:Tm(3+))/CaF₂ core/shell nanoparticles with efficient near-infrared to near-infrared upconversion for high-contrast deep tissue bioimaging. *ACS Nano* 6(9):8280–8287. doi:[10.1021/nm302972r](https://doi.org/10.1021/nm302972r)
50. Xie MY, Peng XN, Fu XF, Zhang JJ, Lia GL, Yu XF (2009) Synthesis of Yb³⁺/Er³⁺ co-doped MnF₂ nanocrystals with bright red up-converted fluorescence. *Scripta Mater* 60(3):190–193. doi:[10.1016/j.scriptamat.2008.10.010](https://doi.org/10.1016/j.scriptamat.2008.10.010)
51. Zeng JH, Xie T, Li ZH, Li YD (2007) Monodispersed nanocrystalline fluoroperovskite up-conversion phosphors. *Cryst Growth Des* 7(12):2774–2777. doi:[10.1021/Cg070477n](https://doi.org/10.1021/Cg070477n)
52. Cai W, Hong H (2011) Peptoid and positron emission tomography: an appealing combination. *Am J Nucl Med Mol Imaging* 1(1):76–79
53. Cai W, Zhang Y, Kamp TJ (2011) Imaging of induced pluripotent stem cells: from cellular reprogramming to transplantation. *Am J Nucl Med Mol Imaging* 1(1):18–28
54. Zhang Y, Cai W (2012) Molecular imaging of insulin-like growth factor I receptor in cancer. *Am J Nucl Med Mol Imaging* 2(2):248–259
55. Zhang Y, Hong H, Engle JW, Yang Y, Barnhart TE, Cai W (2012) Positron emission tomography and near-infrared fluorescence imaging of vascular endothelial growth factor with dual-labeled bevacizumab. *Am J Nucl Med Mol Imaging* 2(1):1–13
56. Xia A, Gao Y, Zhou J, Li C, Yang T, Wu D, Wu L, Li F (2011) Core-shell NaYF₄:Yb³⁺, Tm³⁺@FexOy nanocrystals for dual-modality T₂-enhanced magnetic resonance and NIR-to-NIR upconversion luminescent imaging of small-animal lymphatic node. *Biomaterials* 32(29):7200–7208. doi:[10.1016/j.biomaterials.2011.05.094](https://doi.org/10.1016/j.biomaterials.2011.05.094)
57. Guo H, Li Z, Qian H, Hu Y, Muhammad IN (2010) Seed-mediated synthesis of NaY F₄:Y b, Er/NaGdF₄ nanocrystals with improved upconversion fluorescence and MR relaxivity. *Nanotechnology* 21(12):125602. doi:[10.1088/0957-4484/21/12/125602](https://doi.org/10.1088/0957-4484/21/12/125602)
58. Johnson NJJ, Oakden W, Stanisiz GJ, Scott Prosser R, van Veggel FCJM (2011) Size-Tunable, Ultrasmall NaGdF₄ Nanoparticles: Insights into Their T₁ MRI Contrast Enhancement. *Chemistry of Materials* 23(16):3714–3722. doi:[10.1021/cm201297x](https://doi.org/10.1021/cm201297x)
59. Chen F, Bu W, Zhang S, Liu J, Fan W, Zhou L, Peng W, Shi J (2013) Gd³⁺-Ion-Doped Upconversion Nanoprobes: Relaxivity Mechanism Probing and Sensitivity Optimization. *Adv Funct Mater* 23(3):298–307. doi:[10.1002/adfm.201201469](https://doi.org/10.1002/adfm.201201469)
60. Xing H, Bu W, Zhang S, Zheng X, Li M, Chen F, He Q, Zhou L, Peng W, Hua Y, Shi J (2012) Multifunctional nanoprobes for upconversion fluorescence, MR and CT trimodal imaging. *Biomaterials* 33(4):1079–1089. doi:[10.1016/j.biomaterials.2011.10.039](https://doi.org/10.1016/j.biomaterials.2011.10.039)
61. Xia A, Chen M, Gao Y, Wu D, Feng W, Li F (2012) Gd³⁺ complex-modified NaLuF₄-based upconversion nanophosphors for trimodality imaging of NIR-to-NIR upconversion luminescence, X-Ray computed tomography and magnetic resonance. *Biomaterials* 33(21):5394–5405. doi:[10.1016/j.biomaterials.2012.04.025](https://doi.org/10.1016/j.biomaterials.2012.04.025)
62. Zhou J, Zhu X, Chen M, Sun Y, Li F (2012) Water-stable NaLuF₄-based upconversion nanophosphors with long-term validity for multimodal lymphatic imaging. *Biomaterials* 33(26):6201–6210. doi:[10.1016/j.biomaterials.2012.05.036](https://doi.org/10.1016/j.biomaterials.2012.05.036)

63. Liu Y, Ai K, Liu J, Yuan Q, He Y, Lu L (2012) Hybrid BaYbF₅ nanoparticles: novel binary contrast agent for high-resolution in vivo X-ray computed tomography angiography. *Adv Healthc Mater* 1(4):461–466. doi:[10.1002/adhm.201200028](https://doi.org/10.1002/adhm.201200028)
64. Zeng S, Tsang MK, Chan CF, Wong KL, Hao J (2012) PEG modified BaGdF₅:Yb/Er nanoprobes for multi-modal upconversion fluorescent, in vivo X-ray computed tomography and biomagnetic imaging. *Biomaterials* 33(36):9232–9238. doi:[10.1016/j.biomaterials.2012.09.019](https://doi.org/10.1016/j.biomaterials.2012.09.019)
65. Xiao Q, Bu W, Ren Q, Zhang S, Xing H, Chen F, Li M, Zheng X, Hua Y, Zhou L, Peng W, Qu H, Wang Z, Zhao K, Shi J (2012) Radiopaque fluorescence-transparent TaOx decorated upconversion nanophosphors for in vivo CT/MR/UCL trimodal imaging. *Biomaterials* 33(30):7530–7539. doi:[10.1016/j.biomaterials.2012.06.028](https://doi.org/10.1016/j.biomaterials.2012.06.028)
66. Liu Q, Sun Y, Li C, Zhou J, Li C, Yang T, Zhang X, Yi T, Wu D, Li F (2011) 18F-Labeled magnetic-upconversion nanophosphors via rare-Earth cation-assisted ligand assembly. *ACS Nano* 5(4):3146–3157. doi:[10.1021/nn200298y](https://doi.org/10.1021/nn200298y)
67. Sun Y, Yu M, Liang S, Zhang Y, Li C, Mou T, Yang W, Zhang X, Li B, Huang C, Li F (2011) Fluorine-18 labeled rare-earth nanoparticles for positron emission tomography (PET) imaging of sentinel lymph node. *Biomaterials* 32(11):2999–3007. doi:[10.1016/j.biomaterials.2011.01.011](https://doi.org/10.1016/j.biomaterials.2011.01.011)
68. Chen F, Bu W, Zhang S, Liu X, Liu J, Xing H, Xiao Q, Zhou L, Peng W, Wang L, Shi J (2011) Positive and negative lattice shielding effects co-existing in Gd(III) ion doped bifunctional upconversion nanoprobes. *Adv Funct Mater* 21(22):4285–4294. doi:[10.1002/adfm.201101663](https://doi.org/10.1002/adfm.201101663)
69. Liu Q, Chen M, Sun Y, Chen G, Yang T, Gao Y, Zhang X, Li F (2011) Multifunctional rare-earth self-assembled nanosystem for tri-modal upconversion luminescence/fluorescence/positron emission tomography imaging. *Biomaterials* 32(32):8243–8253. doi:[10.1016/j.biomaterials.2011.07.053](https://doi.org/10.1016/j.biomaterials.2011.07.053)
70. Sun Y, Liu Q, Peng J, Feng W, Zhang Y, Yang P, Li F (2012) Radioisotope post-labeling upconversion nanophosphors for in vivo quantitative tracking. *Biomaterials* 27(12):01306–01303 01306. doi:[10.1016/j.biomaterials.2012.11.047](https://doi.org/10.1016/j.biomaterials.2012.11.047)
71. Yang Y, Sun Y, Cao T, Peng J, Liu Y, Wu Y, Feng W, Zhang Y, Li F (2013) Hydrothermal synthesis of NaLuF₄:153Sm, Yb, Tm nanoparticles and their application in dual-modality upconversion luminescence and SPECT bioimaging. *Biomaterials* 34(3):774–783
72. Cui S, Yin D, Chen Y, Di Y, Chen H, Ma Y, Achilefu S, Gu Y (2012) In vivo targeted deep-tissue photodynamic therapy based on near-infrared light triggered upconversion nanoconstruct. *ACS Nano*. doi:[10.1021/nn304872n](https://doi.org/10.1021/nn304872n)
73. Qian HS, Guo HC, Ho PC, Mahendran R, Zhang Y (2009) Mesoporous-silica-coated upconversion fluorescent nanoparticles for photodynamic therapy. *Small* 5(20):2285–2290. doi:[10.1002/sml.200900692](https://doi.org/10.1002/sml.200900692)
74. Zhao Z, Han Y, Lin C, Hu D, Wang F, Chen X, Chen Z, Zheng N (2012) Multifunctional core-shell upconverting nanoparticles for imaging and photodynamic therapy of liver cancer cells. *Chem Asian J* 7(4):830–837. doi:[10.1002/asia.201100879](https://doi.org/10.1002/asia.201100879)
75. Chen F, Zhang S, Bu W, Chen Y, Xiao Q, Liu J, Xing H, Zhou L, Peng W, Shi J (2012) A uniform sub-50 nm-sized magnetic/upconversion fluorescent bimodal imaging agent capable of generating singlet oxygen by using a 980 nm laser. *Chemistry* 18(23):7082–7090. doi:[10.1002/chem.201103611](https://doi.org/10.1002/chem.201103611)
76. Zhang P, Steelant W, Kumar M, Scholfield M (2007) Versatile photosensitizers for photodynamic therapy at infrared excitation. *J Am Chem Soc* 129(15):4526–4527. doi:[10.1021/ja0700707](https://doi.org/10.1021/ja0700707)
77. Meng H, Xue M, Xia T, Ji Z, Tarn DY, Zink JJ, Nel AE (2011) Use of size and a copolymer design feature to improve the biodistribution and the enhanced permeability and retention effect of doxorubicin-loaded mesoporous silica nanoparticles in a murine xenograft tumor model. *ACS Nano* 5(5):4131–4144. doi:[10.1021/nn200809t](https://doi.org/10.1021/nn200809t)
78. Shan JN, Budijono SJ, Hu GH, Yao N, Kang YB, Ju YG, Prud'homme RK (2011) Pegylated composite nanoparticles containing upconverting phosphors and meso-tetraphenyl porphine

- (TPP) for photodynamic therapy. *Adv Funct Mater* 21(13):2488–2495. doi:[10.1002/adfm.201002516](https://doi.org/10.1002/adfm.201002516)
79. Liu JN, Bu W, Pan LM, Zhang S, Chen F, Zhou L, Zhao KL, Peng W, Shi J (2012) Simultaneous nuclear imaging and intranuclear drug delivery by nuclear-targeted multifunctional upconversion nanoprobe. *Biomaterials* 33(29):7282–7290. doi:[10.1016/j.biomaterials.2012.06.035](https://doi.org/10.1016/j.biomaterials.2012.06.035)
 80. Wang C, Cheng L, Liu Z (2011) Drug delivery with upconversion nanoparticles for multifunctional targeted cancer cell imaging and therapy. *Biomaterials* 32(4):1110–1120. doi:[10.1016/j.biomaterials.2010.09.069](https://doi.org/10.1016/j.biomaterials.2010.09.069)
 81. Wang C, Tao H, Cheng L, Liu Z (2011) Near-infrared light induced in vivo photodynamic therapy of cancer based on upconversion nanoparticles. *Biomaterials* 32(26):6145–6154. doi:[10.1016/j.biomaterials.2011.05.007](https://doi.org/10.1016/j.biomaterials.2011.05.007)
 82. Chatterjee DK, Yong Z (2008) Upconverting nanoparticles as nanotransducers for photodynamic therapy in cancer cells. *Nanomedicine* 3(1):73–82. doi:[10.2217/17435889.3.1.73](https://doi.org/10.2217/17435889.3.1.73)
 83. Xu H, Cheng L, Wang C, Ma X, Li Y, Liu Z (2011) Polymer encapsulated upconversion nanoparticle/iron oxide nanocomposites for multimodal imaging and magnetic targeted drug delivery. *Biomaterials* 32(35):9364–9373. doi:[10.1016/j.biomaterials.2011.08.053](https://doi.org/10.1016/j.biomaterials.2011.08.053)
 84. Cheng L, Yang K, Li Y, Chen J, Wang C, Shao M, Lee ST, Liu Z (2011) Facile preparation of multifunctional upconversion nanoprobe for multimodal imaging and dual-targeted photothermal therapy. *Angew Chem Int Ed* 50(32):7385–7390. doi:[10.1002/anie.201101447](https://doi.org/10.1002/anie.201101447)
 85. Ungun B, Prud'homme RK, Budijon SJ, Shan J, Lim SF, Ju Y, Austin R (2009) Nanofabricated upconversion nanoparticles for photodynamic therapy. *Opt Express* 17(1):80–86
 86. Nichols JW, Bae YH (2012) Odyssey of a cancer nanoparticle: from injection site to site of action. *Nano Today* 7(6):606–618. doi:[10.1016/j.nantod.2012.10.010](https://doi.org/10.1016/j.nantod.2012.10.010)
 87. Zhang F, Braun GB, Pallaoro A, Zhang Y, Shi Y, Cui D, Moskovits M, Zhao D, Stucky GD (2012) Mesoporous multifunctional upconversion luminescent and magnetic “nanorattle” materials for targeted chemotherapy. *Nano Lett* 12(1):61–67. doi:[10.1021/nl202949y](https://doi.org/10.1021/nl202949y)

Chapter 23

Engineering of Mesoporous Silica Nanoparticles for In Vivo Cancer Imaging and Therapy

Feng Chen, Weibo Cai and Hao Hong

23.1 Introduction

In the last one decade, enormous efforts have been devoted to design smart, multifunctional, all-in-one nanosystems, which could not only be used for locating the cancer non-invasively, but also deliver sufficient drugs on-demand with a remotely controlled manner to suppress the growth of cancers [1–4]. Although the majority of these theranostic agents, including iron oxide (Fe_3O_4) nanoparticles [5], gold (Au) nanorods and nanocages [6, 7], carbon nanotubes and graphenes [8, 9], upconversion nanoparticles (UCNPs) [10, 11], could only show enhanced imaging and therapeutic capabilities in the preclinical settings, some of them have already demonstrated their potentials for future cancer diagnosis and therapy in human.

Silica-based nanoparticle is another category of such promising nanoplateforms, which has drawn increasing attentions because of its non-toxic nature, easily modified surface, and good biocompatibility [12–15]. Silica has been accepted as “generally recognized as safe” (GRAS) by the United States Food and Drug Administration (FDA). More excitingly, dye-doped ultrasmall silica nanoparticles,

F. Chen (✉) · W. Cai · H. Hong (✉)
Departments of Radiology, University of Wisconsin—Madison,
Madison, WI 53705, USA
e-mail: FChen@uwhealth.org

H. Hong
e-mail: HHong@uwhealth.org

W. Cai
Departments of Medical Physics, University of Wisconsin—Madison,
Madison, WI 53705, USA
University of Wisconsin Carbone Cancer Center, Madison,
WI 53705, USA
e-mail: wcai@uwhealth.org

also named as Cornell dots (C dots), are the first inorganic nanoparticles which have received approval from FDA for the first investigational new drug (IND) application for clinical cancer imaging trial in human [16].

In comparison with pure silica nanoparticle, mesoporous silica nanoparticles (MSNs) possess even more attractive properties, such as large surface area, high pore volume, uniform and tunable pore size, and low mass density, and have been intensively investigated as novel drug delivery systems since 2001 [17]. With all the attractive characteristics, MSN has been considered as one of the best nanoplatforms for cancer imaging and therapy [13]. The fabrication of MSN is really simple, scalable, cost-effective, and controllable [18, 19]. Based on well-established silica chemistry, the surface of MSN could be easily modified with many active functional groups [15], e.g., thiol ($-SH$) or amino ($-NH_2$), for facilitating the further conjugation of fluorescent dyes, stealth polymer (polyethylene glycol or PEG), targeting ligands (e.g., folic acid [20], transferrin (Tf) [21], aptamer [22], and Herceptin [23]). The large surface area, high pore volume, and tunable pore size make MSN a perfect candidate for loading and controlled delivery of therapeutic drugs for cancer therapy [14]. Besides encapsulating luminescent dyes into uniform MSN matrix for optical tracking imaging *in vitro* and *in vivo* [24], coating functional nanoparticles, e.g., quantum dots (QDs) [25], Au nanorods [26], UCNPs [27, 28], Fe_3O_4 [29, 30], with a shell thickness controllable MSN has become a new trend to develop novel functionalized MSNs (i.e., f-MSNs) for integrating imaging and therapy into one system. With the availability of techniques for creating a big hollow cavity inside original MSN for enhanced drug-loading capacity [13, 31], researchers are now making such hollow MSN (h-MSN) an even better nanoplatform for cancer imaging and therapy.

Although *in vitro* imaging and therapeutic applications by using MSN have been reached a great success [32], transferring these to the *in vivo* level is still facing big challenges and is now under intensive investigations. Also, many questions, such as the fate of MSNs *in vivo*, factors that affect the *in vivo* bio-distribution and clearance of MSNs with varied surface modifications, the strategies for targeting MSNs specifically to sites of interest, are still waiting to be answered. Here, we summarize the very recent progress and future directions of engineering MSNs for biological imaging and therapy *in vivo*.

23.2 Engineering the Morphology and Surface of MSN

Since the first report of MSN with uniform pore size and a long-range ordered pore structure in early 1990s [33], over 20 years of development has witnessed a rapid progress in control synthesis of MSN with varied morphologies, sizes, and surface properties. Many well-written reviews with detailed discussions about the synthesis and surface modifications of MSNs are available for readers [13–15, 18, 19, 34, 35]. The following sections will mainly be focused on strategies which have been developed for engineering of different MSNs for *in vivo* cancer molecular imaging and therapy.

23.3 Engineering of MSNs for Cancer Imaging In Vivo

Molecular imaging, with the definition of “visualization, characterization, and measurement of biological processes at the molecular and cellular levels in humans and other living systems” [36], is now greatly enhancing the way researchers and clinicians visualize and investigate complex biological events. Although still in its infancy, molecular imaging shows great promise in disease diagnosis, therapy monitoring, drug discovery, and, especially, the understanding of nanoscale interactions/reactions [37]. Molecular imaging with MSNs can be used to assess their biodistribution pattern, cell-targeting efficacy, cytotoxicity, and therapeutic output [38]. In the following sections, we will discuss about the engineering of MSN for fluorescence, positron emission tomography (PET), and magnetic resonance imaging (MRI).

23.3.1 Fluorescence Imaging

Fluorescence imaging is economical, easy to handle, and highly sensitive in certain scenarios and has been widely used for monitoring molecular events in live cells and tissues. Although MSN itself emits no light, many strategies have been developed for engineering MSN that can be tracked by fluorescence imaging. Fluorescent dyes with varied excitation/emission combinations have been chemically linked to the surface or loaded into the matrix of MSN for studying the dynamic distribution of MSN in vivo [24, 39]. Moreover, inorganic function nanocrystals, such as QDs [40], UCNPs [41, 42], with even more attractive optical properties [e.g., near-infrared (NIR) excitation and NIR emission] have also been encapsulated into MSN for imaging deeper tissues in vivo.

Fluorescein and rhodamine derivatives are frequently used for MSN modification with the application in cell targeting/labeling [43–45], drug delivery monitoring [46], or subcellular function exploration [47]. However, due to the penetration limitation, most of them were not optimal to be used in live animals [48]. For better in vivo imaging applications, MSNs can be modified or loaded with NIR organic dyes with emissions located in the range of 700–900 nm, which has been well accepted to have minimal skin absorbance and better tissue penetration [37, 49]. In one study, indocyanine green (ICG), an FDA-approved NIR contrast agent with the excitation/emission of 800/820 nm, has been absorbed onto MSNs via electrostatic attraction [50]. As-synthesized MSN-ICG showed high stability over the pH range from acidic to physiological. In vivo imaging in anesthetized rats demonstrated their prominent uptake in the liver with minimal autofluorescence, while significant autofluorescence from different organs (e.g., skin, hair, and urine) has been observed when injecting with fluorescein isothiocyanate (FITC)-conjugated MSN (Fig. 23.1a). By using in vivo fluorescence imaging and inductively coupled plasma mass spectroscopy (ICP-MS), the same

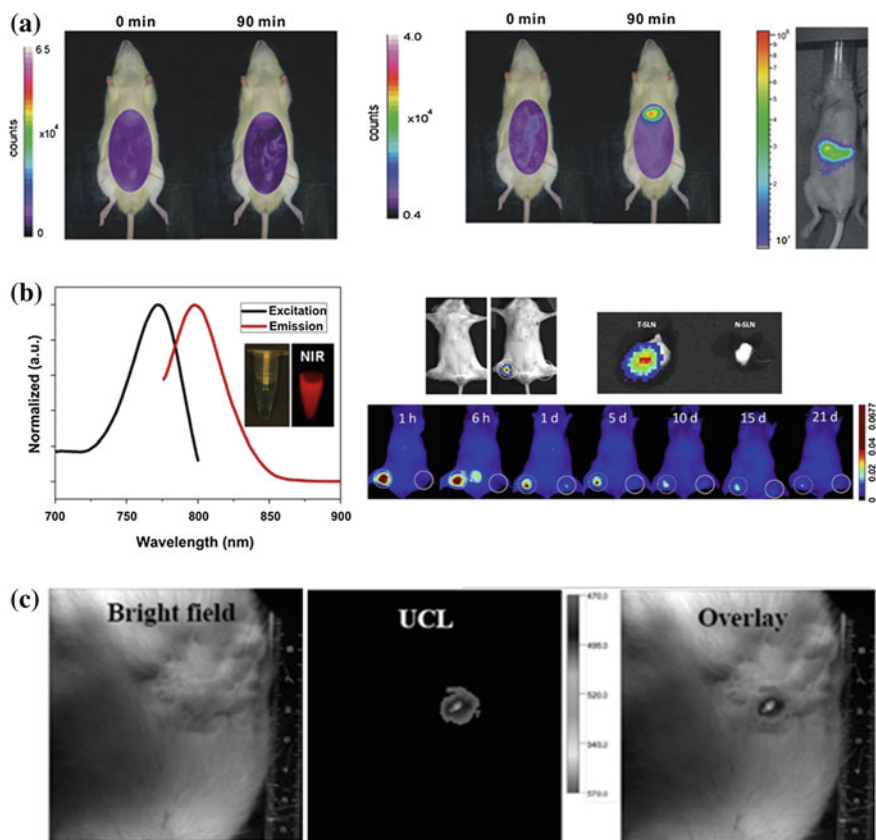


Fig. 23.1 **a** Fluorescence imaging of MSN-NH₂-FITC (*left*) and MSN-ICG (*middle*) in anesthetized rats before and 90 min after i.v. injection. Scanning time was all set to be 30 s. The fluorescence image of mouse injected with MSN-ICG at 3 h p.i. was also included (*right*). **b** (*Left*) Excitation and emission spectra of MSN nanoprobes. *Inset*: the fluorescence imaging of particles which were directly acquired before (*left*) and after (*right*) excitation by Maestro imaging system. (*Right*) In vivo optical imaging of SLNs in a 4T1 tumor metastatic model. The tumor-drained SLNs were confirmed by bioluminescence imaging and monitored by ZW800-modified MSNs for up to 3 weeks. **c** In vivo optical imaging of a tumor-bearing mice after local injection of UCNP@MSNs. From *left* to *right* bright field, upconversion luminescence, and overlay images. Recreated with kind permission from Wiley-VCH Verlag GmbH & Co. KGaA [27, 50] and Elsevier B. V. [49]

groups demonstrated the big differences in distribution patterns of MSN-ICG with different surface charges. MSN-ICG with more highly charged moieties (+34.4 mV at pH = 7.4) has been found excreted quickly from the liver into the gastrointestinal tract, while same nanoparticle with only less charged moieties (-17.6 mV at pH = 7.4) remained sequestered within the liver [51]. In another study, NIR dye ZW800-conjugated MSNs have been designed for tracking 4T1 tumor metastatic sentinel lymph nodes (T-SLNs) in vivo [49]. Significant

differences in uptake of MSNs in T-SLNs and normal lymph nodes (N-SLNs) have been clearly observed and could be maintained for up to 3 weeks (Fig. 23.1b), indicating the high stability of ZW800-conjugated MSNs in vivo and their potential for future tumor metastatic mapping.

Despite the success achieved by using ICG and ZW800-conjugated MSNs for optical imaging, room for further improvement is still available to minimize their inherent disadvantages, such as non-specific interactions with in vivo proteins/enzymes, low photostability, wider emission spectra [52]. Nanoparticles-based fluorescence reagents have tunable and narrow emission peaks, high quantum yields and non-photobleaching, which can serve as another promising candidate for fluorescence imaging [53, 54].

Due to the very small pore size (2–3 nm) of MSN, and to avoid potential optical quenching when decorating fluorescent nanocrystals at the surface of MSN, loading them into the mesoporous silica shell has been demonstrated to be the best way to synthesize high-quality fluorescent MSNs [25, 30]. By using cetyltrimethylammonium bromide (CTAB) as not only organic template for the formation of mesoporous silica shell, but also the stabilizing secondary surfactant for transferring the hydrophobic nanoparticles into water phase, a simple but efficient method for encapsulating any oleic acid-capped nanoparticles into mesoporous silica matrix has been developed and widely used to date [25, 26, 30]. Similar strategy has been used for the synthesis of a PEGylated liposome-coated QDs/MSN core-shell nanoparticles [40]. Although successful cellular imaging was achieved in MCF-7 breast cancer cell line by using such nanoparticles [40], so far no in vivo imaging study has been reported, possibly due to the toxicity concern from traditional cadmium-based QD [55].

In comparison with traditional organic dyes and QDs, UCNP excludes the potential ultraviolet photodamage and has been demonstrated to be much more biocompatible with extremely low toxicity in living systems [56, 57]. Besides, UCNP exhibits other attractive optical features such as sharp emission lines [58], long lifetimes (\sim ms) [59], large anti-Stokes shift [58], superior photostability [60], high detection sensitivity [61], non-blinking and non-bleaching [60, 62], high tissue penetration depth [63], minimal photodamage [64], and extremely low autofluorescence [65]. Moreover, by doping with well-selected lanthanide ions of Gd^{3+} , Er^{3+}/Yb^{3+} , and Tm^{3+}/Yb^{3+} (or combination of these ions) in suitable crystal hosts (e.g., $NaYF_4$), magnetic resonance and multicolor upconversion luminescence (UCL) imaging could be readily achieved [62, 66–68]. With the presence of heavy metal ions like Gd^{3+} , Yb^{3+} , and Lu^{3+} in $NaYF_4$ matrix, such UCNP has also been considered as an intrinsic computed tomography (CT) contrast agent recently [69–71]. Although UCNP@MSN could become a highly attractive candidate for cancer imaging and therapy, so far only very limited papers have been reported regarding the in vivo imaging of UCNP@MSN [27]. In one study, core-shell-structured $NaYF_4:Tm^{3+}/Yb^{3+}/Gd^{3+}@MSN$ nanoparticles have been synthesized with a modified method of that reported by Kim et al. [30] and used for in vivo tumor optical and MR imaging [27]. Although only preliminary in vivo UCL imaging of $NaYF_4:Tm^{3+}/Yb^{3+}/Gd^{3+}@MSN$ nanoparticles after intratumor

injection has been provided (Fig. 23.1c), as-synthesized $\text{NaYF}_4:\text{Tm}^{3+}/\text{Yb}^{3+}/\text{Gd}^{3+}@\text{MSN}$ could become more useful if suitable post-surface modifications, such as PEGylation, targeting ligand conjugations, and anti-cancer drug loading, could be invited in the future.

Although series of fluorescent MSNs have been developed and adopted for fluorescence imaging, most of them are still unsuitable for *in vivo* tumor imaging due to the limited tissue penetration depth. Also, despite NIR dyes (e.g., ICG and ZW800) conjugated MSNs or UCNP@MSN have shown promising *in vivo* imaging, due to the semi-quantitative nature of fluorescence imaging, engineering of MSN to enable a much more sensitive and quantitative imaging is urgently needed and will provide researchers with more accurate information about the fate of MSN *in vivo*.

23.3.2 PET

In PET imaging, internal radiation is administered through a low mass amount of chemicals labeled with a radioisotope. The major advantages of PET imaging over other modalities (e.g., optical and MRI) are that it is highly sensitive (picomolar detection limit) and quantitative with no tissue penetration limit [72]. Labeling nanoparticles with positron-emitting nuclides has been accepted as the most accurate mean for the non-invasive evaluation of their biodistribution [73]. Despite the above-mentioned advantages of radionuclide-based imaging, the numbers of studies using PET for MSN are rather limited.

So far, only one report about radioisotope-labeled MSN has been reported [49], where MSN-based triple-modal (fluorescence/MR/PET) nanoprobe has been developed for tracking 4T1 T-SLNs *in vivo*. To synthesize an MSN-based triple-modal nanoprobe (fluorescence/MR/PET), preprepared NIR dye (i.e., ZW800) doped MSN has been further labeled with gadolinium (Gd^{3+}) or ^{64}Cu through chelation (Fig. 23.2a). Systematic *in vitro* characterization and long-term (up to 3 weeks) *in vivo* T-SLNs mapping confirmed the high stability of as-designed nanoprobe. Based on PET imaging, the accumulation of MSNs in T-SLNs has been found to be very high and reached nearly 80 %ID/g at 1 h post-injection (p.i.), which was about 35-fold higher than that in N-SLNs (Fig. 23.2b). Although much room is still available for improving the current version of triple-modal MSN probes, the advantages for the integration of fluorescence/MR/PET together with one nanoparticle are obvious. PET imaging can be performed first to identify any skeptical “hot spots” in a highly sensitive and quantitative manner. Then, MRI will be used for achieving a better anatomical localization of site of interest. Last, on-spot optical imaging can be invited for providing an imaging guidance during surgery.

It is worthy to know that, different from optical imaging of UCNP@MSN [27], where typically the nanoparticle itself is detected, radionuclide-based imaging detects the radioisotopes rather than MSN itself. The biodistribution of radiolabeled MSN is measured indirectly by assessing the localization of the

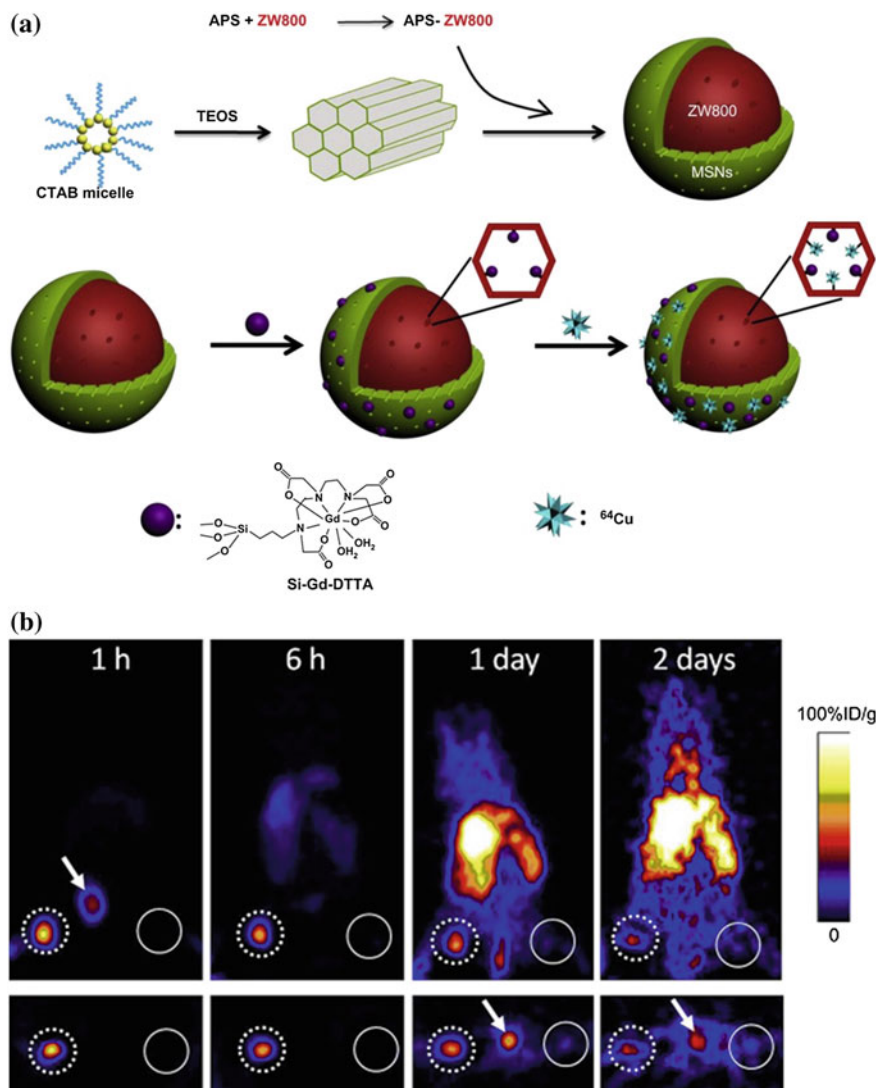


Fig. 23.2 a Schematic illustrations for the synthesis of triple-modal imaging MSN probes. (*up*) Diagram of ZW800-doped MSN fabrication; (*down*) diagram of Gd^{3+} and ^{64}Cu integration. **b** PET imaging of SLNs with ^{64}Cu -labeled triple-modal MSNs in a 4T1 tumor metastatic model. Recreated with kind permission from Elsevier B. V. [49]

radionuclide, which can provide quantitative measurement of the pharmacokinetics only if the radioisotope on MSN is stable enough under physiological conditions. With the possible dissociation of the radionuclide (typically metal ions) from the chelator, and/or the detachment of radionuclide-containing polymer coating from the nanoparticle, significant difference between the real nanoparticle

distribution and the radionuclide distribution may occur. Thus, the biodistribution data of radiolabeled nanoparticles based on PET imaging should only always be interpreted with caution. Rigorous validation of the stability of the radioisotopes on the nanoparticle should always be carried out to obtain more reliable experimental results.

Along with the advantages of PET for sensitive and quantitative *in vivo* imaging, one disadvantage is that their relatively low spatial resolution (>1 mm), which is significantly lower than that of MRI (<100 μm) [74]. MRI, with exquisite soft tissue contrast, is a widely used imaging modality with high clinical relevance due to its high spatial resolution [75]. By conjugating MSN with Gd^{3+} complex [76] or encapsulating with varied nanoparticles (e.g., Fe_3O_4 [77], Gd-doped UCNP [27], MnO_x [78, 79]) that can be demonstrated as MRI contrast agents, such f-MSNs could be ready to be used for MR imaging as well as drug delivery.

23.3.3 Magnetic Resonance Imaging

Generally, two major categories of f-MSNs have been developed. They are gadolinium- or MnO_x - modified MSNs [78, 80–82] for T_1 -weighted MRI and superparamagnetic iron oxide nanoparticle (SPION)@MSN core-shell structure for T_2 -weighted MRI [77, 83, 84].

Gd^{3+} -complex-modified MSNs have been used most frequently in cell tracking, especially in stem cell tracking [85–87]. In one study, dual-functional Gd-FITC mesoporous silica nanoparticles (Gd-Dye@MSN) that possess green fluorescence and paramagnetism have been developed to evaluate their potential as effective T_1 -enhancing trackers for human mesenchymal stem cells (hMSCs). As-synthesized Gd-Dye@MSN showed high biocompatibility with no obvious affection on the cell viability, proliferation, and differentiation capacities and has been suggested to be an ideal vector for stem cell tracking with MRI [85]. High internalizing efficiency, durability, and biocompatibility of Gd^{3+} -complex-modified MSN have also been demonstrated in the other similar studies [86, 88]. More recently, different novel Gd^{3+} -complex-modified MSNs have also been demonstrated useful for tumor targeting and drug delivery [83, 88, 89]. At the same time, different methods for enhancing the relativity of these MSNs are also available [76, 81, 82, 90, 91].

Manganese (II) has been adopted as an MRI contrast agent due to its less toxicity and five unpaired electrons with long electronic relaxation time. MSN-coated hollow manganese oxide (MnO) nanoparticles (HMnO@MSN) have been developed as a powerful tool for serial MR monitoring of adipose-derived mesenchymal stem cells [78], which enabled the long-term monitoring of cell transplants up to 14 days (Fig. 23.3a). Possibly due to the shielding of manganese ions by mesoporous silica coating, results showed that as-synthesized HMnO@MSN had only a very low r_1 value of about $0.99 \text{ mM}^{-1} \text{ s}^{-1}$. In another study, by using an *in situ* redox reaction, Chen et al. reported a novel manganese oxide-based multifunctionalization of hollow mesoporous silica nanoparticles (h-MSN@MnO)

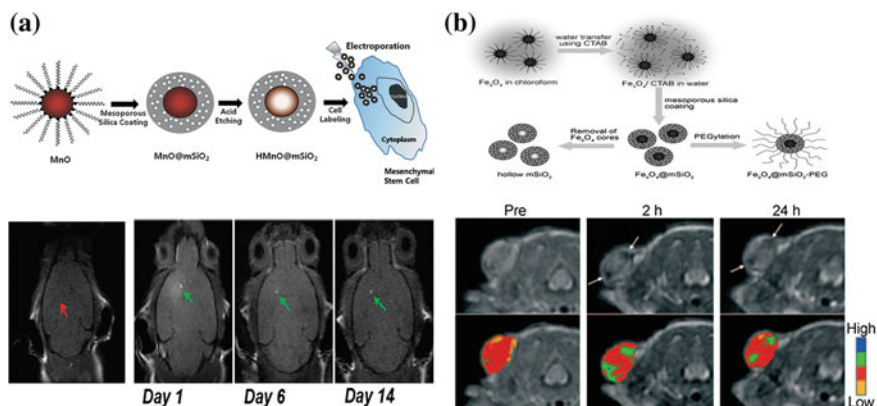


Fig. 23.3 **a** *Up* schematic illustration for the synthesis of HMnO@MSN and labeling of stem cells. *Down* in vivo T₁-weighted MR images of transplanted stem cells. No hyperintense signal has been detected in mouse transplanted with unlabeled stem cells, while observable signals have been detected in labeled stem cells and kept visible for at least 2 weeks p.i. **b** *Up* schematic illustration of the synthetic procedure for SPION@MSN core-shell nanostructures. *Down* in vivo T₂-weighted MR images (*upper row*) and corresponding color maps (*lower row*) of tumor before and after the i.v. injection of SPION@MSN into MCF-7 tumor-bearing nude mouse. Recreated with kind permission from American Chemical Society [78] and Wiley-VCH Verlag GmbH & Co. KGaA [77]

for pH-responsive T₁-weighted MRI to detect the acidic tumor microenvironment [92]. Under weak acid conditions, the release of Mn²⁺ ions from h-MSN@MnO could cause a significant increase in r_1 value (up to 8.81 mM⁻¹s⁻¹), which has been demonstrated to be 11-fold higher than the same value in neutral condition. This is the highest r_1 value that has ever been reported in manganese-based MRI contrast agents, and such pH-responsive MRI contrast enhancement might become a useful technique for future cancer diagnosis.

SPION is among the most well-developed contrast agents for T₂-weighted MRI [5]. Although oleic acid-assisted strategy could guarantee high-quality SPIONs with uniform size and morphology [93], as-synthesized SPIONs are always coated with a layer of oleic acid ligands, which makes them water insoluble. Surface modifications, such as ligand exchange [94] and mesoporous silica coating [77], can efficiently overcome the hydrophobicity of original SPIONs, making them ready for biological applications. Recent research showed that the shell thickness of mesoporous silica could significantly affect the MRI contrast enhancement and might become a simple way to tune r_2 values of SPION@MSN nanoparticles [95]. With the presence of MSN at the surface, small molecular drugs [e.g., docetaxel (DOC) and doxorubicin (DOX)] can be loaded for controlled drug release and cancer therapy, suitable length of PEG could also be added to increase the blood circulation time of SPION@MSN for a better enhanced permeability and retention (EPR) effect. In one study, enhanced tumor uptake of uniform PEGylated SPION@MSN in MCF-7 tumor-bearing nude mice has been achieved based on pure

EPR effect [77] (Fig. 23.3b). Higher in vivo tumor-targeting efficiency could be achieved by conjugating SPION@MSN with certain targeting ligands (e.g., proteins, peptides, or small molecules). Many other studies have further proven the feasibility in using functionalized SPION@MSN as a useful tool for tracking various types of cells with MRI [86, 95–97]. The low cytotoxicity, high cell-labeling efficiency, and high biocompatibility of SPION@MSNs make them attractive choices for a variety of biomedical applications.

23.3.4 Other Modalities and Multimodality Imaging

Although still under intensive investigation, f-MSNs can also be applicable in other molecular imaging modalities such as ultrasound or computed tomography (CT). Compared with other imaging modalities, ultrasound imaging stands out as a versatile, painless, low-risk, non-invasive procedure, which can be done and readily repeated virtually anywhere. Au nanoparticle and perfluorohexane-encapsulated h-MSNs have been used for both contrast-enhanced ultrasound imaging and high-intensity focused ultrasound (HIFU) surgical therapy [98, 99], demonstrating that functionalized h-MSN can serve as a novel theranostic agent for both the imaging and combined therapy under the guidance of intensified ultrasound (Fig. 23.4a). With the support of X-ray, CT can provide high-resolution anatomical information and has indisputable benefits to the practice of medicine. ICG-loaded Au@MSN has been developed recently for dual-modal fluorescence/CT imaging (Fig. 23.4b) [100]. Such probe might have great potential applications for use in applications such as cancer targeting, molecular imaging in combination with radiotherapy, and phototherapy.

Each imaging modality discussed above has its advantages and limitations. For example, it is difficult to accurately quantify a fluorescence signal in living subjects with fluorescence imaging alone, particularly in deep tissues; MRI has high-resolution and good soft tissue contrast but low sensitivity; radionuclide-based imaging techniques are very sensitive but suffer from relatively poor spatial resolution and high costs. Combination of multiple imaging modalities may provide complementary information than a single modality alone. Using MSNs as a multifunctional platform, combination with different imaging modalities will enable the development of “smart” nanomedical platforms with higher clinical potentials. One of the most selected combinations is the integration of fluorescent and magnetic materials into MSNs, which merges the high sensitivity of fluorescence with the high spatial resolution of MRI for real-time monitoring of disease evolution [27, 88] or specific cell tracking [97]. Similar rules can apply to the MSNs for CT/fluorescence dual imaging purpose [100]. Another attractive choice is the unionization of ultrasound and MRI [92]. Using MRI as the presurgical evaluation tool and ultrasound as the real-time guidance during the surgical removal of lesions, this type of MSNs can stand for the next generation of theranostic agents. MSN nanoprobe, with triple-modal (i.e., PET/fluorescence/MRI)

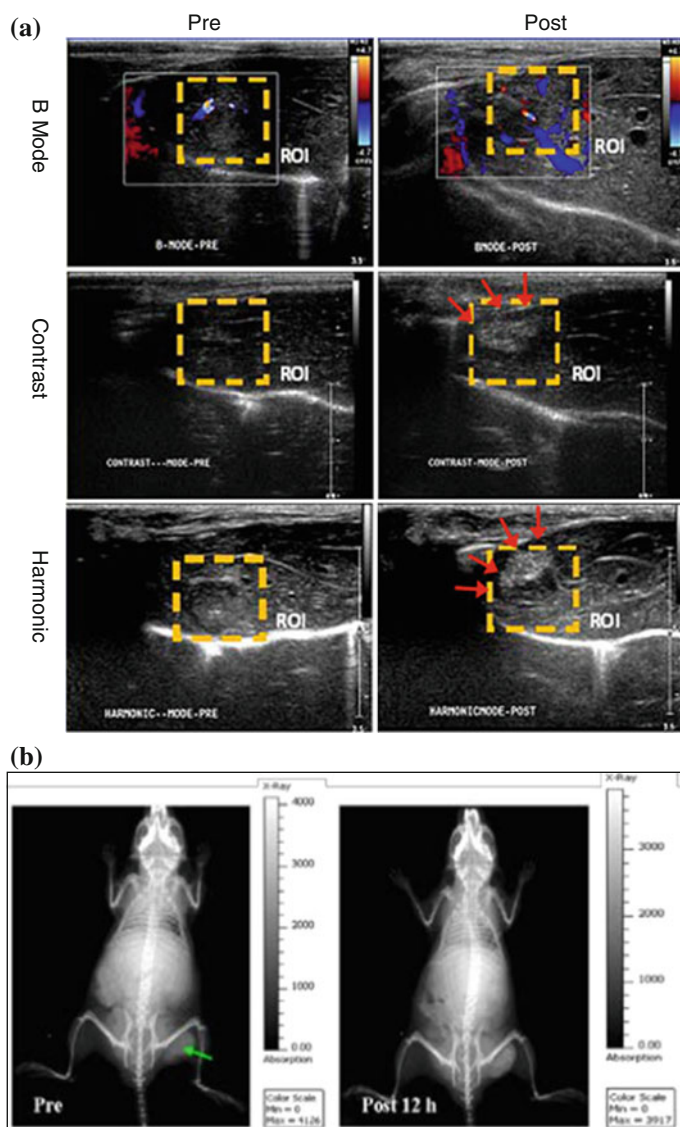


Fig. 23.4 **a** Ultrasound imaging in rabbit VX2 liver tumor before and after the injection of perfluorohexane-encapsulated MSNs. **b** In vivo planar X-ray images before and 12 h after the injection of ICG-loaded Au@MSN. Recreated with kind permission from Elsevier B. V. [98] and OSA [100]

imaging modality, has also been developed and used for long-term monitoring of tumor-draining SLNs [49]. For the multimodality imaging applications, the stability and robustness of MSNs should stay high to guarantee the imaging results from different modalities that are consistent and complementary.

23.4 Engineering of MSNs for Cancer Therapy In Vivo

Besides using MSN as a useful nanoplatform for molecular imaging, thanks to its large surface area, high pore volume, and uniform and tunable pore size, MSN has long been considered as highly attractive candidate for delivering small molecular drugs to tumor site for suppressing the growth of cancer. Despite the huge progress that has been made in the in vitro therapy with drug-loaded MSNs, in vivo translation is still facing big challenges and is now under intensive investigations. In the following sections, only engineering of MSNs for successful in vivo therapeutic studies will be highlighted.

23.4.1 Pure MSNs or h-MSNs for Chemotherapy

Although great efforts have been devoted to improve the in vivo therapeutic efficiency of anti-cancer drugs by using various kinds of drug delivery systems, developing a universal strategy for improving both the passive and active targeted drug delivery is still a huge challenge. By reducing the size of MSN to about 50 nm and further surface functionalized with a polyethyleneimine–polyethylene glycol copolymer (PEI-PEG), Meng et al. demonstrated that such redesigned MSN@PEI/PEG could effectively reduce the particle opsonization while improving the EPR effect and in vivo therapeutic effects [101]. In comparison with similar MSNs with only PEGylation, the further introduction of cationic charged PEI has been shown highly useful to enhance the repulsion between nanoparticles, which increase the particle stability and reduce the chance of their aggregation in saline (Fig. 23.5a). A significantly higher (~12 %) passive tumor-targeting efficiency of NIR dye-incorporated MSN@PEI/PEG has been demonstrated, while only limited tumor uptake has been observed in non-PEGylated (~1 %) and PEGylated (~3 %) control groups (Fig. 23.5b). Although clearly higher fluorescence signal could be seen in MSN@PEI/PEG group based on the optical imaging, due to the semi-quantitative feature of fluorescence, the real differences in EPR effect might deserve further investigation by using more quantitative method, such as PET imaging. Interestingly, no obvious kidney uptake of all three kinds of nanoparticles has been observed after 72 h post-injection, which is inconsistent with similar nanoparticle reported by the same group [102, 103]. After demonstrating the enhanced passive targeting efficiency of MSN@PEI/PEG, the therapeutic effect of DOX-loaded MSN@PEI/PEG on KB-31 tumor model has also been investigated, which showed an 85 % of tumor inhibition, 10 % higher than that of free DOX (i.e., 70 %) (Fig. 23.5c). Importantly, mice treated with DOX-loaded MSN@PEI/PEG showed reduced systemic, hepatic, and renal toxicity compared to free DOX drug. One of the possible drawbacks of these DOX-loaded MSN@PEI/PEG nanoparticles is its high lung uptake, which usually is caused by the aggregation of nanoparticle after intravenous (i.v.) injection. Although the

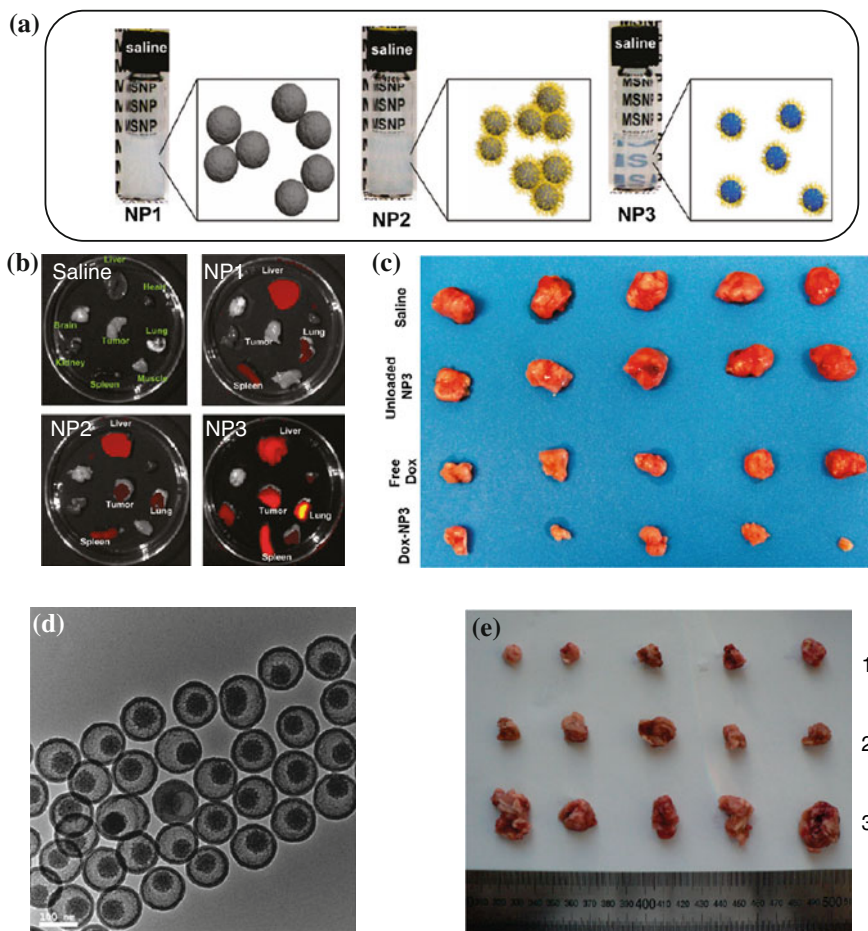


Fig. 23.5 **a** Photographs of three different MSNs in saline (20 mg/mL). *NP1*: 100-nm-sized non-PEGylated MSNs, *NP2*: 50-nm-sized PEGylated MSNs, *NP3*: 50-nm-sized PEI/PEG copolymer-modified MSNs. **b** Ex vivo optical imaging of major organs (heart, lung, spleen, liver, kidney, brain, and muscle) from mice at 72 h post-injection. **c** Photograph of tumor sizes at the end of treatment. **d** TEM image of SN-PEG. **e** In vivo anti-tumor effect of SN-PEG-DOC and Taxotere on H22 liver cancer subcutaneous model (*dose*: 20 mg/kg of DOC, 4 doses in 13 days). Photographs of tumors from different treatment groups of [1] SN-PEG-DOC, [2] Taxotere group, and [3] control group with saline. Recreated with kind permission from American Chemical Society [101, 102]

authors claimed no significant lung damage, no reason for such high lung uptake has been provided yet.

DOC is a hydrophobic drug which could kill cancer cells via stabilizing microtubules to induce cell cycle arrest and caspase-2- and caspase-3-dependent apoptoies [104]. The current clinical formulation of DOC, also named as Taxotere, is known to have severe adverse effect due to the acute hypersensitive reaction

induced by its toxic excipients (i.e., Tween-80) and the severe systematic toxicity of DOC itself [105]. By loading DOC into a well-designed PEGylated silica nanorattle (SN-PEG) (Fig. 23.5d), Li et al. demonstrated the feasibility for enhancing the in vivo therapeutic efficiency of SN-PEG-DOC while reducing the systematic toxicity of DOC in H22 liver cancer subcutaneous model [106]. The absence of toxic Tween-80 surfactants and reduced amount of free DOC after i.v. injection have been suggested to be two of the main factors which contribute the lower systematic toxicity. Their systematic treatment experiments showed a significant inhibition of tumor weight by SN-PEG-DOC up to 72 %, in comparison with that of 57 % in Taxotere groups (Fig. 23.5e). Although no data about the passive targeting efficiency of SN-PEG-DOC in vivo could be found in this study, the author believed the possibility to further enhance such therapeutic efficiency by conjugating nanoparticle with certain targeting ligands.

23.4.2 *f*-MSN@PS for Photodynamic Therapy

Photodynamic therapy (PDT) has arisen as an alternative to chemotherapy and radiotherapy. PDT involves the use of certain photosensitizer (PS) which, upon irradiation with light with specific wavelength and in the presence of oxygen, could lead to the generation of cytotoxic singlet oxygen and consequently cause the killing of cancer cells [107]. Due to the limited light penetration depth, for a long time, PDT has only been effective to certain superficial cancers, such as skin cancer [107]. The combination of PDT with light in the NIR region might hold the potential for extending the treatment to tumors located deeply in body. Recent researches have demonstrated such possibility in *f*-MSNs either by using a well-designed PS which has high two-photo absorption (TPA) cross-section in the biological spectral window (i.e., 700–1,000 nm) [108], or by using UCNPs as an internal light transducer for transferring 980 nm laser to visible light for triggering the generation of singlet oxygen [28].

In one study, Gary-Bobo et al. reported the first example of tumor treatment by using MSNs which were covalently linked with PS and targeting ligands (mannose moiety), denoted as MSN1-mannose (Fig. 23.6a) [108]. Each MSN had about 6,850 units of PS and a hydrodynamic diameter of 118 nm. By irradiation with 760 nm laser (80 mW or 10.6 J cm^{-2}), in vitro two-photo-excitation PDT effect showed a twofold enhanced therapeutic effect of MSN1-mannose in three cancer cell lines, in comparison with group treated with only non-targeted MSN1 nanoparticles. To investigate the potential of MSN1-mannose for in vivo treatment, nude mice-bearing HCT-116 xenografts were used. With only one i.v. injection, the authors have demonstrated a significant reduction in tumor weight (ca. 70 %) in the group treated with MSN1-mannose (dose: 16 mg/kg, light dose: 760 nm laser for three periods of 3 min) compared with control groups (Fig. 23.6b). Surprisingly, it was reported that MSN1-mannose treatment followed by two-photo-excitation PDT prevented macrometastasis formation in liver and colon,

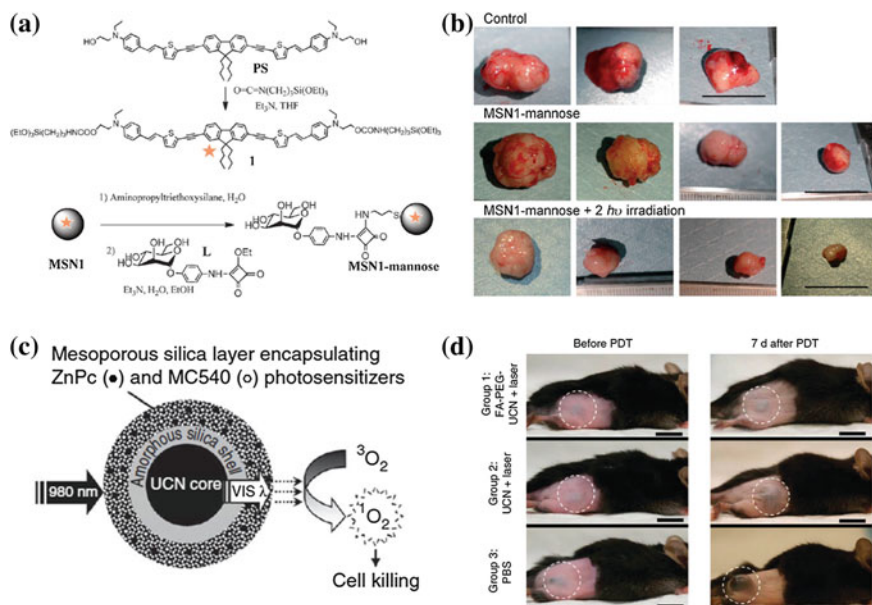


Fig. 23.6 **a** Synthesis of PS and MSN1-mannose. **b** Effect of two-photo-excitation PDT on tumor growth. **c** Schematic of MSN coated with UCNP coloaded with ZnPC and MC540 PSs for PDT. After the excitation of single 980 nm laser, the UCNP can convert the NIR light to visible light of different wavelength, which will be absorbed by the PSs and trigger the generation of singlet oxygen. **d** Representative photos of mice injected with folic acid-conjugated PEGylated UCNP, unmodified UCNP and PBS. Scale bar: 10 mm. Recreated with kind permission from Wiley-VCH Verlag GmbH & Co. KGaA [108] and Nature Publishing Group [28]

while no such effect could be observed in groups of mice treated with saline alone or with MSN1-mannose without 760 nm laser irradiation. The authors suggested the decrease in the subcutaneous tumor growth and its associated neoangiogenesis to be the main reason behind such effect. Although enhanced therapeutic effects have been demonstrated by using MSN1-mannose plus laser in this report, no data about the exact tumor uptake and biodistribution of MSN1-mannose after i.v. injection could be found.

UCNP has gained growing interests owing to their unique UCL features that are highly suitable for multimodal imaging in living subjects [11]. UCL is a unique process where low-energy continuous wave of NIR light (usually 980 nm) is converted to higher-energy light through the sequential absorption of multiple photons or energy transfer [109]. By using the visible emission bands (mostly red emissions) of UCNP for triggering the generation of singlet oxygen, researchers have developed many different versions of UCNP/PS nanocomposites for 980 nm laser-initiated PDT [28, 110–118].

In one well-conducted study, Idris et al. demonstrated that enhanced PDT effect could be achieved by encapsulating two different PSs (i.e., ZnPC and MC540) into

one mesoporous silica-coated NaYF₄:Er/Yb nanoparticle (Fig. 23.6c) [28]. In vitro experiments demonstrated the higher generation rate of singlet oxygen and lower cell viability when shedding 980 nm light on co-PS-loaded nanoparticles. After the injection of B10-F0 melanoma cell that prelabeled with co-PS-loaded UCNP under the skin of C57BL/6 mice, they succeeded in inhibiting the tumor growth rate significantly by irradiating the injected site with a 980 nm laser. However, in the case of injecting the drug either intratumorally or intravenously, only slight tumor growth inhibition could be achieved, indicating such in vivo PDT effect is still limited. Since the half-life of singlet oxygen is very short, on the order of microseconds, and can therefore act only on target structures that are in close proximity to it, in order to guarantee an effective PDT therapeutic outcome, sufficient amount of PDT agents should be able to accumulate in the tumor site and somehow further internalized by the cells. Much room is still available for enhancing the UCNP-based PDT therapeutic effect in the future.

23.4.3 MSN for Gene Delivery and Therapy

Although small interfering RNA (siRNA) holds great promising as a powerful gene therapeutic agent for the treatment of a wide range of diseases from viral infection to cancer [119, 120], it is still a big challenge to deliver effective dose of siRNA into target cells with high gene-silencing efficacy while maintaining its intact chemical structure. Aiming to provide a better solution to these problems, except using previously reported nanoplatforms, such as viral gene or liposomes, Na et al. reported a highly efficient siRNA delivery system based on biocompatible MSNs with large pores of 23 nm in diameter (denoted as MSN23) and have demonstrated their advantages in siRNA delivery for gene silencing both in vitro and in vivo (Fig. 23.7a) [121]. As-designed MSN23 was prepared by expanding the original pores of MSN2 (mesoporous silica with 2 nm pore size) with trimethylbenzene (Fig. 23.7b). With the presence of larger pores, they have demonstrated that siRNA could be loaded into the MSN23 with a decent loading capacity of 1.25 pmol/μg and shown high resistance against the RNase-mediated degradation while maintaining its chemical integrity in vivo. The in vivo siRNA delivery and gene silencing by using siRNA-MSN complex have been demonstrated in mice-bearing green fluorescent protein (GFP) expressing HeLa and MDA-MB-231 xenografts, which showed significantly decreased green fluorescence intensity and inhibition of tumor growth rate in positive groups after intratumoral injection with siGFP (or siVEGF)-MSN complexes vascular endothelial growth factor (VEGF) (Fig. 23.7c, d). Although the intratumoral administration of siRNA-MSN in this study, to a certain degree, limited its application and needed further improvement by optimizing the surface modifications, it ensured the accumulation of sufficient siRNA in tumor site and guaranteed the efficiency in gene silencing.

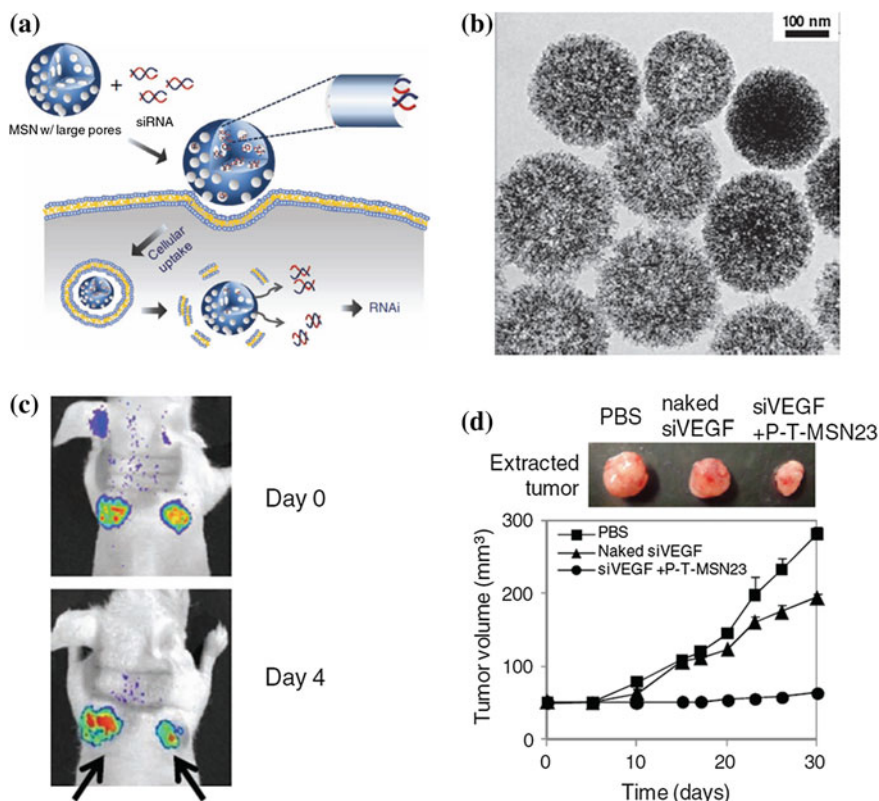


Fig. 23.7 **a** A schematic illustration showing the siRNA delivery with MSN possessing larger pores. **b** Representative TEM image of MSN23. **c** In vivo GFP silencing in GFP-expressing HeLa xenografts on day 0 and day 4. Mice were intratumorally injected with PBS (*left*) and siGFP-MSN complex (*right*). **d** In vivo VEGF silencing in MDA-MB-231 xenografts. Intratumoral injections of siVEGF-P-T-MSN complex, naked siVEGF, and PBS were performed four times at days 0, 5, 10, and 20. Tumor growth was observed for 30 days from the initial injections. Extracted tumors at day 30 were shown for size comparison. Recreated with kind permission from Wiley-VCH Verlag GmbH & Co. KGaA [121]

23.4.4 MSN for MRI-Guided Ultrasound Therapy

HIFU surgery is one of the most promising non-invasive and non-radiative transcutaneous treatment protocols for cancer therapy [122]. Unlike radiation, HIFU is non-ionizing and can be repeated without damaging healthy tissue. Although it is still under investigation in clinical trials and has not received the stamp of approval by the FDA in the United States, HIFU is now being used extensively to treat localized prostate cancer in Europe, Russia, Japan, and other Asian countries. How to realize the accurate positioning of therapeutic targets for focused ultrasound during surgery and achieve an effective HIFU therapy under

simultaneous imaging guidance are two typical challenges before HIFU realize its extensive clinical applications.

To potentially provide a solution to these challenges, Chen et al. have designed an interesting mesoporous composite nanocapsule (MCNC), which is both HIFU synergistic agent for enhancing surgery effect and MRI contrast agent for imaging guiding (Fig. 23.8a) [123]. Specifically, MCNC was formed firstly by reacting strong oxidizing MnO_4^- ions with surfactant (i.e., CTAB) to generate MnO nanoparticles in the mesoporous silica network for T_1 -weighted MR contrast effect and then by loading biocompatible perfluorohexane (PFH) in the hollow cavity for an enhanced HIFU surgery effect (Fig. 23.8b) [99]. The final dynamic light scattering size of MCNCs was found to be ~ 342 nm. Although raw MSN has been known to be highly unstable and easily aggregated in biological buffers, no further surface modification (e.g., PEGylation) has been introduced in this study and all of the following in vitro and in vivo imaging-guided surgeries have been achieved by using such raw MCNCs. The effectiveness of MCNCs as the synergistic agent for HIFU surgery has been evaluated by using degassed bovine liver as the model tissue. To further evaluate the in vivo therapeutic effect of PFH-MCNCs in vivo, an MRI/HIFU apparatus and rabbit-bearing VX2 liver tumor were used. After ear vein injection of PFH-MCNCs (200 μL , 30 mg/mL), tumor was first imaged by using T_1 -weighted MRI and then precisely focused and irradiated by ultrasound (150 W, 5 s). The mean volume of coagulated tumor by HIFU exposure in PFH-MCNCs group was found 8.3 and 1.8 times larger than control groups that only received PBS and MCNCs/PBS, respectively, demonstrating the enhanced synergistic efficiency of PFH-MCNCs for MRI-guided HIFU surgery (Fig. 23.8d, e). Since tumors in liver could already be clearly seen by MRI without using any contrast agents (Fig. 23.8c), other tumor models might be needed to further demonstrate the proposed concept. Moreover, the slight change in signal intensity in tumor after ear vein injection might not be a good evidence to support the uptake of MCNCs in tumor, other more sensitive and quantitative method, such as PET imaging, might be considered to confirm this in the future research.

23.4.5 MSN for Combined Thermal Therapy and Chemotherapy

For the last 5 years, combining hyperthermia and chemotherapeutic agents into one nanosystem (e.g., Au nanocages, carbon nanotubes) for synergistic effects has been intensively pursued [6, 124]. Such synergistic effect of thermal therapy and chemotherapy has been speculated to be caused by the altered kinetics, permeability, and uptake of chemotherapeutic agents during the heating process [125]. With the presence of large hollow cavity for enhanced drug-loading capacity and well-established silica chemistry for surface modifications, biocompatible hollow (or rattle type) mesoporous silica holds great potential as a novel nanopatform for

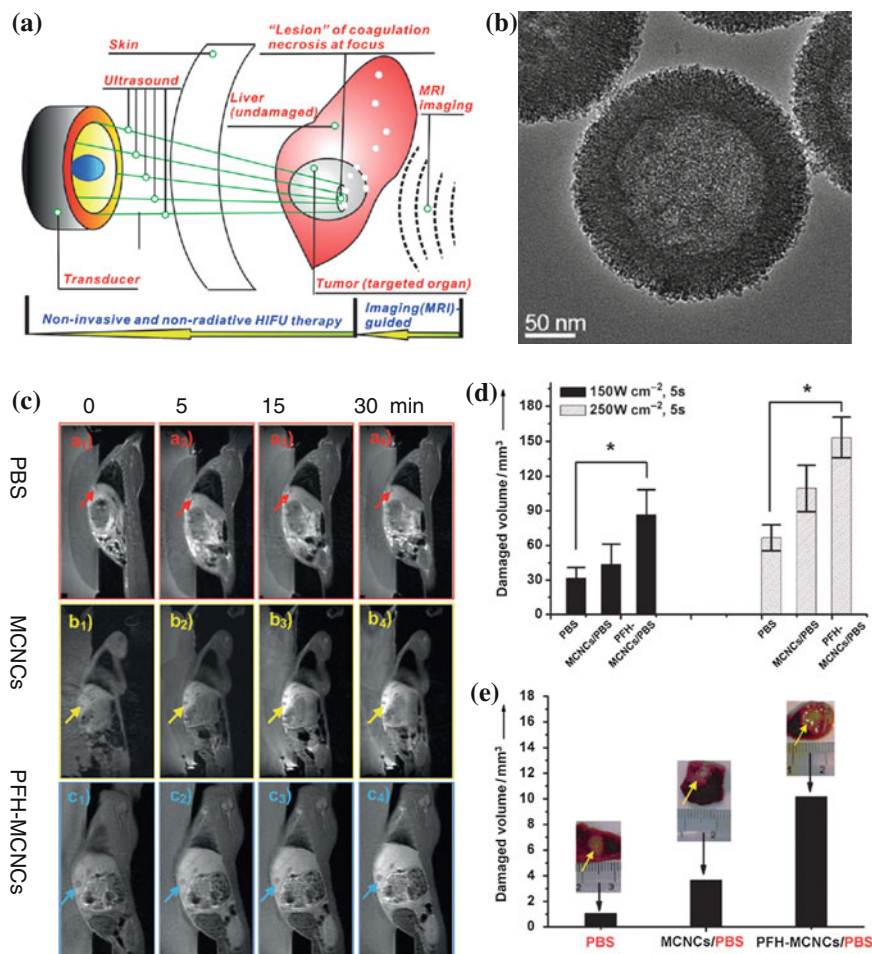


Fig. 23.8 **a** Technical principle of MRI-guided HIFU for the surgery of hepatic neoplasm in rabbits. **b** TEM image of MCNC. **c** In vivo T_1 -weighted MRI of rabbit-bearing VX2 liver tumor after ear vein injection of PBS, MCNCs/PBS and PFH-MCNCs/PBS. **d** In vitro coagulated-tissue volume of degassed bovine liver after intratissue injection of PBS, MCNCs/PBS, and PFH-MCNCs/PBS under the same irradiation power and duration (150 W cm⁻², 5 s and 250 W cm⁻², 5 s). **e** In vivo coagulated necrotic tumor volume by MRI-guided HIFU exposure under the irradiation power of 150 W cm⁻² and duration of 5 s in rabbit liver tumor after ear vein injection (inset digital photos of tumor tissue after HIFU exposure). Recreated with kind permission from Wiley-VCH Verlag GmbH & Co. KGaA [123]

integrating both thermal therapy and chemotherapy in one multifunctional system [126–128].

For example, Liu et al. successfully reported an interesting PEGylated gold nanoshell-coated silica nanorattle (Fig. 23.9a) (denoted as pGSNs), which was further loaded with anti-cancer small molecular drug (i.e., DOC, which has been

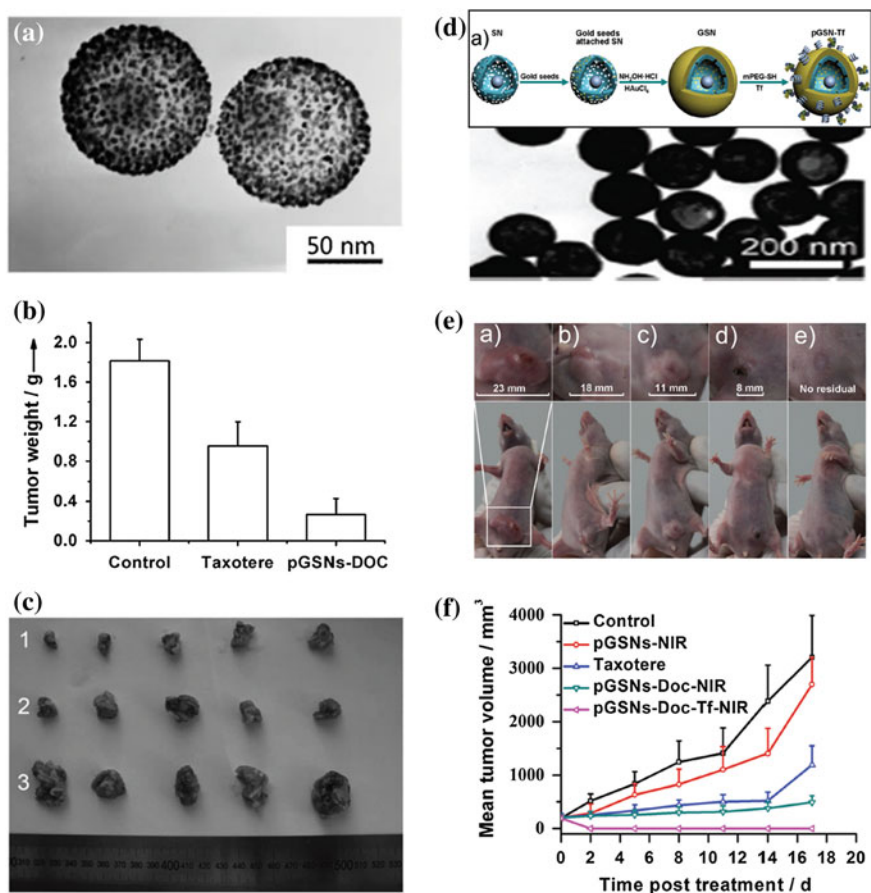


Fig. 23.9 **a** TEM image of gold nanoshell-coated silica nanorattle. **b** Tumor weights of three treatment groups. **c** Photograph of tumor sizes at the end of treatment from group pGSNs-DOC (1), Taxotere (2), and control groups (3). **d** TEM image of GSNs. *Inset* shows the schematic diagram of GSNs synthesis and bioconjugation. **e** Representative images of mice from groups of (a) control, (b) pGSNs-NIR, (c) Taxotere, (d) pGSNs-Doc-NIR, (e) pGSNs-Doc-Tf-NIR on day 17 after treatment. **f** In vivo anti-tumor activities of corresponding groups on MCF-7-bearing nude BALB/c mice. Recreated with kind permission from Wiley-VCH Verlag GmbH & Co. KGaA [127, 130]

reported to have a hyperthermia-enhanced cytotoxicity [129]) for investigation of its synergistic effects in cancer therapy [127]. The shell thickness of Au nanoshell could be easily tuned by altering the precursors and reaction time. After i.v. injection of pGSNs-DOC, the tumor sites of H22 tumor-bearing ICR mice were exposed to NIR laser (808 nm) at 2 W cm^{-2} for 3 min after 6 h p.i. Their results showed the significant tumor inhibition rate in pGSNs-DOC group (85.4 %), higher than that of Taxotere group (57.4 %) (Fig. 23.9b, c). However, some

important control groups (e.g., pGSNs with NIR laser and pure pGSNs-DOC without laser) were missing in this study, and these results should be highly useful to further demonstrate the synergistic effects in cancer therapy. Also, no solid evidence could be found to support the passive targeting of pGSNs-DOC *in vivo* and the detailed targeting efficacy is unknown either. Although the accelerated drug release rate has been observed in other similar nanosystems, i.e., Au@m-SiO₂(DOX) [126], no such effect could be found in pGSNs-DOC system, possibly due to the good thermal and mechanical stability of pGSNs-DOC, as suggested by the authors.

To further ensure a better thermal therapeutic effect, the same group further reported a Tf-targeting ligand-conjugated pGSNs (Fig. 23.9d) (denoted as pGSN-Tf) and demonstrated a complete regression of breast tumor *in vivo* (Fig. 23.9e, f) [130]. Although pGSNs-Tf has been designed for active targeting of nanoparticle to tumor *in vivo* and was expected to show enhanced tumor uptake at the same time post-injection, inductively coupled optical emission spectrometry (ICP-OES) of Au from both pGSNs-Tf and pGSNs in solid tumors failed to show any significant difference in tumor uptake (both were $\sim 3\%$ of injected dose), indicating such cell-based active targeting strategy might not work in this case due to extremely limited extravasation of either pGSNs-Tf or pGSNs *in vivo*. Without clear knowledge of the pGSNs extravasation and suitable evidence to support their hypothesis, the authors attributed the observed enhanced therapeutic effects simply to an enhanced intracellular localization within cancer cells of pGSNs-Tf. Moreover, *in vivo* non-invasive imaging might be needed in the future to better determine the best treatment window for this interesting nanoparticle.

Based on the discussions above, the combination of thermal therapy with chemotherapy is indeed a better option and has shown promise in future clinical translation. Although enhanced therapeutic effects could be achieved in these studies based on passive EPR effect, better outcome should be expected if active targeting strategies could be incorporated.

23.5 Conclusions and Future Perspective

In conclusion, we summarize here the engineering of various kinds of MSNs for *in vivo* molecular imaging and therapy. Although inexpensive fluorescence imaging of f-MSNs will continue to be used in studying the interaction between MSNs and cells *in vitro* and *in vivo*, non-invasive PET imaging of radioisotopes-labeled MSN might become a better choice in the near future for investigating the real-time tumor-targeting efficiency and fate of MSNs in live animals. Engineering of MSNs to integrate two or more imaging modalities into one nanosystem will also become a new trend and provide researchers complementary and more accurate information about the pharmacokinetics of MSNs *in vivo*. Thanks to the huge progress in control synthesis and surface modifications of MSNs for biological imaging applications, the past 5 years have also witnessed a rapid progress in applying MSNs for

preclinical therapeutic studies and have shown great promises in fighting against different cancers. Although most of the designed MSNs so far are still far from perfect, with the increasing awareness of the high potential of biocompatible MSNs in cancer imaging and therapy, even more advances in applying f-MSNs for combined imaging and therapy will be anticipated in the next 5 years.

However, many challenges still remained to be conquered. Firstly, although silica has been accepted as GRAS by the FDA, and silica-based C dots have received approval for the first IND application for human clinical trial for cancer imaging [16], the toxicity concerns of MSN will continue to be an major issue due to the inevitable use of toxic surfactants as templates for creating mesopores during the synthesis of MSN. Systematic short- and long-term toxicity studies in different levels (from cell to big animals) are urgently needed.

Secondly, specifically deliver enhanced amount of anti-cancer drugs to tumor site by in vivo active targeting of f-MSN is still a big challenge by far. Although a few studies could demonstrate an enhanced signal intensity or therapeutic effect by using MSNs conjugated with cell-based targeting ligands, a lot of control experiments, such as targeting efficiency of negative control and blocking groups, are usually unavailable to further confirm the specific targeting of MSNs. Moreover, few quantitative data of tumor uptake could be found, and more sensitive and quantitative imaging modalities (e.g., PET) should be explored in the future cancer imaging studies.

Finally, more effective targeting strategies are needed. Despite the progress in suppressing the tumor growth rate by delivering drugs based on EPR effect, the attempts to further enhance the therapeutic effects by conjugating MSNs with cell-based targeting ligands (e.g., folic acid, transferrin) have failed. Due to the possible limited tumor extravasation of f-MSNs, tumor angiogenesis-based targeting strategy might stand out as a promising alternative to solve this problem. We recently demonstrated the first example of in vivo PET imaging, combined active/passive targeting and enhanced delivery of DOX by using TRC105 (anti-CD105 antibody) as a targeting ligand for targeting tumor vasculature. The highest tumor uptake of as-designed ^{64}Cu -NOTA- mSiO_2 -PEG-TRC105 has been found to be 5.9 %ID/g at 5 h p.i., which is significantly higher than that of non-targeted control group (<2.5 %ID/g) (unpublished data). Based on such promising tumor angiogenesis targeting, progress in more accurate in vivo pharmacokinetics, optimized tumor-targeting efficiency in different tumor models and enhanced therapeutic effect of MSN-based nanosystems are expected in the near future.

References

1. Pan D (2013) Theranostic nanomedicine with functional nanoarchitecture. *Mol Pharm* 10(3):781–782. doi:10.1021/mp400044j
2. Cabral H, Nishiyama N, Kataoka K (2011) Supramolecular nanodevices: from design validation to theranostic nanomedicine. *Acc Chem Res* 44(10):999–1008. doi:10.1021/ar200094a

3. Chen X, Gambhir SS, Cheon J (2011) Theranostic nanomedicine. *Acc Chem Res* 44(10):841–841. doi:[10.1021/ar200231d](https://doi.org/10.1021/ar200231d)
4. Ma X, Zhao Y, Liang X-J (2011) Theranostic nanoparticles engineered for clinic and pharmaceuticals. *Acc Chem Res* 44(10):1114–1122. doi:[10.1021/ar2000056](https://doi.org/10.1021/ar2000056)
5. Ho D, Sun X, Sun S (2011) Monodisperse magnetic nanoparticles for theranostic applications. *Acc Chem Res* 44(10):875–882. doi:[10.1021/ar200090c](https://doi.org/10.1021/ar200090c)
6. Xia Y, Li W, Cobley CM, Chen J, Xia X, Zhang Q, Yang M, Cho EC, Brown PK (2011) Gold nanocages: from synthesis to theranostic applications. *Acc Chem Res* 44(10):914–924. doi:[10.1021/ar200061q](https://doi.org/10.1021/ar200061q)
7. Dreaden EC, Mackey MA, Huang X, Kang B, El-Sayed MA (2011) Beating cancer in multiple ways using nanogold. *Chem Soc Rev* 40(7):3391–3404. doi:[10.1039/c0cs00180e](https://doi.org/10.1039/c0cs00180e)
8. Liu Z, Liang XJ (2012) Nano-carbons as theranostics. *Theranostics* 2(3):235–237. doi:[10.7150/thno.4156](https://doi.org/10.7150/thno.4156)
9. Yang K, Feng L, Shi X, Liu Z (2013) Nano-graphene in biomedicine: theranostic applications. *Chem Soc Rev* 42(2):530–547. doi:[10.1039/c2cs35342c](https://doi.org/10.1039/c2cs35342c)
10. Wang F, Banerjee D, Liu YS, Chen XY, Liu XG (2010) Upconversion nanoparticles in biological labeling, imaging, and therapy. *Analyst* 135(8):1839–1854. doi:[10.1039/c0an00144a](https://doi.org/10.1039/c0an00144a)
11. Zhou J, Liu Z, Li FY (2012) Upconversion nanophosphors for small-animal imaging. *Chem Soc Rev* 41(3):1323–1349. doi:[10.1039/c1cs15187h](https://doi.org/10.1039/c1cs15187h)
12. Ambrogio MW, Thomas CR, Zhao Y-L, Zink JI, Stoddart JF (2011) Mechanized silica nanoparticles: a new frontier in theranostic nanomedicine. *Acc Chem Res* 44(10):903–913. doi:[10.1021/ar200018x](https://doi.org/10.1021/ar200018x)
13. Tang F, Li L, Chen D (2012) Mesoporous silica nanoparticles: synthesis, biocompatibility and drug delivery. *Adv Mater (Deerfield Beach, Fla)* 24(12):1504–1534. doi:[10.1002/adma.201104763](https://doi.org/10.1002/adma.201104763)
14. Vivero-Escoto JL, Huxford-Phillips RC, Lin W (2012) Silica-based nanoprobe for biomedical imaging and theranostic applications. *Chem Soc Rev* 41(7):2673–2685. doi:[10.1039/c2cs15229k](https://doi.org/10.1039/c2cs15229k)
15. Yang P, Gai S, Lin J (2012) Functionalized mesoporous silica materials for controlled drug delivery. *Chem Soc Rev* 41(9):3679–3698. doi:[10.1039/c2cs15308d](https://doi.org/10.1039/c2cs15308d)
16. Benezra M, Penate-Medina O, Zanzonico PB, Schaer D, Ow H, Burns A, DeStanchina E, Longo V, Herz E, Iyer S, Wolchok J, Larson SM, Wiesner U, Bradbury MS (2011) Multimodal silica nanoparticles are effective cancer-targeted probes in a model of human melanoma. *J Clin Invest* 121(7):2768–2780. doi:[10.1172/jci45600](https://doi.org/10.1172/jci45600)
17. Vallet-Regi M, Rámila A, del Real RP, Pérez-Pariente J (2000) A new property of MCM-41: drug delivery system. *Chem Mater* 13(2):308–311. doi:[10.1021/cm0011559](https://doi.org/10.1021/cm0011559)
18. Hoffmann F, Cornelius M, Morell J, Froba M (2006) Silica-based mesoporous organic-inorganic hybrid materials. *Angew Chem Int Ed* 45(20):3216–3251. doi:[10.1002/anie.200503075](https://doi.org/10.1002/anie.200503075)
19. Slowing II, Vivero-Escoto JL, Trewyn BG, Lin VSY (2010) Mesoporous silica nanoparticles: structural design and applications. *J Mater Chem* 20(37):7924–7937. doi:[10.1039/c0jm00554a](https://doi.org/10.1039/c0jm00554a)
20. Rosenholm JM, Meinander A, Peuhu E, Niemi R, Eriksson JE, Sahlgren C, Linden M (2009) Targeting of porous hybrid silica nanoparticles to cancer cells. *ACS Nano* 3(1):197–206. doi:[10.1021/nm800781r](https://doi.org/10.1021/nm800781r)
21. Ferris DP, Lu J, Gothard C, Yanes R, Thomas CR, Olsen JC, Stoddart JF, Tamanoi F, Zink JI (2011) Synthesis of biomolecule-modified mesoporous silica nanoparticles for targeted hydrophobic drug delivery to cancer cells. *Small* 7(13):1816–1826. doi:[10.1002/sml.201002300](https://doi.org/10.1002/sml.201002300)
22. Zhu CL, Song XY, Zhou WH, Yang HH, Wen YH, Wang XR (2009) An efficient cell-targeting and intracellular controlled-release drug delivery system based on MSN-PEM-aptamer conjugates. *J Mater Chem* 19(41):7765–7770. doi:[10.1039/b907978e](https://doi.org/10.1039/b907978e)

23. Tsai CP, Chen CY, Hung Y, Chang FH, Mou CY (2009) Monoclonal antibody-functionalized mesoporous silica nanoparticles (MSN) for selective targeting breast cancer cells. *J Mater Chem* 19(32):5737–5743. doi:[10.1039/b905158a](https://doi.org/10.1039/b905158a)
24. Wang K, He X, Yang X, Shi H (2013) Functionalized silica nanoparticles: a platform for fluorescence imaging at the cell and small animal levels. *Acc Chem Res*. doi:[10.1021/ar3001525](https://doi.org/10.1021/ar3001525)
25. Hu X, Zrazhevskiy P, Gao X (2009) Encapsulation of single quantum dots with mesoporous silica. *Ann Biomed Eng* 37(10):1960–1966. doi:[10.1007/s10439-009-9660-y](https://doi.org/10.1007/s10439-009-9660-y)
26. Gorelikov I, Matsuura N (2008) Single-step coating of mesoporous silica on cetyltrimethyl ammonium bromide-capped nanoparticles. *Nano Lett* 8(1):369–373. doi:[10.1021/nl0727415](https://doi.org/10.1021/nl0727415)
27. Liu J, Bu W, Zhang S, Chen F, Xing H, Pan L, Zhou L, Peng W, Shi J (2012) Controlled synthesis of uniform and monodisperse upconversion core/mesoporous silica shell nanocomposites for bimodal imaging. *Chemistry* 18(8):2335–2341. doi:[10.1002/chem.201102599](https://doi.org/10.1002/chem.201102599)
28. Idris NM, Gnanasammandhan MK, Zhang J, Ho PC, Mahendran R, Zhang Y (2012) In vivo photodynamic therapy using upconversion nanoparticles as remote-controlled nanotransducers. *Nat Med* 18(10):1580–1585. doi:[10.1038/nm.2933](https://doi.org/10.1038/nm.2933)
29. Sathe TR, Agrawal A, Nie S (2006) Mesoporous silica beads embedded with semiconductor quantum dots and iron oxide nanocrystals: dual-function microcarriers for optical encoding and magnetic separation. *Anal Chem* 78(16):5627–5632. doi:[10.1021/ac0610309](https://doi.org/10.1021/ac0610309)
30. Kim J, Lee JE, Lee J, Yu JH, Kim BC, An K, Hwang Y, Shin CH, Park JG, Kim J, Hyeon T (2006) Magnetic fluorescent delivery vehicle using uniform mesoporous silica spheres embedded with monodisperse magnetic and semiconductor nanocrystals. *J Am Chem Soc* 128(3):688–689. doi:[10.1021/ja0565875](https://doi.org/10.1021/ja0565875)
31. Chen Y, Chen H, Shi J (2013) In vivo bio-safety evaluations and diagnostic/therapeutic applications of chemically designed mesoporous silica nanoparticles. *Adv Mater* 25(23):3144–3176. doi:[10.1002/adma.201205292](https://doi.org/10.1002/adma.201205292)
32. Li Z, Barnes JC, Bosoy A, Stoddart JF, Zink JI (2012) Mesoporous silica nanoparticles in biomedical applications. *Chem Soc Rev* 41(7):2590–2605. doi:[10.1039/c1cs15246g](https://doi.org/10.1039/c1cs15246g)
33. Inagaki S, Fukushima Y, Kuroda K (1993) Synthesis of highly ordered mesoporous materials from a layered polysilicate. *J Chem Soc, Chem Commun* 8:680–682. doi:[10.1039/c39930000680](https://doi.org/10.1039/c39930000680)
34. Tarn D, Ashley CE, Xue M, Carnes EC, Zink JI, Brinker CJ (2013) Mesoporous silica nanoparticle nanocarriers: biofunctionality and biocompatibility. *Acc Chem Res*. doi:[10.1021/ar3000986](https://doi.org/10.1021/ar3000986)
35. Wan Y, Zhao D (2007) On the controllable soft-templating approach to mesoporous silicates. *Chem Rev* 107(7):2821–2860. doi:[10.1021/cr068020s](https://doi.org/10.1021/cr068020s)
36. Mankoff DA (2007) A definition of molecular imaging. *J Nucl Med* 48(6):18N–21N
37. James ML, Gambhir SS (2012) A molecular imaging primer: modalities, imaging agents, and applications. *Physiol Rev* 92(2):897–965. doi:[10.1152/physrev.00049.2010](https://doi.org/10.1152/physrev.00049.2010)
38. Chen PJ, Hu SH, Fan CT, Li ML, Chen YY, Chen SY, Liu DM (2013) A novel multifunctional nano-platform with enhanced anti-cancer and photoacoustic imaging modalities using gold-nanorod-filled silica nanobeads. *Chem Commun* 49(9):892–894. doi:[10.1039/c2cc37702k](https://doi.org/10.1039/c2cc37702k)
39. Liang M, Lu J, Kovochich M, Xia T, Ruehm SG, Nel AE, Tamanoi F, Zink JI (2008) Multifunctional inorganic nanoparticles for imaging, targeting, and drug delivery. *ACS Nano* 2(5):889–896. doi:[10.1021/nn800072t](https://doi.org/10.1021/nn800072t)
40. Pan J, Wan D, Gong J (2011) PEGylated liposome coated QDs/mesoporous silica core-shell nanoparticles for molecular imaging. *Chem Commun* 47(12):3442–3444. doi:[10.1039/c0cc05520d](https://doi.org/10.1039/c0cc05520d)
41. Feng J, Song SY, Deng RP, Fan WQ, Zhang HJ (2010) Novel multifunctional nanocomposites: magnetic mesoporous silica nanospheres covalently bonded with near-infrared luminescent lanthanide complexes. *Langmuir* 26(5):3596–3600. doi:[10.1021/la903008z](https://doi.org/10.1021/la903008z)

42. Zhang F, Braun GB, Pallaoro A, Zhang Y, Shi Y, Cui D, Moskovits M, Zhao D, Stucky GD (2012) Mesoporous multifunctional upconversion luminescent and magnetic “nanorattle” materials for targeted chemotherapy. *Nano Lett* 12(1):61–67. doi:[10.1021/nl202949y](https://doi.org/10.1021/nl202949y)
43. Morelli C, Maris P, Sisci D, Perrotta E, Brunelli E, Perrotta I, Panno ML, Tagarelli A, Versace C, Casula MF, Testa F, Ando S, Nagy JB, Pasqua L (2011) PEG-templated mesoporous silica nanoparticles exclusively target cancer cells. *Nanoscale* 3(8):3198–3207. doi:[10.1039/c1nr10253b](https://doi.org/10.1039/c1nr10253b)
44. Roggers RA, Lin VS, Trewyn BG (2012) Chemically reducible lipid bilayer coated mesoporous silica nanoparticles demonstrating controlled release and HeLa and normal mouse liver cell biocompatibility and cellular internalization. *Mol Pharm* 9(9):2770–2777. doi:[10.1021/mp200613y](https://doi.org/10.1021/mp200613y)
45. Hocine O, Gary-Bobo M, Brevet D, Maynadier M, Fontanel S, Raehm L, Richeter S, Look B, Couleaud P, Frochot C, Charnay C, Derrien G, Smaïhi M, Sahmoune A, Morere A, Maillard P, Garcia M, Durand JO (2010) Silicalites and mesoporous silica nanoparticles for photodynamic therapy. *Int J Pharm* 402(1–2):221–230. doi:[10.1016/j.ijpharm.2010.10.004](https://doi.org/10.1016/j.ijpharm.2010.10.004)
46. Lai J, Shah BP, Garfunkel E, Lee KB (2013) Versatile fluorescence resonance energy transfer-based mesoporous silica nanoparticles for real-time monitoring of drug release. *ACS Nano* 7(3):2741–2750. doi:[10.1021/nn400199t](https://doi.org/10.1021/nn400199t)
47. Wu S, Li Z, Han J, Han S (2011) Dual colored mesoporous silica nanoparticles with pH activable rhodamine-lactam for ratiometric sensing of lysosomal acidity. *Chem Commun* 47(40):11276–11278. doi:[10.1039/c1cc14627k](https://doi.org/10.1039/c1cc14627k)
48. He Q, Zhang Z, Gao F, Li Y, Shi J (2011) In vivo biodistribution and urinary excretion of mesoporous silica nanoparticles: effects of particle size and PEGylation. *Small* 7(2):271–280. doi:[10.1002/sml.201001459](https://doi.org/10.1002/sml.201001459)
49. Huang X, Zhang F, Lee S, Swierczewska M, Kiesewetter DO, Lang L, Zhang G, Zhu L, Gao H, Choi HS, Niu G, Chen X (2012) Long-term multimodal imaging of tumor draining sentinel lymph nodes using mesoporous silica-based nanoprobe. *Biomaterials* 33(17):4370–4378. doi:[10.1016/j.biomaterials.2012.02.060](https://doi.org/10.1016/j.biomaterials.2012.02.060)
50. Lee CH, Cheng SH, Wang YJ, Chen YC, Chen NT, Souris J, Chen CT, Mou CY, Yang CS, Lo LW (2009) Near-infrared mesoporous silica nanoparticles for optical imaging: characterization and in vivo biodistribution. *Adv Funct Mater* 19(2):215–222. doi:[DOI10.1002/adfm.200800753](https://doi.org/10.1002/adfm.200800753)
51. Souris JS, Lee CH, Cheng SH, Chen CT, Yang CS, Ho JA, Mou CY, Lo LW (2010) Surface charge-mediated rapid hepatobiliary excretion of mesoporous silica nanoparticles. *Biomaterials* 31(21):5564–5574. doi:[10.1016/j.biomaterials.2010.03.048](https://doi.org/10.1016/j.biomaterials.2010.03.048)
52. Resch-Genger U, Grabolle M, Cavaliere-Jaricot S, Nitschke R, Nann T (2008) Quantum dots versus organic dyes as fluorescent labels. *Nat Methods* 5(9):763–775. doi:[10.1038/nmeth.1248](https://doi.org/10.1038/nmeth.1248)
53. Gao X, Dave SR (2007) Quantum dots for cancer molecular imaging. *Adv Exp Med Biol* 620:57–73
54. Zrazhevskiy P, Sena M, Gao X (2010) Designing multifunctional quantum dots for bioimaging, detection, and drug delivery. *Chem Soc Rev* 39(11):4326–4354. doi:[10.1039/b915139g](https://doi.org/10.1039/b915139g)
55. Derfus AM, Chan WCW, Bhatia SN (2003) Probing the cytotoxicity of semiconductor quantum dots. *Nano Lett* 4(1):11–18. doi:[10.1021/nl0347334](https://doi.org/10.1021/nl0347334)
56. Xiong L, Yang T, Yang Y, Xu C, Li F (2010) Long-term in vivo biodistribution imaging and toxicity of polyacrylic acid-coated upconversion nanophosphors. *Biomaterials* 31(27):7078–7085. doi:[10.1016/j.biomaterials.2010.05.065](https://doi.org/10.1016/j.biomaterials.2010.05.065)
57. Cheng L, Yang K, Li Y, Chen J, Wang C, Shao M, Lee S-T, Liu Z (2011) Facile preparation of multifunctional upconversion nanoprobe for multimodal imaging and dual-targeted photothermal therapy. *Angew Chem Int Ed* 50(32):7385–7390. doi:[10.1002/anie.201101447](https://doi.org/10.1002/anie.201101447)
58. Haase M, Schafer H (2011) Upconverting nanoparticles. *Angew Chem Int Ed* 50(26):5808–5829. doi:[10.1002/anie.201005159](https://doi.org/10.1002/anie.201005159)

59. Ju Q, Tu D, Liu Y, Li R, Zhu H, Chen J, Chen Z, Huang M, Chen X (2012) Amine-functionalized lanthanide-doped KGdF₄ nanocrystals as potential optical/magnetic multimodal bioprobes. *J Am Chem Soc* 134(2):1323–1330. doi:[10.1021/ja2102604](https://doi.org/10.1021/ja2102604)
60. Wu S, Han G, Milliron DJ, Aloni S, Altoe V, Talapin DV, Cohen BE, Schuck PJ (2009) Non-blinking and photostable upconverted luminescence from single lanthanide-doped nanocrystals. *Proc Natl Acad Sci USA* 106(27):10917–10921. doi:[10.1073/pnas.0904792106](https://doi.org/10.1073/pnas.0904792106)
61. Cheng L, Wang C, Liu Z (2012) Upconversion nanoparticles and their composite nanostructures for biomedical imaging and cancer therapy. *Nanoscale* 5(1):23–37. doi:[10.1039/c2nr32311g](https://doi.org/10.1039/c2nr32311g)
62. Park YI, Kim JH, Lee KT, Jeon KS, Bin Na H, Yu JH, Kim HM, Lee N, Choi SH, Baik SI, Kim H, Park SP, Park BJ, Kim YW, Lee SH, Yoon SY, Song IC, Moon WK, Suh YD, Hyeon T (2009) Nonblinking and nonbleaching upconverting nanoparticles as an optical imaging nanoprobe and T1 magnetic resonance imaging contrast agent. *Adv Mater* 21(44):4467–4471. doi:DOI [10.1002/adma.200901356](https://doi.org/10.1002/adma.200901356)
63. Chatterjee DK, Rufaihah AJ, Zhang Y (2008) Upconversion fluorescence imaging of cells and small animals using lanthanide doped nanocrystals. *Biomaterials* 29(7):937–943. doi:[10.1016/j.biomaterials.2007.10.051](https://doi.org/10.1016/j.biomaterials.2007.10.051)
64. Nam SH, Bae YM, Park YI, Kim JH, Kim HM, Choi JS, Lee KT, Hyeon T, Suh YD (2011) Long-term real-time tracking of lanthanide ion doped upconverting nanoparticles in living cells. *Angew Chem Int Ed* 50(27):6093–6097. doi:[10.1002/anie.201007979](https://doi.org/10.1002/anie.201007979)
65. Xiong L, Chen Z, Tian Q, Cao T, Xu C, Li F (2009) High contrast upconversion luminescence targeted imaging in vivo using peptide-labeled nanophosphors. *Anal Chem* 81(21):8687–8694. doi:[10.1021/ac901960d](https://doi.org/10.1021/ac901960d)
66. Chen F, Bu WB, Zhang SJ, Liu XH, Liu JN, Xing HY, Xiao QF, Zhou LP, Peng WJ, Wang LZ, Shi JL (2011) Positive and negative lattice shielding effects co-existing in Gd(III) ion doped bifunctional upconversion nanoprobe. *Adv Funct Mater* 21(22):4285–4294. doi:DOI [10.1002/adfm.201101663](https://doi.org/10.1002/adfm.201101663)
67. Kumar R, Nyk M, Ohulchanskyy TY, Flask CA, Prasad PN (2009) Combined optical and MR bioimaging using rare earth ion doped NaYF₄ nanocrystals. *Adv Funct Mater* 19(6):853–859. doi:[10.1002/adfm.200800765](https://doi.org/10.1002/adfm.200800765)
68. Zhou J, Sun Y, Du X, Xiong L, Hu H, Li F (2010) Dual-modality in vivo imaging using rare-earth nanocrystals with near-infrared to near-infrared (NIR-to-NIR) upconversion luminescence and magnetic resonance properties. *Biomaterials* 31(12):3287–3295. doi:[10.1016/j.biomaterials.2010.01.040](https://doi.org/10.1016/j.biomaterials.2010.01.040)
69. He M, Huang P, Zhang CL, Hu HY, Bao CC, Gao G, He R, Cui DX (2011) Dual phase-controlled synthesis of uniform lanthanide-doped NaGdF₄ upconversion nanocrystals via an OA/ionic liquid two-phase system for in vivo dual-modality imaging. *Adv Funct Mater* 21(23):4470–4477. doi:DOI [10.1002/adfm.201101040](https://doi.org/10.1002/adfm.201101040)
70. Liu Y, Ai K, Liu J, Yuan Q, He Y, Lu L (2012) A high-performance ytterbium-based nanoparticulate contrast agent for in vivo X-ray computed tomography imaging. *Angew Chem Int Ed* 51(6):1437–1442. doi:[10.1002/anie.201106686](https://doi.org/10.1002/anie.201106686)
71. Zhu X, Zhou J, Chen M, Shi M, Feng W, Li F (2012) Core-shell Fe₃O₄@NaLuF₄:Yb, Er/Tm nanostructure for MRI, CT and upconversion luminescence tri-modality imaging. *Biomaterials* 33(18):4618–4627. doi:[10.1016/j.biomaterials.2012.03.007](https://doi.org/10.1016/j.biomaterials.2012.03.007)
72. Hong H, Zhang Y, Sun J, Cai W (2009) Molecular imaging and therapy of cancer with radiolabeled nanoparticles. *Nano Today* 4(5):399–413. doi:[10.1016/j.nantod.2009.07.001](https://doi.org/10.1016/j.nantod.2009.07.001)
73. Cai W, Chen X (2008) Multimodality molecular imaging of tumor angiogenesis. *J Nucl Med* 49(Suppl 2):113S–128S. doi:[10.2967/jnumed.107.045922](https://doi.org/10.2967/jnumed.107.045922)
74. Weissleder R (1999) Molecular imaging: exploring the next frontier. *Radiology* 212(3):609–614
75. Villaraza AJ, Bumb A, Brechbiel MW (2010) Macromolecules, dendrimers, and nanomaterials in magnetic resonance imaging: the interplay between size, function, and pharmacokinetics. *Chem Rev* 110(5):2921–2959. doi:[10.1021/cr900232t](https://doi.org/10.1021/cr900232t)

76. Huang CC, Tsai CY, Sheu HS, Chuang KY, Su CH, Jeng US, Cheng FY, Lei HY, Yeh CS (2011) Enhancing transversal relaxation for magnetite nanoparticles in MR imaging using Gd(3) + - chelated mesoporous silica shells. *ACS Nano* 5(5):3905–3916. doi:[10.1021/nm200306g](https://doi.org/10.1021/nm200306g)
77. Kim J, Kim HS, Lee N, Kim T, Kim H, Yu T, Song IC, Moon WK, Hyeon T (2008) Multifunctional uniform nanoparticles composed of a magnetite nanocrystal core and a mesoporous silica shell for magnetic resonance and fluorescence imaging and for drug delivery. *Angew Chem Int Ed* 47(44):8438–8441. doi:[10.1002/anie.200802469](https://doi.org/10.1002/anie.200802469)
78. Kim T, Momin E, Choi J, Yuan K, Zaidi H, Kim J, Park M, Lee N, McMahon MT, Quinones-Hinojosa A, Bulte JW, Hyeon T, Gilad AA (2011) Mesoporous silica-coated hollow manganese oxide nanoparticles as positive T1 contrast agents for labeling and MRI tracking of adipose-derived mesenchymal stem cells. *J Am Chem Soc* 133(9):2955–2961. doi:[10.1021/ja1084095](https://doi.org/10.1021/ja1084095)
79. Peng YK, Lai CW, Liu CL, Chen HC, Hsiao YH, Liu WL, Tang KC, Chi Y, Hsiao JK, Lim KE, Liao HE, Shyue JJ, Chou PT (2011) A new and facile method to prepare uniform hollow MnO/functionalized mSiO(2) core/shell nanocomposites. *ACS Nano* 5(5):4177–4187. doi:[10.1021/nn200928r](https://doi.org/10.1021/nn200928r)
80. Taylor KM, Kim JS, Rieter WJ, An H, Lin W (2008) Mesoporous silica nanospheres as highly efficient MRI contrast agents. *J Am Chem Soc* 130(7):2154–2155. doi:[10.1021/ja710193c](https://doi.org/10.1021/ja710193c)
81. Shao YZ, Liu LZ, Song SQ, Cao RH, Liu H, Cui CY, Li X, Bie MJ, Li L (2011) A novel one-step synthesis of Gd3 + -incorporated mesoporous SiO2 nanoparticles for use as an efficient MRI contrast agent. *Contrast Media Mol Imaging* 6(2):110–118. doi:[10.1002/cmml.412](https://doi.org/10.1002/cmml.412)
82. Vivero-Escoto JL, Taylor-Pashow KM, Huxford RC, Della Rocca J, Okoruwa C, An H, Lin W, Lin W (2011) Multifunctional mesoporous silica nanospheres with cleavable Gd(III) chelates as MRI contrast agents: synthesis, characterization, target-specificity, and renal clearance. *Small* 7(24):3519–3528. doi:[10.1002/sml.201100521](https://doi.org/10.1002/sml.201100521)
83. Chen Y, Chen H, Zeng D, Tian Y, Chen F, Feng J, Shi J (2010) Core/shell structured hollow mesoporous nanocapsules: a potential platform for simultaneous cell imaging and anticancer drug delivery. *ACS Nano* 4(10):6001–6013. doi:[10.1021/nn1015117](https://doi.org/10.1021/nn1015117)
84. Xuan S, Wang F, Lai JM, Sham KW, Wang YX, Lee SF, Yu JC, Cheng CH, Leung KC (2011) Synthesis of biocompatible, mesoporous Fe(3)O(4) nano/microspheres with large surface area for magnetic resonance imaging and therapeutic applications. *ACS Appl Mater Interfaces* 3(2):237–244. doi:[10.1021/am1012358](https://doi.org/10.1021/am1012358)
85. Hsiao JK, Tsai CP, Chung TH, Hung Y, Yao M, Liu HM, Mou CY, Yang CS, Chen YC, Huang DM (2008) Mesoporous silica nanoparticles as a delivery system of gadolinium for effective human stem cell tracking. *Small* 4(9):1445–1452. doi:[10.1002/sml.200701316](https://doi.org/10.1002/sml.200701316)
86. Liu HM, Wu SH, Lu CW, Yao M, Hsiao JK, Hung Y, Lin YS, Mou CY, Yang CS, Huang DM, Chen YC (2008) Mesoporous silica nanoparticles improve magnetic labeling efficiency in human stem cells. *Small* 4(5):619–626. doi:[10.1002/sml.200700493](https://doi.org/10.1002/sml.200700493)
87. Shen Y, Shao Y, He H, Tan Y, Tian X, Xie F, Li L (2013) Gadolinium(3 +)-doped mesoporous silica nanoparticles as a potential magnetic resonance tracer for monitoring the migration of stem cells in vivo. *Int J Nanomed* 8:119–127. doi:[10.2147/ijn.s38213](https://doi.org/10.2147/ijn.s38213)
88. Yeh CS, Su CH, Ho WY, Huang CC, Chang JC, Chien YH, Hung ST, Liao MC, Ho HY (2013) Tumor targeting and MR imaging with lipophilic cyanine-mediated near-infrared responsive porous Gd silicate nanoparticles. *Biomaterials* 34(22):5677–5688. doi:[10.1016/j.biomaterials.2013.04.020](https://doi.org/10.1016/j.biomaterials.2013.04.020)
89. Huang X, Zhang F, Wang H, Niu G, Choi KY, Swierczewska M, Zhang G, Gao H, Wang Z, Zhu L, Choi HS, Lee S, Chen X (2013) Mesenchymal stem cell-based cell engineering with multifunctional mesoporous silica nanoparticles for tumor delivery. *Biomaterials* 34(7):1772–1780. doi:[10.1016/j.biomaterials.2012.11.032](https://doi.org/10.1016/j.biomaterials.2012.11.032)
90. Carniato F, Tei L, Arrais A, Marchese L, Botta M (2013) Selective anchoring of Gd(III) chelates on the external surface of organo-modified mesoporous silica nanoparticles: a new

- chemical strategy to enhance relaxivity. *Chemistry* 19(4):1421–1428. doi:[10.1002/chem.201202670](https://doi.org/10.1002/chem.201202670)
91. Shao Y, Tian X, Hu W, Zhang Y, Liu H, He H, Shen Y, Xie F, Li L (2012) The properties of Gd₂O₃-assembled silica nanocomposite targeted nanoprobe and their application in MRI. *Biomaterials* 33(27):6438–6446. doi:[10.1016/j.biomaterials.2012.05.065](https://doi.org/10.1016/j.biomaterials.2012.05.065)
 92. Chen Y, Yin Q, Ji X, Zhang S, Chen H, Zheng Y, Sun Y, Qu H, Wang Z, Li Y, Wang X, Zhang K, Zhang L, Shi J (2012) Manganese oxide-based multifunctionalized mesoporous silica nanoparticles for pH-responsive MRI, ultrasonography and circumvention of MDR in cancer cells. *Biomaterials* 33(29):7126–7137. doi:[10.1016/j.biomaterials.2012.06.059](https://doi.org/10.1016/j.biomaterials.2012.06.059)
 93. Park J, An K, Hwang Y, Park JG, Noh HJ, Kim JY, Park JH, Hwang NM, Hyeon T (2004) Ultra-large-scale syntheses of monodisperse nanocrystals. *Nat Mater* 3(12):891–895. doi:[10.1038/nmat1251](https://doi.org/10.1038/nmat1251)
 94. Zhang T, Ge J, Hu Y, Yin Y (2007) A general approach for transferring hydrophobic nanocrystals into water. *Nano Lett* 7(10):3203–3207. doi:[10.1021/nl071928t](https://doi.org/10.1021/nl071928t)
 95. Ye F, Laurent S, Fornara A, Astolfi L, Qin J, Roch A, Martini A, Toprak MS, Muller RN, Muhammed M (2012) Uniform mesoporous silica coated iron oxide nanoparticles as a highly efficient, nontoxic MRI T₂ contrast agent with tunable proton relaxivities. *Contrast Media Mol Imaging* 7(5):460–468. doi:[10.1002/cmml.1473](https://doi.org/10.1002/cmml.1473)
 96. Gandhi S, Sethuraman S, Krishnan UM (2012) Synthesis, characterization and biocompatibility evaluation of iron oxide incorporated magnetic mesoporous silica. *Dalton Trans* 41(40):12530–12537. doi:[10.1039/c2dt30853c](https://doi.org/10.1039/c2dt30853c)
 97. Zhang L, Wang Y, Tang Y, Jiao Z, Xie C, Zhang H, Gu P, Wei X, Yang GY, Gu H, Zhang C (2013) High MRI performance fluorescent mesoporous silica-coated magnetic nanoparticles for tracking neural progenitor cells in an ischemic mouse model. *Nanoscale* 5(10):4506–4516. doi:[10.1039/c3nr00119a](https://doi.org/10.1039/c3nr00119a)
 98. Wang X, Chen H, Zheng Y, Ma M, Chen Y, Zhang K, Zeng D, Shi J (2013) Au-nanoparticle coated mesoporous silica nanocapsule-based multifunctional platform for ultrasound mediated imaging, cytolysis and tumor ablation. *Biomaterials* 34(8):2057–2068. doi:[10.1016/j.biomaterials.2012.11.044](https://doi.org/10.1016/j.biomaterials.2012.11.044)
 99. Wang X, Chen H, Chen Y, Ma M, Zhang K, Li F, Zheng Y, Zeng D, Wang Q, Shi J (2012) Perfluorohexane-encapsulated mesoporous silica nanocapsules as enhancement agents for highly efficient high intensity focused ultrasound (HIFU). *Adv Mater* 24(6):785–791. doi:[10.1002/adma.201104033](https://doi.org/10.1002/adma.201104033)
 100. Luo T, Huang P, Gao G, Shen G, Fu S, Cui D, Zhou C, Ren Q (2011) Mesoporous silica-coated gold nanorods with embedded indocyanine green for dual mode X-ray CT and NIR fluorescence imaging. *Opt Express* 19(18):17030–17039
 101. Meng H, Xue M, Xia T, Ji Z, Tarn DY, Zink JI, Nel AE (2011) Use of size and a copolymer design feature to improve the biodistribution and the enhanced permeability and retention effect of doxorubicin-loaded mesoporous silica nanoparticles in a murine xenograft tumor model. *ACS Nano* 5(5):4131–4144. doi:[10.1021/nn200809t](https://doi.org/10.1021/nn200809t)
 102. Lu J, Liang M, Li Z, Zink JI, Tamanoi F (2010) Biocompatibility, biodistribution, and drug-delivery efficiency of mesoporous silica nanoparticles for cancer therapy in animals. *Small* 6(16):1794–1805. doi:[10.1002/smll.201000538](https://doi.org/10.1002/smll.201000538)
 103. Lu J, Li Z, Zink JI, Tamanoi F (2012) In vivo tumor suppression efficacy of mesoporous silica nanoparticles-based drug-delivery system: enhanced efficacy by folate modification. *Nanomedicine* 8(2):212–220. doi:[10.1016/j.nano.2011.06.002](https://doi.org/10.1016/j.nano.2011.06.002)
 104. Wang LG, Liu XM, Kreis W, Budman DR (1999) The effect of antimicrotubule agents on signal transduction pathways of apoptosis: a review. *Cancer Chemother Pharmacol* 44(5):355–361
 105. Montero A, Fossella F, Hortobagyi G, Valero V (2005) Docetaxel for treatment of solid tumours: a systematic review of clinical data. *Lancet Oncol* 6(4):229–239. doi:[10.1016/s1470-2045\(05\)70094-2](https://doi.org/10.1016/s1470-2045(05)70094-2)

106. Li L, Tang F, Liu H, Liu T, Hao N, Chen D, Teng X, He J (2010) In vivo delivery of silica nanorattle encapsulated docetaxel for liver cancer therapy with low toxicity and high efficacy. *ACS Nano* 4(11):6874–6882. doi:[10.1021/nm100918a](https://doi.org/10.1021/nm100918a)
107. Agostinis P, Berg K, Cengel KA, Foster TH, Girotti AW, Gollnick SO, Hahn SM, Hamblin MR, Juzeniene A, Kessel D, Korbelik M, Moan J, Mroz P, Nowis D, Piette J, Wilson BC, Golab J (2011) Photodynamic therapy of cancer: an update. *CA Cancer J Clin* 61(4):250–281. doi:[10.3322/caac.20114](https://doi.org/10.3322/caac.20114)
108. Gary-Bobo M, Mir Y, Rouxel C, Brevet D, Basile I, Maynadier M, Vaillant O, Mongin O, Blanchard-Desce M, Morere A, Garcia M, Durand JO, Raehm L (2011) Mannose-functionalized mesoporous silica nanoparticles for efficient two-photon photodynamic therapy of solid tumors. *Angew Chem Int Ed* 50(48):11425–11429. doi:[10.1002/anie.201104765](https://doi.org/10.1002/anie.201104765)
109. Auzel F (2004) Upconversion and anti-stokes processes with f and d ions in solids. *Chem Rev* 104(1):139–173. doi:[10.1021/cr020357g](https://doi.org/10.1021/cr020357g)
110. Cui S, Yin D, Chen Y, Di Y, Chen H, Ma Y, Achilefu S, Gu Y (2012) In vivo targeted deep-tissue photodynamic therapy based on near-infrared light triggered upconversion nanoconstruct. *ACS Nano*. doi:[10.1021/nn304872n](https://doi.org/10.1021/nn304872n)
111. Shan JN, Budijono SJ, Hu GH, Yao N, Kang YB, Ju YG, Prud'homme RK (2011) Pegylated composite nanoparticles containing upconverting phosphors and meso-tetraphenyl porphine (TPP) for photodynamic therapy. *Adv Funct Mater* 21(13):2488–2495. doi:[DOI10.1002/adfm.201002516](https://doi.org/10.1002/adfm.201002516)
112. Park YI, Kim HM, Kim JH, Moon KC, Yoo B, Lee KT, Lee N, Choi Y, Park W, Ling D, Na K, Moon WK, Choi SH, Park HS, Yoon SY, Suh YD, Lee SH, Hyeon T (2012) Theranostic probe based on lanthanide-doped nanoparticles for simultaneous in vivo dual-modal imaging and photodynamic therapy. *Adv Mater* 24(42):5755–5761. doi:[10.1002/adma.201202433](https://doi.org/10.1002/adma.201202433)
113. Wang C, Tao H, Cheng L, Liu Z (2011) Near-infrared light induced in vivo photodynamic therapy of cancer based on upconversion nanoparticles. *Biomaterials* 32(26):6145–6154. doi:[10.1016/j.biomaterials.2011.05.007](https://doi.org/10.1016/j.biomaterials.2011.05.007)
114. Zhao Z, Han Y, Lin C, Hu D, Wang F, Chen X, Chen Z, Zheng N (2012) Multifunctional core-shell upconverting nanoparticles for imaging and photodynamic therapy of liver cancer cells. *Chem Asian J* 7(4):830–837. doi:[10.1002/asia.201100879](https://doi.org/10.1002/asia.201100879)
115. Chatterjee DK, Yong Z (2008) Upconverting nanoparticles as nanotransducers for photodynamic therapy in cancer cells. *Nanomedicine* 3(1):73–82. doi:[10.2217/17435889.3.1.73](https://doi.org/10.2217/17435889.3.1.73)
116. Ungun B, Prud'homme RK, Budijon SJ, Shan J, Lim SF, Ju Y, Austin R (2009) Nanofabricated upconversion nanoparticles for photodynamic therapy. *Opt Express* 17(1):80–86
117. Qian HS, Guo HC, Ho PC, Mahendran R, Zhang Y (2009) Mesoporous-silica-coated up-conversion fluorescent nanoparticles for photodynamic therapy. *Small* 5(20):2285–2290. doi:[10.1002/smll.200900692](https://doi.org/10.1002/smll.200900692)
118. Chen F, Zhang S, Bu W, Chen Y, Xiao Q, Liu J, Xing H, Zhou L, Peng W, Shi J (2012) A uniform sub-50 nm-sized magnetic/upconversion fluorescent bimodal imaging agent capable of generating singlet oxygen by using a 980 nm laser. *Chemistry* 18(23):7082–7090. doi:[10.1002/chem.201103611](https://doi.org/10.1002/chem.201103611)
119. Hamilton AJ, Baulcombe DC (1999) A species of small antisense RNA in posttranscriptional gene silencing in plants. *Science* 286(5441):950–952
120. Bumcrot D, Manoharan M, Kotliansky V, Sah DW (2006) RNAi therapeutics: a potential new class of pharmaceutical drugs. *Nat Chem Biol* 2(12):711–719. doi:[10.1038/nchembio839](https://doi.org/10.1038/nchembio839)
121. Na HK, Kim MH, Park K, Ryoo SR, Lee KE, Jeon H, Ryoo R, Hyeon C, Min DH (2012) Efficient functional delivery of siRNA using mesoporous silica nanoparticles with ultralarge pores. *Small* 8(11):1752–1761. doi:[10.1002/smll.201200028](https://doi.org/10.1002/smll.201200028)

122. Schmitz AC, Gianfelice D, Daniel BL, Mali WP, van den Bosch MA (2008) Image-guided focused ultrasound ablation of breast cancer: current status, challenges, and future directions. *Eur Radiol* 18(7):1431–1441. doi:[10.1007/s00330-008-0906-0](https://doi.org/10.1007/s00330-008-0906-0)
123. Chen Y, Chen H, Sun Y, Zheng Y, Zeng D, Li F, Zhang S, Wang X, Zhang K, Ma M, He Q, Zhang L, Shi J (2011) Multifunctional mesoporous composite nanocapsules for highly efficient MRI-guided high-intensity focused ultrasound cancer surgery. *Angew Chem Int Ed* 50(52):12505–12509. doi:[10.1002/anie.201106180](https://doi.org/10.1002/anie.201106180)
124. Madani SY, Naderi N, Dissanayake O, Tan A, Seifalian AM (2011) A new era of cancer treatment: carbon nanotubes as drug delivery tools. *Int J Nanomedicine* 6:2963–2979. doi:[10.2147/ijn.s16923](https://doi.org/10.2147/ijn.s16923)
125. Hauck TS, Jennings TL, Yatsenko T, Kumaradas JC, Chan WCW (2008) Enhancing the toxicity of cancer chemotherapeutics with gold nanorod hyperthermia. *Adv Mater* 20(20):3832–3838. doi:[10.1002/adma.200800921](https://doi.org/10.1002/adma.200800921)
126. Zhang Z, Wang L, Wang J, Jiang X, Li X, Hu Z, Ji Y, Wu X, Chen C (2012) Mesoporous silica-coated gold nanorods as a light-mediated multifunctional theranostic platform for cancer treatment. *Adv Mater* 24(11):1418–1423. doi:[10.1002/adma.201104714](https://doi.org/10.1002/adma.201104714)
127. Liu H, Chen D, Li L, Liu T, Tan L, Wu X, Tang F (2011) Multifunctional gold nanoshells on silica nanorattles: a platform for the combination of photothermal therapy and chemotherapy with low systemic toxicity. *Angew Chem Int Ed* 50(4):891–895. doi:[10.1002/anie.201002820](https://doi.org/10.1002/anie.201002820)
128. Ma M, Chen H, Chen Y, Wang X, Chen F, Cui X, Shi J (2012) Au capped magnetic core/mesoporous silica shell nanoparticles for combined photothermo-/chemo-therapy and multimodal imaging. *Biomaterials* 33(3):989–998. doi:[10.1016/j.biomaterials.2011.10.017](https://doi.org/10.1016/j.biomaterials.2011.10.017)
129. Mohamed F, Stuart OA, Glehen O, Urano M, Sugarbaker PH (2004) Docetaxel and hyperthermia: factors that modify thermal enhancement. *J Surg Oncol* 88(1):14–20. doi:[10.1002/jso.20117](https://doi.org/10.1002/jso.20117)
130. Liu H, Liu T, Wu X, Li L, Tan L, Chen D, Tang F (2012) Targeting gold nanoshells on silica nanorattles: a drug cocktail to fight breast tumors via a single irradiation with near-infrared laser light. *Adv Mater* 24(6):755–761. doi:[10.1002/adma.201103343](https://doi.org/10.1002/adma.201103343)

Chapter 24

Engineering Carbon Nanomaterials for Stem Cell-Based Tissue Engineering

Tapas R. Nayak and Weibo Cai

24.1 Introduction

Tissue engineering and regenerative medicine is an incipient multidisciplinary field involving biology, medicine, and engineering. It is expected to revolutionize the ways to enhance the health and quality of life for millions of people worldwide by restoring, maintaining, or improving tissue and organ functions (NIH, USA). It is associated with interesting therapeutic applications, where the tissue is either grown inside a patient's body or built outside the patient and subsequently transplanted. Alternatively, tissue engineering can be exploited in terms of diagnostic applications, where the tissue is grown in vitro and used for testing drug uptake, metabolism, toxicity, and pathogenicity. In other words, the basis of tissue engineering/regenerative medicine for either therapeutic or diagnostic applications is the ability to exploit living cells in a variety of ways.

Tissue engineering and regenerative medicine aims to control and guide specific tissue regeneration in order to restore structure and function of a defect by utilizing the body's natural healing response. It may provide functional substitutes for native tissues to serve not only as grafts for implantation [1], but also as physiologically relevant models for controlled studies of development and function of specific tissue [2]. In addition to supporting factors such as sequencing and expression analysis of genes and proteins, quantitative cellular and tissue analysis, in silico tissue and cell modelling, and quality assurance, there are three most

T. R. Nayak (✉)

University of Wisconsin-Madison, 1111 Highland Avenue, Madison,
WI 53705-2275, USA

e-mail: tnayak@uwhealth.org

W. Cai

University of Wisconsin-Madison, Room 7137, 1111 Highland Avenue,
Madison, WI 53705-2275, USA

e-mail: Wcai@uwhealth.org

important elements associated with tissue engineering and regenerative medicine. They are as follows:

- **Cells and Tissues:** They constitute and are responsible for regeneration of specific tissues. They can be further exploited by (a) their acquisition from appropriate source (such as autologous cells, allogeneic cells, xenogeneic cells, stem cells, and genetically engineered cells), (b) use of appropriate methods for their proliferation and differentiation into specific tissues, and (c) their immunological manipulation.
- **Biomolecules:** They comprise several angiogenic factors, growth factors, differentiation factors, and bone morphogenic proteins which help in accelerating cell differentiation into specific tissue lineage and functionality.
- **Biomaterials and Scaffolds:** They provide the optimal microenvironment in the form of physical and chemical cues conducive for growth and regeneration of specific tissues [3]. Therefore, these novel biomaterials are currently being designed to direct the organization, growth, and differentiation of cells in the process of forming functional tissues.

24.1.1 Stem Cells in Tissue Engineering

Since the late 1980s, autologous grafts have been the gold standard for their application in tissue repair and regeneration [4–7]. A patient’s own tissue not only lacks immunogenicity, but also can be directly delivered at the implant site. Once implanted, these autologous grafts recruit stem cells and induce them to differentiate into specific tissues through exposure to specific growth factors [5, 8]. Although there are many advantages associated with this tissue source, there has been a search for alternatives for several decades owing to major drawbacks in the form of limited tissue harvesting sites without loss of function [9], morbidity at donor sites due to extra surgery involved [8, 10], postoperative continuous pain [11], hypersensitivity [5], and infection [8, 11].

A possible solution to this problem is represented by the use of allografts (from human to human). This eliminates the need for harvesting tissue from patient, and therefore, the quantity of available tissue is no longer an issue. Nevertheless, the quality of allografts is worse, as they have a poor degree of cellularity, less revascularization, and a higher resorption rate compared to autologous grafts [8], resulting in a slower rate of new tissue regeneration, as observed in several studies [12]. Additionally, the immunogenic potential of these allografts and the risks of virus transmission to the recipient are serious disadvantages [13]. In case of bone tissue repair, metals such as iron, cobalt, and titanium have been utilized as permanent implant in bone to fill defects and provide internal fixation [14]. However, problems in the form of fatigue, corrosion, tissue infections, poor implant-tissue interface, and stress-shielding effects were found to be associated with patients undergoing such procedures. To overcome these drawbacks of the current graft

materials and metal implants, new tissue engineering approaches utilizing stem cells have been suggested as promising techniques for regenerative medicine.

Current tissue engineering strategies tend to combine biomaterials or scaffolds with living cells to develop biological substitutes that can restore tissue functions [15–17]. The cells are essential for regeneration of new tissues through extracellular matrix synthesis [18] during which they proliferate, fill up the scaffold, and grow into a three-dimensional (3D) tissue [19, 20]. However, tissue-specific cell types are not always available in sufficient amounts to guarantee complete recovery of damaged tissue; therefore, stem cells symbolize a remarkable alternative for tissue engineering. They include pluripotent stem cells, such as embryonic stem cells (ESCs) and reprogrammed induced pluripotent stem cells (iPSCs), and multipotent (adult) stem cells, such as mesenchymal stem cells (MSCs) and neural stem cells (NSCs). Both the pluripotent stem cells and adult stem cells have specific advantages and disadvantages involving their application in tissue engineering. Pluripotent stem cells have immense differentiation potential or plasticity compared to adult stem cells, as they can differentiate into any number or type of diversified tissue lineages. However, they are not only prone to tumor formation but also may be subjected to immune rejection. In contrast, adult stem cells have the potential to differentiate into limited tissue lineages but have the ability to modulate the activity of immune cells of the host body and hence may not be subjected to immune rejection. Depending on the specific requirements, both stem cell types are promising and attractive for tissue engineering-based therapy aimed at treating previously incurable disorders [21]. Numerous experimental and preclinical studies are currently being undertaken to evaluate their potential in tissue engineering and regenerative medicine.

24.1.2 Growth Factors in Tissue Engineering

Several biomolecules in the form of proteins and growth factors that play a key role in proliferation and differentiation of cells have frequently been applied to tissue engineering. They include bone morphogenetic proteins (BMPs), basic fibroblast growth factor (bFGF or FGF-2), vascular endothelial growth factor (VEGF), and transforming growth factor- β (TGF- β) [22]. In addition, biomolecules such as dexamethasone, ascorbic acid, hydrocortisone, and insulin are also being used as induction factors for specific differentiation of the pluripotent or multipotent stem cells.

24.1.3 Biomaterials as Scaffold for Tissue Engineering

Biomaterials are critical in the success of tissue engineering approaches, as they modulate the shape and structure of developing tissues, provide mechanical

stability, and present opportunities to deliver inductive molecules to transplanted or migrating cells [23]. Therefore, the selection of the appropriate biomaterial can have a profound impact on the quality of newly formed tissue. But the fact that very few biomaterials possess all the characteristics necessary to perform ideally, and the identification of materials capable of promoting the desired cellular and tissue behavior is still a major challenge facing the field of tissue engineering. To alleviate this problem, engineers and clinicians alike have been pursuing the development of different nanomaterials and their composite as biomaterials to synergize their beneficial properties into a superior matrix. These nanomaterials and their composite are expected to augment cellular interaction, embolden integration into host tissues, and provide tunable material properties and degradation kinetics [23]. In this book chapter, we have focused on recent studies pertaining to engineering and development of carbon nanomaterials and their composite for their application in synthetic scaffolds in tissue engineering and regenerative medicine.

24.2 Carbon Nanomaterials

Nanostructured carbons or carbon-based nanomaterials are mostly composed of carbon in the form of zero-dimensional (0D) fullerene, one-dimensional (1D) carbon nanotubes (CNTs), two-dimensional (2D) graphene, and three-dimensional (3D) nanodiamond and amorphous carbon dots [24]. Since their discovery, they are being researched extensively for several applications owing to their unique physicochemical properties. The enormous aspect ratio and surface area exhibited by some of these carbon nanomaterials allow functionalization with multiple therapeutic moieties. These multiple functionalities augment their functions, and hence, they are being widely regarded as attractive biomaterials. Simultaneously, recent development of nanofabrication techniques has led to further engineering of these carbon nanomaterials for production of several derivatives having more advantageous properties than the starting materials. The growing popularity of these carbon nanomaterials has been embraced by the field of biomedical research as many of its applications rely heavily on the performance of biomaterials [25].

Currently, most artificial scaffolds being researched for tissue engineering are made of polymers and peptide fibers. However, these materials have relatively low strength and are often susceptible to immune rejection [26]. The discovery of carbon nanomaterials and their extraordinary physical and chemical properties has fuelled intense research and paved way for recent developments of synthetic scaffolds for tissue engineering. Because of their structural dimensions, they can be considered as a physical analog of extracellular matrix (ECM) components (e.g., collagen fibers). In addition, they are one of the strongest known materials known on this earth [27]. Coupled with their outstanding flexibility and elasticity, they can potentially reinforce the organic/inorganic synthetic scaffolds. Furthermore, these nanomaterials possess high electrical conductivity, which can be utilized to provide electrical stimulation required for specific cell types growing on

synthetic scaffolds [28]. While some of these carbon nanomaterials have been found to be incompatible with biological milieu, the development of different functionalization methods have led to reduced toxicity and enhanced biocompatibility of such nanomaterials [29, 30]. This book chapter will focus only on tissue engineering applications of carbon nanotubes, graphene, and their derivatives due to the insufficient literature reports pertaining to such application of fullerenes, nanodiamonds, and carbon dots.

24.3 Carbon Nanotubes

CNTs are allotropes of carbon with a 1D cylindrical nanostructure. The first reported observation of CNT was by Iijima [31]. Depending on the number of concentric layers, they can be further classified into (1) single-walled CNT (SWCNT), which is made up of a single layer of carbon atoms wrapped into a cylindrical form, and (2) multi-walled CNT (MWCNT), which has a central tube surrounded by several graphitic layers spaced by a distance of about 0.34 nm [32, 33]. CNTs exhibit many unique intrinsic physical and chemical properties, and therefore, they are being intensively explored for several biomedical applications including scaffold for tissue engineering in the past few years [34, 35]. Since the creation of microenvironments for stem cells similar to ECM is important in the development of suitable scaffolds for tissue regeneration, therefore, CNTs have been engineered by different methods to fabricate both 2D and 3D scaffolds. Table 24.1 lists all such scaffolds engineered from CNT and its derivatives for tissue engineering with various stem cells.

24.3.1 Carbon-Nanotube-Based 2D Scaffold for Tissue Engineering

The successful growth and differentiation of stem cells on CNT-based 2D scaffold was initially demonstrated by Jan et al., who studied the behavior of mouse cortical neural stem cells (NSCs) on layer-by-layer (LBL)-assembled SWCNTs [36]. The NSCs grown on this SWCNT/polyethyleneimine (PEI) polyelectrolyte composite multilayer thin film showed increased differentiation into neurons and oligodendrocytes and decreased differentiation into astrocytes compared to NSCs grown on poly-L-ornithine (PLO), one of the most widely used substrata for neural stem cells.

Similarly, SWCNT/laminin composite fabricated by LBL method was also reportedly found to support growth, proliferation, and differentiation of NSCs into neurons [37]. Extensive functional neural networks along with the presence of synaptic connections were observed on this composite scaffold. Furthermore, application of pulsed electrical stimulation through the SWCNT substrate revealed

Table 24.1 List of CNT-based engineered scaffolds for tissue engineering with stem cells

Engineered nanostructure	Stem cell	Differentiated cell	Proposed mechanism	Reference
LBL-assembled SWCNT/PEI polyelectrolyte composite	mNSCs	Neurons, oligodendrocytes, astrocytes	Chemical structure better suitable as neural electrode	[36]
LBL-assembled SWCNT/laminin composite	mNSCs	Neurons	Chemical structure better suitable as neural electrode	[37]
MWCNT micropatterns network	hNSCs	Neurons and astroglial cells	Nanotopography	[38]
Monolayer of SWCNT micropatterns network	hMSCs	No differentiation		[39]
Monolayer of SWCNT micropatterns network modified by fibronectin	hMSCs	No differentiation		[40]
SWCNT film	hMSCs	Neurons	Nano roughness	[41]
MWCNT sheet	hMSCs	Neurons	Nano roughness	[42]
SWCNTs/collagen matrix rigid fibril bundles	hESCs	Ectodermal lineage	Preconcentration platform	[43]
MWCNTs (PAA/PMA) thin film	hESCs	Neuron	Preconcentration platform	[44, 45]
MWCNTs/PEG thin film	hMSCs	Osteocytes	Nanotopography	[47]
MWCNT/PCL composite	BMSCs	Osteocytes	Nanotopography	[48]
SWCNT monolayer	hMSCs	Osteocytes	Nanotopography	[49]
Aligned CNT network	hMSCs	Osteocytes	High cytoskeletal tension	[50]
3D CNT rope	hNSCs	Neurons	Electrical stimulation	[51]
3D porous US-SWCNTs/ppf composite	Rat MSCs	No differentiation/in vivo implantation		[52, 53]
MWCNTs/PLA	hMSCs	Cardiomyocytes	Electrical stimulation	[54, 55]

generation of action potential with simultaneous excitation of NSCs. The above results indicate the potential application of these SWCNT composite materials for neural tissue engineering and nerve injury repair using neural stem cells due to their chemical structure better suitable as neural electrode leading to their long-term integration with neural tissues.

Behavior of hNSCs and their selective neuronal differentiation has also been investigated on different MWCNT network patterns [38]. Topographical cues obtained from these micropatterns were found to provide optimal surface roughness for selective growth and adhesion of hNSCs on to MWCNT regions. Furthermore, differentiation of these hNSCs into neurons or astroglial cells was found to depend on shape and dimensions of the MWCNT micropatterns. The results suggest that these CNT patterns were able to induce the adhesion, growth, and selective differentiation of hNSCs even better than conventional cell culture substrates such as bare glass.

CNT micropatterns based on SWCNTs have also been reported for growth and morphogenesis of human mesenchymal stem cells (hMSCs). These micropatterns were fabricated by adsorbing SWCNTs onto self-assembled monolayer patterns and further modified with adhesion protein such as fibronectin [39, 40]. The hMSCs growing on these patterns exhibited a stronger affinity to SWCNTs region with an elongated morphology compared to bare glass, CNT, or only fibronectin regions. Further studies have reported upregulation of neurogenic expression of hMSCs grown on SWCNT film [41] and aligned MWCNT sheets [42]. hMSCs showed increased neurite outgrowth along the CNTs implying that the differentiation of hMSCs is controlled by the nanoroughness of the CNTs. The above results provide solid evidence that CNT-based nanofibrillar surfaces mimic the characteristics of ECM with enhanced cell adhesion and growth factor adsorption and promote stem cell differentiation. In other words, the role of ECM molecules in cell-nanostructure interactions is important in designing nanostructure-based surface arrays to control and monitor activity and behavior of stem cells.

CNTs modified with natural or synthetic polymers have also been reported for growth and differentiation of pluripotent cells like human embryonic stem cells (hESCs). The hESCs grown on SWCNTs grafted into collagen matrix were found to form rigid fibril bundles with polarized growth [43]. Additionally, 90 % of the hESCs were differentiated into ectodermal lineage indicated by their long and bipolar filaments aligned with CNT/collagen matrix. Similarly, hESCs grown on MWCNTs grafted with poly(acrylic acid) [44] (PAA) and poly(methacrylic acid) [45] (PMA) via in situ polymerization showed not only better viability but also enhanced differentiation into B-tubulin-positive neurons compared to thin films made up of individual polymer or PLO. Further surface analysis and cell adhesion studies indicated that above result could be due to enhanced cell adhesion and protein adsorption resulting from large surface area and nanoscale fiber morphology created by CNTs. The lineage selection in hESCs generally depends on growth factors and small molecules in the media and the microenvironment provided by the scaffold. These results confirm the responsiveness of the hESCs to matrix properties and thereby provide a simple and efficient way to direct hESC

differentiation. Specifically, in these cases, CNT/polymer composite showed potential for their future application in forming neural-cell-based biodevices.

Similar to the above results pertaining to use of CNT and its composite for neural tissue engineering, many researchers have also investigated the suitability of CNTs as a substrate material for bone tissue engineering. Initial *in vivo* investigation showed high bone–tissue compatibility, new bone integration, and accelerated bone formation stimulated by recombinant human bone morphogenetic protein-2 (rhBMP-2) along with little local inflammatory reaction for MWCNTs adjoining bone [46]. This result encouraged several studies exploring use of engineered carbon nanomaterials as scaffold for bone tissue engineering. One such study done by Nayak et al. explored the homogenous thin film formed by polyethylene glycol (PEG)-conjugated multiwalled carbon nanotubes sprayed on to plain coverslips to induce hMSCs differentiation into osteogenic lineages (Fig. 24.1) [47]. This compact and thin film of MWCNT–PEG having nanometric irregularities was able to provide suitable microenvironment for differentiation of hMSCs into osteogenic lineage visualized by upregulation of osteogenic proteins like osteocalcin and osteopontin, without the need of any biochemical inducers like BMP-2. This study clearly demonstrates that such carbon nanomaterial-based scaffolds can direct and support differentiation of multipotent stem cells like hMSCs into other tissue types through subtle modification of the matrix and induction with specific media.

Similar CNT/polymer composite scaffolds based on MWCNTs/polycaprolactone (PCL) were fabricated by the solution evaporation technique and have been studied for attachment, proliferation, and differentiation of the rat bone marrow-derived stromal cells (BMSCs) [48]. Incorporation of MWCNTs into PCL led to increase in surface roughness and tensile strength of the matrix. The proliferation and osteogenic differentiation of BMSCs were found to depend on the concentration of MWCNTs in the polymer, and the optimum concentration of MWCNTs to grow BMSCs was 0.5 %.

The results from another study pertaining to growth of hMSCs on SWCNT monolayer showed enhanced adhesion, proliferation, and osteogenic differentiation due to oxygen plasma treatment without any induction medium [49]. The osteogenic proteins such as osteocalcin, alkaline phosphatase (ALP), and early markers for osteogenic commitment such as CBFA1 were found to be upregulated. The possible explanation could be stress on hMSCs due to enhanced cell spreading brought about by chemical effects along with normal topological effects. In addition to the above effects, enhanced proliferation and osteogenic differentiation were also exhibited by hMSCs growing on aligned CNT networks compared to those on randomly oriented CNT networks [50]. In other words, hMSCs grown on CNT networks could recognize the arrangement of individual CNTs in the CNT networks, which implies that direction of growth and differentiation of hMSCs can be controlled by alignment direction of the individual CNTs. In this study, enhanced proliferation and osteogenic differentiation were proposed to be due to mechanotransduction pathways triggered by high cytoskeletal tension in the aligned hMSCs.

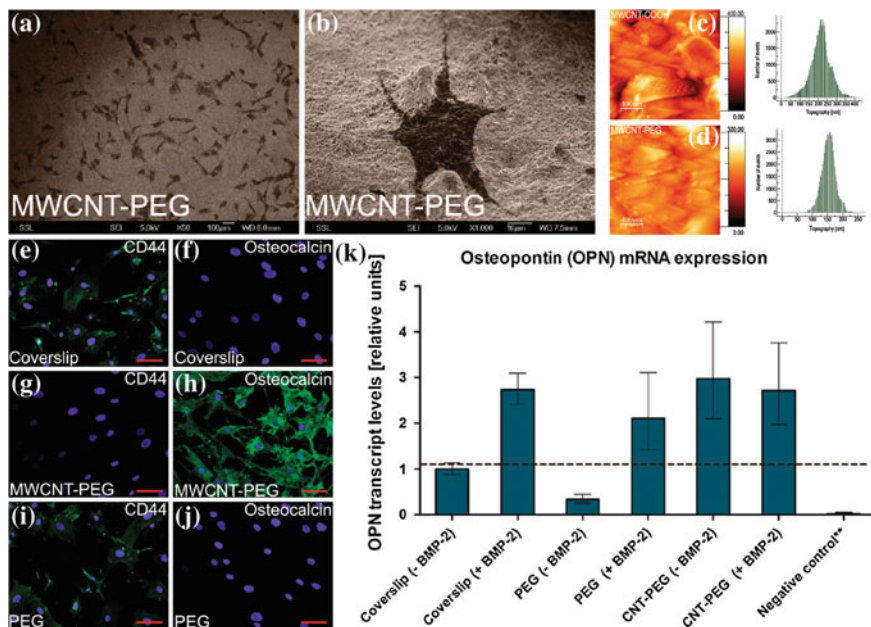


Fig. 24.1 a, b SEM images of hMSCs growing in normal medium on MWCNT-PEG-coated coverslips at day four of incubation showing growth of lots of cells in a large field of view (Scale bar is 100 μ m) and growth of a single cell in a small field of view (Scale bar is 10 μ m), respectively. c, d Atomic force microscopy images showing the topography of the surfaces of MWCNT-COOH- and MWCNT-PEG-coated coverslips, respectively. e-j Immunofluorescence image of cells subjected to osteoinduction without BMP-2 (Scale bars are 100 μ m). e, f Plain coverslips showing the presence of CD44 and absence of OCN; g, h MWCNT-PEG-coated coverslips showing the absence of CD44 and presence of OCN; i, j only PEG-coated coverslips showing the presence of CD44 and absence of OCN. k qPCR analysis of relative expression levels of OPN for hMSCs cultured on different types of substrates and osteoinduced with osteogenic media with or without BMP-2 for 14 days. **Negative control consists of a coverslip without BMP-2 and without induction with osteogenic media. Figure adapted from Nayak et al. [47]. Copyright@ACS

24.3.2 Carbon-Nanotube-Based 3D Scaffold for Tissue Engineering

CNTs have been engineered to develop various 3D architectures, and several of these structures have been found to support growth, proliferation, and differentiation of NSCs, MSCs, and pluripotent hESCs. A 3D rope like structure with a diameter of 1 mm and length of 1.5 cm was prepared by elongating bulk CNTs and twisting the resulting CNT strips. This rope was evaluated as a scaffold for growth and differentiation of NSCs. NSCs growing on these CNT ropes displayed enhanced differentiation into neurons even in the early culture stage compared to conventional tissue culture plates [51]. In addition, the neurite outgrowth was

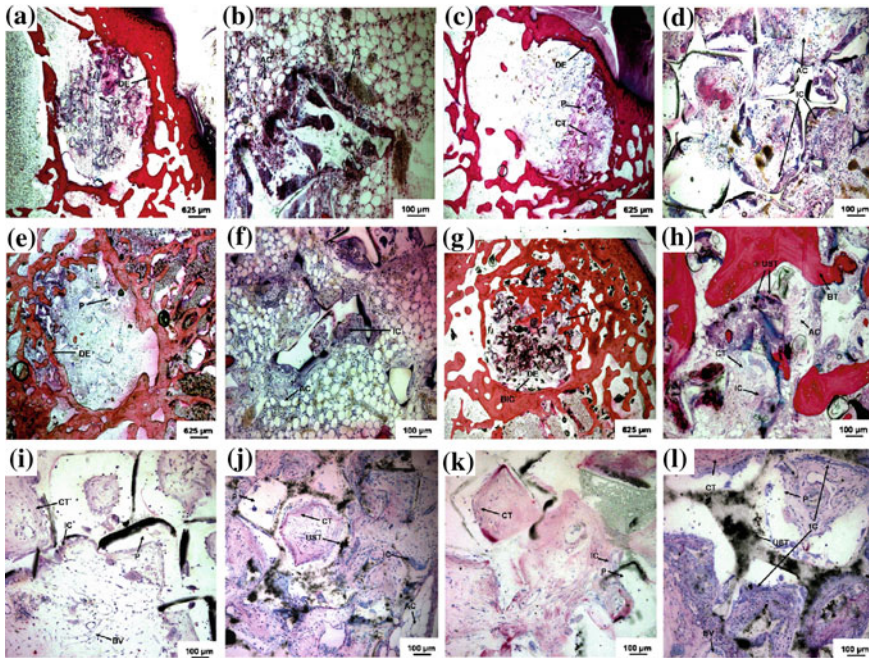


Fig. 24.2 Representative histological sections of CNT-based 3D scaffolds implanted in femoral condyle defects (a–h) and subcutaneously (i–l): a, b, and i a PPF scaffold 4 weeks after implantation, c, d, and j a US-tube/PPF scaffold after 4 weeks, e, f, and k a PPF scaffold after 12 weeks, and g, h, and l a US-tube/PPF scaffold after 12 weeks implantation. The PPF scaffold (*P*) appears in all images as *white* areas. The US-tubes (*UST*) appear as *black* aggregates in the nanocomposite images and are distinctly different from the other *black* artifacts generated during the sectioning process. Direct bone implant contact (*BIC*) occurred with the US-tube/PPF nanocomposite scaffold 12 weeks after implantation. The original defect edge (*DE*) is visible in the low magnification images. Connective tissue (*CT*), adipose cells (*AC*), blood vessels (*BV*), and inflammatory cells (*IC*) are also visible. Figure adapted from Sitharaman et al. [53]. Copyright@Elsevier

found to polarize along the spiral direction of the rope. Furthermore, electrical stimulation led to increased neuronal maturity with simultaneous increase in speed of neurite outgrowth as determined by upregulation of specific protein markers such as B-tubulin class III and microtubule-associated protein 2 (MAP-2). The above synergistic results pertaining to enhanced differentiation into mature neurons and promotion of neurite outgrowth due to electrical stimulation indicates potential application of such electroconductive CNT rope for therapeutic application of neural tissue regeneration.

The first 3D porous biodegradable scaffold for bone tissue engineering was fabricated by reinforcing poly(propylene fumarate) (PPF) with ultra-short (US) SWCNTs. This porous US-SWCNT nanocomposite scaffold demonstrated good cell attachment and sustained proliferation for rat MSCs [52]. The *in vivo* biocompatibility of this scaffold was evaluated in a rabbit model by implanting them

in femoral condyles and in subcutaneous pockets (Fig. 24.2) [53]. Addition of US-SWCNTs did not change the scaffold's structure, but improved its mechanical properties. The porous composite scaffold exhibited favorable hard and soft tissue responses and a threefold greater bone tissue ingrowth compared to control polymer scaffolds as determined by microcomputed tomography (microCT), histology, and histomorphometry at 4 and 12 weeks after implantation. The results indicate that presence of US-SWCNTs may be assisting in osteogenesis by rendering nanocomposite scaffolds bioactive.

Another method of fabricating 3D porous biocompatible scaffold that could possibly mimic the structure of ECM is electrospinning which helps in easy incorporation of CNTs into polymeric nanofibers by spinning a homogenous mixture of CNTs and polymers. Scaffolds made up of such CNT composites have been found to possess enhanced tensile modulus. The behavior of such electrospun scaffold was initially evaluated by incorporating varying concentration of MWCNTs into poly(lactic acid) (PLA) and seeding adipose-derived mesenchymal stem cells on them [54]. At the end of two weeks, hMSCs were found to be alive and proliferating as determined by DNA quantification and live and dead cell assay. Moreover, hMSCs growing on the 1 % MWCNT composite showed morphological differences as they were closely packed and longitudinally aligned compared to hMSCs growing on PLA only scaffold. Recently, another study done on the MSCs cultured on SWCNT/PLA nanocomposite and subjected to electrical stimulation showed upregulated expression of cardiac gene and proteins [55]. Several other studies have also been done utilizing these electrospun CNT composite scaffolds for growth and proliferation of cells such as osteoblasts [56] and skeletal myoblasts [57].

24.4 Graphene

Graphene is a 2D sheet of sp^2 bonded one-atom-thick monolayer of carbon atoms arranged in a honeycomb structure [58, 59]. It is a basic building block for other graphitic materials such as graphite, CNT, and fullerene. Because of their unique and desirable characteristics, graphene and its derivatives such as graphene foam, graphene oxide (GO), reduced graphene oxide (rGO), and GO nanocomposites have received extraordinary attention for a wide variety of applications such as nanoelectronics, sensors, and energy storage [60]. In addition, single-layered graphene has ultra-high surface area as every atom is exposed on its surface allowing efficient loading of drugs/genes leading to versatile surface functionalization. Therefore, within the realm of biomedical engineering, graphene-based nanomaterials are currently being explored as novel nanoplatfoms for drug and gene delivery, multimodal imaging, image-guided cancer therapy including tissue engineering and regenerative medicine [60, 61]. While there is a continuous search for biocompatible scaffolds with desired physical, chemical, and mechanical characteristics for engineering appropriate biomimetic materials [47], graphene

Table 24.2 List of graphene-based engineered scaffolds for tissue engineering with stem cells

Engineered nanostructure	Stem cell	Differentiated cell	Proposed mechanism	Reference
Graphene coated on different substrates (Glass, SiO ₂ , PET, and PDMS)	hMSCs	Osteocytes	Preconcentration platform	[68]
GO film with varying surface roughness	hMSCs	Osteocytes	Increased cytoskeletal tension due to nanotopography	[71]
Graphene layer	hNSCs	Neuron	Good electrical coupling	[74]
Fluorinated graphene	hMSCs	Neurons	Electrostatic induction resulting from polarization effect of carbon–fluorine bond	[75]
GO coated on SiO ₂	hMSCs	Adipocytes	Electrostatic interaction	[69]
GO coated on SiO ₂	iPSCs	Endodermal lineages	Physiochemical properties of surface	[76]
Graphene foam	hNSCs	Neurons and astrocytes	Efficient conductive platform	[86]
Graphene foam	hMSCs	Osteocytes	–	[87]

and its derivatives with unique properties such as high elasticity, flexibility, and adaptability to flat or irregular shaped surfaces can play key roles in promoting the adhesion, proliferation, and differentiation of various stem cells such as hMSCs, hNSCs, and iPSCs [62–64]. Table 24.2 lists scaffolds engineered from graphene and its derivatives for tissue engineering with various stem cells.

24.4.1 Graphene-Based 2D Scaffold for Tissue Engineering

The potential of graphene as 2D biocompatible scaffold was initially evaluated as a substrate for mammalian NIH 3T3 fibroblast cells [65], mammalian colorectal adenocarcinoma HT-29 cells [66], human osteoblasts, and mesenchymal stromal cells [67]. It was found to promote growth, proliferation, and adhesion of these mammalian cells. Cellular functions such as gene transfection and expressions were also found to be enhanced on graphene-based scaffolds without any toxicity. In addition, mesenchymal stromal cells grown on graphene showed spindle-shaped morphology compared to normal polygonal-shaped morphology achieved on SiO₂ substrate. While all of the above results suggested high affinity of mammalian cells toward scaffold based on graphene family of nanomaterials, the results pertaining to difference in morphology of mesenchymal stromal cells indicated its future application on regulating specific lineage direction of pluripotent or multipotent stem cells. Since then, several studies have been reported for differentiation of hMSCs, hNSCs, iPSCs, and hESCs growing on scaffolds based on graphene family of nanomaterials into specific lineages.

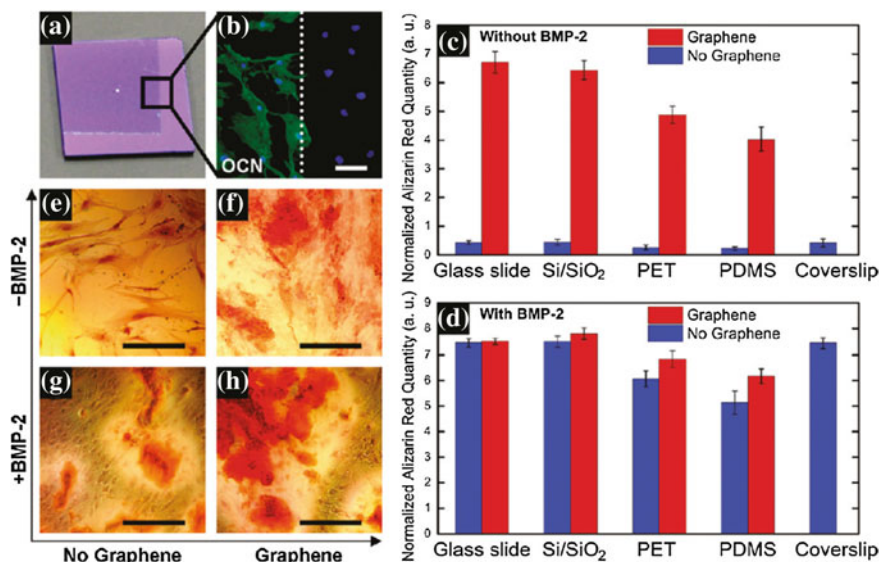


Fig. 24.3 **a** Optical image of 1 × 1 cm, partially graphene-coated Si/SiO₂ chip, showing the graphene boundary. **b** Osteocalcin (OCN) marker showing bone cell formation on the same chip only on the graphene-coated area; the graphene boundary is also clearly visible here. **c, d** Alizarin red quantification of hMSCs grown for 15 days on substrates with or without graphene coating. **c** Cells grown in the absence of BMP-2. Control with coverslips is shown as a reference. **d** Cells grown in the presence of BMP-2. Conventional plain coverslips were used as a positive control. **e–h** PET substrate stained with alizarin red showing calcium deposits due to osteogenesis. **e** PET without BMP-2 and without graphene; **f** PET without BMP-2 and with graphene; **g** PET with BMP-2 and without graphene; **h** PET with both BMP-2 and graphene. Scale bars are 100 μm. Figure adapted from Nayak et al. [68]. Copyright@ACS

One such study was done for evaluation of graphene coated on different substrates (glass, SiO₂, PET, and PDMS) for osteogenesis of hMSCs [68]. Graphene not only supported unhindered growth and proliferation of hMSCs irrespective of the below substrate but also accelerated their differentiation into osteocytes as indicated by enhanced expression of typical protein marker for osteoblasts such as osteocalcin, osteopontin, and calcium deposition (Fig. 24.3). The rate of osteogenic differentiation was found to be comparable to that of specific differentiation factor such as BMP-2. This particular result was further confirmed by Lee et al., who attributed the role of unique physiochemical properties of graphene surface which act as a preconcentration platform due to the noncovalent binding of growth factors including osteogenic inducers [69].

Since some of the prior studies have reported significant increase in osteogenic differentiation of hMSCs growing on scaffolds with nanopopography [70], therefore, surface morphology of graphene owing to its highly wrinkled structure has also been proposed to be the driving force for osteogenic differentiation [68, 69]. This role of surface topography was evaluated by growing hMSCs on graphene oxide (GO) films

with different surface roughness created by crosslinking methacrylate functionalized GO by the process of free radical polymerization [71]. The extent of mineralization as determined by calcium precipitation on the roughest GO film was found to be four times higher than the smoother GO film. Moreover, spontaneous osteogenic differentiation of hMSCs was observed on rough GO film without the use of any chemical inducers. The above result was attributed to the increased cytoskeletal tension created due to the nanotopography on the surface of GO film which provides more anchoring points for the adhesion and hence facilitates the proliferation and differentiation of hMSCs. Such kind of engineering of graphene nanomaterials has opened up the possibility of preparing biocompatible scaffolds for potential use in bone tissue engineering and regenerative medicine.

Recently, graphene and its derivatives have also been investigated for their potential application in neural tissue engineering. Being electroactive, behavior of neural cells can be influenced by electrical properties of graphene [28]. Such possibility was initially explored with growth of mouse neuronal hippocampal cells on graphene [72] and neuroendocrine PC12 cells on reduced graphene oxide (rGO) [73]. In both the cases, morphology of these cells remains unaltered and increased neurite outgrowth was observed. Similar to the above results, hNSCs grown on graphene displayed long-term viability and enhanced neuronal differentiation indicated by neural activity of the differentiated cells as confirmed by electrical stimulation using the graphene electrode [74]. In other words, graphene had a good electrical coupling with the differentiated neurons for electrical stimulation.

In addition to the graphene, fluorinated graphene has been reported for promoting transdifferentiation of hMSCs into neural lineage [75]. This neuroinductive effect was suggested to be due to polarization effect of carbon–fluorine bond which results in electrostatic induction at the interface of the cell and fluorinated graphene facilitating cellular alignment and nucleus elongation. These results suggest that graphene and its family of nanomaterials can be utilized as an excellent nanostructured scaffolds for promoting neuronal differentiation leading to their potential applications in neural tissue engineering.

Compared to the results pertaining to osteogenesis and neurogenesis, adipogenesis of hMSCs was found to be suppressed on graphene [69]. This was explained by the fact that insulin, a key regulator for fatty acid synthesis, gets denatured due to π – π interactions with graphene. Contrastingly, graphene oxide (GO) did not suppress the process of adipogenesis due to the surface oxygen content which helped in electrostatic interaction without affecting function of insulin. In other words, GO promoted adipogenic differentiation of hMSCs due to the increased adsorption of insulin. These results suggest that graphene displays different binding interactions with different growth factors and hence has a different influence on the growth of different stem cells and their subsequent differentiation to specific tissue lineages.

This particular aspect could be only be confirmed by evaluating growth, proliferation, and differentiation of pluripotent stem cells like hESCs or iPSCs on scaffolds engineered from graphene and its derivatives. One such study done utilizing cultured mouse induced pluripotent stem cells (iPSCs) growing on

graphene and GO surfaces displayed distinct proliferation and differentiation characteristics [76]. GO-based scaffold showed better iPSCs attachment and proliferation than graphene, due to the presence of oxygen atoms (e.g., OH) on their surface. Additionally, unlike graphene, GO was found to promote the differentiation of iPSCs toward an endodermal lineage. However, the differentiation toward ectodermal and mesodermal lineages was comparable for both surfaces. This result indicated the importance of surface properties of graphene-based scaffolds in controlling the behavior of stem cells.

24.4.2 Graphene-Based 3D Scaffold for Tissue Engineering

While unique surface properties of 2D graphene and its derivatives can induce stem cells to differentiate into specific lineages, their 3D porous structures engineered via different processes such as hydrothermal reduction [77–80], supramolecular interaction [81–83], electrospinning [84], and chemical vapor deposition might provide in vivo 3D microenvironment resembling natural ECM. Among various graphene-based 3D scaffolds, hydrogels are most attractive biomaterials as their mechanical properties can be controlled by utilizing different polymeric materials and altering crosslinking density and swelling degree. Graphene and its derivatives act as reinforcing materials in these 3D polymeric scaffolds leading to increased tensile and compressive strength without any change in their biocompatibility. The results from a preliminary study suggest that one such rGO hydrogel-based 3D polymeric scaffold promoted growth and proliferation of osteoblasts [85].

While all the above graphene-based 3D scaffolds are yet to be evaluated with regard to stem cells, graphene foam (GF), a 3D porous structure, was reportedly utilized as a novel 3D scaffold for NSCs (Fig. 24.4) [86]. The 3D GF not only supported NSCs growth, but also kept cells at a more active proliferation state as indicated by upregulated expression of Ki67 (a cellular marker for proliferation). Additionally, 3D GF was able to enhance differentiation of NSCs toward neurons as well as astrocytes as determined by phenotypic analysis. Furthermore, 3D GF was observed to be an efficient conductive platform mediating effective electrical stimulation for differentiated NSCs. Graphene foam as part of another study was found to support growth, proliferation, and spontaneous osteogenic differentiation of hMSCs [87]. Above results implicate great potential of 3D GFs for neural and bone tissue engineering.

24.5 Toxicity of Carbon Nanomaterials

While carbon nanomaterials are relatively new nanoplateforms for tissue engineering and regenerative medicine compared to other biomaterials such as polymeric scaffolds, they hold tremendous potential owing to their unique

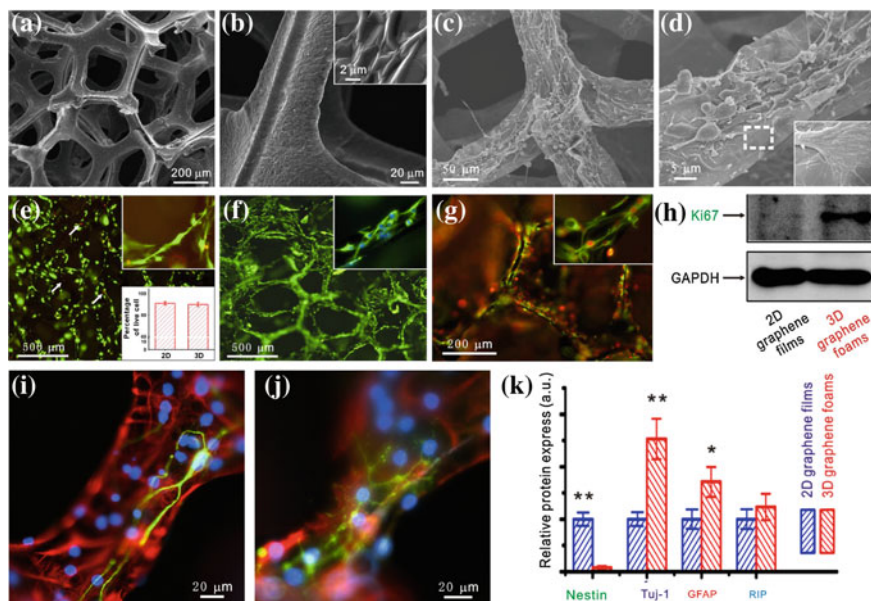


Fig. 24.4 SEM micrographs of 3D GFs at **a** low and **b** high magnification, the inset shows an enlarged view of 3D GF skeleton surface. **c** Low and **d** high magnified SEM micrographs of NSCs cultured on 3D GFs under the proliferation medium. The inset illustrates the interaction between the cell filopodia and 3D GF surface. **e** Cell viability assay of NSCs on 3D GFs after 5 days of culture as determined by live/dead assay. Live cells are stained green, and dead cells are red, white arrow points to dead cell. The lower right inset depicts the percentage of live cell on 2D graphene films and 3D GFs. **f** Fluorescence images of NSCs proliferated on 3D GFs for 5 days, immunostaining markers were nestin (green) for neural stem cells and DAPI (blue) for nuclei. **g** NSCs were double-immunostained with anti-Ki67 (red) and anti-nestin (green) antibodies, and Ki67 is a marker for cell proliferation. **h** Western blot analysis of Ki67 expression on 2D graphene films and 3D GFs. **i, j** Representative fluorescence images of differentiated NSCs under differentiation conditions. The cells were immunostained with Tuj-1 for neuron (green, **i**), GFAP for astrocyte (red, **i** and **j**), O4 for oligodendrocyte (green, **j**) and DAPI for nuclei (blue, **i** and **j**). **k** Relative expression of nestin, Tuj1, GFAP, and RIP as determined by Western blot analysis. The data are presented as mean \pm standard error (s. e. m.), * p , 0.05, ** p , 0.01. Figure adapted from Li et al. [86]. Copyright@NPG

physicochemical characteristics. However, their production with identical characteristics, good quality control, and minimal impurities is still a challenge for their potential biomedical applications. In addition, significant barriers also persist due to their lack of solubility in most solvents compatible with the biological milieu as the pristine form of these nanomaterials are inherently hydrophobic. However, these barriers have been overcome by mainly focusing on covalent and noncovalent functionalization of carbon nanomaterials with different biomolecules or polymers, which render them more hydrophilic with enhanced biocompatibility and toxicity profile. Subsequently, it is important to determine the potential toxic effects of these nanomaterials before their clinical translation can become a reality.

Therefore, several studies detailing the *in vitro* and *in vivo* toxicity of both pristine and functionalized carbon nanomaterials and their derivatives are currently being investigated.

24.5.1 Toxicity of CNTs

The adverse and unintended effects of pristine CNTs on human health have been a concern [88]. Several *in vitro* studies involving lung epithelial cells [89–91], keratinocytes [92, 93], macrophages [94], cardiac muscle cells [95], mouse embryonic stem cells [96], and mesenchymal stem cells [94] have indicated dose-dependent cytotoxicity for pristine CNTs. *In vivo* study involving intratracheally instilled pristine CNTs have been found showing pulmonary toxicity including unusual inflammation and fibrotic reactions due to the aggregation of CNTs in the lung airways [97–100]. Similarly, intraperitoneal injection of large MWCNTs has resulted in asbestos-like pathogenic consequences such as mesothelioma [101]. Contrastingly, PEGylated SWCNTs intravenously injected into mice (3 mg/kg of mouse BW) and monitored for over four months were found to be biocompatible and safe for *in vivo* biological applications [102, 103]. Since, in most cases, CNTs are required to be made biocompatible by process of functionalization, therefore, the results obtained from toxicity studies pertaining to pristine CNTs may not be relevant in the context of biomedical applications. However, it can be a concern for occupational safety considerations [104], and therefore, further investigations using parameters such as animal models, routes of administration, and surface functionalization are needed to fully address the toxicity concerns of CNTs.

24.5.2 Toxicity of Graphene

Several *in vitro* studies have been undertaken to evaluate the cytotoxicity of graphene and its derivatives. Studies done with macrophages [105–107], kidney cells [108], neuronal cells [109, 110], lung epithelial cells [111], fibroblasts [112], erythrocytes [112], and hepatoma cells [113] have indicated dose-dependent cytotoxicity associated with both graphene and GO. The main reason behind this cytotoxicity was found to be due to generation of intracellular/extracellular reactive oxygen species (ROS) in response to accumulation of graphene and GO which hinders nutrient uptake. Additionally, some of the above studies have also suggested size-dependent cytotoxicity for GO. The loss of viability of lung epithelial cells [114] and hemolysis of erythrocytes [115] was found to be inversely proportional to the size of the GO. In contrast, macro-sized GO showed better biocompatibility with macrophages in comparison to nanosized GO [116]. In other words, different types of cells are influenced differently by the dimensions and

surface properties of GO. However, graphene functionalized with biocompatible polymers such as PEG [117] and dextran [118] exhibited good biocompatibility.

Unlike CNTs, very few *in vivo* studies detailing biocompatibility and toxicity have been reported for graphene and its derivatives. One such *in vivo* study done after intravenous (IV) injection of GO in mice indicated chronic toxicity in the form of pulmonary edema and lung granuloma, as they get deposited primarily in the lung [119, 120]. However, similar study done after IV injection of dextran functionalized GO exhibited very good biocompatibility without any noticeable toxicity to mice as they accumulate in the reticuloendothelial systems (e.g., liver and spleen) and are cleared from the mouse body within one week [121]. *In vivo* studies done with graphene nanoplatelets (which are consisted of several layers of graphene sheets) have indicated inflammation in both the lung and pleural space, associated with increased expression of IL-1 β [122]. In contrast, PEGylated nanographene sheets did not elicit any toxicity in mice for a period of 3 months, even at a dose of 20 mg/kg, as indicated by blood biochemistry, hematological analysis, and histological examination [123]. Results from both *in vitro* and *in vivo* studies demonstrate that the development of functionalized graphene derivatives is essential for their potential biomedical applications such as regenerative medicine.

24.6 Conclusion and Perspectives

The recent interest in the use of carbon nanomaterials and their derivatives for biomedical applications including tissue engineering and regenerative medicine has led to continuous progress in this research area. Several studies pertaining to tissue engineering have demonstrated carbon nanomaterials as biocompatible substrates for enhanced growth, adhesion, proliferation, and spontaneous differentiation of various stem cells such as hMSCs, hNSCs, and iPSCs. Simultaneously, they have also been found to be amenable to transduction and genetic manipulation.

Different mechanisms have been proposed by these studies outlining the role of these scaffolds based on carbon nanomaterials for the behavior of stem cells growing on them. While some reports have suggested the role of these scaffolds as a preconcentration platform to growth factors and inductive peptides, others have implicated such responsibility on nanotopography of these scaffolds. Alternatively, several reports have also indicated the role of specific interaction of specific growth factors with the chemical interface of these scaffolds responsible for specific differentiation of both multipotent and pluripotent stem cells. In other words, the different surface properties of scaffolds based on carbon nanomaterials modulate differential behavior of different stem cells, indicating the broad potential of these nanomaterials as extracellular scaffolds to guide osteogenesis, neurite outgrowth, and adipogenesis, among others. These findings provide new insights regarding the capability of stem cells to recognize nanostructures and their interaction with growth factors and proteins, which indicates their potential applications for regenerative tissue engineering.

The development of these carbon nanomaterials for potential tissue engineering applications must proceed in tandem with the documentation of their toxicological side effects. The toxicity associated with the pristine carbon nanomaterials as reported in some of the previous studies may not be highly relevant, as they need to be functionalized for any such potential applications. However, robust chemistry for functionalization and the quality control of such functionalized carbon nanomaterials are the two most important prerequisites for any future clinical applications such as tissue engineering and regenerative medicine.

Overall, the exploration of carbon nanomaterials and their derivatives has culminated in many exciting and intriguing literature reports indicating them as excellent nanoplatforms for tissue engineering and stem cell-based regenerative medicine. However, most of these literature reports consist only of *in vitro* studies of specific stem cells. Subsequently, these are relatively new materials, and research on their potential applications in tissue engineering and regenerative medicine is still at a nascent stage. Therefore, sufficient *in vivo* investigations are necessary for their future application as an implantable tissue engineering material.

References

1. Langer R, Vacanti JP (1993) Tissue engineering. *Science* 260(5110):920–926
2. Freed LE, Vunjak-Novakovic G (2000) Tissue engineering bioreactors. In: Lanza RP, Langer R, Vacanti J (eds) *Principles of tissue engineering*, 2nd edn. Academic Press, San Diego, pp 143–156
3. Meinel L, Karageorgiou V, Fajardo R, Snyder B, Shinde-Patil V, Zichner L, Kaplan D, Langer R, Vunjak-Novakovic G (2004) Bone tissue engineering using human mesenchymal stem cells: effects of scaffold material and medium flow. *Ann Biomed Eng* 32(1):112–122
4. de Boer HH (1988) The history of bone grafts. *Clin Orthop Relat Res* 226:292–298
5. Damien CJ, Parsons JR (1991) Bone graft and bone graft substitutes: a review of current technology and applications. *J Appl Biomater* 2(3):187–208. doi:10.1002/jab.770020307
6. Coombes AG, Meikle MC (1994) Resorbable synthetic polymers as replacements for bone graft. *Clin Mater* 17(1):35–67
7. Yaszemski MJ, Payne RG, Hayes WC, Langer R, Mikos AG (1996) Evolution of bone transplantation: molecular, cellular and tissue strategies to engineer human bone. *Biomaterials* 17(2):175–185. doi:0142961296857620 [pii]
8. Lane JM, Tomin E, Bostrom MP (1999) Biosynthetic bone grafting. *Clin Orthop Relat Res* (367 Suppl):S107–117
9. Brown KL, Cruess RL (1982) Bone and cartilage transplantation in orthopaedic surgery, a review. *J Bone Joint Surg Am* 64(2):270–279
10. Northington JW, Brown MJ (1982) Acute canine idiopathic polyneuropathy, a Guillain-Barre-like syndrome in dogs. *J Neurol Sci* 56(2–3):259–273
11. Arrington ED, Smith WJ, Chambers HG, Bucknell AL, Davino NA (1996) Complications of iliac crest bone graft harvesting. *Clin Orthop Relat Res* 329:300–309
12. Anderson ML, Dhert WJ, de Bruijn JD, Dalmeijer RA, Leenders H, van Blitterswijk CA, Verbout AJ (1999) Critical size defect in the goat's os ilium, a model to evaluate bone grafts and substitutes. *Clin Orthop Relat Res* 364:231–239
13. Strong DM, Friedlaender GE, Tomford WW, Springfield DS, Shives TC, Burchardt H, Enneking WF, Mankin HJ (1996) Immunologic responses in human recipients of osseous and osteochondral allografts. *Clin Orthop Relat Res* 326:107–114

14. Mistry AS, Mikos AG (2005) Tissue engineering strategies for bone regeneration. *Adv Biochem Eng Biotechnol* 94:1–22
15. Sittinger M, Bujia J, Rotter N, Reitzel D, Minuth WW, Burmester GR (1996) Tissue engineering and autologous transplant formation: practical approaches with resorbable biomaterials and new cell culture techniques. *Biomaterials* 17(3):237–242. doi:[014296129685561X](https://doi.org/10.1016/0142-9612(96)85561-X) [pii]
16. Vacanti JP, Langer R (1999) Tissue engineering: the design and fabrication of living replacement devices for surgical reconstruction and transplantation. *Lancet* 354 Suppl 1:S132–34
17. Khademhosseini A, Vacanti JP, Langer R (2009) Progress in tissue engineering. *Sci Am* 300(5):64–71
18. Bonassar LJ, Vacanti CA (1998) Tissue engineering: the first decade and beyond. *J Cell Biochem Suppl* 30–31:297–303
19. Schultz O, Sittinger M, Haeupl T, Burmester GR (2000) Emerging strategies of bone and joint repair. *Arthritis Res* 2(6):433–436
20. Moroni L, de Wijn JR, van Blitterswijk CA (2008) Integrating novel technologies to fabricate smart scaffolds. *J Biomater Sci Polym Ed* 19(5):543–572. doi:[10.1163/156856208784089571](https://doi.org/10.1163/156856208784089571)
21. Satija NK, Singh VK, Verma YK, Gupta P, Sharma S, Afrin F, Sharma M, Sharma P, Tripathi RP, Gurudutta GU (2009) Mesenchymal stem cell-based therapy: a new paradigm in regenerative medicine. *J Cell Mol Med* 13(11–12):4385–4402. doi:[10.1111/j.1582-4934.2009.00857.x](https://doi.org/10.1111/j.1582-4934.2009.00857.x)
22. Ikada Y (2006) Challenges in tissue engineering. *J R Soc Interface* 3(10):589–601. doi:[10.1098/rsif.2006.0124](https://doi.org/10.1098/rsif.2006.0124) [pii] 3KJ54G03J182H66P
23. Davis HE, Leach JK (2008) Hybrid and composite biomaterials in tissue engineering. In: Ashammakhi N (ed) *Topics in multifunctional biomaterials and devices*, vol 1
24. Liu Z, Liang XJ (2012) Nano-carbons as theranostics. *Theranostics* 2(3):235–237. doi:[10.7150/thno.4156](https://doi.org/10.7150/thno.4156) thnov02p0235 [pii]
25. Cha C, Shin SR, Annabi N, Dokmeci MR, Khademhosseini A (2013) Carbon-based nanomaterials: multifunctional materials for biomedical engineering. *ACS Nano* 7(4):2891–2897. doi:[10.1021/nn401196a](https://doi.org/10.1021/nn401196a)
26. Veetil JV, Ye KM (2009) Tailored carbon nanotubes for tissue engineering applications. *Biotechnol Prog* 25(3):709–721. doi:[10.1002/btpr.165](https://doi.org/10.1002/btpr.165)
27. Yu MF, Files BS, Arepalli S, Ruoff RS (2000) Tensile loading of ropes of single wall carbon nanotubes and their mechanical properties. *Phys Rev Lett* 84(24):5552–5555
28. Ku SH, Lee M, Park CB (2013) Carbon-based nanomaterials for tissue engineering. *Adv Healthcare Mater* 2(2):244–260. doi:[10.1002/adhm.201200307](https://doi.org/10.1002/adhm.201200307)
29. Lin Y, Taylor S, Li H, Fernando KAS, Qu L, Wang W, Gu L, Zhou B, Sun Y-P (2004) Advances toward bioapplications of carbon nanotubes. *J Mater Chem* 14(4):527. doi:[10.1039/b314481j](https://doi.org/10.1039/b314481j)
30. Kuila T, Bose S, Mishra AK, Khanra P, Kim NH, Lee JH (2012) Chemical functionalization of graphene and its applications. *Prog Mater Sci* 57(7):1061–1105. doi:[10.1016/j.pmatsci.2012.03.002](https://doi.org/10.1016/j.pmatsci.2012.03.002)
31. Iijima S (1991) Helical microtubules of graphitic carbon. *Nature* 354(6348):56–58
32. Haddon RC (2002) Carbon nanotubes. *Acc Chem Res* 35(12):997
33. Dai H (2002) Carbon nanotubes: synthesis, integration, and properties. *Acc Chem Res* 35(12):1035–1044. doi:[ar0101640](https://doi.org/10.1021/ar0101640) [pii]
34. Hong H, Gao T, Cai W (2009) Molecular imaging with single-walled carbon nanotubes. *Nano today* 4(3):252–261. doi:[10.1016/j.nantod.2009.04.002](https://doi.org/10.1016/j.nantod.2009.04.002)
35. Liu Z, Tabakman S, Welsher K, Dai H (2009) Carbon nanotubes in biology and medicine: in vitro and in vivo detection, imaging and drug delivery. *Nano Res* 2(2):85–120. doi:[10.1007/s12274-009-9009-8](https://doi.org/10.1007/s12274-009-9009-8)

36. Jan E, Kotov NA (2007) Successful differentiation of mouse neural stem cells on layer-by-layer assembled single-walled carbon nanotube composite. *Nano Lett* 7(5):1123–1128. doi:[10.1021/nl0620132](https://doi.org/10.1021/nl0620132)
37. Kam NW, Jan E, Kotov NA (2009) Electrical stimulation of neural stem cells mediated by humanized carbon nanotube composite made with extracellular matrix protein. *Nano Lett* 9(1):273–278. doi:[10.1021/nl802859a](https://doi.org/10.1021/nl802859a) 10.1021/nl802859a [pii]
38. Park SY, Choi DS, Jin HJ, Park J, Byun KE, Lee KB, Hong S (2011) Polarization-controlled differentiation of human neural stem cells using synergistic cues from the patterns of carbon nanotube monolayer coating. *ACS Nano* 5(6):4704–4711. doi:[10.1021/Nn2006128](https://doi.org/10.1021/Nn2006128)
39. Park SY et al (2007) Carbon nanotube monolayer patterns for directed growth of mesenchymal stem cells. *Adv Mater*, 19 (18):2530–2534. doi:[10.1002/adma.200600875](https://doi.org/10.1002/adma.200600875)
40. Namgung S, Kim T, Baik KY, Lee M, Nam JM, Hong S (2011) Fibronectin-carbon-nanotube hybrid nanostructures for controlled cell growth. *Small* 7(1):56–61. doi:[10.1002/sml.201001513](https://doi.org/10.1002/sml.201001513)
41. Tay CY, Gu H, Leong WS, Yu H, Li HQ, Heng BC, Tantang H, Loo SCJ, Li LJ, Tan LP (2010) Cellular behavior of human mesenchymal stem cells cultured on single-walled carbon nanotube film. *Carbon* 48(4):1095–1104. doi:[10.1016/j.carbon.2009.11.031](https://doi.org/10.1016/j.carbon.2009.11.031)
42. Kim JA, Jang EY, Kang TJ, Yoon S, Ovalle-Robles R, Rhee WJ, Kim T, Baughman RH, Kim YH, Park TH (2012) Regulation of morphogenesis and neural differentiation of human mesenchymal stem cells using carbon nanotube sheets. *Integr Biol (Camb)* 4(6):587–594. doi:[10.1039/c2ib20017a](https://doi.org/10.1039/c2ib20017a)
43. Sridharan I, Kim T, Wang R (2009) Adapting collagen/CNT matrix in directing hESC differentiation. *Biochem Biophys Res Commun* 381(4):508–512. doi:[10.1016/j.bbrc.2009.02.072](https://doi.org/10.1016/j.bbrc.2009.02.072)
44. Chao TI, Xiang S, Chen CS, Chin WC, Nelson AJ, Wang C, Lu J (2009) Carbon nanotubes promote neuron differentiation from human embryonic stem cells. *Biochem Biophys Res Commun* 384(4):426–430. doi:[10.1016/j.bbrc.2009.04.157](https://doi.org/10.1016/j.bbrc.2009.04.157) [pii] S0006-291X(09)00851-1
45. Chao TI, Xiang S, Lipstate JF, Wang C, Lu J (2010) Poly(methacrylic acid)-grafted carbon nanotube scaffolds enhance differentiation of hESCs into neuronal cells. *Adv Mater* 22(32):3542–3547. doi:[10.1002/adma.201000262](https://doi.org/10.1002/adma.201000262)
46. Usui Y, Aoki K, Narita N, Murakami N, Nakamura I, Nakamura K, Ishigaki N, Yamazaki H, Horiuchi H, Kato H, Taruta S, Kim YA, Endo M, Saito N (2008) Carbon nanotubes with high bone-tissue compatibility and bone-formation acceleration effects. *Small* 4(2):240–246. doi:[10.1002/sml.200700670](https://doi.org/10.1002/sml.200700670)
47. Nayak TR et al (2010) Thin films of functionalized multiwalled carbon nanotubes as suitable scaffold materials for stem cells proliferation and bone formation. *ACS Nano*. doi:[10.1021/nn102738c](https://doi.org/10.1021/nn102738c)
48. Pan LL, Pei XB, He R, Wan QB, Wang J (2012) Multiwall carbon nanotubes/polycaprolactone composites for bone tissue engineering application. *Colloids and Surfaces B-Biointerfaces* 93:226–234
49. Baik KY, Park SY, Heo K, Lee KB, Hong S (2011) Carbon nanotube monolayer cues for osteogenesis of mesenchymal stem cells. *Small* 7(6):741–745. doi:[10.1002/sml.201001930](https://doi.org/10.1002/sml.201001930)
50. Namgung S, Baik KY, Park J, Hong S (2011) Controlling the growth and differentiation of human mesenchymal stem cells by the arrangement of individual carbon nanotubes. *ACS Nano* 5(9):7383–7390. doi:[10.1021/nn2023057](https://doi.org/10.1021/nn2023057)
51. Huang YJ, Wu HC, Tai NH, Wang TW (2012) Carbon nanotube rope with electrical stimulation promotes the differentiation and maturity of neural stem cells. *Small* 8(18):2869–2877
52. Shi X, Sitharaman B, Pham QP, Liang F, Wu K, Edward Billups W, Wilson LJ, Mikos AG (2007) Fabrication of porous ultra-short single-walled carbon nanotube nanocomposite scaffolds for bone tissue engineering. *Biomaterials* 28(28):4078–4090. doi:[10.1016/j.biomaterials.2007.05.033](https://doi.org/10.1016/j.biomaterials.2007.05.033)
53. Sitharaman B, Shi X, Walboomers X, Liao H, Cuijpers V, Wilson L, Mikos A, Jansen J (2008) In vivo biocompatibility of ultra-short single-walled carbon nanotube/biodegradable

- polymer nanocomposites for bone tissue engineering. *Bone* 43(2):362–370. doi:[10.1016/j.bone.2008.04.013](https://doi.org/10.1016/j.bone.2008.04.013)
54. McCullen SD, Stevens DR, Roberts WA, Clarke LI, Bernacki SH, Gorga RE, Lobo EG (2007) Characterization of electrospun nanocomposite scaffolds and biocompatibility with adipose-derived human mesenchymal stem cells. *Int J Nanomed* 2(2):253–263
 55. Mooney E, Mackle JN, Blond DJ, O’Cearbhaill E, Shaw G, Blau WJ, Barry FP, Barron V, Murphy JM (2012) The electrical stimulation of carbon nanotubes to provide a cardiomimetic cue to MSCs. *Biomaterials* 33(26):6132–6139. doi:[10.1016/j.biomaterials.2012.05.032](https://doi.org/10.1016/j.biomaterials.2012.05.032) S0142-9612(12)00573-X [pii]
 56. Shao S, Zhou S, Li L, Li J, Luo C, Wang J, Li X, Weng J (2011) Osteoblast function on electrically conductive electrospun PLA/MWCNTs nanofibers. *Biomaterials* 32(11):2821–2833. doi:[10.1016/j.biomaterials.2011.01.051](https://doi.org/10.1016/j.biomaterials.2011.01.051) S0142-9612(11)00077-9 [pii]
 57. McKeon-Fischer KD, Flagg DH, Freeman JW (2011) Coaxial electrospun poly(epsilon-caprolactone), multiwalled carbon nanotubes, and polyacrylic acid/polyvinyl alcohol scaffold for skeletal muscle tissue engineering. *J Biomed Mater Res, Part A* 99A(3):493–499. doi:[10.1002/jbm.a.33116](https://doi.org/10.1002/jbm.a.33116)
 58. Geim AK, Novoselov KS (2007) The rise of graphene. *Nat Mater* 6(3):183–191. doi:[10.1038/nmat1849](https://doi.org/10.1038/nmat1849) [pii] nmat1849
 59. Feng L, Wu L, Qu X (2012) New horizons for diagnostics and therapeutic applications of graphene and graphene oxide. *Adv Mater:ePub*. doi:[10.1002/adma.201203229](https://doi.org/10.1002/adma.201203229)
 60. Zhang Y, Nayak TR, Hong H, Cai W (2012) Graphene: a versatile nanoplatform for biomedical applications. *Nanoscale* 4(13):3833–3842. doi:[10.1039/c2nr31040f](https://doi.org/10.1039/c2nr31040f)
 61. Yang K, Feng L, Shi X, Liu Z (2012) Nano-graphene in biomedicine: theranostic applications. *Chem Soc Rev:ePub*. doi:[10.1039/c2cs35342c](https://doi.org/10.1039/c2cs35342c)
 62. Frank IW, Tanenbaum DM, Van der Zande AM, McEuen PL (2007) Mechanical properties of suspended graphene sheets. *J Vac Sci Technol, B* 25(6):2558–2561. doi:[10.1116/1.2789446](https://doi.org/10.1116/1.2789446)
 63. Lee C, Wei X, Kysar JW, Hone J (2008) Measurement of the elastic properties and intrinsic strength of monolayer graphene. *Science* 321(5887):385–388. doi:[10.1126/science.1157996](https://doi.org/10.1126/science.1157996) [pii] 321/5887/385
 64. Lee Y, Bae S, Jang H, Jang S, Zhu SE, Sim SH, Song YI, Hong BH, Ahn JH (2010) Wafer-scale synthesis and transfer of graphene films. *Nano Lett* 10(2):490–493. doi:[10.1021/nl903272n](https://doi.org/10.1021/nl903272n)
 65. Ryoo SR, Kim YK, Kim MH, Min DH (2010) Behaviors of NIH-3T3 fibroblasts on graphene/carbon nanotubes: proliferation, focal adhesion, and gene transfection studies. *ACS Nano* 4(11):6587–6598. doi:[10.1021/nn1018279](https://doi.org/10.1021/nn1018279)
 66. Ruiz ON, Fernando KA, Wang B, Brown NA, Luo PG, McNamara ND, Vangsness M, Sun YP, Bunker CE (2011) Graphene oxide: a nonspecific enhancer of cellular growth. *ACS Nano* 5(10):8100–8107. doi:[10.1021/nn202699t](https://doi.org/10.1021/nn202699t)
 67. Kalbacova M, Broz A, Kong J, Kalbac M (2010) Graphene substrates promote adherence of human osteoblasts and mesenchymal stromal cells. *Carbon* 48(15):4323–4329. doi:[10.1016/j.carbon.2010.07.045](https://doi.org/10.1016/j.carbon.2010.07.045)
 68. Nayak TR et al (2011) Graphene for controlled and accelerated osteogenic differentiation of human mesenchymal stem cells. *ACS Nano*. doi:[10.1021/nn200500h](https://doi.org/10.1021/nn200500h)
 69. Lee WC, Lim C, Shi H, Tang LAL, Wang Y, Lim CT, Loh KP (2011) Origin of enhanced stem cell growth and differentiation on graphene and graphene oxide. *ACS Nano* 5(9):7334–7341. doi:[10.1021/nn202190c](https://doi.org/10.1021/nn202190c)
 70. Dalby MJ, Gadegaard N, Tare R, Andar A, Riehle MO, Herzyk P, Wilkinson CD, Oreffo RO (2007) The control of human mesenchymal cell differentiation using nanoscale symmetry and disorder. *Nat Mater* 6(12):997–1003. doi:[10.1038/nmat2013](https://doi.org/10.1038/nmat2013) [pii] nmat2013
 71. Tang LA, Lee WC, Shi H, Wong EY, Sadovoy A, Gorelik S, Hobbey J, Lim CT, Loh KP (2012) Highly wrinkled cross-linked graphene oxide membranes for biological and charge-storage applications. *Small* 8(3):423–431. doi:[10.1002/smll.201101690](https://doi.org/10.1002/smll.201101690)

72. Li N, Zhang X, Song Q, Su R, Zhang Q, Kong T, Liu L, Jin G, Tang M, Cheng G (2011) The promotion of neurite sprouting and outgrowth of mouse hippocampal cells in culture by graphene substrates. *Biomaterials* 32(35):9374–9382. doi:[10.1016/j.biomaterials.2011.08.065](https://doi.org/10.1016/j.biomaterials.2011.08.065) [pii] S0142-9612(11)01013-1
73. Agarwal S, Zhou X, Ye F, He Q, Chen GC, Soo J, Boey F, Zhang H, Chen P (2010) Interfacing live cells with nanocarbon substrates. *Langmuir* 26(4):2244–2247. doi:[10.1021/la9048743](https://doi.org/10.1021/la9048743)
74. Park SY, Park J, Sim SH, Sung MG, Kim KS, Hong BH, Hong S (2011) Enhanced differentiation of human neural stem cells into neurons on graphene. *Adv Mater* 23(36):H263–H267. doi:[10.1002/adma.201101503](https://doi.org/10.1002/adma.201101503)
75. Wang Y, Lee WC, Manga KK, Ang PK, Lu J, Liu YP, Lim CT, Loh KP (2012) Fluorinated graphene for promoting neuro-induction of stem cells. *Adv Mater* 24(31):4285–4290. doi:[10.1002/adma.201200846](https://doi.org/10.1002/adma.201200846)
76. Chen GY, Pang DW, Hwang SM, Tuan HY, Hu YC (2012) A graphene-based platform for induced pluripotent stem cells culture and differentiation. *Biomaterials* 33(2):418–427. doi:[10.1016/j.biomaterials.2011.09.071](https://doi.org/10.1016/j.biomaterials.2011.09.071) [pii] S0142-9612(11)01147-1
77. Xu Y, Sheng K, Li C, Shi G (2010) Self-assembled graphene hydrogel via a one-step hydrothermal process. *ACS Nano* 4(7):4324–4330. doi:[10.1021/nn101187z](https://doi.org/10.1021/nn101187z)
78. Jiang X, Ma YW, Li JJ, Fan QL, Huang W (2010) Self-assembly of reduced graphene oxide into three-dimensional architecture by divalent ion linkage. *J Phys Chem C* 114(51):22462–22465. doi:[10.1021/Jp108081g](https://doi.org/10.1021/Jp108081g)
79. Hou CY, Duan YR, Zhang QH, Wang HZ, Li YG (2012) Bio-applicable and electroactive near-infrared laser-triggered self-healing hydrogels based on graphene networks. *J Mater Chem* 22(30):14991–14996. doi:[10.1039/C2jm32255b](https://doi.org/10.1039/C2jm32255b)
80. Tang Z, Shen S, Zhuang J, Wang X (2010) Noble-metal-promoted three-dimensional macroassembly of single-layered graphene oxide. *Angew Chem Int Ed Engl* 49(27):4603–4607. doi:[10.1002/anie.201000270](https://doi.org/10.1002/anie.201000270)
81. Xu Y, Wu Q, Sun Y, Bai H, Shi G (2010) Three-dimensional self-assembly of graphene oxide and DNA into multifunctional hydrogels. *ACS Nano* 4(12):7358–7362. doi:[10.1021/nl1027104](https://doi.org/10.1021/nl1027104)
82. Bai H, Li C, Wang X, Shi G (2010) A pH-sensitive graphene oxide composite hydrogel. *Chem Commun (Camb)* 46(14):2376–2378. doi:[10.1039/c000051e](https://doi.org/10.1039/c000051e)
83. Bai H, Sheng KX, Zhang PF, Li C, Shi GQ (2011) Graphene oxide/conducting polymer composite hydrogels. *J Mater Chem* 21(46):18653–18658. doi:[10.1039/C1jm13918e](https://doi.org/10.1039/C1jm13918e)
84. Wan C, Chen B (2011) Poly (epsilon-caprolactone)/graphene oxide biocomposites: mechanical properties and bioactivity. *Biomed Mater* 6(5):055010. doi:[10.1088/1748-6041/6/5/055010](https://doi.org/10.1088/1748-6041/6/5/055010) S1748-6041(11)99617-X [pii]
85. Lim HN, Huang NM, Lim SS, Harrison I, Chia CH (2011) Fabrication and characterization of graphene hydrogel via hydrothermal approach as a scaffold for preliminary study of cell growth. *Int J Nanomed* 6:1817–1823. doi:[10.2147/ijn.s23392](https://doi.org/10.2147/ijn.s23392)
86. Li N, Zhang Q, Gao S, Song Q, Huang R, Wang L, Liu L, Dai J, Tang M, Cheng G (2013) Three-dimensional graphene foam as a biocompatible and conductive scaffold for neural stem cells. *Sci Rep* 3:1604. doi:[10.1038/srep01604](https://doi.org/10.1038/srep01604) srep01604 [pii]
87. Crowder SW, Prasai D, Rath R, Balikov DA, Bae H, Bolotin KI, Sung HJ (2013) Three-dimensional graphene foams promote osteogenic differentiation of human mesenchymal stem cells. *Nanoscale* 5(10):4171–4176. doi:[10.1039/c3nr00803g](https://doi.org/10.1039/c3nr00803g)
88. Ji SR et al (2010) Carbon nanotubes in cancer diagnosis and therapy. *Biochim Biophys Acta* 1806 (1):29–35. doi:[10.1016/j.bbcan.2010.02.004](https://doi.org/10.1016/j.bbcan.2010.02.004) S0304-419X(10)00014-4 [pii]
89. Davoren M, Herzog E, Casey A, Cottineau B, Chambers G, Byrne HJ, Lyng FM (2007) In vitro toxicity evaluation of single walled carbon nanotubes on human A549 lung cells. *Toxicol In Vitro* 21(3):438–448. doi:[10.1016/j.tiv.2006.10.007](https://doi.org/10.1016/j.tiv.2006.10.007) [pii] S0887-2333(06)00232-3
90. Casey A, Herzog E, Lyng FM, Byrne HJ, Chambers G, Davoren M (2008) Single walled carbon nanotubes induce indirect cytotoxicity by medium depletion in A549 lung cells. *Toxicol Lett* 179(2):78–84. doi:[10.1016/j.toxlet.2008.04.006](https://doi.org/10.1016/j.toxlet.2008.04.006) S0378-4274(08)00107-0 [pii]

91. Ye SF, Wu YH, Hou ZQ, Zhang QQ (2009) ROS and NF-kappaB are involved in upregulation of IL-8 in A549 cells exposed to multi-walled carbon nanotubes. *Biochem Biophys Res Commun* 379(2):643–648. doi:[10.1016/j.bbrc.2008.12.137](https://doi.org/10.1016/j.bbrc.2008.12.137) S0006-291X(08)02565-5 [pii]
92. Manna SK, Sarkar S, Barr J, Wise K, Barrera EV, Jejelowo O, Rice-Ficht AC, Ramesh GT (2005) Single-walled carbon nanotube induces oxidative stress and activates nuclear transcription factor-kappaB in human keratinocytes. *Nano Lett* 5(9):1676–1684. doi:[10.1021/nl0507966](https://doi.org/10.1021/nl0507966)
93. Monteiro-Riviere NA, Nemanich RJ, Inman AO, Wang YY, Riviere JE (2005) Multi-walled carbon nanotube interactions with human epidermal keratinocytes. *Toxicol Lett* 155(3):377–384. doi:[10.1016/j.toxlet.2004.11.004](https://doi.org/10.1016/j.toxlet.2004.11.004) [pii] S0378-4274(04)00506-5
94. Kalbacova M, Kalbac M, Dunsch L, Kataura H, Hempel U (2006) The study of the interaction of human mesenchymal stem cells and monocytes/macrophages with single-walled carbon nanotube films. *Physica Status Solidi B-Basic Solid State Physics* 243(13):3514–3518. doi:[10.1002/pssb.200669167](https://doi.org/10.1002/pssb.200669167)
95. Garibaldi S, Brunelli C, Bavastrello V, Ghigliotti G, Nicolini C (2006) Carbon nanotube biocompatibility with cardiac muscle cells. *Nanotechnology* 17(2):391–397. doi:[10.1088/0957-4484/17/2/008](https://doi.org/10.1088/0957-4484/17/2/008)
96. Zhu L, Chang DW, Dai L, Hong Y (2007) DNA damage induced by multiwalled carbon nanotubes in mouse embryonic stem cells. *Nano Lett* 7(12):3592–3597. doi:[10.1021/nl071303v](https://doi.org/10.1021/nl071303v)
97. Lam CW, James JT, McCluskey R, Hunter RL (2004) Pulmonary toxicity of single-wall carbon nanotubes in mice 7 and 90 days after intratracheal instillation. *Toxicol Sci* 77(1):126–134. doi:[10.1093/toxsci/kfg243](https://doi.org/10.1093/toxsci/kfg243) kfg243 [pii]
98. Warheit DB (2003) Comparative pulmonary toxicity assessment of single-wall carbon nanotubes in rats. *Toxicol Sci* 77(1):117–125. doi:[10.1093/toxsci/kfg228](https://doi.org/10.1093/toxsci/kfg228)
99. Shvedova AA et al (2005) Unusual inflammatory and fibrogenic pulmonary responses to single-walled carbon nanotubes in mice. *Am J Physiol Lung Cell Mol Physiol* 289(5):L698–L708. doi:[10.1152/ajplung.00084.2005](https://doi.org/10.1152/ajplung.00084.2005) [pii] 00084.2005
100. Muller J, Huaux F, Moreau N, Misson P, Heilier JF, Delos M, Arras M, Fonseca A, Nagy JB, Lison D (2005) Respiratory toxicity of multi-wall carbon nanotubes. *Toxicol Appl Pharmacol* 207(3):221–231. doi:[10.1016/j.taap.2005.01.008](https://doi.org/10.1016/j.taap.2005.01.008)
101. Poland CA, Duffin R, Kinloch I, Maynard A, Wallace WA, Seaton A, Stone V, Brown S, Macnee W, Donaldson K (2008) Carbon nanotubes introduced into the abdominal cavity of mice show asbestos-like pathogenicity in a pilot study. *Nat Nanotechnol* 3(7):423–428. doi:[10.1038/nnano.2008.111](https://doi.org/10.1038/nnano.2008.111) [pii] nnano.2008.111
102. Schipper ML, Nakayama-Ratchford N, Davis CR, Kam NWS, Chu P, Liu Z, Sun X, Dai H, Gambhir SS (2008) A pilot toxicology study of single-walled carbon nanotubes in a small sample of mice. *Nat Nanotechnol* 3(4):216–221. doi:[10.1038/nnano.2008.68](https://doi.org/10.1038/nnano.2008.68)
103. Liu Z, Davis C, Cai W, He L, Chen X, Dai H (2008) Circulation and long-term fate of functionalized, biocompatible single-walled carbon nanotubes in mice probed by Raman spectroscopy. *Proc Natl Acad Sci USA* 105(5):1410–1415. doi:[10.1073/pnas.0707654105](https://doi.org/10.1073/pnas.0707654105)
104. Liu Z, Tabakman S, Welsher K, Dai H (2009) Carbon nanotubes in biology and medicine: in vitro and in vivo detection, imaging and drug delivery. *Nano Res* 2(2):85–120. doi:[10.1007/s12274-009-9009-8](https://doi.org/10.1007/s12274-009-9009-8)
105. Li Y, Liu Y, Fu Y, Wei T, Le Guyader L, Gao G, Liu RS, Chang YZ, Chen C (2012) The triggering of apoptosis in macrophages by pristine graphene through the MAPK and TGF-beta signaling pathways. *Biomaterials* 33(2):402–411. doi:[10.1016/j.biomaterials.2011.09.091](https://doi.org/10.1016/j.biomaterials.2011.09.091) S0142-9612(11)01183-5 [pii]
106. Sasidharan A, Panchakarla LS, Sadanandan AR, Ashokan A, Chandran P, Girish CM, Menon D, Nair SV, Rao CN, Koyakutty M (2012) Hemocompatibility and macrophage response of pristine and functionalized graphene. *Small* 8(8):1251–1263. doi:[10.1002/sml.201102393](https://doi.org/10.1002/sml.201102393)

107. Chen GY, Yang HJ, Lu CH, Chao YC, Hwang SM, Chen CL, Lo KW, Sung LY, Luo WY, Tuan HY, Hu YC (2012) Simultaneous induction of autophagy and toll-like receptor signaling pathways by graphene oxide. *Biomaterials* 33(27):6559–6569. doi:[10.1016/j.biomaterials.2012.05.064](https://doi.org/10.1016/j.biomaterials.2012.05.064) S0142-9612(12)00618-7 [pii]
108. Sasidharan A, Panchakarla LS, Chandran P, Menon D, Nair S, Rao CN, Koyakutty M (2011) Differential nano-bio interactions and toxicity effects of pristine versus functionalized graphene. *Nanoscale* 3(6):2461–2464. doi:[10.1039/c1nr10172b](https://doi.org/10.1039/c1nr10172b)
109. Zhang Y, Ali SF, Dervishi E, Xu Y, Li Z, Casciano D, Biris AS (2010) Cytotoxicity effects of graphene and single-wall carbon nanotubes in neural pheochromocytoma-derived pc12 cells. *ACS Nano* 4(6):3181–3186. doi:[10.1021/nn1007176](https://doi.org/10.1021/nn1007176)
110. Lv M, Zhang Y, Liang L, Wei M, Hu W, Li X, Huang Q (2012) Effect of graphene oxide on undifferentiated and retinoic acid-differentiated SH-SY5Y cells line. *Nanoscale* 4(13):3861–3866. doi:[10.1039/c2nr30407d](https://doi.org/10.1039/c2nr30407d)
111. Chang Y, Yang S-T, Liu J-H, Dong E, Wang Y, Cao A, Liu Y, Wang H (2011) In vitro toxicity evaluation of graphene oxide on A549 cells. *Toxicol Lett* 200(3):201–210. doi:[10.1016/j.toxlet.2010.11.016](https://doi.org/10.1016/j.toxlet.2010.11.016)
112. Liao K-H, Lin Y-S, Macosko CW, Haynes CL (2011) Cytotoxicity of graphene oxide and graphene in human erythrocytes and skin fibroblasts. *ACS Appl Mater Interfaces* 3(7):2607–2615. doi:[10.1021/am200428v](https://doi.org/10.1021/am200428v)
113. Yuan J, Gao H, Sui J, Duan H, Chen WN, Ching CB (2012) Cytotoxicity evaluation of oxidized single-walled carbon nanotubes and graphene oxide on human hepatoma HepG2 cells: an iTRAQ-coupled 2D LC-MS/MS proteome analysis. *Toxicol Sci* 126(1):149–161. doi:[10.1093/toxsci/kfr332](https://doi.org/10.1093/toxsci/kfr332) [pii] kfr332
114. Chang Y, Yang ST, Liu JH, Dong E, Wang Y, Cao A, Liu Y, Wang H (2011) In vitro toxicity evaluation of graphene oxide on A549 cells. *Toxicol Lett* 200(3):201–210. doi:[10.1016/j.toxlet.2010.11.016](https://doi.org/10.1016/j.toxlet.2010.11.016) S0378-4274(10)01776-5 [pii]
115. Liao KH, Lin YS, Macosko CW, Haynes CL (2011) Cytotoxicity of graphene oxide and graphene in human erythrocytes and skin fibroblasts. *ACS Appl Mater Interfaces* 3(7):2607–2615. doi:[10.1021/am200428v](https://doi.org/10.1021/am200428v)
116. Yue H, Wei W, Yue Z, Wang B, Luo N, Gao Y, Ma D, Ma G, Su Z (2012) The role of the lateral dimension of graphene oxide in the regulation of cellular responses. *Biomaterials* 33(16):4013–4021. doi:[10.1016/j.biomaterials.2012.02.021](https://doi.org/10.1016/j.biomaterials.2012.02.021) S0142-9612(12)00187-1 [pii]
117. Wojtoniszak M, Chen X, Kalenczuk RJ, Wajda A, Lapczuk J, Kurzewski M, Drozdziak M, Chu PK, Borowiak-Palen E (2012) Synthesis, dispersion, and cytocompatibility of graphene oxide and reduced graphene oxide. *Colloids Surf B Biointerfaces* 89:79–85. doi:[10.1016/j.colsurfb.2011.08.026](https://doi.org/10.1016/j.colsurfb.2011.08.026) [pii] S0927-7765(11)00504-2
118. Zhang S, Yang K, Feng L, Liu Z (2011) In vitro and in vivo behaviors of dextran functionalized graphene. *Carbon* 49(12):4040–4049. doi:[10.1016/j.carbon.2011.05.056](https://doi.org/10.1016/j.carbon.2011.05.056)
119. Wang K, Ruan J, Song H, Zhang JL, Wo Y, Guo SW, Cui DX (2011) Biocompatibility of graphene oxide. *Nanoscale Res Lett* 6:8. doi:[10.1007/s11671-010-9751-6](https://doi.org/10.1007/s11671-010-9751-6)
120. Zhang XY, Yin JL, Peng C, Hu WQ, Zhu ZY, Li WX, Fan CH, Huang Q (2011) Distribution and biocompatibility studies of graphene oxide in mice after intravenous administration. *Carbon* 49(3):986–995. doi:[10.1016/j.carbon.2010.11.005](https://doi.org/10.1016/j.carbon.2010.11.005)
121. Zhang SA, Yang K, Feng LZ, Liu Z (2011) In vitro and in vivo behaviors of dextran functionalized graphene. *Carbon* 49(12):4040–4049. doi:[10.1016/j.carbon.2011.05.056](https://doi.org/10.1016/j.carbon.2011.05.056)
122. Schinwald A, Murphy FA, Jones A, MacNee W, Donaldson K (2012) Graphene-based nanoplatelets: a new risk to the respiratory system as a consequence of their unusual aerodynamic properties. *ACS Nano* 6(1):736–746. doi:[10.1021/nn204229f](https://doi.org/10.1021/nn204229f)
123. Yang K, Wan J, Zhang S, Zhang Y, Lee ST, Liu Z (2011) In vivo pharmacokinetics, long-term biodistribution, and toxicology of PEGylated graphene in mice. *ACS Nano* 5(1):516–522. doi:[10.1021/nn1024303](https://doi.org/10.1021/nn1024303)

Chapter 25

Engineering Peptide-based Carriers for Drug and Gene Delivery

Jo-Ann Chuah, David L. Kaplan and Keiji Numata

25.1 Introduction

An efficient delivery system is the key element to ensure that new drugs (small molecules, peptides, proteins, DNA, RNA) can serve their purpose as useful medicines. These molecules encompass a range of sizes and need to be delivered intracellularly to produce therapeutic effects in the cytoplasm or in specific organelles such as the nucleus, mitochondria, or lysosomes. The lipophilic nature of the cell membrane, however, is a barrier that prevents the diffusion of large and charged molecules into cells. Physical techniques such as microinjection and electroporation are well established and have been found to be effective with most cells and species, but these methods cause damage to the cell membrane [1, 2]. Viral vectors (adenoviruses, retroviruses, herpes) have unparalleled success in delivering membrane-impermeable molecules, surpassing all other methods in terms of efficiency. With these vectors, however, immunogenicity, cytotoxicity, and insertional mutagenesis are major limitations [3, 4].

Although less efficient, non-viral vectors are safer alternatives. Some common non-viral delivery systems include liposomes, polyethylenimine, dendrimers, chitosan, polylysine, and various peptides. Once molecules are inside the cell by any of these delivery methods, trafficking of the different biological active molecules to appropriate intracellular compartments becomes the next challenge. A potential problem here is that molecules traveling via the endocytic pathway may become trapped in the endosome and eventually end up being enzymatically degraded in the lysosome [5]. In this regard, any vehicle that can deliver molecules directly into

J.-A. Chuah · K. Numata (✉)
Enzyme Research Team, Biomass Engineering Program, RIKEN, 2-1 Hirosawa, Wako-shi,
Saitama 351-0198, Japan
e-mail: keiji.numata@riken.jp

D. L. Kaplan
Department of Biomedical Engineering, Tufts University, 4 Colby Street, Medford,
Massachusetts 02155, USA

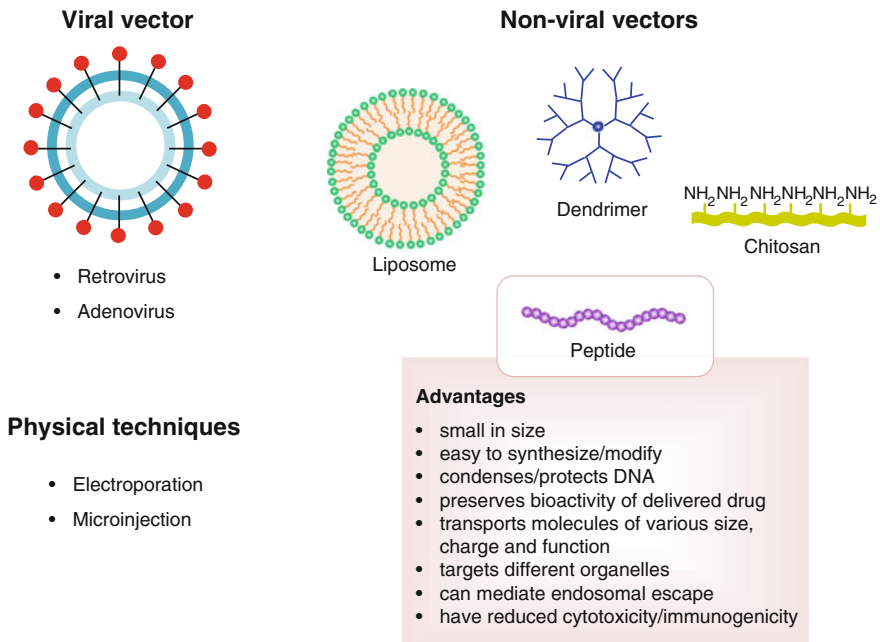


Fig. 25.1 Examples of established delivery systems. Physical techniques such as electroporation and microinjection, viral vectors in the form of retrovirus or adenovirus, as well as non-viral vectors which include liposomes, dendrimers, chitosan, and peptides are commonly used for delivery of genes/drugs into cells. Among these methods/carriers, peptides are advantageous as they are small in size, easily synthesized and modified, can condense DNA into compact particles for transport, preserve bioactivity of the drug until it is delivered to the target site, disrupt the endosomal membrane and escape proteasomal degradation, traffic therapeutic molecules of various size, charge and function to targeted intracellular compartments, and additionally, have reduced cytotoxicity and immunogenicity

the cytoplasm of target cells and to specific organelles would be highly desirable. Ideally, the carrier should (1) be biodegradable and biocompatible, (2) lack intrinsic toxicity, (3) not accumulate in the body, (4) retain the original specificity for the target, and (5) preserve bioactivity of the drug until it is delivered to the target site.

Peptides stand out among the non-viral vectors as no other class of biomolecules is able to simultaneously condense and protect DNA [6, 7], mediate endosomal escape [8, 9], and localize to specific organelles for cargo delivery [10–12] (Fig. 25.1). Peptides also have the amazing ability to transport cargoes with molecular weights significantly greater than their own [13]. For intracellular trafficking of peptide carriers, two major strategies have been described: (1) the covalent linkage of the cargo to the peptide, thereby forming a conjugate, achieved by chemical cross-linking, cloning, or expression of a protein fused to the peptide and (2) the formation of a non-covalent complex between the two partners. As yet, there is no consensus as to the mechanism of translocation by these peptides except for various proposed mechanisms detailed in recent reviews [14–16].

Aside from the useful qualities exhibited by peptides, the ability to deliver bioactive molecules and drugs in a slow, sustained, controlled release format is also important. The applicability of such a delivery system would be further expanded if the carriers were also biodegradable, biocompatible, mechanically durable, and could be prepared and processed under ambient aqueous conditions to preserve the bioactivity of the drug to be delivered. Silk proteins are promising biomaterials that can fulfill these needs. In addition, they have advantages of slow biodegradability, biocompatibility, self-assembly, excellent mechanical properties (tensile strength and Young's modulus), and controllable structure and morphology [17, 18]. Silk proteins have been produced by spiders and insects such as silkworms, and they form fibrous materials. Recombinant silks are also synthesized by the elucidation of silk genetics, structures, and biophysics.

We describe in this chapter peptide/protein-based carriers for intracellular gene or drug delivery as well as organelle-targeted delivery and highlight some of the recent advances in designs. Diverse applications where these peptides have been harnessed are presented, as well as how these carriers have helped to advance the field of cell biology. The use of silk-based biomaterials to deliver bioactive molecules, such as small drugs, proteins, and genes, is also described in this review.

25.2 Peptide-based Drug/Gene Carrier

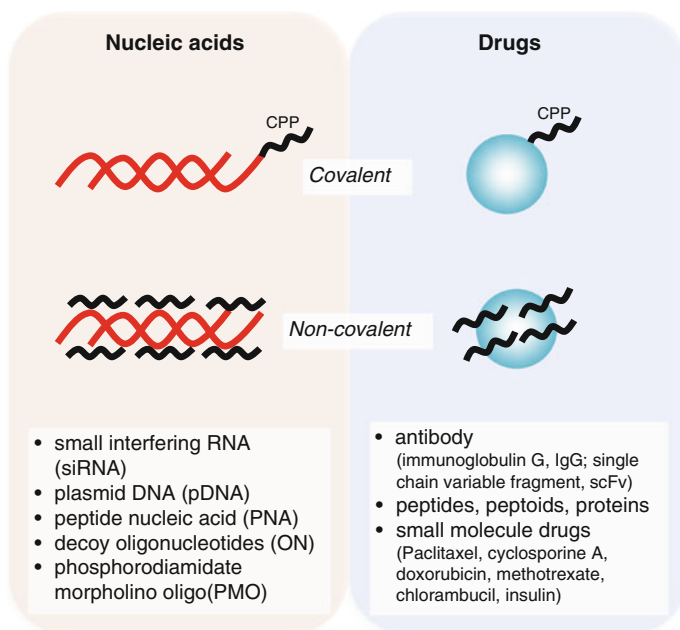
Peptides possess many advantages as delivery vehicles in comparison with viral vectors and outperform even other non-viral vectors with the small size, ease of synthesis and modification, and good biocompatibility. A highly versatile and efficient class of transporters, known as cell-penetrating peptides (CPPs), comprises short peptide sequences (6–30 amino acids) with the ability to traverse plasma membranes. CPPs vary significantly in sequence, hydrophobicity, and polarity. These peptides are typically cationic and exist as naturally occurring protein transduction domains or can be rationally designed [14] (Table 25.1). Tat [19] represents CPPs derived from naturally occurring proteins. A second group contains chimeric CPPs such as transportan, which has 12 amino acids derived from the neuropeptide galanin fused with 14 amino acids derived from the wasp venom mastoparan [20]. A third group contains synthetic CPPs, and of these the polyarginines [21] are the most studied. Identification of the first CPP, the trans-activating transcriptional activator (Tat) of HIV-1, dates back to 1988 from two research groups working on HIV [22, 23]. Other CPPs have been discovered since, and the list continues to grow.

Although the mechanism underlying the internalization of CPPs across the cellular membrane remains to be elucidated, recent studies have helped to shed some light on the subject [24]. To date, these peptides have successfully delivered a wide range of exogenous molecules including nucleic acids, proteins, antibodies, nanoparticles, and liposomes (Fig. 25.2). An intense and ongoing subject of

Table 25.1 Examples of cell-penetrating peptides described in this review, sequences and origins

Peptide	Sequence	Origin	Reference
Tat (48–59)	GRKKRRQRRRAP	Protein-derived	[19]
Penetratin	RQIKIWFQNRRMKWKK-NH ₂	Protein-derived	[42]
pVEC	LLIILRRRIRKQAHHSK-NH ₂	Protein-derived	[72]
PTD4	YARAAARQARA	Protein-derived	[82]
Transportan	GWTLNSAGYLLGKINLKALAALAKKIL-NH ₂	Chimeric	[20]
PepFect6	Stearyl-AGYLLGK(ϵ NH ^a)INLKALAALAKKIL-NH ₂	Chimeric	[37]
Tetravalent decaarginine (10R-p35 ^{tet})	R ₁₀ GEYFTLQIRGRERFEMFRELNEALELKDAQA	Chimeric	[57]
Bombesin (6–14)	NQWAVGHLM-NH ₂	Chimeric	[109]
Pep-1	Ac ^b -KETWWETWWTEWSQPK KKRKV-cya ^c	Synthetic	[15, 87]
Polyarginine	R _n (n = 6–12)	Synthetic	[21]
CADY	Ac-GLWRALWRLRSLWRL WRA-cya	Synthetic	[40]
YTA2	YTAIAWVKAFIRKLRK-NH ₂	Synthetic	[73]
YTA4	IAWVKAFIRKLRKGPLG-NH ₂	Synthetic	[73]

^a lysine tree with trifluoromethylquinoline derivative modifications; ^b acetyl group; ^c cysteamine

**Fig. 25.2** Covalent and non-covalent linkages of cell-penetrating peptide (CPP) to various drug and nucleic acid cargoes

research is the intracellular delivery of genes due to their tremendous potential as therapeutic agents for many acquired or inherited diseases. The selective permeability of the plasma membrane presents a major challenge for internalization of these large and negatively charged molecules. Unassisted uptake of nucleic acids, if at all, occurs only at negligible levels [25]. Cationic CPPs, on the other hand, are not only able to destabilize the cell membrane but can also bind and compact nucleic acid molecules via electrostatic interactions [26], thereby aiding the translocation of these molecules across the cell membrane.

For efficient uptake, the size of CPP–nucleic acid complexes should preferentially be in the range of 100–300 nm. An equally important criterion is the stability of complexes which can be regulated by varying the charge ratio, as overly strong electrostatic interactions may prevent dissociation of nucleic acids from the carrier inside the cell [27]. Although CPP–nucleic acid complexes face the risk of being trapped in endosomes, the current state of research on CPPs enables modifications of peptides to improve their endosomal escape [28–30]. Most importantly, CPPs have been found to have minimal cytotoxicity at concentrations required to mediate the delivery of various cargoes [31]. Additionally, the versatility of CPPs lies in their ability to undergo structural modifications to suit different types of cargoes. For instance, CPPs can be conjugated covalently as well as non-covalently with siRNAs [32, 33].

The discovery of siRNA as a powerful strategy for the modulation of gene expression [34] led to various approaches to modify the systems to optimize potency, specificity, and delivery [35, 36]. The past few years have seen the emergence of new CPPs such as PepFect6 (variant of TP-10) [37], gastrin-related peptides [38], and bLFcin₆ (derived from bovine lactoferricin) [39], specifically designed for optimized delivery of siRNA. The first secondary amphiphilic peptide, CADY, showed improvement in terms of higher affinity for siRNA and higher viability (more than 80 %) with all tested cell lines [40]. Tat peptide, crosslinked to siRNA, effectively increased cellular uptake of the oligonucleotide [41]. The degree of silencing achieved by Tat-mediated siRNA delivery matched that using the highly efficient transfection reagent, Lipofectamine 2000. Reduced gene expression for up to 7 days could be attained with penetratin [42] and transportan covalently linked to modified siRNA [43], while CPPs in the form of polyarginine and an MPG derivative formed non-covalent complexes with siRNA for delivery [44, 45]. A separate study boasted an efficient and persistent silencing effect with minimum cytotoxicity using siRNA packaged in octaarginine-modified MEND (R8-MEND) for cell transfection [46]. In another report, a type of CPP termed “peptide for ocular delivery” (POD) successfully transported siRNA into human embryonic retinal cells to result in a gene silencing effect of more than 50 % [47]. POD also delivered plasmid DNA (pDNA) to cells with gene expression exceeding 50 %. In addition, macrobranched Tat [48], arginine- or histidine-rich CPPs [49, 50] and some well-known synthetic peptide analogs such as GALA [51], KALA [52], JTS1 [53], and ppTG1 [54] were found to function efficiently as carriers of pDNA. Multimers of Tat increased transfection efficiency of plasmids by 6–8 times more than poly-L-arginine or mutant Tat2-M1 and by 390 times compared

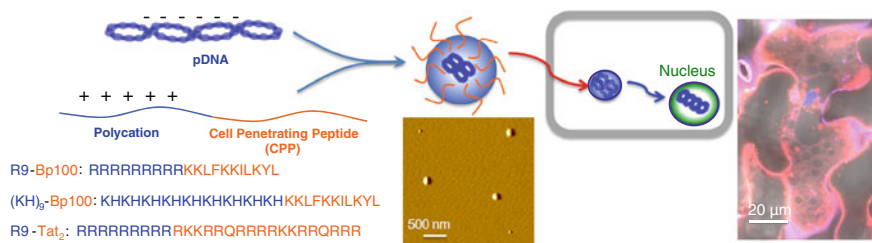


Fig. 25.3 A useful strategy for rapid and efficient gene delivery which is based on the combination of a cell-penetrating peptide (Bp100 or Tat2) and a polycation (nona-arginine or a copolymer of histidine and lysine) (adapted from [57])

with other standard vectors [55]. We recently developed peptide carriers, which were fusions of different CPPs and polycations, as a new tool for gene delivery (Fig. 25.3). The designed peptides facilitated rapid delivery of pDNA and showed better transfection efficiency compared to either just the CPP or polycationic region alone [56]. Related to the idea of a fusion peptide, multivalency also improves the activity of CPP. Tetrameric CPPs performed 10–100 times better in cellular uptake and mediated as high as a 1,000-fold increase in activity relative to their monomeric counterparts [57].

Apart from siRNA and plasmids, CPPs have also been used widely in the delivery of DNA mimics such as peptidic nucleic acid (PNA), decoy oligonucleotide (ON), and phosphorodiamidate morpholino oligomer (PMO). CPP (transportan or penetratin) conjugates of PNA analog exhibited inhibition of Tat-dependent trans-activation in HeLa cells within 6 h when coadministered with chloroquine [58]. Nuclear localization of splice-correcting ON analogs was accomplished by CPP-mediated delivery [59]. A specific example is the delivery of double-stranded decoy ONs targeting the transcription factor nuclear factor kappa-light-chain-enhancer of activated B cells and Myc protein by TP or TP10 [60, 61]. R8-MEND, which can transport siRNA, also transported antisense oligodeoxynucleotides to functionally inhibit cytosolic mRNA [62]. CPPs have also been applied for PMO delivery into mouse models of Duchenne muscular dystrophy, to enable splice correction of a nonsense mutation at exon 23 in the dystrophin gene [63, 64].

Intriguingly, the Rath peptide, derived from VP5 protein of avian infectious bursal disease virus, rapidly delivered not just DNA but also antibody within 30 min for the former, and 1 h for the latter [65]. Similar to their application in nucleic acid delivery, CPPs are just as commonly used for cellular delivery of a variety of drugs, with sizes ranging from 30 to 150 kDa. CPPs can deliver these molecules by chemical modifications, non-covalent transduction, or using fusion proteins. Polyarginine conjugates of paclitaxel enhanced the water solubility, and thus cellular uptake of this hydrophobic drug [66, 67]. The same CPP, when conjugated with cyclosporine A, showed potential use for treatment of psoriasis as well as other skin diseases [21]. Penetratin, on the other hand, made delivery of photoactive drugs possible by mitigating their extreme lipophilicity and poor trafficking properties [68].

Some of these CPPs also play a pivotal role in cancer therapy. Doxorubicin conjugated to Tat and transferrin successfully inhibited the growth of multidrug-resistant tumor cells [69, 70]. This well-characterized chemotherapeutic was also employed to evaluate the anti-tumor efficacy of a new and potential glioma-targeted drug delivery vector, gHoPe2 [71]. In this study, the authors reported construction of the new vector by covalent conjugation of pVEC [72], gHo, and a cargo, and the efficiency of drug delivery by gHoPe2 highlighted the feasibility of the strategy. In another study, two different CPPs, YTA2 and YTA4, increased uptake of methotrexate in resistant tumor cells [73]. CPPs are invaluable tools in cancer therapy primarily because they can be modified to improve selectivity for cancer cells. Conjugation of a Tat derivative to AHNP, a mimetic that binds selectively to an epidermal growth factor receptor overexpressed in breast cancers, yielded a cell-specific transporter [74]. Subsequently, this transporter successfully delivered the intended therapeutic to cancer cells both *in vivo* and *in vitro*, without compromising the activity of the drug. Tumor-homing domains can also be engineered into CPP, for instance, a PEGA-homing domain known to accumulate in breast tumor vasculature was conjugated to pVEC CPP, and the resultant construct was effective and selectively taken up into breast tumor blood vessels [75]. Conjugation of a chemotherapeutic agent, chlorambucil, to the same CPP enhanced efficacy of the drug as much as 4 times.

In comparison with the delivery of small molecule therapeutics for the treatment of cancer and other diseases, a more challenging task is the translocation of large molecules such as antibodies into cells. Tat peptide, known for its remarkable translocation capacity, was first exploited for such a function two decades ago [76]. Since then, Tat has been used to deliver ^{111}In -labeled anti-mouse IgG for radiotherapeutic applications [77] and anti-p21 for sensitizing cancer cells to cytotoxic therapies [78]. Some recent achievements include the delivery of single-chain antibody fragments into mouse brain cells to target prion diseases [79] and into hepatocytes to inhibit hepatitis B virus replication [80]. The ability of CPPs to overcome various barriers is showcased with examples, such as the blood–brain barrier, membrane barrier of hepatocytes and, additionally, the intestinal barrier for the delivery of insulin [81]. An impressive point to note was that covalent attachment of the CPP to insulin was not required; instead, the simple coadministration sufficed. Bioactive macromolecules in the form of peptides, peptoids, and proteins have also been successfully delivered to modulate intracellular processes. A representative example for each of these different types of cargo is described. The peptide inhibitor of transcription factor STAT-6 was conjugated to the HIV-Tat-derived PTD4 CPP [82], and internalization of the conjugate attenuated ovalbumin-induced inflammatory responses and mucus production in mice [83]. Anti-apoptotic proteins, Bcl-x_L and its BH4 domain, were conjugated to Tat for administration to mice to treat bacterial sepsis, which pioneered the use CPP in such applications [84]. The conjugation of Tat and Penetratin, individually, to a peptoid inhibitor improves cell membrane permeability, with higher inhibition observed using the penetratin conjugate [85]. Antigens, with ovalbumin as a model, were conjugated to the translocation motif of the hepatitis B virus for

intracellular delivery [86]. The authors observed improvements of both cellular and humoral immune system responses. Interestingly, it is possible for a single carrier, such as the amphiphilic peptide Pep-1, to promote cellular uptake of both small peptides as well as large proteins regardless of their nature and target cell type [15, 87].

25.3 Organelle-Specific Delivery System

The ultimate goal in designing a peptide carrier is to make one with target specificity or the ability to carry therapeutics not just to a specific cell, but to a specific organelle within the cell. This is crucial as a majority of therapeutic agents need to be in particular intracellular compartments to fully exert their therapeutic potential. Some diseases and corresponding treatments have been associated with specific organelles—the cell nucleus is a well-known target for gene therapy; the mitochondrion itself is important for proapoptotic cancer therapy, while its genome is a prime target for manipulation; and the lysosomes are recognized for targeting of enzymes to treat lysosomal storage diseases. An effective strategy for organelle-specific targeting is by the use of signal peptides, which have specific amino acid sequences for recognition by the cellular machinery in order to direct attached cargoes toward correct destinations in the cell [88] (illustrated in Fig. 25.4).

The most established system for transport of molecules between the cytoplasm and the nucleus is the classical nuclear import pathway, whereby proteins containing nuclear localization signals (NLS) are transported into the nucleus. Since characterization of the NLS from simian virus 40 (SV40) large T antigen in 1984 [10], this and other NLS peptides have been used to traffic DNA to the nucleus [89]. These NLS peptides ensure entry of DNA through the nuclear pore complexes by active transport as free diffusion is an unlikely route for DNA passage due to size restrictions [90, 91]. NLSs are characterized by short clusters of basic amino acids and are typically about 10 amino acids in length. They form complexes with DNA by ionic interactions, covalent attachments, or site-specific attachment using a peptide nucleic acid clamp [92]. In the field of gene therapy, the most notable NLS originated from the large tumor antigen of SV40. This peptide of 7 amino acids enabled a 100-fold increase in the speed of nuclear uptake of pDNA compared to a reversed NLS sequence [93]. In another study, the M9 sequence of the heterogeneous nuclear ribonucleoprotein attached to DNA in a non-covalent manner improved nuclear import of DNA. Conjugation of the M9 sequence to a cationic peptide for DNA condensation resulted in a 10-fold increase in reporter gene expression [94]. As nuclear-targeted drug delivery can kill cancer cells more directly and efficiently, some recent work featured design strategies using different NLSs and doxorubicin as model drug. In one of the studies, Tat was conjugated with mesoporous silica nanoparticles and was found to efficiently target the cell nucleus, killing cancer cells effectively [95]. Another study reported

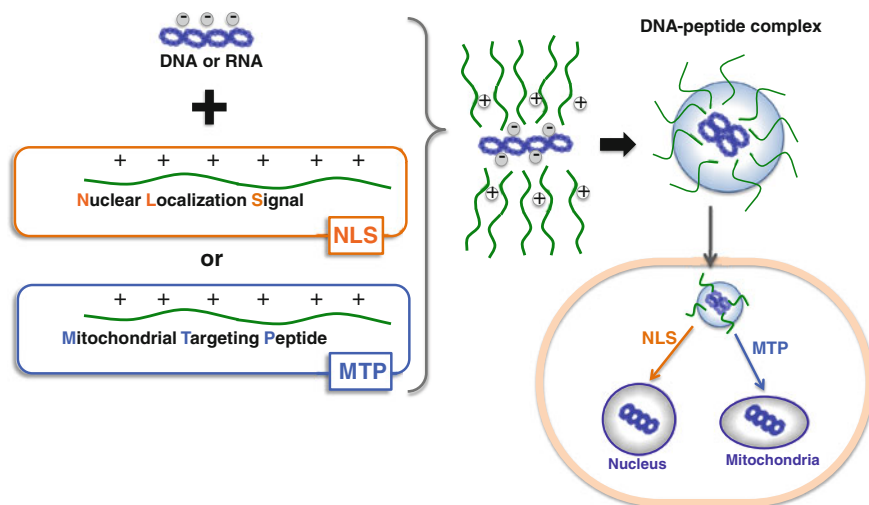


Fig. 25.4 Peptide carrier loading and targeting strategies for gene delivery. Non-covalent complex of signal peptides (nuclear localization signal or mitochondrial targeting peptide) and cargo (DNA or RNA) for localization to specific organelles (nucleus or mitochondria). The complex is formed by electrostatic and hydrophobic interactions between the peptide and the cargo

on a novel nucleus-targeting carrier comprising NLS conjugated to cholesterol-modified glycol chitosan, which facilitated nuclear localization of higher doxorubicin amounts than unassisted uptake of the drug [96].

As mentioned earlier, mitochondria represent another important target for intracellularly delivered DNA and drugs. Not only is this organelle responsible for ATP production, the mitochondrion is also involved in various metabolic pathways essential for the regulation of fundamental cellular processes. Mitochondria dysfunction therefore contributes to a variety of disorders and diseases namely cancer [97], Parkinson's disease [98], Alzheimer's disease [99], diabetes [100], and atherosclerosis [101], among others. Since the discovery of peptides with mitochondria-targeting ability, a variety of innovative approaches to develop new peptides or fine-tune properties of existing peptides to achieve efficient mitochondrial localization have surfaced. Introduction of lipophilic residues and modification of charge distribution in a CPP yielded peptides with mitochondrial targeting ability [102]. A different approach was taken in a separate study where artificial signal sequences were created, and the fabricated sequences worked favorably to target the mitochondria just as well as natural signal sequences [12]. Zhao and coworkers successfully used tetrapeptide sequences containing radical scavenging properties to deliver antioxidants to the mitochondria. The versatile Tat peptide, when fused to a mitochondrial targeting sequence from malate dehydrogenase, efficiently translocated proteins across mitochondrial membranes [103]. These mitochondrial targeting peptides (MTPs) are typically N-terminal

motifs predicted to form amphipathic helices approximately 15–70 residues in length and enriched in positively charged basic residues [104]. To date, different MTPs have been discovered for the delivery of various cargoes. The DNA alkylating drug chlorambucil was delivered as an MTP conjugate [105], while histatin 5, an anti-microbial peptide, can be used as a carrier molecule for leishmanicidal molecules to target mitochondria ATP synthesis in *Leishmania* [106]. Fusion of adeno-associated virus capsid with a mitochondrial targeting sequence provided a platform for introduction of large DNA fragments (~5 kb) into mitochondria [107], which was applied in a follow-up study for mutant gene delivery to successfully induce visual loss and optic atrophy in mice [108]. In other new cancer-related studies, a chimeric peptide analog of bombesin targeted mitochondria-disrupting peptides to the mitochondria in tumor cells [109], while a combination of mitochondria-targeting genes (*LETM1* and *CTMP*) and 2A-peptide sequence induced anti-tumor effect and mediated mitochondria apoptosis [110].

In the case of lysosomes, delivery of enzymes is the only means of treatment for lysosomal storage diseases (LSDs) such as glucocerebrosidase, phenylalanine ammonia lyase, and many others. More than forty of the known LSDs are caused, directly or indirectly, by the absence of one or more enzymes in the lysosome [111]. Hence, enzyme replacement therapy for LSDs is being actively pursued although advancement in the area still falls short compared to well-established therapeutic strategies for diseases associated with the mitochondria or nucleus. Nevertheless, recent progress related to lysosomal targeting is highlighted. LeBowitz and coworkers tested an alternative, peptide-based targeting system for delivery of enzymes to lysosomes. Their strategy involved a chimeric protein containing a portion of mature human IGF-II fused to the C terminus of human β -glucuronidase, which was delivered effectively and reversed the storage pathology in mice as models [11]. The same research group reported recently on lysosomal targeting of acid α -glucosidase to enhance muscle glycogen clearance in mice with Pompe disease, where human clinical studies are currently underway [112]. Other researchers evaluated subcellular targeting and delivery of nanoparticles to the lysosome in mammalian cells using a novel carrier comprising cell-penetrating peptide and lysosomal sorting peptide domains [113]. Another approach taken in the development of new vectors was to synthesize, by click chemistry, an inhibitor-Tat conjugate, which was successfully delivered to lysosomes for inhibition of lysosomal cysteine proteases [114].

25.4 Drug Delivery Via Silk Nanoparticles

Silk proteins have been used successfully for several decades as sutures and have also been explored as biomaterials for drug delivery systems, due to their excellent mechanical properties, versatility in processing, and low cytotoxicity [18, 115, 116]. The degradation products of silk proteins with beta-sheet structures, when exposed to alpha-chymotrypsin, have been identified and shown to have no

cytotoxicity to in vitro neuron cells [117, 118]. The combination of silk protein and nanoparticles makes useful delivery systems because silk nanoparticles are advantageous over other delivery methods in terms of biodegradability and biocompatibility. In this section, silk-based nanoparticles and their preparation methods, which have been widely studied by many groups, are summarized.

Silk nanoparticles from silk fibroin solutions of *Bombyx mori* and tropical tasar silkworm *Antheraea mylitta* were stable, spherical, negatively charged, 150–170 nm in average diameter, and showed no toxicity [119]. The silk nanoparticles were observed in the cytosol of murine squamous cell carcinoma cells, and the growth factor release from the nanoparticles showed significantly sustained release over 3 weeks, implying potential application as a growth factor delivery system [119]. Silk nanoparticles were also used to increase mechanical properties of silk-based porous scaffolds [120]. Several types of silk nanoparticles hybridized with chitosan, sericin, elastin, and genes have been developed due to their excellent availability and biocompatibility [121–125]. Silk fibroin-based nanoparticles (<100 nm) for local and sustained therapeutic curcumin delivery to cancer cells were fabricated by blending with non-covalent interactions to encapsulate curcumin in various proportions with pure silk fibroin or silk fibroin with chitosan. The silk-based nanoparticles containing curcumin showed a higher efficiency against breast cancer cells and have potential to treat in vivo breast tumors by local, sustained, and long-term therapeutic delivery [126]. Silk sericin-polyoxamer nanoparticles loaded with both hydrophilic and hydrophobic drugs were reported to be stable in aqueous solution, small in size (100–110 nm), and rapidly taken up by cells [122]. Conjugation of bioactive agents such as drugs or peptides into silk-based nanoparticles is also an efficient methodology for delivery of these molecules into target sites. The crystalline silk protein nanoparticles (40–120 nm) have been conjugated with insulin via covalent crosslinking [127]. It was confirmed that in vitro stability of insulin in human serum was enhanced and the half-life of insulin prolonged by conjugating with silk protein nanoparticles. Silk fibroin was also bioconjugated with L-asparaginase to form crystalline nanoparticles with diameters of 50–120 nm [124]. These bioconjugates had an increased resistance to trypsin digestion, better stability in serum, storage stability in solution, and no leakage of the enzyme from the nanoparticles.

The reconstituted dragline silk proteins from the spider *Araneus diadematus* have been used to prepare microcapsules for drug delivery using self-assembly of the proteins at an emulsion interface [128]. These microcapsules were suggested to be useful to encapsulate small active ingredients, provided that the active ingredient does not impede the adsorption of the silk and/or that the encapsulation process does not alter the ingredient [128]. Microspheres of bioengineered spider silks, which were derived from ADF4 from *A. diadematus*, were formed by several methods such as dialysis and micromixing [129]. As a result of their material strength, biocompatibility, and the possibility of functionalization via recombinant protein techniques, spider silk microspheres may offer potential for the development of targeted drug delivery systems.

We recently developed a facile ethanol-based method for preparing silk nanoparticles, and then fabricated a biodegradable and biocompatible dual-drug release system based on silk nanoparticles and the molecular networks of silk hydrogels [130]. This is the first fully silk-based biocompatible and slowly biodegradable dual-drug delivery system. Model drugs incorporated in the silk nanoparticles and silk hydrogels showed fast and constant release, respectively, indicating successful dual-drug release from silk hydrogel containing silk nanoparticles. The present silk-based system containing silk nanoparticles for dual-drug release demonstrated no significant cytotoxicity against human mesenchymal stem cells (hMSCs), and thus this silk-based dual-drug release system has potential as a versatile and useful new platform of polymeric materials for various types of dual delivery of bioactive molecules.

25.5 Recombinant Silk-based Gene Delivery

Spider silk-based block copolymers have been designed via genetic engineering and used for drug/gene delivery systems. In particular, recombinant silk proteins containing transition peptides or ligand molecules have been designed for target-specific delivery, such as into tumor cells. The bioengineered silk proteins with additional functional features are classified as a new family of highly tailored gene delivery systems. The nanoparticles composed of DNA and recombinant silks, which contained cell-penetrating peptide, tumor-homing peptide, Arg-Gly-Asp (RGD) motifs, and/or cationic sequences, were recently reported and are summarized here [18, 131–135].

The authors designed silk-based block copolymers by combining spider silk consensus repeats with poly(L-lysine) for gene delivery [135]. Poly(L-lysine) is a polycation that interacts with genes through electrostatic interactions to assemble into ionic complexes, is hydrolyzed inside cells, and has been considered as an alternative to recombinant viruses for the delivery of genes into cells. The silk-based block copolymers formed ion complexes with pDNA, and sizes were controllable based on the polymer/DNA ratio or molecular weight of poly(L-lysine) bioengineered into the designs [135]. The pDNA complexes of silk-based block copolymers with less than 30 lysines showed no cytotoxicity toward human embryonic kidney (HEK) cells. This demonstrated the feasibility of bioengineering highly designed silk-based pDNA complexes for gene delivery systems; however, the transfection efficiency was too low to be useful for gene vectors.

By combining CPPs with the silk and lysine sequences, the authors aimed to enhance the transfection efficiency of the silk-based gene delivery system. These biosynthesized recombinant silk proteins contained one of the CPPs, ppTG1 [54], and their pDNA complexes were used for *in vitro* gene transfection to HEK cells [132]. The pDNA complexes of silk-polylysine-ppTG1 dimer recombinant proteins prepared at an N/P 2 (the ratio of number of amines/phosphates from pDNA) showed the highest transfection efficiency into HEK cells, the level of which was

comparable to the transfection reagent Lipofectamine 2000. The assemblies showed a globular morphology with an average hydrodynamic diameter of 99 nm and almost no beta-sheet structure. Additionally, the silk-based pDNA complexes demonstrated excellent DNase resistance as well as efficient release of the pDNA by enzymes that degrade silk proteins. Comparisons with beta-sheet induced silk-based pDNA complexes indicated that the beta-sheet structure content of the silk sequence of the pDNA complexes controlled the enzymatic degradation rate and hence can be used to regulate the release profile of genes from the complexes. The bioengineered silk-based gene delivery vehicles containing cell membrane-destabilizing peptides were concluded to have potential for less toxic and controlled release gene delivery systems.

To add target specificity into the silk-based gene delivery systems, transfection of silk-based polymers that contained ligand molecules such as arginyl-glycyl-aspartic acid (RGD)(s) was expected via receptor-mediated endocytosis. The RGD sequence is known to selectively recognize and bind $\alpha_v\beta_3$ and $\alpha_v\beta_5$ integrins that are expressed on cell surfaces of endothelial cells, osteoclasts, macrophages, and platelets [136–139]. The integrins are considered to be a class of transmembrane glycoproteins that interact with the extracellular matrix and are exploited for cell binding and entry by receptor-mediated endocytosis, a representative pathway for gene delivery [139]. RGD sequences are therefore a useful candidate as a ligand for gene vectors. The silk-based block copolymers containing both poly(L-lysine) domains to interact with pDNA and RGD to enhance cell binding and transfection efficiency were reported as a new gene delivery system via endocytosis [131]. Ionic complexes of these silk-polylysine-RGD block copolymers with pDNA were prepared, characterized, and utilized for gene delivery to HeLa cells and HEK cells. Sizes and surface charges of the pDNA complexes were regulated by the polymer/nucleotide molar ratio. Samples with 30 lysine residues and 11 RGD sequences, prepared at N/P of 2, had an average solution diameter of 186 nm and showed the highest transfection efficiency. The results demonstrated that a few RGDs were not enough to be recognized by integrin receptors at the cell surface membrane. The position of the RGD motif, at the N- or C-terminus of the recombinant silks, did not influence the transfection efficiency of the pDNA complexes.

Tumor vasculature, which is important in cardiovascular diseases and cancer, is a target for anti-cancer therapy. However, most drug/gene carriers are relatively poor at target-specific delivery. Selective targeting to tumor cells has been reported using several tumor-homing peptides. Peptides include antibodies that recognize tumor-specific vascular signatures, identified by *in vivo* screening of phage libraries, revealed extensive heterogeneity in tumor blood vessels and lymphatics [140]. We also demonstrated that pDNA complexes of recombinant silk proteins containing poly(L-lysine) and tumor-homing peptides (THPs), which are globular and approximately 150–250 nm in diameter, showed significant enhancement of target specificity to tumor cells by additions of F3 [141, 142] and CGKRK [143]. Novel silk-based ionic complexes containing pDNA able to home specifically to tumor cells were also reported with particular focus on how the THP, F3

(KDEPQRRSARLSAKPAPPKPEPKPKKAPAKK) [141, 142] and CGKRK [143], enhanced transfection specificity to tumor cells. Silk proteins containing both poly(L-lysine) domains to interact with pDNA and the THP to bind to specific tumor cells for target-specific pDNA delivery were examined for *in vitro* and *in vivo* transfection experiments into MDA-MB-435 melanoma cells and the highly metastatic human breast tumor MDA-MB-231 cells. Nanoscale complexes of recombinant silk molecules containing THPs with DNA were also designed as less cytotoxic and highly target-specific gene carriers [133]. Recombinant silk proteins (MaSp1 monomer) containing poly(L-lysine) domains and the THP for target-specific pDNA delivery were investigated for *in vitro* transfection experiments into the same cells as above. The silk–poly(L-lysine) block copolymer containing F3 was the most useful candidate for target delivery into tumorigenic cells with respect to less cytotoxicity to healthy cells and transfection efficiency to tumorigenic cells. The target specificity of the pDNA complexes to tumorigenic cells seemed to be regulated by specific adsorption processes on the cell surface, based on field emission scanning electron microscopy observations. These results demonstrated that combinations of the bioengineered silk delivery systems and THP can serve as a versatile and useful new platform for non-viral gene delivery.

25.6 Future Perspectives

Comprehensive studies on peptides, silk proteins, and their utility as transport vectors for various types of bioactive cargo have made available large amounts of useful information to improve our understanding of such systems. The ability to incorporate genes or drugs into functionalized peptide- or silk-based carriers has informed the fields of medicine, pharmacology, and cell biotechnology. Continuous investigations into this rapidly developing area of research have opened up new avenues for the application of these carriers. Some vital issues that need to be addressed before these systems can be used clinically remain, such as poor delivery, low bioavailability, and lack of specific targeting.

Due to their favorable properties, CPPs have tremendous potential as tools for gene and protein transfer into various cell types. Further characterization of peptide size, sequence, and structure is imperative to understand features that influence CPP function and to allow rational engineering of CPPs. The secondary structure of peptides, in particular, is most critical in influencing membrane interaction and hence efficiency of CPP uptake into cells. Customization of peptide carriers for each type of cargo is necessary to circumvent bioavailability problems. In addition, stability of peptide–cargo conjugates in solution and in the cell requires further studies and optimization. The complex needs include to be sufficiently stable to prevent dissociation before arriving at the target intracellular compartment and, conversely, be able to dissociate when the cargo needs to be released. Ultimately, the discovery of new CPPs will provide a wider array of properties for selection and aid elucidation of the mechanism governing their entry

into cells. One of the greater merits of using CPPs for drug/gene delivery compared to lipid- or polymer-based vectors is due to the absence of cytotoxicity at their required concentrations. Thus far, there has been no known report of long-term *in vivo* cytotoxicity evaluation for peptides currently being used as shuttle systems. New strategies for the design and synthesis of peptide-based carriers need to be developed to make these systems simple and reproducible on an industrial scale as well as economically feasible for commercialization in the future. Despite the growing number of therapeutic strategies that involve targeting therapeutics to specific organelles in the cell, some novel intracellular targets have received less attention. One such example and a promising target for therapeutic endeavors is the endoplasmic reticulum, which has been associated with Alzheimer's disease and cystic fibrosis due to its involvement in signaling pathways regulating cell growth and differentiation.

The remarkable mechanical properties, processability in an aqueous environment, biocompatibility, and controlled degradation suggest that silks (both native as well as recombinant) are attractive biomaterials for controlled and sustained release, stabilization, and delivery of bioactive molecules. Silk solutions can be morphed into a variety of biomaterial formats, and the degradation rate of these materials can be controlled during processing. In addition to these useful properties, silk proteins derived from recombinant DNA technology are amenable to bioengineering efforts to greatly expand the suite of options for targeted delivery. Targeted delivery function is a significant factor in drug delivery; hence, these silk proteins can be prepared with functional sequences to home to specific cells, tissues, or organs. The ability of silk to self-assemble, combined with all the other inherent features of silk proteins, makes them a unique and versatile delivery platform for small molecules, large proteins, DNA, and RNA. Hybrid or composite silk-based materials containing other biopolymers have not been extensively studied, and they should provide applicable mechanical, thermal, and biological properties for not only drug/gene delivery but also tissue engineering, medical imaging, and regenerative medicine.

References

1. Chakrabarti R, Wylie DE, Schuster SM (1989) Transfer of monoclonal antibodies into mammalian cells by electroporation. *J Biol Chem* 264:15494–15500
2. Arnheiter H, Haller O (1988) Antiviral state against influenza virus neutralized by microinjection of antibodies to interferon-induced Mx proteins. *EMBO J* 7:1315–1320
3. Glover DJ, Lipps HJ, Jans DA (2005) Towards safe, non-viral therapeutic gene expression in humans. *Nat Rev Genet* 6:299–310. doi:[10.1038/nrg1577](https://doi.org/10.1038/nrg1577)
4. Schwartz JJ, Zhang S (2000) Peptide-mediated cellular delivery. *Curr Opin Mol Ther* 2:162–167
5. Varga CM, Wickham TJ, Lauffenburger DA (2000) Receptor-mediated targeting of gene delivery vectors: insights from molecular mechanisms for improved vehicle design. *Biotechnol Bioeng* 70:593–605. doi:[10.1002/1097-0290\(20001220\)70:6](https://doi.org/10.1002/1097-0290(20001220)70:6)

6. Wadhwa MS, Collard WT, Adami RC, McKenzie DL, Rice KG (1997) Peptide-mediated gene delivery: influence of peptide structure on gene expression. *Bioconjug Chem* 8:81–88. doi:[10.1021/bc960079q](https://doi.org/10.1021/bc960079q)
7. Adami RC, Rice KG (1999) Metabolic stability of glutaraldehyde cross-linked peptide DNA condensates. *J Pharm Sci* 88:739–746. doi:[10.1021/js990042p](https://doi.org/10.1021/js990042p)
8. Deshayes S, Morris MC, Divita G, Heitz F (2005) Cell-penetrating peptides: tools for intracellular delivery of therapeutics. *Cell Mol Life Sci* 62:1839–1849. doi:[10.1007/s00018-005-5109-0](https://doi.org/10.1007/s00018-005-5109-0)
9. Gupta B, Levchenko TS, Torchilin VP (2005) Intracellular delivery of large molecules and small particles by cell-penetrating proteins and peptides. *Adv Drug Deliv Rev* 57:637–651. doi:[10.1016/j.addr.2004.10.007](https://doi.org/10.1016/j.addr.2004.10.007)
10. Kalderon D, Richardson WD, Markham AF, Smith AE (1984) Sequence requirements for nuclear location of simian virus 40 large-T antigen. *Nature* 311:33–38. doi:[10.1038/311033a0](https://doi.org/10.1038/311033a0)
11. LeBowitz JH, Grubb JH, Maga JA, Schmiel DH, Vogler C, Sly WS (2004) Glycosylation-independent targeting enhances enzyme delivery to lysosomes and decreases storage in mucopolysaccharidosis type VII mice. *Proc Natl Acad Sci USA* 101:3083–3088. doi:[10.1073/pnas.0308728100](https://doi.org/10.1073/pnas.0308728100)
12. Zhao K, Zhao G-M, Wu D, Soong Y, Birk AV, Schiller PW, Szeto HH (2004) Cell-permeable peptide antioxidants targeted to inner mitochondrial membrane inhibit mitochondrial swelling, oxidative cell death, and reperfusion injury. *J Biol Chem* 279:34682–34690. doi:[10.1074/jbc.M402999200](https://doi.org/10.1074/jbc.M402999200)
13. Schwarze SR, Ho A, Vocero-Akbani A, Dowdy SF (1999) In vivo protein transduction: delivery of a biologically active protein into the mouse. *Science* 285:1569–1572. doi:[10.1126/science.285.5433.1569](https://doi.org/10.1126/science.285.5433.1569)
14. Fischer R, Fotin-Mleczek M, Hufnagel H, Brock R (2005) Break on through to the other side—biophysics and cell biology shed light on cell-penetrating peptides. *ChemBioChem* 6:2126–2142. doi:[10.1002/cbic.200500044](https://doi.org/10.1002/cbic.200500044)
15. Morris MC, Deshayes S, Heitz F, Divita G (2008) Cell-penetrating peptides: from molecular mechanisms to therapeutics. *Biol Cell* 100:201–217. doi:[10.1042/bc20070116](https://doi.org/10.1042/bc20070116)
16. Zorko M, Langel Ü (2005) Cell-penetrating peptides: mechanism and kinetics of cargo delivery. *Adv Drug Deliv Rev* 57:529–545. doi:[10.1016/j.addr.2004.10.010](https://doi.org/10.1016/j.addr.2004.10.010)
17. Elzoghby AO, Samy WM, Elgindy NA (2012) Protein-based nanocarriers as promising drug and gene delivery systems. *J Controlled Release* 161:38–49. doi:[10.1016/j.jconrel.2012.04.036](https://doi.org/10.1016/j.jconrel.2012.04.036)
18. Numata K, Kaplan DL (2010) Silk-based delivery systems of bioactive molecules. *Adv Drug Deliv Rev* 62:1497–1508. doi:[10.1016/j.addr.2010.03.009](https://doi.org/10.1016/j.addr.2010.03.009)
19. Vivès E, Brodin P, Lebleu B (1997) A truncated HIV-1 Tat protein basic domain rapidly translocates through the plasma membrane and accumulates in the cell nucleus. *J Biol Chem* 272:16010–16017. doi:[10.1074/jbc.272.25.16010](https://doi.org/10.1074/jbc.272.25.16010)
20. Pooga M, Hällbrink M, Zorko M, Langel Ü (1998) Cell penetration by transportan. *FASEB J* 12:67–77
21. Rothbard JB, Garlington S, Lin Q, Kirschberg T, Kreider E, McGrane PL, Wender PA, Khavari PA (2000) Conjugation of arginine oligomers to cyclosporin facilitates topical delivery and inhibition of inflammation. *Nat Med* 6:1253–1257. doi:[10.1038/81359](https://doi.org/10.1038/81359)
22. Green M, Loewenstein PM (1988) Autonomous functional domains of chemically synthesized human immunodeficiency virus Tat trans-activator protein. *Cell* 55:1179–1188. doi:[10.1016/0092-8674\(88\)90262-0](https://doi.org/10.1016/0092-8674(88)90262-0)
23. Frankel AD, Pabo CO (1988) Cellular uptake of the Tat protein from human immunodeficiency virus. *Cell* 55:1189–1193. doi:[10.1016/0092-8674\(88\)90263-2](https://doi.org/10.1016/0092-8674(88)90263-2)
24. Mishra A, Lai GH, Schmidt NW, Sun VZ, Rodriguez AR, Tong R, Tang L, Cheng J, Deming TJ, Kamei DT, Wong GCL (2011) Translocation of HIV TAT peptide and analogues induced by multiplexed membrane and cytoskeletal interactions. *Proc Natl Acad Sci USA* 108:16883–16888. doi:[10.1073/pnas.1108795108](https://doi.org/10.1073/pnas.1108795108)

25. Akhtar S, Juliano RL (1992) Cellular uptake and intracellular fate of antisense oligonucleotides. *Trends Cell Biol* 2:139–144. doi:[10.1016/0962-8924\(92\)90100-2](https://doi.org/10.1016/0962-8924(92)90100-2)
26. Bloomfield VA (1996) DNA condensation. *Curr Opin Struct Biol* 6:334–341. doi:[10.1016/S0959-440X\(96\)80052-2](https://doi.org/10.1016/S0959-440X(96)80052-2)
27. Adami RC, Collard WT, Gupta SA, Kwok KY, Bonadio J, Rice KG (1998) Stability of peptide-condensed plasmid DNA formulations. *J Pharm Sci* 87:678–683. doi:[10.1021/js9800477](https://doi.org/10.1021/js9800477)
28. Abes S, Moulton HM, Clair P, Prevot P, Youngblood DS, Wu RP, Iversen PL, Lebleu B (2006) Vectorization of morpholino oligomers by the (R-Ahx-R)₄ peptide allows efficient splicing correction in the absence of endosomolytic agents. *J Controlled Release* 116:304–313. doi:[10.1016/j.jconrel.2006.09.011](https://doi.org/10.1016/j.jconrel.2006.09.011)
29. Abes S, Turner JJ, Ivanova GD, Owen D, Williams D, Arzumanov A, Clair P, Gait MJ, Lebleu B (2007) Efficient splicing correction by PNA conjugation to an R6-Penetratin delivery peptide. *Nucleic Acids Res* 35:4495–4502. doi:[10.1093/nar/gkm418](https://doi.org/10.1093/nar/gkm418)
30. Lundberg P, El-Andaloussi S, Sütülü T, Johansson H, Langel Ü (2007) Delivery of short interfering RNA using endosomolytic cell-penetrating peptides. *FASEB J* 21:2664–2671. doi:[10.1096/fj.06-6502com](https://doi.org/10.1096/fj.06-6502com)
31. Vivès E, Schmidt J, Pèlerin A (2008) Cell-penetrating and cell-targeting peptides in drug delivery. *Biochim Biophys Acta Rev Cancer* 1786:126–138. doi:[10.1016/j.bbcan.2008.03.001](https://doi.org/10.1016/j.bbcan.2008.03.001)
32. Crombez L, Divita G (2007) A non-covalent peptide-based strategy for siRNA delivery. *Biochem Soc Trans* 683:349–360. doi:[10.1007/978-1-60761-919-2_25](https://doi.org/10.1007/978-1-60761-919-2_25)
33. Detzer A, Overhoff M, Wünsche W, Rompf M, Turner JJ, Ivanova GD, Gait MJ, Sczakiel G (2009) Increased RNAi is related to intracellular release of siRNA via a covalently attached signal peptide. *RNA* 15:627–636. doi:[10.1261/rna.1305209](https://doi.org/10.1261/rna.1305209)
34. McManus MT, Sharp PA (2002) Gene silencing in mammals by small interfering RNAs. *Nat Rev Genet* 3:737–747. doi:[10.1038/nrg908](https://doi.org/10.1038/nrg908)
35. Meade BR, Dowdy SF (2007) Exogenous siRNA delivery using peptide transduction domains/cell penetrating peptides. *Adv Drug Deliv Rev* 59:134–140. doi:[10.1016/j.addr.2007.03.004](https://doi.org/10.1016/j.addr.2007.03.004)
36. Meade BR, Dowdy SF (2008) Enhancing the cellular uptake of siRNA duplexes following noncovalent packaging with protein transduction domain peptides. *Adv Drug Deliv Rev* 60:530–536. doi:[10.1016/j.addr.2007.10.004](https://doi.org/10.1016/j.addr.2007.10.004)
37. Andaloussi S, Lehto T, Mäger I, Rosenthal-Aizman K, Oprea I, Simonson O, Sork H, Ezzat K, Copolovici D, Kurrikoff K, Viola J, Zaghoul E, Sillard R, Johansson H, Said Hassane F, Guterstam P, Suhorutšenko J, Moreno P, Oskolkov N, Hälldin J, Tedebark U, Metspalu A, Lebleu B, Lehtiö J, Smith C, Langel U (2011) Design of a peptide-based vector, PepFect6, for efficient delivery of siRNA in cell culture and systemically in vivo. *Nucleic Acids Res* 39:3972–3987. doi:[10.1093/nar/gkq1299](https://doi.org/10.1093/nar/gkq1299)
38. Sioud M, Mobergslien A (2012) Efficient siRNA targeted delivery into cancer cells by gastrin-releasing peptides. *Bioconjug Chem* 23:1040–1049. doi:[10.1021/bc300050j](https://doi.org/10.1021/bc300050j)
39. Fang B, Guo HY, Zhang M, Jiang L, Ren FZ (2013) The six amino acid antimicrobial peptide bLFCin6 penetrates cells and delivers siRNA. *FEBS J* 280:1007–1017. doi:[10.1111/febs.12093](https://doi.org/10.1111/febs.12093)
40. Crombez L, Aldrian-Herrada G, Konate K, Nguyen QN, McMaster GK, Brasseur R, Heitz F, Divita G (2008) A new potent secondary amphipathic cell-penetrating peptide for siRNA delivery into mammalian cells. *Mol Ther* 17:95–103. doi:[10.1038/mt.2008.215](https://doi.org/10.1038/mt.2008.215)
41. Chiu Y-L, Ali A, Chu C-Y, Cao H, Rana TM (2004) Visualizing a correlation between siRNA localization, cellular uptake, and RNAi in living cells. *Chem Biol* 11:1165–1175. doi:[10.1016/j.chembiol.2004.06.006](https://doi.org/10.1016/j.chembiol.2004.06.006)
42. Derossi D, Joliot AH, Chassaing G, Prochiantz A (1994) The third helix of the Antennapedia homeodomain translocates through biological membranes. *J Biol Chem* 269:10444–10450

43. Muratovska A, Eccles MR (2004) Conjugate for efficient delivery of short interfering RNA (siRNA) into mammalian cells. *FEBS Lett* 558:63–68. doi:[10.1016/S0014-5793\(03\)01505-9](https://doi.org/10.1016/S0014-5793(03)01505-9)
44. Veldhoen S, Laufer SD, Trampe A, Restle T (2006) Cellular delivery of small interfering RNA by a non-covalently attached cell-penetrating peptide: quantitative analysis of uptake and biological effect. *Nucleic Acids Res* 34:6561–6573. doi:[10.1093/nar/gkl941](https://doi.org/10.1093/nar/gkl941)
45. Kumar P, Wu H, McBride JL, Jung K-E, Hee Kim M, Davidson BL, Kyung Lee S, Shankar P, Manjunath N (2007) Transvascular delivery of small interfering RNA to the central nervous system. *Nature* 448:39–43. doi:[10.1038/nature05901](https://doi.org/10.1038/nature05901)
46. Nakamura Y, Kogure K, Futaki S, Harashima H (2007) Octaarginine-modified multifunctional envelope-type nano device for siRNA. *J Controlled Release* 119:360–367. doi:[10.1016/j.jconrel.2007.03.010](https://doi.org/10.1016/j.jconrel.2007.03.010)
47. Johnson LN, Cashman SM, Kumar-Singh R (2007) Cell-penetrating peptide for enhanced delivery of nucleic acids and drugs to ocular tissues including retina and cornea. *Mol Ther* 16:107–114. doi:[10.1038/sj.mt.6300324](https://doi.org/10.1038/sj.mt.6300324)
48. Liu Z, Li M, Cui D, Fei J (2005) Macro-branched cell-penetrating peptide design for gene delivery. *J Controlled Release* 102:699–710. doi:[10.1016/j.jconrel.2004.10.013](https://doi.org/10.1016/j.jconrel.2004.10.013)
49. Liu BR, Lin M-D, Chiang H-J, Lee H-J (2012) Arginine-rich cell-penetrating peptides deliver gene into living human cells. *Gene* 505:37–45. doi:[10.1016/j.gene.2012.05.053](https://doi.org/10.1016/j.gene.2012.05.053)
50. Kichler A, Mason AJ, Bechinger B (2006) Cationic amphipathic histidine-rich peptides for gene delivery. *Biochim Biophys Acta Biomembr* 1758:301–307. doi:[10.1016/j.bbmem.2006.02.005](https://doi.org/10.1016/j.bbmem.2006.02.005)
51. Li W, Nicol F, Szoka FC Jr (2004) GALA: a designed synthetic pH-responsive amphipathic peptide with applications in drug and gene delivery. *Adv Drug Deliv Rev* 56:967–985. doi:[10.1016/j.addr.2003.10.041](https://doi.org/10.1016/j.addr.2003.10.041)
52. Wyman TB, Nicol F, Zelphati O, Scaria PV, Plank C, Szoka FC (1997) Design, synthesis, and characterization of a cationic peptide that binds to nucleic acids and permeabilizes bilayers. *Biochemistry* 36:3008–3017. doi:[10.1021/bi9618474](https://doi.org/10.1021/bi9618474)
53. Gottschalk S, Sparrow JT, Hauer J, Mims MP, Leland FE, Woo SL, Smith LC (1996) A novel DNA-peptide complex for efficient gene transfer and expression in mammalian cells. *Gene Ther* 3:448–457
54. Rittner K, Benavente A, Bompard-Sorlet A, Heitz F, Divita G, Brasseur R, Jacobs E (2002) New basic membrane-destabilizing peptides for plasmid-based gene delivery in vitro and in vivo. *Mol Ther* 5:104–114. doi:[10.1006/mthe.2002.0523](https://doi.org/10.1006/mthe.2002.0523)
55. Rudolph C, Plank C, Lausier J, Schillinger U, Müller RH, Rosenacker J (2003) Oligomers of the arginine-rich motif of the HIV-1 TAT protein are capable of transferring plasmid DNA into cells. *J Biol Chem* 278:11411–11418. doi:[10.1074/jbc.M211891200](https://doi.org/10.1074/jbc.M211891200)
56. Lakshmanan M, Kodama Y, Yoshizumi T, Sudesh K, Numata K (2012) Rapid and efficient gene delivery into plant cells using designed peptide carriers. *Biomacromolecules* 14:10–16. doi:[10.1021/bm301275g](https://doi.org/10.1021/bm301275g)
57. Kawamura KS, Sung M, Bolewska-Pedyczak E, Gariépy J (2006) Probing the impact of valency on the routing of arginine-rich peptides into eukaryotic cells. *Biochemistry* 45:1116–1127. doi:[10.1021/bi051338e](https://doi.org/10.1021/bi051338e)
58. Turner JJ, Ivanova GD, Verbeure B, Williams D, Arzumanov AA, Abes S, Lebleu B, Gait MJ (2005) Cell-penetrating peptide conjugates of peptide nucleic acids (PNA) as inhibitors of HIV-1 Tat-dependent trans-activation in cells. *Nucleic Acids Res* 33:6837–6849. doi:[10.1093/nar/gki991](https://doi.org/10.1093/nar/gki991)
59. Resina S, Abes S, Turner JJ, Prevot P, Travo A, Clair P, Gait MJ, Thierry AR, Lebleu B (2007) Lipoplex and peptide-based strategies for the delivery of steric-block oligonucleotides. *Int J Pharm* 344:96–102. doi:[10.1016/j.ijpharm.2007.04.039](https://doi.org/10.1016/j.ijpharm.2007.04.039)
60. Fisher L, Soomets U, Cortés Toro V, Chilton L, Jiang Y, Langel U, Iverfeldt K (2004) Cellular delivery of a double-stranded oligonucleotide NFκB decoy by hybridization to complementary PNA linked to a cell-penetrating peptide. *Gene Ther* 11:1264–1272. doi:[10.1038/sj.gt.3302291](https://doi.org/10.1038/sj.gt.3302291)

61. El-Andaloussi S, Johansson H, Magnusdottir A, Järver P, Lundberg P, Langel U (2005) TP10, a delivery vector for decoy oligonucleotides targeting the Myc protein. *J Controlled Release* 110:189–201. doi:[10.1016/j.jconrel.2005.09.012](https://doi.org/10.1016/j.jconrel.2005.09.012)
62. Nakamura Y, Yamada Y, Kogure K, Harashima H, Futaki S (2006) Significant and prolonged antisense effect of a multifunctional envelope-type nano device encapsulating antisense oligodeoxynucleotide. *J Pharm Pharmacol* 58:431–437. doi:[10.1211/jpp.58.4.0002](https://doi.org/10.1211/jpp.58.4.0002)
63. Fletcher S, Honeyman K, Fall AM, Harding PL, Johnsen RD, Steinhaus JP, Moulton HM, Iversen PL, Wilton SD (2007) Morpholino oligomer-mediated exon skipping averts the onset of dystrophic pathology in the mdx mouse. *Mol Ther* 15:1587–1592. doi:[10.1038/sj.mt.6300245](https://doi.org/10.1038/sj.mt.6300245)
64. Gebiski BL, Mann CJ, Fletcher S, Wilton SD (2003) Morpholino antisense oligonucleotide induced dystrophin exon 23 skipping in mdx mouse muscle. *Hum Mol Genet* 12:1801–1811. doi:[10.1093/hmg/ddg196](https://doi.org/10.1093/hmg/ddg196)
65. Bais MV, Kumar S, Tiwari AK, Kataria RS, Nagaleekar VK, Shrivastava S, Chindera K (2008) Novel Rath peptide for intracellular delivery of protein and nucleic acids. *Biochem Biophys Res Commun* 370:27–32. doi:[10.1016/j.bbrc.2008.03.023](https://doi.org/10.1016/j.bbrc.2008.03.023)
66. Goun EA, Pillow TH, Jones LR, Rothbard JB, Wender PA (2006) Molecular transporters: synthesis of oligoguanidinium transporters and their application to drug delivery and real-time imaging. *ChemBioChem* 7:1497–1515. doi:[10.1002/cbic.200600171](https://doi.org/10.1002/cbic.200600171)
67. Kirschberg TA, VanDeusen CL, Rothbard JB, Yang M, Wender PA (2003) Arginine-based molecular transporters: the synthesis and chemical evaluation of releasable taxol-transporter conjugates. *Org Lett* 5:3459–3462. doi:[10.1021/ol035234c](https://doi.org/10.1021/ol035234c)
68. Dixon MJ, Bourré L, MacRobert AJ, Eggleston IM (2007) Novel prodrug approach to photodynamic therapy: Fmoc solid-phase synthesis of a cell permeable peptide incorporating 5-aminolaevulinic acid. *Bioorg Med Chem Lett* 17:4518–4522. doi:[10.1016/j.bmcl.2007.05.095](https://doi.org/10.1016/j.bmcl.2007.05.095)
69. Mazel M, Clair P, Rousselle C, Vidal P, Scherrmann J-M, Mathieu D, Temsamani J (2001) Doxorubicin-peptide conjugates overcome multidrug resistance. *Anticancer Drugs* 12:107–116. doi:[10.1097/00001813-200102000-00003](https://doi.org/10.1097/00001813-200102000-00003)
70. Liang JF, Yang VC (2005) Synthesis of doxorubicin-peptide conjugate with multidrug resistant tumor cell killing activity. *Bioorg Med Chem Lett* 15:5071–5075. doi:[10.1016/j.bmcl.2005.07.087](https://doi.org/10.1016/j.bmcl.2005.07.087)
71. Eriste E, Kurrikoff K, Suhorutšenko J, Oskolkov N, Copolovici DM, Jones S, Laakkonen P, Howl J, Langel U (2013) Peptide-based glioma-targeted drug delivery vector gHoPe2. *Bioconjugate Chem* 24:305–313. doi:[10.1021/bc300370w](https://doi.org/10.1021/bc300370w)
72. Elmquist A, Lindgren M, Bartfai T, Langel U (2001) VE-cadherin-derived cell-penetrating peptide, pVEC, with carrier functions. *Exp Cell Res* 269:237–244. doi:[10.1006/excr.2001.5316](https://doi.org/10.1006/excr.2001.5316)
73. Lindgren M, Rosenthal-Aizman K, Saar K, Eiríksdóttir E, Jiang Y, Sassian M, Östlund P, Hällbrink M, Langel U (2006) Overcoming methotrexate resistance in breast cancer tumour cells by the use of a new cell-penetrating peptide. *Biochem Pharmacol* 71:416–425. doi:[10.1016/j.bcp.2005.10.048](https://doi.org/10.1016/j.bcp.2005.10.048)
74. Tan M, Lan K-H, Yao J, Lu C-H, Sun M, Neal CL, Lu J, Yu D (2006) Selective inhibition of ErbB2-overexpressing breast cancer in vivo by a novel TAT-based ErbB2-targeting signal transducers and activators of transcription 3-blocking peptide. *Cancer Res* 66:3764–3772. doi:[10.1158/0008-5472.can-05-2747](https://doi.org/10.1158/0008-5472.can-05-2747)
75. Myrberg H, Zhang L, Mäe M, Langel U (2007) Design of a tumor-homing cell-penetrating peptide. *Bioconjugate Chem* 19:70–75. doi:[10.1021/bc0701139](https://doi.org/10.1021/bc0701139)
76. Anderson DC, Nichols E, Manger R, Woodle D, Barry M, Fritzberg AR (1993) Tumor cell retention of antibody Fab fragments is enhanced by an attached HIV TAT protein-derived peptide. *Biochem Biophys Res Commun* 194:876–884. doi:[10.1006/bbrc.1993.1903](https://doi.org/10.1006/bbrc.1993.1903)
77. Cornelissen B, Hu M, McLarty K, Costantini D, Reilly RM (2007) Cellular penetration and nuclear importation properties of ¹¹¹In-labeled and ¹²³I-labeled HIV-1 tat peptide

- immunoconjugates in BT-474 human breast cancer cells. *Nucl Med Biol* 34:37–46. doi:[10.1016/j.nucmedbio.2006.10.008](https://doi.org/10.1016/j.nucmedbio.2006.10.008)
78. Hu M, Wang J, Chen P, Reilly RM (2006) HIV-1 Tat peptide immunoconjugates differentially sensitize breast cancer cells to selected antiproliferative agents that induce the cyclin-dependent kinase inhibitor p21WAF-1/CIP-1. *Bioconjug Chem* 17:1280–1287. doi:[10.1021/bc060053r](https://doi.org/10.1021/bc060053r)
79. Škrlić N, Drevenšek G, Hudoklin S, Romih R, Čurin Šerbec V, Dolinar M (2013) Recombinant single-chain antibody with the Trojan peptide penetratin positioned in the linker region enables cargo transfer across the blood-brain barrier. *Appl Biochem Biotechnol* 169:159–169. doi:[10.1007/s12010-012-9962-7](https://doi.org/10.1007/s12010-012-9962-7)
80. Xun Y, Pan Q, Tang Z, Chen X, Yu Y, Xi M, Zang G (2013) Intracellular-delivery of a single-chain antibody against hepatitis B core protein via cell-penetrating peptide inhibits hepatitis B virus replication in vitro. *Int J Mol Med* 31:369–376. doi:[10.3892/ijmm.2012.1210](https://doi.org/10.3892/ijmm.2012.1210)
81. Morishita M, Kamei N, Ehara J, Isowa K, Takayama K (2007) A novel approach using functional peptides for efficient intestinal absorption of insulin. *J Controlled Release* 118:177–184. doi:[10.1016/j.jconrel.2006.12.022](https://doi.org/10.1016/j.jconrel.2006.12.022)
82. Wang H, Chen X, Chen Y, Sun L, Li G, Zhai M, Zhai W, Kang Q, Gao Y, Qi Y (2013) Antitumor activity of novel chimeric peptides derived from cyclinD/CDK4 and the protein transduction domain 4. *Amino Acids* 44:499–510. doi:[10.1007/s00726-012-1360-5](https://doi.org/10.1007/s00726-012-1360-5)
83. McCusker CT, Wang Y, Shan J, Kinyanjui MW, Villeneuve A, Michael H, Fixman ED (2007) Inhibition of experimental allergic airways disease by local application of a cell-penetrating dominant-negative STAT-6 peptide. *J Immunol* 179:2556–2564
84. Hotchkiss RS, McConnell KW, Bullock K, Davis CG, Chang KC, Schwulst SJ, Dunne JC, Dietz GPH, Bähr M, McDunn JE, Karl IE, Wagner TH, Cobb JP, Coopersmith CM, Piwnicka-Worms D (2006) TAT-BH4 and TAT-Bcl-xL peptides protect against sepsis-induced lymphocyte apoptosis in vivo. *J Immunol* 176:5471–5477
85. Orzáez M, Mondragón L, Marzo I, Sanclimens G, Messeguer À, Pérez-Payá E, Vicent MJ (2007) Conjugation of a novel Apaf-1 inhibitor to peptide-based cell-membrane transporters: effective methods to improve inhibition of mitochondria-mediated apoptosis. *Peptides* 28:958–968. doi:[10.1016/j.peptides.2007.02.014](https://doi.org/10.1016/j.peptides.2007.02.014)
86. Bleifuss E, Kammertoens T, Hutloff A, Quarcoo D, Dorner M, Straub P, Uckert W, Hildt E (2006) The translocation motif of hepatitis B virus improves protein vaccination. *Cell Mol Life Sci* 63:627–635. doi:[10.1007/s00018-005-5548-7](https://doi.org/10.1007/s00018-005-5548-7)
87. Gros E, Deshayes S, Morris MC, Aldrian-Herrada G, Depollier J, Heitz F, Divita G (2006) A non-covalent peptide-based strategy for protein and peptide nucleic acid transduction. *Biochim Biophys Acta Biomembr* 1758:384–393. doi:[10.1016/j.bbamem.2006.02.006](https://doi.org/10.1016/j.bbamem.2006.02.006)
88. Heijne G (1990) The signal peptide. *J Membr Biol* 115:195–201. doi:[10.1007/bf01868635](https://doi.org/10.1007/bf01868635)
89. Cartier R, Reszka R (2002) Utilization of synthetic peptides containing nuclear localization signals for nonviral gene transfer systems. *Gene Ther* 9:157–167. doi:[10.1038/sj.gt.3301635](https://doi.org/10.1038/sj.gt.3301635)
90. Nigg EA (1997) Nucleocytoplasmic transport: signals, mechanisms and regulation. *Nature* 386:779–787. doi:[10.1038/386779a0](https://doi.org/10.1038/386779a0)
91. Goldfarb DS, Gariépy J, Schoolnik G, Kornberg RD (1986) Synthetic peptides as nuclear localization signals. *Nature* 322:641–644. doi:[10.1038/322641a0](https://doi.org/10.1038/322641a0)
92. Escriou V, Carrière M, Scherman D, Wils P (2003) NLS bioconjugates for targeting therapeutic genes to the nucleus. *Adv Drug Deliv Rev* 55:295–306. doi:[10.1016/S0169-409X\(02\)00184-9](https://doi.org/10.1016/S0169-409X(02)00184-9)
93. Collas P, Husebye H, Aleström P (1996) The nuclear localization sequence of the SV40 T antigen promotes transgene uptake and expression in zebrafish embryo nuclei. *Transgenic Res* 5:451–458. doi:[10.1007/bf01980210](https://doi.org/10.1007/bf01980210)
94. Subramanian A, Ranganathan P, Diamond SL (1999) Nuclear targeting peptide scaffolds for lipofection of nondividing mammalian cells. *Nat Biotech* 17:873–877. doi:[10.1038/12860](https://doi.org/10.1038/12860)

95. Pan L, He Q, Liu J, Chen Y, Ma M, Zhang L, Shi J (2012) Nuclear-targeted drug delivery of TAT peptide-conjugated monodisperse mesoporous silica nanoparticles. *J Am Chem Soc* 134:5722–5725. doi:[10.1021/ja211035w](https://doi.org/10.1021/ja211035w)
96. Yu J, Xie X, Zheng M, Yu L, Zhang L, Zhao J, Jiang D, Che X (2012) Fabrication and characterization of nuclear localization signal-conjugated glycol chitosan micelles for improving the nuclear delivery of doxorubicin. *Int J Nanomed* 7:5079–5090. doi:[10.2147/ijn.s36150](https://doi.org/10.2147/ijn.s36150)
97. de Moura MB, dos Santos LS, Van Houten B (2010) Mitochondrial dysfunction in neurodegenerative diseases and cancer. *Environ Mol Mutagen* 51:391–405. doi:[10.1002/em.20575](https://doi.org/10.1002/em.20575)
98. Schapira AH, Mann VM, Cooper JM, Krige D, Jenner PJ, Marsden CD (1992) Mitochondrial function in Parkinson's disease. The royal kings and queens Parkinson's disease research group. *Ann Neurol* 32(Suppl):S116–S124. doi:[10.1002/ana.410320720](https://doi.org/10.1002/ana.410320720)
99. Hirai K, Aliev G, Nunomura A, Fujioka H, Russell RL, Atwood CS, Johnson AB, Kress Y, Vinters HV, Tabaton M, Shimohama S, Cash AD, Siedlak SL, Harris PLR, Jones PK, Petersen RB, Perry G, Smith MA (2001) Mitochondrial abnormalities in Alzheimer's disease. *J Neurosci* 21:3017–3023
100. Green K, Brand MD, Murphy MP (2004) Prevention of mitochondrial oxidative damage as a therapeutic strategy in diabetes. *Diabetes* 53:S110–S118. doi:[10.2337/diabetes.53.2007.S110](https://doi.org/10.2337/diabetes.53.2007.S110)
101. Di Lisa F, Kaludercic N, Carpi A, Menabo R, Giorgio M (2009) Mitochondria and vascular pathology. *Pharmacol Rep* 61:123–130
102. Horton KL, Stewart KM, Fonseca SB, Guo Q, Kelley SO (2008) Mitochondria-penetrating peptides. *Chem Biol* 15:375–382. doi:[10.1016/j.chembiol.2008.03.015](https://doi.org/10.1016/j.chembiol.2008.03.015)
103. Gaizo VD, MacKenzie JA, Payne RM (2003) Targeting proteins to mitochondria using TAT. *Mol Genet Metab* 80:170–180. doi:[10.1016/j.ymgme.2003.08.017](https://doi.org/10.1016/j.ymgme.2003.08.017)
104. Bolender N, Sickmann A, Wagner R, Meisinger C, Pfanner N (2008) Multiple pathways for sorting mitochondrial precursor proteins. *EMBO Rep* 9:42–49. doi:[10.1038/sj.embor.7401126](https://doi.org/10.1038/sj.embor.7401126)
105. Fonseca SB, Pereira MP, Mourtada R, Gronda M, Horton KL, Hurren R, Minden MD, Schimmer AD, Kelley SO (2011) Rerouting chlorambucil to mitochondria combats drug deactivation and resistance in cancer cells. *Chem Biol* 18:445–453. doi:[10.1016/j.chembiol.2011.02.010](https://doi.org/10.1016/j.chembiol.2011.02.010)
106. Luque-Ortega J, van't Hof W, Veerman E, Saugar J, Rivas L (2008) Human antimicrobial peptide histatin 5 is a cell-penetrating peptide targeting mitochondrial ATP synthesis in Leishmania. *FASEB J* 22:1817–1828. doi:[10.1096/fj.07-096081](https://doi.org/10.1096/fj.07-096081)
107. Yu H, Koilkonda RD, Chou T-H, Porciatti V, Ozdemir SS, Chiodo V, Boye SL, Boye SE, Hauswirth WW, Lewin AS, Guy J (2012) Gene delivery to mitochondria by targeting modified adenoassociated virus suppresses Leber-hereditary optic neuropathy in a mouse model. *Proc Natl Acad Sci USA* 109:E1238–E1247. doi:[10.1073/pnas.1119577109](https://doi.org/10.1073/pnas.1119577109)
108. Yu H, Ozdemir SS, Koilkonda RD, Chou TH, Porciatti V, Chiodo V, Boye SL, Hauswirth WW, Lewin AS, Guy J (2012) Mutant NADH dehydrogenase subunit 4 gene delivery to mitochondria by targeting sequence-modified adeno-associated virus induces visual loss and optic atrophy in mice. *Mol vision* 18:1668–1683
109. Yang H, Cai H, Wan L, Liu S, Li S, Cheng J, Lu X (2013) Bombesin analogue-mediated delivery preferentially enhances the cytotoxicity of a mitochondria-disrupting peptide in tumor cells. *PLoS One* 8:e57358. doi:[10.1371/journal.pone.0057358](https://doi.org/10.1371/journal.pone.0057358)
110. Shin JY, Chung YS, Kang B, Jiang HL, Yu DY, Han K, Chae C, Moon JH, Jang G, Cho MH (2013) Co-delivery of LETM1 and CTMP synergistically inhibits tumor growth in H-ras12 V liver cancer model mice. *Cancer Gene Ther* 20:186–194. doi:[10.1038/cgt.2013.6](https://doi.org/10.1038/cgt.2013.6)
111. Grabowsky G, Desnick R (1981) Enzyme replacement in genetic diseases. In: Holcenberg J, Roberts J (eds) *Enzymes as drugs*. Wiley, New York
112. Maga JA, Zhou J, Kambampati R, Peng S, Wang X, Bohnsack RN, Thomm A, Golata S, Tom P, Dahms NM, Byrne BJ, LeBowitz JH (2013) Glycosylation-independent lysosomal

- targeting of acid α -glucosidase enhances muscle glycogen clearance in Pompe mice. *J Biol Chem* 288:1428–1438. doi:[10.1074/jbc.M112.438663](https://doi.org/10.1074/jbc.M112.438663)
113. Dekiwadia CD, Lawrie AC, Fecondo JV (2012) Peptide-mediated cell penetration and targeted delivery of gold nanoparticles into lysosomes. *J Pept Sci* 18:527–534. doi:[10.1002/psc.2430](https://doi.org/10.1002/psc.2430)
 114. Loh Y, Shi H, Hu M, Yao SQ (2010) “Click” synthesis of small molecule-peptide conjugates for organelle-specific delivery and inhibition of lysosomal cysteine proteases. *Chem Commun* 46:8407–8409. doi:[10.1039/c0cc03738a](https://doi.org/10.1039/c0cc03738a)
 115. Altman GH, Diaz F, Jakuba C, Calabro T, Horan RL, Chen J, Lu H, Richmond J, Kaplan DL (2003) Silk-based biomaterials. *Biomaterials* 24:401–416. doi:[S0142961202003538](https://doi.org/S0142961202003538)
 116. Wang Y, Kim HJ, Vunjak-Novakovic G, Kaplan DL (2006) Stem cell-based tissue engineering with silk biomaterials. *Biomaterials* 27:6064–6082. doi:[10.1016/j.biomaterials.2006.07.008](https://doi.org/10.1016/j.biomaterials.2006.07.008)
 117. Numata K, Kaplan DL (2011) Differences in cytotoxicity of beta-sheet peptides originated from silk and amyloid beta. *Macromol Biosci* 11:60–64. doi:[10.1002/mabi.201000250](https://doi.org/10.1002/mabi.201000250)
 118. Numata K, Cebe P, Kaplan DL (2010) Mechanism of enzymatic degradation of beta-sheet crystals. *Biomaterials* 31:2926–2933. doi:[10.1016/J.Biomaterials.2009.12.026](https://doi.org/10.1016/J.Biomaterials.2009.12.026)
 119. Kundu J, Chung YI, Kim YH, Tae G, Kundu SC (2010) Silk fibroin nanoparticles for cellular uptake and control release. *Int J Pharm* 388:242–250. doi:[10.1016/j.ijpharm.2009.12.052](https://doi.org/10.1016/j.ijpharm.2009.12.052)
 120. Rajkhowa R, Gil ES, Kluge J, Numata K, Wang LJ, Wang XD, Kaplan DL (2010) Reinforcing silk scaffolds with silk particles. *Macromol Biosci* 10:599–611. doi:[10.1002/Mabi.200900358](https://doi.org/10.1002/Mabi.200900358)
 121. Anumolu R, Gustafson JA, Magda JJ, Cappello J, Ghandehari H, Pease LF (2011) Fabrication of highly uniform nanoparticles from recombinant silk-elastin-like protein polymers for therapeutic agent delivery. *ACS Nano* 5:5374–5382. doi:[10.1021/Nn103585f](https://doi.org/10.1021/Nn103585f)
 122. Mandal BB, Kundu SC (2009) Self-assembled silk sericin/poloxamer nanoparticles as nanocarriers of hydrophobic and hydrophilic drugs for targeted delivery. *Nanotechnology* 20:355101. doi:[10.1088/0957-4484/20/35/355101](https://doi.org/10.1088/0957-4484/20/35/355101)
 123. Zhang YQ, Shen WD, Xiang RL, Zhuge LJ, Gao WJ, Wang WB (2007) Formation of silk fibroin nanoparticles in water-miscible organic solvent and their characterization. *J Nanopart Res* 9:885–900. doi:[10.1007/S11051-006-9162-X](https://doi.org/10.1007/S11051-006-9162-X)
 124. Zhang YQ, Wang YJ, Wang HY, Zhu L, Zhou ZZ (2011) Highly efficient processing of silk fibroin nanoparticle-L-asparaginase bioconjugates and their characterization as a drug delivery system. *Soft Matter* 7:9728–9736. doi:[10.1039/C0sm01332c](https://doi.org/10.1039/C0sm01332c)
 125. Zhu L, Hu RP, Wang HY, Wang YJ, Zhang YQ (2011) Bioconjugation of neutral protease on silk fibroin nanoparticles and application in the controllable hydrolysis of sericin. *J Agric Food Chem* 59:10298–10302. doi:[10.1021/Jf202036v](https://doi.org/10.1021/Jf202036v)
 126. Gupta V, Aseh A, Rios CN, Aggarwal BB, Mathur AB (2009) Fabrication and characterization of silk fibroin-derived curcumin nanoparticles for cancer therapy. *Int J Nanomedicine* 4:115–122. doi:[10.2147/IJN.S5581](https://doi.org/10.2147/IJN.S5581)
 127. Yan HB, Zhang YQ, Ma YL, Zhou LX (2009) Biosynthesis of insulin-silk fibroin nanoparticles conjugates and in vitro evaluation of a drug delivery system. *J Nanopart Res* 11:1937–1946. doi:[10.1007/S11051-008-9549-Y](https://doi.org/10.1007/S11051-008-9549-Y)
 128. Hermanson KD, Huemmerich D, Scheibel T, Bausch AR (2007) Engineered microcapsules fabricated from reconstituted spider silk. *Adv Mater* 19:1810–1815. doi:[10.1002/Adma.200602709](https://doi.org/10.1002/Adma.200602709)
 129. Lammel A, Schwab M, Slotta U, Winter G, Scheibel T (2008) Processing conditions for the formation of spider silk microspheres. *Chemsuschem* 1:413–416. doi:[10.1002/Cssc.200800030](https://doi.org/10.1002/Cssc.200800030)
 130. Numata K, Yamazaki S, Naga N (2012) Biocompatible and biodegradable dual-drug release system based on silk hydrogel containing silk nanoparticles. *Biomacromolecules* 13:1383–1389. doi:[10.1021/bm300089a](https://doi.org/10.1021/bm300089a)

131. Numata K, Hamasaki J, Subramanian B, Kaplan DL (2010) Gene delivery mediated by recombinant silk proteins containing cationic and cell binding motifs. *J Controlled Release* 146:136–143. doi:[10.1016/J.Jconrel.2010.05.006](https://doi.org/10.1016/J.Jconrel.2010.05.006)
132. Numata K, Kaplan DL (2010) Silk-based gene carriers with cell membrane destabilizing peptides. *Biomacromolecules* 11:3189–3195. doi:[10.1021/Bm101055m](https://doi.org/10.1021/Bm101055m)
133. Numata K, Mieszawska-Czajkowska AJ, Kvenvold LA, Kaplan DL (2012) Silk-based nanocomplexes with tumor-homing peptides for tumor-specific gene delivery. *Macromol Biosci* 12:75–82. doi:[10.1002/mabi.201100274](https://doi.org/10.1002/mabi.201100274)
134. Numata K, Reagan MR, Goldstein RH, Rosenblatt M, Kaplan DL (2011) Spider silk-based gene carriers for tumor cell-specific delivery. *Bioconjug Chem* 22:1605–1610. doi:[10.1021/bc200170u](https://doi.org/10.1021/bc200170u)
135. Numata K, Subramanian B, Currie HA, Kaplan DL (2009) Bioengineered silk protein-based gene delivery systems. *Biomaterials* 30:5775–5784. doi:[10.1016/j.biomaterials.2009.06.028](https://doi.org/10.1016/j.biomaterials.2009.06.028)
136. Oba M, Fukushima S, Kanayama N, Aoyagi K, Nishiyama N, Koyama H, Kataoka K (2007) Cyclic RGD peptide-conjugated polyplex micelles as a targetable gene delivery system directed to cells possessing alphavbeta3 and alphavbeta5 integrins. *Bioconjug Chem* 18:1415–1423. doi:[10.1021/Bc0700133](https://doi.org/10.1021/Bc0700133)
137. Kim WJ, Yockman JW, Lee M, Jeong JH, Kim YH, Kim SW (2005) Soluble Flt-1 gene delivery using PEI-g-PEG-RGD conjugate for anti-angiogenesis. *J Controlled Release* 106:224–234. doi:[10.1016/J.Jconrel.2005.04.016](https://doi.org/10.1016/J.Jconrel.2005.04.016)
138. Connelly JT, Garcia AJ, Levenston ME (2007) Inhibition of in vitro chondrogenesis in RGD-modified three-dimensional alginate gels. *Biomaterials* 28:1071–1083. doi:[10.1016/J.Biomaterials.2006.10.006](https://doi.org/10.1016/J.Biomaterials.2006.10.006)
139. Renigunta A, Krasteva G, Konig P, Rose F, Klepetko W, Grimminger F, Seeger W, Hanze J (2006) DNA transfer into human lung cells is improved with Tat-RGD peptide by Caveolin-mediated endocytosis. *Bioconjug Chem* 17:327–334. doi:[10.1021/Bc050263o](https://doi.org/10.1021/Bc050263o)
140. Arap W, Pasqualini R, Ruoslahti E (1998) Cancer treatment by targeted drug delivery to tumor vasculature in a mouse model. *Science* 279:377–380. doi:[10.1126/Science.279.5349.377](https://doi.org/10.1126/Science.279.5349.377)
141. Christian S, Pilch J, Akerman ME, Porkka K, Laakkonen P, Ruoslahti E (2003) Nucleolin expressed at the cell surface is a marker of endothelial cells in angiogenic blood vessels. *J Cell Biol* 163:871–878. doi:[10.1083/Jcb.200304132](https://doi.org/10.1083/Jcb.200304132)
142. Porkka K, Laakkonen P, Hoffman JA, Bernasconi M, Ruoslahti E (2002) A fragment of the HMGN2 protein homes to the nuclei of tumor cells and tumor endothelial cells in vivo. *Proc Natl Acad Sci USA* 99:7444–7449. doi:[10.1073/Pnas.062189599](https://doi.org/10.1073/Pnas.062189599)
143. Hoffman JA, Giraudo E, Singh M, Zhang LL, Inoue M, Porkka K, Hanahan D, Ruoslahti E (2003) Progressive vascular changes in a transgenic mouse model of squamous cell carcinoma. *Cancer Cell* 4:383–391. doi:[10.1016/S1535-6108\(03\)00273-3](https://doi.org/10.1016/S1535-6108(03)00273-3)

Chapter 26

Activation Approaches on Delivery of Imaging and Therapeutic Agents

Mitulkumar A. Patel and Benedict Law

26.1 Introduction

For many years, chemotherapy has been used as the first-line treatment for cancer, yet it can have many adverse effects due to off-targeting activity. In the past, a number of prodrugs were synthesized to improve the therapeutic index [1, 2]. Some prodrugs such as capecitabine and cyclophosphamide were approved by the US Food and Drug Administration (FDA) for the treatment for various cancers [3–6]. With advances in nanomedicine, chemotherapeutic agents have been incorporated into nanometer-sized materials to serve as carriers to enhance tumoral delivery through passive and/or active targeting [7, 8]. However, the kinetics of drug release may affect the pharmacokinetics, biodistribution, therapeutic activity, and toxicity of these inherited carriers; consequently, they can influence the therapeutic outcome [9–11]. Thus, many of the carriers were designed to be activatable. That is, the intention of drug release is to be controlled by specific trigger [12–14]. Such activatable agents are typically composed of materials, such as lipids, peptide, inorganic salts, and polymers, which undergo changes in structure, hydrophobic–lipophilic balance, solubility, charge, and chemical bonding to promote drug release under the influence of internal or external triggers [15–19]. The ultimate goal is to allow a sufficient accumulation of the drug carrier at the target site that will provide a rapid drug release upon activation [20, 21]. The results were proved to improve efficacy [22, 23] and to decrease the side effects and the dose require [24, 25].

The internal triggers are dependent on the biochemical or physiological difference between the disease and the healthy states, such as a lower pH or a higher enzyme level at the tumor site [26–29]. This approach is self-regulatory, since the drugs are released in response to the detected difference [30–32]. External triggers

M. A. Patel · B. Law (✉)

Department of Pharmaceutical Sciences, College of Pharmacy, North Dakota State University, Department 2665, 6050 Fargo, ND 58108, USA
e-mail: Shek.law@ndsu.edu

are physical stimuli, such as higher temperature, light, and magnetic field, which are applied locally to the accessible target area to promote spatial (space/target site specific) and temporal (time dependent) control over the drug release from a predelivered nanomedicine [33, 34]. This chapter includes a discussion of the methods used to engineer activatable agents. Specific examples were chosen to illustrate not only their mechanism of common trigger to activate them, but also the effectiveness both in vitro and in vivo. Some of them have been used to develop contrast agents for functional imaging as well as for the reduction in the imaging background [35–37].

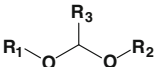
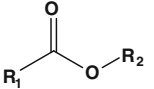
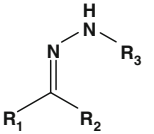
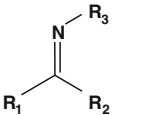
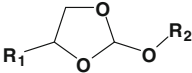
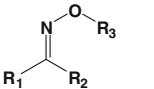
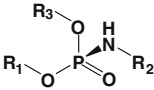
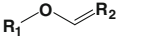
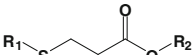
26.2 pH-Activatable Agents

In the context of cancer, the microenvironment of tumors can be slightly acidic (pH \sim 7.0) because a tumor normally has a higher metabolic rate than normal tissue [38–40]. As a result of the higher metabolic rate, specifically from glycolysis under aerobic or anaerobic conditions, the tumor produces substantial amounts of lactic acid and carbonic acid as the major sources of H^+ ions. In contrast, regardless of whether a cell is in a cancerous or a normal state, certain intracellular organelles, such as endosomes and lysosomes, are always acidic (pH \sim 5.0–6.0). Maintaining a low pH in these organelles is essential to the function of >50 acid hydrolase enzymes for breaking down various biological molecules [41]. Hence, a drug delivery system that can be activated by an acidic pH to release a payload will not only enhance the efficacy, but also reduce the incidence of side effect [42, 43]. In fact, the concept of a pH-activatable system can be traced back to the time when a prodrug, methenamine (or hexamine), was introduced by Schering in 1899. It was shown to decompose in acidic urine to formaldehyde for the treatment for urinary tract infection. Today, many pH-activatable delivery systems are designed differently, mostly are nanocarriers that can be dissolved, disassembled, or swelled in response to acidic pH to release the therapeutic payload. In addition to therapeutic agents, the similar designs have also been applied to the delivery of contrast agents for tumor imaging [44–47].

26.2.1 Acid-sensitive Linkers

One of the pH-activatable approaches is to covalently conjugate a therapeutic or an imaging agent to a carrier via acid-sensitive linkers, such as acetal, ester, hydrazone, imine, orthoester, oxime, phosphoramidate, vinyl ether, or β -thiopropionate (Table 26.1). Although these linkers are relatively stable in physiological pH, they can be hydrolyzed in an acidic environment. The choice of linkers is made based on the accessibility of functional groups that are available from the drug molecule and the carrier. Hydrazone is the most widely used linker, primarily because its

Table 26.1 Examples of pH-sensitive linkers used to develop prodrugs

Linkers	Chemical structures	Therapeutic agents	References
Acetal		Diethylstilboestrol	[63]
		Doxorubicin	[64]
Ester		Bortezomib	[65]
		Doxorubicin	[66]
Hydrazone		Cisplatin	[51]
		Doxorubicin	[49, 50, 52]
		Geldanamycin	[67]
Imine		Gemcitabine	[68]
		Chromone	[69]
Orthoester		Doxorubicin	[70]
		Paclitaxel	[71]
Oxime		Daunorubicin	[54, 55]
		Doxorubicin	[57]
		Oligonucleotide	[56]
Phosphoramidate		Oligonucleotide	[60]
Vinyl ether		Oligonucleotide	[72]
β -Thiopropionate		Oligonucleotide	[61, 62]

conjugation chemistry is mild and flexible. Various functional groups, including –COOH, –OH, or –CHO, from a carrier can be easily converted to hydrazide by using hydrazine. The hydrazide can then react with another carbonyl from a drug molecule, such as the ketone of doxorubicin, to form an acid-labile linkage [48–53] (Fig. 26.1a). Oxime has also been employed in many drug delivery systems [54–57], although studies have shown that it was more resistant to acid hydrolysis than hydrazone [58]. For oligonucleotides, phosphoramidate and β -thiopropionate are the better choices, given that they can be introduced to DNA or RNA via the phosphate group at the 5' position [59–62].

In some cases, acid-sensitive linkers are incorporated into the carriers. This strategy does not require the chemical modification of a drug or an imaging agent. For example, acid-sensitive micelles have been described in the literature. They were composed of polyethylene glycol (PEG) that was conjugated to stearic acids

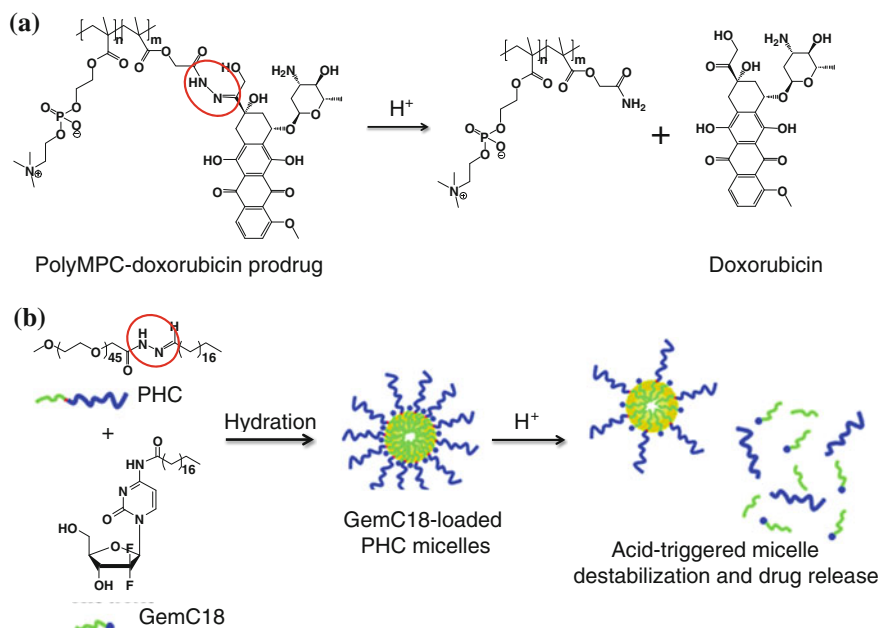


Fig. 26.1 Examples of pH-activatable agents which utilize hydrazone linker. **a** PolyMPC–DOX prodrugs that integrate pH-responsive hydrazone linkages into the poly(methacryloyloxyethyl phosphorylcholine) (polyMPC) structure. **b** Acid-sensitive micelles. The micelles were assembled by acid-sensitive copolymers, which were synthesized by conjugating the hydrophilic PEG segment to a hydrophobic stearic acid derivative with a hydrazone bond. Recreated with permission from ACS Publications [68]

(C18) via hydrazone linkages (Fig. 26.1b). These linkages were destabilized at a low pH and, subsequently, triggered the release of 4-(*N*-stearoyl-gemcitabine (GemC18), a deoxycytidine nucleoside analog of gemcitabine used for the treatment for many cancers [68]. In another study, hydrazone linkages were introduced between the PEG chains and the phospholipids of long-circulating liposomes. Following the cleavage of the hydrazone bonding at low pH, the PEG was removed, leading to multiple cell-penetrating peptides exposing on the liposome surfaces to promote the intracellular delivery of the encapsulated doxorubicin [73].

26.2.2 Demicellization of Micelles

Some materials used to construct the acid-sensitive micelles are intrinsically sensitive to pH changes [74, 75], whereas others are introduced with functional groups that are known to be neutral at physiological pH and ionizable in an acidic environment (Fig. 26.2a). Poly(β -amino ester) is commonly used to construct

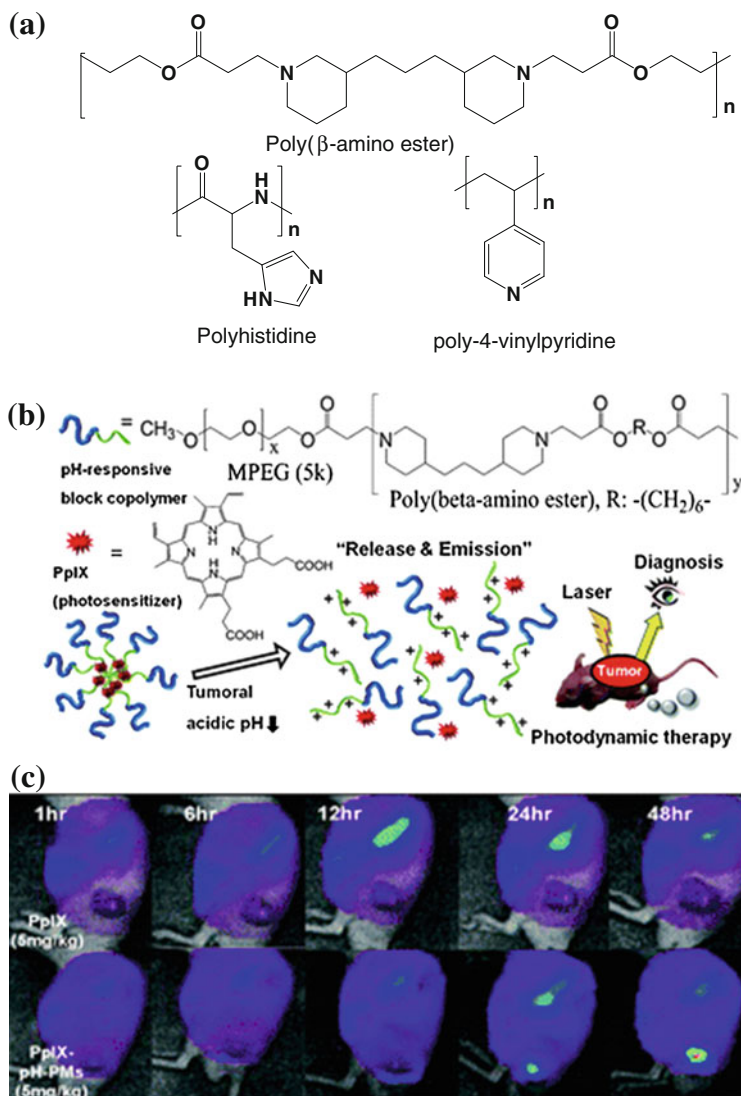


Fig. 26.2 **a** Examples of functional group that is neutral at a physiological pH, but ionizable in an acidic environment. **b** The design of the MPEG-poly(β -amino ester) micelles system. **c** Fluorescence images of SCC7 tumor-implanted mice injected with free PpIX (*top panel*) and PpIX encapsulated in the MPEG-poly(β -amino ester) micelles (PpIX-pH-PMs). Recreated with permission from RSC Publishing [79]

acid-sensitive micelles [76, 77]. The advantage of poly(β -amino ester) is that it responds abruptly to pH changes. Given that the tertiary amino groups in the hydrophobic amino ester can be protonated (with a pK_b of 6.5) in an acidic environment, the polymers can become hydrophilic. Subsequently, the micelles

lose stability (dissociate) and release the encapsulated drug contents rapidly. For example, camptothecin was encapsulated in the micelles assembled from PEG and poly(β -amino ester) copolymers. The resulting micelles can be activated inside the endosomes and the lysosomes to release the drug contents [78]. Protoporphyrin IX (PpIX) is a photosensitizer that has been loaded into the pH-responsive MPEG-poly(β -amino ester) polymeric micelles [79]. The resulting micelles could be delivered to the tumors by the EPR effect and, subsequently, destabilized to release the PpIX. Upon laser irradiation, the PpIX generated near-infrared (NIR) fluorescence for tumoral imaging and, simultaneously, singlet oxygen for photodynamic therapy (Fig. 26.2b and c). In another study, to synthesize an acid-sensitive magnetic resonance imaging (MRI) probe, iron oxide (Fe_3O_4) nanoparticles were encapsulated inside an acid-sensitive micelle composed of copolymers of PEG, poly(β -amino ester), and poly(amido amine). This MRI probe released the Fe_3O_4 nanoparticles at a lower pH to image the ischemic area of the brain [80]. Other acid-sensitive micelles were also created by introducing polyhistidine or poly-4-vinylpyridine to the polymeric constructs (Fig. 26.2a) [81, 82].

26.2.3 Decomposition or Desorption of Inorganic Materials

Certain inorganic materials, such as calcium phosphate (CaPO_4), are insoluble in physiological pH, but can be completely dissolved at $\text{pH} < 6.5$. Thus, pH-sensitive delivery systems have been designed either by encapsulating hydrophobic drug molecules inside the particles made up of inorganic materials [83] or by adsorbing the drugs onto the particle surfaces [84]. For instance, CaPO_4 has been used to form a deposit layer on a polymer micelle through the mineralization process [85]. Doxorubicin molecules were securely trapped inside the micelle in physiological pH and were readily released after rapid dissolution of the CaPO_4 layer (Fig. 26.3a). In another design, zinc oxide (ZnO) quantum dots were employed to seal the nanopores of mesoporous silica nanoparticles [86]. The dots were decomposed in an acidic environment, which caused the pores to open to promote the release of the drug contents (Fig. 26.3b).

Some therapeutic agents such as doxorubicin have potential metal-binding sites [87]. They can be adsorbed onto the surfaces of inorganic particles, including titanium dioxide (TiO_2), magnesium oxide (MnO), and ZnO via electrostatic and hydrophobic interactions [88–92]. Despite the fact that the exact drug release mechanism is not completely understood, it can be explained as the protonation of the chemisorbed doxorubicin molecules under an acidic condition and lead to a reduction in binding to particles. Some inorganic nanoparticles, such as MnO, have been described as T_1 MRI contrast agents [93]. When loaded with doxorubicin, these particles can also be theranostic agents [89, 90].

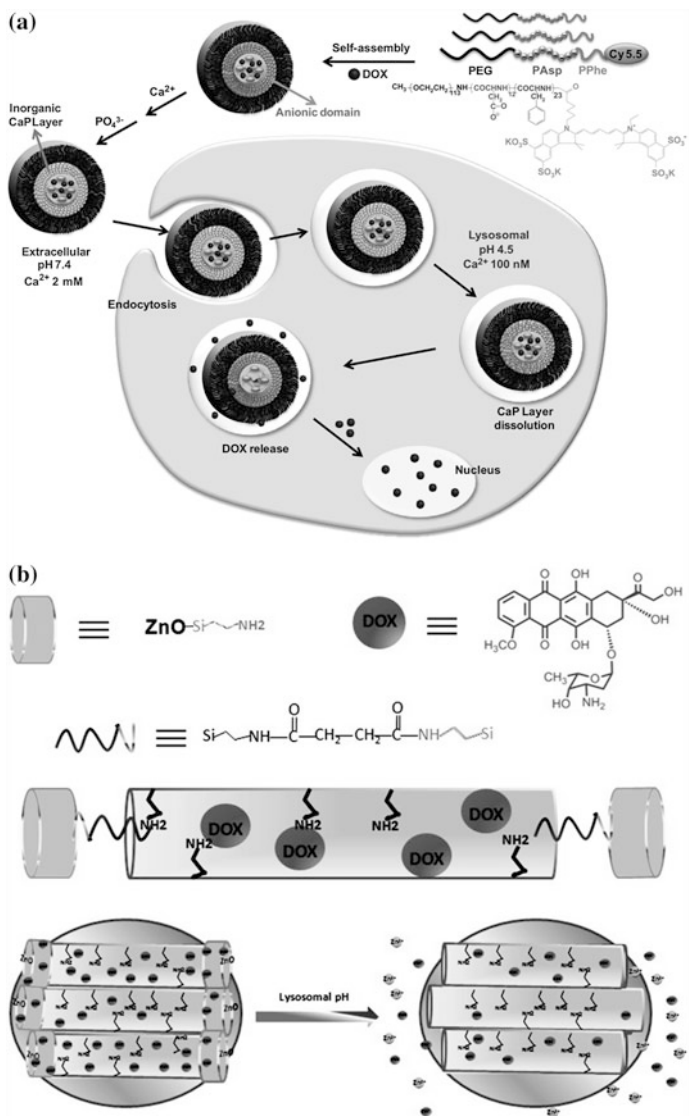


Fig. 26.3 Design of pH-sensitive agents using inorganic materials. **a** Calcium phosphate (CaP) was deposited onto micelles assembled from copolymers of polyethylene glycol, poly(L-aspartic acid), and poly(L-phenylalanine) through the mineralization process. The release of doxorubicin content was facilitated inside the cells at the endosomal pH because of the rapid dissolution of the CaP layer. Recreated with permission from Elsevier [85]. **b** ZnO quantum dots were used as a lid to seal the pores of mesoporous silica nanoparticles, which could be efficiently dissolved in the acidic intracellular compartments of cancer cells, resulting in the release of doxorubicin into the cytosol. Recreated with permission from ACS Publications [86]

26.2.4 Microgels

Acid-sensitive microgels are composed of polymeric materials that can undergo phase transition (swelling) in response to pH [94]. At low pH, the protonation of certain functional groups, such as amino groups, generates positive charges that cause swelling. As a result, the gel permeability increases and leads to the release of drug content. Chitosan is one of the most commonly used acid-sensitive polymers for preparing microgels because it is also biocompatible. A chitosan derivative, *N*-[(2-hydroxy-3-trimethylammonium)propyl]chitosan chloride, has been employed to prepare acid-sensitive microgels for the delivery of methotrexate into HeLa cells [95]. The polymer has also been copolymerized with a variety of polymers, such as PEG, poly(methacrylic acid), and poly(*N*-isopropylacrylamide) (PNIPAM), for the delivery of other chemotherapeutic agents including 5-fluorouracil, temozolomide, and oridonin [96–98].

26.3 Enzyme-Activatable Agents

Aberration of enzyme activity or protein concentration occurs in most diseases. In the past, therapeutic agents were developed with the goal of inhibiting the action of a particular enzyme or protein. Enzyme-sensitive motifs can be incorporated into different nanoparticles, which can be readily activated by the disease-associated enzyme to release a payload at the target site [99]. The advantage of this approach is that the target enzyme behaves similarly to a self-propelled machine, where one enzyme can potentially activate hundreds to thousands of delivery systems. Further, enzyme-activatable agents can also act as substrate inhibitors. Therefore, numerous enzyme-activatable agents have been proposed for the purpose of drug delivery, therapy, and imaging in recent years [100]. To ensure the success of an enzyme-activatable agent, it is essential to have a profound understanding of the mechanism of the target enzymes (Fig. 26.4) and the heterogeneity between the disease and normal states.

26.3.1 Protease

Protease belongs to a class of enzyme that has the ability to hydrolyze the amide bonding of a protein or peptide (Fig. 26.4). In 2012, there were 581 human proteases in the Degradome database, which covers approximately 2–4 % of a typical mammalian genome [101]. Each of the proteases exhibits distinct functions to maintain “normality” in a healthy state. For example, pepsin, trypsin, and chymotrypsin are secreted from the stomach and duodenum to digest proteins in food [102]. Thrombin, plasmin, and the Hageman factor are involved in the normal

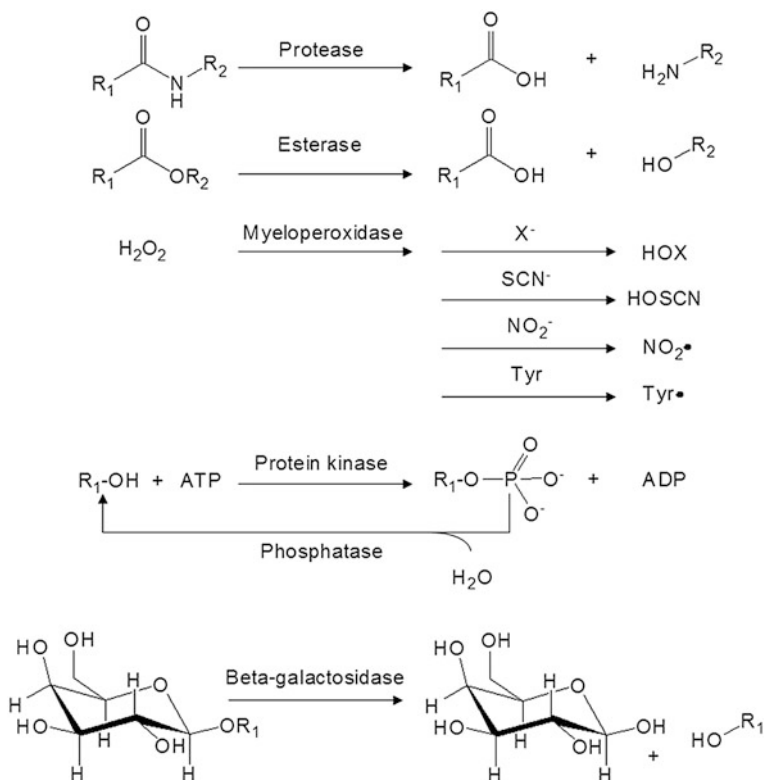


Fig. 26.4 General mechanisms of some target enzymes used to activate an enzyme-activatable agent

function of blood clotting [103]. Inside a cell, some proteases, such as cathepsin D, are stored within the lysosomes for breaking down waste material and cellular debris. Other intracellular proteases are known to regulate gene expression, cell growth, and apoptosis [104, 105]. Because of the diverse functionality and abundant amount of proteases, many of them are abolished or elevated during disease progression. For instance, dysregulated protease activities are commonly found in atherosclerosis [106–108], thrombosis [109], arthritis [110], asthma [111], emphysema [112], and osteoporosis [113]. In the context of cancer, cathepsins [114], matrix metalloproteinases (MMPs) [115], urokinase plasminogen activators (uPA) [116], and prostate-specific antigen (PSA) have been shown to play distinct roles in tumor growth, invasion, migration, and angiogenesis by facilitating the breakdown of extracellular matrix (ECM) [116–118].

Advances in solid-phase peptide synthesis and combinatorial chemistry have led to the discovery of many peptide sequences that are specific to individual proteases [119, 120]. When these peptides are conjugated to chemotherapeutic agents, the resulting conjugates become prodrugs that can be activated by targeted

Table 26.2 Some of the drug–peptide conjugates

Active drug metabolite	Peptide substrate	Target protease	Disease	References
Amiloride	LFGGGG	Enkephalinase	Ischemia	[136]
Cycloamine	SSKYQ	PSA	Cancer	[137]
Cyclophosphamide	Cbz-SSFY	PSA	Cancer	[138]
Doxorubicin	BLAL	TOP	Cancer	[139]
	PLGL, PVGLIG	MMP-2/9	Cancer	[126, 140, 141]
	aFK	Plasmin/urokinase	Cancer	[142, 143]
	RSSYYSR	PSA	Cancer	[144]
	AANL	Legumain	Cancer	[145]
Fluorodeoxyuridine	HSSKLQL	PSA	Cancer	[146]
Gentamicin	GfPRGFAGG	Thrombin	Infection	[147]
Methotrexate	aFKK	Cathepsin, plasmin	Arthritis	[148]
Paclitaxel	aFK, vLK	Plasmin	Cancer	[149]
	V-Cit	Cathepsin B	Cancer	[150]
	GPLGIAGQ	MMP-2	Cancer	[151]
Pyropheophorbide-a	TSGPNQEYK	FAP	Cancer	[152]
	DEVD	Caspase 3	Cancer	[153]
TGX-221	SSKYQ	PSA	Cancer	[154]
Thapsigargin	HSSKLQL	PSA	Cancer	[155]
	GKAFRR	Hk2	Cancer	[156]
Vinblastine	Hyp-SS-Chg-QSSP	PSA	Cancer	[127]

Note The small letters indicate that particular amino acids are in D-configuration. The amino acid derivatives are shown by a group of three italics. *Cbz* *N*-benzyloxycarbonyl; *Chg* *L*-cyclohexylglycine; *Cit* citrulline; *FAP* fibroblast activation protein; *Hk2* human glandular kallikrein 2; *Hyp* *trans*-4-hydroxy-*L*-proline; *MMP* matrix metalloproteinase; *PSA* prostate-specific antigen; *Pyr* *L*-pyroglutamic acid; *TOP* thimet oligopeptidase

proteases [121–127]. A peptide (Mu-HSSKLQL) that is specific to PSA cleavage was coupled to the primary amine of doxorubicin. The drug–peptide conjugate exhibited a specific cytotoxic response to PSA-positive prostate cancer cell lines [128]. In another example, a synthetic semenogelin I peptide analog was covalently conjugated to the aminoglycoside of doxorubicin. The resulting L-377,202 showed a significant reduction in dose-limiting systemic toxicities compared to free doxorubicin [129]. In the clinical context, L-377,202 was well tolerated in patients with advanced hormone-refractory prostate cancer. The prodrug could be cleaved by PSA to release the active metabolites [130]. The similar design has been applied to numerous other drug–peptide conjugates (Table 26.2). Unfortunately, peptide-based therapeutic agents normally exhibit short elimination half-lives. Further, they are difficult to administer over a prolonged dosing interval [131].

To increase circulation time, these prodrugs can be covalently attached to a biomolecule. Antibodies are frequently used as the biomolecules because they are specific. These so-called antibody–drug conjugates can deliver the therapeutic agents inside the target cell. In a successful case, monomethylauristatin E (MMAE) was conjugated to a monoclonal antibody (cAC10) that was specific CD30 via a dipeptide (V-Cit) [132]. In vitro study showed that the resulting

antibody–drug conjugate (brentuximab vedotin) could target CD30-expressing malignant cells and could be cleaved by cathepsin B to release the active MMAE. In vivo study showed that brentuximab vedotin was able to suppress subcutaneous Karpas 299 anaplastic large cell lymphoma (ALCL) tumors [132]. In 2011, brentuximab vedotin was approved by the FDA for the treatment for ALCL and Hodgkin's lymphoma [133]. However, some studies have shown that using peptides might not be superior to using a pH-cleavable linker when designing an antibody–drug conjugate [134]. Occasionally, a protein may be selected as the biomolecular carrier. For example, paclitaxel has been conjugated to albumin via a peptide (RSSYYSL) that is specific to PSA cleavage. The albumin improved the pharmacokinetic and the solubility of the drug. The macromolecular prodrug was three times more potent toward PSA-positive LNCaP prostate cancer cells, and the maximum-tolerated dose in vivo was twice that of free paclitaxel [135].

A number of macromolecular prodrugs have been designed using synthetic polymers (Table 26.3). *N*-(2-hydroxypropyl)methacrylamide (HPMA) copolymers have been used extensively. For example, prostaglandin E1 (PGE1) has been conjugated to HPMA through a cathepsin K-sensitive peptide linker (GGP-*Nle*, where *Nle* = norleucine) [157]. Incubation of the polymer with cathepsin K-expressing osteoblasts caused a rapid release of PGE1 for the treatment for osteoporosis [158]. The same polymer has been used to deliver many other chemotherapeutic agents including 5-fluorouracil, anthracycline, platinum (II), and TNP-470 for the treatment for different cancers [159–164], except the drugs were conjugated to the polymer via a cathepsin B-sensitive peptide (GFLG).

Recently, many fluorophores, including fluorescein, indocyanine green (ICG), cresyl violet, isosulfan blue, methylene blue, and porphyrins, have been identified as contrast agents for optical imaging [175–181]. By simply replacing the drug molecule with a fluorophore to conjugate it to a macromolecule, a protease-activatable probe can be developed (Fig. 26.5). For example, multiple peptides (GSGRSANA) capped with different NIR fluorophores (Cy5.5 or Cy7) have been conjugated to PEG and poly-*L*-lysine copolymer. The probe was optically silent (quenched) in its native state, as the fluorophores orientated in a close proximity. Upon digestion by a serine protease (uPA), the polymer released fluorophore–peptide fragments, which resulted in the recovery of fluorescence [182]. The probe was used to visualize the uPA activity in HT1080 tumor xenografts [183]. Using the same strategy, other peptide substrates have also been applied to imaging other disease-associated proteases including cathepsins, MMPs, caspases, and thrombin [184–189].

For therapeutic agents that are too fragile to be chemically modified or do not have a spare functional group for bioconjugation, a drug can be encapsulated in a carrier that can be degraded by proteases. Some materials used for engineering nanoparticles, such as gelatin, can be intrinsically degraded by proteases; therefore, they have been used for the delivery of chemotherapeutic agents, such as paclitaxel [190]. On the other hand, enzyme-activatable nanoparticles have been custom-designed by incorporating peptide substrates as part of the components. Short chains of PEG (~480 Da) have been cross-linked with peptide substrates

Table 26.3 Some of the macromolecular prodrugs

Macromolecule	Active drug metabolite	Peptide substrate	Target protease	Disease	References
<i>Protein</i>					
Avidin	Equinatoxin II	CNKSRLGLGK	Cathepsin B/ MMP-7	Cancer	[165]
Albumin	Camptothecin	RRALALA	Cathepsin B	Cancer	[166]
		Doxorubicin	FK, RRALAL	Cathepsin B	Cancer
	Paclitaxel	GPLGIAGQ	MMP-2/9	Cancer	[168, 169]
		RSSYYSR	PSA	Cancer	[144]
		GGGRR	Urokinase	Cancer	[170]
	RSSYYSL	PSA	Cancer	[135]	
<i>Antibody</i>					
CBR96	MMAE	V-Cit	Cathepsin B	Cancer	[132]
cAC10	MMAE	V-Cit	Cathepsin B	Lymphoma	[132]
<i>Polymer</i>					
CM-Dextran-PA	Exatecan	GGFG	Cathepsin B	Cancer	[171]
Dextran	Methotrexate	PVGLIG	MMP-2/9	Cancer	[172]
HPMA	5-Fluorouracil	GFLG	Cathepsin B	Cancer	[159]
		Doxorubicin	GFLG	Cathepsin B	Cancer
	Daunorubicin	GFLG	Cathepsin B	Leukemia	[162]
	L12ADT	SSKYQ	PSA	Cancer	[173]
	Platinum (II)	GFLG	Cathepsin B	Cancer	[163]
	Prostaglandin E1	GGP-Nle	Cathepsin K	Osteoporosis	[157, 158]
	TNP-470	GFLG	Cathepsin B	Cancer	[164]
PGA	Paclitaxel	(E) _x	Cathepsin B	Cancer	[174]

Note The amino acid derivatives are shown in a group of three italics
Cit citrulline, *Nle* norleucine, *PSA* prostate-specific antigen

(RVRR) to form nanocapsules to protect and carry a recombinant myogenic transcription factor across the cell membrane [191]. Upon uptake by the cell, the intracellular furin, a ubiquitous endoprotease, degraded the capsules and, subsequently, released the encapsulated protein. In another example, sodium poly(styrene-4-sulfonate), a polymeric microbicide used to treat HIV infection, was encapsulated in the microgel particles composed of HPMA and 2-aminopropyl-methacrylamide (APMA) copolymers cross-linked with PSA substrates (GIS-SFYSSK) [192]. The resulting particles were degraded by the PSA in human seminal plasma (HSP) and released the entrapped antiviral polymer.

26.3.2 Esterase

Esterase is an enzyme that breaks down the ester, amide, and thioester bonding of an organic molecule. It can be found in many organs including the liver, lung epithelia, small intestine, kidney, and plasma [193]. To improve the solubility

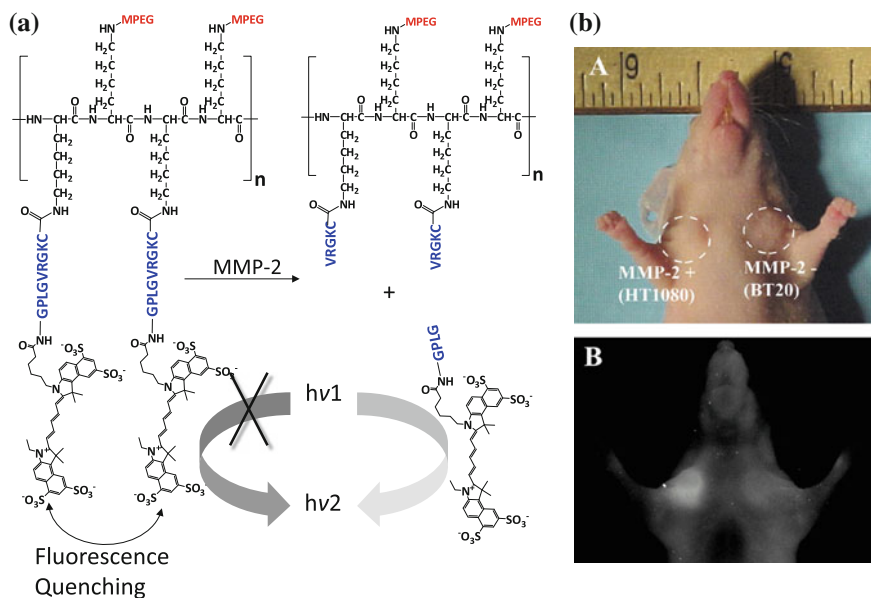


Fig. 26.5 An enzyme-activatable probe designed to be activated by MMP-2-associated protease. **a** The probe was composed of multiple peptide motifs that were terminally capped with different Cy5.5 and a pegylated poly-L-lysine graft copolymer. **b** In vivo imaging. NIRF imaging of a nude mouse implanted with HT1080 (MMP-2+) and BT20 (MMP-2-) tumors. Photograph and fluorescence image of the mouse 2 h after intravenous injection of the probe. Recreated with permission from RSNA [187]

and/or bioavailability of the drug formulation [194–198], prodrugs such as capecitabine, oseltamivir, meperidine, and methylphenidate were designed. They can be converted by carboxylesterase to the active pharmacophores (Fig. 26.6). Esterase-activatable nanoparticles have only been reported recently. Lipid nanoparticles assembled from ester-containing polysorbate 60 and PEG6000 monostearate have been synthesized [199]. Silica mesoporous nanoparticles (MCM-41) have been employed for the delivery of camptothecin [200]. The pore outlets of MCM-41 were capped with ester glycol moieties as the stoppers, which could be hydrolyzed by esterase in the lysosome inside HeLa cells to release the active drug contents. In another example, micelles were constructed from amphiphilic dendrimers functionalized with hexyl ester (as the lipophilic unit) and pentaethylene glycol (as the hydrophilic unit). In the presence of porcine liver esterase, the enzyme hydrolyzed the ester functionalities and caused the demicellization of the micelles, leading to the release of hydrophobic guest molecules at the target site [201].

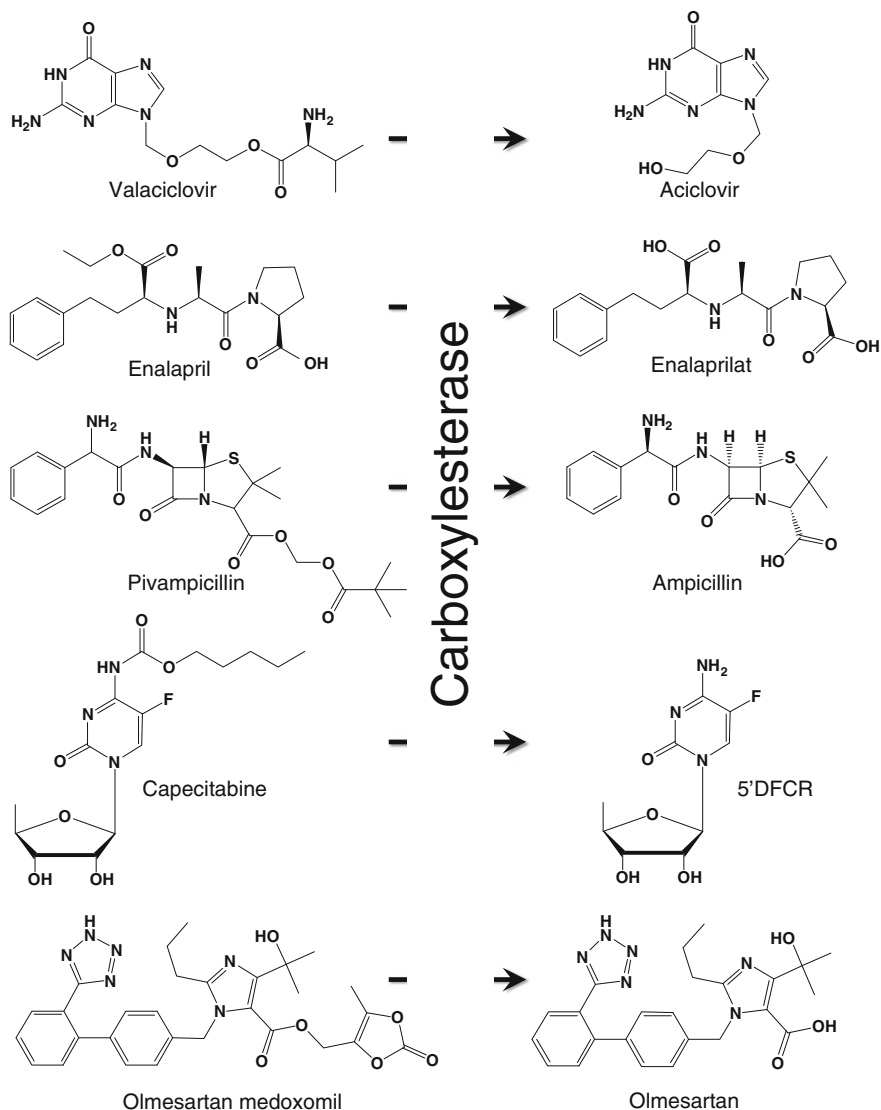


Fig. 26.6 Examples of carboxylesterase-activatable prodrugs and their metabolites

26.3.3 Myeloperoxidase

Myeloperoxidase (MPO) is an enzyme that is predominantly stored in azurophilic granules of polymorphonuclear neutrophils and macrophages. The enzyme consumes hydrogen peroxide to produce hypochlorous acid and tyrosyl radicals during neutrophil's respiratory burst. During inflammation, MPO is released into

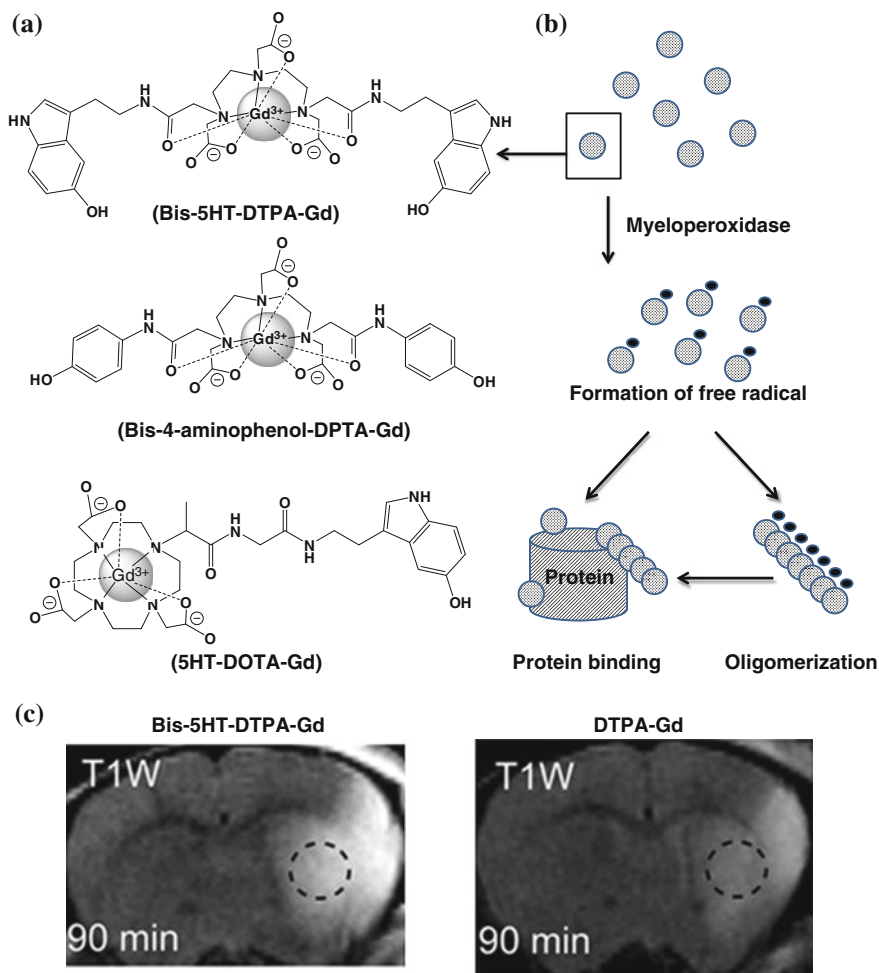


Fig. 26.7 Myeloperoxidase-activatable MRI contrast agents. **a** The chemical structures of some of the developed myeloperoxidase-activatable contrast agents. **b** Upon enzyme activation, bis-5HT-DTPA-Gd radicalized to form oligomers and/or to bind to other proteins, which resulted in the increase in r_1 relaxivity. **c** A comparison of the T_1 -weighted brain images of animals injected with bis-5HT-DTPA-Gd and DTPA-Gd. Recreated with permission from PNAS [211]

extracellular fluid; consequently, it has been implicated in many diseases including Alzheimer's disease, atherosclerosis, Parkinson's disease, stroke, and vasculitis [202–206]. For these reasons, a number of myeloperoxidase-activatable contrast agents have been developed for MRI [207–210]. They were designed with the attachment of an MPO substrate, such as 5-hydroxytryptamine-(serotonin) and tyramide, to a paramagnetic gadolinium chelate, such as DOTA-Gd or DTPA-Gd, via amide bonding (Fig. 26.7). Upon enzyme activation, these contrast agents form

radical species and oligomerize or bind to proteins, which results in an increase in the T_1 -weighted signal in MRI. For example, *bis*-5HT-DTPA-Gd has been used to image the MPO activity of a living animal with cerebral ischemia [211]. The post-contrast T_1 -weighted image of the brain was enhanced compared to the conventional DTPA-Gd (Fig. 26.7). The same contrast agent has also been applied to visualize the MPO activity in atherosclerotic plaques and myositis [212, 213].

26.3.4 Miscellaneous Enzymes

Numerous innovative agents have been for activation by other enzymes. However, their application in vivo still needs to be addressed. A multiple protein kinase A (PKA) substrate kemptide, and an NIR fluorophore, Cy5.5, have been incorporated into positively charged polyethylenimine [214]. The polymer was coassembled with the negatively charged polyacrylic acid (PAA) to form an optically silent polyion-induced complex (PIC). The PIC has been used for imaging protein phosphorylation in single living cell. Upon enzyme activation, the particle became phosphorylated, dissolved, and resulted in the recovery of NIR fluorescence. The same peptide has also been grafted to polyacrylamide, resulting in the formation of a cationic polymer (PAK) [215]. PAK formed a stable complex with DNA and halted gene expression. Ex vivo study showed that the activated protein kinase A (PKA) in abnormal cells could destabilize the complex via phosphorylation to release the DNA for gene transcription. Other prodrugs that can be activated by β -galactosidase were also developed as potential candidates for chemotherapy [216–220] and imaging purposes [221].

26.4 Thermo-Activatable Agents

In certain medical conditions such as hyperpyrexia, body temperature can be elevated up to 41.5 °C. In other disease states, including cancer, the microenvironment of tumors is slightly hyperthermic. In the past, numerous thermo-activatable agents have been developed for drug delivery with the aim of enhancing local drug release and cellular uptake. Another advantage of applying additional heat [i.e., hyperthermia therapy (HT)] to the tumor is that it can sensitize the cancer cells when responding to radiation and chemotherapy; therefore, HT has been proposed as an adjunctive therapy [222–226]. Many micelles have been assembled from thermo-responsive polymers (Table 26.4). In particular, PNIPAM has been widely used as the thermo-activatable polymer. It has a lower critical solution temperature (LCST) of 32 °C and can be dissolved at temperature below 32 °C. When the temperature is above the LCST, the polymer can undergo phase transition to form a gel. Thus, PNIPAM has been used in combination with other hydrophobic constructs. The resulting copolymers were able to assemble into a

Table 26.4 Some of the polymers employed to assemble into thermo-activatable micelles

Polymers	Drug	LCST ($^{\circ}\text{C}$)	References
PIPROX-PAA	N/A	32	[231]
PNIPAM-PBMA	Doxorubicin	33	[234]
PNIPAM-(PHEMA -PCL) _x	Paclitaxel	36	[235]
(PNIPAM-PNHMAM) _x -PLLA	Methotrexate	37	[236]
(PNIPAM-PHEMA) _x -(PLLA-PCL) _y	Doxorubicin	38	[237]
(PNIPAM-PDMAM) _x -PLGA	Doxorubicin	39	[238]
(PNIPAM-PAM) _x -PLLA	Docetaxel	41	[229, 230]
PLLA-PEG-PLLA	Doxorubicin	42	[239]

PAA poly(amino acid), *PAM* poly(acrylamide), *PBMA* poly(butylmethacrylate), *PDMAM* poly(N,N-dimethylacrylamide), *PHEMA* poly(2-hydroxyethylmethacrylate), *PIPROX* poly(2-isopropyl-2-oxazoline), *PNHMAM* poly(N-hydroxymethylacrylamide), *PNIPAM* poly(N-isopropylacrylamide), *PCL* poly(ϵ -caprolactone), *PLGA* poly(D,L-lactide-co-glycolide), and *PLLA* poly(L-lactide)

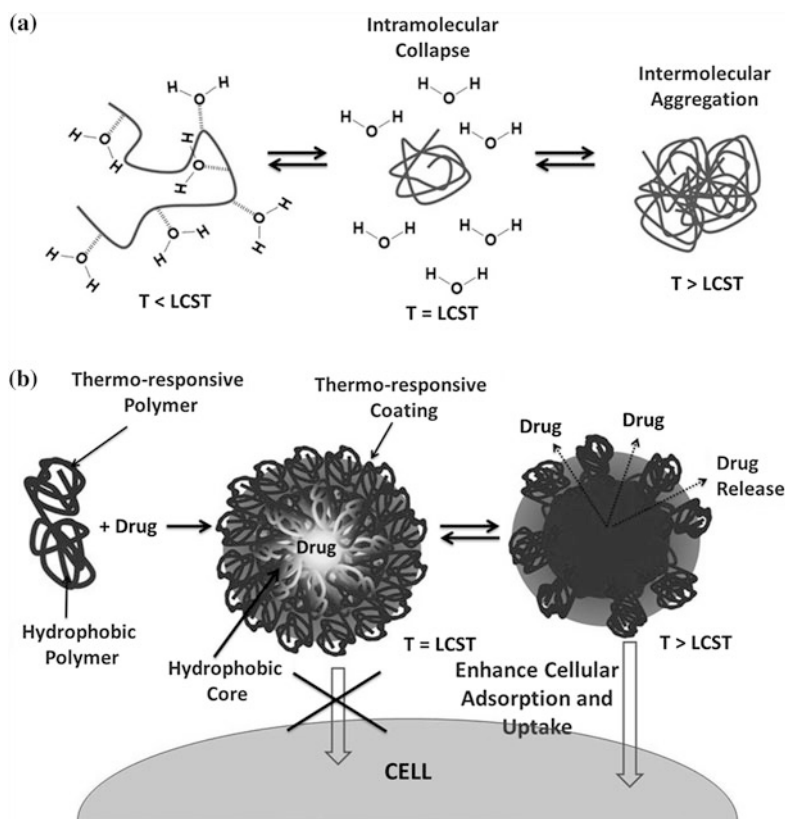


Fig. 26.8 The concept of thermo-activatable micelle. **a** The mechanism of the phase transition of the polymer (e.g., PNIPAM) employed in a thermo-responsive micelle. **b** The micelle can be designed by assembling the thermo-responsive and hydrophobic copolymer

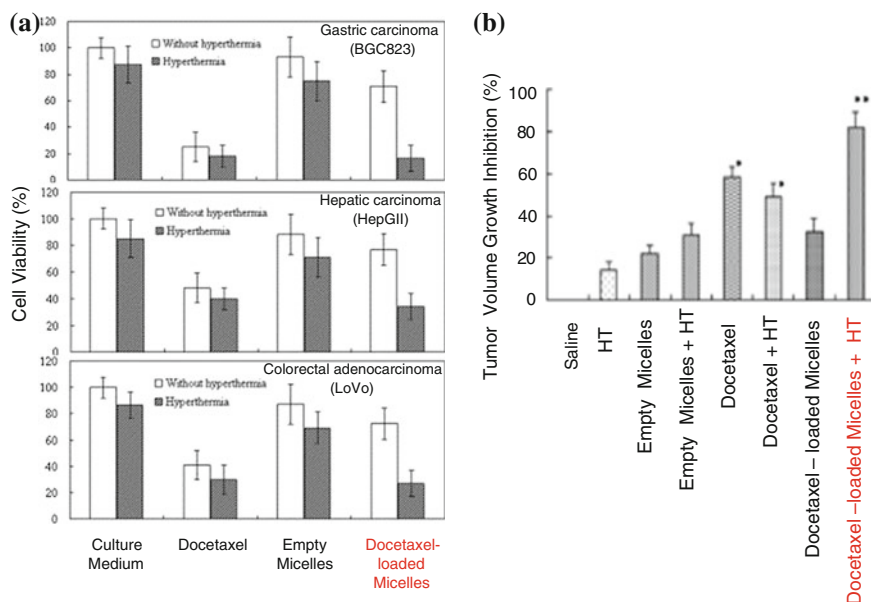


Fig. 26.9 A comparison of the cytotoxicity of docetaxel-loaded thermo-responsive micelles with and without hyperthermia therapy **a** ex vivo and **b** in vivo. Recreated with permission from Wiley InterScience [229, 230]

micelle consisting a thermo-responsive coating (Fig. 26.8). Furthermore, therapeutic agents, such as doxorubicin, could be encapsulated inside micelles. Upon heating, the coatings collapsed and resulted in the release of drug contents and/or enhanced cell attachment [227, 228]. Docetaxel has been loaded into micelles assembled from copolymer, poly(*N*-isopropylacrylamide-co-acrylamide)-*b*-poly(DL-lactide). The cytotoxicity of the micelles was significantly increased with hyperthermia therapy (Fig. 26.9) [229]. In vivo study using human BCG gastric tumor-implanted nude mice demonstrated that HT could significantly enhance the tumor inhibition of the docetaxel-loaded micelles compared to animals without hyperthermia treatment (82 vs. 32 %) (Fig. 26.9) [230]. Other newer types of polymers have also been used to generate thermo-activatable particles or micelles [231–233]. However, their performance still needs to be confirmed in vivo.

In addition to the thermo-sensitive polymer, a thermo-sensitive liposome was introduced in the late 1970s [240]. By changing the lipid compositions, the resulting liposomes could be fine-tuned to release the drug contents quickly at a desired temperature [241, 242]. ThermoDox[®] is a low-temperature-sensitive liposome (LTSL) composed of dipalmitoylphosphatidylcholine (DPPC), monostearoylphosphatidylcholine (MSPC), and pegylated distearoylphosphatidylethanolamine (DSPE-PEG2000) in 90:10:4 molar ratio [243]. It is currently undergoing clinical trials for the treatment for liver and recurrent breast cancers. The liposome exhibited a lower phase transition temperature and a faster drug

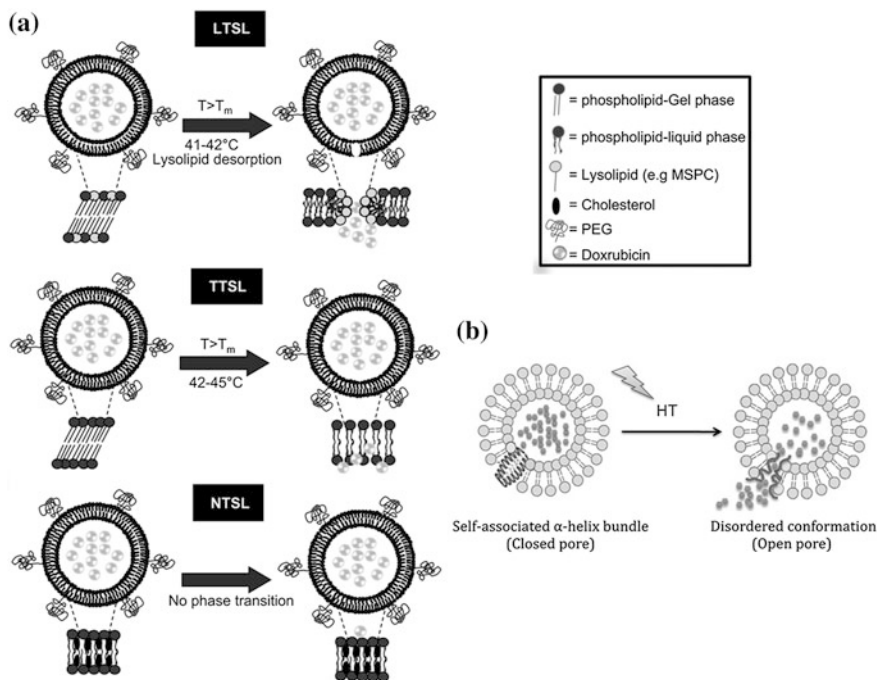


Fig. 26.10 A design of thermo-sensitive liposome. **a** Schematic presentation of the drug release mechanisms of LSTL, TTSL, and NTSL. The additional lysolipid in LSTL stabilizes the pore formed at the phase transition temperature (T_m) to enhance the drug release kinetic. Recreated with permission from Elsevier [301]. **b** A thermo-responsive liposome system was developed by anchoring a temperature-sensitive amphiphilic peptide within the lipid bilayer. At hyperthermia, the peptide unfolded, which made the liposome become sufficiently leaky to release the drug content. Recreated with permission from ACS Publications [245]

release kinetic compared to the “traditional” TSL (TTSL) and non-temperature-sensitive liposome (NTSL) (Fig. 26.10). It was shown to be more effective in reducing tumor growth rate *in vivo* when used in combination with HT [244]. Recently, a new class of thermo-sensitive liposome was developed by incorporating a leucine zipper peptide that has the ability to dissociate at 40 °C into the LSTL (Fig. 26.10). The liposome exhibited a similar thermo-responsive nature, but appeared to be more stable in serum [245].

26.5 Photo-Activatable Agents

The use of light as an external trigger in drug delivery has received a great deal of attention recently. An external light source can be remotely and accurately controlled in a temporal (when the light source is switched on) and spatial (the area to

which the light is directed) manner with a resolution as high as approximately 1 μM . The early design involved the introduction of photo-isomerizable groups, such as azobenzene or stilbene, in the hydrophobic chains [246]. Micelles or vesicles composed of diblock copolymer of poly(azobenzene) and poly(*tert*-butyl acrylate) and poly(acrylic acid) have been designed to undergo disruption and reformation upon alternating UV and visible light illumination [246]. Currently, many materials used for engineering photo-activatable agents are covalently incorporated with photo-cleavable moieties [247]. For example, a photo-labile *o*-nitrobenzyl group has been introduced between a hydrophobic poly(γ -methyl- ϵ -caprolactone) and a hydrophilic poly(acrylic acid). The resulting micelles or vesicles assembled from this polymeric construct showed significant reduction in size and number after exposure to UV irradiation [248]. Nanoparticles constructed from photodegradable 2-nitrophenylethylene glycol polymers have also been reported. The particles could be triggered by UV light to release the anticancer agent, Tagalsin G [249]. Because UV light may also cause damage to healthy cells, NIR light has recently been proposed as the preferred trigger for in vivo applications. Furthermore, it can also penetrate more deeply into the tissue. It has been shown that micelles composed of a hydrophilic poly(ethylene oxide) (PEO) and hydrophobic poly([7-(dimethylamino)coumarin-4-yl]methyl methacrylate (PDEACMM) diblock copolymer could be triggered by two-photon NIR absorption at 794 nm. The micelles were also encapsulated with a model drug (Nile Red). As a result of photo-solvolysis, the hydrophobic component of PDEACMM, [7-(dimethylamino)coumarin-4-yl]methyl esters, was cleaved, which led to changes in the hydrophilic-hydrophobic balance and, subsequently, the disruption of the micelles [250]. Similarly, a photo-sensitive polymer containing multiple quinone-methide self-immolative moieties have been formulated into nanoparticles. In vitro studies demonstrated a burst release of the encapsulated contents upon irradiation at 750 nm by the two-photon process [247].

The two-photon absorption of NIR light can sometimes be slow and inefficient. Micelles that can be directly activated by NIR have been designed. These micelles were composed of the diblock copolymer of PEO and poly(4,5-dimethoxy-2-nitrobenzyl methacrylate) encapsulated with NaYF₄:TmYb upconverting nanoparticles (Fig. 26.11). Upon absorption of NIR light, the nanoparticles emitted photons in the UV and visible regions, which were absorbed by the *o*-nitrobenzyl groups of the polymeric components to initiate a photo-cleavage reaction. Subsequently, the micelles dissociated to release the content [251]. In another design, gold nanorods were encapsulated in thermo-sensitive microspheres. The system utilized the photo-thermal effect of gold. Upon NIR light exposure, the encapsulated gold nanorods converted the light into heat and triggered the release of the doxorubicin from the microspheres [252].

Although many photo-activatable agents have been reported in the literatures, their applications in vivo have not yet been confirmed. On the other hand, photo-thermal conducting agents, such as various gold (Au) nanostructures [253–257] and copper monosulfide (CuS) nanoparticles [258], were shown to be clinically applicable to photo-thermal ablation therapy (PAT) [259]. They acted by

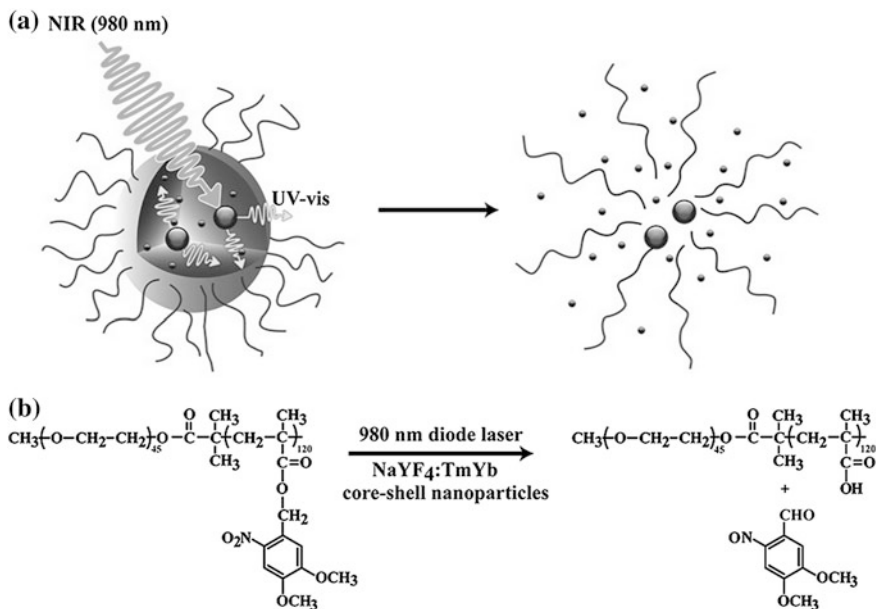


Fig. 26.11 A photo-activatable micelle triggered by a direct excitation of NIR light. **a** The encapsulated UCNP absorbed the light and emitted photons at a shorter wavelength (i.e., in the UV–visible region), which were absorbed by the *o*-nitrobenzyl groups of the polymeric constructs to initiate a photo-cleavage reaction. Subsequently, the micelle dissociated and released the content. **b** NIR light-triggered photoreaction of the polymeric constructs. Recreated with permission from ACS Publications [251]

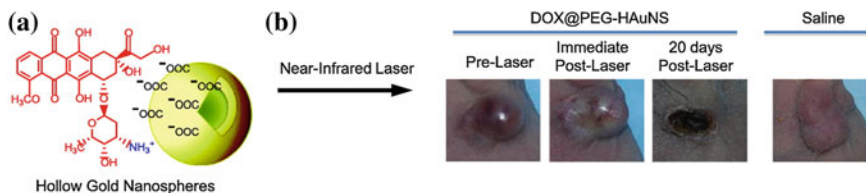


Fig. 26.12 A combination of PTA and chemotherapy. **a** Doxorubicin was coated at both the outer and the inner surfaces of HAuNS. Therefore, irradiation with an NIR laser could induce photo-thermal conversion for PTA and could also trigger the release of doxorubicin for chemotherapy. **b** Photographs of MDA-MB-231 tumors after treatment with DOX@PEG-HAuNS. Recreated with permission from Elsevier [260]

converting the absorbed light energy into heat to eradicate the cancer cells. For example, α -melanocyte-stimulating hormone analog, NDP-MSH, has been conjugated to pegylated hollow Au nanospheres (HAuNSs) and was shown to effectively target murine B16/F10 melanoma for PAT [256]. Doxorubicin has also been loaded to HAuNSs. In addition to PAT, the resulting particles, DOX@PEG-HAuNS, could be triggered by NIR laser irradiation to release the drug locally at

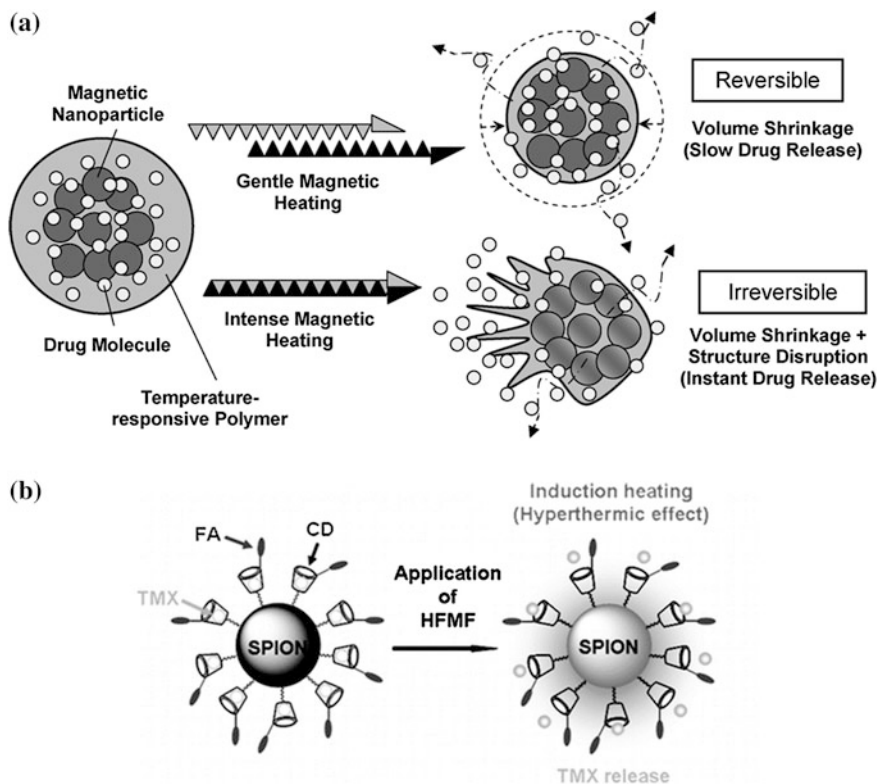


Fig. 26.13 **a** Schematic illustration of the mechanisms of magnetic-activatable agents. Recreated with permission from Elsevier [302]. **b** A multimodal magnetic-activatable agent. Recreated with permission from ACS Publications [278]

the tumor site (Fig. 26.12) [260]. Some photo-thermal conducting agents, such as AuroShell (TM), are currently undergoing clinical trials for the treatment for patients with refractory and/or recurrent tumors of the head and neck.

26.6 Magnetic-Activatable Agents

The majority of magnetic-activatable agents are designed to induce hyperthermic effects when placed in an alternating magnetic field (AMF) [261–263]. These agents are often composed of supermagnetic nanoparticles embedded in materials, such as porous scaffolds, polymers, liposomes, microspheres, microcapsules, and nanospheres that are thermo-responsive [264–269]. Depending on the degree of heat generated by the magnetic particles as a result of Néel and Brown relaxation [270], the materials collapse, deform, or rupture, and result in the release of drug content (Fig. 26.13a). Iron oxide (Fe_3O_4), together with a model drug (ibuprofen),

has been embedded into silica nanospheres [271]. It was shown that the drug release could be enhanced by the formation of porous channels upon contactless exposure to a high-frequency magnetic field (HFMF).

Magnetic-activatable liposomes (MALs) have also been developed through encapsulation of small superparamagnetic iron oxide nanoparticles (SPIONs) within the aqueous core [272] or by insertion of SPIONs within the lipid bilayers [273, 274]. When used as a combined hyperthermia and chemotherapy (i.e., chemohyperthermia), MALs were shown to be effective for the eradication of solid tumors [275, 276]. For example, MALs were prepared by loading Fe_3O_4 nanoparticles and 4-*S*-cysteaminyphenol (4-*S*-CAP), a melanoma tyrosinase substrate, into the cationic liposomes [276]. Results from in vivo study on B16 melanoma-implanted mice demonstrated that the therapeutic efficacy of a combined MALs and hyperthermia treatment was significantly higher compared to the MALs or hyperthermia alone. A similar design using MALs loaded with docetaxel has been proposed for the treatment for gastric cancer [277]. A multimodal SPIONs functionalized with β -cyclodextrin (CD) and folic acid have been reported recently as a magnetic-activatable agent [278]. The CD was served as a container for tamoxifen. The heat generated upon application of high-frequency magnetic field (HFMF) triggered the release of the drug from the CD cavity (Fig. 26.13b). One advantage of using MALs is that the encapsulated magnetic iron oxide nanoparticles can also be used as MRI contrast agent. For example, MALs containing cathepsin protease inhibitor JPM-565 have been used for both the imaging (via the T_2 -weighted MRI contrast) and the therapy of tumor [279].

Another approach to design magnetic-activatable system is in the form of a cargo and a cap. The cargo is normally filled with the payload and sealed by a thermo-sensitive cap. In the presence of an external magnetic field, the heat generated by the magnetic nanoparticle will open the cap, leading to the release of the encapsulated drug from the cargo. For example, magnetic mesoporous silica decorated with single-stranded DNA was served as a cargo, whereas the pores of the cargo were capped by magnetic nanoparticles functionalized with the complementary strand (Fig. 26.14). Upon magnetic activation, the heat generated from magnetic nanoparticle was sufficient to dehybridize the DNA, open the cap, and release the drug molecules [280]. In another study, zinc-doped iron oxide nanocrystals (ZnNCs) were encapsulated within mesoporous silica nanoparticles that were surface-modified with pseudorotaxanes. Application of AMF caused internal heating of the nanoparticles and, subsequently, disassembled the pseudorotaxanes to release the drug content [281].

26.7 Prospective

We have described examples of some activatable agents. It is noteworthy that many others can be triggered by reducing the environment, hydrogen peroxide, electric field, and ultrasound that are not reported here [282–292]. There is no rule

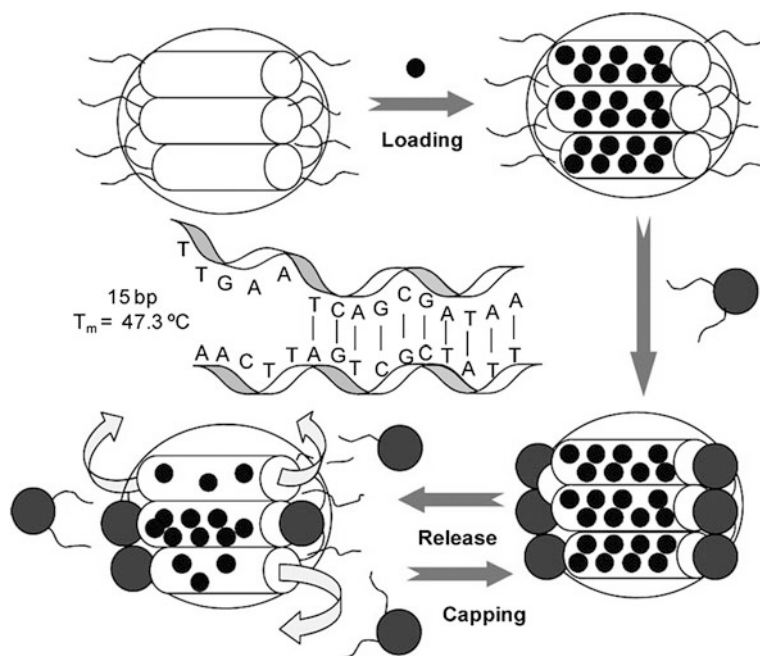


Fig. 26.14 A schematic representation of magnetic-activatable system based on cargo-cap concept. Drug releases from the magnetic mesoporous silica through DNA hybridization/dehybridization. Recreated with kind permission from ACS Publications [280]

of thumb on how to design an activatable agent. Multiple factors, including the nature and the progression of the disease, the accessibility to external stimuli, and the components of the activatable agents, should be taken into account on a case-by-case basis. To achieve better control over drug release kinetics, some activatable agents were designed to have more than one trigger [293–295]. In the case of an imaging agent, it is important to establish a clinical purpose to distinguish between normal and abnormal anatomy, locate a specific disease, evaluate the function, and/or improve patient management.

Many other activatable agents have been reported for the treatment for diseases other than cancer. For example, microaggregates that are sensitive to high fluid shear have been developed for the treatment for pulmonary embolism [296]. Self-regulated glucose-sensitive delivery systems have been created to treat diabetics [297–299]. Further, activatable imaging agents have been used to monitor disease progression, such as acute pancreatitis and ischemic injury [208, 300]. Until now, although only a few of the activatable agents have been examined in *in vivo* testing, many of them were shown to have great potentials. The state-of-the-art research in multidisciplinary areas is expected to yield more sophisticated activatable systems that are biocompatible and possess favorable pharmacokinetic properties as prospective candidates for future clinical trials.

References

1. Mittal S, Tsume Y, Landowski CP, Lee KD, Hilfinger JM, Amidon GL (2007) Proline prodrug of melphalan, prophalan-L, demonstrates high therapeutic index in a murine melanoma model. *Eur J Pharm Biopharm* 67(3):752–758
2. Garsky VM, Lumma PK, Feng DM, Wai J, Ramjit HG, Sardana MK, Oliff A, Jones RE et al (2001) The synthesis of a prodrug of doxorubicin designed to provide reduced systemic toxicity and greater target efficacy. *J Med Chem* 44(24):4216–4224
3. Ryan Q, Ibrahim A, Cohen MH, Johnson J, C-W Ko, Sridhara R, Justice R, Pazdur R (2008) FDA drug approval summary: lapatinib in combination with capecitabine for previously treated metastatic breast cancer that overexpresses HER-2. *Oncologist* 13(10):1114–1119
4. Koukourakis GV, Kouloulis V, Koukourakis MJ, Zacharias GA, Zabatis H, Kouvaris J (2008) Efficacy of the oral fluorouracil pro-drug capecitabine in cancer treatment: a review. *Molecules* 13(8):1897–1922
5. Casak SJ, Lemery SJ, Shen YL, Rothmann MD, Khandelwal A, Zhao H, Davis G, Jarral V et al (2011) US food and drug administration approval: rituximab in combination with fludarabine and cyclophosphamide for the treatment of patients with chronic lymphocytic leukemia. *Oncologist* 16(1):97–104
6. Blagosklonny MV (2004) Analysis of FDA approved anticancer drugs reveals the future of cancer therapy. *Cell Cycle* 3(8):1033–1040
7. Chow TH, Lin YY, Hwang JJ, Wang HE, Tseng YL, Wang SJ, Liu RS, Lin WJ et al (2009) Improvement of biodistribution and therapeutic index via increase of polyethylene glycol on drug-carrying liposomes in an HT-29/luc xenografted mouse model. *Anticancer Res* 29(6):2111–2120
8. Alexis F, Basto P, Levy-Nissenbaum E, Radovic-Moreno AF, Zhang L, Pridgen E, Wang AZ, Marein SL et al (2008) HER-2-targeted nanoparticle–affibody bioconjugates for cancer therapy. *Chem Med Chem* 3(12):1839–1843
9. Lim HJ, Masin D, McIntosh NL, Madden TD, Bally MB (2000) Role of drug release and liposome-mediated drug delivery in governing the therapeutic activity of liposomal mitoxantrone used to treat human A431 and LS180 solid tumors. *J Pharmacol Exp Ther* 292(1):337–345
10. Lim HJ, Masin D, Madden TD, Bally MB (1997) Influence of drug release characteristics on the therapeutic activity of liposomal mitoxantrone. *J Pharmacol Exp Ther* 281(1):566–573
11. Charrois G, Allen TM (2004) Drug release rate influences the pharmacokinetics, biodistribution, therapeutic activity, and toxicity of pegylated liposomal doxorubicin formulations in murine breast cancer. *Biochim Biophys Acta* 1663(1–2):167
12. Andresen TL, Jensen SS, Kaasgaard T, Jorgensen K (2005) Triggered activation and release of liposomal prodrugs and drugs in cancer tissue by secretory phospholipase A2. *Curr Drug Deliv* 2(4):353–362
13. Huan M, Zhang B, Teng Z, Cui H, Wang J, Liu X, Xia H, Zhou S et al (2012) In vitro and in vivo antitumor activity of a novel pH-activated polymeric drug delivery system for doxorubicin. *PLoS One* 7(9):e44116
14. Lu J, Choi E, Tamanoi F, Zink JJ (2008) Light-activated nanoimpeller-controlled drug release in cancer cells. *Small* 4(4):421–426
15. Griset AP, Walpole J, Liu R, Gaffey A, Colson YL, Grinstaff MW (2009) Expansile nanoparticles: synthesis, characterization, and in vivo efficacy of an acid-responsive polymeric drug delivery system. *J Am Chem Soc* 131(7):2469–2471
16. Obata Y, Tajima S, Takeoka S (2010) Evaluation of pH-responsive liposomes containing amino acid-based zwitterionic lipids for improving intracellular drug delivery in vitro and in vivo. *J Control Release* 142(2):267–276
17. Morgan TT, Muddana HS, Altinoğlu EI, Rouse SM, Tabaković A, Tabouillot T, Russin TJ, Shanmugavelandy SS et al (2008) Encapsulation of organic molecules in calcium phosphate

- nanocomposite particles for intracellular imaging and drug delivery. *Nano Lett* 8(12):4108–4115
18. Satarakar NS, Hilt JZ (2008) Magnetic hydrogel nanocomposites for remote controlled pulsatile drug release. *J Control Release* 130(3):246–251
 19. She W, Li N, Luo K, Guo C, Wang G, Geng Y, Gu Z (2013) Dendronized heparin–doxorubicin conjugate based nanoparticle as pH-responsive drug delivery system for cancer therapy. *Biomaterials*
 20. Spratt T, Bondurant B, O'Brien DF (2003) Rapid release of liposomal contents upon photoinitiated destabilization with UV exposure. *Biochim Biophys Acta* 1611(1):35–43
 21. Chen KJ, Liang HF, Chen HL, Wang Y, Cheng PY, Liu HL, Xia Y, Sung HW (2012) A thermoresponsive bubble-generating liposomal system for triggering localized extracellular drug delivery. *ACS Nano* 7(1):438–446
 22. Huang IP, Sun SP, Cheng SH, Lee CH, Wu CY, Yang CS, Lo LW, Lai YK (2011) Enhanced chemotherapy of cancer using pH-sensitive mesoporous silica nanoparticles to antagonize P-glycoprotein-mediated drug resistance. *Mol Cancer Ther* 10(5):761–769
 23. Gang J, Park SB, Hyung W, Choi EH, Wen J, Kim HS, Shul YG, Haam S et al (2007) Magnetic poly ϵ -caprolactone nanoparticles containing Fe₃O₄ and gemcitabine enhance anti-tumor effect in pancreatic cancer xenograft mouse model. *J Drug Target* 15(6):445–453
 24. Leite EA, Souza CM, Carvalho-Júnior AD, Coelho LG, Lana AM, Cassali GD, Oliveira MC (2012) Encapsulation of cisplatin in long-circulating and pH-sensitive liposomes improves its antitumor effect and reduces acute toxicity. *Int J Nanomedicine* 7:5259
 25. Lee JH, Chen KJ, Noh SH, Garcia MA, Wang H, Lin WY, Jeong H, Kong BJ et al (2013) On-demand drug release system for in vivo cancer treatment through self-assembled magnetic nanoparticles. *Angewandte Chemie International Edition*
 26. DeBerardinis RJ, Sayed N, Ditsworth D, Thompson CB (2008) Brick by brick: metabolism and tumor cell growth. *Curr Opin Genet Dev* 18(1):54–61
 27. Kessenbrock K, Plaks V, Werb Z (2010) Matrix metalloproteinases: regulators of the tumor microenvironment. *Cell* 141(1):52–67
 28. Cantero D, Friess H, Deflorin J, Zimmermann A, Bründler M, Riesle E, Korc M, Büchler M (1997) Enhanced expression of urokinase plasminogen activator and its receptor in pancreatic carcinoma. *Br J Cancer* 75(3):388–395
 29. Berdowska I (2004) Cysteine proteases as disease markers. *Clin Chim Acta* 342(1–2):41–69
 30. Du JZ, Du XJ, Mao CQ, Wang J (2011) Tailor-made dual pH-sensitive polymer–doxorubicin nanoparticles for efficient anticancer drug delivery. *J Am Chem Soc* 133(44):17560–17563
 31. Garripelli VK, Kim JK, Son S, Kim WJ, Repka MA, Jo S (2011) Matrix metalloproteinase-sensitive thermogelling polymer for bioresponsive local drug delivery. *Acta Biomater* 7(5):1984–1992
 32. Lee S, Saito K, Lee HR, Lee MJ, Shibasaki Y, Oishi Y, Kim BS (2012) Hyperbranched double hydrophilic block copolymer micelles of poly (ethylene oxide) and polyglycerol for pH-responsive drug delivery. *Biomacromolecules* 13(4):1190–1196
 33. Li G, Fei G, Xia H, Han J, Zhao Y (2012) Spatial and temporal control of shape memory polymers and simultaneous drug release using high intensity focused ultrasound. *J Mater Chem* 22(16):7692–7696
 34. Braun GB, Pallaoro A, Wu G, Missirlis D, Zasadzinski JA, Tirrell M, Reich NO (2009) Laser-activated gene silencing via gold nanoshell–siRNA conjugates. *ACS Nano* 3(7):2007–2015
 35. Huang X, Lee S, Chen X (2011) Design of “smart” probes for optical imaging of apoptosis. *Am J Nucl Med Mol Imaging* 1(1):3–17
 36. Ogawa M, Regino CA, Choyke PL, Kobayashi H (2009) In vivo target-specific activatable near-infrared optical labeling of humanized monoclonal antibodies. *Mol Cancer Ther* 8(1):232–239

37. Ogawa M, Kosaka N, Longmire MR, Urano Y, Choyke PL, Kobayashi H (2009) Fluorophore–quencher based activatable targeted optical probes for detecting in vivo cancer metastases. *Mol Pharm* 6(2):386–395
38. Vaupel P, Kallinowski F, Okunieff P (1989) Blood flow, oxygen and nutrient supply, and metabolic microenvironment of human tumors: a review. *Cancer Res* 49(23):6449–6465
39. Gatenby RA, Gillies RJ (2008) A microenvironmental model of carcinogenesis. *Nat Rev Cancer* 8(1):56–61
40. Hashim AI, Zhang X, Wojtkowiak JW, Martinez GV, Gillies RJ (2011) Imaging pH and metastasis. *NMR Biomed* 24(6):582–591
41. Cesen MH, Pegan K, Spes A, Turk B (2012) Lysosomal pathways to cell death and their therapeutic applications. *Exp Cell Res* 318(11):1245–1251
42. Rodrigues PC, Beyer U, Schumacher P, Roth T, Fiebig HH, Unger C, Messori L, Orioli P et al (1999) Acid-sensitive polyethylene glycol conjugates of doxorubicin: preparation, in vitro efficacy and intracellular distribution. *Bioorg Med Chem* 7(11):2517–2524
43. MacKay JA, Chen M, McDaniel JR, Liu W, Simnick AJ, Chilkoti A (2009) Self-assembling chimeric polypeptide-doxorubicin conjugate nanoparticles that abolish tumours after a single injection. *Nat Mater* 8(12):993–999
44. Park HS, Lee JE, Cho MY, Hong JH, Cho SH, Lim YT (2012) Hyaluronic acid/poly(beta-amino ester) polymer nanogels for cancer-cell-specific NIR fluorescence switch. *Macromol Rapid Commun* 33(18):1549–1555
45. Murthy N, Thng YX, Schuck S, Xu MC, Frechet JM (2002) A novel strategy for encapsulation and release of proteins: hydrogels and microgels with acid-labile acetal cross-linkers. *J Am Chem Soc* 124(42):12398–12399
46. Indira Chandran V, Matesic L, Locke JM, Skropeta D, Ranson M, Vine KL (2012) Anti-cancer activity of an acid-labile N-alkylisatin conjugate targeting the transferrin receptor. *Cancer Lett* 316(2):151–156
47. Barth BM, Sharma R, Altinoglu EI, Morgan TT, Shanmugavelandy SS, Kaiser JM, McGovern C, Matters GL et al (2010) Bioconjugation of calcium phosphosilicate composite nanoparticles for selective targeting of human breast and pancreatic cancers in vivo. *ACS Nano* 4(3):1279–1287
48. Braslawsky GR, Edson MA, Pearce W, Kaneko T, Greenfield RS (1990) Antitumor activity of adriamycin (hydrazone-linked) immunoconjugates compared with free adriamycin and specificity of tumor cell killing. *Cancer Res* 50(20):6608–6614
49. Colombo PE, Boussta M, Poujol S, Jarlier M, Bressolle F, Teulon I, Ladjemi MZ, Pinguet F et al (2011) Intraperitoneal administration of novel doxorubicin loaded polymeric delivery systems against peritoneal carcinomatosis: experimental study in a murine model of ovarian cancer. *Gynecol Oncol* 122(3):632–640
50. Chen X, Parelkar SS, Henchey E, Schneider S, Emrick T (2012) PolyMPC-Doxorubicin prodrugs. *Bioconjug Chem* 23(9):1753–1763
51. Lin CH, Cheng SH, Liao WN, Wei PR, Sung PJ, Weng CF, Lee CH (2012) Mesoporous silica nanoparticles for the improved anticancer efficacy of cis-platin. *Int J Pharm* 429(1–2):138–147
52. Kiziltepe T, Ashley JD, Stefanick JF, Qi YM, Alves NJ, Handlogten MW, Suckow MA, Navari RM et al (2012) Rationally engineered nanoparticles target multiple myeloma cells, overcome cell-adhesion-mediated drug resistance, and show enhanced efficacy in vivo. *Blood Cancer J* 2(4):1–10
53. Moktan S, Perkins E, Kratz F, Raucher D (2012) Thermal targeting of an acid-sensitive doxorubicin conjugate of elastin-like polypeptide enhances the therapeutic efficacy compared to the parent compound in vivo. *Mol Cancer Ther* 11(7):1547–1556
54. Orban E, Mezo G, Schlage P, Csik G, Kulic Z, Ansorge P, Fellingner E, Moller HM et al (2011) In vitro degradation and antitumor activity of oxime bond-linked daunorubicin-GnRH-III bioconjugates and DNA-binding properties of daunorubicin-amino acid metabolites. *Amino Acids* 41(2):469–483

55. Szabo I, Manea M, Orban E, Csampai A, Bosze S, Szabo R, Tejeda M, Gaal D et al (2009) Development of an oxime bond containing daunorubicin-gonadotropin-releasing hormone-III conjugate as a potential anticancer drug. *Bioconjug Chem* 20(4):656–665
56. Carmona S, Jorgensen MR, Kolli S, Crowther C, Salazar FH, Marion PL, Fujino M, Natori Y et al (2009) Controlling HBV replication in vivo by intravenous administration of triggered PEGylated siRNA-nanoparticles. *Mol Pharm* 6(3):706–717
57. Jin Y, Song L, Su Y, Zhu L, Pang Y, Qiu F, Tong G, Yan D et al (2011) Oxime linkage: a robust tool for the design of pH-sensitive polymeric drug carriers. *Biomacromolecules* 12(10):3460–3468
58. Kalia J, Raines RT (2008) Hydrolytic stability of hydrazones and oximes. *Angew Chem Int Ed Engl* 47(39):7523–7526
59. Oishi M, Nagasaki Y, Itaka K, Nishiyama N, Kataoka K (2005) Lactosylated poly(ethylene glycol)-siRNA conjugate through acid-labile beta-thiopropionate linkage to construct pH-sensitive polyion complex micelles achieving enhanced gene silencing in hepatoma cells. *J Am Chem Soc* 127(6):1624–1625
60. Jeong JH, Kim SW, Park TG (2003) Novel intracellular delivery system of antisense oligonucleotide by self-assembled hybrid micelles composed of DNA/PEG conjugate and cationic fusogenic peptide. *Bioconjug Chem* 14(2):473–479
61. Ali MM, Oishi M, Nagatsugi F, Mori K, Nagasaki Y, Kataoka K, Sasaki S (2006) Intracellular inducible alkylation system that exhibits antisense effects with greater potency and selectivity than the natural oligonucleotide. *Angew Chem Int Ed Engl* 45(19):3136–3140
62. Oishi M, Nagatsugi F, Sasaki S, Nagasaki Y, Kataoka K (2005) Smart polyion complex micelles for targeted intracellular delivery of PEGylated antisense oligonucleotides containing acid-labile linkages. *Chem Bio Chem* 6(4):718–725
63. Vicent MJ, Tomlinson R, Brocchini S, Duncan R (2004) Polyacetal-diethylstilboestrol: a polymeric drug designed for pH-triggered activation. *J Drug Target* 12(8):491–501
64. Tomlinson R, Heller J, Brocchini S, Duncan R (2003) Polyacetal-doxorubicin conjugates designed for pH-dependent degradation. *Bioconjug Chem* 14(6):1096–1106
65. Su J, Chen F, Cryns VL, Messersmith PB (2011) Catechol polymers for pH-responsive, targeted drug delivery to cancer cells. *J Am Chem Soc* 133(31):11850–11853
66. Cr K, Thapa B, Xu P (2012) pH and redox dual responsive nanoparticle for nuclear targeted drug delivery. *Mol Pharm* 9(9):2719–2729
67. Bae Y, Alani AW, Rockich NC, Lai TS, Kwon GS (2010) Mixed pH-sensitive polymeric micelles for combination drug delivery. *Pharm Res* 27(11):2421–2432
68. Zhu S, Lansakara PD, Li X, Cui Z (2012) Lysosomal delivery of a lipophilic gemcitabine prodrug using novel acid-sensitive micelles improved its antitumor activity. *Bioconjug Chem* 23(5):966–980
69. Wang B, Xu C, Xie J, Yang Z, Sun S (2008) pH controlled release of chromone from chromone-Fe₃O₄ nanoparticles. *J Am Chem Soc* 130(44):14436–14437
70. Xu S, Luo Y, Graeser R, Warnecke A, Kratz F, Hauff P, Licha K, Haag R (2009) Development of pH-responsive core-shell nanocarriers for delivery of therapeutic and diagnostic agents. *Bioorg Med Chem Lett* 19(3):1030–1034
71. Griset AP, Walpole J, Liu R, Gaffey A, Colson YL, Grinstaff MW (2009) Expansile nanoparticles: synthesis, characterization, and in vivo efficacy of an acid-responsive polymeric drug delivery system. *J Am Chem Soc* 131(7):2469–2471
72. Xu Z, Gu W, Chen L, Gao Y, Zhang Z, Li Y (2008) A smart nanoassembly consisting of acid-labile vinyl ether PEG-DOPE and protamine for gene delivery: preparation and in vitro transfection. *Biomacromolecules* 9(11):3119–3126
73. Koren E, Apte A, Jani A, Torchilin VP (2012) Multifunctional PEGylated 2C5-immunoliposomes containing pH-sensitive bonds and TAT peptide for enhanced tumor cell internalization and cytotoxicity. *J Control Release* 160(2):264–273
74. Lee ES, Na K, Bae YH (2003) Polymeric micelle for tumor pH and folate-mediated targeting. *J Control Release* 91(1–2):103–113

75. Lee ES, Na K, Bae YH (2005) Doxorubicin loaded pH-sensitive polymeric micelles for reversal of resistant MCF-7 tumor. *J Control Release* 103(2):405–418
76. Song W, Tang Z, Li M, Lv S, Yu H, Ma L, Zhuang X, Huang Y et al (2012) Tunable pH-sensitive poly(beta-amino ester)s synthesized from primary amines and diacrylates for intracellular drug delivery. *Macromol Biosci* 12(10):1375–1383
77. Kim JH, Li Y, Kim MS, Kang SW, Jeong JH, Lee DS (2012) Synthesis and evaluation of biotin-conjugated pH-responsive polymeric micelles as drug carriers. *Int J Pharm* 427(2):435–442
78. Shen Y, Tang H, Zhan Y, Van Kirk EA, Murdoch WJ (2009) Degradable poly(beta-amino ester) nanoparticles for cancer cytoplasmic drug delivery. *Nanomedicine* 5(2):192–201
79. Koo H, Lee H, Lee S, Min KH, Kim MS, Lee DS, Choi Y, Kwon IC et al (2010) In vivo tumor diagnosis and photodynamic therapy via tumoral pH-responsive polymeric micelles. *Chem Commun (Camb)* 46(31):5668–5670
80. Gao GH, Lee JW, Nguyen MK, Im GH, Yang J, Heo H, Jeon P, Park TG et al (2011) pH-responsive polymeric micelle based on PEG-poly(beta-amino ester)/(amido amine) as intelligent vehicle for magnetic resonance imaging in detection of cerebral ischemic area. *J Control Release* 155(1):11–17
81. Kim D, Lee ES, Park K, Kwon IC, Bae YH (2008) Doxorubicin loaded pH-sensitive micelle: antitumoral efficacy against ovarian A2780/DOXR tumor. *Pharm Res* 25(9):2074–2082
82. Kondo S, Yamamoto K, Sawama Y, Sasai Y, Yamauchi Y, Kuzuya M (2011) Characterization of novel pH-sensitive polymeric micelles prepared by the self-assembly of amphiphilic block copolymer with poly-4-vinylpyridine block synthesized by mechanochemical solid-state polymerization. *Chem Pharm Bull (Tokyo)* 59(9):1200–1202
83. Kester M, Heikal Y, Fox T, Sharma A, Robertson GP, Morgan TT, Altinoglu EI, Tabakovic A et al (2008) Calcium phosphate nanocomposite particles for in vitro imaging and encapsulated chemotherapeutic drug delivery to cancer cells. *Nano Lett* 8(12):4116–4121
84. Barroug A, Glimcher MJ (2002) Hydroxyapatite crystals as a local delivery system for cisplatin: adsorption and release of cisplatin in vitro. *J Orthop Res* 20(2):274–280
85. Min KH, Lee HJ, Kim K, Kwon IC, Jeong SY, Lee SC (2012) The tumor accumulation and therapeutic efficacy of doxorubicin carried in calcium phosphate-reinforced polymer nanoparticles. *Biomaterials* 33(23):5788–5797
86. Muhammad F, Guo M, Qi W, Sun F, Wang A, Guo Y, Zhu G (2011) pH-triggered controlled drug release from mesoporous silica nanoparticles via intracellular dissolution of ZnO nanolids. *J Am Chem Soc* 133(23):8778–8781
87. Fiallo MM, Garnier-Suillerot A, Matzanke B, Kozlowski H (1999) How Fe³⁺ binds anthracycline antitumour compounds. The myth and the reality of a chemical sphinx. *J Inorg Biochem* 75(2):105–115
88. Chen Y, Wan Y, Wang Y, Zhang H, Jiao Z (2011) Anticancer efficacy enhancement and attenuation of side effects of doxorubicin with titanium dioxide nanoparticles. *Int J Nanomedicine* 6:2321–2326
89. Chen Y, Chen H, Zhang S, Chen F, Sun S, He Q, Ma M, Wang X et al (2012) Structure-property relationships in manganese oxide-mesoporous silica nanoparticles used for T1-weighted MRI and simultaneous anti-cancer drug delivery. *Biomaterials* 33(7):2388–2398
90. Shin J, Anisur RM, Ko MK, Im GH, Lee JH, Lee IS (2009) Hollow manganese oxide nanoparticles as multifunctional agents for magnetic resonance imaging and drug delivery. *Angew Chem Int Ed Engl* 48(2):321–324
91. Zhang H, Wang C, Chen B, Wang X (2012) Daunorubicin-TiO₂ nanocomposites as a “smart” pH-responsive drug delivery system. *Int J Nanomedicine* 7:235–242
92. Muhammad F, Guo M, Guo Y, Qi W, Qu F, Sun F, Zhao H, Zhu G (2011) Acid degradable ZnO quantum dots as a platform for targeted delivery of an anticancer drug. *J Mater Chem* 21(35):13406–13412

93. Na HB, Lee JH, An K, Park YI, Park M, Lee IS, Nam DH, Kim ST et al (2007) Development of a T1 contrast agent for magnetic resonance imaging using MnO nanoparticles. *Angew Chem Int Ed Engl* 46(28):5397–5401
94. Deepa G, Thulasidasan AK, Anto RJ, Pillai JJ, Kumar GS (2012) Cross-linked acrylic hydrogel for the controlled delivery of hydrophobic drugs in cancer therapy. *Int J Nanomedicine* 7:4077–4088
95. Zhang H, Mardiyani S, Chan WC, Kumacheva E (2006) Design of biocompatible chitosan microgels for targeted pH-mediated intracellular release of cancer therapeutics. *Biomacromolecules* 7(5):1568–1572
96. Zhou T, Xiao C, Fan J, Chen S, Shen J, Wu W, Zhou S (2012) A nanogel of on-site tunable pH-response for efficient anticancer drug delivery. *Acta Biomater* 9(1):4546–4557
97. Wu W, Shen J, Banerjee P, Zhou S (2010) Chitosan-based responsive hybrid nanogels for integration of optical pH-sensing, tumor cell imaging and controlled drug delivery. *Biomaterials* 31(32):8371–8381
98. Duan C, Zhang D, Wang F, Zheng D, Jia L, Feng F, Liu Y, Wang Y et al (2011) Chitosan-g-poly(N-isopropylacrylamide) based nanogels for tumor extracellular targeting. *Int J Pharm* 409(1):252–259
99. Andresen TL, Thompson DH, Kaasgaard T (2010) Enzyme-triggered nanomedicine: drug release strategies in cancer therapy. *Mol Membr Biol* 27(7):353–363
100. Law B, Tung CH (2009) Proteolysis: a biological process adapted in drug delivery, therapy, and imaging. *Bioconjug Chem* 20(9):1683–1695
101. Puente XS, Sanchez LM, Gutierrez-Fernandez A, Velasco G, Lopez-Otin C (2005) A genomic view of the complexity of mammalian proteolytic systems. *Biochem Soc Trans* 33(Pt 2):331–334
102. Silk DB (1980) Digestion and absorption of dietary protein in man. *Proc Nutr Soc* 39(1):61–70
103. Nilsson IM (1987) Coagulation and fibrinolysis. *Scand J Gastroenterol Suppl* 137:11–18
104. Tong W, Zhang L (2012) Fetal hypoxia and programming of matrix metalloproteinases. *Drug Discov Today* 17(3–4):124–134
105. Hyman BT, Yuan J (2012) Apoptotic and non-apoptotic roles of caspases in neuronal physiology and pathophysiology. *Nat Rev Neurosci* 13(6):395–406
106. Cipollone F, Prontera C, Pini B, Marini M, Fazio M, De Cesare D, Iezzi A, Uchino S et al (2001) Overexpression of functionally coupled cyclooxygenase-2 and prostaglandin E synthase in symptomatic atherosclerotic plaques as a basis of prostaglandin E(2)-dependent plaque instability. *Circulation* 104(8):921–927
107. Loftus IM, Naylor AR, Goodall S, Crowther M, Jones L, Bell PR, Thompson MM (2000) Increased matrix metalloproteinase-9 activity in unstable carotid plaques. A potential role in acute plaque disruption. *Stroke* 31(1):40–47
108. Papalambros E, Sigala F, Georgopoulos S, Panou N, Kavatzas N, Agapitos M, Bastounis E (2004) Vascular endothelial growth factor and matrix metalloproteinase 9 expression in human carotid atherosclerotic plaques: relationship with plaque destabilization via neovascularization. *Cerebrovasc Dis* 18(2):160–165
109. Baruah DB, Dash RN, Chaudhari MR, Kadam SS (2006) Plasminogen activators: a comparison. *Vascul Pharmacol* 44(1):1–9
110. Burrage PS, Mix KS, Brinckerhoff CE (2006) Matrix metalloproteinases: role in arthritis. *Front Biosci* 11:529–543
111. Gueders MM, Foidart JM, Noel A, Cataldo DD (2006) Matrix metalloproteinases (MMPs) and tissue inhibitors of MMPs in the respiratory tract: potential implications in asthma and other lung diseases. *Eur J Pharmacol* 533(1–3):133–144
112. Churg A, Wright JL (2005) Proteases and emphysema. *Curr Opin Pulm Med* 11(2):153–159
113. Deaton DN, Tavares FX (2005) Design of cathepsin K inhibitors for osteoporosis. *Curr Top Med Chem* 5(16):1639–1675
114. Kobayashi H, Schmitt M, Goretzki L, Chucholowski N, Calvete J, Kramer M, Gunzler WA, Janicke F et al (1991) Cathepsin B efficiently activates the soluble and the tumor cell

- receptor-bound form of the proenzyme urokinase-type plasminogen activator (Pro-uPA). *J Biol Chem* 266(8):5147–5152
115. Nabeshima K, Inoue T, Shimao Y, Sameshima T (2002) Matrix metalloproteinases in tumor invasion: role for cell migration. *Pathol Int* 52(4):255–264
 116. Blasi F, Carmeliet P (2002) uPAR: a versatile signalling orchestrator. *Nat Rev Mol Cell Biol* 3(12):932–943
 117. Lee M, Fridman R, Mobashery S (2004) Extracellular proteases as targets for treatment of cancer metastases. *Chem Soc Rev* 33(7):401–409
 118. Koblinski JE, Ahram M, Sloane BF (2000) Unraveling the role of proteases in cancer. *Clin Chim Acta* 291(2):113–135
 119. Maly DJ, Huang L, Ellman JA (2002) Combinatorial strategies for targeting protein families: application to the proteases. *Chem Bio Chem* 3(1):16–37
 120. Aureli L, Gioia M, Cerbara I, Monaco S, Fasciglione GF, Marini S, Ascenzi P, Topai A et al (2008) Structural bases for substrate and inhibitor recognition by matrix metalloproteinases. *Curr Med Chem* 15(22):2192–2222
 121. Carl PL, Chakravarty PK, Katzenellenbogen JA, Weber MJ (1980) Protease-activated “prodrugs” for cancer chemotherapy. *Proc Natl Acad Sci USA* 77(4):2224–2228
 122. Chakravarty PK, Carl PL, Weber MJ, Katzenellenbogen JA (1983) Plasmin-activated prodrugs for cancer chemotherapy. 1. Synthesis and biological activity of peptidylacivicin and peptidylphenylenediamine mustard. *J Med Chem* 26(5):633–638
 123. Balajthy Z, Aradi J, Kiss IT, Elodi P (1992) Synthesis and functional evaluation of a peptide derivative of 1-beta-D-arabinofuranosylcytosine. *J Med Chem* 35(18):3344–3349
 124. Albright CF, Graciani N, Han W, Yue E, Stein R, Lai Z, Diamond M, Dowling R et al (2005) Matrix metalloproteinase-activated doxorubicin prodrugs inhibit HT1080 xenograft growth better than doxorubicin with less toxicity. *Mol Cancer Ther* 4(5):751–760
 125. Timar F, Botyanszki J, Suli-Vargha H, Babo I, Olah J, Pogany G, Jeney A (1998) The antiproliferative action of a melphalan hexapeptide with collagenase-cleavable site. *Cancer Chemother Pharmacol* 41(4):292–298
 126. Kline T, Torgov MY, Mendelsohn BA, Cerveny CG, Senter PD (2004) Novel antitumor prodrugs designed for activation by matrix metalloproteinases-2 and -9. *Mol Pharm* 1(1):9–22
 127. DeFeo-Jones D, Brady SF, Feng DM, Wong BK, Bolyar T, Haskell K, Kiefer DM, Leander K et al (2002) A prostate-specific antigen (PSA)-activated vinblastine prodrug selectively kills PSA-secreting cells in vivo. *Mol Cancer Ther* 1(7):451–459
 128. Denmeade SR, Nagy A, Gao J, Lilja H, Schally AV, Isaacs JT (1998) Enzymatic activation of a doxorubicin-peptide prodrug by prostate-specific antigen. *Cancer Res* 58(12):2537–2540
 129. DeFeo-Jones D, Garsky VM, Wong BK, Feng DM, Bolyar T, Haskell K, Kiefer DM, Leander K et al (2000) A peptide-doxorubicin ‘prodrug’ activated by prostate-specific antigen selectively kills prostate tumor cells positive for prostate-specific antigen in vivo. *Nat Med* 6(11):1248–1252
 130. DiPaola RS, Rinehart J, Nemunaitis J, Ebbinghaus S, Rubin E, Capanna T, Ciardella M, Doyle-Lindrud S et al (2002) Characterization of a novel prostate-specific antigen-activated peptide-doxorubicin conjugate in patients with prostate cancer. *J Clin Oncol* 20(7):1874–1879
 131. Szeto HH, Lovelace JL, Fridland G, Soong Y, Fasolo J, Wu D, Desiderio DM, Schiller PW (2001) In vivo pharmacokinetics of selective mu-opioid peptide agonists. *J Pharmacol Exp Ther* 298(1):57–61
 132. Doronina SO, Toki BE, Torgov MY, Mendelsohn BA, Cerveny CG, Chace DF, DeBlanc RL, Gearing RP et al (2003) Development of potent monoclonal antibody auristatin conjugates for cancer therapy. *Nat Biotechnol* 21(7):778–784
 133. Gualberto A (2012) Brentuximab Vedotin (SGN-35), an antibody-drug conjugate for the treatment of CD30-positive malignancies. *Expert Opin Investig Drugs* 21(2):205–216

134. Gianolio DA, Rouleau C, Bauta WE, Lovett D, Cantrell WR Jr, Recio A 3rd, Wolstenholme-Hogg P, Busch M et al (2012) Targeting HER2-positive cancer with dolastatin 15 derivatives conjugated to trastuzumab, novel antibody-drug conjugates. *Cancer Chemother Pharmacol* 70(3):439–449
135. Elsadek B, Graeser R, Esser N, Schafer-Obodozie C, Abu Ajaj K, Unger C, Warnecke A, Saleem T et al (2010) Development of a novel prodrug of paclitaxel that is cleaved by prostate-specific antigen: an in vitro and in vivo evaluation study. *Eur J Cancer* 46(18):3434–3444
136. Palandoken H, By K, Hegde M, Harley WR, Gorin FA, Nantz MH (2005) Amiloride peptide conjugates: prodrugs for sodium-proton exchange inhibition. *J Pharmacol Exp Ther* 312(3):961–967
137. Kumar SK, Roy I, Anchoori RK, Fazli S, Maitra A, Beachy PA, Khan SR (2008) Targeted inhibition of hedgehog signaling by cyclopamine prodrugs for advanced prostate cancer. *Bioorg Med Chem* 16(6):2764–2768
138. Jiang Y, Dipaola RS, Hu L (2009) Synthesis and stereochemical preference of peptide 4-aminocyclophosphamide conjugates as potential prodrugs of phosphoramidate mustard for activation by prostate-specific antigen (PSA). *Bioorg Med Chem Lett* 19(9):2587–2590
139. Dubois V, Nieder M, Collot F, Negrouk A, Nguyen TT, Gangwar S, Reitz B, Wattiez R et al (2006) Thimet oligopeptidase (EC 3.4.24.15) activates CPI-0004Na, an extracellularly tumour-activated prodrug of doxorubicin. *Eur J Cancer* 42(17):3049–3056
140. Shi NQ, Gao W, Xiang B, Qi XR (2012) Enhancing cellular uptake of activable cell-penetrating peptide-doxorubicin conjugate by enzymatic cleavage. *Int J Nanomedicine* 7:1613–1621
141. Lim SH, Jeong YI, Moon KS, Ryu HH, Jin YH, Jin SG, Jung TY, Kim IY et al (2010) Anticancer activity of PEGylated matrix metalloproteinase cleavable peptide-conjugated adriamycin against malignant glioma cells. *Int J Pharm* 387(1–2):209–214
142. de Groot FM, Broxterman HJ, Adams HP, van Vliet A, Tesser GI, Elderkamp YW, Schraa AJ, Kok RJ et al (2002) Design, synthesis, and biological evaluation of a dual tumor-specific motive containing integrin-targeted plasmin-cleavable doxorubicin prodrug. *Mol Cancer Ther* 1(11):901–911
143. de Groot FM, de Bart AC, Verheijen JH, Scheeren HW (1999) Synthesis and biological evaluation of novel prodrugs of anthracyclines for selective activation by the tumor-associated protease plasmin. *J Med Chem* 42(25):5277–5283
144. Graeser R, Chung DE, Esser N, Moor S, Schachtele C, Unger C, Kratz F (2008) Synthesis and biological evaluation of an albumin-binding prodrug of doxorubicin that is cleaved by prostate-specific antigen (PSA) in a PSA-positive orthotopic prostate carcinoma model (LNCaP). *Int J Cancer* 122(5):1145–1154
145. Liu C, Sun C, Huang H, Janda K, Edgington T (2003) Overexpression of legumain in tumors is significant for invasion/metastasis and a candidate enzymatic target for prodrug therapy. *Cancer Res* 63(11):2957–2964
146. Mhaka A, Denmeade SR, Yao W, Isaacs JT, Khan SR (2002) A 5-fluorodeoxyuridine prodrug as targeted therapy for prostate cancer. *Bioorg Med Chem Lett* 12(17):2459–2461
147. Tanihara M, Suzuki Y, Nishimura Y, Suzuki K, Kakimaru Y, Fukunishi Y (1999) A novel microbial infection-responsive drug release system. *J Pharm Sci* 88(5):510–514
148. Fiehn C, Kratz F, Sass G, Muller-Ladner U, Neumann E (2008) Targeted drug delivery by in vivo coupling to endogenous albumin: an albumin-binding prodrug of methotrexate (MTX) is better than MTX in the treatment of murine collagen-induced arthritis. *Ann Rheum Dis* 67(8):1188–1191
149. de Groot FM, Loos WJ, Koekkoek R, van Berkomp LW, Busscher GF, Seelen AE, Albrecht C, de Bruijn P et al (2001) Elongated multiple electronic cascade and cyclization spacer systems in activatable anticancer prodrugs for enhanced drug release. *J Org Chem* 66(26):8815–8830

150. Liang L, Lin SW, Dai W, Lu JK, Yang TY, Xiang Y, Zhang Y, Li RT et al (2012) Novel cathepsin B-sensitive paclitaxel conjugate: Higher water solubility, better efficacy and lower toxicity. *J Control Release* 160(3):618–629
151. Yamada R, Kostova MB, Anchoori RK, Xu S, Neamati N, Khan SR (2010) Biological evaluation of paclitaxel-peptide conjugates as a model for MMP2-targeted drug delivery. *Cancer Biol Ther* 9(3):192–203
152. Lo PC, Chen J, Stefflova K, Warren MS, Navab R, Bandarchi B, Mullins S, Tsao M et al (2009) Photodynamic molecular beacon triggered by fibroblast activation protein on cancer-associated fibroblasts for diagnosis and treatment of epithelial cancers. *J Med Chem* 52(2):358–368
153. Chen J, Stefflova K, Niedre MJ, Wilson BC, Chance B, Glickson JD, Zheng G (2004) Protease-triggered photosensitizing beacon based on singlet oxygen quenching and activation. *J Am Chem Soc* 126(37):11450–11451
154. Tai W, Shukla RS, Qin B, Li B, Cheng K (2011) Development of a peptide-drug conjugate for prostate cancer therapy. *Mol Pharm* 8(3):901–912
155. Denmeade SR, Jakobsen CM, Janssen S, Khan SR, Garrett ES, Lilja H, Christensen SB, Isaacs JT (2003) Prostate-specific antigen-activated thapsigargin prodrug as targeted therapy for prostate cancer. *J Natl Cancer Inst* 95(13):990–1000
156. Janssen S, Jakobsen CM, Rosen DM, Ricklis RM, Reineke U, Christensen SB, Lilja H, Denmeade SR (2004) Screening a combinatorial peptide library to develop a human glandular kallikrein 2-activated prodrug as targeted therapy for prostate cancer. *Mol Cancer Ther* 3(11):1439–1450
157. Pan H, Kopeckova P, Wang D, Yang J, Miller S, Kopecek J (2006) Water-soluble HPMA copolymer–prostaglandin E1 conjugates containing a cathepsin K sensitive spacer. *J Drug Target* 14(6):425–435
158. Pan H, Liu J, Dong Y, Sima M, Kopeckova P, Brandi ML, Kopecek J (2008) Release of prostaglandin E(1) from N-(2-hydroxypropyl)methacrylamide copolymer conjugates by bone cells. *Macromol Biosci* 8(7):599–605
159. Putnam D, Kopecek J (1995) Enantioselective release of 5-fluorouracil from N-(2-hydroxypropyl)methacrylamide-based copolymers via lysosomal enzymes. *Bioconjug Chem* 6(4):483–492
160. Seymour LW, Ferry DR, Kerr DJ, Rea D, Whitlock M, Poyner R, Boivin C, Hesselwood S et al (2009) Phase II studies of polymer-doxorubicin (PK1, FCE28068) in the treatment of breast, lung and colorectal cancer. *Int J Oncol* 34(6):1629–1636
161. Etrych T, Kovar L, Strohalm J, Chytil P, Rihova B, Ulbrich K (2011) Biodegradable star HPMA polymer-drug conjugates: Biodegradability, distribution and anti-tumor efficacy. *J Control Release* 154(3):241–248
162. Duncan R, Kopeckova P, Strohalm J, Hume IC, Lloyd JB, Kopecek J (1988) Anticancer agents coupled to N-(2-hydroxypropyl)methacrylamide copolymers. II. Evaluation of daunomycin conjugates in vivo against L1210 leukaemia. *Br J Cancer* 57(2):147–156
163. Gianasi E, Buckley RG, Latigo J, Wasil M, Duncan R (2002) HPMA copolymers platinates containing dicarboxylate ligands. Preparation, characterisation and in vitro and in vivo evaluation. *J Drug Target* 10(7):549–556
164. Satchi-Fainaro R, Puder M, Davies JW, Tran HT, Sampson DA, Greene AK, Corfas G, Folkman J (2004) Targeting angiogenesis with a conjugate of HPMA copolymer and TNP-470. *Nat Med* 10(3):255–261
165. Potrich C, Tomazzolli R, Dalla Serra M, Anderluh G, Malovrh P, Macek P, Menestrina G, Tejuca M (2005) Cytotoxic activity of a tumor protease-activated pore-forming toxin. *Bioconjug Chem* 16(2):369–376
166. Schmid B, Chung DE, Warnecke A, Fichtner I, Kratz F (2007) Albumin-binding prodrugs of camptothecin and doxorubicin with an Ala-Leu-Ala-Leu-linker that are cleaved by cathepsin B: synthesis and antitumor efficacy. *Bioconjug Chem* 18(3):702–716

167. Abu Ajaj K, Graeser R, Fichtner I, Kratz F (2009) In vitro and in vivo study of an albumin-binding prodrug of doxorubicin that is cleaved by cathepsin B. *Cancer Chemother Pharmacol* 64(2):413–418
168. Mansour AM, Dreves J, Esser N, Hamada FM, Badary OA, Unger C, Fichtner I, Kratz F (2003) A new approach for the treatment of malignant melanoma: enhanced antitumor efficacy of an albumin-binding doxorubicin prodrug that is cleaved by matrix metalloproteinase 2. *Cancer Res* 63(14):4062–4066
169. Kratz F, Dreves J, Bing G, Stockmar C, Scheuermann K, Lazar P, Unger C (2001) Development and in vitro efficacy of novel MMP2 and MMP9 specific doxorubicin albumin conjugates. *Bioorg Med Chem Lett* 11(15):2001–2006
170. Chung DE, Kratz F (2006) Development of a novel albumin-binding prodrug that is cleaved by urokinase-type-plasminogen activator (uPA). *Bioorg Med Chem Lett* 16(19):5157–5163
171. Shiose Y, Ochi Y, Kuga H, Yamashita F, Hashida M (2007) Relationship between drug release of DE-310, macromolecular prodrug of DX-8951f, and cathepsins activity in several tumors. *Biol Pharm Bull* 30(12):2365–2370
172. Chau Y, Dang NM, Tan FE, Langer R (2006) Investigation of targeting mechanism of new dextran-peptide-methotrexate conjugates using biodistribution study in matrix-metalloproteinase-overexpressing tumor xenograft model. *J Pharm Sci* 95(3):542–551
173. Chandran SS, Nan A, Rosen DM, Ghandehari H, Dennebde SR (2007) A prostate-specific antigen activated N-(2-hydroxypropyl) methacrylamide copolymer prodrug as dual-targeted therapy for prostate cancer. *Mol Cancer Ther* 6(11):2928–2937
174. Chipman SD, Oldham FB, Pezzoni G, Singer JW (2006) Biological and clinical characterization of paclitaxel polyglumex (PPX, CT-2103), a macromolecular polymer-drug conjugate. *Int J Nanomedicine* 1(4):375–383
175. Dan AG, Saha S, Monson KM, Wiese D, Schochet E, Barber KR, Ganatra B, Desai D et al (2004) 1 % lymphazurin vs 10 % fluorescein for sentinel node mapping in colorectal tumors. *Arch Surg* 139(11):1180–1184
176. Dettler C, Russ D, Iffland A, Wipper S, Schurr MO, Reichenspurner H, Buess G, Reichart B (2002) Near-infrared fluorescence coronary angiography: a new noninvasive technology for intraoperative graft patency control. *Heart Surg Forum* 5(4):364–369
177. Lane PM, Lam S, McWilliams A, Leriche JC, Anderson MW, Macaulay CE (2009) Confocal fluorescence microendoscopy of bronchial epithelium. *J Biomed Opt* 14(2):024008
178. Albayrak Y, Oren D, Gundogdu C, Kurt A (2011) Intraoperative sentinel lymph node mapping in patients with colon cancer: study of 38 cases. *Turk J Gastroenterol* 22(3):286–292
179. Varghese P, Abdel-Rahman AT, Akberali S, Mostafa A, Gattuso JM, Carpenter R (2008) Methylene blue dye—a safe and effective alternative for sentinel lymph node localization. *Breast J* 14(1):61–67
180. Goetz M, Toerner T, Vieth M, Dunbar K, Hoffman A, Galle PR, Neurath MF, Delaney P et al (2009) Simultaneous confocal laser endomicroscopy and chromoendoscopy with topical cresyl violet. *Gastrointest Endosc* 70(5):959–968
181. Xia Zhang, Lovejoy KS, Jasanoff A, Lippard SJ (2007) Water-soluble porphyrins as a dual-function molecular imaging platform for MRI and fluorescence zinc sensing. *Proc Natl Acad Sci USA* 104(26):10780–10785
182. Law B, Curino A, Bugge TH, Weissleder R, Tung CH (2004) Design, synthesis, and characterization of urokinase plasminogen-activator-sensitive near-infrared reporter. *Chem Biol* 11(1):99–106
183. Hsiao JK, Law B, Weissleder R, Tung CH (2006) In-vivo imaging of tumor associated urokinase-type plasminogen activator activity. *J Biomed Opt* 11(3):34013
184. Tung CH, Mahmood U, Bredow S, Weissleder R (2000) In vivo imaging of proteolytic enzyme activity using a novel molecular reporter. *Cancer Res* 60(17):4953–4958

185. Abd-Elgaliel WR, Cruz-Monserrate Z, Logsdon CD, Tung CH (2011) Molecular imaging of cathepsin E-positive tumors in mice using a novel protease-activatable fluorescent probe. *Mol BioSyst* 7(12):3207–3213
186. Jaffer FA, Kim DE, Quinti L, Tung CH, Aikawa E, Pande AN, Kohler RH, Shi GP et al (2007) Optical visualization of cathepsin K activity in atherosclerosis with a novel, protease-activatable fluorescence sensor. *Circulation* 115(17):2292–2298
187. Bremer C, Bredow S, Mahmood U, Weissleder R, Tung CH (2001) Optical imaging of matrix metalloproteinase-2 activity in tumors: feasibility study in a mouse model. *Radiology* 221(2):523–529
188. Bremer C, Tung CH, Weissleder R (2001) In vivo molecular target assessment of matrix metalloproteinase inhibition. *Nat Med* 7(6):743–748
189. Messerli SM, Prabhakar S, Tang Y, Shah K, Cortes ML, Murthy V, Weissleder R, Breakefield XO et al (2004) A novel method for imaging apoptosis using a caspase-1 near-infrared fluorescent probe. *Neoplasia* 6(2):95–105
190. Lu Z, Yeh TK, Tsai M, Au JL, Wientjes MG (2004) Paclitaxel-loaded gelatin nanoparticles for intravesical bladder cancer therapy. *Clin Cancer Res* 10(22):7677–7684
191. Biswas A, Liu Y, Liu T, Fan G, Tang Y (2012) Polyethylene glycol-based protein nanocapsules for functional delivery of a differentiation transcription factor. *Biomaterials* 33(21):5459–5467
192. Clark MR, Aliyar HA, Lee CW, Jay JI, Gupta KM, Watson KM, Stewart RJ, Buckheit RW et al (2011) Enzymatic triggered release of an HIV-1 entry inhibitor from prostate specific antigen degradable microparticles. *Int J Pharm* 413(1–2):10–18
193. Fukami T, Yokoi T (2012) The emerging role of human esterases. *Drug Metab Pharmacokinet* 27(5):466–477
194. Montagnani F, Chiriatti A, Licitra S, Aliberti C, Fiorentini G (2010) Differences in efficacy and safety between capecitabine and infusional 5-fluorouracil when combined with irinotecan for the treatment of metastatic colorectal cancer. *Clin Colorectal Cancer* 9(4):243–247
195. Tang M, Mukundan M, Yang J, Charpentier N, LeCluyse EL, Black C, Yang D, Shi D et al (2006) Antiplatelet agents aspirin and clopidogrel are hydrolyzed by distinct carboxylesterases, and clopidogrel is transesterified in the presence of ethyl alcohol. *J Pharmacol Exp Ther* 319(3):1467–1476
196. Shi D, Yang J, Yang D, LeCluyse EL, Black C, You L, Akhlaghi F, Yan B (2006) Anti-influenza prodrug oseltamivir is activated by carboxylesterase human carboxylesterase 1, and the activation is inhibited by antiplatelet agent clopidogrel. *J Pharmacol Exp Ther* 319(3):1477–1484
197. Zhang J, Burnell JC, Dumaul N, Bosron WF (1999) Binding and hydrolysis of meperidine by human liver carboxylesterase hCE-1. *J Pharmacol Exp Ther* 290(1):314–318
198. Sun Z, Murry DJ, Sanghani SP, Davis WI, Kedishvili NY, Zou Q, Hurley TD, Bosron WF (2004) Methylphenidate is stereoselectively hydrolyzed by human carboxylesterase CES1A1. *J Pharmacol Exp Ther* 310(2):469–476
199. Howard MD, Lu X, Rinehart JJ, Jay M, Dziubla TD (2012) Carboxylesterase-triggered hydrolysis of nanoparticle PEGylating agents. *Langmuir* 28(33):12030–12037
200. Agostini A, Mondragon L, Pascual L, Aznar E, Coll C, Martinez-Manez R, Sancenon F, Soto J et al (2012) Design of enzyme-mediated controlled release systems based on silica mesoporous supports capped with ester-glycol groups. *Langmuir* 28(41):14766–14776
201. Azagarsamy MA, Sokkalingam P, Thayumanavan S (2009) Enzyme-triggered disassembly of dendrimer-based amphiphilic nanocontainers. *J Am Chem Soc* 131(40):14184–14185
202. Green PS, Mendez AJ, Jacob JS, Crowley JR, Growdon W, Hyman BT, Heinecke JW (2004) Neuronal expression of myeloperoxidase is increased in Alzheimer's disease. *J Neurochem* 90(3):724–733
203. Zhang R, Brennan ML, Fu X, Aviles RJ, Pearce GL, Penn MS, Topol EJ, Sprecher DL et al (2001) Association between myeloperoxidase levels and risk of coronary artery disease. *JAMA* 286(17):2136–2142

204. Choi DK, Pennathur S, Perier C, Tieu K, Teismann P, Wu DC, Jackson-Lewis V, Vila M et al (2005) Ablation of the inflammatory enzyme myeloperoxidase mitigates features of Parkinson's disease in mice. *J Neurosci* 25(28):6594–6600
205. Re G, Azzimondi G, Lanzarini C, Bassein L, Vaona I, Guarnieri C (1997) Plasma lipoperoxidative markers in ischaemic stroke suggest brain embolism. *Eur J Emerg Med* 4(1):5–9
206. Ishida-Okawara A, Oharaseki T, Takahashi K, Hashimoto Y, Aratani Y, Koyama H, Maeda N, Naoe S et al (2001) Contribution of myeloperoxidase to coronary artery vasculitis associated with MPO-ANCA production. *Inflammation* 25(6):381–387
207. Chen JW, Pham W, Weissleder R, Bogdanov A Jr (2004) Human myeloperoxidase: a potential target for molecular MR imaging in atherosclerosis. *Magn Reson Med* 52(5):1021–1028
208. Nahrendorf M, Sosnovik D, Chen JW, Panizzi P, Figueiredo JL, Aikawa E, Libby P, Swirski FK et al (2008) Activatable magnetic resonance imaging agent reports myeloperoxidase activity in healing infarcts and noninvasively detects the antiinflammatory effects of atorvastatin on ischemia-reperfusion injury. *Circulation* 117(9):1153–1160
209. Querol M, Chen JW, Weissleder R, Bogdanov A Jr (2005) DTPA-bisamide-based MR sensor agents for peroxidase imaging. *Org Lett* 7(9):1719–1722
210. Rodriguez E, Nilges M, Weissleder R, Chen JW (2010) Activatable magnetic resonance imaging agents for myeloperoxidase sensing: mechanism of activation, stability, and toxicity. *J Am Chem Soc* 132(1):168–177
211. Breckwoldt MO, Chen JW, Stangenberg L, Aikawa E, Rodriguez E, Qiu S, Moskowitz MA, Weissleder R (2008) Tracking the inflammatory response in stroke in vivo by sensing the enzyme myeloperoxidase. *Proc Natl Acad Sci USA* 105(47):18584–18589
212. Ronald JA, Chen JW, Chen Y, Hamilton AM, Rodriguez E, Reynolds F, Hegele RA, Rogers KA et al (2009) Enzyme-sensitive magnetic resonance imaging targeting myeloperoxidase identifies active inflammation in experimental rabbit atherosclerotic plaques. *Circulation* 120(7):592–599
213. Chen JW, Querol Sans M, Bogdanov A Jr, Weissleder R (2006) Imaging of myeloperoxidase in mice by using novel amplifiable paramagnetic substrates. *Radiology* 240(2):473–481
214. Kim JH, Lee S, Park K, Nam HY, Jang SY, Youn I, Kim K, Jeon H et al (2007) Protein-phosphorylation-responsive polymeric nanoparticles for imaging protein kinase activities in single living cells. *Angew Chem Int Ed Engl* 46(30):5779–5782
215. Oishi J, Kawamura K, Kang JH, Kodama K, Sonoda T, Murata M, Niidome T, Katayama Y (2006) An intracellular kinase signal-responsive gene carrier for disordered cell-specific gene therapy. *J Control Release* 110(2):431–436
216. Fernandes A, Viterisi A, Coutrot F, Potok S, Leigh DA, Aucagne V, Papot S (2009) Rotaxane-based propeptides: protection and enzymatic release of a bioactive pentapeptide. *Angew Chem Int Ed Engl* 48(35):6443–6447
217. Kamal A, Tekumalla V, Krishnan A, Pal-Bhadra M, Bhadra U (2008) Development of pyrrolo[2,1-c][1,4]benzodiazepine beta-galactoside prodrugs for selective therapy of cancer by ADEPT and PMT. *Chem Med Chem* 3(5):794–802
218. Thomas M, Rivault F, Tranoy-Opalinski I, Roche J, Gesson JP, Papot S (2007) Synthesis and biological evaluation of the suberoylanilide hydroxamic acid (SAHA) beta-glucuronide and beta-galactoside for application in selective prodrug chemotherapy. *Bioorg Med Chem Lett* 17(4):983–986
219. Fang L, Battisti RF, Cheng H, Reigan P, Xin Y, Shen J, Ross D, Chan KK et al (2006) Enzyme specific activation of benzoquinone ansamycin prodrugs using HuCC49DeltaCH2-beta-galactosidase conjugates. *J Med Chem* 49(21):6290–6297
220. Yu Y, Fang L, Sun D (2010) Biodistribution of HuCC49DeltaCH2-beta-galactosidase in colorectal cancer xenograft model. *Int J Pharm* 386(1–2):208–215

221. Ho NH, Weissleder R, Tung CH (2007) A self-immolative reporter for beta-galactosidase sensing. *Chem Bio Chem* 8(5):560–566
222. Valdagni R, Amichetti M (1994) Report of long-term follow-up in a randomized trial comparing radiation therapy and radiation therapy plus hyperthermia to metastatic lymph nodes in stage IV head and neck patients. *Int J Radiat Oncol Biol Phys* 28(1):163–169
223. Vernon CC, Hand JW, Field SB, Machin D, Whaley JB, van der Zee J, van Putten WL, van Rhoon GC et al (1996) Radiotherapy with or without hyperthermia in the treatment of superficial localized breast cancer: results from five randomized controlled trials. International Collaborative Hyperthermia Group. *Int J Radiat Oncol Biol Phys* 35(4):731–744
224. Sneed PK, Stauffer PR, McDermott MW, Diederich CJ, Lamborn KR, Prados MD, Chang S, Weaver KA et al (1998) Survival benefit of hyperthermia in a prospective randomized trial of brachytherapy boost \pm hyperthermia for glioblastoma multiforme. *Int J Radiat Oncol Biol Phys* 40(2):287–295
225. Hamazoe R, Maeta M, Kaibara N (1994) Intraperitoneal thermochemotherapy for prevention of peritoneal recurrence of gastric cancer. Final results of a randomized controlled study. *Cancer* 73(8):2048–2052
226. Kawai N, Ito A, Nakahara Y, Futakuchi M, Shirai T, Honda H, Kobayashi T, Kohri K (2005) Anticancer effect of hyperthermia on prostate cancer mediated by magnetite cationic liposomes and immune-response induction in transplanted syngeneic rats. *Prostate* 64(4):373–381
227. Okano T, Yamada N, Sakai H, Sakurai Y (1993) A novel recovery system for cultured cells using plasma-treated polystyrene dishes grafted with poly(N-isopropylacrylamide). *J Biomed Mater Res* 27(10):1243–1251
228. Okano T, Yamada N, Okuhara M, Sakai H, Sakurai Y (1995) Mechanism of cell detachment from temperature-modulated, hydrophilic-hydrophobic polymer surfaces. *Biomaterials* 16(4):297–303
229. Yang M, Ding Y, Zhang L, Qian X, Jiang X, Liu B (2007) Novel thermosensitive polymeric micelles for docetaxel delivery. *J Biomed Mater Res A* 81(4):847–857
230. Liu B, Yang M, Li X, Qian X, Shen Z, Ding Y, Yu L (2008) Enhanced efficiency of thermally targeted taxanes delivery in a human xenograft model of gastric cancer. *J Pharm Sci* 97(8):3170–3181
231. Park JS, Akiyama Y, Yamasaki Y, Kataoka K (2007) Preparation and characterization of polyion complex micelles with a novel thermosensitive poly(2-isopropyl-2-oxazoline) shell via the complexation of oppositely charged block ionomers. *Langmuir* 23(1):138–146
232. Toti US, Moon SH, Kim HY, Jun YJ, Kim BM, Park YM, Jeong B, Sohn YS (2007) Thermosensitive and biocompatible cyclotriphosphazene micelles. *J Control Release* 119(1):34–40
233. Bae KH, Choi SH, Park SY, Lee Y, Park TG (2006) Thermosensitive pluronic micelles stabilized by shell cross-linking with gold nanoparticles. *Langmuir* 22(14):6380–6384
234. Chung JE, Yokoyama M, Yamato M, Aoyagi T, Sakurai Y, Okano T (1999) Thermosensitive drug delivery from polymeric micelles constructed using block copolymers of poly(N-isopropylacrylamide) and poly(butylmethacrylate). *J Control Release* 62(1–2):115–127
235. Zhu JL, Zhang XZ, Cheng H, Li YY, Cheng SX, Zhuo RX (2007) Synthesis and characterization of well-defined, Amphiphilic Poly(N-isopropylacrylamide)-b-[2-hydroxyethyl methacrylate-poly(epsilon-caprolactone)](n) graft copolymers by RAFT polymerization and macromonomer method. *J Polym Sci [A1]* 45(22):5354–5364
236. Wei H, Chen WQ, Chang C, Cheng C, Cheng SX, Zhang XZ, Zhuo RX (2008) Synthesis of star block, thermosensitive poly(L-lactide)-star block-poly(N-isopropylacrylamide-co-N-hydroxymethylacrylamide) copolymers and their self-assembled micelles for controlled release. *J Phys Chem* 112(8):2888–2894

237. Nakayama M, Okano T, Miyazaki T, Kohori F, Sakai K, Yokoyama M (2006) Molecular design of biodegradable polymeric micelles for temperature-responsive drug release. *J Control Release* 115(1):46–56
238. Liu SQ, Tong YW, Yang YY (2005) Incorporation and in vitro release of doxorubicin in thermally sensitive micelles made from poly(N-isopropylacrylamide-co-N, N-dimethylacrylamide)-b-poly(D, L-lactide-co-glycolide) with varying compositions. *Biomaterials* 26(24):5064–5074
239. Na K, Lee KH, Lee DH, Bae YH (2006) Biodegradable thermo-sensitive nanoparticles from poly(L-lactic acid)/poly(ethylene glycol) alternating multi-block copolymer for potential anti-cancer drug carrier. *Eur J Pharm Sci* 27(2–3):115–122
240. Yatvin MB, Weinstein JN, Dennis WH, Blumenthal R (1978) Design of liposomes for enhanced local release of drugs by hyperthermia. *Science* 202(4374):1290–1293
241. Needham D, Anyarambhatla G, Kong G, Dewhirst MW (2000) A new temperature-sensitive liposome for use with mild hyperthermia: characterization and testing in a human tumor xenograft model. *Cancer Res* 60(5):1197–1201
242. Chen Q, Tong S, Dewhirst MW, Yuan F (2004) Targeting tumor microvessels using doxorubicin encapsulated in a novel thermosensitive liposome. *Mol Cancer Ther* 3(10):1311–1317
243. Chang HI, Yeh MK (2012) Clinical development of liposome-based drugs: formulation, characterization, and therapeutic efficacy. *Int J Nanomedicine* 7:49–60
244. Kong G, Anyarambhatla G, Petros WP, Braun RD, Colvin OM, Needham D, Dewhirst MW (2000) Efficacy of liposomes and hyperthermia in a human tumor xenograft model: importance of triggered drug release. *Cancer Res* 60(24):6950–6957
245. Al-Ahmady ZS, Al-Jamal WT, Bossche JV, Bui TT, Drake AF, Mason AJ, Kostarelos K (2012) Lipid-Peptide vesicle nanoscale hybrids for triggered drug release by mild hyperthermia in vitro and in vivo. *ACS Nano* 6(10):9335–9346
246. Tong X, Wang G, Soldera A, Zhao Y (2005) How can azobenzene block copolymer vesicles be dissociated and reformed by light? *J Phys Chem B* 109(43):20281–20287
247. Fomina N, McFearin C, Serssakdi M, Edigin O, Almutairi A (2010) UV and near-IR triggered release from polymeric nanoparticles. *J Am Chem Soc* 132(28):9540–9542
248. Cabane E, Malinova V, Meier W (2010) Synthesis of photocleavable amphiphilic block copolymers: toward the design of photosensitive nanocarriers. *Macromol Chem Phys* 211(17):1847–1856
249. Lv C, Wang Z, Wang P, Tang X (2012) Photodegradable polyurethane self-assembled nanoparticles for photocontrollable release. *Langmuir* 28(25):9387–9394
250. Babin J, Pelletier M, Lepage M, Allard JF, Morris D, Zhao Y (2009) A new two-photon-sensitive block copolymer nanocarrier. *Angew Chem Int Ed Engl* 48(18):3329–3332
251. Yan B, Boyer JC, Branda NR, Zhao Y (2011) Near-infrared light-triggered dissociation of block copolymer micelles using upconverting nanoparticles. *J Am Chem Soc* 133(49):19714–19717
252. Hribar KC, Lee MH, Lee D, Burdick JA (2011) Enhanced release of small molecules from near-infrared light responsive polymer-nanorod composites. *ACS Nano* 5(4):2948–2956
253. Hirsch LR, Stafford RJ, Bankson JA, Sershen SR, Rivera B, Price RE, Hazle JD, Halas NJ et al (2003) Nanoshell-mediated near-infrared thermal therapy of tumors under magnetic resonance guidance. *Proc Natl Acad Sci USA* 100(23):13549–13554
254. Skrabalak SE, Au L, Lu X, Li X, Xia Y (2007) Gold nanocages for cancer detection and treatment. *Nanomedicine (Lond)* 2(5):657–668
255. Huang X, El-Sayed IH, Qian W, El-Sayed MA (2006) Cancer cell imaging and photothermal therapy in the near-infrared region by using gold nanorods. *J Am Chem Soc* 128(6):2115–2120
256. Lu W, Xiong C, Zhang G, Huang Q, Zhang R, Zhang JZ, Li C (2009) Targeted photothermal ablation of murine melanomas with melanocyte-stimulating hormone analog-conjugated hollow gold nanospheres. *Clin Cancer Res* 15(3):876–886

257. Melancon MP, Lu W, Yang Z, Zhang R, Cheng Z, Elliot AM, Stafford J, Olson T et al (2008) In vitro and in vivo targeting of hollow gold nanoshells directed at epidermal growth factor receptor for photothermal ablation therapy. *Mol Cancer Ther* 7(6):1730–1739
258. Zhou M, Zhang R, Huang M, Lu W, Song S, Melancon MP, Tian M, Liang D et al (2010) A chelator-free multifunctional [64Cu]CuS nanoparticle platform for simultaneous micro-PET/CT imaging and photothermal ablation therapy. *J Am Chem Soc* 132(43):15351–15358
259. Melancon MP, Zhou M, Li C (2011) Cancer theranostics with near-infrared light-activatable multimodal nanoparticles. *Acc Chem Res* 44(10):947–956
260. You J, Zhang R, Zhang G, Zhong M, Liu Y, Van Pelt CS, Liang D, Wei W et al (2012) Photothermal-chemotherapy with doxorubicin-loaded hollow gold nanospheres: A platform for near-infrared light-triggered drug release. *J Control Release* 158(2):319–328
261. Regmi R, Bhattarai SR, Sudakar C, Wani AS, Cunningham R, Vaishnava PP, Naik R, Oupicky D et al (2010) Hyperthermia controlled rapid drug release from thermosensitive magnetic microgels. *J Mater Chem* 20(29):6158–6163
262. Katagiri K, Imai Y, Koumoto K (2011) Variable on-demand release function of magnetoresponsive hybrid capsules. *J Colloid Interface Sci* 361(1):109–114
263. Liu TY, Hu SH, Liu KH, Shaiu RS, Liu DM, Chen SY (2008) Instantaneous drug delivery of magnetic/thermally sensitive nanospheres by a high-frequency magnetic field. *Langmuir* 24(23):13306–13311
264. Liu J, Zhang Y, Wang C, Xu R, Chen Z, Gu N (2010) Magnetically sensitive alginate-templated polyelectrolyte multilayer microcapsules for controlled release of doxorubicin. *J Phys Chem C* 114(17):7673–7679
265. Hu SH, Tsai CH, Liao CF, Liu DM, Chen SY (2008) Controlled rupture of magnetic polyelectrolyte microcapsules for drug delivery. *Langmuir* 24(20):11811–11818
266. Liu C, Guo J, Yang W, Hu J, Wang C, Fu S (2009) Magnetic mesoporous silica microspheres with thermo-sensitive polymer shell for controlled drug release. *J Mater Chem* 19(27):4764–4770
267. Oliveira H, Pérez-Andrés E, Thevenot J, Sandre O, Berra E, Lecommandoux S (2013) Magnetic field triggered drug release from polymersomes for cancer therapeutics. *J Control Release*
268. Zhao X, Kim J, Cezar CA, Huebsch N, Lee K, Bouhadir K, Mooney DJ (2011) Active scaffolds for on-demand drug and cell delivery. *Proc Natl Acad Sci USA* 108(1):67–72
269. Hu SH, Liu TY, Huang HY, Liu DM, Chen SY (2008) Magnetic-sensitive silica nanospheres for controlled drug release. *Langmuir* 24(1):239–244
270. Brazel CS (2009) Magnetothermally-responsive nanomaterials: combining magnetic nanostructures and thermally-sensitive polymers for triggered drug release. *Pharm Res* 26(3):644–656
271. Hu SH, Liu TY, Huang HY, Liu DM, Chen SY (2009) Stimuli-responsive controlled drug release from magnetic-sensitive silica nanospheres. *J Nanosci Nanotechnol* 9(2):866–870
272. Clares B, Biedma-Ortiz RA, Sáez-Fernández E, Prados JC, Melguizo C, Cabeza L, Ortiz R, Arias JL (2013) Nano-engineering of 5-fluorouracil-loaded magnetoliposomes for combined hyperthermia and chemotherapy against colon cancer. *Eur J Pharm Biopharm*
273. Chen Y, Bose A, Bothun GD (2010) Controlled release from bilayer-decorated magnetoliposomes via electromagnetic heating. *ACS Nano* 4(6):3215–3221
274. Qiu D, An X (2012) Controllable release from magnetoliposomes by magnetic stimulation and thermal stimulation. *Colloids Surf B Biointerfaces* 104:326–329
275. Yoshida M, Sato M, Yamamoto Y, Maehara T, Naohara T, Aono H, Sugishita H, Sato K et al (2012) Tumor local chemohyperthermia using docetaxel-embedded magnetoliposomes: Interaction of chemotherapy and hyperthermia. *J Gastroenterol Hepatol* 27(2):406–411
276. Ito A, Fujioka M, Yoshida T, Wakamatsu K, Ito S, Yamashita T, Jimbow K, Honda H (2007) 4-S-Cysteaminyphenol-loaded magnetite cationic liposomes for combination

- therapy of hyperthermia with chemotherapy against malignant melanoma. *Cancer Sci* 98(3):424–430
277. Yoshida M, Watanabe Y, Sato M, Maehara T, Aono H, Naohara T, Hirazawa H, Horiuchi A et al (2010) Feasibility of chemohyperthermia with docetaxel-embedded magnetoliposomes as minimally invasive local treatment for cancer. *Int J Cancer* 126(8):1955–1965
 278. Hayashi K, Ono K, Suzuki H, Sawada M, Moriya M, Sakamoto W, Yogo T (2010) High-frequency, magnetic-field-responsive drug release from magnetic nanoparticle/organic hybrid based on hyperthermic effect. *ACS Appl Mater Interfaces* 2(7):1903–1911
 279. Mikhaylov G, Mikac U, Magaeva AA, Itin VI, Naiden EP, Psakhye I, Babes L, Reinheckel T et al (2011) Ferri-liposomes as an MRI-visible drug-delivery system for targeting tumours and their microenvironment. *Nat Nanotechnol* 6(9):594–602
 280. Ruiz-Hernández E, Baeza A, Ma Vallet-Regí (2011) Smart drug delivery through DNA/magnetic nanoparticle gates. *ACS Nano* 5(2):1259–1266
 281. Thomas CR, Ferris DP, Lee JH, Choi E, Cho MH, Kim ES, Stoddart JF, Shin JS et al (2010) Noninvasive remote-controlled release of drug molecules in vitro using magnetic actuation of mechanized nanoparticles. *J Am Chem Soc* 132(31):10623–10625
 282. Wang YC, Wang F, Sun TM, Wang J (2011) Redox-responsive nanoparticles from the single disulfide bond-bridged block copolymer as drug carriers for overcoming multidrug resistance in cancer cells. *Bioconj Chem* 22(10):1939–1945
 283. Liu J, Pang Y, Huang W, Zhu Z, Zhu X, Zhou Y, Yan D (2011) Redox-responsive polyphosphate nanosized assemblies: a smart drug delivery platform for cancer therapy. *Biomacromolecules* 12(6):2407–2415
 284. Zhao M, Biswas A, Hu B, Joo KI, Wang P, Gu Z, Tang Y (2011) Redox-responsive nanocapsules for intracellular protein delivery. *Biomaterials* 32(22):5223–5230
 285. Kuang Y, Balakrishnan K, Gandhi V, Peng X (2011) Hydrogen peroxide inducible DNA cross-linking agents: targeted anticancer prodrugs. *J Am Chem Soc* 133(48):19278–19281
 286. Liu J, Pang Y, Zhu Z, Wang D, Li C, Huang W, Zhu X, Yan D (2013) Therapeutic nanocarriers with hydrogen peroxide-triggered drug release for cancer treatment. *Biomacromolecules*
 287. Ge J, Neofytou E, Cahill TJ III, Beygui RE, Zare RN (2011) Drug release from electric-field-responsive nanoparticles. *ACS Nano* 6(1):227–233
 288. Zhu Y, Liu H, Li F, Ruan Q, Wang H, Fujiwara M, Wang L, Lu G (2010) Dipolar molecules as impellers achieving electric-field-stimulated release. *J Am Chem Soc* 132(5):1450–1451
 289. Fantozzi F, Arturoni E, Barbucci R (2010) The effects of the electric fields on hydrogels to achieve antitumoral drug release. *Bioelectrochemistry* 78(2):191–195
 290. Yudina A, de Smet M, Lepetit-Coiffe M, Langereis S, Van Ruijssevelt L, Smirnov P, Bouchaud V, Voisin P et al (2011) Ultrasound-mediated intracellular drug delivery using microbubbles and temperature-sensitive liposomes. *J Control Release* 155(3):442–448
 291. Yin T, Wang P, Li J, Zheng R, Zheng B, Cheng D, Li R, Lai J et al. (2013) Ultrasound-sensitive siRNA-loaded nanobubbles formed by hetero-assembly of polymeric micelles and liposomes and their therapeutic effect in gliomas. *Biomaterials*
 292. Yan F, Li L, Deng Z, Jin Q, Chen J, Yang W, Yeh CK, Wu J et al (2013) Paclitaxel-liposome-microbubble complexes as ultrasound-triggered therapeutic drug delivery carriers. *J Control Release* 166(3):246–255
 293. Han D, Tong X, Zhao Y (2012) Block copolymer micelles with a dual-stimuli-responsive core for fast or slow degradation. *Langmuir* 28(5):2327–2331
 294. Li Y, Tong R, Xia H, Zhang H, Xuan J (2010) High intensity focused ultrasound and redox dual responsive polymer micelles. *Chem Commun* 46(41):7739–7741
 295. Tong R, Xia H, Lu X (2013) Fast release behavior of block copolymer micelles under high intensity focused ultrasound/redox combined stimulus. *J Mater Chem* 1(6):886–894
 296. Korin N, Kanapathipillai M, Matthews BD, Crescente M, Brill A, Mammoto T, Ghosh K, Jurek S et al (2012) Shear-activated nanotherapeutics for drug targeting to obstructed blood vessels. *Science* 337(6095):738–742

297. Matsumoto A, Yamamoto K, Yoshida R, Kataoka K, Aoyagi T, Miyahara Y (2010) A totally synthetic glucose responsive gel operating in physiological aqueous conditions. *Chem Commun* 46(13):2203–2205
298. Yao Y, Zhao L, Yang J, Yang J (2012) Glucose-responsive vehicles containing phenylborate ester for controlled insulin release at neutral pH. *Biomacromolecules* 13(6):1837–1844
299. Traitel T, Cohen Y, Kost J (2000) Characterization of glucose-sensitive insulin release systems in simulated in vivo conditions. *Biomaterials* 21(16):1679–1687
300. Agarwal A, Boettcher A, Kneuer R, Sari-Sarraf F, Donovan A, Woelcke J, Simic O, Brandl T et al (2013) In vivo imaging with fluorescent smart probes to assess treatment strategies for acute pancreatitis. *PLoS One* 8(2):e55959
301. Al-Jamal WT, Al-Ahmady ZS, Kostarelos K (2012) Pharmacokinetics and tissue distribution of temperature-sensitive liposomal doxorubicin in tumor-bearing mice triggered with mild hyperthermia. *Biomaterials* 33(18):4608–4617
302. Liu TY, Hu SH, Liu DM, Chen SY, Chen IW (2009) Biomedical nanoparticle carriers with combined thermal and magnetic responses. *Nano Today* 4(1):52–65

Chapter 27

Opportunities for New Photodynamic Molecular Beacon Designs

Kun Lou and Jonathan F. Lovell

27.1 Introduction to Molecular Beacons

27.1.1 Classic Molecular Beacons

Molecular beacons were originally described as single-stranded nucleic acid molecules with a stem-and-loop structure [1]. Molecular beacons make use of Förster resonance energy transfer (FRET) or contact quenching, and complementary base-pairing principles [2]. Generally, molecular beacons consist of three parts: loop, stem, and fluorophore/photosensitizer/quencher groups. The loop portion, with approximately 15–30 nucleotides, is usually designed to be complementary to the target sequence. Typically composed of 5–7 nucleotides, the stem portion acts as the flanking ends of the molecular beacon and is designed to be complementary to itself (at the other end). Thus, before hybridization with the target, a molecular beacon is a closed structure composed of a hairpin stem and a loop. Fluorophores (donors) and quenchers (acceptors) are covalently linked to the 5' ends and 3' ends, respectively. In this way, molecular beacons are closed before binding to the target, bringing fluorophores and quenchers close together, and attenuating the fluorescence.

Several types of nucleic acid hybridization assays were used before the emergence of molecular beacons [1, 3]. Two fluorophores could be brought in close proximity with the binding of two fluorescently labeled nucleic acids to a target strand at closely spaced positions [4]. Donor and acceptor fluorophores were also covalently attached to two ends of the same oligodeoxyribonucleotide at 5' and 3' ends of two complementary strands [5]. Molecular beacons, flanked by two complementary stem portions, are also based on nucleic acid hybridization. Their advantage lies in the enhancement of selectivity and specificity brought by the

K. Lou · J. F. Lovell (✉)

Department of Biomedical Engineering; Department of Chemical and Biological Engineering, University at Buffalo, The State University of New York, Buffalo, NY 14260, USA

e-mail: jflovell@buffalo.edu

hairpin stem. Hybridization specificity can be considered match versus mismatch discrimination, and stem-loop molecular beacons excel in this regard, being able to detect even a single base-pair mismatch [6]. Real-time polymerase chain reaction (real-time PCR), where molecular beacons are often employed, benefits from their selectivity and sensitivity since there is no need to remove excess unhybridized probes prior to detection. The distance between fluorophores attached to linear oligonucleotides in solution varies randomly since they behave like a random coil, thus lowering sensitivity. The stable double-helix stem structure of molecular beacons keeps the fluorophore close to the quencher so that fluorescence is highly quenched prior to target binding. Another desirable target recognition feature is that molecular beacons are able to detect single-nucleotide variations [7]. Probes do not hybridize with mismatched target sequence as long as the reaction is carried out at appropriate temperatures [8].

Regarding their mechanism, when a fluorescently labeled beacon encounters a target strand, the loop portion that is complementary to the target opens into a duplex hybrid. This duplex hybrid between the loop and the target is longer and more stable than the stem [1]. Zippering of the base pairs between the beacon loop and the target results in unfolding of the hairpin stems [9]. Hybridization between complementary probes and targets leads to spatial separation of the fluorophores and quenchers covalently attached to the probe ends. The separation between fluorophores and quenchers makes the target nucleic acids detectable by fluorescence measurements. Fluorescence can be viewed as light emission (of photons) following excitation. The fluorophore is raised to a higher excitation level by light absorption. This step is rapidly followed by a return to the lowest stable vibrational level with heat loss. Finally, the fluorophore returns to the ground state with light emission or non-radiative energy transfer, to which FRET and contact quenching can be attributed [10]. In the case of photodynamic beacons, energy may ultimately be dissipated by the generation of singlet oxygen following photosensitizer intersystem crossing to its triplet state. Fluorescence and singlet oxygen are quenched before separation between fluorophores and quenchers. High quenching efficiency is of significance because a low background enhances the specificity of the probes. In most cases, fluorescence of molecular beacons is quenched by FRET or contact quenching [11], depending on the distance between the fluorophores and quenchers. When fluorophores are brought close enough to quenchers, fluorescence emission intensity of the fluorophores decreases [3]. A closer distance may trigger contact quenching (also referred as static quenching), resulting in the formation of a non-fluorescent ground-state complex. It is believed that contact quenching assumes a principal role to the close proximity of fluorophore and quencher in most molecular beacons [12, 13].

Förster theory indicates that the energy transfer efficiency is inversely proportional with 6 powers to the distance between the fluorophores and quenchers [2, 14]. Two prerequisites are necessary: a required interaction distance between donors and acceptors (fluorophores and quenchers) as well as an overlap between the emission spectrum of fluorophore and absorption spectrum of quencher [15]. Effective distance between fluorophores and quenchers ranges from 10 to 100 Å, which is

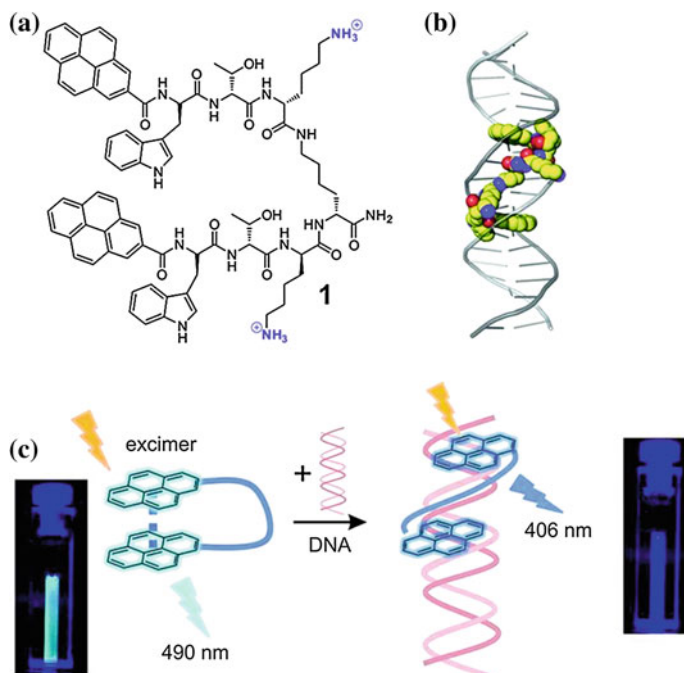


Fig. 27.1 **a** Molecular structure of a pyrene-functionalized cationic oligopeptide. **b** Binding of the beacon to double-stranded DNA. **c** Schematic working mechanism (Recreated with kind permission from American Chemical Society; *J. Am. Chem. Soc.* 2012; 134(4):1958–61)

roughly the distance of 3–30 nucleotides of double-helix DNA [10, 16]. Contact quenching, however, is irrespective of spectral overlap. In this mode, most absorbed energy is dissipated as heat instead of light emission [17]. Lifetime fluorescence measurements may help distinguish the two quenching modes [12]. FRET may be predicted by spectral overlap and the distance between fluorophores and quenchers, and also directly applies to photosensitizers in an analogous manner [18].

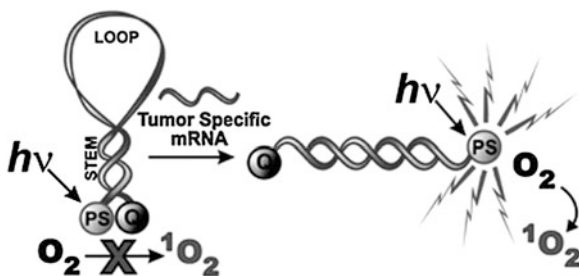
Although most focus to date has been on DNA molecular beacons and their corresponding fluorescence emission changes, the molecular beacon family has been expanding. As an example, consider a peptide molecular beacon for DNA imaging in cells [19]. Figure 27.1 illustrates this oligopeptide-derived molecular beacon that changed conformation to switch to excimer emission at 490 nm from monomer emission at 406 nm after binding to specific double-stranded DNA. Structurally, a lysine spacer is centered laterally by two Trp-Thr-Lys tripeptide units via C-terminus. A pyrene is attached to each N-terminus. These cationic peptides are useful for cellular imaging due to their ability to penetrate cells [20]. Thus, the field of molecular beacons has expanded greatly beyond traditional DNA stem-loop structures. Photodynamic molecular beacons in many ways can be constructed in the same ways as classical and emerging molecular beacons, but have not been explored to as great an extent.

27.1.2 Photodynamic Molecular Beacons

With the same sensitive detection ability as molecular beacons, photodynamic molecular beacons feature light-activated singlet oxygen generating properties of photosensitizers, which are altered, reduced, or intensified by molecular recognition or environmental changes. Historically, development of photodynamic molecular beacons has not been based on nucleic acids. For instance, activatable photosensitizers can control how singlet oxygen is quenched and activated via protease control [21]. Cytotoxic singlet oxygen is only produced upon irradiation if the photosensitizer is liberated from the quencher. Compared to fluorophores of conventional molecular beacons, the excited singlet state can alternatively enter a lower-energy triplet state via intersystem crossing [12]. Surrounded by diffused oxygen molecules, triplet-state photosensitizers can interact with these to yield singlet oxygen [22]. As for the photosensitizer spectral properties, those absorbing at near-infrared wavelengths (650–900 nm) are usually selected since deeper tissue penetration and lower background fluorescence are possible in this range due to intrinsic optical properties of tissues [23]. The localization of photosensitizers is also important, and partitioning into organelles like the mitochondria and endoplasmic reticulum can improve efficacy [22, 24]. The principles in designing photodynamic molecular beacons for controlling singlet oxygen generation are essentially the same as for fluorescence beacons and must enable beacon activation upon target recognition [25, 26].

DNA-based activatable photosensitizers have been constructed as a means to control on-and-off switching of singlet oxygen in response to nucleic acid target binding [27]. Pyropheophorbide and Black Hole Quencher were conjugated to two separate complimentary oligonucleotide strands to serve as photosensitizer and quencher, respectively. Both fluorescence emission and singlet oxygen production were almost completely shut down, while an excess of complimentary sequence was able to recover 85 % of the singlet oxygen after hybridization. Figure 27.2 shows the conversion of a classic molecular beacon into a photodynamic one [28]. Further innovations include a pH-sensitive DNA *i*-motif controlling photosensitized singlet oxygen [29]. The *i*-motif quadruplex was able to keep the photosensitizer and quencher in close proximity in the absence of acidic conditions. The formation of the triplet state of the sensitizer was prevented by quenching. The *i*-motif was not stable when the pH was raised above five, resulting in increased distance between photosensitizer and quencher and increased singlet oxygen production. This approach successfully permits the modulation of photodynamic activity in response to pH change. A peptide photodynamic molecular beacon was synthesized for the diagnosis and treatment of epithelial cancer [30]. The photocytotoxicity is triggered via fibroblast activation protein (FAP), which is a cell-surface serine protease in cancer-related fibroblasts of human epithelial carcinomas but not healthy tissues. The peptide loop specific to FAP could be cleaved and allowed restoration of fluorescence and singlet oxygen. Specific photocytotoxicity was observed toward HEK cells expressing FAP, demonstrating a feasible therapeutic option as well.

Fig. 27.2 The concept of mRNA photodynamic molecular beacon (Recreated with kind permission from Royal Society of Chemistry; Photochem. Photobiol. Sci. 2008; 7(7):775–81)



As photosensitizers are also fluorescent, they can be used for imaging combined with photodynamic therapy (PDT). PDT is a minimally invasive therapeutic method that avoids repeated dosage resistance and other side effects [22, 24]. PDT aims at destroying target cells using three elements: light irradiation, photosensitizers, and cytotoxic singlet oxygen [31]. Reactive oxygen species activated from irradiated photosensitizers are responsible for killing targeted cells. PDT requires careful planning to limit damage to surrounding healthy tissues. PDT and imaging can be conveniently carried out with a single fluorescent photosensitizer, with porphyrins being a good example [32]. Porphyrins have a long history as tumor-specific diagnostic fluorescence imaging agents. For PDT applications, porphyrins meet the demands of good availability, conjugation compatibility, quencher compatibility, singlet oxygen quantum yield, and fluorescence quantum yield [22]. Thus, for photodynamic beacons, porphyrin-related compounds are suitable candidates to use in engineer beacons. Quenchers are important for photodynamic molecular beacons since any unquenched beacons might exert unwanted singlet oxygen on healthy tissues under irradiation. Thus, the signal-to-noise ratio is important for therapeutic applications. Carotenoid (CAR) has been studied as a unique quencher since it is able to directly scavenge singlet oxygen [33]. CAR has dual quenching ability, which helps to improve beacon efficacy; photosensitizer excited-state deactivation and singlet oxygen scavenging.

For photodynamic beacons, a linker sequence specific to the target, such as a tumor-specific enzyme, can act as the recognition probe. The goal is to trigger the enzymatic cleavage of the linker in disease-specific cells to restore light-induced singlet oxygen, which is quenched in the inactive beacon. Figure 27.3 illustrates an engineered photodynamic beacon targeting breast cancer cells [34]. Breast cancer is a common disease and requires more effective diagnosis and treatment options. The proposed photodynamic peptide-based beacon offers promise for non-invasive and site-selective treatment. In this approach, the beacon was able to be activated by matrix metalloproteinases (MMPs), proteases implicated in the disease. Another example was a membrane-permeable, cancer-specific beacon with a built-in apoptosis sensor to carry out therapeutic and imaging functions [35]. The beacon contained a fluorescent pyromoiety as a photosensitizer and a BHQ-3 quencher connected by the caspase-3-cleavable sequence (KGDEVDGSGK), while folate served as a targeting moiety. The folate-carrying beacon preferentially accumulated where folate receptors were overexpressed. Following uptake, the

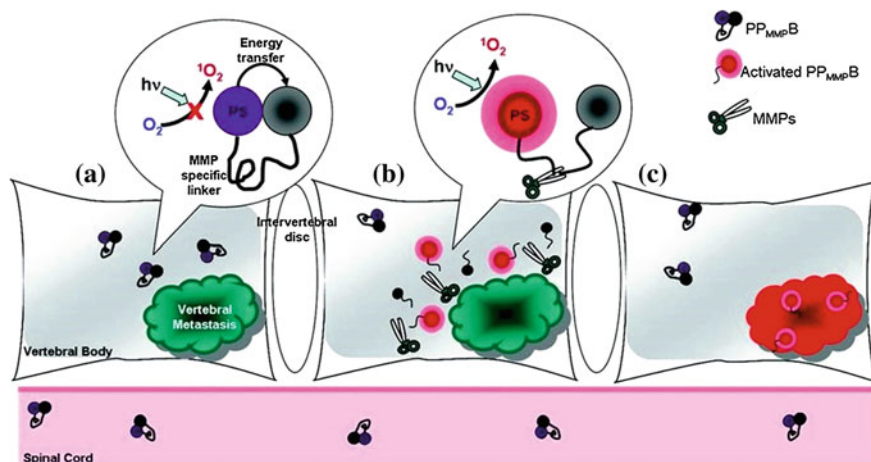


Fig. 27.3 Three phases of molecular beacon triggered by vertebral metastases. **a** Molecular beacons are quenched when accumulated in tissue. **b** MMPs within vertebral metastases cleave the loop portion of the beacon. **c** Beacons relieved from quenched status restore fluorescence and trigger singlet oxygen (Recreated with kind permission from American Chemical Society; *Bioconjugate Chem.* 2011; 22(6):1021–30)

next step involved light activation and singlet oxygen was generated. Apoptosis led to the activation of caspase-3, which specifically cleaved the beacon. Thus, dying cells were able to be identified by the restoration of photosensitizer emission. Although measurements of singlet oxygen luminescence and photobleaching of photosensitizers have been taken to gauge tissue damage during the course of PDT treatment, these methods only behave indirectly to give feedback. A subsequent approach made use of 5-carboxy-X-rhodamine (Rox) as a donor, along with the acceptor pyro and a caspase-3-specific peptide sequence. This beacon was more effectively able to both induce and detect apoptosis [36]. This represents a new strategy that enables light to be regulated to activate photosensitizer dosage with direct molecular feedback. Another approach involved the combination of photosensitizers with single-walled carbon nanotubes as quenchers [37]. Single-walled carbon nanotubes have been regarded as efficient quenchers [38] and intracellular carriers [39]. Chlorine 6 was attached to a single-stranded aptamer for fluorescence and singlet oxygen generation. Upon binding to single-walled carbon nanotubes, fluorescence and light-activated singlet oxygen were quenched. Targets that bound to the aptamer modulated its interaction with single-walled carbon nanotubes and released the Ce6 from quenched state. Irradiation then caused the production of singlet oxygen.

The strategy of singlet oxygen control with photodynamic molecular beacons is no longer limited to classic designs. An X-ray-activated system that used a lanthanum fluoride nanoparticle covalently linked to a photosensitizer was capable of yielding singlet oxygen. This approach offers opportunity for the application of photodynamic beacons deep in human tissue [40].

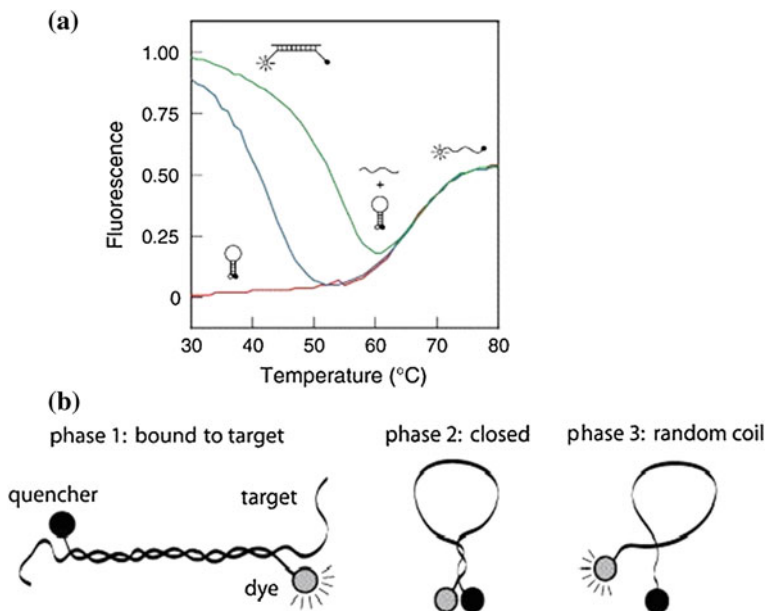


Fig. 27.4 Phase transition of molecular beacons in solutions. **a** Molecular beacons denaturation curves: solo molecular beacons without target nucleotides (*red curve*), with perfectly complementary targets (*green curve*) and with excess mismatched targets (*blue curve*) (Recreated with kind permission from Elsevier; real-time assays with molecular beacons and other fluorescent nucleic acid hybridization probes. *Clin. Chim. Acta.* 2006 Jan; 363(1–2):48–60. **b** Schematic representation of three transition states. Phase 1: hybridization hybrid between molecular beacons and targets. Phase 2: independent molecular beacons without targets. Phase 3: molecular beacons melt into random-coiled state. Recreated with kind permission from Oxford University Press; *Nucl. Acids Res.* 2003; 15,31(4):1319–30)

27.1.3 Thermodynamic Properties of Molecular Beacons

Most studies of molecular beacon thermodynamics have been related to nucleic acid-based beacons. Figure 27.2 demonstrates the first nucleic acid-based photodynamic molecular beacon [28], which follows the same principles as standard molecular beacons. To investigate thermodynamic effects of molecular beacons, an understanding of a three-state transition model of classic molecular beacons, based on temperature, is useful to avoid false positives (activation in the absence of targets) and false negatives (no activation with targets present) [8]. The thermal denaturation profile of molecular beacons without targets is shown in Fig. 27.4. Within the low-temperature phase, molecular beacons exist as loop–stem structures. Gradual increase in temperature results in the transition from a hairpin-loop structure to a random-coil structure, as indicated as Phase 3. Note that in this case, the increase in fluorescence with temperature increase is not due to hybridization. High fluorescence can be achieved when all molecular beacons come to this

completely unquenched state. Hybridization can take place between molecular beacons and target oligonucleotides at temperatures below the DNA hybrid melting temperature (Phase 1). The high fluorescence of the hybridized beacons (compared to that of closed molecular beacons at corresponding temperatures) drops noticeably with ascending temperature, due to breaking of hydrogen bonds that form hybridized double helix. The dehybridization of the target oligonucleotides enables the remaining single-stranded molecular beacons to recover to stable stem-loop structures with fluorophores becoming quenched again. This fluorescence turning point indicates the transition of molecular beacons back into hairpin structures (Phase 2). A portion of molecular beacons does not undergo transition from Phase 1 to Phase 2 at all and become randomly coiled, that is, going from Phase 1 directly to Phase 3. Eventually, all molecular beacons tend to open to a random-coiled phase as the temperature is elevated. It is interesting that fluorescence of random-coiled molecular beacons (Phase 3) is lower than that of hybridization status (Phase 1) and can be attributed to incomplete quenching of fluorophores in the random-coil form. Molecular beacons with a single-nucleotide mismatch target experience similar transitions but with a lower transition temperature at the turning point. This permits discrimination between matched and mismatched targets and demonstrates the specificity and selectivity of molecular beacons [8].

Melting temperature (T_m), the most important property in beacon transitions, is defined as the temperature at which 50 % of the strands are hybridized in the double-helix state [41]. Numerous factors are responsible for determining T_m : base stacking [42], guanine-cytosine content (GC content), buffer composition, stem length, and secondary structure [2, 8]. Since the thermodynamic stability of the G-C bond is greater than the A-T bond, rich GC content sequences tend to have a higher T_m [41, 43, 44]. A longer stem length is found to change the melting profile by broadening the transition between free molecular beacons in loop-stem structure to hybridized double helices [9]. Interactions between nucleotides within the same strand may occur with secondary internal loops. These loops are regarded as competitors against target oligonucleotide binding and decrease the T_m of the hybrid. General thermodynamic analysis of ion effects has been studied in terms of hairpin structure, indicating that reduced ion concentration may add to the loop free energy and destabilize the structure [45], but once the stabilization effect is saturated, a higher ion concentration does not further enhance stability [46]. As to the effect of a target probe length, T_m generally grows with longer probe lengths. Stem length also exerts significant influence on the T_m . A 2.7 °C reduction in hybrid T_m was observed by increasing the stem length by one base [9]. Thermodynamic analysis of molecular beacons is important due to the fact that it is closely related to the selectivity of molecular beacons [11]; the difference between phase transition temperature of a perfect beacon-target double helix and a mismatched duplex determines the selectivity of any given molecular beacon.

27.2 Classic Molecular Beacon Design Considerations

Thanks to vast online bioinformatics tools and database resources such as basic local alignment search tool (BLAST), we are able to target various wild-type gene sequences from huge databases and use the corresponding complementary sequences as beacon probes. However, several considerations should be taken to carefully design a molecular beacon. In this section, some of these general design considerations of classic molecular beacons will be discussed. Recent progress in molecular beacons involves new ideas in beacon design either to enhance their performance or to expand their applications.

The probe length, typically a 15–25-base oligonucleotide [47], should be of suitable length in order to position the fluorophore as far as possible from the quencher upon hybridization, or to be at least twice the length of each stem sequence [1]. Longer probes are also beneficial for faster hybridization kinetics. However, the different requirement of GC content between probe and stem portions is a barrier that makes this challenging. Bounded by three hydrogen bonds, GC pairs are more stable than AT pairs, which have only two hydrogen bonds. GC pairs should comprise at least half of the stem pairs in order to form a secure, rigid hairpin structure, while too much overall GC content should be avoided to avoid secondary internal loops formation. These loops, however, may appear even though GC pairs are not dominating, for example, consecutive AT pairs may also break the loop into secondary ones. To minimize the sliding of the hybridized target along the probe, GC residues are expected to occupy end positions of the loop [8]. Given that a wild-type sequence is a natural genetic code, it is not always straightforward to select sequences meeting all requirements, although the relative long length of genes compared to the molecular beacon permits many options. The stem portion is less difficult to design, with respect to length and GC content. Longer stems contribute to provide discrimination between mutant mismatch targets and perfectly matched ones within a large temperature range and increase the T_m gap between perfectly matched duplexes and mismatched ones. However, longer stems require longer loop sequences to overcome the energy barrier encountered in unzipping the stems and a decrease in hybridization rate may be observed [8]. They may also lead to false-negative results, whereas short and unstable stems give false-positive signals and higher background fluorescence [2, 9].

Fluorophores, analogous photosensitizers, and their quenchers should be selected carefully. Overall, fluorophores and photosensitizers should be chosen to have maximum emission spectral overlap with quencher absorption. Good quenching efficiency is required so that accuracy and sensitivity in fluorescence detection can be achieved with a low background signal. Fortunately, many quenchers like dabcyll can be applied to a very wide range of fluorophores. These universal quenchers usually exert both FRET and contact quenching [47]. Selection of fluorophores is based on various criteria [48]: an easily tuned photophysical and spectral range, stability against chemical, thermal, or light effects, and good bioconjugation properties. To avoid being quenched by nucleotides, it is best not to link fluorophores next to guanosine bases, which themselves can act like quenchers [10, 49].

Apart from design strategies, specific experimental conditions are important to consider. For example, the reaction buffer can have profound effects on performance. Since nucleic acid backbones are strongly negatively charged, cations such as sodium and magnesium help balance the charge so that molecular beacons are properly folded and fluorescence is quenched before the addition of target oligonucleotides. Ion concentration and size are important factors [46, 50]. For in vitro analysis, most molecular beacons are used in aqueous solutions. Organic solvents also have been studied as a buffer for molecular beacons. Although hybridization reactions in most common organic solvents do not take place to a full extent, faster kinetics are observed. T_m is found to have a solvent concentration-dependent decrease [51]. Fortunately, there are several online simulation tools that can assist the design of DNA molecular beacons, for example, the UNAFold Web Server of University at Albany [52]. These tools are able to give predicted thermodynamic properties and schematic hybridization possibilities, which can greatly lower the potential of unwanted secondary structure during the design process.

27.3 Next-Generation Molecular Beacon Designs

Numerous publications regarding optimization of molecular beacons have described enhancements to the performance of molecular beacons and have largely expanded the types of applications they are used in. In this section, we will introduce some of the more recent developments in design, from adjusting the beacon itself to incorporation with other technologies. These efforts not only improve molecular beacon efficacy but also reveal innovative ideas that may serve as future engineering options for photodynamic molecular beacons.

27.3.1 *Optimization of Fluorophores and Quenchers*

Since activatable photosensitizers share similar mechanisms with normal fluorophores of molecular beacons, approaches for selecting photosensitizers can benefit from examining recent trends in the selection of fluorophores and quenchers for standard molecular beacons [22]. Compared to the challenge of designing an optimal beacon stem and loop sequence, it is more straightforward to optimize fluorophores and quenchers; for example, by using fluorophores with more desirable spectral properties or by using quenchers that have higher quenching efficiency. As mentioned above, the efficacy of certain quenchers can be predicted by spectral properties alone. To further enhance sensitivity of molecular beacons, a “super-quencher” array of multiple quenchers was proposed [53]. 99.7 % quenching efficiency was observed using super-quenchers, which may result from higher absorption efficiency and the increased dipole–dipole coupling between the quenchers and the fluorophores. The architecture of super-quenchers can be

modified as multiple quenchers linked to a trebler phosphoramidite that branches one end of the beacon stem or a series of quenchers linearly connected to a photodynamic beacon [54]. Further development of this beacon led to programmed lipoprotein and liposome nanoparticle aggregation due to the hydrophobic character of the super-quenchers, which is inserted into the nanoparticles to induce irreversible aggregation upon target nucleic acid recognition [55].

Other than changes in type and number of quenchers, improvements can be achieved with other design aspects. Synthesis of classic molecular beacons involves two steps: conjugation of quenchers and conjugation of fluorophores [1]. However, a deprotection step is often required between these two steps, and therefore, more cost-effective and simplified conjugation schemes are useful [56]. Quencher-free molecular beacons simplify beacon design and synthesis [57]. The first example of this approach came from attaching a fluorophore to the loop portion so the probe provided a fluorescence differential to discriminate between perfectly matched targets and single-base mismatches [58]. Other quencher-free molecular beacons were subsequently reported. Analogous to contact quenching of conventional molecular beacons, formation of H-type dimers by two identical dye molecules tethered to both ends allowed silencing of fluorescence with restoration upon hybridization [59]. Similarly, a spectral shift from excimer fluorescence to monomer fluorescence with a different emission wavelength is feasible [60, 61]. These so-called excimer–monomer switching (EMS) molecular beacons differ from non-fluorescent dye dimerization beacons since the fluorescence intensity ratio between excimer and monomer emissions becomes the key discriminating criteria instead of total fluorescence intensity. Fluorescent groups themselves are able to act as “quenchers”, with terminal fluorophores serving as quenchers for each other. The determination of beacon opening is based on the ratio of fluorescence intensity emitted by the two fluorophores at their respective wavelengths [62]. This type of molecular beacon functions via wavelength shifting. Molecular beacons that do not have typical quenchers exist. As previously mentioned, certain nucleotide bases, especially guanosine, can quench fluorescence, so it is possible that nucleotide bases can take the role of quenchers in well-designed schemes. This is because these nucleotide bases tend to transfer electrons to fluorophores in terms of a photoelectron transfer [63]. The geometry of the attached fluorophores is important to take full advantage of nucleotide bases as quenchers. An interesting design used a fluorophore tethered to the center of the loop, accompanied by two guanosines on either side, to generate effective quenching [64]. Development of a quencher-free molecular beacon that has a fluorophore within its stem portion was also reported [56]. In this case, the microenvironment plays an important role in quenching. Making use of the fact that some fluorophores have solvent polarity preferences and there is a hydrophobic environment within the hybridization duplex between beacons and targets, fluorescence can be switched on or off based on the position of fluorophores. A linear probe with such strategy was synthesized [65]. As shown in Fig. 27.5, this approach was carried out so that hybridization controlled the local environment of the dye molecule, which was attached to the middle of one stem [56]. 7-hydroxycoumarin, whose fluorescence is controlled by protonation or

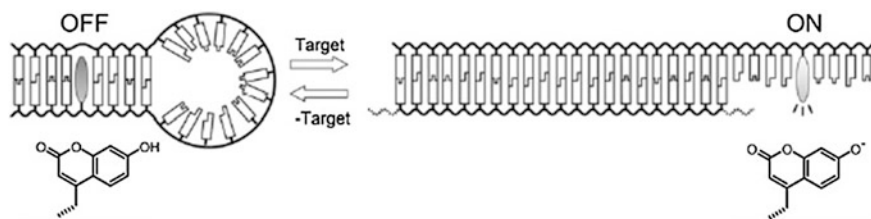


Fig. 27.5 A quencher-free molecular beacon with a fluorophore (7-hydroxycoumarin) embedded within the stem (Recreated with kind permission from Elsevier; *Bioorg. Med. Chem.* 2012; 15; 20(14):4310–5)

deprotonation, was used as the fluorophore. A similar approach made use of thiazole orange (TO) and thiazole red (TR) adjacently embedded on two arms of the stem. The incorporation of two fluorophores makes the beacon emit red when the beacon is closed and the fluorophores are kept within the hydrophobic stem. When the complementary target binds, the stem opens and shifts the red emission to a blue one. This “DNA Traffic Light” approach successfully combined concepts of wavelength shifting and in-stem labeling together to produce a smart probe that is suitable for living cell applications. These combined strategies help to reduce false-positive and false-negative signals given from autofluorescence or undesired quenching, which usually occur in single-emission molecular beacons [66]. Photodynamic molecular beacons could take advantage of the same approaches.

Considering that organic dye molecules may have short biological lifetimes, there may be limitations for *in vivo* applications, and therefore, inorganic particles have been considered as alternate reporters for molecular beacons [67]. Silver nanoclusters (Ag NC) were proposed as a new class of fluorophore [68]. Upon the addition of the complementary target, dark Ag NCs were transformed to bright red-emitting ones. Rather than being quenched, Ag NCs did not show fluorescence signal until they were brought close to guanine bases at the end of the target. Although details of this new signal reporting are still emerging, this approach provides advantages over classic organic dye molecules. For example, the synthesis is straightforward and involves only a single step. Since Ag alone does not produce any signal, excess reagents do not contribute to fluorescence, whereas free organic dye molecules need to be carefully removed during purification. Quantum dots (QDs) have also been used to label molecular beacons as fluorophores. Compared to conventional organic fluorescent dyes, QDs are capable of serving as fluorophores with decent quantum yields, excellent stability, tunable absorption and emission, and a wide UV absorption spectrum [69]. Just as multicolor molecular beacons have been used to detect multiple targets by simultaneously using different molecular beacons with different fluorophores in the same solution [13], different color QDs have also been synthesized and conjugated to molecular beacons to make this possible [70]. Other efforts include replacing fluorophores with CdSe–ZnS core–shell QDs for real-time visualization of virus replication in living cells [71]. Water-soluble QDs may release toxic ions like Cd^{2+} and must be

carefully prepared to meet the demands of *in vivo* diagnostics [72]. The stabilization of QDs in a wide range of environmental conditions is enhanced through the use of silica and amphiphilic polymers. Further improvements in encapsulation technology focus on controlling the size to lead to more efficient energy transfer while maintaining the high quantum yield of QDs in harsh chemical environments [73]. The size of QDs is important in that a certain distance between fluorophores and quenchers is required for Förster energy transfer.

If these new design strategies are applied to photodynamic molecular beacons, several advantages could be achieved. For example, enhanced singlet oxygen quenching could lead to the more efficient beacons. Quencher-free options are interesting to explore to generate more potent beacons. Ultimately, these designs may lead to superior photodynamic molecular beacons that require less dosage with enhanced efficacy.

27.3.2 New Designs of Loops and Stems

Besides the importance of quenching before activation, fast kinetics of fluorescence restoration and singlet oxygen generation are desirable for accurate and effective treatment using photodynamic molecular beacons. The time needed for either peptide cleavage or nucleic acid hybridization is an important parameter and in some situation can be improved using new designs of loops and stems.

It may be challenging to optimize conventional molecular beacons only through base-pair adjustment, but many new ideas have emerged that involve modification of the loop and stem portions. Regarding the probe length of molecular beacons, which is usually less than 30 nucleotides, it is known that very long probes may negatively impact hybridization kinetics. However, in certain applications, such as homogeneous PCR screening assays as an example, an unusual long or “sloppy” probe may be useful [74]. The aim is to use the probe in such a manner that it can hybridize with amplicons from different species despite the presence of mismatched base pairs. By looking into the T_m of hybrids, each mycobacterium sample featured a unique thermodynamic profile, regardless of the initial bacterial concentration. Sloppy molecular beacons have been shown to be compatible with various real-time PCR platforms in clinical microbiology detection. To determine rifampin resistance in mycobacterium tuberculosis, the characteristic thermodynamic profiles of sloppy beacons were used to differentiate wild-type resistance sequences from mutant ones in approximately 2 h [75].

The development of molecular beacons with peptide stems has been explored. While common photosensitizers suffer from killing healthy tissue from non-specific accumulation, photodynamic peptide beacons show better selectivity [34]. Singlet oxygen can be generated from photosensitizers activated by both enzymes and target nucleic acids [21, 25]. The fact that proteases are usually overexpressed by tumors affords opportunity for cancer diagnostics and treatment with photodynamic molecular beacons. Protease-targeted molecular beacons operate on the

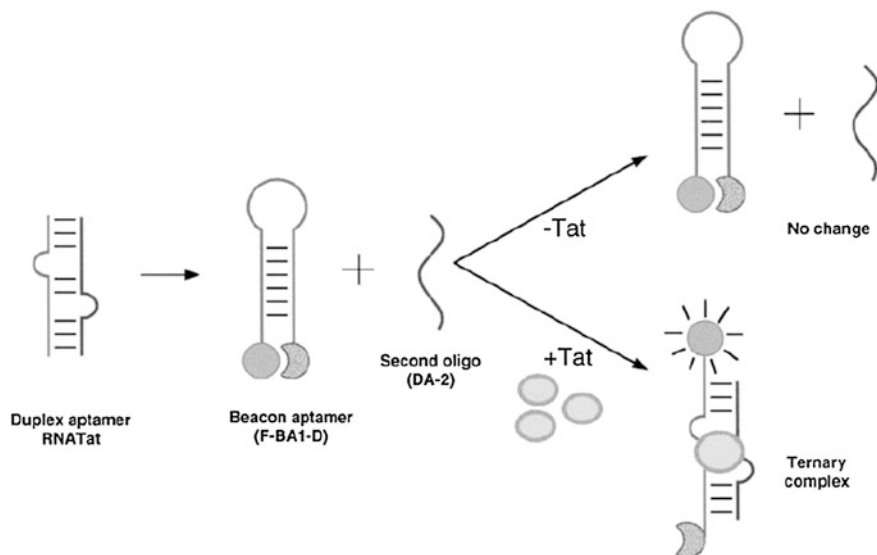


Fig. 27.6 Molecular beacon aptamer for HIV-1 Tat protein detection (Recreated with kind permission from John Wiley and Sons; *Genes to Cells*. 2000; 5(5):389–96)

basis of proteases breaking down proteins through hydrolysis of specific peptide bonds [26, 76, 77]. Other enzymes such as nucleases have also been used as the activating agent of molecular beacons [78]. Nucleic acid-based molecular beacons are also capable of protein recognition. Aptamers that recognize a specific protein can form the basis of split oligomers that report protein binding (Fig. 27.6). The beacon responded only to Tat-1 or its peptides, while fluorescence emission was not observed in the presence of other RNA-binding proteins [79]. Enhancement of beacon fluorescence activation can also be achieved by protease cleavage since a single protease can cleave multiple beacons [21]. Conventional fluorescence beacons have been functionalized with enzyme-recognizing linkers in a similar fashion [80]. Protease molecular beacons have fluorophores and quenchers just like classic nucleic acid molecular beacons. They are connected by a peptide sequence, which is cleaved in the presence of a target protease. In preclinical studies, protease-based beacons have high delivery yield, low toxicity, and low immunogenicity [81]. Adjacency of quenchers and fluorophores in peptide beacons is realized through random or deliberate self-folding peptide sequences. Polyarginine/polyglutamate electrostatic hairpins have also been reported to keep quenchers and photosensitizers in close proximity [82]. Peptide nucleic acid linkers, which recognize other nucleic acids, have been described that are based on oligonucleotide mimics using an N-(2-aminoethyl)glycine backbone [83]. Compared to analogous DNA:DNA or DNA:RNA duplexes, peptide nucleic acid sequences tend to hybridize faster into stronger complexes due to their non-negatively charged backbone [84].



Fig. 27.7 A molecular beacon with stems connected by a PEG loop (Recreated with kind permission from American Chemical Society; *J. Am. Chem. Soc.* 2006; 1; 128(31):9986–7)

The expansion of the molecular beacon family is more than target-oriented. Several pragmatic considerations have also given rise to modified beacons. Degradation of oligonucleotide backbones by endogenous nucleases makes molecular beacons vulnerable during cellular imaging applications [85, 86]. By including 2'-O-methyl-modified bases, molecular beacons become resistant to degradation. This involves the replacement of a hydrogen atom by a methoxy group at the 2' base position and prevents enzymatic activity by RNase H [87]. An interesting hybrid molecular beacon linker was designed using a donor and acceptor linked by a poly(ethylene glycol) (PEG) polymer chain [88]. As shown in Fig. 27.7, hybridization brought the two terminal ends together, without the use of any type of loop component. This design used PEG to create spacing between the fluorophore and quencher, while at the same time was flexible enough to permit effective hybridization. This type of molecular beacons is suitable for applications in living cells since this construct avoids nuclease degradation, protein binding, or thermodynamic fluctuations from which conventional molecular beacons may suffer from [89]. On the other extreme, stem-less molecular beacons (Fig. 27.8) have been developed with fast hybridization kinetics and good signal-to-noise (S/N) ratios for biological applications [57, 90]. Another positive feature of stem-less molecular beacons is that the sequence design is greatly simplified. Most molecular beacons make use of a self-complementary stem sequence to silence fluorescence by keeping fluorophores and quenchers in close proximity. Another stem-hybridization strategy consists of a cleavable polyanionic peptide arm and a polycationic peptide arm (Fig. 27.9) [82]. This photodynamic beacon was activated in the two steps of cleavage and stem dissociation. Furthermore, the polycationic arm acted as a cell-penetrating peptide to facilitate cellular uptake.

Conventional molecular beacons are usually designed based on one desired target sequence. However, this specificity is lost with undesired transitions from hairpin structure to random coil. Within complex cellular systems, intermolecular interactions between stems and their complementary sequences may hinder the designed hybridization scheme and largely increase the background signal [89]. To overcome this problem, unnatural enantiomeric L-DNA can be used to replace natural DNA or RNA in the stem. The insertion of L-DNA does not affect physical properties of the molecule and eliminates the possibility of "stem invasion" by non-specific nucleic acids. Molecular beacons with a homo-DNA stem also protect

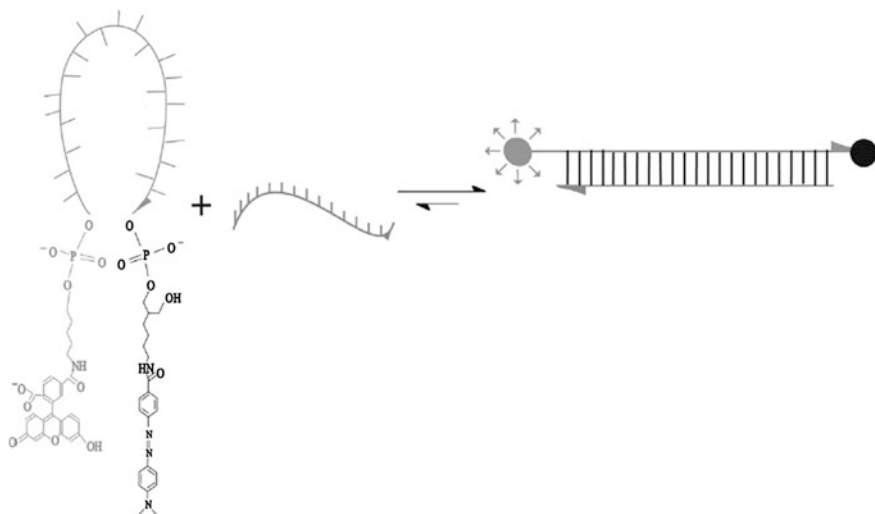


Fig. 27.8 Schematic working mechanism of a stem-less molecular beacon (Recreated with kind permission from Elsevier; *Anal. Biochem.* 2005, 1; 347 [1]:77–88)

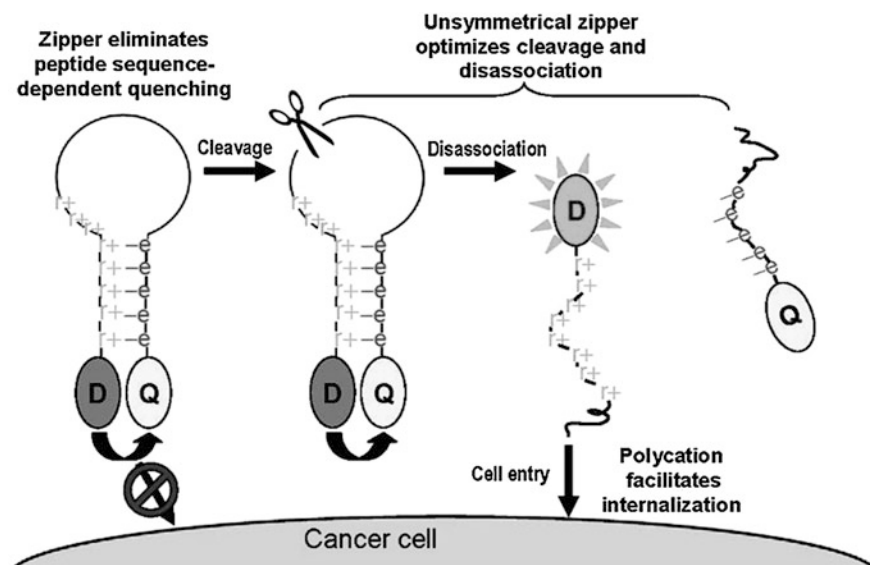


Fig. 27.9 A beacon composed of a pair of polycation and polyanion arms holding the dye (*D*) and quencher (*Q*) in close proximity due to electrostatic attraction (Recreated with kind permission from American Chemical Society; *Bioconjug. Chem.* 2009, 21; 20(10):1836–42)

the stem part from unwanted interactions. Similar to L-DNA, homo-DNA stems are orthogonal DNA analogs that do not hybridize with natural nucleic acids. The preparation of homo-DNA can be carried out with the standard automated phosphoramidite chemistry used in DNA synthesis [91]. A similar concept has been proposed with the incorporation of locked nucleic acid (LNA). Molecular beacons with LNA backbones have superior resistance to degradation and non-specific opening in complex biological environments. LNA molecular beacons exhibit better thermostability and selectivity compared to standard DNA beacons [92]. The stronger stability is related to slow hybridization kinetics; thus, efforts have been made to engineer hybrid LNA/DNA molecular beacons with faster hybridization kinetics while maintaining low background and resistance to degradation. Insertion of LNA in the loop portion of the beacon maintains degradation resistance while improving hybridization kinetics [93].

27.3.3 Other Considerations for Molecular Beacons

Several diverse improvements have been developed for various parts of molecular beacons that deserve mention. FRET quenching and contact quenching form a central tool for molecular beacons. However, these mechanisms have limitation in certain applications due to interference induced by biological environments [94]. The desire for improved energy transfer mechanism comes from the fact that acceptors may be coexcited along with the energy donors because of the overlap of their excitation spectra [95]. Solutions to this problem could involve strategies mentioned before, such as quencher-free designs or alternatively, to apply two-photon excitation (TPE) to molecular beacons. TPE involves the simultaneous absorption of two photons with lower energies to excite the fluorophores. The coexcitation phenomenon can be avoided since TPE fluorophores are excited in near-infrared region so that biological fluorescence and quencher TPE may be reduced [96]. Although numerous optimized methods have been described to maximize beacon fluorescence increase, in theory, there is only one action, i.e., stem disassociation, which is responsible for the signal amplification. Recently, another step to further amplify the signal was developed by cleaving the loop after the hybridization with the target. The beacon in this study was composed of a RNA loop and DNA stem, while consequent addition of thermostable RNase H activated the cleavage of RNA loop. The targets released from the cleaved loops could then hybridize with other beacons, creating an amplification step. This enzymatic amplification resulted in the detection of a small amount of enzyme [97].

The most developed field for molecular beacon use is real-time PCR monitoring. As a detection tool, molecular beacons are helpful to recognize the presence of small amounts of nucleic acids in biological samples. Since molecular beacons remain dark before being activated, separation of probe–target hybrids is not essential to determine the amplicon number [98]. Besides nucleic acid detection, molecular beacons have been involved in other applications. As has been discussed,

molecular beacons can be regarded as a therapeutic tool when transformed into photodynamic molecular beacons to destroy target tissues [21, 25]. Furthermore, molecular beacons are also capable of actuating drug release. Gold nanoparticles, which have been used to quench fluorescence, can serve not only as a quencher, but also as a substrate to carry drug delivery agents as well. In this approach, multiple molecular beacons were immobilized onto gold nanoparticles. For each beacon, Doxorubicin (Dox) was intercalated into the double-stranded 5'-GC-3' or 5'-CG-3' sequences of DNA or RNA stems. Sequestered within the stem, Dox cytotoxicity was largely attenuated. However, Dox was released when targets opened the hairpin structure. This strategy can be used for drug release against cancer targets by selecting appropriate tumor-related mRNAs [99].

As a detection agent, molecular beacons have been used as to sense various targets. Several new targets have been detected using molecular beacons recently, including glutathione and cysteine [100], thrombin [101], human prostate cancer cells [102]. A rapid molecular beacon-based assay has been developed to determine gene fragments along with PCR amplification products related to chronic myelogenous leukemia (CML) [103]. Recently, a TO-labeled peptide nucleic acid molecular beacon was applied in real time for in vivo imaging of endogenous mRNA with single-nucleotide polymorphism (SNP) resolution [84]. A recent demonstration of LNA molecular beacons involved the evaluation of UV induced DNA damage. The discrimination between the damaged and undamaged DNA was based on the finding that the UV-affected configuration has a lower T_m , which resulted in lower fluorescence [104]. The result demonstrated that detection of damaged DNA was possible in low target concentration, while high ionic strength can improve the process [105]. Protein molecules can be detected using novel approaches to molecular beacons. A gold-supported solid-state molecular beacon without classic hairpin structure was designed (Fig. 27.10). The distance between the gold, the quencher, and the labeled Cy3 controlled the fluorescence signal intensity, eliminating the role for a hairpin structure. The left part of Fig. 27.10 shows the working mechanism of a single-stranded DNA probe detecting a single-stranded DNA-binding protein (SSBP). Due to the flexibility of single-stranded DNA, the Cy3 attached to the 3' end of the probe was quenched by the gold substrate. The addition of SSBP moves the Cy3 away from the gold by forming a rigid double helix. Conversely, the detection of a histone protein resulted in a decrease in fluorescence. Taking advantage of the fact that histone is able to wind and condense double-stranded DNA, the distance between Cy3 and the gold could be shortened, thus lowering the fluorescence [106]. In this protein detection design, the gold served as both the quenching and immobilization agent at the same time. DNA damage caused by chemotherapeutic effects could be assessed via molecular beacons. Cisplatin (cis-ziamminedichloroplatinum(II)), an anti-cancer drug, reacts with cellular DNA and cross-links either AG or GG bases, leading to cell division inhibition and cell death [107]. Damaged target DNA could be detected via the decrease in fluorescence due to the mismatch base pairs. The advantage of molecular beacons over conventional chromatographical methods to assess DNA damage is that there is no need to isolate the damaged DNA [108].

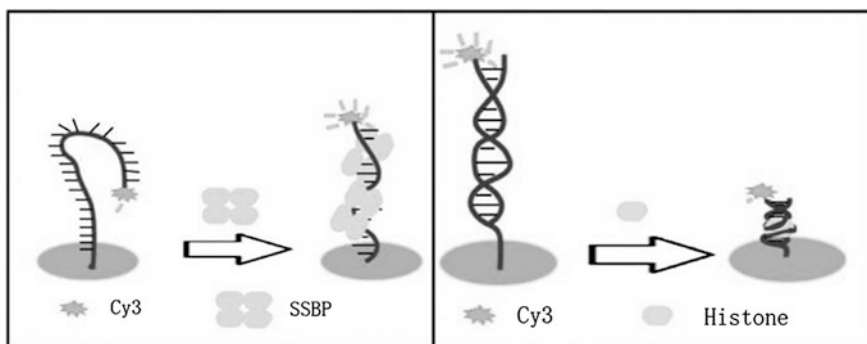


Fig. 27.10 Molecular beacon sensor that is able to detect single-stranded DNA-binding protein (*SSBP*) and histone protein (Recreated with kind permission from American Chemical Society; *Anal. Chem.* 2011; 1; 83(9):3528–32)

Ions can also be detected through molecular beacons. As shown in Fig. 27.11, a beacon was designed consisting of two phosphorylated and pyrene-labeled oligonucleotides (P1 and P2). Although they had five matching base pairs close to labeled pyrene that served as the stem, the T_m of this hybrid was 6.5 °C less than the experimental condition (25 °C). Thus, free P1 and P2 did not hybridize with each other until the target Zr^{4+} ions were introduced to form a strong $-PO_3^{2-}-Zr^{4+}-PO_3^{2-}$ -structure between the ends so that the two labeled pyrene molecules were brought close to each other to give rise to strong excimer fluorescence. Furthermore, γ -cyclodextrin was found to further amplify the signal [109]. The key to triggering fluorescence emission in this work was the change in T_m reflected by the structural change induced by the target ions, which is different from the traditional beacon opening scheme. A similar metal ion-activated linker, T-Hg-T, that directly controlled the on/off state of the molecular beacon was embedded across two sides within a beacon stem portion. The in-stem bridge acted to bring the fluorophore and quencher together to silence the fluorescence. The beacon was reopened with the addition of a biomarker of oxidative stress and cardiovascular disease, homocysteine [110].

Graphene oxide has emerged as an exciting material that can be used as a quencher [111]. A hairpin molecular beacon labeled with carboxyfluorescein was linked to graphene oxide as a quencher. The fluorescence was sharply quenched by graphene. The complementary target was able to restore part of the fluorescence and lower the quenching efficiency due to the weaker adsorption of the hybrid to the graphene oxide sheet. Damaged DNA targets failed to form intact duplex structures with molecular beacon, which retained higher quenching [112]. Recent trends in applying graphene oxide as quenchers include optimization of the distance range for fluorescence signaling on graphene oxide, measuring beacon adsorption energy, and optimizing the washing process required to remove adsorbed beacons [113, 114]. Other than quenching, graphene oxides use its rigidity for molecular beacons applications. LNA-modified molecular beacons formed a delivery system together

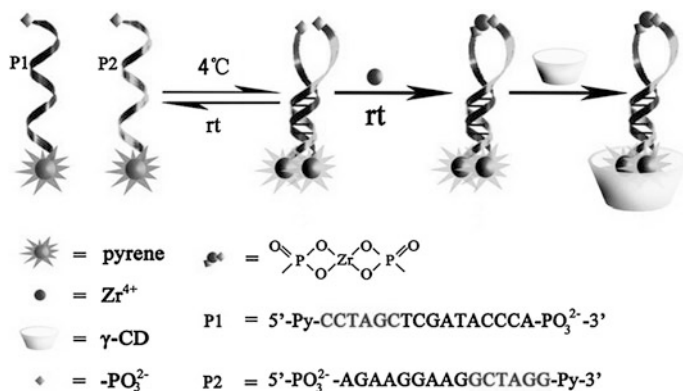


Fig. 27.11 The schematics of molecular beacon detection of Zr^{4+} and use γ -CD as a signal amplifier (Recreated with kind permission from American Chemical Society; *Anal. Chem.* 2012; 6; 84(5):2124–8)

with polyethylenimine-grafted graphene nanoribbons (PEI-g-GNR). In this study, graphene contributed to higher transfection efficiency due to its excellent affinity and improvements to the resistance of the beacon [115].

27.4 Final Remarks

Researchers have been focusing on molecular beacons since the first classic molecular beacons were reported in 1996 [1]. Their unique biorecognition ability comes with their rationally designed structure which can target any desired nucleic acid sequence and more recently several other target molecules. They form the starting point to develop photodynamic molecular beacons as a new detection and therapeutic tools. In this chapter, we introduced some fundamentals of molecular beacons and design considerations. Recent improvements and designs of molecular beacons can provide inspiration for future photodynamic molecular beacon design.

Instead of evolutionary improvements to the classic beacon design, many highly novel ideas have been proposed to improve beacon performance. By modulating the structure in numerous ways, beacons can exhibit improved performance in complex biological environments. New biorecognition schemes using molecular beacons will continue to be developed and inspire more novel ideas. These changes in structure can be related back to classic molecular beacon design and serve as future design considerations for photodynamic molecular beacons as well. There is enormous opportunity in converting some of the molecular beacons described in the chapter into new photodynamic molecular beacons. By replacing the fluorophores with light-activatable photosensitizers, seamless conversion of an imaging probe to a therapeutic probe is achieved. Thus, photodynamic molecular beacons have a bright future ahead as they follow in the footsteps of classic molecular beacons.

References

1. Tyagi S, Kramer FR (1996) Molecular beacons: probes that fluoresce upon hybridization. *Nat Biotechnol* 14:303–308
2. Li Y, Zhou X, Ye D (2008) Molecular beacons: an optimal multifunctional biological probe. *Biochem Biophys Res Commun* 373:457–461
3. Marras SAE, Kramer FR, Tyagi S (2002) Efficiencies of fluorescence resonance energy transfer and contact-mediated quenching in oligonucleotide probes. *Nucl Acids Res* 30:e122–e122
4. Cardullo RA, Agrawal S, Flores C, Zamecnik PC, Wolf DE (1988) Detection of nucleic acid hybridization by nonradiative fluorescence resonance energy transfer. *PNAS* 85:8790–8794
5. Morrison LE, Halder TC, Stols LM (1989) Solution-phase detection of polynucleotides using interacting fluorescent labels and competitive hybridization. *Anal Biochem* 183:231–244
6. Fuchs J, Podda M (2004) *Encyclopedia of medical genomics and proteomics-2 Volume Set*. CRC Press
7. Marras SAE, Russell Kramer F, Tyagi S (1999) Multiplex detection of single-nucleotide variations using molecular beacons. *Genet Anal Biomol Eng* 14:151–156
8. Bonnet G, Tyagi S, Libchaber A, Kramer FR (1999) Thermodynamic basis of the enhanced specificity of structured DNA probes. *PNAS* 96:6171–6176
9. Tsourkas A, Behlke MA, Rose SD, Bao G (2003) Hybridization kinetics and thermodynamics of molecular beacons. *Nucl Acids Res* 31:1319–1330
10. Marras SAE (2006) Selection of fluorophore and quencher pairs for fluorescent nucleic acid hybridization probes. *Methods Mol Biol* 335:3–16
11. Wang K, Tang Z, Yang CJ et al (2009) Molecular engineering of DNA: molecular beacons. *Angewandte Chemie Int Ed* 48:856–870
12. Lakowicz JR (2006) *Principles of fluorescence spectroscopy*. Springer
13. Tyagi S, Bratu DP, Kramer FR (1998) Multicolor molecular beacons for allele discrimination. *Nat Biotechnol* 16:49–53
14. Förster T (1948) Zwischenmolekulare energiewanderung und fluoreszenz. *Ann Phys* 437:55–75
15. Stryer L (1978) Fluorescence energy transfer as a spectroscopic ruler. *Ann Rev Biochem* 47:819–846
16. Haugland RP, Yguerabide J, Stryer L (1969) Dependence of the kinetics of singlet energy transfer on spectral overlap. *PNAS* 63:23–30
17. Bernacchi S, Mély Y (2001) Exciton interaction in molecular beacons: a sensitive sensor for short range modifications of the nucleic acid structure. *Nucleic Acids Res* 29:e62
18. Lovell JF, Chen J, Jarvi MT, Cao W-G, Allen AD, Liu Y, Tidwell TT, Wilson BC, Zheng G (2009) FRET quenching of photosensitizer singlet oxygen generation. *J Phys Chem B* 113:3203–3211
19. Wu J, Zou Y, Li C, Sicking W, Piantanida I, Yi T, Schmuck C (2012) A molecular peptide beacon for the ratiometric sensing of nucleic acids. *J Am Chem Soc* 134:1958–1961
20. Said Hassane F, Saleh AF, Abes R, Gait MJ, Lebleu B (2010) Cell penetrating peptides: overview and applications to the delivery of oligonucleotides. *Cell Mol Life Sci* 67:715–726
21. Chen J, Stefflova K, Niedre MJ, Wilson BC, Chance B, Glickson JD, Zheng G (2004) Protease-triggered photosensitizing beacon based on singlet oxygen quenching and activation. *J Am Chem Soc* 126:11450–11451
22. Lovell JF, Liu TWB, Chen J, Zheng G (2010) Activatable photosensitizers for imaging and therapy. *Chem Rev* 110:2839–2857
23. Stefflova K, Chen J, Zheng G (2007) Killer beacons for combined cancer imaging and therapy. *Curr Med Chem* 14:2110–2125
24. Wilson BC, Patterson MS (2008) The physics, biophysics and technology of photodynamic therapy. *Phys Med Biol* 53:R61–R109

25. Zheng G, Chen J, Stefflova K, Jarvi M, Li H, Wilson BC (2007) Photodynamic molecular beacon as an activatable photosensitizer based on protease-controlled singlet oxygen quenching and activation. *PNAS* 104:8989–8994
26. Liu TWB, Chen J, Zheng G (2011) Peptide-based molecular beacons for cancer imaging and therapy. *Amino Acids* 41:1123–1134
27. Cló E, Snyder JW, Voigt NV, Ogilby PR, Gothelf KV (2006) DNA-programmed control of photosensitized singlet oxygen production. *J Am Chem Soc* 128:4200–4201
28. Chen J, Lovell JF, Lo P-C, Stefflova K, Niedre M, Wilson BC, Zheng G (2008) A tumor mRNA-triggered photodynamic molecular beacon based on oligonucleotide hairpin control of singlet oxygen production. *Photochem Photobiol Sci* 7:775–781
29. Tørring T, Toftegaard R, Arnbjerg J, Ogilby PR, Gothelf KV (2010) Reversible pH-regulated control of photosensitized singlet oxygen production using a DNA i-Motif. *Angewandte Chemie Int Ed* 49:7923–7925
30. Lo P-C, Chen J, Stefflova K, Warren MS, Navab R, Bandarchi B, Mullins S, Tsao M, Cheng JD, Zheng G (2009) Photodynamic molecular beacon triggered by fibroblast activation protein on cancer-associated fibroblasts for diagnosis and treatment of epithelial cancers. *J Med Chem* 52:358–368
31. Jin CS, Lovell JF, Chen J, Zheng G (2013) Ablation of hypoxic tumors with dose-equivalent photothermal, but not photodynamic, therapy using a nanostructured porphyrin assembly. *ACS Nano* 7:2541–2550. doi: [10.1021/nm3058642](https://doi.org/10.1021/nm3058642)
32. Zhang Y (2012) Porphyrins as theranostic agents from prehistoric to modern times. *Theranostics* 2:905–915
33. Chen J, Jarvi M, Lo P-C, Stefflova K, Wilson BC, Zheng G (2007) Using the singlet oxygen scavenging property of carotenoid in photodynamic molecular beacons to minimize photodamage to non-targeted cells. *Photochem Photobiol Sci* 6:1311–1317
34. Liu TW, Akens MK, Chen J, Wise-Milestone L, Wilson BC, Zheng G (2011) Imaging of specific activation of photodynamic molecular beacons in breast cancer vertebral metastases. *Bioconjugate Chem* 22:1021–1030
35. Stefflova K, Chen J, Li H, Zheng G (2006) Targeted photodynamic therapy agent with a built-in apoptosis sensor for in vivo near-infrared imaging of tumor apoptosis triggered by its photosensitization in situ. *Mol Imaging* 5:520–532
36. Lovell JF, Chan MW, Qi Q, Chen J, Zheng G (2011) Porphyrin FRET acceptors for apoptosis induction and monitoring. *J Am Chem Soc* 133:18580–18582
37. Zhu Z, Tang Z, Phillips JA, Yang R, Wang H, Tan W (2008) Regulation of singlet oxygen generation using single-walled carbon nanotubes. *J Am Chem Soc* 130:10856–10857
38. Zhu Z, Yang R, You M, Zhang X, Wu Y, Tan W (2010) Single-walled carbon nanotube as an effective quencher. *Anal Bioanal Chem* 396:73–83
39. Kam NWS, Liu Z, Dai H (2006) Carbon nanotubes as intracellular transporters for proteins and DNA: an investigation of the uptake mechanism and pathway. *Angewandte Chemie Int Ed* 45:577–581
40. Liu Y, Chen W, Wang S, Joly AG (2008) Investigation of water-soluble x-ray luminescence nanoparticles for photodynamic activation. *Appl Phys Lett* 92:043901–043901–3
41. SantaLucia J (1998) A unified view of polymer, dumbbell, and oligonucleotide DNA nearest-neighbor thermodynamics. *PNAS* 95:1460–1465
42. Yakovchuk P, Protozanova E, Frank-Kamenetskii MD (2006) Base-stacking and base-pairing contributions into thermal stability of the DNA double helix. *Nucleic Acids Res* 34:564–574
43. Vologodskii AV, Amirikyan BR, Lyubchenko YL, Frank-Kamenetskii MD (1984) Allowance for heterogeneous stacking in the DNA helix-coil transition theory. *J Biomol Struct Dyn* 2:131–148
44. Breslauer KJ, Frank R, Blöcker H, Marky LA (1986) Predicting DNA duplex stability from the base sequence. *PNAS* 83:3746–3750
45. Tan Z-J, Chen S-J (2008) Salt dependence of nucleic acid hairpin stability. *Biophys J* 95:738–752

46. Tan Z-J, Chen S-J (2006) Nucleic acid helix stability: effects of salt concentration, cation valence and size, and chain length. *Biophys J* 90:1175–1190
47. Tsourkas A, Bao G (2003) Shedding light on health and disease using molecular beacons. *Brief Funct Genomic Proteomic* 1:372–384
48. Nesterova IV, Verdree VT, Pakhomov S, Strickler KL, Allen MW, Hammer RP, Soper SA (2007) Metallo-phthalocyanine near-IR fluorophores: oligonucleotide conjugates and their applications in PCR assays. *Bioconj Chem* 18:2159–2168
49. Seidel CAM, Schulz A, Sauer MHM (1996) Nucleobase-specific quenching of fluorescent dyes. I. nucleobase one-electron redox potentials and their correlation with static and dynamic quenching efficiencies. *J Phys Chem* 100:5541–5553
50. Owczarzy R, You Y, Moreira BG, Manthey JA, Huang L, Behlke MA, Walder JA (2004) Effects of sodium ions on DNA duplex oligomers: improved predictions of melting temperatures. *Biochemistry* 43:3537–3554
51. Dave N, Liu J (2010) Fast molecular beacon hybridization in organic solvents with improved target specificity. *J Phys Chem B* 114:15694–15699
52. Zuker M (2003) Mfold web server for nucleic acid folding and hybridization prediction. *Nucleic Acids Res* 31:3406–3415
53. Yang CJ, Lin H, Tan W (2005) Molecular assembly of superquenchers in signaling molecular interactions. *J Am Chem Soc* 127:12772–12773
54. Lovell JF, Chen J, Huynh E, Jarvi MT, Wilson BC, Zheng G (2010) Facile synthesis of advanced photodynamic molecular beacon architectures. *Bioconj Chem* 21:1023–1025
55. Lovell JF, Jin H, Ng KK, Zheng G (2010) Programmed nanoparticle aggregation using molecular beacons. *Angewandte Chemie Int Ed* 49:7917–7919
56. Kashida H, Yamaguchi K, Hara Y, Asanuma H (2012) Quencher-free molecular beacon tethering 7-hydroxycoumarin detects targets through protonation/deprotonation. *Bioorg Med Chem* 20:4310–4315
57. Venkatesan N, Seo YJ, Kim BH (2008) Quencher-free molecular beacons: a new strategy in fluorescence based nucleic acid analysis. *Chem Soc Rev* 37:648–663
58. Hwang GT, Seo YJ, Kim BH (2004) A highly discriminating quencher-free molecular beacon for probing DNA. *J Am Chem Soc* 126:6528–6529
59. Knemeyer J-P, Marmé N, Häfner B, Habl G, Schäfer G, Müller M, Nolte O, Sauer M, Wolfrum J (2005) Self-quenching DNA probes based on dye dimerization for identification of mycobacteria. *Int J Env Anal Chem* 85:625–637
60. Fujimoto K, Shimizu H, Inouye M (2004) Unambiguous detection of target DNAs by excimer-monomer switching molecular beacons. *J Org Chem* 69:3271–3275
61. Berndt S, Wagenknecht H-A (2009) Fluorescent color readout of DNA hybridization with thiazole orange as an artificial DNA base. *Angewandte Chemie Int Ed* 48:2418–2421
62. Zhang P, Beck T, Tan W (2001) Design of a molecular beacon DNA probe with two fluorophores. *Angewandte Chemie Int Ed* 40:402–405
63. Heinlein T, Knemeyer J-P, Piestert O, Sauer M (2003) Photoinduced electron transfer between fluorescent dyes and guanosine residues in DNA-hairpins. *J Phys Chem B* 107:7957–7964
64. Ryu JH, Seo YJ, Hwang GT, Lee JY, Kim BH (2007) Triad base pairs containing fluorene unit for quencher-free SNP typing. *Tetrahedron* 63:3538–3547
65. Okamoto A, Tainaka K, Ochi Y, Kanatani K, Saito I (2006) Simple SNP typing assay using a base-discriminating fluorescent probe. *Mol BioSyst* 2:122–127
66. Holzhauser C, Wagenknecht H-A (2011) In-stem-labeled molecular beacons for distinct fluorescent color readout. *Angewandte Chemie Int Ed* 50:7268–7272
67. Kim JH, Morikis D, Ozkan M (2004) Adaptation of inorganic quantum dots for stable molecular beacons. *Sens Actuators B Chem* 102:315–319
68. Yeh H-C, Sharma J, Han JJ, Martinez JS, Werner JH (2010) A DNA—silver nanocluster probe that fluoresces upon hybridization. *Nano Lett* 10:3106–3110
69. Huang K, Martí AA (2012) Recent trends in molecular beacon design and applications. *Anal Bioanal Chem* 402:3091–3102

70. Kim JH, Chaudhary S, Ozkan M (2007) Multicolour hybrid nanoprobe of molecular beacon conjugated quantum dots: FRET and gel electrophoresis assisted target DNA detection. *Nanotechnology* 18:195105
71. Yeh H-Y, Yates MV, Mulchandani A, Chen W (2010) Molecular beacon-quantum dot-Au nanoparticle hybrid nanoprobe for visualizing virus replication in living cells. *Chem Commun* 46:3914–3916
72. Hu X, Gao X (2010) Silica-polymer dual layer-encapsulated quantum dots with remarkable stability. *ACS Nano* 4:6080–6086
73. Wu C-S, Oo MKK, Cupps JM, Fan X (2011) Robust silica-coated quantum dot-molecular beacon for highly sensitive DNA detection. *Biosens Bioelectron.* doi: [10.1016/j.bios.2011.02.049](https://doi.org/10.1016/j.bios.2011.02.049)
74. El-Hajj HH, Marras SAE, Tyagi S, Shashkina E, Kamboj M, Kiehn TE, Glickman MS, Kramer FR, Alland D (2009) Use of sloppy molecular beacon probes for identification of mycobacterial species. *J Clin Microbiol* 47:1190–1198
75. Chakravorty S, Kothari H, Aladegbami B et al (2012) Rapid, high-throughput detection of rifampin resistance and heteroresistance in *Mycobacterium tuberculosis* by use of sloppy molecular beacon melting temperature coding. *J Clin Microbiol* 50:2194–2202
76. Law B, Tung C-H (2009) Proteolysis: a biological process adapted in drug delivery, therapy, and imaging. *Bioconj Chem* 20:1683–1695
77. Turk B (2006) Targeting proteases: successes, failures and future prospects. *Nat Rev Drug Discov* 5:785–799
78. Li JJ, Geyer R, Tan W (2000) Using molecular beacons as a sensitive fluorescence assay for enzymatic cleavage of single-stranded DNA. *Nucleic Acids Res* 28:e52
79. Yamamoto R, Kumar PKR (2000) Molecular beacon aptamer fluoresces in the presence of Tat protein of HIV-1. *Genes Cells* 5:389–396
80. Matayoshi ED, Wang GT, Krafft GA, Erickson J (1990) Novel fluorogenic substrates for assaying retroviral proteases by resonance energy transfer. *Science* 247:954–958
81. Tung C-H (2004) Fluorescent peptide probes for in vivo diagnostic imaging. *Biopolymers* 76:391–403
82. Chen J, Liu TWB, Lo P-C, Wilson BC, Zheng G (2009) “Zipper” molecular beacons: a generalized strategy to optimize the performance of activatable protease probes. *Bioconj Chem* 20:1836–1842
83. Egholm M, Buchardt O, Christensen L, Behrens C, Freier SM, Driver DA, Berg RH, Kim SK, Norden B, Nielsen PE (1993) PNA hybridizes to complementary oligonucleotides obeying the Watson-Crick hydrogen-bonding rules. *Nature* 365:566–568
84. Kam Y, Rubinstein A, Nissan A, Halle D, Yavin E (2012) Detection of endogenous K-ras mRNA in living cells at a single base resolution by a PNA molecular beacon. *Mol Pharm* 9:685–693
85. Tsourkas A, Behlke MA, Bao G (2002) Hybridization of 2'-O-methyl and 2'-deoxy molecular beacons to RNA and DNA targets. *Nucl Acids Res* 30:5168–5174
86. Zamaratski E, Pradeepkumar PI, Chattopadhyaya J (2001) A critical survey of the structure-function of the antisense oligo/RNA heteroduplex as substrate for RNase H. *J Biochem Biophys Methods* 48:189–208
87. Teplova M, Minasov G, Tereshko V, Inamati GB, Cook PD, Manoharan M, Egli M (1999) Crystal structure and improved antisense properties of 2'-O-(2-methoxyethyl)-RNA. *Nat Struct Biol* 6:535–539
88. Yang CJ, Martinez K, Lin H, Tan W (2006) Hybrid molecular probe for nucleic acid analysis in biological samples. *J Am Chem Soc* 128:9986–9987
89. Kim Y, Yang CJ, Tan W (2007) Superior structure stability and selectivity of hairpin nucleic acid probes with an I-DNA stem. *Nucl Acids Res* 35:7279–7287
90. Gifford LK, Jordan D, Pattanayak V, Vernovsky K, Do BT, Gewirtz AM, Lu P (2005) Stemless self-quenching reporter molecules identify target sequences in mRNA. *Anal Biochem* 347:77–88

91. Crey-Desbiolles C, Ahn D-R, Leumann CJ (2005) Molecular beacons with a homo-DNA stem: improving target selectivity. *Nucleic Acids Res* 33:77
92. Wang L, Yang CJ, Medley CD, Benner SA, Tan W (2005) Locked nucleic acid molecular beacons. *J Am Chem Soc* 127:15664–15665
93. Wu Y, Yang CJ, Moroz LL, Tan W (2008) Nucleic acid beacons for long-term real-time intracellular monitoring. *Anal Chem* 80:3025–3028
94. Chen Z, Chen H, Hu H, Yu M, Li F, Zhang Q, Zhou Z, Yi T, Huang C (2008) Versatile synthesis strategy for carboxylic acid-functionalized upconverting nanophosphors as biological labels. *J Am Chem Soc* 130:3023–3029
95. Liu L, Dong X, Lian W, Peng X, Liu Z, He Z, Wang Q (2010) Homogeneous competitive hybridization assay based on two-photon excitation fluorescence resonance energy transfer. *Anal Chem* 82:1381–1388
96. Liu L, Li H, Qiu T, Zhou G, Wong K-Y, He Z, Liu Z (2011) Construction of a molecular beacon based on two-photon excited fluorescence resonance energy transfer with quantum dot as donor. *Chem Commun* 47:2622–2624
97. Jacroux T, Rieck DC, Cui R, Ouyang Y, Dong W-J (2012) Enzymatic amplification of DNA/RNA hybrid molecular beacon signaling in nucleic acid detection. *Anal Biochem* 432:106–114
98. Vet JAM, Van der Rijt BJM, Blom HJ (2002) Molecular beacons: colorful analysis of nucleic acids. *Expert Rev Mol Diagn* 2:77–86
99. Qiao G, Zhuo L, Gao Y, Yu L, Li N, Tang B (2011) A tumor mRNA-dependent gold nanoparticle–molecular beacon carrier for controlled drug release and intracellular imaging. *Chem Commun* 47:7458–7460
100. Xu H, Hepel M (2011) Molecular beacon-based fluorescent assay for selective detection of glutathione and cysteine. *Anal Chem* 83:813–819
101. Cheng G, Shen B, Zhang F, Wu J, Xu Y, He P, Fang Y (2010) A new electrochemically active-inactive switching aptamer molecular beacon to detect thrombin directly in solution. *Biosens Bioelectron* 25:2265–2269
102. Jiang YL, McGoldrick CA, Yin D, Zhao J, Patel V, Brannon MF, Lightner JW, Krishnan K, Stone WL (2012) A specific molecular beacon probe for the detection of human prostate cancer cells. *Bioorg Med Chem Lett* 22:3632–3638
103. Liu A, Sun Z, Wang K, Chen X, Xu X, Wu Y, Lin X, Chen Y, Du M (2012) Molecular beacon-based fluorescence biosensor for the detection of gene fragment and PCR amplification products related to chronic myelogenous leukemia. *Anal Bioanal Chem* 402:805–812
104. Yarasi S, McConachie C, Loppnow GR (2005) Molecular beacon probes of photodamage in thymine and uracil oligonucleotides. *Photochem Photobiol* 81:467–473
105. El-Yazbi A, Loppnow GR (2011) Locked nucleic acid hairpin detection of UV-induced DNA damage. *Can J Chem* 89:402–408
106. Wang J, Onoshima D, Aki M, Okamoto Y, Kaji N, Tokeshi M, Baba Y (2011) Label-free detection of DNA-binding proteins based on microfluidic solid-state molecular beacon sensor. *Anal Chem* 83:3528–3532
107. Crul M, Van Waardenburg RCAM, Beijnen JH, Schellens JHM (2002) DNA-based drug interactions of cisplatin. *Cancer Treat Rev* 28:291–303
108. Shire ZJ, Loppnow GR (2012) Molecular beacon probes for the detection of cisplatin-induced DNA damage. *Anal Bioanal Chem* 403:179–184
109. Meng H-M, Fu T, Zhang X-B, Wang N-N, Tan W, Shen G-L, Yu R-Q (2012) Efficient fluorescence turn-on probe for zirconium via a target-triggered DNA molecular beacon strategy. *Anal Chem* 84:2124–2128
110. Stobiecka M, Molinero AA, Chalupe A, Hepel M (2012) Mercury/homocysteine ligation-induced ON/OFF-switching of a T–T mismatch-based oligonucleotide molecular beacon. *Anal Chem* 84:4970–4978
111. Wang Y, Li Z, Hu D, Lin C-T, Li J, Lin Y (2010) Aptamer/graphene oxide nanocomplex for in situ molecular probing in living cells. *J Am Chem Soc* 132:9274–9276

112. Zhou J, Lu Q, Tong Y, Wei W, Liu S (2012) Detection of DNA damage by using hairpin molecular beacon probes and graphene oxide. *Talanta* 99:625–630
113. Huang P-JJ, Liu J (2012) Molecular beacon lighting up on graphene oxide. *Anal Chem* 84:4192–4198
114. Huang P-JJ, Liu J (2012) DNA-length-dependent fluorescence signaling on graphene oxide surface. *Small* 8:977–983
115. Dong H, Ding L, Yan F, Ji H, Ju H (2011) The use of polyethylenimine-grafted graphene nanoribbon for cellular delivery of locked nucleic acid modified molecular beacon for recognition of microRNA. *Biomaterials* 32:3875–3882

Part IV
Biomedical Instrumentation

Chapter 28

Engineering the Next-Generation PET Detectors

Arne Vandenbroucke and Craig S. Levin

28.1 Introduction

Positron emission tomography (PET) is a *functional* imaging modality whereby contrast is generated by the biological activity of the tissue of interest. A patient is injected with a radioactively labeled tracer that preferably accumulates in the tissue of interest, for example a cancerous lesion, an amyloid-beta plaque in the brain, or myocardial anomalies. The radioactive label is a positron emitting isotope. Upon decay, the emitted positron deposits its energy in the surrounding tissue before it annihilates with an electron [1]. This results in two 511 keV photons emitted in opposite directions. There is a small acolinearity effect in the emission of both photons when there is a finite momentum of the electron–positron system in the laboratory reference frame at the time of annihilation. The observed acolinearity is dependent on the system diameter D and is measured to be $0.00243 \pm 0.00014 \times D$ [2]. A PET camera detects many of these 511 keV photon pairs in coincidence. These pairs are then assigned to lines of response (LOR) which are used in the image reconstruction process to yield a tomographic 3D image of the tracer distribution in the human body. The concept of PET photon creation and collection is sketched in Fig. 28.1. Due to the finite width of the pixel elements, the LORs are actually tubes-of-response. The width of these tubes is related to the spatial resolution of the system.

In order to obtain high-quality images, contrast needs to be enhanced as much as possible, e.g. by reducing background present in PET images. There are two

A. Vandenbroucke (✉)

Molecular Imaging Program at Stanford, Department of Radiology,
Stanford University, Stanford, CA, USA
e-mail: arnevdb@stanford.edu

C. S. Levin

Molecular Imaging Program at Stanford, Department of Radiology, Physics,
Electrical Engineering and Bioengineering, Stanford University, Stanford, CA, USA
e-mail: cslevin@stanford.edu

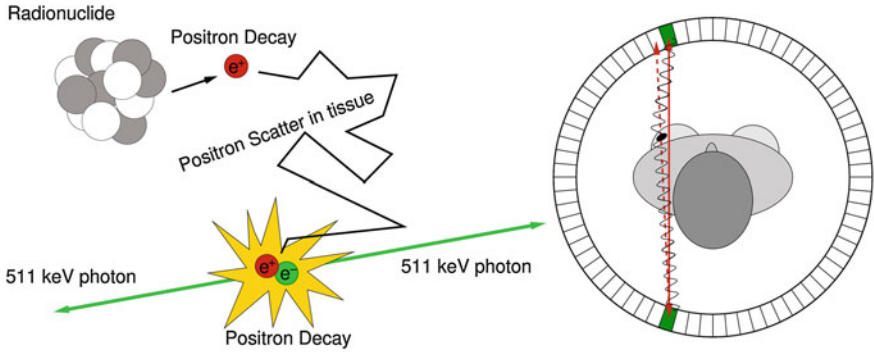


Fig. 28.1 *Left* The mechanism for signal generation in PET: a positron is emitted by a proton rich nucleus. After thermalization, the positron annihilates with an electron from the surrounding medium, resulting in the emission of two 511 keV photons back-to-back. *Right* The *solid red line* is an observed line of response (LOR) in a PET camera, obtained by combining the interaction locations of the two 511 keV photons. If the center of mass momentum of the positron and electron is nonzero in the lab reference frame when they annihilate, the photons have a slight acolinearity. The *dashed red line* is the true LOR

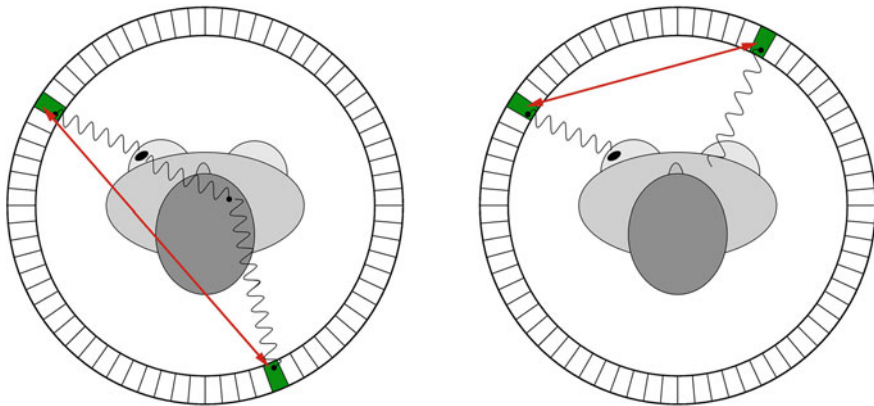


Fig. 28.2 Object scatter (*left*) and random coincidences (*right*) cause positioning errors that reduce image contrast and quantitative accuracy

main background mechanisms in PET: scatter and random coincidences, schematically shown in Fig. 28.2.

Since a scattered photon will have lost some energy, object scatter can be identified by measuring the energy of the detected photon accurately. Therefore, it is desirable for a PET camera to have excellent energy resolution.

A random coincidence occurs when two photons, each originating from a different location, are assumed to be part of the same pair. This will happen, for instance, when only one of the two annihilation photons is detected, a situation that may happen frequently given the limited coincidence photon detection sensitivity of PET cameras. The number of random coincidences is reduced by utilizing a

smaller coincidence time window, which is the time during which a PET system considers two photons as being simultaneously emitted. PET cameras with a fine time resolution allow for tighter coincidence windows and less random coincidence background.

Newer systems with time resolution <1 ns are able to use timing information to assign probabilities to where along the line of response the tracer was emitted, yielding “time-of-flight” (TOF) PET, which we will come back to later in this chapter (Sect. 28.6).

In order to precisely localize the tracer distribution, PET cameras should also have a fine spatial resolution, preferably uniform across the field of view (FOV).

A fourth requirement for a PET camera is high sensitivity to detect emitted radiation. This efficiency can be expressed as a product of a geometric form factor ϵ_{geo} and an intrinsic detection efficiency ϵ_{int}^2 . The former depends on the solid angle coverage of the detection elements, which in turn depend on the system form factor and the packing fraction of the active detector elements. ϵ_{int} on the other hand measures the efficiency to detect an incident 511-keV photon and depends on the Z_{eff} and the density and thickness of the detector material. Since PET requires coincident photon detection, the intrinsic detection efficiency needs to be squared.

Since the contrast mechanism in PET images is mainly caused by biochemical activity, it is often difficult to localize regions of high focal uptake relative to anatomical landmarks that show little or no tracer uptake such as the organs and skeleton in a patient’s body. The combination of a PET camera with an X-ray *computed tomography* (CT) camera results in a hybrid PET/CT image and enables precise localization of areas with high tracer uptake. In addition, the CT camera can be used for calculating an attenuation correction, i.e. a compensation for the nonuniform attenuation of 511-keV photons in the different tissues of the human body. Attenuation correction results in higher-quality images. Another advantage of this dual modality is the confirmation of suspicious lesions on both PET and CT images, hence, reducing the number of false-positive lesions. The combination of PET and CT camera is currently considered the best imaging modality in oncologic settings [3, 4].

The number of PET/CT procedures in the clinic has steadily been increasing since the introduction of this modality around the start of the millennium. The volume of studies increased by 7.1 % between 2008 and 2010 in the United States. In 2011, 1.85 million patient studies were performed at 2,209 sites, up from 2,000 sites in 2008 [5]. The number of PET only sites decreased from 215 to 120 over the same period. In 2012, 94 % of the PET/CT procedures were oncology related, 3 % cardiology related, and 3 % in neurology. In oncology, 68 % of procedures are for lung, breast, lymphoma, and colorectal cancer. Among these, 19 % is used for diagnosis, 38 % for staging, 13 % for treatment planning, and 30 % therapy follow-up. The increased availability of PET/CT cameras resulted in a reduced wait time from 7 to 4 days [5].

The vast majority (96 %) of PET studies use fluoro-deoxyglucose (FDG) as a tracer, which is a glucose analog, where the 2' OH group is replaced by ^{18}F . Due to

the enhanced anaerobic sugar metabolism of cancer cells (i.e., the Warburg effect, see, e.g., [6]), FDG molecules preferably accumulate in these cells. Due to the lack of the 2' OH group, FDG cannot be fully metabolized, and thus, remains in these cells until ^{18}F decays into ^{18}O . In addition, the 110 min half-life of ^{18}F makes the isotope practical for use in the clinic. Other tracers are, for example, ^{82}Rb for myocardial studies [7] and ^{11}C labeled PiB (Pittsburg compound B) for beta-amyloid imaging [8], in the quest to predict and diagnose early appearance of Alzheimer's disease. A large number of other tracers have been developed or are under study [9].

The development of disease-specific tracers could potentially yield enhanced contrast in PET images due to the higher specific uptake. This would result in higher-quality images without significant improvement in instrumentation. It is also likely that patient dose can be reduced by development of very specific tracers. However, it is important as well to note that the fact that the Warburg effect is present in most cancer cells has resulted in the success and usability of FDG-PET in the clinic.

Over the last two decades, large progress has been made in the development of PET cameras. Both clinical as well as preclinical (small animal) PET cameras have improved spatial, energy, and time resolution, resulting in reliable visualization and quantification of smaller tumors. A general paradigm in medicine is that earlier detection of smaller lesions results in better patient outcome. In addition, improved spatial resolution enables improved monitoring of the effects of radio- or chemotherapy, which often show up earlier on PET images than the corresponding CT images. This chapter discusses the potential improvements in PET detectors that can be implemented in the next-generation PET cameras and will result in better image quality. In order to discuss these improvements, we start with a description of the current generation. Throughout the chapter, we will only focus on the improvement of the PET detectors. We refer the reader to the literature to study improvements in CT images.

28.2 Current-Generation Commercially Available PET Cameras

It is instructive to look at the performance of current commercially available state-of-the-art PET/CT cameras by the leading manufacturers Philips, Siemens, and GE Healthcare. All three manufacturers use a traditional “block-detector” scheme for their cameras: a scintillation crystal is used to stop and convert the 511-keV photons into many optical photons, which are then converted to electronic charge using a photomultiplier-tube (PMT). The charge is further digitized and processed by data acquisition (DAQ) boards and stored to disk. A “block detector” typically consists of an array of PMTs coupled to a segmented scintillation crystal. In these, the number of PMTs is smaller than the number of crystal elements. The segmentation is optimized to maximize interaction location resolvability. Figure 28.3

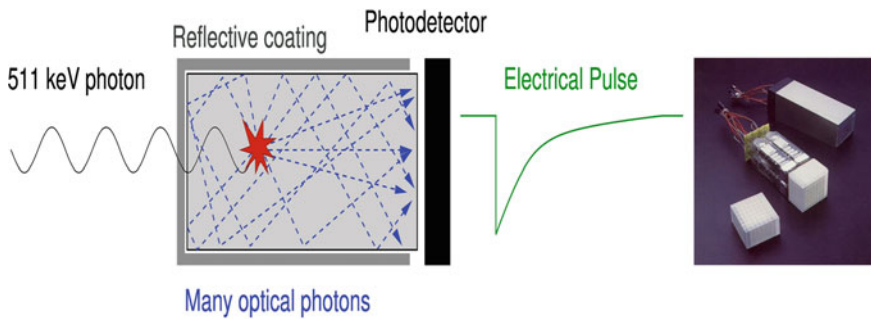


Fig. 28.3 *Left* Optical photons are created in a scintillation crystal upon absorption of a 511-keV photon. After a number of reflections, the optical photons reach the photodetector where they are converted into electric charge. *Right* A block detector in a standard PET camera. An 8×8 scintillation crystal array (*lower left corner*) is coupled to 4 PMTs (*middle*) and placed in a specially designed housing (*upper right corner*). Figure courtesy of Siemens Healthcare

shows a photograph of a typical block detector along with a schematic of the interaction process.

Table 28.1 gives an overview of hardware configuration and associated performance of state-of-the-art cameras. We see that all manufacturers have a similar axial field-of-view (FOV) of about 16–18 cm. The Siemens biograph comes with a *TrueV* (sic) option, which allows an extended axial FOV. Array crystal element size is typically $4 \times 4 \times 20 \text{ mm}^3$, resulting in about 25,000 crystal elements per camera. The GE design uses a slightly larger crystal resulting in about 14,000 crystals in the entire camera. Acquisition time is about 15–40 min. The scintillation material used by all manufacturers is Lutetium based, with an unspecified “lutetium-based scintillator” for GE, and LYSO and LSO for Philips and Siemens, respectively. These specifications are readily available on the manufacturer’s website.

The National Electrical Manufacturers Association (NEMA) defined procedures for evaluating performance of PET systems in order to standardize these [10]. The sensitivity, as measured by these NEMA standards, varies between 0.5 and 0.7 % ($=5 - 7 \text{ counts per second (cps)/kBq}$), thus smaller than 1 % for all systems. Transaxial spatial resolution is about 4.4–5.2 mm, with slightly inferior axial resolution for the GE system due to the use of rectangular cross-sectional crystal elements. In the most recent systems, all manufacturers have omitted the use of septa to increase sensitivity. All systems acquire data in 3D.

28.3 Progress for Scintillation Crystals

This section covers the progress towards improving the active detector elements in PET cameras, which are responsible for absorbing and converting the 511-keV annihilation radiation. We first cover the more traditional method of using

Table 28.1 Hardware and performance parameters of state-of-the-art commercially available PET/CT cameras

		Philips TruFlight	Siemens Biograph TruePoint	GE Discovery 710
<i>Hardware</i>				
Axial FOV	cm	18	16.2 (21.6) ^a	15.7
Number of crystals		28,336	24,336 (32,448) ^a	13,824
Number of PMTs		420	576 (768) ^a	256 ^b
Detector material		LYSO	LSO	LBS ^c
Crystal size	mm ³	4 × 4 × 22	4 × 4 × 20	4.2 × 6.3 × 25
Acquisition time	min	15	20 (10) ^a	N.A.
<i>NEMA performance</i>				
Sensitivity center	cps/kBq	4.5	4.4(7.9) ^a	7
Transverse spatial resolution @1 cm	mm	4.7	4.4	4.9 ^d
Transverse spatial resolution @10 cm	mm	5.2	4.9	6.3 ^d
Axial spatial resolution @1 cm	mm	4.7	4.5	5.6 ^d
Axial spatial resolution @10 cm	mm	5.2	5.9	6.3 ^d
Peak NECR	kcps@kBq/ ml	65@20	96@25(165@35) ^a	130@19.5

CT performance is omitted in this table. Data taken from respective manufacturer's websites [11, 12] and Ref. [13]

^a Value between brackets reflects performance with *TrueV* option, which extends the FOV

^b Quad anode

^c Lutetium-based scintillator

^d 4;4.5;5 and 5 are mentioned, respectively, using advanced reconstruction techniques. See Sect. 28.3.2.6

scintillation crystals. We will discuss various modern crystal types, the configuration of these in so-called block detectors, and progress on light extraction methods. A discussion on photodetectors coupled to these scintillators is given in Sect. 28.4. We will discuss semiconductor detectors, which directly convert the incident photon into electric charge, in Sect. 28.5.

28.3.1 Scintillation Crystals

An optimal scintillation crystal for a PET camera should have a high stopping power for 511 keV photons, a high light yield, fast rise and fall time, and a fine energy resolution. In order to increase sensitivity, it is desirable to have crystals with a high density and a high atomic number Z (or Z_{eff}). A high light output is desirable in order to increase the signal from the detector, which facilitates event positioning methods and moderates the requirements on the readout electronics.

The energy resolution of typical scintillation crystals is only indirectly related to the light output: given the roughly 10,000 photons created in LSO upon 511 keV photoelectric absorption, one would expect a variation of about 1 % when using Poisson counting statistics alone. Due to the nonproportionality of the scintillation process [14], the energy resolution for LSO crystals is not better than 9 % FWHM at 511 keV. Nonproportionalities in light output as a function of energy may become more important if lower-energy detector scatter events are included in the event-list. Currently, the detector response is often assumed linear and calibration is done using the 511-keV photopeak position.

Another increasingly important parameter for scintillation crystals is their rise and decay time. These are important because they impose fundamental limits on the coincidence timing resolution of PET detectors. While the rise time is experimentally difficult to assess, it is of great importance to the time resolution [15]. Rise time optimization will likely yield to improved timing resolution as we will discuss in Sect. 28.6.

The peak emission wavelength of scintillation crystals for PET detectors should match the maximum quantum efficiency (QE) of the photon detector, in order to increase signal output. Matching of the index of refraction of the scintillator to the photodetector entrance window is important as well in order to reduce reflective losses and hence to maximize the signal.

Table 28.2 gives an overview of a number of scintillation detectors and their properties. BGO used to be a popular choice, because of its high Z_{eff} and relatively high density, yielding a large photon detection efficiency (PDE). However, due to its poor decay time, moderate light output, and high index of refraction, it has been replaced by LSO or LYSO in many recently constructed cameras. LYSO has similar properties to LSO and is not included in the table. It is instructive to see that calcium co-doping in LSO yields a better energy resolution and a faster decay time [16], indicating that dopant concentration is very important for scintillator performance.

LaBr₃ has excellent energy resolution and a very short decay time. However, its drawbacks include its poor photofraction and its hygroscopic nature, which makes it necessary to avoid contact with moisture when utilizing this crystal.

LuAP combines a fast decay time with a high density. The latter results in a short attenuation ($1/e$) length. Using praseodymium (Pr) as the activating dopant instead of cerium (Ce), as in the case of LuAg, results in an improved energy resolution, while maintaining the fast decay. The drawbacks of LaBr₃, LuAP, and LuAg are their short emission wavelengths, resulting in tight requirements on the photodetector.

Among the newer crystals, LuI₃ has some interesting properties: very high light yield, excellent energy resolution, a short decay time, and a better attenuation length than LaBr₃. Its emission wavelength is redshifted which may be beneficial when used with silicon-based photodetectors.

As seen from Table 28.1, the big three clinical PET system vendors all choose Lutetium-based crystals, whereas BGO used to be the material of choice. Philips and Siemens use LYSO and LSO respectively, GE uses a nonspecified lutetium-based material. LuAG is currently used in an application-specific PET camera for breast imaging [17].

Table 28.2 Properties of selected scintillation crystals for PET imaging, data from Refs. [18–25]

	BGO	GSO:Ce	LSO:Ce	LSO:Ca	LaBr ₃ :Ce	LuAP:Ce	LuAg:Pr	LuI ₃
Formula	Bi ₄ Ge ₃ O ₁₂	Gd ₂ SiO ₅ :Ce	Lu ₂ SiO ₅ :Ce	Lu ₂ SiO ₅ :Ca	LaBr ₃ :Ce	LuAlO ₃ :Ce	Lu ₃ Al ₅ O ₁₂ :Pr	LuI ₃ :Ce
Density	7.13 g/cm ³	6.71	7.40	7.40	5.29	8.34	7.4	5.68
Z _{eff}	75	59	66	66	47	65	63	60
Photofraction	0.44	0.26	0.34	0.34	0.13	0.32	0.29	0.22
↓ Length PE ^a	2.5 cm	5.7	3.6	3.6	16.3	3.5	4.4	8.7
↓ Length all	1.1 cm	1.5	1.2	1.2	2.2	1.1	1.3	1.9
Light output	8,200 photons/MeV	12,500	27,000	29,400	57,700	16,300	18,000	115,000
E _{res} @662	10.2 % FWHM	9.2	8.2	6.8	2.7	10.6	5.2	3.6
Decay time	300 ns	30–60	40	30	18	17	22	33
Peak emission	480 nm	430	420	420	356	365	320	505
Index of refraction	2.15	1.85	1.82	1.82	1.88	1.97	1.84	NA

Italic values indicate “best in category”

^a PE = photoelectric interactions

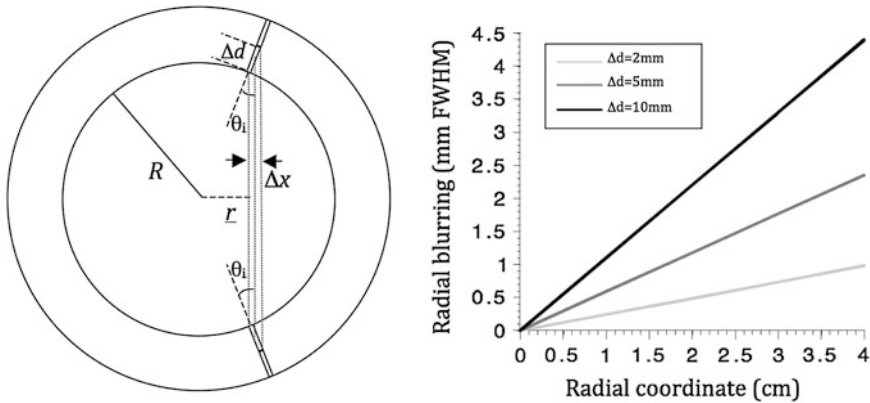


Fig. 28.4 Left shows the coordinates used in Eq. 28.1. Right is a numerical evaluation of the same equation for different DOI resolutions Δd

28.3.2 DOI Configurations

When comparing the newest generation of clinical PET cameras with older ones, we see that there has been a drive to increase spatial resolution by utilizing smaller crystals. Indeed, manufacturers use $4 \times 4 \text{ mm}^2$ crystals today, compared to $6 \times 12 \text{ mm}^2$ that was state-of-the-art in 1991 for the GE “4096+” system.

While the area of the crystals has been made smaller over the years, their length has stayed more or less the same in order to maintain sensitivity. As a consequence, spatial resolution of PET cameras only improved in two dimensions. The lack of resolution in the radial dimension (i.e., along an LOR) results in a non-uniform resolution across the FOV. This becomes apparent through increased blurring of point sources when going from center to the edge of a camera. This effect is also known as the parallax error, or LOR blurring and is indicated in Fig. 28.4.

With r the radial coordinate varying between 0 and the ring radius $R (= D/2)$, and Δd the interaction depth resolution, we obtain

$$r = (R + (\Delta d/2)) \sin \theta_i.$$

Looking at the figure, the precision in r , Δr , can now be expressed as

$$\begin{aligned} \Delta r &\approx \Delta x/2 = (\Delta d/2) \sin \theta_i \quad (\text{FWHM}) \\ &= (\Delta d/2)r/[R + (\Delta d/2)] \\ &= r/[(D/\Delta d) + 1]. \end{aligned} \tag{28.1}$$

This equation is plotted in the right panel of Fig. 28.4 for different Δd values. We see that the blurring increases when going away from the center of the FOV, and for larger interaction depth resolutions.

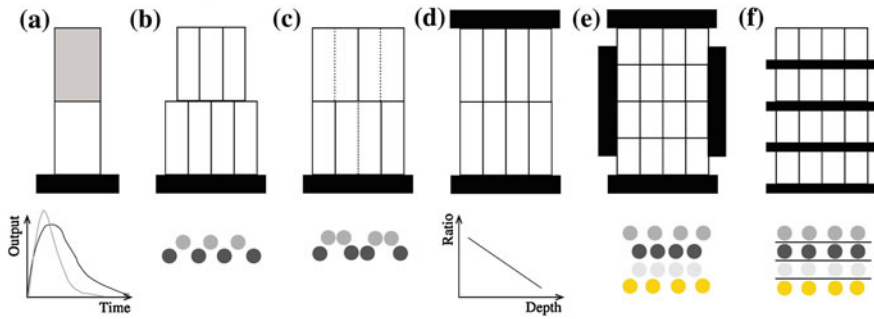


Fig. 28.5 Different DOI designs referred to in the text. **a** Phoswich; **b** crystal offset; **c** light sharing; **d** dual-ended readout, **e** and **f** direct DOI measurement. The *bottom row* shows how the detector output is used to obtain depth information: **a** uses different pulse shapes; **d** uses a ratio between top and bottom detector signals; **b**, **c**, **e**, and **f** utilize crystal positions in the flood histogram to localize interaction depth: the *circles* in **b**, **c**, **e**, and **f** represent the resulting crystal element positions in a flood histogram

Improving the resolution in the radial dimension by so-called depth-of-interaction (DOI) measurements will increase spatial resolution uniformity across the FOV and yield images with better resolution and contrast.¹ Research groups at universities across the globe have been investigating various detector configurations to improve DOI detection. Over the next sections, we will discuss a number of DOI configurations pursued by different research groups. An overview of these is seen in Fig. 28.5. A more comprehensive overview can be found in [26].

28.3.2.1 Pulse Shape Discrimination

One of the first attempts to obtain DOI information was using pulse shape discrimination (PSD): two or more scintillation crystals with different decay times are coupled together. Based on the pulse shape observed, estimations are made whether the interaction happened in the top or the bottom crystal. The design is schematically represented in Fig. 28.5a. These configurations are also known as “phoswich” configurations, a combination of “phosphor” and “sandwich”. Phoswich designs originate from X- and gamma-ray astronomy experiments [27].

The PSD approach is still being investigated as a method to improve DOI in the next-generation scanners. Mosset et al. [28] built an LSO/LuYAP combination which is 98 % efficient in determining the correct interaction location. As shown in simulations by Jung et al. [29], identification may be improved depending on the optical coupling between different crystals. More recently, Vaquero et al. [30]

¹ Better resolution only leads to better contrast if the size of structures are on the order of the resolution.

investigated a combination of LYSO and GSO coupled to a matrix of silicon photomultipliers (Si-PMs, see Sect. 28.4.3) and evaluated a delayed charge integration method.

While several research groups have reported low misidentification and high efficiency, the PSD approach has a number of drawbacks. One problem is that the pulse shape needs to be determined, which increases requirements on the readout electronics. Another disadvantage is that optical photons created in the first scintillator need to propagate through the second scintillator in order to be detected. This may cause a dispersion in pulse shape and degrade the timing resolution achievable with this design. The different light output and associated differences in energy resolution of the crystals used in a PSD design may also introduce nonuniformities in scatter rejection capabilities.

It is worth noting that PSD has also been used in the LabPET scanner [31] in order to reduce the number of electronic readout channels. In this design, two crystals with different decay times are positioned next to each other and are coupled to the same photosensor, thus multiplexing the readout by a factor of two.

In order to circumvent the discrete nature of the phoswich approach, Du et al. [32] proposed a continuous phoswich crystal, whereby the far end and part of the sides of a crystal are coated with a phosphor powder. The phosphor re-emits absorbed scintillation light at a later time point and at a lower frequency. Using different pulse shape discrimination and advanced analysis techniques [33], continuous DOI can be obtained. The authors obtained an 8 mm FWHM DOI resolution for a 2-cm-thick array.

28.3.2.2 Crystal Offset Method

A solution to the different response from the different scintillators in a phoswich design is to use a stack of the *same* scintillator material, albeit with an offset. The offset causes the optical light created in the different layers to follow different paths, resulting in different patterns on the photodetector surface, as shown in Fig. 28.5b. The location of the focal light spot on the photodetector surface thus gives DOI information. Liu et al. [34] stacked a 6×6 array of $1.8 \times 1.8 \times 10 \text{ mm}^3$ LSO crystals on top of a 7×7 array of the same crystals. The lower array was coupled to a position-sensitive PMT (PS-PMT). Using this approach, the authors observed an improvement from 4.5 mm FWHM to 3.4 mm FWHM at 30° photon incidence, with uniform energy and timing resolution. Zhang et al. [35] stacked a 9×9 layer of $2.1 \times 2.1 \times 6.5 \text{ mm}^3$ BGO crystals on top of a 10×10 array of $2.1 \times 2.1 \times 11.5 \text{ mm}^3$ BGO crystals, though with moderate crystal identification performance. Ito et al. [36] used a similar approach to stack 4 layers of 29×29 , 29×28 , 28×28 , and 28×27 LSO crystals of $1.5 \times 1.5 \times 7 \text{ mm}^3$ each. The second layer was offset by half a pitch in the X direction, the third by half a pitch in the Y direction, and the fourth by an additional half pitch in the X direction. Even and odd rows in the flood histogram would thus correspond to even and odd layers. Each individual crystal was wrapped with

a reflector. Crystal resolving power in individual layers was excellent, yet the different DOI layers overlapped at the edges of the flood and thus were inseparable, presumably due to loss of photon collection efficiency at the edge. In these designs, the array closest to the photodetector is referred to as the “frontal” layer, and the one further away from the photodetector is the “distal” layer.

While the crystal offset method bypasses some of the disadvantages of the phoswich design, it has its own drawbacks. An offset method will result in non-uniform sensitivity as inevitably the second “distal” layer has less solid angle coverage than the first. A bigger problem is the light collection problem from the distal layer, similar to that of the phoswich design, but worse since light collection for the back crystal elements are split between two front element crystals. In addition, it is often hard to reliably distinguish both layers, in particular for incident photon angles larger than 0° , the angles for which DOI improvement is relevant.

28.3.2.3 Light Sharing Method

In an attempt to improve the nonuniform sensitivity caused by the crystal offset method, various researchers have experimented using different reflector arrangements for different layers, instead of physically offsetting different crystal layers. This method also results in a distinct pattern on the photodetector surface, as shown in Fig. 28.5c. Different reflector configurations are schematically drawn with full and dotted lines in the figure. The crystal location pattern observed on the photodetector is not equidistant in each row, as opposed to the offset design.

Using the light sharing method, Tsuda et al. [37] made a stack of 4 layers of 16×16 GSO crystals each measuring $1.42 \times 1.42 \times 4.5 \text{ mm}^3$. Each stack contained a different arrangement of light reflectors, so that a different pattern appears on the surface of the photodetector for each individual layer. They were able to achieve separation between the four layers, but with quite significant overlap, leading to layer misidentification.

Inadama et al. [38] used a combination of the light sharing and the phoswich approach to build an 8-layer DOI detector, organized as a 4-layer stack of a phoswich of 10×10 arrays of $2.9 \times 2.9 \times 3.75 \text{ mm}^3$ GSO crystals with 0.5 mol% Ce dopant and $2.9 \times 2.9 \times 3.60 \text{ mm}^3$ GSO crystals with 1.5 mol% Ce. Each phoswich layer had a different reflector orientation. The authors were able to separate all layers, but also observed large overlap and hence misidentification.

28.3.2.4 Dual-Ended Readout

The previously discussed DOI approaches all feature the drawback that the dispersion in the optical photons from the most distal layer will be larger than the dispersion from the proximal crystals, potentially compromising energy and timing resolution of those distal layers. A solution to this problem could be to collect the

scintillation light on both sides of the crystal using two photodetectors. Depth information is obtained by the ratio of the signal collected in both photodetectors, as shown in Fig. 28.5d. Dual-ended readout was already proposed in 1988 [39]. These authors placed PMTs in the transaxial direction on both ends of a 4×8 array of $3 \times 5 \times 50 \text{ mm}^3$ BGO crystals. The setup thus had a radial length of 20 mm. They were able to obtain a FWHM of 9.5 mm across the 50 mm transaxial direction when irradiating at 0.5 mm intervals.

The development of small silicon-based avalanche photodiodes (APDs) as a replacement for PMTs allowed dual readout in the radial direction. Such an approach was used by the ClearPEM group [40] for use in a dedicated breast PET camera. These researchers coupled two APDs to a 4×8 array of $2 \times 2 \times 20 \text{ mm}^3$ LSO crystals. The introduction of the APD and a thin circuit board between the LSO crystals and the 511-keV source only introduces minimal scatter.

James et al. [41] used position-sensitive APDs (PSAPDs) to read out both sides of an array comprising $0.5 \times 0.5 \times 20 \text{ mm}^3$ LSO crystals. A DOI resolution of $1.9 \pm 0.1 \text{ mm}$ was obtained at a temperature of 0°C in a design intended to be used for small animal imaging.

The dual-ended readout seems a promising solution to estimate DOI. However, it comes with a number of drawbacks: the number of photodetectors needs to be doubled and positioning these inside the photon path will introduce additional scatter. Moreover, the continuous approach currently only *estimates* where the interaction happened, which yields an uncertainty in the DOI coordinate and hence a potentially large misidentification.

28.3.2.5 Direct DOI Measurement

Instead of making an estimate of the interaction location using the ratio of the charge collected at both ends of a scintillation crystal, the AXPET design [42] placed a number of wavelength shifting strip (WLS) underneath an 1×8 array of $3 \times 3 \times 100 \text{ mm}^3$ LYSO crystals. The WLS measured $3 \times 40 \times 0.9 \text{ mm}^2$. Both scintillation crystal and WLS are read out by a Si-PM. The authors measured an axial resolution of less than 1.7 mm. A similar approach for a small animal PET camera was used in the COMPET design [43]. The drawback of this approach is the need for photodetectors on four sides of the “block,” and the low light yield of the WLS, potentially reducing the efficiency of the method.

In order to obtain direct interaction location measurements in three dimensions, Yamaya et al. [44] built a $16 \times 16 \times 16$ cube of $0.993 \times 0.993 \times 0.993 \text{ mm}^3$ LGSO crystals (X'tal cube). Each of the six faces of the cube was coupled to a 4×4 array of Si-PMs. Almost all of the 4,096 crystals were identified in the flood map, albeit with 12.9% cross talk at the edge and 6.0% cross talk in the center. The fabrication was improved using a laser to cut microcracks in an LYSO block, resulting in a 3D grid [45]. A $9 \times 9 \times 9$ grid with 2 mm pitch was produced using

this method. An intrinsic resolution of 2.1 mm was obtained. The design of the X'tal cube is shown in Fig. 28.5e. The obtained flood histogram is actually a 3D histogram.

Another approach for 3D imaging was first proposed conceptually by Levin [46]. In this approach, an array of crystals is coupled to a thin APD. Every layer is directly read out by a photodetector, as shown in Fig. 28.5f. A stack of these detectors forms a 3D block detector. In this particular design, scintillation photons are collected from the sides rather than ends of long scintillation crystal elements, increasing the light yield and removing the dependence of light collection on DOI. Vandenbroucke et al. [47] measured an intrinsic spatial resolution of 0.84 ± 0.05 mm, using an 8×8 array of $0.9 \times 0.9 \times 1$ mm³ LSO crystals coupled to a PSAPD. The PSAPDs themselves are mounted on a thin Kapton readout circuit in order to decrease the dead area [48]. Because of the small crystals used in this design, and their readout in small cohorts of two 8×8 arrays, each individual interaction location of a multiple photon interaction events (MIPE) can be identified. These are events whereby the 511 keV photon Compton scatters once or more than once before it undergoes photoelectric absorption. In order to include these MIPE, the readout electronics need to be carefully designed, so that the trigger threshold can be set as low as possible. A feasibility study of measuring these MIPE events in this stacked design is shown in Ref. [49]. This design is currently incorporated in the construction of a high-resolution breast PET camera [50].

28.3.2.6 Monolithic Crystals

As opposed to utilizing very small crystals for DOI estimation, a recently revived trend in PET detector development is to use large monolithic crystals, read out by a PS-PMT or an array of SiPMs to measure the distribution of scintillation photons on the surface of the crystal (this design is not shown in Fig. 28.5). The position of the 511 keV interaction can be estimated using a maximum likelihood (ML) method. Ling et al. [51] used a $50 \times 50 \times 8$ mm³ crystal coupled to a 64-channel flat-panel PMT. The interaction reconstruction algorithm utilizes look-up tables to estimate the interaction location. The authors used two DOI regions in their experiment and determined a misclassification rate of 25 %, compared to a 3.5 % misclassification in simulations. The difference is presumably due to MIPEs in the crystal, where the 511 keV undergoes one or more Compton interactions followed by a photoelectric absorption in the crystal. The large difference between simulations and experiments indicates that it is often hard to exactly model light distributions in a crystal.

The use of thick monolithic crystals seems advantageous for increasing the sensitivity of PET cameras, yet the spatial resolution is compromised when going to larger crystals. Bruyndonckx et al. [52] used the Cramer-Rao inequality to estimate the lower limit on the intrinsic resolution. Using a Monte Carlo simulation, they determined this limit to be 1.7-mm-FWHM intrinsic resolution for 10-

mm-thick LSO blocks and 2.0 mm FWHM for 20-mm-thick blocks. In a more realistic simulation, and using a k -nearest neighbor algorithm, vanderLaan et al. [53] determined a Cramer-Rao bound of 1.2 mm FWHM for both $20 \times 10 \times 20$ and $20 \times 10 \times 10 \text{ mm}^3$ LYSO crystals. These authors also experimentally measured the spatial resolution using a 4×8 APD array to be 1.6 mm FWHM and 1.5 mm FWHM, respectively. The differences between experiment and simulation are attributed to Compton scatter and X-ray fluorescence.

Both GE [54] and Siemens researchers [55] have studied the use of light propagation models in their crystals to obtain DOI resolution. These models are based on measured point spread functions. Reference [54] for instance determines that using this PSF model the axial spatial resolution at 1 cm improves from 5.6 to 5.0 mm, and at 10 cm from 6.3 to 5.0 mm.

28.3.3 Scintillation Light Collection

When coupling scintillation crystals to a photodetector, much attention needs to be given to the light propagation inside the crystal and onto the surface of the photodetector, both in case of monolithic crystals and in case of discrete crystal arrays. Researchers have investigated polished as well as *as-cut* surface treatments to maximize light output or crystal identification. Various kinds of coupling materials and reflectors have been studied, including specular reflectors, acting as perfect mirrors, and diffuse reflectors that reflect incident light over a continuum of angles. Many researchers use optical simulation packages to investigate the implications of various design choices. DETECT [56] has long been the workhorse for many scientists. However, it uses a simplified model of light propagation. In addition, determining accurate parameters for the simulation is tricky and not always done accurately. In an attempt to improve existing simulation packages, Janecek et al. [57] built a tool to directly measure surface reflectance using common surface treatments, reflectors and bonding types. They implemented their results in a look-up table which can be interpolated in a simulation. The simulation code based on the LUT mimics experimental data more accurately than the Geant4 [58] code. As a consequence, attempts were made to incorporate these LUTs in Geant4. An alternative package to simulate optical light propagation based on its electromagnetic properties is Litrani [59], originally written to model the crystals of the electromagnetic calorimeter of the CMS experiment at CERN.

When the incident optical photon angle is larger than the critical angle, total internal reflection occurs, and the light is trapped in the scintillator. In order to avoid total internal reflection, Kronberger et al. [60] coupled a photonic crystal (PhC) slab to the collecting phase of a standard scintillator. The PhC consists of a lattice of holes, with the lattice constant a about 0.8 of the wavelength λ . Doing so, these researchers were able to recover all incident photon angles, including those larger than the critical angle. This novel method of light extraction is very promising, in particular for improving the time resolution (see Sect. 28.6).

28.4 Photodetectors

In the last section, we focused on the design of scintillation crystals. The optical photons created by these crystals are converted to photoelectrons in the entrance window of the photodetector. These electrons usually are further amplified by the photodetector in question. It is important to realize that in scintillation detection, we are counting photoelectrons, not photons. In this section, we will discuss PMTs, APDs, and SiPMs, since these are most commonly used in PET scintillation detection.

28.4.1 Photomultiplier Tubes

Currently, most commercial PET systems still use PMTs [61]. These typically feature a set of dynodes in a vacuum tube, each at a different voltage. Multiple electrons emerge upon incidence of an electron on a dynode, thus establishing amplification. 6 dynodes, each having a multiplication gain of 10 yield a total gain of 10^6 . PMTs present a mature technology that has been around since about 1930 [62]. Thanks to massive use in astronomy, medical, nuclear, and particle physics, ever since 1930, PMTs represent a robust technology [63]. There are a myriad of different PMTs available, with various form factors ranging from about 1 cm to over 50 cm in diameter, and a variety of different shapes. Their sensitivity ranges from UV light at 115 nm to IR light at 1,200 nm, with the bulk of the available devices having a peak sensitivity of about 420 nm [64].

The QE defined as the ratio of emitted photoelectrons to the number of incident photons varies as a function of wavelength. For PET applications, the QE is about 30–35 % for blue light at around 400 nm. The gain of these PMTs typically is of the order of 10^6 . A supply voltage that varies between 100 and 2,000 V is needed. PMTs are in general fast, with rise times ranging from 0.4 to 1.5 ns.

In order to reduce the number of readout channels, it is desirable to couple a large number of crystal elements with as few PMTs as possible, as was shown in the right panel of Fig. 28.3, which exploits the sharing of scintillation light into multiple PMTs. For designs that use these arrays of PMTs, an approach to further reduce the number of readout channels is to combine the signals of multiple PMTs, which essentially shares charge rather than light to reduce the number of readout channels. This concept is now generally known in the field as “Anger logic.” Using a resistive network, Anger [65] was able to readout a cluster of 7 PMTs with 3 analog signals X , Y , and Z , as shown in Fig. 28.6.

$$\begin{aligned}
 Z &= \sum_{i=1}^{i=7} P_i \\
 X &= \frac{X^+ - X^-}{Z} X^+ = P_1 + P_2 + P_6 \\
 X^- &= P_3 + P_4 + P_5
 \end{aligned} \tag{28.2}$$

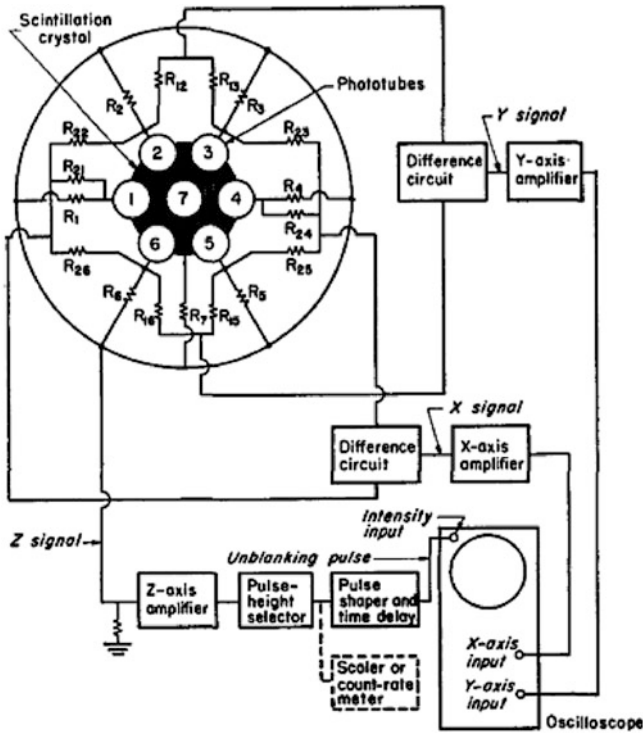


Fig. 28.6 Anger logic as described in [65]. Three readout lines are required to read out 7 PMTs, as displayed on the *right*. Figure on the right reprinted with permission from [65]. Copyright 1958, American Institute of Physics

$$\begin{aligned}
 Y &= \frac{Y^+ - Y^-}{Z} X^+ = P_2 + P_3 \\
 X^- &= P_5 + P_6
 \end{aligned}
 \tag{28.3}$$

Instead of using arrays of single PMTs, multianode PMTs have been developed. These are also known as position sensitive PMTs (PS-PMTs) and typically feature multiple PMTs in one housing, utilizing advanced charge multiplication systems [66]. The multiple channels can be read out individually or combined using resistors to form an Anger logic readout scheme. Alternative approaches to make more compact schemes have been proposed as well [67, 68]. Manufacturers were able to reduce the size of a 64-channel PMT to a volume of $25 \times 25 \times 20 \text{ mm}^3$ with a narrow peripheral zone. These PMTs are referred to as “flat-panel” PMTs [69].

Today, PS-PMTs remain very popular devices for the readout of scintillation crystals. These are for example used in a commercially available breast PET camera [70], a low-cost small animal imaging PET camera [71], and a dual-ended DOI capable block detector intended to be used in a breast PET camera [72].

Despite their reliability, PMTs suffer a number of drawbacks. First of all, they are bulky, which is an inconvenience in the clinic. In particular when trying to combine PET with another imaging modality such as CT. Even the most advanced flat-panel PMTs remain quite large compared to the scintillation crystals used. A second drawback is their relatively low QE. This low QE will ultimately influence timing resolution of these devices. The rather high supply voltage required by PMTs is detrimental as well. Finally, PMTs are sensitive to magnetic fields, since the electrons generated in the dynodes are subject to the Lorenz force. This forms a major difficulty when attempting to combine PET and MR into a single clinical unit (see Sect. 28.7), where the PMTs would be located inside or close to the MR magnetic field. Such a configuration requires extensive shielding with μ -metals. Finally, PMTs always require significant manual labor for assembly.

28.4.2 Avalanche Photodiodes

An alternative to PMTs are solid-state photodetectors. Due to the low number of photons created in scintillation crystals upon absorption of an annihilation quantum, the use of photodetectors without internal gain would enforce the use of extremely sensitive electronics. Since the 1950s, however, electron multiplication in silicon has been studied [73–76] resulting in the development of APDs. These devices feature a reverse biased p - n junction, with a very high electric field across the depletion region. The photoelectron created upon photoabsorption gains energy from this field and becomes ionizing, thus creating more electron–hole pairs on its path and establishing an avalanche, similar to a proportional counter. Gain factors between 100 and 1,000 are achievable. Due to the statistical nature of the avalanche process, signals created by an APD are subject to an “excess-noise” factor [77].

APDs typically have a higher QE than PMTs, about 80–90 % at 400 nm. Another advantage compared to PMTs is their insensitivity to magnetic fields. APDs are typically only 300 μm thick and thus offer a tremendous advantage compared to PMTs in terms of size. Because their limited thickness, various multiple layer DOI designs now become feasible. APDs have been studied in combination with a scintillator detector for PET imaging since the 1980s [78, 79].

A multitude of different APDs have been designed, optimized for specific applications. In scintillation detection, three types of APDs are commonly used: “reach-through” APDs, buried-junction “reverse” APDs, and diffused-junction “beveled-edge” APDs. Cross sections of these devices are shown in Fig. 28.7, and a brief summary of their performance is given in Table 28.3.

Reach-through APDs, produced since the 1960s, are by far most commonly used in scintillation applications. These devices feature a relatively thin multiplication region (1–10 μm) that has a large electric field across ($O(10^6)$ V/cm). The multiplication region is located opposite to the entrance window. Photoelectrons thus need to transverse a large drift region (about 100–150 μm) before

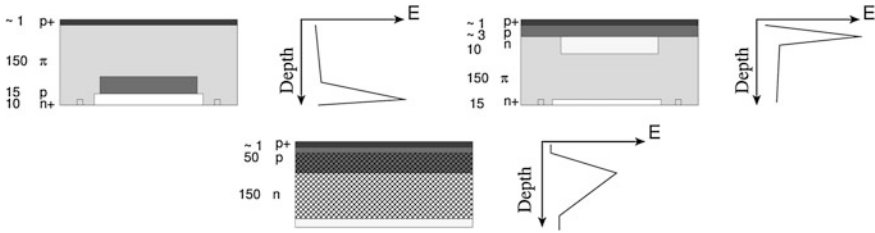


Fig. 28.7 Cross section and electric field profile of various APDs. *Upper left* shows a “reach-through” APD; *upper right*, a “buried-junction”; *lower center*, a “diffused-junction” APD. The numbers on the left give the thicknesses of the various layers in μm

Table 28.3 Qualitative properties of different types of APDs

Type	Drift region (μm)	Multiplication region (μm)	Gain	Bias voltage	$k_{\text{eff}} 10^{-2}$
Reach through	100–150	1–10	100	100	1–5
Buried junction ¹	<10	1–10	<250	400	0.700
Diffused junction ²	20	100	2,000	1,800	0.072

Values are approximate

¹ Ref. [87], ² Ref. [88]

they are amplified. Buried-junction APDs [80, 81] resolve the problems related to the large drift region by having the amplification region “buried” about 10 μm below the surface.

Diffused-junction APDs have a relatively wide multiplication region (about 100 μm) in combination with a slightly smaller electric field (about 10^5 V/cm). These were initially referred to as “beveled-edge” APDs [82–84], because of the physical bevel present to prevent HV arching across the device. These types of APDs have been characterized for radiation detection for example in Ref. [85]. A new production process [86] allowed construction of these diffused-junction APDs without the need for physical bevel formation, thus allowing for a smaller dead area.

One of the most appealing features of APDs is its small form factor that allows novel DOI design configurations to be designed and investigated: dual layer designs [89], dual-ended readout [90], or 3D detectors [91]. Furthermore, these devices are potentially produced at low cost compared to PMTs.

An APD-based small animal PET camera was first proposed in Ref. [92]. The full system achieved a 2-mm-FWHM spatial resolution, and a sensitivity of 0.51 % [93]. The same group made two more APD-based small animal cameras LabPET [94] and LabPET II [95].

Catana et al. [96] and Judenhofer et al. [97] have built APD-based systems that are capable of operating inside a magnetic field. These were the first PET/MR systems available. Another example of the practicality of using APDs in a compact

space inside a magnetic field is the CMS electromagnetic calorimeter, which exists of tapered PbWO_4 crystals coupled to APDs. The calorimeter uses over 120,000 APDs that have been running reliably during a 2 month cosmic run at 4 T [98].

Compared to PMTs, APDs have a lower gain, putting more stringent requirements on the noise parameters of the front-end electronics. Another disadvantage of APDs is their lower rise time, resulting in a less performant coincidence time resolution compared to PMTs. However, in small animal designs or dedicated breast PET cameras, the requirements on coincidence time resolution are less stringent, due to the smaller activity in the FOV compared to human whole-body cameras.

APDs are very sensitive to bias voltage and temperature variations [99, 100]. This requires careful implementation of temperature regulation in systems using these devices [101].

Shah et al. [102] designed position-sensitive APDs (PSAPDs), which have a resistive sheet coupled to the n -side of the junction, that results in spatially dependent charge sharing over the four corners of the sheet. Reading out these four corners of the PSAPD and applying Anger logic allow one to readout an 8×8 array of small crystals with only four electronic channels [103]. The electronic channel density can be further reduced by multiplexing multiple PSAPDs together [104].

28.4.3 Silicon Photomultipliers

When biased above the breakdown voltage, APDs operate in the so-called Geiger-mode. Analogous to gas-based Geiger counters, the obtained signal is no longer proportional to the incoming radiation. When a photoelectron is created in these devices, the device breaks down inducing large charge on the readout pads. It is essentially a binary device. However, in scintillation detection, we want to measure a signal proportional to the incoming photon energy. Proportionality is obtained by combining many Geiger-mode APDs into a single device. These devices are referred to as “multipixel proportional counters” (MPPCs) by one of the manufacturers (Hamamatsu). A more common name for these devices is SiPM, because these devices feature a high gain and are able to detect single photoelectrons, just like PMTs. Individual pixel sizes range from 25×25 to $100 \times 100 \mu\text{m}^2$, with 100–1,600 pixels per $1 \times 1 \text{cm}^2$ device.

Much research and progress has been made in recent years in the design and development of SiPMs for usage in radiation detection [105–107]. A model of scintillation induced response in these devices can be found in Ref. [108]. Indeed, these devices have desirable properties for PET applications: their large signal amplitude loosens the requirement on subsequent readout electronics. Second, SiPMs are fast thus enabling improved timing resolution. Moreover, SiPMs are insensitive to magnetic fields, have a small form factor and only require a

moderate bias voltage (<100 V). It is worth noting that these devices are also under consideration for photon detection in particle physics and astronomy experiments [109]. The combined demand of various research fields for SiPMs will further encourage the improvement of these devices.

28.4.3.1 SiPM Photon Detection Efficiency

One of the most important performance parameters for SiPMs is the PDE, which is defined as:

$$\text{PDE}(\lambda, V, T) = \text{FF} \times P_g(V, T) \times \text{QE}(\lambda),$$

where λ is the wavelength of the incident photon, V the bias voltage, and T the temperature. FF is the fill factor, the fraction of the sensitive area occupied by active pixels; $P_g(V, T)$ the probability of a Geiger discharge, and $\text{QE}(\lambda)$ the QE. Some authors also include a factor related to the recovery time in the above empirical formula [106].

The FF ranges from 20 to 80 %. Given that each pixel is surrounded by some dead area, the fill factor will in general be larger for larger pixel sizes.

Since not all photons incident on the SiPM surface will create a Geiger discharge, a finite probability $P_g(V, T)$ is assigned to each incident photon. The probability is dependent on temperature and bias voltage and has been studied for individual diodes since the 1970s [110, 111]. The probability increases with increased bias voltage and, in general, varies somewhere between 0.5 and 1. Since the breakdown voltage is temperature dependent [112], the breakdown probability is temperature dependent as well. Absorption of optical photons in silicon is strongly wavelength dependent: blue photons have an absorption length of about 0.1 μm , red photons an absorption length of about 10 μm . As a consequence, the quantum efficiency $\text{QE}(\lambda)$ will be wavelength dependent. In general, a good efficiency in the blue region is required, since most scintillators emit blue light. QE optimization is exploited in so-called *p-on-n* devices [113]. It is also worth noting that the efficiency for wavelengths shorter than blue light decreases because these photons do not make it to the multiplication region in the device.

28.4.3.2 Other SiPM Properties

The Geiger discharge in SiPMs needs to be quenched in order to be ready to detect the next event. Quenching is achieved by lowering the bias voltage below the breakdown voltage, which effectively halts the Geiger discharge, followed by a recharge of the device above the breakdown voltage. There are two modes of quenching: “passive” and “active”. In the former, the voltage drop is achieved by a bias resistor: when the current through the resistor increases, the voltage drop across this resistor becomes sufficiently large to lower the bias voltage below

breakdown and thus decreases the current. This approach is also often implemented for conventional APDs that will occasionally reach breakdown. The advantage of the passive quenching method is its simplicity, disadvantageous is the relatively long recovery time. Active quenching [114, 115] uses a comparator-based sensing circuitry in combination with a quenching transistor to reduce the bias voltage. For high-count-rate application, active quenching is preferred.

The gain of SiPMs increases with increasing bias voltage and decreasing temperature. However, when plotting the gain as a function of overvoltage (i.e., the voltage applied above breakdown voltage), temperature dependence vanishes [116]. Also linearity depends on the applied bias voltage: When the overvoltage is too large, too many pixels will trigger with a loss of linearity as a consequence. This will be apparent in unrealistically low-energy-resolution measurements [106].

Thermally generated electron–hole pairs that trigger avalanche breakdown are responsible for the dark count rate that also increases with overvoltage and temperature. At lower temperatures, the incidence of these random pairs is less; hence, the dark count rate drops. At lower overvoltage, the probability for these thermally generated electron–hole pairs to trigger a breakdown is lower.

One important source of background signal in SiPMs is optical cross talk [117]: electrons or hole transitions between different energy bands may result in photon emission [118]. When such a photon is absorbed in a neighboring cell, a breakdown may be triggered. Optical cross talk is higher at higher bias voltage. Several methods have been investigated to reduce optical breakdown. Examples are engineering intra-cell trenches to prevent photons from reaching neighboring cells, or to design double p – n junctions [119].

Apart from optical cross talk, the so-called afterpulsing may influence SiPM behavior, which is caused by carrier trapping and delayed release at impurities in the silicon, and may influence the recovery time. The delayed release is longer at lower temperatures.

28.4.3.3 Advanced Readout Techniques for SiPMs

In recent years, efforts were made to exploit the digital nature of the SiPM signal. Frach et al. [120, 121] added dedicated cell electronics next to each single pixel to sense the voltage at each pixel using a standard CMOS process. Photons are detected and counted as digital signals, thus creating a “digital” SiPM. The integration with CMOS logic reduces the requirements on subsequent readout electronics.

Much progress is to be expected from SiPMs that integrate some circuitry in the silicon bulk. References [122] and [123] placed the quenching resistor inside the bulk to increase PDE for instance. Berube et al. [124] developed a single-photon avalanche diode (SPAD) array with deep-submicron CMOS readout electronics to realize a 3D single-photon-counting module. Through silicon vias are used to realize the 3D heterogeneous bonding.

Several attempts are being made to reduce the number of readout channels from SiPM arrays. Similar to position-sensitive APDs, position-sensitive SiPMs (PS-SiPM) are currently being studied [125, 126]. In these PS-SiPMs, all micropixels are combined to a resistive network from which the four corners are read out. Spatial coordinates are retrieved using Anger logic. The disadvantage of this approach is that the noise of all cells is combined.

Fischer and Piemonte [127] propose an Interpolating SiPM (ISiPM), where each cell is connected to *one* of 4 readout channels, such that the weighted sum of a group of cells yields the center of gravity of the group. In a first prototype, all pixels in a 3×3 scintillator array with a pitch of 2 mm were clearly resolved.

References [128–130] investigate compressed sensing in order to further reduce the readout channel count. The compressed sensing method employs nonadaptive linear projections that preserve the underlying signal information at a lower sampling rate than is required by Nyquist theory. From these projections, optimization algorithms can be implemented to decode the original set of detector signals. When combined with a good sensing matrix, this approach can produce superior SNR compared to Anger or cross-strip multiplexing.

28.5 Semiconductor Detectors

Semiconductor detectors form an alternative to scintillation detectors. In these detectors, electron–hole pairs created during interactions of the photo- or Compton electron obtained by the primary gamma interaction are detected directly. Due to this direct conversion, the energy resolution of these devices is very high, on the order of a few % FWHM. Semiconductor detectors have the additional advantage that their spatial resolution is determined by the pitch of the readout strip and thus is not limited by the ability of manufacturing and organizing tiny crystals.

The most commonly used semiconductor in particle and nuclear physics experiments is silicon. However, due to its low Z and low density, silicon is not a very efficient absorber for annihilation radiation. Therefore, CdZnTe (CZT) and CdTe have been considered as more appropriate alternative room temperature semiconductors for PET imaging. Both materials have a density of about 5.85 g/cm^3 and an effective Z of roughly 50. The main difference between the materials is the bandgap and charge transport properties. We see that both Z_{eff} and density of CZT are slightly better than those of LaBr₃.

Another advantage of using CZT is that the ratio of anode to cathode signals can be used to estimate the depth of interaction [131]. Gu et al. [132] used this approach in a prototype small animal CZT PET camera, achieving 1 mm resolution in the direction orthogonal to the electrode planes.

Other researchers that have investigated CZT as active detector element for a PET camera have done so in view of developing preclinical PET systems [133–135]. The poor timing resolution achievable with semiconductor detectors makes

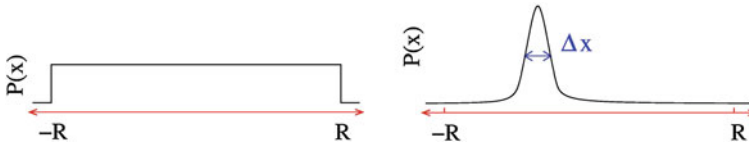


Fig. 28.8 Difference between non-TOF and TOF imaging. In case of non-TOF imaging, the annihilation event occurred anywhere along the LOR (*left*). In TOF imaging, we can estimate where along the line of response the annihilation occurred, with precision Δx , which is dependent on the time resolution: $\Delta x = c \cdot \Delta t/2$

them difficult to use in clinical PET system designs. Timing resolution is not that much of an issue in small animal imaging systems due to the higher geometric efficiency and low activity used, that reduces the number of random coincidences, and the lack of need for TOF information.

Due to the relatively low Z , a large number of photons will undergo Compton scatter in the CZT detector. In order to maintain sensitivity, it is desirable to include these MIPE in the data set and ultimately in the reconstruction. This also requires estimating the first point of interaction, which could be done by using Bayesian estimators [136] for example. In addition, care needs to be taken to design low-noise electronics, so the energy threshold can be set low.

28.6 Improvements in Timing Resolution

Traditionally, timing resolution was only used to reduce the random coincidences. However, the ability to localize where along the line of response the annihilation occurred is also enhanced by improved time resolution, see Fig. 28.8. Systems that are able to do so are called “time-of-flight” systems. The advantage is that the reconstruction converges faster or at lower counts and that more contrast is observed in the resulting image. Better lesion contrast, and thus, detectability is achieved using TOF imaging [137]. Typical state-of-the-art clinical systems have a time resolution of about 500–900 ps (i.e., 7.5–13.5 cm). These resolutions help lesion detectability in particular in larger patients [138]. Unfortunately, the current commercially available timing resolution is insufficient to improve image quality for smaller lesions. A lot of research currently is being performed to enhance timing resolution. Improvements in scintillator material, light extraction, novel photodetectors, and signal processing are likely to improve time resolution in clinical systems in the next couple of years [139]. We present here a brief overview of recent accomplishments toward TOF-PET.

Traditionally, the contribution from the scintillator to time resolution is characterized by three parameters: R the total number of photoelectrons generated, Q the photoelectron number on which the discriminator is triggering, and τ , the decay time of the scintillator [140]:

$$t_Q = \tau \ln\left(\frac{1}{2}\left(Q - R + \sqrt{(Q - R)^2 + 4R}\right)\right), \quad (28.4)$$

t_Q being the most probable interval in which the Q th photon is detected or in other words the time precision. The formula above yields superior timing for smaller Q , larger R , and smaller τ . The small Q requirement shows the need for the design of low-noise electronics, so low-trigger thresholds can be set. Contributions of each parameter individually were calculated in Ref. [141]. Taking $R = 2, 200$, $\tau = 40$ ns (comparable to LSO) and $Q = 5$, we achieve 73 ps. If we take $Q = 2$, we obtain 18 ps. Using the above formula, we see that because of its higher light yield and its faster decay time, LaBr₃ is superior to LSO for timing resolution. Coincidence resolving time of about 100 ps FWHM has been achieved with small ($3 \times 3 \times 5$ mm³) LaBr₃ crystals [142]. The crystal was used in a prototype TOF-PET camera [143] that achieved 375 ps timing resolution.

In a more realistic approximation compared to the one of Eq. 28.2, both the optical transit time and the scintillation rise time need to be taken into account. The optical transit time is dependent on the crystal type, crystal dimensions and surface treatment [144]. For a 1-cm-length LSO crystal, Powolny [141] calculated a propagation time of 75 ps.

The rise time of the scintillation pulse has long been ignored, since it is experimentally hard to assess, as it is typically quite short. Derenzo et al. [145] measured a two-component rise time for a $3 \times 3 \times 30$ mm LSO crystal of 30 ± 30 ps (88 %) and 350 ± 70 ps (12 %). A single-component rise time of 72 ± 12 ps was measured by Seifert et al. [146] for the same crystal type. For LaBr₃, the same authors determined three exponential rise time contributions to the overall signal rise

time: $\tau_{r,1} = 270 \pm 70$ ps (72 %), $\tau_{r,2} = 2.0 \pm 0.9$ ns (26 %), $\tau_{r,3} = 130 \pm 50$ ns (2 %). The influence of a finite rise time was characterized using a bi-exponential timing model in Ref. [147]:

$$f(t) = a \int_0^t (e^{-t/\tau_d} (1 - e^{-t/\tau_r})) dt, \quad (28.5)$$

with a a constant, τ_d the decay time, and τ_r the rise time. Note that if $\tau_r = 0$, the traditional model without rise time is obtained. Lecoq et al. [148] calculated a fivefold increase in the arrival time of the first photoelectron and a 2.5-fold increase in arrival of the first five photoelectrons for a rise time of 0.2 ns with $Q = 2, 200$ and $\tau_d = 40$ ns.

When combining the effects of rise time ($\sigma_{\text{rise}} \approx 20$ ps), propagation time ($\sigma_{\text{prop}} \approx 75$ ps) and photoproduction time ($\sigma_{\text{phot}} \approx 18$ ps), the total time precision intrinsic to the scintillator can be calculated:

$$\sigma_{\text{scint}} = \sqrt{\sigma_{\text{rise}}^2 + \sigma_{\text{prop}}^2 + \sigma_{\text{phot}}^2} \approx 80 \text{ ps}. \quad (28.6)$$

The numeric values in the above equation show that the propagation time is an important contribution. One way of reducing the uncertainty in propagation time is to use DOI methods: light propagation is more constrained when the location of the interaction of the 511 keV photon can be estimated [144, 149]. Seifert et al. [150] measured 200 ps FWHM for a monolithic $18 \times 16.2 \times 10.0 \text{ mm}^3$ LaBr_3 crystal coupled to SiPMs using ML estimates of the interaction location. Other methods to reduce σ_{prop} are to decrease the aspect ratio of the crystal for instance by coupling the side of the crystal to the photodetector rather than the edge [151], or to optimize light extraction using photonic crystals [60] as mentioned in Sect. 28.3.3.

Another reason for timing degradation are the electronics attached to the photodetector. For standard time pickoff, the single detector time resolution is given by [152]

$$\Delta t_{\text{FWHM}} = \frac{\sigma_V}{dV/dt}. \quad (28.7)$$

When using a constant fraction discriminator (CFD) for time pickoff, the exact expression of time resolution is more complicated. A more elaborate expression can be found in [153].

It is clear that in order to improve timing, we need fast rise and decay times (i.e., fast light production), large light output, low noise, and low optimal transit time spread. Also being able to trigger on a signal level as low as a few photoelectrons would improve timing. Due to the high QE of SiPMs compared to PMTs, the former may yield superior timing resolution, provided the noise is sufficiently low.

Fishburn and Charbon [154] showed that the best timing is not always achieved by triggering on the first photoelectron when using SiPMs: as the light detection efficiency increases, the arrival time variances of the initial primary photoelectrons are dominated by the Gaussian jitter rather than the exponential light emission, and hence, the initial primary photoelectron with the minimum-variance arrival time is not always the first primary photoelectron. According to Ref. [155], optimal timing resolution can be further improved by 10–20 % when measuring the timestamp of the first n photons, rather than only measuring the n th photon. For LYSO, best results are obtained at $n \approx 10$.

The decay time of light production is dependent on the activator. For inorganic scintillators with Ce^{3+} activators for example, the ultimate scintillation decay time is around 15–17 ns [156]. The 5d–4f emission responsible for scintillation light is roughly two times faster in Pr^{3+} . The fundamental limit for Pr activators is around 7–9 ns [156]. Alternatively, direct bandgap semiconductors could be used: Derenzo et al. [157] measured for example the decay of Ga-doped ZnO powder to have three principal components with decay times of 0.11 ns (37 %), 0.29 ns (23 %) and 0.78 ns (28 %). The material was further evaluated in Ref. [158].

Alternative to scintillation light, one could use the Cherenkov light produced by the photoelectron to obtain faster timing, since these Cherenkov photons are

produced quasi instantaneously. A few tens of Cherenkov photons are created upon absorption of 511 keV photons [148]. Korpar et al. [159] measured coincidence resolution of 71 ps FWHM by detecting Cherenkov radiation in PbF₂ crystals. A drawback of this approach is the poor associated energy resolution.

28.7 MR Compatibility

In the last decade, much interest was generated in combining PET and MR imaging modalities. MR has excellent soft tissue contrast combined with high spatial resolution. There has been a desire and need to combine PET and MR modalities in order to take advantage of both modalities' unique features [160–163].

In general, two approaches are used to combine PET and MR imaging: one is the so-called sequential approach, where a subject first undergoes one of both modalities, followed by the next. Advanced registration mechanisms have been developed to co-register these images [164]. However, as patients are moved from one bed to another, organs may move and it becomes quite challenging to fuse images from both modalities. When using a highly specific tracer, this is even more challenging due to the absence of anatomical landmarks. In order to mitigate these problems, both PET and MR cameras can be located in the same room. The bed is then translated to each scanner individually, without the need for the subject to leave the bed. Some commercial vendors (GE and Philips) have chosen this approach for combined PET and MR imaging. The advantage of the sequential approach is a reduced technological challenge.

The alternative method is to place the PET camera inside the bore of the magnet. This allows simultaneous acquisition of both modalities. However, the space available is often limited due to the limited bore diameter, and there are significant technological challenges to be solved. The first generation of PET/MR systems typically used light guides to bring the scintillation photons outside of the magnetic field, with PMTs operating in the fringe field. The advances in APD and SiPM technology yielded second-generation PET/MR systems, which have both the scintillator and photodetectors inside the bore, made possible by the insensitivity of these solid-state photodetectors to magnetic fields. However, as pointed out in Ref. [163], the PET part of these early second-generation small animal imaging systems features an order of magnitude lower sensitivity, combined with a worse spatial resolution compared to stand-alone PET systems. The challenge of building high-sensitivity and high-resolution PET inserts is as of today still unmet.

The difficulty of designing PET cameras inside the MR bore is that the PET part should be shielded from the intense RF field generated by the MR coils. The MR signals, i.e., the RF waves emitted by the subject upon spin relaxation, are extremely weak, and therefore, one needs to ensure that the PET component does not interfere with the MR-receiving electronics. In addition, the uniformity of the field in MR is extremely important. Care needs to be taken that the magnetic susceptibility of the materials used in the PET component do not influence field

homogeneity. MR gradients can for instance induce eddy currents in conductive PET components, which generate opposing magnetic fields and hence influence field uniformity [165]. It should also be noted that shielding is strongly field dependent: shielding designed for a 3T magnet may not work for a 7T magnet, and vice versa.

When using combined PET and MR scanners, it is desirable to use the MR image to perform attenuation correction. However, as opposed to using CT for attenuation correction, the MR protocol does not directly measure tissue attenuation. MR rather measures tissue composition. Bone density varies for example largely across patients, yet the MR only determines that a certain tissue is bone, without directly measuring its attenuation coefficient [166, 167].

28.8 Improvements in Image Reconstruction Techniques

After collection of many LORs in a PET detector, an image reconstruction process is applied to obtain a 3D image of the tracer concentration in a subject. The reconstruction process is essentially an inverse Radon transform that attempts to reconstruct the original density from projection data [168].

Statistical iterative methods to reconstruct images such a maximum likelihood expectation maximization (MLEM) in general yield more desirable images than the ones obtained with more conventional filtered back projection (FBP) methods due to a better trade-off between noise and resolution. Iterative reconstruction methods enable to incorporate information about the image formation process in the reconstruction, such as the Poisson nature of the detection of 511-keV photons. In addition, geometry, scatter, and attenuation corrections can be included in these iterative algorithms.

Each iteration essentially contains a number of forward and backprojection operations. The forward projection is represented as a matrix-vector multiplication. The vector is a discretization of the object being imaged, and the matrix describes the linear response of the imaging system. Because the matrix is sparse, the multiplication occurs implicitly. The backprojection involves matrix transposition. Both matrix transposition and matrix-vector multiplication form the bulk of the computation.

Graphics processing units (GPU) have become of large interest to the PET community to perform these computationally intensive iterative image reconstruction algorithms [169]. GPUs feature several hundred of cores and allow over 10^{12} floating-point operations per second (>1 TFLOP). The speed at which GPUs operate has been increasing faster than the increase in CPU speed. GPUs were used for the first time in image reconstruction in 1994 [170].

Thanks to the development of readily accessible application programming interfaces (APIs) such as NVIDIA's CUDA, Microsoft DirectCompute or

OpenCL, it has become relatively straightforward to use GPUs for image reconstruction. CUDA for example provides a set of extensions to the C language that allows the programmer to access computing resources on the GPU, without the need to access the graphics pipeline directly as for instance was done by Pratz et al. [171]. The many matrix transposition and matrix-vector multiplication needed for iterative reconstruction can easily be executed in parallel on the GPU. Also TOF reconstruction methods have been implemented on the GPU [172].

Fast image reconstruction, enabled by the use of GPUs, allows an operator for instance to change some of the reconstruction parameters to optimize lesion detectability as a function of patient size, lesion size, or tracer uptake. The practical advantage of a fast image reconstruction procedure is easily seen.

There also is an ongoing development to improve the quality of the reconstructed images using scatter reduction techniques [173], random estimation and correction [174], incorporating temporal data [175] and positron range correction [176]. A discussion of these is beyond the scope of this chapter, a detailed overview can be found for example in [177].

28.9 Summary and Conclusions

We have given an overview of the current state-of-the-art commercially available clinical whole-body PET-CT systems, followed by a discussion of various detector design improvements under development in various academic centers and research laboratories across the globe. It is likely that some of the techniques currently being developed make their way to the clinic. As a consequence, in the next couple of years significant improvements can be made toward improved clinical PET cameras. In particular, progress is to be expected in TOF imaging in the very near future. The use of SiPMs or novel 3D SPAD designs may improve timing resolution significantly, in combination with low-noise electronics that would allow triggering on small signals. Improved light extraction methods and scintillation crystals may also help to further improve timing resolution. The benefits of TOF imaging would be an enhanced image signal to noise ratio, yielding higher-contrast images, and potentially improving detectability of low-contrast lesions.

If the QE of various novel photodetectors can be enhanced in the shorter wavelength region, Pr-doped scintillators like LuAg:Pr may show to have improved characteristics compared to LSO, the current workhorse crystal in PET.

There is a clinical demand to increase the sensitivity of current clinical PET cameras. Today's best systems have a sensitivity $<1\%$. Increasing the sensitivity may enable a higher patient throughput and/or a reduced injected dose. Avoiding gaps between block detectors, including detector scattered MIPE in the reconstruction, or the use of thick monolithic crystals may help to increase sensitivity. The demand here is for low-noise electronics with low-trigger threshold in combination with an excellent energy resolution.

In terms of spatial resolution improvement, progress is to be expected when some of the DOI methods developed by various researchers in the field are implemented in clinical systems. Enhancing the spatial resolution, and its uniformity across the FOV will lead to detectability of smaller lesions, which is important when using PET for staging.

The large interest in combined PET and MR imaging modalities will likely lead toward MR compatible PET systems with higher sensitivity than the current available PET-MR systems. Also here, the development and increased reliability of SiPMs will trigger progress.

Acknowledgments The authors would like to thank Virginia Spanoudaki, David Hsu, and David Freese for discussions regarding this manuscript.

References

1. Levin CS, Hoffman EJ (1999) Calculation of positron range and its effect on the fundamental limit of positron emission tomography system spatial resolution. *Phys Med Biol* 44:781–799
2. Shibuya K, Yoshida E, Nishikido F, Suzuki T, Tsuda T, Inadama N, Yamaya T, Murayama H (2007) Annihilation photon acollinearity in PET: volunteer and phantom FDG studies. *Phys Med Biol* 52:5249–5261
3. Delbeke D, Schöder H, Martin WH, Wahl RL (2009) Hybrid imaging (SPECT/CT and PET/CT): improving therapeutic decisions. *Semin Nucl Med* 39:308–340
4. von Schulthess GK, Steinert HC, Hany TF (2006) Integrated PET/CT: current applications and future directions. *Radiology* 238:405–422
5. IMV Medical Information Division (2012) 2012 PET Imaging market summary report. Technical Report
6. Hanahan D, Weinberg RA (2011) Hallmarks of Cancer: the next generation. *Cell* 144:646–674
7. Valenta I, Schindler TH (2012) Rb PET/CT: entering a new area of myocardial perfusion imaging? *Eur J Nucl Med Mol Imaging* 39:1231–1232
8. Landau SM, Breault C, Joshi AD, Pontecorvo M, Mathis CA, Jagust WJ, Mintun MA, and Alzheimer's Disease Neuroimaging Initiative (2013) Amyloid- β imaging with Pittsburgh compound B and florbetapir: comparing radiotracers and quantification methods. *J Nucl Med* 54:70–77
9. Chen K, Chen X (2011) Positron emission tomography imaging of cancer biology: current status and future prospects. *Semin Oncol* 38:70–86
10. National Electrical Manufacturers Association (2013) NEMA NU 2-2012
11. Siemens Medical (2006) TruePoint PET/CT technology. pp 1–16
12. Philips Healthcare (2011) Time-of-Flight technology within your reach. pp 1–4
13. Imaging Technology News (2013), PET/CT system comparison charts. <http://www.itnonline.com/comparison-charts>
14. Payne SA, Moses WW, Sheets S, Ahle L, Cherepy NJ et al (2011) Nonproportionality of scintillator detectors: theory and experiment. II. *IEEE Trans. Nucl. Sci* 58:3392–3402
15. Wiener R, Kaul M, Surti S (2010) Signal analysis for improved timing resolution with scintillation detectors for TOF PET imaging. *IEEE NSS-MIC Conf Rec.* pp 1991–1995
16. Yang K, Melcher CL, Koschan M, Zhuravleva M (2011) Effect of Ca co-doping on the luminescence centers in LSO: Ce single crystals. *IEEE Trans Nucl Sci* 58:1394–1399

17. Yanagida T, Yoshikawa A, Yokota Y, Kamada K, Usuki Y, Yamamoto S, Miyake M, Baba M et al (2010) Development of Pr: LuAG scintillator array and assembly for positron emission mammography. *IEEE Trans Nucl Sci* 57:1492–1495
18. Chewpraditkul W, Swiderski L, Moszynski M, Szczesniak T, Syntfeld-Kazuch A, Wanarak C, Limsuwan P (2009) Scintillation properties of LuAG:Ce, YAG:Ce and LYSO:Ce crystals for gamma-ray detection. *IEEE Trans Nucl Sci* 56:3800–3805
19. Conti M, Eriksson L, Rothfuss H, Melcher CL (2009) Comparison of fast scintillators with TOF PET potential. *IEEE Trans Nucl Sci* 56:926–933
20. Kamada K, Yanagida T, Tsutsumi K, Usuki Y, Sato M, Ogino H, Novoselov A, Yoshikawa A et al (2009) Scintillation properties of 2-inch-diameter Pr: Lu₂Al₅O₁₂(LuAG) single crystal. *IEEE Trans Nucl Sci* 56:570–573
21. Balcerzyk M, Moszynski M, Kapusta M, Wolski D, Pawelke J, Melcher CL (2000) YSO, LSO, CSO and LGSO. A study of energy resolution and nonproportionality. *Nucl Sci* 47:1319–1323
22. Swiderski L, Moszynski M, Nassalski A, Syntfeld-Kazuch A, Szczesniak T, Kamada K, Tsutsumi K, Usuki Y et al (2009) Scintillation properties of praseodymium doped LuAG scintillator compared to cerium doped LuAG, LSO and LaBr. *IEEE Trans Nucl Sci* 56:2499–2505
23. Balcerzyk M, Galazka Z, Kapusta M, Syntfeld A, Lefaucheur JL (2004) Perspectives for high resolution and high light output LuAP:Ce crystals. *IEEE NSS-MIC Conf Rec* 2:986–992
24. Auffray E, Abler D, Brunner S, Frisch B, Knapitsch A, Lecoq P, Mavromanolakis G, Poppe O et al (2009) LuAG material for dual readout calorimetry at future high energy physics accelerators. *IEEE NSS-MIC Conf Rec*, pp 2245–2249
25. van Loef EV, Higgins WM, Glodo J, Churilov AV, Shah KS (2008) Crystal growth and characterization of rare earth iodides for scintillation detection. *J Cryst Growth* 310:2090–2093
26. Ito M, Hong SJ, Lee JS (2011) Positron emission tomography (PET) detectors with depth-of-interaction (DOI) capability. *Biomed Eng Lett* 1:70–81
27. Costa E, Massaro E, Piro L (1986) A BGO-CsI(Tl) phoswich: a new detector for X- and γ -ray astronomy. *Nucl Instr Meth A* 243:572–577
28. Mosset J-B, Devroede O, Krieguer M, Rey M, Vieira JM, Jung JH, Kuntner C, Streun M et al (2006) Development of an optimized LSO/LuYAP phoswich detector head for the Lausanne ClearPET demonstrator. *IEEE Trans Nucl Sci* 53:25–29
29. Jung JH, Choi Y, Chung YH, Devroede O, Krieguer M, Bruyndonckx P, Tavernier S (2007) Optimization of LSO/LuYAP phoswich detector for small animal PET. *Nucl Instr Meth A* 571:669–675
30. Vaquero J, Sanchez J, Lage E (2011) Design of DOI PET detector modules using phoswich and SiPMs: first results. *IEEE NSS-MIC Conf Rec*. pp 3311–3313
31. Fontaine R, Bélanger F, Viscogliosi N (2009) The hardware and signal processing architecture of LabPETTM, a small animal APD-based digital PET scanner. *Nucl Sci* 56:3–9
32. Du H, Yang Y, Glodo J, Wu Y, Shah K, Cherry SR (2009) Continuous depth-of-interaction encoding using phosphor-coated scintillators. *Phys Med Biol* 54:1757–1771
33. Roncali E, Phipps J, Marcu L (2012) Pulse shape discrimination and classification methods for continuous depth of interaction encoding PET detectors. *Phys Med Biol* 57:6571–6585
34. Liu H, Omura T, Watanabe M, Yamashita T (2001) Development of a depth of interaction detector for γ -rays. *Nucl Instr Meth A* 459:182–190
35. Zhang N, Thompson CJ, Togane D, Cayouette F, Nguyen KQ (2002) Anode position and last dynode timing circuits for dual-layer BGO scintillator with PS-PMT based modular PET detectors. *IEEE Trans Nucl Sci* 49:2203–2207
36. Ito M, Lee JS, Kwon SI, Lee GS, Hong B, Lee KS, Sim K-S, Lee SJ et al (2010) A four-layer DOI detector with a relative offset for use in an animal PET system. *IEEE Trans Nucl Sci* 57:976–981

37. Tsuda T, Murayama H, Kitamura K, Yamaya T, Yoshida E, Omura T, Kawai H, Inadama N et al (2004) A four-Layer depth of interaction detector block for small animal PET. *IEEE Trans Nucl Sci* 51:2537–2542
38. Inadama N, Murayama H, Hamamoto M, Tsuda T, Ono Y, Yamaya T, Yoshida E, Shibuya K et al (2006) 8-Layer DOI encoding of 3-dimensional crystal array. *IEEE Trans Nucl Sci* 53:2523–2528
39. Shimizu K, Ohmura T, Watanabe M, Uchida H, Yamashita T (1988) Development of 3-D detector system for positron CT. *IEEE Trans Nucl Sci* 35:717–720
40. Abreu M, Aguiar J, Almeida F, Almeida P, Bento P, Carrico B, Ferreira M, Ferreira N et al (2006) Design and evaluation of the Clear-PEM scanner for positron emission mammography. *IEEE Trans Nucl Sci* 53:71–77
41. James SS, Yang Y, Wu Y, Farrell R, Dokhale P, Shah KS, Cherry SR (2009) Experimental characterization and system simulations of depth of interaction PET detectors using 0.5 mm and 0.7 mm LSO arrays. *Phys Med Biol* 54:4605–4619
42. Beltrame P, Bolle E, Braem A, Casella C, Chesi E, Clinthorne N, Cochran E, De Leo R et al (2011) Construction and tests of demonstrator modules for a 3-D axial PET system for brain or small animal imaging. *Nucl Instr Meth A* 636:S226–S230
43. Bolle E, Rissi M, Bjaalie JG, Buskenes JI, Dorholt O, Røhne O, Skretting A, Stapnes S (2011) COMPET—high resolution and high sensitivity PET scanner with novel readout concept: setup and simulations. *Nucl Instr Meth A* 648:S93–S95
44. Yamaya T, Mitsuhashi T, Matsumoto T, Inadama N, Nishikido F, Yoshida E, Murayama H, Kawai H et al (2011) A SiPM-based isotropic-3D PET detector X'tal cube with a three-dimensional array of 1 mm³ crystals. *Phys Med Biol* 56:6793–6807
45. Yoshida E, Tashima H, Inadama N, Nishikido F, Moriya T, Omura T, Watanabe M, Murayama H et al (2012) Intrinsic spatial resolution evaluation of the X'tal cube PET detector based on a 3D crystal block segmented by laser processing. *Radiol Phys Technol* 6:21–27
46. Levin CS (2002) Design of a high-resolution and high-sensitivity scintillation crystal array for PET with nearly complete light collection. *IEEE Trans Nucl Sci* 49:2236–2243
47. Vandenbroucke A, Foudray AMK, Olcott PD, Levin CS (2010) Performance characterization of a new high resolution PET scintillation detector. *Phys Med Biol* 55:5895–5911
48. Zhang J, Foudray A, Olcott P, Farrell R, Shah K, Levin C (2007) Performance characterization of a novel thin position-sensitive avalanche photodiode for 1 mm resolution positron emission tomography. *IEEE Trans Nucl Sci* 54:415–421
49. Vandenbroucke A, Lau FWY, Reynolds PD, Levin CS (2011) Measuring 511 keV photon interaction locations in three dimensional position sensitive scintillation detectors. *IEEE NSS-MIC Conf Rec* 2011:1–4
50. Lau FWY, Fang C, Reynolds PD, Olcott PD, Vandenbroucke A, Spanoudaki VC, Olutade F, Horowitz MA et al (2008) 1 mm³ resolution breast-dedicated PET system. *IEEE NSS-MIC Conf Rec*, pp 5619–5622
51. Ling T, Lewellen TK, Miyaoka RS (2007) Depth of interaction decoding of a continuous crystal detector module. *Phys Med Biol* 52:2213–2228
52. Bruyndonckx P, Lematre C, Schaart D, Maas M (2007) Towards a continuous crystal APD-based PET detector design. *Nucl Instr Meth NIM A* 571:182–186
53. van der Laan DJJ, Maas MC, Bruyndonckx P, Schaart DR (2012) Limits on the spatial resolution of monolithic scintillators read out by APD arrays. *Phys Med Biol* 57:6479–6496
54. Ross S, Stearns C (2010) SharpIR, white paper. GE Healthcare, pp 1–8
55. Siemens Medical (2007) TruePoint PET. pp 1–10
56. Cayouette F, Laurendeau D, Moisan C (2003) DETECT2000: an improved Monte-Carlo simulator for the computer aided design of photon sensing devices. In: Lessard RA, Lampropoulos GA, Schinn GW (eds) *Proceedings of SPIE*, pp 69–76, SPIE
57. Janeczek M, Moses WW (2010) Simulating scintillator light collection using measured optical reflectance. *IEEE Trans Nucl Sci* 57:964–970

58. Agostinelli S, Allison J, Society AC, Apostolakis J, Araujo H, Arce P, Asai M, Axen D et al (2003) Geant4—a simulation toolkit. *Nucl Instr Meth A* 506:250–303
59. Gentil F (2002) Litrani: a general purpose Monte Carlo program simulating light propagation in isotropic or anisotropic media. *Nucl Instr Meth A* 4486:35–39
60. Kronberger M, Auffray E, Lecoq P (2010) Improving light extraction from heavy inorganic scintillators by photonic crystals. *IEEE Trans Nucl Sci* 57:2475–2482
61. Flyckt SO, Marmonier C (2002) Photomultiplier tubes—principles and applications. *Photonis*, 2 edn
62. Iams H, Salzberg B (1935) The secondary emission phototube. *Proc. IRE* 23:55–64
63. Iijima T (2011) Status and perspectives of vacuum-based photon detectors. *Nucl Instr Meth A* 639:137–143
64. Hamamatsu (2013) Electron tube division. <http://sales.hamamatsu.com/en/products/electron-tube-division/detectors/photomultiplier-tubes.php>
65. Anger HO (1958) Scintillation camera. *Rev Sci Inst* 29:27–33
66. Pani R, Pellegrini R, Cinti MN, Mattioli M, Trotta C, Montani L, Iurlaro G, Trotta G et al (2004) Recent advances and future perspectives of position sensitive PMT. *Nucl Instr Meth B* 213:197–205
67. Olcott P, Talcott JA, Levin CS, Habte F (2005) Compact readout electronics for position sensitive photomultiplier tubes. *IEEE Trans Nucl Sci* 52:21–27
68. Pani R, Cinti MN, Pellegrini R, Betti M, Bennati P, Trotta G, Del Guerra A (2005) Reduced parallel anode readout for 256 ch flat panel PMT. *IEEE NSS-MIC Conf Rec* 5:2954–2958
69. Kyushima H, Shimoi H, Atsumi A, Ito M, Oba K, Yoshizawa YNSSCRI (2000) The development of flat panel PMT. *IEEE NSS-MIC Conf. Rec.* 7:3–7
70. Luo W, Anashkin E, Matthews CG (2008) First test results of a commercially available clinical PET scanner using the NEMA NU4-2008 small animal PET standards. *IEEE NSS-MIC Conf Rec*, pp 4718–4723
71. Gu Z, Taschereau R, Vu NT, Wang H, Prout DL, Silverman RW, Stout DB, Phelps ME et al (2011) Design and initial performance of PETbox4, a high sensitivity preclinical imaging tomograph. *IEEE NSS-MIC Conf Rec*, 2328–2331
72. Godinez F, Chaudhari AJ, Yang Y, Farrell R, Badawi RD (2012) Characterization of a high-resolution hybrid DOI detector for a dedicated breast PET/CT scanner. *Phys Med Biol* 57:3435–3449
73. Wolff P (1954) Theory of electron multiplication in silicon and germanium. *Phys Rev* 95:1415–1420
74. Chynoweth AG (1960) Uniform silicon p–n junctions. II. Ionization rates for electrons. *J Appl Phys* 31:1161–1165
75. Baraff GA (1962) Distribution functions and ionization rates for hot electrons in semiconductors. *Phys Rev* 128:2507–2517
76. Huth G, Trice J, McKinney R (1964) Internal pulse amplification in silicon pn junction radiation detection junctions. *Rev Sci Inst* 35:1220–1222
77. McIntyre R (1966) Multiplication noise in uniform avalanche diodes. *IEEE Trans Electr Dev* 13:164–168
78. Petrillo G, McIntyre R, Lecomte R, Lamoureux G, Schmitt D (1984) Scintillation detection with large-area reach-through avalanche photodiodes. *Nucl. Sci.* 31:417–423
79. Lecomte R, Schmitt D, Lightstone A, McIntyre R (1985) Performance characteristics of BGO-silicon avalanche photodiode detectors for PET. *IEEE Trans Nucl Sci* 32:482–486
80. McIntyre R, Webb P, Dautet H (1996) A short-wavelength selective reach-through avalanche photodiode. *IEEE Trans Nucl Sci* 43:1341–1346
81. Lecomte R, Pepin C, Rouleau D, Saoudi A, Andreaco M, Casey M, Nutt R, Dautet H et al (2002) Investigation of GSO, LSO and YSO scintillators using reverse avalanche photodiodes. *Nucl Sci* 45:478–482
82. Huth G, Bergeson H, Trice J (1963) Stable, high field silicon pn junction radiation detectors. *Rev Sci Inst* 34:1283–1285

83. Locker R, Huth G (1966) A new ionizing radiation detection concept which employs semiconductor avalanche amplification and the tunnel diode element. *Appl Phys Lett* 9:227–230
84. Farrell R, Olschner F, Frederick E, McConchie L, Vanderpuye K, Squillante M, Entine G (1990) Large area silicon avalanche photodiodes for scintillation detectors. *Nucl Instr Meth A* 288:137–139
85. Moszynski M, Szawlowski M, Kapusta M, Balcerek M (2002) Large area avalanche photodiodes in scintillation and X-rays detection. *Nucl Instr Meth A* 485:504–521
86. Farrell R, Shah K, Vanderpuye K, Grazioso R, Myers R, Entine G (2000) APD arrays and large-area APDs via a new planar process. *Nucl Instr Meth A* 442:171–178
87. Pepin CM, Dautet H, Bergeron M, Cadorette J, Beaudoin J-F, Jacques-Bedard X, Couture M, Lecomte R (2010) New UV-enhanced, ultra-low noise silicon avalanche photodiode for radiation detection and medical imaging. *IEEE NSS-MIC Conf Rec*, pp 1740–1746
88. Redus R, Farrell R (1996) Gain and noise in very high-gain avalanche photodiodes: theory and experiment. *Proc. SPIE* 2859:288–297
89. McElroy D, Pimpl W, Pichler B, Rafecas M, Schüler T, Ziegler SI (2005) Characterization and readout of MADPET-II detector modules: validation of a unique design concept for high resolution small animal PET. *IEEE Trans Nucl Sci* 52:199–204
90. Moses WW, Derenzo SE, Budinger TF (1994) PET detector modules based on novel detector technologies. *Nucl Instr Meth A* 353:189–194
91. Levin CS, Foudray A, Olcott P, Habte F (2004) Investigation of position sensitive avalanche photodiodes for a new high-resolution PET detector design. *IEEE Trans Nucl Sci* 51:805–810
92. Lightstone AW, McIntyre RJ, Lecomte R, Schmitt D (1986) A bismuth germanate-avalanche photodiode module designed for use in high resolution positron emission tomography. *IEEE Trans Nucl Sci* 33:456–459
93. Lecomte R, Cadorette J, Rodrigue S, Lapointe D, Rouleau D, Bentourkia M, Yao R, Msaki P (1996) Initial results from the Sherbrooke avalanche photodiode positron tomograph. *IEEE Trans Nucl Sci* 43:1952–1957
94. Fontaine R, Bélanger F, Cadorette J, Leroux JD, Martin JP, Michaud JB, Pratte J-F, Robert S et al (2005) Architecture of a dual-modality, high-resolution, fully digital positron emission tomography/computed tomography (PET/CT) scanner for small animal imaging. *IEEE Trans Nucl Sci* 52:691–696
95. Bergeron M, Thibaudeau C, Cadorette J, Pepin CM, Tetrault MA, Davies M, Dautet H, Deschamps P et al (2011) LabPET II, an APD-based PET detector module with counting CT imaging capability. *IEEE NSS-MIC Conf Rec*, pp 3543–3547
96. Catana C, Wu Y, Judenhofer MS, Qi J, Cherry SR (2006) Simultaneous acquisition of multislice PET and MR images: initial results with a MR-compatible PET scanner. *J Nucl Med* 47:1968–1976
97. Judenhofer MS, Catana C, Swann BK, Siegel SB, Jung W-I, Nutt RE, Cherry SR, Claussen CD et al (2007) Is MR-guided attenuation correction a viable option for dual-modality PET/MR imaging? *Radiology* 244:639–642
98. CMS Collaboration (2010) Performance and operation of the CMS electromagnetic calorimeter. *JINST* 5:T03010–T03010
99. Spanoudaki VC, McElroy D, Torres-Espallardo I, Ziegler SI (2008) Effect of temperature on the performance of proportional APD-based modules for gamma ray detection in positron emission tomography. *Nucl Sci* 55:469–480
100. Vandenbroucke A, McLaughlin TJ, Levin CS (2012) Influence of temperature and bias voltage on the performance of a high resolution PET detector built with position sensitive avalanche photodiodes. *JINST* 7:P08001–P08001
101. Cadorette J, Rodrigue S, Lecomte R (1993) Tuning of avalanche photodiode PET camera. *IEEE Trans Nucl Sci* 40:1062–1066
102. Shah K, Farrell R, Grazioso R, Harmon ES, Karplus E (2002) Position-sensitive avalanche photodiodes for gamma-ray imaging. *Nucl Sci* 49:1687–1692

103. Vandembroucke A, Levin CS (2008) Study of scintillation crystal array parameters for an advanced PET scanner dedicated to breast cancer imaging. *IEEE NSS-MIC Conf Rec*, pp 4914–4919
104. Lau FWY, Vandembroucke A, Reynolds PD, Olcott PD, Horowitz MA, Levin C (2010) Analog signal multiplexing for PSAPD-based PET detectors: simulation and experimental validation. *Phys Med Biol* 55:7149
105. Renker D (2006) Geiger-mode avalanche photodiodes, history, properties and problems. *Nucl Instr Meth A* 567:48–56
106. Spanoudaki VC, Levin CS (2010) Photo-detectors for time of flight positron emission tomography (ToF-PET). *Sensors* 10:10484–10505
107. Roncali E, Cherry SR (2011) Application of silicon photomultipliers to positron emission tomography. *Ann Biomed Eng* 39:1358–1377
108. Spanoudaki VC, Levin CS (2011) Scintillation induced response in passively-quenched Si-based single photon counting avalanche diode arrays. *Opt Express* 19:1665–1679
109. Britvitch I, Renker D (2006) Measurements of the recovery time of Geiger-mode avalanche photodiodes. *Nucl Instr Meth A* 567:260–263
110. Oldham W, Samuelson R (1972) Triggering phenomena in avalanche diodes. *IEEE Trans Electr Dev* 19:1056–1060
111. McIntyre R (1973) On the avalanche initiation probability of avalanche diodes above the breakdown voltage. *IEEE Trans Electr Dev* 20:637–641
112. Mars P (1972) Temperature dependence of avalanche breakdown voltage temperature dependence of avalanche breakdown voltage in p–n junctions. *Int J Electron* 32:23–37
113. Mazzillo M, Abbisso S, Condorelli G, Sanfilippo D, Valvo G, Carbone B, Piana A, Fallica G et al (2011) Enhanced blue-light sensitivity P on N silicon photomultipliers. *IEEE NSS-MIC Conf Rec*, pp N12–1
114. Brown RGW, Jones R, Rarity JG, Ridley KD (1987) Characterization of silicon avalanche photodiodes for photon correlation measurements 2: active quenching. *Appl Opt* 26:2383
115. Cova S, Ghioni M, Lacaita A, Samori C, Zappa F (1996) Avalanche photodiodes and quenching circuits for single-photon detection. *Appl Opt* 35:1956–1976
116. Ramilli M, Allevi A, Nardo L, Bondani M, Caccia M (2012) Silicon photomultipliers: characterization and applications. *Photodetector (Sanka Gateva Edt., InTech, Rijeka, Croatia)*, pp 77–100
117. Chynoweth A, McKay K (1956) Photon emission from avalanche breakdown in silicon. *Phys Rev* 102:369–376
118. Lacaita AL, Zappa F, Bigliardi S, Manfredi M (1993) On the bremsstrahlung origin of hot-carrier-induced photons in silicon devices. *IEEE Trans Electr Dev* 40:577–582
119. Buzhan P, Dolgoshein B, Ilyin A, Kaplin V, Klemin S, Mirzoyan R, Popova E, Teshima M (2009) The cross-talk problem in SiPMs and their use as light sensors for imaging atmospheric Cherenkov telescopes. *Nucl Instr Meth A* 610:131–134
120. Frach T, Prescher G, Degenhardt C (2009) The digital silicon photomultiplier—principle of operation and intrinsic detector performance. *IEEE NSS-MIC Conf Rec*
121. Frach T, Prescher G, Degenhardt C, Zwaans B (2010) The digital silicon photomultiplier—system architecture and performance evaluation. *IEEE NSS-MIC Conf Rec*, pp 1959–1965
122. Ninković J, Andriček L, Liemann G, Lutz G, Moser H-G, Richter R, Schopper F (2009) SiMPI—novel high QE photosensor. *Nucl Instr Meth A* 610:142–144
123. Jendrysik C, Andriček L, Liemann G, Moser H-G, Ninković J, Richter R, Schopper F (2013) Characterization of the first prototypes of silicon photomultipliers with bulk-integrated quench resistor fabricated at MPI semiconductor laboratory. *Nucl Instr Meth A* 718:262–265
124. Berube B-L, Rheume V-P, Corbeil-Therrien A, Boisvert A, Carini G, Charlebois S, Fontaine R, Pratte J-F (2012) Development of a single photon avalanche diode (SPAD) array in high voltage CMOS 0.8 μm dedicated to a 3D integrated circuit (3DIC). *IEEE NSS-MIC Conf Rec*, pp 1835–1839

125. McClish M, Dokhale P, Christian J, Johnson E, Stapels C, Robertson R, Shah KS (2010) Characterization of CMOS position sensitive solid-state photomultipliers. *Nucl Instr Meth A* 624:492–497
126. McClish M, Dokhale P, Christian J (2011) Performance measurements from LYSO scintillators coupled to a CMOS position sensitive SSPM detector. *Nucl Instr Meth A* 652:264–267
127. Fischer P, Piemonte C (2013) Interpolating silicon photomultipliers. *Nucl Instr Meth A* 718:320–322
128. Olcott P, Chinn G, Levin CS (2011) Compressed sensing for the multiplexing of PET detectors. *IEEE NSS-MIC Conf Rec*, pp 3224–3226
129. Chinn G, Olcott PD, Levin CS (2010) Improving SNR with a maximum likelihood compressed sensing decoder for multiplexed PET detectors. *IEEE NSS-MIC Conf Rec*, pp 3353–3356
130. Chinn G, Olcott PD, Levin CS (2012) Improved compressed sensing multiplexing PET readout. *IEEE NSS-MIC Conf Rec*, pp 2472–2474
131. Hong J, Bellm EC, Grindlay JE, Narita T (2003) Cathode depth sensing in CZT detectors. *arXiv preprint astro-ph/0310475*
132. Gu Y, Matteson J, Skelton R, Deal A, Stephan E, Duttweiler F, Gasaway T, Levin C (2011) Study of a high-resolution, 3D positioning cadmium zinc telluride detector for PET. *Phys Med Biol* 56:1563
133. Morimoto Y, Ueno Y, Kojima S, Takeuchi W, Ishitsu T, Matsuzaki K, Umegaki K, Kubo N et al (2010) Development of a prototype 3D PET scanner using semiconductor detectors and depth of interaction information. *Mol Imaging Integr Med Ther Drug Dev*, pp 30–41, Springer
134. Mitchell G, Sinha S, Stickel JR, Bowen S, Cirignano L, Dokhale P, Kim H, Shah KS et al (2008) CdTe strip detector characterization for high resolution small animal PET. *IEEE Trans Nucl Sci* 55:870–876
135. Vaska P, Bolotnikov A, Carini G, Camarda G, Pratte J-F, Dilmanian FA, Park SJ, James RB (2005) Studies of CZT for PET Applications. *IEEE NSS-MIC Conf Rec* 5:2799–2802
136. Prax G, Levin CS (2009) Bayesian reconstruction of photon interaction sequences for high-resolution PET detectors. *Phys Med Biol* 54:5073
137. Surti S, Karp JS (2008) Experimental evaluation of a simple lesion detection task with time-of-flight PET. *Phys Med Biol* 54:373–384
138. Karp JS, Surti S, Daube-Witherspoon ME, Muehllehner G (2008) Benefit of time-of-flight in PET: experimental and clinical results. *J Nucl Med* 49:462–470
139. Lecoq P (2012) New approaches to improve timing resolution in scintillators. *IEEE Trans Nucl Sci* 59:2313–2318
140. Lynch FJ (1966) Improved timing with NaI(Tl). *IEEE Trans Nucl Sci* 13:140–147
141. Powolny F (2009) Characterization of time resolved photodetector systems for positron emission tomography. Ph.D. thesis, Université de Neuchâtel
142. Schaart DR, Seifert S, Vinke R (2010) LaBr₃:Ce and SiPMs for time-of-flight PET: achieving 100 ps coincidence resolving time. *Phys Med Biol* 55:N179–N189
143. Daube-Witherspoon ME, Surti S, Perkins A, Kyba CCM, Wiener R, Werner ME, Kulp R, Karp JS (2009) The imaging performance of a LaBr₃-based PET scanner. *Phys Med Biol* 55:45–64
144. Spanoudaki VC, Levin CS (2010) Investigating the temporal resolution limits of scintillation detection from pixellated elements: comparison between experiment and simulation. *Phys Med Biol* 56:735–756
145. Derenzo SE, Weber MJ, Moses WW, Dujardin C (2000) Measurements of the intrinsic rise times of common inorganic scintillators. *IEEE Trans Nucl Sci* 47:860–864
146. Seifert S, Steenbergen J, van Dam H, Schaart DR (2012) Accurate measurement of the rise and decay times of fast scintillators with solid state photon counters. *JINST* 7:P09004
147. Shao Y (2007) A new timing model for calculating the intrinsic timing resolution of a scintillator detector. *Phys Med Biol* 52:1103

148. Lecoq P, Auffray E, Brunner S, Hillemanns H, Jarron P, Knapitsch A, Meyer T, Powolny F (2010) Factors influencing time resolution of scintillators and ways to improve them. *IEEE Trans Nucl Sci* 57:2411–2416
149. Moses WW, Derenzo SE (1999) Prospects for time-of-flight PET using LSO scintillator. *IEEE Trans Nucl Sci* 46:474–478
150. Seifert S, van Dam H, Huizenga J, Vinke R, Dendooven P, Löhner H, Schaart DR (2012) Monolithic LaBr₃: Ce crystals on silicon photomultiplier arrays for time-of-flight positron emission tomography. *Phys Med Biol* 57:2219
151. Levin C (2008) New imaging technologies to enhance the molecular sensitivity of positron emission tomography. *Proc IEEE* 96:439–467
152. Spieler H (1982) Fast timing methods for semiconductor detectors. *IEEE Trans Nucl Sci* 29:1142–1158
153. Lecomte R, Pepin C, Rouleau D, Dautet H, McIntyre R, McSween D, Webb P (1999) Radiation detection measurements with a new “Buried Junction” silicon avalanche photodiode. *Nucl Instr Meth A* 423:92–102
154. Fishburn MW, Charbon E (2010) System tradeoffs in gamma-ray detection utilizing SPAD arrays and scintillators. *IEEE Trans Nucl Sci* 57:2549–2557
155. Seifert S, van Dam HT, Schaart DR (2012) The lower bound on the timing resolution of scintillation detectors. *Phys Med Biol* 57:1797–1814
156. Dorenbos P (2010) Fundamental limitations in the performance of Ce³⁺, Pr³⁺, and Eu²⁺ activated scintillators. *IEEE Trans Nucl Sci* 57:1162–1167
157. Derenzo SE, Weber MJ, Klintonberg MK (2002) Temperature dependence of the fast, near-band-edge scintillation from CuI, HgI₂, PbI₂, ZnO:Ga and CdS:In. *Nucl Instr Meth A* 486:214–219
158. Bourret-Courchesne ED, Derenzo SE, Weber MJ (2009) Development of ZnO:Ga as an ultra-fast scintillator. *Nucl Instr Meth A* 601:358–363
159. Korpar S, Dolenc R, Križan P, Pestotnik R, Stanovnik A (2011) Study of TOF PET using cherenkov light. *Nucl Instr Meth A* 654:532–538
160. Pichler BJ, Judenhofer MS, Wehrl HF (2008) PET/MRI hybrid imaging: devices and initial results. *Eur Radiol* 18:1077–1086
161. Judenhofer MS, Wehrl HF, Newport DF, Catana C, Siegel SB, Becker M, Thielscher A, Kneilling M et al (2008) Simultaneous PET-MRI: a new approach for functional and morphological imaging. *Nat Med* 14:459–465
162. Cherry SR, Louie AY, Jacobs RE (2008) The integration of positron emission tomography with magnetic resonance imaging. *Proc IEEE* 96:416–438
163. Judenhofer MS, Cherry SR (2013) Applications for preclinical PET/MRI. *Semin Nucl Med* 43:19–29
164. Li G, Xie H, Ning H, Capala J, Arora BC, Coleman CN, Camphausen K, Miller RW (2005) A novel 3D volumetric voxel registration technique for volume-view-guided image registration of multiple imaging modalities. *Int J Radiat Oncol Biol Phys* 63:261–273
165. Vaska P, Cao T (2013) The state of instrumentation for combined positron emission tomography and magnetic resonance imaging. *Semin Nucl Med* 43:11–18
166. Hofmann M, Pichler B, Schölkopf B, Beyer T (2008) Towards quantitative PET/MRI: a review of MR-based attenuation correction techniques. *Eur J Nucl Med Mol Imaging* 36:93–104
167. Wagenknecht G, Kops ER, Mantlik F, Fried E, Pilz T (2011) Attenuation correction in MR-BrainPET with segmented T1-weighted MR images of the patient’s head—a comparative study with CT. *IEEE NSS-MIC Conf Rec*, pp 2261–2266
168. Deans SR (2007) The radon transform and some of its applications. Courier Dover Publications
169. Prax G, Xing L (2011) GPU computing in medical physics: a review. *Med Phys* 38:2685–2697

170. Cabral B, Cam N, Foran J (1994) Accelerated volume rendering and tomographic reconstruction using texture mapping hardware. In: Proceedings of the volume visualization, New York, USA. ACM Press, pp 91–98
171. Prax G, Chinn G, Olcott P, Levin CS (2009) Fast, accurate and shift-varying line projections for iterative reconstruction using the GPU. *IEEE Trans Med Imag* 28:435–445
172. Cui J, Prax G, Prevrhal S, Levin CS (2011) Fully 3D list-mode time-of-flight PET image reconstruction on GPUs using CUDA. *Med Phys* 38:6775–6786
173. Chinn G, Levin CS (2011) A maximum NEC criterion for compton collimation to accurately identify true coincidences in PET. *IEEE Trans Med Imag* 30:1341–1352
174. Oliver JF, Rafecas M (2010) Improving the singles rate method for modeling accidental coincidences in high-resolution PET. *Phys Med Biol* 55:6951–6971
175. Grotus N, Reader AJ, Stute S, Rosenwald JC, Giraud P, Buvat I (2009) Fully 4D list-mode reconstruction applied to respiratory-gated PET scans. *Phys Med Biol* 54:1705–1721
176. Lin F, Qi J (2010) A residual correction method for high-resolution PET reconstruction with application to on-the-fly Monte Carlo based model of positron range. *Med Phys* 37:704
177. Reader AJ, Zaidi H (2007) Advances in PET image reconstruction. *PET Clin* 2:173–190

Chapter 29

Photoacoustic Imaging: Development of Imaging Systems and Molecular Agents

Adam de la Zerda

29.1 Photoacoustic Effect

Photoacoustic imaging is based on the conversion of light into sound waves, an effect that was first observed by Alexander Graham Bell in 1880 [1]. In photoacoustic imaging, the light excitation is typically a nanosecond-pulsed laser and the sound waves that are emitted and detected are in the frequency of ultrasound waves. A light absorbing material that is illuminated with a short laser pulse will lead to a local temperature increase ΔT in time and space. This produces an initial pressure p_0 due to the thermoelastic expansion $p_0 = \beta \cdot \Delta T / \kappa$, where β is the thermal expansion coefficient and κ is the isothermal compressibility. If the duration of the laser pulse that causes ΔT is short enough, the initial pressure p_0 can be represented in terms of the energy density that was absorbed by the material, A , as follows: $p_0 = \Gamma \cdot A$, where Γ is the Grüneisen coefficient, a dimensionless quantity that provides a measure of the conversion efficiency of absorbed energy density to pressure. Γ is given by $\Gamma = \beta c^2 / C_p$, where c is the speed of sound in the medium and C_p is the specific heat capacity. This rapid increase in pressure can be modeled as an impulse response that propagates outward according to the wave equation. A bulk change in temperature of 10^{-3} °C will result in a pressure rise of 800 Pa, which is well within the detectable levels of modern ultrasound detectors. In cases where a long laser pulse is used, some of the absorbed energy can be lost through conduction and convection processes, in which case the temperature increase will not be linearly related to the absorbed energy density, A , and therefore, p_0 will not be linearly related to A .

The energy density that is absorbed by a tissue A (measured in J/cm^3) satisfies $A = \mu_a \cdot F$, where μ_a is the absorption coefficient of the material (measured in

A. de la Zerda (✉)

Departments of Structural Biology and Electrical Engineering, and Bio-X Program,
School of Medicine, Stanford University, Fairchild Building, D141, 299,
Campus Drive W, Stanford, CA 94305, USA
e-mail: adlz@stanford.edu

cm^{-1}) and F is the excitation light fluence (measured in J/cm^2). In a living tissue, A is a function of time and space. The Grüneisen coefficient Γ , on the other hand, does not vary significantly across a tissue, and hence, Γ would often be treated as a constant. Situations where Γ is not constant gave rise to new measurement outcomes of photoacoustic imaging, such as the ability to measure temperature in deep tissue through the weak dependency of Γ on local temperature [2].

29.2 Conditions for Creating Photoacoustic Signals

An important aspect of building a tomographic imaging system is the ability to localize the origin of a signal in space. In photoacoustic imaging, this requirement is translated to a number of conditions imposed primarily, but not entirely, on the laser excitation system. Consider a laser pulse of long duration that is illuminating a small optically absorbing particle. During the course of illumination, the heat generated by the particle will begin to diffuse to its surroundings, leading to photoacoustic waves originating from around the particle as well. Similarly, photoacoustic waves will be created throughout the course of illumination and until the laser pulse is over, which reduces the effective spatial resolution of the system. These two situations are summarized below as the thermal confinement condition and the stress confinement condition, respectively.

29.2.1 Thermal Confinement Condition

Let L_p be the size of an object that is intended to be visualized by a photoacoustic system. Hence, over the course of the pulse illumination, the heat produced by the object should not diffuse more than the size of an object itself (Fig. 29.1). The heat diffusion distance is given by the thermal diffusion length: $\delta_T = 2\sqrt{D_T t_p}$, here D_T is the thermal diffusivity of the tissue (a constant with a typical value for most tissues of $\sim 1.4 \times 10^{-3} \text{ cm}^2/\text{s}$) and t_p is the laser pulse duration. Hence, the thermal confinement condition can be written as follows: $\delta_T < L_p$. For example, a laser pulse duration of $t_p = 0.5 \mu\text{s}$ (a relatively long laser pulse) will result in $\delta_T = 0.5 \mu\text{m}$. This can easily be achieved, as the spatial resolution of most photoacoustic tomography (PAT) systems is typically much larger than $0.5 \mu\text{m}$.

29.2.2 Stress Confinement Condition

Similarly to the thermal confinement condition, the stress confinement condition requires that over the course of the light excitation pulse, photoacoustic waves produced by the object should not travel longer than the size of the object

Fig. 29.1 Thermal confinement

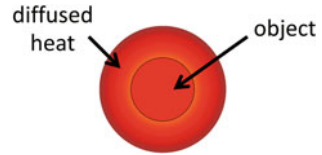
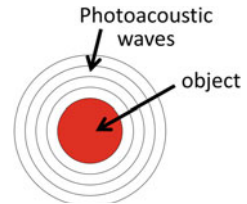


Fig. 29.2 Stress confinement



(Fig. 29.2). Over the course of one pulse duration, photoacoustic waves travel a distance of $t_p c$ ($c = 1.54 \text{ mm}/\mu\text{s}$ in soft tissues). Hence, the stress confinement condition requires that $t_p c < L_p$. For example, for a laser pulse duration of $t_p = 0.5 \mu\text{s}$, the photoacoustic waves travel $t_p c = 770 \mu\text{m}$, which greatly smears the spatial resolution of most photoacoustic systems. To allow a spatial resolution of $150 \mu\text{m}$ (i.e., $L_p = 150 \mu\text{m}$), the laser pulse duration t_p must be no more than 97 ns . As can be seen, it is much harder to satisfy the stress confinement than the thermal confinement.

29.3 Photoacoustic Tomography

PAT has rapidly developed over the past two decades into a powerful imaging modality that provides high tissue depth of penetration while maintaining high spatial and temporal resolutions. It has found a diverse range of applications in oncology [3], ophthalmology [4], endoscopy [5], dermatology [6], cardiology [7], and neurology [8]. Based on the photoacoustic effect, the principle of PAT is the conversion of pulsed light into ultrasound waves by absorbing molecules in a tissue and the detection of these ultrasound waves using an ultrasound transducer(s) to form an image. In photoacoustic tomography, a tissue will be illuminated by a broad diffuse laser pulse. The pulse energy will propagate through the tissue as it is scattered and absorbed by chromophores in the tissue. The absorbed photons are converted into heat, leading to a local transient temperature rise. This increase in temperature generates a local pressure rise, according to the thermoelastic expansion. The pressure propagates as an ultrasound wave until it gets to the surface of the tissue. An ultrasound transducer or an array of transducers is measuring a time trace of the ultrasound waves as they reach the surface of the tissue. The traces are then reconstructed into a full three-dimensional photoacoustic image that represents the origin of the photoacoustic waves. Various

reconstruction algorithms were devised for various photoacoustic system geometries and are the topic of other reviews [9]. The photoacoustic signal is proportional to the product of the object absorption coefficient and the fluence of light reaching this object, which represents the absorbed energy density by the object. Because the absorption and scattering of ultrasound waves by a tissue are relatively minimal, PAT provides high tissue depth of penetration as well as a high spatial resolution. Finally, unlike in ultrasound imaging, PAT exhibits minimal speckle artifacts. This is because the ultrasound waves forming the image propagate in one direction (from the tissue to the transducer) and therefore do not have an opportunity to coherently interfere with each other.

29.3.1 Intrinsic Contrasts

A number of chromophores are endogenously expressed by different tissues. Of particular relevance are the chromophores which are highly abundant and exhibit an absorption profile in the visible or near-infrared range. Such molecules include hemoglobin, melanin, water, fats, and certain proteins (Fig. 29.3). Since in most tissues hemoglobin absorption dominates most other endogenous chromophores, a photoacoustic image of a tissue would primarily show the distribution of blood within the tissue. Hemoglobin at different oxygen saturation levels will display different absorption spectra. This difference in optical absorption between oxygenated and deoxygenated hemoglobin can be exploited to map the blood oxygenation levels within a tissue, by acquiring multiple photoacoustic imaging at different wavelengths and quantifying the spectra of each pixel in the image using a spectral component analysis algorithm [10]. Melanin is also a major absorber in tissues such as skin and the retinal pigment epithelium (RPE) in the eye. In those tissues, melanin will be the main contributor for the photoacoustic signal at the visible and near-infrared wavelengths. Applications of photoacoustic imaging of melanin include visualizing melanoma tumors in the skin [11] and imaging the retina [4, 12]. Finally, morphological changes in a tissue, such as those occurred during a thermal burn, can cause changes in the optical absorption of the skin that outlines the physical extent of the burn and may help in classifying burns based on their depth [13].

29.3.2 PAT Imaging Configurations

There are largely two categories for PAT setups, a first using diffuse light and an unfocused transducer array and a second using diffuse light and a focused transducer. The second implementation is also referred to as acoustic-resolution photoacoustic microscopy (AR-PAM) and should not be confused with optical-resolution photoacoustic microscopy (OR-PAM), where light is also tightly

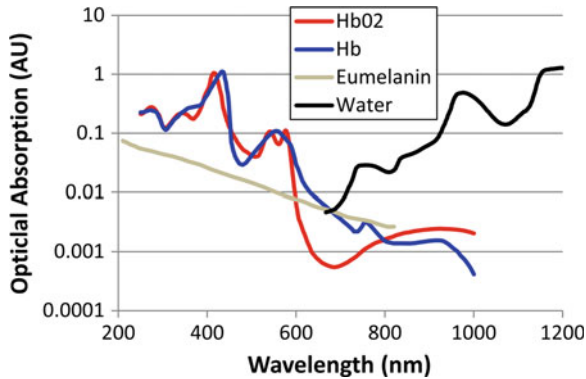


Fig. 29.3 Optical absorption spectra of the common endogenous absorbers in tissues. Deoxygenated and oxygenated hemoglobin (*Hb* and *HbO₂*, *blue* and *red*, respectively; <http://omlc.ogi.edu/spectra/hemoglobin/summary.html>), melanin (Eumelanin, *gray*; <http://omlc.ogi.edu/spectra/melanin/>), and water [84] (*black*; <http://omlc.ogi.edu/spectra/water/data/kou93b.dat>) in arbitrary units. The final absorption coefficient of a tissue will constitute some linear combination of these components, where the relative weights will vary across tissues

focused with a lens, thereby providing optical resolution in the lateral plane of the image. Previous reviews have covered in detail the various PAT setups [14, 15]. Here, we briefly review some of the common PAT setups at the context of the applications to which they are best suited for.

29.3.2.1 Spherical Scanners

Since the photoacoustic waves that are formed by an optically absorbing object travel in all directions, the ultimate tomography system would provide a good coverage of the tissue surface where ultrasound waves can be measured. Ultrasound detectors arranged in a half sphere would therefore provide a near ideal arrangement for imaging the breast [16], as depicted in Fig. 29.4. The excitation light in this system is delivered through a fiber that is attached to an Nd:YAG laser source that is further converted using an optical parametric oscillator (OPO) to any wavelength of choice in the near infrared at a pulse repetition rate of 10 Hz. The ultrasound array is composed of 128 individual unfocused transducers with a center frequency of 5 MHz arranged in a sparse spiral patterns on a bowl. To further improve the spatial coverage of the tissue surface, the ultrasound array is incrementally rotating so by the end of the acquisition, most of the tissue surface has been sampled. This provides an isotropic spatial resolution of $\sim 250 \mu\text{m}$ across a 5-cm-diameter field of view. Since all 128 ultrasound transducers are sampled simultaneously, a photoacoustic image made from 240 rotational positions can be acquired in 24 s. In addition to imaging the breast, this system has been used for whole-body small animal imaging [17] (Fig. 29.4c). Another implementation of a

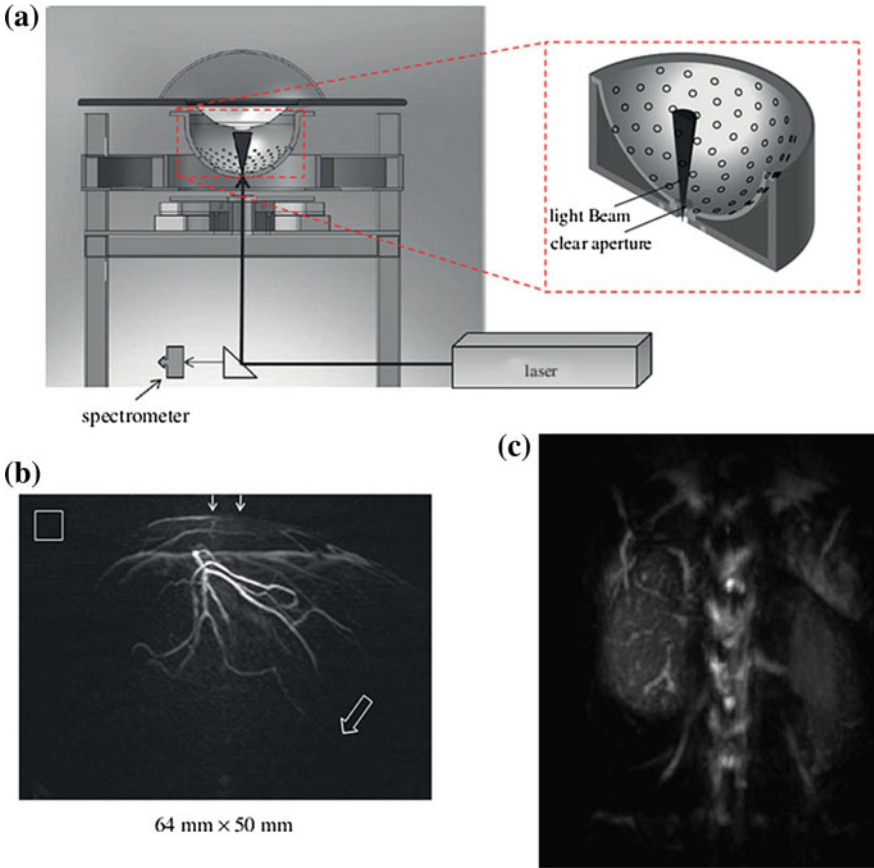


Fig. 29.4 Hemispherical photoacoustic tomography breast scanner. **a** Schematic of system. **b** Maximum intensity projection of the *left* breast of a healthy individual taken at an excitation wavelength of 800 nm. *Arrows* at the *top* represent the direction of the excitation light illumination, and the hollow arrow shows the position of a blood vessel at a depth of 40 mm. *Hollow box* is 1×1 cm in size. **c** Maximum intensity projection photoacoustic image of the abdominal section of a mouse. Note the clear vasculature detail evident in the kidney. Recreated with kind permission from American Association of Physicists in Medicine and SPIE [16, 17]

spherical scanner is through a linear ultrasound array arranged as an arc that is rotating about an object [18, 19]. Whatever the arrangement of transducers is, the common reconstruction method for spherical scanners is the spherical back projection algorithm [9]. However, it is possible to incorporate some prior knowledge on the structures and elements that make up the tissue to form an even higher-quality photoacoustic image using wavelet filtering [19]. This allowed the system to generate detailed images of a mouse abdomen (Fig. 29.5). The arc array is made of 64 transducer elements at a center frequency of 3.1 MHz. Over a 360° rotation, this covers nearly a perfect sphere for an accurate reconstruction, resulting in an

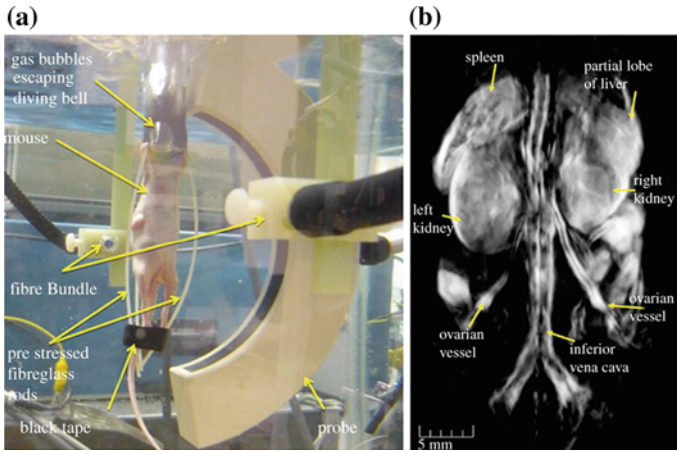


Fig. 29.5 Whole-body small animal photoacoustic tomography spherical scanner. **a** An arch-shaped ultrasound array made with 64 elements that rotate 360° around the animal. **b** Three-dimensional rendering of a photoacoustic image of a nude mouse. Several anatomical structures can be clearly seen including the kidneys and spleen. Recreated with kind permission from SPIE [19]

isotropic 0.5 mm spatial resolution. To achieve high signal-to-noise ratio, each ultrasound measurement is taken by averaging the response from 32 laser pulses. This greatly compromises the temporal resolution of the system, which was 8 min per three-dimensional image of a whole mouse.

29.3.2.2 Cylindrical Scanners

Similarly to spherical PAT scanners, in cylindrical scanners, photoacoustic waves are measured across the surface of a cylinder that surrounds the object. This has been implemented either using a single-element transducer that rotates around the object [20], or using an ultrasound transducer array arranged in a circle [21]. The single-element transducer implementation is particularly popular among the cylindrical scanners, primarily for its simplicity and low cost. Figure 29.6 shows the implementation of such cylindrical system, comprising a 3.5 MHz transducer focused on the elevation (z) axis. The illumination and the object are not moving during the scan, while the transducer is rotating around the object in circles. The object is illuminated from the top using an Nd:YAG laser of 532 nm at a safe laser energy density of less than 10 mJ/cm^2 . This resulted in a system with $200 \mu\text{m}$ spatial resolution. Such cylindrical scanners have found applications in monitoring tumor growth [22], early detection of arthritis [23], and monitoring brain hemodynamics [24].

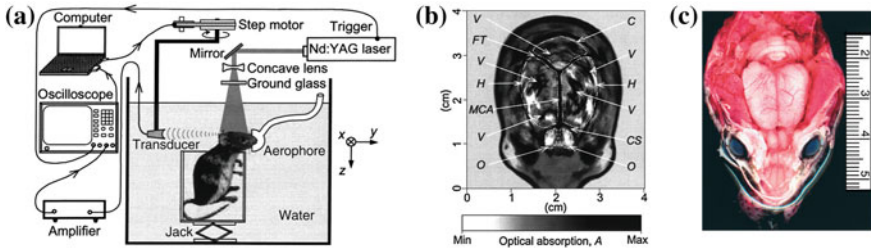


Fig. 29.6 Cylindrical photoacoustic tomography scanner. **a** A semi-focused transducer rotated around the animal head and a jack moved the animal *up* and *down* to allow for a full cylindrical coverage of the animal brain. **b** Non-invasive photoacoustic image of the superficial layer of a rat brain acquired with the skin and skull intact. Optical absorption shown in *gray scale* (darker areas indicate greater absorption). *C* cerebellum; *H* cerebral hemispheres; *O* olfactory bulbs; *MCA* middle cerebral artery; *CS* cruciate sulcus; *FT* fissura transversa; *V* blood vessels. Total image size is 4×4 cm in lateral dimension. The blood vessels distributed in the superficial layer of the cerebrum and the cerebellum are clearly visible with high optical contrast and accurate localization. **c** Open skull photograph of the rat brain surface acquired after the photoacoustic experiment. Recreated with kind permission from Nature Publishing Group [8]

29.3.2.3 Planar Scanners

In tissues such as skin or tissues containing bone structures, acquiring the large angular aperture needed for spherical and cylindrical scanners is not feasible. In such cases, acquiring photoacoustic signals over a flat surface with a planar scanner is preferable. Planar scanners can be implemented either as a single transducer that is raster scanning the surface in two-dimensions, a one-dimensional ultrasound array that scans the surface in the other direction [25], or a two-dimensional ultrasound arrays [26, 27]. The main trade-off between these options is speed, cost, and ease of use. Most planar scanners have been implemented as one-dimensional array systems that are assembled into a handheld device. Such systems also have the capability to acquire ultrasound images in addition to photoacoustic images (some photoacoustic scanners were even adapted from an ultrasound scanner) so to allow the coregistered acquisition of an ultrasound and a photoacoustic image [28, 29]. While the ultrasound image provides anatomical information, the photoacoustic image provides physiological and possibly molecular information (if molecular agents are used). Planar scanners typically suffer from image artifacts and lower lateral resolution due to their limited aperture compared to the spherical and cylindrical counterparts.

Recently, a planar photoacoustic scanner capable of producing real-time photoacoustic images at 50 frames per second has been devised [30, 31]. The scanner is made of 48 elements with a central frequency of 30 MHz to allow for high spatial resolution across the first 3 mm of the tissue (Fig. 29.7). By rapidly scanning the array, a full volumetric frame rate of 1 frames per second can be achieved for 166 B-scans volume. Other similar scanners with larger number of elements have been devised as well [32], including a 64-element 7.5 MHz linear

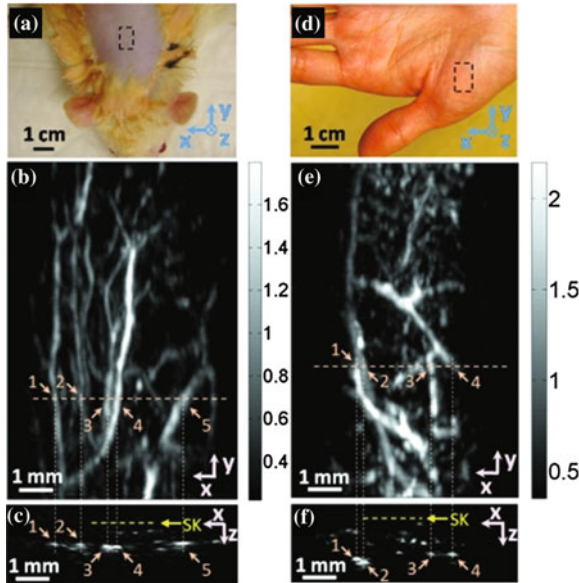


Fig. 29.7 Planar photoacoustic scanner. **a** Photograph of a Sprague–Dawley rat with hair removed before photoacoustic imaging, where x represents the beam forming (B-scan) direction, y represents the mechanical scanning direction, and z represents the depth direction. The *dashed rectangle* indicates the imaged area. **b** Photoacoustic maximum amplitude projection (MAP) image of the rat. The *gray scale* represents relative optical absorption. **c** Photoacoustic B-scan image corresponding to the *dashed horizontal line* in **(b)**, showing the depths of the blood vessels: SK skin surface. Numbers 1–5 indicate corresponding blood vessels in **(b)** and **(c)**. **d** Photograph of a human hand. The *dashed rectangle* indicates the imaged area. **e** Photoacoustic MAP image of the hand. **f** Photoacoustic B-scan image corresponding to the *dashed horizontal line* in **(e)**. Numbers 1–4 indicate corresponding blood vessels in **(e)** and **(f)**. Recreated with kind permission from SPIE [30]

array that provides a frame rate of 7.5 frames per second [29] and used to visualize blood vessels at a depth of 10 mm in the leg. Another planar scanner system has employed a commercial ultrasound system with 128 elements operating at 5 MHz was used to image the vascular bed in the human arm [33].

Another implementation of a planar scanner is based on an all-optical ultrasound sensor (Fig. 29.8a). The sensor is essentially a transparent Fabry–Perot film etalon, where a thin polymer spacer is sandwiched in between two reflectors [34, 35]. When an acoustic wave hits the etalon, it slightly modifies the spacer thickness, which locally and temporally affects the optical reflection conditions of the etalon. By scanning the etalon surface with a coherent laser beam, an effective two-dimensional ultrasound array results. This approach has numerous advantages over conventional ultrasound arrays, including low cost, simplicity, ability to transmit the exciting laser pulse through the etalon, and an ultrawide frequency bandwidth from 100 kHz to 22 MHz. Moreover, this approach allows for a fine

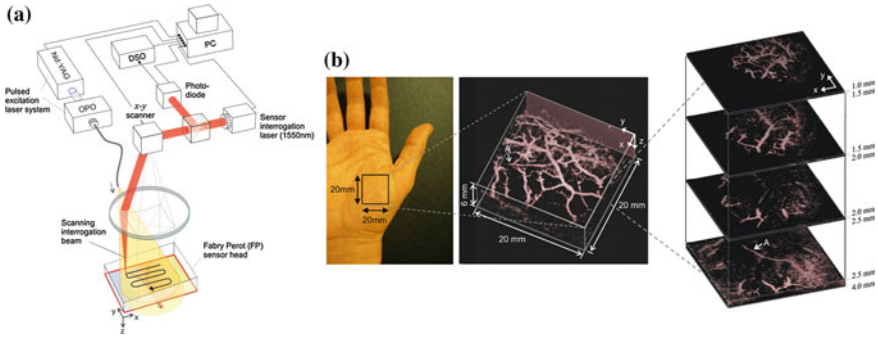


Fig. 29.8 All-optical photoacoustic planar scanner. **a** The Fabry–Perot (*FP*) sensor head is placed in acoustic contact with the surface of the skin. Nanosecond excitation laser pulses emitted by a tuneable OPO laser system are directed onto the sensor head and transmitted through it into the underlying tissue, thereby exciting acoustic waves. A second laser operating at 1,550 nm provides a focused sensor interrogation laser beam that is raster scanned over the surface of the sensor to map the distribution of the photoacoustic waves arriving at the sensor head. From the 2D distribution of the photoacoustic waves, a 3D image is then reconstructed. **b** In vivo photoacoustic image of the vasculature in the palm using an excitation wavelength of 670 nm. *Left* photograph of the imaged region, *middle* volume-rendered image, *right* lateral slices at different depths. The arrow ‘A’ indicates the deepest visible vessel, which is located 4 mm beneath the surface of the skin. Recreated with kind permission from IOP Publishing [37]

spatial sampling of the etalon, where the only limit to the ultrasound element size is the diffraction limit of the sampling laser beam on the etalon surface. This allows for element sizes as small as tens of micrometers without loss of sensitivity. The challenge with such systems is the sequential reading of the etalon, which limits their speed, although this limitation can be overcome by either using higher repetition rate lasers or employing multiple optical beams to sample the etalon simultaneously [36]. This system was used to image a variety of tissues, including a human hand (Fig. 29.8b) and subcutaneous tumors that were implanted in mice [37] and in the mouse brain [38].

29.3.2.4 Acoustic-Resolution Photoacoustic Microscopy

AR-PAM systems typically employ a single-element-focused transducer that is raster scanning the tissue. Similarly to conventional ultrasound systems, the scanner acquires individual vertical line scans (*A-scans*) and combining consecutive *A-scans* into a two-dimensional *B-scan* image or a three-dimensional volumetric image. These systems are typically slower than array systems due to the sequential scanning nature. However, they are less vulnerable to motion artifacts or acoustically scattering objects such as bones, as every *A-scan* is reconstructed independently of its neighboring *A-scans*. In most AR-PAM scanners, light is weakly focused as a spot or a hollow ring on the tissue below the transducer. This can be done either with a conical lens [39] or with a fiber-optic ring [40, 41].

Figure 29.9 shows a common implementation of an acoustic-resolution photoacoustic microscope scanner and its application in imaging the blood vessels in a human hand [39]. In addition to visualizing blood vessels in a tissue, such photoacoustic systems were used to assess the oxygen saturation level of the blood vessels (Fig. 29.10). This is done by acquiring photoacoustic images of a tissue at multiple excitation wavelengths and fitting the known spectra of oxygenated hemoglobin and deoxygenated hemoglobin to the acquired photoacoustic response. Once the relative amplitudes of the oxygenated and deoxygenated hemoglobin signals have been isolated, oxygen saturation levels can be easily calculated as $\text{HbO}_2/(\text{HbO}_2 + \text{Hb})$. Another application of acoustic-resolution photoacoustic microscopy has been ocular imaging (Fig. 29.11). While the spatial resolution may be lower than other retina imaging methods such as optical coherence tomography, the depth of penetration provided by photoacoustic imaging allows visualizing the entire ocular globe. The image was acquired at 740 nm wavelength with a 25 MHz transducer and consisted of 48 by 32 A-scans combined into one volumetric image spanning 12×8 mm lateral scan area (250 μm lateral step size). With the 25 MHz focused transducer, the system provides a spatial resolution of 50 μm (axial) and 240 μm (lateral), which allowed visualizing the major blood vessels of the retina and the choroid as well as other pigmented structures in the eyes of non-albino animals [4].

29.4 Optical-Resolution Photoacoustic Microscopy

If the target tissue is superficial or optically clear, it is possible to generate photoacoustic images at a spatial resolution superior to what acoustic transducers may allow. This is done by focusing the excitation light beam onto the tissue of interest, such that the spatial lateral localization is provided by the optical beam, while the axial localization is provided by the ultrasound transducer. This leads to anisotropic spatial resolution, high lateral resolution, and lower axial resolution. Nonetheless, this approach has found many important niche applications, including ocular imaging [12, 42, 43], microvessels imaging [44, 45], and oximetry [46].

29.4.1 System Configurations

A variety of optical-resolution photoacoustic scanners have been constructed. Because the spatial localization of this technique is dependent on optical confinement, the depth of penetration is limited to not more than 1 mm in optically scattering tissues. An important distinguishing feature between AR-PAM and OR-PAM is that in AR-PAM, the acoustic transducer needs to physically move to allow the raster scan to take place, whereas in OR-PAM, only the optical beam needs to move. This has major ramifications on the scan speed as optical beams

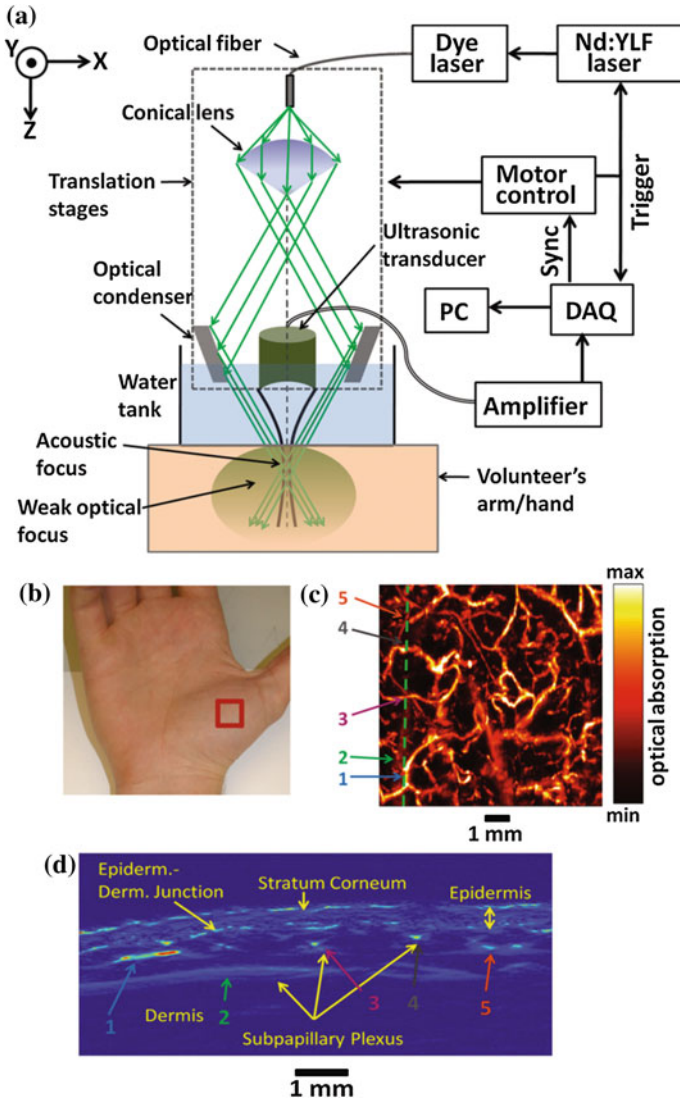


Fig. 29.9 Acoustic-resolution photoacoustic microscopy scanner. **a** Schematic of the photoacoustic microscope used in the described experiments. **b** Photograph of the palm of the volunteer. The *red* box indicates the imaged area 8×8 mm. **c** B-scan PA image taken along the *dashed line* in **(d)**. Notable features including the stratum corneum, epidermal–dermal junction, and subpapillary blood vessels, are all labeled. Selected vessels have been labeled with *color arrows* for reference with the image in **(d)**. **d** Maximum amplitude projection PA image taken from the palm using a 584-nm laser excitation wavelength. The *green dashed line* indicates the cross section shown in **(c)**. Recreated with kind permission from SPIE [39]

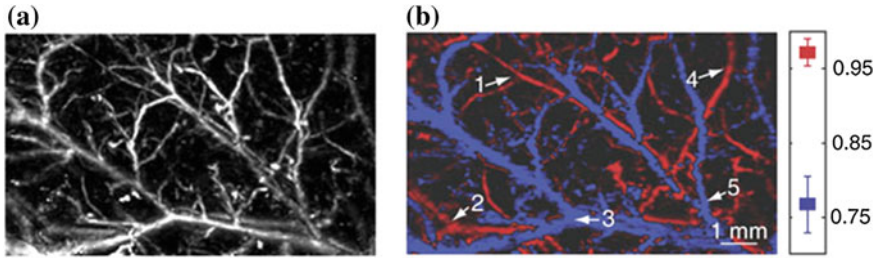


Fig. 29.10 Photoacoustic imaging of blood oxygen saturation levels. Four wavelengths (578, 584, 590, and 596 nm) were employed to acquire four photoacoustic images. **a** Structural image acquired at 584 nm. **b** Vessel-by-vessel sO_2 mapping based on a least squares fitting of the four images. The calculated sO_2 values are shown in the *color bar*. Recreated with kind permission from Nature Publishing Group [3]

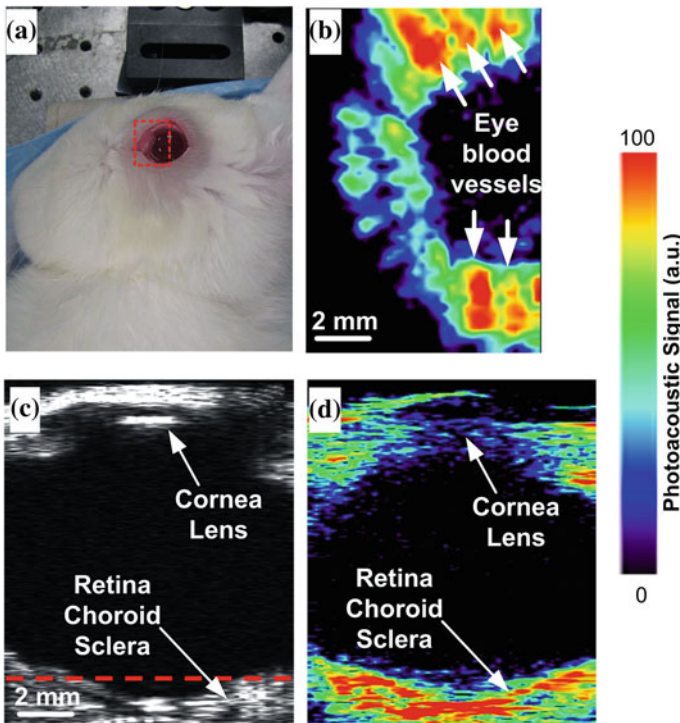


Fig. 29.11 Photoacoustic ocular imaging. **a** Photograph of the rabbit eye. **b** Horizontal photoacoustic, **c** vertical ultrasound, and **d** vertical photoacoustic images of the eye of the live rabbit. The area of the eye imaged in **(b)** is outlined by the *red boundary (dotted box)* in **(a)**, and the depth is noted by the *dashed red line* in **(c)**. Recreated with kind permission from the Optical Society [4]

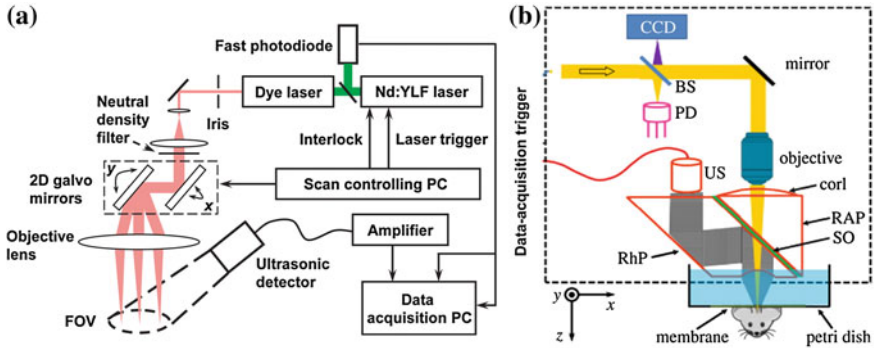


Fig. 29.12 Optical-resolution photoacoustic microscopy (OR-PAM) scanners. **a** An OR-PAM system implemented with a 2D galvo mirrors for ultrafast raster scanning of a tissue. A static unfocused ultrasound transducer is positioned at an angle to the excitation beam path. **b** A scanning head OR-PAM scanner is implemented with the head being physically moved across an object to form a three-dimensional photoacoustic image. *BS* beam splitter; *PD* photodiode; *CorL* correction lens; *RAP* right-angled prism; *SO* silicone oil; *RhP* rhomboid prism; *US* ultrasonic transducer (50 MHz). The CCD is used to view the imaging region. The components that lie within the dotted rectangle form the scan head, which is mechanically translated in order to acquire an image. Recreated with kind permission from The Royal Society and the Optical Society [15, 44, 85]

can be steered ultrafast using galvo mirrors (Fig. 29.12a). Moreover, because the laser excitation spot size in OR-PAM is significantly smaller than that in AR-PAM, the total energy per pulse should be significantly reduced to stay below the 20 mJ/cm^2 pulse energy density limit set by American National Standards Institute (ANSI) [47]. This allows the use of pulsed laser diodes, which are significantly cheaper than the traditional Nd:YAG lasers that are typically used in photoacoustic imaging. However, using lower pulse energies reduces the total signal and therefore limits the sensitivity of the system.

Another common implementation of OR-PAM is shown in Fig. 29.12b. A high numerical aperture lens is focusing the excitation light to the surface of a tissue. Acoustic waves that return from the tissue propagate through an acoustic lens that collimate the wave, reflected off an optically transparent acoustical mirror, and detected by an unfocused transducer. The entire scanning head is raster scanning a two-dimensional surface by being moved mechanically and acquiring an A-scan at each position, resulting in a three-dimensional photoacoustic image.

29.4.2 Applications of OR-PAM

The high spatial resolution offered by OR-PAM can produce en-face images of the target tissue. En-face images of blood vessel capillaries [45] as well as individual red blood cells [44] have been demonstrated (Fig. 29.13a, b). Moreover, by

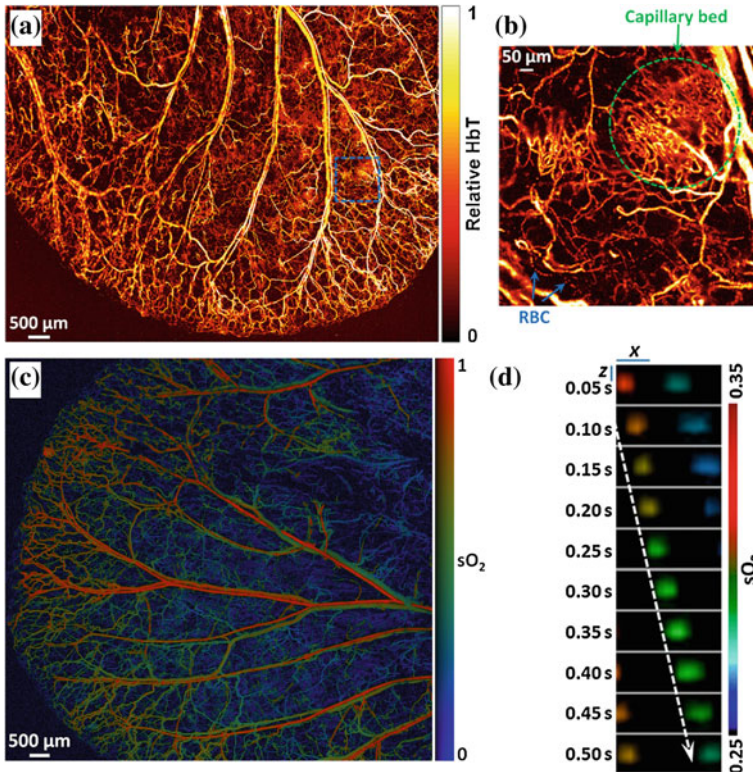


Fig. 29.13 OR-PAM images of capillaries. **a** OR-PAM of total hemoglobin (*HbT*) in a living mouse ear, revealing the vascular anatomy. **b** Inset shows a densely packed capillary bed and individual red blood cells traveling along a capillary. **c** Dual-wavelength (561 and 570 nm) OR-PAM calculation of blood oxygen saturation levels (sO_2) in a living mouse ear. **d** Sequential snapshots of single RBCs releasing oxygen in a mouse brain. Scale bars: $x = 10 \mu\text{m}$, $z = 30 \mu\text{m}$. Blood flows from *left to right*. The *dashed arrow* follows the trajectory of a single flowing RBC. Recreated with kind permission from the Optical Society and the National Academy of Sciences [44, 46]

acquiring several OR-PAM images at multiple wavelengths, OR-PAM can be used to create an oxygen saturation map of the ear (Fig. 29.13b). Note that while the lateral spatial resolution is approximately $2.5 \mu\text{m}$, the axial resolution is approximately $10 \mu\text{m}$. The ability to calculate oxygen saturation levels has recently been applied for the dynamic imaging of individual red blood cells in vivo. Figure 29.13d shows the dynamic transition of an individual red blood cell in a capillary of a living mouse brain [46]. The dynamic images monitor the oxygen capacity of the individual red blood cell as it is traveling through the capillary vessel. In addition to visualizing blood vessels in skin applications, OR-PAM has shown great promise for ocular imaging, primarily because of the optical clarity of the eye. Imaging of both the retina [12, 48] and the iris [42] has been demonstrated

by different groups using OR-PAM. Importantly, despite the retina being ~ 8 mm or 25 mm under the cornea in mice and human, respectively, the clarity of the cornea, lens, and vitreous gel of the eye allows OR-PAM to focus the light onto the retina and achieve high lateral resolution photoacoustic images. In fact, OR-PAM of the retina is using the focusing capability of the animal lens to focus the light onto the retina, so in theory, no additional optical lens is required. The contrasts provided by the eye are primarily hemoglobin and melanin. The RPE is a highly pigmented layer located between the retina and the choroid and exhibits a high scattering and absorption coefficient. Hence, OR-PAM can clearly visualize the RPE but not the choroid structures under it.

29.5 Photoacoustic Molecular Imaging

Photoacoustic imaging scanners has been optimized over the past two decades to provide superb imaging performance of the endogenous pigments in tissues, primarily hemoglobin and melanin. However, most biomolecules are transparent in the visible and near-infrared range and hence will not provide a photoacoustic contrast. Therefore, to allow photoacoustic imaging to reach its full potential, exogenous imaging agents should be used. Such imaging agents can be either molecularly targeted to a given biomolecule or non-targeted. A wide variety of photoacoustic contrast-producing agents (aka, contrast agents) have been demonstrated, including small-molecule optical dyes, organic and metallic nanoparticles [49]. By conjugating these contrast agents to targeting moieties such as antibodies [50] or peptides [41], they can be targeted to a specific biomolecule of interest, providing it with an observable photoacoustic signal. Another common targeting mechanism is leveraging biological activities that can that leads to the accumulation of the agents in the target tissue, such as the enhanced retention and permeation effect (EPR) of tumors [51]. The following sections discuss the design requirements of photoacoustic contrast agents, the process needed to validate them in vivo, and the diverse range of applications they are applied to.

29.5.1 Design of Photoacoustic Imaging Agents

Simply put, a good photoacoustic imaging agent should produce as high signal as possible, accumulate in high levels in the target tissue and as minimally as possible in non-target tissues, and be non-toxic. To maximize the photoacoustic signal of a particle, it is not enough to have a high absorption cross section. Indeed, the absorbed energy should be converted into heat, and not, for example, to fluorescent light. In addition, it is preferred that the imaging agent will circulate in the blood stream just long enough to accumulate in the target tissue, but not too long that it produces a non-specific signal when the tissue is being imaged. If the imaging

agent is molecularly targeted to a specific biomolecule of interest, the affinity between the agent and the target should be strong enough so the agent is rapidly accumulating in the target region and does not fall off, but yet specific enough so it does not bind to similar biomolecules in the tissue. Finally, the imaging agent should be well tolerable by a living subject with no adverse toxic effects. Often the toxicity of an agent is a function of dose. Since the photoacoustic signal of an agent will determine the dose needed to visualize the target tissue, the photoacoustic signal of an agent is closely related to the potential toxicity of the agent. Below we outline several additional conditions that affect the photoacoustic signal of an agent and discuss the experiments needed to validate a photoacoustic agent.

29.5.1.1 Conditions

Beyond the thermal and stress confinement conditions outlined in Sect. 29.2, photoacoustic imaging agents should satisfy several additional conditions [52]. First, most of the absorbed energy should be converted into heat. Second, most of the heat should remain within the imaging agent particle. Finally, the absorbed heat should not produce damage to the surrounding tissue over a single or a sequence of laser excitation pulses.

Optical Absorption Condition

To provide maximal photoacoustic effect, most absorbed energy should be transformed into heat, which occurs when $\tau_{NR} < \tau_R$, where τ_{NR} and τ_R are the characteristic times of non-radiative and radiative relaxation, respectively. In most nanoparticles, this confinement is fulfilled ($\tau_{NR} \sim 10^{-12}$ – 10^{-11} s, $\tau_R \sim 10^{-9}$ – 10^{-10} s), while in some fluorescent dyes, it is not [53]. This inefficiency of heat conversion, along with their relatively low absorption cross section, renders small-molecule fluorescent dyes less effective as photoacoustic contrast agents compared to nanoparticles. Nevertheless, photoacoustic signals from larger fluorescent nanoparticles, such as quantum dots, have been measured [54]. Noteworthy, the fluorescence of dye molecules can be quenched and therefore contribute to the photoacoustic signal by conjugating the dyes to metal nanoparticles [54].

Thermal Diffusivity Condition

In addition to the previously discussed thermal confinement, when contrast agents are being used, one needs to consider the thermal diffusion within the contrast agent itself. To provide efficient heating of nanoparticles without heat loss, the pulse duration, t_p , should be less than the characteristic thermal relaxation time, τ_T , of the nanoparticle $t_p \leq \tau_T$. Fulfillment of this condition means achieving the maximal nanoparticle temperature possible without heat exchange with the near

environment of the nanoparticle. For example, for a solid nanosphere with radius R , $\tau_T = R^2/6.75 k$, where k is thermal diffusivity [53]. For targets with $R = 50, 500 \text{ nm}, 5, \text{ and } 50 \text{ }\mu\text{m}$ (e.g., nanoparticles, cellular organelles, cells, or bulk media illuminated with a $100 \text{ }\mu\text{m}$ laser spot), τ_T is $\sim 3 \text{ ns}, 0.3, 30 \text{ }\mu\text{s}, \text{ and } 3 \text{ ms}$, respectively. In strongly absorbing nanoparticles such as gold particles or carbon nanotubes, the absorbed energy in the nanoparticle surface is almost instantaneously transformed into thermal energy (characteristic time $\sim 10^{-12} \text{ s}$) and very quickly averaged in the absorbing layers. The heat is then transferred to the core of the particle as well as to surrounding water. For example, in a particle made of silica core and a gold shell, heat will be conducted six times faster into the silica as compared to the surrounding water. Therefore, the particle itself will reach thermal equilibrium before much heat will be lost to surrounding water. As a first approximation, τ_T can be estimated by considering the nanoparticle as an equivalent heated quasi-solid nanoparticle with an average heat capacity C_{NP} and a density ρ_{NP} . The characteristic thermal relaxation (i.e., cooling) time for heat transfer between the nanoparticle surrounding water with the coefficient of thermal conductivity K_W can be estimated as $\tau_T = R^2 \rho_{\text{NP}} C_{\text{NP}} / n K_W$, where coefficient n depends on the nanoparticle shape [53]. Hence, in cases of very small particles or very long laser pulses, significant heat will be exchanged with surrounding water and the thermal diffusivity condition will not be met and the photoacoustic signal will therefore be reduced. A more rigorous analysis of thermal effects in multilayer nanoparticles can be found elsewhere [55, 56]. Importantly, while diffusion of heat from an absorbing nanoparticle to its surroundings will not affect the spatial resolution of the image, it may, however, limit the intensity of the photoacoustic wave that is generated as the Grüneisen coefficients of metals are higher than those of water.

Overheating Condition

Overheating of the target tissue could be the result of either an individual laser pulse or a net accumulation of heat due to a sequence of laser pulses. Since the laser pulse duration t_p in most photoacoustic systems is in the order of nanoseconds, significant heat could be built in the tissue during this short time frame. Since both heat conduction and convection out of the target tissue occur at much longer timescales, the maximum permissible energy per pulse is measured in J/cm^2 , or energy of an individual laser pulse per irradiated tissue surface area. The laser irradiation safety limits were determined by the ANSI, which suggests a limit of $\sim 20 \text{ mJ}/\text{cm}^2$ for visible wavelength nanosecond laser pulse and a slightly higher limit for near-infrared light [47].

The previous confinement does not take into account possible temporal overlapping of thermal effects at high laser pulse rate, f_{REP} . Such condition could result in accumulating heat and hence a need to use less powerful lasers, which will

result in a decreased photoacoustic signal. To avoid this effect, the thermal confinement for successive laser pulses is defined as $f_{\text{REP}} \leq 1/\tau_T$, when there is enough time for target cooling before the next pulse comes. For targets with $R = 50, 500 \text{ nm}, 5, \text{ and } 50 \text{ }\mu\text{m}$, $f_{\text{REP}}^{\text{MAX}}$ was estimated as $\sim 330, 3.3 \text{ MHz}, 33 \text{ kHz}, \text{ and } 330 \text{ Hz}$, respectively.

29.5.1.2 Validation of a Photoacoustic Imaging Agent

Once a new photoacoustic contrast agent is synthesized and conjugated to a targeting moiety of some kind, a number of validation steps need to be performed to confirm the utility of the imaging agent against its specific molecular target. Some of these steps are quite similar to those taken for imaging agents of other molecular imaging modalities, and some are specific to the photoacoustic character of the particle. Table 29.1 summarizes the different validation experiments needed, sectioned into *in vitro* studies (i.e., not in animals), *in vivo* studies (i.e., in living animals), and *ex vivo* (i.e., in dead tissues).

29.5.2 Applications and Examples

A wide variety of photoacoustic contrast agents have been devised, spanning a wide spectrum of materials, sizes, and shapes [49]. Since the expression levels of the disease-relevant molecular markers are typically in low concentration, a photoacoustic contrast agent should be detectable at a level of 100 nM or less, preferably 1 nM or less. This is the primary reason for the high prevalence of nanoparticle-based photoacoustic imaging agents versus their smaller counterparts, the small-molecule dyes [57, 58]. Beyond greater sensitivity, some additional advantages of using nanoparticles as photoacoustic contrast agents include minimal photobleaching effect, higher affinity to molecular targets through a multivalency effect, and relatively short blood half-life time. However, the primary limitation of nanoparticles as contrast agents includes their non-specific uptake by the reticuloendothelial system (RES, namely liver, spleen, and bone marrow), and the difficulty of targeting them to biomolecules beyond the vasculature [59]. In cases where the photoacoustic agent is not molecularly targeted to a given biomolecule, the poor sensitivity of small molecules can be compensated by using high concentration of dye. This is particularly useful for visualizing blood perfusion [21], or the uptake of a small-molecule dye by the lymphatic system [60]. In the sections below, we review some of the main types of nanoparticles-based photoacoustic imaging agents, including single-walled carbon nanotubes (SWNTs), small dye-SWNT conjugates, gold-coated nanotubes, as well as gold-based nanoparticles.

Table 29.1 Validation steps of a photoacoustic imaging agent

Test	System	Description/comments	Purpose
Photoacoustic spectrum	in vitro	Measure the photoacoustic signal from the contrast agent across a range of possible excitation wavelengths. If agent is non-scattering and non-fluorescent, optical absorbance measurement is equivalent	Identify optimal excitation wavelength
Signal–concentration relation	in vitro	Quantify the change in photoacoustic signal as contrast agent concentration increases	Correlate imaging agent concentration with photoacoustic signal
Serum stability	in vitro	Measure the molecular integrity of agent and its photoacoustic signal as it is exposed to an animal serum	Mimic the enzymatic activity the agent is exposed to in the animal's systemic circulation
Photobleaching	in vitro	Measure photoacoustic signal degradation as the agent is exposed to extended durations of light exposure	Mimic laser light exposure of agent in the animal
Cell uptake study	in vitro	Incubation of cells expressing the molecular target with either the contrast agent or with control (untargeted) contrast agent	Quantify molecular target specificity of the contrast agent
Sensitivity	in vivo	Quantify the photoacoustic signal from a series of subcutaneous injections of the imaging agent in an animal and compare that to the background signal	Find the lowest detectable concentration (i.e., sensitivity)
Targeting capability	in vivo	Administration of the targeted contrast agents to diseased animal models (e.g., tumor-bearing mice via intravenous injection) while administering additional animals the control (untargeted) contrast agent	Establish that the contrast agent is delivered in a specific way to the target site and in a sufficient amount to produce a detectable photoacoustic signal
Validation	in vivo or ex vivo	Validate with an independent way of measuring, either in vivo or ex vivo, the delivery of imaging agent to the target site	Validate the in vivo targeting results

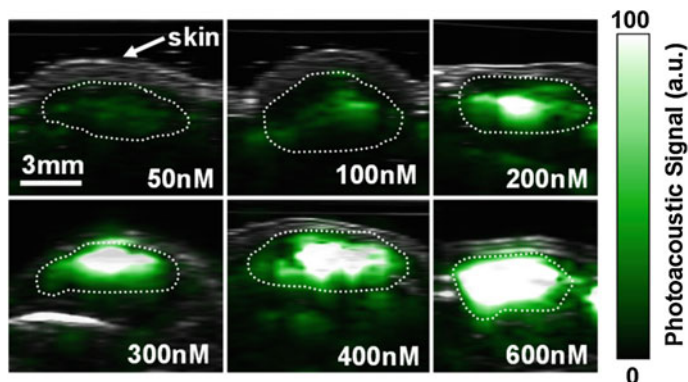


Fig. 29.14 Photoacoustic detection of SWNTs in living mice. Mice were injected subcutaneously with SWNTs at increasing concentrations from 50 to 600 nM. An ultrasound image slice (gray) showing the skin level was overlaid on the photoacoustic image (green), which showed the SWNT photoacoustic contrast. The dotted lines on the images illustrate the edges of each inclusion. The photoacoustic signal produced by 50 nM of SWNT is equal to the average photoacoustic background signal produced by tissues. Recreated with kind permission from Nature Publishing Group [41]

29.5.2.1 Single-Walled Carbon Nanotubes

Recently, SWNTs conjugated with RGD peptide (SWNT-RGD) through PL-PEG₅₄₀₀ were demonstrated to target $\alpha_v\beta_3$ in tumors, an important vascular integrin associated with tumor angiogenesis [61]. By radiolabeling the SWNTs with ⁶⁴Cu, the tumor accumulation has been quantified to be ~ 14 %ID/g (percent injected dose per gram of tissue) [61], while control-untargeted SWNTs without the RGD peptide showed significantly lower accumulation of ~ 3 %ID/g. This first demonstration of molecular targeting of SWNTs in living subjects led to multiple imaging studies utilizing various physical properties of SWNTs including Raman scattering [62, 63] as well as photoacoustic imaging [41]. While photoacoustic imaging takes advantage of the high optical absorption character of SWNTs, Raman imaging utilizes the characteristic Raman scattering spectrum of sp² carbon materials (G-band at 1,582 cm⁻¹).

Perhaps of most importance among the characterization experiments listed in Table 29.1 were the in vivo sensitivity and in vivo targeting tests of SWNT-RGD [41]. The lowest detectable concentration of SWNTs in living mice was found to be 50 nM (i.e., 50 nM of SWNT-RGD gave the equivalent photoacoustic signal as the background tissue signal) (Fig. 29.14). Furthermore, mice-bearing U87 glioblastoma xenograft tumors injected with SWNT-RGD intravenously showed significantly higher photoacoustic signal in the tumor as compared with mice injected

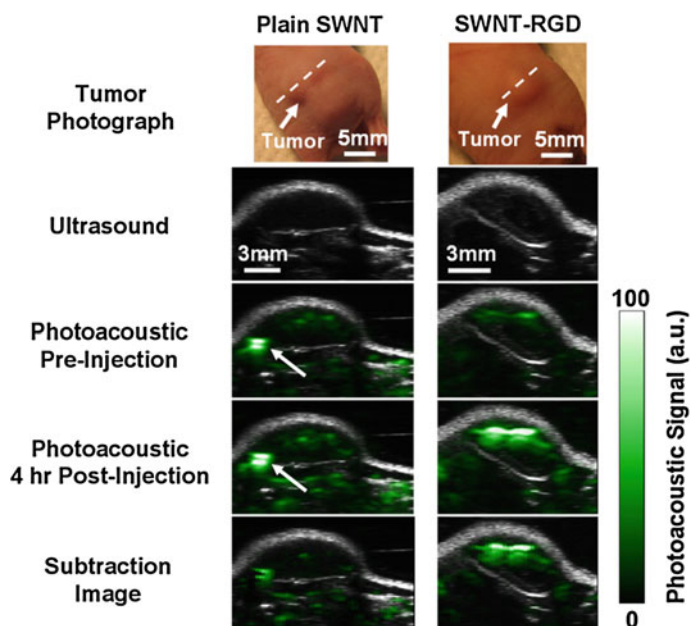


Fig. 29.15 SWNT-RGD tumor targeting in living mice. Ultrasound (*gray*) and photoacoustic (*green*) images of a *vertical slice* (*white dotted line*) through the tumors of mice injected with SWNT-RGD (*right column*) and control plain SWNTs (*left column*). Subtraction images were calculated as 4 h post-injection minus preinjection to remove tissue background signal from the photoacoustic image. The high photoacoustic signal in the mouse injected with plain SWNTs (indicated with *white arrow*) is not seen in the subtraction image, suggesting that it is due to a large blood vessel and not SWNTs. Recreated with kind permission from Nature Publishing Group [41]

with untargeted SWNTs (Fig. 29.15). Importantly, the fact that SWNTs produce a strong Raman signal allowed for *ex vivo* validation of the SWNT presence in the target tissue. Such independent way of visualizing SWNTs is critical for complete validation of a new photoacoustic imaging agent.

29.5.2.2 Optical Dye-SWNT Hybrids

While the optical absorption spectrum of SWNTs is very broad covering the visible and NIR wavelengths, their spectrum can be altered by adding dye molecules such as indocyanine green (ICG) or QSY₂₁ on the surface of the nanotubes [64, 65]. Taking advantage over the very high surface area to volume ratio of SWNTs, potentially many such small optical dyes can be attached to the surface of a single SWNT. As SWNTs have hydrophobic benzene ring structures on their

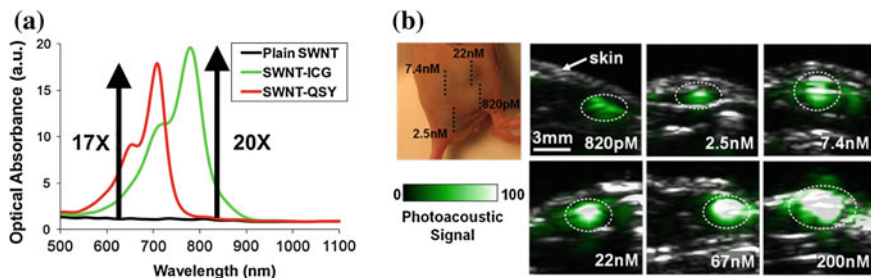


Fig. 29.16 Optical dye-SWNT hybrids. **a** Optical spectra of plain SWNTs (*black*), SWNT-ICG (*green*), and SWNT-QSY (*red*). **b** Photoacoustic detection of SWNT-ICG in living mice. Vertical slices ultrasound images (*gray*) and photoacoustic images (*green*) of mice injected subcutaneously with SWNT-ICG-RGD at concentrations of 0.82–200 nM (*dotted black line*). The *white dotted lines* on the images illustrate the approximate edges of each inclusion. Quantitative analysis of the images estimated that 170 pM of SWNT-ICG-RGD gives the equivalent photoacoustic signal as the tissue. Recreated with kind permission from American Chemical Society [64, 65]

surface, it is possible to stably load molecules onto the SWNTs through non-covalent π - π stacking bonds. Upon incubation of SWNTs with ICG or QSY₂₁, a strong and stable binding of the ICG or QSY₂₁ molecules to the surface of the SWNT has occurred, leading to ~ 20 -fold increase in the optical absorption of the SWNT (Fig. 29.16a). Interestingly, small optical dyes are far more efficient in absorbing light than nanoparticles. For example, ICG has 30-fold and 5×10^3 -fold lower optical absorbance than SWNT and gold nanorods (GNRs) 10 nm \times 40 nm in size, respectively. However, ICG is also 220-fold and 45×10^6 -fold lighter than SWNT and GNRs, respectively. Hence, on an absorbance-per-weight basis, ICG is \sim sevenfold more efficient than SWNT and $\sim 9,000$ -fold more efficient than GNRs in absorbing light. Also, unlike ICG and SWNT for which absorbance represents only light absorption, GNRs absorbance represents both optical absorption and scattering, where the latter do not contribute to the photoacoustic signal of the particle. If volume is considered instead of molecular weight for measure of efficiency, GNR would be considered more efficient in light absorption than SWNTs. Finally, unlike most nanoparticles, ICG can be photobleached, which will affect photoacoustic signal accordingly. This concept of carrying small optical dyes on an SWNT can likely be extended to other nanoparticle systems and other optical dyes.

The shape of ICG-enhanced SWNTs is very similar to that of plain SWNTs, as the ICG molecules are bound to the SWNT surface, leaving the protective layer of PEG on the exterior of the particle intact. However, despite their similarity, one cannot assume that the ICG-modified SWNT-RGD (SWNT-ICG-RGD) will behave similarly to SWNT-RGD *in vivo*. The two particles may have different molecular weights, charge, or zeta potential and therefore potentially different biodistribution in the body. Hence, in order to validate that SWNT-ICG-RGD can also be used as a photoacoustic imaging agent, one has to study the particle against

all the tests in Table 29.1. In vitro testing of the SWNT-ICG-RGD contrast agents discovered that they are highly stable in serum; however, unlike plain SWNT-RGD, some degree of photobleaching was observed to the extent of $\sim 30\%$ over 1 h of strong nanosecond-pulsed laser illumination. Despite the fact that SWNTs are highly resistive to photobleaching, small-molecule optical dyes, such as ICG, are more susceptible to photobleaching, and hence, this observed photobleaching is likely due to photobleaching of the ICG molecules. The sensitivity of ICG-modified SWNT-RGD in living mice has been estimated to be 170 pM (Fig. 29.16b). This is a significant improvement in sensitivity of over 300-fold as compared with plain SWNT-RGD. This improvement in sensitivity is primarily due to the higher optical absorption of the new nanoparticle as well as the ability to shift the laser excitation wavelength from 690 to 780 nm (the absorption spectrum maximum of SWNT-ICG-RGD) in which the background tissue absorption is significantly reduced. Finally, in a similar experiment as was previously described for SWNT-RGD, SWNT-ICG-RGD as well as QSY₂₁-modified SWNT-RGD have been shown to specifically target the $\alpha_v\beta_3$ integrin in living tumor-bearing mice [64, 65]. Importantly, SWNT is only one possible platform for carrying optical dyes. Other options include ICG-loaded into silicate structures [66], vesicle structures such as perfluorocarbon double emulsion [67] or bubble-shaped particles [68].

Finally, the different spectra of SWNT-ICG and SWNT-QSY were used to multiplex the photoacoustic signals of the two imaging agents in vivo [65]. By acquiring 5 photoacoustic images at 700, 730, 760, 780, and 800 nm, the signals of the two agents were unmixed from each other using a similar least squares technique as was used for measuring oxygen saturation levels of blood vessels using photoacoustic imaging (Fig. 29.17).

29.5.2.3 Golden SWNTs

Despite the excellent biological and physical properties of SWNTs as non-toxic [69] photoacoustic imaging agents, their optical absorption cross section is still lower than that of gold nanoparticles (GNPs). While this is partially due to the smaller size of SWNT versus some of the GNPs, the GNPs also exhibit a resonance effect that greatly enhances their optical absorbance. To improve the photoacoustic effect of SWNTs, new types of hybrid GNPs consisting of a SWNT core surrounded by a gold layer were recently introduced (Fig. 29.18) [70]. The new SWNT-mediated hybrid nanoparticle combines the optical NIR absorbance of SWNTs and the biocompatibility and bioconjugation potential of gold to realize the advantages of both SWNTs and GNPs. The synthesis process involves SWNTs and gold salts in water and does not require additional chemical reductant or catalyst agents. Hybrid rod-shaped gold-plated SWNTs (termed golden carbon nanotubes—GNTs), with a thin layer of gold around the SWNT core, were synthesized using short (~ 100 nm) and well-dispersed SWNTs in water. When even shorter SWNTs (~ 30 nm) were used, monodisperse plasmonic hexagonal

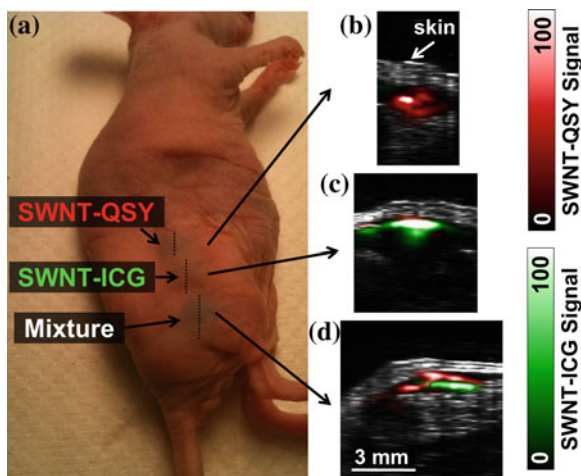


Fig. 29.17 Multiplexing of SWNT-ICG and SWNT-QSY in vivo. **a** A mouse was injected with 30 μL of 50 nM SWNT-QSY (*upper injection*), 30 μL of 50 nM SWNT-ICG (*middle injection*), and 30 μL of an equal mixture of 50 nM SWNT-QSY and SWNT-ICG (*lower injection*). **b** Unmixed photoacoustic vertical slice through the upper injection area, showing only SWNT-QSY signal (*red*). **c** Unmixed photoacoustic slice through the middle injection area, showing mostly SWNT-ICG signal (*green*). **d** Unmixed photoacoustic slice through the lower injection area, showing both SWNT-QSY and SWNT-ICG signals spread throughout the injection area. Image reconstruction artifacts as well as inhomogeneous light penetration into the tissue are likely the cause for the separation of the *green* and *red* signals in the image. Recreated with kind permission from American Chemical Society [65]

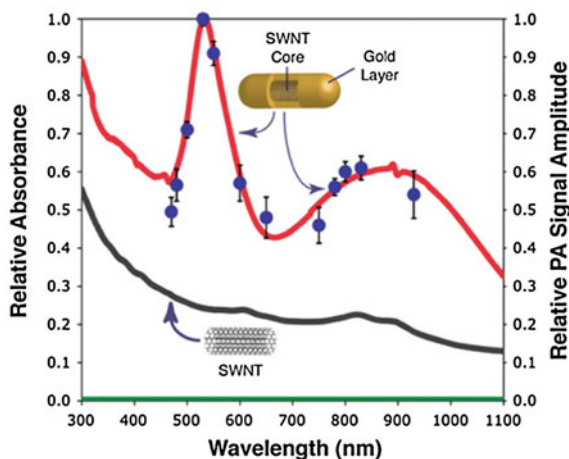


Fig. 29.18 Spectra of SWNTs and golden nanotubes (GNTs). *Lines* represent normalized optical absorbance spectra (*left vertical axis*) of GNTs in water (*red curve*), SWNTs in water (*black curve*), and water only (*green curve*). The dots represent the normalized photoacoustic signal amplitude (*blue dots, right axis*) of GNTs in water. The concentration of the SWNTs is ~ 35 times higher than that of GNTs; hence, 85- to 100-fold enhanced contrast is achieved by the hybrid GNTs. Recreated with kind permission from Nature Publishing Group [70]

bipyramidal gold nanocrystals with well-defined size and shape resulted [71]. The GNTs exhibited two plasmon absorption maxima (Fig. 29.18) in the visible region of 520–530 nm (similar to transverse absorption of gold nanospheres) and in the NIR region of 800–900 nm, similar to the longitudinal response of GNRs. Their plasmon responses in the NIR were significantly higher (85 to 100-fold for GNTs; 25 to 30-fold for bipyramidal nanocrystals) than those of the SWNTs without the gold layer. This implies that potentially lower concentrations would be required for effective photoacoustic molecular imaging. Moreover, it is possible to control the absorbance peak of GNTs, which allowed for multiplexing the photoacoustic signals of these particles [72]. The GNTs can be easily conjugated with targeting moieties for molecular imaging applications. An antibody specific to the lymphatic endothelial hyaluronan receptor-1 (LYVE-1) was conjugated to the GNTs and used for photoacoustic mapping of lymphatic endothelial cells in mouse mesentery [70]. The LYVE-1 receptor is one of the most widely used lymphatic markers of endothelial cells, and their expression and functional activity are closely correlated with the regulation of cell migration, metastasis, inflammation, and other important processes. Other applications of GNTs have been the photoacoustic detection followed by photothermal ablation of GNT-labeled tumor cells in sentinel lymph nodes (SLNs). As SLN is typically the first occurrence of metastasis from primary tumors, visualizing tumor cells in the SLN would be desirable. In addition, the ability to destroy the tumor cells through overheating the SLN selectively through GNTs optical absorption is highly complementary to the diagnostic capability of photoacoustic imaging [72].

29.5.2.4 Gold Nanoparticles

GNPs represent a significant portion of the photoacoustic imaging agents developed to date. They exhibit unique properties rendering them attractive photoacoustic imaging agents including high optical absorption cross section, easy functionalization chemistry to targeting moieties, and minimal to no cytotoxicity. The use of GNPs for photoacoustic imaging has been reviewed elsewhere and broadly covers the subcategories of gold nanospheres [51, 73–75], GNRs [76], gold nanocages [77], and other gold nanostructures [78, 79].

Gold nanospheres are perhaps the most common gold nanoparticle in biomedical research [80]. They exhibit a strong plasmon resonance peak at ~ 520 nm that allows them to produce strong photoacoustic contrast at that wavelength. Because at that wavelength the tissue optical absorption is quite high, gold nanospheres suffer from poor sensitivity compared to other gold nanoparticles, which in turn limits their imaging applications to non-targeted applications. For example, gold nanospheres were used to amplify the bulk photoacoustic signal of blood vessel in rat's brain [74] or for imaging the trafficking of macrophages to atherosclerotic plaques through the uptake of the gold particles by macrophages that later trafficked to the atherosclerotic plaque [81].

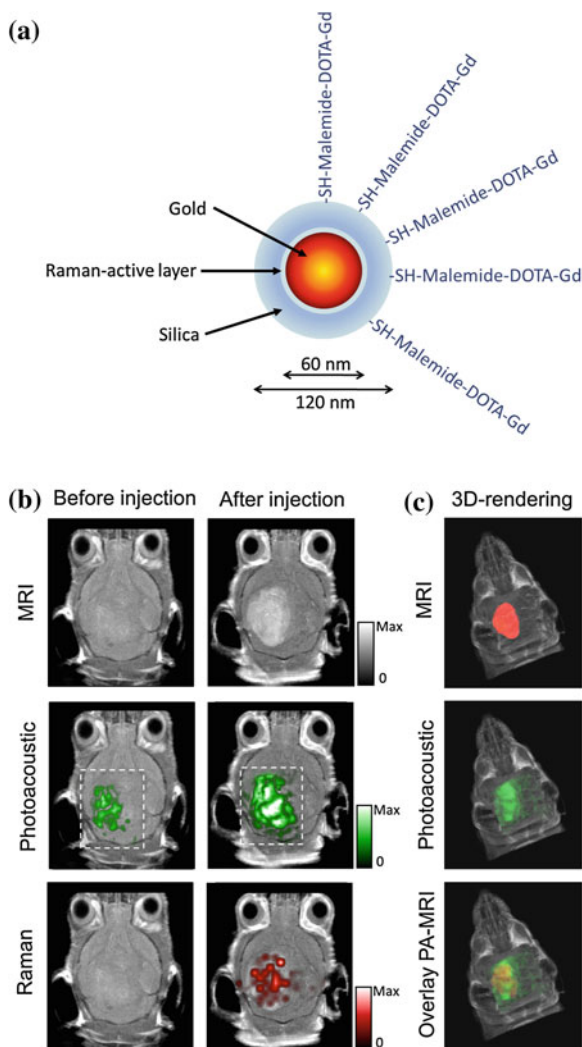


Fig. 29.19 Triple-modality gold nanospheres imaging agents for photoacoustic, magnetic resonance, and Raman imaging. **a** A 60-nm gold core is surrounded by a thin Raman active layer that is protected by a 30-nm silica coating. The silica coating was further functionalized with Maleimide-DOTA-Gd which was conjugated to the sulfide group on the silica. **b** Triple-modality detection of brain tumors in living mice with the gold nanospheres. Three weeks after orthotopic inoculation, tumor-bearing mice were injected intravenously with the nanoparticles. Photoacoustic, Raman, and MRI images of the brain (skin and skull intact) were acquired before and 2, 3, and 4 h post-injection, respectively. 2D coronal MRI, photoacoustic, and Raman images are shown. The post-injection images of all three modalities demonstrated clear tumor visualization. The photoacoustic and Raman images were coregistered with the MRI image, demonstrating good colocalization between the three modalities. **c** 3D rendering of MRI image with the tumor segmented in red (top), overlay of MRI and 3D photoacoustic images (middle) and overlay of MRI, segmented tumor and photoacoustic image (bottom) showing good colocalization of the photoacoustic signal with the tumor. Recreated with kind permission from Nature Publishing Group [51]

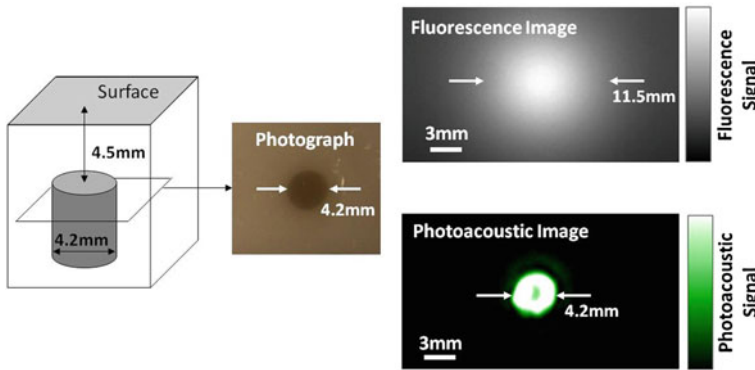


Fig. 29.20 Photoacoustic imaging versus fluorescence imaging. *Left* Schematic of a tissue mimicking phantom, with a well containing both fluorescent and optically absorbing materials that is placed 4.5 mm under the phantom surface. *Right* Fluorescence and photoacoustic images of the phantom. Due to the scattering nature of the phantom, the fluorescence image depicts the 4.2-mm well as a 11.5-mm object (full width half max), whereas the photoacoustic image clearly depicts the real width of the well. Note the reduced signal at the center of the photoacoustic image is due to the lack of full light penetration into the center of the well. Recreated with kind permission from Nature Publishing Group [41]

A more recent application of gold nanospheres was imaging brain cancer tumors by leveraging the leaky vasculature of the tumor in a multimodal approach [51]. The nanoparticle was made of a 60-nm gold core covered with a Raman molecular tag that was itself covered with a 30-nm silica coating, which was then modified with DOTA-Gd. This resulted in a triple-modality particle producing an imaging contrast for photoacoustic imaging, due to the gold optical absorption, Raman imaging, due of the surface-enhanced Raman scattering (SERS) effect between the Raman tag and the gold nanoparticle, and T_1 -weighted magnetic resonance imaging (MRI), due to the gadolinium conjugate (Fig. 29.19a). Upon intravenous administration of the particle to mice-bearing brain cancer tumors, the nanoparticles leaked out of the tumor vasculature and produced a clear imaging signal in all three imaging modalities within 30 min post-injection (Fig. 29.19b). Such triple-modality approach is highly beneficial in clinical settings: Detectability by MRI allows preoperative detection and surgical planning; photoacoustic imaging with its relatively high-resolution and deep tissue penetration is then able to guide bulk tumor resection intraoperatively; Raman imaging with its ultrahigh sensitivity and spatial resolution [62, 63, 82] can then be used to remove residual microscopic tumor burden. Resected specimen can subsequently be examined with a Raman probe *ex vivo* to verify clear margins. Such MRI photoacoustic modality approach has also been proposed using gold–cobalt nanoparticles [79].

Table 29.2 Characteristics of the available molecular imaging modalities

	Photoacoustic imaging	Ultrasound	Fluorescence imaging	MRI	PET
Type of energy measured	High-frequency sound waves	High-frequency sound waves	Visible or near-infrared light	Radio waves	High-energy gamma rays
Spatial resolution	50–500 μm	50–500 μm	2–10 mm (depth dependent)	0.1–1 mm	1–3 mm
Time resolution	Seconds to minutes	Seconds to minutes	Seconds	Minutes	Minutes
Sensitivity	pM	Not well characterized	nM	μM –mM	pM
Depth	<5 cm	<5 cm	<5 mm	No limit	No limit
Type of contrast agents	Nanoparticles	Microbubbles	Small molecules, nanoparticles	Small molecules, nanoparticles	Small molecules, nanoparticles
Cost	Low	Low	Medium	High	High

29.5.3 Comparison of Photoacoustic Molecular Imaging to Other Molecular Imaging Modalities

The uniqueness aspect of photoacoustic imaging, the conversion of light into sound, is also the source of its main advantages over conventional molecular imaging modalities: high spatial resolution, high tissue penetration depth, and high sensitivity. The frequency bandwidth of the sounds that results in a photoacoustic system is very broad covering the range of DC to $\sim 1/t_p$, where t_p is the time duration of the light pulse. Therefore, for light pulse durations shorter than 1 μ s, pressure waves in frequencies up to several MHz (ultrasound) will emerge. A tissue mimicking phantom with a well containing both fluorescent and absorbing nanoparticles (quantum dots emitting at 800 nm and SWNTs), 4.5 mm under the surface of the phantom was prepared. While the photoacoustic image of the phantom clearly shows the width of the well with high accuracy and signal-to-noise ratio (SNR), the fluorescent image is blurred, due to the scattering nature of the phantom (Fig. 29.20). Table 29.2 provides a high-level comparison between several of the leading molecular imaging modalities. As is evident from the table, neither fluorescence imaging, nor MRI or PET can provide molecular images at reasonable sensitivities (i.e., less than 100 nM) and submillimeter resolution level of an entire tumor (i.e., depth of penetration >3 –4 mm). Ultrasound imaging of targeted microbubbles can provide similar imaging parameters as photoacoustic molecular imaging, with the caveat that the image quality is much worse due to the formation of speckles in the ultrasound image [83].

References

1. Bell A (1880) On the production and reproduction of sound by light. *Am J Sci* 305–324
2. Pramanik M, Wang LV (2009) Thermoacoustic and photoacoustic sensing of temperature. *J Biomed Opt* 14(5):054024. doi:[10.1117/1.3247155](https://doi.org/10.1117/1.3247155)
3. Zhang HF, Maslov K, Stoica G, Wang LV (2006) Functional photoacoustic microscopy for high-resolution and noninvasive in vivo imaging. *Nat Biotechnol* 24(7):848–851
4. de la Zerda A, Paulus YM, Teed R, Bodapati S, Dollberg Y, Khuri-Yakub BT, Blumenkranz MS, Moshfeghi DM, Gambhir SS (2010) Photoacoustic ocular imaging. *Opt Lett* 35(3):270–272
5. Yang JM, Maslov K, Yang HC, Zhou Q, Shung KK, Wang LV (2009) Photoacoustic endoscopy. *Opt Lett* 34(10):1591–1593
6. Zhang EZ, Povazay B, Laufer J, Alex A, Hofer B, Pedley B, Glittenberg C, Treeby B, Cox B, Beard P, Drexler W (2011) Multimodal photoacoustic and optical coherence tomography scanner using an all optical detection scheme for 3D morphological skin imaging. *Biomed Opt Express* 2(8):2202–2215. doi:[10.1364/BOE.2.002202](https://doi.org/10.1364/BOE.2.002202)
7. Jansen K, van der Steen AF, van Beusekom HM, Oosterhuis JW, van Soest G (2011) Intravascular photoacoustic imaging of human coronary atherosclerosis. *Opt Lett* 36(5):597–599. doi:[10.1364/OL.36.000597](https://doi.org/10.1364/OL.36.000597)

8. Wang X, Pang Y, Ku G, Xie X, Stoica G, Wang LV (2003) Noninvasive laser-induced photoacoustic tomography for structural and functional in vivo imaging of the brain. *Nat Biotechnol* 21(7):803–806. doi:[10.1038/nbt839](https://doi.org/10.1038/nbt839)
9. Xu MH, Wang LHV (2006) Photoacoustic imaging in biomedicine. *Rev Sci Instrum* 77(4):041101–043100
10. Wang X, Xie X, Ku G, Wang LV, Stoica G (2006) Noninvasive imaging of hemoglobin concentration and oxygenation in the rat brain using high-resolution photoacoustic tomography. *J Biomed Opt* 11(2):024015
11. Oh JT, Li ML, Zhang HF, Maslov K, Stoica G, Wang LV (2006) Three-dimensional imaging of skin melanoma in vivo by dual-wavelength photoacoustic microscopy. *J Biomed Opt* 11(3):034032
12. Jiao S, Jiang M, Hu J, Fawzi A, Zhou Q, Shung KK, Puliafito CA, Zhang HF (2010) Photoacoustic ophthalmoscopy for in vivo retinal imaging. *Opt Express* 18(4):3967–3972. doi:[10.1364/OE.18.003967](https://doi.org/10.1364/OE.18.003967)
13. Zhang HF, Maslov K, Stoica G, Wang LV (2006) Imaging acute thermal burns by photoacoustic microscopy. *J Biomed Opt* 11(5):054033
14. Wang LV, Hu S (2012) Photoacoustic tomography: in vivo imaging from organelles to organs. *Science* 335(6075):1458–1462. doi:[10.1126/science.1216210](https://doi.org/10.1126/science.1216210)
15. Beard P (2011) Biomedical photoacoustic imaging. *Interface Focus* 1(4):602–631. doi:[10.1098/rsfs.2011.0028](https://doi.org/10.1098/rsfs.2011.0028)
16. Kruger RA, Lam RB, Reinecke DR, Del Rio SP, Doyle RP (2010) Photoacoustic angiography of the breast. *Med Phys* 37(11):6096–6100
17. Lam RB, Kruger RA, Reinecke DR, DelRio SP, Thornton MM, Picot PA, Morgan TG (2010) Dynamic optical angiography of mouse anatomy using radial projections. In: *Proceedings of SPIE 7564, photons plus ultrasound: imaging and sensing 2010*, pp 756405–756405. doi:[10.1117/12.841024](https://doi.org/10.1117/12.841024)
18. Kruger RA, Kiser WL, Reinecke DR, Kruger GA, Miller KD (2003) Thermoacoustic molecular imaging of small animals. *Mol Imaging* 2(2):113–123
19. Brecht HP, Su R, Fronheiser M, Ermilov SA, Conjusteau A, Oraevsky AA (2009) Whole-body three-dimensional photoacoustic tomography system for small animals. *J Biomed Opt* 14(6):064007. doi:[10.1117/1.3259361](https://doi.org/10.1117/1.3259361)
20. Wang X, Pang Y, Ku G, Stoica G, Wang LV (2003) Three-dimensional laser-induced photoacoustic tomography of mouse brain with the skin and skull intact. *Opt Lett* 28(19):1739–1741
21. Buehler A, Herzog E, Razansky D, Ntziachristos V (2010) Video rate photoacoustic tomography of mouse kidney perfusion. *Opt Lett* 35(14):2475–2477. doi:[10.1364/OL.35.002475](https://doi.org/10.1364/OL.35.002475)
22. Lao Y, Xing D, Yang S, Xiang L (2008) Noninvasive photoacoustic imaging of the developing vasculature during early tumor growth. *Phys Med Biol* 53(15):4203–4212. doi:[10.1088/0031-9155/53/15/013](https://doi.org/10.1088/0031-9155/53/15/013)
23. Wang X, Chamberland DL, Jamadar DA (2007) Noninvasive photoacoustic tomography of human peripheral joints toward diagnosis of inflammatory arthritis. *Opt Lett* 32(20):3002–3004
24. Li C, Aguirre A, Gamelin J, Maurudis A, Zhu Q, Wang LV (2010) Real-time photoacoustic tomography of cortical hemodynamics in small animals. *J Biomed Opt* 15(1):010509. doi:[10.1117/1.3302807](https://doi.org/10.1117/1.3302807)
25. Zemp RJ, Song L, Bitton R, Shung KK, Wang LV (2008) Realtime photoacoustic microscopy of murine cardiovascular dynamics. *Opt Express* 16(22):18551–18556. doi:[173047](https://doi.org/10.1364/OE.16.021855)
26. Vaithilingam S, Ma TJ, Furukawa Y, Wygant IO, Zhuang X, De La Zerda A, Oralkan O, Kamaya A, Gambhir SS, Jeffrey RB Jr, Khuri-Yakub BT (2009) Three-dimensional photoacoustic imaging using a two-dimensional CMUT array. *IEEE Trans Ultrason Ferroelectr Freq Control* 56(11):2411–2419. doi:[10.1109/TUFFC.2009.1329](https://doi.org/10.1109/TUFFC.2009.1329)

27. Kothapalli SR, Ma TJ, Vaithilingam S, Oralkan O, Khuri-Yakub BT, Gambhir SS (2012) Deep tissue photoacoustic imaging using a miniaturized 2-D capacitive micromachined ultrasonic transducer array. *IEEE Trans Bio-med Eng* 59(5):1199–1204. doi:[10.1109/TBME.2012.2183593](https://doi.org/10.1109/TBME.2012.2183593)
28. Kim C, Erpelding TN, Jankovic L, Pashley MD, Wang LV (2010) Deeply penetrating in vivo photoacoustic imaging using a clinical ultrasound array system. *Biomed Opt Express* 1(1):278–284. doi:[10.1364/BOE.1.000278](https://doi.org/10.1364/BOE.1.000278)
29. Niederhauser JJ, Jaeger M, Lemor R, Weber P, Frenz M (2005) Combined ultrasound and optoacoustic system for real-time high-contrast vascular imaging in vivo. *IEEE Trans Med Imaging* 24(4):436–440
30. Song L, Maslov K, Shung KK, Wang LV (2010) Ultrasound-array-based real-time photoacoustic microscopy of human pulsatile dynamics in vivo. *J Biomed Opt* 15(2):021303. doi:[10.1117/1.3333545](https://doi.org/10.1117/1.3333545)
31. Song L, Maslov K, Bitton R, Shung KK, Wang LV (2008) Fast 3-D dark-field reflection-mode photoacoustic microscopy in vivo with a 30-MHz ultrasound linear array. *J Biomed Opt* 13(5):054028. doi:[10.1117/1.2976141](https://doi.org/10.1117/1.2976141)
32. Aguirre A, Guo P, Gamelin J, Yan S, Sanders MM, Brewer M, Zhu Q (2009) Coregistered three-dimensional ultrasound and photoacoustic imaging system for ovarian tissue characterization. *J Biomed Opt* 14(5):054014. doi:[10.1117/1.3233916](https://doi.org/10.1117/1.3233916)
33. Fronheiser MP, Ermilov SA, Brecht HP, Conjusteau A, Su R, Mehta K, Oraevsky AA (2010) Real-time optoacoustic monitoring and three-dimensional mapping of a human arm vasculature. *J Biomed Opt* 15(2):021305. doi:[10.1117/1.3370336](https://doi.org/10.1117/1.3370336)
34. Beard PC, Perennes F, Mills TN (1999) Transduction mechanisms of the Fabry-Perot polymer film sensing concept for wideband ultrasound detection. *IEEE Trans Ultrason Ferroelectr Freq Control* 46(6):1575–1582. doi:[10.1109/58.808883](https://doi.org/10.1109/58.808883)
35. Zhang E, Laufer J, Beard P (2008) Backward-mode multiwavelength photoacoustic scanner using a planar Fabry-Perot polymer film ultrasound sensor for high-resolution three-dimensional imaging of biological tissues. *Appl Opt* 47(4):561–577
36. Lamont M, Beard P (2006) 2D imaging of ultrasound fields using CCD array to map output of Fabry-Perot polymer film sensor. *Electron Lett* 42(3):187–189
37. Zhang EZ, Laufer JG, Pedley RB, Beard PC (2009) In vivo high-resolution 3D photoacoustic imaging of superficial vascular anatomy. *Phys Med Biol* 54(4):1035–1046. doi:[10.1088/0031-9155/54/4/014](https://doi.org/10.1088/0031-9155/54/4/014)
38. Laufer J, Zhang E, Raivich G, Beard P (2009) Three-dimensional noninvasive imaging of the vasculature in the mouse brain using a high resolution photoacoustic scanner. *Appl Opt* 48(10):D299–D306
39. Favazza CP, Jassim O, Cornelius LA, Wang LV (2011) In vivo photoacoustic microscopy of human cutaneous microvasculature and a nevus. *J Biomed Opt* 16(1):016015. doi:[10.1117/1.3528661](https://doi.org/10.1117/1.3528661)
40. Vaithilingam S, Ma T-J, Furukawa Y, Zerda Adl, Oralkan O, Kamaya A, Keren S, Gambhir SS, Jr RBJ, Khuri-Yakub BT (2007) A co-axial scanning acoustic and photoacoustic microscope. In: *Proceedings of IEEE ultrasonics symposium, 2007*, pp 2413–2416
41. de la Zerda A, Zavaleta C, Keren S, Vaithilingam S, Bodapati S, Liu Z, Levi J, Smith BR, Ma TJ, Oralkan O, Cheng Z, Chen X, Dai H, Khuri-Yakub BT, Gambhir SS (2008) Carbon nanotubes as photoacoustic molecular imaging agents in living mice. *Nat Nanotechnol* 3(9):557–562
42. Hu S, Rao B, Maslov K, Wang LV (2010) Label-free photoacoustic ophthalmic angiography. *Opt Lett* 35(1):1–3. doi:[10.1364/OL.35.000001](https://doi.org/10.1364/OL.35.000001)
43. Zhang HF, Puliafito CA, Jiao S (2011) Photoacoustic ophthalmoscopy for in vivo retinal imaging: current status and prospects. *Ophthalmic Surg, Lasers Imaging: Official J Int Soc Imaging Eye* 42(Suppl):S106–S115. doi:[10.3928/15428877-20110627-10](https://doi.org/10.3928/15428877-20110627-10)
44. Hu S, Maslov K, Wang LV (2011) Second-generation optical-resolution photoacoustic microscopy with improved sensitivity and speed. *Opt Lett* 36(7):1134–1136. doi:[10.1364/OL.36.001134](https://doi.org/10.1364/OL.36.001134)

45. Maslov K, Zhang HF, Hu S, Wang LV (2008) Optical-resolution photoacoustic microscopy for in vivo imaging of single capillaries. *Opt Lett* 33(9):929–931
46. Wang L, Maslov K, Wang LV (2013) Single-cell label-free photoacoustic flowoxigraphy in vivo. *Proc Natl Acad Sci USA* 110(15):5759–5764. doi:[10.1073/pnas.1215578110](https://doi.org/10.1073/pnas.1215578110)
47. American National Standards Institute (2000) American national standard for the safe use of lasers, ANSI Standard Z1361-2000, ANSI, Inc, New York
48. Jiao S, Xie Z, Zhang HF, Puliafito CA (2009) Simultaneous multimodal imaging with integrated photoacoustic microscopy and optical coherence tomography. *Opt Lett* 34(19):2961–2963
49. Kim C, Favazza C, Wang LV (2010) In vivo photoacoustic tomography of chemicals: high-resolution functional and molecular optical imaging at new depths. *Chem Rev* 110(5):2756–2782. doi:[10.1021/cr900266s](https://doi.org/10.1021/cr900266s)
50. Xiang L, Yuan Y, Xing D, Ou Z, Yang S, Zhou F (2009) Photoacoustic molecular imaging with antibody-functionalized single-walled carbon nanotubes for early diagnosis of tumor. *J Biomed Opt* 14(2):021008. doi:[10.1117/1.3078809](https://doi.org/10.1117/1.3078809)
51. Kircher MF, de la Zerda A, Jokerst JV, Zavaleta CL, Kempen PJ, Mittra E, Pitter K, Huang R, Campos C, Habte F, Sinclair R, Brennan CW, Mellinghoff IK, Holland EC, Gambhir SS (2012) A brain tumor molecular imaging strategy using a new triple-modality MRI-photoacoustic-Raman nanoparticle. *Nat Med* 18(5):829–834. doi:[10.1038/nm.2721](https://doi.org/10.1038/nm.2721)
52. de la Zerda A, Kim J-W, Galanzha EI, Gambhir SS, Zharov VP (2011) Advanced contrast nanoagents for photoacoustic molecular imaging, cytometry, blood test and photothermal theranostics. *Contrast Media Mol Imaging* 6(5):346–369
53. Zharov VP, Galanzha EI, Shashkov EV, Kim JW, Khlebtsov NG, Tuchin VV (2007) Photoacoustic flow cytometry: principle and application for real-time detection of circulating single nanoparticles, pathogens, and contrast dyes in vivo. *J Biomed Opt* 12(5):051503. doi:[10.1117/1.2793746](https://doi.org/10.1117/1.2793746)
54. Shashkov EV, Everts M, Galanzha EI, Zharov VP (2008) Quantum dots as multimodal photoacoustic and photothermal contrast agents. *Nano Lett* 8(11):3953–3958. doi:[10.1021/nl802442x](https://doi.org/10.1021/nl802442x)
55. Pustovalov V, Astafyeva LG, Galanzha E, Zharov VP (2010) Thermo-optical analysis and selection of the properties of absorbing nanoparticles for laser applications in cancer nanotechnology. *Cancer Nano* 1(1–6):35–46. doi:[10.1007/s12645-010-0005-1](https://doi.org/10.1007/s12645-010-0005-1)
56. Pustovalov VK, Smetannikov AS, Zharov VP (2008) Photothermal and accompanied phenomena of selective nanophotothermolysis with gold nanoparticles and laser pulses. *Laser Phys Lett* 5(11):775–792. doi:[10.1002/lapl.200810072](https://doi.org/10.1002/lapl.200810072)
57. Razansky D, Distel M, Vinegoni C, Ma R, Perrimon N, Koster RW, Ntziachristos V (2009) Multispectral opto-acoustic tomography of deep-seated fluorescent proteins in vivo. *Nat Photon* 3(7):412–417
58. Razansky D, Vinegoni C, Ntziachristos V (2007) Multispectral photoacoustic imaging of fluorochromes in small animals. *Opt Lett* 32(19):2891–2893
59. Jain RK, Stylianopoulos T (2010) Delivering nanomedicine to solid tumors. *Nat Rev Clin Oncol* 7(11):653–664. doi:[10.1038/nrclinonc.2010.139](https://doi.org/10.1038/nrclinonc.2010.139)
60. Song KH, Stein EW, Margenthaler JA, Wang LV (2008) Noninvasive photoacoustic identification of sentinel lymph nodes containing methylene blue in vivo in a rat model. *J Biomed Opt* 13(5):054033–054033. doi:[10.1117/1.2976427](https://doi.org/10.1117/1.2976427)
61. Liu Z, Cai W, He L, Nakayama N, Chen K, Sun X, Chen X, Dai H (2007) In vivo biodistribution and highly efficient tumour targeting of carbon nanotubes in mice. *Nat Nanotechnol* 2(1):47–52
62. Keren S, Zavaleta C, Cheng Z, de la Zerda A, Gheysens O, Gambhir SS (2008) Noninvasive molecular imaging of small living subjects using Raman spectroscopy. *Proc Natl Acad Sci* 105(15):5844–5849. doi:[10.1073/pnas.0710575105](https://doi.org/10.1073/pnas.0710575105)
63. Zavaleta C, de la Zerda A, Liu Z, Keren S, Cheng Z, Schipper M, Chen X, Dai H, Gambhir SS (2008) Noninvasive Raman spectroscopy in living mice for evaluation of tumor targeting with carbon nanotubes. *Nano Lett* 8(9):2800–2805

64. de la Zerda A, Liu Z, Bodapati S, Teed R, Vaithilingam S, Khuri-Yakub BT, Chen X, Dai H, Gambhir SS (2010) Ultrahigh sensitivity carbon nanotube agents for photoacoustic molecular imaging in living mice. *Nano Lett* 10(6):2168–2172. doi:[10.1021/nl100890d](https://doi.org/10.1021/nl100890d)
65. de la Zerda A, Bodapati S, Teed R, May SY, Tabakman SM, Liu Z, Khuri-Yakub BT, Chen X, Dai H, Gambhir SS (2012) Family of enhanced photoacoustic imaging agents for high-sensitivity and multiplexing studies in living mice. *ACS Nano* 6(6):4694–4701. doi:[10.1021/nn204352r](https://doi.org/10.1021/nn204352r)
66. Kim G, Huang SW, Day KC, O'Donnell M, Agayan RR, Day MA, Kopelman R, Ashkenazi S (2007) Indocyanine-green-embedded PEBBLES as a contrast agent for photoacoustic imaging. *J Biomed Opt* 12(4):044020
67. Rajian JR, Fabiilli ML, Fowlkes JB, Carson PL, Wang X (2011) Drug delivery monitoring by photoacoustic tomography with an ICG encapsulated double emulsion. *Opt Express* 19(15):14335–14347. doi:[10.1364/OE.19.014335](https://doi.org/10.1364/OE.19.014335)
68. Xu RX (2011) Multifunctional microbubbles and nanobubbles for photoacoustic imaging. *Contrast Media Mol Imaging* 6(5):401–411. doi:[10.1002/cmmi.442](https://doi.org/10.1002/cmmi.442)
69. Schipper ML, Nakayama-Ratchford N, Davis CR, Kam NWS, Chu P, Liu Z, Sun X, Dai H, Gambhir SS (2008) A pilot toxicology study of single-walled carbon nanotubes in a small sample of mice. *Nat Nano* 3(4):216–221
70. Kim JW, Galanzha EI, Shashkov EV, Moon HM, Zharov VP (2009) Golden carbon nanotubes as multimodal photoacoustic and photothermal high-contrast molecular agents. *Nat Nanotechnol* 4(10):688–694. doi:[nnano.2009.231](https://doi.org/10.1038/nnano.2009.231) 1038/nnano.2009.231
71. Kim JW, Moon HM, Benamara M, Sakon J, Salamo GJ, Zharov VP (2010) Aqueous-phase synthesis of monodisperse plasmonic gold nanocrystals using shortened single-walled carbon nanotubes. *Chem Commun (Camb)* 46(38):7142–7144. doi:[10.1039/c0cc00218f](https://doi.org/10.1039/c0cc00218f)
72. Galanzha EI, Kokoska MS, Shashkov EV, Kim JW, Tuchin VV, Zharov VP (2009) In vivo fiber-based multicolor photoacoustic detection and photothermal purging of metastasis in sentinel lymph nodes targeted by nanoparticles. *J Biophotonics* 2(8–9):528–539. doi:[10.1002/jbio.200910046](https://doi.org/10.1002/jbio.200910046)
73. Zhang Q, Iwakuma N, Sharma P, Moudgil BM, Wu C, McNeill J, Jiang H, Grobmyer SR (2009) Gold nanoparticles as a contrast agent for in vivo tumor imaging with photoacoustic tomography. *Nanotechnology* 20(39):395102
74. Wang Y, Xie X, Wang X, Ku G, Gill KL, O'Neal DP, Stoica G, Wang LV (2004) Photoacoustic tomography of a nanoshell contrast agent in the in vivo rat brain. *Nano Lett* 4(9):1689–1692. doi:[10.1021/nl049126a](https://doi.org/10.1021/nl049126a)
75. Luke GP, Yeager D, Emelianov SY (2012) Biomedical applications of photoacoustic imaging with exogenous contrast agents. *Ann Biomed Eng* 40(2):422–437. doi:[10.1007/s10439-011-0449-4](https://doi.org/10.1007/s10439-011-0449-4)
76. Manohar S, Ungureanu C, Van Leeuwen TG (2011) Gold nanorods as molecular contrast agents in photoacoustic imaging: the promises and the caveats. *Contrast Media Mol Imaging* 6(5):389–400. doi:[10.1002/cmmi.454](https://doi.org/10.1002/cmmi.454)
77. Li W, Brown PK, Wang LV, Xia Y (2011) Gold nanocages as contrast agents for photoacoustic imaging. *Contrast Media Mol Imaging* 6(5):370–377. doi:[10.1002/cmmi.439](https://doi.org/10.1002/cmmi.439)
78. Pan D, Pramanik M, Senpan A, Yang X, Song KH, Scott MJ, Zhang H, Gaffney PJ, Wickline SA, Wang LV, Lanza GM (2009) Molecular photoacoustic tomography with colloidal nanobeacons. *Angew Chem Int Ed Engl* 48(23):4170–4173. doi:[10.1002/anie.200805947](https://doi.org/10.1002/anie.200805947)
79. Bouchard LS, Anwar MS, Liu GL, Hann B, Xie ZH, Gray JW, Wang X, Pines A, Chen FF (2009) Picomolar sensitivity MRI and photoacoustic imaging of cobalt nanoparticles. *Proc Natl Acad Sci USA* 106(11):4085–4089
80. Boisselier E, Astruc D (2009) Gold nanoparticles in nanomedicine: preparations, imaging, diagnostics, therapies and toxicity. *Chem Soc Rev* 38(6):1759–1782. doi:[10.1039/b806051g](https://doi.org/10.1039/b806051g)
81. Wang B, Yantsen E, Larson T, Karpouk AB, Sethuraman S, Su JL, Sokolov K, Emelianov SY (2009) Plasmonic intravascular photoacoustic imaging for detection of macrophages in atherosclerotic plaques. *Nano Lett* 9(6):2212–2217. doi:[10.1021/nl801852e](https://doi.org/10.1021/nl801852e)

82. Zavaleta CL, Smith BR, Walton I, Doering W, Davis G, Shojaei B, Natan MJ, Gambhir SS (2009) Multiplexed imaging of surface enhanced Raman scattering nanotags in living mice using noninvasive Raman spectroscopy. *Proc Natl Acad Sci USA* 106(32):13511–13516
83. Deshpande N, Needles A, Willmann JK (2010) Molecular ultrasound imaging: current status and future directions. *Clin Radiol* 65(7):567–581. doi:[10.1016/j.crad.2010.02.013](https://doi.org/10.1016/j.crad.2010.02.013)
84. Kou L, Labrie D, Chylek P (1993) Refractive indices of water and ice in the 0.65- to 2.5-micron spectral range. *Appl Opt* 32(19):3531–3540. doi:[10.1364/AO.32.003531](https://doi.org/10.1364/AO.32.003531)
85. Xie Z, Jiao S, Zhang HF, Puliafito CA (2009) Laser-scanning optical-resolution photoacoustic microscopy. *Opt Lett* 34(12):1771–1773

Chapter 30

Engineering Miniature Imaging Instruments

Zhen Qiu and Thomas D. Wang

30.1 Introduction

Rapid advances in technology have allowed for miniature imaging instruments to be engineered with unprecedented performance with reduced size to visualize biological phenomena in vivo. The increased variety of light sources, improved sensitivity of detectors, and availability of optical fibers are accelerating these engineering breakthroughs. A number of prototype instruments have been demonstrated using sophisticated engineering techniques to scale down instrument packaging to millimeter dimensions. The primary dimension criteria are compatibility with medical endoscopes to allow for broad application in imaging of hollow organs, including bladder, colon, esophagus, stomach, and lung. Also, these tiny microscopes can be implanted within freely moving animals for repetitive imaging studies to better understand biology on a molecular level over time. This small size allows for visualizing cellular behavior in vivo that has never been seen previously to generate new knowledge that may challenge current paradigms in biology. Novel optical designs, miniature scanning mechanisms, and innovative packaging strategies are needed to further advance this field. In the future, these instruments will provide images with multiple colors, more tissue depth, and in numerous dimensions. Here, we focus our discussion on miniature technologies that perform imaging. Methods based primarily on spectroscopy are beyond the scope of this chapter. Here, we will provide only a few representative examples rather than an exhaustive discussion of the vast number of efforts in this field.

Z. Qiu

Department of Biomedical Engineering, University of Michigan, 1728,
109 Zina Pitcher Place, Ann Arbor, MI 48109, USA
e-mail: zqiu@umich.edu

T. D. Wang (✉)

Department of Medicine, Biomedical Engineering and Mechanical Engineering,
University of Michigan, Ann Arbor, MI 48109, USA
e-mail: thomaswa@umich.edu

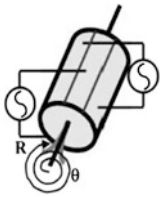

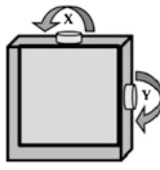
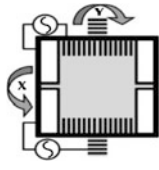
30.2 Unmet Needs for Endomicroscopy

Miniature imaging instruments have great potential to make an important contribution to clinical medicine as an adjunct to conventional endoscopy. Currently, management of almost all diseases that occur in hollow organs, including early detection, image-guided therapy, and drug monitoring, is performed with conventional white-light endoscopy and physical biopsy [1]. This technique is based on the collection of reflected light from the mucosal surface to detect gross structural changes, such as masses, polyps, and ulcers, and abnormalities in color. While this technique is adequate for localizing large, elevated lesions on the tissue surface, visualization of disease that is flat in appearance, focal in size, and patchy in distribution is much more difficult. Also, evaluation of disease as it extends below the mucosal surface is needed for staging purposes. Light is well suited for imaging with high resolution in real time. Endomicroscopy can help the physician to guide tissue biopsies, in particular, in regions where the surface texture alone is not adequate to identify the diseased regions. A number of medical conditions are characterized by flat lesions that reside in a premalignant state and are not visible endoscopically, including dysplasia in Barrett's esophagus, gastric atrophy, and ulcerative colitis. Precancers lie dormant for a period of ~ 10 – 15 years before progressing on to frank carcinoma and provide a window of opportunity for prevention if adequate imaging tools are available to increase the yield for detection. Endomicroscopes that perform optical sectioning can be used to non-destructively sample tissue to guide biopsy to prevent blood from obscuring the endoscopic image. Moreover, *in vivo* endomicroscopy can be used to assist the physician in performing therapeutic procedures, such as endoscopic mucosal resection, ablation, cryotherapy, and electrocautery, by accurately identifying the disease margins, thus minimizing destruction of healthy tissue. Finally, endomicroscopes can provide great clinical utility by differentiating between precancerous or malignant lesions and inflammation in individuals who are at increased risk for developing cancer.

30.3 Scanning Mechanisms

The scanning mechanism plays the key role in image formation and performance in miniature instruments. The technical challenges in designing this component include generation of a distortion-free scan pattern with sufficient speed to mitigate *in vivo* motion artifacts with millimeter package dimensions. For effective *in vivo* imaging to be performed, frame rates of at least 4 Hz or faster are needed to accommodate movement created by respiratory displacement, heart beating, and organ peristalsis. The size of the scanner determines its location at either the proximal end or distal end of the instrument. A much greater control of the focal volume, including axial scanning for imaging into the tissue, can be achieved with the scanner positioned distally. For endoscope compatibility, the distal end of the

Table 30.1 Scanning mechanisms for in vivo endomicroscopy. A description and summary of performance for various scanners

	Spiral	Rotational	Galvo	MEMS
Scanner				
Location	Distal	Distal	Proximal	Distal
Fast axis	>1 kHz	>1 kHz	1–5 kHz	>3 kHz
Slow axis	NA	NA	<10 Hz	<30 Hz
Footprint	<3 mm	<3 mm	<1 cm	<1 mm
Fiber (mode)	Single	Single	Multi-mode bundle	Single
Batch fabrication	No	No	No	Yes

Note Devices must generate high speeds in a small package on the millimeter scale. Recreated with kind permission from McGraw-Hill Professional [2]

instrument should be ~5 mm or less. A description and summary of performance for several different scanner designs that are currently being developed for in vivo endomicroscopy are summarized in Table 30.1 [2].

A spiral scanner consists of a tubular piezoelectric actuator that drives the distal tip of a single optical fiber using sinusoidal waveforms near resonance. This method is used in the scanning fiber endoscope (SFE) and in some multi-photon endomicroscopes. The spiral scan pattern can achieve much faster frame rates than that for raster scanning. The rotational scanner mechanically “rotates” the laser beam circumferentially around the longitudinal axis of the instrument after a 45° deflection off a mirror or prism and is used in OCT and photoacoustic endomicroscopes. The galvo-scanner is an electromechanical mechanism that performs beam scanning by deflecting a mounted mirror. The relatively large size limits its use to steering a focused beam into the proximal end of a coherent bundle of optical fibers. This technique is used in confocal endomicroscopy (Cellvizio®, Mauna Kea Technologies). This scanner provides deflections in the slow axis and is used with an oscillating mirror that performs scanning in the fast axis. Micro-mirrors have been developed with micro-electro-mechanical systems (MEMS) technologies that use either electrothermal or electrostatic actuators to achieve large deflection angles and high dynamic bandwidths with excellent linearity. These scanners can be batch fabricated on silicon wafers to achieve devices with large yield. MEMS scanners require complicated fabrication processes but have great flexibility in scanning speed and device dimensions.

Since the emergence of MEMS, various scanners and actuators have been widely used in imaging prototypes. Based on different working principles, there are several types of miniature micromirrors for endomicroscope (Table 30.2),

Table 30.2 MEMS scanners for in vivo endomicroscopy

Parameter	Electrostatic	Electrothermal	Electromagnetic	Bulky piezo	Thin-film piezo
Footprint	Compact	Compact	Bulk	Large	Compact
Integration complexity	Simple	Simple	Complex	Medium	Simple
Maximum z-axis	~1 mm in vacuum	>1 mm at ambient	>1 mm at ambient	~0.3 mm in-plane motion	>0.5 mm at ambient
Mechanical tilting angle	±10	±20	±20	N/A	>±10
Driving voltage (V)	Medium (20–150)	Low (<10)	Low (<20)	High (>100)	Low (<20)
Driving current (mA)	~0	~15	~50–100	~0	~0
Power consumption	Low	~100 mW	~200 mW	Low	Ultralow

A description and summary of performance for various MEMS scanners

including bulky piezoelectric [3], electrostatic [4, 5], electrothermal [6–8], electromagnetic scanner [9–11], and thin-film piezoelectric [12]. Electrostatic devices are most commonly used because of the fast scan speeds that can be achieved with low power consumption, but the driving voltage may be too high for clinical use (>100 V). By comparison, thin-film piezoelectric devices have very good performance with low driving voltage and ultralow power consumption and may be the future for scanners and actuators in endomicroscopy. The low fill-in factor (<50 %) of existing micromirrors is a common problem that may be solved by microassembly or advanced manufacturing processes [8].

30.4 Scanning Fiber Endoscopy

In the SFE, a tubular piezoelectric actuator scans a single-mode optical fiber in a spiral pattern to create an image with a large field of view, Fig. 30.1a. Laser light at three excitation wavelengths ($\lambda_{\text{ex}} = 440, 532, \text{ and } 635 \text{ nm}$) is delivered through the scanning fiber, and a multi-lens objective located in the distal tip of the endoscope focuses the beams onto the tissue surface. Reflectance and fluorescence is collected by a ring of multi-mode optical collection fibers arranged around the perimeter of the instrument, Fig. 30.1b. Images are collected at video rate (30 frames/s) to overcome motion artifacts in vivo. The SFE imaging technology was first developed for the early detection of cancer in the esophagus, pancreatic duct, and peripheral airways of the lung using reflected white light [13]. Recently, it has been adapted for collection of fluorescence to visualize over expressed molecular targets [14].

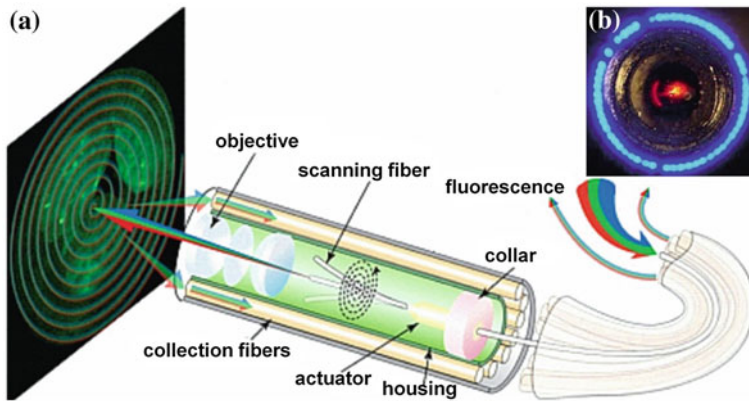


Fig. 30.1 Scanning fiber endoscope. **a** System design of multi-spectral scanning fiber endoscope (SFE). **b** En-face view of distal tip shows scanning fiber (red) in center surrounded by a ring of multi-mode collection fibers for light collection (blue). Recreated with kind permission from SPIE [14]

The detection system make use of a set of additive and subtractive filters (longpass $\lambda_{LP} = 450$ nm and notch $\lambda_{N1} = 532$ nm and $\lambda_{N2} = 632.8$ nm) to reject reflectance from the laser excitation sources. The distal tip is 1.6 mm in outer diameter and has a 10 mm rigid end. Three peptides with unique amino acid sequences were identified using phage display technology and were used as molecular probes that bind specifically to premalignant colonic mucosa (adenoma). These peptides were fluorescently labelled with fluorophores that emitted light in different parts of the spectrum (non-overlapping). Diethylaminocoumarin-3-carboxylic acid (DEAC) with absorption and emission peaks at 432 and 472 nm, 5-carboxytetramethylrhodamine (TAMRA) with absorption and emission peaks at 541 and 568 nm, and CF633 with absorption and emission peaks at 630 and 650 nm were used. The excitation wavelengths nearly matched the three lasers used.

Application of this technology was demonstrated in vivo in CPC: Apc mice that are genetically engineered to develop adenomas spontaneously [15]. These mice are developed with a mutation in the APC genes that also frequently found in human colorectal cancer; thus, this mouse model is highly representative of the clinical condition. First, white-light images were collected with a conventional endoscope, Fig. 30.2a–d. Fluorescence images were collected in vivo after topical application of the fluorescently labelled peptides KCCFPAQ-DEAC (blue), AK-PGYLS-TAMRA (green), and LTTHYKL-CF633 (red). Specific binding of each peptide to the adenoma but not to the surrounding normal colonic mucosa can be seen in Fig. 30.2e–g. The peptides could also be combined as a “cocktail”, Fig. 30.2h. This capability has potential to detect multiple molecular targets in a broad patient population where the genetic changes are heterogeneous.

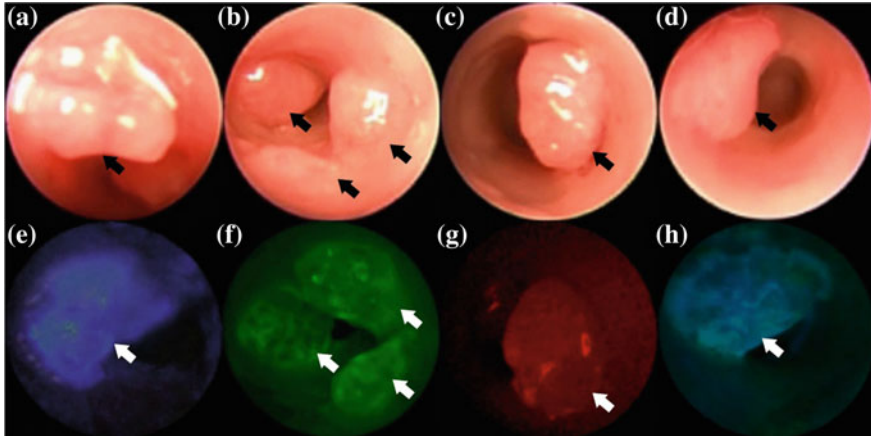


Fig. 30.2 In vivo multi-spectral images. **a–d** Conventional white-light images collected from distal colon of *CPC Apc* mice genetically engineered to develop adenomas (*arrow*) spontaneously. Fluorescence images collected with SFE after topical administration of fluorescently labelled peptides, **e** KCCFPAQ-DEAC, **f** AKPGYLS-TAMRA, and **g** LTTHYKL-CF633 demonstrate specific binding to premalignant lesion in comparison with adjacent normal mucosa, **h** image from “cocktail” of peptides. Recreated with kind permission from Elsevier [15]

30.5 Optical Coherence Tomography Endomicroscopy

Optical coherence tomography (OCT) is an interferometric technique that uses near-infrared (NIR) light to penetrate deeply into tissue to perform minimally invasive imaging. Backscattered light is collected coherently to provide cross-sectional images with micron-scale resolution. Optical frequency-domain imaging (OFDI) is an enhancement of OCT that detects the individual spectral components of low coherence light separately with a fast detector to improve the signal-to-noise ratio and allow for faster frame rates [16]. This method visualizes tissue morphology and has been shown previously to be sensitive to the presence of Barrett’s esophagus and high-grade dysplasia (HGD) [17]. OCT endomicroscopy has been further developed into a tethered pill that can be swallowed to collect reflectance images. This engineering advance allows for imaging in an unsedated patient to potentially improve compliance with screening for early detection of cancer.

The capsule is transparent and cylindrical in shape with a diameter of 12.8 mm and a length of 24.8 mm, Fig. 30.3 [18]. The focusing optics consists of an optical fiber and gradient-index (GRIN) lens, and 45° prism that are contained within the shell. The spot size of the focused beam is 30 μm (full width at half maximum). The capsule is tethered to flexible sheath (0.96 mm diameter) that encloses a driveshaft and the optical fiber that transmits light to and from the tissue. The driveshaft rotates the optics inside the shell to collect circumferential, cross-sectional reflectance images continuously. The OFDI system uses NIR light with

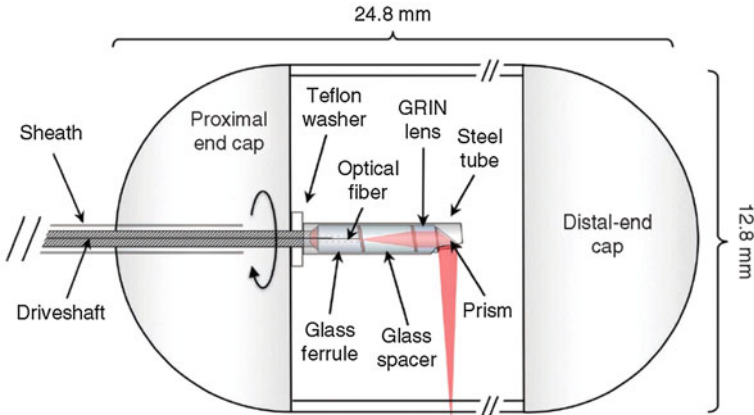


Fig. 30.3 Tethered capsule OCT. A driveshaft encloses the optical fiber and is connected to a steel tube that contains the miniature optics. A ferrule, spacer, gradient-index (*GRIN*) lens, and 45° reflecting prism are rotated to scan the focused beam around the circumference of the hollow organ. Recreated with kind permission from Nature America [18]

frequency ranging from 1,250 to 1,380 nm. Images are collected at 20 frames/s using 2,048 axial (depth) scans per image. The axial resolution is 7 μm in tissue, and the system sensitivity is ~ 110 dB. The images are reconstructed at full resolution (2,900 \times 2,900 pixels) and displayed them using an inverse grayscale lookup table.

Clinical use of this endomicroscope has been demonstrated in unsedated patients who swallowed the capsule using a sip of water. The capsule was held by the tether and allowed to gently descend through the esophagus into the stomach, while images were collected. In vivo cross-sectional images of normal esophagus, stomach, and Barrett's esophagus are shown in Fig. 30.4a–c. Features of normal esophagus can be appreciated on the expanded image (3X), including squamous epithelium (E), muscularis mucosa (MM), lamina propria (L), submucosa (S) containing blood vessels (arrowheads), inner muscularis (IM), outer muscularis (OM), and myenteric plexus (MP), scale bar 0.5 mm, Fig. 30.4d. An expanded image of normal stomach shows characteristic glandular “pits” (arrowheads), Fig. 30.4e. The expanded image of Barrett's esophagus shows an irregular luminal surface, heterogeneous backscattering, and glands within the mucosa (arrowheads), Fig. 30.4f.

30.6 Photoacoustic Endomicroscopy

Photoacoustic imaging is an emerging technology based on optical absorption and ultrasound detection that can achieve high spatial resolution, bright image contrast, and deep tissue penetration [19]. This novel imaging modality can be combined

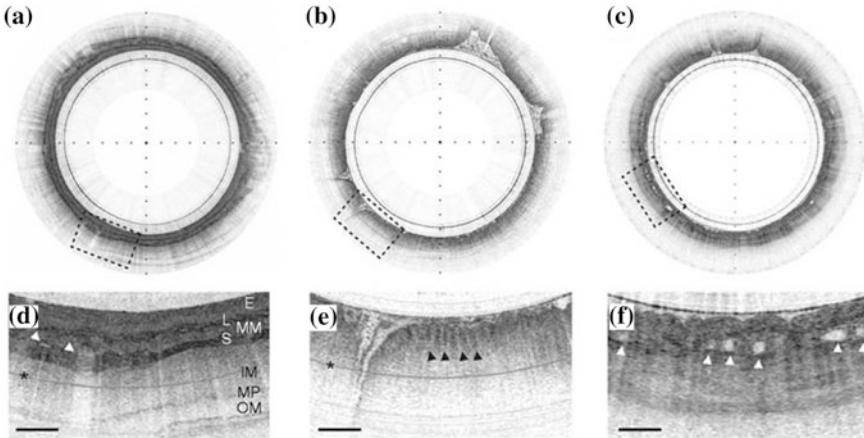


Fig. 30.4 OCT images in vivo. Cross-sectional OCT images in vivo of normal **a** esophagus and **b** stomach and of **c** Barrett's esophagus, tick marks 1 mm. **d** Expanded image (3X) of normal esophagus shows the squamous epithelium (*E*), muscularis mucosa (*MM*), lamina propria (*L*), submucosa (*S*) containing blood vessels (*arrowheads*), inner muscularis (*IM*), outer muscularis (*OM*), and myenteric plexus (*MP*), scale bar 0.5 mm. The asterisk indicates a multiple reflection artifact; **e** expanded image (3X) of normal stomach shows characteristic glandular "pits" (*arrowheads*); **f** expanded image (3X) of Barrett's esophagus shows an irregular luminal surface, heterogeneous backscattering, and glands within the mucosa (*arrowheads*). Recreated with kind permission from Nature America [18]

with endoscopic ultrasound to achieve a multi-modal imaging strategy. The photoacoustic images are formed through the detection of acoustic waves generated by rapid thermoelastic expansion caused by optical absorption of short laser pulses to provide biological function. The ultrasonic images are produced with conventional pulse-echo imaging that detects reflected acoustic waves to provide tissue microstructure.

The microendoscope scan head is ~ 35 mm in length and is enclosed within a 2.5 mm-diameter stainless steel and polyethyleneterephthalate plastic tube [20], Fig. 30.5a. A multi-mode optical fiber (OF, 0.22 NA, 365 μm core diameter) delivers laser pulses that reflect off the 45° deflection dielectric-coated fused silica scanning mirror (SM) that is mechanically rotated at a B-scan frame rate of ~ 4 Hz, driven by a geared micromotor (GM). The mirror reflects both the laser light and acoustic waves, and the imaging window is formed from an optically and acoustically transparent plastic membrane (JPM) with ~ 70 μm thickness. The optical fiber and ring-shaped focused ultrasound transducer (UST) are coaxially aligned to maximize the detection sensitivity of both the photoacoustic and ultrasound pulse-echo signals. The sealed inner cavity is filled with deionized water (WM) to provide acoustic coupling between the imaging window and the transducer. A set of magnets (MN) provides the torque to rotate the scan mirror through a glass partition (GP). A rigid stainless steel housing is sheathed with a polyethyleneterephthalate tube (~ 25 μm thick) to fix the micromotor's 4 electric

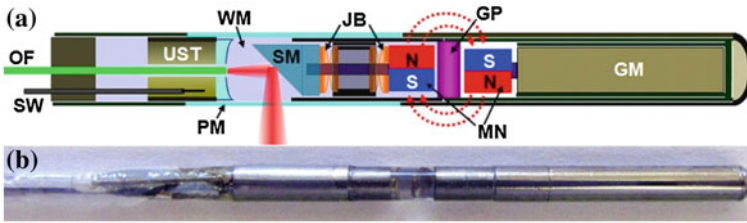


Fig. 30.5 Multi-modal photoacoustic and ultrasound endomicroscope. **a** Schematic instrument. *GM* geared micromotor, *GP* glass partition, *JB* jewel bearings, *MN* magnets, *OF* optical fiber, *PM* plastic membrane (imaging window), *SM* scanning mirror, *SW* signal wire, *UST* ultrasonic transducer, *WM* water medium. **b** Photograph of integrated instrument (2.5 mm diameter and ~ 35 mm length). Recreated with kind permission from OSA [20]

wires ($\sim 200 \mu\text{m}$ thickness for each wire). The angular field of view is partially blocked by the electric wires and thus covers only $\sim 310^\circ$. Another polyethyleneterephthalate tube encloses the wires and optical fiber over the 2 m long flexible section. A photograph of integrated instrument (2.5 mm diameter and ~ 35 mm length) is shown, Fig. 30.5b.

The focused ultrasonic transducer detects one-dimensional depth-resolved signals (or A-lines), and cross-sectional images (or B-scans) are produced by rotating the scanning mirror that directs both the optical and acoustic waves [21]. The endoscope system records and displays a set of dual-wavelength photoacoustic and ultrasonic B-scan images in real time during the constant rotation (~ 4 Hz) of the mirror. By interleaving two optical pulses of different wavelengths and one acoustic pulse at each angular step of the mirror, spatially coincident images are recorded from the generated photoacoustic and ultrasonic A-line signals, even during periods of substantial motion of the target. Volumetric data sets are acquired by recording sequential A-line data during the constant rotational motion of the mirror and mechanical pullback of the probe at a speed of $\sim 200 \mu\text{m s}^{-1}$. This instrument has been used to collect three-dimensional photoacoustic and ultrasound images of rat colon in vivo. The photoacoustic image was acquired using $\lambda_{\text{ex}} = 584 \text{ nm}$ where light is absorbed primarily by hemoglobin. These volumetric data sets cover a 4 cm long cylindrical volume with a 10 mm diameter (i.e., ~ 3.7 mm radial imaging depth), which required a scan time of ~ 4 min at the 4 frames/s. The radial-maximum amplitude projection photoacoustic and ultrasound images from the volumetric image are shown in Fig. 30.6a, b. The volume-rendered PA image shows the vasculature in and near the colon wall, while the US image reveals the density distribution of the tissues. In a representative B-scan section, the US image shows clear contrast at the boundary of the colon wall and the photoacoustic image shows contrast originating from the vasculature in the wall shown in Fig. 30.6c. In the future, this integrated imaging strategy can be combined with molecular probes for staging disease and detection of subsurface pathology.

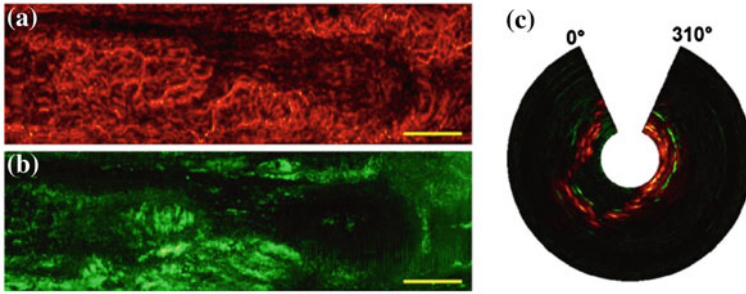


Fig. 30.6 In vivo images of rat colon. **a** Photoacoustic endoscopy. **b** Endoscopic ultrasound maximum amplitude projection images from the distal colon and anus are shown over a 4 cm range with a 10 mm image diameter (3.7 mm radial imaging depth), scale bar 5 mm. **c** Coregistered images are shown over 310° radial image. Recreated with kind permission from OSA [20]

30.7 Confocal Endomicroscopy

A confocal endomicroscope uses the individual optical fibers to deliver the illumination, and each core of the fiber acts as the collection pinhole to reject scattered light from regions outside of the focal plane. The Cellvizio® (Mauna Kea Technologies) is an FDA-approved confocal instrument that uses a coherent optical bundle consisting of $\sim 30,000$ individual, multi-mode fibers coupled to a miniature objective [22]. The advantage of this simple design is that it can be easily assembled in a package on the millimeter scale to pass through the instrument channel of a medical endoscope. A semiconductor laser ($\lambda_{\text{ex}} = 488 \text{ nm}$) provides the illumination, and beam scanning is performed at the proximal end of the fiber bundle by a 4 kHz oscillator for horizontal scanning (lines) and a 12 Hz galvo-mirror for vertical scanning (frames). A dichroic mirror reflects fluorescence to a photodetector, and a longpass filter blocks the residual excitation. A flexible fiber-based confocal endomicroscope (arrow) that has a diameter of 2.6 mm and delivers $<2 \text{ mW}$ of excitation at $\lambda_{\text{ex}} = 488 \text{ nm}$ has been used in the clinic. This level of power has been determined to be non-significant risk by the FDA. Images are collected at 8 frames/s over a $240 \times 240 \mu\text{m}^2$ field of view. The working distance of this instrument was 50 μm , and the resolution in the lateral and axial dimensions was 1.4 and 7 μm , respectively. Separate miniprobes are available that have different working distances for imaging at different tissue depths.

This instrument has been demonstrated clinically to target premalignant mucosa in Barrett's esophagus using a fluorescently labeled peptide to collect horizontal cross-sectional images [23]. ASYNYDA-FITC at a concentration of 100 μM in 5 ml of saline was delivered topically to the esophageal mucosa. After 5 min for incubation, the unbound peptides are rinsed off, and the confocal endomicroscope (arrow) was placed in contact with the esophageal mucosa, Fig. 30.7a. The image of squamous epithelium shows minimal peptide binding with a faint outline of

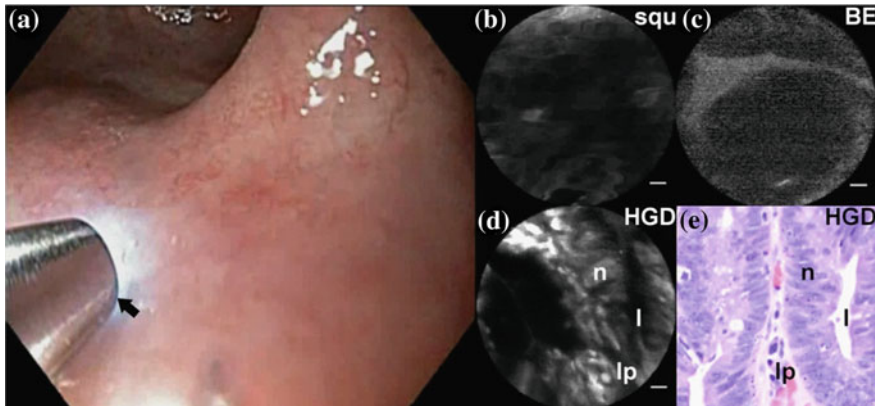


Fig. 30.7 Confocal endomicroscopy. **a** Flexible fiber instrument (*arrow*) is passed through the biopsy channel of a medical endoscope and placed into contact with esophageal mucosa. Molecular images collected with an FITC-labeled peptide show minimal intensity for **b** squamous (normal) and **c** Barrett's esophagus, but significant signal for **d** high-grade dysplasia (*HGD*). **e** Findings are confirmed on histology (H&E)

squamous cells, scale bar 20 μm , Fig. 30.7b. The image of Barrett's esophagus showed a vague outline of a benign crypt with a circular shape, Fig. 30.7c. The image from a region of HGD in Barrett's esophagus showed strong fluorescence intensity from the surface of distorted crypts, Fig. 30.7d. The corresponding histology (H&E) shows crypts with an elongated appearance, Fig. 30.7e. The lumen (l) is tubular in shape, nuclei (n) appear stratified, and the lamina propria (lp) is crowded. These images provide a high magnification of 1,000X and are useful to validate specific binding of molecular probes being clinically validated for over-expressed molecular targets [24].

30.8 Dual Axes Confocal Endomicroscopy

The dual axes design is a novel confocal configuration that separates the illumination and collection beams along different optical axes, using the region of overlap between the two beams (focal volume) to define the resolution [25]. Low numerical aperture objectives are used to create a long working distance so that the scan mirror can be placed in the post-objective position. In this geometry, the two beams are always incident to the objective on axis so that the scan mirror can sweep a diffraction-limited focal volume over an arbitrarily large field of view that is limited only by the maximum deflection angle of the mirror. This feature allows for the size of the instrument to be scaled down to millimeter dimensions without losing performance. In addition, very little of the light that is scattered by tissue along the illumination path is collected to result in a much higher dynamic range.

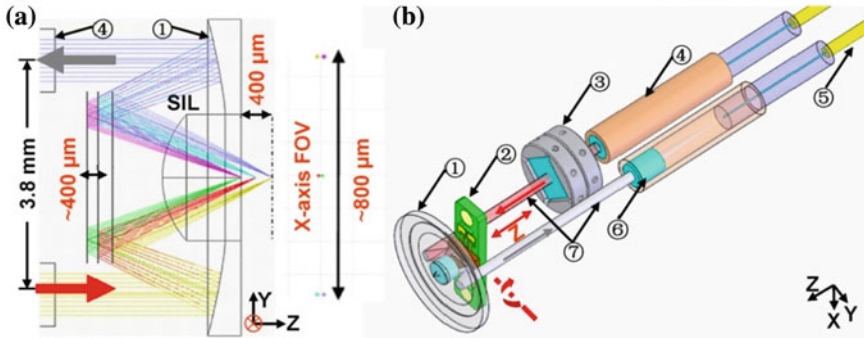


Fig. 30.8 Dual axes confocal endomicroscope. **a** Schematic of dual axes architecture shows ray-trace simulation for achieving large field of view ($800 \times 400 \mu\text{m}^2$) in vertical cross-section using post-objective scanning. **b** Packaging strategy for fiber-coupled instrument. Components are as follows: (1) aluminum-coated parabolic mirror with solid immersion lens (SIL) in center; (2) MEMS mirror with PCB holder; (3) prism with holder; (4) achromatic doublet-lens-based collimator; (5) single-mode fiber; (6) achromatic lens; (7) illumination (red) and collection beam (gray). Recreated with kind permission from OSA [27]

This improvement enables optical sections to be collected in the vertical cross-section to achieve deep tissue imaging using NIR light [26]. This view shows the relationship among tissue microstructures as they vary with depth and provides important diagnostic information about variations in the differentiation pattern of the tissue.

We first determined the scan parameters needed to achieve vertical cross-sectional images with the miniature dual axes design by performing ray-trace simulations in ZEMAX, Fig. 30.8a. We found that we can achieve vertical cross-sectional images with $800 \mu\text{m}$ in the transverse dimension (x-axis) using a MEMS mirror that has a mechanical scan angle of $\pm 6^\circ$. The three pairs of spots represent the focus points of the illumination and collection beams at either extent of the scanning range and on axis. The z-axis actuator moves the focal volume over a range of $\sim 400 \mu\text{m}$ below the tissue surface, which is sufficient for imaging the epithelium in hollow organs, as shown in Fig. 30.8b.

A 1D MEMS resonant scanner was developed for x-axis scanning using a working principle based on electrostatic, parametric resonant tilting to achieve a scan angle greater than the desired $\pm 6^\circ$ with a low drive voltage ($< 40 \text{ V}$) in a small $3 \times 2 \text{ mm}^2$ footprint, Fig. 30.9a. The tilting mirror steers the two overlapping beams (illumination and collection) together over the field of view with a geometry that has a high fill-in factor of 90.3 % ($2.71 \text{ mm}/3 \text{ mm}$) in the lateral dimension of the device. Each device is dry-released from the module by breaking off the link-arm struts with laser cutting (or tweezers). With the simple robust fabrication and fully dry post-process, the new application-driven MEMS scanner design and its fabrication process guarantee a high device yield ($> 90 \%$). With parametric resonance, the mirror is driven by a square waveform (50 % duty cycle) with drive frequency

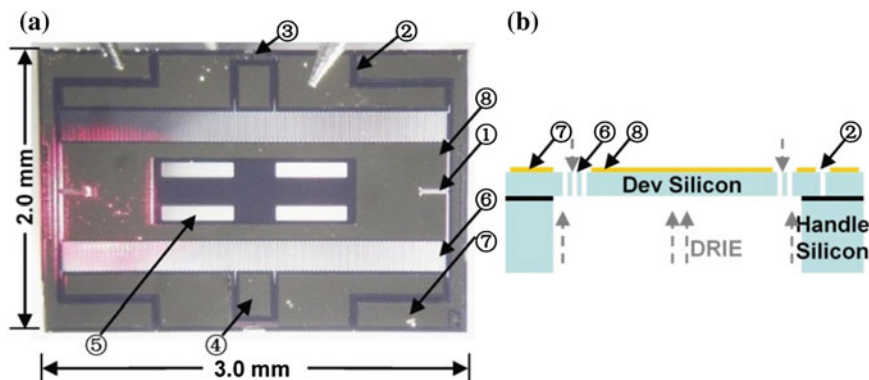


Fig. 30.9 MEMS scanner. **a** Stereomicroscope image of device. Components are as follows: (1) hinge; (2) electric isolation trench; (3) link-arm struts; (4) sensor pad; (5) four weight-reducing holes; (6) electrostatic comb-drive actuators; (7) electric Au/Cr pad; (8) Au/Cr-coated reflective mirror surface. **b** Schematic of cross-sectional view of the MEMS 1D scanner design for a $3 \times 2 \text{ mm}^2$ SOI device with pattern gold coating using DRIE on the *top* and *bottom* layers. Recreated with kind permission from OSA [27]

$f_d = 2 \times f_r/N$ ($N = 1, 2, 3, \dots$, in ambient air, we use $N = 1$). The mirror surface is first coated with a 10 nm layer of chrome followed by a 120 nm layer of gold (Au), for enhanced reflectivity (>85 %, 640–785 nm) in the NIR. A cross-sectional view of the MEMS shows patterning of gold to on the mirror surface, Fig. 30.9b.

Vertical cross-sectional images were collected of NIR fluorescence to illustrate the high dynamic range of the dual axes geometry [27]. The 10 mm-diameter scan head integrates the MEMS mirror for lateral scanning and a bulk PZT actuator for axial scanning. The microscope images in a raster-scanning pattern with a $\pm 6^\circ$ (mechanical) scan angle at $\sim 3 \text{ kHz}$ in the x-axis (fast) and up to 10 Hz (0–400 μm) in the z-axis (slow). Vertical cross-sectional fluorescence images are collected with a transverse and axial resolution of 4 and 5 μm , respectively. A Cy5.5-labeled peptide specific for colonic dysplasia was intravenously administered at a concentration of 400 μM , Fig. 30.10a. The mice were then euthanized, and the colon was excised and imaged immediately with 2 mW of excitation at $\lambda_{\text{ex}} = 671 \text{ nm}$. NIR fluorescence images show dysplastic crypts in the vertical orientation (Fig. 30.10b), demonstrating the histology-like performance. The contrast from specific binding of the peptide can be appreciated by the image of the border between normal colonic mucosa and dysplasia, Fig. 30.10c. Vertically oriented crypts can be appreciated in the corresponding histology (H&E), scale bar 200 μm , Fig. 30.10d.

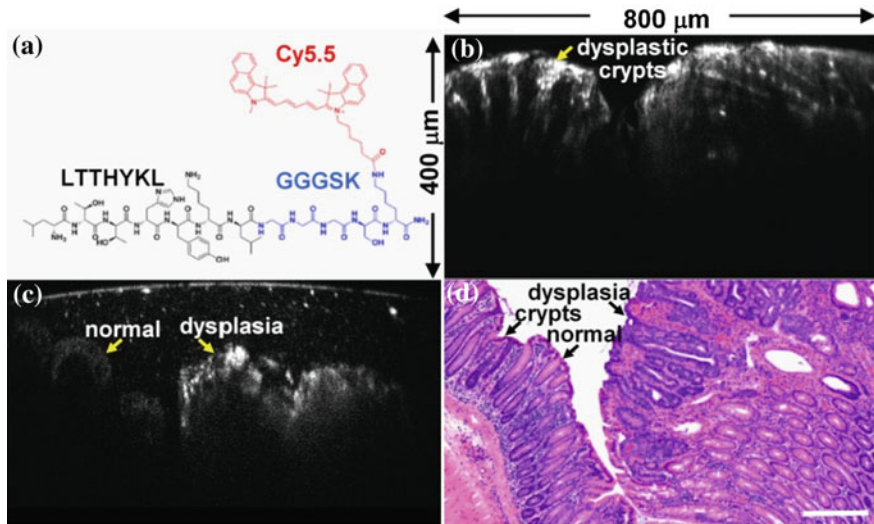


Fig. 30.10 Vertical cross-sectional imaging. **a** Chemical structure of Cy5.5-labeled peptide. **b** NIR fluorescence image from colonic adenoma in ex vivo shows vertically oriented dysplastic crypts ($800 \times 400 \mu\text{m}^2$). **c** Border between normal and premalignant colonic mucosa shows increased contrast from specific binding of molecular probe. **d** Corresponding histology (H&E), scale bar $200 \mu\text{m}$. Recreated with kind permission from OSA [27]

30.9 Multi-Photon Endomicroscope

Multi-photon microscopy uses nonlinear light–tissue interactions to generate image contrast. Fluorescence is generated when two lower-energy (longer wavelength) photons in the NIR regime arrive at tissue biomolecules simultaneously [28]. These photons combine their energies to promote electrons into higher energy levels to produce fluorescence emission. Excitation is provided by ultra-short, 70–200 fs, high peak-intensity pulses of light that localize the energy in space and time to maximize the fluorescence signal.

The scan head of the multi-photon endomicroscope consists of a small tubular piezoelectric actuator that spirally scans a double-clad fiber [29], Fig. 30.11. This fiber is effective for delivery of femtosecond laser pulses for excitation and collection of fluorescence [30]. Excitation is delivered through the core ($3.5 \mu\text{m}$ diameter and 0.19 NA), and fluorescence is collected by the core and by the inner cladding ($103 \mu\text{m}$ diameter and 0.24 NA). The beam is focused by a GRIN lens with 0.22 pitch and a 1.8 mm diameter. The distal end of the instrument is housed in a thin-wall hypodermic tube with an overall diameter of 2.4 mm. The en-face image is produced by a resonant scan of the double-clad fiber in a spiral pattern. The optical fiber extends out of the tubular piezoelectric actuator as a free-standing cantilever. The outer surface of the piezoelectric tube is divided symmetrically into four quadrants that form two orthogonal pairs of drive electrodes. Each pair of

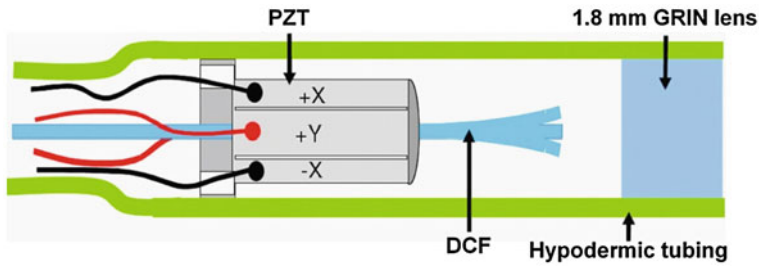


Fig. 30.11 Multi-photon endomicroscope. Double-clad fiber (*DCF*) extends out of a piezoelectric transducer tube (*PZT*) as a cantilever and is spiral scanned by mechanical resonance. The beam is focused by a GRIN lens, and fluorescence is focused by this objective into the core and inner cladding of the fiber. The distal end of the instrument is encased with hypodermic tubing, resulting in an overall outer diameter of 2.4 mm. Recreated with kind permission from OSA [29]

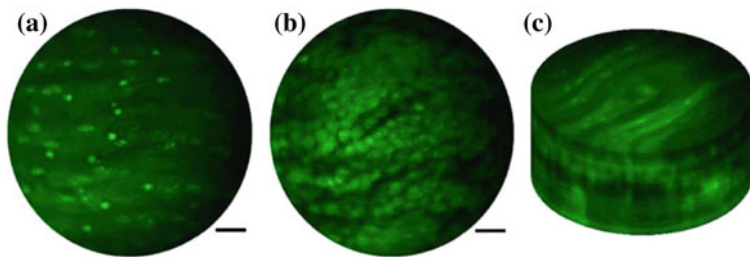


Fig. 30.12 Multi-photon images. Rat oral mucosa was stained with acridine orange, and fluorescence images reveal nucleus density from the **a** superficial layer at 10 μm depth and **b** basal layer at 50 μm depth; **c** images are Z-stacked for 3D volumetric representation. Used with permission. Recreated with kind permission from OSA [29]

opposing quadrants is driven independently out of phase at the mechanical resonance of the fiber cantilever at $\sim 1,690$ Hz. At this frequency, images consisting of 512 circular scans are generated at 3.3 frames/s. The diameter of the field of view is ~ 160 μm using the GRIN lens with a magnification of 0.5.

The potential of multi-photon endomicroscopy to perform optical sectioning was demonstrated with rat oral mucosa stained with acridine orange. The density of the epithelial cell nuclei was observed to increase from the superficial to the basal layers at tissue depths of 10 and 50 μm , respectively, Fig. 30.12a, b. This finding is consistent with that seen on histology. A three-dimensional volumetric image was generated by collecting horizontal (*en face*) cross-sections at 5 μm increments from the mucosal surface to 120 μm below, Fig. 30.12c.

30.10 Conclusion and Future Direction

Miniature imaging system is becoming very important tool for visualizing the mucosa of hollow organs in vivo, such as oropharynx, esophagus, lung, stomach, colon, and rectum. Advanced endomicroscopes have been realized by modern technologies, including light sources, microoptics, fiber optics, miniature scanner. Endomicroscopy, such as OCT, confocal, multi-photon, and photoacoustic, can perform optical sectioning for looking below the tissue surface with subcellular resolution. These methods are relying on novel optics, ultrathin scanning mechanisms based on micromachining and piezoelectric technologies. In addition, innovative target-specific molecular probes significantly improve the specificity of early disease detection before morphology changes occur. In the future, with the development of new technologies, the miniature imaging system will allow physicians to see beyond gross anatomical structures to appreciate biological function. Rapid progress in the biomedical optics field will further expand the capabilities of the imaging system through multi-spectral image collection, higher sensitivity, better resolution, deeper tissue penetration, and 3D volumetric imaging for diagnosis.

References

1. Maitland K, Wang TD (2013) Endoscopy. In: Moore J, Maitland D (eds) *Biomedical Technology and Devices Handbook*, 2nd edn. Taylor & Francis, New York. doi:[10.1201/9780203491492.ch11](https://doi.org/10.1201/9780203491492.ch11)
2. Piyawattanametha W, Wang TD (2011) In vivo microendoscopy. In: Tunnell J (ed) *In vivo clinical imaging and diagnosis*. McGraw Hill Professional, New York, pp 45–76. ISBN: 9780071626842
3. Domke JF, Rhee CH, Liu Z et al (2011) Amplifying transmission and compact suspension for a low-profile, large-displacement piezoelectric actuator. *J Micromech Microeng* 21(6):067004-1–8. doi:[10.1088/0960-1317/21/6/067004](https://doi.org/10.1088/0960-1317/21/6/067004)
4. Piyawattanametha W, Patterson PR, Hah D et al (2005) Surface- and bulk- micromachined two-dimensional scanner driven by angular vertical comb actuators. *J Microelectromech Syst* 14(6):1329–1338. doi:[10.1109/JMEMS.2005.859073](https://doi.org/10.1109/JMEMS.2005.859073)
5. Aguirre AD, Paul RH, Chen Yu et al (2007) Two-axis MEMS scanning catheter for ultrahigh resolution three-dimensional and en face imaging. *Opt Express* 15(5):2445–2453. doi:[10.1364/OE.15.002445](https://doi.org/10.1364/OE.15.002445)
6. Pan Y, Xie H, Fedder GK (2001) Endoscopic optical coherence tomography based on a microelectromechanical mirror. *Opt Lett* 26(24):1966–1968. doi:[10.1364/OL.26.001966](https://doi.org/10.1364/OL.26.001966)
7. Sun J, Guo S, Wu L et al (2010) 3D in vivo optical coherence tomography based on a low-voltage, large-scan-range 2D MEMS mirror. *Opt Express* 18(12):12065–12075. doi:[10.1364/OE.18.012065](https://doi.org/10.1364/OE.18.012065)

8. Samuelson SR, Wu L, Sun J et al (2012) A 2.8 mm imaging probe based on a high-fill-factor MEMS mirror and wire-bonding-free packaging for endoscopic optical coherence tomography. *J Microelectromech Syst* 21(6):1291–1302. doi:[10.1109/JMEMS.2012.2209404](https://doi.org/10.1109/JMEMS.2012.2209404)
9. Kim KH, Park BH, Maguluri GN et al (2007) Two-axis magnetically-driven MEMS scanning catheter for endoscopic high-speed optical coherence tomography. *Opt Express* 15(26):18130–18140. doi:[10.1364/OE.15.018130](https://doi.org/10.1364/OE.15.018130)
10. Mansoor H, Zeng H, Tai IT et al (2013) A handheld electromagnetically actuated fiber optic raster scanner for reflectance confocal imaging of biological tissues. *IEEE Trans Biomed Eng* 60(5):1431–1438. doi:[10.1109/TBME.2012.2236326](https://doi.org/10.1109/TBME.2012.2236326)
11. Mansoor H, Zeng H, Chen K et al (2011) Vertical optical sectioning using a magnetically driven confocal microscanner aimed for in vivo clinical imaging. *Opt Express* 19(25):25161–25172. doi:[10.1364/OE.19.025161](https://doi.org/10.1364/OE.19.025161)
12. Qiu Z, Pulskamp JS, Lin X et al (2010) Large displacement vertical translational actuator based on piezoelectric thin films. *J Micromech Microeng* 20(7):1–10. doi:[10.1088/0960-1317/20/7/075016](https://doi.org/10.1088/0960-1317/20/7/075016)
13. Lee CM, Engelbrecht CJ, Soper TD et al (2010) Scanning fiber endoscopy with highly flexible, 1 mm catheterscopes for wide-field, full-color imaging. *J Biophotonics* 5–6:385–407. doi:[10.1002/jbio.200900087](https://doi.org/10.1002/jbio.200900087)
14. Miller SJ, Lee CM, Joshi BP et al (2012) Targeted detection of murine colonic dysplasia in vivo with flexible multi-spectral scanning fiber endoscopy. *J Biomed Optics* 17(2):1–11. doi:[10.1117/1.JBO.17.2.021103](https://doi.org/10.1117/1.JBO.17.2.021103)
15. Joshi BP, Miller SJ, Lee CM et al (2012) Multispectral endoscopic imaging of colorectal dysplasia in vivo. *Gastroenterology* 143(6):135–137. doi:[10.1053/j.gastro.2012.08.053](https://doi.org/10.1053/j.gastro.2012.08.053)
16. Yun SH, Tearney GJ, Vakoc BJ et al (2006) Comprehensive volumetric optical microscopy in vivo. *Nat Med* 12(12):1429–1433. doi:[10.1038/nm1450](https://doi.org/10.1038/nm1450)
17. Evans JA, Poneros JM, Bouma BE et al (2006) Optical coherence tomography to identify intramucosal carcinoma and high-grade dysplasia in Barrett's esophagus. *Clin Gastroenterol Hepatol* 4(1):38–43. doi:[10.1016/S1542-3565\(05\)00746-9](https://doi.org/10.1016/S1542-3565(05)00746-9)
18. Gora MJ, Sauk JS, Carruth RW et al (2013) Tethered capsule endomicroscopy enables less invasive imaging of gastrointestinal tract microstructure. *Nat Med* 19(2):238–240. doi:[10.1038/nm.3052](https://doi.org/10.1038/nm.3052)
19. Wang LV, Hu S (2012) Photoacoustic tomography: in vivo imaging from organelles to organs. *Science* 335(6075):1458–1462. doi:[10.1126/science.1216210](https://doi.org/10.1126/science.1216210)
20. Yang JM, Chen R, Favazza C et al (2012) A 2.5 mm diameter probe for photoacoustic and ultrasonic endoscopy. *Opt Express* 20(21):23944–23953. doi:[10.1364/OE.20.023944](https://doi.org/10.1364/OE.20.023944)
21. Yang JM, Favazza C, Chen R et al (2012) Simultaneous functional photoacoustic and ultrasonic endoscopy of internal organs in vivo. *Nat Med* 18(8):1297–1302. doi:[10.1038/nm.2823](https://doi.org/10.1038/nm.2823)
22. Wang TD, Friedland S, Sahbaie P et al (2007) Functional imaging of colonic mucosa with a fibered confocal microscope for real time in vivo pathology. *Clin Gastroenterol Hepatol* 5(11):1300–1405. doi:[10.1016/j.cgh.2007.07.013](https://doi.org/10.1016/j.cgh.2007.07.013)
23. Sturm MB, Joshi BP, Lu S et al (2013) Targeted endoscopic imaging of Barrett's neoplasia with specific fluorescent-labeled peptide: first in-humans results. *Sci Trans Med* 5(184):184ra61-1-0. doi:[10.1126/scitranslmed.3004733](https://doi.org/10.1126/scitranslmed.3004733)
24. Hsiung P, Hardy J, Friedland S (2008) Detection of colonic dysplasia in vivo using a targeted heptapeptide and confocal microendoscopy. *Nat Med* 14(4):454–458. doi:[10.1038/nm1692](https://doi.org/10.1038/nm1692)
25. Wang TD, Mandella MJ, Contag CH et al (2003) Dual axes confocal microscope for high resolution in vivo imaging. *Opt Lett* 28(6):414–416. doi:[10.1364/OL.28.000414](https://doi.org/10.1364/OL.28.000414)

26. Liu JTC, Mandella MJ, Crawford JM et al (2006) A dual-axes confocal reflectance microscope for distinguishing colonic neoplasia. *J Biomed Opt* 11(5):054019-1–10. doi:[10.1117/1.2363363](https://doi.org/10.1117/1.2363363)
27. Qiu Z, Liu Z, Duan X et al (2013) Targeted vertical cross-sectional imaging with handheld near-infrared dual axes confocal fluorescence endomicroscope. *Biomed Opt Express* 4(2):322–330. doi:[10.1364/BOE.4.000322](https://doi.org/10.1364/BOE.4.000322)
28. Denk W, Strickler JH, Webb WW (1990) Two-photon laser scanning fluorescence microscopy. *Science* 248(4951):73–76. doi:[10.1126/science.2321027](https://doi.org/10.1126/science.2321027)
29. Wu Y, Leng Y, Xi J et al (2009) Scanning all-fiber-optic endomicroscopy system for 3D nonlinear optical imaging of biological tissues. *Opt Express* 17(10):7907–7915. doi:[10.1364/OE.17.007907](https://doi.org/10.1364/OE.17.007907)
30. Myaing MT, Ye JY, Norris TB et al (2003) Enhanced two-photon biosensing with double-clad photonic crystal fibers. *Opt Lett* 28(14):1224–1226. doi:[10.1364/OL.28.001224](https://doi.org/10.1364/OL.28.001224)

Chapter 31

Engineering Small Animal Conformal Radiotherapy Systems

Magdalena Bazalova and Edward E. Graves

List of Abbreviations

BLI	Bioluminescence imaging
CBCCT	Cone-beam computed tomography
CT	Computed tomography
DETR	Dose-enhanced radiotherapy
IGRT	Image-guided radiotherapy
kV	Kilovoltage
LPS	Lipopolysaccharides
MC	Monte Carlo
MLC	Multileaf collimator
MV	Megavoltage
NPC	Neural progenitor cells
NTCP	Normal tissue complication probability
PDT	Photodynamic therapy
SARRP	Small animal radiation research platform
TCP	Tumor control probability

M. Bazalova · E. E. Graves (✉)
Department of Radiation Oncology, Stanford University, 875 Blake Wilbur, Stanford, CA,
USA
e-mail: egraves@stanford.edu

M. Bazalova
e-mail: bazalova@stanford.edu

31.1 The Need for Small Animal Conformal Radiotherapy Systems

State-of-the-art image-guided radiotherapy (IGRT) is clinically delivered with megavoltage (MV) photon beams generated by medical linear accelerators (linacs). High geometrical accuracy with a millimeter precision to ensure lethal radiation dose to the tumor and minimal dose to critical organs and normal tissue is a requisite for clinical radiotherapy. The prescription doses to the tumors and maximum tolerable doses to critical structures are determined based on patient outcomes, such as tumor control probability (TCP) and normal tissue complication probability (NTCP). TCP and NTCP are derived from patient follow-up studies that typically take 5–20 years. Radiation therapy outcome studies can be performed much faster with small animals due to their short life span and the ability to rigorously control experiments. In order to be able to compare small animal studies to clinical data, a close match between clinical dose delivery and preclinical dose delivery must be achieved.

Historically, small animal radiotherapy studies were commonly nonconformal and performed using a single X-ray beam and a lead shield with an opening cut in the shape of the tumor. Whereas this setup ensures irradiation of the tumor, other organs, and normal tissue in the path of the beam also receive a radiation dose. The results of the radiation study might then be affected by the dose to normal tissues.

For radiotherapy conformal small animal studies with clinical implications, clinical radiotherapy systems must be significantly downscaled. The need to treat submillimeter targets in small animals requires submillimeter dose delivery accuracy. High-resolution anatomical imaging is therefore an integral part of small animal conformal radiotherapy systems. Small animal radiotherapy requires a higher spatial accuracy compared to clinical radiotherapy (Fig. 31.1).

31.2 Components of a Small Animal Conformal Radiotherapy System

A typical small animal conformal radiotherapy system consists of a source of radiation, a collimation system mounted on a gantry, a movable specimen table, and an imaging system. Prior to treatment, the subject is typically imaged with X-ray cone-beam computed tomography (CBCT), reconstructed 3D CBCT volumes are used for specimen positioning and treatment planning. Animals are irradiated with a number of beams calculated by a treatment-planning program, an integral part of every system. Treatment beams have to be collimated to a large degree, so that the beam penumbra (unsharpness) does not degrade the quality of dose distributions and small target volumes can be irradiated while surrounding healthy tissue is spared. The individual components of a small animal conformal radiotherapy system depicted in Fig. 31.2 are described in detail in the following sections.

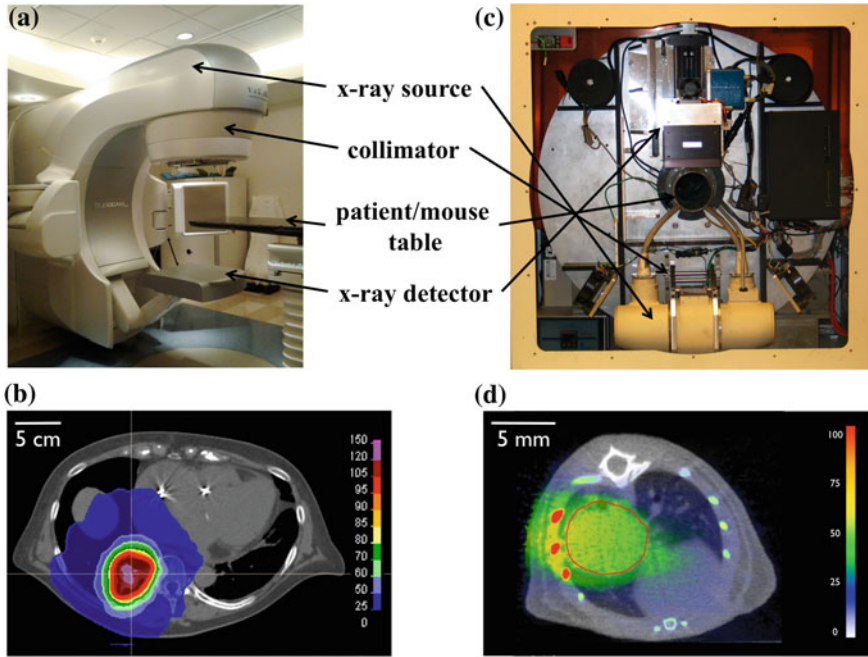


Fig. 31.1 State-of-the-art medical linear accelerator (a) and a patient dose distribution generated by a treatment technique called RapidArc (b). Small animal conformal radiotherapy system at Stanford University based on a modified microCT scanner (c) and a mouse dose distribution delivered by the system (d)

Fig. 31.2 The main components of a small animal conformal radiotherapy system: source of radiation, collimator, X-ray detector, animal bed, and a gantry

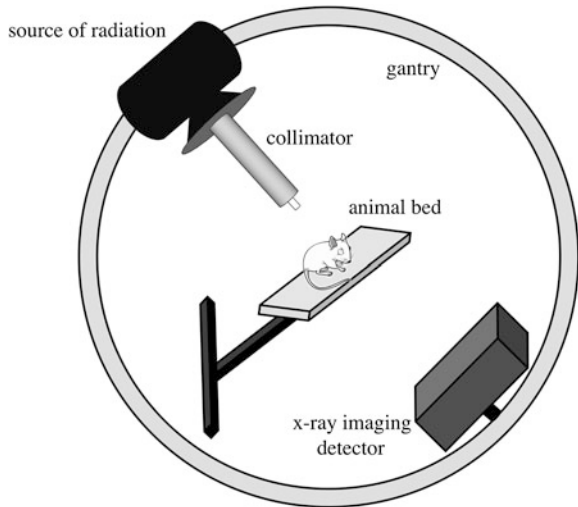
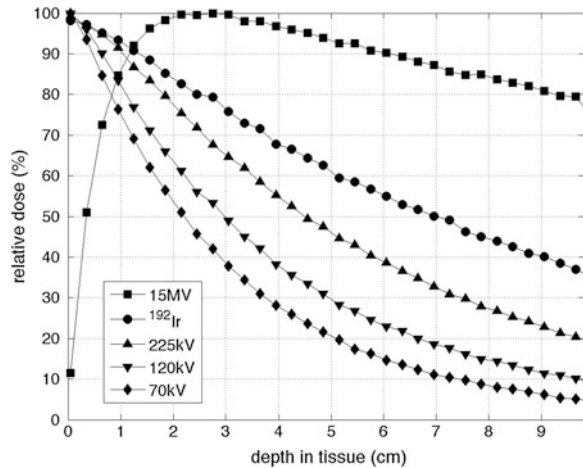


Fig. 31.3 Dose deposition by a 1×1 cm beam as a function of depth for a 15 MV, 70, 120, 225 kV X-ray beams and an ^{192}Ir γ -ray source calculated by Monte Carlo simulation



31.2.1 Sources of Radiation

Due to the typical size of small animals, clinically used high-energy MV photon beams with maximum dose deposition at depths of 1.5–3.5 cm are not suitable for preclinical irradiations. Kilovoltage (kV) photon beams are preferred for small animal radiotherapy systems for three primary reasons:

1. More suitable depth–dose deposition for irradiation of small animals compared to MV beams.
2. Less collimation material needed to generate conformal beams.
3. Lower radiation-shielding requirements compared to clinical radiotherapy shielded by thick concrete walls.
4. Generated by more cost-effective and compact X-ray tubes compared to clinical linear accelerators.

As mentioned above, radiotherapy in most current small animal conformal systems is delivered by kV X-ray beams generated with X-ray tubes, but radionuclide sources have also been considered. Dose deposition of a clinical 15-MV linac photon beam, X-ray tube generated 70, 120, and 225 kV beams, and an ^{192}Ir radionuclide source are plotted in Fig. 31.3. Small animals with sizes from 1 to 5 cm can be conveniently treated with kV photon beams and an ^{192}Ir source.

31.2.1.1 X-Ray Tubes

X-ray tubes are used for radiotherapy of small animals because of their compactness and the dose deposition properties of kV X-ray beams. In an X-ray tube, electrons emitted from a cathode are accelerated over a high voltage (50–300 kV) toward an angled anode usually made of tungsten. Electrons interact with the

anode material over an area defined by the electron beam size (the focal spot) and generate X-rays in the form of Bremsstrahlung and characteristic radiation. The tube voltage determines the energy and penetration power of the X-ray beam, the higher the energy the deeper the beam penetration.

The output of an X-ray tube (i.e., the dose rate) linearly scales with tube current and with square of tube voltage. For highest dose rate, the X-ray tube current and tube voltage are maximized and limited by the generator power. Small animal conformal radiotherapy is typically done with 120–225 kV and 10–50 mA.

X-ray beam attenuation (beam quality) can be modified by inserting filters in the path of the X-ray beam, generally directly in front of the X-ray tube window. While filtration increased the mean beam energy resulting in less steep attenuation, it decreases the dose rate. A compromise between beam attenuation and output must be found. Mean energies of X-ray beams used for small animal radiotherapy are between 80 and 150 keV corresponding to tube voltages of 120–225 keV.

For larger subjects irradiated with large X-ray beams, the X-ray beam heel effect caused by the angled anode must be accounted for, because it results in uneven beam intensity across the direction of the anode angle. For example, for a 12° anode and a 120 kV beam, the difference between the central axis dose and dose 2 cm off axis at 1 cm depth in tissue and 30 cm source-to-skin distance is 10 %. To accurately account for the heel effect during irradiation, Monte Carlo (MC) dose calculations are performed (Sect. 31.3). The focal spot size is one of the factors determining the geometric beam penumbra (Fig. 31.4a, c). The larger the focal spot size, the larger the beam penumbra. With a larger beam penumbra, it becomes more difficult to irradiate the tumor in a conformal fashion. Typical X-ray tubes offer focal spot sizes with diameters from 0.3 to 5 mm. While use a smaller focal spot is preferred for penumbra reasons, small focal spots exacerbate tube heating, and ultimately limit output.

31.2.1.2 Radioisotopes

As an alternative to X-ray tube sources, radioisotopes can be used as treatment sources in small animal conformal radiotherapy systems. The source should have γ -ray energy between 40 and 500 keV for reasonable dose deposition without significant shielding requirements. Moreover, the activity of the source must be high to ensure a high-dose rate, and the half-life of the radionuclide should be reasonable long so that it does not need to be replaced frequently. Moreover, the size of the source affects the geometric beam penumbra (Fig. 31.4), so source sizes in the order of a few millimeters are desirable.

Similar to clinical ^{60}Co source with 1.25 MeV mean beam energy, an ^{192}Ir source with 380 keV γ -ray mean energy can be used for small animal radiotherapy. The deposition of a ^{192}Ir source with a half-life of 74 days is shown in Fig. 31.3. The dose rates of a ^{192}Ir high-dose-rate brachytherapy source are typically on the order of 12 Gy/min at 1 cm distance. Unlike electrically controlled X-

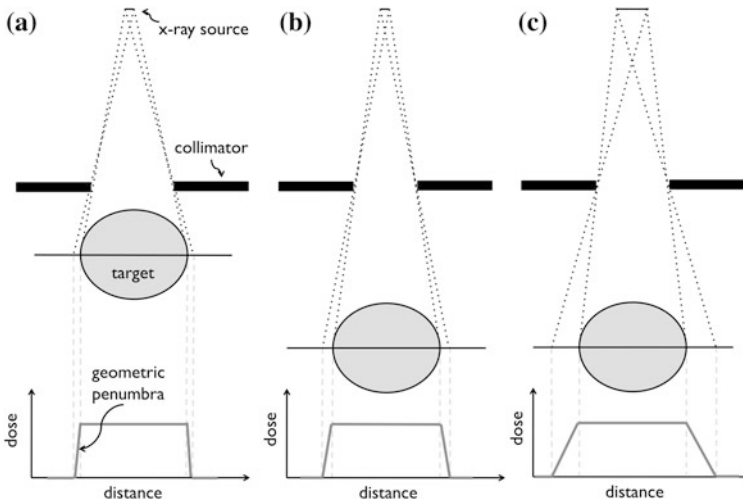


Fig. 31.4 Demonstration of small (a), medium (b), and large (c) geometric beam penumbra (unsharpness) due to treatment source size and collimator-to-target distance. In (a), a small X-ray source and short collimator-to-target distance results in small geometric penumbra. The collimator-to-target distance is enlarged in (b), generating a larger penumbra. In (c), enlarging the X-ray source further increases the beam penumbra. The ideal geometry consists of a small radiation source and a short collimator-to-target geometry

ray tubes, radioisotopes cannot be switched off and special care must be taken concerning shielding and personnel exposure.

31.2.2 Collimation Systems

Delivery of conformal radiotherapy is dependent upon shaping the treatment beam to the shape of the target (the tumor). This is clinically achieved by blocking the radiation beam using thick collimators made of high-density materials (typically tungsten). Clinical collimators are designed with various degrees of complexity. Even though small animal radiotherapy beams are of lower energies than clinical beams and therefore require smaller collimator thicknesses, these beams must be smaller, sharper and delivered with a higher spatial accuracy. This presents a challenge in designing collimators for small animal radiotherapy.

Collimator material and thickness are chosen to attenuate the X-ray beam in a small thickness of material. As such, high-density materials are preferred; however, the clinically used costly tungsten is typically replaced by lead or brass. Collimators must attenuate the X-ray beam to 0.1 % of the initial X-ray fluence. The thicknesses of lead and brass can be calculated using the linear attenuation coefficients obtained from the XCOM database [1] based on Beer's law:

Table 31.1 Linear attenuation coefficient μ and collimator thickness d required to attenuate initial X-ray beam to 0.1 % of its original fluence as a function of beam energy and collimator material

Mean energy (keV)	Lead		Brass ^a	
	μ (cm ⁻¹)	d (mm)	μ (cm ⁻¹)	d (cm)
80	25.8	2.7	6.7	10.3
120	37.4	1.8	2.8	24.7
150	21.5	3.2	1.9	35.8

^a Brass is considered to consist of 60 % copper and 40 % zinc with mass density of 8.5 g/cm³

$$I = I_0 e^{(-\mu d)},$$

where I and I_0 are the intensity of the attenuated and initial X-ray beam, respectively, μ is the linear attenuation coefficient of the collimator material and d is collimator thickness. Table 31.1 summarizes collimator thicknesses required to attenuate initial X-ray beam with a number of mean energies to 0.1 % of the original X-ray fluence. Lead attenuates X-rays more efficiently and is preferred over brass.

In order to generate a sharp beam with a small geometric penumbra, collimators should be placed as close to the target as possible (Fig. 31.4a, b). The distance from the collimator to the isocenter of the machine (the radiation target) is limited by the size of the irradiated animal. Typical distances between the source and the target are 5–15 cm.

Beam-targeting accuracy is driven by the positioning accuracy of the collimators. Careful beam alignment is performed by irradiating a film from a number of beam angles and observing the intersection of the beams.

The four main collimator designs considered for conformal small animal radiotherapy are discussed in the following sections.

31.2.2.1 Removable Collimators

A simple way of collimating the beam is to attach a static removable collimator to the X-ray tube (Fig. 31.5a). Removable collimators typically employ circular openings to create circular fields, or rectangular openings to create rectangular fields. Removable collimators offer the advantage of being in general closer to the target and thus suffer less from geometric penumbra. However, such collimators have to be manually mounted before each beam if the beam size varies for a multibeam treatment. A state-of-the art modulated arc therapy is therefore not possible with removable collimators that have to be inserted manually. Moreover, removable collimators typically offer only a limited number of beam sizes and they are symmetric.

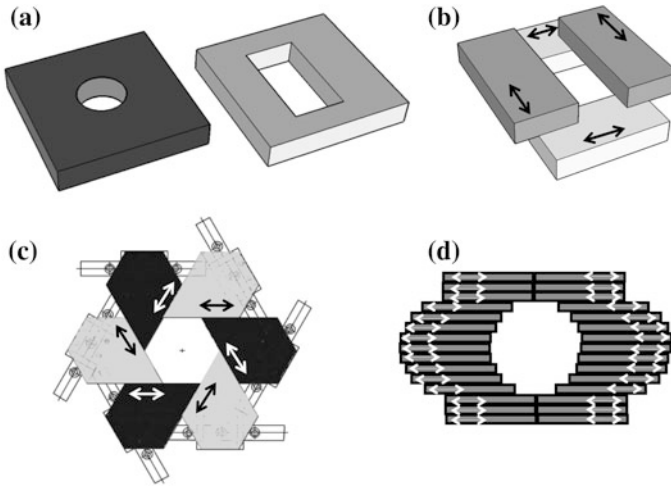


Fig. 31.5 Collimation systems for small animal radiotherapy: removable collimators with *circular* and *rectangular* openings (a), movable collimator jaws (b), an iris collimator with six collimator blocks forming a *hexagonal* opening (c), and a multileaf collimator (d). Arrows indicate the direction of motion of movable parts

31.2.2.2 Movable Jaws

Movable jaws, also used in clinical radiotherapy machines, consist of two pairs of motorized jaws shaping the beam in two perpendicular directions (Fig. 31.5b). The geometric beam penumbra is larger in the direction of the jaw closer to the X-ray tube. Movable jaws can generate rectangular shapes of any sizes in any location. Moreover, X-ray beams shaped by movable jaws can be asymmetric. In principle, the jaws can move during irradiation, which can result in a sophisticated angled dose distribution resembling the clinical enhanced wedge.

31.2.2.3 Iris Collimators

An iris collimator (Fig. 31.5c) consists of a number (n) of motorized blocks organized in a circular geometry so that they form a symmetric polygon opening. The iris collimator has been recently been added to the CyberKnife, a 6 MV clinical linear accelerator mounted on a robotic arm [2]. The iris collimator in Fig. 31.5c generates hexagonal shapes that for small target can approximate circular beams. In order to create more circular-like beam, two n -sided iris collimators rotated by $180/n$ can be placed in two stages in a similar setup to the movable jaws described above. The size of an iris collimator can be adjusted to any desirable opening. The shape, however, is defined the number of collimator blocks (n) and cannot be modified, and moreover the aperture is always isocentric. This design has been implemented for small animal radiotherapy [3].

31.2.2.4 Multileaf Collimators

The treatment beam in state-of-the art clinical irradiators is shaped by the so-called multileaf collimator (MLC, Fig. 31.5d). A large number of 2.5–5 mm tungsten leaf-pairs (approximately 120) move independently forming the field in practically any beam shape. MLCs have not been yet implemented in small animal conformal radiotherapy, but the field is moving toward their application. Based on Table 31.1, it is most likely that the collimator leaves will be made of lead. Assuming a 1 mm resolution at the target, a small focal spot size, and location of the MLC halfway between the focal spot and target, the MLC leaves must be 0.5 mm wide. To cover a 3 cm field in the isocentric plane, 30 leaf-pairs are needed. Packing a large amount of electronics to operate each of the 60 leaves independently presents an engineering challenge.

31.2.3 Gantry and Animal Bed

Conformal radiotherapy also depends upon delivering treatment beams from multiple angles, which results in lowering the skin and normal tissue dose. For this purpose, the treatment X-ray source is mounted on a gantry enabling its rotation. The rotational gantry also supports beam collimation. Ideally, a full arc 360° rotation is available; however, attempts have been made to deliver small animal and clinical conformal radiotherapy over a smaller angle.

The rotational gantry must support the weight of the equipment (the X-ray tube or radioisotope source, and in some cases the imaging panel) while performing accurate rotation with high positioning accuracy and minimal sagging. Gantry rotation speed requirements are similar to clinical radiotherapy machines that can only rotate at 1 rpm according to IEC rotation limits. If the gantry also contains imaging equipment, a faster rotation of 6 rpm is desirable for faster imaging.

In order to irradiate a target anywhere in a small animal body, it is necessary to either allow off-isocenter beams or to place the target into the isocenter of the gantry, where all beams intersect. As most collimation systems do not allow the former at present, a motorized three-dimensional translation animal bed is therefore an important part of a small animal conformal system. Bed positioning accuracy must be within 0.2 mm in all directions. It should have a high reproducibility with travel ranges at least 10 cm to cover the entire small animal body. Lasers along two or three perpendicular directions can be used for a more accurate animal positioning.

Small animals are irradiated under anesthesia that is either delivered by intraperitoneal injection prior to the experiment, or via inhalation during the procedure. In the latter, more common case, a mixture of oxygen and isoflurane gas is supplied to the animal from outside of the shielded system by tubes. Moreover, due to possible long irradiation times, animals are kept on an electric heating pad to maintain body temperature. Tubing and cables are run through a special entry port in order to minimize radiation leakage from the irradiator.

31.2.4 Integrated Imaging

Imaging is a crucial component of conformal radiotherapy machines, as it is important to accurately locate and define the radiation target. Historically, X-ray computed tomography (CT) imaging has been used for localization of the target, as well as for dose calculations. Similar to clinical radiotherapy, CT images must also be acquired for accurate calculation of radiation dose to the small animal. More recently, molecular bioluminescence imaging (BLI) has been considered for the use in targeting small animal conformal radiotherapy. Both of these techniques are discussed in the following sections.

31.2.4.1 X-Ray Computed Tomography Imaging

X-ray CT imaging provides information about the anatomy of the animal. CT images show the X-ray attenuation properties of tissues and can be used to delineate regions of pathology. During CT imaging, X-rays pass through the subject and an X-ray detector consisting of a large number of pixels detects the attenuated beam. The X-ray tube is rotated about the animal, and attenuation through the animal is detected with the detector at a large number of beam angles. CT images are reconstructed from the attenuation data acquired at multiple X-ray tube angles. Due to the high spatial resolution needed in small animal imaging (50–200 μm), CT images are commonly acquired in the cone-beam geometry and reconstructed using the Feldkamp algorithm [4]. In the cone-beam geometry, a large volume of the animal is imaged during a single X-ray tube rotation. The large acquired volume of data results in long CBCT image reconstruction times, which are often shortened by using multiple GPU processors [5].

X-Ray Tubes

Imaging X-ray tubes for small animal radiotherapy systems operate with lower tube voltages (50–100 kV) than treatment X-ray tubes (120–225 kV). In principle, a single X-ray tube can be the source for both treatment and imaging X-rays, if it can be operated at two different tube voltages. Low-energy X-rays are preferentially attenuated in soft tissues relative to high-energy X-rays and therefore provide higher tissue contrast. CBCT imaging spatial resolution must be high so that small targets (≤ 1 mm) can be localized for radiation treatment. Even though CBCT imaging spatial resolution is primarily defined by the resolution of the X-ray detector, it is also affected by the size of the X-ray tube focal spot. For imaging, a small focal spot size of less than 1 mm is desirable.

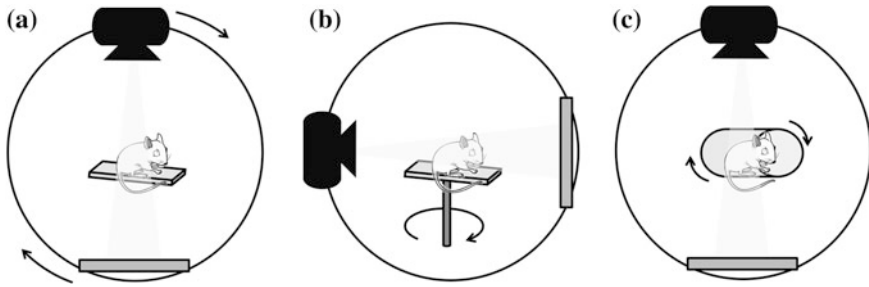


Fig. 31.6 CBCT imaging geometries used in small animal conformal radiotherapy system. Stationary animal is imaged using an X-ray tube and detector rotating about the animal (a), using a stationary X-ray tube and detector by rotating animal bed (b) or by rotating animal placed in a restraining device (c)

Detectors

Small animal X-ray imaging detectors are typically amorphous silicon-based sensors with $1,000 \times 1,000$ – $2,000 \times 2,000$ pixels of size 50×50 – $100 \times 100 \mu\text{m}$, covering an area of approximately 10×10 cm. High-resolution, high-detection efficiency detectors operate at 15 frames/s in order to achieve fast imaging times. Projection data over 360–720 projection angles are needed for reconstruction of three-dimensional images. It is critical that the imaging detectors are fast and efficient in absorbing X-rays, so that minimal animal motion occurs during the imaging time. Small animal CBCT imaging times vary from 20 s to 1 h in existing microCT scanners. During long acquisition times, animal motion can occur resulting in imaging artifacts that severely degrade image quality. In the case of radiotherapy targeting, these artifacts prevent identification of small targets and also complicate treatment planning dose calculations.

CBCT Imaging Geometry

CBCT images are reconstructed based on X-rays attenuation data from the imaged animal that are acquired over a large number of angles. CBCT imaging data can be acquired with three different geometries:

1. The X-ray tube and detector rotate while the animal bed is stationary (Fig. 31.6a).
2. The animal bed rotates with the X-ray tube and detector stationary (Fig. 31.6b).
3. The animal rotates in a restraining device about its long axis with X-ray tube and detector stationary (Fig. 31.6c).

In general, the first approach provides best image quality, because X-rays pass through a smaller thickness of animal and the detected signal used in image formation is maximized. In the second approach, the animal is placed on a 3D

motion bed that is mounted on a rotation stage and the animal is rotated during imaging. The signal through the long animal axis is significantly lower than through the short animal axis, resulting in decrease in imaging quality. Modulation of the X-ray tube current, although not currently used in small animal CT imaging, can mitigate this loss of signal-to-noise ratio. The X-ray tube and detector are also stationary in the third approach. Additionally, the animal is placed into a restraining device and rotated about its long axis. This approach in combination with a reliable restraining device can potentially provide similar imaging quality as the first technique.

31.2.4.2 Bioluminescence Imaging

Researchers at John Hopkins University (JHU) have incorporated BLI into a small animal radiotherapy system. In contrast to anatomical X-ray CT imaging, BLI offers molecular information about the location of the target [6]. During BLI imaging, the subject is injected with luciferin, which is metabolized by the light-emitting enzyme luciferase that has been transfected into specific cells in the animal. As a result of the luciferin–luciferase interaction, optical photons with eV energies are emitted from the target and detected by a CCD camera. Since the photons are in the visible light range, the penetration depth in tissue is low and the imaging system needs to be enclosed in a black light-tight box. In addition, scattering is high in this photon energy range, and sophisticated data reconstruction and processing methods are needed to properly localize the source of bioluminescent light in the subject. Optical imaging plays a unique role in preclinical research, but it is unfeasible in clinical settings due the small penetration depth of optical photons and the difficulty of transfecting human subjects with a bioluminescent enzyme. The most common systems use planar projection imaging, although optical CT facilitating 3D information about the location of the target is becoming available.

31.3 Dose Calculations and Treatment Planning

Dose calculations and treatment planning are an integral part of small animal conformal radiotherapy systems. Interactions of lower-energy-kV X-ray beams are more complex compared to clinical MV X-ray beams and as a result, no simplified, generalized, accurate dose calculation techniques are available. Although approximate kV dose calculation techniques that calculate dose to water accurately exist [7, 8], the dose deposited in tissue by these beams is most accurately calculated using MC techniques [9–11].

First, the treatment beam must be accurately modeled for reliable MC dose calculations. An X-ray source is modeled according to manufacturer's specifications, and validated against dose measurements. Dose measurements can be

performed by ionization chambers or more conveniently by films that have a higher spatial resolution than ionization chambers [12]. Once a beam model is built, MC dose calculations for each animal are performed based on the animal CT images. Each voxel of the CT images, representing the linear attenuation coefficient, is converted into a mass density and tissue type to achieve accurate dose calculation results [13]. The kV beams used in small animal radiotherapy deposit more dose in bony tissues (Fig. 31.1d) relative to MV beams due to the high probability of photoelectric effect, which must be accounted for in the dose calculation process.

Once CT images are acquired, the radiation target is identified and delineated, and the treatment planning process begins. Small animal conformal radiotherapy has yet to evolve to include inverse planning and other clinical treatment planning innovations, and at present, only simple forward planning and optimization methods have been implemented. In one such approach, the user manually selects beam angles and adjusts the collimator size visually to completely cover the target at each angle. In a more advanced technique, collimator sizes are adjusted automatically after beam angle selection [14]. The treatment planning system then calculates the dose based on the MC model of the X-ray beam and the animal CT images. If the outcome of the planning process is not satisfactory in terms of target coverage or dose to critical organs, the user manipulates the number of beams, angles, and collimator settings until an acceptable dose distribution is found. Clearly, the described small animal treatment optimization process lags behind the clinically used workflow employing inverse treatment planning optimization, and more work is needed in this field.

Generally, animal CT images are acquired just prior treatment, and therefore, small animal conformal radiotherapy is a true form of IGRT. In clinical radiotherapy, on the other hand, planning CT images for each patient are acquired multiple days prior treatment due to the lack of high-quality imaging equipment in treatment rooms and to allow time to carefully plan the treatment. Patient positioning on the treatment day is the most time-consuming process.

31.4 Radiation Shielding and Safety

Access to and use of small animal irradiators must be controlled as they can potentially cause harm to the operating personnel if not handled properly. The system can be either enclosed in a lead cabinet that provides radiation shielding to the operator, or the system can be open and located in a separate room from the control computer with a shielded door. In the first case, users can stand right next to the irradiator while operating the machine. In the second case, the system controller is located outside the shielded room and an electronic interlock is mounted on the door to prevent operation of the system with the door open. Additionally, interlocks should be placed on the system itself. The interlock stops the beam when the small animal irradiator door is open. Warning signs consisting

of blinking X-ray warning sign while the beam is on must also be included with the system.

Each user of a small animal radiotherapy system must be trained to use the equipment and must wear a radiation dosimeter while operating the system. The shielding of the system or of the room must be designed in such a way that the exposure to personnel operating the system is below the limits set for radiation workers (50 mSv/year in the USA).

31.5 Quality Assurance

It is important to understand the characteristics of small animal conformal irradiators and to test them on a monthly basis. No protocol has been developed for quality assurance of small animal radiotherapy systems. We will give an overview what such a protocol should include in terms of verifying the mechanical properties of the system and measuring the dose output and beam target accuracy. Moreover, imaging quality assurance must be performed for small animal conformal radiotherapy systems with imaging capabilities.

31.5.1 Mechanical Quality Assurance

The positioning of the animal bed and the rotation of the gantry can be tested in a number of ways. For example, a high-density object visible with the X-ray imaging beam in combination with the imaging panel (a high-density marker, a pin) can be used for both animal bed positioning and gantry rotation testing (Winston-Lutz test).

To assess the accuracy of rotation of the gantry, a high-density marker is carefully positioned at the isocenter of the machine and repeatedly imaged with the CBCT imaging panel from a number of angles. If the gantry rotation is accurate and the position of the X-ray tube and detector with respect to the isocenter constant, the position of the marker in the image is identical for each image acquired at each tube angle. The maximum deviation in images acquired over these gantry angles corresponds to the uncertainty in gantry rotation. The maximum marker position deviation in images acquired at different angles defines the diameter of the radiation isocenter.

A high-density marker placed at the isocenter can also be used to determine bed positioning accuracy. The marker is placed on the bed and imaged with the CBCT imaging panel at two angles separated by 90° (from the top and from the left). The bed is then translated by approximately 1 cm in each direction and the location of the marker on the images is noted. Based on the difference in the positions of the imaged marker before and after the shift, bed shifts are calculated and applied. The marker is imaged again after the bed is shifted. The differences between the

original images and repositioned images of the marker define the bed positioning accuracy in all three directions. Bed positioning accuracy should be within 0.2 mm.

31.5.2 Dose Output Quality Assurance

Dose output is an important quantity in any radiotherapy system. For large fields (> 3 cm), dose output can be measured with an ionization chamber calibrated for the treatment beam. For smaller fields, Gafchromic films should be used for output measurements. Two formalisms can be followed for dose measurements using an ionization chamber according to the AAPM TG-61 protocol [15]: (1) dose is measured in air, or (2) dose is measured in a phantom. For measurements of dose in air, it is important to place the center of the ionization chamber exactly at the isocenter of the machine with no horizontal or vertical tilt. Placement of the chamber is simpler when the “in-phantom” method is used, because the orientation of the chamber with respect to the phantom is known. A small phantom with an opening for the chamber for output measurement calibrated in a kV beam must be designed. We recommend that output be checked for all beam energy and filtration combinations for beam sizes > 3 mm used for small animal irradiations on a monthly basis.

For smaller beam sizes, the process of output calibration with films is more labor-intensive. Film measurements, however, offer more measured data points compared to the single-point measurement with an ionization chamber. An example of dose output measurement is presented in Fig. 31.7a. Gafchromic films are stacked between tissue-equivalent plastic slabs and irradiated with a small beam of the small animal conformal irradiator from the direction perpendicular to the films. The films are subsequently digitized in a flatbed scanner and calibrated based on films irradiated with known doses in a beam of similar quality. As a result of this measurement, beam output, depth-dose curves, and beam profiles at a number of depths are measured. The measurement is repeated for all beam sizes used for radiotherapy annually. We recommend that output values be within 2 % of the actual value for all beam sizes.

31.5.3 Beam-Targeting Quality Assurance

Beam-targeting accuracy can also be measured using Gafchromic films. An example of beam target accuracy with films is demonstrated in Fig. 31.7b, and it is similar to the clinically used star-shot test. A circularly cut film with a small circular hole of approximately 1 mm diameter is inserted between two cylindrical blocks made of a tissue-equivalent material and positioned on the animal bed with the axis parallel to the rotation axis of CT imaging. The phantom is imaged, and

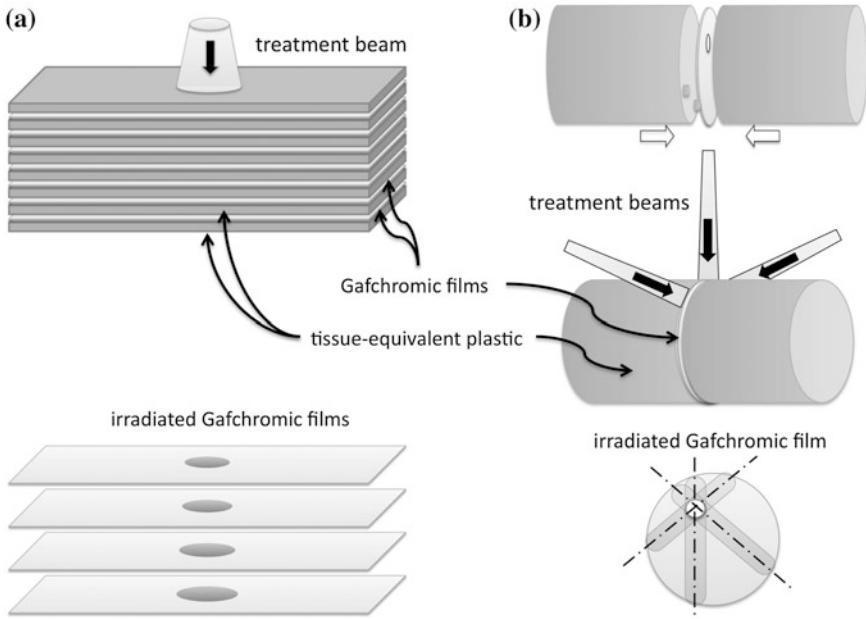


Fig. 31.7 Schematics of film phantoms for small-field output and depth-dose measurements (a) and beam-targeting accuracy (b)

the small hole in the film is identified on CBCT images. After the center of the hole is positioned at the isocenter of the irradiator using the linear translation stages, the film is irradiated with three beams separated by 60° . The film is digitized on a scanner and the axes of all three beams are identified based on the darkness of the film. The accuracy of the intersection of the beams with respect to the center of the hole in the film is evaluated. In order to fully exploit the potential of an advanced small animal conformal radiotherapy system, beam-targeting accuracy should be within 0.2 mm.

31.5.4 Imaging Quality Assurance

Imaging quality assurance can be conveniently performed using the Shelley phantom [16]. The phantom consists of section for testing CT number linearity, uniformity, noise, and accuracy, as well as spatial resolution and geometric accuracy. All these parameters should be checked annually to ensure imaging performance has not degraded in the system over time.

31.6 Overview of Existing Systems

To date, five small animal conformal radiotherapy systems have been developed by groups at JHU, Princess Margaret Hospital (PMH), Washington University, Stanford University, and the University of Texas Southwestern. The systems differ primarily in terms of imaging and treatment geometry and in radiation sources. The existing systems are described in detail below.

31.6.1 John Hopkins University System

The JHU system [8, 17, 18] consists of a dual-focal spot X-ray tube mounted on a gantry rotating over 120°. The X-ray tube operates with the smaller 0.4 mm focal spot at 80–100 kV for imaging and with both the smaller and the larger 3 mm focal spot at 225 kV for radiotherapy. X-ray CBCT imaging is performed by rotating the animal on the couch (Fig. 31.6b), with a nominal resolution of the CBCT images of 0.27 mm. The output of the X-ray radiotherapy source varies between 22 and 375 cGy/min at 1 cm depth depending on the beam size and focal spot size. More recently, this group has incorporated BLI into their small animal radiotherapy system.

Xstrahl (formerly Gulmay Medical, Surrey, United Kingdom) commercialized the JHU system in 2009 under the name Small Animal Radiation Research Platform (SARRP, Fig. 31.8a). The commercial SARRP allows full 360° rotation of the 225 kV X-ray source. CT imaging is performed with a 50–100 kV tube voltage using a high-resolution amorphous silicon detector. The treatment beam can be shaped by collimators of 0.5–10 × 10 mm in size resulting in dose rates 43–229 cGy/min at 1 cm depth. Additionally, beam sizes up to 10 × 10 cm are available.

31.6.2 Princess Margaret Hospital System

PMH developed a standalone small animal irradiation system that has been commercialized by Precision X-ray Inc. (North Branford, CT) under the name X-RAD 225Cx (Fig. 31.8b). In the PMH system [19], both treatment and imaging are performed with a 225 kV X-ray tube. The tube is operated with the large 5.5 mm focal spot at 225 kV and 13 mA with a 0.3 mm Cu filter for radiotherapy, and with the small 1.0 mm focal spot at 40–100 kV and 0.1–0.5 mA with a 2 mm Al filter for imaging. The X-ray tube and the amorphous silicon detector are mounted on a C-arm gantry capable of 360° rotation. Unlike the JHU system, CBCT imaging with resolution of 0.3 mm is performed in the standard geometry, in which the long axis of the animal coincides with the rotation axis of the gantry. The targeting

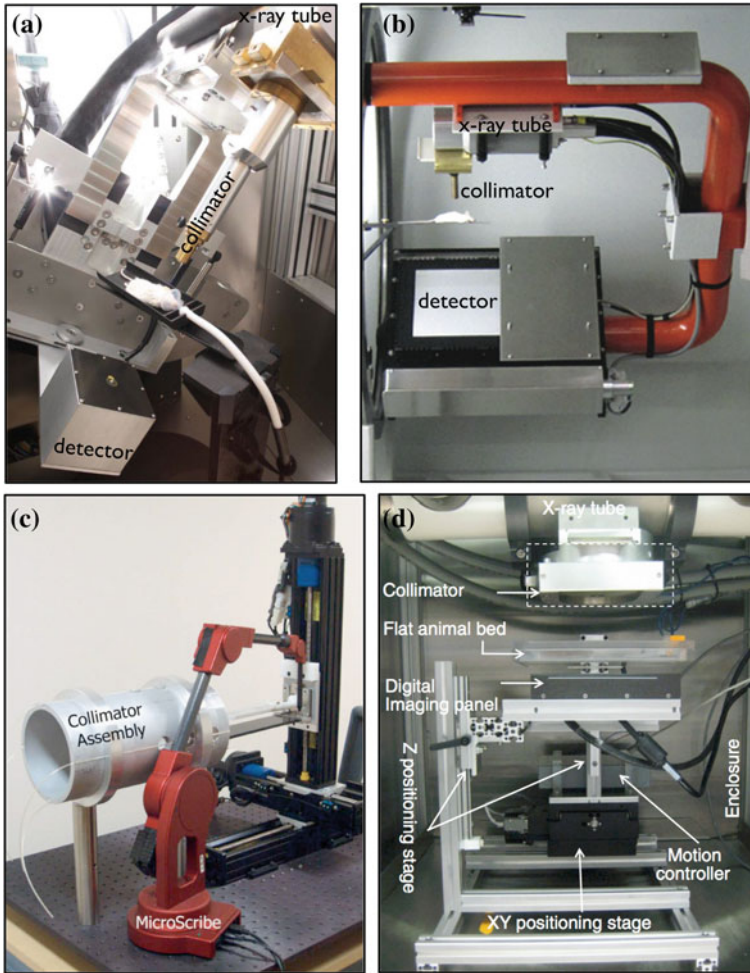


Fig. 31.8 Photographs of four out of five main current small animal conformal radiotherapy systems: JHU system (a), PMH system (b), Washington University system (c), and UT Southwestern system (d). The Stanford University system is shown in Fig. 31.1b. (Images courtesy of Xstrahl, Ltd, Surrey, UK (a), PXi, North Branford, CT (b), and recreated with kind permission of AAPM from Ref. [7] (c) and recreated with kind permission of IoP Publishing from Ref. [22])

accuracy of the system is 0.2 mm. The output of the 225 kV treatment beam at 1 cm depth is 0.96–3.02 Gy/min for beam sizes of 1–20 mm in diameter. Additionally, square and rectangular beams of 3×3 – 10×10 mm are available. Planar BLI has recently been added to the system.

31.6.3 Washington University System

The Washington University MicroRT system [7] is unique because of the ^{192}Ir radioisotope source used to produce the treatment beam (Fig. 31.8c). The radioisotope is installed in a collimator assembly with a remote brachytherapy afterloader. The system can currently deliver dose from four beam portals separated by 90° , the source-to-isocenter distance can be varied between 1 and 8 cm, and the beam can be collimated to field sizes of 5–15 cm using the tungsten collimator assembly. No imaging is included in the current system. Small animals are anesthetized, placed in an immobilization bed with built-in markers and imaged with standalone imaging system, such as microCT, microMRI, or microPET. Small animals are positioned in the MicroRT system for radiation therapy according to the bed markers visible in the imaging modality of choice. Dose rates can be as high as 90 cGy/min. The positioning accuracy of the system is within 0.2 mm.

31.6.4 Stanford University System

A prototype GE 120RS microCT scanner was modified for conformal irradiations of small animals [20] at Stanford University. The irradiation geometry takes advantage of the existing rotational geometry of the microCT scanner (Fig. 31.1c). A two-stage hexagonal iris collimator is mounted in front of the X-ray tube that generates 12-sided polygonal beams with any sizes between 1 to 102 mm (open field for imaging) in diameter. A 2D linear translational stage was mounted on the imaging bed to allow for position of any target at the isocenter of the machine for irradiations. The 70–120 kV X-ray tube is used in the lower tube voltage mode for imaging, and irradiations are performed with the higher tube voltage. The CBCT imaging performance of this system has the highest spatial resolution of all discussed systems, 0.14 mm, due to the original purpose of the system. The X-ray tube output at 1 cm depth is 1.2–1.4 Gy/min for beam sizes of 2–20 mm in diameter. Positioning accuracy of the linear motion stage is 0.1 mm.

31.6.5 University of Texas Southwestern System

The UT Southwestern platform (Fig. 31.8d) employs a 320 kV X-ray tube operated at 250 kV for radiotherapy, which results in high output up to 20 Gy/min for a 50 mm field [21, 22]. The X-ray tube (pointing down) and the imaging panel are stationary, while the animal is inserted in a rotation tube with a restraining device placed on a 2D motion horizontal stage attached to a 1D vertical motion stage. CBCT imaging is performed with rotating the small animal in a restraining device (Fig. 31.6c). The X-ray tube operates at 30 kV and 10 mA for imaging and

250 kV and 15 mA at for radiotherapy. Treatment beams can be shaped by tungsten–copper alloy collimators to sizes of 1–10 mm resulting in dose rates of 4.3–12.8 Gy/min at 1 cm depth. The overall targeting accuracy for cranial radiation was shown to be 0.3 mm [23].

31.7 Applications

Small animal conformal radiotherapy systems are especially critical for small animal studies, in which dose to normal tissue influences the results of the study and must therefore be minimized. Translational radiation oncology and biology studies in small animals should be performed using a conformal radiotherapy system to properly simulate the clinical situation.

Preclinical studies of dose fractionation schemes for all major anatomical sites (brain, lung, breast, pancreas, liver, colon, and prostate) can be efficiently investigated using small animal conformal radiotherapy systems. The effects of radiotherapy alone or in conjunction with chemotherapy and/or surgery can be studied with small animal models.

Brain tumor models were studied using a small animal conformal radiotherapy system to investigate the effect of sparing neural progenitor cells (NPCs) in order to decrease neurocognitive toxicity following radiotherapy [24]. It was shown that conformal plans targeting a hypothetical tumor location in the cortex while avoiding the ipsilateral ventricles and hippocampus spared proliferating cells 24 h after radiation compared to the plan delivering 5.2 Gy to the ipsilateral ventricle and 2.8 Gy to the dentate gyrus of the hippocampus. The results of the study suggest that treatment planning of human brain tumors should be modified to avoid neurologic toxicity from radiotherapy.

The lumbar vertebrae of rats were irradiated using small animal radiotherapy to study the effect on photodynamic therapy (PDT) on bone enhancement following secondary metastatic breast cancer [25]. Rats inoculated with human breast cancer cells were irradiated under image guidance to 4 Gy with a single beam on day 7 postinoculation. On day 14, PDT was delivered to a subgroup of both RT-treated and nontreated rats. All rats were sacrificed on day 21 and bone properties studied in microCT. It was found that PDT may be a viable adjuvant treatment for spinal metastasis postirradiation.

The effects of lipopolysaccharides (LPS) as a treatment of radiation-induced injuries were studied in mice using the X-RAD 225Cx irradiator [26]. The entire thorax of mice was irradiated under image guidance with two parallel-opposed (anterior-posterior and posterior anterior) beams to a dose of 10 Gy. It was determined that early exposure to LPS mitigated the injury caused by irradiation of lungs in mice.

Another research area utilizing small animal radiotherapy systems and currently under development is dose-enhanced radiation therapy (DERT). In DERT, tumors

are injected (either intratumorally or intravenously) with high atomic number (Z) material, such as iodine or gold nanoparticles, and irradiated with kV X-ray beams [27]. The high interaction probability of kV X-rays with the high- Z materials causes dose enhancement in the tumor, effectively reducing dose to healthy tissue and it results in superior treatment outcomes compared to radiotherapy alone [28]. Up to date, DERT small animal studies have been performed with nonconformal irradiations. Small animal conformal radiotherapy systems are the ideal instruments for investigating the benefits of DERT because they use kV X-ray beams.

Researchers will gain valuable insight into radiation biology and the clinical application of radiotherapy from small animal studies. Unlike in the clinical settings, treatment response in a large group of genetically matched animals and tumors treated with the exactly same regimen can be followed. Alternatively, nontreated control and treated small animal tissues can be harvested and stained for radiation damage using various markers at a number of time points after treatment. Small animal studies result in complex sets of data, around which models of radiation therapy response translatable to humans can be created and validated. In the future, the models derived from small animal studies will facilitate the development of personalized medicine: they will aid physicians to decide on the best treatment for every cancer patient.

References

1. Berger MJ, Hubbell JH, Seltzer SM, Chang J, Coursey JS, Sukumar R, Zucker D (2005) XCOM: photon cross section database NBSIR 87-3597. Web version 1.3 (<http://physics.nist.gov/PhysRefData/Xcom/Text/XCOM.html>)
2. Adler JR, Chang SD, Murphy MJ, Doty J, Geis P, Hancock SL (1997) The cyberknife: a frameless robotic system for radiosurgery. *Stereotact Funct Neurosurg* 69(1–4):124–128
3. Graves EE, Zhou H, Chatterjee R, Keall PJ, Gambhir SS, Contag CH, Boyer AL (2007) Design and evaluation of a variable aperture collimator for conformal radiotherapy of small animals using a microCT scanner. *Med Phys* 34(11):4359–4367. doi:10.1118/1.2789498
4. Feldkamp LA, Davis LC, Kress JW (1984) Practical cone-beam algorithm. *J Opt Soc Am a: Opt Im Sci and Vis* 1(6):612–619. doi:10.1364/josaa.1.000612
5. Yan G, Tian J, Zhu S, Dai Y, Qin C (2008) Fast cone-beam CT image reconstruction using GPU hardware. *J X-Ray Sci Tech* 16(4):225–234
6. Jenkins DE, Oei Y, Hornig YS, Yu SF, Dusich J, Purchio T, Contag PR (2003) Bioluminescent imaging (BLI) to improve and refine traditional murine models of tumor growth and metastasis. *Clin Exp Metastasis* 20(8):733–744. doi:10.1023/b:clin.0000006815.49932.98
7. Stojadinovic S, Low DA, Hope AJ, Vicic M, Deasy JO, Cui J, Khullar D, Parikh PJ, Malinowski KT, Izaguirre EW, Mutic S, Grigsby PW (2007) MicroRT: small animal conformal irradiator. *Med Phys* 34(12):4706–4716. doi:10.1118/1.2799887
8. Tryggestad E, Armour M, Iordachita I, Verhaegen F, Wong JW (2009) A comprehensive system for dosimetric commissioning and Monte Carlo validation for the small animal radiation research platform. *Phys Med Biol* 54(17):5341–5357. doi:10.1088/0031-9155/54/17/017

9. Kawrakow I, Rogers DWO (2003) The EGSnrc code system: Monte Carlo simulation of electron and photon transport. NRCC Report PIRS-701, National Research Council, Ottawa, Canada
10. Agostinelli S, Allison J, Amako K, Apostolakis J, Araujo H, Arce P, Asai M, Axen D, Banerjee S, Barrand G, Behner F, Bellagamba L, Boudreau J, Broglia L, Brunengo A, Burkhardt H, Chauvie S, Chuma J, Chytracsek R, Cooperman G, Cosmo G, Degtyarenko P, Dell'Acqua A, Depaola G, Dietrich D, Enami R, Feliciello A, Ferguson C, Fesefeldt H, Folger G, Foppiano F, Forti A, Garelli S, Giani S, Giannitrapani R, Gibin D, Cadenas JGG, Gonzalez I, Abril GG, Greeniaus G, Greiner W, Grichine V, Grossheim A, Guatelli S, Gumplinger P, Hamatsu R, Hashimoto K, Hasui H, Heikkinen A, Howard A, Ivanchenko V, Johnson A, Jones FW, Kallenbach J, Kanaya N, Kawabata M, Kawabata Y, Kawaguti M, Kelner S, Kent P, Kimura A, Kodama T, Kokoulin R, Kossov M, Kurashige H, Lamanna E, Lampen T, Lara V, Lefebvre V, Lei F, Liendl M, Lockman W, Longo F, Magni S, Maire M, Medernach E, Minamimoto K, de Freitas PM, Morita Y, Murakami K, Nagamatu M, Nartallo R, Nieminen P, Nishimura T, Ohtsubo K, Okamura M, O'Neale S, Oohata Y, Paech K, Perl J, Pfeiffer A, Pia MG, Ranjard F, Rybin A, Sadilov S, Di Salvo E, Santin G, Sasaki T, Savvas N, Sawada Y, Scherer S, Seil S, Sirotenko V, Smith D, Starkov N, Stoecker H, Sulikimo J, Takahata M, Tanaka S, Tcherniaev E, Tehrani ES, Tropeano M, Truscott P, Uno H, Urban L, Urban P, Verderi M, Walkden A, Wander W, Weber H, Wellisch JP, Wenaus T, Williams DC, Wright D, Yamada T, Yoshida H, Zschiesche D (2003) GEANT4-a simulation toolkit. Nucl Instrum Method Phys Res Sect A: Acceler Spectrom Det Assoc Equip 506(3):250–303. doi:[10.1016/s0168-9002\(03\)01368-8](https://doi.org/10.1016/s0168-9002(03)01368-8)
11. Pelowitz DB (2008) MCNPX User's Manual, Version 2.6.0. Los Alamos National Laboratory Report No. LA-CP-07-1473, Los Alamos, NM
12. Bazalova M, Zhou H, Keall PJ, Graves EE (2009) Kilovoltage beam Monte Carlo dose calculations in submillimeter voxels for small animal radiotherapy. Med Phys 36(11):4991–4999. doi:[10.1118/1.3238465](https://doi.org/10.1118/1.3238465)
13. Bazalova M, Graves EE (2011) The importance of tissue segmentation for dose calculations for kilovoltage radiation therapy. Med Phys 38(6):3039–3049. doi:[10.1118/1.3589138](https://doi.org/10.1118/1.3589138)
14. Motomura AR, Bazalova M, Zhou H, Keall PJ, Graves EE (2010) Investigation of the effects of treatment planning variables in small animal radiotherapy dose distributions. Med Phys 37(2):590–599. doi:[10.1118/1.3276738](https://doi.org/10.1118/1.3276738)
15. Ma CM, Coffey CW, DeWerd LA, Liu C, Nath R, Seltzer SM, Seuntjens JP (2001) AAPM protocol for 40–300 kV x-ray beam dosimetry in radiotherapy and radiobiology. Med Phys 28(6):868–893. doi:[10.1118/1.1374247](https://doi.org/10.1118/1.1374247)
16. Du LY, Umoh J, Nikolov HN, Pollmann SI, Lee TY, Holdsworth DW (2007) A quality assurance phantom for the performance evaluation of volumetric micro-CT systems. Phys Med Biol 52(23):7087–7108. doi:[10.1088/0031-9155/52/23/021](https://doi.org/10.1088/0031-9155/52/23/021)
17. Wong J, Armour E, Kazanzides P, Iordachita U, Tryggstad E, Deng H, Matinfar M, Kennedy C, Liu ZJ, Chan T, Gray O, Verhaegen F, McNutt T, Ford E, DeWeese TL (2008) High-resolution, small animal radiation research platform with X-ray tomographic guidance capabilities. Int J Rad Oncol Biol Phys 71(5):1591–1599. doi:[10.1016/j.ijrobp.2008.04.025](https://doi.org/10.1016/j.ijrobp.2008.04.025)
18. Matinfar M, Ford E, Iordachita I, Wong J, Kazanzides P (2009) Image-guided small animal radiation research platform: calibration of treatment beam alignment. Phys Med Biol 54(4):891–905. doi:[10.1088/0031-9155/54/4/005](https://doi.org/10.1088/0031-9155/54/4/005)
19. Clarkson R, Lindsay PE, Ansell S, Wilson G, Jelveh S, Hill RP, Jaffray DA (2011) Characterization of image quality and image-guidance performance of a preclinical microirradiator. Med Phys 38(2):845–856. doi:[10.1118/1.3533947](https://doi.org/10.1118/1.3533947)
20. Zhou H, Rodriguez M, van den Haak F, Nelson G, Jogani R, Xu J, Zhu X, Xian Y, Tran PT, Felsner DW, Keall PJ, Graves EE (2010) Development of a micro-computed tomography-based image-guided conformal radiotherapy system for small animals. Int J Rad Oncol Biol Phys 77(2):384–391

21. Pidikiti R, Stojadinovic S, Speiser M, Song KH, Hager F, Saha D, Solberg TD (2011) Dosimetric characterization of an image-guided stereotactic small animal irradiator. *Phys Med Biol* 56(8):2585–2599. doi:[10.1088/0031-9155/56/8/016](https://doi.org/10.1088/0031-9155/56/8/016)
22. Song KH, Pidikiti R, Stojadinovic S, Speiser M, Seliounine S, Saha D, Solberg TD (2010) An x-ray image guidance system for small animal stereotactic irradiation. *Phys Med Biol* 55(23):7345–7362. doi:[10.1088/0031-9155/55/23/011](https://doi.org/10.1088/0031-9155/55/23/011)
23. Kiehl EL, Stojadinovic S, Malinowski KT, Limbrick D, Jost SC, Garbow JR, Rubin JB, Deasy JO, Khullar D, Izaguirre EW, Parikh PJ, Low DA, Hope AJ (2008) Feasibility of small animal cranial irradiation with the microRT system. *Med Phys* 35(10):4735–4743. doi:[10.1118/1.2977762](https://doi.org/10.1118/1.2977762)
24. Redmond KJ, Achanta P, Grossman SA, Armour M, Reyes J, Kleinberg L, Tryggestad E, Quinones-Hinojosa A, Ford EC (2011) A radiotherapy technique to limit dose to neural progenitor cell niches without compromising tumor coverage. *J Neur Oncol* 104(2):579–587. doi:[10.1007/s11060-011-0530-8](https://doi.org/10.1007/s11060-011-0530-8)
25. Lo VCK, Akens MK, Moore S, Yee AJM, Wilson BC, Whyne CM (2012) Beyond radiation therapy: photodynamic therapy maintains structural integrity of irradiated healthy and metastatically involved vertebrae in a pre-clinical in vivo model. *Breast Cancer Res Treat* 135(2):391–401. doi:[10.1007/s10549-012-2146-x](https://doi.org/10.1007/s10549-012-2146-x)
26. Zaidi A, Jelveh S, Mahmood J, Hill RP (2012) Effects of lipopolysaccharide on the response of C57BL/6 J mice to whole thorax irradiation. *Rad Oncol* 105(3):341–349. doi:[10.1016/j.radonc.2012.08.003](https://doi.org/10.1016/j.radonc.2012.08.003)
27. Chithrani DB, Jelveh S, Jalali F, van Prooijen M, Allen C, Bristow RG, Hill RP, Jaffray DA (2010) Gold nanoparticles as radiation sensitizers in cancer therapy. *Radiat Res* 173(6):719–728. doi:[10.1667/rr1984.1](https://doi.org/10.1667/rr1984.1)
28. Hainfeld JF, Slatkin DN, Smilowitz HM (2004) The use of gold nanoparticles to enhance radiotherapy in mice. *Phys Med Biol* 49(18):N309–N315. doi:[10.1088/0031-9155/49/18/n03](https://doi.org/10.1088/0031-9155/49/18/n03)

Part V
Theranostics and Other Novel
Approaches

Chapter 32

Plasmonic Nanobubbles for Cancer Theranostics

Ekaterina Y. Lukianova-Hleb and Dmitri O. Lapotko

32.1 Introduction

32.1.1 *Limitations of Macromedicine*

Use of current medical practices such as surgery and chemotherapy or chemoradiation therapy for cancers occurring in vitally important anatomic locations such as the head and neck (brain, prostate, lungs, and other sites) is limited by several factors. (1) Incomplete resection of tumors results in microscopic residual disease [1–5]. (2) Resection of tumors intertwined with functionally or cosmetically important organs causes functional and cosmetic damage [6–9]. (3) Residual cancer cells often become highly resistant to chemotherapy and radiotherapy, rendering these interventions ineffective and greatly increasing the risk of local regional recurrence [10, 11]. (4) High doses of drugs and radiation induce severe nonspecific toxicities, further complicating treatment [5]. These limitations ultimately reduce patients' survival rates (which for head and neck cancers have not improved over the past 30 years [12, 13]) and profoundly impact their quality of life, cosmesis, and psychological health. Therefore, the development of novel methods that will selectively detect and efficiently and rapidly eliminate treatment-resistant residual cancer cells and tumors, preserve the functionality of co-localized normal tissue, and reduce nonspecific toxicity and treatment time is urgently needed. Such methods that unite the diagnosis and treatment in one procedure are defined as theranostics.

E. Y. Lukianova-Hleb · D. O. Lapotko (✉)
Department of Biochemistry and Cell Biology, Department of Physics and Astronomy,
Rice University, 6100 Main Street, MS-140 Houston 77005 TX, USA
e-mail: dl5@rice.edu

32.1.2 Nanotheranostics

Nanoparticle (NP) medicine is considered as one of the most promising approaches in resolving the above medical challenges, and the main effort was historically focused on the nanoparticle properties to achieve the theranostic functions, i.e., diagnosis and treatment, in one package. The recent advances in chemistry allowed to employ a phenomenon of plasmon resonance [14] for the conversion of light into medically relevant processes at nanoscale via metal (plasmonic) nanoparticles that show a million times higher optical absorbance than any natural molecules. Among them, gold nanoparticles have both the highest optical absorbance and the lowest biological toxicity. Interestingly, gold nanoparticles are not new. In fact, they were invented by Michael Faraday in the nineteenth century [15] and have been used in clinics for more than 50 years [16]. On the other hand, the recent advances in laser technologies allowed the use of near-infrared continuous and pulsed light with the maximal tissue penetration depth (up to 70 mm [17]) and safety. Fiber optical technologies allowed the delivery of light even deeper, up to 300–400 mm, thus enabling laser microsurgery [18]. Finally, advances in conjugation chemistry made possible the precise delivery of gold NPs to specific pathological cells, where these NPs can be remotely and instantaneously activated with visible or near-infrared (NIR) laser light. All the above created a unique interdisciplinary platform for the development and clinical translation of the nanoparticle-based theranostics.

32.1.3 Limitations of the Nanoparticle-based Approaches

As we stated, metal plasmonic NPs are the best photothermal (PT) converters through the mechanism of surface plasmon resonance [14, 19–22]. This unique mechanism enables precise manipulations of thermal energy at nanoscale, including in biomedical applications at cell and molecular level [23]. The spectral region and efficacy of this PT conversion were so far controlled by engineering the specific optical absorbance of NPs during their synthesis [24–43]. An increase in the PT efficacy of such NPs was achieved through increasing the absorbed optical energy by augmenting the local amount of NPs through their clustering, or by raising the level of optical excitation energy at the wavelength of plasmon resonance, or by both. The active development of this field (referred to as plasmonics) during the two decades revealed several problems which are typical of most PT applications of plasmonic NPs:

1. Limitation of PT efficacy: Most common stationary optical excitation creates high thermal losses [44–46] that, in turn, require a further increase in the excitation energy, while the short pulse excitation involves high optical intensities that destroy the NP structure and, thus, reduce its optical absorbance. Both effects reduce PT efficacy.

2. Limitation of spectral selectivity: The spectral width of the absorption band of single NPs is tens of nanometers at best [19, 20, 23, 47–57], while their random clustering further broadens their absorption spectra to hundreds of nanometers [19, 41, 47–51, 54, 58–60].
3. Limitation of spatial selectivity: Thermal diffusive losses under stationary excitation increase the heated volume from the nanosize of an NP to micro- or even macrosized.

These challenges prevent the PT conversion of sufficient energy with both high efficacy and high spectral, spatial and temporal resolution. Instead, the PT effects of NPs often default to macroscale, stationary, and broadband processes, thus losing the main advantage of NPs as nanoscale PT agents. An ability to combine high PT efficacy with high spectral resolution and minimal thermal losses would therefore significantly improve the current applications of plasmonic materials and stimulate new ones.

Until now, the PT properties of metal NPs were preset during their synthesis [23–43] and were assumed to remain constant during their optical excitation. Unlike this stationary paradigm that cannot overcome the above limitations, we propose an alternative approach based on the nonstationary excitation of NPs that can potentially create new transient states with improved PT and spectral properties. This can be realized through the *dynamic modification* of the optical absorbance of an NP during its nonstationary excitation with a short intense laser pulse. Previous studies of metal NPs under pulsed excitation show that laser-induced NP reshaping, fragmentation, melting, and ionization [61–69] modify their plasmonic properties.

We hypothesized that the absorption of a short laser pulse by a metal NP and the induced nonstationary modification of this NP will enhance its optical absorbance (and hence the PT efficacy) in a narrow, nanometer-wide, spectral window. This was realized by replacing stationary NPs with transient nonstationary event, vapor nanobubbles generated with a short laser pulse around plasmonic NPs and termed as “plasmonic nanobubbles” (PNB). By developing this novel nonstationary plasmonic method, we (1) created a new engineering approach, namely nonstationary plasmonics that will improve our understanding of nanoscale energy conversion and applications of current nanomaterials and (2) improved the biomedical potential of available nanomaterials and will facilitate their translation to clinic. In particular, this improved the NIR PT efficacy of gold solid spheres (known as gold colloids for 150 years [15, 70]) for various biomedical applications that require NIR optical radiation. These safe, inexpensive, and easily available NPs were so far not considered for NIR excitation due to their poor optical absorbance. With enhanced NIR PT efficacy, these basic NPs may replace complex specifically engineered NPs that are often expensive, physiologically unsafe, and unstable compared to solid gold spheres. Below we discuss the physical properties of PNBs in the Part I, the methods for their generation and detection in cells and tissues in Part II, and the theranostic applications of PNBs in vitro and in vivo in the Part III.

32.2 Part I Physical Properties of Plasmonic Nanobubbles

32.2.1 *Generation and Detection of Plasmonic Nanobubbles*

Transient thermal evaporation and the generation of vapor bubbles are one of the basic processes accompanying nonstationary high-temperature heat and mass transfer in liquids. The science and the methods for the detection of inertial vapor bubbles of various origins were well developed for macro- and microsized bubbles and mainly employ their ability to emit pressure and to scatter the incident light [71–96]. Recent developments in nanoscience reduced the spatial and temporal scale of vapor bubbles to nanometers and nanoseconds [77–80, 93, 97–103]. Unlike their larger analogs, vapor nanobubbles require much higher sensitivity and resolution of the detection methods for their imaging, quantification, and identification among other phenomena such as transient heating and the generation of stress waves. Here, we analyze several experimental techniques for the imaging and quantitative analysis of transient vapor nanobubbles as single events, and we troubleshoot some related errors. Due to the multiple biomedical applications of nanobubbles and related phenomena [104–108], it should be noted that we consider the transient events, but not the materials (particles) that are often also called plasmonic nanobubbles [109, 110]. We also do not consider the cavitation of preexisting bubbles that is well studied elsewhere [111].

While PNBs may have various sources of energy (the heating of liquid above the boiling threshold, local rarefaction, and plasma discharge), we focus on the mechanism that provides maximal precision, control, and reproducibility in a PNB generation through the localized transient photothermal heating of liquid above the evaporation point (Fig. 32.1). This was achieved through the optical excitation of individual gold nanospheres in water with single short laser pulses at specific fluences above the PNB generation threshold. We used the plasmonic conversion of optical energy into heat to control the maximal diameter and lifetime of the PNBs through the fluence of a single laser pulse, as described in detail previously [78–80, 103]. This experimental model includes an internal metal NP that acts as the source of the PNB energy during PNB generation and prevents the development of extreme temperatures and sonoluminescence at the collapse stage [78, 112], unlike “classical” bubbles that are generated in homogeneous media [113, 114]. Another important difference in the model employed is the absence of an external acoustic field that is often used alone or in combination with optical energy to generate a vapor bubble [114, 115]. The above conditions and the nanoscale size resulted in a single cycle of the vapor nanobubble that did not oscillate (Fig. 32.1).

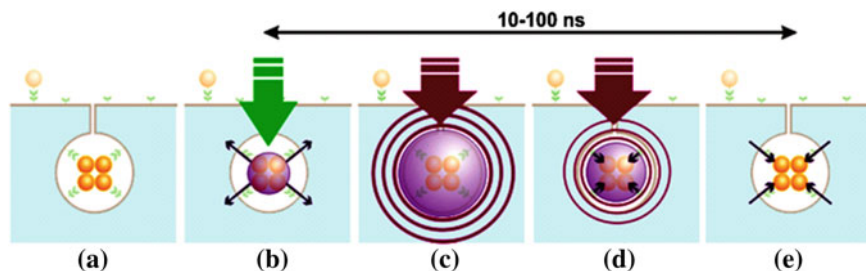


Fig. 32.1 Plasmonic bubble generation and detection: **a** cluster of gold nanoparticles in target cell, **b** laser pulse (*green*) nucleates the vapor bubble, **c** bubble expands and scatters a probe laser beam (*purple*), **d–e** bubble collapse

32.2.2 Methods for Plasmonic Nanobubble Detection

PNB detection employs several universal techniques that have to provide sufficient sensitivity, resolution, and speed. First, we consider imaging methods. Optical scattering phenomena allow both PNB imaging and monitoring of its dynamics [77–80, 84–88, 116].

The imaging of a transient PNB can also be realized with much more affordable equipment using slow cameras and pulsed light sources (Fig. 32.2) by using (1) pulsed illumination with a shorter duration than a PNB lifetime within a nano- and pico-second range; (2) sufficient energy of the optical pulse to compensate the very small scattering cross section of the PNB; (3) precise synchronization of the illuminating pulse with the PNB source. These requirements suggest a pulsed laser as the illumination source. The illumination angle and the numerical aperture of the collecting lens further determine the signal-to-noise ratio of this imaging scheme. Forward scattering results in the maximal scattering efficacy but cannot be fully separated from incident light that creates a high background. We achieved the best results with angled side illumination (Fig. 32.2a), providing that the numerical aperture of the imaging (collecting) lens is lower than the angle of incidence of the illuminating radiation. In this case, the lens collects only the light scattered by the PNB. This scheme allows the imaging of a single transient PNB with a lifetime down to 10 ns (Fig. 32.3). The 100 ps illumination pulse of 1 μJ at 576 nm was directed at 45° to the sample cuvette with an optically variable delay relative to the excitation pulse, and the PNB was imaged with 10X–63X microscope objectives. Most of the current CCD- and CMOS-based cameras can do such imaging. We used EMCCD (charged coupled device with electronic multiplication) cameras. In this method, the pixel image amplitude is used as a PNB metric, but it is not very practical: (1) any deviation in the alignment of the probe beam would require the re-calibration of the system, and (2) this metric will not characterize the maximal diameter of a PNB when one fixed time delay is applied. The advantage of this method is in the relatively precise identification of a PNB and its location. It also shows the number of PNBs if multiple events occur.

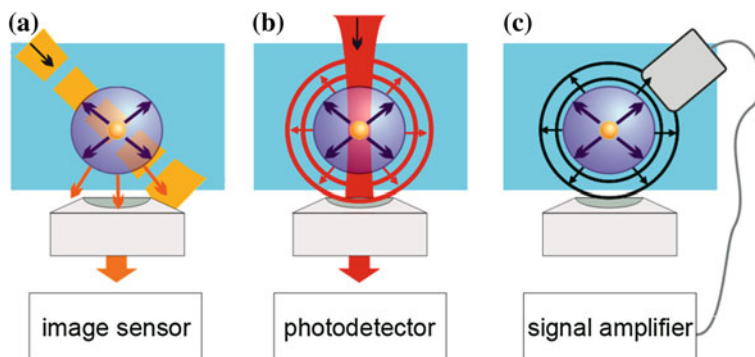


Fig. 32.2 Methods for detecting plasmonic nanobubbles in liquid: **a** optical time-resolved scattering imaging is obtained with a short probe laser pulse and a slow image detector, **b** optical scattering (extinction) time response is obtained with a continuous focused probe laser pulse and a fast photodetector, **c** acoustical time response is obtained with an ultrasound detector. Recreated by kind permission of AIP [116]

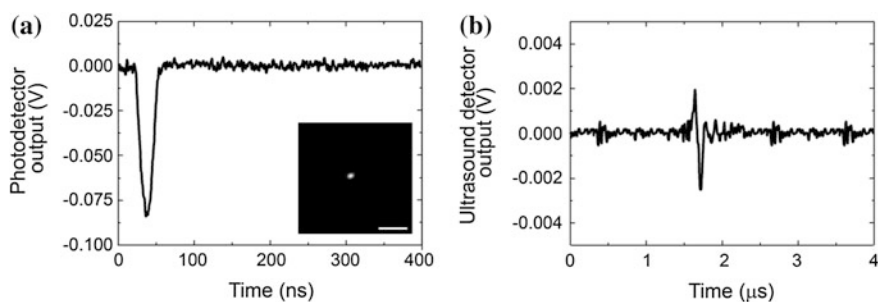


Fig. 32.3 Three methods of detecting a single PNB. **a** Optical scattering (extinction) time response obtained with continuous probe laser shows the expansion and collapse of an PNB (metrics—amplitude and duration) and time-resolved optical scattering imaging (insert) with a pulsed probe laser (metric—a pixel image amplitude). **b** Acoustical time response obtained with an ultrasound sensor (metric—amplitude). Scale bar is 15 μm . Recreated by kind permission of AIP [116]

The maximal diameter of a PNB is the most important parameter that also characterizes the amount of energy received by the bubble [71–76, 78]. It can be measured with another optical scattering technique that employs the monitoring of the intensity of a continuous probe beam with a broadband high-speed photodetector. The beam is focused at the PNB and its scattering by the PNB changes its axial intensity which is measured as a time response with the photodetector. In one method, the beam is pointed at the low noise detector through the aperture and produces a high base level (Fig. 32.2b). A PNB scatters the light and thus increasingly reduces the axial intensity of the probe beam during its expansion stage and brings it back to the base level during its collapse stage. This results in

the bubble-specific shape of the time response (Fig. 32.3a). Technically, the detector measures the optical extinction of the probe beam, but since a PNB does not absorb any optical energy, the extinction becomes equal to its scattering component. Due to the scattering nature of such a signal, we define it as a “scattering”. This definition assumes the absence of any transient optical absorbance developed simultaneously with a PNB. If such absorbance emerges (due to plasma formation or any nonlinear modification of the optical properties of the media), the method may characterize a PNB incorrectly [117, 118]. In another method, the beam is pointed off the detector aperture and produces a low base level at the detector. In this case, only the light scattered by a PNB will reach the detector and will increase its output signal, also producing a time response with a bubble-specific shape.

The most precise way to measure the maximal diameter of a single PNB is to measure the duration of the PNB-specific signal (Fig. 32.3a) which was shown to correlate to its maximal diameter [71–76, 78]. The amplitude of the PNB response also depends upon the maximal diameter of the PNB, but is very sensitive to experimental factors that are difficult to control. The first is the diameter and divergence of the probe beam at the PNB’s plane. The smaller the beam waste, the higher the sensitivity of PNB detection. An increase in the beam’s diameter by 10–15 % and/or a slight deviation of the beam axis may cause a several-fold decrease in the signal amplitude of a dip-shaped PNB signal. Such conditions occur during changing the sample chamber or while scanning a heterogeneous sample across the beam. The simultaneous generation of multiple PNBs around different sources of thermal energy (for example, in suspension around optically absorbing molecules or NPs) instead of a single one, increases the signal amplitude, but such an increase is just an ensemble effect. The simultaneous generation of several PNBs of different maximal sizes influences not only the amplitude but also the shape of the PNB time response. Smaller PNBs form a sharp front and fewer large PNBs form a long tail of lower amplitude. While the generation of PNBs under some settings may typically involve such a multi-PNB pattern, it is still possible to estimate the lifetime of the largest PNBs that represent the maximal deposition of the thermal energy by measuring the duration of the time response at the reduced level instead of at half of maximum. However, the best rule is to avoid such distorted signals because they may lead to misinterpretation of the bubble parameters [117]. In all three considered cases (single PNB, single PNB with misaligned probe beam, multiple PNBs), the durations of the bubble-specific signals could be linked to the maximal diameter of the PNB, while their amplitudes differed significantly, and therefore, their use as PNB metrics may lead to artifacts [118].

The third method of PNB detection employs the pressure waves generated during the bubble expansion and collapse [93, 96] (Fig. 32.2c). In the case of a single inertial bubble, the pressure and rarefaction waves produce a typical signal (Fig. 32.3b). This is definitely the simplest and the least expensive method of the three, because it does not require expensive optical sources, optics, and sensors. In addition, it detects PNBs in optically opaque media, so is probably the most

universal of the methods. The most obvious metric of the acoustic signal is its maximal (peak-to-peak) amplitude. However, the correct identification and measurement of a PNB with a standard acoustic detector can be challenging in a single pulse mode. Most detectors have a resonant frequency of 10 MHz and lower where their sensitivity is the maximal. For small PNBs with lifetimes from 5 to 100 ns, the corresponding pressure rise times and associated frequencies seem to be higher than the resonant frequencies of most acoustic sensors. Therefore, the sensor signal does not show the real pressure, but rather represents a response function of the sensor. In this case, the amplitude of the output signal of the acoustic sensor significantly depends upon its resonant frequency and may cause a significant error. For a specific acoustic sensor, the amplitude of its output also depends upon the number of simultaneously generated PNBs. Therefore, a reliable measurement of the PNB diameter through the amplitude of acoustic response assumes that a single PNB is generated.

The next important task is the identification of a PNB and its discrimination from other phenomena such as transient heating or stress waves (Fig. 32.4). The optical scattering response identifies heating through a thermal lens effect that allows the detection and measurement of rapid heating and gradual cooling due to thermal diffusion (Fig. 32.4a). This purely refractive effect does not produce any optical scattering like a PNB does. Next, under high transient temperatures at short time scales, the generation of stress waves (and shock waves) also influences the refractive index of the media and creates a distinct short (relative to the bubble and heating time scale) signal of nanosecond duration that is determined by the speed of sound and the aperture of the probe beam (Fig. 32.4c). Both phenomena can be clearly distinguished from the bubble (Fig. 32.4b). However, all these three different phenomena do not much influence the shape of the acoustic response, but rather its amplitude, which is minimal for heating, increases for a bubble and becomes the maximal for stress waves. Therefore, an acoustic time response is much less bubble specific than an optical scattering time response.

32.2.3 Tunability of Plasmonic Nanobubbles

The above analysis compares three methods for the detection of PNBs under fixed excitation conditions above the bubble generation fluence. It is important to understand the range of the linear correlation between the PNB maximal diameter and its excitation conditions. We compared the four discussed above metrics, the pixel amplitude of the scattering image, the amplitude and duration of the optical scattering time response, and the amplitude of the acoustic response, as functions of the fluence of the excitation laser pulse, the parameter that, in this model, determines the maximal diameter of the PNB when the fluence exceeds the PNB generation threshold. All bubbles were generated in water around individual identical gold nanospheres.

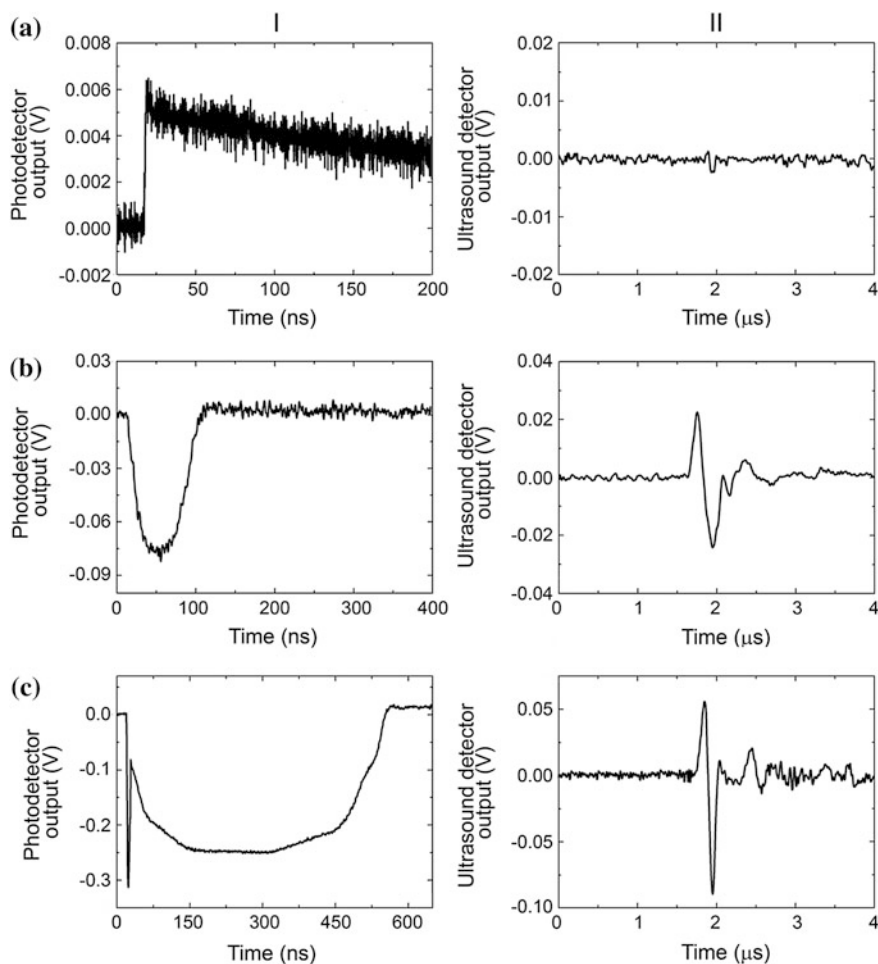


Fig. 32.4 Simultaneously obtained optical scattering (or extinction) (*left*) and acoustic (*right*) time responses of three different phenomena. **a** Transient heating of the gold nanoparticle and the media with a single laser pulse at a fluence below the PNB generation threshold. **b** Single transient vapor PNB generated around gold nanoparticle. **c** PNB accompanied by a stress wave that produces a sharp and short optical signal in the very beginning of the time response. Recreated by kind permission of AIP [116]

For the scattering image, we observed the relatively early saturation and non-linear behavior of the pixel image amplitude compared to the duration of the time response (Fig. 32.5a). Time-resolved scattering images were obtained under a fixed delay between the excitation and probe laser pulses. With an increase in the maximal PNB diameter and lifetime, the moment of illumination moved further from the moment when the PNB reaches its maximal diameter.

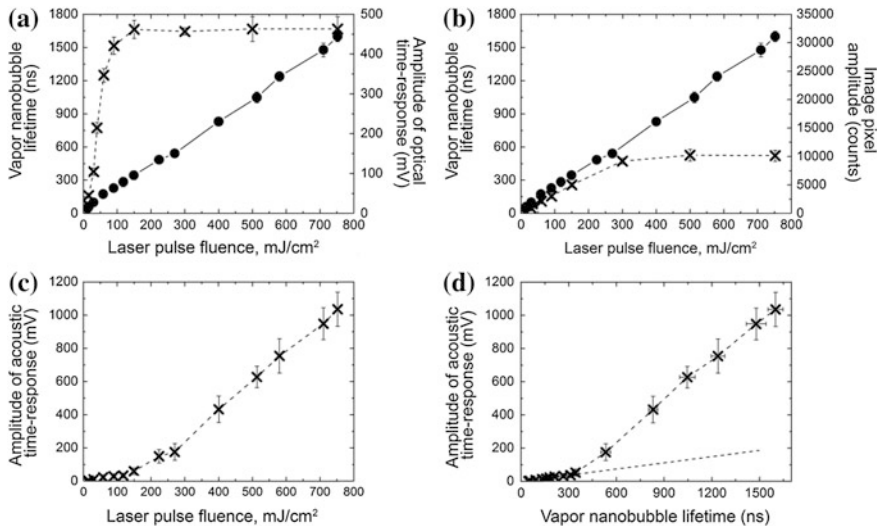


Fig. 32.5 Dependence of the PNB metrics upon the optical excitation fluence that determines the maximal size of PNB. **a** Lifetime (*dots*) and amplitude of the optical scattering time response (*cross*). **b** Lifetime (*dots*) of the optical scattering time response and the pixel image amplitude of the time-resolved optical scattering image (*cross*) at the fixed delay of 10 ns. **c** Amplitude of acoustic time response. **d** Amplitude of acoustic time response versus the lifetime of optical time response. Recreated by kind permission of AIP [116]

Next, we analyzed the amplitude of optical scattering time responses (Fig. 32.5b). The dependence of their amplitude and lifetime upon the fluence showed a nonlinear saturation of the amplitude compared to the lifetime. The nonlinear behavior of the response can be explained by the effect of the limited numerical aperture of the collecting lens and the blocking effect of the large bubble on the probe beam. In addition, at high excitation energies, the amplitude of the response can be influenced by the concurrent optical signal associated with the stress wave. Therefore, the use of the optical response amplitude as a metric of the bubble or even of the energy conversion efficacy is not appropriate and may lead to artifact data for the photothermal responses of ensemble of gold NPs [118]. In contrast, the dynamics of the optical response can be much better quantified through the lifetime that correctly describes both the maximal diameter of a PNB and the efficacy of the energy conversion.

The amplitude of the acoustic response demonstrated two quasi-linear zones (Fig. 32.5c). To explain their origin, we detected the acoustical and optical responses simultaneously for single PNBs under a wide range of excitation fluences and plotted the acoustic amplitude as a function of the PNB lifetime (Fig. 32.5d). Two zones for acoustic signals became even more pronounced with an apparent threshold associated with the PNB lifetime around 350 ns that also corresponded to the fluence of 150 mJ/cm². A detailed analysis of the optical time responses revealed one difference: the optical responses of PNBs larger than

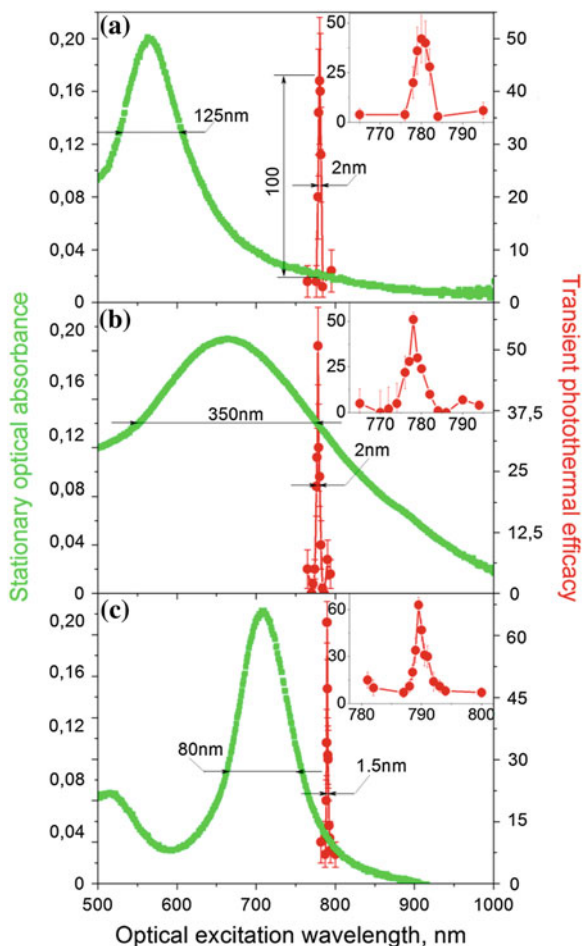
350 ns included an additional component that can be attributed to a stress wave generated due to the high laser-induced temperature in a gold NP (Fig. 32.4c-II). Its additional impact added to the PNB-generated pressure at the acoustic sensor. However, this effect occurs when the PNB lifetime exceeds 300 ns, which corresponds to the maximal diameter above a micrometer, so this is no longer a “nano” bubble. For smaller bubbles of nanosize, both the acoustic amplitude and the duration of the optical scattering time responses provided almost linear signal-energy dependence and showed a good correlation.

The best quantitative analysis of vapor PNBs in the widest range of excitation energies and bubble diameters can be achieved by measuring the duration (lifetime) of the optical scattering time response by using a low-power continuous laser and matching photodetector. In the case of opaque media, the amplitude of the acoustical time response provides good sensitivity and linearity in a range of excitation conditions that are limited by the onset of stress waves that additionally increase the amplitude of the nanobubble signal. The simultaneous use of two or three of these methods provides the best results in the identification, imaging, and measuring of transient nanobubbles in a single event experiment [116].

32.2.4 Spectral Properties of Plasmonic Nanobubbles

An ability to combine high NIR PT efficacy with gold nanospheres is an attractive alternative to specifically engineered NPs with NIR resonances such as nanorods, nanocages, and nanoshells. We recently observed 20–130-fold amplification of the PNB generation efficacy of solid gold nanospheres in a very narrow (2–3 nm) NIR region at 780 nm (far from their regular plasmon resonance at 530–540 nm), where they are usually considered to have poor PT performance (Fig. 32.6a). The experiments were performed with single 70 ps laser pulses at low fluence levels (10–100 mJ/cm²) associated with the generation of vapor PNBs around gold nanospheres in water. The lifetime of the nanobubble was used as the PT metric because it correlates to the thermal energy released by the NP [119, 120]. NIR amplification of the PT efficacy of nanospheres achieved or exceeded their PT efficacy at the visible wavelength of plasmon resonance. The amplification effect and the NIR peak wavelength of 780 nm were reproduced for a wide range of laser pulse fluence from 10 to 500 mJ/cm², NP diameters (20–120 nm), aggregation states (single NPs, aggregated NP clusters and suspensions of NPs), and environments including in vitro and in vivo conditions [105, 121]. The observed NIR amplification effect has a low optical fluence threshold (>10 mJ/cm²), and its transient and resonant nature can be associated not with the nanosphere itself, but with a transient nanostructure that creates a high optical absorbance at 780 nm (where a sphere itself does not absorb well). Thus, solid gold nanospheres, which are cheap, easily available, biologically safe, stable, and easily functionalized, can be successfully employed instead of more complex and unstable NIR-engineered NPs.

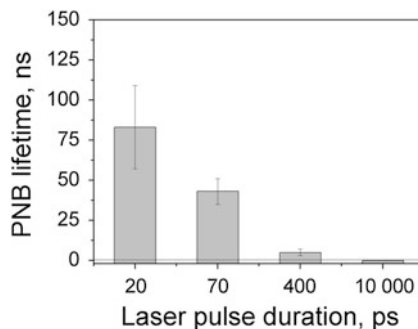
Fig. 32.6 Spectra of the photothermal efficacy of gold solid spheres (a) [121], nanoshells (b), and nanorods (c) (recreated by kind permission of ACS [119]) under stationary (green) and nonstationary transient high energy (red) optical excitation with short 70 ps single laser pulse



Similar narrow spectral peaks were also observed for other types of NPs, gold nanorods, and hollow nanoshells (Fig. 32.6b, c) [119]. Though these NPs are specifically engineered for NIR, the observed 1–3-nm-wide peaks were significantly red-shifted and narrowed compared to their preset properties (for nanorods, plasmon resonance wavelength is at 710 nm and spectral width >100 nm, and for hollow nanoshells, plasmon resonance wavelength is at 665 nm and spectral width >160 nm).

Such narrow PT spectral peaks were never observed previously for single NPs and for their random clusters in a wide range of the excitation pulse fluences, not only near the threshold of PNB generation. Therefore, the discovered phenomenon is not a threshold energy-specific effect like in the case of nonlinear spectroscopy methods [122, 123]. On the contrary, the PT output of the NP can be precisely

Fig. 32.7 Dependence of the PNB lifetime upon duration of the laser pulse (532 nm, 100 mJ/cm²). PNBs were generated in water around isolated solid gold spheres of 60 nm



controlled by varying the laser fluence [78, 119, 121]. A wide range of tested NP parameters and conditions revealed the very stable and universal nature of the observed nonstationary PT amplification and spectral narrowing.

Discovered NIR spectral peaks depend on the duration, not energy, of the excitation laser pulse. We observed very strong influence of the laser pulse duration (from 20 ps to 10 ns) on the PNB generation (Fig. 32.7). The shortest pulses delivered the maximal efficacy. For longer pulses of 400 ps and 10 ns, we observed strong suppression of the PNB generation for all types of NPs, spheres, rods, and shells [119]. This suppression effect can be explained by general thermal diffusion and, in addition, by the dynamic modification of the plasmonic structures during NP interaction with a laser pulse. Thus, only short laser pulses (< 400 ps) induced large PNBs and provided the described above spectral narrowing.

To summarize, these results demonstrate the existence of the nonstationary mechanism with unprecedented amplification and spectral narrowing of the PT efficacy of metal NPs.

32.3 Part II Generation and Detection of Plasmonic Nanobubbles in Cells and Tissues

32.3.1 Cellular Specificity of Plasmonic Nanobubbles

The most important feature of the PNB generation mechanism that distinguishes PNBs from all other nanoprobe and nanosources is the optical energy threshold for the bubble generation around gold NP (Fig. 32.8a). Most of other photoinduced phenomena have nonthreshold nature (including fluorescence, photothermal, and photoacoustic phenomena). We have found that this threshold energy radically depends upon the diameter of the NP and the size of the NP clusters: The threshold energy decreases with the size (Fig. 32.8b) [124]. A low laser pulse fluence was sufficient to generate PNBs around large NP clusters but was not sufficient to induce PNBs around single NPs or small NP clusters. This was demonstrated by exposing multiple NP clusters of various sizes to a single laser pulse of low

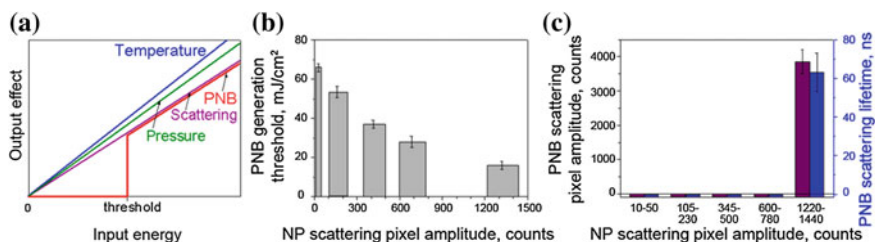


Fig. 32.8 **a** Threshold nature of the PNB generation compared to nonthreshold nature of other photoactivated phenomena (photoacoustic effect due to thermo-elastic expansion, optical scattering, and photothermal effect). **b**, **c** Parameters of PNBs generated around gold NP clusters in water for gold nanoshells [124]. **b** PNB generation threshold fluence of the excitation laser pulse as function of NP cluster size (measured through optical scattering amplitude of NP cluster image for individual clusters); **c** PNB lifetime and scattering brightness as function of the NP cluster size (measured through optical scattering amplitude of NP cluster image) at specific fluence of the excitation pulse (778 nm, 22 mJ/cm²)

fluence. We observed the selective generation of PNBs only around the largest NP clusters (Fig. 32.8c) whose threshold was lower than the applied fluence [124]. The PNB threshold for smaller clusters was above this fluence, and therefore, such small NP clusters did not return PNBs in response to optical excitation.

The dependence of the PNB threshold fluence upon cluster size can be explained through the mechanism of PNB generation around superheated NPs. Merged thermal fields of several tightly aggregated NPs form a common thermal field and vapor layer around the cluster. The initial vapor pressure in such a vapor layer is determined by the fluence of the laser pulse that is converted into heat by each NP in a cluster. Next, the external pressure of surface tension (that needs to be overcome to allow the expansion of the vapor) is inversely proportional to the radius of the vapor–liquid boundary [125–127] and, therefore, decreases with cluster size. We previously analyzed the mechanism of PNB generation around NP clusters versus single NPs [78]. In addition to the above thermal and hydrodynamic factors, NP clustering may enhance their optical absorbance [58, 128], thus additionally increasing the released thermal energy and the initial vapor pressure. All these factors cause the decrease in the PNB generation threshold fluence with cluster size. With the fluence of the excitation pulse below the threshold, the PNB does not emerge and, therefore, creates no impact, unlike NPs (Fig. 32.8c).

This unique property creates the fundamental opportunity to improve the cellular selectivity of PNBs in say, cancer cells, via cancer cell-specific clustering of gold NPs conjugated to cancer-specific vectors, such as antibodies. Target cell-specific formation of the largest gold NP clusters involves several steps (Fig. 32.9a):

- At the first stage, we used target-specific antibodies to provide higher accumulation of gold NPs at the membranes of target cells compared to the NP accumulation at membranes of nontarget cells. This stage did not provide desired specificity of the targeting but at the same time delivered much more NPs to target cells compared to nontarget cells.

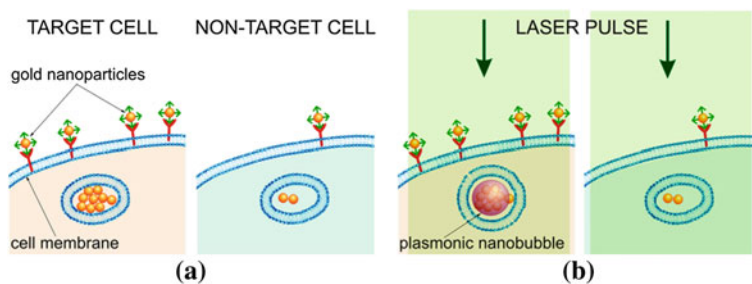


Fig. 32.9 PNBs and NPs in target (*left panels*) versus nontarget (*right panels*) cells. **a** Gold NP conjugates are collected at cellular membranes and are clustered during endocytosis resulting in the largest NP clusters in target cells. **b** Excitation laser pulse (*green*) of low fluence induces PNBs only around the largest NP clusters (i.e., only in target cells) because the PNB generation threshold fluence for single NPs and small clusters (nontarget cells) is higher than the fluence of the laser pulse

- At the second stage, we engaged receptor-mediated endocytosis so that target cells self-assembled the large clusters of gold NPs in their endosomal systems [104, 129–136].

The targeting parameters such as the concentration of NPs and the incubation time were optimized to achieve maximal difference in NP uptake between the target and nontarget cells. Such targeting does not eliminate the nonspecific uptake of NPs by nontarget cells; however, it provides the formation of the largest NP clusters only in target cells for target-specific generation of PNBs. Sphere- and shell-type NP conjugates did not induce any considerable cytotoxicity in either target or nontarget cells. The difference in the NP cluster size between cancer and normal cells create the difference in the PNB generation threshold fluence in cancer (low threshold) and normal (high threshold) cells so that the single laser pulse of specific fluence induces the PNB only in cancer cells (Fig. 32.9b).

Since the largest NP clusters can be selectively formed in target cells through the receptor-mediated endocytosis of NPs [104, 129–136], we further studied the NP cluster–PNB mechanism in living cells in order to compare the cellular specificity of NPs and PNBs under identical conditions of NP targeting and optical excitation. Several different molecular targets were investigated *in vitro* in cell systems that included cells with a high level of molecular target expression (target cells) and a low level of the expression of the same molecular target (nontarget cells). We studied cell models representing lung (A549), head and neck (HN31), prostate (C4-2B), epithelial (HES, a WISH/HeLa derivative), and blood (Jurkat J32) cancers, and also human T cells that are used for gene therapies of cancer. In all six cases, we observed a higher level of NP signals in target cells, but all nontarget cells also showed a significant level of NP uptake and formation of NP clusters (Figs. 32.10a, 32.11a) so that the ratio of the NP signal for target versus nontarget cells was below 10. However, higher pixel image amplitudes in

target cells indicated the formation of the largest NP clusters in target cells. Next, target and nontarget cells were identically treated with single laser pulses within the range of pulse fluences for PNB generation around NP clusters. For each cell model, we experimentally determined the level of excitation pulse fluence that provided the generation of PNBs mainly in target cells and did not induce PNBs in nontarget cells (Fig. 32.10b–d). The optical scattering images and time responses of individual cells were processed to compare the corresponding metrics for NP accumulation (Fig. 32.11a) and PNB generation (Fig. 32.11b, c) in target and nontarget cells. Compared to NP signals, the PNB signals showed a much higher discrimination between target and nontarget cells in all six. Cellular specificity of NPs and PNB was quantitatively shown through the ratios of the target cell signals to the corresponding signals in nontarget cells (shown as colored numbers in each frame of Fig. 32.11). Compared to NPs, the PNBs improved cellular specificity in some models by more than one order of magnitude. While the nontarget cells showed significant uptake of NPs and even their potential aggregation into small clusters, no PNBs, or very small ones, were observed in nontarget cells under identical treatment conditions (Figs. 32.10 and 32.11) [124].

The difference in cellular specificity of NPs and PNBs can be clearly seen in experiments with a co-culture of target (labeled with green fluorescent protein for identification) and nontarget cells (Fig. 32.10). At a specific fluence of the excitation laser pulse (25 mJ/cm² at 778 nm), only target cells yielded PNBs while even adjacent nontarget cells with gold NPs did not. Such a difference between NP and PNB signals was observed for all six cell models: adherent (HN31, HES, and A549) and suspension (C4-2B, T cells, and Jurkat) cells, and for all molecular targets: receptors (EGFR, CD3, and PSMA) and glycoproteins (MUC1). These results indicate the universal nature of the high cellular specificity of PNBs compared to that of gold NPs. Therefore, PNB provided better discrimination between target and nontarget cells even when such cells were heterogeneously mixed [124].

As can be seen from Fig. 32.11, the PNB method can better discriminate between target and nontarget cells compared to NPs. Cellular specificity of PNBs was more than one order of magnitude higher than that of NPs (this can be clearly seen by comparing the ratios of the corresponding signals for target and nontarget cells) [124]. Such an effect was achieved through the cluster-threshold mechanism of PNBs that prevents the generation of PNBs around nonspecifically targeted single NPs (and their small clusters).

32.3.2 NP Clustering and Plasmonic Nanobubbles Generation and Detection in Cancer Cells

The mechanism of the formation of mixed gold NP–drug carrier clusters and on-demand generation of PNBs around such clusters was studied in a co-culture of drug-resistant head and neck squamous cell carcinoma (HNSCC) cells and normal cells.

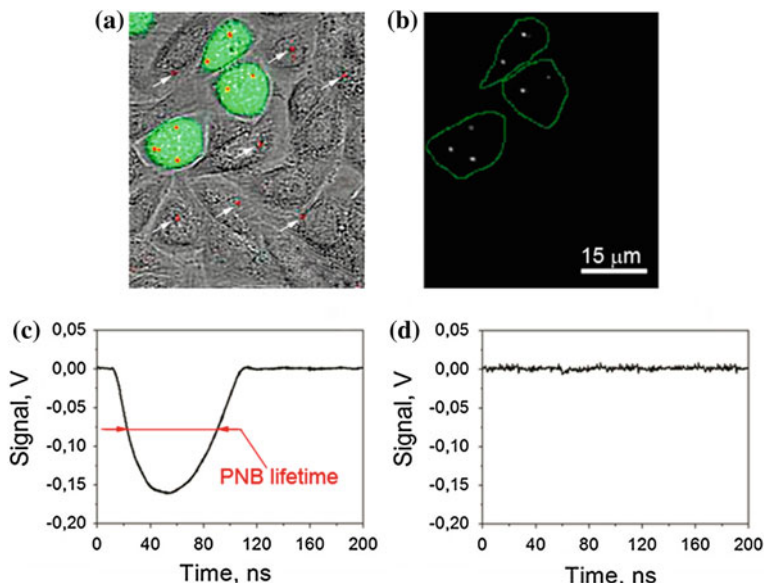


Fig. 32.10 Images and signals of gold NPs and PNBs in co-culture of target (HN31, labeled with green fluorescent protein for identification) and nontarget (NOM9) cells identically treated with 60 nm gold NSP-C225 conjugates (specific to EGFR that is overexpressed in target cells) [124]. **a** Overlay of bright field, fluorescent, and scattering images shows target cells (*green*) and gold NPs (*red*) that can be found in both types of cells (the arrows show NP clusters in nontarget cells); **b** time-resolved scattering image of the same field shows PNB images (*bright white spots*) only in target cells; **c, d** optical scattering time responses of individual target **c** and nontarget **d** cells show the PNB-specific signal only for target cell and the definition of the PNB lifetime of PNBs; time is measured from the moment of the exposure to the excitation laser pulse

32.3.2.1 Selective Formation of Mixed Intracellular Clusters of Gold NPs and Doxil

The NP clustering and co-localization with Doxil was analyzed with confocal microscopy in scattering (for gold NPs) and fluorescent (for Doxil that contains fluorescent doxorubicin) modes (Fig. 32.12a). A co-culture of HN31 (HNSCC) and NOM9 (normal) cells was treated with C225 conjugates of solid gold 60 nm spheres and Doxil liposomes. The antibody C225 (Erbixux) was clinically proven to target the epidermal growth factor receptor (EGFR) in HNSCC [137–139] and provided intracellular clustering of gold NP-C225 conjugates through the mechanism of EGFR-mediated endocytosis [103, 129, 130]. Individual HN31 cells were identified through the fluorescence of the transfected green fluorescent protein (Fig. 32.10a). Analysis of the confocal images of cancer cells revealed complex clusters with gold NPs (blue in Fig. 32.12a) co-localized with Doxil (red in Fig. 32.12a). Adjacent normal cells also showed occasional NPs due to their nonspecific accumulation, but no large NP–Doxil clusters were detected in normal

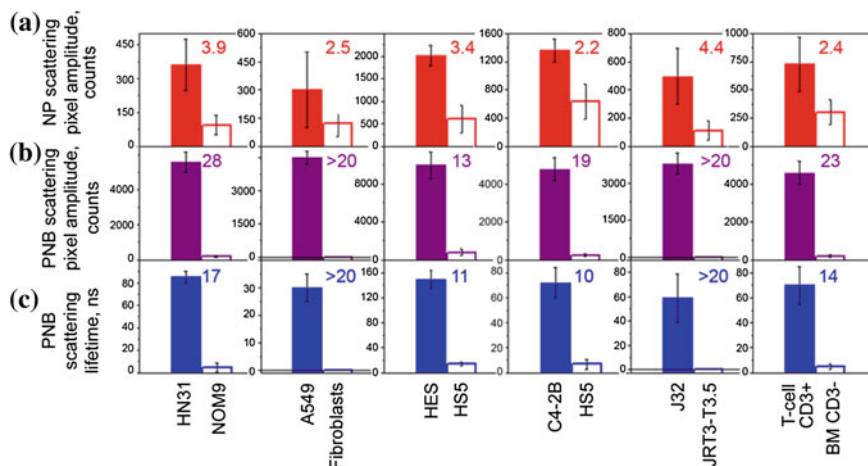


Fig. 32.11 Cell population-averaged levels of optical scattering signals obtained for individual target (*solid bar*) and nontarget (*hollow bar*) cells in six cell models represented by target/nontarget cells/molecular targets [124]: squamous cell carcinoma, HN31/NOM9/EGFR (treated with 50 nm NS-panitumumab conjugates); lung cancer, A549/Fibroblast/EGFR (treated with 60 nm NSP-C225 conjugates); epithelial cancer, HES/HS5/MUC1 (treated with 60 nm NSP-214D4 conjugates); prostate cancer, C2-4B/HS5/PSMA (treated with 60 nm NSP-anti-PSMA conjugates); leukemia, J32/JRT3-T3.5/CD3; and human T cells, T cell/BM/CD3 (treated with 60 nm NSP-OKT3 conjugates) for: row (a) (*red*): gold NP amplitude of scattering image of gold NPs (a metric for the uptake of NPs by cells); row (b) (*purple*): time-resolved scattering image amplitudes of PNBs; row (c) (*blue*): PNB lifetimes. The ratio of the signals for target/nontarget cell is shown for each parameter and cell model and indicates the cellular specificity of NPs (row (a)) and PNBs (rows (b, c))

cells (Fig. 32.12a). Thus, the complex large NP-Doxil clusters were selectively self-assembled only by cancer cells during the separate administration of Doxil and gold NPs [105].

32.3.2.2 Generation and Detection of Plasmonic Nanobubbles in Individual Cells

We next determined the conditions of the PNB generation in the complex NP-Doxil clusters in cells. PNBs were generated by exposing the co-culture of HN31 and NOM9 cells to single NIR laser pulses (70 ps, 780 nm) of broad diameter (that provided the simultaneous irradiation of cancer and normal cells) and varying laser fluence (the energy per unit of square) in the range of 10–100 mJ/cm². In this work, we applied for the first time the safest combination of FDA-approved solid gold spheres and NIR laser radiation in a low dose that provides the deepest tissue penetration and the minimal biodamage [140]. Optical scattering time-resolved imaging (Fig. 32.12b) and optical scattering time responses were obtained for

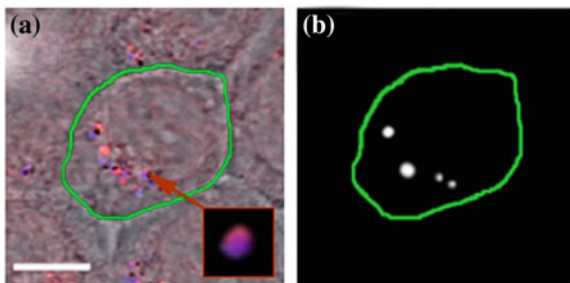


Fig. 32.12 PNB-enhanced endosomal escape in vitro. **a** Confocal microscopy images of cancer (green boarder) and normal (adjacent) cells show NPs (blue) and Doxil (red) co-localized in the large mixed clusters (inset) only in cancer cell, while adjacent normal cells show nonspecific uptake of NPs and Doxil (scale bar is 5 μm); **b** time-resolved optical scattering image of the same sample shows PNBs selectively generated with a broad single laser pulse (780 nm, 70 ps, 40 mJ/cm²) only in cancer cell and their co-localization with NP–Doxil cluster. Recreated by kind permission of Ivyspring International Publisher [105]

individual cancer and normal cells simultaneously with the excitation laser pulses and were employed to image and quantify PNBs in the irradiated cells.

Both images (Fig. 32.12b) and time responses [105] showed the cancer cell-specific generation of PNBs, while normal bystander cells in the co-culture produced no or very small PNBs in a wide range of laser pulse fluences (Fig. 32.12b). This demonstrated the selectivity of the cluster-threshold mechanism of PNB generation. The comparison of the optical scattering images of PNBs (Fig. 32.12b) and NP–Doxil clusters (Fig. 32.12a) revealed their good co-localization in cells. Thus, the mixed NP–Doxil clusters acted as PNB sources, and the mechanical impact of PNBs was co-localized to Doxil liposomes. In this experiment, PNBs provided optical detection of cancer cells with high specificity and sensitivity.

32.3.3 NP Targeting, Plasmonic Nanobubbles Generation, and Detection in HNSCC Tumor In Vivo

In order to translate the achieved result in vivo and to address the impact of tissue on the propagation of light and NPs, we first studied the delivery of NPs, laser radiation, and the generation and detection of PNBs in a xenograft mouse model of HNSCC that used the same cancer cell line, HN31.

32.3.3.1 NP Delivery and Clustering In vivo

The formation of NP clusters in the tumor was imaged and quantified by using TEM microscopy and the PNB generation in the tumor slices. NP–C225 conjugates of solid gold 60 nm spheres were administered locally (intratumoral

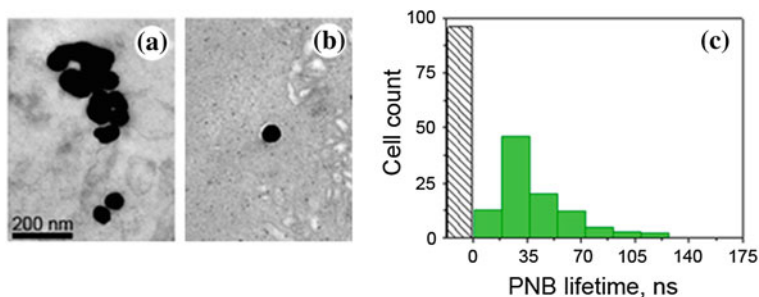


Fig. 32.13 NP-C225, solid gold 60 nm spheres conjugates in HNSCC-bearing mouse: transmission electron microscopy image of a tumor (a) and adjacent muscle tissue (b) in 24 h after systemic injection of NP-C225 to mouse [105]. c Histogram of the PNB lifetime obtained for individual cells in slices of tumor for cancer (green) and normal (gray) cells after being extracted from mice in 24 h after systemic administering of NP-C225. Recreated by kind permission of Ivyspring International Publisher [105]

injection of $1 \mu\text{L}$ at 9×10^{12} NP/mL ($0.8 \mu\text{g/g}$) and systemically (intravenous injection in a tail vein of $200 \mu\text{L}$ at 4.5×10^{10} NP/mL ($0.8 \mu\text{g/g}$) at two diameters of NPs, 20 and 60 nm). In 24 h after systemic administering 60 nm gold NP-C225, TEM analysis of the tumor and adjacent normal muscle tissue showed large clusters of gold NPs (an average size 297 ± 135 nm) only in the tumor (Fig. 32.13a), while nonspecific uptake resulted in occasional single NPs in normal tissue (an average size close to that of a single NP, 64 ± 15 nm, Fig. 32.13b). Thus, despite a nonspecific uptake of single gold NPs by normal tissues, the sources of PNBs, larger NP clusters, were observed only in tumors and not in normal tissues [105].

32.3.3.2 Selectivity of Plasmonic Nanobubble Generation in Tumor

Next, gold NP clusters were analyzed as PNB sources in tumor slices. Each individual cell in a slice was identically exposed to a single laser pulse, and the PNB lifetimes were obtained for cancer (fluorescently identified) and normal cells in a similar way to the above in vitro experiment. At the fluence of 40 mJ/cm^2 , single pulse excitation resulted in the generation of PNBs only in cancer cells, while normal cells did not generate PNBs under such a low fluence level (Fig. 32.13c). This result indicated that tumor-specific gold NP clusters (not present in normal cells and tissues) provided selective generation of PNBs only in tumor cells. The mechanism of such high selectivity is based on the dependence of the PNB generation threshold upon the size of the NP or its cluster: The threshold fluence decreases with the cluster size [79, 107, 124, 130]. The level of laser pulse fluence applied was below the PNB generation threshold for single NPs but above the PNB generation threshold for large NP clusters. These results correlated well to those obtained previously in vitro and demonstrated selective formation of NP

clusters and PNB generation only in tumor, while the nonspecifically taken gold NPs in normal tissue did not form clusters and therefore were unable to generate PNBs [105].

32.3.3.3 Detection of Plasmonic Nanobubbles In vivo in Opaque Tissue

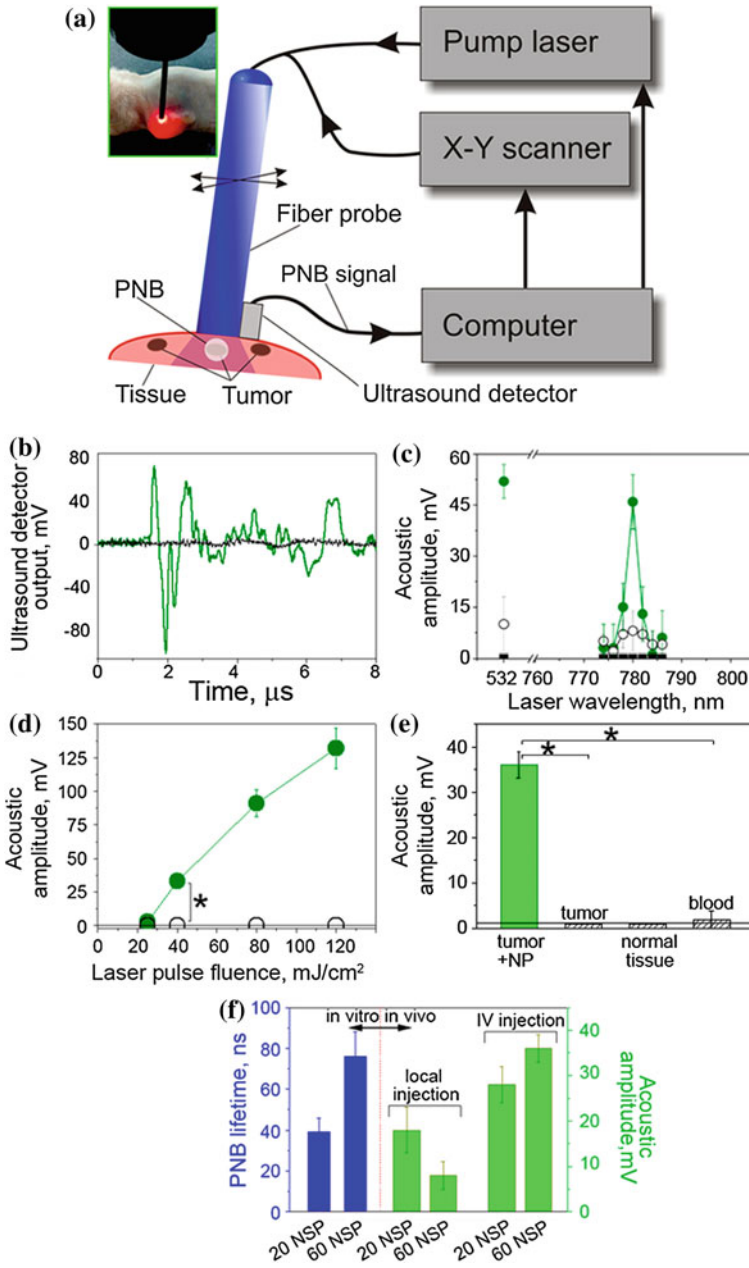
Due to the limited optical transparency of real tissue in animals, we replaced the optical detection of PNBs with the acoustic method (Fig. 32.14a). Briefly, the expansion and collapse of a PNB produce pressure pulses that can be remotely detected in opaque tissue in animals with an ultrasound detector as PNB-specific acoustic time responses (Fig. 32.14b). The amplitude of the acoustic response of a PNB was found to be almost linearly proportional to the optically measured lifetime of the same PNB. Thus, we employed the acoustic signal amplitude as an in vivo metric of PNB [105].

32.3.3.4 Near-Infrared Pulsed Excitation of Plasmonic Nanobubbles in Tumor

Next, in order to optimize the laser wavelength for NIR excitation, the acoustic amplitudes of PNBs were obtained as the spectra of the excitation laser wavelength in tumor and normal tissue in animals that received intravenous gold NP-C225 conjugates and for an intact tumor in animals that did not receive any gold NPs (Fig. 32.14c). Spectrum of the tumor in the NP-treated animal showed a 3 nm-wide peak at 780 nm. Other NIR wavelengths returned much lower signals comparable to the background level. The normal tissue of the NP-treated animal showed very small acoustic signals that were also comparable to the background level, while intact tumor returned zero signals under identical optical excitation (Fig. 32.14c). We concluded that the detected acoustic signals of the NP-treated tumor were associated with gold NP clusters that were selectively formed in the tumor cells as we found previously (Fig. 32.13a). We therefore employed the NIR wavelength of 780 nm for the experiments in vivo [105].

32.3.3.5 Real-Time Detection of the Tumor with Acoustic Signals of Plasmonic Nanobubbles

The specificity and sensitivity of the tumor detection were studied through the amplitude of acoustic signal of PNBs that was measured as function of tissue type and of the laser excitation fluence. The amplitude of PNB signal increased with the fluence of the excitation laser pulse (Fig. 32.14d). It should be noted that just a single laser pulse was required to detect a tumor-specific acoustic signal. The duration of this diagnostic process was limited by the speed of the ultrasound detector and was below one millisecond.



◀ **Fig. 32.14** PNBs in HNSCC-bearing mouse. **a** Functional diagram of the experimental setup. Optical fiber delivers short laser pulse through the surface of the tissue, and PNBs are detected with ultrasound detector, which signals, the scan of the fiber and laser pulse generation are controlled by computer program; **b** acoustic responses to single laser pulses (70 ps, 780 nm, 40 mJ/cm²) obtained from a tumor (*green*) and adjacent muscle (*black*) in mouse systemically treated with 60 nm solid gold sphere conjugates, NP-C225; **c** spectrum of PNB amplitudes of acoustic responses obtained from a squamous cell carcinoma tumor (*solid green*) and normal tissue (*hollow black circles*) of a mouse systemically treated with C225-conjugated 60 nm gold spheres, tumor in intact animal (*solid black squares*) and (40 mJ/cm²); **d** dependence of the amplitudes of acoustic responses upon laser pulse fluence (energy per square unit) for the same animals obtained from the tumor (*green*) and adjacent muscle (*black*) (**p* < 0.001); **e** acoustic amplitudes obtained during the scans of the tumor, muscle and blood of NP-treated animals and of a tumor of an intact animal (**p* < 0.001); **f** dependence of PNB lifetime (*blue*, optical response obtained from individual tumor cells in vitro) and the acoustic amplitude of PNB (*green*, acoustic response obtained from a tumor in animal) as function of NP size (20 nm and 60 nm) and in vivo administration route (local intratumor injection and intravenous injection) under identical laser excitation (single pulse, 70 ps, 780 nm, 40 mJ/cm²). Recreated by kind permission of Ivyspring International Publisher [105]

During the laser scans of a tumor and normal adjacent tissue in the NP-treated animals, the detectable acoustic signal of the PNBs was observed only for the tumor and not for normal muscle tissue and blood (Fig. 32.14d). Tumors in intact animals (that did not receive gold NPs) did not yield any detectable acoustic signal under the identical fluence of laser pulse (Fig. 32.14d). Therefore, the optical fluence of 40 mJ/cm² was below the bubble generation threshold in blood and other normal tissues for the employed NIR wavelength (780 nm) and duration (70 ps) of laser pulse. The results demonstrated high sensitivity, specificity, safety, and speed of tumor detection in a single NIR laser pulse procedure [105].

32.3.3.6 Optimization of the NP Size and Delivery Route for Plasmonic Nanobubble Generation In Vivo

In addition, we analyzed the influence of the NP diameter and delivery route on PNBs generation in vitro and in vivo. The intravenous systemic delivery of NPs resulted in larger PNBs compared to local intratumor injection of the same NPs under identical optical excitation (Fig. 32.14e). In both cases, the NP-C225 conjugates were administered 24 h prior to the laser treatment. Larger 60 nm NPs generated larger PNBs compared to smaller 20 nm NPs both in vivo and in vitro conditions (Fig. 32.14f). We therefore used systemic intravenous delivery of solid gold 60 nm sphere conjugates, NP-C225, for the next, therapeutic stage.

32.3.4 Plasmonic Nanobubble Diagnostics Versus Nanoparticle-based Diagnostic Methods

The diagnostic part of PNB theranostics *in vivo* is technically close to photoacoustic methods [141], but PNBs provide higher sensitivity and specificity of tumor detection compared to broadly used gold NPs as photoacoustic probes. Conventional photoacoustics employ acoustic emission from all NPs, instead of cancer cell-specific generation of PNBs only around NP clusters (Fig. 32.10c, d, 32.14b). Under identical optical excitation, PNBs emit stronger pressure pulses compared to those emitted by gold NPs [142]. This explains the high specificity of PNB signals as shown in Fig. 32.14b, c and the high sensitivity that allows to detect even single tumor cells among normal ones [103]. Thus, the PNB method provided high sensitivity, specificity, and speed of tumor detection in a single NIR laser pulse procedure [105] under relatively low optical fluence of 40 mJ/cm², which is within the medical safety limits for laser radiation [143] and with the safest solid gold spheres.

To summarize, PNBs present excellent diagnostic opportunity via optical scattering detection *in vitro* and acoustic detection *in vivo*. In both cases, PNBs provide much higher cancer cell specificity than any nanoparticle-based imaging can provide because the threshold nature of PNBs overcomes the problem of unavoidable nonspecific uptake of imaging probes by nontarget cells.

32.4 Part III Theranostic Applications of Plasmonic Nanobubbles

One of the major limitations of traditional treatments of cancers and other dangerous diseases is the inability to surgically remove a pathology completely without having to remove large areas of normal tissue that serve critical functions. For example, residual tumor cells form the nidus for local recurrences and delayed metastases, which are seen commonly in head and neck, prostate, and other cancers. Not only does this profoundly impact patients' overall survival, but also their quality of life, due to extensive treatment-related anatomic and functional alterations. The residual cancer cells at the surgical margins often show high resistance to local and systemic adjuvant chemotherapy and radiotherapy [12], thus requiring toxic levels of these treatments. This is of particular concern in HNSCC, the sixth most common cancer diagnosis worldwide, with an estimated 263,000 newly diagnosed cases and over 128,000 deaths occurring yearly [13]. Hence, there is a critical need to develop novel diagnostic and therapeutic modalities that not only complement current therapies to enhance tumor control, but also simultaneously limit the treatment-related morbidity that ensues from treatment intensification, and can be applied as intra- or postoperative treatments.

Recently introduced approaches have employed NPs and external energies to develop putative tumor-targeting capabilities through drug delivery [144–161], hyperthermia [25–28, 100, 162–167], and photodynamic therapy [28, 168, 169]. However, the promises of these new modalities did not provide their fast translation from the laboratory to the clinic for the following reasons: (1) low NP targeting specificity, (2) tumor cell heterogeneity, (3) resistance of phenotypes [12, 144, 145], and (4) NP or energy-delivery toxicities [25–27, 100, 161–166, 170–172]. Therefore, the development of novel technologies that will (a) selectively detect and eliminate drug-resistant residual cancer cells to prevent local and regional recurrence, (b) preserve the functionality of normal tissues and (c) reduce non-specific toxicity, is highly significant. In addition, an ability to unite both tumor detection and its treatment in one real-time intraoperative theranostic procedure will improve the principal limitations of cancer surgery cited above.

In order to overcome the limitations of the NP- and external energy-based medicine, we recently introduced a new class of threshold-activated cellular nanoagents, called PNBs. A PNB is a laser pulse-induced nanoscale explosive event that develops only if the energy (fluence) of laser pulse exceeds specific threshold of the evaporation of NP environment, a vapor nanobubble and not a NP, although it employs a gold NPs or their cluster to convert optical energy into heat for the evaporation of the liquid surrounding superheated NP. The major difference that distinguishes PNBs from existing nanoagents is their on-demand threshold and transient nature, dynamic tunability, and mechanical, not thermal, therapeutic mechanisms [103, 104, 106, 173]. PNBs offer several unique opportunities that are not addressed by current methods (both traditional and those using various NPs and external energies). These are as follows: (1) broad-spectrum efficacy against the major mechanisms of drug resistance, (2) selectivity due to efficient discrimination of cancer from normal cells, and (3) multifunctionality of diagnosis (through optical and acoustic signals [79, 103, 104]) and guided cell level therapeutics [103, 104, 106, 107, 173].

Based on the above, we hypothesized that the synergistic effect of PNBs coupled with low doses of traditional cytotoxic chemotherapies, gold NPs, and optical energy would rapidly and selectively eliminate drug-resistant microtumors in a single pulse treatment (Fig. 32.15). We further hypothesized that the acoustic detection of PNB will provide simultaneous diagnostic tumor imaging and guidance of drug delivery (Fig. 32.15). Utilizing models of HNSCC, we studied the *in vitro* and *in vivo* PNB generation, detection, and intracellular delivery of encapsulated drug (Doxil) with the focus on providing high diagnostic and therapeutic efficacy and reducing nonspecific therapeutic toxicity and the treatment time in a single theranostic procedure.

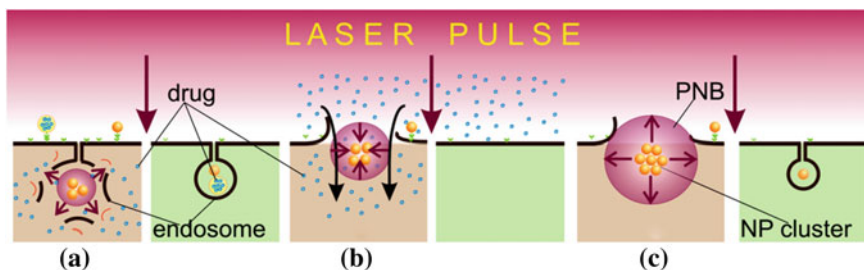
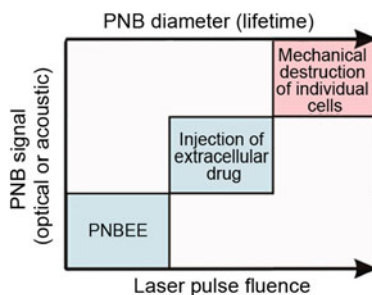


Fig. 32.15 Variation in the size of NP clusters in cancer cells (*brown*) results in different PNBs in response to identical optical excitation. **a** The smallest PNB supports endosomal escape of internalized drug; **b** medium PNB injects free extracellular drug; **c** the largest PNB mechanically destroys the cell. Normal (*green*) cells cannot generate PNBs with nonspecifically taken NPs due to the higher threshold of PNB generation around single NPs or small NP clusters

Fig. 32.16 Therapeutic mechanisms of PNB are determined by its maximal diameter (lifetime) which, in turn, is controlled via the laser pulse fluence



32.4.1 Therapeutic Functions of PNB

The size of the intracellular NP cluster and the optical fluence determines the maximal size of the PNB that, in turn, determines three different PNB therapeutics (Fig. 32.16, Table 32.1):

1. Intracellular drug release with a small noninvasive intracellular PNB that being co-localized with internalized by cancer cell therapeutic nanocarriers (liposomes, micelles, and other drug carriers) disrupt them and endosome and instantaneously eject the drug into the cellular cytoplasm (plasmonic nanobubble-enhanced endosomal escape—PNBEE) [105, 173].
2. Plasmonic nanobubble-induced injection of the extracellular drug (PNBII) [106, 174–177] employs larger PNBs that transiently perforate cellular membrane and create a small hole. Furthermore, expanding and collapsing nanobubble creates the localized jet near the membrane that injects the external solution into the cells much faster than this is done through the gradient-induced diffusion.

Table 32.1 Plasmonic nanobubbles therapeutic mechanisms

Mechanism	PNBEE	Injection	Destruction
PNB function and mechanism	Disruption of drug capsules and endosomes, ejection of drug into cytoplasm	Transient disruption of cellular membrane and induction of inbound nanojet that injects external drug into cytoplasm	Explosive and irreversible disruption of cellular membrane and other components
Targeting components	Drug capsules co-localized with gold NPs in mixed endosomal clusters	Free extracellular drug and gold NPs	Gold NPs
PNB range, ns	25–50	40–90	150–300

3. Even larger PNB with the maximal size exceeding that of the cell mechanically destroy the cell via the instantaneous lysis [104, 129, 177–181]. Each of these mechanisms employs PNBs of a specific size (lifetime).

32.4.2 Drug-Free Mechanical Destruction of Cancer Cells

The direct mechanical destruction of cells with relatively large PNBs (lifetime > 150 ns) does not require any drug and works through the explosive disruption of the cellular membrane and other components and can be defined as immediate lysis, not apoptosis or necrosis [104, 129, 177–181]. The PNB destruction of a cell is a mechanical process contrary to the widely used NP-based hyperthermia. A head-to-head comparison of PNB and hyperthermia in a co-culture of target and nontarget cells pretreated with cancer cell-specific gold conjugates demonstrated the higher therapeutic efficacy and selectivity of PNBs versus hyperthermia (Fig. 32.17). The PNB treatment was realized with a broad single laser pulse, at 40 mJ/cm². Most of cancer cells (97 %) died in 72 h after the PNB treatment, while most of the normal cells survived the PNB treatment (cell death level was <21 %), even those adjacent to the cancer cells where PNBs were generated (Fig. 32.17a). The level of cell destruction correlated with that of PNB lifetime >150 ns. In contrast, hyperthermia mode applied to the same cells under a reduced fluence of laser pulses (40 Hz for 10 min) required a 600-fold higher optical dose to destroy the cancer cells (61 %), but at the same time destroyed 91 % of normal cells (Fig. 32.17b) [175]. This proof of principle experiment confirmed the higher efficacy and selectivity of PNBs over nanohyperthermia.

Mechanical nature of the cell destruction was studied with a scanning electron microscope. Figure 32.18a, b shows the cell after the incubation with gold NPs. Gold NPs were initially accumulated at the cellular membrane (Fig. 32.18) and eventually were internalized due to receptor-mediated endocytosis (Fig. 32.18b). The cells were exposed to laser pulses with parallel monitoring of the PNBs and their lifetime (size). Cells were fixed with glutaraldehyde immediately after the

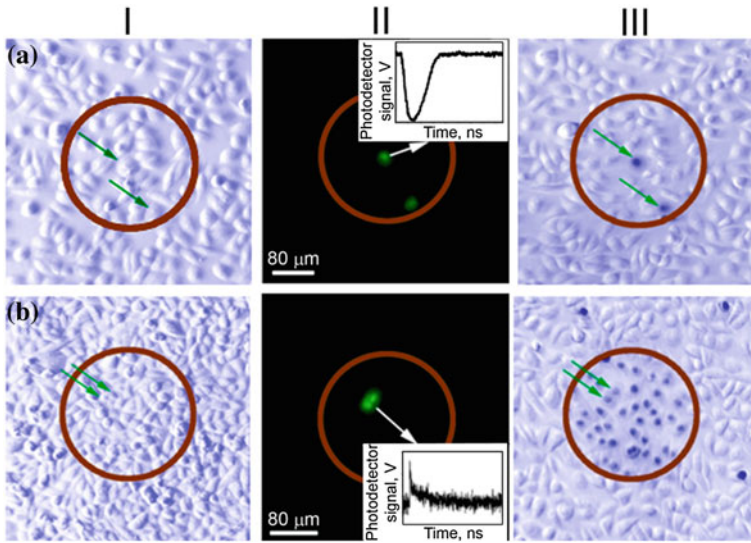


Fig. 32.17 **a** PNB single pulse at 40 mJ/cm^2 ; **b** NP-hyperthermia at 24 J/cm^2 treatments of a co-culture of normal and squamous cell carcinoma (green or shown with green arrows) cells identically treated with gold NPs. I, II: before and III after treatment (blue—dead cells, white—live cells). The time responses of cancer cells show a PNB (insert in II(a)) and heating–cooling process (insert in II(b)) [175]

exposure to laser pulses (within 1 min). Figure 32.18c and d shows the cells after the exposure to a single pump laser pulse that resulted in the PNB with $25 \pm 5 \text{ ns}$ lifetime (the 1st PNB) and $300 \pm 42 \text{ ns}$ lifetime (ablative, the 2nd PNB), respectively. While the first PNB did not change the cell structure (Fig. 32.18c vs. b), the second, bigger PNB had a dramatic effect on the size, shape, and structure of the cell (Fig. 32.18d vs. c, b). Such changes assume the mechanical damage of the membrane and presumably the cytoskeleton [104].

32.4.3 Plasmonic Nanobubble-Induced Injection Method of Drug Delivery

The injection of free extracellular drugs uses PNBs of larger size and is aimed at increasing the efficacy of conventional chemotherapy that employs systemic drug delivery at high doses due to their poor penetration through cellular membrane. PNB-induced transmembrane injection into target cells overcome this barrier and allow for lower drug concentrations to be used. This therapeutic mode uses PNBs for active and fast injection of the external drug through the cellular membrane by inducing a transient hole in the membrane and inbound jet. Unlike other methods of drug delivery, PNB injection uses active injection instead of passive diffusion of

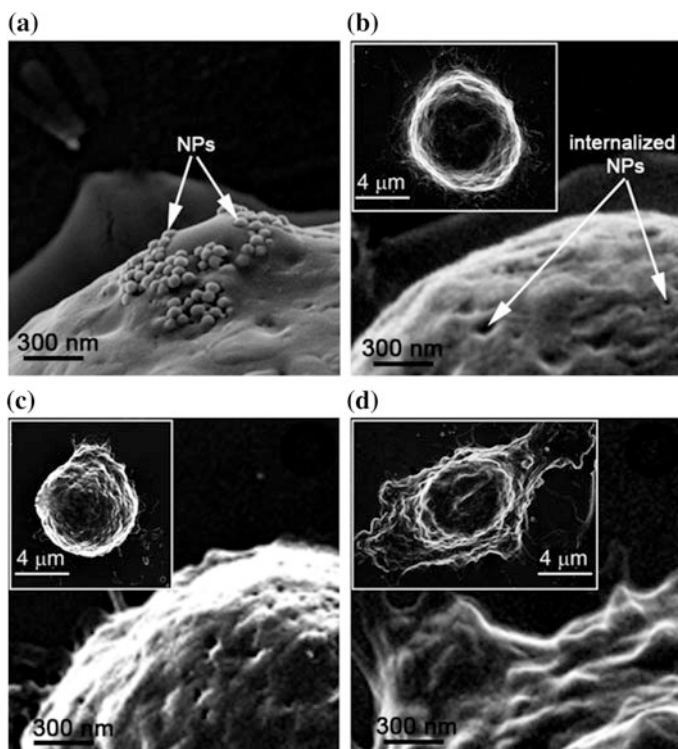


Fig. 32.18 Scanning electron microscopy images of cancer cells after the incubation with gold NPs show their membrane coupling (a) and internalization (b), and the result of the exposure to a single pump laser pulse that resulted in the noninvasive PNB with the lifetime of 25 ± 5 ns (c), and the ablative PNB with the lifetime of 300 ± 42 ns (d). The inserts show the images of the whole cells. Recreated by kind permission of Elsevier [104]

the drug. Unlike other optoinjection methods, the PNB method is cell specific even when many cells are simultaneously exposed to a laser pulse, due to the cellular specificity of PNB generation instead of the perforation of all cells, target and nontarget, as is typical for current optoinjection methods. PNBII method thus can be used for drug delivery and gene transfer [106, 174–177]. It was evaluated for multifunctional processing of heterogeneous cells suspension to perform simultaneous injection of one cell subtype and destruction of the another cell subtype [177].

The heterogeneous cell system was modeled by mixing NSP–OKT3-targeted and NS–OKT3-targeted J32 cells that modeled human T lymphocytes. NSP–OKT3-targeted cells were labeled with blue fluorescent marker (DAPI) to identify the cells and their nuclei, and NS–OKT3-targeted J32 cells were labeled with red fluorescent marker (calcein red) to identify the cells and to monitor their integrity and viability [182] after PNB generation. Then, the blue and red cells were mixed into one suspension to model a heterogeneous cell system, and green fluorescent

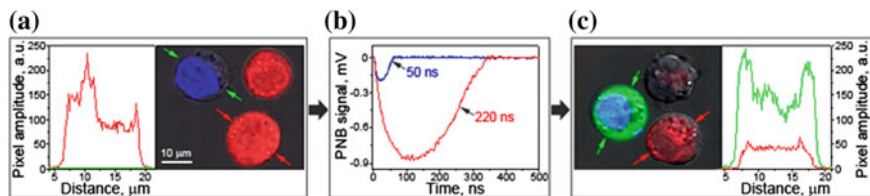


Fig. 32.19 **a** J32 cells with intracellular clusters of gold spheres (NSP–OKT3, blue DAPI marker) and shells (NS–OKT3, calcein red marker); **b** optical scattering PNB-specific time responses of individual cells to a single laser pulse show simultaneous generation of small PNBs in blue and large PNBs in red cells in presence of extracellular molecular cargo FITC–dextran (the lifetimes of PNBs are shown); **c** postlaser treatment blue cells show the injected FITC–dextran (green fluorescence) and red cells show leaked out calcein red dye and distorted membranes due to their destruction. The fluorescence intensity profiles of individual cells in (a) and (c) are indicated by small color-matched arrows. Recreated by kind permission of ACS [177]

dye (FITC–dextran) was added to the cell suspension as a model of the molecular cargo. Next, the suspension was scanned with a broad (0.22 mm diameter) excitation laser beam for the bulk PNB treatment. The broad laser beam simultaneously and identically irradiated hundreds of mixed red and blue cells in one pulse. All the cells received a single pulse exposure. We used the above data to set the pulse fluence to the level of 60 mJ/cm^2 that corresponds to the PNB lifetime of 60–65 ns in NSP–OKT3-treated cells and 200–220 ns in NS–OKT3-treated cells. After the laser irradiation, FITC–dextran was immediately washed off. The experiment was performed in three steps [177]: (1) fluorescent imaging of the mixed cells before exposure to FITC–dextran and the laser, (2) adding FITC–dextran and exposing the cells to broad single laser pulses that induced PNBs, and (3) fluorescent imaging of the cells immediately after the PNB treatment.

Prior to the PNB treatment, we obtained tricolor confocal fluorescent images of the cells (Fig. 32.19a) and measured the levels of red (to characterize the viability) and green (to characterize the presence of the external cargo) fluorescence in individual cells. The viability of the cells was measured by monitoring the level of calcein red fluorescence [182] and with trypan blue exclusion test. Treatment of the cells with a single laser pulse of the fluence of 60 mJ/cm^2 provided the generation of $64 \pm 8 \text{ ns}$ PNBs in blue cells and $237 \pm 38 \text{ ns}$ PNB in red cells (Fig. 32.19b) and resulted in a significant increase in green fluorescence of FITC–dextran only in the blue cells and in a significant decrease of red fluorescence of calcein red in the red cells (Fig. 32.19c). Blue NSP–OKT3-targeted cells showed the presence of FITC–dextran in their cytoplasm (Fig. 32.19c) that was not found there before the PNB treatment (Fig. 32.19a). Intracellular delivery of FITC–dextran was achieved through the PNB-specific mechanism of the localized injection of the extracellular molecules. We recently demonstrated that a small PNB of 40–90 ns lifetime creates a small transient hole in the cellular membrane and induces a nanojet that actively injects the external molecules into the cytoplasm without compromising the cell [103, 106]. Comparison of the concentration

and viability of the blue cells before and after the PNB treatment showed that such small PNBs (64 ns) were relatively safe to the cells.

Red (NS–OKT3-targeted) cells showed a totally different response to the same laser pulse that induced much larger PNBs (237 ± 38 ns) (Fig. 32.19b). Calcein red apparently leaked out and the shape of the cells changed showing the blebbing bodies and damaged membrane in the bright field image (Fig. 32.19c). A comparison of the concentration and viability of the red cells before and after the PNB treatment showed that such large PNBs destroyed 86 % of these cells [177]. The PNB-induced changes in the cell shape, level of red fluorescence, cell concentration, and viability were observed within 10 min after the PNB treatment. The character and speed of these changes indicate that cell death occurred simultaneously through a lysis-like process and not through necrosis or apoptosis. Such an immediate cell death effect was caused by the mechanical explosive action of a large intracellular PNB and not by laser-induced heating of gold NPs because PNBs effectively insulate the thermal effect of gold NPs [78]. Our recent detailed study of the PNB-induced cell death mechanism revealed the disruptive irreversible damage of the cell structure after generating even a single large intracellular PNB [104].

32.4.4 Plasmonic Nanobubble-Enhanced Endosomal Escape Mechanism of Instantaneous Intracellular Drug Release

To overcome drug resistance of HNSCC and to reduce nonspecific toxicity of anti-tumor drug, we applied active and HNSCC cell-specific delivery of encapsulated doxorubicin (Doxil) into the cytoplasm of HNSCC cells in order to create a high local concentration of the drug. Instead of the existing passive diffusion-based mechanisms, we employ the PNB-induced localized, mechanical ejection of the drug from liposome and from endosomes (Fig. 32.20). This is achieved by generating small intracellular PNBs (noninvasive on their own), co-localized with drug liposomes in the complex intracellular clusters. The key to this method is in the separate administration of Doxil (Doxorubicin encapsulated into 85 nm liposomes) at significantly reduced doses and the conjugates of gold NPs with C225 antibody (Erbbitux). Solid gold spheres of 20 and 60 nm diameter, the most available and FDA-approved gold NPs, were employed because they showed high PNB generation efficacy under NIR (780 nm) pulsed optical excitation. Gold NPs and Doxil are nontoxic even when they are internalized by the cells, including their nonspecific uptake by normal cells (Fig. 32.20). The therapeutic mechanism is provided by two steps: (1) cancer cells selectively self-assemble large, complex clusters of gold NPs co-localized with drug liposomes (Fig. 32.20c) through receptor-mediated endocytosis (while normal cells cannot accumulate so many gold NPs and build clusters of the same size as cancer cells (Fig. 32.20d)),

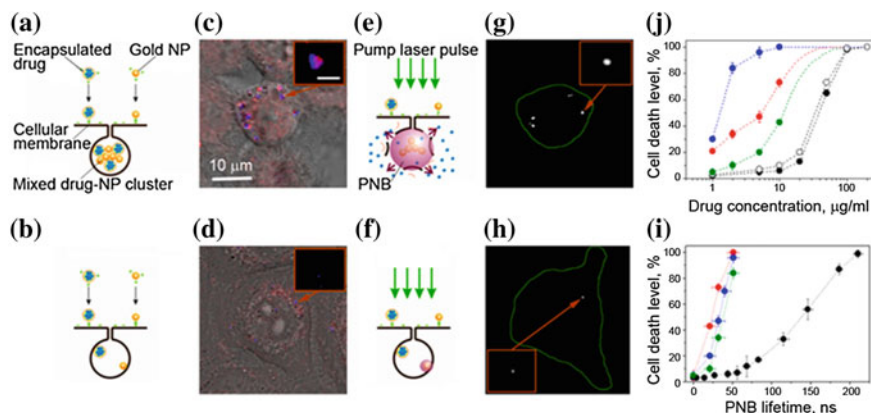


Fig. 32.20 Targeting of cancer (*top panel*) and normal (*bottom panel*) cells with NSs, Doxil (doxorubicin in liposomes), and PNBs. (a, b) Selective formation of the self-assembled mixed drug–NS clusters in target cells through separate administration of gold NPs. (c, d) Co-localization of NS (blue) and Doxil (red) shows the mixed clusters only in cancer (c) but not in normal (d) cells (scale bar is 400 nm insert). e PNBEE mechanism: co-localized PNB disrupts Doxil and endosome and ejects the drug into cytoplasm in nanoseconds. f Lack of PNB and Doxil in normal cell prevents the release of nonspecifically drug. g, h Time-resolved image shows selectivity and co-localization of PNBs with NS–Doxil. i, j, Cell death level among cancer (*solid*) and normal (*hollow*) cells measured in 72 h after PNBEE treatment as function of the concentration of Doxil and of the PNB lifetime (black—0 (no PNB), green: 21 ns, red: 32 ns, blue: 51 ns); Doxil concentrations in I ($\mu\text{g/ml}$): black—0 (no drug), green: 2, blue: 5, red: 10. In all cases, the uncoupled drug was removed before generating PNBs. Recreated by kind permission of Elsevier [173]

and (2) the threshold generation of PNBs around gold NPs in these clusters with a single laser pulse at 780 nm, 70 ps. Gold spheres efficiently generated PNBs with this short NIR laser pulse through our new method that employs the specific duration and low, safe fluence of the single laser pulse. These PNBs are small and therefore noninvasive alone [103, 173], but they simultaneously deliver two important functions. Their optical scattering and acoustic emission provide the remote and immediate detection of cancer cells, and their mechanical, not thermal, impact immediately disrupts the liposome and endosome membranes and the pressure created by the expanding PNB ejects the drug into the cellular cytoplasm. This fast (nanosecond) and localized (submicrometer) mechanism creates a high local intracellular concentration of the drug that is impossible to achieve through conventional slow delocalized diffusive processes of drug delivery. This overcomes most of the known mechanisms of drug resistance and, in addition, allows the reduction in the initial dose of the drug to a level that does not cause non-specific toxicity.

The mechanism of intracellular delivery and on-demand release of an encapsulated drug (doxorubicin in Doxil liposomes) was studied in the same co-culture of HN31 and NOM9 cells.

32.4.4.1 Therapeutic Effect of PNBs In Vitro

Therapeutic effect of PNBs in vitro was measured 72 h after a single pulse laser treatment as the level of cancer cell death in several different treatment modes. We correlated the size of PNBs (measured by their lifetimes, obtained as the duration of time responses of individual cells) to their therapeutic effect. Relatively small PNBs of 20–90 ns lifetime showed the low therapeutic efficacy (low death level for cancer cells) and the low nonspecific toxicity (low death level for normal cells) when used alone (Fig. 32.20i). Earlier we found that only large PNBs with a lifetime >130 ns mechanically kill the cells [103, 104].

32.4.4.2 Synergistic Effect of PNB and Doxil

Direct exposure of cells to Doxil and gold NPs without laser pulses had a limited effect on cancer cells due to their drug resistance coupled with a relatively low dose of Doxil (5 $\mu\text{g}/\text{ml}$, 20-fold lower than the effective therapeutic dose [183]). Such a low dose of the drug reduced nonspecific toxicity, as we observed minimal damage to normal cells. However, when PNBs were generated in the mixed NP–Doxil clusters, the cell death level increased by 30-fold among cancer cells (relative to the drug alone mode) but remained relatively low among normal cells where no PNBs were generated. The optimal PNB–Doxil combination corresponded to noninvasive PNBs of 51 ± 7 ns lifetime (when used alone without the drug) and nontoxic doses of Doxil of 3 $\mu\text{g}/\text{ml}$ (when used alone without the PNB).

This selective and efficient therapeutic effect was achieved due to the localized, active, mechanical release (ejection) of the drug from liposomes and endosomes that were disrupted by an expanding co-localized PNB. This process took tens of nanoseconds and required a single laser pulse of a low dose to provide the selective intracellular release of the drug only in cancer cells. We termed this mechanism as a PNB-enhanced endosome escape. Normal cells did not develop PNBs under identical laser and NP treatment, and thus, the Doxil liposomes nonspecifically taken by normal cells were not disrupted by PNBs and did not release the drug. Unique to this technology, PNBs provided the optical detection of cancer cells and their selective destruction in a single, fast theranostic procedure.

The therapeutic mode of PNBs employed both the above methods of generation and detection of PNBs in vivo and of PNB-enhanced endosome escape intracellular delivery of the encapsulated drug. We next determined the therapeutic efficacy of tumor-targeted PNBs and Doxil in a mouse model of HNSCC.

32.4.4.3 In Vivo Administration of NPs, Doxil, and Laser Radiation for Cancer Therapeutics

We separately administered Doxil and gold 60 nm NP–C225 conjugates to an HNSCC-bearing mouse. Doxil was administered locally at the concentration of

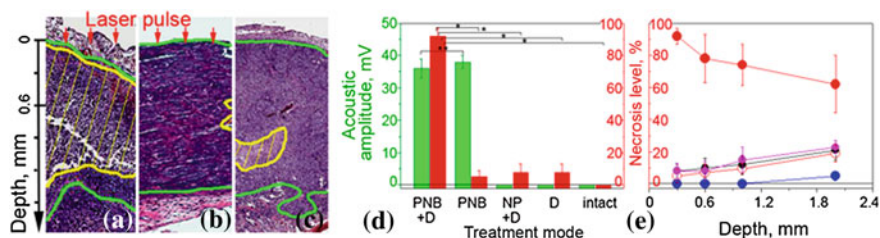


Fig. 32.21 PNB therapeutics of HNSCC tumor in mouse. Tumor depth profiles in (a–c) show tumor (green) and necrotic tumor (yellow) for the treatment modes: (a, e, solid red): PNB + D: small PNBs (40 mJ/cm² @780 nm, 70 ps, single pulse, NP: gold 60 nm spheres conjugated to C225) and Doxil (1 mg/kg); (b, e, hollow red): PNBs alone; (c, e, hollow black): Doxil + NP; **d** level of necrosis (red bars) at 0.3 mm depth and acoustic signals of PNBs (green bars) for the listed treatment modes ($p < 0.001$, $** p > 0.05$). **e** Dependence of the level of necrosis in tumor upon tissue depth (PNB + D: solid red, PNB: hollow red, NP + D: hollow black, magenta, intact tumor: blue). Recreated by kind permission of Ivyspring International Publisher [105]

1 mg/kg, 3-fold lower than therapeutic concentration [183]. NP–C225 conjugates were administered intravenously simultaneously with Doxil at the concentration of 4.5×10^{10} NP/mL (200 μ l). After 24 h, one-half of the tumor and the adjacent normal tissue were scanned with single laser pulses at 20 Hz, while the intact part of the tumor was used as the nonirradiated control. We applied the single laser pulse irradiation with the same parameters as those established earlier in vitro, 780 nm, 70 ps, 40 mJ/cm², and increased the laser beam diameter to 0.25 mm in order to improve the tissue penetration depth [140]. The part of animal surface with the tumor and normal tissue was scanned with the laser beam at the rate 1 mm²/s. Real-time acoustic monitoring showed the PNB signals of 36 ± 3 mV amplitude for the tumor (Fig. 32.21d) and 0 mV for the adjacent muscle tissue. This result approximated the previous in vivo diagnostic experiment [105] and confirmed the tumor-specific generation of PNBs in therapeutic mode.

32.4.4.4 Therapeutic Effects of Plasmonic Nanobubbles and Doxil

Next, we analyzed the effect of several treatment combinations for tumor and for adjacent normal muscle tissue: (1) single laser pulse + NP + Doxil, (2) single laser pulse + NP (PNBs alone, similar to the diagnostic mode), (3) NP + Doxil (evaluation of the toxicity of NPs and drug), (4) Doxil (analog of standard chemotherapy at the reduced dose), and (5) intact tumor or muscle. After 72 h, the tumor and normal tissue were harvested, and the relative level of necrosis was analyzed with a standard histopathological technique. The analysis of the level of necrosis in the tumor (Fig. 32.21a–c) showed a high damage zone only for the combination laser pulse + NP + Doxil (Fig. 32.21a, d) that was associated with the generation of small PNBs. This result corresponded to in vitro case of the co-localized PNBs and Doxil (Fig. 32.20c, g). The therapeutic effects of the PNBs or Doxil alone were low,

less than 7 % each (Fig. 32.21b, d), meaning that only small noninvasive PNBs were generated. This noninvasive nature of PNBs alone was in line with the corresponding *in vitro* results that also showed low PNB-induced cell death (Fig. 32.20). The toxic effect of NPs was also low (Fig. 32.21c, d). Therefore, the single low dose of Doxil applied coupled with the drug-resistant nature of the HNSCC tumor resulted in the low therapeutic efficacy. In contrast, the joint action of PNBs and Doxil resulted in the synergistic enhancement of the necrosis level up to 80–92 %, while the additive effects of PNBs alone and Doxil alone did not exceed the necrosis level of 13 % (Fig. 32.21d). This demonstrates how PNB-enhanced endosomal escape mechanism overcomes the drug resistance of HNSCC even under the low dose of the drug. In addition, the level of necrosis correlated well to the acoustic amplitude of PNBs in drug-treated animals (Fig. 32.21d), thus allowing the real-time guidance of the therapeutic efficacy of PNBs during the laser scan.

32.4.4.5 Correlation of In Vitro and In Vivo Results and the Plasmonic Nanobubble Therapeutic Mechanism

A comparison of the corresponding treatment modes *in vivo* and *in vitro* [105] demonstrated the high similarity of the therapeutic effects in both models, thus confirming the earlier established therapeutic mechanism of PNB-enhanced endosomal escape of the drug from liposomes and endosomes. Regardless of the mechanism of drug resistance, the cancer cell failed to protect itself from the mechanical explosive action of PNBs that ejected the drug into cellular cytoplasm. The nanosecond speed of this process was much higher than traditional diffusion-based release processes. Such fast release of the drug resulted in its high local intracellular concentration that was sufficient to kill drug-resistant cells after a single administration of a 3-fold reduced dose of Doxil. This, in turn, reduced the treatment time from up to a week [183] to less than 1 min of laser scan.

32.4.4.6 Reduction of Nonspecific Toxicity

As a result of the reduction in the drug, NP and optical doses, we observed very low nonspecific toxicity. The levels of necrosis in normal tissue under an identical treatment combination (NP-C225 + Doxil + single laser pulse) were found to be 0 %, even despite nonspecific uptake of NPs and the drug by normal cells and tissues. The threshold mechanism of PNBs prevented their generation in normal tissue and thus prevented the nonspecific release of the drug in normal tissue. This demonstrated the high safety and selectivity of PNB therapeutics [105].

32.4.4.7 Penetration Depth of the Plasmonic Nanobubble Treatment

In order to study the effect of the optical attenuation by the tumor, we measured the level of necrosis level as a function of the tissue depth for all treatment modes (Fig. 32.21e). The laser–NP–Doxil mode demonstrated high therapeutic efficacy (70–92 %), up to 1.5–1.8 mm depth for the laser beam of 0.25 mm diameter. This was achieved by using the NIR wavelength (780 nm) that previously was shown to provide the maximal penetration depth and minimal phototoxicity on a tissue [140]. Since the penetration depth of laser radiation increases with the diameter of the laser beam [140], this parameter can be further improved by using broader laser beam.

To summarize the therapeutic studies *in vivo*, the application of small noninvasive PNBs for intracellular release of the low doses of encapsulated drug allowed us to overcome drug resistance and to reduce nonspecific toxicity and treatment time.

32.4.5 Mechanisms of Plasmonic Nanobubble Therapy Versus Current Therapeutic Mechanisms

Our results demonstrated simultaneous ability of PNBs to deliver high sensitive diagnosis and selective, efficient, and localized therapeutics in a single laser pulse theranostic procedure. The therapeutic mechanism of PNBs is based on active intracellular drug delivery through rapid mechanical, nonthermal, disruption of drug carriers and endosomes, and localized ejection of drug into cytoplasm. This mechanism is distinct from the existing drug delivery mechanisms that are slow or nonspecific. Current approaches for *in vivo* drug delivery, direct or enhanced by hyperthermia or photodynamic therapy employ various NPs [144, 149, 150, 154, 155], external energies [26–28, 156, 158, 159, 165–167], or their combinations [28, 152, 153, 161, 162, 165, 168, 169]. However, their efficacy is limited by the slow diffusive nature of the drug release, while nonspecific uptake of NPs or the nonspecific nature of the external energy-stimulated release increase required doses of drugs and NPs and cause significant nonspecific toxicity.

There are also well-established delivery methods that employ cavitation bubbles as ultrasound- or optically induced events [158, 159, 170–172, 184, 185] or nanobubbles as particles [186–191]. Similar to the previously discussed methods, these “bubble” methods have a nonspecific release mechanism, generate large bubbles that cannot discriminate cancer from normal cells, and increase nonspecific toxicity. Furthermore, an ultrasound cannot be applied as a single short (<1 ms) pulse.

In contrast, PNBs reduced the NP dose by 2–4 orders of magnitude compared to the photothermal therapies [25–28, 162, 167] optical energy dose by 10^{1-4} -fold compared to photothermal drug delivery [152, 153], photodynamic therapies [28, 168, 169],

and drug dose by >3-fold compared to standard chemotherapy [183]. Most of all, PNBs provided a single cell selectivity of the therapeutics and spared even adjacent normal cells.

32.4.6 Plasmonic Nanobubble Theranostics

The results reported above were achieved due to the novel biophysical properties of PNB's: (1) explosive nanoevent whose mechanical, not thermal, action rapidly creates a high intracellular concentration of the released drug; (2) ability to scatter the light and to emit a pressure pulse makes it a sensitive cellular diagnostic probe [103, 124]; (3) the cluster-threshold mechanism of PNBs overcomes nonspecific uptake of gold NPs by normal cells because the PNB generation threshold is minimal for large clusters of NPs self-assembled by cancer cells [103, 124, 173]; (4) a single NP cluster of 5–50 NPs per cell and a single laser pulse are sufficient for detecting and elimination the cancer cells with single PNB, thus substantially reducing the NP and laser energy doses; (5) therapeutic and diagnostic functions of PNBs can be activated simultaneously in a single pulse theranostic procedure [104, 178]; (6) a PNB can be generated with FDA-approved gold spheres and a single NIR laser pulse of low dose and the maximal tissue penetration depth [140], thus eliminating the need in specially engineered NIR NPs (such as nanorods and other NPs) and in prolonged optical excitation.

32.4.7 Translational Potential of Plasmonic Nanobubble Theranostics

The major limitations of the PNB theranostics are associated with the limited penetration of light and gold NPs into heterogeneous tumors and with phototoxicity. The energy of commercial lasers allows an increase in the diameter of the laser beam of up to 3–4 mm and thus to achieve 5–7 mm range of tissue depth [140] and 100 mm²/s scan speed. Both metrics match the needs of intraoperative treatment of residual disease. The optical dose if NIR laser radiation required for PNB generation is relatively low 10–40 mJ/cm², 4–6 orders of magnitude lower than those employed in previously reported in vivo studies of photothermal hyperthermia with gold NPs ($3\text{--}72 \times 10^2$ J/cm²) [25–27, 152, 153]. Such a reduction in optical dose was achieved by using a single pulse of low fluence instead of prolonged, continuous irradiation. In our method, the optical dose becomes equal to the pulse fluence and is comparable to the established laser safety limits of 30–50 mJ/cm² for pulsed laser radiation [183]. Using off-resonant NIR excitation of FDA-approved solid gold spheres reduces the laser-induced NP temperature and, therefore, the thermal damage to NPs and to surrounding tissues.

The combination of the efficacy, cell selectivity, safety, single pulse speed and multifunctionality of PNB theranostics demonstrated in our experiments have not been achieved to date *in vivo* with any current technologies. This all demonstrates translational potential of PNBs for the intraoperative treatment of surgical bed for monitoring and eliminating residual disease in real time.

We demonstrated for the first time *in vivo* the novel concept of PNB theranostics that enables diagnosis through the acoustic detection of the PNBs and the simultaneous efficient treatment of drug-resistant tumors through the PNB-enhanced endosomal escape mechanism of intracellular drug delivery in a single laser pulse procedure:

1. The tumor-preferred clustering of gold nanoparticle conjugates, coupled with the threshold mechanism of PNB generation, provided the cell level specificity of tumor detection and elimination.
2. Plasmonic nanobubbles increased the therapeutic efficacy of the standard drug by more than 10-fold compared to chemotherapy alone and eliminated >80 % of the drug-resistant tumor in a fast single treatment.
3. Cumulated nonspecific toxicity of the drug, gold nanoparticles, and laser radiation was reduced below a detectable level.
4. The treatment time was reduced to less than one min for a tumor of 5 mm size by noninvasively scanning single NIR laser pulses at the safe optical dose.

By using the safest and commercially available gold NPs, solid spheres, a low dose of NIR single laser pulse, and standard encapsulated drugs (not linked to NPs), PNB technology can be applied for local and real-time adjuvant treatment of poorly detectable and curable residual drug-resistant microtumors during or immediately after surgery. The universal mechanism of PNB technology allows its extension to many cancers and other pathologies that require precise local treatment and thus may complement existing surgical and chemotherapeutic approaches.

32.5 Conclusions

Our approach demonstrates that the efficacy, functionality, safety, and precision of nanomedicine may be radically increased by replacing nanomaterials with preset properties by the transient on-demand nanoevents with dynamically tunable diagnostic and therapeutic functions. The described plasmonic nanobubbles (which are, in fact, the smallest controllable nanoexplosions) represent entirely new paradigm of the event-based nanomedicine. Their transient on-demand nature delivers unprecedented multifunctionality and thus allows to unite diagnosis and therapy in one cell level theranostic procedure. Plasmonic nanobubble theranostics presents the entirely new platform for the future medicine that will achieve cell level efficacy, safety, and high speed through the novel intracellular diagnostic and therapeutic mechanisms.

References

1. Looser KG, Shah JP, Strong EW (1978) The significance of “positive” margins in surgically resected epidermoid carcinomas. *Head Neck Surg* 1:107–111. doi:[10.1002/hed.2890010203](https://doi.org/10.1002/hed.2890010203)
2. Vikram B, Strong EW, Shah JP, Spiro R (1984) Failure at the primary site following multimodality treatment in advanced head and neck cancer. *Head Neck Surg* 6:720–723. doi:[10.1002/hed.2890060303](https://doi.org/10.1002/hed.2890060303)
3. Yuen PW, Lam KY, Chan AC, Wei WI, Lam LK (1998) Clinico- pathological analysis of local spread of carcinoma of the tongue. *Am J Surg* 175:242–244. doi:[10.1016/S0002-9610\(97\)00282-1](https://doi.org/10.1016/S0002-9610(97)00282-1)
4. Meier JD, Oliver DA, Varvares MA (2005) Surgical margin determination in head and neck oncology: current clinical practice. The results of an International American Head and Neck Society Member Survey. *Head Neck* 27:952–958. doi:[10.1002/hed.20269](https://doi.org/10.1002/hed.20269)
5. <http://www.cancer.gov/cancertopics/factsheet/Sites-Types/head-and-neck>
6. Seikaly H, Rieger J, Wolfaardt J, Moysa G, Harris J, Jha N (2003) Functional outcomes after primary oropharyngeal cancer resection and reconstruction with the radial forearm free flap. *Laryngoscope* 113:897–904. doi:[10.1097/00005537-200305000-00023](https://doi.org/10.1097/00005537-200305000-00023)
7. Taylor RJ, Chepeha JC, Teknos TN, Bradford CR, Sharma PK, Terrell JE, Hogikyan ND, Wolf GT, Chepeha DB (2002) Development and validation of the neck dissection impairment index: a quality of life measure. *Arch Otolaryngol Head Neck Surg* 128:44–49. doi:[10.1001/archotol.128.1.44](https://doi.org/10.1001/archotol.128.1.44)
8. Langendijk JA, Doornaert P, Verdonck-de IMLeeuw, Leemans CR, Aaronson NK, Slotman BJ (2008) Impact of late treatment-related toxicity on quality of life among patients with head and neck cancer treated with radiotherapy. *J Clin Oncol* 26:3770–3887. doi:[10.1200/JCO.2007.14.6647](https://doi.org/10.1200/JCO.2007.14.6647)
9. Pauloski BR, Rademaker AW, Logemann JA, Lazarus CL, Newman L, Hamner A, MacCracken E, Gaziano J, Stachowiak L (2002) Swallow function and perception of dysphagia in patients with head and neck cancer. *Head Neck* 24:555–565. doi:[10.1002/hed.10092](https://doi.org/10.1002/hed.10092)
10. Jemal A, Siegel R, Ward E, Hao Y, Xu J, Murray T, Thun MJ (2008) Cancer statistics, 2008. *CA Cancer J Clin* 58:71–96. doi:[10.3322/CA.2007.0010](https://doi.org/10.3322/CA.2007.0010)
11. Zackrisson B, Mercke C, Strander H, Wennerberg J, Cavallin-Stahl E (2003) A systemic overview of radiation therapy effects in head and neck cancer. *Acta Oncol* 42:443–461. doi:[10.1081/02841860310014886](https://doi.org/10.1081/02841860310014886)
12. Jemal A, Siegel R, Xu J, Ward E (2010) Cancer statistics. *CA: Cancer J Clin* 60:277–300. doi:[10.3322/caac.20073](https://doi.org/10.3322/caac.20073)
13. Jemal A, Bray F, Center MM, Ferlay J, Ward E, Forman D (2011) Global cancer statistics. *CA: A Cancer J Clin* 61:69-90. doi: [10.3322/caac.20107](https://doi.org/10.3322/caac.20107)
14. Mie G (1908) Beiträge zur Optik trüber Medien, speziell kolloidaler Metallösungen. *Annalen der Physik Vierte Folge Band* 25:377–445. doi:[10.1002/andp.19083300302](https://doi.org/10.1002/andp.19083300302)
15. Faraday M (1857) The Bakerian lecture: Experimental relations of gold (and other metals) to light. *Philos Trans R Soc London* 147:145–181. doi:[10.1098/rstl.1857.0011](https://doi.org/10.1098/rstl.1857.0011)
16. Merchant B (1998) Gold, the noble metal and the paradoxes of its toxicology. *Biologicals* 26:49–59. doi:[10.1006/biol.1997.0123](https://doi.org/10.1006/biol.1997.0123)
17. Weissleder R (2001) A clearer vision for in vivo imaging. *Nat Biotechnol* 19:316–317. doi:[10.1038/86684](https://doi.org/10.1038/86684)
18. Ambrosch P (2007) The role of laser microsurgery in the treatment of laryngeal cancer. *Curr Opin Otolaryngol Head Neck Surg*. 15:82–88. doi:[10.1097/MOO.0b013e3280147336](https://doi.org/10.1097/MOO.0b013e3280147336)
19. Kreibitz U, Vollmer M (1995) *Optical properties of metal clusters*. Springer-Verlag, Berlin
20. Bohren CF, Huffman DR (1983) *Absorption and scattering of light by small particles*. Wiley Interscience, New York

21. Harris N, Ford MJ, Cortie MB (2006) Optimization of plasmonic heating by gold nanospheres and nanoshells. *J Chem Phys B* 110:10701–10707. doi:[10.1021/jp0606208](https://doi.org/10.1021/jp0606208)
22. Link S, El-Sayed MA (2000) Shape and size dependence of radiative, non-radiative and PTT properties of gold nanocrystals. *Int Rev Phys Chem* 19:409–453. doi:[10.1080/01442350050034180](https://doi.org/10.1080/01442350050034180)
23. Dreaden EC, Alkilany AM, Huang X, Murphy CJ, El-Sayed MA (2012) The golden age: gold nanoparticles for biomedicine. *Chem Soc Rev* 41:2740–2779. doi:[10.1039/c1cs15237h](https://doi.org/10.1039/c1cs15237h)
24. Yu Y–Y, Chang S–S, Lee C–L, Wang CRC (1997) Gold nanorods: electrochemical synthesis and optical properties. *J Phys Chem B* 101:6661–6664. doi:[10.1021/jp971656q](https://doi.org/10.1021/jp971656q)
25. Dickerson EB, Dreaden EC, Huang X, El-Sayed I, Chu H, Pushpanketh S, McDonald JF, El-Sayed M (2008) Gold nanorod assisted near-infrared plasmonic photothermal therapy (PPTT) of squamous cell carcinoma in mice. *Cancer Lett* 269:57–66. doi:[10.1016/j.canlet.2008.04.026](https://doi.org/10.1016/j.canlet.2008.04.026)
26. Choi W, Kim J–Y, Kang C, Byeon C, Kim YH, Tae G (2011) Tumor regression in vivo by photothermal therapy based on gold-nanorod-loaded, functional nanocarriers. *ACS Nano* 5:1995–2003. doi:[10.1021/nn103047r](https://doi.org/10.1021/nn103047r)
27. Li Z, Huang P, Zhang X, Lin J, Yang S, Liu B, Gao F, Xi P, Ren Q, Cui D (2010) RGD-conjugated dendrimer-modified gold nanorods for in vivo tumor targeting and photothermal therapy. *Mol Pharm* 7:94–104. doi:[10.1021/mp9001415](https://doi.org/10.1021/mp9001415)
28. Jang B, Park JY, Tung CH, Kim IH, Choi Y (2011) Gold nanorod-photosensitizer complex for near-infrared fluorescence imaging and photodynamic/photothermal therapy in vivo. *ACS Nano* 5:1086–1094. doi:[10.1021/nn102722z](https://doi.org/10.1021/nn102722z)
29. Khlebtsov BN, Panfilova EV, Terentyuk GS, Maksimova IL, Ivanov AV, Khlebtsov NG (2012) Plasmonic nanopowders for photothermal therapy of tumors. *Langmuir* 28:8994–9002. doi:[10.1021/la300022k](https://doi.org/10.1021/la300022k)
30. Oldenburg SJ, Averitt RD, Westcott SL, Halas NJ (1998) Nanoengineering of optical resonances. *Chem Phys Lett* 288:243–247. doi:[10.1016/S0009-2614\(98\)00277-2](https://doi.org/10.1016/S0009-2614(98)00277-2)
31. Gobin AM, Lee MH, Halas NJ, James WD, Drezek RA, West JL (2007) Near-infrared resonant nanoshells for combined optical imaging and photothermal cancer therapy. *Nano Lett* 7:1929–1934. doi:[10.1021/nl070610y](https://doi.org/10.1021/nl070610y)
32. Chen J, Saeiki F, Wiley BJ, Cang H, Cobb MJ, Li Z–Y, Au L, Zhang H, Kimmey MB, Li X, Xia Y (2005) Gold nanocages: bioconjugation and their potential use as optical imaging contrast agents. *Nano Lett* 5:473–477. doi:[10.1021/nl047950t](https://doi.org/10.1021/nl047950t)
33. Chen J, Glaus C, Laforest R, Zhang Q, Yang M, Gidding M, Welch MJ, Xia Y (2010) Gold nanocages as photothermal transducers for cancer treatment. *Small* 6:811–817. doi:[10.1002/smll.200902216](https://doi.org/10.1002/smll.200902216)
34. Guerrero-Martínez A, Grzelczak M, Liz-Marzán LM (2012) Molecular thinking for nanoplasmonic design. *ACS Nano* 6:3655–3662. doi:[10.1021/nn301390s](https://doi.org/10.1021/nn301390s)
35. Jana N, Gearheart L, Murphy C (2001) Wet chemical synthesis of high aspect ratio cylindrical gold nanorods. *J Phys Chem B* 105:4065–4067. doi:[10.1021/jp0107964](https://doi.org/10.1021/jp0107964)
36. Nikoobakht B, El-Sayed MA (2003) Preparation and growth mechanism of gold nanorods (NRs) using seed-mediated growth method. *Chem Mater* 15:1957–1962. doi:[10.1021/cm020732l](https://doi.org/10.1021/cm020732l)
37. Pérez-Juste J, Pastoriza-Santos I, Liz-Marzán LM, Mulvaney P (2005) Gold nanorods: synthesis, characterization and applications. *Coord Chem Rev* 249:1870–1879. doi:[10.1016/j.ccr.2005.01.030](https://doi.org/10.1016/j.ccr.2005.01.030)
38. Hirsch LR, Gobin AM, Lowery AR, Tam F, Drezek RA, Halas NJ, West JL (2006) Metal nanoshell. *Ann Biomed Eng* 34:15–22. doi:[10.1007/s10439-005-9001-8](https://doi.org/10.1007/s10439-005-9001-8)
39. Sun Y, Xia Y (2004) Mechanistic study on the replacement reaction between silver nanostructures and chloroauric acid in aqueous medium. *J Am Chem Soc* 126:3892–3901. doi:[10.1021/ja039734c](https://doi.org/10.1021/ja039734c)
40. Skrabalak SE, Au L, Li X, Xia Y (2007) Facile synthesis of Ag nanocubes and Au nanocages. *Nat Protoc* 2:2182–2190. doi:[10.1038/nprot.2007.326](https://doi.org/10.1038/nprot.2007.326)

41. Xia Y, Xiong Y, Lim B, Skrabalak SE (2009) Shape-controlled synthesis of metal nanocrystals: simple chemistry meets complex physics? *Angew Chem Int Ed* 48:60–103. doi:[10.1002/anie.200802248](https://doi.org/10.1002/anie.200802248)
42. Guerrero-Martínez A, Barbosa S, Pastoriza-Santos I, Liz-Marzán LM (2011) Nanostars shine bright for you: colloidal synthesis, properties and applications of branched metallic nanoparticles. *Curr Opin Colloid & Interface Sci* 16:118–127. doi:[10.1016/j.cocis.2010.12.007](https://doi.org/10.1016/j.cocis.2010.12.007)
43. Boisselier E, Astruc D (2009) Gold nanoparticles in nanomedicine: preparations, imaging, diagnostics, therapies and toxicity. *Chem Rev* 38:1759–1782. doi:[10.1039/b806051g](https://doi.org/10.1039/b806051g)
44. Anderson RR, Parrish JA (1983) Selective photothermolysis: precise microsurgery by selective absorption of pulsed radiation. *Science* 220:524–527. doi:[10.1126/science.6836297](https://doi.org/10.1126/science.6836297)
45. Govorov A, Richardson H (2007) Generating heat with metal nanoparticles. *Nano Today* 2:30–38. doi:[10.1016/S1748-0132\(07\)70017-8](https://doi.org/10.1016/S1748-0132(07)70017-8)
46. Koblinski P, Cahill D, Bodapati A, Sullivan CR, Taton TA (2006) Limits of localized heating by electromagnetically excited nanoparticles. *J Appl Phys* 100:054308. doi:[10.1063/1.2335783](https://doi.org/10.1063/1.2335783)
47. Khlebtsov NG (2008) Optics and biophotonics of nanoparticles with a plasmon resonance. *Quantum Electron* 38:504–529. doi:[10.1070/QE2008v038n06ABEH013829](https://doi.org/10.1070/QE2008v038n06ABEH013829)
48. Pelton M, Aizpurua J, Bryant G (2008) Metal-nanoparticle plasmonics. *Laser & Photon Rev* 2:136–159. doi:[10.1002/lpor.200810003](https://doi.org/10.1002/lpor.200810003)
49. Zhao J, Pinchuk AO, McMahon JM, Li S, Ausman LK, Atkinson AL, Schatz GC (2008) Methods for describing the electromagnetic properties of silver and gold nanoparticles. *Acc Chem Res* 41:1710–1720. doi:[10.1021/ar800028j](https://doi.org/10.1021/ar800028j)
50. Myroshnychenko V, Rodríguez-Fernández J, Pastoriza-Santos I, Funston AM, Novo C, Mulvaney P, Liz-Marzán L-M, García de FJAbajo (2008) Modelling the optical response of gold nanoparticles. *Chem Soc Rev* 37:1792–1805. doi:[10.1039/B711486A](https://doi.org/10.1039/B711486A)
51. Quinten M (2011) Optical properties of nanoparticle systems: Mie and beyond. Wiley-VCH Verlag, GmbH & Co. KGaA, London
52. Huang X, Jain PK, El-Sayed IH, El-Sayed MA (2008) Plasmonic PTT therapy (PPTT) using gold nanoparticles. *Lasers Med Sci* 23:217–228. doi:[10.1007/s10103-007-0470-x](https://doi.org/10.1007/s10103-007-0470-x)
53. Khlebtsov BN, Zharov VP, Melnikov AG, Tuchin VV, Khlebtsov NG (2006) Optical amplification of PTT therapy with gold nanoparticles and nanoclusters. *Nanotechnology* 17:5167–5179. doi:[10.1088/0957-4484/17/20/022](https://doi.org/10.1088/0957-4484/17/20/022)
54. Arbouet A, Christofilos D, Del Fatti N, Vallée F, Huntzinger JR, Arnaud L, Billaud P, Broyer M (2004) Direct measurement of the single-metal-cluster optical absorption. *Phys Rev Lett* 93:127401. doi:[10.1103/PhysRevLett.93.127401](https://doi.org/10.1103/PhysRevLett.93.127401)
55. Berciaud S, Cognet L, Tamarat P, Lounis B (2005) Observation of intrinsic size effects in the optical response of individual gold nanoparticles. *Nano Lett* 5:515–518. doi:[10.1021/nl050062t](https://doi.org/10.1021/nl050062t)
56. Muskens OL, Del Fatti N, Vallée F, Huntzinger JR, Billaud P, Broyer M (2006) Single metal nanoparticle absorption spectroscopy and optical characterization. *Appl Phys Lett* 88:0634109. doi:[10.1063/1.2172143](https://doi.org/10.1063/1.2172143)
57. Del Fatti N, Christofilos D, Vallée F (2008) Optical response of a single gold nanoparticles. *Gold Bull* 41:147–158. doi:[10.1007/BF03216592](https://doi.org/10.1007/BF03216592)
58. Khlebtsov NG, Melnikov AG, Dykman LA, Bogatyrev VA (2004) Optical properties and biomedical applications of nanostructures based on gold and silver bioconjugates. In: Videen G, Yatskiv YS, Mishchenko MI (eds) *Photopolarimetry in remote sensing*. Kluwer Academic Publishers, Dordrecht, pp 265–308
59. Shalaev VM, Poliakov EY, Markel VA (1996) Small-particle composites. II. Nonlinear optical properties. *Phys Rev B* 53:2437–2449. doi:[10.1103/PhysRevB.53.2437](https://doi.org/10.1103/PhysRevB.53.2437)
60. Storhoff JJ, Lazarides AA, Mucic RC, Mirkin CA, Letsinger RL, Schatz GC (2000) What controls the optical properties of DNA-linked gold nanoparticle assemblies? *J Am Chem Soc* 122:4640–4650. doi:[10.1021/ja993825l](https://doi.org/10.1021/ja993825l)

61. Link S, Burda C, Mohamed MB, Nikoobakht B, El-Sayed MA (1999) Laser photothermal melting and fragmentation of gold nanorods: energy and laser pulse-width dependence. *J Phys Chem A* 103:1165–1170. doi:[10.1021/jp983141k](https://doi.org/10.1021/jp983141k)
62. Inasava S, Sugiyama M, Yamaguchi Y (2005) Laser-induced shape transformation of gold nanoparticles below the melting point: the effect of surface melting. *J Phys Chem B* 109:3104–3111. doi:[10.1021/jp045167j](https://doi.org/10.1021/jp045167j)
63. Hashimoto S, Werner D, Uwada T (2012) Studies on the interaction of pulsed lasers with plasmonic gold nanoparticles toward light manipulation, heat management, and nanofabrication. *J Photochem Photobiol* 13:28–54. doi:[10.1016/j.jphotochemrev.2012.01.001](https://doi.org/10.1016/j.jphotochemrev.2012.01.001)
64. Habenicht A, Olapinski M, Burmeister F, Leiderer P, Boneberg J (2005) Jumping nanodroplets. *Science* 309:2043–2045. doi:[10.1126/science.1116505](https://doi.org/10.1126/science.1116505)
65. Petrova H, Hu M, Hartland GV (2007) Photothermal properties of gold nanoparticles. *Z Phys Chem* 221:361–376. doi:[10.1524/zpch.2007.221.3.361](https://doi.org/10.1524/zpch.2007.221.3.361)
66. Kurita H, Takami A, Koda S (1998) Size reduction of gold particles in aqueous solution by pulsed laser irradiation. *Appl Phys Lett* 72:789–791. doi:[10.1063/1.120894](https://doi.org/10.1063/1.120894)
67. Fujiwara H, Yanagida S, Kamat PV (1999) Visible laser induced fusion and fragmentation of thionicotinamide-capped gold nanoparticles. *J Phys Chem B*. 103:2589–2591. doi:[10.1021/jp984429c](https://doi.org/10.1021/jp984429c)
68. Aguirre CM, Moran CE, Young JF, Halas NJ (2004) Laser-induced reshaping of metalodielectric nanoshells under femtosecond and nanosecond plasmon resonant illumination. *J Phys Chem B* 108:7040–7045. doi:[10.1021/jp036222b](https://doi.org/10.1021/jp036222b)
69. Akchurin G, Khlebtsov B, Akchurin G, Tuchin V, Zharov V, Khlebtsov N (2008) Gold nanoshell photomodification under single nanosecond laser pulse accompanied by color-shifting and bubble formation phenomena. *Nanotechnology* 19:015701. doi:[10.1088/0957-4484/19/01/015701](https://doi.org/10.1088/0957-4484/19/01/015701)
70. Zsigmondy R (1898) Üeber wassrige Lösungen metallischen Goldes. *Ann Chem* 301:29–54. doi:[10.1002/jlac.18983010104](https://doi.org/10.1002/jlac.18983010104)
71. Raleigh L (1917) On the pressure developed in a liquid during the collapse of a spherical cavity. *Philos Mag* 34:94–98. doi:[10.1080/14786440808635681](https://doi.org/10.1080/14786440808635681)
72. Plesset MS (1949) The dynamics of cavitation bubbles. *Trans ASME: J Appl Mech* 16:277–282. doi:[10.1080/14786440808635681](https://doi.org/10.1080/14786440808635681)
73. Askaryan GA, Prokhorov AM, Chanturiya GF, Shapiro GP (1963) The effects of a laser beam in a liquid. *Sov Phys JEPT* 17:1463
74. Barnes PA, Rieckhoff KE (1968) Laser induced underwater sparks. *Appl Phys Lett* 13:282. doi:[10.1063/1.1652611](https://doi.org/10.1063/1.1652611)
75. Neumann J, Brinkmann R (2007) Nucleation dynamics around single microabsorbers in water heated by nanosecond laser irradiation. *J Appl Phys* 101:114701. doi:[10.1063/1.2740348](https://doi.org/10.1063/1.2740348)
76. Roeder J, El Hifnawi ES, Birngruber R (1998) Bubble formation as primary interaction mechanism in retinal laser exposure with 200-ns laser pulses. *Lasers Surg Med* 22:240–248. doi: [10.1002/\(SICI\)1096-9101\(1998\)22:4<240::AID-LSM9>3.0.CO;2-P](https://doi.org/10.1002/(SICI)1096-9101(1998)22:4<240::AID-LSM9>3.0.CO;2-P)
77. Lapotko D, Lukianova E, Shnip S, Zheltov G, Potapnev M, Savitsky V, Klimovich O, Oraevsky A (2005) Laser activated nanothermolysis of leukemia cells monitored by photothermal microscopy. *Proc SPIE* 5697:82. doi:[10.1117/12.596372](https://doi.org/10.1117/12.596372)
78. Lukianova-Hleb EY, Hu Y, Latterini L, Tarpani L, Lee S, Drezek R, Hafner JH, Lapotko DO (2010) Plasmonic nanobubbles as transient vapor nanobubbles generated around plasmonic nanoparticles. *ACS Nano* 4:2109–2123. doi:[10.1021/nn1000222](https://doi.org/10.1021/nn1000222)
79. Hleb EY, Lapotko DO (2009) Influence of transient environmental photothermal effects on optical scattering by gold nanoparticles. *Nano Lett* 9:2160–2166. doi:[10.1021/ml9007425](https://doi.org/10.1021/ml9007425)
80. Lapotko DO (2009) Optical excitation and detection of vapor bubbles around plasmonic nanoparticles. *Opt Express* 17:2538–2556. doi:[10.1364/OE.17.002538](https://doi.org/10.1364/OE.17.002538)
81. Kling CL, Hammit FG (1972) A photographic study of spark-induced cavitation bubble collapse. *Trans ASME D: J Basic Eng* 94:825–832. doi:[10.1115/1.3425571](https://doi.org/10.1115/1.3425571)

82. Lauterborn W (1972) High-speed photography of laser-induced breakdown in liquids. *Appl Phys Lett* 21:27. doi:[10.1063/1.1654204](https://doi.org/10.1063/1.1654204)
83. Ohl CD, Philipp A, Lauterborn W (1995) Cavitation bubble collapse studied at 20 million frames per second. *Annr Phys* 507:26–34. doi:[10.1002/andp.19955070104](https://doi.org/10.1002/andp.19955070104)
84. Yavas O, Leiderer P, Park HK, Grigoropoulos CP, Poon CC, Leung WP, Do N, Tam AC (1993) Optical reflectance and scattering studies of nucleation and growth of bubbles at a liquid-solid interface induced by pulsed laser heating. *Phys Rev Lett* 70:1830–1833. doi:[10.1103/PhysRevLett.70.1830](https://doi.org/10.1103/PhysRevLett.70.1830)
85. Vogel A, Lauterborn W (1988) Acoustic transient generation by laser-produced cavitation bubbles near solid boundaries. *J Acoust Soc Am* 84:719–731. doi:[10.1121/1.396852](https://doi.org/10.1121/1.396852)
86. Marston PL (1979) Critical angle scattering by a bubble: physical-optics approximation and observation. *J Opt Soc Am* 69:1205–1211. doi:[10.1364/JOSA.69.001205](https://doi.org/10.1364/JOSA.69.001205)
87. Stroud JS, Marston PL (1993) Optical detection of transient bubble oscillations associated with the underwater noise of rain. *J Acoust Soc Am* 94:2788–2792. doi:[10.1121/1.407362](https://doi.org/10.1121/1.407362)
88. Asaki TJ, Thiessen DB, Marston PL (1995) Effect of an insoluble surfactant on capillary oscillations of bubbles in water: observation of a maximum in the damping. *Phys Rev Lett* 75:2686–2689. doi: [10.1103/PhysRevLett.75.2686](https://doi.org/10.1103/PhysRevLett.75.2686). (E) 75:4336 (1995). [10.1103/PhysRevLett.75.4336](https://doi.org/10.1103/PhysRevLett.75.4336)
89. Fujimoto JG, Lin WZ, Ippen EP, Puliafito CA, Steinert RF (1985) Time-resolved studies of Nd:YAG laser-induced breakdown. Plasma formation, acoustic wave generation, and cavitation. *Invest Ophthalmol Vis Sci* 26:1771–1777
90. Gaitan DF, Crum LA, Church CC, Roy RA (1992) Sonoluminescence and bubble dynamics for a single, stable cavitation bubble. *J Acoust Soc Am* 91:3166–3183. doi:[10.1121/1.402855](https://doi.org/10.1121/1.402855)
91. Barber BP, Putterman SJ (1992) Light scattering measurements of the repetitive supersonic implosion of a sonoluminescing bubble. *Phys Rev Lett* 69:3839–3842. doi:[10.1103/PhysRevLett.69.3839](https://doi.org/10.1103/PhysRevLett.69.3839)
92. Plech A, Kotaidis V, Lorenc M, Boneberg J (2006) Femtosecond laser near-field ablation from gold nanoparticles. *Nature Phys* 2:44–47. doi:[10.1038/nphys191](https://doi.org/10.1038/nphys191)
93. Lin CP, Kelly MW (1998) Cavitation and acoustic emission around laser-heated microparticles. *Appl Phys Lett* 72:2800. doi:[10.1063/1.121462](https://doi.org/10.1063/1.121462)
94. Neumann J, Brinkmann R (2008) Self-limited growth of laser-induced vapor bubbles around single microabsorbers. *Appl Phys Lett* 93:033901. doi:[10.1063/1.2957030](https://doi.org/10.1063/1.2957030)
95. Brinkmann R, Hüttmann G, Rögner J, Roeder J, Birngruber R, Lin CP (2000) Origin of retinal pigment epithelium cell damage by pulsed laser irradiance in the nanosecond to microsecond time regimen. *Lasers Surg Med* 27:451–464. doi:[10.1002/1096-9101\(2000\)27:5<451::AID-LSM1006>3.0.CO;2-1](https://doi.org/10.1002/1096-9101(2000)27:5<451::AID-LSM1006>3.0.CO;2-1)
96. Chen H, Diebold G (1995) Chemical generation of acoustic waves: a giant photoacoustic effect. *Science* 270:963–966. doi:[10.1126/science.270.5238.963](https://doi.org/10.1126/science.270.5238.963)
97. Lapotko D, Kuchinsky G (1995) Photothermal microscopy for cell imaging and diagnostics. *Proc SPIE* 2390:89–100. doi:[10.1117/12.205988](https://doi.org/10.1117/12.205988)
98. Vogel A, Linz N, Freidank S, Paltauf G (2008) Femtosecond-laser-induced nanocavitation in water: implications for optical breakdown threshold and cell surgery. *Phys Rev Lett* 100:038102. doi:[10.1103/PhysRevLett.100.038102](https://doi.org/10.1103/PhysRevLett.100.038102)
99. Vogel A, Noack J, Hüttmann G, Paltauf G (2005) Mechanisms of femtosecond laser nanosurgery of cells and tissues. *Appl Phys B* 81:1015–1047. doi:[10.1077/s00340-005-2036-6](https://doi.org/10.1077/s00340-005-2036-6)
100. Pitsillides CM, Joe EK, Wie X, Anderson RR, Lin CP (2003) Selective cell targeting with light-absorbing microparticles and nanoparticles. *Biophys J* 84:4023–4032. doi:[10.1016/S0006-3495\(03\)75128-5](https://doi.org/10.1016/S0006-3495(03)75128-5)
101. Kotaidis V, Dahmen C, von Plessen G, Springer F, Plech A (2006) Excitation of nanoscale vapor bubbles at the surface of gold nanoparticles in water. *J Chem Phys* 124:184702. doi:[10.1063/1.2187476](https://doi.org/10.1063/1.2187476)
102. Kotaidis V, Plech A (2005) Cavitation dynamics on the nanoscale. *Appl Phys Lett* 87:213102. doi:[10.1063/1.2132086](https://doi.org/10.1063/1.2132086)

103. Lukianova-Hleb EY, Ren X, Zasadzinski JA, Wu X, Lapotko DO (2012) Plasmonic nanobubbles enhance efficacy and selectivity of chemotherapy against drug-resistant cancer cells. *Adv Mater* 24:3831–3837. doi:[10.1002/adma.201103550](https://doi.org/10.1002/adma.201103550)
104. Wagner DS, Delk NA, Lukianova-Hleb EY, Hafner JH, Farach-Carson MC, Lapotko DO (2010) The in vivo performance of plasmonic nanobubbles as cell theranostic agents in zebrafish hosting prostate cancer xenografts. *Biomaterials* 31:7567–7574. doi:[10.1016/j.biomaterials.2010.06.031](https://doi.org/10.1016/j.biomaterials.2010.06.031)
105. Lukianova-Hleb EY, Ren X, Townley D, Wu X, Kupferman M, Lapotko D (2012) Plasmonic nanobubbles rapidly detect and destroy drug-resistant tumors. *Theranostics* 2:976–987. doi:[10.7150/thno.5116](https://doi.org/10.7150/thno.5116)
106. Lukianova-Hleb E, Wagner D, Brenner M, Lapotko D (2012) Cell-specific transmembrane injection of molecular cargo with gold nanoparticle-generated transient plasmonic nanobubbles. *Biomaterials* 33:5441–5450. doi:[10.1016/j.biomaterials.2012.03.077](https://doi.org/10.1016/j.biomaterials.2012.03.077)
107. Lapotko D, Lukianova E, Oraevsky A (2006) Selective laser nano-thermolysis of human leukemia cells with microbubbles generated around clusters of gold nanoparticles. *Lasers Surg Med* 38:631–642. doi:[10.1002/lsm.20359](https://doi.org/10.1002/lsm.20359)
108. Lapotko D, Shnip A, Lukianova E (2003) Photothermal detection of laser-induced damage in single intact cells. *Lasers Surg Med* 33:320–329. doi:[10.1002/lsm.10285](https://doi.org/10.1002/lsm.10285)
109. Jain KK (2010) Advances in the field of nanooncology. *BMC Med* 8:83. doi:[10.1186/1741-7015-8-83](https://doi.org/10.1186/1741-7015-8-83)
110. O'Neill BE, Rapoport N (2011) Phase-shift, stimuli-responsive drug carriers for targeted delivery. *Ther Deliv* 2:1165–1187. doi:[10.4155/tde.11.81](https://doi.org/10.4155/tde.11.81)
111. Ashokkumar M (2011) The characterization of acoustic cavitation bubbles—An overview. *Ultrason Sonochem* 18:864–872. doi:[10.1016/j.ultsonch.2010.11.016](https://doi.org/10.1016/j.ultsonch.2010.11.016)
112. Lapotko D, Lukianova K (2005) Laser-induced micro-bubbles in cells. *Int J Heat Mass Transfer* 48:227–234. doi:[10.1016/j.ijheatmasstransfer.2004.08.012](https://doi.org/10.1016/j.ijheatmasstransfer.2004.08.012)
113. Lauterborn W, Kurz T, Geisler R, Schanz D, Lindau O (2007) Acoustic cavitation, bubble dynamics and sonoluminescence. *Ultrason Sonochem* 14:484–491. doi:[10.1016/j.ultsonch.2006.09.017](https://doi.org/10.1016/j.ultsonch.2006.09.017)
114. Kurz T, Kröninger D, Geisler R, Lauterborn W (2006) Optic cavitation in an ultrasonic field. *Phys Rev E: Stat, Nonlin, Soft Matter Phys* 74:066307. doi:[10.1103/PhysRevE.74.066307](https://doi.org/10.1103/PhysRevE.74.066307)
115. Krasovitski B, Kislev H, Kimmel E (2007) Modeling photothermal and acoustical induced microbubble generation and growth. *Ultrasonics* 47:90–101. doi:[10.1016/j.ultras.2007.08.004](https://doi.org/10.1016/j.ultras.2007.08.004)
116. Lukianova-Hleb EY, Lapotko DO (2012) Experimental techniques for imaging and measuring transient vapor nanobubbles. *Appl Phys Lett* 101:264102. doi:[10.1063/1.4772958](https://doi.org/10.1063/1.4772958)
117. Boulais E, Lachaine R, Meunier M (2012) Plasma mediated off-resonance plasmonic enhanced ultrafast laser-induced nanocavitation. *Nano Lett* 12:4763–4769. doi:[10.1021/nl302200w](https://doi.org/10.1021/nl302200w)
118. Zharov V (2011) Ultrasharp nonlinear photothermal and photoacoustic resonances and holes beyond the spectral limit. *Nat Photonics* 5:110–116. doi:[10.1038/nphoton.2010.280](https://doi.org/10.1038/nphoton.2010.280)
119. Lukianova-Hleb EY, Sassaroli E, Jones A, Lapotko D (2012) Transient photothermal spectra of plasmonic nanobubbles. *Langmuir* 28:4858–4866. doi:[10.1021/la205132x](https://doi.org/10.1021/la205132x)
120. Siems A, Weber SAL, Boneberg J, Plech A (2011) Thermodynamics of nanosecond nanobubble formation at laser-excited metal nanoparticles. *New J Phys* 13:043018. doi:[10.1088/1367-2630/13/4/043018](https://doi.org/10.1088/1367-2630/13/4/043018)
121. Lukianova-Hleb E, Volkov A, Wu X, Lapotko D (2012) Transient enhancement and spectral narrowing of the photothermal effect of plasmonic nanoparticles under pulsed excitation. *Adv Materials* 25:772–776. doi:[10.1002/adma.201203609](https://doi.org/10.1002/adma.201203609)
122. Demtroder W (2008) *Laser Spectroscopy: basic concepts and instrumentation*. Springer, Berlin
123. Orrit M, Bernard J, Personov RI (1993) High-resolution spectroscopy of organic molecules in solids: from fluorescence line narrowing and hole burning to single molecule spectroscopy. *J Phys Chem* 97:10256–10268. doi:[10.1021/j100142a003](https://doi.org/10.1021/j100142a003)

124. Lukianova-Hleb EY, Ren X, Constantinou P, Danysh B, Shenefelt D, Carson D, Farach-Carson MC, Kulchitsky VA, Wu X, Wagner DS, Lapotko DO (2012) Improved cellular specificity of plasmonic nanobubbles versus nanoparticles in heterogeneous cell systems. *PLoS ONE* 7:e34537. doi:[10.1371/journal.pone.0034537](https://doi.org/10.1371/journal.pone.0034537)
125. Adamson AWG, Gast AP (1997) *Physical chemistry of surfaces*. Wiley, London, pp 784
126. Dean JA (ed) (1999) *Lange's handbook of chemistry*. McGraw-Hill, New York
127. de Gennes PGF, Brochard-Wyart F, Quere D (2004) *Capillary and wetting phenomena—drops, bubbles, pearls, waves*. Springer, Berlin, pp 291
128. Khlebtsov NG, Dykman LA, Krasnov Ya M, Melnikov AG (2000) Extinction of light by colloidal clusters of gold and silver particles formed in slow and fast aggregation regimes. *Colloid J* 62:765–779
129. Hleb E, Hafner JH, Myers JN, Hanna EY, Rostro BC, Zhdanok SA, Lapotko DO (2008) LANTCET: elimination of solid tumor cells with photothermal bubbles generated around clusters of gold nanoparticles. *Nanomedicine (Lond)* 3:647–667. doi:[10.2217/17435889.3.5.647](https://doi.org/10.2217/17435889.3.5.647)
130. Lapotko DO, Lukianova-Hleb EY, Oraevsky AA (2007) Clusterization of nanoparticles during their interaction with living cells. *Nanomedicine (Lond)* 2:241–253. doi:[10.2217/17435889.2.2.241](https://doi.org/10.2217/17435889.2.2.241)
131. Chithrani BD, Chan WCW (2007) Elucidating the mechanism of cellular uptake and removal of protein-coated gold nanoparticles of different sizes and shapes. *Nano Lett* 7:1542–1550. doi:[10.1021/nl070363y](https://doi.org/10.1021/nl070363y)
132. Salmaso S, Caliceti P, Amendola V, Meneghetti M, Magnusson JP, Pasparakis G, Alexander C (2009) Cell up-take control of gold nanoparticles functionalized with a thermoresponsive polymer. *J Mater Chem* 19:1608–1615. doi:[10.1039/B816603J](https://doi.org/10.1039/B816603J)
133. Mandal D, Maran A, Yaszemski MJ, Bolander ME, Sarkar G (2009) Cellular uptake of gold nanoparticles directly cross-linked with carrier peptides by osteosarcoma cells. *J Mater Sci Mater Med* 20:347–350. doi:[10.1007/s10856-008-3588-x](https://doi.org/10.1007/s10856-008-3588-x)
134. Haigler HT, McKanna JA, Cohen S (1979) Direct visualization of the binding and internalization of a ferritin conjugate of epidermal growth factor in human carcinoma cells A-431. *J Cell Biol* 81:382–395. doi:[10.1083/jcb.81.2.382](https://doi.org/10.1083/jcb.81.2.382)
135. Shukla R, Bansal V, Chaudhary M, Basu A, Bhonde RR, Sastry M (2005) Biocompatibility of gold nanoparticles and their endocytotic fate inside the cellular compartment: A microscopic overview. *Langmuir* 21:10644–10654. doi:[10.1021/la0513712](https://doi.org/10.1021/la0513712)
136. Chithrani BD, Ghazani AA, Chan WCW (2006) Determining the size and shape dependence of gold nanoparticle uptake into mammalian cells. *Nano Lett* 6:662–668. doi:[10.1021/nl052396o](https://doi.org/10.1021/nl052396o)
137. Mamot C, Drummond DC, Greiser U, Hong K, Kirpotin DB, Marks JD, Park JW (2003) Epidermal growth factor receptor (EGFR)-targeted immunoliposomes mediate specific and efficient drug delivery to EGFR- and EGFRvIII-overexpressing tumor cells. *Cancer Res* 63:3154–3161
138. Herbst RS, Langer CJ (2002) Epidermal growth factor receptors as a target for cancer treatment: the emerging role of IMC-C225 in the treatment of lung and head and neck cancers. *Semin Oncol* 29:27–36
139. Yokoyama T, Tam J, Kuroda S, Scott AW, Aaron J, Larson T et al (2011) EGFR-targeted hybrid plasmonic magnetic nanoparticles synergistically induce autophagy and apoptosis in non-small cell lung cancer cells. *PLoSOne* 6:e25507. doi:[10.1371/journal.pone.0025507](https://doi.org/10.1371/journal.pone.0025507)
140. Welch AJ, van Gemert MJC (eds) (2011) *Optical-thermal response of laser-irradiated tissue*, 2nd edn. Springer, Berlin
141. Zhang HF, Maslov K, Stoica G, Wang LV (2006) Functional photoacoustic microscopy for high-resolution and noninvasive in vivo imaging. *Nat Biotechnol* 24:848–851. doi:[10.1038/nbt1220](https://doi.org/10.1038/nbt1220)
142. Conjusteau A, Ermilov S, Lapotko D, Liao H, Hafner J, Eghtedari M, Motamedi M, Kotov N, Oraevsky A (2006) Metallic nanoparticles as optoacoustic contrast agents for medical imaging. *Proc SPIE* 6086:155–165. Doi: [10.1117/12.658065](https://doi.org/10.1117/12.658065)

143. Laser Institute of America (2007) American national standard for safe use of lasers (ANSI Z136.1–2007)
144. Cho K, Wang X, Nie S, Chen ZG, Shin DM (2008) Therapeutic nanoparticles for drug delivery in cancer. *Clin Cancer Res* 14:1310–1316. doi:[10.1158/1078-0432.CCR-07-1441](https://doi.org/10.1158/1078-0432.CCR-07-1441)
145. Peer D, Karp JM, Hong S, Farokhzad OC, Margalit R, Langer R (2007) Nanocarriers as An emerging platform for cancer therapy. *Nat Nanotechnol* 2:751–760. doi:[10.1038/nnano.2007.387](https://doi.org/10.1038/nnano.2007.387)
146. Kim B, Han G, Toley BJ, Kim CK, Rotello VM, Forbes NS (2010) Tuning payload delivery in tumour cylindroids using gold nanoparticles. *Nat Nanotechnol* 5:465–472. doi:[10.1038/nnano.2010.58](https://doi.org/10.1038/nnano.2010.58)
147. Pissuwan D, Niidome T, Cortie MB (2011) The forthcoming applications of gold nanoparticles in drug and gene delivery systems. *J Control Release* 149:65–71. doi:[10.1016/j.jconrel.2009.12.006](https://doi.org/10.1016/j.jconrel.2009.12.006)
148. Braun GB, Pallaoro A, Wu G, Missirlis D, Zasadzinski JA, Tirrell M, Reich NO (2009) Laser-activated gene silencing via gold nanoshell-siRNA conjugates. *ACS Nano* 3:2007–2015. doi:[10.1021/nm900469q](https://doi.org/10.1021/nm900469q)
149. Biswas S, Dodwadkar NS, Deshpande PP, Torchilin VP (2012) Liposomes loaded with paclitaxel and modified with novel triphenylphosphonium-PEG-PE conjugate possess low toxicity, target mitochondria and demonstrate enhanced antitumor effects in vitro and in vivo. *J Control Release* 159:393–402. doi:[10.1016/j.jconrel.2012.01.009](https://doi.org/10.1016/j.jconrel.2012.01.009)
150. Woo HN, Chung HK, Ju EJ, Jung J, Kang HW, Lee SW et al (2012) Preclinical evaluation of injectable sirolimus formulated with polymeric nanoparticle for cancer therapy. *Int J Nanomedicine* 7:2197–2208. doi:[10.2147/IJN.S29480](https://doi.org/10.2147/IJN.S29480)
151. Koning GA, Eggermont AM, Lindner LH, Ten Hagen TL (2010) Hyperthermia and thermosensitive liposomes for improved delivery of chemotherapeutic drugs to solid tumors. *Pharm Res* 27:1750–1754. doi:[10.1007/s11095-010-0154-2](https://doi.org/10.1007/s11095-010-0154-2)
152. Agarwal A, Mackey MA, El-Sayed MA, Bellamkonda RV (2011) Remote triggered release of doxorubicin in tumors by synergistic application of thermosensitive liposomes and gold nanorods. *ACS Nano* 5:4919–4926. doi:[10.1021/nm201010q](https://doi.org/10.1021/nm201010q)
153. Park JH, von Maltzahn G, Ong LL, Centrone A, Hatton TA, Ruoslahti E, Bhatia SN, Sailor MJ (2010) Cooperative nanoparticles for tumor detection and photothermally triggered drug delivery. *Adv Mater* 22:880–885. doi:[10.1002/adma.200902895](https://doi.org/10.1002/adma.200902895)
154. Stathopoulos GP, Antoniou D, Dimitroulis J, Michalopoulou P, Bastas A, Marosis K et al (2010) Liposomal cisplatin combined with paclitaxel versus cisplatin and paclitaxel in non-small-cell lung cancer: a randomized phase III multicenter trial. *Ann Oncol* 21:2227–2232. doi:[10.1093/annonc/mdq234](https://doi.org/10.1093/annonc/mdq234)
155. Zhang F, Zhu L, Liu G, Hida N, Lu G, Eden HS, Niu G, Chen X (2011) Multimodality imaging of tumor response to Doxil. *Theranostics* 1:302–309. doi:[10.7150/thno/v01p0302](https://doi.org/10.7150/thno/v01p0302)
156. Kost J, Leong K, Langer R (1989) Ultrasound-enhanced polymer degradation and release of incorporated substances. *Proc Natl Acad Sci U S A* 86:7663–7666. doi:[10.1073/pnas.86.20.7663](https://doi.org/10.1073/pnas.86.20.7663)
157. McCarthy MJ, Soong DS, Edelman ER (1984) Control of drug release from polymer matrices impregnated with magnetic beads—a proposed mechanism and model for enhanced release. *J Control Release* 1:143–147. doi:[10.1016/0168-3659\(84\)90006-3](https://doi.org/10.1016/0168-3659(84)90006-3)
158. Husseini GA, Pitt WG (2008) The use of ultrasound and micelles in cancer treatment. *J Nanosci Nanotechnol* 8:2205–2215. doi:[10.1166/jnn.2008.225](https://doi.org/10.1166/jnn.2008.225)
159. Rapoport N (2012) Ultrasound-mediated micellar drug delivery. *Int J Hyperthermia* 28:374–385. doi:[10.3109/02656736.2012.665567](https://doi.org/10.3109/02656736.2012.665567)
160. Shukla R, Chanda N, Zambre A, Upendran A, Katti K, Kulkarni RR et al (2012) Laminin receptor specific therapeutic gold nanoparticles (¹⁹⁸AuNP-EGCg) show efficacy in treating prostate cancer. *Proc Natl Acad Sci U S A* 109:12426–12431. doi:[10.1073/pnas.1121174109](https://doi.org/10.1073/pnas.1121174109)

161. Yuan H, Fales AM, Vo-Dinh T (2012) TAT peptide-functionalized gold nanostars: enhanced intracellular delivery and efficient NIR photothermal therapy using ultralow irradiance. *J Am Chem Soc* 134:11358–11361. doi:[10.1021/ja304180y](https://doi.org/10.1021/ja304180y)
162. Huang HC, Yang Y, Nanda A, Korla P, Rege K (2011) Synergistic administration of photothermal therapy and chemotherapy to cancer cells using polypeptide-based degradable plasmonic matrices. *Nanomedicine* 6:459–473. doi:[10.2217/nmm.10.133](https://doi.org/10.2217/nmm.10.133)
163. Cherukuri P, Glazer ES, Curley SA (2010) Targeted hyperthermia using metal nanoparticles. *Adv Drug Deliver Rev* 62:339–345. doi:[10.1016/j.addr.2009.11.006](https://doi.org/10.1016/j.addr.2009.11.006)
164. Huff TB, Tong L, Zhao Y, Hansen MN, Cheng JX, Wei A (2007) Hyperthermic effects of gold nanorods on tumor cells. *Nanomedicine (Lond)* 2:125–132. doi:[10.2217/17435889.2.1.125](https://doi.org/10.2217/17435889.2.1.125)
165. Gilstrap K, Hu X, Lu X, He X (2011) Nanotechnology for energy-based cancer therapies. *Am J Cancer Res* 1:508–520
166. Gobin AM, O’Neal DP, Watkins DM, Halas NJ, Drezek RA, West JL (2005) Near infrared laser-tissue welding using nanoshells as an exogenous absorber. *Lasers Surg Med* 37:123–129. doi:[10.1002/lsm.20206](https://doi.org/10.1002/lsm.20206)
167. Gormley AJ, Larson N, Sadekar S, Robinson R, Ray A, Ghandehari H (2012) Guided delivery of polymer therapeutics using plasmonic photothermal therapy. *Nano Today* 7:158–167. doi:[10.1016/j.nantod.2012.04.002](https://doi.org/10.1016/j.nantod.2012.04.002)
168. Záruba K, Králová J, Režanka P, Poučková P, Veverková L, Král V (2010) Modified porphyrin-brucine conjugated to gold nanoparticles and their application in photodynamic therapy. *Org Biomol Chem* 8:3202–3206. doi:[10.1039/c002823a](https://doi.org/10.1039/c002823a)
169. Cheng Y, Meyers JD, Broome A-M, Kenney ME, Basilion JP, Burda C (2011) Deep penetration of a PDT drug into tumors by noncovalent drug-gold nanoparticle conjugates. *J Am Chem Soc* 133:2583–2591. doi:[10.1021/ja108846h](https://doi.org/10.1021/ja108846h)
170. Prentice P, Cuschierp A, Dholakia K, Prausnitz M, Campbell P (2005) Membrane disruption by optically controlled microbubble cavitation. *Nat Phys* 1:107–110. doi:[10.1038/nphys148](https://doi.org/10.1038/nphys148)
171. Liu HL, Chen WS, Chen JS, Shih TC, Chen YY, Lin WL (2006) Cavitation-enhanced ultrasound thermal therapy by combined low- and high-frequency ultrasound exposure. *Ultrasound Med Biol* 32:759–767. doi:[10.1016/j.ultrasmedbio.2006.01.010](https://doi.org/10.1016/j.ultrasmedbio.2006.01.010)
172. Arita Y, Torres-Mapa ML, Lee WM, Cizmar T, Campbell P, Gunn-Moore FJ, Dholakia K (2011) Spatially optimized gene transfection by laser-induced breakdown of optically trapped nanoparticles. *Appl Phys Lett* 98:093702. doi:[10.1063/1.3554415](https://doi.org/10.1063/1.3554415)
173. Lukianova-Hleb E, Belyanin A, Kashinath S, Wu X, Lapotko D (2012) Plasmonic nanobubble-enhanced endosomal escape processes for selective and guided intracellular delivery of chemotherapy to drug-resistant cancer cells. *Biomaterials* 33:1821–1826. doi:[10.1016/j.biomaterials.2011.11.015](https://doi.org/10.1016/j.biomaterials.2011.11.015)
174. Lukianova-Hleb E, Samaniego A, Wen J, Metelitsa L, Chang C–C, Lapotko D (2011) Selective gene transfection of individual cells in vitro with plasmonic nanobubbles. *J Control Release* 152:286–293. doi:[10.1016/j.jconrel.2011.02.006](https://doi.org/10.1016/j.jconrel.2011.02.006)
175. Lukianova-Hleb EY, Ren X, Zasadzinski JA, Wu X, Lapotko D (2012) Plasmonic nanobubbles enhance efficacy and selectivity of chemotherapy against drug-resistant cancer cells. *Adv Mater* 24:3831–3837. doi:[10.1002/adma.201103550](https://doi.org/10.1002/adma.201103550)
176. Anderson L, Hansen E, Lukianova-Hleb EY, Hafner JH, Lapotko DO (2010) Optically guided controlled release from liposomes with tunable plasmonic nanobubbles. *J Control Release* 144:151–158. doi:[10.1016/j.jconrel.2010.02.012](https://doi.org/10.1016/j.jconrel.2010.02.012)
177. Lukianova-Hleb EY, Mutonga M, Lapotko DO (2012) Cell-specific multifunctional processing of heterogeneous cell systems in a single laser pulse treatment. *ACS Nano* 6:10973–10981. doi:[10.1021/nn3045243](https://doi.org/10.1021/nn3045243)
178. Lukianova-Hleb E, Oginsky AO, Samaniego AO, Shenefelt DL, Wagner DS, Hafner JH, Farach-Carson MC, Lapotko DO (2011) Tunable plasmonic nanoprobe for theranostics of prostate cancer. *Theranostics* 1:3–17. doi:[10.7150/thno/v01p0003](https://doi.org/10.7150/thno/v01p0003)

179. Lapotko D, Lukianova E, Potapnev M, Aleinikova O, Oraevsky A (2006) Method of laser activated nano-thermolysis for elimination of tumor cells. *Cancer Lett* 239:36–45. doi:[10.1016/j.canlet.2005.07.031](https://doi.org/10.1016/j.canlet.2005.07.031)
180. Lukianova-Hleb EY, Koneva II, Oginsky AO, La Francesca S, Lapotko DO (2011) Selective and self-guided micro-ablation of tissue with plasmonic nanobubbles. *J Surg Res* 166:e3–e13. doi:[10.1016/j.jss.2010.10.039](https://doi.org/10.1016/j.jss.2010.10.039)
181. Lukianova-Hleb E, Hanna EY, Hafner JH, Lapotko DO (2010) Tunable plasmonic nanobubbles for cell theranostics. *Nanotechnology* 21:85102. doi:[10.1088/0957-4484/21/8/085102](https://doi.org/10.1088/0957-4484/21/8/085102)
182. Mueller H, Kassack MU, Wiese M (2004) Comparison of the usefulness of the MTT, ATP, and Calcein assays to predict the potency of cytotoxic agents in various human cancer cell lines. *J Biomol Screen* 9:506–515. doi:[10.1177/1087057104265386](https://doi.org/10.1177/1087057104265386)
183. Doxil: Product Information Book (2011) Centocor Ortho Biotech Products, L.P. USA 3/2011
184. McDannold NJ, Vykhodtseva NI, Hynynen K (2006) Microbubble contrast agent with focused ultrasound to create brain lesions at low power levels: MR imaging and histologic study in rabbits. *Radiology* 241:95–106. doi:[10.1148/radiol.24111051170](https://doi.org/10.1148/radiol.24111051170)
185. Kennedy JE (2005) High-intensity focused ultrasound in the treatment of solid tumours. *Nat Rev Cancer* 5:321–327. doi:[10.1038/nrc1591](https://doi.org/10.1038/nrc1591)
186. Rapoport NY, Kennedy AM, Shea JE, Scaife CL, Nam KH (2009) Controlled and targeted tumor chemotherapy by ultrasound-activated nanoemulsions/microbubbles. *J Control Release* 138:268–276. doi:[10.1016/j.jconrel.2009.05.026](https://doi.org/10.1016/j.jconrel.2009.05.026)
187. Ferrara KW (2008) Driving delivery vehicles with ultrasound. *Adv Drug Deliv Rev* 60:1097–1102. doi:[10.1021/la2011259](https://doi.org/10.1021/la2011259)
188. Wang CH, Huang YF, Yeh CK (2011) Aptamer-conjugated nanobubbles for targeted ultrasound molecular imaging. *Langmuir* 27:6971–6976. doi:[10.1021/la2011259](https://doi.org/10.1021/la2011259)
189. Yin T, Wang P, Zheng R, Zheng B, Cheng D, Zhang X, Shuai X (2012) Nanobubbles for enhanced ultrasound imaging of tumors. *Int J Nanomedicine* 7:895–904. doi:[10.2147/IJN.S28830](https://doi.org/10.2147/IJN.S28830)
190. Cavalli R, Bisazza A, Trotta M, Argenziano M, Civra A, Donalisio M, Lembo D (2012) New chitosan nanobubbles for ultrasound-mediated gene delivery: preparation and in vitro characterization. *Int J Nanomedicine* 7:3309–3318. doi:[10.2147/IJN.S30912](https://doi.org/10.2147/IJN.S30912)
191. Cochran MC, Eisenbrey J, Ouma RO, Soulen M, Wheatley MA (2011) Doxorubicin and Paclitaxel loaded microbubbles for ultrasound triggered drug delivery. *Int J Pharm* 414:161–170. doi:[10.1016/j.ijpharm.2011.05.030](https://doi.org/10.1016/j.ijpharm.2011.05.030)

Chapter 33

Cell-based Microfluidic Assays in Translational Medicine

Eric K. Sackmann, Benjamin P. Casavant,
S. Farshid Moussavi-Harami, David J. Beebe
and Joshua M. Lang

33.1 Introduction

Microfluidics is the study and use of techniques that manipulate $10^{-9} - 10^{-18}$ l of fluid within channels of micrometer dimensions [1]. The field of microfluidics can be traced back to the latter part of the twentieth century, and its rapid evolution coincided with the advent of sensitive chemical analysis techniques and high-throughput genomic studies. This chapter discusses the history of microfluidics, including techniques used to construct microfluidic channels, and microfluidic functional assays for clinical practice. For the purpose of this discussion, we define functional assays as the isolation and analysis of clinically relevant living cells. Clinical assay development can be expensive and time-consuming, but coupling rapid prototyping techniques with microfluidics can shorten development time of clinical assays. Furthermore, these microfluidic assays can be integrated with

E. K. Sackmann · B. P. Casavant · S. F. Moussavi-Harami · D. J. Beebe
University of Wisconsin Carbone Cancer Center and Department of Biomedical
Engineering, 6028 Wisconsin Institutes for Medical Research,
1111 Highland Avenue, 53705 Madison, WI, USA
e-mail: eric.sackmann@me.com

B. P. Casavant
e-mail: bcasavant@wisc.edu

S. F. Moussavi-Harami
e-mail: moussavihara@wisc.edu

D. J. Beebe
e-mail: djbeebe@wisc.edu

J. M. Lang (✉)
Department of Medicine, University of Wisconsin Carbone Cancer Center,
7151 Wisconsin Institutes for Medical Research, 1111 Highland Avenue, 53705
Madison, WI, USA
e-mail: jmlang@medicine.wisc.edu

high-throughput liquid handling techniques, enabling automated laboratory diagnostic platforms. To illustrate the complexity of assay development, we will review the discovery of human chorionic gonadotropin (hCG), which led to the development of the home pregnancy test. After introducing these topics, we will discuss two categories of microfluidic functional assays. One category includes microfluidic devices used to study gradient-dependent cell migration. The second category includes those used to isolate and analyze rare cells including circulating tumor cells (CTCs). These cells are shed from solid tumors, including breast and prostate cancer tumors, into peripheral blood and are used in the clinic as prognostic and predictive biomarkers.

33.1.1 History

Some of the drivers for the development of microfluidics include the following: chemical analysis, bio-defense, genomic analysis, and microelectronics. The use of microfluidics for chemical analysis can be traced back to microanalytical techniques including gas-phase chromatography (GPC), capillary electrophoresis, and high-pressure liquid chromatography (HPLC) [2–4]. These techniques enabled chemical analysis of small sample volumes with high sensitivity and high resolution. Microfluidics has also been effectively utilized in bio-defense applications. As a result of the Cold War, the United States government identified chemical and biological weapons as a threat to national security and safety. The Defense Advanced Research Projects Agency (DARPA) supported the development of field-deployable microfluidic-based detectors of chemical and biological weapons. This provided financial support that advanced the nascent field of microfluidics. Yet, another driver of microfluidics is the field of genomics including high-throughput DNA sequencing. Specifically, microfluidic technologies have been developed to conduct polymerase chain reactions (PCR) within small droplets, enabling quantification of gene expression of single cells or small cell populations [5–8]. Finally, the field of microfluidics has also been driven by microelectronics. Techniques originally developed for microelectronics including photolithography have been adapted to the field of microfluidics. These techniques have enabled the design of microfluidic devices with small features using polydimethylsiloxane (PDMS), an optically transparent and vapor-permeable material [9–12]. Microfluidics was first employed in cell biology in the late 1990s, where primary human keratinocytes were cultured on microposts created through soft lithography and PDMS [9]. Further development followed including microchannels that enabled coculture of various cell types [10]. One of the first cell-based assays, the “Christmas tree” channel enabled the study of chemotaxis within controlled gradients [13], followed by a microfluidic cell-sorting device [14].

33.1.2 Production of Microfluidic Device

Early microchannel platforms were developed using solvent etching on a glass and silicon substrates. In this process, solvents such as hydrofluoric acid were used to create indentations and patterns within a glass surface. However, this process was time-consuming and dangerous to the researchers, therefore limiting the accessibility of this technique to chemists and engineers. To address these shortcomings, researchers transitioned to a more accessible rapid prototyping method using photolithography, a technique used in microelectronics. Using this approach, photoresist is poured onto a silicon wafer and is patterned using a photomask, a high-resolution black and white transparency and ultraviolet (UV) light. The UV light polymerizes photoresist in areas where the mask is optically transparent, producing a copy of the black and white pattern of the photomask. At the end of the lithography process, non-polymerized photoresist is removed by a solvent, creating a master mold for subsequent device fabrication. PDMS is poured onto the master mold and is polymerized in a pattern that is a negative of the master. The PDMS channels are removed and bonded to a glass or plastic substrate. The use of photolithography and PDMS has made microfluidics accessible to engineering researchers. But, PDMS has rarely been used by mainstream biology, especially compared to thermoplastic materials such as polystyrene (PS). Therefore, to make microfluidic assays more accessible to non-engineers, it would be preferable to produce these microfluidic assays from PS or other commonly used polymers [15]. In order to fabricate microfluidic devices with thermoplastic materials, techniques are under development for manufacturing microfluidic channels using injection molding, soft lithography, micromilling, hot embossing, and 3D printing. Generally speaking, PDMS devices are more suitable for research and pilot studies due to the ease of manufacturing and ability to perform rapid design iterations, while hot embossing and micromilling are more conducive to larger studies and product development. Beyond the manufacturing considerations, there are other differences in the materials that should be weighed during the design of microfluidic devices for cell biology applications. These include the high gas permeability of PDMS versus PS that can be important for long-term biological studies, although this can also contribute to evaporation issues that can be detrimental to microscale experiments [16, 17]. PDMS has also been shown to absorb hydrophobic molecules, which makes PDMS unsuitable for steroid studies [18]. Other materials are being utilized more in the field of microfluidics, such as paper-based microchannels [19, 20]. These microchannels are made from paper patterned into hydrophobic and hydrophilic regions. Sample liquid, for example, urine or blood, is wicked into these channels toward regions containing the detection agent, for example, antibodies or chemicals for measuring urine glucose content.

33.1.3 Successful Microfluidic Assays in Clinical Practice: Home Pregnancy Test

One example of microfluidics in medical practice and a successful point-of-care diagnostics assay is the lateral flow pregnancy test. The earliest recorded attempt at a pregnancy test is described in Egyptian hieroglyphs. The Egyptians believed that urine from a pregnant woman induced growth of wheat or barley seeds, with barley sprout indicating a male unborn and wheat sprout indicating a female unborn. While scientific evidence disputes the efficacy of this test for identifying a fetus' sex, experiments in the 1960s suggested that urine from pregnant females induced seed growth [21]. Many failed attempts at pregnancy tests were made throughout history, including visual inspection of urine by "piss prophets"; however, little scientific advancement was made until the discovery of various sex and pregnancy-related hormones [22]. In the 1920s, scientists in Austria and Germany identified a substance that induced ovary development and another that was specifically present in pregnant females. This pregnancy hormone was later identified as human chorionic gonadotropin (hCG) hormone. In the 1960s, scientists developed the hemagglutination inhibition test for detecting hCG, which was the earliest scientific assay for the detection of pregnancy. This test employed purified hCG, mixed with urine as sample, and antibodies directed against hCG. In a positive test, the red blood cells would clump, indicating a pregnancy [23]. This test proved unreliable as it resulted in many false negatives, and many medications caused false positives. In the early 1970s, two clinicians, Griff Ross and Judish Vaitukaitis, at the National Institutes of Health, discovered that hCG activity was only dependent on its β -subunit and created specific antibodies against the β -subunit of hCG [24, 25]. This discovery paved the way for the first at-home pregnancy test. The first version of this test took 2 h and was more accurate for positive than negative results (high sensitivity, low specificity). The test was described as follows, "for your \$10...you get premeasured ingredients consisting of a vial of purified water, a test tube containing, among other things, sheep red blood cells...as well as medicine dropper and clear plastic support for the test tube" [26]. These descriptions help to illuminate the complexity of the assay. In the late 1980s, a new advancement was made with the use of the lateral flow (LF) assay pregnancy test. The LF pregnancy tests came preloaded with all reagents required for measurement and detection. The technology used a porous capillary bed to flow the sample from the collection well through an antibody and detection well. While LF technology predates the field of microfluidics, these features are the hallmark of modern microfluidic technologies. The simplicity of the assay enabled its use at home and in resource-limited settings. Due to their simplicity, low-cost, and minimal sample size, lateral flow assays are considered the gold standard for microfluidic-based clinical assays. A recent extension of these LF assays can be found in paper-based microfluidic channels that involve the use of patterning to control the wetting of a preloaded paper [20]. Paper-based microfluidic assays are being developed as simple and cheap point-of-care assays [19].

33.1.4 Chapter Scope

Currently, microfluidic assays are under development for detecting various proteins and biomarkers from biofluids, and we refer the readers to reviews and articles on this topic [27–29]. The aim of the current chapter is to introduce readers to recent developments related to microfluidic assays for functional biologic measurements including cell migration and the analysis of rare cells. Topics covered include chemotaxis [30] (gradient-dependent cell migration) and isolation of rare cells including circulating tumor cells [31]. We will also summarize early clinical studies involving these microfluidic functional assays and future research directions.

33.2 Chemotaxis

The human body is made up of 100 trillion cells [32], with over 200 cell types that perform a variety of important biological functions. Cell migration is one of the most critical functions for the proper execution of several physiological processes. For example, cell migration is central to wound healing to repair damaged tissue [33] and mobilization of white blood cells to mount the innate immune response in an acute infection [34]. In some cases, cell motility can be detrimental, as is the case when metastatic cancer cells spread rapidly throughout the body during cancer progression [35–37]. Cellular migration is rarely random, but rather guided by extracellular cues that direct cell movement. There are several types of extracellular cues that can direct cell migration, including gradients in cellular adhesion sites (haptotaxis), mechanical cues in the cell microenvironment (durotaxis), changes in the electrical field (electrotaxis), and the presence of soluble proteins (chemotaxis). For chemotaxis to occur, a cell senses an extracellular biochemical gradient and responds by migrating directionally toward, or away from, the increasing concentration of the attractant molecule. Cell chemotaxis is an area of intense study in the cell biology community, and many chemotaxis assays have been developed in order to study this phenomenon in depth. In this section, we will describe the physiology of eukaryotic cell chemotaxis, provide an overview of macroscale and microscale chemotaxis assays that have been developed over the last 50 years, and explore the potential of translating appropriately designed chemotaxis techniques beyond the research setting and into the clinic.

33.2.1 Eukaryotic Cell Chemotaxis

Cellular chemotaxis is a complex, multistage process during which receptors on the cell membrane recognize external biochemical cues and induce intracellular signaling changes, leading to polarization of the cytoskeleton and cell migration.

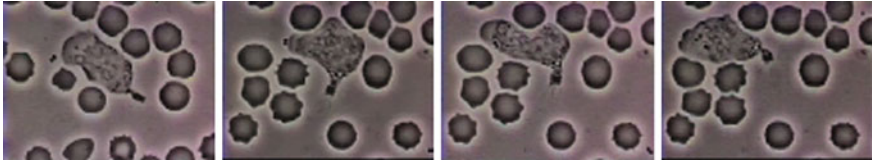


Fig. 33.1 A famous example of neutrophil chemotaxis and phagocytosis. The neutrophil is seen migrating toward a bacterium as it secretes some kind of unknown chemoattractant (e.g., N-formyl peptides like fMLP). The neutrophil polarizes its cytoskeleton and extends lamellepodia toward an increasing concentration of proteins that guide the cell toward the bacterium. Note the ability of the neutrophil to rapidly change direction and polarization in response to movement of the bacterium, as well as its ability to navigate around red blood cells. In its final fate, the bacterium is engulfed by the neutrophil and killed during phagocytosis. (The above images were taken from a 16 mm video recorded by David Rogers of Vanderbilt University in the 1950s. Details can be found at www.biochemweb.org/neutrophil.shtml)

Prokaryotic and eukaryotic cell types both have the ability to undergo chemotaxis, though prokaryotic chemotaxis is characterized by significantly different mechanisms and signaling pathways. Two classic chemotaxis models that have been well characterized in the literature include *Dictyostelium discoideum* amoebae and neutrophils, which exhibit many of the characteristics of eukaryotic cell chemotaxis. However, there are mechanistic differences between the various chemotactic cell types that cannot be covered in this chapter. For details on cell types that will not be discussed here, we refer readers to the following reviews on chemotaxis for bacteria [38]; *Dictyostelium discoideum* [39, 40]; dendritic cells [41]; natural killer cells [42], and macrophages [43]. In order to provide an example of the biology of chemotaxis in a cell type that is currently being exploited in translational medicine, we will focus on neutrophils—the most abundant cell type in the innate immune system and first responders during inflammation and wound healing (Fig. 33.1).

Neutrophil chemotaxis can be broken down into three distinct but overlapping stages: chemosensing, polarization, and locomotion (reviewed in [44, 45]). When a neutrophil senses a concentration gradient of external secreted proteins known as chemokines, the cell polarizes its cytoskeleton and engages in sustained directional migration toward the attractant molecules (i.e., chemoattractant). We will provide a brief overview of the biology of chemotaxis for neutrophils and refer the reader to the aforementioned reviews for a more in-depth treatment of the subject.

33.2.1.1 Chemosensing

Neutrophils stay in an inactive and immobile state until they are activated by external cues. When a chemoattractant is present, neutrophils extend and retract lamellipodia—protrusions of the cell membrane comprised of actin filaments—to dynamically form pseudopods for about 60s intervals. If a uniform concentration

of chemoattractant is present, neutrophils migrate more or less randomly until the cell senses a gradient of chemoattractant and begins to migrate directionally. Neutrophils sense chemoattractants using transmembrane chemoattractant receptors (e.g., fMLP-R and C5a-R) that become occupied by extracellular chemokines, and these receptors activate heterotrimeric G-proteins that transduce the extracellular signals and initiate an intracellular activation cascade. The chemoattractant receptors are relatively uniformly distributed on the cell membrane, and the local and temporary nature of the pseudopod formation allows neutrophils to rapidly change the extension of pseudopodia in reaction to location changes of the source of chemoattractant. Once the cell becomes polarized, neutrophils maintain the original leading edge of the cell and turns toward the new source of chemoattractant rather than forming new pseudopodia.

33.2.1.2 Polarization and Locomotion

Neutrophils can become polarized in a uniform concentration of chemoattractant; however, polarization is much more likely when a concentration gradient exists, resulting in persistent migration toward the source of chemoattractant (chemotaxis). When there is a difference as little as 1–2 % in the number of receptors on opposite ends of the cell occupied by chemoattractants, the neutrophil polarizes its cytoskeleton by increasing the number of advancing pseudopodia on the anterior portion of the cell and enriching retracting uropods with myosin in the posterior portion of the cell. Once activated and polarized, neutrophils have the ability to persistently migrate toward a site of inflammation that is sending inflammatory signals (chemokines) or chase down pathogens such as bacteria to phagocytose and clear the pathogen. The persistent migration of neutrophils is determined by a variety of factors such as type of chemoattractant, steepness, and profile of the concentration gradient and other biophysical and biochemical factors in the neutrophils' extracellular microenvironment.

33.2.2 Chemotaxis in Disease

In the introduction, we described chemotaxis as central to the pathophysiology of many diseases. Indeed, chemotaxis is relevant to the spread of metastatic cancer [36], wound healing [33, 46, 47], the inflammatory response by the innate immune system [48, 49], rheumatoid arthritis [50], chronic obstructive pulmonary disorder (COPD [51]), and asthma [52–54]. The role of chemotaxis in the pathogenesis of these and many other diseases has been intensely studied over the last 50 years. Researchers have made progress in identifying chemotactic cell types central to the pathogenesis of a disease, as well as the identification of cytokines orchestrating cell mobility.

For example, the dissemination of metastatic cancer cells from a primary tumor site throughout the body is central to the pathophysiology of the disease. If a primary tumor is detected early, treatment regimens and prognosis are greatly improved compared to late-stage detection [55]. In other words, the cancer becomes much harder to treat once the cells have migrated away from the primary tumor site, entered the bloodstream (after angiogenesis has been initiated), and extravasated from the blood stream to form a secondary tumor. If the cancer cells have not left the primary tumor site, the cancer can often be surgically removed or treated with local irradiation. Although directional migration is not necessary for this process, there is evidence that metastases occur more efficiently when the cells migrate directionally [56]. Researchers have also shown that the chemotaxis of tumor cells toward macrophages is important for intravasation into blood vessel and for invasion into the tissue of a secondary site [57]. Minimizing or disrupting the ability of cancer cells to undergo chemotaxis may lead to a reduction in the metastatic potential of cancer cells, resulting in improved prognostic outcomes for cancer patients.

In asthma, the dysregulation of inflammatory response contributes to the pathogenesis of the syndrome. Asthma is a condition characterized by chronic inflammation of the lungs that ultimately leads to obstruction of airflow, resulting in clinical symptoms including wheezing, coughing, and shortness of breath. The condition has far-reaching impact and affects more than 300 million people worldwide [58]. Furthermore, asthma prevalence has increased significantly over the last 30 years in many regions, with some indications that it may be reaching a plateau in the developed world [52, 59]. Researchers have made progress uncovering the mechanisms and pathophysiology of asthma, leading to improved treatment and management. However, diagnosing asthma still remains a challenge for physicians [60–62], and misdiagnosis can lead to unnecessary treatment, greatly increased medical costs [63], or missed treatment for vulnerable populations such as the elderly [61, 62]. In this case, mitigating the hyperchemotactic activity of inflammatory cells could lead to improved clinical outcomes for asthmatic patients.

Cancer metastasis and asthma represent two diseases in which chemotaxis can play a central role in the pathophysiology of disease. Researchers have studied these pathways in an attempt not only to understand the biology of a disease, but also to develop targeted therapies. For instance, a therapy blocking the production of interleukin-5 (IL-5)—a cytokine that is implicated in mucus secretion, the recruitment of eosinophils to the lungs (leading to eosinophilia for asthmatic patients), and airway hyper-responsiveness (AHR)—might decrease eosinophil and mast cell recruitment to the lungs, resulting in symptom relief for the patient [64]. Anti-IL-5 clinical trials are currently underway [65, 66], demonstrating how therapeutic interventions can be developed once the underlying pathway is uncovered. In order to understand the role of cell chemotaxis in various diseases and facilitate the development of drug therapies, researchers require robust *in vitro* assays to controllably and systematically study cell chemotaxis. In the following sections, we will explore both traditional macroscale chemotaxis assays and more

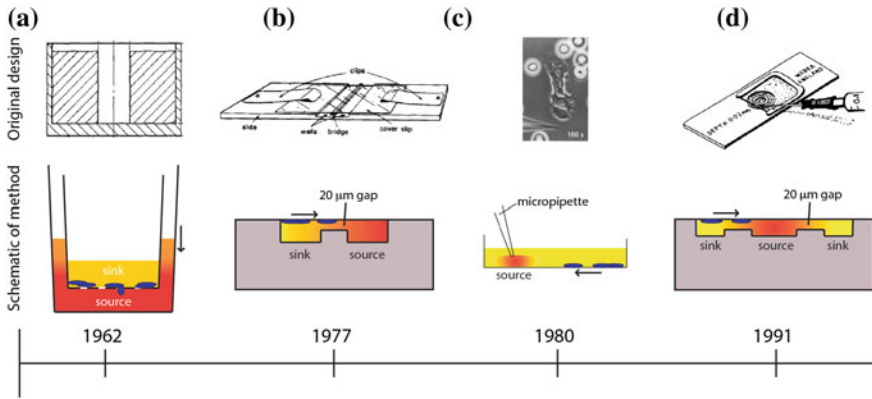


Fig. 33.2 Overview of macroscale chemotaxis assays that have been developed over the years. The timeline below each assay indicates the date the technology was invented below each assay (not to scale). The direction of the arrow indicates the direction of cell chemotaxis. The color shading indicates the formation of the chemical gradient of chemoattractant [67–70]. **a** Boyden/Transwell. **b** Zigmod. **c** Micropipette/Needle. **d** Dunn

recently developed microfluidic systems. Furthermore, we will explore how properly designed microfluidic chemotaxis devices can potentially be used in a clinical setting for diagnostic and therapeutic purposes.

33.2.3 Traditional Methods for Studying Cell Chemotaxis

Several assays have been developed to study cellular chemotaxis (Fig. 33.2). The first widely adopted in vitro assay was developed by Stephen Boyden in 1962 [67], known as the “Boyden chamber” or “Transwell” assay. The Transwell assay is a two-chamber system, with each chamber filled with media and separated by a microporous membrane (Fig. 33.2a). The lower chamber contains a test substance of interest (e.g., chemoattractants), and the upper chamber contains cells. During the course of an experiment, the source compound diffuses across the porous membrane due to the concentration gradient that exists between the two chambers. Chemotactic cells sense the spatial distribution of chemoattractant and, depending on the cell type and chemoattractant, migrate across the membrane and toward the source. Multiple wells can be studied simultaneously and in parallel, allowing incorporation of proper controls (i.e., no concentration gradient) or to test varying doses in order to characterize the chemotactic response of the cell type–compound combination. Several early studies demonstrated the utility of having an in vitro chemotaxis assay by characterizing the chemotactic response of several cell types under various experimental conditions [67, 71–73]. Following the successes of the Boyden chamber, researchers sought to develop new designs that offered different approaches to measuring cell chemotaxis.

Alternative *in vitro* chemotaxis assays that have been utilized in the biology community include the Zigmond chamber [68]; the Dunn chamber, which is a modification of the Zigmond chamber design [70]; the under-agarose assay [74]; and micropipette-based assays [69]. A comparison of some of these chemotaxis techniques is shown in Fig. 33.2. The Zigmond chamber consists of two etched wells—a chemoattractant (source) well and a well containing cells and media (sink)—that are separated by bridge that restricts convection of fluid from one well to the other (Fig. 33.2b). The cells are placed on an inverted coverslip spanning the two wells, allowing the investigator to observe cellular chemotaxis across the bridge in response to a chemical gradient. However, the gradients are short-lived (~ 1 h) and are somewhat unstable due to the evaporation that occurs in this design. The Dunn chamber design [70] sought to overcome these disadvantages and employs a spherical geometry, allowing the wells to be completely encapsulated by the coverslip to limit evaporation (Fig. 33.2d). The under-agarose assay is another early example of a technique that allowed the investigator to visually observe the migration of cells over time. In this assay, holes are punched in agarose gel, and a chemoattractant is placed in the holes to act as a source for the concentration gradient. Due to the concentration gradient between the source and the surrounding gel, the compound diffuses into the gel and cells sense the changing spatial distribution of the source compound over time and migrate toward the source under the agarose gel. This method is a simple and robust technique for creating one or more chemical gradients, while visualizing the response of cells in a physically confined environment. Foxmann et al. utilized the multisource capabilities of the under-agarose assay to characterize the neutrophil chemotactic function in competing gradients [75], and there are many other studies that utilize this technique [76, 77]. However, as useful as these *in vitro* chemotaxis assays have been over the years, researchers have discovered several limitations that limit their utility.

Technological limitations of these assays include the following: large sample volume requirements, unstable or unpredictable gradient profiles, and usability issues that make it difficult to run the desired experiment. For example, the most common macroscale chemotaxis assay in use today—the Transwell assay—develops unstable chemical gradient profiles [78]; filters cells by size and deformability due to the rigid microporous membrane the cells must cross [79]; and delivers ambiguous results as chemotaxis and chemokinesis are difficult to differentiate in this system [80]. The under-agarose assay allows for visualization of the cell migration path, but produces an unstable chemical gradient in all directions [78]. Additionally, under-agarose assays have low spatial resolution with respect to source and cell placement because of the way the experiment is conducted. The user is required to define these locations with a micropipet and crude hole-punching methods for the source of chemoattractant, both of which can be subject to significant variability. Therefore, while the method is relatively simple to perform and can be useful for visualizing cell migration paths, the under-agarose assay is not well-suited for reliable quantification of cell chemotaxis. Another popular and more modern visual chemotaxis assay is the Micropipette

assay (also known as the “Needle assay”). This technique offers significant technical advances over these older techniques, such as high-resolution real-time imaging (Fig. 33.2c and [81]). However, the method is also best suited for qualitative analysis because its onerous labor requirements limit investigators to low-throughput sampling. Another significant limitation of most macroscale assays is that they require large sample volumes in order to isolate specific cell types of interest. For example, to perform a neutrophil chemotaxis experiment using these common macroscale techniques, the sample preparation includes a blood draw and cell purification protocols [82] requiring tens of milliliters of blood. This sample volume requirement limits the number of times a subject can be sampled to probe their neutrophil chemotactic function, thereby restricting the time resolution of the experiment. Additionally, the large blood volumes needed makes sampling infants or small animals (e.g., mice, rats, etc.) for neutrophil chemotaxis logistically complex, if not impossible.

Microfluidic technologies play an important role in providing solutions to many of these limitations. Indeed, over the last decade, microfluidic engineers have either solved or minimized the gradient stability and sample volume limitations of macroscale assays. What properties of microfluidic systems enable them to improve upon current chemotaxis assays? In the following sections, we will detail why microfluidic technologies are particularly useful for chemotaxis assays by exploring the physics of fluids at the microscale.

33.2.4 Microfluidic Methods for Studying Cell Chemotaxis

Microfluidic devices are ideally suited to perform chemotaxis assays and offer significant advantages over macroscale approaches. As previously described, chemotactic eukaryotic cells can sense spatial and temporal perturbations in their microenvironment, and respond by directionally migrating toward the increasing concentration of the stimulus. The cell cannot undergo chemotaxis, however if the concentration changes so suddenly that the receptors on the cell membrane are unable to discern a difference in soluble factors from one side of the cell to the other. Fortunately, the physics of fluids at the micro/nanoliter scale makes creating diffusion dominant mass transport a relatively trivial task. Fluids at this scale are often characterized by a series of dimensionless quantities [83]; the quantity that is most widely cited is the Reynolds number (Re, Eq. 33.1):

$$\text{Re} = \frac{vL_0}{\eta} \quad (33.1)$$

where v is the characteristic velocity of the fluid; L_0 is the characteristic length scale in which the fluid is traveling; and η is the kinematic viscosity of the fluid. For devices with dimensions on the micrometer scale that manipulate fluids with typical velocities ($v \ll \text{m/s}$) and kinematic viscosity (e.g., aqueous solutions, oils, etc.), the

Reynolds number, $Re \ll 1$, is well under the transition from turbulent to laminar flow. Thus, the size scale of microfluidic technologies dictates that fluids generally behave according to the laminar flow regime. The implications of this phenomenon as applied to creating controllable gradients of soluble proteins are significant. Laminar fluids can be manipulated, combined, and separated in highly predictable and reproducible ways without the introduction of stochastic convective currents (turbulence). Specifically, two or more neighboring microfluidic streams can run adjacently to each other without turbulent mixing; instead, molecular diffusion dominates the mass transport between the laminar fluids.

Diffusion is a process governed by Brownian motion, where molecules move from a higher concentration to a lower concentration (i.e., thermodynamically driven). The kinetics of this process are determined by the activation energy required to move the diffusing molecule (e.g., proteins) through a particular medium (e.g., aqueous solution). In one dimension, diffusion can be modeled by (Eq. 33.2):

$$d = \sqrt{2Dt} \quad (33.2)$$

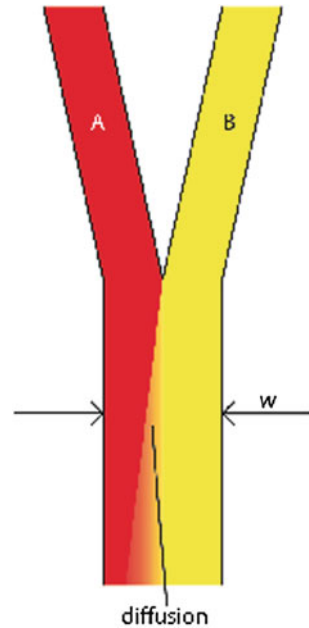
where d is the distance a molecule with diffusivity D travels in time t . There is another dimensionless quantity that describes the ratio of convection of a fluid compared to diffusion of a molecule within that fluid, known most commonly as the Peclet number (Eq. 33.3):

$$Pe = \frac{vL_0}{D} \quad (33.3)$$

where v and L_0 are the characteristic velocity of the fluid and length scale of the system, respectively, and D is still the diffusivity of a molecule from one fluid into the medium of an adjacent fluid. This number helps to determine the relative importance of diffusion compared to the convection of the fluid. In practice, the Pe number can be used to determine the necessary length of a microchannel to allow a complete diffusion of a molecule from one fluid stream to another. For example, consider two fluids—Fluid A and Fluid B—flowing in adjacent laminar flow streams at $10 \mu\text{m/s}$ in a microchannel with width of $500 \mu\text{m}$, and we wish to calculate the channel length required for a protein with diffusivity of $50 \mu\text{m}^2/\text{s}$ to diffuse from Fluid B to the channel edge of Fluid A (Fig. 33.3). Due to the lack of convective mixing on this scale, the protein B will take 20 channel widths or 5 cm to diffuse across Fluid A (a distance a few times the diameter of a human hair). These numbers demonstrate that diffusion can be well controlled within microchannels, but without convection, transport of molecules from one area of a microchannel to another takes considerable time.

Microfluidic engineers have leveraged the unique properties of fluids at the microscale to make significant advancements in the capabilities of chemotaxis assays. Microfluidic devices are ideally suited tools for chemotaxis assays because they can simulate the diffusion-dominant phenomena present in the cellular microenvironment. A classic example of a microfluidic chemotaxis device that

Fig. 33.3 Generic design of two fluids flowing through a microchannel in the laminar flow regime. Diffusion of molecules from fluid B occurs transverse to the fluid flow and down the concentration gradient toward fluid A



leverages microfluidic fluid phenomena is the “Christmas tree” design developed by George Whitesides’ lab in 2000 [13]. In this system, multiple concentration gradients are created by mixing fluid streams with different source concentrations in serpentine microchannels (Fig. 33.4a), then recombining the fluids with different combinations of the source concentration once the serpentine channels meet downstream. The result is a user-defined concentration gradient of the original source molecules (Fig. 33.4b). This channel design exploits laminar flow phenomena to generate highly reproducible concentration gradients that are difficult or impossible to achieve using macroscale techniques. The laminar flow properties of the system allow for the components of each source fluid to be separated and then recombined in a predictable and controllable fashion. However, the lack of convection in the system means a serpentine channel design must be utilized to achieve complete mixing due to the high Peclet number. This channel design has been used for developing chemical gradients for multiple cell types, including neutrophils [13], neural stem cells [84], *Dictyostelium discoideum* [85], and metastatic breast cancer cells [86].

The “Christmas tree” design is one example of leveraging microfluidic phenomena to develop highly predictable chemical gradients; however, many other gradient devices have been developed over the years using microfluidics. For example, Wong et al. describe a microfluidic system that utilizes hydrogel barriers to compartmentalize the source, sink, and cell channels [87].

Here, the authors make use of properties of the hydrogel that enable its use in cell culture—namely the high viscosity of the hydrogel that prevents convective

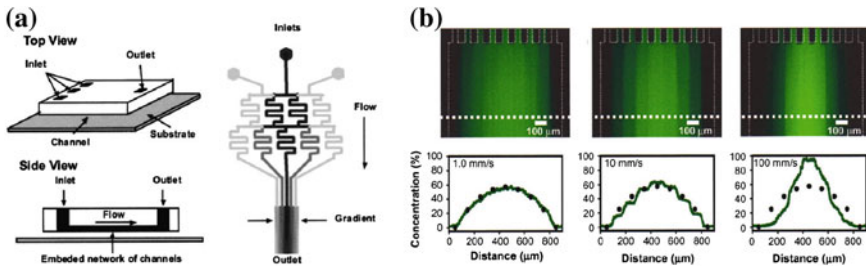


Fig. 33.4 Schematic and data of the microfluidic “Christmas tree” gradient generator. **a** Design of the serpentine gradient generator that shows the splitting and recombination of multiple fluid streams to create a chemical gradient. **b** Gradient profiles of fluorescent dye that show the versatility of the technique [88]

mass transport and the permeability of hydrogels, allowing protein diffusion from one compartment to another (e.g., from the source, to the cells, to the sink). In another class of static, no-flow microfluidic gradient generators, engineers have taken advantage of the greatly increased resistance to fluids as microchannel height is decreased:

$$Q = \frac{\Delta P}{R} \quad (33.4)$$

where Q is the flow rate of the fluid, ΔP is the pressure drop across the microchannel, and R is the fluidic resistance of the microchannel. Equation 33.4 shows that the convection rate of the fluid is inversely proportional to the resistance in of the microchannel. For a microchannel with rectangular cross section and high aspect ratio (width of channel far greater/less than the height of the microchannel), the resistance in the microchannel is given by:

$$R = \frac{12\mu L}{\omega h^3} \quad (33.5)$$

where h and w are the height and width of the channel, respectively; L is the length of the microchannel; and μ is the viscosity of the fluid [89]. From Eq. 33.5, we see that the resistance of a microchannel with a high aspect ratio is inversely proportional to the cube of its height. Therefore, a device can be engineered to be highly resistive to convection by decreasing the height of the microchannel (e.g., 7–15 μm) compared to the height of the cell, source, and sink channels. This technique of separating microchannels containing cells and reagents by low-height “diffusion channels” has been exploited to create no-flow gradient devices [90, 91] and for microfluidic multiculture systems [92]. This approach offers the benefits of highly controlled chemical gradients without requiring tubing or active pumping systems and conserves intercellular signaling that would normally be lost in a convection-based design. Other microfluidic designs have been reported that emphasize user-friendly operation to facilitate adoption by biologists, while

generating robust chemical gradient profiles [93]. For example, our lab recently reported a two-component chemotaxis device that sorts neutrophils within minutes and can easily form a chemical gradient by placing a lid with chemoattractant onto a base where the neutrophils have been sorted [30]. This technique enabled a new set of applications that were difficult or impossible to conduct using macroscale chemotaxis assays, demonstrating how microfluidic systems can not only simplify, but also enhance the capabilities of biomedical researchers. The technological advancements in microfluidics combined with their demonstrated advantages over macroscale assays lead to another potential application, which is clinical diagnostic chemotaxis assays.

33.2.5 Microfluidic Chemotaxis for Translational Research

Assays that directly assess cellular chemotactic function have the potential to make valuable contributions to medicine. The concept of probing the function of a cell type to confirm disease state is beginning to show promising results. This approach seeks to elicit information from the cell type of interest in order to diagnose disease, or perhaps monitor drug therapies. However, the approach of using cell chemotaxis as a readout for clinical medicine is at an embryonic stage, with few studies demonstrating this approach to-date. The few existing published studies share several characteristics, including superior control of the biochemical gradient compared to macroscale chemotaxis assays; user-friendly operation helped by utilizing passive pumping techniques [94] for fluid handling and the use of visual readouts that track cell migration over time.

Neutrophils are a possible candidate cell type for eliciting disease information based on chemotaxis function because of their central role in the pathophysiology of several diseases, as well as their robust ability to undergo chemotaxis. Several studies have probed neutrophils for diagnostic information [90, 91, 95]. For example, Butler et al. described a neutrophil chemotaxis platform that analyzed neutrophils from burn patients to characterize their health status [91]. In this study, the authors found that the magnitude of the burn injury negatively correlated with the speed of neutrophil migration toward the chemoattractant and impaired neutrophil chemotaxis observed as early as 24 h after the patient was burned. This result validates trends observed in previous studies using traditional chemotaxis techniques, such as the Transwell and Zigmond assays [96], although those studies did not document changes in neutrophil function until 72 h after the patient was burned. Additionally, the authors found a correlation between total body surface area of the burn and neutrophil chemotaxis function of the patient. The improved detection of disease phenotypes for the burn patients compared to macroscale techniques is likely due to the improved sensitivity that microfluidic gradient generators can achieve. Keeping user-friendly design considerations in mind, the authors designed this microfluidic chemotaxis device to operate without any external fluid handling equipment (Fig. 33.5a). In contrast, most traditional

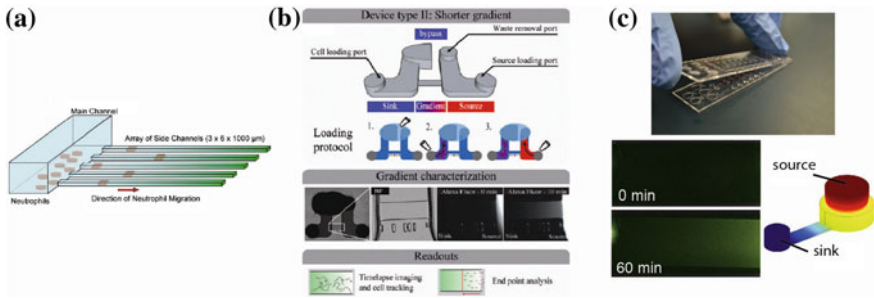


Fig. 33.5 Recent user-friendly chemotaxis devices that have been utilized for clinical applications. **a** Neutrophil chemotaxis through cell-sized microchannels ($3 \mu\text{m} \times 6 \mu\text{m}$) that allow for easy quantification, robust persistent neutrophil chemotaxis, and percent convection from the source to the sink [91]. **b** A chemotaxis device that also utilizes a low-height “diffusion channel” to prevent convection, along with a low-resistance “bypass” to direct any potential convection in the diffusion channel [90]. **c** A neutrophil chemotaxis device that operates by placing a lid containing chemoattractant onto a base containing the cells. Once the connection is made, the chemoattractant can diffuse into the microchannel where the cells are visually tracked over time. Experimental and modeling data of the gradient development are shown. Importantly, all three of these methods can be operated using only a micropipette, and do not require complex fluid handling equipment of expertise [30]

macroscale chemotaxis assays would be difficult to operate in a clinical setting. This study demonstrates how microfluidic assessment of chemotactic function can provide rich, functional information that can potentially be used as a diagnostic, prognostic, and/or therapeutic biomarker.

In our research lab, we have also explored the possibility of using neutrophil chemotaxis for diagnostic applications [90]. Berthier et al. describe a microfluidic chemotaxis device that can easily establish biochemical gradients in a high-throughput screen and automatically track neutrophil chemotactic function (Fig. 33.5b). This study analyzed the neutrophil chemotactic function from an infant who presented recurrent bacterial infections. The analysis showed a significantly retarded neutrophil chemotactic response for the patient compared to both healthy controls and the infant’s parents ($0.7 \mu\text{m/s}$ vs. $0.15\text{--}0.17 \mu\text{m/s}$, respectively). The assay enabled analysis of changing neutrophil morphology and quantitative characterization of the neutrophil chemotaxis. Importantly, both pieces of information conveyed a signaling defect for the patient. Indeed, the patient was later diagnosed with a rare genetic mutation in a GTPase Rac2 (D57 N) that has been previously reported in the literature for an infant with immunodeficiency [97]. This sort of rare immunodeficiency is difficult to diagnose clinically, but this study demonstrates that a functional readout based on cell chemotaxis can potentially aid in making the diagnosis. In another clinical study, we are employing an adaptation of a previously published chemotaxis platform (Fig. 33.5c, [30]) to study whether neutrophil chemotaxis can be used as a biomarker to characterize or diagnose asthma. In this study, we have utilized a microfluidic kit design, where all the reagents required to run the assay are

assembled in a complete, user-friendly assay. Additionally, the method employs a neutrophil sorting technique [93] that can be performed in several minutes using blood obtained from a lancet puncture. These features make it simple to rapidly perform the chemotaxis assay and make the system well suited for implementation in a clinical setting. Preliminary results from this study indicate that neutrophil chemotactic function may be impaired for asthmatic patients compared to non-asthmatic, allergic rhinitis patients. Although the results still need to be confirmed with additional experiments, the study illustrates how microfluidic solutions can provide significant advantages over macroscale assays for clinical applications. Furthermore, these reports demonstrate that chemotaxis can be a useful readout in the clinic to assist physicians with diagnosis or management of a variety of diseases.

Currently, there are few studies that use chemotactic readouts in a clinical setting, and other cell types beyond neutrophils have not been utilized for this purpose. However, given there are several migratory cell types central to the pathophysiology of many diseases, there is no technical or biological reason why the chemotactic function of other cell types could not be measured for clinical applications in the future. A new class of user-friendly chemotaxis assays combined with sophisticated automated tracking software have been published in recent years. These assays provide a compelling solution for physicians that wish to incorporate additional tools for generating a differential diagnosis.

33.2.6 Future Outlook

The use of microfluidic chemotaxis technologies in biology and translational research is still its infancy, and the likelihood of these techniques penetrating mainstream clinical practice remains unclear. To-date, there have been proof-of-concept studies that demonstrate how cell chemotaxis can be used to characterize or diagnose clinical symptoms, and these functional readouts have the potential to yield highly personalized insights into the disease phenotype for patients. However, the adoption of these techniques will likely be determined by whether chemotactic information can aid physicians in making diagnostic or therapeutic choices. This information needs to add to the characterization of the patient beyond the clinical symptoms the patient exhibits and the genetic/proteomic analysis that could be performed. Does the morphology of a migrating cell reveal information about the disease? Does directionality or chemotaxis velocity of a cell indicate hyperactivity that is useful for diagnostics or management of patient therapies? Recent studies have demonstrated that in some cases, the answer to these questions is “yes,” but more studies are required in order to cement these techniques into mainstream clinical practice. What is clear is that the advantages of microfluidic technologies for personalized analysis of a patient are compelling, and microfluidics appears to offer the most promising technological platform on which to build these novel assays.

33.3 Detecting Rare Cells

Rare cell analysis is critical to understanding many biological systems, and often the quantification or analysis of specific cell subtypes has the potential to drive clinical decision-making. The complete cell blood count (CBC) is the simplest and most ubiquitous example of the analysis of cellular subtypes, and this method is used in clinics globally. The CBC is used to monitor a variety of health conditions, from simple dehydration to more complex infections or cellular diseases. The collected blood sample cannot be used directly; instead, the initial sample must be prepared according to a specific protocol to isolate three specific cellular subtypes for quantification. In the case of the CBC, sample preparation is accomplished using density centrifugation to isolate nucleated leukocytes from erythrocytes, with platelets remaining in suspension. While CBCs are useful for a plethora of medical evaluations, their utility is limited by the non-specific nature of the CBC numerical readout. Moving beyond bulk leukocyte enumeration, evaluating subpopulations within the layer of isolated leukocytes has proven to be very useful for a variety of diseases, including the use of T cell counts for monitoring the progression of HIV [98, 99] and neutrophils in the diagnosis and study of asthma [90, 100]. The ability to capture specific subpopulations of cells from the layer of leukocytes obtained via density centrifugation has been pivotal for the diagnosis and treatment of many diseases [101, 102].

Cancer biology is another field wherein cell subpopulations act on larger systems. In the early 1700s, the London physician Percivall Pott was the first to notice the link between the high incidences of scrotal cancer among the population of chimney sweeps, thereby relating an environmental factor to cancer. Importantly, cancer stems from an initial mutation that causes cells to replicate without regulation by normal inhibitory signals from the body, resulting in a tumor mass. Furthermore, either the initial mutation causes increased replication or the replication event itself can further influence cells within the centralized tumor to undergo additional mutations. As a result, cells that make up the primary tumor may have many different mutations and characteristics that can vary by location within the tumor mass [103, 104]. For this reason, understanding the heterogeneity of primary tumors is considered important for personalized medicine and predicting resistance to therapy. Evidence also indicates that within these primary tumors are the subpopulations of stem cells that may act as specific initiators of tumor progression, and these cells may be resistant to chemotherapy. Cancer stem cells (CSCs) are particularly rare, but may be important in understanding the initiation and progression of tumors [105].

Cancer patient mortality is not typically a result of the primary tumor, but due to the spread of cancer and establishment of metastatic sites [107]. There are various ways that tumor cells can progress to metastasis. For instance, in kidney cancer, cases have been reported of a primary tumor growing into and through the vasculature, following the vena cava through to the tricuspid valve. One of the more common forms of metastasis is a result of the shedding of tumor cells into

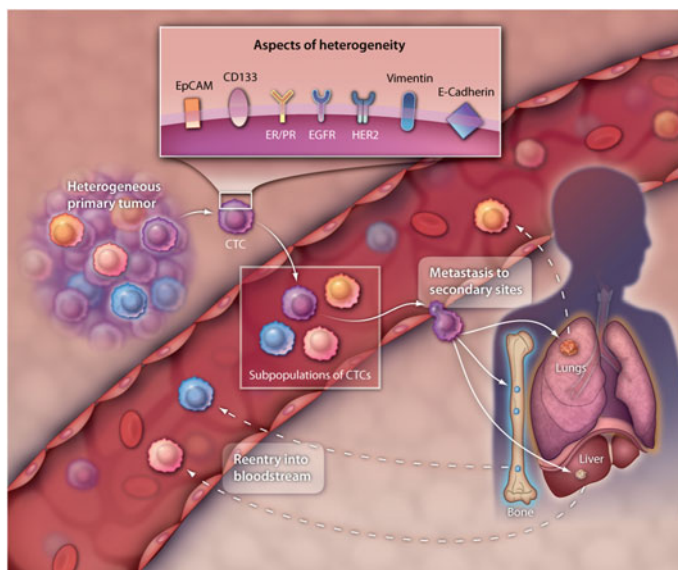


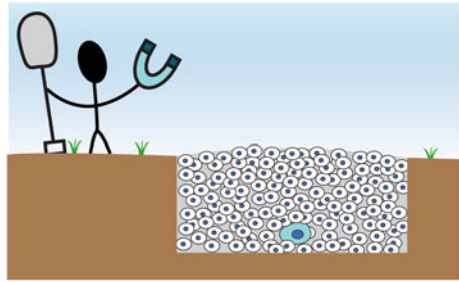
Fig. 33.6 Heterogeneity of CTCs. Heterogeneity of primary tumors and metastatic lesions is well established, and evidence supports the existence of heterogeneity in subpopulations of circulating tumor cells. The ability to define this heterogeneity may be pivotal in using CTCs as a clinical tool for the treatment of advanced cancers [106]

the blood circulation, allowing single or small clusters of cells to reach metastatic sites through the vasculature (Fig. 33.6). These cells, termed circulating tumor cells (CTCs), can be measured from the blood of patients with advanced cancer and may be responsible for hematogenous spread and metastasis to distance sites [31, 99, 106, 108, 109]. In recent years, CTC enumeration has shown to be prognostically relevant, with enumeration of these cells indicative of progression-free survival and overall survival [110–112]. A particularly challenging aspect of working with these cells, however, is their rarity. The prognostic threshold for CTC enumeration is 5 cells per 7.5 mLs in breast and prostate cancer a value that places CTC frequency at approximately 1 cell per 1 billion background cells. The potential value of these cells has resulted in the development of numerous methods to capture this rare cell type, and researchers endeavor to use the information contained within these cells as a “liquid biopsy.”

33.3.1 Macroscale Assays

In 1869, an Austrian physician Thomas Ashworth first detected CTCs microscopically in a patient who died from metastatic late-stage cancer [113]. The clinical utility of this discovery was realized 135 years later, when the Veridex

Fig. 33.7 The problem of CTCs. CTCs exist in *very low* abundance in the blood stream of late-stage cancer patients. Two methods to collect CTCs exist: positive (shown with the CTC magnet) or negative (shown by the shovel)



CellSearch[®] platform was launched and is currently the only FDA-approved method for detecting and enumerating CTCs. The Veridex assay targets a protein called the epithelial cell adhesion molecule (EpCAM), which is known to exist on the surface of epithelial cells but not on other cells in circulation. EpCAM is the main target for the positive selection of CTCs from the background of leukocytes present in the blood sample. There are three other methods for isolating CTCs using macroscale methods. These techniques are compatible with high-throughput platforms but unsatisfactorily isolate rare cells from a large volume of blood (Fig. 33.7).

33.3.1.1 Positive Selection

The Veridex CellSearch[®] platform and many other macroscale methods rely on biologic properties of the CTC to capture (also termed positive selection) the cell of interest from the background populations. Most positive selection techniques rely on the expression of EpCAM by potential CTCs. However, the ability to capture cells using alternative cell markers has been hypothesized including the use of antibodies against markers of epithelial–mesenchymal transition [114]. The FDA-approved definition of a CTC (based on the Veridex CellSearch) includes cells that are EpCAM positive, CD45 negative, and positive for a nucleus.

33.3.1.2 Negative Selection

Similar to the way that density centrifugation isolates leukocytes from erythrocytes, there are certain physical characteristics of CTCs that differentiate them from “not CTCs.” Methods that take advantage of negative selection techniques include OncoQuick[®], which separates cells present in blood using density gradients. OncoQuick selects nucleated cells (removing erythrocytes) and then removes leukocytes through the use of specific cell markers (usually CD45+). This method has the advantage of not relying on specific surface markers, enabling analysis of less common CTC cell surface markers that may be implicated in the progression of metastatic disease.

33.3.1.3 Functional Analyses

CTCs can also be selected using methods that benchmark the functionality of these cells compared to background cells. One method for CTC detection utilizes flow cytometers to isolate cells stained positively for specific proteins. In the case of CTCs, both EpCAM and another protein unique to epithelial cells called cytokeratin can be used in conjunction with fluorescently tagged antibodies to isolate and enumerate CTCs. Another method for functional CTC analysis is the epithelial immunospot (EPISPOT) method. The EPISPOT relies on cellular secretions to enumerate and distinguish CTCs from background leukocytes. In the case of prostate cancer, the EPISPOT captures the secretion of prostate-specific antigen (PSA) from a population of CTCs enriched using density centrifugation. Benefits of functional analyses include the ability to perform evaluation beyond simple enumeration and improving the understanding of cellular characteristics beyond surface or generic physical features.

Macroscale techniques offer many advantages and are simple to employ as demonstrated by the ubiquity of the 96-well plate and cell culture flasks, which are items standard to most biology labs. However, these methods rely on the availability of large amounts of cells—a limitation of macroscale methods when working the CTCs. Macroscale methods are generally not amenable to working with low cell numbers, making it difficult to observe rare cell events (CTCs). Furthermore, the sensitivity of most macroscale techniques is insufficient for identifying CTCs which exist in a low cell-to-background ratio. The low sensitivity inherent in most macroscale techniques results in the inability to detect CTCs due to the presence of contaminating cells. In addition, the contaminating cell types limit the ability to perform certain analytical techniques, including RNA and DNA analyses. For these reasons, the microscale is particularly advantageous for the isolation and analyses of these CTCs.

33.3.2 *Microscale Assays*

The microscale is particularly well suited for CTC research as capture and enumeration of these cells require a high-sensitivity, high-specificity assay. Because of the increased control enabled by the microscale, parameters can be more finely tuned to accommodate the frequency of CTCs. The precision afforded at the microscale allows researchers to capture cells within a more confined viewing window. Furthermore, microscale assays are able to create flow profiles specifically for cells with physical characteristics of CTCs and permit other specific manipulations that would be difficult on the macroscale. In addition, microscale isolation techniques preserve the viability of CTCs, permitting the use of these cells in functional assays to better understand their characteristics including tumor susceptibility to specific chemotherapies. Because of the unique advantages afforded to researchers by studying CTCs at the microscale, many technologies

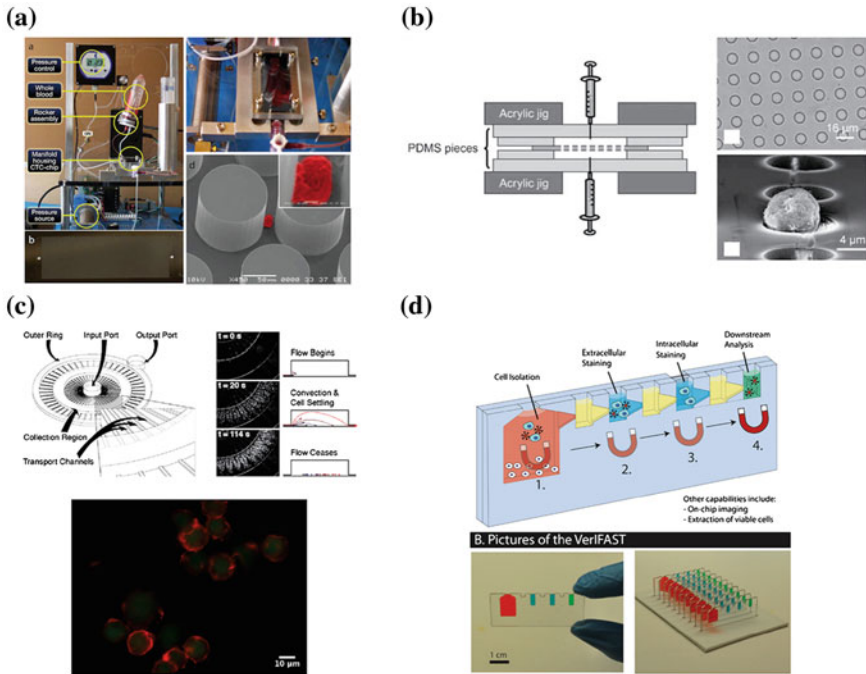


Fig. 33.8 Example microscale microfluidics technologies [31, 117, 119, 120]. **a** CTC chip. **b** Microfluid filter. **c** Microfluidic cell concentrator. **d** The VeriFAST

have recently been developed to capture and enumerate CTCs. We will briefly review a few of these microfluidic-based isolation techniques here. For a more detailed assessment of microfluidic cell sorting technologies, we refer the readers to more comprehensive reviews [115, 116].

33.3.2.1 CTC Chip

Shortly after the Veridex CellSearch platform was developed (Fig. 33.8a), researchers at joint MIT-Harvard facilities developed the CTC Chip [117]. Based on the herringbone chip, an array of posts functionalized with anti-EpCAM antibodies are housed within a microfluidic device such that whole blood can be flowed through the device. When the EpCAM-positive cells come into contact with a post, they are captured and subsequently stained for CTC-positive markers in the same fashion as the Veridex CellSearch platform. The ability to stain cells for specific RNA sequences using fluorescence in situ hybridization techniques (FISH) [118] on the CTC Chip has been recently demonstrated, further highlighting the utility of performing assays at the microscale.

33.3.2.2 CTC Filter

Similar to many negative-selection techniques, the CTC filter uses physical characteristics of CTCs to isolate them from background cells (Fig. 33.8b). Boasting a particularly high throughput for microscale techniques, filter technologies have demonstrated the ability to use a size-exclusion membrane to capture CTCs and allow the billions of background cells through the mesh [119].

33.3.2.3 Microfluidic Cell Concentrator

The microfluidic cell concentrator uses negative selection methodology in the macroscale to isolate CTCs using density centrifugation and CD45+ cell removal (Fig. 33.8c). The depleted mixture is then placed into a microfluidic device wherein cells settle in a specific region, facilitating downstream analysis of the cells for functional or other endpoints, as fluid washes can be performed without any cell loss [120].

33.3.2.4 VerIFAST

Using positive selection method, the VerIFAST leverages the dominance of surface tension over gravity at the microscale to create a “virtual wall” of oil between two aqueous phases (Fig. 33.8d). One phase contains magnetic beads bound to CTCs through a flexible capture method. The analyte-bound magnetic beads are pulled with a magnet to the oil–aqueous interface and escorted through the interface to the second aqueous phase. This method reduces the need for washes, as cell transfer takes the place of fluid wash steps. This method preserves the ability to manipulate cells following isolation. For example, intracellular staining of isolated CTCs allows in-depth molecular analysis of CTCs [31].

33.3.3 *Future Directions*

Microscale methods can be used to facilitate downstream cellular analyses. Enabling analysis of CTCs beyond enumeration will be important to the future advancement of CTC-based medical devices. Microfluidic methods have facilitated this progression by allowing increased control of interactions at the microscale to realize the potential of CTCs as a “liquid biopsy.” Moving forward, increased understanding of these cells to enhance their utility in the clinic is still necessary to see CTCs used as a widespread biomarker, but as methods for analysis of this rare cell population become more accessible, the possibilities for clinical relevance of this cell population grow. Future engineering solutions to isolate single cells for high-content molecular interrogation (next-generation

sequencing, RNA sequencing, etc.) have the potential to discriminate rare cell populations that exhibit intrinsic or evolving mechanisms of resistance to molecular targeting therapies.

33.4 Conclusion

The utility of cell-based microfluidic assays in clinical practice is expanding. Numerous assays beyond those described in this chapter are under development for clinical practice. Microfluidic assays are enabling quantification and analysis of cellular characteristics that were previously not possible using standard macroscale techniques. Furthermore, cell-based microfluidic assays simplify these measurements for clinical practice. The small sample volumes required for microfluidic assays enable readouts at multiple time points, providing a more complete picture of the patient for the clinician. This is an exciting time for microfluidic assay development, especially cell-based assays, as the field looks to make greater contributions to clinical practice within this decade.

References

1. Whitesides GM (2006) The origins and the future of microfluidics. *Nature* 442(7101):368–373. doi:[10.1038/nature05058](https://doi.org/10.1038/nature05058) nature05058 [pii]
2. Jacobson SC, Hergenroder R, Moore AW, Ramsey JM (1994) Precolumn Reactions with Electrophoretic Analysis Integrated on a Microchip. *Anal Chem* 66(23):4127–4132. doi:[10.1021/Ac00095a003](https://doi.org/10.1021/Ac00095a003)
3. Jacobson SC, Koutny LB, Hergenroder R, Moore AW, Ramsey JM (1994) Microchip Capillary Electrophoresis with an Integrated Postcolumn Reactor. *Anal Chem* 66(20):3472–3476. doi:[10.1021/Ac00092a027](https://doi.org/10.1021/Ac00092a027)
4. Regnier FE, He B, Lin S, Busse J (1999) Chromatography and electrophoresis on chips: critical elements of future integrated, microfluidic analytical systems for life science. *Trends Biotechnol* 17(3):101–106. doi:[10.1016/S0167-7799\(98\)01294-3](https://doi.org/10.1016/S0167-7799(98)01294-3)
5. Kopp MU, Mello AJ, Manz A (1998) Chemical amplification: continuous-flow PCR on a chip. *Science* 280(5366):1046–1048
6. Waters LC, Jacobson SC, Kroutchinina N, Khandurina J, Foote RS, Ramsey JM (1998) Microchip device for cell lysis, multiplex PCR amplification, and electrophoretic sizing. *Anal Chem* 70(1):158–162. doi:[10.1021/Ac970642d](https://doi.org/10.1021/Ac970642d)
7. Northrup MA, Benett B, Hadley D, Landre P, Lehew S, Richards J, Stratton P (1998) A miniature analytical instrument for nucleic acids based on micromachined silicon reaction chambers. *Anal Chem* 70(5):918–922
8. Summerer D (2009) Enabling technologies of genomic-scale sequence enrichment for targeted high-throughput sequencing. *Genomics* 94(6):363–368. doi:[10.1016/j.ygeno.2009.08.012](https://doi.org/10.1016/j.ygeno.2009.08.012) S0888-7543(09)00201-8 [pii]
9. Folch A, Ayon A, Hurtado O, Schmidt MA, Toner M (1999) Molding of deep polydimethylsiloxane microstructures for microfluidics and biological applications. *J Biomech Eng* 121(1):28–34

10. Folch A, Jo BH, Hurtado O, Beebe DJ, Toner M (2000) Microfabricated elastomeric stencils for micropatterning cell cultures. *J Biomed Mater Res* 52(2):346–353
11. McDonald JC, Duffy DC, Anderson JR, Chiu DT, Wu H, Schueller OJ, Whitesides GM (2000) Fabrication of microfluidic systems in poly(dimethylsiloxane). *Electrophoresis* 21(1):27–40. doi:[10.1002/\(sici\)1522-2683\(20000101\)21:1<27::aid-elps27>3.0.co;2-c](https://doi.org/10.1002/(sici)1522-2683(20000101)21:1<27::aid-elps27>3.0.co;2-c)
12. Duffy DC, McDonald JC, Schueller OJ, Whitesides GM (1998) Rapid prototyping of microfluidic systems in poly(dimethylsiloxane). *Anal Chem* 70(23):4974–4984. doi:[10.1021/ac980656z](https://doi.org/10.1021/ac980656z)
13. Li Jeon N, Baskaran H, Dertinger SK, Whitesides GM, Van de Water L, Toner M (2002) Neutrophil chemotaxis in linear and complex gradients of interleukin-8 formed in a microfabricated device. *Nat Biotechnol* 20 (8):826–830. doi:[10.1038/nbt712](https://doi.org/10.1038/nbt712) nbt712 [pii]
14. Fu AY, Chou HP, Spence C, Arnold FH, Quake SR (2002) An integrated microfabricated cell sorter. *Anal Chem* 74(11):2451–2457
15. Berthier E, Young EW, Beebe D (2012) Engineers are from PDMS-land. Biologists are from Polystyrenia. *Lab Chip* 12(7):1224–1237. doi:[10.1039/c2lc20982a](https://doi.org/10.1039/c2lc20982a)
16. Berthier E, Warrick J, Yu H, Beebe DJ (2008) Managing evaporation for more robust microscale assays. Part 2. Characterization of convection and diffusion for cell biology. *Lab Chip* 8(6):860–864. doi:[10.1039/b717423c](https://doi.org/10.1039/b717423c)
17. Berthier E, Warrick J, Yu H, Beebe DJ (2008) Managing evaporation for more robust microscale assays. Part 1. Volume loss in high throughput assays. *Lab Chip* 8(6):852–859. doi:[10.1039/b717422e](https://doi.org/10.1039/b717422e)
18. Regehr KJ, Domenech M, Koepsel JT, Carver KC, Ellison-Zelski SJ, Murphy WL, Schuler LA, Alarid ET, Beebe DJ (2009) Biological implications of polydimethylsiloxane-based microfluidic cell culture. *Lab Chip* 9(15):2132–2139. doi:[10.1039/b903043c](https://doi.org/10.1039/b903043c)
19. Pollock NR, Rolland JP, Kumar S, Beattie PD, Jain S, Noubary F, Wong VL, Pohlmann RA, Ryan US, Whitesides GM (2012) A paper-based multiplexed transaminase test for low-cost, point-of-care liver function testing. *Sci Transl Med* 4 (152):152ra129. doi:[10.1126/scitranslmed.3003981](https://doi.org/10.1126/scitranslmed.3003981)
20. Martinez AW, Phillips ST, Whitesides GM (2008) Three-dimensional microfluidic devices fabricated in layered paper and tape. *Proc Natl Acad Sci U S A* 105(50):19606–19611. doi:[10.1073/pnas.0810903105](https://doi.org/10.1073/pnas.0810903105) 0810903105 [pii]
21. Ghalioungui P, Khalil S, Ammar AR (1963) On an ancient Egyptian method of diagnosing pregnancy and determining foetal sex. *Med Hist* 7:241–246
22. Burstein J, Braunstein GD (1995) Urine pregnancy tests from antiquity to the present. *Early Pregnancy* 1(4):288–296
23. Robbins JL, Hill GA, Carle BN, Carlquist JH, Marcus S (1962) Latex agglutination reactions between human chorionic gonadotropin and rabbit antibody. *Proc Soc Exp Biol Med* 109:321–325
24. Vaitukaitis JL, Braunstein GD, Ross GT (1972) A radioimmunoassay which specifically measures human chorionic gonadotropin in the presence of human luteinizing hormone. *Am J Obstet Gynecol* 113(6):751–758. doi:[0002-9378\(72\)90553-4](https://doi.org/0002-9378(72)90553-4) [pii]
25. Vaitukaitis JL, Ross GT, Braunstein GD, Rayford PL (1976) Gonadotropins and their subunits: basic and clinical studies. *Recent Prog Horm Res* 32:289–331
26. Early Pregnancy Test Advertisement (1978). *Mademoiselle*
27. Chin CD, Laksanasopin T, Cheung YK, Steinmiller D, Linder V, Parsa H, Wang J, Moore H, Rouse R, Umvilighozo G, Karita E, Mwambarangwe L, Braunstein SL, van de Wijgert J, Sahabo R, Justman JE, El-Sadr W, Sia SK (2011) Microfluidics-based diagnostics of infectious diseases in the developing world. *Nat Med* 17(8):1015–1019. doi:[10.1038/nm.2408](https://doi.org/10.1038/nm.2408) nm.2408 [pii]
28. Yager P, Edwards T, Fu E, Helton K, Nelson K, Tam MR, Weigl BH (2006) Microfluidic diagnostic technologies for global public health. *Nature* 442(7101):412–418. doi:[10.1038/nature05064](https://doi.org/10.1038/nature05064) nature05064 [pii]

29. Berry SM, Maccoux LJ, Beebe DJ (2012) Streamlining immunoassays with immiscible filtrations assisted by surface tension. *Anal Chem* 84(13):5518–5523. doi:[10.1021/ac300085m](https://doi.org/10.1021/ac300085m)
30. Sackmann EK, Berthier E, Young EW, Shelef MA, Wernimont SA, Huttenlocher A, Beebe DJ (2012) Microfluidic kit-on-a-lid: a versatile platform for neutrophil chemotaxis assays. *Blood* 120(14):e45–53. doi:[10.1182/blood-2012-03-416453](https://doi.org/10.1182/blood-2012-03-416453) [pii]
31. Casavant BP, Guckenberger DJ, Berry SM, Tokar JT, Lang JM, Beebe DJ (2013) The VerIFAST: an integrated method for cell isolation and extracellular/intracellular staining. *Lab Chip* 13(3):391–396. doi:[10.1039/c2lc41136a](https://doi.org/10.1039/c2lc41136a)
32. Ahn AC, Tewari M, Poon CS, Phillips RS (2006) The limits of reductionism in medicine: could systems biology offer an alternative? *PLoS Med* 3(6):e208. doi:[10.1371/journal.pmed.0030208](https://doi.org/10.1371/journal.pmed.0030208) 05-PLME-ES-0675R1 [pii]
33. Poujade M, Grasland-Mongrain E, Hertzog A, Jouanneau J, Chavrier P, Ladoux B, Buguin A, Silberzan P (2007) Collective migration of an epithelial monolayer in response to a model wound. *Proc Natl Acad Sci U S A* 104(41):15988–15993. doi:[10.1073/pnas.0705062104](https://doi.org/10.1073/pnas.0705062104) 0705062104 [pii]
34. Nathan C (2006) Neutrophils and immunity: challenges and opportunities. *Nat Rev Immunol* 6(3):173–182. doi:[10.1038/nri1785](https://doi.org/10.1038/nri1785) nri1785 [pii]
35. Condeelis J, Singer RH, Segall JE (2005) The great escape: when cancer cells hijack the genes for chemotaxis and motility. *Annu Rev Cell Dev Biol* 21:695–718. doi:[10.1146/annurev.cellbio.21.122303.120306](https://doi.org/10.1146/annurev.cellbio.21.122303.120306)
36. Roussos ET, Condeelis JS, Patsialou A (2011) Chemotaxis in cancer. *Nat Rev Cancer* 11(8):573–587. doi:[10.1038/nrc3078](https://doi.org/10.1038/nrc3078) nrc3078 [pii]
37. Muller A, Homey B, Soto H, Ge N, Catron D, Buchanan ME, McClanahan T, Murphy E, Yuan W, Wagner SN, Barrera JL, Mohar A, Verastegui E, Zlotnik A (2001) Involvement of chemokine receptors in breast cancer metastasis. *Nature* 410(6824):50–56. doi:[10.1038/3506501635065016](https://doi.org/10.1038/3506501635065016) [pii]
38. Adler J (1975) Chemotaxis in bacteria. *Annu Rev Biochem* 44:341–356. doi:[10.1146/annurev.bi.44.070175.002013](https://doi.org/10.1146/annurev.bi.44.070175.002013)
39. Affolter M, Weijer CJ (2005) Signaling to cytoskeletal dynamics during chemotaxis. *Dev Cell* 9(1):19–34. doi:[10.1016/j.devcel.2005.06.003](https://doi.org/10.1016/j.devcel.2005.06.003) S1534-5807(05)00215-7 [pii]
40. Parent CA (2004) Making all the right moves: chemotaxis in neutrophils and Dictyostelium. *Curr Opin Cell Biol* 16(1):4–13. doi:[10.1016/j.ceb.2003.11.008](https://doi.org/10.1016/j.ceb.2003.11.008) S09555067403001662 [pii]
41. Sozzani S, Allavena P, Vecchi A, Mantovani A (2000) Chemokines and dendritic cell traffic. *J Clin Immunol* 20(3):151–160
42. Robertson MJ (2002) Role of chemokines in the biology of natural killer cells. *J Leukoc Biol* 71(2):173–183
43. Mosser DM, Edwards JP (2008) Exploring the full spectrum of macrophage activation. *Nat Rev Immunol* 8(12):958–969. doi:[10.1038/nri2448](https://doi.org/10.1038/nri2448) nri2448 [pii]
44. Iglesias PA, Devreotes PN (2008) Navigating through models of chemotaxis. *Curr Opin Cell Biol* 20(1):35–40. doi:[10.1016/j.ceb.2007.11.011](https://doi.org/10.1016/j.ceb.2007.11.011) S0955-0674(07)00179-2 [pii]
45. Van Haastert PJ, Devreotes PN (2004) Chemotaxis: signalling the way forward. *Nat Rev Mol Cell Biol* 5(8):626–634. doi:[10.1038/nrm1435](https://doi.org/10.1038/nrm1435)
46. Fong E, Tzllil S, Tirrell DA (2010) Boundary crossing in epithelial wound healing. *Proc Natl Acad Sci U S A* 107(45):19302–19307. doi:[10.1073/pnas.1008291107](https://doi.org/10.1073/pnas.1008291107) 1008291107 [pii]
47. Martin P, Leibovich SJ (2005) Inflammatory cells during wound repair: the good, the bad and the ugly. *Trends Cell Biol* 15(11):599–607. doi:[10.1016/j.tcb.2005.09.002](https://doi.org/10.1016/j.tcb.2005.09.002) S0962-8924(05)00227-8 [pii]
48. Ley K, Laudanna C, Cybulsky MI, Nourshargh S (2007) Getting to the site of inflammation: the leukocyte adhesion cascade updated. *Nat Rev Immunol* 7(9):678–689. doi:[10.1038/nri2156](https://doi.org/10.1038/nri2156) nri2156 [pii]
49. Soehnlein O, Lindbom L (2010) Phagocyte partnership during the onset and resolution of inflammation. *Nat Rev Immunol* 10(6):427–439. doi:[10.1038/nri2779](https://doi.org/10.1038/nri2779) nri2779 [pii]

50. Murphy G, Caplice N, Molloy M (2008) Fractalkine in rheumatoid arthritis: a review to date. *Rheumatology (Oxford)* 47(10):1446–1451. doi:[10.1093/rheumatology/ken197ken197](https://doi.org/10.1093/rheumatology/ken197ken197) [pii]
51. Barnes PJ (2010) Medicine. Neutrophils find smoke attractive. *Science* 330(6000):40–41. doi:[10.1126/science.1196017330/6000/40](https://doi.org/10.1126/science.1196017330/6000/40) [pii]
52. Eder W, Ege MJ, von Mutius E (2006) The asthma epidemic. *N Engl J Med* 355(21):2226–2235. doi:[10.1056/NEJMra054308](https://doi.org/10.1056/NEJMra054308) 355/21/2226 [pii]
53. Wenzel SE (2006) Asthma: defining of the persistent adult phenotypes. *Lancet* 368(9537):804–813. doi:[10.1016/S0140-6736\(06\)69290-8](https://doi.org/10.1016/S0140-6736(06)69290-8) S0140-6736(06)69290-8 [pii]
54. Fahy JV (2009) Eosinophilic and neutrophilic inflammation in asthma: insights from clinical studies. *Proc Am Thorac Soc* 6(3):256–259. doi:[10.1513/pats.200808-087RM6/3/256](https://doi.org/10.1513/pats.200808-087RM6/3/256) [pii]
55. Chambers AF, Groom AC, MacDonald IC (2002) Dissemination and growth of cancer cells in metastatic sites. *Nat Rev Cancer* 2(8):563–572. doi:[10.1038/nrc865nrc865](https://doi.org/10.1038/nrc865nrc865) [pii]
56. Roussos ET, Balsamo M, Alford SK, Wyckoff JB, Gligorijevic B, Wang Y, Pozzuto M, Stobezki R, Goswami S, Segall JE, Lauffenburger DA, Bresnick AR, Gertler FB, Condeelis JS (2011) Mena invasive (MenaINV) promotes multicellular streaming motility and transendothelial migration in a mouse model of breast cancer. *J Cell Sci* 124(Pt 13):2120–2131. doi:[10.1242/jcs.086231124/13/2120](https://doi.org/10.1242/jcs.086231124/13/2120) [pii]
57. Condeelis J, Pollard JW (2006) Macrophages: obligate partners for tumor cell migration, invasion, and metastasis. *Cell* 124(2):263–266. doi:[10.1016/j.cell.2006.01.007](https://doi.org/10.1016/j.cell.2006.01.007) S0092-8674(06)00055-9 [pii]
58. Masoli M, Fabian D, Holt S, Beasley R (2004) The global burden of asthma: executive summary of the GINA Dissemination Committee report. *Allergy* 59(5):469–478. doi:[10.1111/j.1398-9995.2004.00526.xALL526](https://doi.org/10.1111/j.1398-9995.2004.00526.xALL526) [pii]
59. Foy AL, Knuiaman MW, Divitini ML, Hui J, Hunter M, Palmer LJ, Maier G, Musk AW (2010) Changes in the prevalence of asthma in adults since 1966: the Busselton health study. *Eur Respir J* 35(2):273–278. doi:[10.1183/09031936.0019430809031936.00194308](https://doi.org/10.1183/09031936.0019430809031936.00194308) [pii]
60. Aaron SD, Vandemheen KL, Boulet LP, McIvor RA, Fitzgerald JM, Hernandez P, Lemiere C, Sharma S, Field SK, Alvarez GG, Dales RE, Doucette S, Fergusson D (2008) Overdiagnosis of asthma in obese and nonobese adults. *CMAJ* 179(11):1121–1131. doi:[10.1503/cmaj.081332179/11/1121](https://doi.org/10.1503/cmaj.081332179/11/1121) [pii]
61. Enright PL, McClelland RL, Newman AB, Gottlieb DJ, Lebowitz MD (1999) Underdiagnosis and undertreatment of asthma in the elderly. *Cardiovascular Health Study Research Group. Chest* 116(3):603–613
62. Urso DL (2009) Asthma in the elderly. *Curr Gerontol Geriatr Res*:858415. doi:[10.1155/2009/858415](https://doi.org/10.1155/2009/858415)
63. Serra-Batllés J, Plaza V, Morejon E, Comella A, Brugues J (1998) Costs of asthma according to the degree of severity. *Eur Respir J* 12(6):1322–1326
64. Lloyd CM, Hessel EM (2010) Functions of T cells in asthma: more than just T(H)2 cells. *Nat Rev Immunol* 10(12):838–848. doi:[10.1038/nri2870nri2870](https://doi.org/10.1038/nri2870nri2870) [pii]
65. Haldar P, Brightling CE, Hargadon B, Gupta S, Monteiro W, Sousa A, Marshall RP, Bradding P, Green RH, Wardlaw AJ, Pavord ID (2009) Mepolizumab and exacerbations of refractory eosinophilic asthma. *N Engl J Med* 360(10):973–984. doi:[10.1056/NEJMoa0808991360/10/973](https://doi.org/10.1056/NEJMoa0808991360/10/973) [pii]
66. Nair P, Pizzichini MM, Kjarsgaard M, Inman MD, Efthimiadis A, Pizzichini E, Hargreave FE, O’Byrne PM (2009) Mepolizumab for prednisone-dependent asthma with sputum eosinophilia. *N Engl J Med* 360(10):985–993. doi:[10.1056/NEJMoa0805435360/10/985](https://doi.org/10.1056/NEJMoa0805435360/10/985) [pii]
67. Boyden S (1962) The chemotactic effect of mixtures of antibody and antigen on polymorphonuclear leucocytes. *J Exp Med* 115:453–466
68. Zigmond SH (1977) Ability of polymorphonuclear leukocytes to orient in gradients of chemotactic factors. *J Cell Biol* 75(2 Pt 1):606–616

69. Gerisch G, Keller HU (1981) Chemotactic reorientation of granulocytes stimulated with micropipettes containing fMet-Leu-Phe. *J Cell Sci* 52:1–10
70. Zicha D, Dunn GA, Brown AF (1991) A new direct-viewing chemotaxis chamber. *J Cell Sci* 99(Pt 4):769–775
71. Schiffmann E, Corcoran BA, Wahl SM (1975) N-formylmethionyl peptides as chemoattractants for leucocytes. *Proc Natl Acad Sci U S A* 72(3):1059–1062
72. Tseng HY, Sun S, Shu Z, Ding W, Reems JA, Gao D (2011) A microfluidic study of megakaryocytes membrane transport properties to water and dimethyl sulfoxide at suprzero and subzero temperatures. *Biopreserv Biobank* 9(4):355–362. doi:[10.1089/bio.2011.002710.1089/bio.2011.0027](https://doi.org/10.1089/bio.2011.002710.1089/bio.2011.0027) [pii]
73. Wilkinson PC, Borel JF, Stecher-Levin VJ, Sorkin E (1969) Macrophage and neutrophil specific chemotactic factors in serum. *Nature* 222(5190):244–247
74. Nelson RD, Quie PG, Simmons RL (1975) Chemotaxis under agarose: a new and simple method for measuring chemotaxis and spontaneous migration of human polymorphonuclear leukocytes and monocytes. *J Immunol* 115(6):1650–1656
75. Foxman EF, Campbell JJ, Butcher EC (1997) Multistep navigation and the combinatorial control of leukocyte chemotaxis. *J Cell Biol* 139(5):1349–1360
76. Foxman EF, Kunkel EJ, Butcher EC (1999) Integrating conflicting chemotactic signals. The role of memory in leukocyte navigation. *J Cell Biol* 147(3):577–588
77. Heit B, Tavener S, Raharjo E, Kubes P (2002) An intracellular signaling hierarchy determines direction of migration in opposing chemotactic gradients. *J Cell Biol* 159(1):91–102. doi:[10.1083/jcb.200202114jcb.200202114](https://doi.org/10.1083/jcb.200202114jcb.200202114) [pii]
78. Lauffenburger DA, Zigmond SH (1981) Chemotactic factor concentration gradients in chemotaxis assay systems. *J Immunol Methods* 40(1):45–60. doi:[0022-1759\(81\)90079-X](https://doi.org/0022-1759(81)90079-X) [pii]
79. Wilkinson PC (1998) Assays of leukocyte locomotion and chemotaxis. *J Immunol Methods* 216(1–2):139–153. doi:[S0022-1759\(98\)00075-1](https://doi.org/S0022-1759(98)00075-1) [pii]
80. Wei SH, Parker I, Miller MJ, Cahalan MD (2003) A stochastic view of lymphocyte motility and trafficking within the lymph node. *Immunol Rev* 195:136–159. doi:[076](https://doi.org/076) [pii]
81. Xiao Z, Zhang N, Murphy DB, Devreotes PN (1997) Dynamic distribution of chemoattractant receptors in living cells during chemotaxis and persistent stimulation. *J Cell Biol* 139(2):365–374
82. Bach MK, Brashler JR (1970) Isolation of subpopulations of lymphocytic cells by the use of isotonicity balanced solutions of Ficoll. I. Development of methods and demonstration of the existence of a large but finite number of subpopulations. *Exp Cell Res* 61(2):387–396
83. Squires TM, Quake SR (2005) Microfluidics: Fluid physics at the nanoliter scale. *Rev Mod Phys* 77(3):977–1026. doi:[10.1103/Revmodphys.77.977](https://doi.org/10.1103/Revmodphys.77.977)
84. Chung BG, Flanagan LA, Rhee SW, Schwartz PH, Lee AP, Monuki ES, Jeon NL (2005) Human neural stem cell growth and differentiation in a gradient-generating microfluidic device. *Lab Chip* 5(4):401–406. doi:[10.1039/b417651k](https://doi.org/10.1039/b417651k)
85. Song L, Nadkarni SM, Bodeker HU, Beta C, Bae A, Franck C, Rappel WJ, Loomis WF, Bodenschatz E (2006) Dictyostelium discoideum chemotaxis: threshold for directed motion. *Eur J Cell Biol* 85(9–10):981–989. doi:[10.1016/j.ejcb.2006.01.012](https://doi.org/10.1016/j.ejcb.2006.01.012) S0171-9335(06)00026-4 [pii]
86. Wang SJ, Saadi W, Lin F, Minh-Canh Nguyen C, Li Jeon N (2004) Differential effects of EGF gradient profiles on MDA-MB-231 breast cancer cell chemotaxis. *Exp Cell Res* 300(1):180–189. doi:[10.1016/j.yexcr.2004.06.030S0014-4827\(04\)00386-6](https://doi.org/10.1016/j.yexcr.2004.06.030S0014-4827(04)00386-6) [pii]
87. Wong AP, Perez-Castillejos R, Christopher Love J, Whitesides GM (2008) Partitioning microfluidic channels with hydrogel to construct tunable 3-D cellular microenvironments. *Biomaterials* 29(12):1853–1861. doi:[10.1016/j.biomaterials.2007.12.044S0142-9612\(07\)01053-8](https://doi.org/10.1016/j.biomaterials.2007.12.044S0142-9612(07)01053-8) [pii]
88. Jeon NL, Dertinger SKW, Chiu DT, Choi IS, Stroock AD, Whitesides GM (2000) Generation of solution and surface gradients using microfluidic systems. *Langmuir* 16(22):8311–8316. doi:[10.1021/La000600b](https://doi.org/10.1021/La000600b)

89. Beebe DJ, Mensing GA, Walker GM (2002) Physics and applications of microfluidics in biology. *Annu Rev Biomed Eng* 4:261–286. doi:[10.1146/annurev.bioeng.4.112601.125916112601.125916](https://doi.org/10.1146/annurev.bioeng.4.112601.125916112601.125916) [pii]
90. Berthier E, Surfus J, Verbsky J, Huttenlocher A, Beebe D (2010) An arrayed high-content chemotaxis assay for patient diagnosis. *Integr Biol (Camb)* 2(11–12):630–638. doi:[10.1039/c0ib000030b](https://doi.org/10.1039/c0ib000030b)
91. Butler KL, Ambraveswaran V, Agrawal N, Bilodeau M, Toner M, Tompkins RG, Fagan S, Irimia D (2010) Burn injury reduces neutrophil directional migration speed in microfluidic devices. *PLoS ONE* 5(7):e11921. doi:[10.1371/journal.pone.0011921](https://doi.org/10.1371/journal.pone.0011921)
92. Domenech M, Yu H, Warrick J, Badders NM, Meyvantsson I, Alexander CM, Beebe DJ (2009) Cellular observations enabled by microculture: paracrine signaling and population demographics. *Integr Biol (Camb)* 1(3):267–274. doi:[10.1039/b823059e](https://doi.org/10.1039/b823059e)
93. Agrawal N, Toner M, Irimia D (2008) Neutrophil migration assay from a drop of blood. *Lab Chip* 8(12):2054–2061. doi:[10.1039/b813588f](https://doi.org/10.1039/b813588f)
94. Walker G, Beebe DJ (2002) A passive pumping method for microfluidic devices. *Lab Chip* 2(3):131–134. doi:[10.1039/b204381e](https://doi.org/10.1039/b204381e)
95. Kotz KT, Xiao W, Miller-Graziano C, Qian WJ, Russom A, Warner EA, Moldawer LL, De A, Bankey PE, Petritis BO, Camp DG 2nd, Rosenbach AE, Goverman J, Fagan SP, Brownstein BH, Irimia D, Xu W, Wilhelmy J, Mindrinos MN, Smith RD, Davis RW, Tompkins RG, Toner M (2010) Clinical microfluidics for neutrophil genomics and proteomics. *Nat Med* 16(9):1042–1047. doi:[10.1038/nm.2205nm.2205](https://doi.org/10.1038/nm.2205nm.2205) [pii]
96. Solomkin JS, Nelson RD, Chenoweth DE, Solem LD, Simmons RL (1984) Regulation of neutrophil migratory function in burn injury by complement activation products. *Ann Surg* 200(6):742–746
97. Kurkchubasche AG, Panepinto JA, Tracy TF Jr, Thurman GW, Ambruso DR (2001) Clinical features of a human Rac2 mutation: a complex neutrophil dysfunction disease. *J Pediatr* 139(1):141–147. doi:[10.1067/mpd.2001.114718](https://doi.org/10.1067/mpd.2001.114718) S0022-3476(01)70980-8 [pii]
98. Gurkan UA, Anand T, Tas H, Elkan D, Akay A, Keles HO, Demirci U (2011) Controlled viable release of selectively captured label-free cells in microchannels. *Lab Chip* 11(23):3979–3989. doi:[10.1039/c1lc20487d](https://doi.org/10.1039/c1lc20487d)
99. Lowes LE, Goodale D, Keeney M, Allan AL (2011) Image cytometry analysis of circulating tumor cells. *Methods Cell Biol* 102:261–290. doi:[10.1016/B978-0-12-374912-3.00010-9B978-0-12-374912-300010-9](https://doi.org/10.1016/B978-0-12-374912-3.00010-9B978-0-12-374912-300010-9) [pii]
100. Warner EA, Kotz KT, Ungaro RF, Abouhamze AS, Lopez MC, Cuenca AG, Kelly-Scumpia KM, Moreno C, O'Malley KA, Lanz JD, Baker HV, Martin LC, Toner M, Tompkins RG, Efron PA, Moldawer LL (2011) Microfluidics-based capture of human neutrophils for expression analysis in blood and bronchoalveolar lavage. *Lab Invest* 91(12):1787–1795. doi:[10.1038/labinvest.2011.94labinvest201194](https://doi.org/10.1038/labinvest.2011.94labinvest201194) [pii]
101. Khan MG, Bhaskar KR, Salam MA, Akther T, Pluschke G, Mondal D (2012) Diagnostic accuracy of loop-mediated isothermal amplification (LAMP) for detection of Leishmania DNA in buffy coat from visceral leishmaniasis patients. *Parasit Vectors* 5:280. doi:[10.1186/1756-3305-5-2801756-3305-5-280](https://doi.org/10.1186/1756-3305-5-2801756-3305-5-280) [pii]
102. Salam MA, Khan MG, Bhaskar KR, Afrad MH, Huda MM, Mondal D (2012) Peripheral blood buffy coat smear: a promising tool for diagnosis of visceral leishmaniasis. *J Clin Microbiol* 50(3):837–840. doi:[10.1128/JCM.05067-11JCM.05067-11](https://doi.org/10.1128/JCM.05067-11JCM.05067-11) [pii]
103. Schmitt MW, Prindle MJ, Loeb LA (2012) Implications of genetic heterogeneity in cancer. *Ann N Y Acad Sci* 1267:110–116. doi:[10.1111/j.1749-6632.2012.06590.x](https://doi.org/10.1111/j.1749-6632.2012.06590.x)
104. Al-Hajj M, Wicha MS, Benito-Hernandez A, Morrison SJ, Clarke MF (2003) Prospective identification of tumorigenic breast cancer cells. *Proc Natl Acad Sci U S A* 100(7):3983–3988. doi:[10.1073/pnas.05302911000530291100](https://doi.org/10.1073/pnas.05302911000530291100) [pii]
105. Clevers H (2011) The cancer stem cell: premises, promises and challenges. *Nat Med* 17(3):313–319. doi:[10.1038/nm.2304nm.2304](https://doi.org/10.1038/nm.2304nm.2304) [pii]
106. Lang JM, Casavant BP, Beebe DJ (2012) Circulating tumor cells: getting more from less. *Sci Transl Med* 4 (141):141ps113. doi:[10.1126/scitranslmed.3004261](https://doi.org/10.1126/scitranslmed.3004261) 4/141/141ps13 [pii]

107. Mundy GR (2002) Metastasis to bone: causes, consequences and therapeutic opportunities. *Nat Rev Cancer* 2(8):584–593. doi:[10.1038/nrc867nrc867](https://doi.org/10.1038/nrc867nrc867) [pii]
108. Lianidou ES, Markou A (2011) Circulating tumor cells in breast cancer: detection systems, molecular characterization, and future challenges. *Clin Chem* 57(9):1242–1255. doi:[10.1373/clinchem.2011.165068clinchem.2011.165068](https://doi.org/10.1373/clinchem.2011.165068clinchem.2011.165068) [pii]
109. Dharmasiri U, Witek MA, Adams AA, Soper SA (2010) Microsystems for the capture of low-abundance cells. *Annu Rev Anal Chem (Palo Alto Calif)* 3:409–431. doi:[10.1146/annurev.anchem.111808.073610](https://doi.org/10.1146/annurev.anchem.111808.073610)
110. Cristofanilli M, Budd GT, Ellis MJ, Stopeck A, Matera J, Miller MC, Reuben JM, Doyle GV, Allard WJ, Terstappen LW, Hayes DF (2004) Circulating tumor cells, disease progression, and survival in metastatic breast cancer. *N Engl J Med* 351(8):781–791. doi:[10.1056/NEJMoa040766351/8/781](https://doi.org/10.1056/NEJMoa040766351/8/781) [pii]
111. de Bono JS, Scher HI, Montgomery RB, Parker C, Miller MC, Tissing H, Doyle GV, Terstappen LW, Pienta KJ, Raghavan D (2008) Circulating tumor cells predict survival benefit from treatment in metastatic castration-resistant prostate cancer. *Clin Cancer Res* 14(19):6302–6309. doi:[10.1158/1078-0432.CCR-08-087214/19/6302](https://doi.org/10.1158/1078-0432.CCR-08-087214/19/6302) [pii]
112. Giuliano M, Giordano A, Jackson S, Hess KR, De Giorgi U, Mego M, Handy BC, Ueno NT, Alvarez RH, De Laurentiis M, De Placido S, Valero V, Hortobagyi GN, Reuben JM, Cristofanilli M (2011) Circulating tumor cells as prognostic and predictive markers in metastatic breast cancer patients receiving first-line systemic treatment. *Breast Cancer Res* 13(3):R67. doi:[10.1186/bcr2907bcr2907](https://doi.org/10.1186/bcr2907bcr2907) [pii]
113. Ashworth TR (1869) A case of cancer in which cells similar to those in the tumours were seen in the blood after death. *Aust Med J* 14:146–149
114. Bitting RL, Boominathan R, Rao C, Embree E, George DJ, Connelly MC, Kemeny G, Garcia-Blanco M, Armstrong AJ (2012) Isolation of circulating tumor cells using a novel EMT-based capture method. In: Paper presented at the Journal of Clinical Oncology, ASCO Annual Meeting Proceedings
115. Autebert J, Coudert B, Bidard FC, Pierga JY, Descroix S, Malaquin L, Viovy JL (2012) Microfluidic: an innovative tool for efficient cell sorting. *Methods* 57(3):297–307. doi:[10.1016/j.ymeth.2012.07.002S1046-2023\(12\)00157-0](https://doi.org/10.1016/j.ymeth.2012.07.002S1046-2023(12)00157-0) [pii]
116. Li P, Stratton ZS, Dao M, Ritz J, Huang TJ (2013) Probing circulating tumor cells in microfluidics. *Lab Chip* 13(4):602–609. doi:[10.1039/c2lc90148j](https://doi.org/10.1039/c2lc90148j)
117. Nagrath S, Sequist LV, Maheswaran S, Bell DW, Irimia D, Ulkus L, Smith MR, Kwak EL, Digumarthy S, Muzikansky A, Ryan P, Balis UJ, Tompkins RG, Haber DA, Toner M (2007) Isolation of rare circulating tumour cells in cancer patients by microchip technology. *Nature* 450(7173):1235–1239. doi:[10.1038/nature06385](https://doi.org/10.1038/nature06385) nature06385 [pii]
118. Yu M, Ting DT, Stott SL, Wittner BS, Oszolak F, Paul S, Ciciliano JC, Smas ME, Winokur D, Gilman AJ, Ulman MJ, Xega K, Contino G, Alagesan B, Brannigan BW, Milos PM, Ryan DP, Sequist LV, Bardeesy N, Ramaswamy S, Toner M, Maheswaran S, Haber DA (2012) RNA sequencing of pancreatic circulating tumour cells implicates WNT signalling in metastasis. *Nature* 487(7408):510–513. doi:[10.1038/nature11217](https://doi.org/10.1038/nature11217) nature11217 [pii]
119. Lin HK, Zheng S, Williams AJ, Balic M, Groshen S, Scher HI, Fleisher M, Stadler W, Datar RH, Tai YC, Cote RJ (2010) Portable filter-based microdevice for detection and characterization of circulating tumor cells. *Clin Cancer Res* 16(20):5011–5018. doi:[10.1158/1078-0432.CCR-10-11051078-0432.CCR-10-1105](https://doi.org/10.1158/1078-0432.CCR-10-11051078-0432.CCR-10-1105) [pii]
120. Warrick J, Casavant B, Frisk M, Beebe D (2010) A microfluidic cell concentrator. *Anal Chem* 82(19):8320–8326. doi:[10.1021/ac101866p](https://doi.org/10.1021/ac101866p)

Chapter 34

Engineering of Photomanipulatable Hydrogels for Translational Medicine

Mingtao He and Yan Zhang

34.1 Introduction

Photomanipulation with controllable wavelength and intensity on light source has the advantage of having high temporal and special resolution. Through the use of filters, photomasks or lasers, fabrication of complex features and exposure areas to light source with resolution as small as approximately 1 μm can now be realized. The advent of confocal microscopy further increased resolution with three-dimensional control. Light is a particularly attractive source of energy for use in manipulating behavior of biomolecules and biomaterials. Photomanipulation is an important approach to better understanding the cell and tissue dynamic response to the biomolecules and biomaterials, which then enables scientists to design drugs and medical devices with more flexibility.

Biomaterials developed for tissue engineering and regenerative medicine have important implications in translational medicine to improve existed therapy or to address clinical need which have not been met before [1]. Regenerative medicines have found good opportunities in cardiovascular and peripheral vascular repair, tissue-engineered vascular grafts, and cell-based therapies [2]. New therapeutic strategies based on stem-cell therapy with a supply of appropriate three-dimensional matrix for the repair of injured tissue are hot topics in translational medicine. Three-dimensional scaffolds designed for the selective manipulation of cell growth have high relevance with applications in regenerative medicine. The fabrication of hydrogel that supports long-term survival, proliferation, and unidirectional growth of embedded cells has been considered as a promising method to obtain scaffolds with oriented morphologies to guide the restoration of specific

M. He · Y. Zhang (✉)

School of Chemistry and Chemical Engineering, State Key Laboratory of Analytical Chemistry for Life Science, Nanjing University,
Nanjing 210093, People's Republic of China
e-mail: njuzy@nju.edu.cn

tissues [3]. Photomanipulatable hydrogels serve well as candidates in the engineering of photomanipulatable biomaterials for translational medicine.

In this chapter, we will firstly explain the general principle and chemical moieties developed for the photomanipulation of biomaterials. Then, the focus will be on the illustration of photomanipulatable hydrogels with respect to the engineering strategies and biomedical applications.

34.2 Chemistry Involved in the Design of Photomanipulatable Systems

Chemical moiety with photoresponse is the key structural component integrated into the functional units of biomaterials to realize photomanipulation. Usually, the photoresponsive moieties could undergo chemical reactions such as reversible isomerization, rapid bond cleavage or intermolecular ligation upon photoirradiation. With proper integration of these photoresponsive chemical moieties into biomolecules or building blocks of biomaterials, photoirradiation could induce the macroscopic change on the property or function of the biomaterials through the photoinduced reactions. In this part, we will summarize both the traditional photoreactions that have been commonly used for the engineering of photomanipulatable materials and the emerging ones with fast kinetics to be used in future design and engineering.

34.2.1 Photoinitiated Polymerization

Photoinitiated polymerization is the commonly used approach to synthetic polymeric hydrogels. This kind of polymerization usually needs photoinitiators that create free radicals upon visible or UV light irradiation to initiate the formation of crosslinked networks. Three major classes of photoinitiation, depending on the mechanism involved in photolysis, include radical photopolymerization through photocleavage, hydrogen abstraction, and cationic photopolymerization [4]. Photoinitiated polymerization has advantages over conventional polymerization including spatial and temporal control over polymerization, fast curing rates, at room or physiological temperatures and minimal heat production. Moreover, the photopolymerization can be conducted *in vivo* by injecting the precursor solution under the skin and photopolymerizing upon the light transmitted across the skin with defined volume and shape.

Polymerization of monomers using visible or UV irradiation has been thoroughly investigated. While such systems work well for many applications, their applications as biomaterials are partially restricted due to the cytotoxicity of the monomer and the photo-initiator. Thus, the photopolymerizable macromolecular

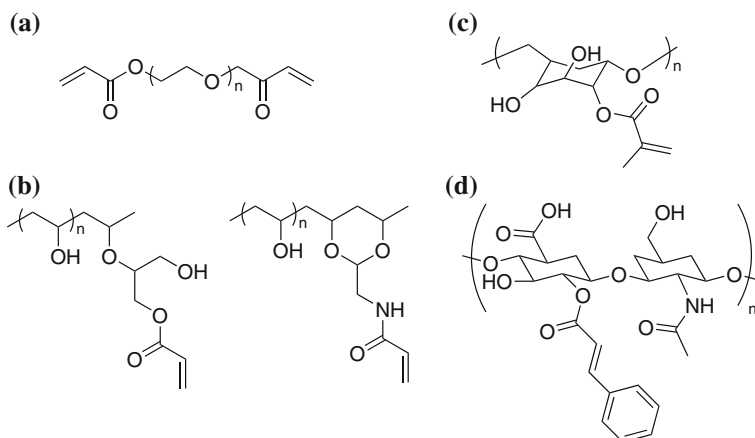


Fig. 34.1 Structure of photopolymerizable macromolecular precursors: **a** PEG acrylate derivatives, **b** polyvinyl alcohol (PVA) derivatives, **c** dextran methacrylate, and **d** hyaluronic acid derivatives

precursors have got increasing attentions for the last few years. These precursors usually are water-soluble polymers with two or more reactive groups including PEG acrylate derivatives, PEG methacrylate derivatives, polyvinyl alcohol (PVA) derivatives, and modified polysaccharides such as hyaluronic acid (HA) derivatives and dextran methacrylate (Fig. 34.1). Among them, the photopolymerizable HA derivatives are intrinsically biodegradable by hyaluronidase that cleaves HA into polysaccharide fragments. More functional groups can be incorporated into the side chain of the macromolecules with diverse bioactivity enabling the researchers to rationally design biomaterials for translational medicine and other purposes.

34.2.2 Photoclick Reactions for Fast Crosslinking or Ligation

34.2.2.1 Thiol-ene

The radical-mediated thiol-ene reaction has all the desirable features of a click reaction, being highly efficient, simple to execute with no side products and proceeding rapidly to give the ligated products with high yields. The photoinitiated thiol-ene reaction is now frequently used for photopolymerization to get highly uniform polymer networks. Thiol-ene photopolymerized networks have a tremendous advantage over networks through traditional photopolymerization in that they form rapidly and quantitatively under ambient atmospheric conditions to yield nearly ideal, uniform polymer networks through a controllable combination of step-growth and chain-growth [5].

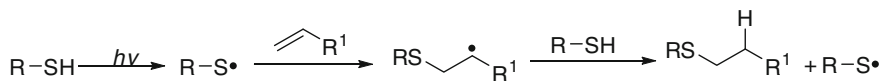


Fig. 34.2 The thiol-ene reaction

In the ideal purely step-growth thiol-ene reaction, the net reaction is simply the combination of the thiol and ene functional groups (Fig. 34.2). For a given thiol, electron-rich enes polymerize more rapidly than electron-poor enes and 1,2-substituted internal enes gave reduced rates and conversions. The original photo induced thiol-ene photopolymerizations utilized abstraction-type photoinitiators such as benzophenone which at the excited triplet state is able to abstract a hydrogen from the thiol and thus initiate the polymerization. Visible and UV-light-sensitive type I initiators with excellent photoinitiation efficiency are better choices owing to improved initiation efficiency. By choosing appropriate excitation wavelength and monomer combinations, initiator-free thiol-ene photopolymerization reactions have been realized. The initiatorless photopolymerizations are very useful to polymerize thick samples without the generation of any colored or volatile by-products.

34.2.2.2 Thiol-yne

The first discovery of radical addition of thiols to alkynes can be dated back to eighty years ago, but only in recent years, the reaction was rediscovered as a click process for the facile preparation of multifunctional polymer structures (Fig. 34.3). It was then considered as a sound candidate for replacing or complementing other popular click reactions such as the thiol-ene coupling and the Cu-catalyzed azide-alkyne cycloaddition. The photoinitiation capability of the thiol-yne coupling is successfully exploited for a number of emerging applications including that for both spatially and temporally controlled functionalization of surfaces [6]. Since the vinyl radicals upon photoinitiation are formed in an irreversible manner and can abstract a hydrogen atom from the thiol reagent more rapidly than their alkyl counterparts, the thiol-yne coupling is most efficient when it is carried out with equimolar amounts of thiol and alkyne. It is noteworthy that highly diluted reaction system might result in appreciable side reactions such as dimerization of sulfanyl radicals to give the corresponding disulfide.

34.2.2.3 Tetrazole-Alkene

In the late 1960s, Huisgen and co-workers described the first photoinduced 1,3-dipolar cycloaddition reaction between 2,5-diphenyltetrazole and methyl crotonate in benzene at 20 °C. Not until 2007, was the reaction revisited and developed as a “photoclick” reaction which was able to be initiated with a hand-held UV lamp to

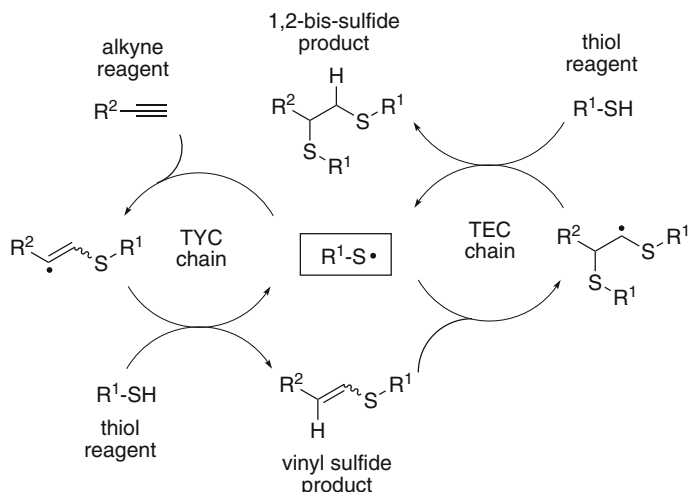


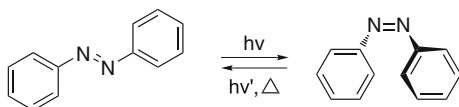
Fig. 34.3 Mechanism of thiol-yne coupling (TYC) and thiol-ene coupling (TEC) radical chains

drive the reaction to completion within two hours [7]. The optimized “photoclick” reaction between tetrazole and alkenes have revealed full water compatibility, high photoactivation quantum yield, tunable photoactivation wavelength and broad substrate scope. Moreover, the formation of fluorescent cycloadducts was claimed as an added benefit in its applications as a spatiotemporally controllable tool to visualize proteins in live cells [8]. The fast reaction kinetics (up to $11.0\text{ M}^{-1}\text{ s}^{-1}$) under mild photoirradiation conditions and the fluorescent cycloadducts of this type of photoclick reactions make them attractive for the engineering of photomanipulatable biomaterials.

34.2.3 Photoisomerization for Reversible Regulation

The ability to reversibly manipulate the physical and chemical properties of a material with an external stimulus forms the basis of stimuli-responsive systems. The application of photochromism to photoresponsive systems has led to the development of new tailored smart materials for photonics and biomedical fields. Within a polymeric matrix, photochromic isomerizations can be stimulated by light to reversibly alter the physical and chemical properties of a material such as phase, shape, self-assembly, size, and fluorescence [9]. Many of the ideas for such photoresponsive systems have been inspired by nature which has evolved many complex biological systems able to exploit light as an external source of energy and information. The underlying principles behind photoresponsive behavior are the photoisomerization of chemical moieties such as azobenzene, spiropyran, and diarylethene.

Fig. 34.4 Reversible isomerization of azobenzene



34.2.3.1 Azobenzene

Azobenzene and its derivatives have been widely used as molecular switches in the area of polymer materials, surface modifications, protein probes, and molecular machines due to their reversible transformations of the *trans* and *cis* form upon irradiation with UV or visible light (Fig. 34.4). Photoinduced isomerism of azobenzene also proceeds with large structural change as reflected in the dipole moment and change in geometry. Quantum yields of the transformation are generally high for the isomerization of azobenzene, and there are no competing reactions of significance [10]. Generally, the *trans*-azobenzene is more stable than the *cis* form with a *trans-cis* transform activation barrier of 10–12 kJ mol⁻¹ in solution. It is also worth mentioning that continuous irradiation of *trans*-azobenzene with either 313 or 436 nm radiation results in a photostationary state comprised of ~20 or ~90 % of *trans*-azobenzene, respectively.

Different ring substitutions have great impact on the absorption, emission, and photochemical property of the azobenzenes. For example, the electron denoting group at the *ortho* or *para* position of the phenyl group can dramatically red-shifted the spectrum. Though the red-shifted azobenzenes with increased dipolar character normally exhibit faster thermal relaxation processes (i.e., short-lived *cis* species), absorption at longer wavelengths with long-lived *cis* species were found to be possible by modifying delocalization and steric effects. Substituents also can make the *cis* form more thermodynamically stable than the *trans* form [11]. With these advances in the development of azobenzene switches, effective control of a large variety of biomaterials for translation medicine can be realized.

34.2.3.2 Spiropyran

Spiroyrans are widely presented in modern scientific literature due to their unique photochromism properties. Upon UV irradiation, molecules with spiroyrans moiety are able to be transformed into the MC forms, which reverse transformation can be realized both thermally and photochemically (by irradiation with visible light) (Fig. 34.5). The ring open form is characterized by a significant charge separation, which is usually depicted as zwitter-ionic structure. In general, the ring-closed spiroyrans form has absorption in visible range, whereas the merocyanine form is dominated by a strong absorption in the visible range [12]. This photochrome moiety has been subjected to various biological environments like RNA, DNA, and proteins for spatial-temporal control over the bimolecular functions.

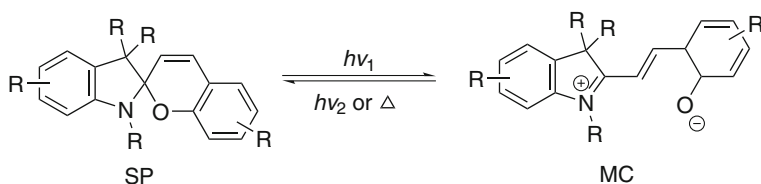
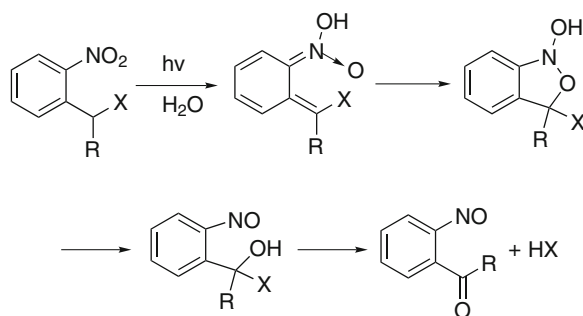


Fig. 34.5 Reversible isomerization of spiropyrans

Fig. 34.6 Mechanism on the photolysis of *o*-nitrobenzyl groups (for NB, R = H and for NPE, R = CH₃)



The most widely studied spiropyran is the 1',3',3'-trimethyl-6-nitrospiro [2H-1-benzopyran-2,2-indoline] having the nitro group in the 6 position of the chromene moiety. The nitro-substituted spiropyran possesses a high quantum yield of photochromic reaction. And the nitro group strongly enhances the intersystem crossing, thereby changing the reaction pathway in photochromism and shift the equilibrium toward the open form. In addition, this kind of spiropyran has been found to undergo hydrolysis in aqueous solutions and lose switching efficiency in the presence of a biomolecule [13].

34.2.4 Photocleavage Reactions for Photodegradation

Unlike the photoclick reactions, the photocleavage reactions are widely used in the photomanipulatable materials for photodegradation of the materials or the release of bioactive molecules to modulate the biomechanical and biochemical properties of the biomaterials. One of the most commonly used photolabile groups is the photocleavable *o*-nitrobenzyl group with all its derivatives [14]. The mechanism of the photolysis of nitrobenzyl (NB) or nitrophenylethyl (NPE) caged compounds has been established to be an intramolecular H-abstraction by the excited nitro group, which is followed by the formation of the aci-nitro form and the rearrangement to the nitroso derivatives [15] (Fig. 34.6). One disadvantage of the ortho-nitrobenzyl group is that upon photolysis a nitrosoaldehyde is formed which can be harmful in a

biological systems. The NPE group can be deprotected faster and results in the formation of a nitrosoketone. Excitation wavelength and kinetics of the cleavage process can be fine tuned by the methoxy substituents. Very recently, the nitro-dibenzofurane chromophore has been reported to have a significant high extinction coefficient and quantum yield in the near UV region and also suitable for two-photon activation. Other photolabile groups containing coumarin-4-ylmethyl and its derivatives, *p*-hydroxyphenacyl group, 7-nitroindolinyl-based group have also got increased interest in the photomanipulatable materials.

34.3 Photomanipulatable Hydrogel

Hydrogels have emerged as promising synthetic analogs of extracellular matrixes for basic cell studies as well as promising biomaterials for regenerative medicine applications [16]. The artificial matrixes based on hydrogels have critical advantages over natural networks in that bioactive functionalities, such as cell adhesive sequences and growth factors, can be incorporated in precise densities without influence on the substrate mechanical properties. Therefore, hydrogels have become a class of biomaterial scaffolds that have been widely used in complex device fabrication, drug release, and tissue engineering.

Tissue engineering employs cells seeded on or in three-dimensional natural or synthetic scaffolds for tissue regeneration or replacement. The static hydrogel systems for tissue engineering have been well developed so far, while the design of dynamic tunable and biomimetic hydrogel systems for cell scaffold just emerged at the beginning of this century. One of the challenges in the engineering of manipulatable hydrogels is to directly control the gelation process under physiological conditions with no harm to the cell encapsulated in the hydrogel system. Due to the spatial and temporal resolution of photoregulation, light irradiation becomes an ideal external stimuli to manipulate the properties and functions of biomaterials including hydrogels. The engineering of photomanipulatable hydrogels is of great research interests as well as potential applications in translational medicine.

Photolabile moieties and photosensitive reactions provide a means to spatially and temporally manipulate mechanical and biochemical microenvironment of the hydrogels. Biocompatible ways to build the photomanipulatable hydrogels have been developed and their applications as drug release systems, and cell-culture matrices in translational medicine have been demonstrated. Photopolymerizable and photodegradable hydrogels are the most widely applied photomanipulatable biomaterials in the field of tissue engineering for the engineering of tissues such as bone, cartilage, and liver [17]. The spatial and temporal control afforded by photoinitiated polymerization has promoted the development of injectable materials that can deliver cells and growth factors, as well as for the fabrication of scaffolding with complex structures.

34.3.1 Photopolymerizable Hydrogels

Photopolymerized hydrogels have been investigated for a number of tissue engineering applications because the in situ formation of these materials provides a minimally invasive manner compared with other methods such as injection. Quite a lot of hydrogel materials formed *via* photopolymerization processes mild enough to be carried out in the presence of living cells. The biocompatibility and cellular toxicity of the photopolymerized hydrogels have been widely explored. The UV or visible light used and different kinds of photoinitiators were examined by different groups with different cell lines [18]. With low irradiation intensity and photoinitiator concentrations [≤ 0.01 % (w/w)], cell survival and cell proliferation were not impaired in general. Different cell types may have variable responses to the same photoinitiator, which was indicated by variable correlation between cellular proliferation rate and increased cytotoxicity of the photoinitiator [19]. The use of photoinitiator-free photopolymerization technique for hydrogel preparation has also been developed [20].

With advances in synthetic chemistry, multifunctional monomers and macromers have been synthesized for photopolymerization to form functional hydrogels. Photoreactive groups, such as acrylates and methacrylates, were introduced into the macromers to give photocrosslinkable synthetic polymers including polyanhydrides [21], poly(ethylene glycol) [22], poly(propylene fumarates) [23], poly(α -hydroxy esters) [24], poly(vinyl alcohol) [25], poly(β -amino esters) [26] etc. Natural polymers, such as collagen [27, 28] and polysaccharides [29–32], have also been modified with photoreactive groups including methacrylates, benzophenone and styrene to be further photocrosslinked. These photopolymerizable synthetic or natural polymers have been developed as degradable biomaterials for tissue engineering applications [33]. We will give some representative or recent examples of each type of photopolymerizable hydrogels for tissue engineering applications after those being reviewed elsewhere [4].

Photoencapsulation of chondrocytes into the polymeric networks was reported [34]. An in vitro analysis of bovine and ovine chondrocytes photoencapsulated in a poly(ethylene oxide)-dimethacrylate and poly(ethylene glycol) semi-interpenetrating network showed that the chondrocyte survived well after one day's encapsulation and continued to grow in the following four weeks. Biochemical analysis indicated significant increase on the proteoglycan and collagen contents over two weeks' static incubation, indicating good biocompatibility and efficacy of the photopolymerizable hydrogels for the encapsulation of chondrocyte cell with low-intensity UVA light. In another work using the photoencapsulation of osteoblasts in injectable RGD-modified PEG hydrogels for bone tissue engineering [35], it was reported that a majority of the osteoblasts survived the photoencapsulation process when gels were formed with 10 % macromer. However, a decrease in osteoblast viability of ~ 25 and 38 % was observed for the encapsulated cells after 1 day of in vitro culture when the macromer concentration was increased to 20 and 30 %, respectively.

The photopolymerized poly(ethylene glycol)-based hydrogel has been demonstrated as regenerative medicine for *in vitro* chondrogenesis of the bone marrow-derived mesenchymal stem cells (MSCs) [36]. The MSCs from skeletally mature goats encapsulated in the hydrogel were cultured with or without transforming growth factor β_1 (TGF). It turned out that the encapsulated MSCs in the chondrogenic medium with TGF proliferated, while the glycosaminoglycan and total collagen content of the hydrogels increased to 3.5 % dry weight and 5.0 % dry weight in 6 weeks. The results demonstrated the potential of the photopolymerizing hydrogel to encapsulate MSCs and induce the formation of cartilage-like tissue for stem-cell translation medicine.

HA is a naturally derived polysaccharide. The monomer of HA is composed of D-glucuronic acid and N-acetyl-D-glucosamine. It is attractive for biomaterial applications, because it can be modified with various functional groups which make covalent crosslinking reactions possible and it is degradable upon treatment of the enzyme hyaluronidase. Besides, HA has proved to play roles in the promotion of cell motility and proliferation, wound healing, angiogenesis, and the reduction of long-term inflammation [37]. It has been reported that photopolymerized HA-based hydrogels and interpenetrating networks were readily degraded by hyaluronidase and their mechanical properties could be modulated by factors such as molecular weight of HA and concentration of PEG-DA [38]. The incorporation of RGD peptides further allowed modulation of the HA properties from cell nonadhesive to adhesive.

Visible-light crosslinkable hydrogel based on methacrylated glycol chitosan (MeGC) has been presented recently [39]. Three blue light initiators, camphorquinone (CQ), fluorescein (FR), and riboflavin (RF), were tested in the photocrosslinking. A minimal irradiation time of 120 s was required to produce MeGC gels able to encapsulate cells with CQ or FR. Prolonged irradiation up to 600 s improved the mechanical strength of CQ- or FR-initiated gels but drastically reduced viability by 5 and 25 % for chondrocyte encapsulated in the photocrosslinked gels initiated by CQ and FR, respectively. Increasing the irradiation time up to 300 s significantly improved the compressive modulus of the RF-initiated MeGC gels without reducing cell viability. RF-photoinitiated hydrogels supported proliferation of encapsulated chondrocytes and extracellular matrix deposition. In osteochondral and chondral defect models, the *in situ* gelling hydrogels using RF was further demonstrated for potential cartilage tissue engineering.

The step-growth thiol-ene photoclick hydrogels have also showed superior properties including cytocompatibility of the reactions and improved hydrogel physical properties. The thiol-ene or thiol-yne reaction involves the sequential propagation of a thiyl radical with an alkyl or vinyl functional group followed by chain transfer of the radical to another thiol to form the network [40, 41]. Thiol-ene click reactions provide an attractive means to fabricate PEG hydrogels with superior gel properties for *in situ* cell encapsulation, as well as to generate and recover 3D cellular structures for regenerative medicine applications. Compared with the disordered network formed by polymerization of PEG diacrylate analogs, thiol-ene step-growth photopolymerizations have demonstrated the advantage of

forming highly ordered polymer networks. McCall and Anseth compared the differences in recovery of bioactive proteins when exposed to similar photoinitiation conditions during thiol-ene versus acrylate polymerizations [40]. After exposure to chain polymerization of acrylates, lysozyme bioactivity was approximately 50 %, after step-growth thiol-ene reaction, lysozyme retained nearly 100 % of its prereaction activity. Bioactive protein recovery was enhanced 1,000-fold in the presence of a thiol-ene reaction, relative to recovery from solutions containing identical primary radical concentrations, but without the thiol-ene components. This showed a potential for this polymerization method in the bioactive macromolecules encapsulation and controlled delivery *in vivo*.

The step-growth thiol-ene photoclick hydrogels also demonstrated the ability for 3D culture of pancreatic β -cells. Cells encapsulated in the thiol-ene hydrogels formed spherical clusters naturally and were retrieved via rapid chymotrypsin-mediated gel erosion. The recovered cell spheroids released insulin upon glucose treatment, demonstrating the cytocompatibility of thiol-ene hydrogels and the enzymic mechanism of cell spheroids recovery [42]. Hydrogels synthesized by a step-growth reaction mechanism *via* thiol-norbornene photopolymerization have also been reported to be with rapid gelation time and high cell viability for cell encapsulated [43]. It has also been demonstrated that the hydrogel combined the advantages of ideal, homogeneous polymer network formation, facile incorporation of peptides without post-synthetic modification, and spatial and temporal control over the network evolution into a single system with enzyme- and cell-responsive characteristics. The high degree of spatial and temporal control over gelation, combined with robust material properties, makes step-growth thiol-ene photoclick hydrogels hydrogels an excellent tool for a variety of medical applications.

In 2006, Engler et al. demonstrated that microenvironments appear important in stem-cell lineage specification. Soft matrices that mimic brain are neurogenic, stiffer matrices that mimic muscle are myogenic, and comparatively rigid matrices that mimic collagenous bone prove osteogenic [44]. As for naive MSCs, during the initial week in culture, reprogramming of these lineages is possible with addition of soluble induction factors, but after several weeks in culture, the cells commit to the lineage specified by matrix elasticity, consistent with the elasticity-insensitive commitment of differentiated cell types. The results have significant implications for understanding physical effects of the *in vivo* microenvironment and also for therapeutic uses of stem cells, but it can be difficult to adequately characterize or control with soft tissues or static *in vitro* models. Hence, the photo enhanced hydrogel provides a unique and dynamic way for studying relationships of the stem-cell differentiation and the microenvironment changes.

Dynamic stiffening of cellular microenvironment has been reported to use a stepwise addition then light-mediated crosslinking approach to fabricate hydrogels that stiffen in the presence of cells. The short-term (minutes to hours) and long-term (days to weeks) cell response to the dynamic stiffening of their microenvironment were then studied [45]. When substrates were stiffened, adhered human MSCs increased their area from similar 500 to 3,000 μm^2 and exhibit greater traction from similar 1 to 10 kPa over a timescale of hours. For longer cultures up to 14 days,

human MSCs selectively differentiate based on the period of culture, before or after stiffening, such that adipogenic differentiation is favored for later stiffening, whereas osteogenic differentiation is favored for earlier stiffening. These results demonstrated that the sequential crosslinking technique was a powerful tool to investigate dynamic changes in biological processes, an approach that may be useful to investigate tissue development, wound healing, and disease progression.

By using this kind of sequential photopolymerization, the underlying mechanisms of the cell–matrix adhesive interactions that are known to regulate stem-cell differentiation are well studied by Burdick's group [46]. In the photopolymerized HA hydrogels, the differentiation of human mesenchymal stem cells (hMSCs) is determined by the biodegradation-mediated cellular traction, instead of cell morphology or matrix mechanics. Moreover, through delayed photocrosslinking, the hydrogels can be switched from biodegradable state to the restrictive state which prevents further degradation. This kind of change suppressed the cellular traction and caused the adipogenesis of the hMSCs rather than osteogenesis without changing of the cellular morphology. Further inhibiting or upregulating tension-mediated signaling proved the mechanism of the cellular traction induced stem-cell differentiation in the HA hydrogels. This method showed a powerful tool in studying cell–matrix interactions that is crucial for further applications in tissue engineering and translational medicine.

X-ray irradiation have been found to be possible for the in situ formation of a three-dimensional hydrogel based on poly(ethylene glycol) diacrylate (PEG-DA) with the option of heparin incorporation to enhance cell adhesion [47]. With the trimmed or focused X-ray beam, the polymerization reaction can be completed in tens of seconds and precisely controlled in administration deep in the tissue without surgery. They also tried addition of Au nanoparticles to the precursor solution to enhance the X-ray sensitive of the biopolymers which is necessary for reducing the X-ray dose to allow cell encapsulation procedures.

In tissue engineering, the biomaterials are required to be degradable, so that the growing tissue eventually replaces them. In drug delivery, degradable polymers are used to entrap various molecules that are released as the polymer degrades or through diffusion mechanisms. If growth factors are released, this method can lead to alterations in cellular differentiation and the type and quality of tissue that forms. Thus, there is a growing interest in designing photoinitiated polymeric hydrogels with degradation based on the hydrolytic or enzymatic degradation of bonds in the polymer backbone or crosslinks. The degradation also ranges from purely bulk to entirely surface degrading, based on the backbone and degradable units. It is also needed to be incorporated to enable cell migration for studying cancer metastasis, angiogenesis, and wound healing and to facilitate cell–cell interactions for controlling cell function and directing tissue morphogenesis [48].

Li et al. reported a biodegradable, photocrosslinkable and multifunctional macromer, poly(6-aminoethyl propylene phosphate) (PPE-HA)-ACRL [49]. It was synthesized by conjugation of different fractions acrylate groups to the side chains of PPE-HA. The hydrogels with different crosslinking densities lost between 4.3 and 37.4 % of their mass in 84 days when incubated in phosphate-

buffered saline at 37°C. Bone marrow–derived MSCs from goat GMSCs encapsulated in the photopolymerized gel maintained their viability when cultured in osteogenic medium for three weeks with clear mineralization in the hydrogel scaffold revealed by Von Kossa staining. Other hydrolytic backbones, such as beta-malic acid, have also been used to form biodegradable and biocompatible hydrogels for tissue engineering application [50].

Different from the hydrolytic biodegradable hydrogel, the enzymatic degradable hydrogel can mimic certain aspects of natural cell migration and ECM remodeling, by allowing cell-dictated degradation through the incorporation of enzymatically degradable sequences [48]. Enzymatically degradable sequences utilized in photopolymerized hydrogels include GGLGPAGGK degraded by collagenase; AAAAAAAAAAK, AAPVR, and AAP(Nva) degraded by elastase; and GPQGIWGQ, GPQGIAGQ, and GPQGILGQ, which are degraded by collagenase and various matrix metalloproteinases (MMPs), such as MMP-1, MMP-2, MMP-3, MMP-7, MMP-8, and MMP-9. Deciding which degradable sequences to use and knowing how cells are degrading their local environment is cell-type-dependent, and because of this feature, tailoring the gel degradation properties to a particular cellular system is still largely empirical.

Efforts have also been taken to make the photopolymerized hydrogels more functional, like antibacterial, or induce the differentiation of cells by incorporating bio-functional groups into the system. For example, photopolymerized hydrogels made from epsilon-poly-l-lysine-graft-methacrylamide (EPL-MA) have been found to have wide spectrum antimicrobial activity against both bacteria and fungi [51]. The EPL-MA hydrogel also possesses in vitro biocompatibility and EPL-MA solution is relatively nonhemolytic. Furthermore, the hydrogel can be conveniently photoimmobilized onto plasma-treated plastic surfaces to form thin highly adherent antimicrobial hydrogel coatings for medical devices and implants.

Advances in tissue engineering require biofunctional scaffolds that not only provide cells with structural support, but also interact with cells in a biological manner. To achieve this goal, a frequently used cell adhesion peptide Arg-Gly-Asp (RGD) was covalently incorporated into poly(ethylene glycol) diacrylate (PEODA) hydrogel. The effect on osteogenesis of marrow stromal cells in a three-dimensional environment was examined [52]. Expression of bone-related markers, osteocalcin (OCN) and alkaline phosphatase (ALP), increased significantly as the RGD concentration increased. Also, RGD helped MSCs maintain *cbfa-1* expression when shifted from a two-dimensional environment to a three-dimensional environment.

34.3.2 Photodegradable Polymeric Hydrogels

Early examples of photodegradable hydrogels can be dated back to 1990s. In 1990, Suzuki and Tanaka constructed a photoresponsive hydrogel with a combination of a thermosensitive hydrogel and a chromophore. The light absorbed by the chromophores is dissipated as heat and increase the local temperature, which affects

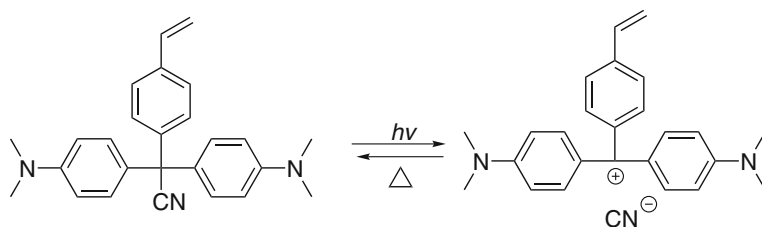


Fig. 34.7 Chemical process involved in the first photoinduced phase-transitions of polymeric hydrogelator monomer

thermosensitive hydrogel network to induce phase transition resulting in a photodegradable hydrogel [53]. In the same year, Masahiro and coworkers reported the photoinduced phase-transition of gels formed by polymerization of bis(4-(dimethylamino)phenyl)methyl leucocyanide in which the leucocyanide moiety upon irradiation gave increased ionization degree and induced the phase-transition of the hydrogel [54] (Fig. 34.7). However, due to poor biocompatibility of the photodegradable material or methods, photodegradable hydrogels were rarely applied as biomaterial until Kloxin et al. reported the nitrobenzyl ether-derived photolabile hydrogel in 2009 [55].

Kloxin et al. developed the strategy to create photodegradable poly(ethylene glycol)-based hydrogels through rapid polymerization of cytocompatible macromers for remote manipulation of gel properties in situ and applied the strategy in the synthesis of photodegradable hydrogels as dynamically tunable cell culture platforms [56] (Fig. 34.8). The cytocompatible macromers were prepared from anitrobenzyl ether-derived monomer attached with a pendant carboxylic acid to poly(ethylene glycol) (PEG)-bis-amine. Then, the photocleavable crosslinking diacrylatemacromer formed PEG-based photodegradable hydrogels. The hydrogel itself is cleaved upon light exposure, decreasing the local network crosslink density and resulting in macroscopic property changes such as stiffness, water content, diffusivity, or complete erosion, all in the presence of cells [57]. They used the phototunable hydrogels for external manipulation of cellular microenvironment through controlled photodegradation [58]. With the biocompatible photodegradation of hydrogels, the advantages of post-gelation control of the gel properties have been well-demonstrated, which led to a renaissance of research on various types of photodegradable hydrogels for applications range from design of drug delivery vehicles to tissue engineering systems [59–61].

It was believed that hydrogels can be used in tissue engineering and regenerative medicine to deliver therapeutic cells to injured or diseased tissue through controlled degradation. For sequential or staged release of cells from hydrogels, Griffin and Kasko synthesized and characterized a series of macromers incorporating photodegradable ortho-nitrobenzyl (*o*-NB) groups in the macromer backbone allowing for staged and sequential release of cells (Fig. 34.9). Hydrogels were formed via redox polymerization and quantified the apparent rate constants of degradation

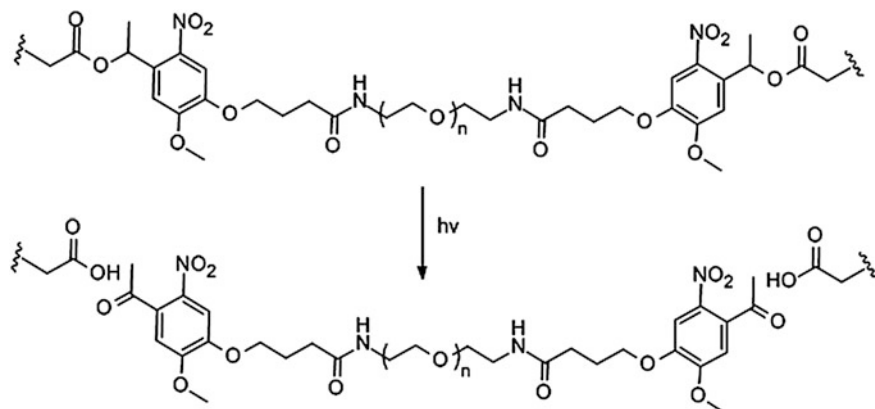


Fig. 34.8 The photoresponse of the nitrobenzyl ether-derived photolabile macromer

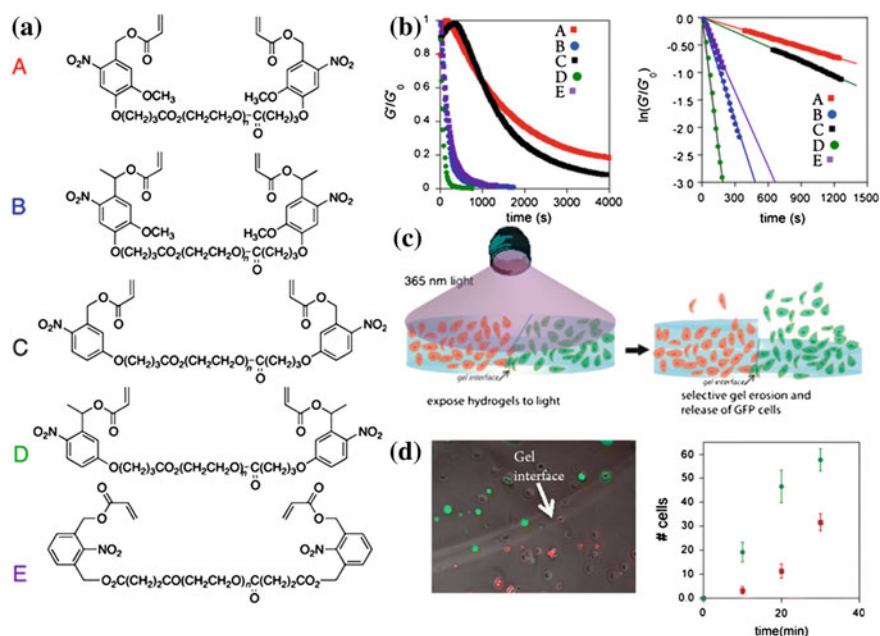


Fig. 34.9 **a** Different structure of degradable ortho-nitrobenzyl (*o*-NB) monomers. **b** Kinetics of the photodegradation. **c** Illustration of wavelength-biased release of encapsulated cells and **d** the selective release of cells encapsulated in the photodegradable hydrogel. Recreated with kind permission of American Chemical Society [62]

[62]. Decreasing the number of aryl ethers on the *o*-NB group increases the apparent rate constants of degradation, and changing the functionality from primary to secondary at the benzylic site dramatically increases the apparent rate constants

of degradation. hMSCs survived encapsulation in the hydrogels with high viability. By exploiting the differences in reactivity of two different *o*-NB linkers, they quantitatively demonstrate the biased release of one stem-cell population (green-fluorescent protein expressing hMSCs) over another (red-fluorescent protein expressing hMSCs). Hydrogels are also commonly used in biomedical applications to sequester and release therapeutics. By using this difference of the degrading rate among different *o*-NB groups, they succeeded in sequential release of three different model therapeutics from a single hydrogel [63].

The combination of the photocleavable moiety in the macromer and novel materials allows innovative photodegradation of hydrogels. For example, Yan et al. recently reported a photosensitive hybrid hydrogel loaded with upconversion nanoparticles (UCNPs) which allowed photodegradation of the hydrogel using near-infrared (NIR) light (980 nm) irradiation [64]. Their results demonstrated that continuous-wave NIR light was able to induce the gel/sol transition and release large, inactive biomacromolecules (protein and enzyme) entrapped in the hydrogel into aqueous solution “on demand”, where their bioactivity is recovered. Using the inclusion complex of trans-azobenzene and cyclodextrin as a photoswitchable crosslinker, a dextran-based photoresponsive hydrogel system has been constructed and employed for a light-controlled protein release system [65].

34.3.3 Photopatternable Hydrogel

Photopatternable hydrogel allows manipulation of specific area in macroscopic hydrogel media with spatial and temporal resolution and is emerging as functional biomaterials for translational medicines. The ability to tailor the biochemical and biomechanical properties of 3D biomaterials at the microscale is important for a range of biotechnology applications, including the engineering of complex tissues, the development of biosensors, the elucidation of cell–cell and cell–material interactions, and the guidance of cellular differentiation [66]. To this end, techniques have emerged for the fabrication of 3D micro-controlled materials, including electrochemical deposition, 3D printing, and soft-lithographic approaches. However, these patterning methods need to be repeated in a layer-by-layer fashion to build an internally complex 3D materials. An alternative approach to the fabrication of complex 3D scaffolds is the photolithography technique which can create extremely small patterns (tens of nanometers in size) and afford exact control over the shape and size of the biomaterials. In this part, we briefly review recent efforts to engineer mechanically and/or biochemically patterned 3D hydrogels to control cellular behavior for translational medicine applications.

It has been confirmed that mechanical properties are important variation of the extra cellular matrix. The spatial photomechanical patterning of hydrogels, motivated by the microscale heterogeneity of native tissue architectures, has recently been a focus. DeForest and Anseth reported strategies to create channels photopatterned within a hydrogel-containing encapsulated cells that allow cell

migration [67]. The photopatternable hydrogels allow real-time manipulation of material properties and provide dynamic environments with the scope to answer fundamental questions about material regulation of live cell function. Further efforts from the same group focused on the development of advanced material systems that allow dynamic alteration of the three-dimensional cellular environment with orthogonal reactions to enable multiple levels of control of biochemical and biomechanical signals. One recent work from the group demonstrated the three-dimensional culture system using cytocompatible and wavelength-specific photoreactions for independent spatiotemporally regulated photocleavage of crosslinks and photoconjugation of pendant functionalities to create hydrogels that allow orthogonal and dynamic control of material properties [68].

Khetan et al. developed a process to synthesize HA hydrogels using multiple modes of crosslinking applied sequentially [69]; a primary addition reaction to introduce protease degradable peptide crosslinks, then a UV-light-induced secondary radical reaction to introduce nondegradable kinetic chains. These differential network structures either permitted or inhibited cellular remodeling. This behavior was validated by controlling the outgrowth from chick aortic arches or the spreading of encapsulated MSCs, where only UV regions permitted arch outgrowth and MSC spreading [70]. Additionally, network structures dictated adipogenic/osteogenic MSC fate decisions, with spatial control, by controlling encapsulated MSC spreading. This manipulation of microenvironmental cues may be valuable for advanced tissue engineering applications requiring the spatial control of cells in 3D [71].

Luo and Shoichet reported the first example of three-dimensional photobiochemical patterning of hydrogel-guided axonal growth [72]. An agarose hydrogel modified with a cysteine compound containing a sulfhydryl protecting group allowed photopatterning with biochemical cues. The transparent hydrogel was immobilized with the adhesive fibronectin peptide fragment, glycine–arginine–glycine–aspartic acid–serine (GRGDS), in selected volumes of the matrix using a focused laser. The photobiochemical patterned hydrogel showed guidance effects in the GRGDS oligopeptide-modified channels on the 3D cell migration and neurite outgrowth. Using similar method, spatially controlled immobilization of different growth factors in distinct volumes in 3D hydrogels and specifically guided differentiation of stem/progenitor cells have realized [73]. The technique should be broadly applicable to the patterning of a wide range of proteins. Stem-cell differentiation factors sonic hedgehog (SHH) and ciliaryneurotrophic factor (CNTF) were simultaneously immobilized using orthogonal physical binding pairs, barnase/barstar and streptavidin–biotin, respectively [74]. Barnase and streptavidin were sequentially immobilized using two-photon chemistry for subsequent concurrent complexation with fusion proteins barstar-SHH and biotin-CNTF, resulting in bioactive 3D-patterned hydrogels. This method for immobilizing biomolecules in 3D matrices can generally be applied to any optically clear hydrogel, offering a solution to construct scaffolds with programmed spatial features for tissue engineering applications [75]. Two-photon laser-scanning photolithography was also applied into this system to increase the penetration of the light and more precise control over the photochemical pattern [76].

Reversible patterning of bioactive molecules into the hydrogel has also realized through the combination of two bioorthogonal photoreactions which enabled the reversible spatial presentation of a biological cue and the formation of complex, well-defined, biomolecular gradients within a hydrogel, respectively [77]. One of the bioorthogonal photoreactions was the thiol-ene reaction which was readily initiated by visible light and an appropriate photoinitiator. The second reaction was the photocleavage of an *o*-NB ether leading to a nitroso compound and an acid byproduct upon exposure to UV light. The biological molecule of interest was modified to contain both the thiol group for photocoupling reaction and the photolabile *o*-NB moiety which allowed the attachment and the subsequent removal of the covalently bound bioepitopes in hydrogel networks, respectively. The use of light allowed dynamic manipulation not only on the intrinsic cellular regulatory machinery, but also on the external microenvironment of the cells encapsulated.

34.3.4 Photomanipulatable Supramolecular Hydrogels

Supramolecular hydrogels have emerged as novel biomaterials with promising applications in regenerative medicine. Most of the reported supramolecular hydrogels were based on the self-assembling of biomimetic epitopes inspired by the chemical structure of natural proteins or polysaccharides. For example, Hu et al. has designed and synthesized a small library of supramolecular hydrogelators inspired by the chemical structure of collagen and found that four of the hydrogels were suitable for NIH 3T3 cell culture [78]. Hamachi screened and optimized low-molecular-weight hydrogelators through combinatorial solid-phase synthesis of glyco-lipid mimics and found that an *N*-acetyl-galactosamine-appended amino acid derivatives displayed an excellent hydrogelation capability [79]. In these supramolecular hydrogels, small molecules self-assembled into nanofibers and then entangled each other to form macroscopic hydrogel. Supramolecular hydrogels with responses to external stimuli are considered as “smart” biomaterials and have been of great research interests in the past decades [80–83].

Integration of photoreactive moieties into the chemical structure of small molecular hydrogelator has proved to be effective strategy to construct photoreponsive supramolecular hydrogels. The hydrogelation properties of the short peptides (Fig. 34.10) linked with the conformational switch azobenzene have been studied in detail by Huang et al. with respect to dependence on amino acid, residue, pH, and salt effect [84]. Photoresponsive supramolecular hydrogels were realized based on the *E*-/*Z*-transition of the conformational switch azobenzene upon light irradiation. The hydrogel formed by azo-Gln-Phe-Ala gel has demonstrated its potentials as photoresponsive soft material for controlled release of drug molecules. The same group also reported a “smart” supramolecular hydrogel with dual responses to both light irradiation and ligand–receptor interaction [85]. Integration of photosensitive spiropyran with dipeptide D-Ala–D-Ala in one small

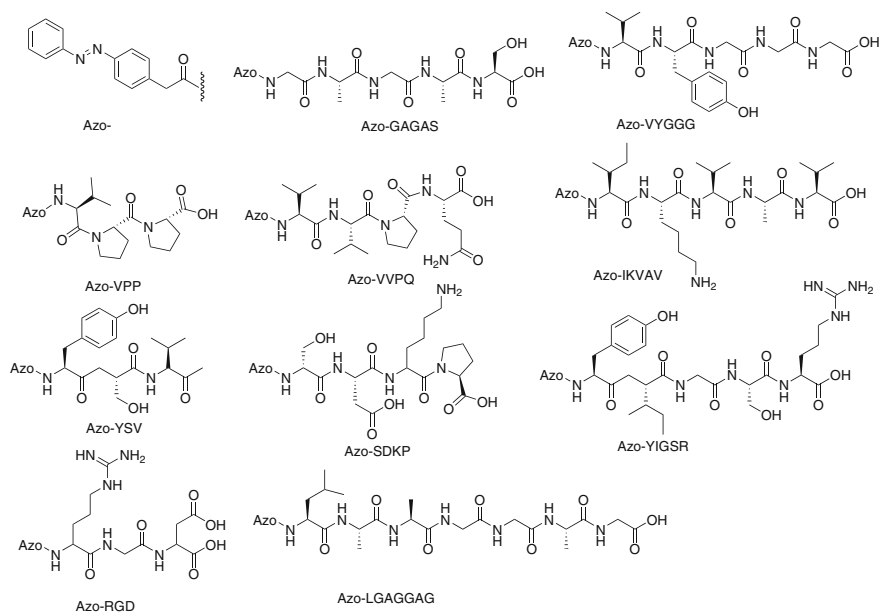


Fig. 34.10 Chemical structure of azobenzene-linked bioactive short peptides

molecule resulted in a hydrogelator which can form supramolecular hydrogel with responses not only to light but to ligand–receptor interaction between D-Ala-D-Ala and vancomycin (Fig. 34.11). This novel example of photoregulated “smart” supramolecular hydrogel suggested the possibility of developing various multifunctional biomaterials through integration of photoresponse and specific response to biomimetic interaction in a small molecule hydrogel. Li et al. also showed an enzymatic formation of a photoresponsive supramolecular hydrogel with an azobenzene-modified oligopeptide [86].

Haines et al. have developed a simple light-activated hydrogelation system that employs a designed peptide whose ability to self-assemble into hydrogel material is dependent on its intramolecular folded conformational state [87] (Fig. 34.12). An iterative design strategy afforded MAX7CNB, a photocaged peptide remains unfolded and unable to self-assemble in aqueous medium; a 2 wt% solution of freely soluble unfolded peptide is stable to ambient light and has the viscosity of water. Irradiation of the solution ($260 < \lambda < 360$ nm) releases the photocage and triggers peptide folding to produce amphiphilic beta-hairpins that self-assemble into hydrogel. NIH 3T3 fibroblasts seeded onto the gel indicates that the gel surface is noncytotoxic, conducive to cell adhesion, allows cell migration and have equivalent proliferate rate compared with cells seeded onto a tissue culture-treated polystyrene control surface. Stupp’s group reported a peptide amphiphile that contains both the photocleavable 2-nitrobenzyl group as well as the bioactive epitope Arg-Gly-Asp-Ser (RGDS) [88]. Photoirradiation at 350 nm cleaves the 2-

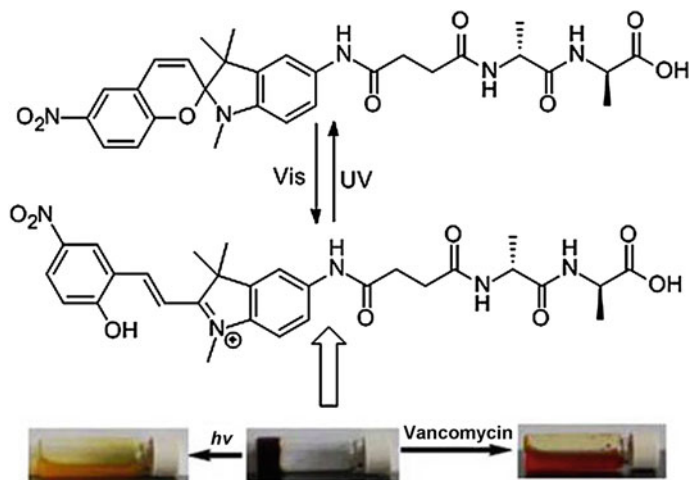


Fig. 34.11 Structure of the spiropyran-D-Ala-D-Ala and its photoresponse and ligand-receptor interaction with vancomycin

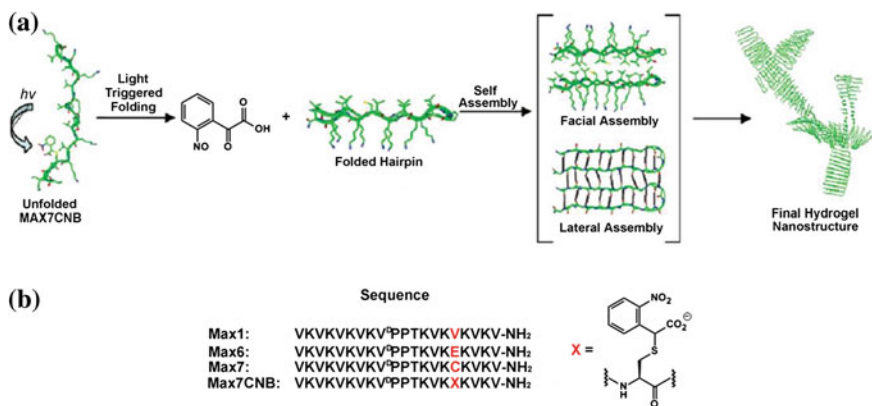


Fig. 34.12 a UV irradiation of MAX7CNB results in side-chain decaging and β -hairpin intramolecular folding for the hydrogel formation. b The peptide sequences used for the control and light-activated hydrogel formation. Recreated with kind permission of American Chemical Society [87]

nitrobenzyl group to form the β sheet which induces the formation of a transparent hydrogel. This small structural change induced a significant change in the supra-molecular structure from nanospheres to nanofibers, affecting the response of cells surrounded by the nanostructures. They found that the vinculin expression levels of the NIH/3T3 mouse embryonic fibroblasts encapsulated in the light-induced hydrogel were 1.9 times higher than the cells in the control hydrogels or solutions. Lately, Takashima et al. reported a photoresponsive supramolecular hydrogel by

integrating host–guest interactions and photoswitching ability in a hydrogel [89]. A photoresponsive supramolecular hydrogel with α -cyclodextrin as a host molecule and an azobenzene derivative as a photoresponsive guest molecule exhibits reversible macroscopic changes in both size and shape when irradiated by UV light at 365 nm or visible light at 430 nm. The deformation of the supramolecular hydrogel depends on the incident direction which allows plate-shaped hydrogels to bend in water. Irradiating with visible light immediately restores the deformed hydrogel. These stimulus-responsive expansion–contraction properties are similar to that of muscle fibrils, such as sarcomere, which consists of actin filaments. These stimulus-responsive stretching properties may eventually be used in stents and drug delivery carriers to selectively release drugs for the translational medicine.

34.4 Summary and Perspective

Photomanipulatable hydrogels are emerging as important biomaterials in translational medicine. With photoreactive chemical moieties modified in the monomers or macromers of synthetic or natural polymeric hydrogelators, it is now possible to realize spatial- and temporal-resoluted control on the properties and function of hydrogels used in regenerative medicines or tissue engineering. Except for the traditional photopolymerizable hydrogels, new types of photoresponsive hydrogels that allow cytocompatible photomanipulation have showed promising applications in the controlled delivery of drug or biomacromolecules, and in the direction of cell growth and differentiation for tissue engineering. The discovery of novel photoreactive molecules and new types of hydrogelators is sure to promote the engineering of new-generation photomanipulatable biomaterials. Construction of photoregulatable supramolecular hydrogels with excellent biocompatibility and mechanical properties for the applications in translational medicine will bring new insight into the structural control at molecular level. The combination of photo-reactive moieties with bioorthogonal functionalities is emerging as a powerful strategy in dynamic tuning the physical and chemical properties of hydrogel which forms the microenvironment for cell growth. With the discovery of more bioorthogonal reactions, it is possible to engineer photomanipulatable and multifunctional biomaterials for translational medicine in the future.

Acknowledgments Financial support from the Natural Science Foundation of Jiangsu Province (BK2012012) was acknowledged.

References

1. Bryan T, Janet H, William S, Russell AJ, Parenteau NL (2013) Meeting the need for regenerative therapies: translation-focused analysis of U.S. regenerative medicine opportunities in cardiovascular and peripheral vascular medicine using detailed incidence data. *Tissue Eng Part B* 19:99–115
2. Ratcliffe A (2011) Difficulties in the translation of functionalized biomaterials into regenerative medicine clinical products. *Biomaterials* 32:4215–4217
3. Slaughter BV, Khurshid SS, Fisher OZ, Khademhosseini A, Peppas NA (2009) Hydrogels in regenerative medicine. *Adv Mater* 21:3307–3329
4. Nguyen KT, West JL (2002) Photopolymerizable hydrogels for tissue engineering applications. *Biomaterials* 23:4307–4314
5. Hoyle CE, Bowman CN (2010) Thiol-ene click chemistry. *Angew Chem Int Ed* 49:1540–1573
6. Massi A, Nanni D (2012) Thiol-yne coupling: revisiting old concepts as a breakthrough for up-to-date applications. *Org Biomol Chem* 10:3791–3807
7. Wang YZ, Vera CIR, Lin Q (2007) Convenient synthesis of highly functionalized Pyrazolines via Mild, Photoactivated 1,3-Dipolar Cycloaddition. *Org Lett* 9:4155–4158
8. Lim RKV, Lin Q (2011) Photoinducible Bioorthogonal Chemistry: a spatiotemporally controllable tool to visualize and Perturb Proteins in live cells. *Acc Chem Res* 44:828–839
9. Ercole F, Davis TP, Evans RA (2010) Photo-responsive systems and biomaterials: photochromic polymers, light-triggered self-assembly, surface modification, fluorescence modulation and beyond. *Polym Chem* 1:37–54
10. Kumar GS, Neckers DC (1989) Photochemistry of azobenzene-containing polymers. *Chem Rev* 89:1915–1925
11. Beharry AA, Woolley GA (2011) Azobenzene photoswitches for biomolecules. *Chem Soc Rev* 40:4422–4437
12. Minkin VI (2004) Photo-, Thermo-, Solvato-, and Electrochromic spiroheterocyclic compounds. *Chem Rev* 104:2751–2776
13. Kohl-landgraf J, Braun M, Ozcoban C, Goncalves DPN, Heckel A, Wachtveitl J (2012) Ultrafast dynamics of a Spiropyran in water. *J Am Chem Soc* 134:14070–14077
14. Mayer G, Heckel A (2006) Biologically active molecules with a “light switch”. *Angew Chem Int Ed* 45:4900–4921
15. Yu HT, Li JB, Wu DD, Qiu ZJ, Zhang Y (2010) Chemistry and biological applications of photo-labile organic molecules. *Chem Soc Rev* 39:464–473
16. Khatiwala C, Law R, Shepherd B, Dorfman S, Csete M (2012) 3D Cell Bioprinting For Regenerative Medicine Research And Therapies. *Gene Ther Regul* 7:1230004
17. Ifkovits JL, Burdick JA (2007) Photopolymerizable and degradable biomaterials for tissue engineering applications. *Tissue Eng* 13:2369–2385
18. Bryant SJ, Nuttelman CR, Anseth KS (2000) Cytocompatibility of UV and visible light photoinitiating systems on cultured NIH/3T3 fibroblasts in vitro. *J Biomat Sci Polym E* 11:439–457
19. Williams CG, Malik AN, Kim TK, Manson PN, Elisseff JH (2005) Variable cytocompatibility of six cell lines with photoinitiators used for polymerizing hydrogels and cell encapsulation. *Biomaterials* 26:1211–1218
20. Ng L, Ng K, Stein DB (2009) *Handbook of hydrogels*. Nova Science, New York
21. Anseth KS, Shastri VR, Langer R (1999) Photopolymerizable degradable polyanhydrides with osteocompatibility. *Nat Biotechnol* 17:156–159
22. Cruise GM, Scharp DS, Hubbell JA (1998) Characterization of permeability and network structure of interfacially photopolymerized poly(ethylene glycol) diacrylate hydrogels. *Biomaterials* 19:1287–1294

23. Timmer MD, Carter C, Ambrose CG, Mikos AG (2003) Fabrication of poly(propylene fumarate)-based orthopaedic implants by photo-crosslinking through transparent silicone molds. *Biomaterials* 24:4707–4714
24. John G, Morita M (1999) Synthesis and characterization of photo-cross-linked networks based on L-lactide/serine copolymers. *Macromolecules* 32:1853–1858
25. Schmedlen KH, Masters KS, West JL (2002) Photocrosslinkable polyvinyl alcohol hydrogels that can be modified with cell adhesion peptides for use in tissue engineering. *Biomaterials* 23:4325–4332
26. Anderson DG, Tweedie CA, Hossain N, Navarro SM, Brey DM, Van VKJ, Langer R, Burdick JA (2006) A combinatorial library of photocrosslinkable and degradable materials. *Adv Mater* 18:2614–2618
27. Brinkman WT, Nagapudi K, Thomas BS, Chaikof EL (2003) Photo-cross-linking of type I collagen gels in the presence of smooth muscle cells: mechanical properties, cell viability, and function. *Biomacromolecules* 4:890–895
28. Dong CM, Wu XY, Caves J, Rele SS, Thomas BS, Chaikof EL (2005) Photomediated crosslinking of C6-cinnamate derivatized type I collagen. *Biomaterials* 26:4041–4049
29. Smeds KA, Pfister-Serres A, Hatchell DL, Grinstaff MW (1999) Synthesis of a novel polysaccharide hydrogel. *J Macromol Sci Pure Appl Chem* 36:981–989
30. Leach JB, Bivens KA, Patrick CW, Schmidt CE (2003) Photocrosslinked hyaluronic acid hydrogels: Natural, biodegradable tissue engineering scaffolds. *Biotechnol Bioeng* 82:578–589
31. Ishihara M, Nakanishi K, Ono K, Sato M, Kikuchi M, Saito Y, Yura H, Matsui T, Hattori H, Uenoyama M, Kurita A (2002) Photocrosslinkable chitosan as a dressing for wound occlusion and accelerator in healing process. *Biomaterials* 23:833–840
32. Matsuda T, Magoshi T (2002) Preparation of vinylated polysaccharides and photofabrication of tubular scaffolds as potential use in tissue engineering. *Biomacromolecules* 3:942–950
33. Ono K, Ishihara M, Ozeki Y, Deguchi H, Sato M, Saito Y, Yura H, Sato M, Kikuchi M, Kurita A, Maehara T (2001) Experimental evaluation of photocrosslinkable chitosan as a biologic adhesive with surgical applications. *Surgery* 130:844–850
34. Elisseeff J, McIntosh W, Anseth K, Riley S, Ragan P, Langer R (2000) Photoencapsulation of chondrocytes in poly(ethyleneoxide)-based semi-interpenetrating networks. *J Biomed Mater Res* 51:164–171
35. Burdick JA, Anseth KS (2002) Photoencapsulation of osteoblasts in injectable RGD-modified PEG hydrogels for bone tissue engineering. *Biomaterials* 23:4315–4323
36. Johnstone B, Hering TM, Caplan AI, Goldberg VM, Yoo JU (2003) In vitro chondrogenesis of bone marrow-derived mesenchymal stem cells in a photopolymerizing hydrogel. *Tissue Eng* 9:679–688
37. Burdick JA, Chung C, Jia XQ, Randolph MA, Langer R (2005) Controlled degradation and mechanical behavior of photopolymerized hyaluronic acid networks. *Biomacromolecules* 6:386–391
38. Park YD, Tirelli N, Hubbell JA (2003) Photopolymerized hyaluronic acid-based hydrogels and interpenetrating networks. *Biomaterials* 24:893–900
39. Hu JL, Hou YP, Park H, Choi B, Hou S, Chung A, Lee M (2012) Visible light crosslinkable chitosan hydrogels for tissue engineering. *Acta Biomater* 8:1730–1738
40. McCall JD, Anseth KS (2012) Thiol-ene photopolymerizations provide a facile method to encapsulate proteins and maintain their bioactivity. *Biomacromolecules* 13:2410–2417
41. Fairbanks BD, Scott TF, Kloxin CJ, Anseth KS, Bowman CN (2009) Thiol-yne photopolymerizations: novel mechanism, kinetics, and step-growth formation of highly cross-linked networks. *Macromolecules* 42:211–217
42. Lin CC, Raza A, Shih H (2011) PEG hydrogels formed by thiol-ene photoclick chemistry and their effect on the formation and recovery of insulin-secreting cell spheroids. *Biomaterials* 32:9685–9695
43. Fairbanks BD, Schwartz MP, Halevi AE, Nuttelman CR, Bowman CN, Anseth KS (2009) A versatile synthetic extracellular matrix mimic via Thiol-Norbornene photopolymerization. *Adv Mater* 21:5005–5010

44. Engler AJ, Sen S, Sweeney HL, Discher DE (2006) Matrix elasticity directs stem cell lineage specification. *Cell* 126:677–689
45. Guvendiren M, Burdick JA (2012) Stiffening hydrogels to probe short- and long-term cellular responses to dynamic mechanics. *Nat Commun.* doi:10.1038/ncomms1792
46. Khetan S, Guvendiren M, Legant WR, Cohen DM, Chen CS, Burdick JA *Nat Mater.* doi:10.1038/nmat3586
47. Tseng SJ, Chien CC, Liao ZX, Chen HH, Kang YD, Wang CL, Hwu Y, Margaritondo G (2012) Controlled hydrogel photopolymerization inside live systems by X-ray irradiation. *Soft Matter* 8:1420–1427
48. Kloxin AM, Kloxin CJ et al (2010) Mechanical properties of cellularly responsive hydrogels and their experimental determination. *Adv Mater* 22:3484–3494
49. Li Q, Wang J et al (2006) Biodegradable and photocrosslinkable polyphosphoester hydrogel. *Biomaterials* 27:1027–1034
50. Poon YF, Cao Y et al (2009) Addition of beta-Malic Acid-Containing Poly(ethylene glycol) Dimethacrylate to form biodegradable and biocompatible hydrogels. *Biomacromolecules* 10:2043–2052
51. Zhou CC, Li P et al (2011) A photopolymerized antimicrobial hydrogel coating derived from epsilon-poly-L-lysine. *Biomaterials* 32:2704–2712
52. Yang F, Williams CG et al (2005) The effect of incorporating RGD adhesive peptide in polyethylene glycol diacrylate hydrogel on osteogenesis of bone marrow stromal cells. *Biomaterials* 26:5991–5998
53. Suzuki A, Tanaka T (1990) Phase-transition in polymer gels induced by visible-light. *Nature* 346:345–347
54. Tanaka T, Mamada A et al (1990) Photoinduced phase-transition of gels. *Macromolecules* 23:1517–1519
55. Kloxin AM, Kasko AM et al (2009) Photodegradable hydrogels for dynamic tuning of physical and chemical properties. *Science* 324:59–63
56. Kloxin AM, Benton JA et al (2010) In situ elasticity modulation with dynamic substrates to direct cell phenotype. *Biomaterials* 31:1–8
57. Kloxin AM, Tibbitt MW et al (2010) Synthesis of photodegradable hydrogels as dynamically tunable cell culture platforms. *Nat Protoc* 5:1867–1887
58. Tibbitt MW, Kloxin AM et al (2010) Tunable hydrogels for external manipulation of cellular microenvironments through controlled photodegradation. *Adv Mater* 22:61–66
59. Peng K, Tomatsu I et al (2011) Dextran based photodegradable hydrogels formed via a Michael addition. *Soft Matter* 7:4881–4887
60. Lewis KJR, Kloxin AM et al (2012) Responsive culture platform to examine the influence of microenvironmental geometry on cell function in 3D. *Integr Biol* 4:1540–1549
61. Wang H, Haeger SM et al (2012) Redirecting Valvular Myofibroblasts into Dormant Fibroblasts through light-mediated reduction in substrate modulus. *PLoS ONE* 7:e39969
62. Griffin DR, Kasko AM (2012) Photodegradable macromers and hydrogels for live cell encapsulation and release. *J Am Chem Soc* 134:13103–13107
63. Griffin DR, Kasko AM (2012) Photoselective delivery of model therapeutics from hydrogels. *ACS Macro Lett* 1:1330–1334
64. Yan B, Boyer JC et al (2012) Near infrared light triggered release of biomacromolecules from hydrogels loaded with upconversion nanoparticles. *J Am Chem Soc* 134:16558–16561
65. Peng K, Tomatsu I et al (2010) Light controlled protein release from a supramolecular hydrogel. *Chem Commun* 46:4094–4096
66. Khetan S, Burdick JA (2011) Patterning hydrogels in three dimensions towards controlling cellular interactions. *Soft Matter* 7:830–838
67. DeForest CA, Anseth KS (2011) Cytocompatible click-based hydrogels with dynamically tunable properties through orthogonal photoconjugation and photocleavage reactions. *Nat Chem* 3:925–931
68. DeForest CA, Anseth KS (2012) Photoreversible patterning of biomolecules within click - based hydrogels. *Angew Chem Int Ed* 124:1852–1855

69. Khetan S, Katz JS et al (2009) Sequential crosslinking to control cellular spreading in 3-dimensional hydrogels. *Soft Matter* 5:1601–1606
70. Marklein RA, Burdick JA (2010) Spatially controlled hydrogel mechanics to modulate stem cell interactions. *Soft Matter* 6:136–143
71. Khetan S, Burdick JA (2010) Patterning network structure to spatially control cellular remodeling and stem cell fate within 3-dimensional hydrogels. *Biomaterials* 31:8228–8234
72. Luo Y, Shoichet MS (2004) A photolabile hydrogel for guided three-dimensional cell growth and migration. *Nat Mater* 3:249–253
73. Wylie RG, Ahsan S et al (2011) Spatially controlled simultaneous patterning of multiple growth factors in three-dimensional hydrogels. *Nat Mater* 10:799–806
74. Wylie RG, Shoichet MS (2011) Three-dimensional spatial patterning of proteins in hydrogels. *Biomacromolecules* 12:3789–3796
75. Hahn MS, Miller JS, West JL (2006) Three-dimensional biochemical and biomechanical patterning of hydrogels for guiding cell behavior. *Adv Mater* 18:2679–2684
76. Lee SH, Moon JJ, West JL (2008) Three-dimensional micropatterning of bioactive hydrogels via two-photon laser scanning photolithography for guided 3D cell migration. *Biomaterials* 29:2962–2968
77. DeForest CA, Anseth KS (2012) Photoreversible patterning of biomolecules within click-based hydrogels. *Angew Chem Int Ed* 51:1816–1819
78. Hu YH, Wang HM, Wang JY, Wang SB, Liao W, Yang YG, Zhang YJ, Kong DL, Yang ZM (2010) Supramolecular hydrogels inspired by collagen for tissue engineering. *Org Biomol Chem* 8:3267–3271
79. Hamachi I (2010) Supramolecular hydrogels as novel stimuli-responsive materials. *Frag J* 38:21–25
80. Appel EA, Loh XJ, Jones ST, Biedermann F, Dreiss CA, Scherman OA (2012) Ultrahigh-water-content supramolecular hydrogels exhibiting Multistimuli responsiveness. *J Am Chem Soc* 134:11767–11770
81. Komatsu H, Tsukiji S, Ikeda M, Hamachi I (2011) Stiff, Multistimuli-responsive supramolecular hydrogels as unique molds for 2D/3D Microarchitectures of live cells. *Chem Asian J* 6:2368–2375
82. Li H, Wang GL, Tang L, Wei Q, Zhen TM, Meng XB (2010) Smart polymer materials for biomedical applications. Nova Science, New York
83. Yang ZM, Liang GL, Xu B (2008) Enzymatic hydrogelation of small molecules. *Acc Chem Res* 41:315–326
84. Huang YC, Qiu ZJ, Xu YM, Shi JF, Lin HK, Zhang Y (2011) Supramolecular hydrogels based on short peptides linked with conformational switch. *Org Biomol Chem* 9:2149–2155
85. Qiu ZJ, Yu HT, Li JB, Wang Y, Zhang Y (2009) Spiropyran-linked dipeptide forms supramolecular hydrogel with dual responses to light and to ligand-receptor interaction. *Chem Commun* 45:3342–3344
86. Li XM, Kuang Y, Gao Y, Xu B (2010) Enzymatic formation of a photoresponsive supramolecular hydrogel. *Chem Commun* 46:5364–5366
87. Haines LA, Ozbas B, Rajagopal K, Salick DA, Pochan DJ (2005) Light-activated hydrogel formation via the triggered folding and self-assembly of a designed peptide. *J Am Chem Soc* 127(48):17025–17029
88. Muraoka T, Cui HG, Koh CY, Stupp SI (2009) Light-triggered bioactivity in three dimensions. *Angew Chem Int Ed* 48:5946–5949
89. Takashima Y, Hatanaka S, Otsubo M, Nakahata M, Kakuta T, Hashidzume A, Yamaguchi H, Harada A (2012) Expansion-contraction of photoresponsive artificial muscle regulated by host-guest interactions. *Nat Commun*. doi:[10.1038/ncomms2280](https://doi.org/10.1038/ncomms2280)

Chapter 35

Engineering Apeptides for Translational Medicine

Haifan Wu and Jianfeng Cai

35.1 Introduction

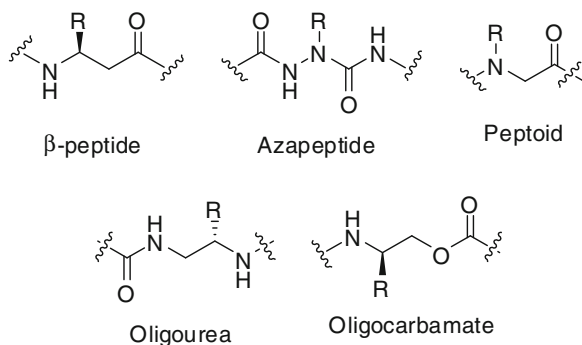
35.1.1 Peptides

Peptides are essential to all aspects of life forms and have found increasing attentions in scientific fields ranging from therapeutics [1–3] to biomaterials [4–7]. They are very attractive for the development of translational medicine, as their synthesis and characterization is straightforward. Meanwhile, they can form defined secondary structures such as helices, β -sheets, and turns and are able to regulate signal transduction pathways and other biological processes. However, there are significant obstacles for the development of peptide-based therapeutics [8]. Despite their high specificity and activity, peptides are more costly than small molecules in large productions, and have susceptibility to protease degradation, short half-live in vivo, and low oral bioavailability [9].

35.1.2 Peptidomimetics

The demand to identify peptide-based translational medicine has led to the creation and development of non-natural peptide mimics, or so-called peptidomimetics, which has become an emerging area in medicinal chemistry [10]. These peptidomimetics contain unnatural backbones and are capable of displaying diverse unnatural side chains. In the last two decades, there have been a wide variety of classes' peptidomimetics that were developed, and many of which have shown great

H. Wu · J. Cai (✉)
Department of Chemistry, University of South Florida, 4202 E. Fowler Ave,
Tampa, FL 33620, USA
e-mail: jianfengcai@usf.edu

Fig. 35.1 Examples of unnatural peptidomimetics

potential in biomedical applications and translational medicines [11]. Examples of these sequence-specific oligomers (Fig. 35.1) include β -peptides [12–14], γ - and δ -peptides [15–17], azapeptides [18, 19], oligoureas [20, 21], α -aminoxy peptides [22], sugar-based peptides [23, 24], α/β -peptides [25, 26], polyamides [27], and peptoids [28].

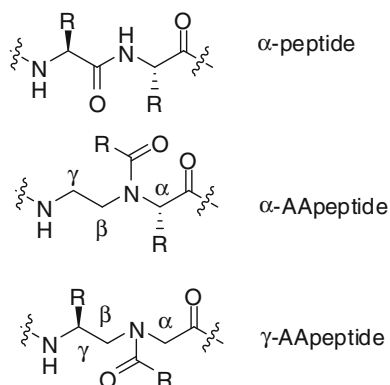
As they are not based on regular peptide backbones, they are often much more stable against proteolysis and have improved bioavailability compared to peptide counterparts [29]. In addition, peptidomimetics greatly enhance structure diversities by not only introducing novel backbones, but also displaying diverse side functional groups with virtually limitless potential. Although peptidomimetics were initially designed to mimic the primary structures of peptides, most classes of these peptide mimics are also able to fold into well-defined discrete three-dimensional structures such as sheets [30–32], helices [33], turns [34–36], and tertiary structures [37–44]. As such, they can mimic structures and functions of peptides and proteins and have begun to find potential applications in translational medicine [45, 46]. These classes of peptidomimetics have been extensively explored in the last two decades and reviewed comprehensively [10, 14, 29, 45, 47–50].

35.1.3 AApeptides

We have recently designed a new class of peptidomimetics termed “AApeptides” based on chiral PNA backbone [51–61]. They are termed “AApeptides” as they contain *N*-acylated-*N*-aminoethyl amino acid residues (Fig. 35.2). Depending on the positions of side chains on the backbone, two related classes of AApeptides— α -AApeptides and γ -AApeptides—were developed.

Both α - and γ -AApeptides were designed to mimic the primary structures of canonical α -peptides so as to facilitate drug discovery. Each AApeptide residue is comparable to a dipeptide residue. Although they have different backbones compared to α -peptides, AApeptides project same number of side chains as regular

Fig. 35.2 The structures of α -peptides, α -AApeptides, and γ -AApeptides



peptides of same lengths do [51, 52]. In addition, AApeptides have limitless diversity in their functional groups, as half of side chains are introduced to the backbones through acylation by any carboxylic acids. Furthermore, due to their unnatural backbone, they are highly resistant to enzymatic degradation [51, 52]. More importantly, the synthesis of AApeptides is modular and straightforward, by utilizing solid-phase synthesis to assemble AApeptide building blocks together [51, 52, 62, 63]. As such, AApeptides can be developed to mimic the structures and functions of bioactive peptides. Indeed, certain AApeptide can bind to RNA with high affinity comparable to the Tat peptide [64], and some AApeptides are efficient cell-penetrating peptidomimetics which can translocate cellular membrane, suggesting their potential for drug delivery [65, 66]. AApeptides also have found great potential in material sciences as some of them are able to form novel nanorods and nanoparticles [67]. In this chapter, we will focus on their application as potential therapeutics for translational medicine, including their development as novel antimicrobial and anticancer agents.

35.2 Antimicrobial Agents

35.2.1 Background

One of the biggest clinical and public concerns worldwide is the antibiotic resistance [68], attributed to antibiotic abuse [69, 70]. The emergence of multi-drug-resistant bacterial strains such as methicillin-resistant *Staphylococcus aureus* (MRSA), vancomycin-resistant enterococci (VRE), and methicillin-resistant *Staphylococcus epidermidis* (MRSE) has largely abolish the efficacy of conventional antibiotics [71–73]. There has been tremendous effort in the search of new and effective antibiotics. Antimicrobial peptides (AMPs) are of significant interest for such development. AMPs exist virtually in all organisms and are their first line

of defense [69, 70, 74–76]. Although the exact bactericidal mechanisms of AMPs may vary from one to the others [71], the hallmark of their structures is that they form globally amphipathic conformations upon interaction with bacterial membranes. In such amphiphilic structures, cationic and hydrophobic side groups segregate into discrete regions. The cationic region first associates with negatively charged bacterial membranes through electrostatic interaction [69, 70, 74–76], and then, the hydrophobic side chains disrupt membranes through hydrophobic interactions. Although such interactions lack defined membrane targets and rather biophysical, the selectivity of AMPs is high because mammalian cell membranes are largely zwitterionic. On the other hand, since antimicrobial activity of AMPs lacks defined bacterial internal and membrane targets, the probability of inducing antibiotic resistance is much lower. Additionally, the amphipathic structures of AMPs are not relevant to precise sequences and defined secondary structures, and in fact, the examples of AMPs embrace α -helices, β -sheets, and extended conformation. [70]

However, there are obstacles for the development of AMPs as new generation of antibiotics. These include susceptibility toward protease degradation, low-to-moderate antimicrobial activity, and limited diversity for optimization. Antimicrobial peptidomimetics, developed to mimic the function of AMPs, can potentially overcome these disadvantages. Many classes of antimicrobial peptidomimetics have been developed, including peptoids [33, 77–81], β -turn mimetics [82, 83], arylamide oligomers [71, 84, 85], and β -peptides [86–88], which have been comprehensively reviewed [69, 70, 89]. The development of these antimicrobial peptidomimetics has led to the recognition that defined secondary structures such as helical or sheet-like structures are not required for antimicrobial activity [62, 63, 90–92].

35.2.2 Design of Antimicrobial AApeptides

AApeptides are expected to be good candidates for the design of novel antimicrobial agents that mimic AMPs, as they possess backbones with limited conformational flexibility and [62, 90] high stability [51, 52, 93]. As such, amphipathic AApeptides can be designed in a very straightforward way by joining amphiphilic AApeptide building blocks, since AApeptides comprising of amphiphilic building blocks (containing one hydrophobic and one cationic side chain) are expected to adopt globally amphipathic structures upon interaction with bacterial membranes (Fig. 35.3). Their activity and selectivity can be further tuned through the introduction of additional hydrophobic (containing two hydrophobic side chains) building blocks, as well as changing the nature of the hydrophobic and cationic groups.

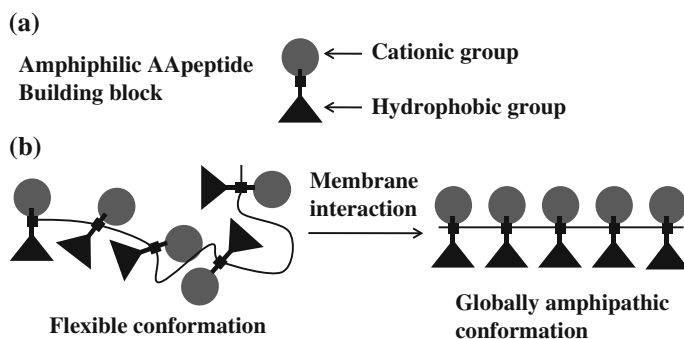


Fig. 35.3 Illustration of the design of antimicrobial AApeptide. **a** The structure of amphiphilic AApeptide building block. **b** The formation of amphipathic structure of AApeptides on bacterial membranes. Adapted from Ref. [90]

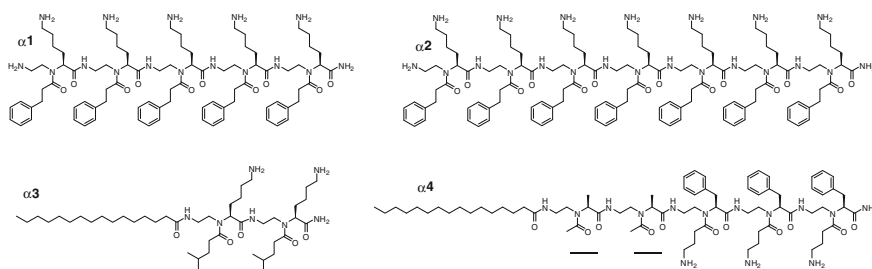


Fig. 35.4 The representative antimicrobial α -AApeptides [62, 94]. Groups underlined are hydrophobic α -AApeptide peptide residues

35.2.3 α -AApeptides as Antimicrobial Agents

35.2.3.1 Linear Antimicrobial α -AApeptides

Following the design strategy, a small library of linear α -AApeptide sequences was prepared, which led to the identification of two lead sequences $\alpha 1$ and $\alpha 2$ (Fig. 35.4) [62]. These linear sequences contain amphiphilic α -AApeptide building blocks and were expected to adopt globally amphipathic structures upon interaction with bacterial membranes so as to kill bacterial pathogens. The amphiphilic sequence $\alpha 1$ is active against *Bacillus subtilis* and *Staphylococcus epidermidis*, and addition of one more amphiphilic building block led to the identification of the more potent antimicrobial agent $\alpha 2$ [62]. Fluorescence microscopy and TEM studies suggested that $\alpha 2$ exert bactericidal activity by damaging bacterial membranes [62]. The preliminary data of linear α -AApeptides antimicrobial agents demonstrate that α -AApeptides are good candidates to mimic the structure and mechanism of AMPs. The design seems straightforward: Amphiphilic building-

block-based α -AApeptides tend to selective kill bacteria pathogens, and longer sequences are more active as they contain more hydrophobic and cationic groups.

35.2.3.2 Lipo-Antimicrobial α -AApeptides

Some natural lipopeptide antibiotics have been used as antibiotics to treat bacterial pathogens [95], although they are different from host-defense peptides in their antimicrobial mechanisms. As they are produced as metabolites in bacteria and fungi [95, 96] and are either anionic [97], cationic [98], and neutral [99], many of these natural lipo-antibiotics are narrow spectrum in their activity. Although their antimicrobial mechanism may vary, lipid tail is generally believed to largely contribute to the antimicrobial activity. Therefore, lipo-sequences with small number of hydrophobic and cationic groups could be very active [100].

It is expected that cationic lipo- α -AApeptides should mimic AMPs because their overall structure is still cationic, and as such, they are active against both Gram-positive and Gram-negative bacteria. Indeed, with just two amphiphilic building blocks, lipidated α -AApeptide α 3 shows potent activity against Gram-positive bacteria [94]. The antimicrobial activity is further enhanced for α 4, which contains two more hydrophobic building blocks and one amphiphilic building block, possibly due to the stronger interaction with bacteria membranes [94].

35.2.4 γ -AApeptides as Antimicrobial Agents

35.2.4.1 Linear Antimicrobial γ -AApeptides

Similar design strategy was used to develop antimicrobial γ -AApeptides. Two most potent linear γ -AApeptides γ 1 and γ 2 are shown in Fig. 35.5 [90]. The amphiphilic sequence γ 1, containing seven amphiphilic building blocks, are active against several Gram-positive bacteria. Replacement of two amphiphilic building blocks in γ 1 with two hydrophobic building blocks led to the identification of γ 2 [90], which are broadly active against a range of Gram-positive and Gram-negative drug-resistant bacterial pathogens. Subsequent drug-resistant studies and fluorescent microscopy supported that γ 2 kill bacteria through membrane disruption [90].

35.2.4.2 Lipo-Antimicrobial γ -AApeptides

Cationic lipo- γ -AApeptides were also investigated for their antimicrobial activity. As shown in Fig. 35.5, both γ 3 and γ 4 have broad spectrum activity. The difference between γ 3 and γ 4 is that γ 4 has an unsaturated bond in its alkyl tail. Interestingly, γ 4 is more selective against bacteria than γ 3. Although mechanistic studies are required to elucidate the behavior, the findings might be significant for

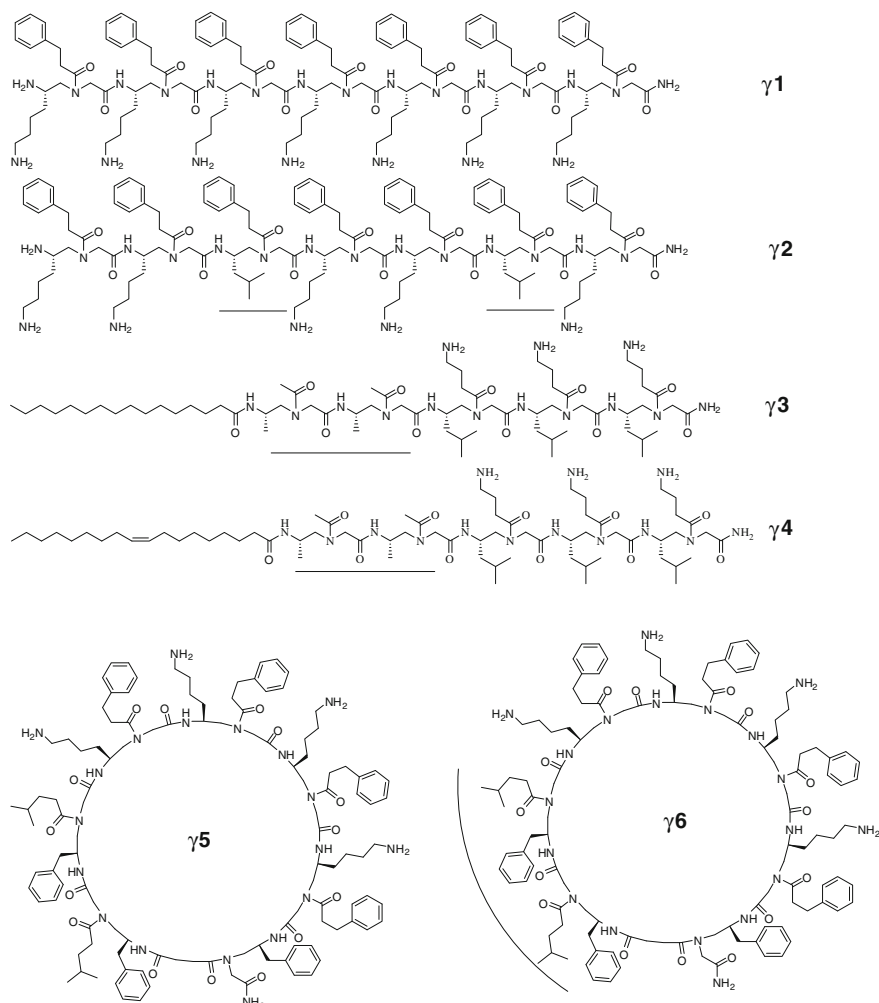


Fig. 35.5 The representative antimicrobial γ -AApeptides [63, 90, 101]. The hydrophobic building blocks are marked by *lines*

the development of new antimicrobial peptidomimetics. Further mechanistic studies including membrane depolarization, fluorescence microscopy, and drug-resistant assays suggested that lipo- γ -AApeptides can also mimic bactericidal mechanism of AMPs by killing bacterial pathogens through the disruption of bacterial membranes [63].

35.2.4.3 Cyclic Antimicrobial γ -AApeptides

Cyclic peptide antibiotics such as tyrocidine and protegrin I are common in nature. These cyclic AMPs have semi-rigid backbone conformations due to cyclization [83], which is believed to improve antimicrobial activity than linear sequences without any constraints, as they may possess more stable amphipathic structures. Similar strategy to design other classes of antimicrobial AApeptides was applied to generate focused cyclic γ -AApeptide library that mimics the mechanisms of AMPs [101]. This is achieved by cyclizing γ -AApeptide amphiphilic building blocks on the solid phase [101]. By varying the ratio of cationic/hydrophobic groups, their antimicrobial activity and selectivity can be fine-tuned [90]. Two cyclic γ -AApeptides γ 5 and γ 6 were identified from the library [101], and they show much improved antimicrobial activity against a range of multi-drug-resistant Gram-positive and Gram-negative bacterial pathogens than linear ones. Moreover, bearing more hydrophobic groups, γ 6 is found to be more potent than γ 5, suggesting that hydrophobic groups are important for the disruption of bacterial membranes.

35.3 Anticancer Agents

35.3.1 *Disruption of MDM2-p53 Protein-Protein Interaction*

The p53 protein is a tumor suppressor that integrates cellular stress signals and functions as a transcription factor with many target genes involved in DNA repair, cell cycle arrest, and activation of apoptosis. MDM2 (murine double minute two protein) is a p53-specific ubiquitin E3 ligase and thus promotes the proteasomal degradation of p53. It binds to the α -helical transactivation domain near the N-terminus of p53 and blocks the DNA-binding activity of p53 [102–104]. The disruption of p53/MDM2 protein-protein interactions can regulate apoptosis and therefore is of significant interest in the development of anticancer agents for translational medicine.

A co-crystal structure of the complex between the MDM2 protein and a peptide corresponding to p53 residues 17–29 was resolved more than a decade ago [102]. The structure reveals that the N-terminal transactivation domain of p53 adopts an amphipathic α -helical conformation and occupies a hydrophobic cleft on the surface of MDM2 (Fig. 35.6). Three hydrophobic side chains from residues Phe19, Trp23, and Leu26 of p53, aligning along one face of the amphipathic α -helix, insert deeply into a compact hydrophobic binding pocket. It is therefore hypothesized that a synthetic molecule displaying three hydrophobic groups in an orientation that mimics the presentation of the Phe19, Trp23, and Leu26 side chains by p53 is able to occupy the MDM2 cleft and thereby disrupt p53/MDM2 interactions. Indeed, both traditional and non-traditional approaches have been adopted to develop new scaffolds that can mimic the α -helical segment of p53 involved in the interaction

Fig. 35.6 The crystal structure of the p53/MDM2 interaction (PDB 1YCR) [102]. Residues 17–29 of p53 are shown as *ribbon*. MDM2 is presented as *gray surface*. The three residues of p53 (F19, W23, and L26) involved in the interaction are shown with *solid sticks*

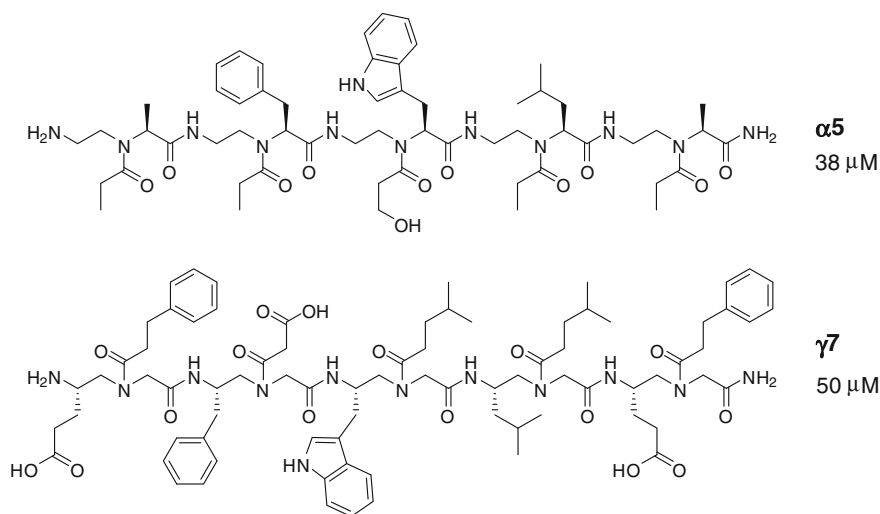
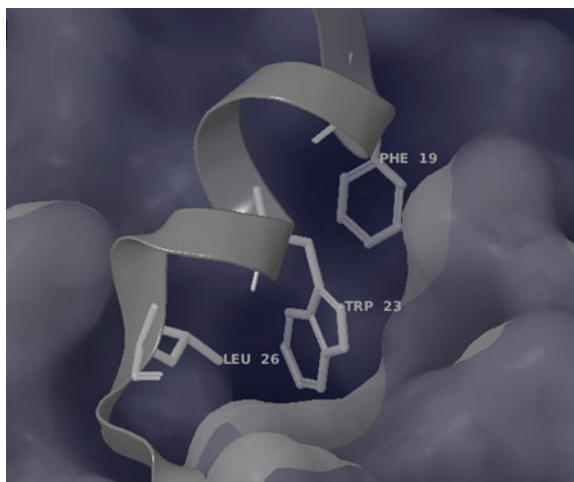


Fig. 35.7 Two representative AApeptides that disrupt MDM2/p53 interaction. IC_{50}s were obtained by ELISA

with MDM2. These antagonists range from small molecules such as syc-7 [105], nutlins [106], sulfonamides [107], benzodiazepinediones [108], to oligomers including peptides [109] and peptidomimetics such as peptoids [110, 111] and β -peptides [112–115].

Both short α -AApeptides and γ -AApeptides have been synthesized and studied for their capability to inhibit MDM2/p53 interaction. As shown in Fig. 35.7, two most potent AApeptides, α -AApeptide $\alpha 5$ and γ -AApeptide $\gamma 7$, are capable of disrupting the interaction, with IC_{50} of 38 and 50 μM , respectively [51, 52]. Both

sequences contain side chains identical to those three critical residues (Phe, Try, and Leu) from p53, and interestingly, these residues are on the same side of backbones. It is probably because these sequences are too short to form any defined fold structures, and as such, they tend to be extended linear structure when interacting with MDM2 hydrophobic pocket. This is also the reason why their activity is modest. However, they are the first examples that AApeptides can have the potential to mimic peptides and disrupt protein–protein interactions, and their activity actually is comparable to other classes of peptidomimetics [110–115]. It is highly possible that with the presence of longer sequences, or introduction of constraints such as cyclization, more potent AApeptides that disrupt p53/MDM2 protein–protein interaction can be identified.

35.3.2 RGD Amimetics

Integrin $\alpha_v\beta_3$ is a cell surface receptor that is tightly involved in tumor angiogenesis. It is frequently overexpressed on many cancer cells (e.g., lung/prostate/breast cancer and glioblastoma), as well as tumor vasculature and therefore is an attractive target for both cancer diagnosis and therapeutic development [116]. As Integrin $\alpha_v\beta_3$ binds very tightly to the Arg-Gly-Asp (RGD) tripeptide epitope existing in many extracellular matrix proteins, a wide variety of peptides/peptidomimetics have been developed to mimic RGD motif so as to be used for anticancer drugs and/or cancer imaging [116, 117]. However, RGD peptides are susceptible to enzymatic degradation, even when cyclization and the use of unnatural amino acids are introduced [117]. To explore the ability of AApeptides to mimic RGD motif, a γ -AApeptide γ -AA1 was designed (Fig. 35.8) [93]. The additional phenyl moiety was introduced to confer the molecule with balanced hydrophilicity and hydrophobicity [116]. Subsequently, DOTA (1, 4, 7, 10-tetraazacyclododecane-1, 4, 7, 10-tetraacetic acid) was linked to γ -AA1 to give γ -AA2 (Fig. 35.8) to enable ^{64}Cu -labeling and PET imaging. Both γ -AA1 and γ -AA2 show very similar binding affinity to c(RGDyK), despite their shorter sequences and linear nature [93]. Next, γ -AA2 was labeled with ^{64}Cu tested with PET for its targeting specificity using a glioblastoma tumor-bearing mouse model. ^{64}Cu -labeled γ -AA2 shows ability to specifically target the tumor site *in vivo*; however, it is much more resistant to enzymatic degradation, augmenting its potential as the novel targeting ligand for cancer imaging and therapeutic applications.

35.4 Future Perspective

Engineering peptidomimetics for the development of translational medicine is an attractive and vibrant research area. It is considerably significant as it can potentially circumvent the drawbacks of peptide-based therapeutics. Exploration

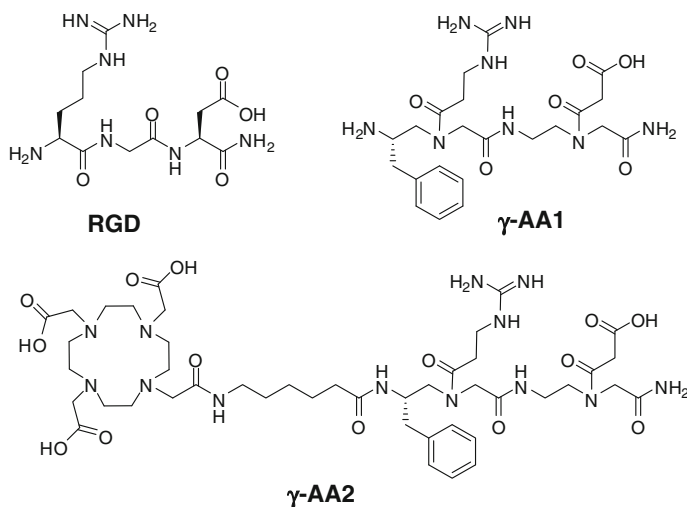


Fig. 35.8 The structures of canonic RGD tripeptide, γ -AApeptides γ -AA1 and γ -AA2

of new classes of peptidomimetics is necessary to identify new sequences, folding structures, and therefore new functions. AApeptides described here are one of such examples. Although the secondary structures of AApeptides have not been resolved, their unique backbone, modular and amendable synthesis, stability against protease hydrolysis and diverse functional groups has led to some important biological applications. It is envisioned that their potential will further expand with continuous development. To fully realize their application for translational medicine, the following approaches will be adopted. First, although many therapeutic peptides do not have secondary structure, it is helpful to understand the folding of AApeptides, so as to facilitate rational design and optimization of lead AApeptides for translational medicine. In this endeavor, 2D-NMR and X-ray crystallography can be employed to investigate their solution and solid 3D structures. Secondly, the synthesis should be further simplified. Current approach needs the preparation of building blocks, which can be laborious even if a small library of AApeptides is prepared. It also limits the potential of mass production and commercialization of AApeptides. Furthermore, to facilitate the therapeutic development for translational medicine, combinatorial chemistry should be explored for AApeptides. As AApeptides have limitless potential for derivatization, the development of combinatorial library is expected to greatly advance peptidomimetics-based translational medicine. With current synthetic organic chemistry development, and state-of-the-art instrumentation, the above questions are expected to be resolved in the near future.

References

1. Saladin PM, Zhang BDD, Reichert JM (2009) Current trends in the clinical development of peptide therapeutics. *Idrugs* 12(12):779–784
2. Guarracino DA, Arora PS (2009) Making strides in peptide-based therapeutics. *Chem Biol* 16(9):919–920
3. Morimoto BH (2012) Progress in peptide therapeutics. *Chimica Oggi-Chem Today* 30(2):2
4. Law B, Weissleder R, Tung CH (2006) Peptide-based biomaterials for protease-enhanced drug delivery. *Biomacromolecules* 7(4):1261–1265
5. Woolfson DN, Ryadnov MG (2006) Peptide-based fibrous biomaterials: some things old, new and borrowed. *Curr Opin Chem Bio* 10(6):559–567
6. Kopecek J, Yang JY (2009) Peptide-directed self-assembly of hybrid biomaterials. Abstracts of Papers of the American Chemical Society 238
7. Khadka DB, Haynie DT (2012) Protein- and peptide-based electrospun nanofibers in medical biomaterials. *Nanomed-Nanotechnol Biol Med* 8(8):1242–1262
8. Brown NJ, Johansson J, Barron AE (2008) Biomimicry of surfactant protein C. *Acc Chem Res* 41(10):1409–1417
9. Chatterjee J, Gilon C, Hoffman A, Kessler H (2008) *N*-methylation of peptides: a new perspective in medicinal chemistry. *Acc Chem Res* 41(10):1331–1342
10. Wu Y-D, Gellman S (2008) Peptidomimetics. *Acc Chem Res* 41(10):1231–1232. doi:10.1021/ar800216e
11. Gellman SH (2011) Foldamer structure and function. Abstracts of Papers of the American Chemical Society 241
12. Cheng RP, Gellman SH, DeGrado WF (2001) Beta-peptides: from structure to function. *Chem Rev* 101(10):3219–3232. doi:cr000045i
13. Seebach D, Ciceri PE, Overhand M, Jaun B, Rigo D, Oberer L, Hommel U, Amstutz R, Widmer H (1996) Probing the helical secondary structure of short-chain beta-peptides. *Helvetica Chimica Acta* 79(8):2043–2066
14. Kritzer JA, Stephens OM, Guarracino DA, Reznik SK, Schepartz A (2005) Beta-peptides as inhibitors of protein–protein interactions. *Bioorg Med Chem* 13(1):11–16
15. Kumbhani DJ, Sharma GV, Khuri SF, Kirdar JA (2006) Fascicular conduction disturbances after coronary artery bypass surgery: a review with a meta-analysis of their long-term significance. *J Card Surg* 21(4):428–434. doi:10.1111/j.1540-8191.2006.00264.x JCS264 [pii]
16. Arndt HD, Ziemer B, Koert U (2004) Folding propensity of cyclohexylether-delta-peptides. *Org Lett* 6(19):3269–3272. doi:10.1021/ol048861q
17. Trabocchi A, Guarna F, Guarna A (2005) Gamma- and delta-amino acids: synthetic strategies and relevant applications. *Curr Org Chem* 9(12):1127–1153
18. Lee HJ, Song JW, Choi YS, Park HM, Lee KB (2002) A theoretical study of conformational properties of *N*-methyl azapeptide derivatives. *J Am Chem Soc* 124(40):11881–11893. doi:10.1021/Ja026496x
19. Graybill TL, Ross MJ, Gauvin BR, Gregory JS, Harris AL, Ator MA, Rinker JM, Dolle RE (1992) Synthesis and evaluation of azapeptide-derived inhibitors of serine and cysteine proteases. *Bioorg Med Chem Lett* 2(11):1375–1380
20. Violette A, Petit MC, Rognan D, Monteil H, Guichard G (2005) Oligoureia foldamers as antimicrobial peptidomimetics. *Biopolymers* 80(4):516
21. Boeijen A, van Ameijde J, Liskamp RMJ (2001) Solid-phase synthesis of oligoureia peptidomimetics employing the Fmoc protection strategy. *J Org Chem* 66(25):8454–8462
22. Li X, Wu YD, Yang D (2008) Alpha-aminoxy acids: new possibilities from foldamers to anion receptors and channels. *Acc Chem Res* 41(10):1428–1438
23. Tuwalska D, Sienkiewicz J, Liberek B (2008) Synthesis and conformational analysis of methyl 3-amino-2,3-dideoxyhexopyranosiduronic acids, new sugar amino acids, and their diglycotides. *Carbohydr Res* 343(7):1142–1152

24. Risseuw MD, Mazurek J, van Langenvelde A, van der Marel GA, Overkleeft HS, Overhand M (2007) Synthesis of alkylated sugar amino acids: conformationally restricted L-Xaa-L-Ser/Thr mimics. *Org Biomol Chem* 5(14):2311–2314
25. Horne WS, Johnson LM, Ketas TJ, Klasse PJ, Lu M, Moore JP, Gellman SH (2009) Structural and biological mimicry of protein surface recognition by alpha/beta-peptide foldamers. *Proc Natl Acad Sci USA* 106(35):14751–14756
26. Horne WS, Gellman SH (2008) Foldamers with heterogeneous backbones. *Acc Chem Res* 41(10):1399–1408
27. Dervan PB (1986) Design of sequence-specific DNA-binding molecules. *Science* 232(4749):464–471
28. Simon RJ, Kania RS, Zuckermann RN, Huebner VD, Jewell DA, Banville S, Ng S, Wang L, Rosenberg S, Marlowe CK et al (1992) Peptoids: a modular approach to drug discovery. *Proc Natl Acad Sci USA* 89(20):9367–9371
29. Patch JA, Barron AE (2002) Mimicry of bioactive peptides via non-natural, sequence-specific peptidomimetic oligomers. *Curr Opin Chem Bio* 6(6):872–877
30. Segman S, Lee MR, Vaiser V, Gellman SH, Rapaport H (2009) Highly stable pleated-sheet secondary structure in assemblies of amphiphilic alpha/beta-peptides at the air-water interface. *Angew Chem Int Ed Engl* 49(4):716–719
31. Levin S, Nowick JS (2009) A new artificial beta-sheet that dimerizes through parallel beta-sheet interactions. *Org Lett* 11(4):1003–1006
32. Levin S, Nowick JS (2007) An artificial beta-sheet that dimerizes through parallel beta-sheet interactions. *J Am Chem Soc* 129(43):13043–13048
33. Chongsiriwatana NP, Patch JA, Czyzewski AM, Dohm MT, Ivankin A, Gidalevitz D, Zuckermann RN, Barron AE (2008) Peptoids that mimic the structure, function, and mechanism of helical antimicrobial peptides. *Proc Natl Acad Sci* 105(8):2794–2799
34. Knijnenburg AD, Spalburg E, de Neeling AJ, Mars-Groenendijk RH, Noort D, Grotenbreg GM, van der Marel GA, Overkleeft HS, Overhand M (2009) Ring-extended derivatives of gramicidin S with furanoid sugar amino acids in the turn region have enhanced antimicrobial activity. *Chem Med Chem* 4(12):1976–1979
35. Pokorski JK, Jenkins LM, Feng H, Durell SR, Bai Y, Appella DH (2007) Introduction of a triazole amino acid into a peptoid oligomer induces turn formation in aqueous solution. *Org Lett* 9(12):2381–2383
36. Seebach D, Jaun B, Sebesta R, Mathad RI, Fogel O, Limbach M, Sellner H, Cottens S (2006) Synthesis, and helix or hairpin-turn secondary structures of ‘mixed’ alpha/beta-peptides consisting of residues with proteinogenic side chains and of 2-amino-2-methylpropanoic acid (Aib). *Helv Chim Acta* 89(9):1801–1825
37. Molski MA, Goodman JL, Craig CJ, Meng H, Kumar K, Schepartz A (2010) Beta-peptide bundles with fluororous cores. *J Am Chem Soc* 132(11):3658–3659
38. Petersson EJ, Schepartz A (2008) Toward beta-amino acid proteins: design, synthesis, and characterization of a fifteen kilodalton beta-peptide tetramer. *J Am Chem Soc* 130(3):821–823
39. Goodman JL, Molski MA, Qiu J, Schepartz A (2008) Tetrameric beta(3)-peptide bundles. *Chem Bio Chem* 9(10):1576–1578
40. Miller CA, Gellman SH, Abbott NL, de Pablo JJ (2009) Association of helical beta-peptides and their aggregation behavior from the potential of mean force in explicit solvent. *Biophys J* 96(11):4349–4362
41. Giuliano MW, Horne WS, Gellman SH (2009) An alpha/beta-peptide helix bundle with a pure beta3-amino acid core and a distinctive quaternary structure. *J Am Chem Soc* 131(29):9860–9861
42. Shu JY, Tan C, DeGrado WF, Xu T (2008) New design of helix bundle peptide-polymer conjugates. *Biomacromolecules* 9(8):2111–2117
43. Horne WS, Price JL, Keck JL, Gellman SH (2007) Helix bundle quaternary structure from alpha/beta-peptide foldamers. *J Am Chem Soc* 129(14):4178–4180

44. Burkoth TS, Beausoleil E, Kaur S, Tang D, Cohen FE, Zuckermann RN (2002) Toward the synthesis of artificial proteins: the discovery of an amphiphilic helical peptoid assembly. *Chem Biol* 9(5):647–654
45. Gellman S (2009) Structure and function in peptidic foldamers. *Biopolymers* 92(4):293
46. Goodman CM, Choi S, Shandler S, DeGrado WF (2007) Foldamers as versatile frameworks for the design and evolution of function. *Nat Chem Biol* 3(5):252–262
47. Gellman SH (1998) Foldamers: a manifesto. *Acc Chem Res* 31(4):173–180
48. Yoo B, Kirshenbaum K (2008) Peptoid architectures: elaboration, actuation, and application. *Curr Opin Chem Biol* 12(6):714–721
49. Zuckermann RN, Kodadek T (2009) Peptoids as potential therapeutics. *Curr Opin Mol Ther* 11(3):299–307
50. Seebach D, Gardiner J (2008) Beta-peptidic peptidomimetics. *Acc Chem Res* 41(10):1366–1375
51. Hu Y, Li X, Sebti SM, Chen J, Cai J (2011) Design and synthesis of AApeptides: a new class of peptide mimics. *Bioorg Med Chem Lett* 21:1469–1471
52. Niu Y, Hu Y, Li X, Chen J, Cai J (2011) [Gamma]-AApeptides: design, synthesis and evaluation. *New J Chem* 35(3):542–545
53. Sforza S, Corradini R, Ghirardi S, Dossena A, Marchelli R (2000) DNA binding of AD-lysine-based chiral PNA: direction control and mismatch recognition. *Eur J Org Chem* 16:2905–2913
54. Tedeschi T, Sforza S, Corradini R, Marchelli R (2005) Synthesis of new chiral PNAs bearing a dipeptide-mimic monomer with two lysine-derived stereogenic centres. *Tetrahedron Lett* 46(48):8395–8399
55. Debaene F, Da Silva JA, Pianowski Z, Duran FJ, Winssinger N (2007) Expanding the scope of PNA-encoded libraries: divergent synthesis of libraries targeting cysteine, serine and metallo-proteases as well as tyrosine phosphatases. *Tetrahedron* 63(28):6577–6586
56. Winssinger N, Damoiseaux R, Tully DC, Geierstanger BH, Burdick K, Harris JL (2004) PNA-encoded protease substrate microarrays. *Chem Biol* 11(10):1351–1360
57. Sforza S, Haaima G, Marchelli R, Nielsen PE (1999) Chiral peptide nucleic acids (PNAs): helix handedness and DNA recognition. *Eur J Org Chem* 1:197–204
58. Dragulescu-Andrasi A, Rapireddy S, Frezza BM, Gayathri C, Gil RR, Ly DH (2006) A simple gamma-backbone modification preorganizes peptide nucleic acid into a helical structure. *J Am Chem Soc* 128(31):10258–10267
59. Lusvardi S, Murphy CT, Roy S, Tanius FA, Sacui I, Wilson WD, Ly DH, Armitage BA (2009) Loop and backbone modifications of peptide nucleic acid improve g-quadruplex binding selectivity. *J Am Chem Soc* 131(51):18415–18424
60. Tedeschi T, Sforza S, Dossena A, Corradini R, Marchelli R (2005) Lysine-based peptide nucleic acids (PNAs) with strong chiral constraint: control of helix handedness and DNA binding by chirality. *Chirality* 17:S196–S204
61. Haaima G, Lohse A, Buchardt O, Nielsen PE (1996) Peptide nucleic acids (PNAs) containing thymine monomers derived from chiral amino acids: hybridization and solubility properties of D-lysine PNA. *Angew Chem Int Ed* 35(17):1939–1942
62. Padhee S, Hu Y, Niu Y, Bai G, Wu H, Costanza F, West L, Harrington L, Shaw LN, Cao C, Cai J (2011) Non-hemolytic alpha-AApeptides as antimicrobial peptidomimetics. *Chem Commun* 47(34):9729–9731
63. Niu Y, Padhee S, Wu H, Bai G, Qiao Q, Hu Y, Harrington L, Burda WN, Shaw LN, Cao C, Cai J (2012) Lipo-gamma-AApeptides as a new class of potent and broad-spectrum antimicrobial agents. *J Med Chem* 55(8):4003–4009
64. Niu Y, Jones AJ, Wu H, Varani G, Cai J (2011) Gamma-AApeptides bind to RNA by mimicking RNA-binding proteins. *Org Biomol Chem* 9(19):6604–6609
65. Niu Y, Bai G, Wu H, Wang RE, Qiao Q, Padhee S, Buzzeo R, Cao C, Cai J (2012) Cellular Translocation of a gamma-AApeptide Mimetic of Tat Peptide. *Mol Pharm*
66. Bai G, Padhee S, Niu Y, Wang RE, Qiao Q, Buzzeo R, Cao C, Cai J (2012) Cellular uptake of an alpha-AApeptide. *Org Biomol Chem* 10(6):1149–1153

67. Niu Y, Wu H, Huang R, Qiao Q, Constanza F, Wang X, Hu Y, Amin MN, Naguyen A, Zhang J, Haller E, Ma S, Li X, Cai J (2012) Nanorods formed from a new class of peptidomimetics. *Macromolecules* 45:7350–7355
68. Spellberg B et al (2011) Combating antimicrobial resistance: policy recommendations to save lives. *Infect Dis Soc Am: Clin Infect Dis* 52(suppl 5):S397–S428
69. Marr AK, Gooderham WJ, Hancock RE (2006) Antibacterial peptides for therapeutic use: obstacles and realistic outlook. *Curr Opin Pharm* 6(5):468–472
70. Hancock RE, Sahl HG (2006) Antimicrobial and host-defense peptides as new anti-infective therapeutic strategies. *Nat Biotech* 24(12):1551–1557
71. Choi S, Isaacs A, Clements D, Liu D, Kim H, Scott RW, Winkler JD, DeGrado WF (2009) De novo design and in vivo activity of conformationally restrained antimicrobial arylamide foldamers. *Pro Natl Aca Sci* 106(17):6968–6973
72. Tew GN, Scott RW, Klein ML, Degrado WF (2009) De novo design of antimicrobial polymers, foldamers, and small molecules: from discovery to practical applications. *Acc Chem Res* 43(1):30–39
73. Scott RW, DeGrado WF, Tew GN (2008) De novo designed synthetic mimics of antimicrobial peptides. *Curr Opin Biotech* 19(6):620–627
74. Zhang L, Dhillon P, Yan H, Farmer S, Hancock RE (2000) Interactions of bacterial cationic peptide antibiotics with outer and cytoplasmic membranes of *Pseudomonas aeruginosa*. *Antimicrob Agents Chemother* 44(12):3317–3321
75. Wu M, Maier E, Benz R, Hancock REW (1999) Mechanism of interaction of different classes of cationic antimicrobial peptides with planar bilayers and with the cytoplasmic membrane of *Escherichia coli*. *Biochemistry* 38(22):7235–7242
76. Friedrich CL, Moyles D, Beveridge TJ, Hancock RE (2000) Antibacterial action of structurally diverse cationic peptides on gram-positive bacteria. *Antimicrob Agents Chemother* 44(8):2086–2092
77. Olsen CA, Ziegler HL, Nielsen HM, Frimodt-Moller N, Jaroszewski JW, Franzyk H (2010) Antimicrobial, hemolytic, and cytotoxic activities of beta-peptoid-peptide hybrid oligomers: improved properties compared to natural AMPs. *Chem Bio Chem* 11(10):1356–1360
78. Chongsiriwatana NP, Miller TM, Wetzler M, Vakulenko S, Karlsson AJ, Palecek SP, Mobashery S, Barron AE (2011) Short alkylated peptoid mimics of antimicrobial lipopeptides. *Antimicrob Agents Chemother* 55(1):417–420
79. Kapoor R, Wadman MW, Dohm MT, Czyzewski AM, Spormann AM, Barron AE (2011) Antimicrobial peptoids are effective against *Pseudomonas aeruginosa* biofilms. *Antimicrob Agents Chemother* 55(6):3054–3057
80. Huang ML, Shin SB, Benson MA, Torres VJ, Kirshenbaum K (2012) A comparison of linear and cyclic peptoid oligomers as potent antimicrobial agents. *Chem Med Chem* 7(1):114–122
81. Kapoor R, Eimerman PR, Hardy JW, Cirillo JD, Contag CH, Barron AE (2011) Efficacy of antimicrobial peptoids against mycobacterium tuberculosis. *Antimicrob Agents Chemother* 55(6):3058–3062
82. Srinivas N, Jetter P, Ueberbacher BJ, Werneburg M, Zerbe K, Steinmann J, Van der Meijden B, Bernardini F, Lederer A, Dias RL, Misson PE, Henze H, Zumbrunn J, Gombert FO, Obrecht D, Hunziker P, Schauer S, Ziegler U, Kach A, Eberl L, Riedel K, DeMarco SJ, Robinson JA (2010) Peptidomimetic antibiotics target outer-membrane biogenesis in *Pseudomonas aeruginosa*. *Science* 327(5968):1010–1013 (New York)
83. Obrecht D, Robinson JA, Bernardini F, Bisang C, DeMarco SJ, Moehle K, Gombert FO (2009) Recent progress in the discovery of macrocyclic compounds as potential anti-infective therapeutics. *Curr Med Chem* 16(1):42–65
84. Hua J, Scott RW, Diamond G (2010) Activity of antimicrobial peptide mimetics in the oral cavity: II. Activity against periopathogenic biofilms and anti-inflammatory activity. *Mol Oral Microbiol* 25(6):426–432

85. Hua J, Yamarthy R, Felsenstein S, Scott RW, Markowitz K, Diamond G (2010) Activity of antimicrobial peptide mimetics in the oral cavity: I. Activity against biofilms of *Candida albicans*. *Mol Oral Microbiol* 25(6):418–425
86. Karlsson AJ, Pomerantz WC, Weisblum B, Gellman SH, Palecek SP (2006) Antifungal activity from 14-helical beta-peptides. *J Am Chem Soc* 128(39):12630–12631
87. Karlsson AJ, Pomerantz WC, Neilsen KJ, Gellman SH, Palecek SP (2009) Effect of sequence and structural properties on 14-helical beta-peptide activity against *Candida albicans* planktonic cells and biofilms. *ACS Chem Bio* 4(7):567–579
88. Karlsson AJ, Flessner RM, Gellman SH, Lynn DM, Palecek SP (2010) Polyelectrolyte multilayers fabricated from antifungal beta-peptides: design of surfaces that exhibit antifungal activity against *Candida albicans*. *Biomacromolecules* 11(9):2321–2328
89. Tew GN, Scott RW, Klein ML, Degrado WF (2010) De novo design of antimicrobial polymers, foldamers, and small molecules: from discovery to practical applications. *Acc Chem Res* 43(1):30–39
90. Niu Y, Padhee S, Wu H, Bai G, Harrington L, Burda WN, Shaw LN, Cao C, Cai J (2011) Identification of gamma-AApeptides with potent and broad-spectrum antimicrobial activity. *Chem Commun* 47(44):12197–12199
91. Schmitt MA, Weisblum B, Gellman SH (2007) Interplay among folding, sequence, and lipophilicity in the antibacterial and hemolytic activities of alpha/beta-peptides. *J Am Chem Soc* 129(2):417–428
92. Mowery BP, Lee SE, Kissounko DA, Epand RF, Epand RM, Weisblum B, Stahl SS, Gellman SH (2007) Mimicry of antimicrobial host-defense peptides by random copolymers. *J Am Chem Soc* 129(50):15474–15476
93. Yang YA, Niu YH, Hong H, Wu HF, Zhang Y, Engle JW, Barnhart TE, Cai JF, Cai WB (2012) Radiolabeled gamma-AApeptides: a new class of tracers for positron emission tomography. *Chem Commun* 48(63):7850–7852
94. Hu Y, Amin MN, Padhee S, Wang R, Qiao Q, Ge B, Li Y, Mathew A, Cao C, Cai J (2012) Lipidated peptidomimetics with improved antimicrobial activity. *ACS Med Chem Lett* 3(8):683–686
95. Makovitzki A, Avrahami D, Shai Y (2006) Ultrashort antibacterial and antifungal lipopeptides. *Pro Natl Acad Sci* 103(43):15997–16002
96. Makovitzki A, Baram J, Shai Y (2008) Antimicrobial lipopolypeptides composed of palmitoyl di- and tricationic peptides: in vitro and in vivo activities, self-assembly to nanostructures, and a plausible mode of action. *Biochemistry* 47(40):10630–10636
97. Weis F, Beiras-Fernandez A, Schelling G (2008) Daptomycin, a lipopeptide antibiotic in clinical practice. *Curr Opin Investig Drugs* 9(8):879–884
98. Zavascki AP, Goldani LZ, Li J, Nation RL (2007) Polymyxin B for the treatment of multidrug-resistant pathogens: a critical review. *J Antimicrob Chemother* 60(6):1206–1215
99. Morris MI, Villmann M (2006) Echinocandins in the management of invasive fungal infections, part 1. *Am J Health Syst Pharm* 63(18):1693–1703
100. Chongsirawatana NP, Miller TM, Wetzler M, Vakulenko S, Karlsson AJ, Palecek SP, Mobashery S, Barron AE (2010) Short alkylated peptoid mimics of antimicrobial lipopeptides. *Antimicrob Agents Chemother*
101. Wu H, Niu Y, Padhee S, Wang RE, Li Y, Qiao Q, Ge B, Cao C, Cai J (2012) Design and synthesis of unprecedented cyclic gamma-AApeptides for antimicrobial development. *Chem Sci* 3:2570–2575
102. Kussie PH, Gorina S, Marechal V, Elenbaas B, Moreau J, Levine AJ, Pavletich NP (1996) Structure of the MDM2 oncoprotein bound to the p53 tumor suppressor transactivation domain. *Science* 274(5289):948–953 (New York)
103. Momand J, Zambetti GP, Olson DC, George D, Levine AJ (1992) The mdm-2 oncogene product forms a complex with the p53 protein and inhibits p53-mediated transactivation. *Cell* 69(7):1237–1245
104. Oliner JD, Kinzler KW, Meltzer PS, George DL, Vogelstein B (1992) Amplification of a gene encoding a p53-associated protein in human sarcomas. *Nature* 358(6381):80–83

105. Zhao J, Wang M, Chen J, Luo A, Wang X, Wu M, Yin D, Liu Z (2002) The initial evaluation of non-peptidic small-molecule HDM2 inhibitors based on p53-HDM2 complex structure. *Cancer Lett* 183(1):69–77
106. Vassilev LT, Vu BT, Graves B, Carvajal D, Podlaski F, Filipovic Z, Kong N, Kammlott U, Lukacs C, Klein C, Fotouhi N, Liu EA (2004) In vivo activation of the p53 pathway by small-molecule antagonists of MDM2. *Science* 303(5659):844–848 New York
107. Galatin PS, Abraham DJ (2004) A nonpeptidic sulfonamide inhibits the p53-mdm2 interaction and activates p53-dependent transcription in mdm2-overexpressing cells. *J Med Chem* 47(17):4163–4165
108. Grasberger BL, Lu T, Schubert C, Parks DJ, Carver TE, Koblisch HK, Cummings MD, LaFrance LV, Milkiewicz KL, Calvo RR, Maguire D, Lattanze J, Franks CF, Zhao S, Ramachandren K, Bylebyl GR, Zhang M, Manthey CL, Petrella EC, Pantoliano MW, Deckman IC, Spurlino JC, Maroney AC, Tomczuk BE, Molloy CJ, Bone RF (2005) Discovery and cocrystal structure of benzodiazepinedione HDM2 antagonists that activate p53 in cells. *J Med Chem* 48(4):909–912
109. Sakurai K, Chung HS, Kahne D (2004) Use of a retroinverso p53 peptide as an inhibitor of MDM2. *J Am Chem Soc* 126(50):16288–16289
110. Alluri PG, Reddy MM, Bachhawat-Sikder K, Olivos HJ, Kodadek T (2003) Isolation of protein ligands from large peptoid libraries. *J Am Chem Soc* 125(46):13995–14004
111. Hara T, Durell SR, Myers MC, Appella DH (2006) Probing the structural requirements of peptoids that inhibit HDM2-p53 interactions. *J Am Chem Soc* 128(6):1995–2004
112. Kritzer JA, Zutshi R, Cheah M, Ran FA, Webman R, Wongjirad TM, Schepartz A (2006) Miniature protein inhibitors of the p53-hDM2 interaction. *ChemBioChem* 7(1):29–31
113. Kritzer JA, Hodsdon ME, Schepartz A (2005) Solution structure of a beta-peptide ligand for hDM2. *J Am Chem Soc* 127(12):4118–4119
114. Kritzer JA, Lear JD, Hodsdon ME, Schepartz A (2004) Helical beta-peptide inhibitors of the p53-hDM2 interaction. *J Am Chem Soc* 126(31):9468–9469
115. Murray JK, Farooqi B, Sadowsky JD, Scalf M, Freund WA, Smith LM, Chen J, Gellman SH (2005) Efficient synthesis of a beta-peptide combinatorial library with microwave irradiation. *J Am Chem Soc* 127(38):13271–13280
116. Cai W, Chen X (2006) Anti-angiogenic cancer therapy based on integrin $\alpha_v\beta_3$ antagonism. *Anti-Cancer Agents Med Chem* 6:407–428
117. Cai W, Niu G, Chen X (2008) Imaging of integrins as biomarkers for tumor angiogenesis. *Curr Pharm Des* 14:2943–2973